Published by
Sri Lankan Geotechnical Society

C/o National Building Research Organisation,
No.99/1, Jawatta Road,
Colombo 05,
Sri Lanka.
www.slgs.lk

ICGE-Colombo-2020 International Conference on Geotechnical Engineering

ICGE Colombo - 2020
International Conference on Geotechnical Engineering

Proceedings of the International Conference on Geotechnical Engineering ICGE-Colombo-2020

Geotechnics in a Challenging Environment

06th & 07th December 2021
executed from
Cinnamon Grand Hotel
Colombo

International Conference on Geotechnical Engineering

ICGE Colombo 2020

Geotechnics in a challenging Environment

Organized by Sri Lankan Geotechnical Society

Executed from Cinnamon Grand Hotel, Colombo, Sri Lanka

6 – 7 December 2021

Preface

ICGEColombo2020 - the third International Conference organized by the Sri Lankan Geotechnical Society (SLGS) was to be held in August 2020. The event was postponed due to Covid-19 pandemic and finally held as a virtual conference on 6-7 December 2021 considering the restrains still prevail. The conference is fully recognized by the International Society for Soil Mechanics and Geotechnical Engineering (ISSMGE).

The conference is held under the theme "Geotechnics in a Challenging Environment" with five keynote lectures and around 100 peer reviewed papers. We are very thankful to the keynote lecturers and all the authors for maintaining their interest and being with us over the last year.

The keynote addresses will cover the current state-of-the-art in the key areas of;

- Unsaturated Soil Mechanics and Bioengineered Soil Slopes with a Focus on Hydrological Effects by Prof Charles W W Ng (Hong Kong University of Science and Technology)
- Ground Improvement for Rail and Road Infrastructure by Distinguished Prof Buddhima Indraratna **(**University of Technology Sydney)
- Lessons Learned from Failures of Embedded Retaining walls by Dr Brian Simpson**,** Arup Fellow Principal of Arup Geotechnics and Honorary Professor at the University of Nottingham, UK
- Foundation Investigation, Analysis and Design for High Rise Buildings by Dr**.** Chris Harberfield Principal, Golder Associates, Australia.
- Modeling Coupled Dynamic Processes in Landfills: Holistic Long-Term Performance Management to Improve Sustainability byProfessor Krishna Reddy, University of Illinois at Chicago

Sri Lankan Geotechnical Engineers have made enormous contributions to the advancement of the field all over the globe. Contributions made by Prof. A Thurairajah who is considered as the father of Soil Mechanics in Sri Lanka in the development of critical state soil mechanics is widely acknowledged by all. Since then many geotechnical engineers who had their initial training in Sri Lanka have excelled in the field as academics researchers and practitioners in the developed part of the world. It is very pleasing to note that a number of them have contributed generously to this conference.

The organizing committee made all possible attempts to encourage young geotechnical engineers from Sri Lanka to publish in the conference. This will give them much needed encouragement to be involved in research and practice in the field with a keen analytical mind. We are very happy to note a significant increase in the number of papers submitted by young Sri Lankan Geotechnical Engineers formulating research projects of great practical value through infrastructure development projects.

We have nominated two young Geotechnical Engineers as Bright Spark lecturers in the conference.

We are hopeful that conference will be a turning point in the field of geotechnical engineering with new encouragement for development of innovative techniques and well directed research to address geotechnical engineering challenges faced by the country.

The papers submitted for the conference went through a thorough review process and all the authors, reviewers and members of the editorial panel should be congratulated for their untiring efforts. The efforts of the five keynote lecturers are also gratefully acknowledged.

Prof Athula Kulathilaka

Eng K L S Sahabandu

Conference Co-Chairs

Editors

Dr Ashani Ranathunga
Dr Asiri Karunawardena
Prof Athula Kulathilaka
Dr Chandana Kurukulasuriya
Dr K H S M Sampath
Dr MCM Nasvi
Dr Nalin De Silva
Dr. Mohamed Nasvi
Dr Nayana Alagiyawanna
Dr NH Priyankara
Dr Prasanna Rathnaweera
Prof Saman Thilakasiri
Dr SK Navaratnarajah
Prof Udeni Nawagamuwa

Reviewers

Dr. Anjula Dassanayake
Dr (Ms) Anuruddhika Jayasinghe
Prof. Anurudhdha Puswewala
Prof Apiniti Jotisankasa
Prof Arul Arulraj
Dr. Ashani Ranathunga
Dr. Asitha Senanayake
Prof. Athula Kulathilaka
Dr. A M K B Abeysinghe
Dr Biyanvilage Dareeju
Dr. Chaminda Gallage
Dr. Chandana Kurukulasuriya
Dr Chiaro Gabriele
Dr (Ms) Dhanya Ganesalingam
Prof. Dharma Wijewickreme
Prof Leong Eng Choon
Dr G Jayathissa
Dr. Harshani Handapangoda
Dr G V I Samaradivakara
Dr. J S M Fowze
Dr. Jay Ameratunga
Prof. Jayantha Kodikara
Dr. K H S M Sampath
Eng. Kirthi Sri Senanayake
Prof M R Madhav
Dr. Muditha Pallewattha
Dr. Nadeej Hansaraj Priyankara
Dr. Nalin De Silva
Dr Nilan Weerakoon
Prof Nimal Rajapakse
Dr (Ms) Nirmali Amarakoon
Dr Prasanna Ratnaweera
Dr (Ms) R A Dilrukshi
Prof. Saman Thilakasiri
Dr (Ms) Samanthi Indiketiya
Dr. (Ms) Samintha Perera
Dr. (Ms) Sanduni Gunaratne
Dr. Sinniah Navaratnarajah
Dr Sothilingam Premkumar
Dr Stanislav Lenart
Dr Takashi Kiyota
Dr (Ms) Thiloththama Nawarathna
Prof Thomas Oommen
Dr Thushara Madanayaka
Prof. Udeni Nawagamuwa
Dr V Sujeevan
Prof. Wasantha Mampearachchi

Advisory Committee

Prof Charles W Ng - President - ISSMGE Hong Kong University of Science and Technology
Prof AS Balasubramaniam - Emeritus Professor, Griffith University, Australia
Prof MR Madhav - Former Vice President Asia – ISSMGE
Prof Ikuo Towhata - Former Vice President Asia - ISSMGE
Dr Gamini Adikari - Chief Technical Principal, Dam Safety, SMEC, Australia
Dr Jayantha Ameratunga - Principal Engineer, Golder Associates, Australia
Dr Upul Athukorala - Principal Engineer, Golder Associates, Canada
Emeritus Prof Dennes T Bergado - Asian Institute of Technology, Thailand
Dr RK Bhandari - Geotechnical Consultant, India
Dr Rajinder Kumar Bhasin - Norwegian Geotechnical Institute, Norway
Prof Jin Chun Chai - Saga University, Japan
Prof Leong Eng Choon - Nanyang Technological University, Singapore
Dr Suraj De Silva - Consultant, Mott MacDonald, Hong Kong
Prof Ranjith Pathegama Gamage - Monash University, Australia
Prof Manjriker Gunaratne - University of South Florida, USA
Prof Hemanta Hazarika - Kyushu University, Japan
Prof An-Bin Huang - National Chiao Tung University, Taiwan
Prof Buddhima Indraratna - University of Technology Sydney, Australia
Prof Priyantha Jayawickrama - Texas Tech University, USA
Assoc Prof Apiniti Jotisankassa - Kasetsart University, Thailand
Prof Jayantha Kodikara - Monash University, Australia
Assoc Prof Diyuan Li - Central South University, Changsha, China
Prof Jianchun Li - South East University, Nanjing, China
Assoc Prof S Liyanapathirana - University of Western, Sydney, Australia
Prof Jay N. Meegoda - New Jersey Institute of Technology, USA
Prof KK Muraleetharan - University of Oklahoma, USA
Assoc Prof Thomas Oommen - Michigan Technological University, USA
Assoc Prof Noppadol Phien-wej - Asian Institute of Technology, Thailand
Emeritus Prof Harry G Poulos - Coffey Services, Australia
Prof Harianto Rahardjo - Nanyang Technological University, Singapore

Prof Nimal Rajapakse	- Simon Fraser University, Canada
Prof Krishna R Reddy	- University of Illinois at Chicago, USA
Prof Kyoji Sassa	- Executive Director, International Consortium on Landslides
Prof APS Selvadurai	- McGill University, Canada
Prof Nimal Seneviratne	- University of Peradeniya, Sri Lanka
Prof Hema Siriwardane	- West Virginia University, USA
Assoc Prof Siva Sivakugan	- James Cook University, Australia
Assoc Prof Suttisak Soralump	- Kasetsart University, Thailand
Prof Fumio Tatsuoka	- Tokyo University, Japan
Emeritus Prof BL Tennakoon	- University of Moratuwa, Sri Lanka
Prof Dharma Wijewickreme	- University of British Columbia, Canada
Prof Sheng-Qi Yang	- China University of Mining Technology, China

Organizing Committee

Co – Chairs

Prof Athula Kulathilaka

Eng K L S Sahabandu

Conference Secretaries

Dr JSM Fowze

Prof Udeni Nawagamuwa

Treasurer

Eng WAAW Bandara

Members

Dr Nayana Alagiyawanna

Dr Nalin De Silva

Dr Asiri Karunawardena

Dr Chandana Kurukulasuriya

Dr Kamal Laksiri

Dr MCM Nasvi

Dr SK Navaratnarajah

Dr NH Priyankara

Dr Ashani Ranathunga

Dr K H S M Sampath

Eng Mahinda Rathnasiri

Dr Prasanna Rathnaweera

Eng Kirthi Sri Senanayake

Prof Saman Thilakasiri

CONTENTS

Keynote Lectures

Transportation Geotechnics

Site Investigation

Foundations, Geosynthetics and Case Histories

Environmental Geotechnics

Ground Improvement

Landslides and slope stability

Analytical and Numerical Modelling

Unsaturated Soil Mechanics and Bioengineered Soil Slopes with a Focus on Hydrological Effects

C. W. W. Ng & J. J. Ni
Department of Civil and Environmental Engineering, Hong Kong University of Science and Technology (HKUST), Hong Kong SAR, China

C. Zhou
Department of Civil and Environmental Engineering, Hong Kong Polytechnic University, Hong Kong SAR, China

ABSTRACT: The negative impact of climate change calls for additional sustainable and environmentally friendly techniques to be developed to improve the engineering performance of slopes. Bioengineering using vegetation can be considered as a low-cost, aesthetically pleasant solution for improving the stability of shallow slopes. The mechanical effects of vegetation for soil reinforcement have been extensively studied, but the hydrological effects of vegetation on soil shear strength and water permeability are unclear. This study presents an interdisciplinary research programme consisting of laboratory, centrifuge modelling and analytical solutions to explore both the hydrological and mechanical effects of plants on slope stability. It is revealed that certain plant species native to southern China and Europe could preserve a credible amount of soil matric suction after heavy rainfall, which is positively correlated with the leaf area index, the root area index and the ratio of root to shoot biomass. Plant-fungus interaction causes a significant increase in root tensile strength, and thus could potentially enhance the mechanical reinforcement of soil. Novel artificial root systems are developed for the geotechnical centrifuge model tests. Heart-shaped roots have stronger pull-out resistance and higher preserved matric suction (hence higher soil shear strength and lower water permeability) than tap- or plate-shaped roots. The heart-shaped root architecture is thus the most effective for improving the stability of slopes.

1. INTRODUCTION

The desire of the public to create and live in a sustainable world has gradually motivated governments and engineers to rediscover vegetation as an engineering material. Bioengineering using vegetation can potentially offer an environmentally friendly, cost-effective and aesthetically pleasant solution for improving the stability of shallow slopes. Although vegetation has been used in slope protection for decades, its purpose has mainly been aesthetic (Coppin and Richards, 1990), likely because the mechanisms of soil–plant–atmosphere interaction are not fully understood. Thus, the current design practice does not scientifically integrate the engineering function of plant roots into the analysis and design of slopes.

It is well known that plant roots can reinforce slopes mechanically (Wu et al., 1979; Stokes et al., 2009). The mechanical effects of roots have been extensively quantified experimentally and theoretically in the past decades (Wu et al., 1979; Pollen and Simon, 2005; Boldrin et al., 2017). By contrast, the hydrological effects of plants have received insufficient attention (Ng, 2017; Ng et al., 2019a). These hydrological effects refer to the increase in soil shear strength and the decrease in water permeability when soil suction is enhanced by vegetation (Ng et al., 2019a). The key to using plants for these purposes is to first understand the fundamentals of unsaturated soil mechanics and soil–plant–atmosphere interactions, which are interdisciplinary subjects involving atmospheric science, soil science, botany, and ecological and geotechnical engineering.

In this keynote, an integrated research approach is introduced to investigate plant hydro−mechanical effects on the stabilisation of shallow soil slopes. First, the fundamentals of unsaturated soil mechanics are reviewed. Second, a series of indoor experiments are reported to quantify the magnitude and distribution of transpiration-induced soil matric suction. Correlations between induced soil matric suction and plant traits are described and discussed. Moreover, how microorganisms (fungi) affect root tensile strength and the mechanical reinforcement of soil is also explored. Third, novel artificial model root systems developed for geotechnical centrifuge tests are introduced. These model root systems can facilitate the study of the combined mechanical and hydrological effects of different root architectures on hydrology, slope stability and failure mechanisms. The influence of root architectures on slope

deformation and failure mechanism can then be identified. More details of the laboratory and centrifuge model tests and findings can be found in Ng et al. (2019a). Finally, analytical solutions are derived to calculate the hydro-mechanical effects of different root architectures on the stability of infinite vegetated soil slopes. Note that some parts of this keynote are verbatim extracts from Ng et al. (2018) and Ng et al. (2019b).

2 FUNDAMENTALS OF UNSATURATED SOIL MECHANICS

All slopes above the ground surface are unsaturated. Saturated soil (i.e., degree of saturation equals to 100%) is just an extreme case of an unsaturated soil. Thus, it is vitally important to understand unsaturated soil behaviour for the stability analysis of soil slopes. In this keynote, relevant theories of unsaturated soil mechanics for slope stability calculations with and without vegetation are briefly introduced and highlighted.

2.1 *Elastoplastic modelling and shear strength*

Many elastoplastic models have been developed for unsaturated soil based on the critical state framework (e.g., Alonso et al., 1990; Wheeler and Sivakumar, 1995; Wheeler et al., 2003; Gens, 2010; Sheng, 2011; D'Onza et al., 2011). Alonso et al. (1990) presented, perhaps, one of the first elastoplastic models for unsaturated soils. This model is also called the Barcelona basic model (BBM) and adopts the Modified Cam Clay model (MCCM) as the reference model at the saturated state. The constitutive variables employed in the model are the mean net stress, p (the difference between mean total stress and pore air pressure), deviator stress, q (the difference between major and minor principal stresses), matric suction, s (the difference between pore air pressure and pore water pressure), and specific volume, v. In the BBM, the relationship between preconsolidation pressure p_0 (or yield stress) and suction is referred to as the loading-collapse (LC) curve. In the three-dimensional p-q-s space, the yield surface consists of a series of ellipses. The size of the ellipse increases with an increase in suction. At a given net stress and density condition, the over-consolidation ratio (OCR) is larger when soil suction is higher. Hence, plant-induced matric suction would increase the OCR of unsaturated soil.

The BBM does not explicitly consider the influence of the degree of saturation, S_r, on the mechanical behaviour of unsaturated soil. Due to the hydraulic hysteresis in the water retention curve during drying and wetting (explained later in detail), two specimens of the same soil at the same suction can have different values of S_r. The influence of S_r is significant, as pointed out by Wheeler et al. (2003). One of the pioneer models that fully couples hydraulic hysteresis and mechanical behaviour of unsaturated soil was presented by Wheeler et al. (2003). The model was developed using Bishop's stress (σ*) and modified suction (s*) rather than net stress and matric suction.

$$\begin{cases} \sigma^* = \sigma_{ij}^t - u_a + S_r(u_a - u_w) \\ s^* = ns \end{cases} \quad (1)$$

where n is the porosity; σ_{ij}^t is the total stress; u_a and u_w are the pore–air pressure and pore–water pressure, respectively. According to Eq. (1), the values of σ* and s* are affected by S_r and n, respectively. Hence, this set of constitutive variables partially describe the coupling effects between mechanical and hydraulic behaviour.

Three yield surfaces (i.e., LC, SI (suction increase) and SD (suction decrease)) are introduced in Wheeler et al. (2003) model. In the p*-s* plane, where p* is the mean Bishop's stress, LC curve is a vertical straight line, while SI and SD form horizontal and straight lines. LC, SI and SD are used to model yielding during compression, drying and wetting, respectively. With defined constitutive variables and hardening laws of yield surfaces, the model is able to describe the influence of hydraulic hysteresis on the mechanical behaviour of unsaturated soil. Effects of soil deformation on water retention behaviour are also captured. It should be noted that this model is only suitable for non-expansive and slightly expansive soils, because the associated flow rule is used for the SD surface. For expansive soil, large volumetric strain is normally observed during the wetting process.

More advanced theories, such as the effects of state-dependent dilatancy on the peak shear strength of unsaturated soil, have been proposed (Chiu and Ng, 2003; Alonso et al., 2007; Ng and Menzies, 2007; Sheng, 2011; Lloret-Cabot et al., 2017). Chiu and Ng (2003) firstly proposed a state-dependent elastoplastic model for unsaturated soil. The model illustrates that the dilatancy of unsaturated soil during shearing depends on void ratio, stress and also suction level:

$$\frac{d\varepsilon_v^p}{d\varepsilon_q^p} = d(s)\left[\exp\left(m\left(e - e_c(s,p)\right)\right) - \frac{q/p}{M}\right] \quad (2)$$

where $d\varepsilon_v^p$ and $d\varepsilon_q^p$ are increments in plastic volumetric and shear strains, respectively, and positive and negative values represent contraction and dilation, respectively; $d(s)$ is the reference amount of dilation which depends on the micro-structure of soil; m is model parameter; e and $e_c(s,p)$ are current and critical state void ratios, respectively; and M is the

stress ratio (q/p) at the critical state. Suction-induced aggregation in fines has two effects on soil dilatancy. First, suction can enhance the interlocking between soil aggregates (i.e., an increase in $d(s)$). Second, it increases the void ratio at critical state $e_c(s,p)$ (Ng and Chiu, 2001). This is mainly because unsaturated soil has a more resistant fabric than saturated soil. At a given e, the value of (e- $e_c(s,p)$), which is defined by Been and Jefferies (1985) as state parameter ψ, is therefore smaller. Consequently, an increase in suction would induce higher dilatancy attributed to a larger d(s) and a smaller ψ. Chiu and Ng (2003) have demonstrated Eq. (2) is able to capture shearing-induced volume changes of unsaturated soil with different suctions, initial densities and confining pressures. For modelling effects of vegetation, plant-induced matric suction would increase the dilatancy and hence peak shear strength of unsaturated soil, as revealed by Eq. (2) (Ng et al., 2019a).

For simplicity, the shear strength of unsaturated soil at failure, τ_f, may be expressed in terms of net stress, water content and matric suction as follows (Vanapalli et al., 1996):

$$\tau_f = c' + (\sigma_n^t - u_a)\tan\phi' + (u_a - u_w)\left[(\tan\phi')\left(\frac{\theta-\theta_r}{\theta_s-\theta_r}\right)\right] \quad (3)$$

where c' is the effective cohesion; σ_n^t is the total normal stress; ϕ' is the effective friction angle; θ is the volumetric water content; θ_s is the saturated volumetric water content; and θ_r is the residual volumetric water content. According to Eq. (3), plant-induced matric suction would increase soil shear strength. More details are given by Ng et al., (2019a).

2.2 *Soil water retention and water permeability function*

In order to carry out transient seepage analysis in unsaturated soil slopes, a water retention curve (WRC) is needed. A WRC defines the relationship between water content (or degree of saturation) and suction. A typical WRC is usually described by the following parameters: air-entry value (AEV), desorption rate, adsorption rate, residual water content, and the size of the hysteresis loop between the drying and wetting curves.

Essentially based on agricultural and soil sciences, many researchers have previously found that the water retention ability of an unsaturated soil is dependent on many factors, including soil type, soil density, drying and wetting history and soil water content during compaction (Fredlund and Rahardjo, 1993), not until Ng and Pang (2000), who developed a new stress-controllable pressure plate apparatus and they observed that the water retention ability of unsaturated soil is strongly affected by net stress. Fig. 1 shows the influence of net stress on the water retention behaviour of CDV (completely decomposed volcanic or clayey silt). It is clear that the water retention ability of the soil specimen increases with net stress. Stress effects on WRC can be partially explained by its dependence on density. When stress increases, so will the density and hence the water retention ability. However, a change in net stress not only affects the density, but more importantly, it alters pore size distribution as well as pore orientation and increases the proportion of micro-pores, thereby enhancing the water retention ability of an unsaturated soil (Zhou and Ng, 2014; Cheng et al., 2019). This was also revealed by Delage and Lefebvre (1984) using a scanning electron microscope. Through one-dimensional consolidation tests on saturated clay, Delage and Lefebvre (1984) found that platy clay particles and soil pores show preferential orientations during the loading process. Another important feature in Fig. 1 is that there is marked hysteresis between the drying and wetting curves at all levels of stress. At a given suction, the equilibrium degree of saturation along the wetting curve is much smaller than that along the drying curve. This phenomenon is referred as "hydraulic hysteresis". The hysteresis loop size decreases with increasing net stress. Based on the above observations, Ng and Pang (2000) introduced the concept of stress-dependent WRC (SDWRC). Moreover, they carried out finite element analysis and illustrated that the factor of safety (FOS) of a soil slope can be overestimated (i.e., on the non-conservative side) if the effects of net stress on WRC are not considered.

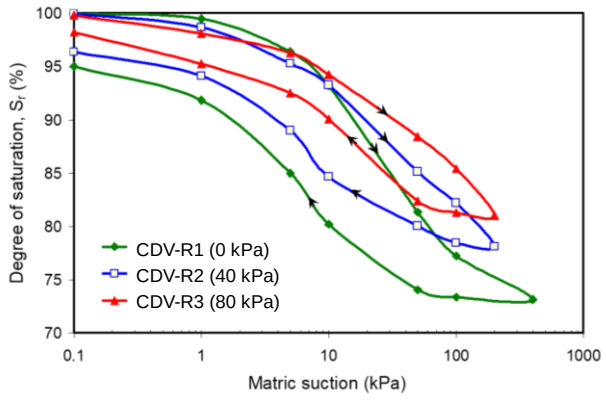

Fig. 1 Stress effects on the water retention curves of compacted unsaturated soil (Ng and Pang, 2000)

Apart from WRC, a water permeability function is the other important hydraulic property for transient seepage analysis of unsaturated soil slopes. Unlike water permeability in saturated soils, that in unsaturated soils not only depends on the void ratio but

is also governed by the degree of saturation or water content. By assuming soil is rigid, for simplicity, a relationship between water permeability and matric suction may be expressed as follows (Fredlund et al., 1994):

$$k(s) = k_s \left[\frac{\int_{ln(s)}^{b} \frac{\theta(e^y) - e(s)}{e^y} \theta'(e^y) dy}{\int_{ln(s_{aev})}^{b} \frac{\theta(e^y) - \theta_s}{e^y} \theta'(e^y) dy} \right] \quad (4)$$

where $b = \ln(10^6)$; k_s is the saturated water permeability; y is a dummy variable for the integration of s; s_{aev} is the air entry value and θ' is the first derivative of function θ. As shown in Fig. 2, water permeability generally reduces with increasing matric suction. This is because pore air is not conductive to liquid water in unsaturated soils. An increase in suction (i.e., a reduction in water content) will lead to a decrease in water permeability. Eqs. (3) and (4) clearly reveal that plant-induced suction not only can increase soil shear strength but also reduces water permeability, thereby decreasing rainfall infiltration into soil slopes and hence helping preserve soil suction in unsaturated soil slopes. The understanding of the hydrological effects of root–water uptake has been greatly improved in the recent years (e.g., Indraratna et al., 2006; Fatahi et al., 2010, 2014; Ng et al., 2013, 2014a, 2016a, 2019a 2020; Ni et al., 2017, 2018, 2019a, b; Ng, 2017).

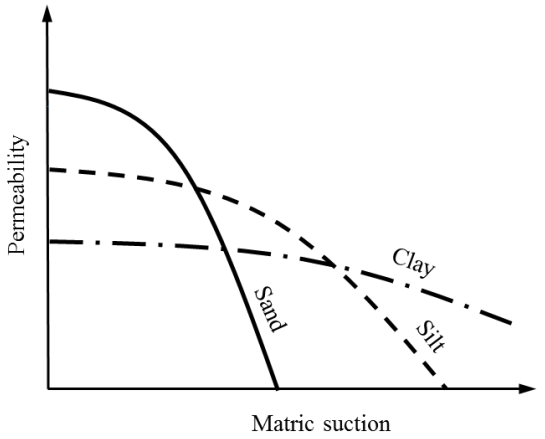

Fig. 2 Schematic relationships between water permeability and suction of three typical types of soils

3 HYDROLOGICAL EFFECTS OF PLANT-INDUCED MATRIC SUCTION

3.1 *Effects of evapotranspiration on suction distribution*

To quantify the effects of evapotranspiration (ET; the sum of soil evaporation and plant transpiration) on matric suction in unsaturated silty sand (see Ng et al. (2016a) for basic soil index properties), a test programme was implemented in a plant room at the Hong Kong University of Science and Technology (HKUST). The room has an air conditioning system, which allows for flexible control of the air temperature from 10°C to 30°C ± 1°C and the air relative humidity (RH) from 40% to 70% ± 5%. A tree species *Schefflera heptaphylla* that is native to southern China including Hong Kong (Ng et al., 2016a) was selected. Compacted soil was planted with multiple tree individuals at a spacing of 120 mm. Three replicates were tested.

Fig. 3 shows the test results comparing the distributions of suction with depth in bare and vegetated soils. Before rainfall, the vegetated soil samples (test T) induced much higher matric suction than the bare sample (test B), both within and below the root zone. After 2 h of rainfall with a constant intensity of 73 mm/h (equivalent to a return period of 10 years in Hong Kong; Lam and Leung, 1995), suction was slightly reduced in the bare soil at depths below 150 mm but greatly reduced at depths above 150 mm. Although suction at the shallow depths of the vegetated samples decreased by up to 60% after the intense rainfall, suction at depths below 250 mm remained largely unchanged due to root water uptake before the rainfall. It can be concluded that suction in vegetated soils was consistently higher than that in the bare soil both before and after the simulated rainfall events.

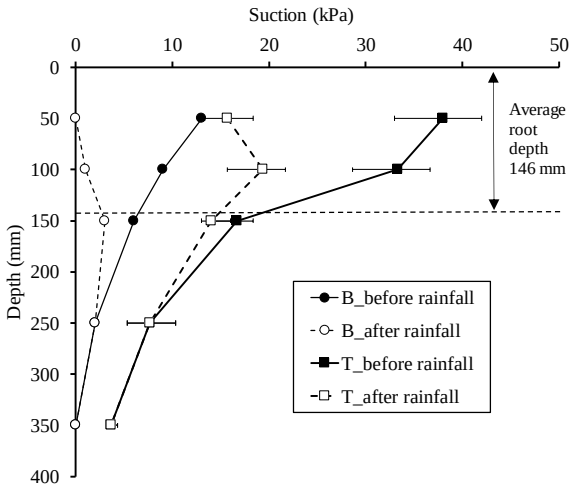

Fig. 3 Distributions of suction with depth before and after intense rainfall

3.2 *Correlation between suction and plant traits*

Fig. 4 shows the correlations between suction induced by *Schefflera heptaphylla* in the root zone and LAI, which is a plant trait defined as the total projected area of leaves per unit soil surface area. The measurement methods of LAI can be found in Ng et al. (2016b). To highlight the effects of tree transpiration, the suction difference Δs between vegetated and bare soils is used in interpretation of test results.

It can be seen from the figure that Δs has a strong linear correlation with LAI (R^2 = 0.91). This is because a tree with a higher LAI would intercept a greater amount of radiant energy, meaning that more stomata are available to absorb energy for transpiration (Kelliher et al., 1995). Thus engineers can predict soil suction simply by measuring the LAI of a plant only, using an unmanned aerial vehicle for example.

Another plant trait that is relevant to root water uptake is RAI, which is defined as the ratio of total root surface area for a given depth range to the circular cross-sectional area of soil in the horizontal plane (Francour and Semroud, 1992). RAI is also a dimensionless number that indicates the water uptake ability of roots. The measurement methods of RAI can be found in Garg et al. (2015). Fig. 5 shows the correlations between Δs and RAI. As expected, for a given RAI, Δs measured after ponding is always lower than that after ET because of infiltration. Δs recorded after either ET or ponding is strongly correlated with RAI (R^2 = 0.96).

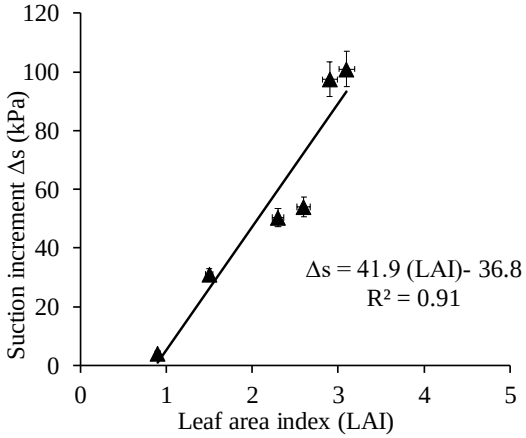

Fig. 4 Relationship between suction increment and LAI after drying for 2 days (Ng et al., 2016b)

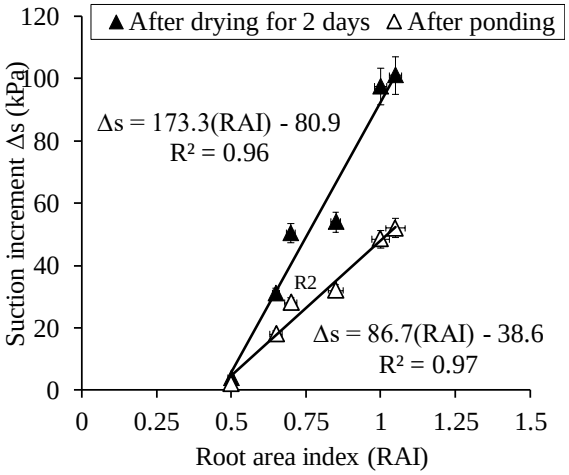

Fig. 5 Relationship between suction and RAI before and after ponding (Ng et al., 2016b)

Boldrin et al. (2017) reported that root water uptake is not correlated with either the above-ground trait or the below-ground trait alone, but with both traits. They investigated the ability of 10 woody shrub species native to Europe to induce matric suction. These species were *Buxus sempervirens* (Bs), *Corylus avellana* (Ca), *Crataegus monogyna* (Cm), *Cytisus scoparius* (Cs), *Euonymus europaeus* (Ee), *Ilex aquifolium* (Ia), *Ligustrum vulgare* (Lv), *Prunus spinosa* (Ps), *Salix viminalis* (Sv) and *Ulex europaeus* (Ue). They defined a new trait, namely the root-to-shoot ratio, which is the ratio of root biomass to shoot biomass. Among the traits examined, this new one has the strongest correlation with induced suction (Fig. 6) for all species except Cs and Ue, which have photosynthetic organs, twigs and thorns that are distinctively different from those of the other eight species.

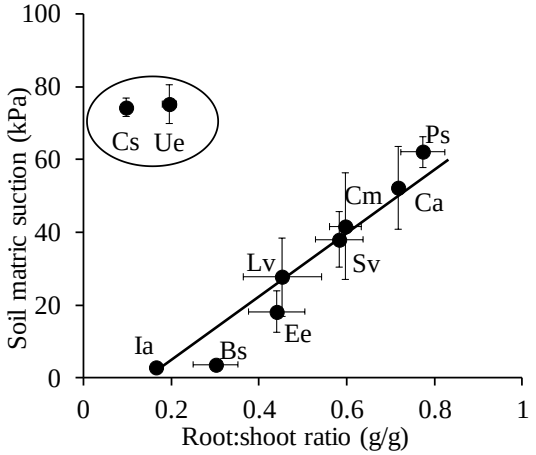

Fig. 6 Relationship between root-to-shoot ratio and matric suction in planted pots. Data are presented as mean (n = 3) ± standard error for 10 species. (Boldrin et al., 2017)

4 EFFECTS OF FUNGI ON ROOT TENSILE STRENGTH

In addition to the hydrological effects of plants discussed above, the mechanical effects of plant roots can also enhance slope stability. The contribution of mechanical root reinforcement primarily depends on root tensile strength. Although root biomechanical properties have been investigated over the past several decades (Wu et al., 1979; Pollen and Simon, 2005; Boldrin et al. 2017), few studies have focused on the effects of microorganisms on any biological change of root tissues or their biomechanical properties. Arbuscular mycorrhizal fungi (AMF) are one of the most important microorganisms that have been associated with plants since 400 million years ago (Smith and Read, 2008). A test programme was designed and implemented at the HKUST to inves-

tigate the effects of various fungi (*Rhizophagus intraradices (Ri), Funneliformis mosseae (Fm) and Glomus aggregatum (Ga)*) on root growth and biomechanical property of vetiver grass (*Chrysopogon zizanioides*). Sterilised inoculum (autoclaved, 121°C for 2 h) was also added to another five empty pots as control (non-mycorrhizal, NM).

Fig. 7 shows the effects of AMF treatment on root tensile strength in different root diameter ranges (Chen et al., 2018). For the stele diameter ranges of 0.1-0.2 and 0.2-0.3 mm, all AMF treatments significantly increased the tensile strength (p-value < 0.05). For the diameter range of 0.3-0.4 mm, only the Ri treatment increased the tensile strength. For the diameter ranges of 0.4-0.5 and 0.5-1.0 mm, both the Ri and Fm treatments enhanced the tensile strength, but not the Ga treatment. These results indicate that the AMF treatments could generally enhance the stele tensile strength, especially the tensile strength of fine stele (0.1-0.3 mm). This is because AMF can easily colonise fine roots, but not coarse roots (Wu et al., 2016), and exert local effects in the colonised cortical cells (Fiorilli et al., 2009). The fungal structures were only found in fine roots in this study. The samples treated with AMF had higher percentages of cellulose and hemicellulose contents than the control samples (Chen et al., 2018). The proportions of lipid and hydrosoluble contents were reduced, and this was compensated only by cellulose and hemicellulose, but not lignin.

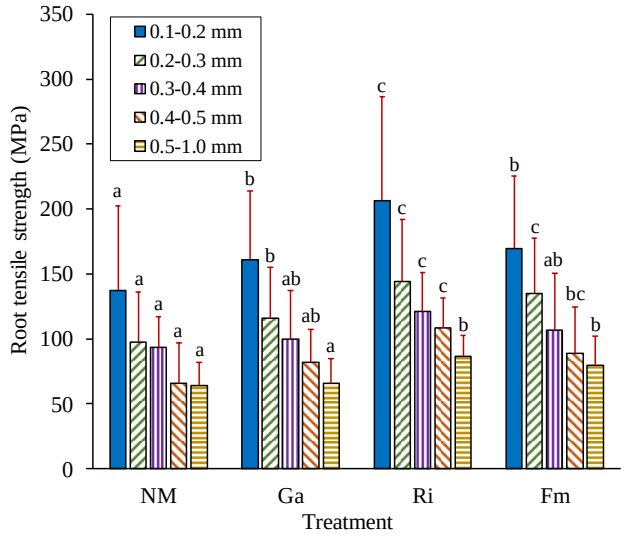

Fig. 7 Comparison of root tensile strengths derived from different mycorrhizal treatments and different ranges of stele diameters. The letters at the top indicate significant differences among treatments for each range of stele diameters. Data are presented as mean ± standard deviation (Chen et al., 2018).

5 CENTRIFUGE MODELLING OF HYDROMECHANICAL EFFECTS OF PLANT ROOTS ON SLOPE STABILITY AND FAILURE MECHANISMS (VERBATIM EXTRACT FROM NG ET AL., 2019B)

Although the mechanical effects of plant roots on slope stability have been reported (Pollen and Simon, 2005; Sonnenberg et al., 2010), the combined hydromechanical effects on deformation mechanism and failure of slopes remain unclear. Therefore, novel artificial root systems were developed for geotechnical centrifuge model tests to study the combined mechanical and hydrological effects of different root architectures on hydrology, slope stability and failure mechanisms (Ng et al., 2014b, 2016c; 2019a; Leung et al., 2017). The novelty of this artificial root system is its capacity to simulate effects of plant transpiration. All dimensions reported in this section have been converted to prototype scale unless stated otherwise.

5.1 *Principle and properties of the novel root model*

Fig. 8 shows the artificial root models of three different architectures (tap, heart and plate) created by Ng et al. (2014b). They were developed by idealising and simplifying the root architectures of real roots retrieved from three species that are commonly used for slope rehabilitation and ecological restoration in tropical and subtropical regions, namely, *Schefflera heptaphylla*, *Rhodomyrtus tomentosa* and *Melastoma sanguineum* (Hau and Corlett, 2003). These artificial root models are made of a porous material called cellulose acetate (CA), whose tensile strength and elastic modulus are fairly close to those typically identified in real roots (Stokes and Mattheck, 1996). In the design of Ng et al. (2014b), these root models are connected to a vacuum system, which includes a vacuum chamber that is partially filled with de-aired water. Through the vacuum source connected to the chamber, vacuum pressures can be applied to the CA; hence, different vacuum pressures up to −100 kPa can be induced in the water reservoir. Given that the CA is in contact with soil, any applied vacuum (and hence reduction in total head inside the root model) would enable water to flow from the soil to the chamber through the filter. The decrease in soil moisture would then induce soil suction. Leung et al. (2017) showed that the distribution of root area ratio with root depth is reasonably captured by the three root models, given the natural variability of plants in the field. Additional details of the test results and calibration can be found in Ng et al. (2019a).

5.2 *Root architecture effects on pore water pressure after rainfall*

Fig. 9 shows a typical centrifuge model setup. Three centrifuge tests were conducted to investigate and compare the contributions of the three different root architectures, namely, tap, heart and plate, to the hydrology and stability of 45° model slopes made of CDG (completely decomposed granite). Each model slope was supported by 15 artificial roots and subjected to a five-day simulated transpiration by the root system, followed by an intense 8-h rainfall event with a constant intensity of 70 mm/h (equivalent to a return period of 1,000 years in Hong Kong; Lam and Leung, 1995). Six pore pressure transducers were installed to monitor the suction (negative pore water pressure, PWP) in each slope. All tests were performed at 15 *g* in the Geotechnical Centrifuge Facility at the HKUST (Ng, 2014). The soil properties, model setup, instrumentation and test procedures can be found in Leung et al. (2017) and Ng et al. (2019a).

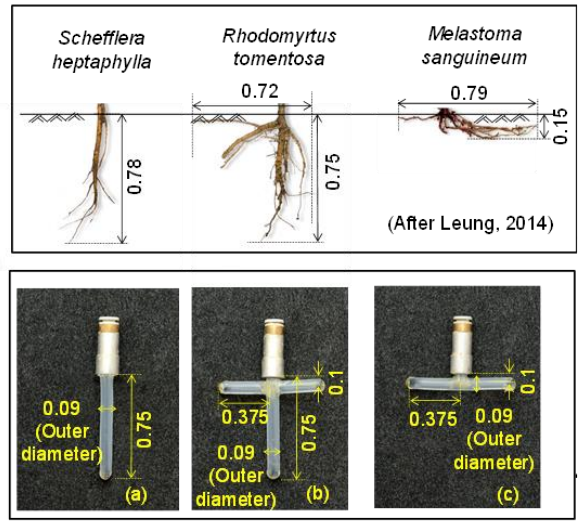

Fig. 8 Idealisation and simplification of plant roots with different root architectures (unit: m; converted to prototype scale)

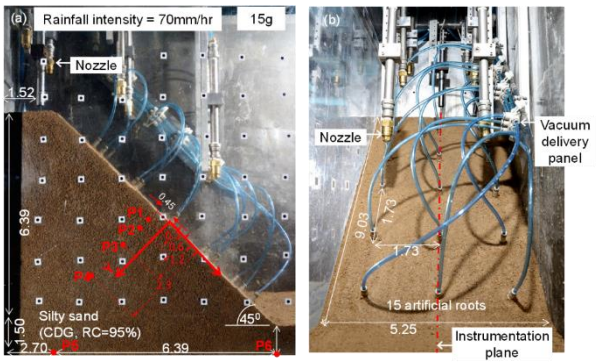

Fig. 9 (a) Elevation and (b) side views of the centrifuge model package and instrumentation (all dimensions are in metres and in prototype scale)

Fig. 10 compares the measured PWP profiles of the three model slopes with different root architectures during rainfall (Ng et al., 2017). Before rainfall, suction within the depths of the tap- and heart-shaped roots increased substantially during the transpiration process. It can be seen that the heart-shaped roots induced higher suction within the root zone than the tap-shaped roots because the former had two branches. For the plate-shaped roots, which did not have any taproot component, suction was the lowest below 0.3 m depth due to their shallow root zone. After a 2-h rain with a constant intensity of 70 mm/h (equivalent to a return period of 10 years), suction at all depths for all types of roots was reduced as expected. Slightly higher suction of 2–3 kPa was retained within the depths of the heart-shaped roots than within the depths of the tap-shaped roots. As the rainfall continued for another 6 h with the same intensity (equivalent to a return period of 1,000 years), a positive PWP distribution was measured in all three root systems. However, the plate-shaped roots showed the highest positive PWP amongst the three root types. This finding suggests that any transpiration performed by this type of root does not help reduce the PWP below the root depth under extreme rainfall very effectively.

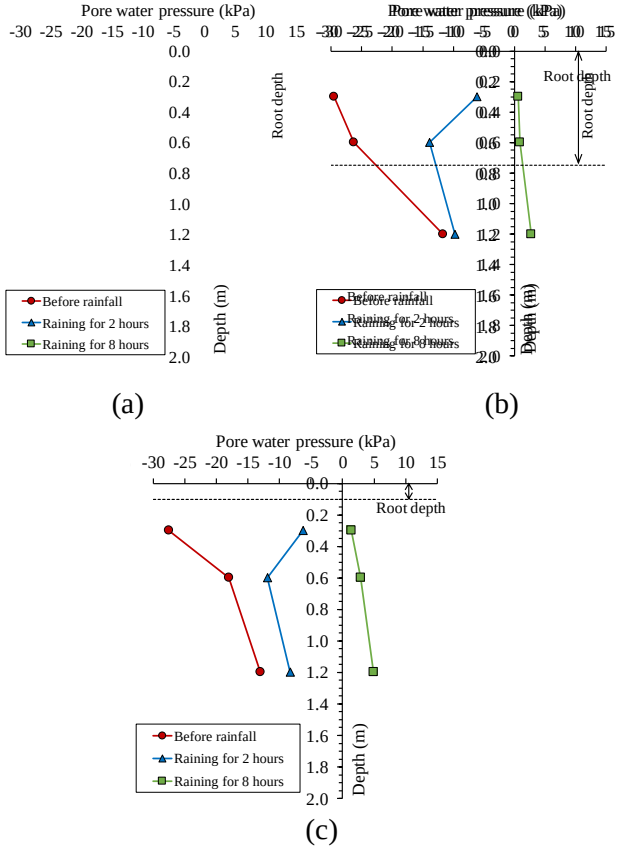

Fig. 10 Distribution of measured and computed pore water pressure along various depths before and after rainfall in the slope models supported by (a) tap-, (b) heart- and (c) plate-shaped roots.

5.3 *Effects of root architecture on pull-out resistance*

Apart from hydrological reinforcement via plant transpiration, the pull-out resistance of plant root systems contributes substantially to the mechanical reinforcement of slopes (Waldron and Dakessian, 1981; Ennos, 1990). Fig. 11 compares the measured relationships between pull-out force and displacement of the tap-, heart- and plate-shaped roots. All pull-out tests were conducted after 8 h of rainfall, when the soil was saturated (Fig. 10). After peaking, the pull-out force in all three cases decreased as the soil–root contact area reduced continuously during the pull-out process. The peak resistance of the heart-shaped roots (3.9 kN) was slightly higher than that of the tap-shaped roots (3.5 kN). Moreover, the post-peak pull-out force of the former architecture decreased more rapidly, given that less pull-out displacement was required to mobilise the same amount of resistance in the former than in the latter. Given the similar positive PWP induced after 8 h of rainfall (Figs. 10(a) and (b)), the difference in pull-out behaviour between these two architectures was primarily attributed to the mechanical reinforcement with the two branches of the heart-shaped root model. In contrast, the plate-shaped root architecture was not effective against the pull-out force. The peak pull-out resistance (1.2 kN) was about three to four times lower than those of the other two root types. Also, the post-peak load reduced much more rapidly than those of the other two architectures. The major reason was that for the plate-shaped root architecture, the two horizontal branches located at much shallower depths failed to provide considerable pull-out resistance.

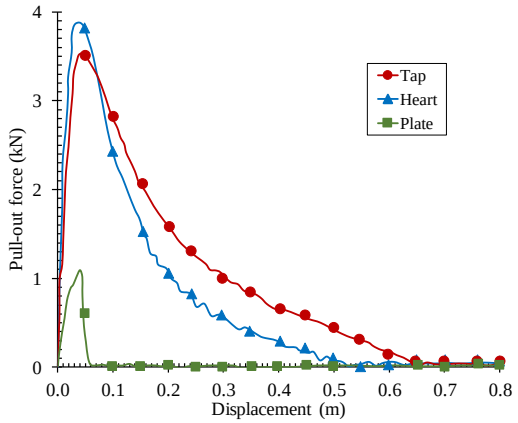

Fig. 11 Comparison of the pull-out behaviour of tap-, heart- and plate-shaped root models (Kamchoom et al., 2014)

5.4 *Effects of root architecture on slope stability and failure mechanisms*

On the basis of the measured PWP response (Fig. 10) and pull-out resistance (Fig. 11), the combined hydro-mechanical effects of plant roots on slope stability and failure mechanisms were studied. Based on the back-analysed PWP responses, slope stability analysis was conducted using SLOPE/W (Geo-Slope Int., 2009) to determine the factor of safety (FOS) in each case. The artificial roots were modelled as a beam element to capture the elastic axial and bending responses (Ng et al., 2016b, 2019a). The computed FOS results are shown in Fig. 12. Before transpiration, the FOS was similar for the three slopes and exceeded 1.0 (i.e., the slopes were stable). When suction was created by simulating transpiration for 5 days, the FOS of each slope increased but not substantially (less than 4%) because transpiration affected mainly the PWP in the top 1.2 m of each slope. After the 8-h rain, the FOS of the three slopes dropped significantly, following a reduction in PWP due to rainfall infiltration. Despite the reduction in FOS, all slopes remained stable, as observed in the model tests. The FOS value of the slope supported by the heart-shaped roots was 16% and 28% higher than those of slopes supported by the tap- and plate-shaped roots respectively. The greater stability provided by the heart-shaped roots came from the substantial suction preserved after rainfall and their higher mechanical pull-out resistance than that of the two other root architectures (Figs. 10 and 11). If the transpiration effects before the rainfall event were ignored in the stability calculations, the values of FOS after rainfall would drop below 1.0 in all the cases. Regardless of the root architecture, neglecting the effects of transpiration on slope stability resulted in a significant underestimation of FOS by up to 50%.

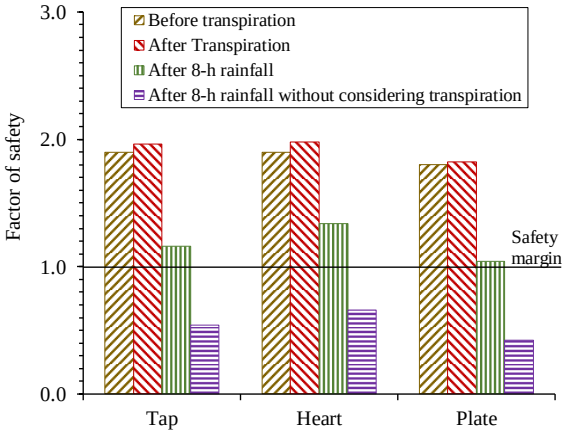

Fig. 12 FOS of slopes supported by different root architectures (Ng et al., 2016c)

To study the role of root architecture in the slope failure mechanism, two more centrifuge tests were conducted for steeper model slopes (i.e., 60°) vegetated with tap- and heart-shaped roots. The two slopes were continuously subjected to an 8-h extreme rainfall event with a constant intensity of 70 mm/h (equivalent to a return period of 1,000 years in Hong Kong) until failure. A comparison of the post-failure geometries between the two slopes in Fig. 13 suggests that a shallower slip was formed and a smaller volume of soil failed in the slope reinforced with heart-shaped roots than in the tap-rooted slope. The runout distance from the toe of the heart-rooted slope was approximately 9% (4.3 m versus 4.7 m) shorter than that from the toe of the tap-rooted slope, suggesting that the heart-shaped roots were more effective for stabilising slopes and reducing the runout distance than the tap- and plate-shaped roots.

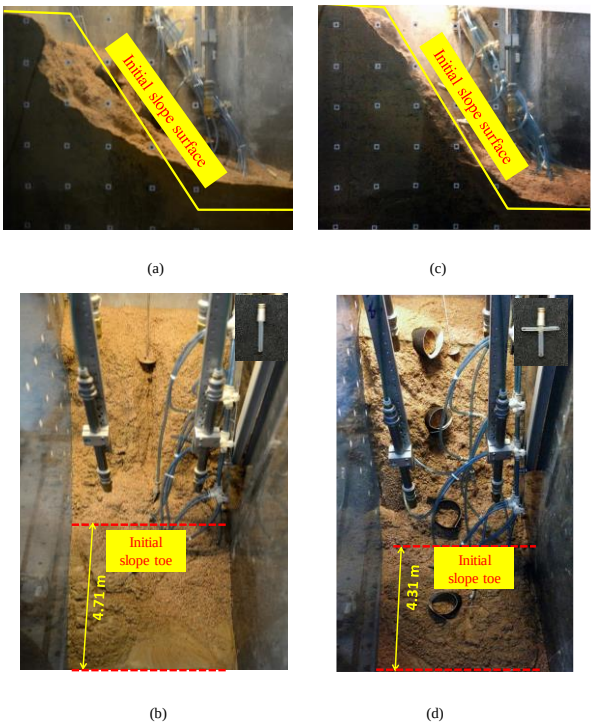

Fig. 13 (a) Elevation view and (b) plan view of a 60° steep slope reinforced with tap-shaped roots; (c) elevation view and (d) plan view of a 60° steep slope reinforced with heart-shaped roots (Ng, 2017)

6. ANALYTICAL SOLUTIONS FOR CALCULATING FOS OF AN INFINITE VEGETATED SOIL SLOPE

In order to calculate hydrological effects of plant roots on soil suction and the combined hydro-mechanical influence on the stability of unsaturated infinite vegetated soil slopes, advanced theoretical solutions have been developed. Closed-form, analytical steady- and transient-state solutions are derived to estimate the magnitude and distribution of plant-induced soil suction and hence the stability of an infinite vegetated slope with different root architectures (Ng et al., 2015; Liu et al., 2016; Feng et a., 2018, 2019, 2020).

6.1 Hydrological effects of roots

Fig. 14 shows the schematic diagram of an infinite vegetated slope, where H_0 is the vertical distance between the slope surface and the slope base, z' is the vertical coordinate, L_1 and L_2 are the perpendicular depth to the slope surface of the outside root zone and the root depth, respectively. The underground water table is assumed at the base of the slope, and rainfall or evaporation is set as the top boundary condition of the slope. Isolines of pore water pressure (PWP) are assumed to be parallel to the slope surface and water seepage in the infinite vegetated slope can thus be simplified as one-dimensional water flow. For a conservative estimation of FOS, surface runoff is not considered. The governing equation of ground water flow can be derived according to a similar procedure to that used by Zhan et al. (2013), but adding a sink term to consider root water uptake as follows:

$$\frac{\partial}{\partial z}(k\frac{\partial h}{\partial z})+\frac{\partial k}{\partial z}\cos\beta-S(z)T_pH(z-L_1)=\frac{\partial\theta_w}{\partial t} \quad (5)$$

where θ_w is the volumetric water content (VWC); t is the elapsed time; z denotes the coordinate perpendicular to the slope surface (Fig. 14); k is the water permeability function of the soil; h is the PWP head ($-h\gamma_w=s$, where γ_w is the unit weight of water); $S(z)$ represents the root architecture function; T_p is the transpiration rate; and $H(z-L_1)$ is the Heaviside function (Polyanin, 2002) defined as follows:

$$H(z-L_1)=\begin{cases}1 & L_1\le z\le(L_1+L_2)\\ 0 & 0\le z<L_1\end{cases} \quad (6)$$

Two representative root architectures (i.e., uniform and exponential; Fig. 15) are considered here to illustrate the derivation of analytical solutions. The corresponding root architecture function can then be expressed as follows:

$$S(z)=\begin{cases}\dfrac{1}{L_2} & \textit{Uniform}\\ \left[\dfrac{\exp(z-L_1)-1}{\exp(L_2)-L_2-1}\right] & \textit{Exponential}\end{cases} \quad (7)$$

In Eq. (7), it is assumed that root grows perpendicular to the slope surface, based on the observation made by Ghestem et al. (2011) and Danjon et al. (2013). To achieve a fair comparison, the integration of *S(z)* over entire root depth is kept constant

for both uniform and exponential roots. In an unsaturated soil, water retention curve and permeability function can be expressed according to Gardner (1958) as follows:

$$\theta_w = \theta_r + (\theta_s - \theta_r)\exp(\alpha h) \quad (8)$$

$$k = k_s \exp(\alpha h) \quad (9)$$

where k_s is the saturated water permeability of soil; α is the desaturation coefficient of soil; and θ_s and θ_r are the saturated and residual water content, respectively. The effects of hydraulic hysteresis are not considered for simplicity. Moreover, root induced changes in soil parameters (e.g., k_s, θ_s and θ_r) are also ignored due to the mathematical difficulties in deriving analytical solutions at transient state. In summary, the unsaturated seepage in an infinite vegetated slope can be described by Eqs. (5)-(9). The obtained analytical solutions for both the steady- and transient-state can be found in Ng et al. (2015).

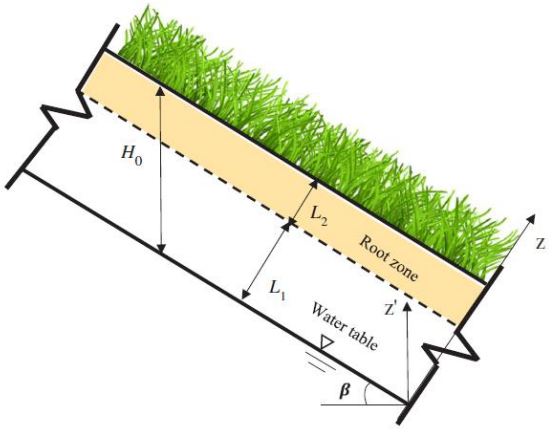

Fig. 14 Schematic diagram of an infinite vegetated soil slope (after Feng et al. (2020)).

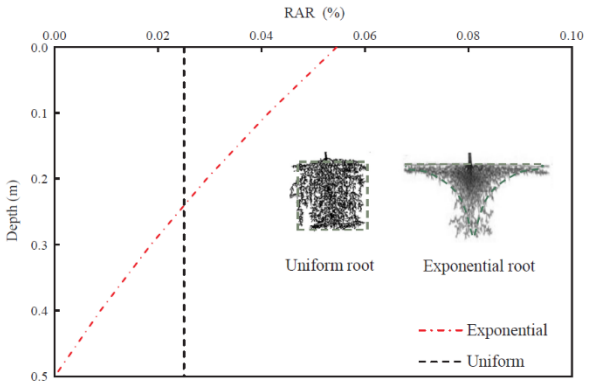

Fig. 15 Two different root architectures and their root area ratios (RARs) (after Feng et al. (2020)).

6.2 Mechanical reinforcement of roots

The root breakage model proposed by Wu et al. (1979) has been widely used over the past decades to estimate the mechanical effects of root on slope stability due to its simplicity. The model assumes that all roots are mobilised and broken simultaneously during shearing. The Wu et al. (1979) model is adopted here to describe the additional increase in soil shear strength induced by the root mechanical reinforcement as follows:

$$c_r = \xi \times T_r \times R_f \times RAR \quad (10)$$

where c_r is the additional apparent cohesion induced by the mechanical effects of roots; ξ is the correction factor, which accounts for the root progressive breakage, and is calibrated to be 0.4 for most species (Preti and Schwarz, 2006). T_r is the average root tensile strength, which is taken to be 2 x 10^4 kPa (Bischetti et al., 2005). R_f is the root orientation factor, which is defined as follows:

$$R_f = \sin\omega + \cos\omega \tan\varphi' \quad (11)$$

where ω is the angle between the root orientation and the failure surface at root breakage. When roots are assumed to grow perpendicularly to the slope surface, ω is equal to be 90^0.

RAR is root area ratio, which is defined as the fraction of the cross-sectional area of the soil occupied by the roots as follows:

$$RAR = \frac{A_r}{A} = \frac{\sum_{i=1}^{n} \pi d_i^2}{4A} \quad (12)$$

where A_r and A represent the cross-sectional area of root and soil, respectively; d_i is the diameter of root i and n the total root number.

6.3 Hydro-mechanical effects of roots on slope stability

By incorporating the additional root-induced apparent cohesion c_r (calculated by Eq. (10)) into the extended Mohr-Coulomb criterion (Fredlund and Rahardjo, 1993), the shear strength of an unsaturated vegetated soil could be obtained. When considering both mechanical and hydrological root reinforcement, the FOS of an infinite vegetated slope with an inclination of β can be expressed as (Feng et al., 2020):

$$FOS = \frac{\left(c' + \xi R_f T_r RAR - u_w \tan\phi^b\right)}{\left[\gamma_d \left(H_0 - z'\right) + \gamma_W \int_{z'}^{H_0} \theta_w dz'\right] \sin\beta\cos\beta} + \frac{\tan\phi'}{\tan\beta} \quad (13)$$

where γ_d and γ_w refer to the unit weight of dry soil and water, respectively; ϕ' is the effective friction

angle and ϕ^b is the angle relating the increase in shear strength to the negative PWP. Based on a series of parametric analyses, Feng et al. (2020) concluded that the hydrological and mechanical effects of roots are more significant in the slope reinforced by an exponential root system (i.e., similar to heart-shaped roots) than in the one reinforced by a uniform root system (i.e., similar to tap-shaped roots). This is because the exponential root architecture has a greater concentration of roots near the slope surface. The mechanical effects of vegetation can only enhance slope stability inside the root zone, while the hydrological effects can improve slope stability in deeper soil zone (i.e., 3-4 times the root depth). This finding is consistent with laboratory and field measurements (refer to Fig. 3 and Ng et al. (2019a)).

7. CONCLUSIONS

Sustainable and ecologically bioengineered slopes that use plants were studied through an interdisciplinary research programme. Various tree, shrub and grass species widespread and native to southern China (*Schefflera heptaphylla* and *Chrysopogon zizanioides*) and Europe with temperate climates (e.g., *Ulex europaeus*, *Salix viminalis*, and *Corylus avellana*) were studied. Some of these species were able to preserve large soil matric suction during and after intense rainfall. The magnitude of suction preserved was positively correlated with plant traits such as the leaf area index, the root area index and the ratio of root to shoot biomass. Moreover, the biological interaction of plant roots with symbiotic fungi in soil enhanced root tensile strength significantly.

Novel artificial root systems with different idealised root architectures were developed to study the combined hydrological and mechanical effects of plant roots on slope stability in centrifuge model tests. The novelty of the root systems lies in their ability to simulate the effects of plant transpiration. The centrifuge experiments were conducted in the Geotechnical Centrifuge Facility at the HKUST. The heart-shaped roots provided greater stabilisation effects in that they preserved higher suction (leading to higher soil shear strength and lower water permeability) and exhibited stronger pull-out resistance than the other two root types during rainfall due to their multiple branching. The FOS was greatly improved (by up to 50%) when plant hydrological effects were considered.

Analytical solutions were derived to calculate the hydrological effects of plants on soil suction and the combined hydro-mechanical influence on the stability of unsaturated infinite vegetated soil slopes with different root architectures. The analytical solutions provide a convenient simple tool for researchers and engineers to carry out preliminary design of sustainable and ecologically engineered slopes worldwide.

ACKNOWLEDGMENTS

The authors acknowledge funding from the Theme-based Research Scheme (grant no. T22-603/15N) and the Areas of Excellence (AoE) Scheme (grant no. AoE/E-603/18) of the Research Grants Council of the Government of Hong Kong SAR.

REFERENCES

Alonso, E. E., Gens, A. and Josa, A. (1990). A Constitutive Model for Partially Saturated Soils, Geotechnique, 40(3): 405-430.

Alonso, E. E., Iturralde, E. F. O. and Romero, E. E. (2007). Dilatancy of coarse granular aggregates. In Experimental unsaturated soil mechanics (pp. 119-135). Springer, Berlin, Heidelberg.

Been, K. and Jefferies, M. G. (1985). A State Parameter for Sands. Geotechnique, 35(2): 99-112.

Bischetti, G. B., Chiaradia, E. A., Simonato, T., Speziali, B., Vitali, B., Vullo, P. and Zocco, A. (2005). Root strength and root area ratio of forest species in Lombardy (northern Italy), Plant and Soil, 278: 11–22.

Boldrin, D., Leung, A.K. and Bengough, A.G. (2017). Root biomechanical properties during establishment of woody perennials, Ecological Engineering, 109:192-206.

Chen, X.W., Kang, Y., So, P.S., Ng, C.W.W. and Wong, M.H. (2018). Arbuscular mycorrhizal fungi increase the proportion of cellulose and hemicellulose in the root stele of vetiver grass, Plant and Soil, 425: 309-319.

Cheng, Q., Ng, C. W. W., Zhou, C. and Tang, C. S. (2019). A new water retention model that con-siders pore non-uniformity and evolution of pore size distribution, Bulletin of Engineering Geology and the Environment, 78(7): 5055-5065.

Chiu, C.F. and Ng, C.W.W. (2003). A state-dependent elasto-plastic model for saturated and unsaturated soils, Géotechnique, 53: 809-829.

Coppin, N.J. and Richards, I.G. (1990). Use of Vegetation in Civil Engineering. Construction Industry Research and Information Association/Butterworths, London, UK.

Danjon, F., Khuder, H. and Stokes, A. (2013). Deep phenotyping of coarse root architecture in R. pseudoacacia reveals that tree root system plasticity is confined within its architectural model, PloS one, 8(12).

Delage, P. and Lefebvre, G. (1984). Study of the structure of a sensitive Champlain clay and of its evolution during consolidation, Canadian Geotechnical Journal, 21(1): 21-35.

D'Onza, F., Gallipoli, D., Wheeler, S., Casini, F., Vaunat, J., Khalili, N., Laloui, L., Mancuso, C., Masin, D., Nuth, M., Pereira, J. M. and Vassallo, R. (2011). Benchmark of constitutive models for unsaturated soils, Geotechnique, 61(4): 283-302.

Ennos, A.R. (1990). The anchorage of leek seedlings: The effect of root length and soil strength, Annals of Botany, 65, 409-416.

Fatahi, B., Khabbaz, H. and Indraratna, B. (2010). Bioengineering ground improvement considering root water uptake model, Ecological Engineering, 36: 222-229.

Fatahi, B., Khabbaz, H. and Indraratna, B. (2014). Modelling of unsaturated ground behaviour influenced by vegetation transpiration, Geomechanics and Geoengineering, 9: 187-207.

Feng, S., Liu, H.W. and Ng, C.W.W. (2018). Dimensional analysis of pore-water pressure response in a vegetated infinite slope, Canadian Geotechnical Journal, 56(8): 1119-1133.

Feng, S., Liu, H.W. and Ng, C.W.W. (2019). Analytical solutions for one-dimensional water flow in vegetated layered soil, International Journal of Geomechanics, 19(2): 04018191.

Feng, S., Liu, H. W. and Ng, C. W. W. (2020). Analytical analysis of the mechanical and hydrological effects of vegetation on shallow slope stability, Computers and Geotechnics, 118: 103335.

Fiorilli, V., Catoni, M., Miozzi, L., Novero, M., Accotto, G.P. and Lanfranco, L. (2009). Global and cell-type gene expression profiles in tomato plants colonized by an arbuscular mycorrhizal fungus, New Phytologist, 184: 975-987.

Francour, P. and Semroud, R. (1992). Calculation for the root area index in Posidonia oceanica in the Western Mediterranean. Aquatic Botany, 42: 281–286.

Fredlund, D. G. and Rahardjo, H. (1993). Soil mechanics for unsaturated soils, Wiley-interscience.

Fredlund, D.G., Xing, A. and Huang, S. (1994). Predicting the permeability functions for unsaturated soils using the soil-water characteristic curve, Canadian Geotechnical Journal, 31, 533-546.

Gardner, W. R. (1958). Some steady-state solutions of the unsaturated moisture flow equation with application to evaporation from a water table, Soil science, 85(4):228–32.

Garg, A., Leung, A.K. and Ng, C.W.W. (2015). Comparisons of soil suction induced by evapotranspiration and transpiration of S. heptaphylla, Canadian Geotechnical Journal, 52: 2149-2155.

Gens, A. (2010). Some issues in constitutive modelling of unsaturated soils, Theoretical and Numerical Advances in Unsaturated Soil Mechanics: 613-626.

Geo-Slope International Ltd. (2009). Stress-Deformation Modeling with SIGMA/W, An Engineering Methodology, 4th edn.

Ghestem, M., Sidle, R. C. and Stokes, A. (2011). The influence of plant root systems on subsurface flow: implications for slope stability, Bioscience, 61(11): 869 – 879.

Hau, B.C. and Corlett, R.T. (2003). Factors affecting the early survival and growth of native tree seedlings planted on a degraded hillside grassland in Hong Kong, China, Restoration Ecology, 4: 483-488.

Indraratna, B., Fatahi, B. and Khabbaz, H. (2006). Numerical analysis of matric suction effects of tree roots. Proceedings of the Institution of Civil Engineers – Geotechnical Engineering, 159:77-90.

Kamchoom, V., Leung, A.K. and Ng, C.W.W. (2014). Effects of root geometry and transpiration on pullout resistance, Géotechnique Letters, 4: 330-336.

Kelliher, F.M., Leuning, R., Raupach, M.R. and Schulze, E.D. (1995). Maximum conductances for evaporation from global vegetation types, Agricultural and Forest Meteorology, 73: 1-16.

Lam, C.C. and Leung, Y.K. (1995). Extreme rainfall statistics and design rainstorm profiles at selected locations in Hong Kong, Royal Observatory, Hong Kong.

Leung, A.K., Kamchoom, V. and Ng, C.W.W. (2017). Influences of root-induced soil suction and root geometry on slope stability: a centrifuge study, Canadian Geotechnical Journal, 54: 291-303.

Leung, F.T.Y. (2014). The use of native woody plants in slope upgrading in Hong Kong. PhD thesis, The University of Hong Kong, Hong Kong, China.

Liu, H.W., Feng, S. and Ng, C.W.W. (2016). Analytical analysis of hydraulic effect of vegetation on shallow slope stability with different root architectures, Computers and Geotechnics, 80: 115–120.

Lloret-Cabot, M., Wheeler, S. J. and Sánchez, M. (2017). A unified mechanical and retention model for saturated and unsaturated soil behaviour, Acta Geotechnica, 12: 1-21.

Ng, C. W. W. and Pang, Y. W. (2000). Influence of stress state on soil-water characteristics and slope stability, Journal of Geotechnical and Geoenvironmental Engineering, ASCE, 126(2), doi.org/10.1061/(ASCE)1090-0241.

Ng, C.W.W. (2014). The 6th ZENG Guo-xi Lecture: The state-of-the-art centrifuge modelling of geotechnical problems at HKUST, Journal of Zhejiang University-Science A (Applied Physics & Engineering), 15: 1-21.

Ng, C. W. W. and Chiu, A. C. F. (2001). Behavior of a loosely compacted unsaturated volcanic soil, Journal of Geotechnical and Geoenvironmental Engineering, ASCE, 127(12): 1027-1036.

Ng, C.W.W., Liu, H. W. and Feng, S. (2015). Analytical solutions for calculating pore water pressure in an infinite unsaturated slope with different root architectures, Canadian Geotechnical Journal, 52(12): 1981-1992.

Ng, C.W.W. (2017). The 20th Huangwenxi Lecture: Atmosphere-plant-soil interaction: Theories and mechanisms, Chinese Journal of Geotechnical Engineering, 39:1-47. (In Chinese).

Ng, C.W.W. and Menzies, B. (2007). Advanced Unsaturated Soil Mechanics and Engineering, Taylor & Francis Group, London, UK. ISBN: 9780415436793.

Ng, C.W.W., Garg, A., Leung, A.K. and Hau, B.C.H. (2016b). Relationships between leaf and root area indices and soil suction induced during drying-wetting cycles, Ecological Engineering, 91: 113-118.

Ng, C.W.W., Kamchoom, V. and Leung, A.K. (2016c). Centrifuge modelling of the effects of root geometry on the transpiration-induced suction and stability of vegetated slopes, Landslides 13:1-14.

Ng, C.W.W., Leung, A.K. and Ni, J.J. (2018). Bioengineering for slope stabilization using plants: hydrological and mechanical effects, Proceedings of the 1st China-Europe Conference on Geotechnical Engineering, Vienna Austria, 1287-1303.

Ng, C.W.W., Leung, A.K. and Ni, J.J. (2019a). Plant-Soil Slope Interaction. Taylor & Francis, USA. ISBN: 9781138197558.

Ng, C.W.W., Leung, A.K. and Woon, K.X. (2014a). Effects of soil density on grass-induced suction distributions in compacted soil subjected to rainfall, Canadian Geotechnical Journal, 311-321.

Ng, C.W.W., Leung, A.K., Kamchoom, V. and Garg, A. (2014b). A novel root system for simulating transpiration-induced soil suction in centrifuge, Geotechnical Testing Journal, 37: 1-15.

Ng, C.W.W., Leung, A.K., Yu, R. and Kamchoom, V. (2017). Hydrological effects of live poles on transient seepage in an unsaturated soil slope: centrifuge and numerical study, Journal of Geotechnical and Geoenvironmental Engineering, ASCE, 143: 04016106.

Ng, C.W.W., Ni, J.J. and Leung, A.K. (2020). Effects of plant growth and spacing on soil hydrological changes: a field study, Géotechnique, https://doi.org/10.1680/jgeot.18.P.207.

Ng, C.W.W., Ni, J.J. and Leung, A.K., Zhou, C. and Wang, Z. J. (2016a). Effects of planting density on tree growth and induced soil suction, Géotechnique, 66: 711-724.

Ng, C.W.W., Ni, J.J. and Zhou, C. (2019b). Interplay between ecology and unsaturated soil mechanics for bioengineered landfill covers and slopes, Proceedings of XVI Pan-American Conference on Soil Mechanics and Geotechnical Engineering, Cancun Mexico.

Ng, C.W.W., Woon, K.X., Leung, A.K. and Chu, L.M. (2013). Experimental investigation of induced suction distributions in a grass-covered soil, Ecological Engineering, 52: 219-223.

Ni, J.J., Leung, A.K. and Ng, C.W.W. (2017). Investigation of plant growth and transpiration induced suction under mixed grass-tree conditions, Canadian Geotechnical Journal, 54: 561-573.

Ni, J.J., Leung, A.K. and Ng, C.W.W. (2018). Modelling soil suction changes due to mixed species planting, Ecological Engineering, 117: 1-17.

Ni, J.J., Leung, A.K. and Ng, C.W.W. (2019a). Unsaturated hydraulic properties of vegetated soil under single and mixed planting conditions, Géotechnique, 69: 554-559.

Ni, J. J., Leung, A. K. and Ng, C. W. W. (2019b). Modelling effects of root growth and decay on soil water retention and permeability, Canadian Geotechnical Journal, 56(7): 1049-1055.

Pollen, N. and Simon, A. (2005). Estimating the mechanical effects of riparian vegetation on stream bank stability using a fiber bundle model, Water Resources Research, 41: W07025.

Polyanin, A.D. (2002). Linear partial differential equations for Engineers and Scientists, Chapman and Hall/CRC.

Preti F. and Schwarz M. (2006). On root reinforcement modelling, Geophysical Research 436 Abstracts, vol. 8, EGU General Assembly 2006, 2–7 April, ISSN: 1029–7006.

Sheng, D. (2011). Review of fundamental principles in modelling unsaturated soil behaviour, Computers and Geotechnics, 38: 757-776.

Smith, S.E. and Read, D.J. (2008). Mycorrhizal Symbiosis. London, UK: Academic Press.

Sonnenberg, R., Bransby, M.F., Hallett, P.D., Bengough, A.G., Mickovski, S.B. and Davies, M.C.R. (2010). Centrifuge modelling of soil slopes reinforced with vegetation, Canadian Geotechnical Journal, 47:1415-1430.

Stokes, A., Atger, C., Bengough, A.G., Fourcaud, T. and Sidle, R.C. (2009). Desirable plant root traits for protecting natural and engineered slopes against landslides, Plant and Soil, 324: 1-30.

Stokes, A., Mattheck, C. (1996). Variation of wood strength in tree roots, Journal of Experimental Botany, 47: 693-699.

Vanapalli, S.K., Fredlund, D.G., Pufahi, D.E. and Clifton, A.W. (1996). Model for the prediction of shear strength with respect to soil suction, Canadian Geotechnical Journal 33: 379–392.

Waldron, L.J. and Dakessian, S. (1981). Soil reinforcement by roots: Calculation of increased soil shear resistance from root properties, Soil Science, 132: 427-435.

Wheeler, S. J. and Sivakumar, V. (1995). An elasto-plastic critical state framework for unsaturated soil, Géotechnique, 45(1): 35-53.

Wheeler, S. J., Sharma, R. S. and Buisson, M. S. R. (2003). Coupling of hydraulic hysteresis and stress-strain behaviour in unsaturated soils, Géotechnique, 53(1): 41-54.

Wu, Q.S., Liu, C.Y., Zhang, D.J., Zou, Y.N., He, X.H. and Wu, Q.H. (2016). Mycorrhiza alters the profile of root hairs in trifoliate orange, Mycorrhiza, 26: 237-247.

Wu, T.H., McKinnell, W.P. and Swanston, D.N. (1979). Strength of tree roots and landslides on Prince of Wales Island, Alaska, Canadian Geotechnical Journal, 16: 19–33.

Zhan, T.L.T., Jia, G.W., Chen, Y.M., Fredlund, D.G. and Li, H. (2013). An analytical solution for rainfall infiltration into an unsaturated infinite slope and its application to slope stability analysis, International Journal for Numerical and Analytical Methods in Geomechanics, 37(12):1737–60.

Zhou, C. and Ng, C. W. W. (2014). A new and simple stress-dependent water retention model for unsaturated soil, Computers and Geotechnics, 62: 216-222.

Ground Improvement for Rail and Road Infrastructure

Buddhima Indraratna

Distinguished Professor, Director, Transport Research Centre, Founding Director, ARC Industrial Transformation Training Centre for Railroad Technologies (ITTC-Rail), University of Technology Sydney, Ultimo, NSW 2007, Australia.
Email: buddhima.indraratna@uts.edu.au, Ph: +61 400 213 046

Trung Ngo

Senior Lecturer, Transport Research Centre, School of Civil and Environmental Engineering, University of Technology Sydney, Ultimo, NSW 2007, Australia.

Email: Trung.Ngo@uts.edu.au

Yujie Qi

Lecturer, Program Co-leader of Transport Research Centre, School of Civil and Environmental Engineering, University of Technology Sydney, Ultimo, NSW 2007, Australia.

Email: yujie.qi@uts.edu.au

Cholachat Rujikiatkamjorn

Professor, Transport Research Centre, School of Civil and Environmental Engineering, University of Technology Sydney, Ultimo, NSW 2007, Australia.

Email: cholachat.rujikiatkamjorn@uts.edu.au

ABSTRACT: The need for transport infrastructure that will perform over the long term has recently been accentuated by an expectation that heavy haul transport networks willbe able to withstand higher speeds and heavier axle loads. Several ground improvement techniques used worldwide to improve track embankments built on soft ground are Prefabricated Vertical Drains (PVDs) combined with surcharge and vacuum preloading. These techniques have proven to be efficient, cost-effective, and popular methods for accelerating consolidation. Moreover, energyabsorbing layers manufactured from waste tyres, such as ballast mats, under sleeper pads, rubber crumbs, and tyre cells will also help to attenuate dynamic train loads and also alleviatethe degradation and deformation of ballast. Recycling these waste materials not only helps to solve geotechnical issues, it is also economically beneficial and environmentally sustainable. This keynote paper briefly reviews some key aspects of soft ground improvement via PVDs combined with surcharge and vacuum preloading, and it also discusses our current knowledge of the ability of energy-absorbing materials to mitigate track deterioration induced by fast-moving heavyhaul trains. Since the factors which govern the stress-strain behaviour and the strength and degradation of ballast, as well as the ability of geosynthetics and synthetic energy-absorbing mats to minimise ballast breakage and track settlement have been analysed, our research outcomes are expected to contribute to design solutions that will enhance track stability and reduce the maintenance costs.

1 INTRODUCTION

The almost 40,000km long network of ballasted rail tracks in Australia is the major infrastructure that caters for public and freight transport and also offers an essential supply chain for agricultural and mining industries. Repeated train loads not only causes significant amounts of ballast breakage, the ballast also becomes fouled and less angular, and its shear strength decreases (Indraratna et al. 2011, Huang et al. 2009, Powrie et al. 2007, Zhai et al. 2004, Selig 1994, Chen et al. 2018, Aursudkij et al. 2009). The rail industryis now placing greater emphasis on the construction of high-speed train corridors and heavier freight operations in a bid to achieve more efficient and cost-effective services. Placing synthetic energy-absorbing products such as rubber mats, end-of-lifetyres, and granulated rubber into rail infrastructure iseven more popular because theirvery high damping properties will ab-

sorb more of the kinetic energy induced by moving trains. These properties help to reduce the stresses transmitted ontothe underlying substructural layer and also reduce track degradation (Biabani, et al. 2016, Sun et al. 2019; Sol-Sanchez et al. 2015, Jayasuriya et al. 2019, Indraratna and Ngo 2018, Fernandeset al. 2008, Rujikiatkamjorn et al. 2013, Suiker et al. 2005). Navaratnarajah et al (2018) found that under ballast mats can reduce ballast breakage by 25-45%, vertical plastic strain by 10-20%, and lateral strain by 5-10%. Sol-Sanchez et al. (2015) found thatmixing 10% granulated rubber by volume into ballast is an efficient way of mitigating ballast degradation, and Ngo et al. (2019) found that rubber mats placed beneath the ballast will reduce the impact forces produced by rail irregularities and imperfections. More importantly, these energy-absorbing materials aremanufactured from end-of-life tyresso we now have a result that is environmentally friendly and economically beneficial.

Prefabricated vertical drains (PVD) with surcharge and vacuum preloading is a very popular, efficient and effective technique for ground improvement (Baral et al. 2019). However, its efficiency with a surcharge can be further enhanced by applying negative pressure along the drain; not only does this decrease the consolidation time, it also helps to reduce the surcharge height and stabilise the ground. Instead of having an outward lateral deformation for PVD with surcharge, a vacuum application results in inward lateral deformation which solves the boundary issues, especially whenconstructing in a marine environmentwhere excessive outward lateral deformation affects the turbidity of water and the lifecycle of aquatic animals.

2 VACUUM CONSOLIDATION FOR SOFT SUBGRADE SOIL

Mohamedelhassan and Shang (2002) introduced theoretical expressions by superimposing vacuum and surcharge alone based on Terzaghi's 1-D consolidation theory. This vacuum consolidation system (Fig. 1a) can be determined by combining the surcharge alone system (Fig. 1b) and the vacuum alone system (Fig. 1c) separately. The average degree of consolidation for combined vacuum and surcharge preloading can then be computed as:

$$U_{vc} = 1 - \sum_{m=0}^{\infty} \frac{2}{M} \exp^{-M^2 T_{vc}} \quad (1)$$

$$T_{vc} = c_{vc} t / H^2 \quad (2)$$

where, $c_{vc}$is the coefficient of consolidation for combined vacuum and surcharge preloading, and $T_{vc}$is a time factor for combined vacuum and surcharge preloading.

Fig. 1 Schematic diagram of a vacuum preloading system (a) combined vacuum and surcharge; (b) surcharge only; and (c) vacuum only (adopted from Mohamedelhassan and Shang 2002)

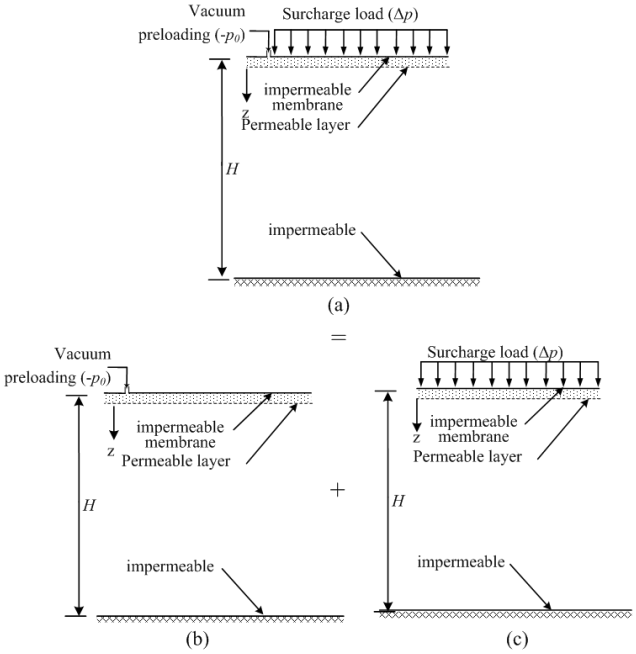

Indraratna et al. (2004) showed that once a vacuum pressure is applied through PVDs, the vacuum pressure decreases along with the depth of drain and its project efficiency is also reduced. Laboratory testsat the University of Wollongong Australia (UOW) using a large-scale consolidometer showed that the vacuum propagates immediately at the topmost area but there is a subsequent loss of vacuum pressure from the pore water pressure transducer along the depth of drain. Based on alaboratory observation to include the pattern of vacuum distribution, Indraratna et al. (2005)introduced a modified radial consolidation theory (Fig. 2). This theory assumes a trapezoidal distribution of vacuum pressure along the length of the PVD which is then applied in various analytical models to consider the loss of vacuum. The average excess pore pressure ratio ($R_u = \Delta p / u_o$) of a soil cylinder for radial drainage that incorporates vacuum preloading, can be estimatedas:

$$R_u = \left(1 + \frac{p_0}{u_o}\frac{(1+k_1)}{2}\right)\exp\left(-\frac{8T_h}{\mu}\right) - \frac{p_0}{u_0}\frac{(1+k_1)}{2} \quad (3)$$

and

$$\mu = \ln\left(\frac{n}{s}\right) + \left(\frac{k_h}{k_s}\right)\ln(s) - 0.75 + \pi z(2l - z)\frac{k_h}{q_w}\left\{1 - \frac{k_h/k_s - 1}{(k_h/k_s)(n/s)^2}\right\} \quad (4)$$

where l: equivalent length of drain;p_0: vacuum applied at the top of the drain;u_0: initial EPWP; k_1: ratio between the vacuum at the top and bottom of the drain;k_h, k_s:horizontal permeability in undisturbed and smeared zones;T_h:time factor;$n = d_e/d_w$ (d_e is the diameter of the equivalent soil cylinder = $2r_e$ and d_w is the diameter of the drain = $2r_w$);$s = d_s/d_w$ (d_s: diameter of the smear zone = $2r_s$with constant permeability), z = depth and q_w = drain discharge capacity.

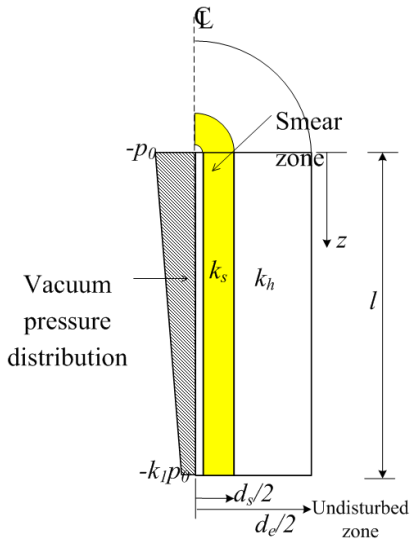

Fig. 2 Vertical distribution of vacuum pressure within a PVD (Indraratna et al. 2005)

2.1 *Case study: Port of Brisbane*

The site at the Port of Brisbane (POB) consists of 30m thick soft compressible clays. To reclaim the sub-tidal area, a 7m thick layer of dredged mud capped with a 2m thick layer of sand was monitored. Sinceit might take more than 50 years for these deposits of soft deep clay and the 2.5-4m deep associated settlements to consolidate with surcharge alone, PVD and surcharge, or PVD combined with vacuum pressure was trialled to accelerate consolidation. Typical settlement and excess pore water pressure (EPWP) predictions and field data are shown in Figure3; note that the predicted settlement curve agrees with the field data. Despite the EPWP dissipation being more difficult to predict than settlement, it still indicates a slower rate of dissipation forthe clays in every section monitored, inspite of the PVDs.

The incremental rate of change inthe lateral displacement/settlement ratio (μ) with time is shown in Figure 4. This rate of change can be evaluated for relatively smalltime increments where a small and decreasing gradient can be considered stable with respect to lateral movement, but a continuously increasing gradient reflects potential lateral instability. The gradient in the non-vacuum area (VC3) increased initially because the final surcharge loading was installed while the clay was still at its early stages of consolidation. However, as the PVDs become fully active and settlement increased at a healthy rate, the gradient of μ decreased, as expected.

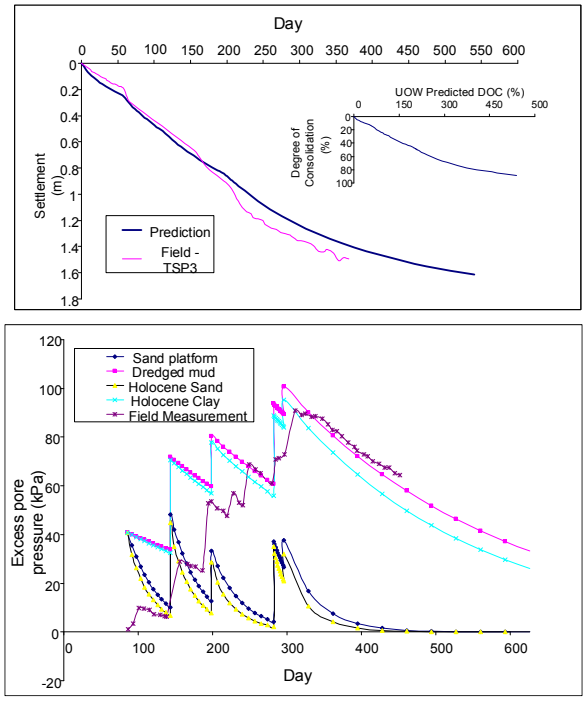

Fig. 3 (a) Settlement; and (b) EPWP predictions and field data for a typical settlement plate location. (Indraratna, 2010, with permission from AGS)

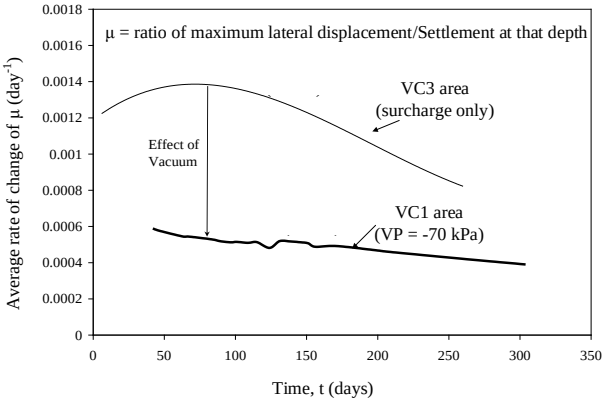

Fig. 4 Rate of change of lateral displacement/settlement ratio with time (Indraratna, 2010, with permission from AGS)

3 SEAL-SYNTHETIC ENERGY ABSORBING LAYER FOR STABILISING SUBSTRUCTURE

Indraratna et al. (2017) developed a synthetic energy absorbing layer (SEAL) for railway subballast using waste mixtures containing steel furnace slag (SFS), coal wash (CW) and rubber crumbs (RC). The comprehensive tests carried out by the authors revealed that a SEAL with a proper blending ratio of SFS, CW and RC has better geotechnical properties than traditional sub-ballast materials. These improved properties include better energy absorption, higher permeability, higher shear strength and acceptable deformation (Qi et al., 2018a; Qi et al., 2018c,b; Qi et al., 2019). However, all the test of the SEAL mixtures were smallscale and only SEAL materials (sub-ballast layer) were involved. Qi et al. (2018a) proposed an energy consumption concept which indicated that if the energy absorbing capacity of the ballast layer is improved, less energy will be imparted to the ballast and the subgrade, and hence ballast degradation and track deformation will be reduced. To verify this concept, a physical model is proposed using the large-scale cubical test apparatus at the University of Wollongong.

3.1 *Materials and testing program*

The steel furnace slag (SFS) by-product is a direct result of steelmaking by processing iron and steel scrap with lime athightemperaturesin Basic Oxygen and Electric ArcFurnaces.Coal wash (CW) is generated from the washery process used to refine run-of-mine coal.The source materials for SFS and CW used in this study came fromIllawarra Coal and Australia Steel Milling Services,and the rubber crumbs (RC) shredded from waste tyres came from Tyre Crumbs Australia. The particle size distribution (PSD) curves of the RC, SFS and CW are shown in Fig. 5.

The physical model hasa ballast layer, a subballast (SEAL) layer, and a layer of structural fill. The ballast and structural fill are from a local quarry near the University of Wollongong. Their PSD curves are shown in Fig. 5; the ballast was prepared according to Australian standard (AS-2758.7, 2015), the SEAL mixture hasan optimal blending ratio of SFS:CW=7:3 (by weight), as suggested by Indraratna *et al.* (2017), and it was then mixed with various percentages of RC (i.e. 0, 10, 20, 30 and 40%). The PSD of the SEAL mixtures with different amounts of RC (R_b,%) are also shown in Fig. 5; the number after SEAL refers to R_b(%).

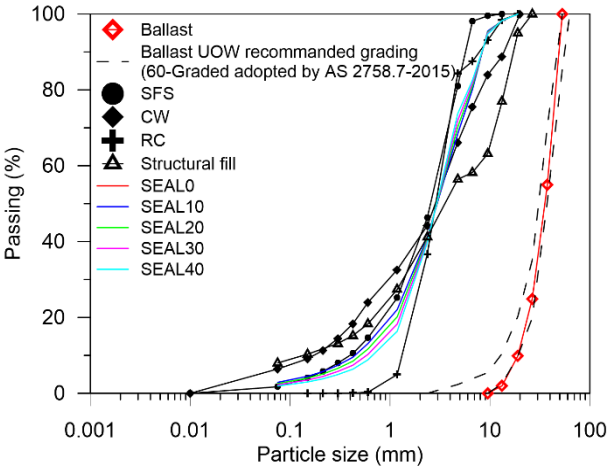

Fig. 5 PSD of SFS, CW, RC, ballast, structural fill and SEAL mixtures

A schematic diagram of the physical model is shown in Fig. 6a. The test specimen was prepared in a 600mm wide by 800mm long by 600mm deep cubical triaxial testing cell.Before being tested the 200mm high ballast, the 150mm high subballast, and the 100mm high subgradewere compacted to field conditions with a dynamic compactor. A 150mm thick concrete sleeper was then placed on top and (red) shoulder ballast was placed around it (Fig. 6b). Five large-scale triaxial tests were carried out during which the amount of RC (0, 10, 20, 30 and 40%) in the SEAL was changed.

A maximum cyclic vertical stress of 230 kPa and a loading frequency of 15 Hz was adopted to simulate a train with a 25-tonne axle load running at 110km/h (Indraratna *et al.*, 2014; Navaratnarajah and Indraratna, 2017; Jayasuriya *et al.*, 2019). A lateral confining pressure $\sigma'_3 = 15kPa$ was applied in a transverse direction of the track to simulate the pressure provided by the crib and shoulder ballast in real track condition (Navaratnarajah *et al.* 2018). After each test, the ballast under the sleeper was sieved to examine the particle breakage. During the test, the specimen with 40% RC failed at around 1,500 cycles due to severe vibration and settlement,while all the othertests were completed successfully up to 500,000 cycles.

3.2 *Measured deformation responses*

The settlement and lateral displacement of the test specimen are shown in Figs7(a-b). Note that settlement increased as the loading cycles increased, while the vertical deformation of most specimensstabilised after 100,000 cycles with a strain accumulation rate of less than 5×10^{-8}. The only exception was the specimen with SEAL40 which failed within 1,500 cycles at a settlement of more than 40 mm. These results indicate that increasing

the RC content in SEAL increased the rate of settlement due to the high compaction of rubber materials. Lateral displacement of the test specimen reduced dilation when the amount of RC ($\leq$ 20%) in the SEAL mixtures increased, but then it fluctuated as more RC was added; this indicates that higher amounts of RC may destabilise the lateral deformation of a track.

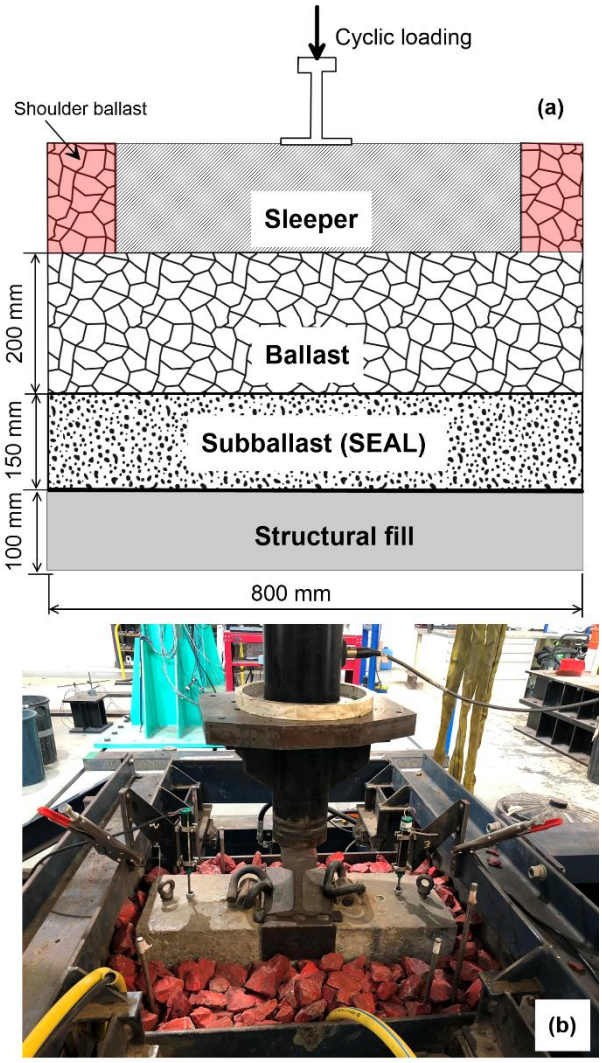

Fig. 6 (a) Schematic illustration of the physical model, (b) a prepared test specimen

Unlike the test specimen with traditional subballast materials tested by Navaratnarajah *et al.* (2018) and Jayasuriya *et al.* (2019) under the same loading conditions, the settlement of test specimens with SEAL0 and SEAL10 were comparable, but the lateral displacement of specimens with SEAL10 and SEAL20 had less dilation.

3.3 *Damping ratio and energy dissipation*

The damping capacity reflects the efficiency at which a material subjected to dynamic or cyclic loading can dissipate energy. To investigate the damping capacity of the test specimen, the damping ratio defined in Fig. 8a was adopted. As expected, the damping ratio increased as the amount of RC in SEAL increased due to the high damping property of rubber crumbs (Fig. 8a). The dissipated energy is the energy the test specimen will consume in terms of permanent deformation, ballast breakage, and heat and sound, etc. This energy can be calculated using the hysteretic loop area of the test specimen (Fig. 8a). The energy dissipated by the test specimen is shown in Fig. 8b; the damping ratio also has a similar trend. Note that the damping ratio and the dissipated energy of the test specimen with SEAL40 increasedmuch faster thanthe other test specimens. Most of the energy was dissipated by deformation which induced the test specimen with SEAL40 to settle deeply and rapidly, as shown in Fig. 7a.

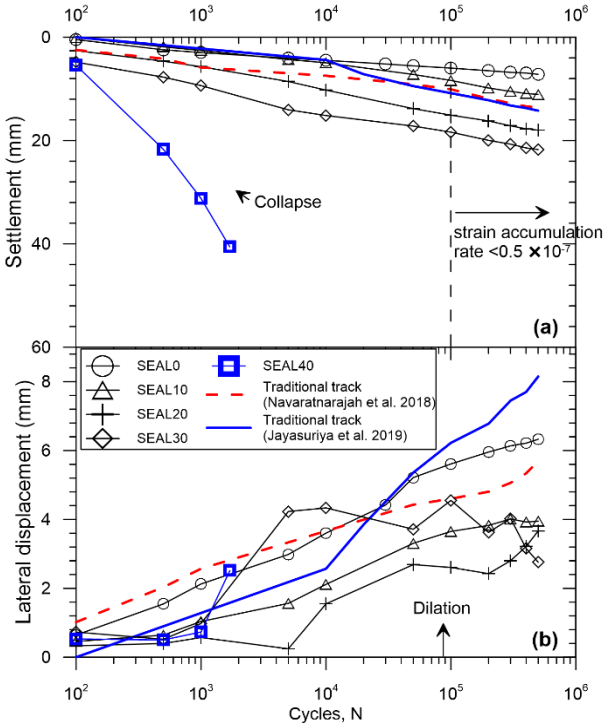

Fig. 7 Cubical triaxial test results: (a) settlement and (b) lateral displacement

3.4 *Ballast degradation (breakage)*

The particle degradation of ballast during cyclic loading was evaluated using the ballast breakage index (BBI) initially proposed by Indraratna *et al.* (2005). It is calculated based on the PSD shown before and after the test; the details are shown in Fig. 9a. The BBI of the test specimen with different amounts of RC is shown in Fig. 9b. As expected, the addition of RC (10%) in SEAL reducesd ballast breakage more than without RC, but

when more RC was added there was no significant reduction in the BBI, in fact it was even higher for the specimen with SEAL20. This maybe because when there is more than 20% RC, the skeleton of the SEAL materials is governed by the rubber particles. Therefore, the specimen with $R_b \geq 20\%$ tended to show a rubber-like behaviour which generated a lot of vibration when subjected to dynamic loading (Qi *et al.*, 2018a); and vibration will induce more ballast degradation.

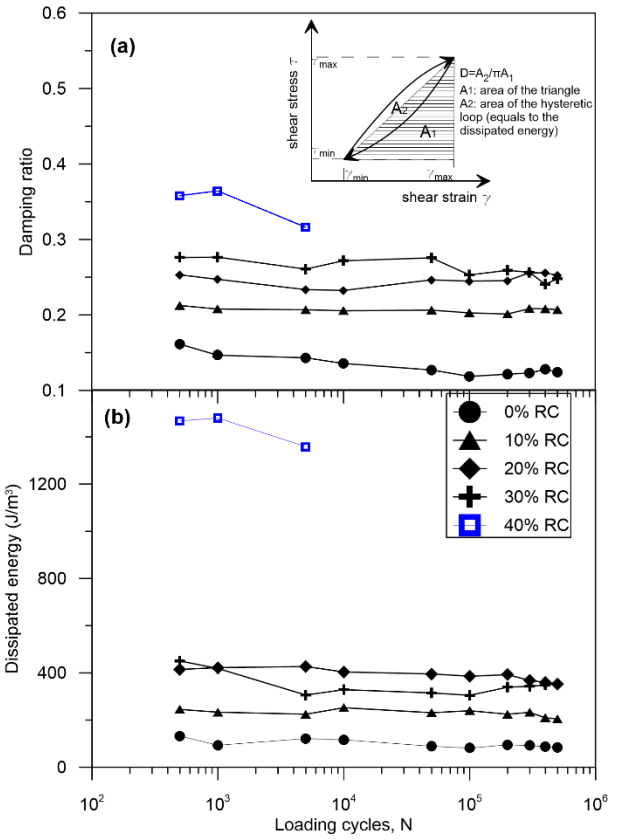

Fig. 8 Damping ratio and dissipated energy of the test specimen

4 USE OF GEOSYNTHETICS AND RECYCLED RUBBER MATS FOR RAIL SUBSTRUCTURE

Defects in rails or wheels such as wheel flats, dipped rails and corrugations and defective welds, may impart large impact forces onto the tracks. These impact loads can also be generated at transitions zones with different degrees of track stiffness such as bridges, tunnels, and road crossings. These loads exacerbate the deterioration of track elements and imply the need for more frequent maintenance (Indraratna 2019).

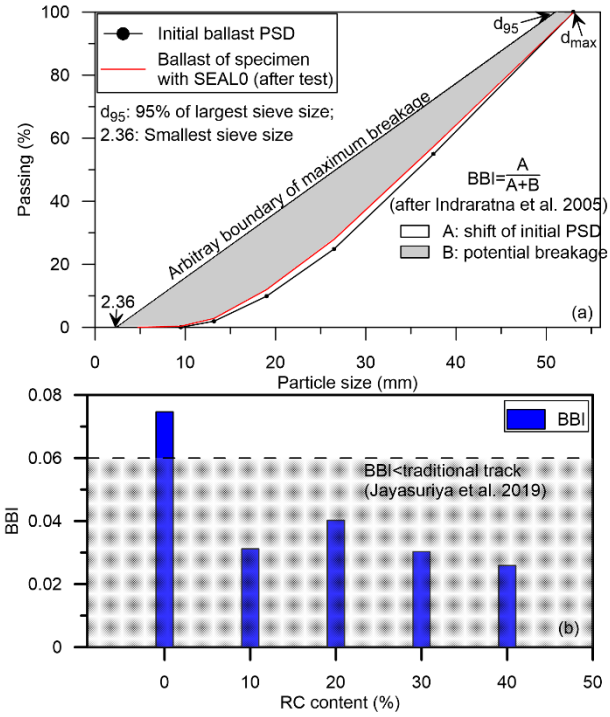

Fig. 9 (a) Definition of ballast breakage index (BBI), and (b) BBI of the test specimen after test

Large drop-weight impact test equipment (Fig.10a) developed at the UOW (Kaewunruen and Remennikov 2010) was used to study the improved performance of ballast reinforced by geogrids (Fig.10b) and resilient rubber mats (Fig.10c) subjected to repeated impact loads. This test apparatus can accommodate specimens within a working area of 1800 × 1500 mm. The transient impact forces are monitored by a dynamic load cell (capacity of 1200 kN) which is attached to the hammer and connected to an automatic data acquisition system. The permanent settlement and radial displacement of the test samples are measured manually after every drop. The free-fall hammer is positioned at the required drop height (h=150 mm) and released through an electronic quick release system. The selected drop height willproduce dynamic stresses that are similar to those generated by the wheelflats and dipped rail joints that aremeasured in the field (Ngo et al. 2019). Data is recorded by automatic triggering via the signal obtained as the hammer falls. Theacquisition frequency was at5000 Hz. The permanent vertical and lateral strains of the test sampleswere measured after each impact at predetermined locations. Allthe tests werecompleted after twelve impact blows due to ballast deformation.

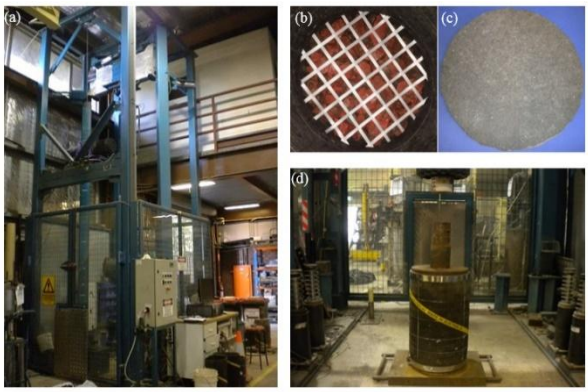

Fig.10(a) Drop-weight impact facility; (b) geogrid sample; (c) rubber mat; (d) assembly ready for testing

The axial and radial strains of ballast over the number of blows are plotted in Figs11a-b. As expected, the ballast deformed more as thenumber of blows progressed. The strain increased quickly as the ballast was rearranged and the corners broke off, but then the rate of strain gradually decreasedafter reaching a certain stage. It was obvious that the deformation of ballast could be mitigated by placing rubber mats either overor under the ballast layer, and moreover, with a rubber mat below the ballast and geogrid placed 100 mm higher will further reduce deformation as the ballast particles interlock within the geogrid apertures. This solution not only confines the ballast aggregates more, it also helps to reduce any lateral displacement.

Sections of tracks built at Bulli and Singleton, NSW were used to examine how geosynthetics and rubber mats improved the performance of ballasted tracks. The technical specifications of various materials used during construction are reported in Indraratna et al. (2010). The experimental sections of this track are monitored such that: (i) the vertical and horizontal displacementsare measured by settlement plates and digital displacement transducers installed at the sleeper-ballast and ballast-capping interfaces, and, (ii) the vertical and lateral stresses are measured by pressure plates.

The vertical and horizontal deformation of ballast is measured in the field at given time intervals. A relationship between the annual rail traffic in million gross tons (MGT) and the axle load (A_t) is needed to determine the number of load cycles N, as proposed by Selig and Waters (1994). This relationship is expressed as:$N_t = 106/(A_t \times N_c)$,where N_t, A_t and N_c are the numbers of load cycles per MGT, the axle load in tonnes, and the number of axles per load cycle (Powrie et al. 2007). When this relationship is used for a traffic tonnage of 60 MGT per year and four axles per load cycle, an axle load of 25 tonnes gives 600,000 load cycles per MGT.

A simple survey technique is then used to record changes in the reduced level of the tip of the settlement pegs. The average ballast settlement against the number of load cycles (N) is shown in Fig.12. Unlike fresh ballast, recycled ballast has less vertical and lateral deformation, possibly due to its moderately graded particle size distribution - PSD (C_u = 1.8) than the uniform PSD (C_u = 1.5) of fresh ballast. These results indicate that geocomposite reinforcement reduced the vertical (S_v) and lateral (S_l) deformation of fresh ballast by around 33% and 49 %, as well as reducing the vertical (S_v) and lateral (S_l) deformation of recycled ballast by about 9% and 11%, respectively. This result meansthe ballast layer candistribute the load better

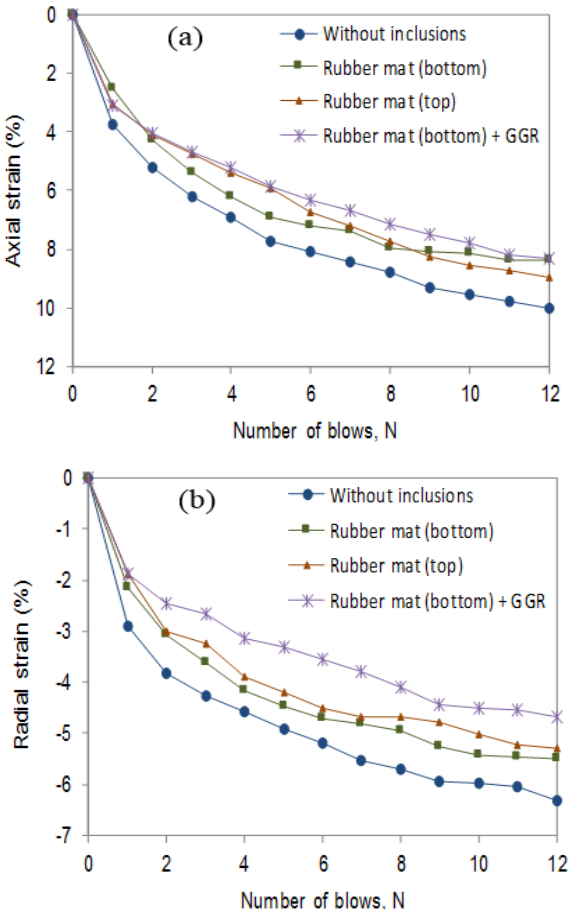

and substantially reduce settlement under high repeated loads.

Fig.11 The roleplayed by the locations of the rubber mas and geogrid inclusion on a) axial strain; b) radial strain (data source: Indraratna et al. 2019)

Figure 13a shows the peak cyclic vertical (σ_v) and lateral (σ_l) stresses recorded at Section 1 (i.e. fresh ballast without geocomposite) due to the passage of a coal train with an axle load of 25 tons. Field data shows that the peak cyclic vertical(σ_v)stressdecreased by 73 % and 82 % at depths of 300 mm and 450 mm, respectively. Thelateral stress (σ_l) only decreased marginally with depth, which meansthat artificial inclusions are needed

for additional restraints, and while most peak cyclic vertical stresses (σ_v) werealmost 230 kPa, one value of σ_v reached 415 kPa (Fig. 13b). This was later found to be associated with a wheel flat, thus proving that much larger stresses and large impact forces are exerted by imperfections in the wheels. The resulting particle breakage could be mitigated by a rubber mat, asIndraratna et al. (2014) showed in the Singleton study.

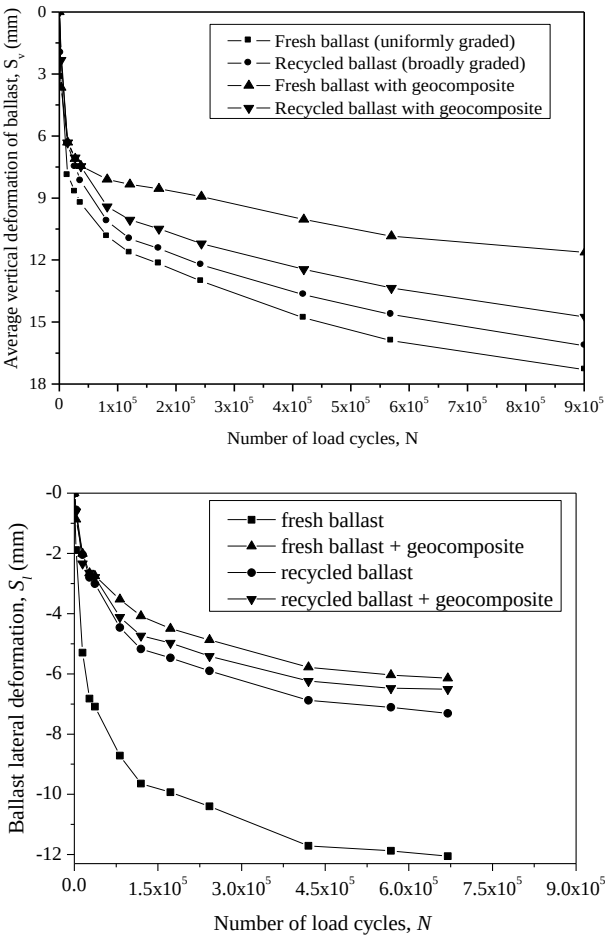

Figure 12. Average vertical deformations of the ballast (data source:Indraratna et al. (2010)-with permission from ASCE).

5 DISCRETE ELEMENT MODELLING OF IMPROVED TRACKS

The discrete element method (DEM) introduced by Cundall and Strack (1979)iswidely to study the behaviour of ballast because it can capture the discrete nature of aggregates which consist of arbitrarily-shaped discrete particles subjected to different loading and boundary conditions(Tutumluer et al. 2012, McDowell et al. 2006, O'Sullivan *et al.* 2008, Ngo *et al.* 2018, Indraratna et al. 2014, Lobo-Guerrero and Vallejo2006, Konietzky et al. 2004). Particle motion is determined using Newton's second law and the interaction between particles is determined using Newton's second law contact laws. At any given time, the force vector $\vec{F}$that represents the interaction between the two particles is resolved into normal ($\vec{F}_N$) and shear component ($\vec{F}_T$) with respect to the contact plane (Itasca 2016):

$$\vec{F}_N = K_N U^n \quad (5)$$

$$\delta\vec{F}_T = -K_T \cdot \delta U^s \quad (6)$$

where K_N, K_T: normal and shear stiffness, U^n: normal penetration between two particles,δU^s: incremental shear displacement, and $\delta\vec{F}_T$: incremental shear force.

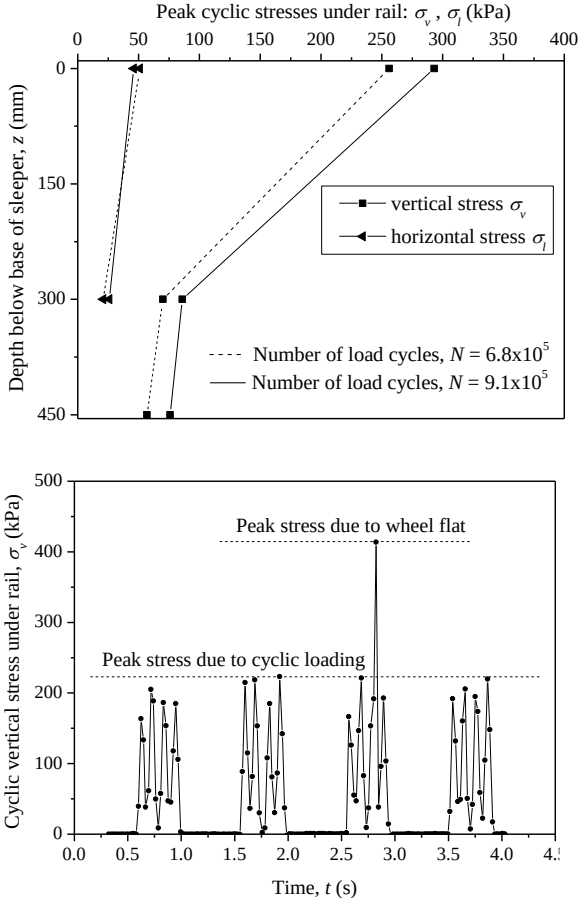

Fig. 13 Cyclic stresses induced by coal train with wagons (100 tons): (a) variation of stresses with depth, (b) additional stress due to wheel flat (data source: Indraratna et al. 2010)

The resistance moment, $\vec{M}_r$ *is* introduced to represent the restraint (i.e. interlocking) between the two particles A and B, and is determined by:

$$\vec{M}_r = \begin{cases} K_r\vec{\omega}_r & if \quad K_r\|\vec{\omega}_r\| < \|\vec{M}_r\|_{lim} \\ \|\vec{M}_r\|_{lim}\frac{\vec{\omega}_r}{\|\vec{\omega}_r\|} & if \quad K_r\|\vec{\omega}_r\| \geq \|\vec{M}_r\|_{lim} \end{cases} \quad (7)$$

where, $\|\vec{M}_r\|_{lim} = \eta_r\|\vec{F}_r\|\frac{R_A+R_B}{2}$;

$K_r = \gamma_r\left(\frac{R_A+R_B}{2}\right)^2$; $\vec{\omega}_r$ is a rolling angular vector representing the relative change in orientation between two particles, it can bedetermined by adding the angular vectors of the incremental rolling; η_r is the dimensionless coefficient, and γ_r is the coefficient of rolling resistance.

5.1 *Modelling irregularshaped ballast*

Ballast particles of variousshapes and sizes were simulated in DEM by clumping a lot ofspheres together to represent actual ballast gradation (Ngo *et al.* 2017), as shownin Fig. 14a.

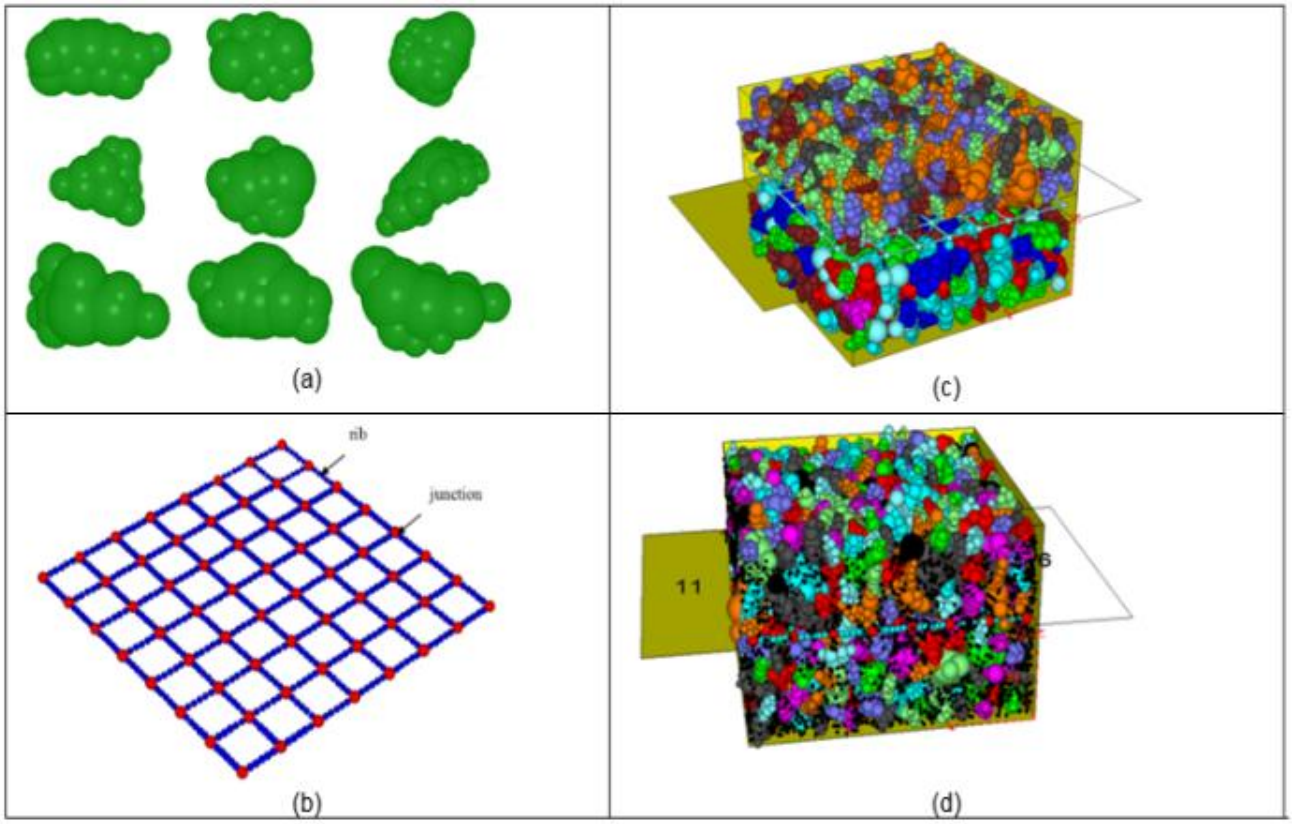

Fig 14. Simulated large-scale direct shear test for geogrid-reinforced ballast (modified after Ngo et al. 2014)

This clump approach is used to generate groups of slaved particles for modelling irregularshaped grains of ballast. The basic properties of a clump are its total mass (m); the location of the centre of itsmass ($x_i^{[G]}$); and the moments and products of inertia (I_{ii}),(I_{ij}). For a clump consisting of N_P particles, witha mass $m^{[p]}$, *a* radius $R^{[p]}$, and centroid location $x_i^{[p]}$, theproperties of this mass is defined by Itasca (2016) as:

$$m = \sum_{p=1}^{N_p} m^{[p]} \quad (8)$$

$$x_i^{[G]} = \frac{1}{m}\sum_{p=1}^{N_p} m^{[p]}x_i^{[p]} \quad (9)$$

$$I_{ii} = \sum_{p=1}^{N_p}\left\{m^{[p]}\left(x_j^{[p]} - x_j^{[G]}\right)\left(x_j^{[p]} - x_j^{[G]}\right) + \frac{2}{5}m^{[p]}R^{[p]}R^{[p]}\right\} \quad (10)$$

$$I_{ij} = \sum_{p=1}^{N_p}\left\{m^{[p]}\left(x_i^{[p]} - x_i^{[G]}\right)\left(x_j^{[p]} - x_j^{[G]}\right)\right\} \; ; \quad i \neq j) \quad (11)$$

The motion of a clump is calculated by the resultant force and moment vectors acting upon it. Because a clump has a rigid body, its motion is described as the translational motion of a point in the clump and the rotational motion of the entire clump. The equation for translational motion is expressed in the vector form:

$$F_i = m(\ddot{x}_i - g_i) \quad (12)$$

where F_i is the resultant force, the sum of all the externallyapplied forces acting on the clump, and

g_i is the body force acceleration vector arising from gravity loading.

5.2 *Modelling direct shear tests for geogrid-reinforced ballast*

Fig. 14 shows how DEM was usedto model ballast reinforced with geogrid in a direct shear test. A bi-axial geogrid with 40 mm × 40 mm apertures was modelled by bonding a number of small spheres together, just like thegeogrids tested in the laboratory (Fig.14b). The DEM of a largescale direct shear test of geogrid-reinforced fresh and 40%VCIfouled ballast are shown in Figs.14c-d.Thedimensions of this model are the same as those in the laboratory (300 mm long× 300 mm wide× 200 mm high). Ballast particles withvarious shapes and sizes weresimulated by clumping a lot ofspheres together to represent actual ballast gradation; they are then placed at random locations within the specified wall boundary without overlapping. The micro-mechanical parameters used to simulate ballast, geogrid and coal-fouling material were determined by calibrating them with the test data (Indraratna et al. 2011).

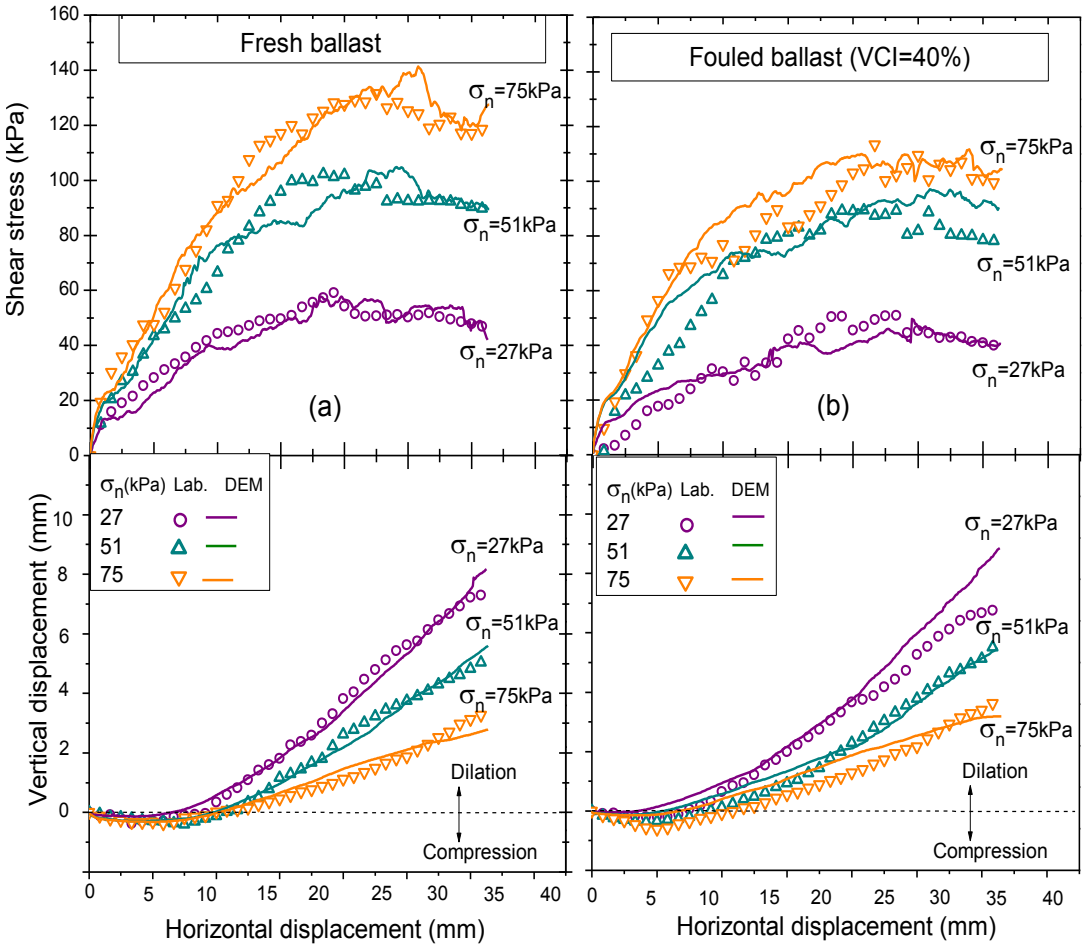

Fig 15. Comparisons of shear stress-strain of geogrid-reinforced ballast between laboratory test and DEM: (a) fresh ballast; and (b) 40%-VCI-fouled ballast (modified after Ngo et al. 2014

The DEM simulations of direct shear tests for fresh and fouled ballast with and without geogrid had three normal stresses of σ_n = 27, 51 and 75kPa. Fig.15compares the shear stress-strain behaviour of ballast from the DEM analysis and the behaviourmeasured with and without geogrid. Note that the simulation agreed reasonably well with the laboratory data by Indraratna *et al.*(2011) for a given normal stress. The strain softening of ballast and volumetric dilation occurred in all the simulations. Notethat the higher σ_n the greater the shear strength and the smaller the dilation; this was due to the ballast particles interlocking and the geogrid.

The strains that developed in the geogrids could not be measured because connecting the strain gauges to the geogrids was complex and preventing the strain gauges from being damagedby the sharp edges of ballast aggregates, as well as compaction,was very difficult (Brown et al. 2007, Duncan et al. 2008). However, the strain could be captured in the numerical simulation so it is presented here to complete the simulation results. Fig. 16shows the typical horizontal contours of strain

that developed across the geogrid at the end of the shear test (shear strain of 13%) offresh ballast. The simulated and actual deformed shape of the geogrid at the end of the test is shown in Figs 16c-d, respectively. Note that these strains developed non-uniformly across the geogrid and their magnitude depends on the degree of interlocking between the geogrid and ballast particles.To design rail tracks properly, understanding the geogrid-ballast interactions under various fouling conditions is imperative, as is the need to determine a threshold value of fouling for track maintenance.

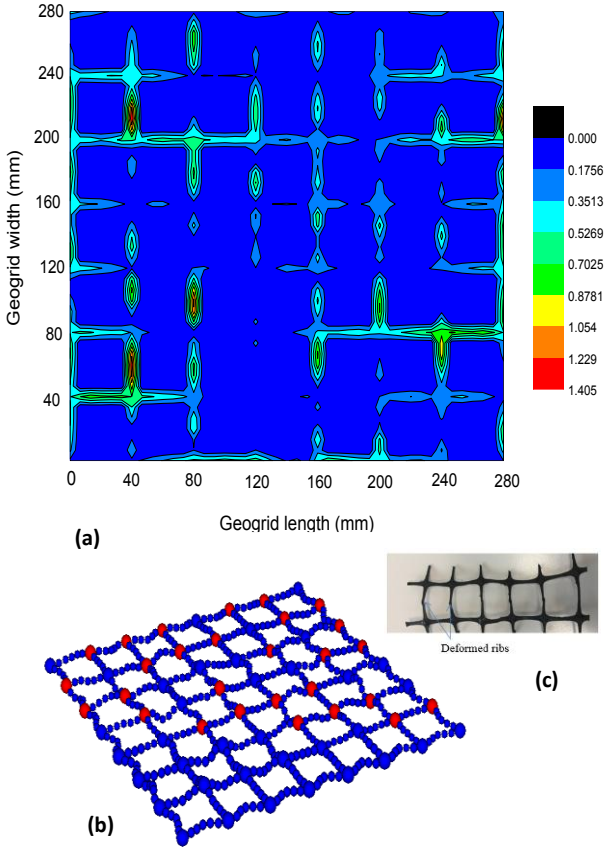

Fig 16. Contour strains developed across the geogrid; (b) simulated deformed geogrid; (c) deformed grid after test

6 FEM MODELLING OF SCRAP RUBBER TYRES FOR ENHANCED CONFINEMENT

Scrap tyres have been usedat UOW to confine the capping (sub-ballast) layer because they provide additional cellular confinement to the infilled-aggregates and also increase the strength and stiffness of railway tracks. Indraratna et al. (2017) proposed using rubber tyres as a base for the capping layer where one sidewall has been cut and the tyres areinfilled with aggregates. Previous studies revealed that from an engineering perspective, a tyre cell has three main effects: (i) it provides extra confinement which increases the stiffness; (ii) it providesa more uniform distribution of stress onto the subgrade; (iii) it will also increase damping all allow the track to attenuate dynamic forces.

Finite element modelling (FEM) was used to study the beneficial effect that recycled tyres have on track embankments, as shown in Fig.17. Details of the FEM model, including the loading and boundary conditions and model parameters can be found in Indraratna et al. (2019). These simulations showed that with waste tyres, the stress imparted onto the subgrade was almost 12% less than if there are no tyres (Fig. 18). This means that a capping layer stabilised with rubber tyres reduces the stress transferred onto the ballast and subgrade layers, mitigates ballast breakage and particle displacement, and enhances damping.

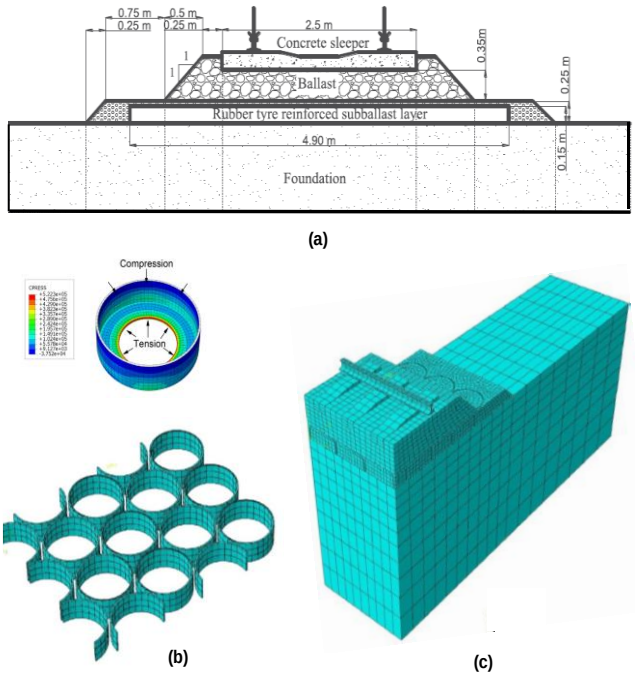

Fig. 17 (a) Track geometry with recycled rubber tyre, (b) FEM mesh for recycled rubber tyres, and (c) Simulated track section with tyres (*modified after Indraratna et al. 2019*)

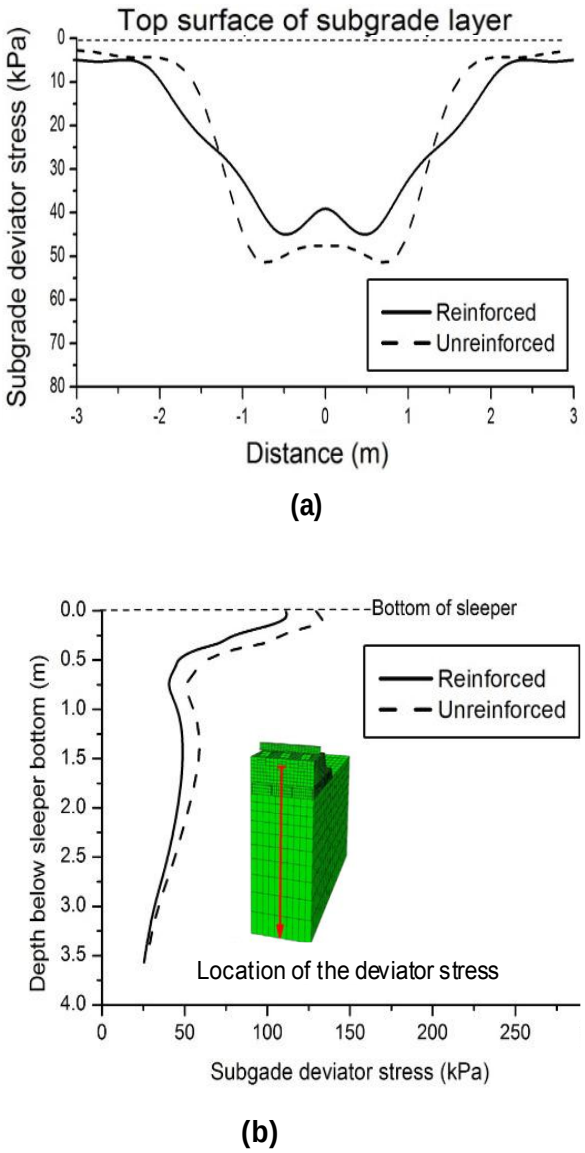

Fig. 18 (a) distribution of subgrade stress, and (b) distribution of stresses along the depth (*Indraratna et al. 2019*)

7 CONCLUSIONS

This paper has reviewed recent studies carried out at the University of Wollongong Australia, to examine the ability of artificial inclusions to minimize ballast deformation and breakage induced by heavy haul freight trains. A series of large-scale tests using the track process simulation testing apparatus were carried out. Computational modelling using DEM and FEM was also conductedto numerically study the micro-mechanical aspects of ballast aggregates and the interaction between the particles and inclusions. The following conclusions can be drawn:

- Vacuum-assistedconsolidation is very successful becausea vacuumhelps to reduce the surcharge height and reachthe same ultimate settlement anddegree of consolidation. Vacuum consolidation is an ideal way of controlling lateral displacement, especially for marine boundaries (e.g. Port of Brisbane) where strict environmental and aquatic regulations are needed to prevent turbidity. It has been previously shown that short PVDs can be used, even under rail tracks, to improve stability by dissipating excess cyclic pore pressure and curtailing lateral displacement.
- Physical model tests using large-scale cubical tri-axial apparatus was developed to investigate the performance of asynthetic energy absorbing layer (SEAL) for railway sub-ballast. The results indicate that when a proper range (i.e. 10%) of rubber crumbs (RC) are added to the SEAL waste mixture, the track specimen had comparable settlement, less lateral displacement, higher damping properties and less ballast degradation. However, adding too much RC (>20%) to the SEAL will cause dramatic settlement, lateral instability, and higher ballast breakage.
- The laboratory tests and DEM simulations on ballast reinforced by geogrids proved that geogrid reinforcement increased the shear strength and helped to controlthe permanent deformation of ballast. This wasattributed to the interlocking mechanism between the aggregates and geogrid which helped to improve the stability of the granular assembly and lead to a more uniform distribution of internal loads.
- An approach of confining the capping layer with recycled rubber tyres to increase the stability and resiliency of track substructure was tested using large-scale tests under cyclic loading conditions. FEM simulations on the use of tyres to provide additional confinement to ballasted tracks were also implemented. The laboratory and FEM results proved that recycled rubber tyres reduced the stress transmitted to the subgrade, a result that could lead to reducing the thickness of ballast and also eliminating the need to have a capping layer composed of natural rock aggregates.
- There is no doubt that the use of rubber products, particularly on harder subgrades, resulted in more resilient tracks with increased stability and longevity; a result with significant implications for the ongoing cost of track maintenance.

ACKNOWLEDGMENTS

The authors wish to acknowledge the Australian Research Council (ARC) and Industry partners for providing support through the ARC Industrial Transformation Training Centre for Advanced Technologies in Rail Track Infrastructure (ITTC-Rail). The efforts of previous PhD students and post-doctoral research fellows, Dr. Sanjay Nimbalkar, Dr ChamindiJayasuriya,Dr. NavaNavaratnarajah, Dr. Qideng Sun, among others, that have contributed to the contents of this paper are also gratefully appreciated, as is the support of A/Prof. Jayan Vinod and Dr. Ana Heitor. The authors sincerely acknowledge Rail Manufacturing Cooperative Research Centre (funded jointly by particpatingrail organisations and the Australian Federal Government's Business Cooperative Research Centres Program) through two Projects, R2.5.1 and R2.5.2. The authors also thank the Australasian Centre for Rail Innovation (ACRI), Global Synthetics, Naue GmbH & Co. KG and Foundation Specialists Group. Salient contents from past articles (ASCE Journal of Geotechnical & Geoenvironmental Engineering, Computers and Geotechnics, Int. J. of Geomechanics, Geotechnique) have been reproduced here with kind permission from the original sources.The authors are also grateful to Cameron Neilson, Duncan Best, Richard Berndt and other CME-technician for their assistance during the laboratory and field tests. The authors also thank Robert Clayton (English editor) for proofreading and professionally editing the manuscript.

REFERENCES

AS-2758.7 (2015). Aggregates and rock for engineering purposes, Part 7: Railway ballast. Sydney, New South Wales, Australia, Standard Australia.

Aursudkij, B., McDowell, G.R. and Collop, A.C. (2009). Cyclic loading of railway ballast under triaxial conditions and in a railway test facility. Granular Matter,11, 391–401.

Biabani, M.M., Ngo, N.T. and Indraratna, B. (2016). "Performance evaluation of railway subballast stabilised with geocell based on pull-out testing." Geotextiles and Geomembranes, 44(4), pp: 579-591.

Baral P, Rujikiatkamjorn C, Indraratna B (2019). Radial consolidation analysis using delayed consolidation approach, Journal of Geotechnical and Geoenvironmental Engineering (in press).

Brown, S.F., Kwan, J. and Thom, N.H. (2007). Identifying the key parameters that influence geogrid reinforcement of railway ballast. Geotextiles and Geomembranes, 25(6), 326-335.

Chen, W.-B., Yin, J.-H., Feng, W.-Q., Borana, L. and Chen, R.-P. (2018). Accumulated permanent axial strain of a subgrade fill under cyclic high-speed railway loading. International Journal of Geomechanics, 18(5), 04018018.

Cundall, P.A. and Strack, O.D.L. (1979). A discrete numerical model for granular assemblies. Géotechnique, 29(1), 47-65.

Indraratna, B., Ngo, N.T. and Rujikiatkamjorn, C. (2011). Behavior of geogrid-reinforced ballast under various levels of fouling. Geotextiles and Geomembranes, 29(3), 313-322.

Indraratna, B., Nimbalkar, S.S., Ngo, N.T. and Neville, T. (2016). Performance improvement of rail track substructure using artificial inclusions – Experimental and numerical studies. Transportation Geotechnics, 8, 69-85.

Duncan-Williams, E. and Attoh-Okine, N.O. (2008). Effect of geogrid in granular base strength - An experimental investigation. Construction and Building Materials, 22(11), 2180-2184.

Huang, H., Tutumluer, E., Hashash, Y.M.A. and Ghaboussi, J. (2009). "Discrete element modeling of aggregate behavior in fouled railroad ballast." Geotechnical Special Publication, 192, pp: 33-41.

Itasca (2016). Particle flow code in three dimensions (PFC3D). . Itasca Consulting Group, Inc., Minnesota.

Indraratna, B., Sun, Q., Heitor, A. and Grant, J. (2017). Performance of Rubber Tire-Confined Capping Layer under Cyclic Loading for Railroad Conditions. Journal of Materials in Civil Engineering, 30(3), 06017021.

Indraratna, B., Nimbalkar, S., Christie, D., Rujikiatkamjorn, C. and Vinod, J. (2010). Field assessment of the performance of a ballasted rail track with and without geosynthetics. Journal of Geotechnical and Geoenvironmental Engineering, 136(7), 907-917.

Indraratna, B., Ngo, N.T., Rujikiatkamjorn, C. and Vinod, J. (2014). Behaviour of fresh and fouled railway ballast subjected to direct shear testing - a discrete element simulation. International Journal of Geomechanics, ASCE, 14(1), 34-44.

Indraratna, B. and Ngo, T. (2018). Ballast Railroad Design: Smart-Uow Approach, CRC Press, Taylor & Francis Group.

Indraratna B. 2010. 2009 EH Davis Memorial Lecture: Recent advances in the application of vertical drains and vacuum preloading in soft soil stabilization. Australian Geomechanics Journal, AGS 45(2):1-43

Indraratna, B., Ngo, N.T., Sun, Q., Rujikiatkamjorn, C. and Ferreira, F.B. Concepts and Methodologies for Track Improvement and Associated Physical Modelling and Field Moni-toring.: Geotechnics for Transportation Infrastructure. Lecture Notes in Civil Engineering, vol 28. pp. 219-246. Springer Singapore (2019).

Indraratna, B., Nimbalkar, S. and Neville, T. (2014). Performance assessment of reinforced ballasted rail track. Proceedings of the ICE - Ground Improvement, 167, 24-34.

Indraratna, B., Rujikiatkamjorn C., and Sathananthan, I. 2005. Analytical and numerical solutions for a single vertical drain including the effects of vacuum preloading. Canadian Geotechnical Journal, 42: 994-1014.

Indraratna, B., Bamunawita, C., and Khabbaz, H. 2004. Numerical modeling of vacuum preloading and field applications. Ca-nadian Geotechechnical Journal, 41: 1098-1110.

Indraratna, B., Lackenby, J. and Christie, D. (2005). Effect of confining pressure on the degradation of ballast under cyclic loading. Géotechnique 55(4): 325-328.

Indraratna, B., Qi, Y. and Heitor, A. (2017). Evaluating the properties of mixtures of steel furnace slag, coal wash, and rubber crumbs used as subballast. Journal of Materials in Civil Engineering 30(1): 04017251.

Lobo-Guerrero, S. and Vallejo, L.E. (2006). Discrete element method analysis of railtrack ballast degradation during cyclic loading. Granular Matter, 8(3-4), 195-204.

Feng, B., Park, E.H., Huang, H., Li, W., Tutumluer, E., Hashash, Y.M.A. and Bian, X. Discrete Element Modeling of Full-Scale Ballasted Track Dynamic Responses from

an Innovative High-Speed Rail Testing Facility. Transportation Research Record, 0(0), 0361198119846475.

Indraratna, B., Qi, Y., Ngo, T.N., Rujikiatkamjorn, C., Neville, T., Ferreira, F.B. and Shahkolahi, A. (2019). Use of geogrids and recycled rubber in railroad infrastructure for enhanced performance. Geosciences, 9(1), 30.

Feng, S.-J., Liu, X., Chen, H.-X. and Zhao, T. (2018). Micromechanical analysis of geomembrane-sand interactions using DEM. Computers and Geotechnics, 94, 58-71.

Fernandes, G., Palmeira, E.M. and Gomes, R.C. (2008). Performance of geosynthetic-reinforced alternative sub-ballast material in a railway track. Geosynthetics International,15(5), 311-321.

Kaewunruen, S. & Remennikov, A.M. 2010. Dynamic crack propagations in prestressed concrete sleepers in railway track systems subjected to severe impact loads. Journal of Structural Engineering, ASCE 136(6): 749-754.

Konietzky, H., te Kamp, L. and Groeger, T. (2004). "Use of DEM to model the interlocking effect of geogrids under static and cyclic loading." Numerical Modeling in Micromechnics via Particle Methods.

Jayasuriya, C., Indraratna, B. and Ngo, T. N. (2019). Experimental Study to Examine the Role of Under Sleeper Pads for Improved Performance of Ballast under Cyclic Loading. Transportation Geotechnics 19: 61-73.

McDowell, G.R., Harireche, O., Konietzky, H., Brown, S.F. and Thom, N.H. (2006). Discrete element modelling of geogrid-reinforced aggregates. Proceedings of the ICE - Geotechnical Engineering 159(1), 35-48.

Mohamedelhassan E., and Shang, J.Q. 2002. Vacuum and surcharge combined one-dimensional consolidation of clay soils, Canadian Geotechnical Journal, 39: 1126-1138.

Navaratnarajah, S. K. and Indraratna, B. (2017). Use of rubber mats to improve the deformation and degradation behavior of rail ballast under cyclic loading. Journal of geotechnical and geoenvironmental engineering 143(6): 04017015.

Navaratnarajah, S. K., Indraratna, B. and Ngo, N. T. (2018). Influence of under sleeper pads on ballast behavior under cyclic loading: experimental and numerical studies. Journal of Geotechnical and Geoenvironmental Engineering 144(9): 04018068.

Ngo, N.T., Indraratna, B. and Rujikiatkamjorn, C. (2014). DEM simulation of the behaviour of geogrid stabilised ballast fouled with coal. Computers and Geotechnics, 55, 224-231.

Ngo, N.T., Indraratna, B. and Rujikiatkamjorn, C. (2017). A study of the geogrid–subballast interface via experimental evaluation and discrete element modelling. Granular Matter, 19(3), 54.

Ngo, T.N., Indraratna, B. and Rujikiatkamjorn, C. (2019). Improved performance of ballasted tracks under impact loading by recycled rubber mats. Transportation Geotechnics, 20, 100239.

Ngo, N.T., Indraratna, B., Ferreira, F.B. and Rujikiatkamjorn, C. (2018). Improved performance of geosynthetics enhanced ballast: laboratory and numerical studies. Proceedings of the Institution of Civil Engineers-Ground Improvement, 171(4), 202-222.

O'Sullivan, C., Cui, L. and O'Neill, C. (2008). "Discrete element analysis of the response of granular materials during cyclic loading." Soils and Foundations, 48(4), pp: 511-530.

Powrie, W., Yang, L.A. and Clayton, C.R.I. (2007). Stress changes in the ground below ballasted railway track during train passage. Proceedings of the Institution of Mechanical Engineers: Part F: Journal of Rail and Rapid Transit, 247-261.

Qi, Y., Indraratna, B., Heitor, A. and Vinod, J. (2019). The influence of rubber crumbs on the energy absorbing property of waste mixtures. Geotechnics for Transportation Infrastructure. Sundaram R., S. J., Havanagi V. Singapore, Springer. 29: 271-281.

Qi, Y., Indraratna, B., Heitor, A. and Vinod, J. S. (2018a). Effect of rubber crumbs on the cyclic behavior of steel furnace slag and coal wash mixtures. Journal of Geotechnical and Geoenvironmental Engineering 144(2): 04017107.

Qi, Y., Indraratna, B. and Vinod, J. S. (2018b). Behavior of Steel Furnace Slag, Coal Wash, and Rubber Crumb Mixtures with Special Relevance to Stress–Dilatancy Relation. Journal of Materials in Civil Engineering 30(11): 04018276.

Qi, Y., Indraratna, B. and Vinod, J. S. (2018c). Dynamic Properties of Mixtures of Waste Materials. GeoShanghai International Conference, Springer.

Rujikiatkamjorn, C., Ngo, N.T., Indraratna, B., Vinod, J. and Coop, M. (2013). Simulation of fresh and fouled ballast behavior using discrete element method. Proceedings of the International Conference on Ground Improvement and Ground Control, (pp. 1585-1592). Singapore: Research Publishing.

Selig, E.T. and Waters, J.M. (1994). Track geotechnology and substructure management, Thomas Telford, London.

Sun, Q., Indraratna, B. and Ngo, N.T. (2019). Effect of increase in load and frequency on the resilience of railway ballast. Géotechnique, 69(9), 833–840.

Suiker, A.S.J., Selig, E.T. and Frenkel, R. (2005). Static and cyclic triaxial testing of ballast and subballast. Journal of Geotechnical and Geoenvironmental Engineering, ASCE 131(6), 771–782.

Tutumluer, E., Huang, H. and Bian, X. (2012). "Geogrid-aggregate interlock mechanism investigated through aggre-gate imaging-based discrete element modeling approach." International Journal of Geomechanics, 12(4), pp: 391-398.

Zhai, W.M., Wang, K.Y. and Lin, l.H. (2004). "Modelling and experiment of railwayballast vibrations." Journal of Sound and Vibration, 673–683, pp: 673–683.

Lessons learned from failures of embedded retaining walls

B. Simpson
Arup, London, UK

ABSTRACT: Embedded retaining walls are widely used, generally successfully, in both permanent and temporary states for construction of deep excavations, including quay walls. This paper sets out to draw lessons from some situations in which walls have failed, causing considerable expense or casualties. Using a categorisation of failure types presented in Eurocode 7, the series of decisions that led to the failures is discussed in each case, showing a strong emphasis on the need for good, clear communication, systematic checking and informed consideration of overall equilibrium of the design situation, adequate safety provisions, vertical as well as horizontal equilibrium, and the possible brittleness of some structural elements.

1 INTRODUCTION

Embedded retaining walls include slurry-trench diaphragm walls, piled concrete walls and driven steel sheet-piled walls. Their common feature is that they are usually constructed from ground level before an excavation is formed, in order to support the sides of the excavation. Their "embedment" implies that they get some of their support from the passive resistance of the ground below the level of the excavation as it progresses.

Embedded walls are widely used to support the sides of excavations for deep basements and most forms of underground infrastructure. They are also used in quay walls, where the excavation may be in the form of dredging in front of the wall, or filling may take place behind them.

Use of embedded retaining walls is usually successful, with principle concerns centering on issues of ground movement and its effect on nearby structures (serviceability limit states). However, more severe failures (ultimate limit states) occasionally occur and Eurocode 7 (BSI 2013) shows a series of possible failure modes that should be considered during the course of design. These are collected together in Fig. 1, which will be used as a reference for the cases studied in this paper.

The series of decisions that led to the failures is discussed in each case, showing a strong emphasis on the need for good, clear communication, systematic checking, and informed consideration of overall equilibrium of the design situation, and the brittleness of some structural elements.

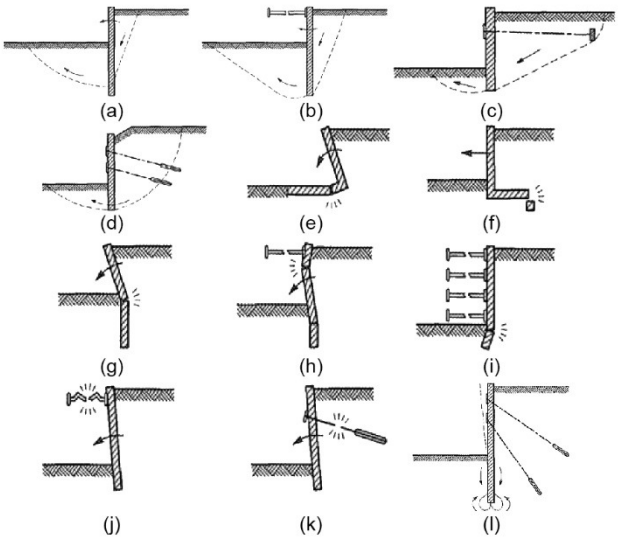

Fig. 1 Failure modes for embedded retaining walls as depicted by Eurocode 7.

2 THINK OF THE BIG PICTURE

2.1 *Construction and history of a quay wall*

Fig. 2 is a schematic diagram of a quay wall originally constructed in the UK early in the 20th century, and subject to later modifications to its configuration. Unlike most embedded walls, this one was built in an open trench. It consisted of steel joists at about 2.5m centres driven about 2m into the bottom of the trench; then unreinforced, curved concrete panels were placed between the joists as backfill was brought up, presumably on both sides

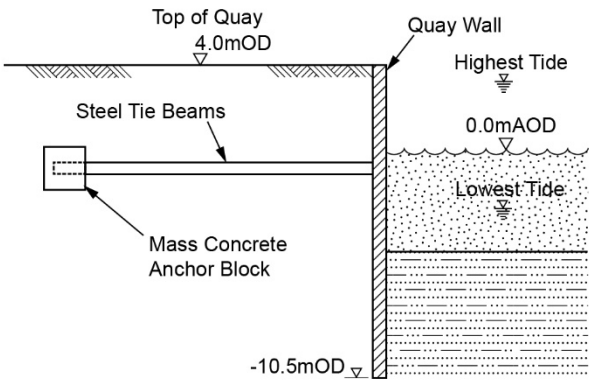

Fig. 2 Quay wall tied back to an anchor block.

of the wall until a tie could be placed to connect the wall to an anchor block. The ties, which were welded to the steel joists, were steel beams and the anchor block was 1m high. The main material surrounding the wall consisted of firm glacial clay with some gravel, much of it placed as fill.

Following construction, the dock was flooded, and the bed level was as shown in Fig. 2. Later in the 20th century, the dock was used as a dry dock. For this purpose, a large berm was placed against the wall and the base of the dock was lowered, as shown in Fig. 3. Subsequently, it was desired to use the dock as a wet dock again, allowing large vessels to access the quayside, and retaining the deeper base level. It was believed that the berm could be removed, leaving the configuration as shown by the broken line in Fig. 3, with the dock again filled with water.

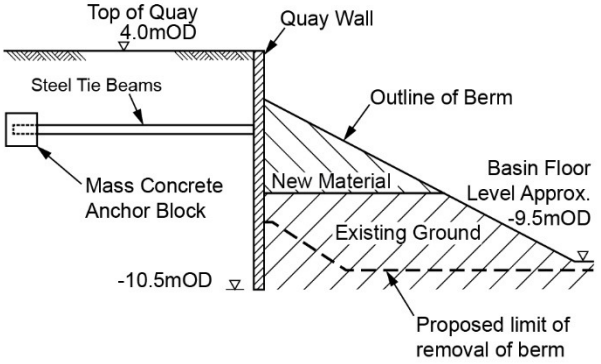

Fig. 3 Berm used for dry dock and proposed limit of removal of berm for wet dock.

2.2 *Removal of the berm*

During excavation of the berm, by dredging from the quayside, a crack was noted in the ground some distance back from the wall. This was located just behind the anchor block, though this might not have been appreciated at the time. Communications between the engineers designing the works and the client seem to have been rather unclear, and the client instructed further dredging a few months later. At this point the crack became alarmingly wide, the wall had moved forward and downwards by hundreds of millimetres, so it was necessary to stop excavation and backfill rapidly. This entailed considerable expense because use of the dock was already booked, and a stronger piled wall had to be constructed very quickly.

2.3 *Reasons for the problem*

To justify excavation of the berm, the stability of the wall had been checked using commonly available software for embedded walls, which essentially checks the horizontal equilibrium of active and passive pressures, treating the tie as a fixed point. This checks failure mode (b) in Fig. 1. Such programs do not consider the overall picture, including the length of the tie and the location of the anchor block – mode (c) in Fig. 1.

Fig. 4 shows a finite element analysis representing the state of the dredging with major movement occurred. This shows the failure extending back to include the anchor block, thus explaining the observed crack at ground level.

Engineers must not allow their thinking to be constrained by the software at hand. Computer programs generally provide answers to the limited questions for which they were designed, but it is the engineer's responsibility to make sure that all possible failure modes have been properly considered and eliminated – "Think of the big picture".

Communication was also a major problem. Engineers must be "brave enough to be afraid" when something is visibly going wrong and must make this known to relevant parties, in this case the client who controlled the dredging.

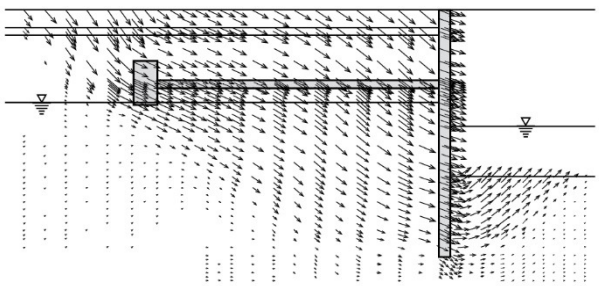

Fig. 4 Finite element computation for situation when failure occurred.

3 BEWARE BRITTLE COMPONENTS

3.1 *Brittleness*

In this paper the term "brittle" will be taken to describe a material or component that achieves a certain peak strength and thereafter loses strength as it deforms further. The loss of strength may be gradual and partial or sudden and complete.

The case described here is an example of failure mode (k) in Fig. 1.

3.2 *Quay wall restrained by high tensile tie bars*

Fig. 5 shows the intended configuration of a quay wall built on a river bank. Backfill was to be placed above the sloping river bank to provide a level quay behind the wall. The wall was tied back to an anchor wall with 22.5m long high tensile steel bars, varying in diameter up to 100mm.

The wall itself was a "combi-wall" consisting of 1220mm diameter steel "soldier piles" at 3.1m centres, separated by three Larssen sheet piles, as shown in Fig. 6. The steel tie rods were to be connected to the soldier piles by embedding them in concrete within the piles, having attached an anchor plate to them with a large nut.

The steel tie bars were laid in trenches in the natural ground and on the surface of the backfill, before being buried in more backfill. Because it was thought that this process might lead to some settlement, pushing the bars downwards, they were laid in the bottom of 250mm plastic sleeves, so that the sleeves could settle 150mm or more before any downward force was applied to the bars.

Shortly after the construction was finished, the wall was observed to move forward a few hundred millimetres. On excavating behind the wall, it was seen that some of the bars had pulled out of the combi-piles, and it was concluded that either the nuts attaching the bars to the anchor plates were missing, or they had not been screwed on adequately.

3.3 *Remedials – and second failure*

To remedy this situation, it was proposed to weld additional fixing plates to the combi-piles and to the high tensile steel bars, as shown in Fig. 7(a and b). The consulting engineer for the project questioned whether the high tensile steel could be welded, but the manufacturer said it could, and so the contractor proceeded with the remedial work.

The backfill was replaced, and, again, shortly afterwards the wall moved forwards appreciably. On excavating once more, it was found that some of the steel bars had snapped – a very clean vertical break through the bars – close to their welded junction with the added fixing plates. Metallurgical investigation showed that the high tensile steel had

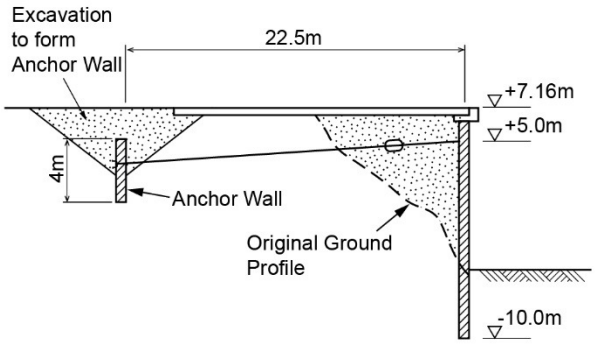

Fig. 5 Quay wall tied back with high tensile steel bar.

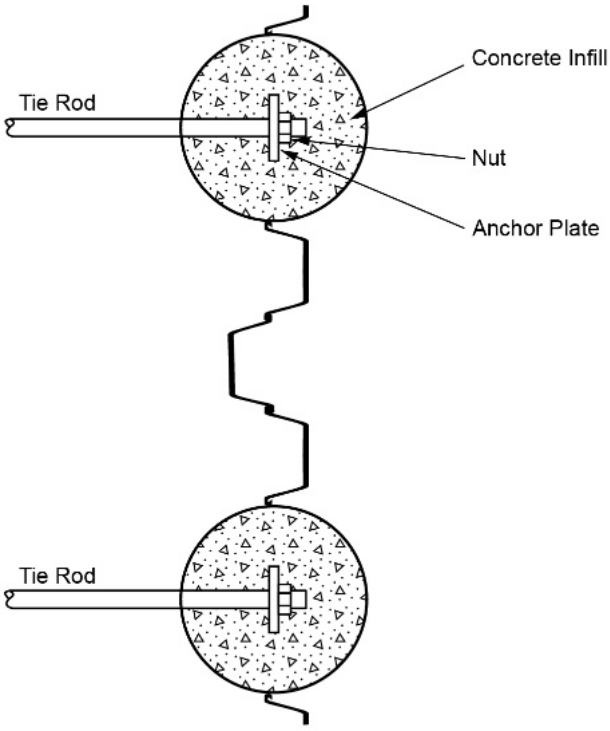

Fig. 6 Detail of attachment of bar to combi-wall.

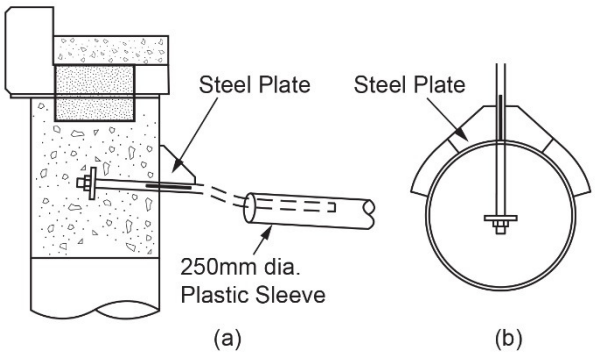

Fig. 7 Tie rod with welded fixing plates – (a) section and (b) plan.

undergone hydrogen embrittlement caused by the welding.

Photographic evidence of the excavation suggests that there had been considerable settlement of the fill material, lowering the plastic sleeves onto the bars and bending them down as shown in Fig. 7(a). It may be fairly common for settlement to drag down steel ties, in the manner shown by the bar in Fig. 7(a) (the broken lines). If this happens, the bars' behaviour may become plastic in bending, but this does not necessarily destroy their ability to take the longitudinal tensile forces for which they are designed. However, the embrittled steel could not bend as shown, and this probably explains why the bars snapped cleanly. Once having been broken, essentially by bending, they were unable to provide the required tensile capacity.

3.4 *Lessons to learn from this case*

No problem was caused by the original design of the wall, so the first obvious lesson is to improve the quality of construction and checking. The situation with regard to the remedial works is more confused: the designer was uncomfortable with the proposed welding of high tensile steel but he was told that the manufacturers claimed that it could be done. In fact, such welding may well be possible in very carefully controlled "factory" conditions, allowing slow cooling after welding, but not in the typical conditions of a construction site. Both designer and contractor should have been more persistent in questioning the validity of this unusual approach. Again the issue of clear and decisive communication between the parties is of paramount importance.

Finally, any design or construction procedure that could introduce a brittle element in to the construction must be reviewed with the utmost care.

4 GEOMETRIC UNCERTAINTY

4.1 *Eurocode 7*

In addition to requirements for factors of safety, Eurocode 7 has a special geometric safety requirement for embedded walls partly restrained by passive earth pressures, as illustrated in Fig. 8. When there is a "normal degree" of construction control, EC7 requires that in the design calculations the level of the resisting soil should be lowered below the nominally expected level by 10% of the retained height for cantilevers, or by 10% of the height below the lowest support for propped or anchored walls.

The case presented here illustrates the reason for this requirement. The type of failure is mode (b) in Fig. 1.

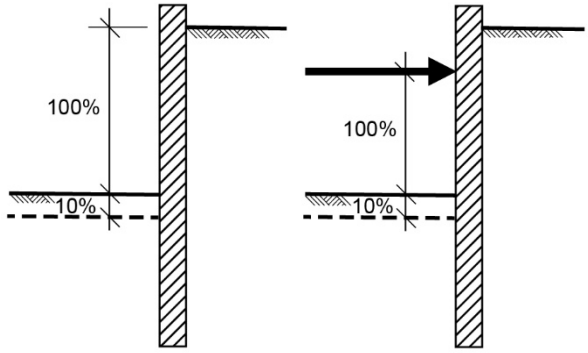

Fig. 8 Eurocode 7 requirement for unplanned excavation.

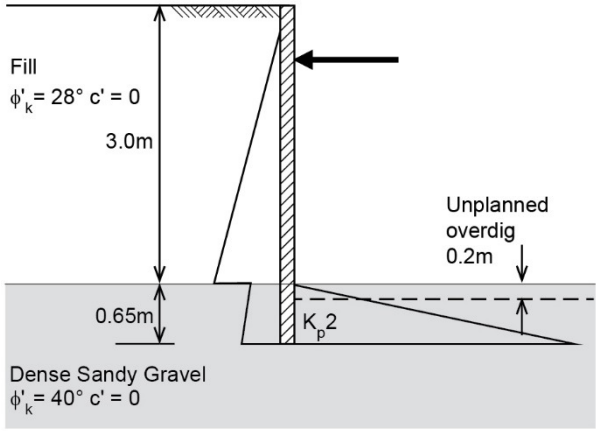

Fig. 9 Wall with small penetration into dense gravel.

4.2 *Propped sheet pile wall*

Figure 9 shows the situation of a small sheet pile wall used for temporary works. It relied on passive resistance derived from dense sandy gravel, for which design calculations showed that a penetration of 0.65m was adequate. So it was driven to a depth of 3.65m from ground level.

During excavation, it was found that the interface between the fill and the dense sandy gravel was slightly lower than anticipated, probably by about 0.2m. Consequently, there was inadequate passive restraint and the wall failed by the toe kicking forward. Had it been compliant with Eurocode 7, it would have been designed to accept a variation in geometric dimensions slightly more than the amount that occurred.

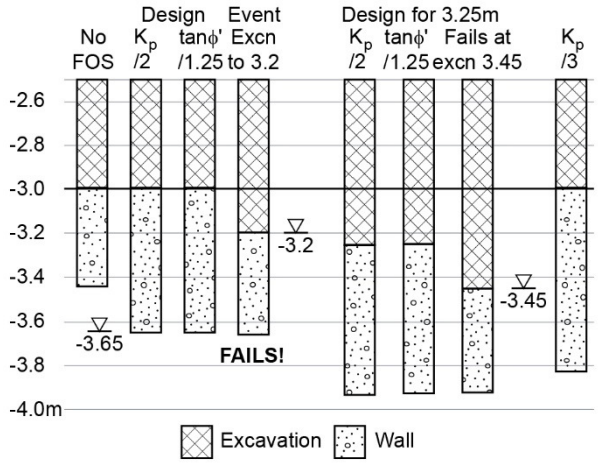

Fig. 10 Comparative wall lengths for wall penetrating into gravel.

4.3 *Comparative designs*

The results of comparative design calculations are illustrated in Figure 10, which will be described here in sequence from left to right. Assuming the type of earth pressure distribution shown in Figure 9, and the anticipated depth to the gravel of 3m, the wall would have had a factor of safety of 1.0 with a length from original ground level of 3.43m. It was actually designed by applying a factor of 2 to the passive resistance (K_p), requiring a length of 3.65m. If, instead, the calculations had used Eurocode 7's factors of safety, following the UK or several other national annexes, the soil's frictional strength, represented by tanϕ' would be reduced by a factor of 1.25 with no further reduction of the passive resistance. In this case, the resulting length would have been almost unchanged at 3.65m.

A wall length of 3.65m is inadequate if the ground surface on the passive side is 0.2m lower, so the wall failed. If the calculations had followed the full EC7 requirements, it would have been designed for the surface of the gravel on the passive side to be 0.25m lower, and so would not have failed. In fact, failure would not occur until the excavation was extended to 3.45m, by which time the over-excavation might well have been noticed and stopped.

Simply increasing the factor of safety is not as effective as direct allowance for variation in geometry. If the wall had originally been designed for a factor of safety of 3 on passive pressure ($K_p/3$), it would probably have accommodated the 0.2m overdig, but it would not be as effective as the requirements of EC7.

4.4 *Discussion*

It is acknowledged that the calculations used here are slightly conservative. It would be possible to redistribute the earth pressure upwards onto the prop, allowing slightly shorter walls for each calculation. Nevertheless, the principle illustrated holds good for all types of calculation.

The principle behind the EC7 requirement is to accommodate a magnitude of variation in geometry that might be overlooked as insignificant during construction, but which is actually of critical importance. In some cases, such as this, factors of safety are unlikely to accommodate even small variations in geometry. For this purpose, it was judged appropriate to require "10% of the retained height for cantilevers, or by 10% of the height below the lowest support".

5 BEWARE VERTICAL EQUILIBRIUM

5.1 *Sheet pile wall in very soft alluvium*

Fig. 11 shows a sheet pile wall, supported by steeply inclined tubular steel piles, constructed in very soft alluvium that had accumulated in a disused tidal basin. The intention was to allow fill to be placed behind the wall to form a working surface that could be used as a car park.

In various ground investigations, the alluvium was described as very soft clay, or silty clay, or clay/silt or silt, often with up to 10% organic content. The common feature was that it was very soft, and it seems to have been accumulated during less than 100 years before the construction works.

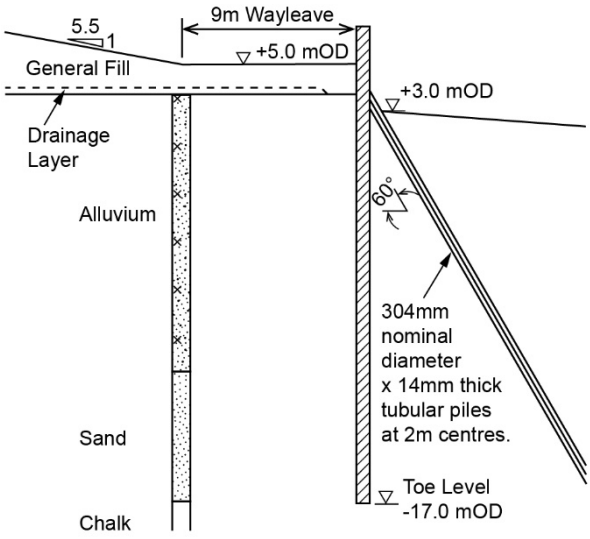

Fig. 11 Propped sheet pile wall in very soft alluvium.

Shear strengths are difficult to measure in such soft material, but the available CPT and vane test results suggest that the peak undrained shear strength of the material increases for about 4kPa near the surface to 8kPa at the base of the alluvium. Measurements of residual strength gave values in the range 1 to 3kPa. These strengths suggest that the alluvium is under-consolidated. At the location of the wall, the ground had been disturbed significantly by previous attempts at construction, so it is possible that available strengths were tending towards residual values.

5.2 *Construction and filling*

In order to install the wall, a double-skin cofferdam was first constructed to provide an access road for plant. This displaced sideways 10 metres, but nevertheless performed its function. The tubular steel piles and sheet piles were then driven and connected, and filling began behind the wall.

The wall was extensively monitored as filling took place, and it was observed that its top was moving forward. The observations also show that it initially moved upwards, so its direction of movement was normal to the direction of the tubular piles, which were being forced to rotate and bend as the wall moved forward. The piles were driven into the dense sand and so were well fixed in their axial direction.

Eventually a major section of the wall collapsed completely, having displaced forward by about 5 metres. By this stage, the upward movement of the top of the wall had been reversed, and the final reading at collapse showed the top of the wall moving downwards abruptly.

5.3 *Mode of failure*

Fig. 12 shows the trajectory of displacement recorded at the top of the wall where the failure occurred. The design intention was that the wall would be prevented from forward movement by the force B from the inclined tubular piles. The design calculations were carried out using the computer program *Oasys* FREW, in which the supporting force is represented by its horizontal component shown as A in Fig. 12. FREW correctly analysed the balance of horizontal forces and earth pressures, and the bending moments in the sheet piles, but it does not check vertical equilibrium.

In order to provide the horizontal component A, the force B has to have a vertical component, which can only be balanced by a downward force C in the sheet piles. The sheet piles can spread this force into the ground through shaft resistance in the alluvium or the sand beneath.

As noted above, the alluvium was initially very soft, and it had been extensively sheared by ground displacement and then disturbed further as the sheet piles were driven, so it probably had only its residual strength available to provide shaft resistance. This would be a negligible contribution to the required force C.

The trajectory of displacement of the top of the sheet piles, initially upwards, shows that the shaft resistance in the sand, D, was not big enough to provide the component C of force B such that the horizontal component A could withstand the forward movement of the wall.

As the wall moved forward it also moved upwards because the vertical restraint was insufficient. The tubular piles would become severely bent, and probably had a bending failure by local buckling at the point at which the wall finally collapsed.

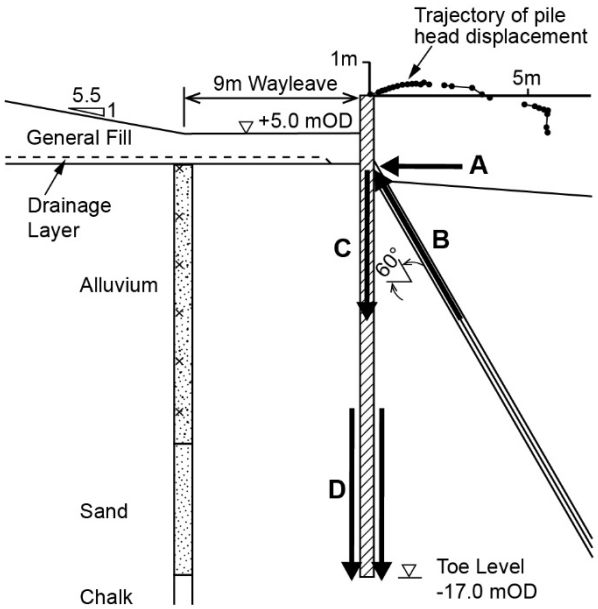

Fig. 12 Propped sheet pile wall – displacement and forces.

5.4 *Lessons derived from this example*

Two lessons are derived from this example. Firstly, it is important in the design of embedded walls to check vertical equilibrium as well as horizontal. Many common computer programs only check horizontal equilibrium and bending moments, so it is important that the engineer makes an independent check on the vertical forces. This mode of failure is represented by case (l) in Fig. 1; the importance of checking vertical as well as horizontal equilibrium is highlighted for embedded walls in EC7.

Secondly, it is important to acknowledge that recently deposited clayey materials can be extremely weak, especially once they are disturbed. EC7 says: "For a steel sheet pile in clay under undrained conditions immediately after driving, no

adhesive or frictional resistance should be assumed. Increases in these values may take place over a period of time."

6 NICOLL HIGHWAY, SINGAPORE

6.1 *Introduction*

In 2004, a major collapse occurred in Singapore during the construction of a metro station at Nicoll Highway. A public enquiry was held and much was published about the incident in the ensuing years. Nevertheless, the lessons to be learnt from this incident are so diverse and significant that it is important that it is known to each generation of geotechnical and structural engineers.

The collapse mode involved elements of (b, h, i and j) in Fig.1.

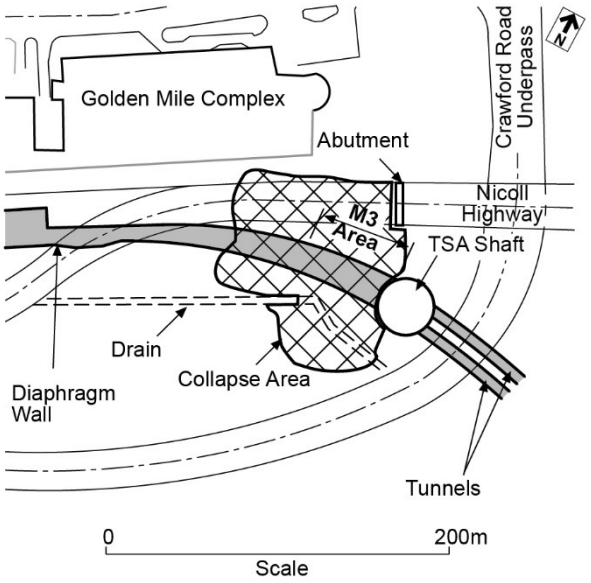

Fig. 13 The collapse area at Nicoll Highway Station, Singapore.

The collapse occurred at around 3:30pm on 20 April 2004, during the construction of Stage 1 of the Circle Line Contract C824 in Singapore (Fig. 13). The collapse involved a 33m deep cut and cover tunnel section, which was being constructed adjacent to the Nicoll Highway in the M3 area of the contract. The collapse tragically resulted in four fatalities, together with the loss of some 110m length of a braced excavation, between 15m and 20m wide and about 30m deep at the time of failure. Substantial ground movements occurred up to about 70m away, resulting in the loss of some 100m of the Nicoll Highway and other utility provisions.

The collapse was investigated by a Committee of Inquiry (Magnus et al 2005) and has been discussed in several publications including: Davies et al (2006); Endicott (2006); Yong and The (2006); Whittle and Davies (2006); Simpson et al (2008).

6.2 *The construction*

Fig. 14 shows the cross section adopted by the designers for the purpose of analysis, including additional details of the stratigraphy. The ground was retained by 800mm thick concrete diaphragm (slurry trench) walls supported by steel strutting as the excavation progressed. Additional support was provided by propping layers of jet grout (JGP), a permanent one beneath the excavation and a sacrificial one between levels 9 and 10.

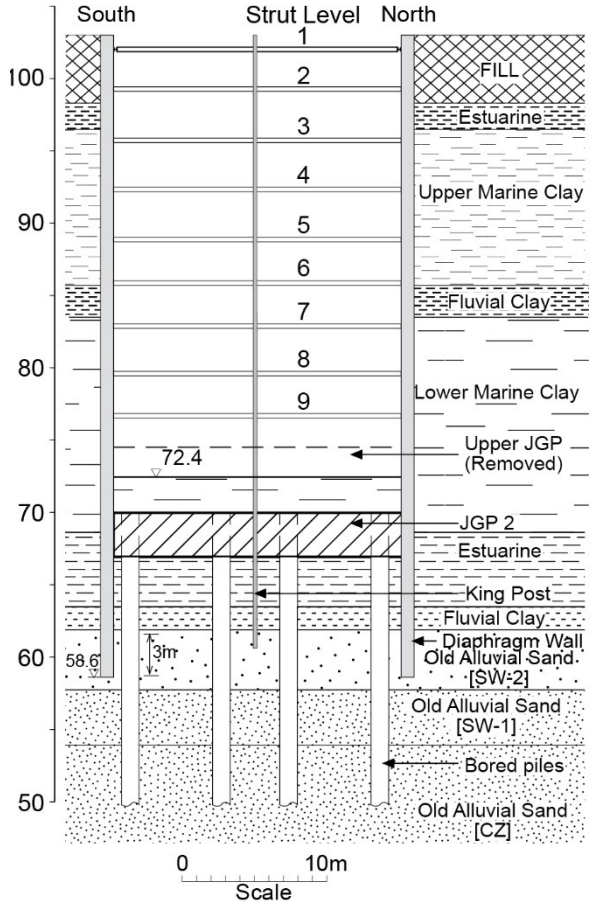

Fig. 14 Design cross-section of the Nicoll Highway excavation.

Fig. 15 shows a more detailed plan at level 9 of the intended construction at the location of the collapse. The area was adjacent to a large diameter shaft, the TSA shaft, which was a launch shaft for tunnelling machines to operate to the east. At level 9, each strut consisted of a pair of steel beams braced together.

The struts transferred their forces to the walls through waler beams. Fig. 16 shows two alternative designs for the steel stiffeners required to transfer the concentrated forces from the struts safely through the walers. In the initial design,

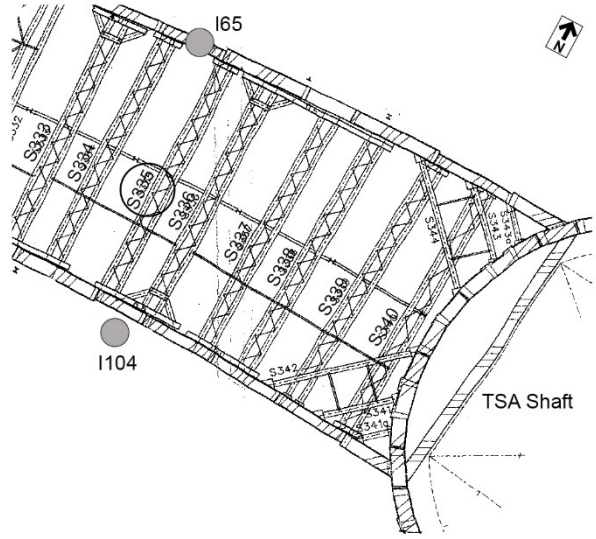

Fig. 15 Strutting plan at the Nicoll Highway excavation.

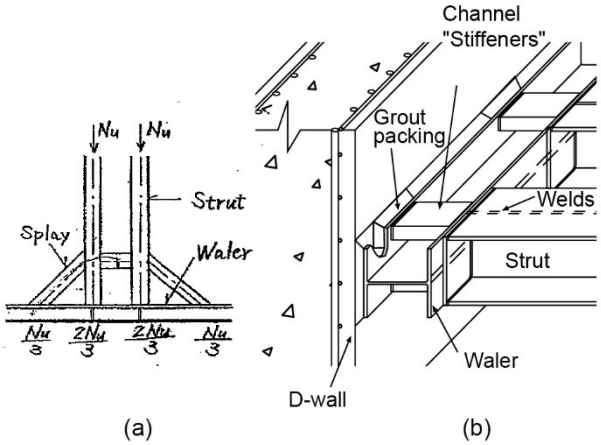

Fig. 16 Waler stiffeners: (a) plate stiffeners; (b) channel stiffeners.

shown in Fig. 16(a), the stiffeners were simple steel plates welded in the pans of the walers. At a later stage, the plates were replaced by channel sections, as shown in Fig. 16(b). Buckling of some of the plate stiffeners had been observed during earlier stages of excavation, but this had not caused a major problem. In some cases the pans of the walers had been filled with concrete to arrest the buckling.

The performance of the structure during excavation was monitored. At the lower levels, strut pair S335, shown ringed in Fig. 15, had four strain gauges to measure the load carried by the strut pair. Some of these had been lost by the time of the collapse, but there were still sufficient to get meaningful readings. Near the north end of the strut there was an inclinometer, I65, in the wall, and I104 was in the ground adjacent to the wall at the south end of the strut.

During construction it was realised that wall displacements were considerably exceeding predictions. At two stages, the contractors and designers re-analysed the design, explaining the large displacements by deriving different, lower, ground strengths by back-analysis. These analyses were claimed to show that it was safe to proceed.

6.3 *The collapse*

The collapse occurred during the excavation for level 10, which required the removal of the upper, sacrificial JGP. At this stage, the struts at level 9 would be expected to be taking their highest load.

During the morning of 20 April, buckling of some of the channel-section strut-waler connections at level 9 was observed. This became progressively worse during the morning, and some workers reported that they could hear sharp “teng” sounds coming form the steelwork; these may have been caused by failure of welds. It was realised that the situation was deteriorating and that remedial action was required. Attempts were made to fill the pans of the walers with concrete, but by this stage they were deforming rapidly. It was not realised, however, that collapse was imminent.

At about 3.30 in the afternoon, the excavation collapsed completely, with massive inward movements of the diaphragm walls.

6.4 *Causes of the collapse*

The collapse was investigated by a Committee of Inquiry (CoI) taking evidence from expert witnesses representing all relevant parties. The CoI’s report (Magnus et al 2005) provides an account of many “contributory factors” which were both administrative and technical in nature. The major technical errors identified by the enquiry were an incorrect use of the geotechnical finite element program Plaxis and incorrect design of the strut-waler connections in the steelwork. It was generally agreed that the steelwork errors were the most significant. The relative importance of the other contributory factors was debated at length during the inquiry, and the discussion was extended in the publications cited above.

Witnesses to the Inquiry identified the following problems with the design and construction.

1. Two errors in the design and construction of the steelwork.
2. Inappropriate use of geotechnical finite element analysis (program Plaxis).
3. Failure to ensure, during construction, that the wall penetrated at least 3m into the Old Alluvium stratum, as required by the design.
4. Failure to check that that the strutting would be adequate if one strut were removed, as required by the contract.

5. Failure to replace a critical piezometer beneath the excavation when it was damaged.
6. Failure to check the toe stability of the walls in accordance with the relevant standard.
7. Failure to provide by calculation adequate factors of safety on load in the steelwork.
8. Failure to respond adequately to observed excessive displacements and bending of the wall and unprecedented compression of the jet grout prop (JGP).
9. Failure to adhere to the Method Statement in relation to the excavation sequence.
10. Uplift of central soldier pile.

It is the opinion of this author that items 1 to 9 contributed significantly to the collapse. If any one of these errors had been avoided, collapse would probably have been averted. This view was broadly upheld by the Committee of Inquiry.

6.5 *Errors in the steelwork*

The experts to the public inquiry agreed that failure was initiated by failure of the strut waler connection at level 9 of the excavation. The performance of this connection was compromised by two major errors in the design, one in the calculation of the load applied and the second in the calculation of the connection capacity. These have been described in some detail by Magnus et al (2005), Simpson et al (2008) and in other publications, so they will only be summarised here.

Fig. 16(a) shows the configuration intended by the design to be used for strut pairs. Two splays helped to spread the force from the strut pair onto the waler, and it was assumed that only two thirds of the force in each beam would be transferred directly from the beam to the waler, the other third going through the splay. Fig. 15 shows, however, that the splays had been omitted from some strut pairs, possibly because there was insufficient space for them. This meant that the force passing from the strut into the waler and its stiffeners was 50% bigger than designed for.

Additionally, the ability of the connection to transfer force from the web of the beam to the web of the waler was over-estimated by about 40%. The combined effect of these two errors was that the design capacity of the connection was less than half the intended capacity.

The original design for the connection at level 9 had two vertical stiffeners between the flanges of the waler (Fig.16(a)). During or after installing the struts at level 7 the connection detail was changed to the channel stiffeners (Fig. 16(b)). Fig. 17 shows the results of finite element analysis of the two connections as they come under compression from the strut. Although the maximum load that can be taken by the channel detail (solid plotted line) is slightly higher than that with two stiffener plates (broken line), the failure modes are very different. For the channel detail it is by buckling and the load capacity drops off significantly. However, for the double stiffener detail the capacity remains high even at significant displacement.

The computed mode of failure of the channel stiffeners is shown in Fig. 18; this was observed to occur as the collapse developed, and recorded photographically (Simpson et al 2008). This brittle mode of behaviour in which capacity is lost as deformation develops greatly exacerbated the problem. As the connections failed at the end of one strut pair, the problem was passed on to other struts at the same level, which then failed, and the forces transferred to other levels caused them to fail, leading to total collapse.

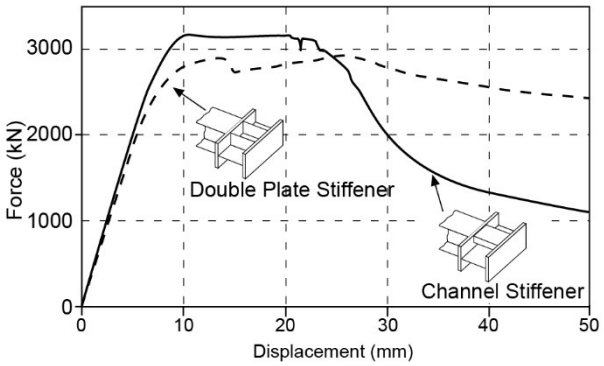

Fig. 17 Computed performance of plate stiffeners (broken line) and channel stiffeners (solid line).

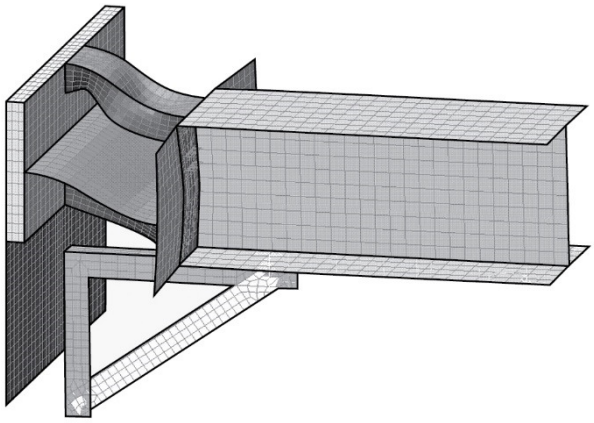

Fig. 18 Computed failure mode of the channel stiffeners.

6.6 *Use of finite element analysis*

The design of retaining walls in such soft materials as the Singapore Marine Clay is dependent on the undrained shear strength of the clay, c_u. This dominates the determination of forces and bending

moments in the structure. These, together with the stiffness of the structure, hopefully largely elastic, determine the displacements of the system. The design analysis is conveniently carried out using a finite element (FE) program; in this case a 2D version of Plaxis was used.

The undrained shear strength profile for the clay could be estimated reasonably well from the results of field vane and cone penetration tests. However, this strength was not input directly into the FE analysis. Instead, the strength of the clay was represented by using its effective angle of shearing resistance and relying on the program to calculate from this the shear strength of the clay.

In principle, this use of effective strength parameters can be successful, but it relies completely on having a material model that correctly computes the changes of pore water pressure that occur during shearing of the clay; in other words, the undrained stress path must be correctly computed in effective stress space. The soil model used by the designers in this case was the simple linear-elastic-Mohr-Coulomb model.

Fig. 19 shows two methods of specifying strength in undrained behaviour, and two undrained stress paths. The "correct" undrained stress path could be obtained in a laboratory test. In the ground, it starts from the initial stress state represented by K_0 and proceeds to failure at the intersection of the Mohr-Coulomb envelope ($t/s'=\sin\phi'$) and the undrained strength c_u.

In the design analysis, Method A, isotropic elastic behaviour is assumed until the Mohr-Coulomb envelope is intersected; as a result the undrained

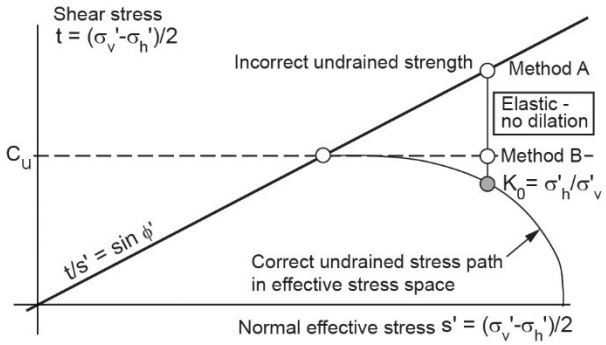

Fig. 19 Modelling undrained behaviour – Methods A and B.

stress path rises vertically and the computed strength is about 40% higher than the correct value.

An alternative simple approach, Method B, is to use the same material model but specifying the undrained strength directly, instead of the effective strength parameters. In this approach the undrained stress path still rises vertically, implying incorrect calculation of pore water pressures, but, crucially, the correct undrained strength is used.

Fig. 20 Shows computed displacements and bending moments in the walls for the design situation shown in Fig. 14. The overestimation of strength in Method A led to an underestimate of maximum displacements and bending moments of about 50%. Critically, the more correct Method B shows that the ultimate bending capacity of the wall would be exceeded (Fig, 20(b)).

The soil profile on the north side of the excavation, near inclinometer I65, was fairly similar to

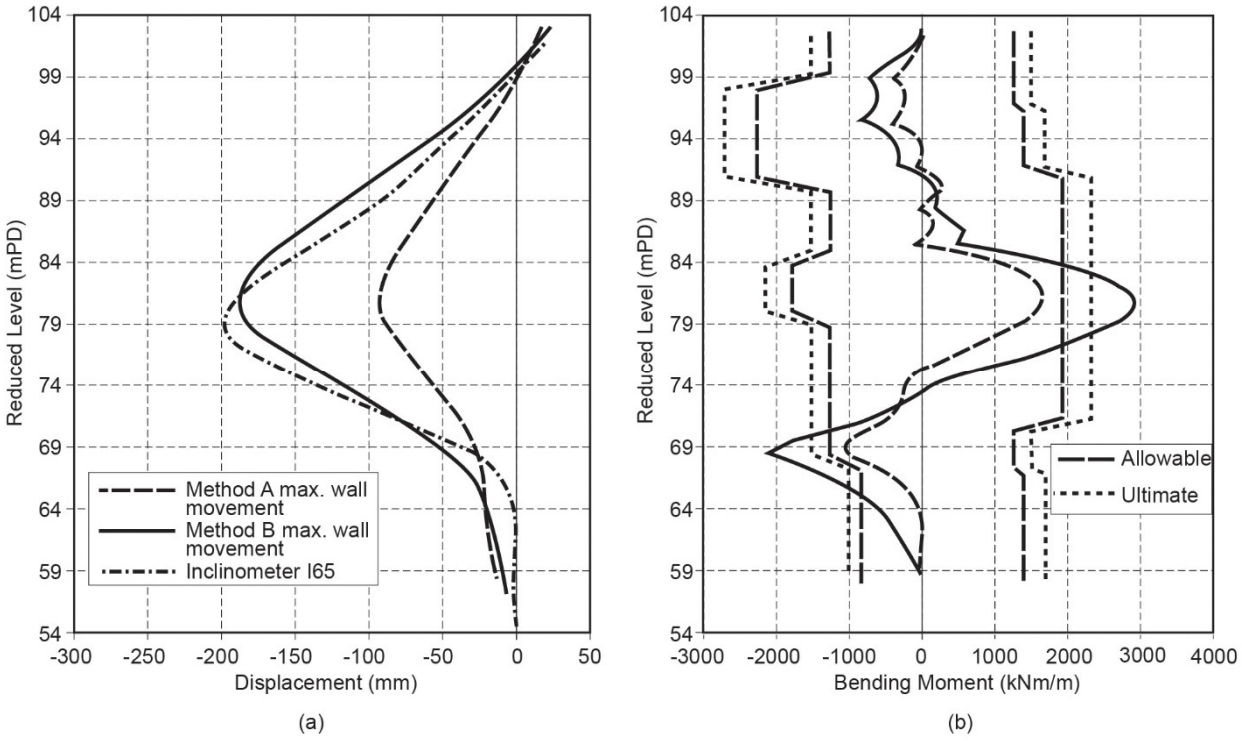

Fig. 20 Computed displacements (a) and bending moments (b) in the walls for Methods A and B.

the assumed profile. Fig. 20(a) shows that use of Method B would predict the observed displacements very well, but the Method A results are much too low.

The important implication of the wall being over-stressed in this way is that when struts started to fail the wall would be unable to protect them by distributing load upwards or downwards.

6.7 *Penetration into Old Alluvium*

The design calculations assumed that the walls should penetrate at least 3m into the Old Alluvium beneath the soft clays, and this was shown as a requirement on the design drawings. At the monitored cross-section, strut S335, this penetration was achieved on the north side of the excavation near Inclinometer I65, giving the displacement results shown in Fig. 20, but not on the south side near Inclinometer I104.

It was known from the established geology of the area that the surface of the Old Alluvium was crossed by small stream channels from erosion before it was overlain by the marine clays. As a way of interpreting the design requirement, the level of the toe of the wall had been fixed before construction by interpolating between levels of the Old Alluvium surface found in boreholes; however, these were not sufficiently closely spaced to pick up the details of the stream channels. When the wall was built at the location of I104, the contractor recorded that it had only 0.3m penetration into the Old Alluvium, which in fact would vary across the base of the diaphragm wall panel.

Fig. 21 shows the wall displacements recorded in the days before the collapse on the north and south sides of the excavation. Where the penetration into the Old Alluvium was very small, the displacement was much larger; in the opinion of some of the experts to the Inquiry, including the author, these displacements indicate that the wall had reached a bending failure, forming a plastic hinge.

A stream channel also affected the north wall, slightly further towards the TSA shaft.

It is likely that this lack of 3m penetration into the Old Alluvium was critical to instability of the excavation. It resulted from a communication failure between the designer, carrying out calculations and producing drawings, and the constructors working on site.

6.8 *Loss of one strut*

It was a design requirement to check that the construction would be stable if a single strut were lost. This requirement was checked in the initial design, but was not checked during the back-analysis stages used to justify continued excavation despite unexpectedly large displacements.

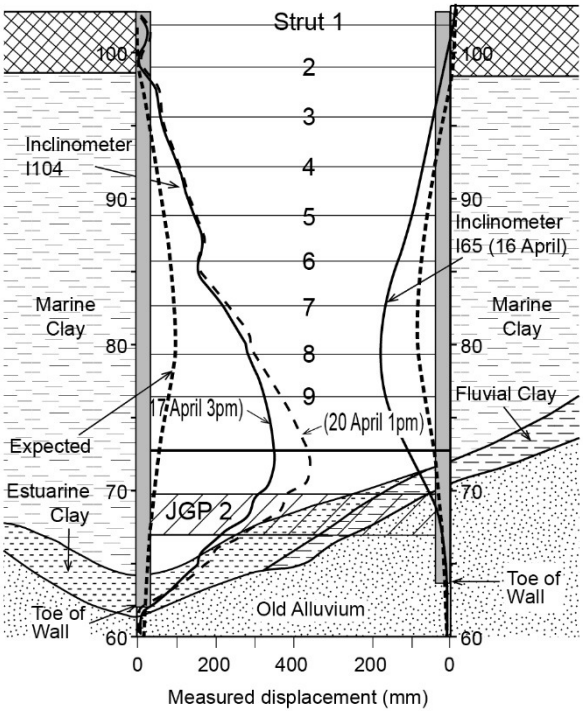

Fig. 21 Wall displacements recorded before the collapse on the north and south sides of the excavation.

Carrying out this check should have led to a need for stronger struts, and in particular strengthening of the strut connections in the walers, which could well have averted the collapse.

6.9 *Replacement of damaged piezometer*

The monitored section had piezometers beneath the excavation, results from which were to be compared with predictions from the finite element work. At around level 4 in the excavation, it seemed likely that the monitored pore water pressures near the toe of the wall would exceed the predictions. At this stage, however, the piezometer was lost and it was not replaced.

It is possible that higher than anticipated water pressures beneath the excavation contributed to the instability, but this cannot be known. It is clearly important to replace instrumentation if it is lost, unless plenty of redundancy has been built into the initial installation of instruments.

6.10 *Calculation check of toe stability*

The design was required to be carried out according to British Standard BS8002 (BSI, 1994). This required that the stability of the wall, and critically of the toe of the wall, should be checked by applying a factor of safety to the soil strength. The code required that the length of the wall and the strength of the supporting structure are consistently checked against this requirement.

With 3m penetration into the Old Alluvium, the length would have been adequate. However, this check would have resulted in a greater demand on the level 9 strut, requiring an increase in its capacity and that or the strut-waler connection.

6.11 *Factors of safety*

The design calculations applied factors of safety only to the structural components. No factors were applied to soil strength or passive resistance. Standard material factors for concrete and reinforcing steel in the diaphragm walls were used, according to BS8110, but a factor of 1.2 was applied to the calculated bending moments. For the steelwork, the material factor on steel strength was 1.0, and a load factor of 1.2 was to be applied to forces in the steelwork.

Load factors of 1.4 would normally have been used for permanent works, but these low factors were considered to be adequate for "temporary works". The Committee of Inquiry concluded that factors of safety should not be lowered for temporary works where failure involves serious consequences. This is in line with the statement in Eurocode 7 that less severe factors may only be used "where the likely consequences justify it".

At the second back-analysis stage, a larger value was computed for the strut force at level 9, implying a reduction in the factor of safety in the steelwork design from 1.2 to 1.06 for the strut-waler connections. However, the design was not changed in response to this calculation.

Had the factor of 1.2 or, more appropriately 1.4, been correctly applied in the design of the strut-waler connections, they would have been stronger and the collapse would probably have been averted. Alternatively, the design could have been checked with reduction factors on ground strength. Eurocode 7's Design Approach 1 requires that both these checks are carried out.

6.12 *Response to excessive displacements*

The location of the excavation was such that large displacements of the walls did not cause serviceability problems for surrounding structures. Some interpreters of limit state thinking might conclude from this that displacements were irrelevant. However, displacements are also relevant to ultimate limit states if they imply such large strains in materials that they would no longer provide the strength assumed in the design.

In this case, as noted above, the displacements shown in Fig. 21 for I104 probably implied that the wall had reached its limiting strength and was unable to provide any additional support if a strut was lost.

The behaviour of the permanent jet grout slab beneath the excavation was also critical. Tests on samples of jet grout showed that they suffered a brittle compression failure at strains typically of about 1%. The displacements at the level of the lower jet grout slab (JGP2) shown in Fig, 21 imply a shortening of the slab of about 2%. Hence it seems likely that the jet grout slab was either faulty or had crushed significantly; in either case it could no longer be relied upon.

Appreciation of these issues, should have led to a very cautious approach to further excavation.

6.13 *The excavation sequence at level 10*

The contractors Method Statement required that not more than four "bays" of excavation should be open at one time before strutting was in place; in this context, a "bay" is defined by each strut pair.

At the time of failure, there was good reason to proceed very cautiously, as explained above. But in the event the length of excavation un-strutted at level 10 was approaching double the intended length. Computations carried out by the author's company suggest that by keeping the length of un-strutted excavation to the intended amount, roughly equal to its width, the forces in the level 9 struts would have been reduced by at least 25%. Such a reduction would probably have averted the failure.

6.14 *Uplift of central soldier pile*

It was also suggested by witnesses to the Inquiry that unexpected heave of the base of the excavation, lifting the central soldier piles so as to distort the failing strut-waler connections, reduced their capacity to carry load. This might also be related to the possibility of excessive pore pressures beneath the excavation, not monitored.

It is not certain whether this occurred; its likelihood has been inferred from observations at other locations in the contract and an interpretation of the observed onset of failure. Heave of the ground beneath the excavation was inevitable, even without excessive water pressures, as the soft clay and jet grout beneath the excavation was squeezed laterally; it might have been exacerbated by a reported failure to reinforce the main load-bearing piles as had been shown in the design. In the opinion of many of the expert witnesses, including the author, it could have been part of the final failure

mechanism, but it only has relevance after the failure of the strut-waler connections, to which the earlier items are critical.

6.15 *Reliance on the strain gauges*

When the channel stiffeners in several of the strut connections were visibly buckling, readings were taken from the strain gauges in strut S335 at level 9. The forces indicated by the gauges were comfortably within the intended design capacities of the struts and the strut-waler connections, and there was no record of the design capacities having been exceeded, though there were critical gaps in the readings.

The strain gauge readings were subsequently studied extensively during the investigation, but the reason for these relatively low readings was not clear. It is possible that they gave some false comfort to the site engineers shortly before the collapse.

6.16 *Reaction to the signs of imminent danger*

The issue of reaction to danger is discussed by Simpson et al (2008), from which the following text is adapted.

The Committee of Inquiry concluded that the collapse was "rooted in history", it "did not develop suddenly. A chain of events preceded the collapse." Nevertheless, the engineers and most of the workforce involved on site were taken by surprise. Four workers were killed and survivors had to run for their lives. By good fortune, traffic lights had stopped the traffic on the heavily used six-lane highway which fell into the excavation; but for this there could well have been many more casualties. It is important to the civil engineering profession to learn from events of this sort (a) what signs should raise alarm, (b) what reactions could be helpful, and (c) what precautionary plans should be in place.

Visual inspection and monitoring made it clear that at least three different elements of the structural system were operating outside their normal performance limits. (a) Displacements of the walls had far exceeded the original predictions. (b) Most of the experts and the Committee of Inquiry concluded that the diaphragm wall was bending excessively and had formed a plastic hinge some days before the collapse. (c) The jet grout prop had compressed by 1% several weeks before the collapse, well beyond the typical working range of about 0.25% compression. (d) In the hours before the collapse, several strut-waler connections were observed to be buckling. Items (c) and (d), and possibly (b), involved brittle behaviour, in the sense that the capacities of the elements to carry load were reducing due to their unintended behaviour, but the engineers involved seem to have been unaware of this at the time.

In the author's opinion, when any element of a structure is known to be performing outside its normal limits, it should be assumed that it is no longer able to serve its intended purpose, unless it can be shown to be safe by rigorous investigation by experienced engineers and specialists. The situation should be one of alarm requiring urgent and cautious action. This should apply to excessive bending, straining or buckling of any components of a structure, including such materials as jet grout and even soil. Systematic monitoring, carefully interpreted, is vitally important, but over-reliance on it, in face of clear adverse events is to be avoided.

In view of the known low factors of safety and large strains in the jet grout excavating to level 10 in very small bays might have provided a way to continue successfully, but even this should have been preceded by a review from which a full understanding of the situation was derived.

7 CONCLUDING REMARKS

The examples presented in this paper have illustrated the need to consider systematically the failure modes noted by Eurocode 7, as shown in Fig. 1. Important issues include overall equilibrium of the design situation, allowance for geometric variations, vertical as well as horizontal equilibrium, and providing adequate margins or factors of safety. Designs or site activities that could lead to brittle behaviour of structural materials or soil should be avoided unless they are very consciously accommodated and monitored. Allowance for minor variations in the ground profile or construction must be included in design, and flexibility is needed to change design details as the profile becomes clear during construction. Several of the examples showed a lack of systematic checking of design or construction by adequately experienced engineers.

Factors of safety are specified by codes and standards at least in part to guard against the risk of major failures. Since risk involves assessment of both likelihood and consequences, any proposed reductions in normal factors of safety should only be allowed if the consequences of a failure would be relatively low.

In the author's experience of investigating failures, errors in civil engineering design and construction are sadly common. Most errors, however, do not lead to significant consequences because they are covered by the factors of safety employed. This gives another reason for caution in reducing standard factors of safety.

Monitoring the performance of structures can provide vital information that could help to avert

disaster. Monitoring points may be difficult to protect during construction, and it is quite common that some are lost. Unless there is ample redundancy in the monitoring system, it is essential that lost monitoring points are replaced quickly.

Although monitoring is extremely valuable, simple observation by engineers and other site personnel is also very important. Where these are in conflict, as in the case of the apparently low loads on the strut connections at Nicoll Highway, though they could be seen to be buckling, basic visual observations of behaviour must not be ignored because of monitoring results.

Most crucially, clear and unambiguous communication is needed between all parties to civil engineering works: clients, designers, checkers, contractors and site workers. Engineers must be "brave enough to be afraid", reacting decisively, with caution and appropriate haste, when there are signs of adverse behaviour of structures and excavations.

ACKNOWLEDGMENTS

The author is grateful for the assistance over the years of many colleagues at Arup and to for discussion with other expert witnesses involved in the Nicoll Highway inquiry.

REFERENCES

BSI (1994) BS8002: British Standards Institution Code of Practice for Earth Retaining Structures.

BSI (2013) BS EN 1997-1:2004 +A1:2013. Eurocode 7: Geotechnical design - Part 1: General rules.

Davies R.V, Fok P, Norrish A and Poh ST (2006) Nicoll Highway Collapse: Field Measurements and Observations. Int. Conf on Deep Excavations, 28-30 June 2006, Singapore.

Endicott, LJ (2006) Nicoll Highway Lessons Learnt. Int. Conf on Deep Excavations, 28-30 June 2006, Singapore.

Magnus, R, Teh, CI and Lau, JM (2005). Report on the Incident at the MRT Circle Line worksite that led to the collapse of the Nicoll Highway on 20 April 2004. Subordinate Courts, Singapore.

Simpson, B, Nicholson, DP, Banfi, M, Grose, WG and Davies, RV (2008) Collapse of the Nicoll Highway excavation, Singapore. Proc Fourth Int Forensic Engineering Conf, ICE, London.

Whittle A.J and Davies RV (2006) Nicoll Highway Collapse: Evaluation of Geotechnical Factors Affecting Design of Excavation Support System. Int. Conf on Deep Excavations, 28-30 June 2006, Singapore.

Yong, KY and Teh, HS (2006) System Failure of Temporary Earth Retaining Structure Leading to Collapse of Nicoll Highway. Int. Conf on Deep Excavations, 28-30 June 2006, Singapore.

Foundation investigation, analysis and design for high rise buildings

C.M. Haberfield
Golder Associates Pty Ltd, Melbourne, Australia

A.L.E. Lochaden
Golder Associates Pty Ltd, Melbourne, Australia

A.L. Henderson
Golder Associates Pty Ltd, Melbourne, Australia

ABSTRACT: The plethora of medium height high rise (high rise) buildings in our modern cities necessitates safe and efficient design of their foundations.The demonstrated success associated with satisfactory performance of foundations for these buildings over the last several decades has led to local precedents in design that result in overly conservative foundations.The knowledge obtained from the analysis, design and construction of foundations for very tall towers provides the methods and confidence to improve the efficiency of the foundations for medium rise buildings.This paper describes the application of technologydeveloped for foundation design in very tall towers to the design of foundations for high rise buildings; in particular, the assessment of relevant engineering properties of the ground, foundation performance and foundation structure interaction. This is illustrated through case studies of medium risebuildings that the authors have been involved in.

1. INTRODUCTION

High rise buildings are a common feature of modern cities. Whilst the number of tall and very tall towers (those in excess of say 50 or 60 levels) continues to increase, it is the medium height high rise (high rise) buildings (i.e. those between about 10 levels and 60 levels) that dominate the constantly changing skylines of our citiesas they have done for at least the last several decades.

As a result, there is significant experience available in every city with respect to the analysis, design and construction of suitable foundations to support such buildings.It may appear that the challenges of designing and building economical and safe foundations for such buildings have significantly reduced over the last 50 years or so, and that now there is little left than can be improved on.This is far from the truth.

In general, the footings for most high rise buildings perform satisfactorily over and beyond their design life.This is primarily due to the prudency adopted in their analysis and design.

In the past, this prudency was necessary due to the relatively limited knowledge (by today's standards) of the properties and behaviour of the ground supporting the foundations, poorer knowledge regarding the performance of foundations, and the use of relatively simplistic analysis tools.

Unfortunately, the success of these foundations has meant that local precedence have been set and become lore, with bearing pressures for new building foundations,for example, being fixed at often highly conservative values.

As a result, the foundations for many new and existing high rise buildings are over engineered.Whilst this may have benefits in some instances (e.g. providing opportunities for increasing the height of an existing building without demolishing the buildingor introducing a new footing system, e.g. Colls, 2019), the push for sustainability and economical solutions requires that we improve the efficiency of foundations for these structures.

On the other hand, there are instances of poor performance of the foundations supporting some high rise buildings (e.g. Mascot Towers in Sydney, Australia, Millennium Tower in San Francisco, USA). Whilst the issues facing these buildings are still being debated and it is unclear whether this poor performance is due to poor design/construction or caused by recent changes in the ground conditions below the buildings, the foundation designer is obliged to provide a safe design that considers reasonably foreseeable future events.

Over the last 30 years there have been significant developments in our ability to assess the engineering properties of the ground, in our understanding of foundation performance and in our ability to analyse and quantify the interaction between a building and the ground (soil structure in-

teraction analysis).Whilst this new knowledge has allowed tall towers of greater heights to be constructed in areas which were previously considered to be infeasible, it also provides the experience and knowledge to overcome local precedence and to design and construct more efficient foundations for high rise buildings.

In addition to the above, modern day safety standards mean that some past site practices (e.g. entering deep, unsupported footing excavations to place reinforcement) are no longer acceptable, and alternative methods of carrying out these activities in a safe manner are required (e.g. prefabricated reinforcement cages for pad footings).

This paper provides a summary of the authors' experience ofinvestigation, analysis and design of foundations for high rise buildings. It demonstrates this experience through case studies.In this paper, only aspects of the foundation system are considered (i.e. basement retention aspects are not considered).

2. FOOTING DESIGN CONCEPTS

2.1 Introduction

The footing system for a highrise building must be able to provide satisfactory support to the building to resist design vertical and lateral loads without displacing excessively.

The critical vertical loads for most high rise buildings usually comprise a combination of dead and live load and are considered to act continuously over the life of the building.It is therefore the long term performance of the footings (and hence of the founding materials) that is often the key consideration.

However, lateral loads from wind or earthquake events, although of relatively short duration, can be critical and must be designed for.These loads are resisted primarily by the near surface soil/rock, although interaction between the footing system and the lower building structure results in some push-pull action which imparts tension and compression vertical loads into the footing system that are in in addition to the gravity loads. The short term performance of the footing system under this additional short term loading is therefore also a key consideration of the footing system design.

The fundamental components of all footing systems for high rise buildings comprise piles and shallow spread footings (pads, strips and rafts) which can be used on their own (e.g. piles, rafts, strips or pads) or in combination (e.g. piled rafts, piled strips and piled pads). The majority of high rise buildings are typically supported on reasonably competent material, comprising either weathered rock or in some cases, very dense / hard soils (such as gravel and sand).Typically, one of the following ground condition scenarios would be expected to be encountered for a tall building footing system:

- Competent founding strata of sufficient strength and stiffness at a shallow depth such that spread footings may be adopted.
- Relatively competent founding strata at a shallow depth but of insufficient strength or stiffness to allow shallow footings to be adopted. In this case a hybrid footing system(such as a piled-raft or piled-pad) could be adopted, where the piles are designed primarily as settlement reducing to limit settlements to acceptable levels.
- Significant depth to competent founding strata such that piled foundations are required to support axial loads. Assuming the soils overlying the founding level are not relatively weak, a variety of pile types could be adopted, such as bored or continuous flight auger (CFA) piles socketed into weathered rock, or driven steel or concrete piles driven to refusal. If there is a significant thickness of weak sediments overlying the founding strata, and the building is relatively tall, the resistance of the overlying soils and the foundation system to lateral wind and earthquake loading can become critical and more heavily reinforced large diameter bored piles may be required to control excessive lateral deformation.

Irrespective of the footing type used to support the columns (and core/s) of the building, group effects between individual columns can be significant and usually result in settlements and lateral movements well in excess of that of a single isolated footing.That is, unless a high rise building is supported at the ground surface on relatively competent rock where displacements are likely to be small enough so that group effects are not of concern, it is not usually sufficient to consider the performance of individual footings in isolation, but instead, the entire footing system as a single entity (potentially together with some portion of the building structure) must be analysed.This is usually done using a soil structure interaction program, of which many are commercially available (e.g. PLAXIS, FLAC, etc).

Nevertheless, before undertaking such analysis, the performance of an individual footing under vertical, lateral and moment loading of short and long term duration must be understood and quantified.

Bearing capacity of individual footings is rarely an issue, and whilst strength considerations need to be checked, they rarely control the design of the footing system. There are very few documented instances of bearing capacity failures of build-

ings.However, excessive settlement, lateral movement, sway and tilt of high rise buildings, (i.e. serviceability issues), although rare, is more common.

For ground conditions which comprise reasonably competent soil or rock from the ground surface, it is usually the long term vertical loads (rather than short term lateral loads) that govern the design of the footing system. In such cases, preliminary sizing of footings is commonly undertaken using estimates of allowable bearing pressure-which are usually based on local experience or precedence, or on estimates of ultimate bearing capacity divided by a factor of safety (FoS) of 2.5 to 3. Settlement calculations are then undertaken to check whether group settlement and differential settlement between columns are satisfactory. The settlement calculations often adopt stiffness parameters that have been assessed based on engineering judgement and perhaps some limited strength-based testing.

However, as settlement considerations typically control the design of the footing system, the economic and sustainable design of footing systems requires that accurate and reliable estimates of settlement be made.The necessary inputs that are required to obtain such estimates include an accurate assessment of deformation properties of the ground, an understanding of the performance of each footing type and appropriate calculation tools. There have been significant advances in all of these aspects over the last several decades which allow us to make much more accurate, reliable and confident settlement estimates.

Despite these advances, in general, standards, codes of practices, reference books, university courses and other sources of design information are lagging behind current knowledge and need to be updated to focus foundation design in more competent geomaterials on displacement rather than strength performance. Ground investigations should also focus on the measurement of soil/rock mass stiffness and defect properties, with less emphasis on strength.

2.2 Preliminary footing design

The design of the footing system for a high rise building usually commences with sizing of individual footings to carry the design vertical compressive loads.

2.2.1Pad footings

For columns supported on pad footings the size of the pad is based on an assessment of an allowable bearing pressure or ultimate bearing pressure divided by a FoS (usually of about 2.5 to 3). Pad footings for heavily loaded columns are usually only a satisfactory option if they bear on rock, which depending on the magnitude of the column loads could comprise rock of very low strength or higher (i.e. rock with an intact unconfined compressive strength (UCS, q_u)of greater than about 1 MPa). In general, our assessment of allowable bearing pressure for pad footings on rock is overly conservative with bearing pressures capped at a fraction of the UCS of the intact rock. For example, Pells (2004) provides classification systems for Hawkesbury sandstone and shale in Sydney based on visual assessment of the rock mass and recommends a maximum allowable bearing pressure of 0.5 x $q_u$to achieve a footing settlement of less than 1% of footing diameter. Pells (2004) also limits the allowable bearing pressures to maximum absolute values for each rock class (e.g. 12 MPa for Class I sandstone which has an intact rock strength generally in the range of 12 MPa to 50 MPa). Whilst the Pells (2004) recommendations provide a site non-specific, sensible and practical approach which can be easily applied by designers, the approach still includes a significant level of conservatism leaving potential for bearing pressuresto be improved on the basis of site specific assessment of relevant mass stiffness properties of the rock.

In general, there appears to be a reluctance to adopt more realistic design parameters for the stronger and stiffer materials, even though documented performance and current knowledge has indicated past designs to be conservative.

In some localities, it is relatively common practice to drill shallow boreholes in the base of every pad footing excavation to confirm the rock mass conditions are consistent with the design assumptions and that no weak or compressible seams are present. However, this is usually unnecessary. Exceptions may include footings in karstic ground conditions or in horizontally bedded variably weathered rock where an undetected compressible horizontal seam may underlie the base of the footing. Such conditions should however be identified from the geotechnical investigation and considered in the footing design. In most other situations, confidence of founding conditions can be obtained by having a good understanding of the geology of the site, the rock formation processes and likely geological history, and by directly observing the structure in the rock in the wall and sides of the footing excavation and surrounding ground surface. If the rock structure is not horizontal and no compressible seams are observed in the walls and floor of the excavation or surrounding ground surface (with a strike and dip that indicates it may underlie the footing) then it is highly unlikely that such seams would underlie the footing.

When founding in relatively strong rock, the minimum size of a pad footing may be limited by

practicality of construction rather than geotechnical considerations. There is no sense in constructing a footing smaller than the column dimensions. In circumstances when the rock is also relatively massive and intact with little rock structure, the merits of excavating rock that is stronger than the concrete to form the footing should be considered carefully. Consideration could be given to forming a flat surface to the rock (by grinding or blinding), grouting starter bars directly into the rock, and then constructing the column directly on the flat surface so formed.

2.2.2Piles

For columns supported on piles, the number of piles and pile diameter are usually chosen on the basis of structural strength considerations. Alternatives for heavily loaded columns include single large diameter bored piles or groups of two or more smaller diameter piles.

The unit shaft resistance of piles in competent soil and rock materials generally reduces with increasing pile diameter (e.g. Haberfield, 2013). This indicates that smaller diameter piles are usually more efficient at carrying axial load than larger diameter piles. In addition, the efficiency of pile construction reduces as pile diameter increases. For this reason, in most applications, the diameter of single piles is chosen as the minimum diameter required to meet pile structural axial strength considerations. The pile length is then designed to meet geotechnical strength and serviceability requirements. An exception is when piles are installed through soft or liquefiable soil, in which case the greater bending strength and stiffness of larger diameter piles may be required to resist lateral earthquake and wind loads.

Lateral restraint to applied lateral loading can be provided by the buildings piles and pile caps. Rather than being governed by the ultimate lateral resistance of the soils, the response of the piled foundations of a building in this situation is often governed by the allowable lateral deformation at the top of the pile or pile group. For this reason, relatively stiff large diameter bored piles reinforced over their full depth are often required to provide increased lateral resistance and reduce lateral movement to allowable levels. In the authors' experience, more lightly / partially reinforced small diameter CFA or bored piles are typically insufficient to reduce lateral deformations to acceptable levels for this situation.

In most circumstances, single piles that support columns are requiredto be founded in very low strength or better rock. The majority of the axial resistance of the pile to vertical load is generated by the shaft resistance and base resistance developed within the length of the pile embedded in the rock, commonly referred to as the rock socket. In general, the performance of well installed piles in rock is underestimated, with design being overly conservative. However, the potential impacts of poor construction on the load versus displacement performance of rock socketed piles aresignificant (e.g. Haberfield,2013, O'Neill and Hassan, 1994) and for this reason, appropriate attention needs to be applied during pile construction to ensure the design performance of the piles is obtained. As rock-socketed piles are probably the most common form of pile support for high rise buildings, further comment on their design is provided below.

A column supported by a single large diameter pile is often more efficient (both in terms of performance under axial and lateral loads and construction savings resulting from not constructing a pile cap) than multiple smaller diameter piles (which require a pile cap). However, in certain ground conditions (e.g. comprising granular or soft soils overlying rock, where bored piles require the use of drilling fluids or casing to support the pile hole during pile construction) it may be more efficient/practical and lower risk to use a group of smaller diameter piles under each column. Such piles could include CFA and driven precast concrete or steel piles or similar.

The performance of driven piles is usually confirmed at end of driving, with piles typically driven to a set which has been assessed (and usually verified through dynamic pile testing) to provide the required performance. The set requirement is effectively a load test, and in practical terms means that every pile is tested as it is installed, thus providing a relatively high level of confidence in the load versus displacement performance and integrity of the piles. The same information is not available for bored concrete castin situ piles and CFA piles without specific load (and integrity) testing of completed piles. As a result, greater prudency, without excessive conservativism, is required in their design.

A historical approach has required piles in a group to be based at minimum spacings of 2.5 to 3 pile diameters to reduce interaction effects. It is commonly thought that these interaction effects reduce the ultimate geotechnical capacity of the piles and hence unless piles are spaced at reasonable spacing more piles are required to carry the column loads. The 2.5 to 3 pile diameter spacing can result in pile caps of significant size. However, consideration of the way in which piles generate their resistance through shaft and base resistance (as set out below) indicates that in reality the geotechnical capacity of the piles remains largely unaffected, but the pile head settlement required to mobilise the same axial resistance is increased. Pile caps comprising closely spaced piles will therefore set-

tle more at the same load than pile caps with the same piles (number, length and diameter) but spaced at larger spacing, however the ultimate geotechnical capacity of the two pile groups will be much the same.

The closest practical spacing of piles in a group depends on construction considerations. For example, the spacing between piles that are installed by driving may need to be greater than piles that are drilled due to potential damage caused if a driven (usually slender) concrete pile hits and is deflected by an already installed pile. Such damage is less likely to occur in drilled piles although construction sequencing needs to be considered so that a pile hole is not drilled too close to a recently completed pile in which the concrete has not attained sufficient strength. The authors have been involved in several successful projects where 600 mm and 750 mm diameter CFA piles have been installed in clusters of 2 to 6 piles at nominal clear spacings of 100 mm.

2.2.3Combined footings

In ground conditions where reasonably competent material occurs below the base of the building for significant depth and for which the stiffness of the material remains constant or increases gradually with depth, building columns may be supported on combined footings which comprise shallow pads, strips or rafts supported on piles (i.e. piled pads, piled strips and piled rafts). In these combined footings, the column loads areusually shared about equally (40% to 60%) between the shallow footing and the pile/s. Preliminary sizing of each component is achieved by undertaking separate simplified analyses of the shallow footing and piles as single units and distributing load between the two so as to match displacements between the pile/s and the shallow footing. Final sizing is undertaken using appropriate soil structure interaction software using realistic input (i.e. unfactored) input parameters and loads (see below). Bearing capacity of the combined footing is checked to ensure an appropriate safety margin (i.e.FoS) on ultimate design loads.

In piled rafts, it is usually more efficient to place piles directly under the main structural columns and walls rather than in a regular grid arrangement. Locating piles beneath main structural elements reduces the bending stresses in the raft and may allow the raft thickness to be reduced below that required for a regular grid spacing. Pile lengths are varied to reduce the overall settlement and dishing of the raft, and in general, the length of the piles beneath the central core and major walls will be longer than those at other columns and around the edge of the building.

Combined footings are not usually suited for ground conditions which comprise relatively compressible soil (e.g. soft to stiff clay) immediately below the pad/strip/raft or if the piles penetrate into a significantly stiffer material at depth. In such cases, the surface footing carries very little of the applied load, with most load resisted by the piles, and a fully piled solution is usually the most appropriate footing solution.

2.3 Design of rock socketed piles

2.3.1Introduction

Rock socketed piles can be constructed in very low strength to very high strength rock and from relatively intact rock to intensely fractured rock. For the reasons set out below, the load carrying capacity of even low strength rock (in most situations) is far in excess of the strength of the structure (e.g. a building column or pile) transmitting the load. Even if bearing capacity can be reasonably quantified, it has little if any significance to the load versus settlement performance of the pile. Performance of a rock socketed pile is usually a displacement issue and is a function of rock mass stiffness rather than rock mass strength. In addition, poor pile performance is much more likely to result from poor construction practices than excessive displacement of the rock mass.

As all loads applied from the surface to the pile must be transferred through the interface between the pile and the ground (i.e. through shaft resistance and base resistance), the performance of the pile is defined by the characteristics of these interfaces, the integrity of the concrete pile and the characteristics of the surrounding rock mass. The characteristics of the shaft and base interfaces are highly dependent on the properties and characteristics of the rock mass, pile diameter and length, and the construction technique adopted (e.g. Haberfield and Lochaden, 2019).

However, these factors are not normally considered in the design of piles in rock. Piles in rock are still predominantly designed based on estimates of ultimate bearing capacity using empirical generic (non-site specific) rules based largely on the UCS of the rock with little if any consideration of other factors. Settlement is often calculated as an afterthought and based on modulus values correlated with UCS. The order of magnitude scatter in the empirical data (Haberfield, 2013) means that the possible range of design values and possible design performance is large,and therefore requiressignificant prudency in design.Howeversignificantly more economical and sustainable footing solutions are possible with a little more thought in analysis and design and the adoption of good construction practices.

Rock socketed pile designers should have an understanding of the basic mechanisms that control pile performance as well as an understanding of how the pile construction processes can affect this performance and be changed to obtain better and more reliable performance. Such information is provided in a number of readily available technical references (e.g. Haberfield and Lochaden, 2019).

2.3.2Base resistance considerations

Due to the relatively higher strength of rock (compared to soil) the ultimate base resistance of a pile in rock can be large and well in excess of the ultimate structural strength of the pile column. This occurs even in piles which contain a significant thickness of debris or softer material at the base of the pile which has been for example, left behind by ineffective base cleaning or settled out of the drilling fluid (or water) in the pile hole during placement of reinforcement or due to delay in concreting. This is because under loading, the pile will displace and will gradually compress the base debris, resulting in a gradual increase in base resistance until the full ultimate base resistance is eventually mobilised.

The ultimate base resistance of a pile in rock is therefore not of great significance to pile design and performance, as it is the rate of mobilisation of the base resistance that is important to the displacement of the pile, and hence the performance of the pile under Serviceability Limit State (SLS) and Ultimate Limit State (ULS) conditions.

The measurement of ultimate base resistance for piles in rock is often impractical due to the very high pile loads required to displace the pile sufficient distance to mobilise ultimate base resistance. Haberfield (2013) provides an analysis of the results of published pile load test results. All of the test results considered were for low to medium strength rocks with UCS less than 10 MPa. On the basis of his analysis, Haberfield (2013) observed that the ultimate bearing capacity was only mobilised in piles with zero embedment and indicated values generally greater than 5 x UCS. Ultimate end bearing was not mobilised in any piles with embedments into rock of more than about 2 pile diameters and piles with embedments greater than about five pile diameters (and which were taken to relatively large displacements) generally mobilised base resistances in excess of 10 x UCS. In extremely fractured rock, however, significantly lower bearing pressures were measured at the same pile displacement.

The lower bound estimate of base resistance of 5 xUCS is reasonably consistent with the ultimate base resistance of piles in clay (e.g. Tomlinson, 1997) of nine times the undrained shear strength s_u (i.e. 9 s_u) which is approximately equivalent to 4.5 x UCS. However, in general, the ultimate base resistance of a pile in rock is usually significantly higher than 5 x UCS, due to the usually low porosity (and compressibility) of the rock which constrains the way in which failure of the rock mass below the toe of the pile can occur.

Haberfield (2013) argued that for many piles in rock there is no practical limit to bearing pressure that can be applied at the base of the pile (other than that defined by the structural strength of the pile column), and for this reason there is no sense in trying to assess an ultimate base bearing pressure. He argued that for a pile toe embedded into a dense dilatant material, the stress bulb present at the toe of the pile expands as the pile load increases eventually resulting in a yield zone developing beneath the pile toe. As the rock is dense, with a low porosity, the yield zone dilates, and this dilation occurs against the stiffness of the surrounding rock, thereby increasing the normal stress on the yielded material and hence increasing its strength. As the pile loading continues to increase, the extent of the yield zone grows until the surrounding rock fractures in tension (Johnston and Choi, 1985). However, the propagation of the tension cracks also occurs against the stiffness of the rock, and as a result the pile continues to take load.

The above mechanism is characteristic of dense dilatant rocks and may be muted or absent in intensely fractured rock masses or high void ratio rocks such as carbonate rocks. Haberfield (2013) argues that the presence of a few defects in the rock mass immediately below the pile toe does not influence to any practical degree the maximum bearing pressure that can be achieved, but does influence the rate at which the end bearing resistance mobilises.

The conclusion from this is that the base response of the majority of piles in rock is a work hardening response, with the pile able to continue to take additional load until the concrete column of the pile fails. However, the displacements required to achieve bearing pressures in excess of 2 to 3 times the intact unconfined strength of the rock are relatively large and usually well past the serviceability considerations for the pile.

As noted above the structural strength of the concrete pile column often provides an upper practical limit to the pile ultimate load. Haberfield and Lochaden (2019) provide an example of design of piles to Australian standards which indicates the structural strength of a pile governs the design of the pile for piles embedded in rock with an intact UCS > 3 MPa. As a result it is the displacement of the pile and SLS considerations that are critical to the design of a pile in rock.

There are a multitude of methods that allow the displacement of the toe of a pile to be calculated,

ranging from simple analytical elastic solution calculations to advanced numerical methods using non-linear constitutive laws. As identified above, the base bearing pressure of a pile in rock increases with pile load, and ultimate bearing pressure (if it could be mobilised) occurs at pile displacements well in excess of 10% of pile diameter. For this reason, only a very small portion of the available pile end bearing resistance is mobilised at pile head displacements that meet usual serviceability requirements for individual piles of about 20 mm. As a result, for well-constructed piles free of base debris, elastic solutions provide a reasonable basis for estimating the pile settlement due to the base bearing pressure.

In order to calculate settlement due to base bearing pressure using elastic solutions (e.g. Poulos and Davis, 1974), the mass Young's modulus of the rock (E_m) is required. Ideally this needs to be measured during a geotechnical investigation (e.g. from pressuremeter tests (Benson and Haberfield, 2013) or estimated from correlations with UCS and knowledge of the discontinuities in the rock (e.g. Hoek and Diederichs, 2006). On the basis of this information, typical ratios of E_m/UCS vary from about 50 in extremely fractured rock to about 400 in intact rock with few fractures.

The above discussion has assumed that there is no debris at the base of the pile. This requires appropriate construction procedures to be implemented. The presence of base debris will not significantly reduce the ultimate base resistance of the pile, but it will significantly increase the displacement required to mobilise the design base resistance. For this reason, it is imperative that piles are constructed with clean bases, or alternatively, the piles should be designed such that a majority (if not all) of the serviceability load can be safely carried by (factored) shaft resistance only. The impact of base debris on pile load settlement performance is considered in detail by Xu *et al.* (2018).

Even if accepted base cleaning methods are adopted and carried out competently, it is likely that some debris will remain at the base of the pile unless specialised base cleaning procedures are implemented (e.g. Ervin and Finlayson, 2006). If concrete is placed with a tremie, some of this base debris may be carried away on the top of the rising concrete column, whilst the remainder will tend to be pushed to the edge of the pile base, potentially forming an annulus of debris material around the outer edge of the pile. For this reason, it is prudent to reduce the effective base area of a pile for serviceability calculations (unless a clean base can be ensured and confirmed). A reasonable and prudent assumption for design would be that 50% of the base area is effective for serviceability calculations. The full base area may be used for ULS calculations, but the designer should be aware that the pile head settlement required to achieve this may be significant.

2.3.3Shaft resistance considerations

Whilst our knowledge and understanding of the development of shaft resistance is reasonably well developed (e.g. Haberfield and Lochaden, 2019), it is still common practice for designers to use non-site specific empirical correlations to estimate design shaft resistance values based only on the strength of the intact rock. In the absence of site specific static load testing to failure, many designers assess ultimate shaft resistance based on a non-project specific, empirical data set obtained from the results of static load testing similar to that shown in Figure 1. The ultimate shaft resistance is obtained from Figure 1by multiplying the adhesion factor assessed from the vertical axis of Figure 1 for the applicable intact rock strength (horizontal axis of Figure 1) by the q_u(or UCS) of the intact rock.

For a clean socket, a conservative designer might adopt a shaft resistance using an ultimate shaft resistance value ($f_{s,ult}$) = $0.2\sqrt{q_u}$, whereas a more optimistic designer might use $f_{s,ult} = 0.45\sqrt{q_u}$, or even higher. For a rock with an UCS of 4 MPa, this equates to design shaft resistance values of 400 kPa and 900 kPa respectively. If the designer is able to influence the way in which the pile is installed (e.g. by providing a specification for roughening, cleaning and concreting and ensuring that these activities are undertaken to his / her satisfaction), then a value towards the upper end of the range might be adopted.

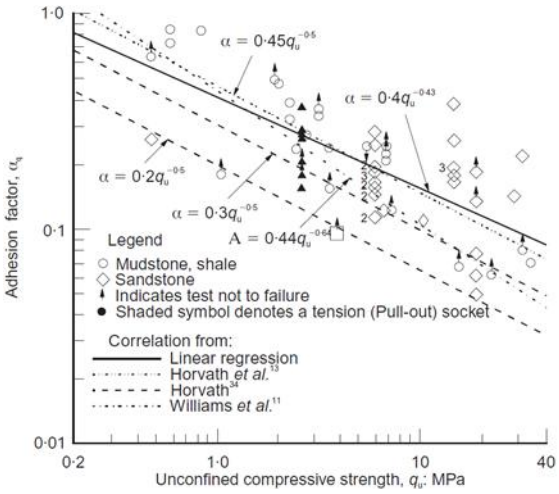

Figure 1. Empirical correlations between ultimate shaft resistance and rock UCS (after Rowe and Armitage, 1984)

It is apparent from the order of magnitude scatter in Figure 1 above that there are other factors that effecttheshaft resistance other than the rock

strength, including (e.g. Haberfield, 2013) rock mass stiffness, pile diameter, socket roughness, rock type, pile length and construction effects (e.g. rock smear and drilling fluid residue). In assessing design shaft resistance, a designer must be aware of these key characteristics and their impact on pile performance.

2.3.4Overall pile performance

The above discussion considers pile shaft and pile base resistances separately. However, these two components of resistance are developed together in response to the load applied (and hence displacement) of the pile. In combining the shaft and base resistance into an overall assessment of pile load displacement response it is essential that the rates of mobilisation of each are considered.

A general rule of thumb based on experience of static load testing is that shaft resistance is fully mobilised at a displacement of about 1% of pile diameter (with a range typically between 0.5% to 2% of pile diameter), whilst base resistance mobilises much more slowly and is not fully mobilised until pile displacements in excess of 10% of pile diameter are attained (Haberfield, 2013).

This highlights the inconsistency in the pile design approaches and recommendations incorporated into most technical reference books, standards and codes of practice around the world. The approach generally adopted in these documents is to calculate the ultimate geotechnical capacity of the pile based on estimates of ultimate shaft and base resistance and then apply a suitable strength reduction factor to the sum of these two components. As pile shaft and base resistance mobilise at very different rates, this approach is only correct at the ultimate geotechnical capacity of the pile.

A more rational approach is to design piles in rock using techniques which account for the different mobilisation rates of shaft and base resistance. Such approaches need to be based on serviceability rather than working or ultimate load considerations. There are a number of pile programs that are commercially available (e.g. RATZ (Randolph, 2003)) as well as other methods that have been developed for piles in soil (e.g. Coyle and Reese, 1966, Ni *et al.*, 2017,Zhang *et al.*, 2010 and Zhang and Zhang,2012) that allow shaft and base resistance to be combined in a rational manner. Whilst these programs have been developed for piles in soil they can also be applied to piles in rock, provided the correct inputs are used. Alternatively, approaches developed specifically for piles in rock (e.g. Kodikara and Johnston, 1994; Seol and Jeong, 2009 and Seol *et al.*, 2009) can be easily implemented into a spreadsheet. In using any of these methods, the designer needs to confirm that the rates of mobilisation of shaft and base resistance assumed in the analyses are reasonable (and consistent with the above observations, or with observations from site-specific load test results).

Due to the different mobilisation rates of shaft and base resistance, the performance of piles in very low to low strength rock at SLS loads is dependent predominantly on shaft resistance. The base resistance also provides some resistance to the serviceability load, but in general its contribution is much less than shaft resistance (particularly for relatively long piles in weak rock). For this reason, it is common for piles in relatively weak rock to be designed such that serviceability loads are carried predominantly by shaft resistance, and that the available base resistance is only relied on for ultimate loads (ULS).

For piles with short sockets (usually in more competent rock), base resistance is the primary component of pile resistance. As with long sockets, serviceability considerations also dictate the design of piles with short sockets.

2.3.5Pile performance

The load deformation performance of a pile is entirely reliant on how well that pile is constructed. Sufficient quality control and quality assurance measures must be in place to ensure that the pile construction process is managed appropriately so that the design intent is achieved (e.g. Haberfield, 2013). If such measures are not implemented, then the design of the piles must be based on lower bound estimates of performance; at least in those aspects that are not appropriately managed during construction.

Such quality control measures must also be practical and safe to undertake. For example:it is often imprudent to dewater pile holes so that concrete can be placed in the dry (rather than by tremie). This is because dewatering of rock sockets, especially in weak rocks can lead to collapse of the socket and poor concrete can result from water seeping into the socket during concreting. In addition, manned entry into pile holes to confirm lithology and to inspect the base of the pile hole is not required and is difficult and costly to perform safely. The lithology can be reasonably confirmed by inspection of drill cuttings and there are a number of devices available suitable for inspecting the base of sockets.

2.4 Designing for serviceability

Designers need to consider variability across the site and with depth and some form of safety factor needs to be applied to the assessment of pile displacement at serviceability loads. This is particularly the case if there is high reliance on end bear-

ing of a pile. Due to the interaction between the various parameters affecting pile response and the different rates of mobilisation of shaft and base resistance, such safety (or reduction) factors should only be applied to the estimated settlement performance of the pile and should not be applied to individual input parameters. Standards should be revised to offer guidance on a safety factors for serviceability based design.

In addition, there are many instances that piles cannot be considered to be acting in isolation, but instead must be considered as part of a group where interaction effects can become significant or need to be considered together with the superstructure (e.g. piles supporting tall buildings or large bridge piers / abutments). There are now a large number of commercially available two-dimensional (2D) and three-dimensional (3D) software packages that allow these complex interactions to be effectively modelled (e.g. FLAC, PLAXIS). In these packages, piles are modelled in a variety of ways, but in many of them, the user has very little control over the modelled pile performance other than to specify pile shaft and base resistance and the axial and bending stiffness of the pile. The user has limited control over the rate of mobilisation of shaft and base resistance which are fundamental to the modelled performance of the piles and the structure. In the authors' experience, in most instances the user rarely considers if the pile performance calculated from the analysis is reasonable for the piles that the user is trying to model. This is described further in Section 4.

3. GEOTECHNICAL INVESTIGATIONS

3.1 *Background*

In order to develop an appropriate geotechnical scope of works for footing design, the expected geological setting,engineering parameters of the founding materials required for design,and the temporary and permanent loading conditions (i.e. vertical, lateral and moment loading) applied to the founding material,must firstly be considered.

Prior to scoping any investigation, the geological history of the site should be outlined and understood, and conceptual ground and foundation models developed. Following this, identification of key risks and the development of an appropriate scope for the geotechnical investigation works can be undertaken.

3.2 *Key geotechnical considerations*

Footing systems for most tall buildings are rarely governed by their ultimate capacity. Rather, the allowable displacement of the footing system is likely to be the primary consideration, and the design of foundationsfor any building should be based on serviceability criteria (i.e. SLS) rather than ultimate failure (i.e. ULS).Any geotechnical investigation must therefore be sufficientto reasonably define the subsurface stratigraphy and thestiffness and load deformation behaviour of the materials within the zone of influence of the proposed building.

For most high rise buildings, it is generally insufficient to only drill boreholes using simplistic investigation techniques such asauger or single / double tube coring drillingand to undertake occasional sampling and standard penetration testing (SPTs). This provides little information of relevance on thestiffness and load deformation behaviour of the ground.

Instead, the investigation techniques that are to be adopted for high rise buildings must be of sufficient quality to reasonably identify the key parameters affecting the performance of building foundations, namely the strength and compressibility of the founding material under serviceability loading. Such an investigation could comprise a combination of cone penetration testing (CPTs) if relatively weak soils are present, along with borehole drilling – initially with standard sampling and testing in the soil materials (e.g. undisturbed tube samples, SPTs) – followed by adopting triple tube coring immediately on encountering competent material (i.e. in extremely weak rock), and performing high quality in situ testing.

The depth of testingshould be developed based on an understanding of expected geological conditions at the site and must be able to define the ground conditions within the zone of influence of the footing system. Where the geology is known and is relatively simplewith a general increase in strength and stiffness with depth, a reasonable depth of testing may be to a distance of about two times the expected footing width below the founding level for shallow footings and about two times the diameter of the likely piled footing size below founding level. For more complex ground conditions with high variability, or where stiffer material overlies less competent material significantly deeper testing in a greater quantity may be required.

In soils, the use of CPT with pore-water pressure measurements,DilatometerMarchetti Testing (DMT) or CPTs with additional shear wave (and P-wave) velocity measurementcan be adopted to supplement borehole drilling and provide useful informationon the stiffness of the ground. If relatively weak soilsare present overlying the expected founding strata, and lateral stability issues become critical with respect to building performance, the use of more accurate soft soil CPT techniques, such as sensitive (i.e. 1 tonne to 2.5 tonne) cones,

T-bar or ball penetrometer testingcan be used. For very dense / very stiff soils, or weathered rock, the use of high pressure pressuremeter (PMT) testing is often undertaken. Other techniques that can be of benefit in more complex ground to provide further informationon the expected engineering behaviour of founding materials include cross hole seismic testing (CHST) in completed boreholes, as well aspreliminary pile testing on sacrificial piles.

3.3 Assessment of engineering properties of founding materials

In order to assess the load deformation response of the founding layers for serviceability design criteria, high quality in situ sampling and testing should be undertaken.

Given that typically founding conditions for high rise buildings will comprise relatively competentstrata, it is the authors experience that in situ PMTs in conjunction with borehole drilling is more commonly undertaken to assess the load-deformation response of the founding materials.

In situPMTs together with appropriate laboratory testing (such as unconfined compression testing) can be used to measure the load-deformation characteristics of the in situ rock mass at discrete test locations.

The results of the pressure expansion curve taken at the initial portion of the curve can be used to assess an initial elastic modulus (E_i), whilst unload-reload data can also be obtained to investigate the deformation characteristics under unload-reload conditions (E_{ur}), which may be of more relevance for transient loading conditions.

In some ground conditions such as where deep granular soil or weak slaking rock is present, quality sampling and PMTs may be impractical to undertake. In such cases, other methods such as high-qualityCHSTcan be adopted to assess the small strain stiffness profile of the ground, provided that appropriate correlations are usedto convertfrom small strain stiffness to larger engineering strains appropriate for footing deformation assessment. Significant benefit with respect to understanding deformation of hybrid footing systems can be realised if CHST is used in conjunction with quality in situ PMTs.

4 ANALYSIS

4.1 Introduction

The analysis of individual shallow footings is reasonably routine for the majority of geotechnical engineers. The settlement of such footings under the loads applied by high rise buildings may be reasonably approximated by simple closed-form hand calculations, but of course is dependent on the adoption of an appropriate stiffness. The design of a shallow footing system for high rise buildings, however, involves the interaction between multiple shallow footings, and more sophisticated analysis methodologies are typically adopted in such cases, such as 2D and 3D numerical analysis. Similarly, more sophisticated analysis methodologies are typically adopted for the assessment of pile group effects.

The assessment of feasibility and the preliminary design of piled / piled raft foundations is typically undertaken using simple closed-form hand calculations (see above and Poulos, 2001) and 2D finite element (FE) analyses which may adopt either plane-strain or axisymmetric conditions. Such methods are useful to assess the approximate required number, diameter, length and location of piles. 3D numerical analysis is now routinely adopted for detailed design, in part due to the availability and relatively low cost of computational power.

4.2 Assessment of pile behaviour

In order to have confidence in the design, it is critical to assess the suitability of the design methodology adopted to model the pile load displacement behaviour. This is typically undertaken by the comparison of the calculated to the known pile load displacement behaviour. The known pile load displacement behaviour will ideally consist of data from site-specific fully instrumented test piles. However, it is the experience of the authors that such data are not routinely available. Comparison of the calculated pile load displacement behaviour to pile data from adjacent sites and sites with similar ground conditions may therefore be required.

The means by which commercially available software consider the interface between the pile and the soil / rock is an important consideration in such a back-analysis. These means have been described by Haberfield and Lochaden (2019) with respect to the PLAXIS suite of software (the use of which has grown significantly in the past ten to fifteen years, to the extent that it is now routinely globally used to model the load deformation performance of piles), and are summarised briefly below.

A pile may be considered as a volume element or as an embedded beam (the latter applicable only for 2D plane-strain and 3D models). When a volume pile is adopted, an interface with a reduced strength and stiffness in comparison to that of the adjacent soil / rock mass is adopted to consider the shear zone between the structural element and the adjacent soil / rock mass. The behaviour of the interface is typically described by linear elastic perfectly plastic behaviour. When an embedded beam is adopted, the interaction of the pile shaft and base

with the adjacent rock is described by linear elastic behaviour with a finite strength and linear elastic perfectly plastic behaviour, respectively. The maximum allowable shaft and base resistance which the embedded beam can mobilise is provided as an input by the user. Alternatively, the shaft resistance can be related to the strength properties of the rock.

Haberfield and Lochaden (2019) conclude that modelling of the pile as a volume element allows the designer significantly more flexibility in the back-analysis of the results of a pile load test, as the stiffness of the interface may be altered without altering that of the adjacent soil / rock mass, and the strength properties of the interface may be modified. However, the adoption of the volume element is more complicated (with respect to geometry and meshing) than the adoption of the embedded beam.

Axisymmetric 2D analysis in which the pile is modelled as a volume element is a useful tool to ensure that the calculated pile load displacement behaviour is similar to the known behaviour. The interface properties required to reasonably match the calculated to the known pile load displacement in the 2D analysis may then be confirmed in a 3D analysis of a single pile. Alternatively, if the pile is modelled as an embedded beam, or if the computational time is not deemed to be excessive, 3D analysis of a single pile under loading may be undertaken without undertaking axisymmetric 2D analysis.

4.3 Selection of ground model

The purpose of this section is to provide a brief discussion of some of the more important considerations in the selection of a model which adequately describes the behaviour of the soil / rock (termed "ground" herein, hence ground model) for the analysis of piled / piled raft foundations. More general guidance on this aspect may be found elsewhere (e.g. Lees, 2017).

All ground models provide only an approximation of the true behaviour of the ground. An increasing degree of complexity is not necessarily either desirable or required, due in part to the potentially extensive and sophisticated nature of testing which may be necessary to assess the inputs to such models. There are many case studies reported in the literature in which very simple constitutive models have been adopted to great effect (e.g. Lochaden *et al.*, 2019). An appropriate ground model should be capable of modelling the critical aspects of the behaviour of the ground for the specific case under consideration.

An appropriate assessment of the stiffness of the ground is of critical importance to the design of the basement and footing system for a high rise building, and as described in Section 3, is a primary consideration in the scoping of an appropriate geotechnical investigation. One of the behavioural aspects which the authors consider to be of primary importance in the design of high rise buildings is the tendency for the stiffness of some materials to be higher in unloading and reloading compared to virgin loading. This tendency may be assessed in the laboratory (e.g. oedometer and triaxial testing) and in the field using PMTs. This effect may be considered in an analysis by either manually changing the stiffness value for the material in question based on consideration of the stress history, or by adopting a constitutive model which automatically considers the stress dependency of the stiffness.

Many high risebuildings have deep basements constructed in rock. In Melbourne, for example, many such basements have been constructed in the Melbourne Formation (MF), the weak weathered siltstone which underlies parts of the city. Haberfield (2017) discusses the engineering implications of the bedding planes present in the MF primarily with respect to basement design and construction. These bedding planes can be persistent for significant lengths (greater than 100 m) and with measured strengths as low as 12°. Such rock is typically considered as either a continuum (i.e. the bedding planes are not explicitly modelled, and relatively lower strength and stiffness values are adopted for the rock), or as a discontinuum (i.e. the bedding planes are explicitly modelled, and relatively higher strength and stiffness values are adopted for the rock). Whilst both of these approaches are valid for the design of basement retention systems, the authors consider that the discontinuum approach is preferable for an analysis in which the footing system of the high rise building is being assessed. The adoption of a continuum approach results in calculated displacements which are significantly greater than those measured, due primarily to the reduced strength and stiffness values which are adopted in such an analysis.

4.4 Limit state design

The adoption of limit state design is now required by many design codes globally. However, many of these design codes provide little guidance on how limit state design should be appropriately considered in soil-structure interaction analyses, noting that it is the understanding of the authors that this will be rectified in revisions which are currently underway to both the Australian standard for retaining wall design (AS4678, 2002) and Eurocode 7. The analysis of the basement / footing system for a high rise building should be based on reasonable and appropriate geotechnical strength and stiffness inputs. The authors therefore consider that a material factoring approach, that is the adop-

tion of shear strength parameters (and stiffness, in some design codes) which have been reduced by some factor, is not appropriate for such analyses. Instead, prudently conservative best-estimate values should be adopted for design. A suitable margin of safety needs to be applied to settlement estimates and recommendations need to be provided in future revisions of relevant standards. The structural ULS may then be considered by applying an appropriate factor to the calculated structural actions. The geotechnical ULS should be considered by reducing the strength of the materials in a stepwise fashion until a valid failure mechanism is deemed to have occurred. Further information is provided in Lees (2013).

5 CASE STUDIES

5.1 Piled-pad footing example

In this case study, a supplementary geotechnical investigation comprising the drilling of additional boreholes, in situ PMTs and associated laboratory testingwas undertaken for several high rise buildings with design column working loads of up to about 14 MN in Melbourne.

The site was underlain by stiff to hard silty or sandy clay underlain by predominantly sandy soils that were dense and very dense.Given the potential to encounter iron cemented lenses within the ground at this site, CPT based investigation techniques were not considered practical for this site, due to the high likelihood of shallow refusal.

The results of in situ PMTs indicated $E_i$values of between about 25 MPa to 80 MPa for the overlying predominantly clayey soils and between about 100 MPa and 160 MPa for the underlying predominantly sandy soils. Calculated E_{ur} values varied between about 120 MPa and 350 MPa for the clayey soils and 250 MPa and 1400 MPa for the sandy soils.

The early footing recommendations called for relatively long CFA piles. Given the subsurface conditions and the magnitude of the design loads, it was considered that a combined piled pad footing solution could provide a less costly satisfactory footing alternative.

Following the geotechnical investigation, a combination of PLAXIS 2D and PLAXIS 3D analyses were used to assess the load settlement performance of the proposed combined footing scheme.

The subsurface profile adopted in the model comprised stiff to hard clay below the base of the proposed footing (initial loading modulus (E_{50}) value of 45 MPa), overlying dense becoming very dense sands (E_{50} values varying between about 125 MPa and 160 MPa).

A hardening soil model was used in a PLAXIS 3D analyses where the unload / reload modulus was equal to three times the initial loading modulus (E_{50}) and long term drained parameters were adopted for the clays.

Various pile sizes and lengths and pad footing dimensions were trialled to achieve a satisfactory footing arrangement with a settlement limitin the range of about 15 mm to 20 mm.As part of the assessment, a group of nine hybrid piled pad footings were also modelled to assess the interaction of adjacent footings and the magnitude of this interaction with respect to settlement.A screenshot of the calculated vertical displacements from the PLAXIS 3D model is presented in Figure 2.

Based on the results of the analysis combined piled-pads comprising pads of between about 2 m to 3 m in plan dimension and piles varying between about 0.6 m in diameter (7 m socket length)and1.2 m in diameter (15 m socket length) were adopted.

To verify the modelled load-settlement response of the pile component, high strain dynamic testing with subsequent signal matching (using CAPWAP) was undertaken on 3% of all piles installed. The results of the high strain dynamic testing typically indicated performance of the pile response to loading in line with the PLAXIS 3D modelling and provided further confidence in the parameters adopted and the performance of CFA piles drilled to a target depth rather than refusal.

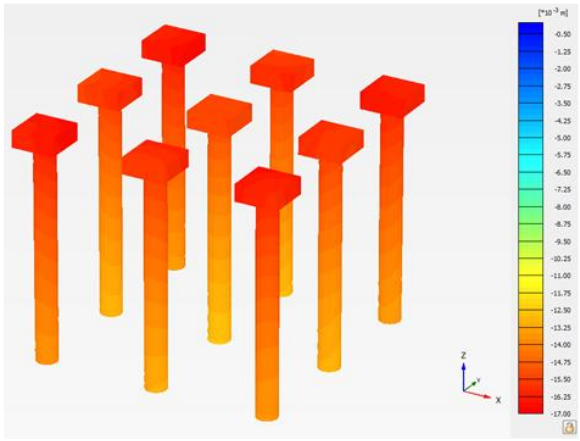

Figure 2.Screenshot of calculated vertical displacements (in units of mm) from PLAXIS 3D model

5.2 Foundation investigation in weak slaking rock

In this case study originally presented in Paul & Haberfield (2008), a foundation investigation and design was completed for a 34 storey building (building column loads up to about 27 MN) in Darwin, Australia, where it was originally proposed to adopt large diameter deep bored piles due to the presence of deeply weathered phyllite rock

across the site. However, suitable piling equipment to undertake drilling of these bored piles was not available in Darwin and an alternative footing solution was sought. Overlying the weathered phyllite is a relatively competentporcellanite, along with weaker siltstone across a smaller portion of the site.

A supplementary investigation comprising triple tube diamond core drilling with PMTs was undertaken to attempt to obtain higher quality estimates of the engineeringproperties of the deeply weathered phyllite. However, due to slaking of this rock and poor core recovery during drilling, this additional investigation was unsuccessful. Suitable samples for laboratory UCS testing could also not be obtainedas recovered core samples exhibited significant disturbance and slaking upon contact with water.

The slaking properties of the phyllite meant that construction of bored piles would be prblematic,and it was likely that socket shaft and base resistance would be compromised by the slaking characteristics of the phyllite. However,based on an understanding of the geological history of the area, it was expected that the in situ mass stiffness of the phyllite wassignificantly higher than that observed in disturbed borehole core samples andthat shallow footings may be suitable for the site (as thesecould be constructed without significantly disturbing the mineral structure of the underlying phyllite). However,adequate testing of the stiffness and load-deformation response of the phyllitewas required to confirm this footing solution was appropriate.

To measure the in situ stiffness at varying depths within the weathered phyllite, pile driving tests on two 450 mm square precast driven piles were undertaken. A 900 mm diameter pre-bored hole was drilled through the upper materials to allow testing to be undertaken within the weathered phyllite. The precast piles were then placed in the pre-drilled hole, and the annulus loosely backfilled with sand. Pile driving was undertaken and monitored by high strain dynamic testing using Pile Driving Analysis (PDA) Equipment. Tests at various elevations were undertaken by removing the precast pile and drilling the pre-bored hole to the new test depth and repeating the above procedure.

Following interpretation of the PDA results using CAPWAP signal matching software, an estimate of the Young's Modulus of the material at the test depth was obtained. The results indicated that the highly weatheredphyllitehad a Young's Modulus of about 300 MPa to 500 MPa and the extremely weathered phyllite had a Young's Modulus of between about 150MPa and 350 MPa.

Analyses were then undertaken using PLAXIS 2D software. Young's modulus values of about 150 MPa and 300 MPa were assumed as a lower-bound and higher-bound estimate of the extremely weathered phyllite, respectively. These adopted Young's Modulus were about five times greater than those adopted previously.

Calculated settlements ranged from about 30 mm to 60 mm at the edge of the building footprint and 60 mm to 110 mm at the centre of the building, with the higher settlement values based on the lower bound mass modulus. These settlement estimates were considered acceptable by the client and structural engineer. Footing displacements measured during construction at various height levels indicated low footing displacement, significantly less than calculated.

5.3 Optimisation of shallow footings for lateral stability

An investigation was undertaken for a proposed high rise buildingof about 35 levels located about 15 km from the Melbourne CBD and founded in deeply weathered, weak siltstone. The investigation comprised borehole drilling using triple tube coring, in situ PMTsand associated laboratory testing.

The results of the investigation indicated predominantly highly to moderately weathered siltstone of low / low to medium strength was expected to be encountered at founding level. The results of the PMTsindicated $E_i$values generally between 470 MPa and 1800 MPa.

Based on the PMT results it was considered that spread footings would provide a satisfactory footing option for axially loaded footings, with design allowable bearing pressures of 4000 kPa recommended.

The initial lateral stability system (designed by others) for the proposed building comprised a fully piled central core footing system with two additional stability footings (one on either side of the core) comprising four 0.9 m diameter piles for each footing. To optimise the lateral stability system and potentially remove / reduce the number of piles required, modelling of the two lateral stability footing systems was undertaken using PLAXIS 3D, with a hardening soil model utilised to represent the increased stiffness experienced by the founding materials under unload-reload conditions. Combined line loads for three critical load combinations were provided by the structural engineer, comprising a SLS case, and two ULS cases (which were deemed to capture the most critical tension (i.e. footing uplift) and compression loads). Lateral loading was also considered for the above combinations.

The results of the analysis indicated that piles were not required for the two stability footing systems, whilst a significantly reduced number of

piles (in the order of about 25%) were required for the central core structure to assist in resisting lateral loads. The maximum calculated bearing pressure under the footings was considered acceptable. The maximum calculated vertical differential displacement under SLS loading for the footings was approximately 10 mm, which was considered acceptable by the structural engineer. A screenshot of the calculated deformed shape from PLAXIS 3D for one of the two lateral stability footings is presented in Figure 3.

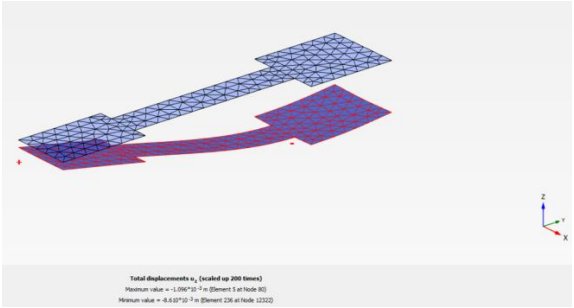

Figure 3:Screenshot of calculated deformed shape of lateral stability footing system from PLAXIS 3D model

5.4 Piled-raft investigation and design

This case study details the investigations, analysis and design for a proposed 60 level high rise building in Mumbai, India in which a piled-raft footing solution has been adopted. The proposed building comprised two central cores with wing structures extending to the north and south. Total working load (dead plus live) was in the order of about 2.4 GN and significant lateral loading due to wind and earthquake had to also be considered.

Several previous investigations had been undertaken across the site, with the results of the investigations indicating variable founding conditions comprising a significantly deep weathering profile of pyroclastic rock and an increased depth to 'hard' bedrock observed over the site. However, these geotechnical investigations comprised little more than single tube cored boreholes (with significant core loss typically greater than 80%) and SPTs at irregular intervals which all refused. The previous recommendations for the proposed building footing system comprised a fully piled solution.

It was considered that a piled raft footing option could be adopted for the building in lieu of a fully piled solution if additional quality investigation was undertaken.

A supplementary investigation was undertaken comprising the drilling of several boreholes using triple tube coring methods, in situ PMTs and laboratory testing. Coring was commenced several metres prior to the proposed founding level of the footing system. Typically, core recovery greater than 90% was observed using the triple tube coring techniques. Following drilling, CHST was also undertaken beneath one core location. The results of the supplementary investigation indicated that the pyroclastic rock, whilst relatively weak near to the founding level, typically increased in strength and stiffness with depth, with modulus values of up to 2000 MPa recorded.

A summary plot of the Young's Modulus estimates from in situ PMTs (E_i), as well as small strain CHST (E_o/N, for N=1, 5, 7 and 10), is presented as Figure 4. Also shown on the plot is the design stiffness stratigraphy adopted for initial design.

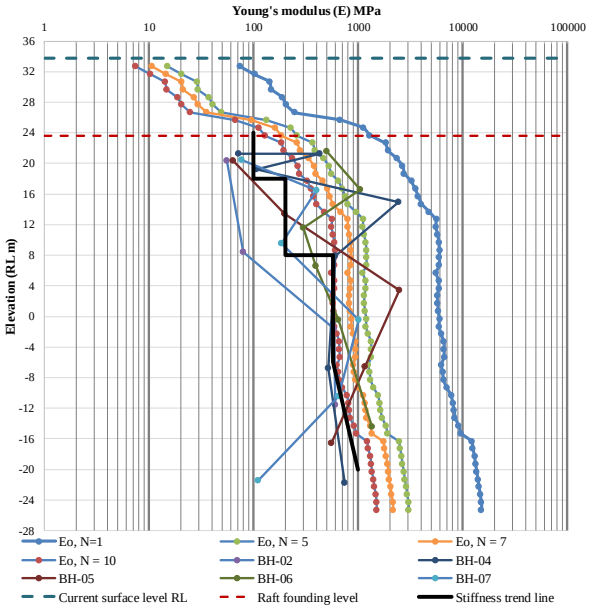

Figure 4.Summary plot of Young's Modulus from supplementary investigation

Based on the results of the supplementary investigation, it was considered that a piled raft footing solution could be adopted in lieu of a fully piled solution. Modelling of the proposed arrangement was undertaken with piles located beneath the main structural elements of the building using PLAXIS 3D.

Individual pile load-deformation responses were assessed based on analysis completed using the software program ROCKET. The pile behaviour as modelled in PLAXIS 3D was matched to the ROCKET analysis results to confirm load-deformation response.

The PLAXIS 3D analysis indicated that 80 no. 1.2 m diameter piles with lengths of between 21 m and 32 m were required to limit calculated settlements to about 30 mm to 35 mm under permanent loads. This resulted in a load share between the raft and piles of about 30% raft / 70% piles. A graphical output of the proposed pile arrangement beneath the raft structure is presented as Figure 5.

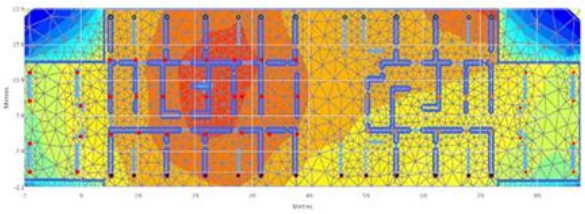

Figure 5. Typical pile arrangement beneath raft structure (piles shown as solid red circles)

5.5 Raft design

A geotechnical investigation was undertaken at a sloping site in the downtown area of Seattle, Washington, USA, for a proposed 27 level building, with a seven level basement extending to a maximum depth of approximately 25 m. The site is approximately square in plan (plan dimensions of approximately 40 m x 40 m).

The geotechnical investigation at the site allowed the characterisation of the founding units, which comprised eithera very stiff to hard grey laminated silty clay to clay lacustrine deposit, and a hardclayey silt to clay and gravelly silty sand glacial deposit, with sand and gravel seams. The groundwater level was measured to be approximately 5 m above basement bulk excavation level.

A suite of in situ investigations was undertaken at the site to allow appropriate characterisation of the deformation behaviour of the sub-surface units. The results from downhole CHST at the site indicated that the average shear wave velocity at and below bulk excavation level was approximately 450 m/s.These test results, in addition to the results of PMTs undertaken at the site, allowed the designers the confidence to adopt Young's Modulus values which were higher than would typically be adopted for the founding materials. This was critical to the assessment of the deformation of the raft under SLS loads.

The purpose of the modelling was to assess calculated settlements and bearing pressures in the SLS case and to provide the structural engineer with indicative raft structural actions in both the SLS and ULS cases.

Effective stress conditions were adopted for the analysis of thesingle SLS load case considered, whilst total stress conditions were considered for the analysis of the four ULS load cases considered. Core and perimeter walls were considered in the analysis to partially account for the stiffness provided by the superstructure of the building.

The output from the model provided to the structural engineer included calculated raft displacements, raft structural actions (shear forces and bending moments), and spring stiffness values. The purpose of the latter wasto allow an iterative approach to be adopted between the geotechnical and structural analyses.

6 CONCLUSION

This paper presents the authors' experience of geotechnical investigation and footing design for high rise buildings. The scope of the investigation must target the specific ground conditions at the site, which must initially be assessed from a desktop study of available information. This desktop study allows the likely subsurface conditions to be identified and preliminary foundation concepts to be developed. The ground investigation is then used to confirm the geological model and refine the geotechnical model and properties of the site. The ground investigation must do more than simply quantify the subsurface stratigraphy and the engineering properties of the primary founding materials; rather it must specifically target the load deformation performance of such materials. Therefore, every site is different, and the scope of the ground investigation must be tailored to suit.

Obtaining suitable samples from significant depth for laboratory testing which are sufficiently undisturbed to provide reliable estimates of load deformation performance is difficult. Greater reliance should be placed on quality in situ testing, which should be focused on the assessment of stiffness and load deformation behaviour. Such testing includes high quality high pressure PMTs, CHST and pile load testing. However, this does not negate the requirement for appropriate high quality laboratory testing.

Once a suitable geotechnical model has been developed, preliminary sizing of individual footings can be undertaken using simplified approaches. This is followed by a detailed analysis of the entire foundation using soil-structure interaction software packages. The geotechnical engineer must understand footing performance and the potential impact of construction effects on footing performance as well as carefully consider a number of issues, including the limitations of the design methodology (including ground and constitutive models) and the means by which the design methodology may be validated (e.g. against measured data). The material factoring approach of limit state design is considered to be inappropriate for such analyses, and prudently conservative best-estimate values should be adopted.

7 ACKNOWLEDGEMENTS

The authors gratefully acknowledge their colleagues within Golder who assisted in the case studies described above, including Darren Paul, Reda Mikhail,Doug Goad, Dr Gary Chapman, Dr Yousef Ansari, Dr Daniel King and Dr David Gu, and their ex-colleagues, including Jim Finlayson

and Dr Shailendra Amatya.The assistance of Dr Julian Seidel in undertaking the CAPWAP analysis as described in Section 5.2 and for the use of the ROCKET programis also gratefully acknowledged.

8 REFERENCES

AS4678 (2002), "Earth-retaining structures", Standards Australia.

Benson, N. D. and Haberfield, C. M. (2003). "Assessment of mass modulus of a weathered argillaceous rock". Proceedings international Society for Rock Mechanics 2003, Southern African Institute of Mining and Metallurgy: Johannesburg.

Colls, S. (2019). "Adding new level to old buildings: a case study in foundation assessment", 13th Australia New Zealand Conference on Geomechanics, Perth, Australia, pp. 309-314.

Coyle, H. M. and Reese, L. C., (1966). "Load transfer for axially loaded piles in clay". Journal Soil Mechanics and Foundation Engineering Division, ASCE, 92 (SM2), pp. 1-26.

EN 1997 (2004). Eurocode 7 – Geotechnical design. European Committee for Standardisation, Brussels.

Ervin, M. C. and Finlayson, J. E. (2006), "Piled foundations for Eureka Tower, Melbourne, Australia". Proceedings of the Institution of Civil Engineers, Geotechnical Engineering 159, July 2006, Issue GE3, pp 187-194.

Haberfield, C.M. (2013). "Performance of footings in rock based on serviceability". EH Davis Memorial Lecture 2007. Australia Geomechanics, 48, no. 1, pp. 1-50.

Haberfield, C.M. (2017). "Practical application of soil structure interaction analysis", Gregory Tschebotarioff Lecture 2017, Proceedings of the 19th International Conference on Soil Mechanics and Geotechnical Engineering, Seoul, South Korea.

Haberfield, C.M., and Lochaden, A.L.E. (2019). "Analysis and design of axially loaded piles in rock", Journal of Rock Mechanics and Geotechnical Engineering, 11, pp. 535-548. https://doi.org/10.1016/j.jrmge.2018.10.001.

Hoek, E. and Diederichs, M.S., (2006) "Empirical estimation of rock mass modulus", International Journal of Rock Mechanics and Mining Sciences, 43, pp. 203-215.

Johnston, I.W. and Choi, S.K. (1985). Failure mechanisms of foundations in soft rock. Proc. 11th Int. Conference on Soil Mechanics and Found. Engineering, Ed Balkema, A.A. Rotterdam, San Francisco, 3, pp. 1397-1400.

Kodikara, J. K., and Johnston, I. W. (1994). "Shear behaviour of irregular triangular rock-concrete joints". International Journal of Rock Mechanics Min. Science and Geomechanics. Abstract., 31, no. 4, pp. 313-22.

Lees, A. (2013). "Using numerical analysis with geotechnical design codes", in Modern Geotechnical Design Cordes of Practice (eds. Arnold, Fenton, Hicks, Schweckendiek & Simpson), IOS Press, Amsterdam, Netherlands, pp. 157-170.

Lees, A. (2016). "Geotechnical finite element analysis", Thomas Telford, London.

Lochaden, A. L. E., and Haberfield, C.M. (2018). "Challenges in the design of basements in Melbourne, Australia", Technical Committee 207 of the International Society for Soil Mechanics and Geotechnical Engineering (ISSMGE) International Conference on Geotechnical Engineering and Architecture, Saint Petersburg, Russia.

Lochaden, A. L. E., Haberfield, C.M., and Francis, B. (2019). "The effect of the in situ stress field on basement performance – a case study from Sydney, Australia", 13th Australia New Zealand Conference on Geomechanics, Perth, Australia, pp. 435-440.

O'Neill, M. W. and Hassan, K. M. (1994), "Drilled shafts: effects of construction on performance and design criteria. Proceedings of the International Conference on Design and Construction of Deep Foundations, Orlando, FL, pp. 137-87.

Ni, P., Song, L., Mei, G., and Zhao, Y. (2017). "Generalized nonlinear softening load-transfer model for axially loaded piles". International Journal of Geomechanics. 17(8).

Paul, D. and Haberfield, C. M. (2018). "Foundation investigation in weak slaking rock, Darwin, Proceedings of the Sydney Chapter 2008 Symposium "Foundations: Innovation and Experience", Sydney, Australia.

Pells, P.J.N. (2004). Substance and mass properties for the design of engineering structures in the Hawkesbury Sandstone. Australian Geomechanics, September, 39, no. 3, pp. 1-23.

PLAXIS. PLAXIS 2D manual (2019), The Netherlands.

PLAXIS. PLAXIS 3D manual (2019), The Netherlands.

Poulos, H.G. (2001). "Piled raft foundations: design and applications". Geotechnique, 51, no. 2, pp. 95-113.

Poulos, H.G. and Davis, E.H. (1974). Elastic solutions for soil and rock mechanics. John Wiley and Sons Inc., New York.

Rowe, R.K. and Armitage, H.H., (1984). "The design of piles socketed into weak rock". Report GEOT-11-84, University of Western Ontario, Canada.

Randolph, M.F.(2003). RATZ manual version 4.2: load transfer analysis of axially loaded piles, RATZ Software Manual, Perth, Australia.

ROCKET 97, (1997), Civil Engineering Monash University.

Seol, H. and Jeong, S. (2009). "Load-settlement behavior of rock-socketed drilled shafts using Osterberg-Cell tests." Computers and Geotechnics, 36, no. 7, pp. 1134-41.

Seol, H., Jeong, S., and Cho, S. (2009). "Analytical method for load-transfer characteristics of rock-socketed drilled shafts". Journal of Geotechnical and Geoenvironmental Engineering, 135, no. 6, pp. 778-89.

Tomlinson, M. J., (1997), "Pile Design and Construction Practice", Viewpoint Publications, Cement and Concrete Association, London.

Xu, M., Ni, P., Mei, G., and Zhao, Y. (2018). "Load-settlement behaviour of bored piles with loose sediments at the pile tip: experimental, numerical and analytical study". Computers and Geotechnics, 102, pp. 92-101.

Zhang, Q.Q., Zhang, Z.M., and He, J.Y. (2010). "A simplified approach for settlement analysis of single pile and pile groups considering interaction between identical piles in multi-layered soils". Computers and Geotechnics, 37, no. 7, pp. 969-76.

Zhang, Q.Q. and Zhang, Z.M. (2012). "A simplified nonlinear approach for single pile settlement analysis". Canadian Geotechnical Journal, 49, no. 11, pp. 1256-66.

Modeling Coupled Dynamic Processes in Landfills: Holistic Long-Term Performance Management to Improve Sustainability

K.R. Reddy & G. Kumar
Department of Civil and Materials Engineering, University of Illinois at Chicago, USA

ABSTRACT: In recent years,the bioreactor landfillswherein leachate recirculation/injection is carried out to enhance the moisture levels within the waste thereby facilitating rapid waste decomposition and leading to early waste stabilization have emerged as an effective waste management option. However, thereis a lack of sound basis for effective design and operation of such landfills due to the fact that there is a limited understanding of the physical, chemical and biological processes and the influence of their coupled interactions on the MSW behavior in landfills. Several researchers have developed numerical models to simulate waste behavior but only a few models have considered the simultaneous interactions of hydraulic, mechanical, biological and thermal processes within the waste in their numerical model. In this study, anew numerical framework incorporating coupled thermo-hydro-bio-mechanical processes is presented. The numerical model can predict the spatial and temporal variation of waste temperatures, moisture distribution, gas generation, pore pressures, waste settlement, waste slope stability, and interface shear response in the landfill liner system. The numerical model has been validated with lab-scale and field-scale experiments. Parametric analyses are performed using the developed model to identify the key variables that influence the effective design of bioreactor landfills.

1 INTRODUCTION

Landfilling of municipal solid waste, although being the least preferred option, is the most dominant method of managing waste in U.S. and many other countries across the globe. In the light of steady increase in the population and rapid urbanization, the amount of waste produced is also increasing considerably. According to United States Environmental Protection Agency (USEPA), about 262 million tons of MSW was produced in 2015 of which nearly 138 million tons was landfilled (USEPA, 2018). The current practices for construction of traditional engineered landfills that just serve as waste containment systems are well established. This isolated system primarily contains the landfilled MSW in a relatively dry state and is designed with soil cover systems at the top of the landfill to prevent infiltration of water from the precipitation and with leachate collection and removal systems to remove any leachate accumulated over the bottom liner system. This results in a relatively dry condition within MSW and causing slow decomposition of the organic matter (biodegradable constituents) within the waste due to the lack of adequate moisture. The slow decomposition of waste leads to several problems such as low gas generation rates, prolonged waste stabilization periods, increased post-closure monitoring requirements, increased leachate treatment and disposal costs, and a long-term liability of the land use with no beneficial purpose.

In recent years the idea of bioreactor landfills has gained wide attention because of its numerous benefits that can lead to sustainable waste management. A schematic of the operation of bioreactor landfill is shown in Fig. 1.

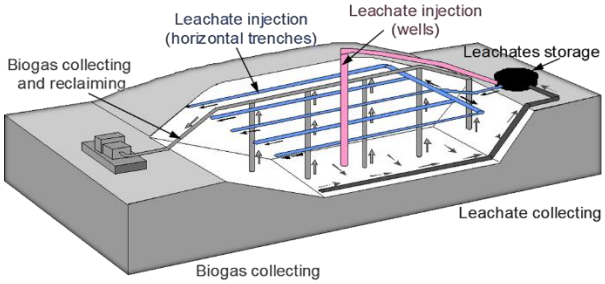

Fig. 1: Schematic of a bioreactor landfill and its fundamental operations

The bioreactor landfill uses the concept of an anaerobic digester, wherein the favorable conditions for rapid biodegradation of organic matter within the waste are maintained to accelerate the waste stabilization except that there is no rapid agitation as in the case of an anaerobic digester. In the field, these favorable conditions are achieved by recirculation of leachate and other permitted liquids along with addition of supplemental nutrients and/or inoculum of microbes, which results in adequate moisture levels and biochemical conditions suitable for rapid waste decomposition. Bioreactor landfills offer several benefits such as rapid waste decomposition, increased gas generation rates,

high settlement rates and early waste stabilization. In addition, there are other secondary benefits such as reduced post-closure monitoring cost, reduced leachate treatment and disposal costs, and landfill space reclamation. Several laboratory studies and field-scale pilot tests have been performed confirming the enhanced decomposition of MSW with leachate recirculation into the waste mass. Although the leachate recirculation seems to be a viable concept, there are no established design practices for leachate recirculation, mainly due to the lack of adequate knowledge and data on the performance of such landfill systems. Unlike conventional landfills where leachate generation is limited, bioreactor landfills operate on intentional leachate/liquid recirculation/injection into the landfill, and if the leachate levels and pore pressures induced by the injection are not properly managed, it may cause instability in landfill resulting in landfill design failures.

In this regard, several numerical modeling efforts were carried out, to investigate the effectiveness of different leachate recirculation systems (LRS) in various configurations for uniformly distributing the injected leachate while maintaining the stability of landfill slopes under pressurized leachate injections (Kulkarni and Reddy 2012; Reddy et al. 2017a). However, most of these studies neglected the effects of biodegradation and its consequent effects from settlement and gas generation on the fluid flow within the waste. The performance of a bioreactor landfill is influenced by several interdependent processes within the waste including the leachate flow and distribution, waste settlement due to the overburden stress and mass loss induced by waste decomposition, changes in the shear strength of the waste with degradation, and changes in temperature and heat generated from waste decomposition. Thus, there exists a complex system of simultaneously occurring and interrelated processes within the waste mass. There have also been several numerical investigations that looked at the coupled behavior of MSW accounting for the hydraulic, biochemical and mechanical behavior of MSW into a numerical model to simulate the coupled hydro-bio-mechanical response of MSW in landfills. But these models do not holistically assess the influence of the coupled processes on the performance of other engineered components of a landfill in terms of their stability and integrity within the landfill. In addition, most of the studies did not account for the heat generation and thermal behavior within the landfill and furthermore, if they did incorporate the effects of heat generation on the transient temperature distribution within the landfill, its influence on the biodegradation of waste was not accounted.

In this paper a numerical framework is presented that can holistically assess the overall performance of the landfill by accounting for the interdependency of hydraulic (fluid flow and pore fluid pressure distribution), mechanical (stress and deformation, waste settlement and slope stability), biological (waste decomposition and gas generation) and thermal (heat generation and temperature distribution) processes within the MSW. Details on the mathematical formulations of each model is presented elsewhere. A brief review of literature on the previous attempts to model MSW behavior in bioreactor landfills is presented and some of the major challenges associated with numerical modeling of MSW behavior in such landfills are presented.These aspects are presented in Kumar and Reddy (2019) and repeated here.

2 COUPLED PROCESSES IN LANDFILLS

Municipal solid waste is a highly heterogeneous porous media with its properties (physical, mechanical and biological) varying spatially across the landfill due to inherent differences in waste composition. In addition, the rapid decomposition of the waste under leachate recirculation further exacerbates the situation by causing temporal changes in the waste properties. Thus, the overall performance of a bioreactor landfill is dictated by the combined effect of several interdependent system processes including hydraulic, mechanical, biochemical and thermal processes. A brief explanation of each of the system processes and their interactions with one another is explained in this section. A schematic of the major system processes and their interactions within the MSW landfills is shown in Fig. 2.

The hydraulic processes within the bioreactor landfills include the fluid flow (leachate flow) and the resulting distribution of moisture and pore-fluid pressures (liquid and gas phase). Due to the relatively low moisture in the MSW pore spaces, the fluid flow is generally and suitably assumed to follow unsaturated fluid flow behavior. Moreover, the decomposition of waste generates landfill gas (predominantly methane and carbon dioxide) leading to the gas flow and development of pore gas pressures within the MSW pore space that can have a great influence on the transient leachate flow and distribution. Thus, a two-phase flow behavior can be used to adequately simulate the fluid flow within the unsaturated waste mass.

The mechanical behavior of the waste is influenced by the overburden stress from the overlying waste layers and this differs spatially based on the landfill geometry and the spatially varying waste properties. The deformation and consequently the

settlement of the waste is partly influenced by the mechanical properties of the waste (e.g. stiffness, strength parameters). However, the mechanical properties of the waste change temporally as the waste degrades and hence the change in the settlement of the waste induced by overburden stress. In addition to this, a significant amount of the waste settlement is borne out of the mass loss (conversion of biodegradable solids to landfill gas) resulting from the contemporaneous increase and decrease in void spaces within the waste due to waste degradation. This contributes to most of the waste settlement in MSW landfills.

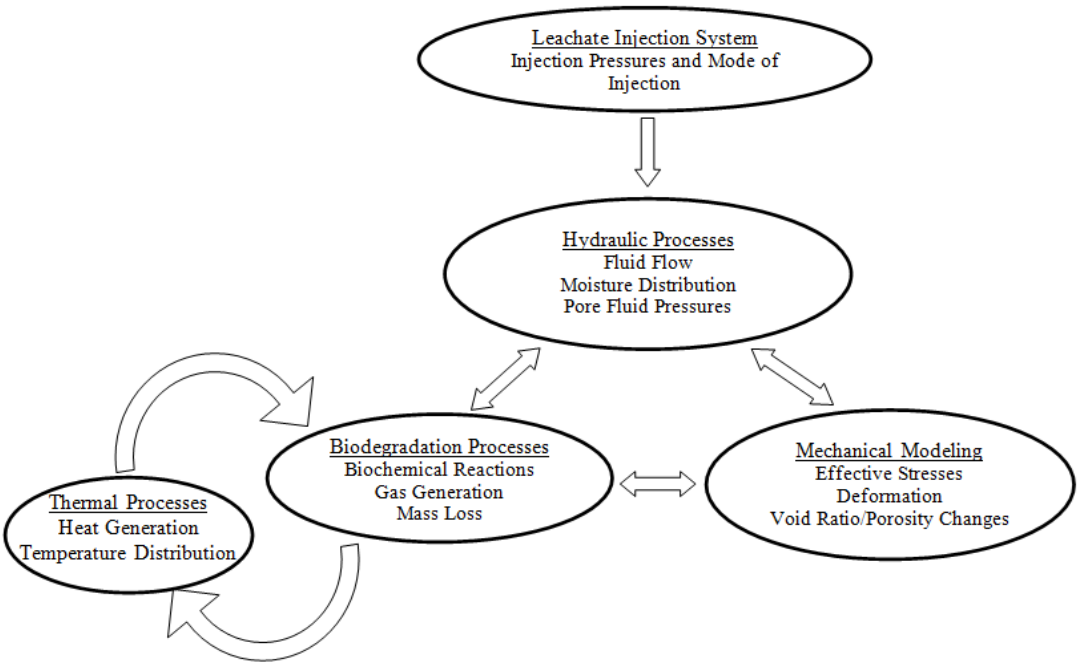

Fig. 2: Major processes and their coupled interactions in MSW landfills

The biochemical behavior of the waste is mainly dependent on the waste composition. Typically, most of the readily degradable matter is found to be cellulosic and hemi-cellulosic in nature and it contributes the most to the total methane gas production (Barlaz et al., 1990). Most of the biodegradation takes place anaerobically due to oxygen deprived conditions within the waste mass. The major biochemical reactions leading to the landfill gas production are hydrolysis involving the breakdown of higher molecular weight organic compounds to easily degradable monomers, followed by acid production (typically acetic acid) by microbially aided acidogenesis through fermentative bacteria, and finally the generation of methane by methanogenic bacteria. In all of this, the leachate chemistry and the biochemical reaction kinetics dictate the generation of landfill gas. Moreover, the biodegradation process is influenced by many factors including, temperature, pH, and moisture among the most influential parameters.

The anaerobic biodegradation of organic matter in the MSW releases heat which influences the temperature within the waste mass. Furthermore, the resulting temperature in turn dictates the biodegradation of waste mass since the optimum degradation of waste by microbes occurs only at a certain temperature range.In addition, the spatial and temporal distribution of temperatures within the waste are influenced by the seasonal temperature changes as well.

Thus, understanding the thermal behavior of MSW and incorporating its influence on the other system processes in a landfill plays a significant role in a better prediction of the overall performance of the landfill.

Each of the above-mentioned processes occur and interact simultaneously influencing the overall behavior of MSW. For example, the fluid flow (leachate and gas) within the MSW is dictated by the porosity, available moisture and the permeability of waste for the fluids. However, the decomposition of waste that occurs simultaneously as the fluid flows through the MSW causes the mass loss resulting in changes in the void spaces (porosity) and in turn influences the fluid flow thereafter. In addition, the increase in the void spaces can cause the waste to settle under the overburden stresses causing changes in the pore fluid pressures. Furthermore, the changing void space (void ratio) al-

ters the moisture availability in MSW across the landfill, consequently influencing the rate of biodegradation MSW. The temperature dependent heat generation constantly influences the biodegradation of MSW and thereby the other processes impacted by the biodegradation of waste. It is quite evident that the landfill system is a unique and complex multiphase system with several processes occurring simultaneously in a coupled manner. It is of utmost importance to understand the individual system processes and their coupled interactions accurately to have a good prediction on the performance of a landfill system thereby enabling safe and effective construction and operation of bioreactor landfills.

3 PREVIOUS INVESTIGATIONS ON BIOREACTOR LANDFILLS

Over the past few years, a comprehensive research has been performed at the University of Illinois at Chicago (UIC) on bioreactor landfills involving field investigations, laboratory tests on MSW samples and numerical modeling of MSW behavior based on the characteristics of MSW as observed from the experimental studies. A list of all the previous studies on bioreactor landfills performed at UIC is shown in Table 1.

Table 1: Previous research on bioreactor landfills at UIC

Research Type	Topic of the Study	Reference
Field Investigation	In-situ properties of MSW at a leachate recirculating landfill	Grellier et al. (2006, 2007)
	Geophysical testing for evaluating dynamic properties of MSW	Carpenter et al. (2013a,b)
	Field Monitoring and performance assessment of bioreactor landfill	Reddy et al. (2009a)
Laboratory Investigation	Laboratory testing of geotechnical properties (compressibility, shear strength, hydraulic conductivity, etc.) of field and synthetic waste samples	Reddy et al. (2009b,d,e); Reddy et al. (2009b); Reddy et al. (2011); Reddy et al. (2015a)
Numerical Modeling/ Simulation	Settlement modeling	Babu et al. (2010, 2011)
	Modeling single phase (liquid) fluid flow in bioreactor landfills to evaluate the moisture distribution by different leachate injection systems	Kulkarni and Reddy (2012); Reddy et al. (2013a,b); Reddy et al. (2014); Giri and Reddy (2014a); Reddy et al. (2015b,c)
	Slope stability under pressurized leachate injection	Giri and Reddy (2014b,c); Giri and Reddy (2015a)
	Modeling of coupled hydro-mechanical processes	Giri and Reddy (2015d)
	Modeling of coupled hydro-bio-mechanical processes	Reddy et al. (2017a,b); Reddy et al. (2018a,b)

A thorough field investigation was performed to determine the variation of in-situ moisture and density variation with depth and leachate injection were monitored to characterize the field waste. In addition, geophysical testing was performed to determine other dynamic and mechanical properties of waste. Several laboratory investigations were performed which involved testing of field MSW samples from a leachate recirculation landfill for their geotechnical properties such as the compressibility, shear strength, hydraulicconductivity, specific gravity, unit weight and other crucial properties. These properties were furtherevaluated at different stages of waste degradation to determine the effect of biodegradation on waste properties. In addition, biochemical testing was performed on the field MSW samples to determine the biochemical properties of MSW. All the tests performed on field MSW samples were also performed on synthetically prepared waste to have a control on the degradation and thereby evaluate the variation in waste properties with time.

Numerical modeling techniques are a great tool in simulating the coupled processes within MSW. It has been extensively used in order to understand the behavior of MSW and the influence it has on the performance of different components of a landfill. It is quite essential to assess the short-term and long-term integrity and stability of landfill components such as the liner and cover systems along with the stability of landfill slopes for a holistic assessment of the performance of a landfill system.In the recent years, a progressive modeling effort has been laid on trying to accurately simulate the different processes and their interactions in waste.

Most of the initial numerical studies on bioreactor landfills performed in this regard neglected the combined effects of different processes and mainly focused on the hydraulic aspects of bioreactor landfills (e.g. moisture and pore pressure distribu-

tion). Some of the studies evaluated the effectiveness of different subsurface leachate recirculation systems (horizontal trenches, vertical injection wells, drainage blankets) in uniformly distributing the injected leachate (Kulkarni and Reddy 2012; Reddy et al. 2013a,b; Reddy et al. 2014; Giri and Reddy 2014a; Reddy et al. 2015b,c). Thereafter, the study was focused on evaluating the stability of landfill slopes under different injection pressures or flow rates (Giri and Reddy 2014b,c; Giri and Reddy 2015a). Design recommendations were developed based on these investigations suggesting the safe injection pressures and setback distance for locating the injection system from the landfill slope that needs to be followed.

Recently, there have also been efforts to incorporate the coupled interactions between hydraulic, mechanical and biological processes into the numerical model to predict the MSW behavior in landfills (Reddy et al. 2017a). These studies focused on simulating the coupled hydro-bio-mechanical processes to try and understand the complexity associated with the MSW behavior within the landfill and how it affects the holistic performance of a bioreactor landfill. In this regard a mathematical modeling framework that incorporates the coupled hydro-bio-mechanical processes and its impacts on the stability and integrity of the landfill system and its components has been formulated. In particular, this mathematical framework integrates a two-phase flow hydraulic model, a 2-D plane strain mechanical model, and a first order decay biodegradation model. The entire numerical framework is implemented in a software named FLAC which is based on a finite different numerical method.

The fluid flow is based on the Darcy's law while the hydraulic conductivity of the fluids under unsaturated conditions is given by the relative permeability functions of the van Genuchten form (van Genuchten, 1980). The mechanical model for MSW involves the 2-D plane strain formulation of Mohr-Coulomb constitutive law to simulate the stress-strain behavior of MSW. The biodegradation of waste is simulated using the first order decay kinetics. The gas generation from waste degradation is similar to the USEPA's LandGEM model. However, the biodegradation model formulated in this study incorporates the effect of changing moisture as fluid flows through the MSW on the rate of biodegradation of waste. The extent of waste degradation at a location in the landfill is derived from the gas produced from the waste at that location over the biochemical methane potential of the waste. As the biodegradation takes place the waste properties also change as per the correlations developed between the extent of degradation and the geotechnical properties of the waste from previous experimental investigations on field MSW samples, thus simulating a transient coupled hydro-bio-mechanical behavior of MSW. A detailed explanation of the entire coupled hydro-bio-mechanical (CHBM) numerical framework and the numerical simulations performed on a typical landfill cell configuration (see Fig. 3) using the CHBM numerical framework is presented in Reddy et al. (2017b). Some of the results obtained from these numerical simulations are presented here to demonstrate the predictive capacities of the model.

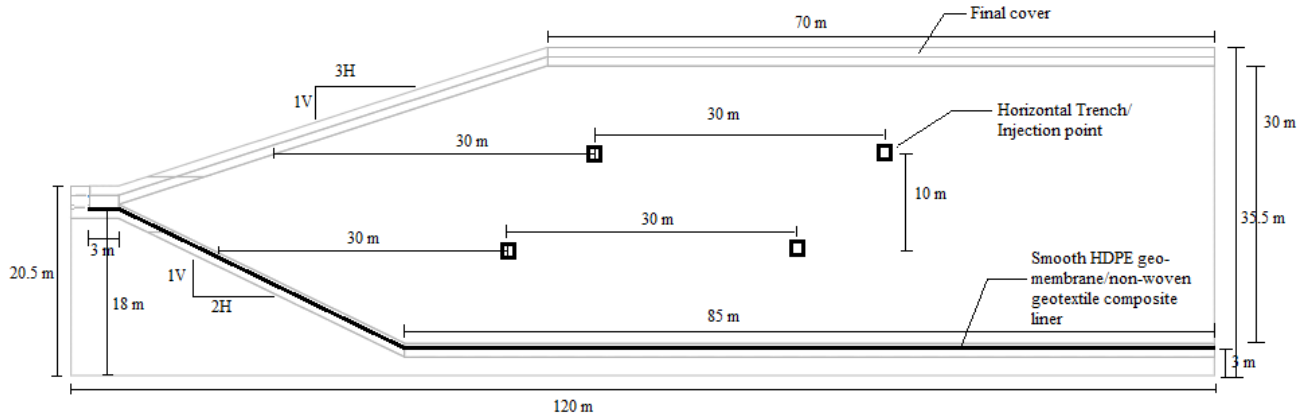

Fig. 3: Schematic of the typical bioreactor landfill cell model used for the numerical analyses

4 RESULTS AND DISCUSSION

Fig. 4 shows the evolution of the extent of moisture within the waste mass with time in terms of wetted area.In this study, wetted area is defined as the cross-sectional area of with a degree of saturation greater than 60%. It is essentially a measure of the extent of moisture distributed across the landfill from leachate recirculation/injection. The value of 60% saturation is considered to be indicative of optimum moisture within the waste for enhanced waste decomposition (ITRC 2006). It can be seen in Fig. 4 that the wetted area increases with time due to leachate injection, but it is dictated by the

fluid flow within the waste. The initial unsaturated state of the waste limits the rapid flow due to low relative permeability of the fluid in the initial stages. However, as the waste saturation increases so does the permeability of the fluid and thereby the extent of moisture distributed across the landfill also increases at a rapid rate. The landfill owners or the operators must be aware of the wetted area in the landfill to be able to estimate the moisture requirements and it is therefore an important operating parameter for bioreactor landfills which needs to be accurately predicted by a numerical model.

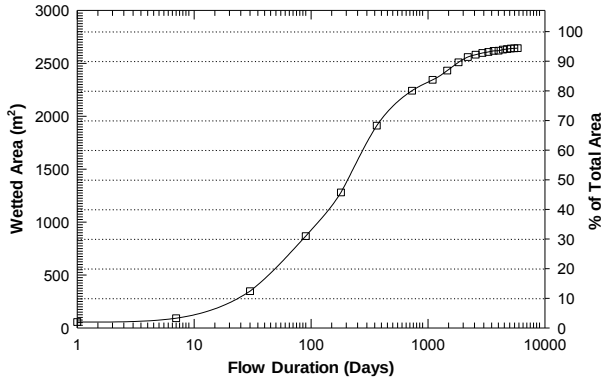

Fig. 4. MSW wetted area with continuous periods of leachate injection at an injection pressure of 100 kPa in bioreactor landfill

Fig. 5 shows the evolution of cumulative volume of methane (CH_4) gas generated with time for the conventional (without leachate injection) and bioreactor landfill (with leachate injection) simulation. The results clearly indicate the distinct rates of CH_4 gas generation between the two simulations indicative of the effect of moisture from leachate injection on the rapid decomposition of the waste in the bioreactor landfill simulation.The gas generation model is simplified to follow a first order decay kinetics which may not be an accurate way of estimating CH_4 gas production.

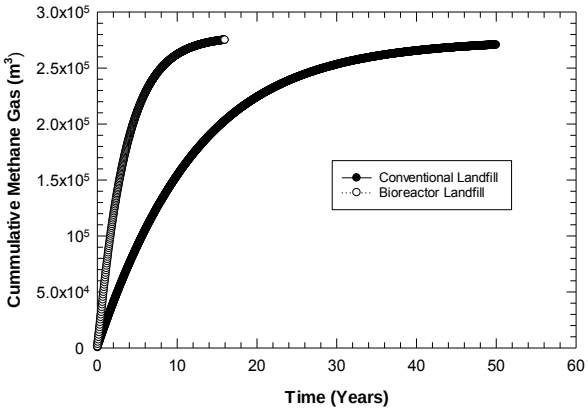

Fig. 5: Cumulative methane gas generation for conventional and bioreactor landfill

Several studies involving more realistic and rational approach towards exclusively for modeling of biodegradation waste have been published and efforts are underway to incorporate a biochemical reactions based model to simulate waste degradation and accurate prediction of CH_4 gas generation.

Fig. 6 shows the comparison of the variation of surface settlement with time for a conventional and bioreactor landfill. It can be observed that total settlement in both the cases is the same due to the same amount of waste and its composition in both conventional and bioreactor landfill simulation. However, the time it takes for attaining the total settlement in a bioreactor landfill is significantly less than the conventional landfill. This is mainly because of the higher rates of biodegradation in bioreactor landfill due to the availability of moisture from leachate injection and its distribution. The numerical model could simulate the different landfill settlement behavior with and without recirculation reasonably well.

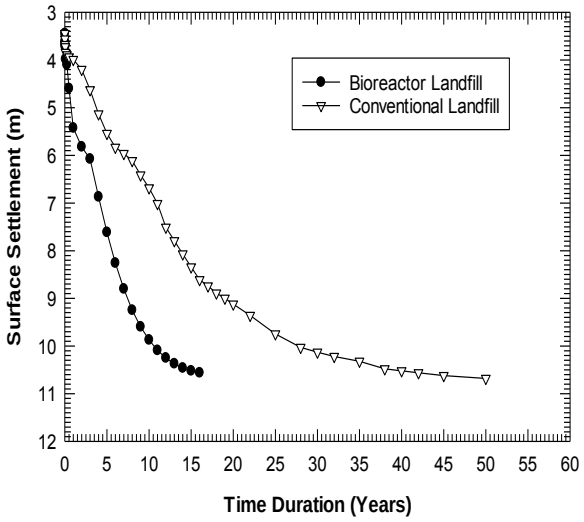

Fig. 6: Variation of surface settlement in a simulated conventional and bioreactor landfill model

Fig 7 shows the results of slope stability in terms of factor of safety (FOS) for three numerical simulations of a landfill with the same waste conditions and landfill geometry. However, each of the three simulations incorporated different system processes.The first simulation represented a bioreactor landfill (involving leachate injection) but neglected the effect of biodegradation on the MSW behavior (coupled hydro-mechanical simulation). The second simulation represented a conventional landfill with no leachate injection (coupled bio-mechanical simulation) and the third simulation represented a bioreactor landfill with leachate injection (coupled hydro-bio-mechanical). The second and the third simulation incorporated the effect of biodegrada-

tion on MSW behavior. The three cases were evaluated for their slope stability under different simulated conditions.

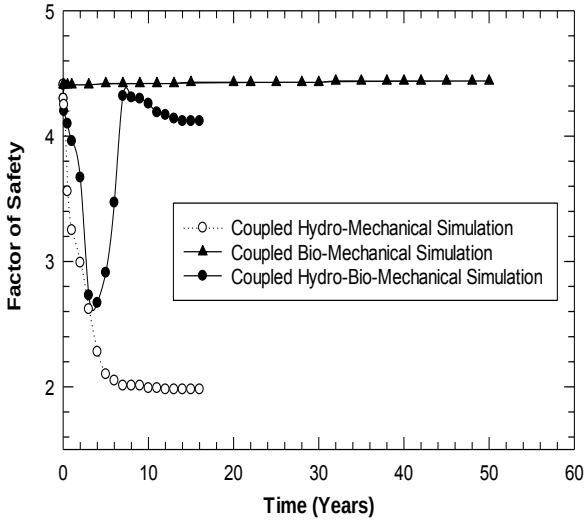

Fig. 7: Variation of factor of safety of landfill slope with elapsed time for coupled hydro-mechanical, coupled bio-mechanical and coupled hydro-bio-mechanical simulation

For the coupled hydro-mechanical simulation the factor of safety (FOS) against slope stability decreased continuously with increasing pore pressures from leachate injection (see Fig. 7). For the coupled bio-mechanical simulation, there were no excess pore pressures as such in the system due to the absence of pressurized leachate injection. Thus, the FOS values almost remained constant over the entire simulation. However, for the coupled hydro-bio-mechanical simulation resulted in an initial decrease in the FOS values until certain time where the effect of increasing pore pressures was dominant. Meanwhile the changes in the waste properties (increasing unit weight, increasing cohesive strength of waste) resulted in an overall increase in the slope stability as indicated by the increase in FOS values. In the long-term with substantial settlement and dissipated pore water pressures and limited changes in the waste properties the FOS values decreased and reached a steady value. Hence, incorporating the effects of biodegradation along with other processes is essential for accurate prediction of the stability of a bioreactor landfill. However, the trend observed in Fig. 7 should be validated with actual field or other relevant experimental data to confirm such behavior.

The unique ability of the CHBM numerical framework is to be able to capture the influence of coupled interactions within the waste on the waste liner interaction. Modern landfills typically consist of composite liner system comprising of weak geosynthetic interfaces. The short-term and long-term stability of the lining systems is mostly dictated by the shear behavior of weak geosynthetic interfaces under the influence of overlying waste.

Fig. 8 shows the shear response (shear stresses and shear displacements) of an interface formed by smooth High-Density Polyethylene (HDPE) geomembrane and nonwoven geotextile in a composite liner system for a bioreactor landfill simulation.

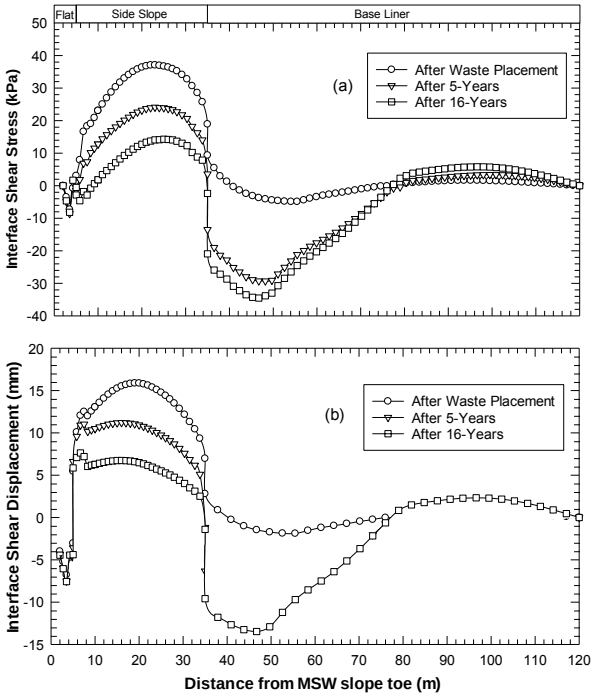

Fig. 8: Evolution of (a) interface shear stress (b) interface shear displacement with elapsed time along the composite liner system for a bioreactor landfill simulation

Fig. 8(a) and Fig 8(b) shows the induced shear stresses and shear displacements, respectively, along the flat run-out anchor, side slope, and base liner interface after the waste placement, after 5 years and after 16 years of leachate injection operation. The results show a characteristic trend in the distribution of the shear stresses and shear displacement along the interface. The shear stresses along the side liner increased, reached a peak value and decreased to zero, from left to right. Similarly, the shear stresses along the base liner from left to right increased, reached a peak value and then decreased to zero towards the right end of the base liner. This characteristic trend may be attributed to the boundary conditions imposed on to the landfill cell configuration (Reddy et al., 2017). Initially after the waste placement higher shear stresses and corresponding higher shear displacements were observed along the side slope liner owing to the

mobilization of the friction between the geomembrane and geotextile interface. However, with time, the shear stresses along the interface were found to be influenced by the changing waste characteristics due to waste degradation and the shear stresses and shear displacements along the side slope liner decreased while the shear stress along the base liner increased with time. It is inferred that the changes in the waste stiffness (from being stiff at the early stages of degradation to being soft as the waste stabilizes) in the region around the side liner is found to have influenced the changes in the shear stresses and displacements along the side slope liner. In the lack of a conclusive evidence and explanation of such behavior there is a need for further study on the effect of changing waste characteristics on the shear response of the liner and consequently on the integrity of the liner. In this regard, the CHBM model expresses a great capacity in being able to associate waste behavior and the shear behavior of such interfaces in the liner system and predict the holistic performance of the bioreactor landfill and its components.

5 SUMMARY AND ONGOING RESEARCH

Bioreactor landfills are an attractive option for effective and efficient management of waste. They offer numerous advantages over the traditionally constructed and operated landfills in several aspects. Moreover, in the light of sustainable development, bioreactor landfills prove to be an ideal concept of waste management. However, there are no rigorous procedures or guidelines for safe and effective design of such landfills. Unlike conventional landfills, the construction and operation of bioreactor landfills require adequate knowledge and accuracy on the required moisture levels within the landfill, the injection pressures and flow rates all of which depends on a good estimation of the properties of waste. One of the major concerns in leachate recirculating landfills is to ensure uniform distribution of moisture across the landfill space, which is hindered by the lack of knowledge on the fluid flow in MSW. In addition, the biodegradation of MSW makes the understanding of the landfill system quite complex due to the interdependency of the hydraulic flow, mechanical response and biodegradation processes. Thus, understanding these individual processes and their interactions will aid in simulating this behavior mathematically thereby allowing us to design safe and effective bioreactor landfills.

Several researchers have performed numerous studies to numerically simulate the coupled processes. However, these studies do have some limitations from the simplification made in simulating the hydraulic, mechanical and biochemical processes. The current research at UIC is focused on addressing the research challenges pertaining to mathematical formulation of the biochemical reactions and their kinetics for realistic simulation of the biodegradation of MSW. More importantly, there are no coupled models that account for the influence of heat generation and temperature distribution within the landfill on the biodegradation of MSW and subsequently on the behavior of MSW and liner systems in landfills. Thus, numerical modeling of temperature distribution and heat generation within the landfill is currently being carried out to have an accurate description of the biodegradation of MSW. In addition, accurate simulation of the mechanical response of the waste undergoing degradation is another complex topic that is being addressed. Understanding the mechanical behavior of waste has always been a challenging task and requires adequate experimental investigation to delineate and formulate the constitutive behavior that can simulate the waste behavior with reasonable accuracy. Finally, integration of all these different aspects into a comprehensive coupled model is crucial to predict overall performance of a bioreactor landfill.

ACKNOWLEDGMENTS

This project is funded by the U.S. National Science Foundation (CMMI # 1537514), which is gratefully acknowledged.

REFERENCES

Barlaz, M. A., Ham, R. K., Schaefer, D. M., and Isaacson, R. (1990). Methane production from municipal refuse: a review of enhancement techniques and microbial dynamics, Critical Reviews in Environmental Science and Technology, 19:557-584.

Carpenter, P.J., Reddy, K.R., and Thompson, M.D. (2013a). Dynamic properties of municipal solid waste in a bioreactor cell at orchard hills landfill, Illinois, USA, Seventh International Conference on Case Histories in Geotechnical Engineering, Wheeling, IL, USA, Paper No. 6.02b, pp 1-6.

Carpenter, P.J., Reddy, K.R., and Thompson, M.D. (2013b). Seismic imaging of a leachate recirculation landfill: Spatial changes in dynamic properties of municipal solid waste, Journal of Hazardous, Toxic, and Radioactive Waste, 17:331-341.

Giri, R.K., and Reddy, K.R. (2014a). Design charts for selecting minimum setback distance from side slope to horizontal trench system in bioreactor landfills, Geotechnical and Geological Engineering Journal, 32:1017-1027.

Giri, R.K., and Reddy, K.R. (2014b). Slope stability of bioreactor landfills during leachate injection: Effects of unsaturated hydraulic properties of municipal solid

waste, International Journal of Geotechnical Engineering, 8:144-156.
Giri, R.K., and Reddy, K.R. (2014c). Slope stability of bioreactor landfills during leachate injection: Effects of heterogeneous and anisotropic municipal solid waste, Waste Management & Research, 32:186-197.
Giri, R.K., and Reddy, K.R. (2015a) Slope stability of bioreactor landfills during leachate injection: Effects of geometric configurations of horizontal trench systems, Geomechanics and Geoengineering, 10:126-138.
Grellier, S., Reddy, K., Gangathulasi, J., Adib, R., and Peters, C. (2006). Electrical resistivity tomography imaging of leachate recirculation in orchard hills landfill, SWANA Conference, Charlotte, 7p.
Grellier, S., Reddy, K.R., Gangathulasi, J., Adib, R., and Peters, C. (2007). US MSW and its biodegradation in a bioreactor landfill, Sardinia 2007, Eleventh International Waste Management and Landfill Symposium, S. Margherita di Pula, Cagliari, Italy, 11p.
ITRC (2006). Characterization, design, construction and monitoring of bioreactor landfills. Washington: Alternative landfill technologies team, Interstate Technology and Regulatory Council (ITRC), <https://clu-in.org/conf/itrc/bioreactors/ALT-3.pdf> (March 4, 2020)
Kulkarni, H.S., and Reddy, K.R. (2012). Moisture distribution in bioreactor landfills: A review, Indian Geotechnical Journal, 42:125-149
Kumar, G., and Reddy, K.R. (2019). Rapid stabilization of municipal solid waste in bioreactor landfills: Predictive performance using coupled modeling. Global NEST Journal, 21: 505-512.
Reddy, K.R., Gangathulasi, J., Parakalla, N., Bogner, J., Carpenter, P., and Lagier, T. (2009a). Field monitoring and performance assessment of Orchard Hills bioreactor landfill, NSF Engineering Research and Innovation Conference, Honolulu, HI, 13p.
Reddy, K.R., Hettiarachchi, H., Gangathulasi, J., Parakalla, N., Bogner, J.E., and Lagier, T. (2009b). Compressibility and shear strength of municipal solid waste under short-term leachate recirculation operations, Waste Management & Research, 27:578-587.
Reddy, K.R., Hettiarachchi, H., Gangathulasi, J., Bogner, J.E., and Lagier, T. (2009c). Geotechnical properties of synthetic municipal solid waste, International Journal of Geotechnical Engineering, 3:429-438.
Reddy, K.R., Hettiarachchi, H., Parakalla, N., Gangathulasi, J., Bogner, J.E., and Lagier, T. (2009d). Hydraulic conductivity of MSW in landfills, Journal of Environmental Engineering, 135:677-683.
Reddy, K.R., Hettiarachchi, H., Parakalla, N.S., Gangathulasi, J., and Bogner, J.E. (2009e). Geotechnical properties of fresh municipal solid waste at Orchard Hills landfill, USA, Waste Management, 29:952-959.
Reddy, K.R., Hettiarachchi, H., Gangathulasi, J., and Bogner, J.E. (2011). Geotechnical properties of municipal solid waste at different phases of degradation, Waste Management, 31:2275-2286
Reddy, K.R., Hettiarachchi, H., Giri, R.K., and Gangathulasi, J. (2015a). Effects of degradation on geotechnical properties of municipal solid waste from Orchard Hills Landfill, USA, International Journal of Geosynthetics and Ground Engineering, 1:1-14
Reddy, K.R., Kulkarni, H.S., and Khire, M.V. (2013a). Two-phase modeling of leachate recirculation using vertical wells in bioreactor landfills, Journal of Hazardous, Toxic and Radioactive Waste, 17:272-284
Reddy, K.R., Kulkarni, H.S., Srivastava, A., and Sivakumar Babu, G.L. (2013b). Influence of spatial variation of hydraulic conductivity of municipal solid waste on performance of bioreactor landfills, Journal of Geotechnical and Geoenvironmental Engineering, 139:1968–1972
Reddy, K.R., Giri, R.K., and Kulkarni, H.S. (2014). Design of drainage blankets for leachate recirculation in bioreactor landfills using two-phase flow modeling, Computers and Geotechnics, 62:77-89
Reddy, K.R., Kulkarni, H.S., and Giri, R.K. (2015b). Design of horizontal trenches for leachate recirculation in bioreactor landfills using two-phase modeling, International Journal of Environment and Waste Management, 15:347-376
Reddy, K.R., Kulkarni, H.S., and Giri, R.K. (2015c). Design of vertical wells for leachate recirculation in bioreactor landfills using two-phase modeling, Journal of Solid Waste Technology and Management, 41:203-218
Reddy, K.R., Kulkarni, H.S., and Giri, R.K. (2015d). Modeling coupled hydro-mechanical behavior of landfilled waste in bioreactor landfills: Numerical formulation and validation, Journal of Hazardous, Toxic and Radioactive Waste, ASCE, 21:D4015004
Reddy, K.R., Kumar, G., and Giri, R.K. (2017a). Modeling coupled processes in municipal solid waste landfills: An overview with key engineering challenges, International Journal of Geosynthetics and Ground Engineering, 3:6
Reddy, K.R., Kumar, G., and Giri, R.K. (2017b). Influence of dynamic coupled hydro-bio-mechanical processes on response of municipal solid waste and liner system in bioreactor landfills, Waste Management, 63:143-160
Reddy, K.R., Kumar, G., and Giri, R.K. (2018a). System effects on bioreactor landfill performance based on coupled hydro-bio-mechanical modeling, Journal of Hazardous, Toxic and Radioactive Waste, ASCE, 22:04017024
Reddy, K.R., Kumar, G., Giri, R.K. and Basha, B.M. (2018b). Reliability assessment of bioreactor landfills using Monte Carlo simulation and coupled hydro-bio-mechanical model, Waste Management, 72:329-338
Sivakumar Babu, G.L., Reddy, K.R., Chouskey, S.K., and Kulkarni, H.S. (2010). Prediction of long-term municipal solid waste landfill settlement using constitutive model, Practice Periodical of Hazardous, Toxic, and Radioactive Waste Management, 14:139-150
Sivakumar Babu, G.L., Reddy, K.R., and Chouskey, S.K. (2011). Parametric study of MSW landfill settlement model, Waste Management Journal, 31:1222-1231
USEPA (2018). Advancing Sustainable Materials Management: 2015 Fact Sheet, <https://www.epa.gov/facts-and-figures-about-materials-waste-and-recycling/advancing-sustainable-materials-management> (March 4, 2020).

Behaviour of Granular Waste Medium with Rubber Particles under Cyclic Loading for Transport Infrastructure

Yujie Qi

Lecturer, Program Co-leader of Transport Research Centre, School of Civil and Environmental Engineering, University of Technology Sydney, Ultimo, NSW 2007, Australia.

Buddhima Indraratna

Distinguished Professor, Director, Transport Research Centre, Founding Director, ARC Industrial Transformation Training Centre for Railroad Technologies (ITTC-Rail), University of Technology Sydney, Ultimo, NSW 2007, Australia.

Email: buddhima.indraratna@uts.edu.au, Ph: +61 400 213 046

Ana Heitor

School of Civil Engineering, University of Leeds, Leeds, UK

Jayan S. Vinod

ARC Training Centre for Advanced Technologies in Rail Track Infrastructure (ITTC-Rail), University of Wollongong Australia, NSW 2522, Australia

Chathuri M. K. Arachchige

PhD candidate, Transport Research Centre, University of Technology Sydney, Ultimo, NSW 2007, Australia.

ABSTRACT: The practical application of waste materials such as steel furnace slag (SFS) and coal wash (CW) is becoming more prevalent in many geotechnical projects. While the inclusion of rubber crumbs (RC) from recycled tyres into mixtures of SFS and CW not only solves the problem of large stockpiles of waste tyres, it can also provide an energy-absorbing medium that will reduce vibration and track degradation due to the high damping properties of RC particles. In this study the influence of RC contents on the cyclic loading behaviour (i.e. deformation, damping ratio and dissipated energy) was investigated based on small-scale cyclic triaxial tests. The results reveal that the inclusion of RC leads to an increase in the total axial strain, a more contractive volumetric strain, and a higher damping ratio with more energy being dissipated. An energy consumption flowchart was developed to show how a synthetic energy absorbing layer (SEAL: SFS+CW+RC mixture) will reduce track degradation by absorbing more energy. This has been further verified by large-scale cubical triaxial tests of track specimens with and without SEAL.

1 INTRODUCTION

Coal mining and steel manufacturing are the two main industries in Australia, and although the country benefits economically, there are problems with the large stockpiles of waste materials (e.g. steel furnace slag and coal wash) that accumulate as they are processed. In the Wollongong region (Australia) alone, the production of steel furnace slag (SFS) and coal wash (CW) can be more than 2mt per year (Chiaro et al. 2015). Were that not enough, the ever increasing stockpile of waste tyres is also creating another environmental problem in developed and developing countries due to the rapidly increasing number of motor vehicles. At present there are more than 50 million tyre equivalent passenger units (EPU) of waste tyres produced in Australia every year (Mountjoy et al. 2015). There is therefore an urgent need to recycle these waste materials, and one efficient method is to utilise them in large civil engineering projects.

To minimise the adverse geotechnical effects of waste materials such as the volumetric expansion of SFS, particle degradation of CW, and the highly deformable properties of RC, these waste materials are usually mixed with other materials before being used. For example, SFS is usually mixed with Class C fly ash, cement, and asphalt or concrete for use in landfill, road construction, and the production of cement (Xue et al. 2006, Yildirim and Prezzi 2015). It has been found that CW can reduce the swelling of SFS, SFS can reduce the particle breakage of CW, and blends of SFS+CW have been successfully used for port reclamation in Wollongong, Australia (Chiaro et al. 2015, Tasalloti et al. 2015). To extend the use of SFS+CW mixtures into dynamic loading projects, Indraratna et al. (2017a) introduced rubber crumbs (RC) made from scrap tyres into the waste

mixture and developed a synthetic energy absorbing layer (SEAL) for railway subballast. The addition of RC can further reduce the swelling of SFS and the particle degradation of CW, while enhancing the energy absorbing properties the waste mixture (Indraratna et al. 2017a, Indraratna et al. 2017b, Qi et al. 2018a, 2019abc, Qi et al. 2018d).

To better understand the effect that RC has on the cyclic loading behaviour (deformation, damping ratio and dissipated energy) of SFS+CW+RC mixtures, a series of small-scale cyclic triaxial tests have been carried out on the waste mixtures with different amounts of RC. The energy absorbing concept of using SEAL to reduce track degradation will be illustrated based on the test results, while a large-scale cubical triaxial test is used to examine the deformation and ballast degradation of test specimens of track that incorporate SEAL.

2 CYCLIC LOADING BEHAVIOUR OF SFS+CW+RC MIXTURES

2.1 *Materials and testing program*

The source materials for SFS and CW are from ASMS (Australia Steel Milling Services) and Illawarra Coal Mining, and the RC shredded from waste tyres came frome Tyre Crumbs Australia. The blending ratio of SFS:CW is 7:3 (by mass) because with this blending ratio the waste matrix will have less particle degradation and acceptable volumetric expansion while maintaining sufficient shear strength (Indraratna et al. 2017a, Qi et al. 2018a). The amount of RC in the matrix was not more than 40% (i.e. 10, 20, 30 and 40% by mass) to prevent the sample skeleton from being totally controlled by RC (Kim and Santamarina 2008, Senetakis et al. 2012). All the specimens (100 mm high and 50 mm in diameter) for the small-scale cyclic triaxial test are prepared with the optimum moisture content and are compacted to 95% of their maximum dry density. Fig. 1 shows the particle size distribution curves (PSD) of the wate materials as well as their mixtures.

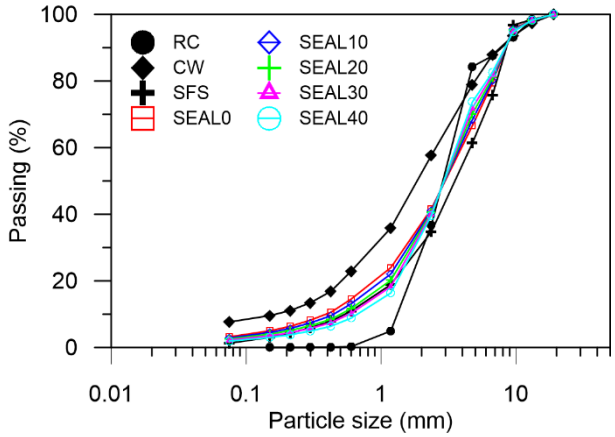

Fig. 1 PSD of waste materials and SEAL mixtures

A series of stress-controlled drained cyclic triaxial tests were carried out on the waste matrix following the procedure suggested by ASTM-D5311/D5311M (2013). The effective confining pressure σ'_3 used for the cyclic loading triaxial tests are 10, 40, and 70 kPa to simulate the low confining pressure under field conditions. The maximum deviator stress q_{max} is determined using the cyclic stress ratio ($CSR = q_{max}/2\sigma'_3$) CSR=0.8 and the effective confining pressure. The loading frequency was 5 Hz. Details regarding specimen preparation and test procedures can be found elsewhere in Indraratna et al. (2017a) and Qi et al. (2018b).

2.2 *Cyclic test results*

The axial strain and volumetric strain from the cyclic loading tests of waste composite with different amounts of RC are shown in Fig. 2. Note that as the amount of RC increases the axial strain of waste mixtures also increases due to the high deformation of rubber materials. The axial strain and volumetric strain of the waste mixture with RC contents <20% gradually stabilise after 10,000 cycles, whereas the axial and volumetric strain of the mixtures with larger amounts of RC continue to increase to the end of the test (50,000 cycles). All the test specimens experience some contraction, and indeed become more contractive as the amount of RC increases.

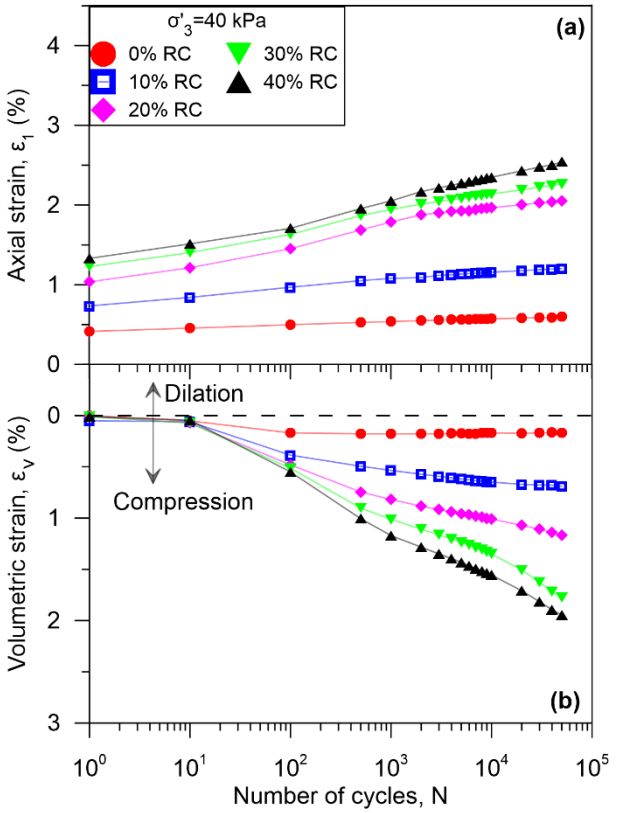

Fig. 2 Cyclic loading test results (5 Hz) for SFS+CW+RC mixtures (a) axial strain and (b) volumetric strain (modified after Qi et al. 2018b)

The damping ratio (D) is the efficiency of dissipating energy for materials subjected to cyclic loading. The dissipated energy during one loading cycle is usually represented by the area of the hysteretic loop. The definition of D and E is shown in Fig. 3.

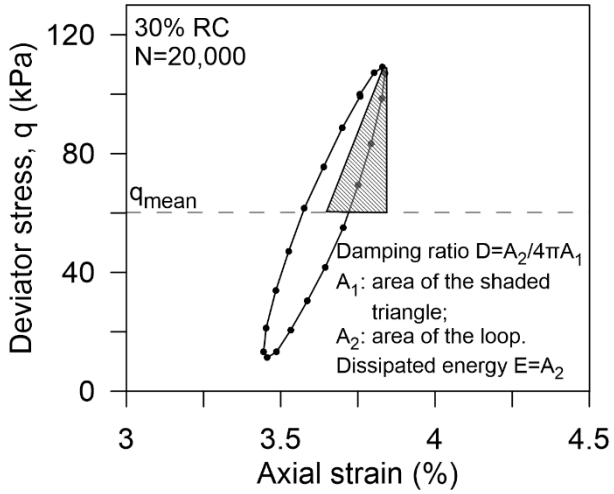

Fig. 3 Definition of damping ratio and dissipated energy

The influence that the amount of RC and σ'_3 has on D and E of the waste matrix is shown in Fig. 4. As expected, as the amount of RC increases the damping ratio and dissipated energy of the waste mixtures also increases due to the high energy absorbing properties of rubber materials. Most of the energy is dissipated at the beginning of the test due to initial densification and particle rearrangement, but then the dissipation rate decreases and stabilises at a low level. Increasing the effective confining pressure reduces the damping ratio but increases the dissipated energy, as shown in Fig. 4b.

2.3 *Energy absorbing concept*

If the total energy input of a given track load is assumed to be a certain amount, the energy applied to the ballast and the subgrade will decrease as the energy absorbing capacity of the subballast layer increases and thus reduces the particle breakage of ballast.

As Fig. 5 shows, the energy consumption flowchart is established based on the comprehensive test results of the waste matrix from current and previous studies by the authors (Indraratna et al. 2020, Indraratna et al. 2017a, Qi et al. 2019b, Qi et al. 2018b, Qi et al. 2018c). Here, the energy absorbed by the synthetic energy absorbing layer (SEAL) from the dynamic loading generally results in permanent deformation or is dissipated by heat and particle breakage. It is noted that as the amount of RC increase, the energy absorbed by the SEAL increases as the area of the shear stress-shear strain triangle increases (Fig. 5a). This indicates that less energy will be transmitted to the subgrade or ballast layer, but accordingly, this energy results in permanent strains (Fig. 5b) and the dissipated energy increases (Fig. 5c). The dissipated energy represented by the area of the hysteresis loop obtained from cyclic loading tests is due to (i) the recoverable deformation of the waste matrix, (ii) particle friction, and (iii) particle breakage (Feng and Sutter 2000, Li et al. 2016). Recoverable deformation is reflected by the resilient modulus M_R. Note that the increase in dissipated energy is mainly due to the rise in the recoverable deformation (M_R decreases, Fig. 5d) as the shear strength (Fig. 5e) and particle breakage (Fig. 5f) decrease when the amount of RC increases.

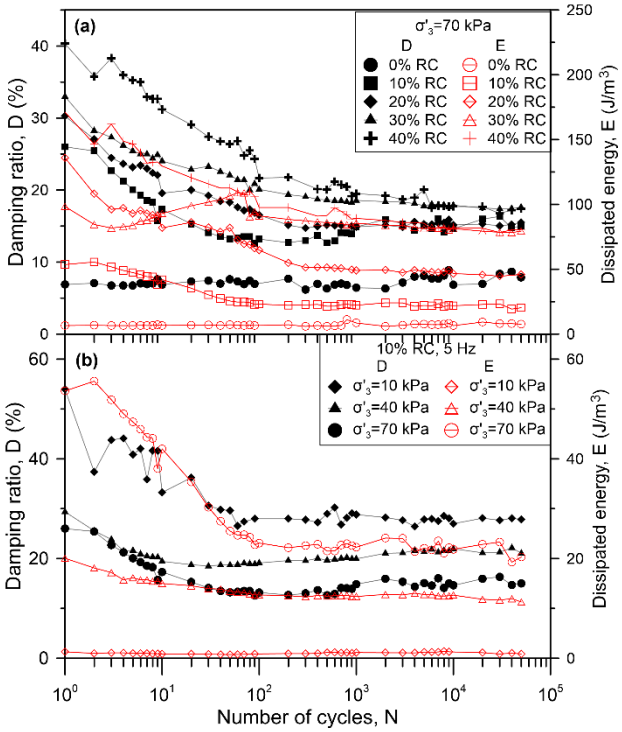

Fig. 4 D and E for the waste mixtures (a) with different RC contents and (b) under different effective confining pressures and f=5 Hz (modified after Qi et al. 2018b)

This analysis reveals that using more rubber ensures the SEAL (SFS+CW+RC mixtures) has a higher energy absorbing capacity and less particle breakage, but it has higher deformation, lower resilient modulus, and less shear strength. Note that 10% of RC is already has a promising energy absorbing capacity (Fig. 5a) and therefore 10% RC is now suggested as the optimal amount of RC needed for an optimal SEAL matrix for subballast.

3 LARGE-SCALE CUBICAL TRIAXIAL TEST

To verify the proposed energy absorbing concept, the deformation and ballast degradation of the track specimen with and without SEAL were investigated by the large-scale cubical triaxial test using the

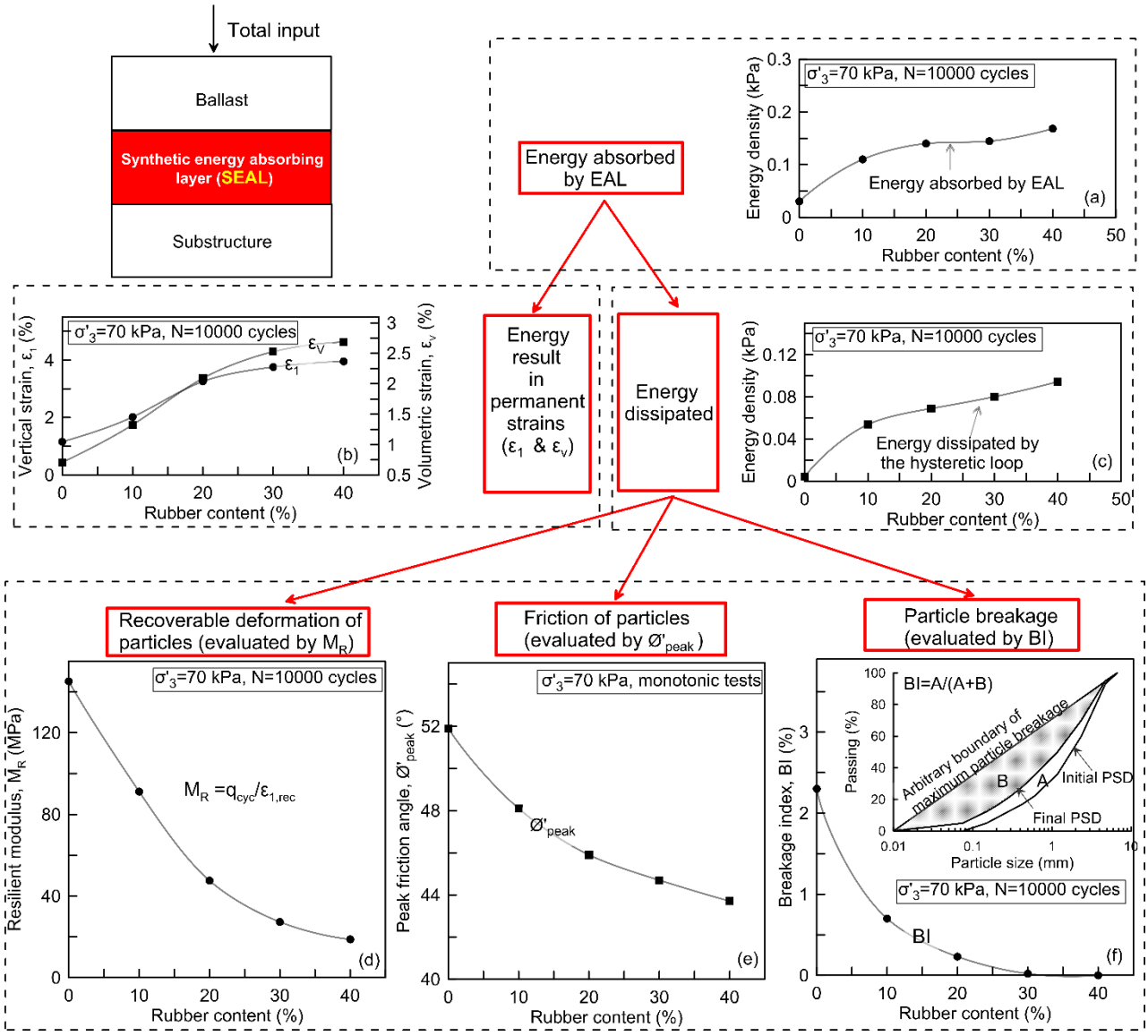

Fig. 5 Energy-consumption flowchart and comprehensive properties of SFS+CW+RC mixtures (SFS:CW=7:3) having different amounts of RC s at the effective confining pressure $\sigma'_3 = 70\ kPa$ and at loading cycles N=10,000 (modified after Qi et al. 2018b)

large-scale process simulation primoidal testing apparatus (PSPTA) designed and built at the University of Wollongong Australia (Fig. 6a).

The area of the cuboid shaped test chamber is 800× 600mm by 600 mm deep. The test specimen shown in Fig. 6b is compacted in three layers, i.e. subgrade layer (100 mm thick) on the bottom, a SEAL (150 mm thick) in the middle, and a ballast layer on the top (200 mm thick). The concrete with the rail is installed on top of the test specimen and the space around the sleeper is filled with shoulder ballast (Fig. 6b). The cyclic loading test was carried out at a frequency f=15 Hz, and the maximum vertical pressure under the sleeper was 230 kPa to simulate a train with 25-tonne axle load running at 115 km/h (Indraratna et al. 2017c). The four sidewalls are movable to allow for lateral deformation. The confining pressure applied to the sidewalls (perpendicular to the sleeper) was 15 kPa and the sidewalls parallel to the sleeper were locked to restrict movement in order to simulate a plain strain condition. After each test, the ballast directly under the sleeper was sieved again to check the ballast degradation. Details of the test procedure can be found elsewhere in Qi and Indraratna (2020).

Ballast degradation is evaluated using the ballast breakage index (BBI) initially proposed by Indraratna et al. (2005). The BBI can be calculated by comparing the particle size distribution curves of ballast before and after the tests (Fig. 7a):

$$BBI=A/(A+B) \quad (1)$$

where A is the area enclosed by the particle size distribution curves of ballast before and after the test, and B is the area enclosed by the arbitrary boundary of maximum breakage and the particle size distribution curve of ballast after tests (Fig. 7a).

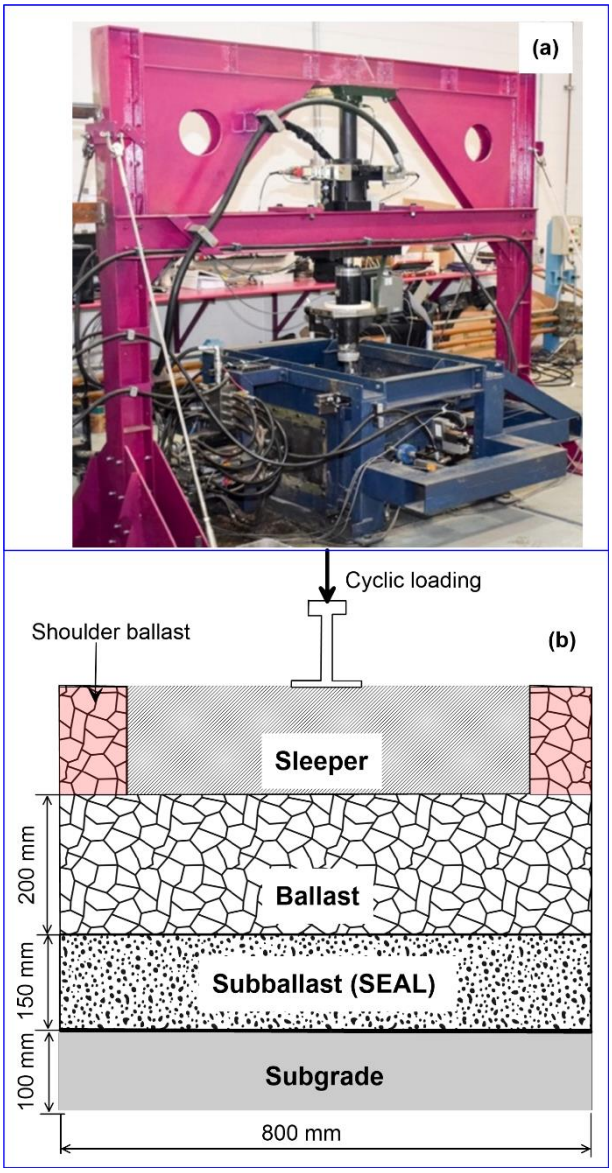

Fig. 6 (a) The large-scale process simulation primoidal testing apparatus (PSPTA) and (b) schematic illustration of the cubical triaxial test specimen

Fig. 7b shows the the plastic vertical strain and ballast degradation for the track specimen with SEAL having different amounts of RC. Note that when increasing the RC content in SEAL, the plastic vertical strain ε_1 increases, which agrees with the small-scale triaxial test results results. It can be seen that the permanent axial strain is almost 10% at the end of the test when 40% RC is included, indicating that too much rubber will induce severe track settlement. Also note that there is a significant decrease in BBI when 10% RC is included in SEAL, but when more RC is added there is no noticeable reduction. To compare with a traditional track, the cubic triaxial tests of traditional track materials tested under the same loading conditions by Jayasuriya et al. (2019) are also shown in Fig. 7b. In comparison with traditional track specimen, the test specimen with SEAL10 (10% RC in SEAL) has less vertical deformation and ballast degradation; this verifies the proposed energy absorbing concept.

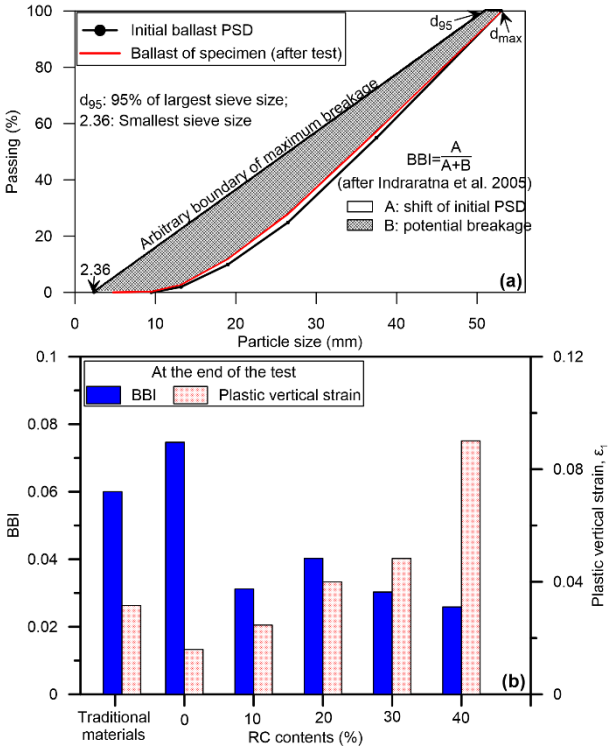

Fig. 7 (a) The definition of BBI and (b) BBI and plastic vertical strain of the track specimen with and without SEAL (data sourced from Qi and Indraratna 2020)

4 CONCLUSIONS

The cyclic loading behaviour of SEAL composites (SFS+CW+RC mixtures) for railway subballast was investigated through a series of small-scale cyclic triaxial tests and large-scale cubical triaxial tests. The following important findings can be concluded from this study:

- When the amount of RC is increased, the SEAL mixture had more vertical deformation and the test specimen became more contractive.
- The increase in RC contents increased the damping ratio and the dissipated energy of the SEAL mixture, and the increase in the effective confining pressure increased the dissipated energy, and reduced the damping ratio.
- The proposed energy absorbing concept indicated that with 10% of RC, SEAL would be the optimal mixture to increase the energy absorb-

ing capacity of a track and also reduce the ballast degradation. This was successfully verified by the large-scale cubical triaxial tests.

ACKNOWLEDGEMENTS

The authors would like to acknowledge the financial assistance provided by the Australian Research Council Discovery Project (ARC-DP) and and ARC Training Centre for Advanced Technologies in Rail Track Infrastructure (ARC-ITTC-Rail). The assistance provided by industry (ASMS, South 32, and Tyre Crumb Australia) in relation to the procurement of material used in this study is gratefully acknowledged. The assistance in the laboratory from Mr. Richard Berndt, Mr. Cameron Neilson, Mr. Jordan Wallace, Mr. Quang Minh Vu and Mr. Salvatore Wedde are appreciated. Some figures in this paper were modified after Qi et al. (2018b) and Qi and Indraratna (2020), whereby the original data has been reproduced with kind permission from ASCE: Journal of Geotechnical and Geoenvironmental Engineering and Journal of Materials in Civil Engineering, respectively.

REFERENCES

ASTM-D5311/D5311M (2013). Standard test method for load controlled cyclic triaxial strength of soil, ASTM International West Conshohocken, PA.

Chiaro, G., Indraratna, B., Tasalloti, S. and Rujikiatkamjorn, C. (2015). "Optimisation of coal wash-slag blend as a structural fill." Proceedings of the Institution of Civil Engineers: Ground Improvement 168(GI1): 33-44.

Feng, Z.-Y. and Sutter, K. G. (2000). "Dynamic properties of granulated rubber/sand mixtures." Geotech. Testing J. 23(3): 338-344.

Indraratna, B., Lackenby, J. and Christie, D. (2005). "Effect of confining pressure on the degradation of ballast under cyclic loading." Géotechnique 55(4): 325-328.

Indraratna, B., Qi, Y. and Heitor, A. (2017a). "Evaluating the properties of mixtures of steel furnace slag, coal wash, and rubber crumbs used as subballast." Journal of Materials in Civil Engineering 30(1): 04017251.

Indraratna, B., Qi, Y., Tawk, M., Heitor, A., Rujikiatkamjorn, C. and Navaratnarajah, S.K. (2020). "Advances in ground improvement using waste materials for transportation infrastructure." Proceedings of the ICE-Grount Improvement, DOI: 10.1680/jgrim.20.00007.

Indraratna, B., Sun, Q. and Grant, J. (2017b). "Behaviour of subballast reinforced with used tyre and potential application in rail tracks." Transportation Geotechnics 12: 26-36.

Indraratna, B., Sun, Q., Heitor, A. and Grant, J. (2017c). "Performance of rubber tire-confined capping layer under cyclic loading for railroad conditions." J. Mater. Civil Engin. 30(3): 06017021.

Jayasuriya, C., Indraratna, B. and Ngo, T. N. (2019). "Experimental Study to Examine the Role of Under Sleeper Pads for Improved Performance of Ballast under Cyclic Loading." Transportation Geotechnics 19: 61-73.

Kim, H.-K. and Santamarina, J. (2008). "Sand–rubber mixtures (large rubber chips)." Can. Geotech. J. 45(10): 1457-1466.

Li, B., Huang, M. and Zeng, X. (2016). "Dynamic behavior and liquefaction analysis of recycled-rubber sand mixtures." J. Mater. Civil Engin. 28(11): 04016122.

Mountjoy, E., Hasthanayake, D. and Freeman, T. (2015). "Stocks & Fate of End of Life Tyres-2013-14 Study." National Environmental Protection Council.

Qi, Y. and Indraratna, B. (2020). "Energy-based approach to assess the performance of a granular matrix consisting of recycled rubber, steel furnace slag and coal wash. " ASCE Journal of Materials in Civil Engineering, 32 (7), 04020169,

Qi, Y., Indraratna, B. and Coop, M.R. (2019a). Predicted Behaviour of Saturated Granular Waste Blended with Rubber Crumbs. *Inter. J. Geomech., ASCE* 19(8): 04019079.

Qi, Y., Indraratna, B., Heitor, A. and Vinod, J. (2019b). The influence of rubber crumbs on the energy absorbing property of waste mixtures. Geotechnics for Transport. Infrastructure. S. J. Sundaram R., Havanagi V. Singapore, Springer. 29: 271-281.

Qi, Y., Indraratna, B., Heitor, A. and Vinod, J. S. (2018a). "Closure to "Effect of Rubber Crumbs on the Cyclic Behavior of Steel Furnace Slag and Coal Wash Mixtures" by Yujie Qi, Buddhima Indraratna, Ana Heitor, and Jayan S. Vinod." J. Geotech. Geoenviron. Engin. 145(1): 07018035.

Qi, Y., Indraratna, B., Heitor, A. and Vinod, J. S. (2018b). "Effect of rubber crumbs on the cyclic behavior of steel furnace slag and coal wash mixtures." Journal of Geotechnical and Geoenvironmental Engineering 144(2): 04017107.

Qi, Y., Indraratna, B., Heitor, A. and Vinod, J. S. (2019c). The influence of rubber crumbs on the energy absorbing property of waste mixtures. Geotechnics for Transportation Infrastructure, Springer: 271-281.

Qi, Y., Indraratna, B. and Vinod, J. S. (2018c). "Behavior of Steel Furnace Slag, Coal Wash, and Rubber Crumb Mixtures with Special Relevance to Stress–Dilatancy Relation." Journal of Materials in Civil Engineering 30(11): 04018276.

Qi, Y., Indraratna, B. and Vinod, J. S. (2018d). Dynamic Properties of Mixtures of Waste Materials. GeoShanghai International Conference, Springer.

Senetakis, K., Anastasiadis, A. and Pitilakis, K. (2012). "Dynamic properties of dry sand/rubber (SRM) and gravel/rubber mixtures in a wide range of shearing strain amplitudes." Soil Dynam. Earthquake Engin. 33(1): 38-53.

Tasalloti, S. M., Indraratna, B., Rujikiatkamjorn, C., Heitor, A. and Chiaro, G. (2015). "A laboratory study on the shear behavior of mixtures of coal wash and steel furnace slag as potential structural fill." Geotech. Test. J. 38(4): 361-372.

Xue, Y., Wu, S., Hou, H. and Zha, J. (2006). "Experimental investigation of basic oxygen furnace slag used as aggregate in asphalt mixture." J. Hazardous Materials 138(2): 261-268.

Yildirim, I. Z. and Prezzi, M. (2015). "Geotechnical properties of fresh and aged basic oxygen furnace steel slag." J. Mater. Civil Engin. 27(12): 04015046.

Developing Realistic "Smart Ballast" for Improved Understanding of Ballasted Tracks – A conceptual Design

A.R. Siddiqui

PhD Candidate, Transport Research Centre, School of Civil and Environmental Engineering, University of Technology Sydney, Ultimo, NSW 2007. Australia

B. Indraratna

Distinguished Professor of Civil Engineering, Founding Director of Australian Research Council's Industrial Transformation Training Centre for Advanced Technologies in Rail Track Infrastructure (ITTC-Rail), Director of Transport Research Centre, School of Civil and Environmental Engineering, University of Technology Sydney, Sydney, NSW 2007, Australia

T. Ngo

Senior Lecturer, Transport Research Centre, School of Civil and Environmental Engineering, University of Technology Sydney, Sydney NSW 2007, Australia.

ABSTRACT: Ballasted tracks settle as the ballast particles are rearranged and spread laterally under the cyclic loads imparted by moving trains. However, despite the movement of ballast particles being the primary mode of track deformation this process is still not fully understood. This study aims to develop an artificial but realistic "Smart Ballast" particle equipped with wireless motion-sensing technology. To achieve this aim, a ballast particle was scanned in 3d to capture its shape, angularity and surface roughness, and the scan data was then used to 3d print smart ballast with a special filament to match the density of actual ballast particle. A 9-axis wireless motion sensor was embedded inside the smart ballast particle to provide driftless and real-time particle orientation and motion data using an extended Kalman filter. This smart ballast with its advanced motion-sensing ability can have wide-ranging applications in the design, analysis, and monitoring of ballasted rail tracks.

1 INTRODUCTION

Ballast is the layer of unbound granular material placed beneath and around railway sleepers. It serves as a foundation for railways and holds the track components in place. Under cyclic train loads ballast gradually degrades and deforms (Indraratna et al. 2011), and if this continues, it increases the risk of track derailment. As a result, huge sums of money are spent worldwide constantly maintaining railway tracks; for example, the NSW government alone has invested over a billion dollars during the last four years maintaining their tracks (RailCorp 2017-18), most of which is spent on ballast and other substructure layers (Selig & Waters 1994).

The deformation of ballast consists of an initial rapid plastic deformation due to rearrangement and densification of ballast particles, and a gradual deformation that occurs afterwards as the particles degrade and spread laterally. The common aspect of both modes of deformation is the movement of ballast particles. While numerous researchers have experimentally investigated the deformation behavior of the ballast layer as a continuum, very few have actually used the discrete approach by considering individual particle motion. Zhai et al. (2004) placed multiple accelerometers in the ballast layer to measure particle accelerations for modelling the vibration of ballast under moving trains. On the other hand, Kumara and Hayano (2016) used particle image velocity (PIV) to track local deformations induced by tamping rather than measuring the total deformation using displacement transducers. This method involves capturing a number of images at specific intervals during a loading cycle and then analysing the images in a PIV software. This study revealed the non-uniform displacement behavior of ballast at different locations and proved the PIV method to be useful. However, the PIV technique could only reliably track the two-dimensional motion of ballast particles.

A recent series of studies monitored the movement of ballast particles using a wireless device called "Smart Rock". Liu et al. (2017) developed this device by encasing a motion-sensing unit in a ballast shaped PLA plastic object and used it to study the motion of ballast particles reinforced with different geogrids. Zeng et al. (2019) however, used small cubes with embedded motion sensors to monitor the movement of ballast and then identify

its condition. In both studies however, the smart rock did not either have the density of an actual rock or the realistic shape of a ballast particle, as shown in Fig. 1, so these devices may not reflect the actual movement a real ballast particle would experience under track forces.

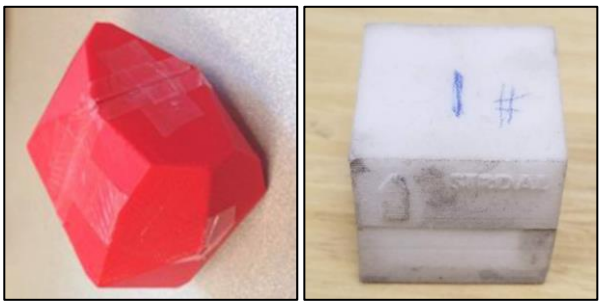

Liu et al. (2016) Zeng et al. (2019)

Fig. 1: Smart Rock

This current study aims to develop an artificial ballast particle with realistic geometry and density, which will provide complete and accurate information about particle motion and orientation.

2 DEVELOPMENT OF SMART BALLAST

In this study, an effort was made to geometrically simulate a real ballast particle as closely as possible because the shape, angularity and surface texture of the particles are important factors that govern the performance of ballast (Sun 2017). A high precision rotary scanner is used to 3d scan an actual ballast particle to capture its geometry and surface roughness, as shown in Fig. 2. Multiple scans were taken as the ballast particle was placed in different positions, and then the data was stitched together to obtain a complete geometric mesh.

The scanned stereolithographic model was then 3d printed to an accuracy of 10 x 10 x 5 Microns and with a precise layer height of 50 Microns so that fairly accurate surface details could be realized. A special kind of PLA filament infused with metal powder was utilised to give the smart ballast a realistic weight. Note that the 3d printed ballast particle was the same weight as actual ballast when 90% print infill density was used. The 3d printing of a smart ballast particle is shown in Fig. 3, while the final product in comparison to an actual ballast particle is shown in Fig. 4. The ballast particle size for this study was selected so as to fit the embedded motion sensor in it (40 mm vs 40 mm x 5 mm).

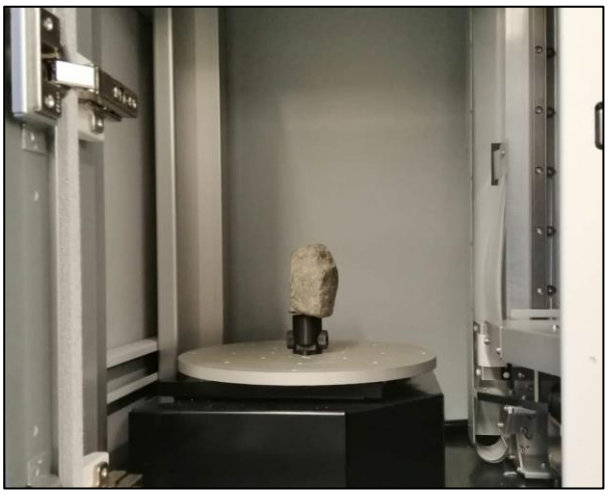

Fig. 2: 3d Scanning of Actual Ballast Particle

Fig. 3: 3d Printing of Smart Ballast Particle

Fig. 4: Smart Ballast particle

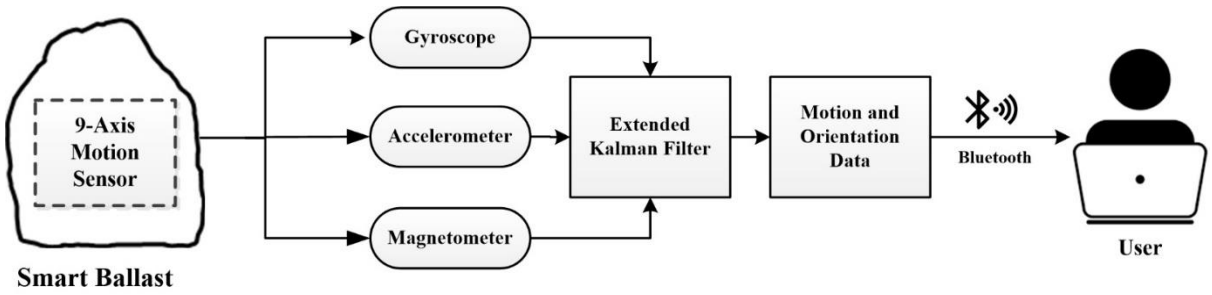

Fig. 5: Working Mechanism of Smart Ballast

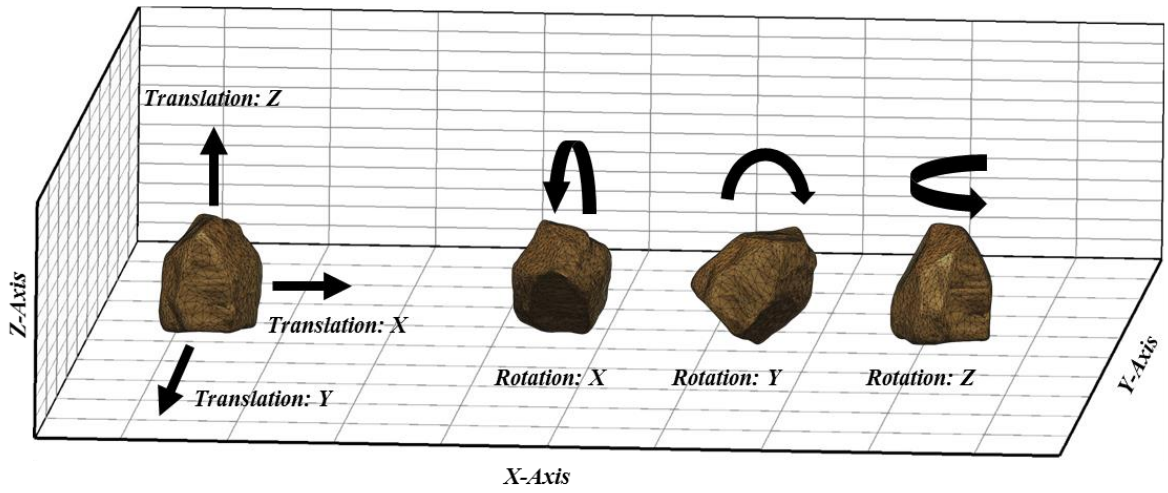

Fig. 6: Six Degrees of Freedom (DOFs) of Smart Ballast

3 MOTION SENSING CAPABILITIES

The "Smart Ballast" had to have advanced motion-sensing capabilities to track its motion and orientation when used under rail tracks. For this purpose, a commercially available 9-axis motion-sensing unit with a gyroscope, an accelerometer, and a magnetometer was used. Generally, a gyroscope and an accelerometer can determine accelerations in all three directions and rotations around each axis, however small errors that arise while integrating the data for absolute position and orientation will have an exponential effect over longer periods. This ultimately leads to instability and cause the absolute values to "drift". This problem can be avoided by using an additional 3-axis magnetometer. The extra information from the magnetic field compensates for the buildup of drifts, and the absolute change in position and orientation of the object can be tracked more accurately.

The motion-sensing unit of smart ballast uses an extended Kalman filter (EKF) for real-time orientation tracking. It filters the raw data obtained from three sensors (gyrometer, accelerometer and magnetometer) to reduce errors in measurement, especially in the case of regular movements as experienced during track vibrations. The data can be sampled at a frequency of 400 Hz and be accessed in real-time by wireless communication. The working mechanism of smart ballast is described in Fig. 5.

The smart ballast has six degrees of freedom, as shown in Fig. 6, so it can track translational motion in three spatial axes as well as rotational motion about those three axes. It can output two types of orientation data: Euler angles and quaternions. Although a ballast particle will not have multiple turns when confined inside a ballast assembly, it may experience multiple full rotations at the top of the ballast layer as the tracks vibrate. In these instances, the Euler angles are prone to "Gimbal lock" and should therefore be ignored. The quaternion representation of orientation should be utilised in these situations. In order to house the motion-sensing unit inside the smart ballast, a very tight embedment hole has been designed in the middle of the particle to ensure that the sensor will not wobble and give noisy data.

4 POTENTIAL APPLICATIONS

The Smart Ballast developed as part of this study can have wide-ranging applications in rail geotechnology. Some examples of when the motion-sensing capabilities of smart ballast could be utilised to great advantage are as follows:

- Smart Ballast can offer real-time monitoring of the ballast layer, especially during the initial compaction stage.
- Different ballast reinforcement techniques such as geogrids can be better evaluated using smart ballast for their ability to arrest ballast particle movement (Liu et al. 2017)
- With the help of acceleration data from smart ballast, the effectiveness of different elastic elements in attenuating the impact forces can now be ascertained more reliably.
- The discrete element method (Cundall & Strack 1979), which has become increasingly popular for modelling granular materials such as ballast, can now be validated using the particle displacement and rotation measured through smart ballast.

ACKNOWLEDGMENTS

This study was funded by Australian Research Council (ARC) through Industrial Transformation Training Centre for Advanced Technologies in Rail Track Infrastructure (ITTC-Rail). The authors gratefully thank and acknowledge the support provided.

REFERENCES

Cundall, PA & Strack, OD 1979, 'A discrete numerical model for granular assemblies', geotechnique, vol. 29, no. 1, pp. 47-65.

Indraratna, B, Salim, W & Rujikiatkamjorn, C 2011, Advanced rail geotechnology-ballasted track, CRC press.

Kumara, JJ & Hayano, K 2016, 'Deformation characteristics of fresh and fouled ballasts subjected to tamping maintenance', Soils and Foundations, vol. 56, no. 4, pp. 652-63.

Liu, S, Huang, H, Qiu, T & Gao, L 2017, 'Comparison of laboratory testing using SmartRock and discrete element modeling of ballast particle movement', Journal of Materials in Civil Engineering, vol. 29, no. 3, p. D6016001.

RailCorp, Annual Report 2017-18, Transport for NSW, NSW Government, Australia

Selig, ET & Waters, JM 1994, Track geotechnology and substructure management, Thomas Telford.

Sun, Y 2017, 'Effect of particle angularity and size distribution on the deformation and degradation of ballast under cyclic loading'.

Zeng, K, Qiu, T, Bian, X, Xiao, M & Huang, H 2019, 'Identification of ballast condition using SmartRock and pattern recognition', Construction and Building Materials, vol. 221, pp. 50-9.

Zhai, W, Wang, K & Lin, J 2004, 'Modelling and experiment of railway ballast vibrations', Journal of Sound and Vibration, vol. 270, no. 4-5, pp. 673-83.

Permeability of Granular Soils through LBM-DEM Coupling

N.M. Phan
Postgraduate Research Student, Centre for Geomechanics and Railway Engineering (CGRE), and ITTC-Rail, University of Wollongong, Australia

B. Indraratna
Distinguished Professor, and Director of Transport Research Centre (TRC), Faculty of Engineering and Information Technology (FEIT), University of Technology Sydney (UTS), Australia

T.T. Nguyen
Research Fellow, Transport Research Centre (TRC), School of Civil and Environmental Engineering, FEIT, University of Technology Sydney (UTS), Australia

ABSTRACT: Permeability of granular soils is one of the important factors when designing foundation as it affects the seepage, stability, and settlement of the foundation. The traditional methods such as experimental and analytical approaches can measure this parameter, however, they become inaccurate when soil properties such as porosity and particle distribution vary during fluid flowing. Therefore, computational methods which can capture both particle and fluid behaviours, and their mutual interactions have received greater attention in recent years. This paper presents a novel numerical approach where fluid variables are coupled with particles to predict hydraulic behaviours. While the particle behaviour can be captured by the Discrete Element Method (DEM) using Newton's second law, the fluid dynamics behaviour will be described by the Lattice Boltzmann Method (LBM) based on a distribution function. The mutual interaction between these two phases is carried out so that particle and fluid variables are updated constantly. The numerical results are validated with experiments showing a good agreement.

1 INTRODUCTION

The permeability of porous materials is a fundamental parameter in the geotechnical field as it can be used for designing the seepage, drainage and many other associated geotechnical purposes. For example, the hydraulic behaviour plays an important role in discharge capacity of natural fibre drains where the porous characteristics are very complex (Nguyen et al. 2018; Nguyen and Indraratna 2019). These characteristics can be measured by traditional methods such as experiments or analytical approaches. However, these methods are lack of the ability to capture the fluid behavior at microscopic level such as localized fluid variables in the porous media. In addition, micro-parameters such as the particle shape and size can have significant influences on the macro-hydraulic conductivity (Nguyen and Indraratna 2017b; Nguyen and Indraratna 2020c), thus more rigorous approach to predict the hydraulic properties of geomaterials is needed. As a result, numerical approaches which can capture the particle and fluid interactions at the microscopic level have been received greater attention in recent years (Tsuji et al. 1993; Kloss et al. 2012; Nguyen and Indraratna 2020b).

This study uses the Discrete Element Method (DEM) coupled with Lattice Boltzmann method (LBM) which is an alternative approach to the conventional Computational Fluid Dynamics (CFD) methods based on Navier-Stoke (NS) equations, to model the permeability of granular soil. Despite considerable success in using CFD-DEM coupling to model hydraulic behaviour of geomaterials, previous studies (Nguyen and Indraratna 2017a, 2020a) also indicate limited accuracy when using NS method to capture microscopic properties of fluid flows. For example, a common numerical technique is using the coarse-grid approach for the CFD-DEM coupling that restricts the scale of predicted fluid variables to the size of particles. LBM, in comparison with conventional CFD, demonstrates a higher degree of resolution as well as the ability to model complex geometries (Feng et al. 2007; Han and Cundall 2013; Indraratna et al. 2021), which is why it is used in this current study.

2 THEORIETICAL BACKGROUND

2.1 *Discrete Element Method*

The DEM was first introduced in (Cundall and Strack 1979) and has been widely used in geotechnical field to model the granular soil, especially at the micromechanical scale. The method uses Newton's Law to calculate particle translational and rotational motion as follows:

$$m_i \frac{dU_{p,i}}{dt} = \sum_{n_c} F_{c,ij} + F_{f,i} + F_{g,i} \quad (1)$$

$$I_i \frac{d\omega_i}{dt} = \sum_{n_c} T_{c,ij} + T_{f,i} \quad (2)$$

where m_i and I_i are the mass and moment of inertia, $U_{p,i}$ and ω_i are the translational and angular velocities, and $T_{c,ij}$ and $T_{f,i}$ are the torques exerting on particle due to other particles and fluid, respectively. F_{cij} is the contact force between adjacent particles. $F_{f,i}$ is the total fluid–particle force interacting on particle. $F_{g,i}$ is the gravitational force. n_c is the total number of contacts.

To simulate particle contact, this current study uses the non-linear contact model which combines Hertz and Mindlin-Deresiewicz theory. This model has been used widely to model particle contact of granular materials with significant success. How to compute contact forces can be found in previous studies (Zhu et al. 2007; Nguyen and Indraratna 2020b)

2.2 *Lattice Boltzmann Method*

The theories of LBM have been thoroughly explained through previous studies (Zou and He 1997; Chen and Doolen 1998; Feng et al. 2007; Krüger et al. 2009). The following section summarizes the important fundamental theory of LBM.

LBM is an immersing alternative method to the conventional CFD solver based on Navier Stoke equation. While the conventional CDF methods are based on using of average fluid variables which leads to less accuracy, LBM has been successful in modelling complex fluid flow such as flow through porous media and multiphase flows (Succi et al. 1989; Aidun and Clausen 2009). Unlike convention CFD using the Navier-Stokes equation to directly solve the macroscopic quantity such as the velocity and pressure, the LBM describes fluid as fluid density distribution function (FDDF) $f_i(x,t)$ moving along the lattice node. This movement involves two consecutive steps streaming and collision. Streaming is the process that $f_i(x,t)$ moves from the current node (x) to the neighbour node ($x+e_i\Delta_t$) at the lattice velocity c and in the direction of the lattice velocity vector e_i (Table 1). Since D3Q19 structure is adopted in this study, the FDDFs are split into 18 directional components (Figure 1). At the new node, the FDDFs are collided and get bouncing back in the opposite direction.

$$\underbrace{f_i(x + e_i\Delta_t, t + \Delta t)}_{streaming} = \underbrace{f_i(x,t) - \frac{1}{\tau}\left(f_i^{eq}(x,t) - f_i(x,t)\right)}_{collision} \quad (3)$$

where Δt the lattice time, τ is the relaxation time and f_i^{eq} is the equilibrium distribution which is computed by:

$$f_i^{eq} = w_i\rho_f\left(1 + \frac{3}{c^2}e_iU_{f,i} + \frac{9}{2c^4}\left(e_iU_{f,i}\right)^2 - \frac{3}{2c^2}U_{f,i}^2\right) \quad (4)$$

in which w_i is the weighting factor shown in Table 1. ρ_f and $U_{f,i}$ are the fluid density and velocity.

The macroscopic observables like density, velocity and pressure can directly be recovered by

$$\rho_f = \sum_{i=0}^{18} f_i \quad (5)$$

$$\vec{U}_f = \frac{1}{\rho_f}\sum_{i=0}^{18} f_i e_i \quad (6)$$

$$P_f = C_s^2\rho_f \quad (7)$$

where $C_s$is the fluid speed of sound. $C_s = c/\sqrt{3}$; $c = \Delta x/\Delta t$ (Δx is lattice spacing).

The kinematic viscosity of fluid can be determined by the relaxation time:

$$\nu = \frac{1}{3}\left(\tau - \frac{1}{2}\right)\frac{\Delta x^2}{\Delta t} \quad (8)$$

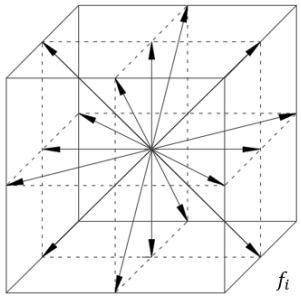

Figure 1: D3Q19 lattice model

From Equation (7), the relaxation time needs to be larger than 0.5 to ensure the viscosity is positive. Given that the stability of LBM model is sensitive to the relaxation time and Mach number. To keep the simulation under the incompressible limit, Mach number needs to be smaller than 0.1

$$M_a = \frac{U_{f,max}}{C_s} \tag{9}$$

Table 1: The velocity vector and weighting factor of D3Q19 model

i	Lattice velocity vector, e_i	Weight, w_i
$i = 0$	(0,0,0)	1/3
$i = 1,..6$	$(\pm c, 0, 0), (0, \pm c, 0), (0, 0, \pm c)$	1/18
$i = 7,..18$	$(\pm c, \pm c, 0), (\pm c, 0, \pm c), (0, \pm c, \pm c)$	1/36

2.3 *LBM-DEM coupling through Immerse Moving Boundary*

In this study, the Immerse Moving Boundary (IMB) proposed by (Noble and Torczynski 1998), is used to consider fluid-solid interaction. This method is widely used to simulate the particle moving in fluid (Feng et al. 2007). The advantage of this boundary is that it considers both solid and fluid in a lattice cell. As a result, it reduces the fluctuation of forces acting on the particles (Feng et al. 2007).

This method introduces a modified collision operator for the fluid nodes that are partially or fully occupied by solid. Equation (3) becomes:

$$\begin{aligned} f_i(x + e_i\Delta_t, t, +\Delta t) - f_i(x,t) \\ = -\frac{1}{\tau}(1-B)\left(f_i(x,t) \right. \\ \left. - f_i^{eq}(x,t)\right) + B\Omega_i^s \end{aligned} \tag{10}$$

where B is the weighting function and can be calculated by:

$$B(\varepsilon, \tau) = \frac{\varepsilon\left(\tau - \frac{1}{2}\right)}{(1-\varepsilon) + \left(\tau - \frac{1}{2}\right)} \tag{11}$$

in which ε is the solid ratio in the lattice cell

And the new additional collision term can be computed by:

$$\begin{aligned} \Omega_i^s = f_{-i}(x,t) - f_i(x,t) + f_i^{eq}(\rho_f, U_p) \\ - f_{-i}^{eq}(\rho_f, U_f) \end{aligned} \tag{12}$$

where U_p is the solid particle velocity

The hydrodynamic force and torques exerting on particles can be computed by:

$$F_f = \sum_{n_s} B_{n_s} \sum_i \Omega_i^s \, e_i \tag{13}$$

$$T_f = \sum_{n_s} (x_{n_s} - x_c) \times \left(B_{n_s} \sum_i \Omega_i^s e_i \right) \tag{14}$$

where n_s is the number of lattice cells covered by the solid particle, and x_c and x_{ns} are the centroid of the solid particle and the lattice node, respectively.

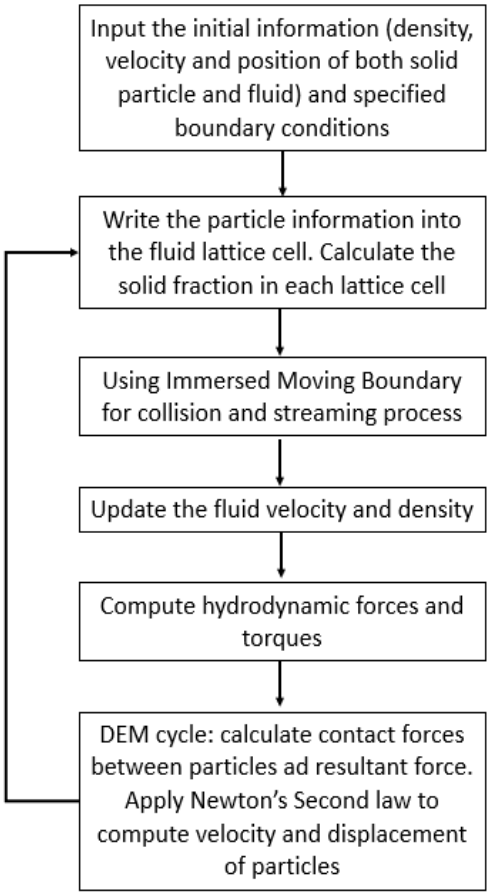

Figure 2: Flow diagram for LBM-DEM coupling algorithms

To sum up, in LBM-DEM numerical model, the LBM exerts the hydrodynamic forces on particles in DEM. If these forces are larger than the body weight of the particles, the particles start to move. Newton's Second Law is applied to determine the-

se movements. The new particle position and orientation are continuously updated and written into the lattice to determine the solid ratio in the lattice cell. Using the modified collision proposed by IBM, the new hydrodynamic force and torque can be computed. The loop continues until simulation time finishes (Figure 2).

3 EXPERIMENT AND NUMERICAL SETUP

In this study, the numerical results are validated with the results obtained from the experiments conducted in this current and a previous studies (Fleshman and Rice 2014). The uniform coarse sand is used for the validation.

3.1 *Experiment*

Figure 3 shows the experimental setup. The permeability of the soil sample can be obtained by:

$$k_T = \frac{QL}{Aht} \tag{15}$$

where Q is the volume of collected water, L is the height of sample, A is sample cross section, h is the water head difference and t is interval time.

The steady flow is established to the inlet at the bottom and the water discharge is collected at the outlet at the top. The water head difference is measured by the manometers. A thin filter layer is laid at the bottom to ensure the uniform water distribution. Further details of the test can be found in other publication of the authors (Indraratna et al. 2021).

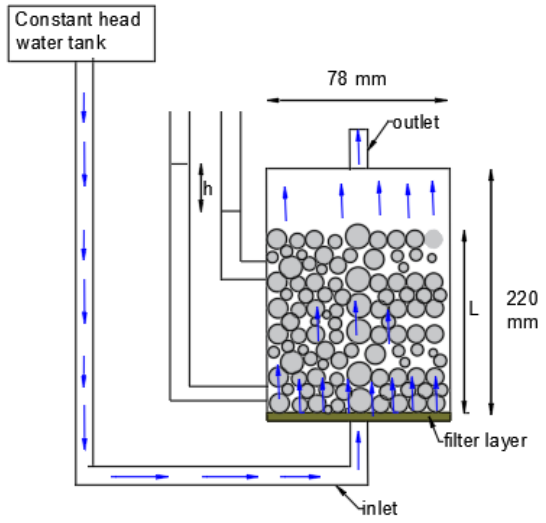

Figure 3: Experimental setup for permeability test

3.2 *Numerical model*

Soil sample having a similar PSD to the experimental sample is generated in DEM. The soil properties are adopted from previous studies (Kafui et al. 2002; Zeghal and El Shamy 2008; Nguyen and Indraratna 2020a) as shown in Table 2.

In this model, the pressure difference is applied at the inlet and outlet. And the discharge velocity (V_d) is obtained. The permeability in the numerical model can be computed by:

$$k = \frac{V_d}{i} \tag{16}$$

where i is the hydraulic gradient

$$i = \frac{\Delta P_f}{\rho g \Delta L} \tag{17}$$

in that ΔP_f is the pressure drop and ΔL is the distance that the fluid travels through soil.

Table 2: Soil and fluid parameters used in this current numerical investigation

Parameters	**Value**	**Unit**
Particles		
Specific gravity	2.65	
Young modulus	6.1×10^5	kPa
Coefficient of friction	0.5	
Coefficient of restitution	0.3	
Poisson's ratio	0.4	
Fluid		
Density	1000	kg/m^3
Kinematic viscosity	10^{-6}	m^2/s

4 RESULTS AND DISCUSSION

4.1 *Permeability*

In this section, the permeability captured by the numerical simulation is validated with experiment result and previous study which has the comparable properties and particle size distribution (PSD) with the soil used in this model. The range of porosity is from 0.39 to 0.46. Overall, the experiment shows a good agreement between numerical and

experimental results (Table 3). The deviations between numerical and experimental results are small, which are 18.9% compared with the current experiment and 11.2% compared with the previous study. Such differences occur due to the difference in cell friction and particle shape. Besides that, the test also proves that the higher the porosity, the higher the permeability.

Table 3: Permeability of soil with different porosities and approaches

	Experiment (Current study)	Numerical results	Experiment (Fleshman and Rice 2014)	Numericla result
Porosity	0.39	0.39	0.45	0.46
Permeability (m/s)	0.0037	0.0044	0.0089	0.0079

4.2 *Localized fluid variables*

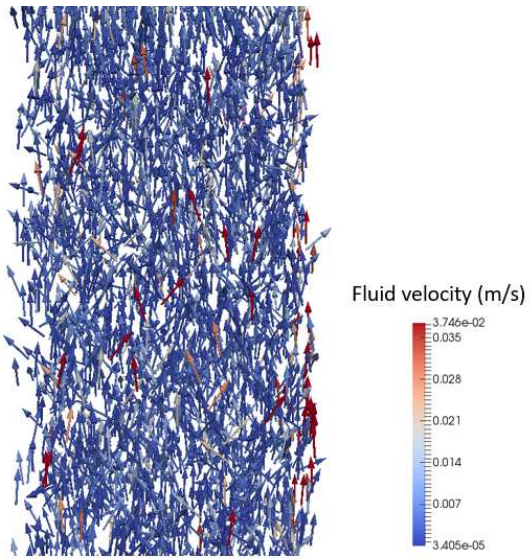

Figure 4: Interstitial micro-fluid vector flowing through particle bed

The advantage of using numerical simulation over the traditional method is the ability to capture localized variables of fluid over detailed porous properties. For instance, the laboratory test can capture the average fluid flow through particle bed, however, it is difficult or almost impossible to measure the local velocity of fluid flowing through the pore space. The arrows in Figure 4 demonstrate the fluid flow through the particle bed. The fluid velocity does not distribute uniformly showing by different colors of the arrows, which due to the different size of the pore. Fundamentally, fluid flow through larger pore has the slower velocity than fluid flow through smaller pore. In addition, it also illustrates that due to the solid obstacles, the fluid can only flow through the gap between particles, therefore, the fluid vectors do not in parallel with each other.

5 CONCLUSION

A study based on LBM-DEM coupling was carried out to investigate the permeability of granular materials. The numerical model represented in this paper showed certain success in predicting hydraulic properties of granular materials. Following conclusions could be highlighted:

The LBM-DEM numerical model can reasonably predict the permeability of the granular soil with different porosities. The deviation between numerical model and experiment is acceptable, from 11.2% to 18.9%. The numerical model can also capture very well the porosity-dependent behaviour of hydraulic conductivity that is understandable well through past experiments.

The fluid-particle coupling based on LBM can capture the localized fluid velocity as well as show how the fluid flows through the porous medium of granular soils. The results showed that the velocity of fluid flowing through the particle bed varies significantly with the localized characteristics of porous systems.

ACKNOWLEDGMENTS

This research was supported by the Australian Government through the Australian Research Council's Linkage Projects funding scheme (project LP160101254) and the Industrial Transformation Training Centre for Advanced Technologies in Rail Track Infrastructure (ITTC), University of Wollongong. The financial and technical supports from SMEC, Coffey, ACRI, Sydney Trains and ARTC (Australian Rail Track Corporation) are acknowledged

REFERENCES

Aidun, C. and Clausen, J. 2009. Lattice-Boltzmann Method for Complex Flows. *Annual Review of Fluid Mechanics*, **42**: 439-472. doi: 10.1146/annurev-fluid-121108-145519.

Chen, S. and Doolen, G.D. 1998. Lattice Boltzmann Method For Fluid Flows. *Annual Review of Fluid Mechanics*, **30**(1): 329-364. doi: 10.1146/annurev.fluid.30.1.329.

Cundall, P.A. and Strack, O.D.L. 1979. A discrete numerical model for granular assemblies. *Géotechnique*, **29**(1): 47-65. doi: 10.1680/geot.1979.29.1.47.

Feng, Y.T., Han, K. and Owen, D.R.J. 2007. Coupled lattice Boltzmann method and discrete element modelling of particle transport in turbulent fluid flows: Computational issues. *International Journal for Numerical Methods in Engineering*, **72**(9): 1111-1134. doi: 10.1002/nme.2114.

Fleshman, M.S. and Rice, J.D. 2014. Laboratory Modeling of the Mechanisms of Piping Erosion Initiation. *Journal of Geotechnical and Geoenvironmental Engineering*, **140**(6): 04014017. doi: 10.1061/(ASCE)GT.1943-5606.0001106.

Han, Y. and Cundall, P.A. 2013. LBM–DEM modeling of fluid–solid interaction in porous media. *International Journal for Numerical and Analytical Methods in Geomechanics*, **37**(10): 1391-1407. doi: 10.1002/nag.2096.

Indraratna, B., Phan, N.M., Nguyen, T.T. and Huang, J. 2021. Simulating Subgrade Soil Fluidization Using LBM-DEM Coupling. *International Journal of Geomechanics*, **21**(5): 04021039. doi: doi:10.1061/(ASCE)GM.1943-5622.0001997.

Kafui, K.D., Thornton, C. and Adams, M.J. 2002. Discrete particle-continuum fluid modelling of gas–solid fluidised beds. *Chemical Engineering Science*, **57**(13): 2395-2410.

Kloss, C., Goniva, C., Hager, A., Amberger, S. and Pirker, S. 2012. Models, algorithms and validation for opensource DEM and CFD-DEM. Vol. 12.

Krüger, T., Varnik, F. and Raabe, D. 2009. Shear stress in lattice Boltzmann simulations. *Physical review. E, Statistical, nonlinear, and soft matter physics*, **79**: 046704. doi: 10.1103/PhysRevE.79.046704.

Nguyen, T.T. and Indraratna, B. 2017a. Experimental and numerical investigations into hydraulic behaviour of coir fibre drain. *Canadian Geotechnical Journal*, **54**(1): 75-87. doi: 10.1139/cgj-2016-0182.

Nguyen, T.T. and Indraratna, B. 2017b. The permeability of natural fibre drains, capturing their micro-features. *Proceedings of the Institution of Civil Engineers - Ground Improvement*, **170**(3): 123-136. doi: 10.1680/jgrim.16.00032.

Nguyen, T.T. and Indraratna, B. 2019. Micro-CT scanning to examine soil clogging behavior of natural fiber drains. *ASCE Journal of Geotechnical and Geoenvironmental Engineering*, **145**(9): 04019037. doi: 10.1061/(ASCE)GT.1943-5606.0002065.

Nguyen, T.T. and Indraratna, B. 2020a. A coupled CFD-DEM approach to examine the hydraulic critical state of soil under increasing hydraulic gradient. *ASCE International Journal of Geomechanics*, **20**(9): 04020138-1:15. doi: https://doi.org/10.1061/(ASCE)GM.1943-5622.0001782.

Nguyen, T.T. and Indraratna, B. 2020b. The energy transformation of internal erosion based on fluid-particle coupling. *Computers and Geotechnics*, **121**: 103475. doi: https://doi.org/10.1016/j.compgeo.2020.103475.

Nguyen, T.T. and Indraratna, B. 2020c. The role of particle shape on hydraulic conductivity of granular soils captured through Kozeny–Carman approach. *Géotechnique Letters*, **10**(3): 398-403. doi: 10.1680/jgele.20.00032.

Nguyen, T.T., Indraratna, B. and Carter, J. 2018. Laboratory investigation into biodegradation of jute drains with implications for field behaviour. *ASCE Journal of Geotechnical & Geoenvironmental Engineering*, **144**(6): 04018026-1:15. doi: https://doi.org/10.1061/(asce)gt.1943-5606.0001885.

Noble, D.R. and Torczynski, J.R. 1998. A Lattice-Boltzmann Method for Partially Saturated Computational Cells. *International Journal of Modern Physics C*, **09**(08): 1189-1201. doi: 10.1142/S0129183198001084.

Succi, S., Foti, E. and Higuera, F. 1989. Three-Dimensional Flows in Complex Geometries with the Lattice Boltzmann Method. *Europhysics Letters (EPL)*, **10**(5): 433-438. doi: 10.1209/0295-5075/10/5/008.

Tsuji, Y., Kawaguchi, T. and Tanaka, T. 1993. Discrete particle simulation of two-dimensional fluidized bed. *Powder Technology*, **77**(1): 79-87. doi: https://doi.org/10.1016/0032-5910(93)85010-7.

Zeghal, M. and El Shamy, U. 2008. Liquefaction of saturated loose and cemented granular soils. *Powder Technology*, **184**(2): 254-265. doi: http://dx.doi.org/10.1016/j.powtec.2007.11.032.

Zhu, H.P., Zhou, Z.Y., Yang, R.Y. and Yu, A.B. 2007. Discrete particle simulation of particulate systems: Theoretical developments. *Chemical Engineering Science*, **62**(13): 3378-3396. doi: https://doi.org/10.1016/j.ces.2006.12.089.

Zou, Q. and He, X. 1997. On pressure and velocity boundary conditions for the lattice Boltzmann BGK model. *Physics of Fluids*, **9**(6): 1591-1598. doi: 10.1063/1.869307.

Piezometer Filter Tip Clogging in Low-lying Acid Sulfate Soils

Senura Athuraliya
PhD Candidate, Transport Research Centre, University of Technology Sydney, Ultimo, NSW 2007, Australia.

Buddhima Indraratna
Distinguished Professor, Director, Transport Research Centre, Founding Director, ARC Industrial Transformation Training Centre for Railroad Technologies (ITTC-Rail), University of Technology Sydney, Ultimo, NSW 2007, Australia.

Ana Heitor
Lecturer of Geotechnical Engineering, School of Civil Engineering, University of Leeds, UK. Formerly Centre for Geomechanics and Railway Engineering, University of Wollongong, Australia.

ABSTRACT: Geotechnical field instruments are essential tools that assist in providing valuable monitoring data, especially when there are major design uncertainties. Piezometers have been reported to produce erroneous readings of pore water pressure (PWP) in numerous case studies attributed to filter tip clogging when installed in acid sulfate soil terrain. It was observed that the excess pore water pressures (EPWP) interpreted from vibrating wire piezometers (VWPs) indicate slowing down of the rate of dissipation after a certain period of time. This paper presents the potential factors that can affect the accuracy and reliability of the PWP measurements in VWPs with special mention to biogeochemical factors that influence clogging of piezometer filter tips. Piezometers affected by coupled clogging, is further evident from the microscopic images and analysis of clogging material.

1 INTRODUCTION

Practising geotechnical and dam engineers have often been puzzled by erroneous piezometer readings which do not follow conventional soil mechanics, for instance, when excess piezometer readings are constant or even increasing even though significant settlement is still taking place in saturated clay foundations. According to previous literature (DiBiagio 1977; Dunnicliff 1993; Hvorslev 1951) piezometers can malfunction due to reasons such as sedimentation and clogging of microscopic soil particles, defective seals, loss of anchorage, corrosion of metal elements, inappropriate aperture sizes of filters or corresponding air entry values as well as severely disturbed soil in the proximity of the filter.

When piezometers are installed in low-lying pyritic clays with a high organic content, erroneous readings may be attributed to biological and chemical factors resulting in the deposition of organic biomass and chemical precipitants such as iron oxides potentially clogging the piezometer filter tip and the surrounding soil (Indraratna et al. 2018; Indraratna et al. 2019). The accumulation of mineral precipitates (Fe and Al oxides/hydroxides) within the pore spaces of soil can result in reducing the porosity and hinder the overall ability for the groundwater to permeate (Indraratna et al. 2014). The bio-clogging is associated with acidophilic bacteria, which promotes biofilm growth as well as catalysing the chemical reactions of mineral precipitation.

2 CLOGGING IN ACID SULFATE SOILS

In low-lying coastal acid sulfate terrain, partial clogging of VWPs with time is mainly attributed to chemical precipitates (e.g. iron oxides and. hydroxides), bacteria-induced cavitation, chemical alteration and growth of biomass, all of which inhibits the dissipation of excess pore water pressure over time (Indraratna et al. 2017). The chemical clogging is further catalysed by acidophilic bacteria, *Acidithiobacillus Ferrooxidans*, where the biological and chemical clogging occurs in tandem, hence the term bio-geochemical clogging. A number of standpipe piezometers, observation and data logger wells that were installed in a coastal acid sulfate floodplain several years ago were exhumed and examined for potential clogging. The clogging had significantly deteriorated the filter zone and the

deposition was mainly biological and chemical origin, including infiltrated particles of fine soil and organic matter, reddish-brown precipitates and dark brown to black biomass/slime that formed a blend of cohesive matrix lining the filters (Fig. 1). Furthermore, sampling of the clogging material revealed that iron oxidising bacterial count was of high aggressivity.

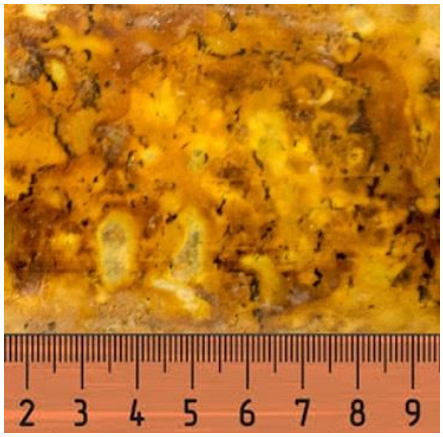

Fig. 1 Iron oxide/hydroxide precipitates clogging the pores of a granular cover surrounding the piezometer tip

To support the clogging phenomenon, a comprehensive microscopic analysis was performed on VWP filter tips before (i.e. a fresh filter) and after clogging (i.e. a filter retrieved from the field 1.5 years after installation) at the UOW-EMC laboratory. These piezometer filter tips were extracted from the Ballina bypass trial embankment, which is an acid sulfate 'hotspot'. A scanning electron microscope (SEM) (JEOL JSM-6490LV) was used to examine the surface of the filter tips. The SEM micrographs show the distinct contrast in the void spaces of the fresh filter prior to clogging (Fig 2(a)), compared to the clogged filter with clogging material deposited within the pores of the filter (Fig 2(b)). An Energy Dispersive X-ray Spectroscopy (EDS) analysis was then coupled with SEM to identify the elemental composition of the filter surface. The primary elemental composition of the filter surface prior to clogging consisted mainly large peaks in Fe, Cr, and Ni, (Fig 3(a) – Spectrum 1) confirming the elemental composition of the stainless steel alloy, whilst the primary elemental composition of the clogging material comprised of Si, Al, Fe and O (Fig 3(b) - Spectrum 2). This further affirms that chemical precipitates deposit on piezometer filter tips, which are transported in their soluble form in acidic groundwater (Indraratna et al. 2010).

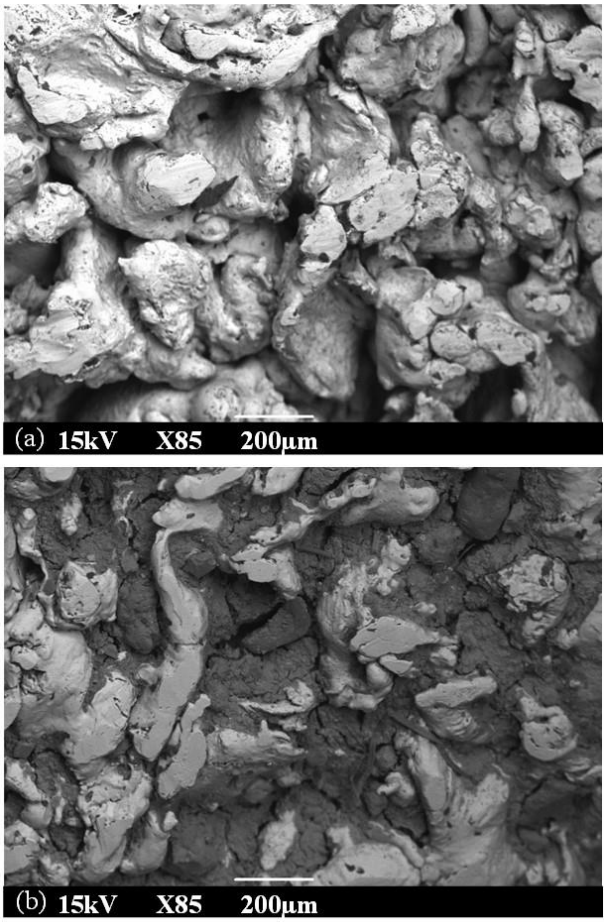

Fig. 2 SEM micrographs of piezometer filters: (a) filter tip prior to clogging, (b) clogged filter tip after deposition of clogging material in filter pores (after Indraratna et al. 2019)

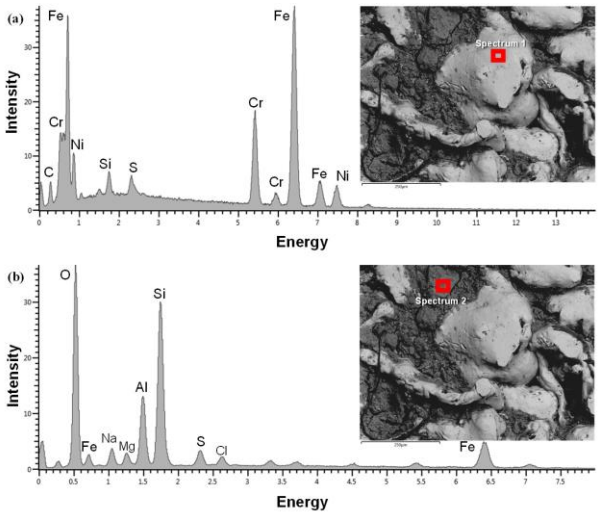

Fig. 3 Comparison of EDS spectra for (a) filter material (spectrum 1); (b) clogging material (spectrum 2)

The potential clogging of VWPs exacerbated by the acidophilic bacteria suggests that for long-term monitoring traditional standpipe piezometers can be easily maintained by flushing would comple-

ment the use of VWPs, although given the longer time lag for standpipes. Recently, fully grouted installations of VWPs have been popular (Dunnicliff 1993), however even then Kelly et al. (2018) have observed discrepancies in pore pressure readings, possibly due to cracking of grout annulus due to large-strain soil movement resulting in tensile strains, paving acidophilic bacteria contaminated groundwater to infiltrate the pore space surrounding the piezometer tip.

3 CASE HISTORIES: PIEZOMETER RESPONSE IN ACID SULFATE TERRAIN

The dissipation trends of excess pore water pressure for four case histories, (i) Port of Brisbane (POB), Australia with wick drains of 1.3 m spacing, (ii) Muar clay embankments, Malaysia with wick drains of 1.3 m spacing, (iii) Pacific Highway-Ballina Bypass, Australia with wick drains of 1.0 m spacing, and (iv) the Second Bangkok (Suwarnabhumi) International Airport (SBIA), Thailand, with wick drains of 1.2 m spacing are presented in Fig 4. For some of the cases, acceptable PWP dissipation rates were observed (e.g. POB and SBIA), however, a sudden retardation of PWP dissipation was observed for the Pacific Highway-Ballina Bypass embankment in Australia after about a year, even with drains installed.

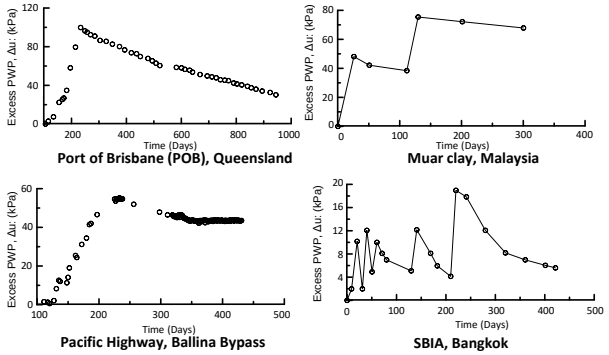

Fig. 4 Selected trends of excess pore water pressure dissipation for various case studies (adapted from Indraratna et al. 2017)

A comparison was made of the Excess PWP trends of embankments at POB and the Pacific Highway (Ballina Bypass, south of Brisbane) to further provide evidence in clogging. Both embankments were raised on similar upper Holocene clay and the piezometer data were recorded at similar depths and at the centreline of each embankment below the groundwater table as shown in Fig 5. VWPs for both cases had stainless steel low air entry filter tips to measure the EPWP in saturated clay.

An accurate prediction of the Excess PWP trend from the selected VWPs were made using the elastic visco-plastic (EVP) model (Baral 2017). This model predicted Excess PWP behaviour very accurately for POB, however, the same model when used to predict the Excess PWP for the site in Ballina, it was only comparable for about a year, after which the measured data remained much higher than the computed or predicted values; whilst the disparity increasing with time (Fig 5).

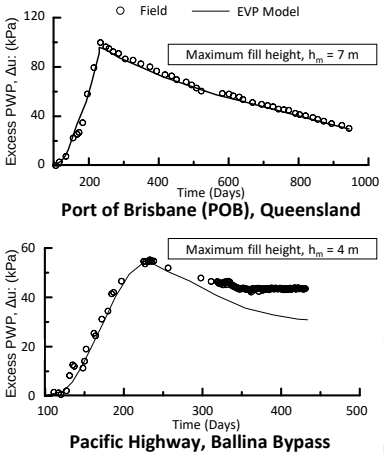

Fig. 5 Vibrating wire piezometer prediction using the EVP model for the Port of Brisbane (POB) and Ballina bypass embankment (adapted from Indraratna et al. 2017)

Unlike the site at POB, the Ballina embankment site is located in a low-lying coastal floodplain in an acid sulfate 'hotspot' with a high organic content (4-6%) and groundwater pH below 5.5. This implies that in the longer term, VWPs installed with ceramic and stainless steel filters can experience clogging when installed in acid sulphate (pyritic) floodplains. At the POB, the stainless-steel filter tips may have been more resistant to bacteria-induced clogging, but the pyrite oxidation problem is not as acute as the Ballina floodplain.

The sudden retarded dissipation of excess PWP at Ballina bypass can be attributed to the potential clogging of piezometers. Based on the EPWP dissipation curve for Ballina Bypass, such clogging in acid sulfate soil conditions can be described using a distinguishable tri-linear trend (Fig 6). During the initial stage of soil consolidation, a piezometer is very accurate and reliable, up until around a year after installation. In the second stage, the piezometer filter tip may begin to partially clog in acid sulfate soils with the continuous deposition of chemical and biological material. Clogging will restrain the flow surrounding the filter tip and will disrupt the pore water pressure dissipation over time. As a

result, a large time lag may be required to establish equilibrium at the soil-filter interface. In the third and final stage the filter may get fully clogged and produce near constant EPWP readings and almost no dissipation. During this stage it can be assumed that the soil would have no 'hydraulic connection' to the filter tip.

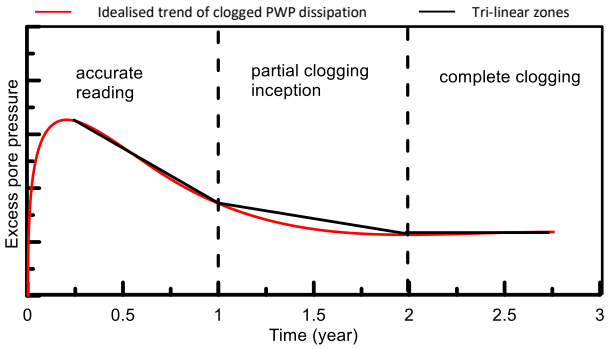

Fig. 6 Trilinear trend for excess PWP dissipation (after Indraratna et al. 2018)

4 CONCLUSIONS

Piezometers may not always respond accurately and reliably as one expects. This is apparent in the case histories discussed, as the piezometer filter tip may be clogged when a retarded dissipation of excess pore pressure is measured even when significant consolidation is still occurring.

In embankments constructed in ASS floodplains with high organic contents, chemical and biological (bacterial) factors may cause VWPs filter tips to gradually lose the reliability and accuracy over time because their filters cannot be backwashed once installed, unlike standpipes piezometers where backwashing is possible as and when required during its entire service life. Therefore it is important that practitioners continue to use alternative methods to verify the VWP readings, such as standpipes that can be backwashed after installation.

ACKNOWLEDGMENTS

Helpful comments from instrumentation manufacturers and discussions with industry colleagues who have had problems measuring the correct pore pressures in the field are greatly appreciated. The authors would like to acknowledge the help from CSIRO, ANSTO and SMEC scientists and engineers in interpreting some past data. The support from of field technicians (Bob Rowland, Frank Crabtree, and Alan Grant) and more than a dozen past PhD and Honours thesis students are acknowledged in the field of acid sulfate soils. The use of facilities and equipment within the University of Wollongong Electron Microscopy Centre (UOW-EMC) should also be acknowledged.

REFERENCES

Baral, P 2017, 'Anisotropic Visco-Plastic Behaviour of Soft Soil with Special Reference to Radial Consolidation', Doctor of Philosophy thesis, University of Wollongong.

DiBiagio, E 1977, 'Field Instrumentation - a Geotechnical Tool', *Norwegian Geotechnical Institute Publication*, no. 115, pp. 29-40.

Dunnicliff, J 1993, *Geotechnical Instrumentation for Monitoring Field Performance*, John Wiley & Sons, New York.

Hvorslev, M 1951, *Time Lag and Soil Permeability in Ground-Water Observations*, Bulletin No. 36, Waterways Experiment Station, Corps of Engineers, US Army, Vicksburg, Mississippi.

Indraratna, B, Baral, P, Ameratunga, J & Kendaragama, B 2017, 'Potential Biological and Chemical Clogging of Piezometer Filters in Acid Sulphate Soil', *Australian Geomechanics Journal*, vol. 52, no. 2, pp. 79-85.

Indraratna, B, Baral, P, Ameratunga, J, Kendaragama, B & Athuraliya, S 2018, 'Potential Biological and Geochemical Clogging of Vibrating Wire Piezometers in Low-Lying Acid Sulphate Soil', in *Proceedings of Australian National Committee on Large Dams (ANCOLD) Conference*, Melbourne, Victoria, vol. Paper ID: 6 (5B).

Indraratna, B, Medawela, SK, Athuraliya, S, Heitor, A & Baral, P 2019, 'Chemical Clogging of Granular Media under Acidic Groundwater', *Environmental geotechnics*, vol. Special Issue: Testing and Modelling of Complex Rockfill Material, 6 (3) doi: 10.1680/jenge.18.00143.

Indraratna, B, Pathirage, PU, Rowe, RK & Banasiak, L 2014, 'Coupled Hydro-Geochemical Modelling of a Permeable Reactive Barrier for Treating Acidic Groundwater', *Computers and Geotechnics*, vol. 55, pp. 429-39.

Indraratna, B, Regmi, G, Nghiem, L & Golab, AN 2010, *Performance of a PRB for the Remediation of Acidic Groundwater in Acid Sulfate Soil Terrain*, Research Online.

Kelly, R, Sloan, S, Pineda, J, Kouretzis, G & Huang, J 2018, 'Outcomes of the Newcastle Symposium for the Prediction of Embankment Behaviour on Soft Soil', *Computers and Geotechnics*, vol. 93, pp. 9-41.

Cyclic behaviour of soft clay railway subgrade prone to mud pumping

Aruni Abeywickrama
Graduate Engineer, Geovert Ground Engineering Pty Ltd, Sydney, NSW 2020, Australia
Buddhima Indraratna
Distinguished Professor, Director, Transport Research Centre, Founding Director, ARC Industrial Transformation Training Centre for Railroad Technologies (ITTC-Rail), University of Technology Sydney, Ultimo, NSW 2007, Australia.
Cholachat Rujikiatkamjorn
Professor, Transport Research Centre, School of Civil and Environmental Engineering, University of Technology Sydney, Ultimo, NSW 2007, Australia.
Mandeep Singh
Senior Technical Support Officer, Transport Research Centre, School of Civil and Environmental Engineering, University of Technology Sydney, Ultimo, NSW 2007, Australia.

ABSTRACT: This paper explicates the cyclic behaviour of soft clay railway subgrade, which is prone to mud pumping using laboratory experiments. Actual field conditions are applied on the soil samples using the Dynamic Triaxial apparatus to simulate the railway subgrades subjected to different train loads and speeds. The objective of this paper is to serve the reader with a rigorous understanding about the different aspects of cyclic behaviour of soil such as the generation of excess pore water pressure, cyclic axial strain development and effect of drainage on mud pumping through these laboratory experiments. For instance, the mechanism and mitigation of mud pumping is still queried. Therefore, an endeavour to understand the mechanism of mud pumping and its mitigation is also given through this research. Evidently, the Dynamic triaxial test results can be exploited to crystalize the understanding in the mechanism of mud pumping and its mitigation.

1 INTRODUCTION

The demand for freight transportation is rapidly increasing mainly due to the industrial and agricultural development all over the world. Moreover, the higher freight capacity, efficiency and low environmental impacts make trains very attractive for inland transportation purposes. The Australian Bureau of Statistics reported that the Australian railway network, which consists of narrow, broad and standard gauge ballasted rail tracks extend up to 41,461 km (Year Book Australia 2005). According to the statistics the freight movement by rail has exceeded all the other modes such as sea and road (BITRE 2009). To meet this boosting demand the speed and the axle loads of the trains moving these heavy freights are also increasing.

When these high speed heavy haul trains pass through vulnerable areas with saturated subgrades, rail tracks are most likely to fail under the higher deformation and pumping of fines (i.e. mud pumping) under repeated loading (Abeywickrama et al. 2019). Cyclic load exerted on the saturated subgrade by the passing train generates higher excess pore water pressures thus resulting a reduction in the effective stress under poor drainage condition. Due to the reduction in the shear strength, the upper layer of the subgrade turns in to slurry. When the train passes, the fines from the slurried subgrade moves upward into the ballast layer. This phenomenon also causes higher deformations along with this fine particle migration and the sinking of ballast into the subgrade. There are several mud pumping incidents which occurred in different countries in the world. A mud pumping prone site in New South Wales, Australia is shown in Fig. 1.

Fig. 1 A railway site which is prone to mud pumping near Wollongong in New South Wales, Australia

It is very important to get an understanding of the causative factors and remedial measures for this mud pumping problem. Since it is understood that the major factors favouring mud pumping are saturated subgrade and poor drainage, which result in higher excess pore pressures under cyclic loading, it is crucial to enhance the drainage and reduce the excess pore pressure generation. Past laboratory investigations have shown that Prefabricated Vertical Drains (PVD) can reduce the generation of excess pore water pressure due to cyclic loading (Indraratna et al. 2010). Therefore, these PVDs can be adopted as a solution to mitigate mud pumping problem in railway subgrades. The experimental investigation on the factors affecting mud pumping and how the mitigation of mud pumping can be implemented is covered through this paper.

2 TEST PROCEDURE

2.1 *Basic soil properties and sample preparation*

The soil used in the laboratory experiments was taken from a site in Wollongong. The soil was classified as a CL type soil with a low plasticity (i.e. PI=10%) (ASTM D2487-17 2017).

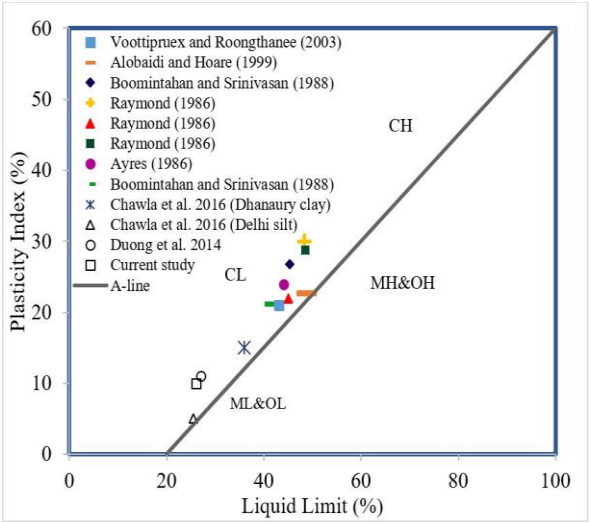

Fig. 2 Plasticity chart of the subgrade soils subjected to mud pumping (Modified after Abeywickrama et al. 2019)

The soils taken from reported mud pumping sites are tested to be low to medium plastic soil (Fig. 2). Thus, the soil susceptible to mud pumping was identified to be CL or ML type soils. The particle size distribution of the soil used in the current study compared with soils from mud pumping sites in the past studies is given in Fig. 3.

Oven dried soil samples were taken and water was added to get an initial moisture content of 20%. The soil was then kept in a humidity-controlled room for 24 hours to get a uniform consistency. The samples were prepared using the moist tamping method in a mould of 50mm in diameter and 100mm in height to a uniform bulk density of 1600kg/m^3. Compaction was done in 10 layers following the nonlinear under-compaction criterion (Jiang et al. 2003).

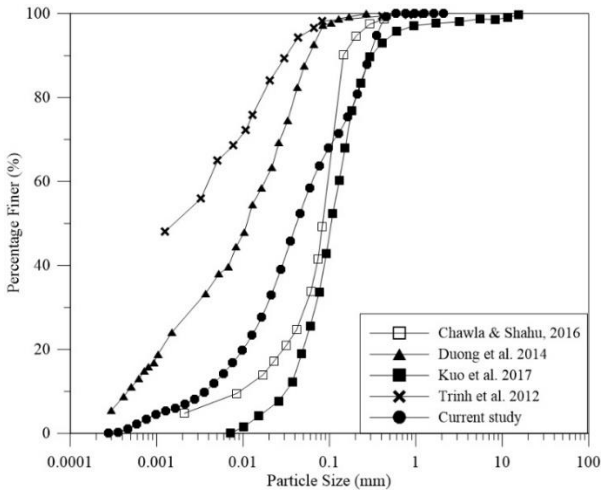

Fig. 3 Particle size distribution of the soil compared with various mud pumping studies

2.2 *Test apparatus and experimental plan*

A series of cyclic triaxial tests was conducted using the dynamic triaxial testing apparatus with an electro-mechanical actuator on the remoulded samples. After setting up the specimen in the triaxial cell, it was saturated using back pressure saturation with an effective radial stress of 10 kPa and a back pressure of 400 kPa for 1-2 days under isotropic condition. Skempton's B value was checked >0.95 to make sure the sample is saturated. After saturation, the sample was anisotropically consolidated ($k_0=\sigma'_h/\sigma'_v$=0.6) to simulate the in situ subgrade stresses (Wood 1991). During consolidation, an effective radial stress of 24 kPa was kept constant. In order to model the cyclic stress state induced by the passage of trains in the field, a stress-controlled loading scheme was adopted in accordance with ASTM D5311-92 2004. A cyclic load with a sinusoidal waveform was applied under undrained condition on the samples with different cyclic stress ratios (CSR) (equation 1) and frequency to simulate the trains with different axle loads moving at different speeds. The frequency was varied from 1-5 Hz and the CSR was varied from 0.2-0.8. Cyclic load was applied for 50000 number of cycles or up to the failure (5% axial strain).

$$CSR = \frac{q_{cyc}}{2\sigma_3'} \quad (1)$$

where, q_{cyc} is the cyclic deviator stress and σ_3' is the effective radial stress. When analysing the results, a membrane correction for undrained testing was applied according to ASTM D4767-95.

3 RESULTS AND DISCUSSION

The undrained stress-controlled cyclic triaxial test results show the behaviour of a saturated subgrade with poor drainage subjected to repeated loading. The most important factors that should be concerned under cyclic loading are the accumulation of excess pore pressure and the permanent axial deformation (Cai et al. 2012).

3.1 *Permanent axial strain*

As can be seen from Fig. (5a), with the increase in the number of cycles the axial strains also increase. The sample did not fail under CSR of 0.2. That is, when the applied cyclic load was below a particular value, the sample remained stable. The stable samples show gradual accumulation of axial strain, and it reaches to a constant value with increasing number of cycles. The maximum axial strain that the stable sample reached is less than 0.4% after 50000 number of cycles, but the samples subjected to cyclic loading >0.2 CSR failed resulting higher deformation. Corresponding to the higher deformation, which occur in the fluidised specimens there is a drop in the deviator stress in the specimens as a result of the loss of shear strength due to fluidization (Fig. 4). Also, it is clear that there is an increment in the accumulation of the plastic deformation with the number of cycles. This increment in the cyclic deformation causes higher stiffness degradation of the soil. Higher cyclic loads cause higher degradation (Zhou et al. 2001).

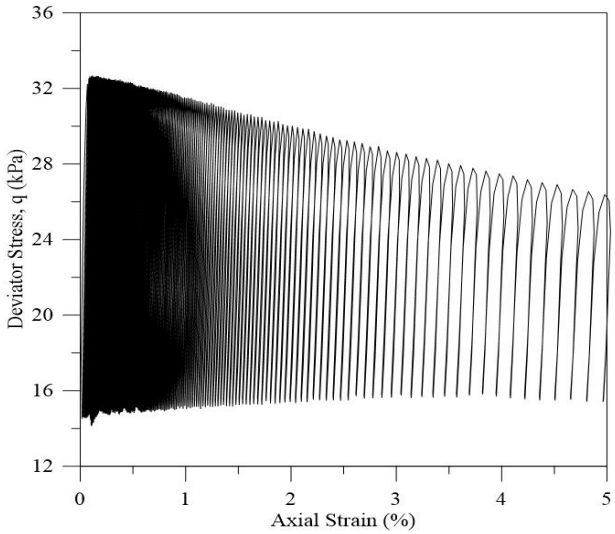

Fig. 4 Deviator stress vs. axial strain (f=2Hz, CSR=0.4)

Fig. (5a) depicts how the axial strains increase rapidly in few cycles for the failed samples. At a given number of cycles before the failure, the axial strains occurred are higher for higher CSR values. Fig. (5b) shows the effect of frequency on the axial strains. With the increase in the frequency, the number of cycles to failure is also increasing. Therefore, the samples subjected to low frequencies failed quicker than the samples subjected to higher frequencies.

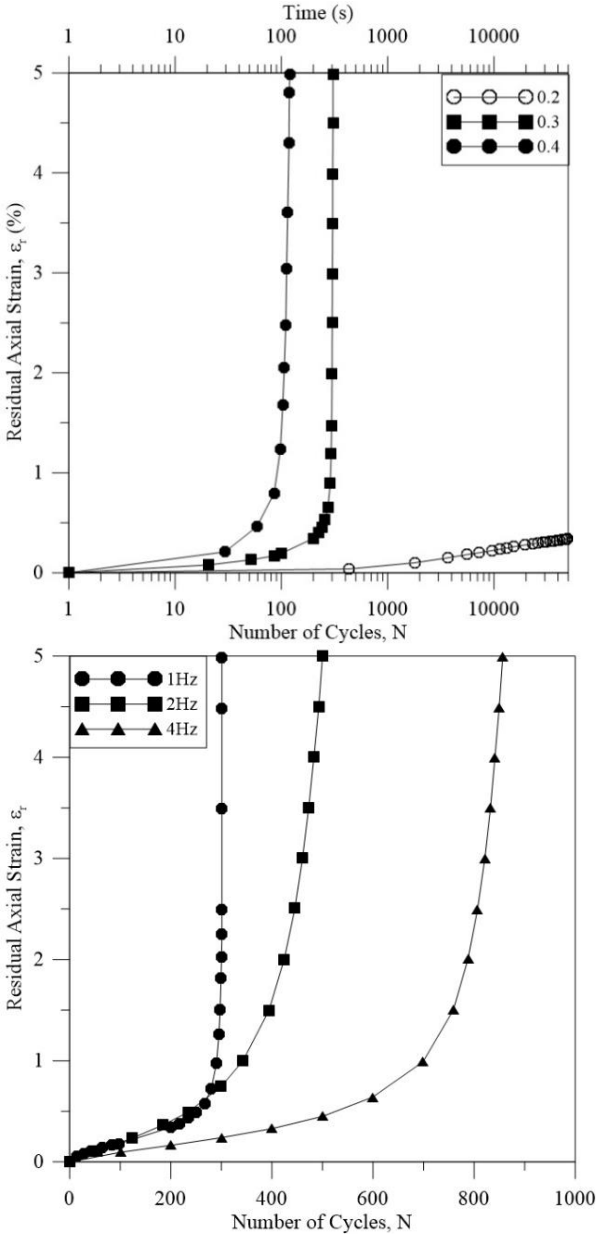

Fig. 5 Effect of (a) CSR (F=1Hz) and (b) frequency (CSR=0.3) on axial strain

3.2 *Excess pore water pressure*

Accumulation of the dynamic excess pore pressure is the major causative factor for railway subgrade mud pumping in the saturated vulnerable areas. The effect of CSR and frequency on the excess pore pressure ratio similar to the development of axial strain. Fig. (6) shows the variation of mean excess pore pressure with the number of cycles. With the increase in the number of cycles, the generated excess pore pressure also increases. The excess pore pressure of the stable sample under 0.2 CSR increased gradually and reached to a maximum constant value. Samples subjected to CSR>0.2 failed with a sudden increase in the excess pore pressure and fluidised. At a given number of cycles, the generated excess pore pressure is higher for a higher CSR value.

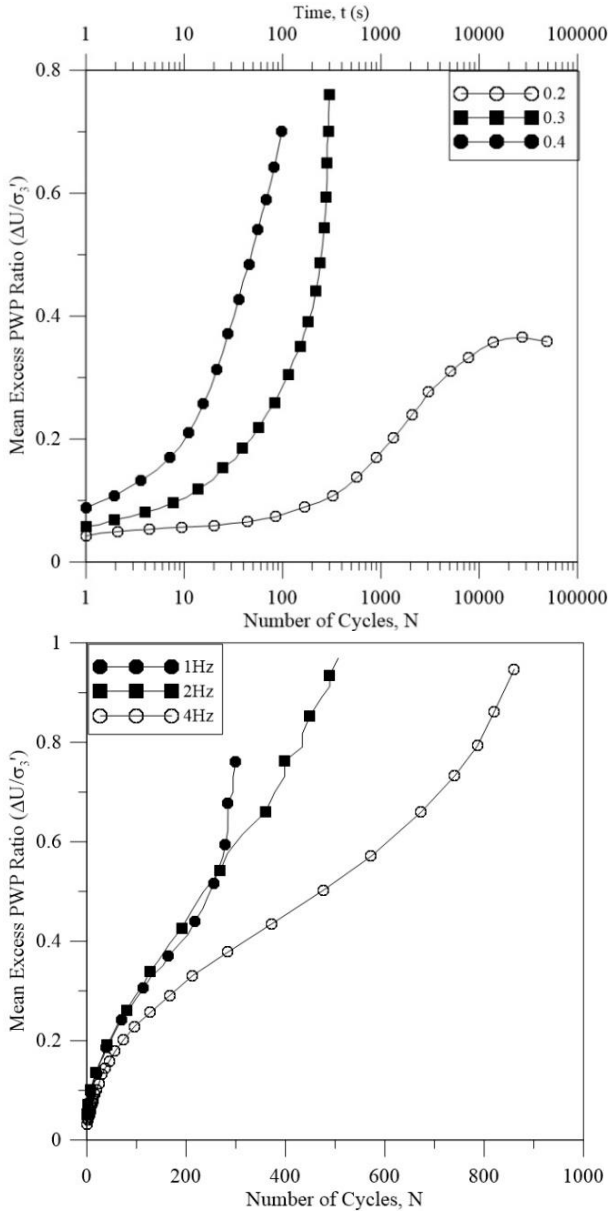

Fig. 6 Effect of (a) CSR (F=1Hz) and (b) frequency (CSR=0.3) on excess pore pressure

Fig. (6b) shows the effect of frequency on the accumulation of excess pore pressure. For a given number of cycles, the generated excess pore pressure is higher for lower frequencies. Therefore, higher the frequency later the failure occurs. A similar behaviour with the effect of frequency on the excess pore pressure as well as the axial strain was observed in previous studies (Dash et al. 2016, Andersen 2009, Voznesenky et al. 1999).

Fig. 7 Fluidized specimen subjected to CSR > CSRc

Under the combined effect of critical cyclic stress and frequency, the triaxial samples fluidised forming a slurry at the upper part of the sample. A typical fluidised specimen under cyclic loading is shown in Fig. 7. For the fluidised specimens, it was observed that there is a redistribution of moisture in the upper regions of the sample along with the upward migration of fine particles. For a selected specimen (F=1 Hz, CSR= 0.3) the water content of the uppermost layer was measured to be 38% whereas the saturated moisture content was 35% after back saturation. Similar findings were reported by the authors elsewhere (Indraratna et al. 2020, Chawla et al. 2016).

3.3 *Partially drained cyclic triaxial tests*

It is clear that under higher cyclic load (> CSR_c), high excess pore pressures and excessive deformations occur under poor drainage conditions in saturated railway subgrades. This higher excess pore pressure generated at the shallow subgrade induces softening and the fine particles accumulate on the top and migrate into the upper ballast layer.

Therefore, it is clear that if the generation of higher excess pore pressure can be reduced this problem can be mitigated to a greater extent.

Past studies show that PVDs are effective in dissipating excess pore pressure generated due to cyclic loading making it more resistant to the next cyclic loading. (Attya et al. 2007; Rujikiatkamjorn et al. 2011) This approach can be adopted in mitigating the mud pumping problem in railways.

This study focuses on a series of cyclic triaxial tests with PVD to investigate the effectiveness of PVD in mitigating mud pumping. By installing a PVD into the soil, it creates a partially drained condition. In undrained condition cyclic excess pore pressure increases with the number of cycles under a zero volume change.

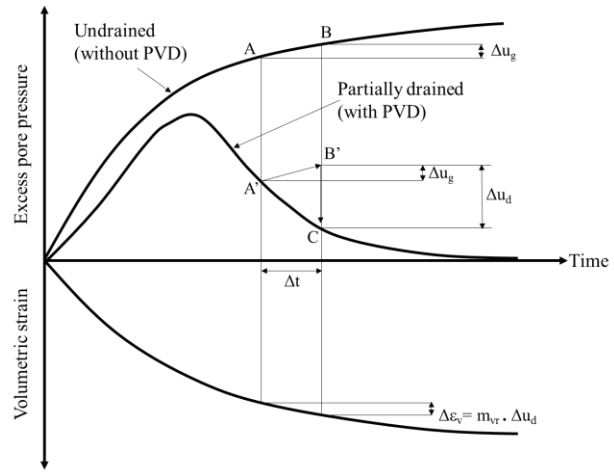

Fig. 8 Schematic diagram of excess pore pressure and volumetric strain variation under undrained and partially drained conditions (Modified after Hyodo et al. 1992).

Unlike in undrained condition, in partially drained condition excess pore pressure increase initially and then it tends to reduce after some number of cycles. The variation of excess pore pressure and the volumetric strain with time under undrained and partially drained conditions are well depicted with a schematic diagram in Fig. (8). With the dissipation of excess pore pressure, the shear strength of the soil is also increases (Yasuhara et al. 1983; Yasuhara 1985; Yasuhara and Hirao 1989). Dissipation of excess pore pressure under partially drained condition depends on the hydraulic conductivity of the subgrade soil as well.

In the Δt time increment the generated excess pore pressure due to cyclic loading during that time period is Δu_g. In the undrained condition there's a continuous accumulation of the excess pore with time resulting a continuous reduction in the effective stress. The void ratio of the samples subjected to undrained loading does not change, thus the volumetric strain is also zero. In the case of partially drained condition the generation and dissipation of excess pore pressure occur simultaneously. With the dissipation of excess pore pressure, the sample is subjected to a volumetric strain of $\Delta \varepsilon_v$ as shown in Fig. 8.

Thus, by enhancing the drainage condition in the subgrade by installing PVD the excess pore pressure accumulation can be retarded. Therefore, the major causative factor for the occurrence of mud pumping in the railway subgrades can be alleviated.

4 CONCLUSIONS

This paper presents a series of undrained cyclic triaxial tests conducted under different CSRs and frequencies for a soil which is susceptible to mud pumping. The effect of CSR and frequency on axial deformation and excess pore pressure generation is determined through the triaxial test results. A mitigation measure for mud pumping problem in saturated railway subgrades is proposed.

- Permanent axial strains and excess pore pressure generated due to cyclic loading under undrained condition increase with the number of cycles irrespective of the CSR and frequency.
- Higher CSR (i.e. higher cyclic load) creates higher axial strains and excess pore pressures compared to a lower CSR.
- Samples are stable below a particular CSR and above that critical CSR (CSR_c), samples fail under undrained cyclic loading resulting instantaneous increase in axial strain and excess pore pressures. For the soil and loading conditions selected in this study, this particular CSR_c value is 0.2. This value is dependent on the soil type and the loading conditions.
- Providing a partially drained environment for the subgrade susceptible to mud pumping would reduce the risk of mud pumping. Further investigation should be done in this regard.

ACKNOWLEDGMENTS

The authors would like to acknowledge the financial and technical support from the Australian Reasearch Council (ARC) Linkage Project (LP160101254), the Industrial Transformation Training Centre for Advanced Technologies in Rail Track Infrastructure (ITTC), University of Wollongong, SMEC-Australia, ARTC (Australian Rail Track Corporation) and the technical staff of University of Wollongong.

REFERENCES

Abeywickrama, A., Indraratna, B. and Rujikiatkamjorn, C. 2019. Excess Pore-Water Pressure Generation and Mud Pumping in Railways Under Cyclic Loading. *In* Geotechnics for Transportation Infrastructure. *Edited*. Springer. pp. 371-383.

Alobaidi, I. and Hoare, D.J. 1996. The development of pore water pressure at the subgrade-subbase interface of a highway pavement and its effect on pumping of fines. Geotextiles and geomembranes, **14**(2): 111-135.

Andersen, K.H. 2009. Bearing capacity under cyclic loading — offshore, along the coast, and on land. The 21st Bjerrum Lecture presented in Oslo, 23 November 2007. Canadian Geotechnical Journal, 46(5): 513-535. doi: 10.1139/t09-003

ASTM D2487-17. 2017. Standard Practice for Classification of Soils for Engineering Purposes (Unified Soil Classification System). West Conshohocken, PA, Pa.

ASTM D4767-95. 1995. Standard Test Method for Consolidated Undrained Triaxial Compression Test for Cohesive Soils. American Society for Testing and Materials (ASTM), West Conshohocken, PA, Pa.

ASTM D5311-92. 2004. Standard test method for load controlled cyclic triaxial strength of soil. American Society for Testing and Materials (ASTM), West Conshohocken, PA, Pa.

Attya, A., Indraratna, B. and Rujikiatkamjorn, C. 2007. Cyclic behaviour of PVD-soft soil subgrade for improvement of railway tracks. *10th Australia New Zealand Conference on Geomechanics.* Brisbane.

Ayres, D.J. 1986. Geotextiles or geomembranes in track? British railways' experience. Geotextiles and Geomembranes, 3(2): 129-142. doi: https://doi.org/10.1016/0266-1144(86)90004-X.

BITRE. 2009. Australian transport statistics Yearbook 2009.

Boomintahan, S. and Srinivasan, G.R. 1988. Laboratory studies on mud-pumping into ballast under repetitive rail loading. Indian Geotechnical Journal, 18(1): 31-47.

Cai, Y., Gu, C., Wang, J., Juang, C.H., Xu, C. and Hu, X. 2012. One-way cyclic triaxial behavior of saturated clay: comparison between constant and variable confining pressure. Journal of Geotechnical and Geoenvironmental Engineering, **139**(5): 797-809.

Chawla, S. and Shahu, J.T. 2016. Reinforcement and mud-pumping benefits of geosynthetics in railway tracks: Model tests. Geotextiles and Geomembranes, 44(3): 366-380. doi: https://doi.org/10.1016/j.geotexmem.2016.01.005.

Dash, H.K. and Sitharam, T.G. 2016. Effect of frequency of cyclic loading on liquefaction and dynamic properties of saturated sand. International Journal of Geotechnical Engineering, 10(5): 487-492. doi: 10.1080/19386362.2016.1171951.

Duong, T.V., Cui, Y.-J., Tang, A.M., Dupla, J.-C., Canou, J., Calon, N. and Robinet, A. 2014. Investigating the mud pumping and interlayer creation phenomena in railway sub-structure. Engineering geology, **171**: 45-58.

Hyodo, M., Yasuhara, K. & Hirao, K. 1992. Prediction of clay behaviour in undrained and partially drained cyclic triaxial tests. Soils and Foundations, 32, 117-127.

Indraratna, B., Ni, J. and Rujikiatkamjorn, C. 2010. Investigation on effectiveness of a prefabricated vertical drain during cyclic loading. *In Proceedings of the* IOP Conference Series: Materials Science and Engineering. IOP Publishing Vol. **10**, pp. 012091.

Indraratna, B.M., Singh; Nguyen,Thanh Trung; Leroueil, Serge; Abeywickrama, Aruni; Kelly, Richard; Neville, Tim. 2020. A laboratory study on fluidization of subgrade under undrained cyclic triaxial tests. Canadian Geotechnical Journal.

Jiang, M.J., Konrad, J.M. and Leroueil, S. 2003. An efficient technique for generating homogeneous specimens for DEM studies. Computers and Geotechnics, 30(7): 579-597. doi: https://doi.org/10.1016/S0266-352X(03)00064-8

Raymond, G.P. 1986. Geotextile Application for a branch line upgrading. Geotextiles and Geomembranes, 3(2): 91-104. doi: https://doi.org/10.1016/0266-1144(86)90002-6.

Rujikiatkamjorn, C., Indraratna, B. and Meng, G. 2011. Experimental study on the effectiveness of prefabricated vertical drains under cyclic loading.

Trinh, V.N., Tang, A.M., Cui, Y.-J., Dupla, J.-C., Canou, J., Calon, N., Lambert, L., Robinet, A. and Schoen, O. 2012. Mechanical characterisation of the fouled ballast in ancient railway track substructure by large-scale triaxial tests. Soils and Foundations, 52(3): 511-523. doi: https://doi.org/10.1016/j.sandf.2012.05.009.

Voznesensky, E.A. and Nordal, S. 1999. Dynamic instability of clays: an energy approach. Soil Dynamics and Earthquake Engineering, 18(2): 125-133. doi: https://doi.org/10.1016/S0267-7261(98)00043-8.

Wood, D.M. 1991. Soil Behaviour and Critical State Soil Mechanics. Cambridge University Press.

Yasuhara, K. (1985). "Undrained and drained cyclic triaxial tests on a marine clay." Proc.11th International Conf. Soil Mech. and Founds. Eng., San Francisco, USA, 2, 1095–1098.

Yasuhara, K., and Hirao, K. (1989). "Changes in undrained strengrh of clay after cyclic loading." Technical Report of Geotechnical Research Institute, Nishinippon Institute of Technology, 5, 15–30.

Yasuhara, K., Ue, S., and Fujiwara, H. (1983). "Undrained shear behaviour of quasioverconsolidated clay." Proc. IUTAM Symp. On Seabed Mechanics, Graham and trotman, London, England, 17–24.

Year Book Australia 2005. no. 87. Commonwealth of Australia, Canberra, Cat, (1301.0)

Zhou, J. and Gong, X. 2001. Strain degradation of saturated clay under cyclic loading. Canadian Geotechnical Journal, 38(1): 208-212. doi: 10.1139/t00-062.

Factors affecting mud pumping of subgrade fines under ballasted rail tracks

Mandeep Singh[a], Buddhima Indraratna[b], Cholachat Rujikiatkamjorn[c]

[a] *Senior Technical Support Officer, Transport Research Centre, School of Civil and Environmental Engineering, University of Technology Sydney, Ultimo, NSW 2007, Australia*
[b] *Distinguished Professor, Director, Transport Research Centre, Founding Director, ARC Industrial Transformation Training Centre for Railroad Technologies (ITTC-Rail), University of Technology Sydney, Ultimo, NSW 2007, Australia.*
[c] *Professor, Transport Research Centre, School of Civil and Environmental Engineering, University of Technology Sydney, Ultimo, NSW 2007, Australia.*

ABSTRACT: With the rapid growth and advancement of the transportation industry across the world, the demand for a faster and sustainable rail network is the priority of all nations. Of the many challenges faced by railway geotechnical engineers, mud pumping of railway subgrade, into ballasted tracks is by far, the most common yet not fully understood phenomenon. Mud pumping occurs when the fine particles from the subgrade migrate upwards due to the dynamic loads acting on the subgrade during the passage of trains. The fouled ballast is compromised on its strength and free draining capability. It requires extensive maintenance costs to repair the affected track, which does not guarantee a permanent solution. The main aim of this article is to summarise the various factors that affect the pumping of subgrade fines. Further, it is emphasised that the cyclic behaviour of the subgrade plays a significant role in understanding the causes of mud pumping. The cyclic excess pore pressure creates a hydraulic gradient which may cause the subgrade slurry to shoot upwards. It is observed that beyond a threshold cyclic stress ratio there is a rapid increment of the mean excess pore pressure and accumulated axial strains which cause the soil to soften.

1 INTRODUCTION

In recent times, there has been a growing interest in the geotechnical community to comprehend on the factors governing the pumping of fines under the railway tracks. Simply said, the migration of the soft subgrade particles into the coarser ballast layer can be termed as mud pumping or subgrade fluidisation. The phenomenon of pumping of fines is not only limited to the railways but has also been reported on airfields (Yoder, 1957) as well as on pavements (Alobaidi and Hoare, 1994; Kermani et al., 2019). Although, mud pumping is a widespread problem there have been limited studies on investigating the governing mechanism (Alobaidi and Hoare, 1999; Duong et al., 2014; Indraratna et al., 2020b). A recent study reported as many as 300 active locations of mud pumping along the coastal railway lines in New South Wales, Australia (Nguyen et al., 2019).

Fig. 1: Perched water table on the subgrade surface at a problematic site near Wollongong City, Australia.

As the fines rise upwards from the subgrade layer, they hinder the free draining capacity of the ballast layer. Under extreme cases of pumping, the subgrade slurry ejects along the sides of the rail track forming miniature soil volcano. This not only reduces the bearing capacity of the ballast layer but also results in differential settlements. In addition to the above problems, the sleepers lose contact with the ballast and this causes a detrimental effect on the sleepers which result in severe track degradation (Fig. 1).

The phenomenon of mud pumping is closely related to the liquefaction behaviour of fine grained soils due to the common causative factor; the development of cyclic excess pore pressure (Indraratna et al., 2020b). Castro and Poulos (1977) define liquefaction as the phenomenon in which saturated sand loses its shear resistance significantly due to static or dynamic loading and flows like a liquid. On the other hand, cyclic mobility is defined as the progressive softening of saturated sand specimen under cyclic loading at constant water content. Indraratna et

al. (2020b) identified subgrade fluidisation or mud pumping as a special case of cyclic mobility involving the redistribution of water content and upward fines migration.

Nguyen et al. (2019) summarised mud pumping into three categories; (i) subgrade fluidisation and infiltration (ii) formation of peat boils on soft subsoils and (iii) upward migration of fouled ballast particles. The main aim of this article is to discuss the factors contributing to the migration of fines under ballasted rail tracks. To address this issue, these factors are divided in two categories: (a) Inherent soil properties and (b) the soil response due to external loading. In this case, the external loading arises due to the passage of trains.

2 SOIL PROPERTIES INFLUENCING THE PUMPING OF FINES

The basic geotechnical properties govern the soil response when subjected to external stresses. Under undrained cyclic loading, the build-up of excess pore pressures reduces the effective stresses in the soil matrix. When the excess pore pressure ratio (i.e., the ratio of the cyclic excess pore water pressure to the mean effective confining pressure) reaches unity, the specimen liquefies. Few researchers have correlated the liquefaction susceptibility of fine grained soils to its water content and Atterberg limits (Bray and Sancio, 2006). In this section, emphasis is laid on understanding the influence of soil plasticity, particle size gradation, water content and relative compaction (RC) on the pumping of fines.

2.1 *Soil plasticity*

Plasticity is an important soil property that governs the ability of the soil to undergo non-recoverable deformation. The water content at which the soil behaves like a liquid is defined as the liquid limit (w_{LL}) whereas the water content at which the soil exhibits plastic behaviour is defined as the plastic limit (w_{PL}). It is seen that the soils having low to medium plasticity are more vulnerable to mud pumping (Singh et al., 2019; Indraratna et al., 2020b) as opposed to highly plastic clays. In the case of highly cohesive soils, these soils have larger specific surface area and for instance, clays containing montmorillonite can adsorb large quantity of water resulting in high liquid limit of clays. Moreover, the cohesion caused by inter-molecular attraction for clayey particles could explain why the low plastic soils are susceptible to mud pumping.

2.2 *Minimum fluidisation velocity*

Kunii and Levenspiel (2013) define fluidisation as the operation by which fine solids are transformed into a fluid-like state through the contact with gas or liquid. Hayashi and Shahu (2000) observed that the pumping of fines involved the washing and continuous loss of fine soil particles. Therefore, the minimum fluidisation velocity, which is the minimum seepage velocity at which the same grain size particles start to flow (Hayashi and Shahu, 2000), plays a crucial role in adjudicating the subgrade fluidisation. The minimum fluidisation velocity can be estimated by computing the pressure, P, required to exceed the effective weight, W of the particles of different sizes (Justin, 1923):

$$W=P=2\frac{v_s^2}{2g}A\rho_w$$

where v_s is the seepage velocity, A is the area of the soil grain subjected to the flow, g is the acceleration due to gravity and ρ_w is the density of water. Hayashi and Shahu (2000) recommend a high factor of safety (FOS = 4.0) while evaluating the minimum fluidisation velocity as the effective size of the soil particles varies significantly on any given plane. Bhowmik et al. (2018) have also reported similar high values of factors of safety against piping failure.

2.3 *In-situ water content*

In the coastal floodplains of Australia, the tracks laid on the soft soil deposits are more vulnerable to pumping (Nguyen et al., 2019). The natural water content of the subgrade is close to the liquid limit and under the action of moving loads, the subgrade softens and pumps upwards. When the ballast is fouled either by ballast degradation or subgrade fines, the free draining characteristic of the ballast gets impeded. The role of fouled ballast will be discussed in the later sections. Due to the lack of proper drainage, there is ponding of free water at the top of the subgrade (as can be seen from Fig. 1). The event of heavy rainfall is also believed to further soften the upper layers of the subgrade. Aw (2007) noted that a rainfall intensity of less than 0.5 cm per unit area caused incremental track degradation on a pumping effected site at Mansfield, Massachusetts.

2.4 *Relative compaction*

Relative compaction (RC) is defined as the ratio of the initial compacted density of the specimen to that of the maximum dry density of the soil as obtained by the Standard Proctor (ASTM D698-07 Standard, 2012). Indraratna et al. (2020b) reported the fluidisation of heavily compacted specimens (RC ≈ 99%) at high cyclic stresses. The ratio of the applied cyclic stress (σ_d) to twice of the effective confining

pressure (σ'_{3c}) is defined as the cyclic stress ratio (CSR) (Indraratna et al., 2020b).

$$CSR = \frac{\sigma_d}{2\sigma'_{3c}} \quad (1)$$

The effect of CSR on subgrade fluidisation is discussed in the later sections. When the specimens are compacted at lower densities i.e. at lower RC, the specimens fluidised at lower values of cyclic stress ratio. This can be attributed to the larger magnitude of excess pore pressure generated in relatively loose specimens. In another study, Indraratna et al. (2020a) found that the soil specimen (w_{LL} = 26%, *PI* = 11, maximum dry density, ρ_{dmax} = 1820 kg/m^3) when compacted to a density of 1620 kg/m^3 fluidised at a CSR of 0.3, whereas the specimen compacted at an initial dry density of 1805 kg/m^3 fluidised at CSR = 1.0 at a loading frequency of 5.0 Hz.

2.5 *Fines content*

Nguyen et al. (2019) summarised the soil properties of the subgrade from the reports of mud pumping from across the world. In majority of the cases, the subgrade soil was found to have at least 25% fines content (< 75 μm). Upon comparison of this finding with the concept of minimum fluidisation velocity, it is likely that the finer fraction of the subgrade soil softens and then fluidises which leads to the pumping of fines under the action of moving rail loads. Indraratna et al. (2020a) observed that the increase in the plastic fines content from 0% to 10% increases the cyclic stability of the subgrade soil. Although, further increment in the plastic fines to 30% led to the reduction in cyclic resistance of the soil.

3 EXTERNAL FACTORS LEADING TO MUD PUMPING IN BALLASTED RAIL TRACKS

With the passage of trains, excess pore water pressures are generated in saturated subgrade soils (Sheng et al., 2014; Indraratna et al., 2020b). Additionally, the moving load also induces the rotation of the major and minor principal stresses. Mamou et al. (2017) noted that the effect of principal stress rotation on the saturated subgrade exacerbates the cyclic stability of soft soils and generates larger magnitude of excess pore pressure. This section lays emphasis on the dynamic stresses arising by the rail loads which result in the generation of high cyclic excess pore pressures leading to mud pumping.

3.1 *Cyclic Stress Ratio (CSR)*

The advent of heavy haul trains can significantly increase the magnitude of stresses being transferred from the ballast to the subgrade layer. The larger magnitude of the cyclic stresses acting on the soft railway subgrade results in a higher cyclic stress ratio (1). As can be seen from Fig. 2, as the CSR increases from 0.4 to 0.5, there is sudden increase in the cyclic axial strains for the specimen (ρ_d = 1790 kg/m^3, f = 1.0 Hz). Thus, there exists a critical cyclic stress ratio beyond which the specimen experiences softening and this leads to the fluidisation of the specimens (Indraratna et al., 2020a; Indraratna et al., 2020b).

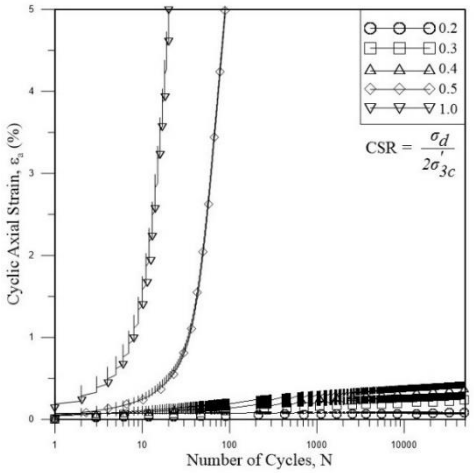

Fig. 2: Variation of cyclic axial strain (ρ_d = 1790 kg/m^3, f = 1.0 Hz) (after Indraratna et al. 2020b)

3.2 *Cyclic excess pore pressure (EPP)*

Alobaidi and Hoare (1996) simulated the subgrade soil layer beneath a stiff subbase particle to investigate the development of excess pore pressure (EPP). The dissipation of the excess pore pressure (EPP) at various time intervals revealed that there exists a very high pressure difference between the centre and the edge of the subbase particle. As can be seen from Fig. 3, after about 0.25 seconds, the hydraulic gradient equivalent to the high pressure difference between the centre and the edge of the particle is as high as 147. This high hydraulic gradient could possibly be the driving force responsible for the flushing of fine particles into the ballast layer.

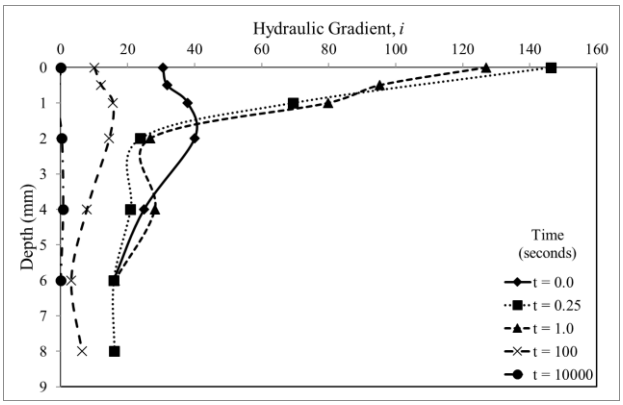

Fig. 3: Hydraulic gradient between the centre and the edge of the subbase particle (Reanalysed based on the results of Alobaidi and Hoare 1996).

A series of undrained cyclic triaxial tests carried out on remoulded subgrade specimens collected from a mud pumping prone site in Wollongong revealed that significantly high cyclic excess pore pressures are generated at high cyclic stresses. As can be seen from Fig. 4, the mean excess pore pressure ratio, which is the ratio of the mean excess pore pressure to the effective confining pressure, rises to 0.6 in less than 100 cycles when subjected to a CSR of 0.5. The rapid rate of increment of the excess pore pressure results in softening of the specimen and forms a slurry at the top of the specimen (Indraratna et al., 2020b).

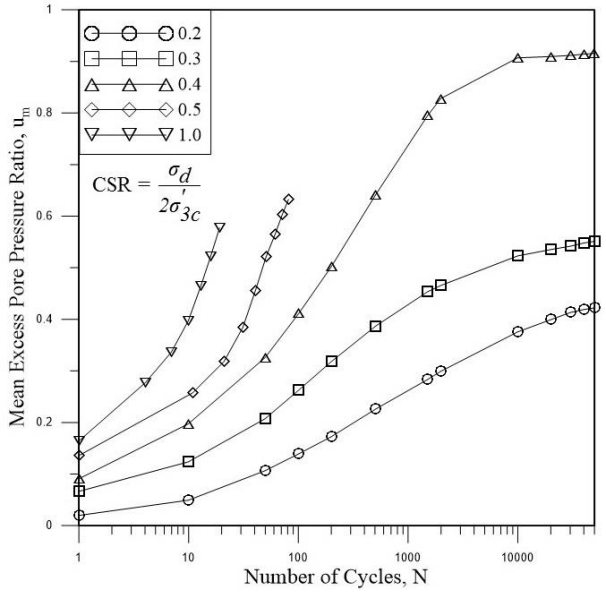

Fig. 4: Development of mean excess pore pressure ratio (ρ_d = 1790 kg/m^3, f = 1.0 Hz) (after Indraratna et al. 2020b)

The excess pore pressures causes an internal redistribution of water contents under cyclic loading along with the migration of fines towards the upper region of the specimen. Indraratna et al. (2020a) evaluated the change in water contents by measuring the liquidity index along the specimen. The liquidity index (LI) is defined as the ratio of the difference of the current water content and the plastic limit to that of the plasticity index (PI = $w_{LL} - w_{PL}$). When the liquidity index, LI is closer to 1.0 it indicates that the water content is near the liquid limit of the soil. From Fig. 5, it is evident that the top portions of the specimen which has fluidised, have the liquidity index nearing 1.0 while the stable specimens have consistent LI throughout the specimen. The specimens prepared with 10% kaolin are designated as K10, whereas the ones with 30% kaolin are denoted as K30. Another inference that can be drawn from Fig. 5 is that the addition of plastic fines improves the resistance of the specimens towards mud pumping (Indraratna et al., 2020a).

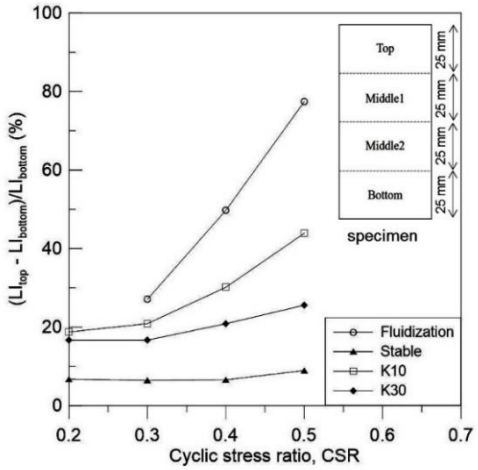

Fig. 5: Effect of CSR on the variation of liquidity index along the specimen height (after Indraratna et al. 2020a)

3.3 *Fouled ballast (impeded drainage)*

With continuous pumping of the subgrade fines into the coarser ballast layer, the voids in ballast gets fouled. There are other sources of ballast fouling which have been investigated in detail by Tennakoon (2012). Tennakoon et al. (2012) investigated the cyclic response of kaolin fouled ballast at different levels of void contamination index (VCI). VCI is defined as the ratio of the bulk volume of fouling material to that of the volume of voids in the clean ballast. As can be seen from Fig. 6, the hydraulic conductivity of the clayey fine sand fouled ballast is significantly reduced when the void contamination index exceeds 20%. In addition to the reduction in the hydraulic conductivity, the peak friction angle of the fouled ballast also decreases with an increase in the void contamination index (Indraratna et al., 2013).

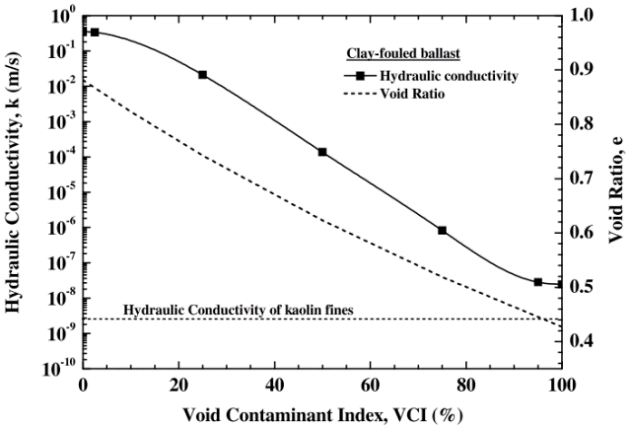

Fig. 6: Effect of plastic fines (Kaolin) on the hydraulic conductivity of the ballast (after Tennakoon et al. 2012)

3.4 *Zones of stress concentration*

Few of the reported locations of mud pumping have been along the transition zones, junction boxes etc.

where the localised stress concentrations aggravates the ballast degradation (Powrie, 2014; Yang et al., 2018; Nguyen et al., 2019). The discontinuities and the unevenness in the contact surface between the wheels and rail joints creates regions of stress concentration (Yang et al., 2018). These stress concentration zones amplify the stresses acting on the subgrade due to sudden change in the stiffness before and after the zones and in general, account for frequent maintenance (Selig and Waters, 1994; Powrie, 2014; Hudson et al., 2016). The phenomenon of mud pumping is enhanced by the presence of such localised stress concentration zones (Nguyen et al., 2019).

4 CONCLUSION

The migration of fines under ballasted railway tracks is a complicated phenomenon involving several external factors as well as inherent soil parameters. The factors that influence the subgrade fluidisation have been summarised in Fig. 7. The passage of heavy haul train generates high cyclic stress on the soft subgrade which results in the development of high cyclic excess pore pressure. When the hydraulic gradient exceeds the minimum fluidisation velocity of the softened subgrade, the cyclic action of the rail loading pushes the fines upward. The presence of perched water at the top of the subgrade further softens the subgrade and exacerbates the pumping of fines. In particular, the localised stress concentration zones which undergo frequent maintenance accelerate mud pumping.

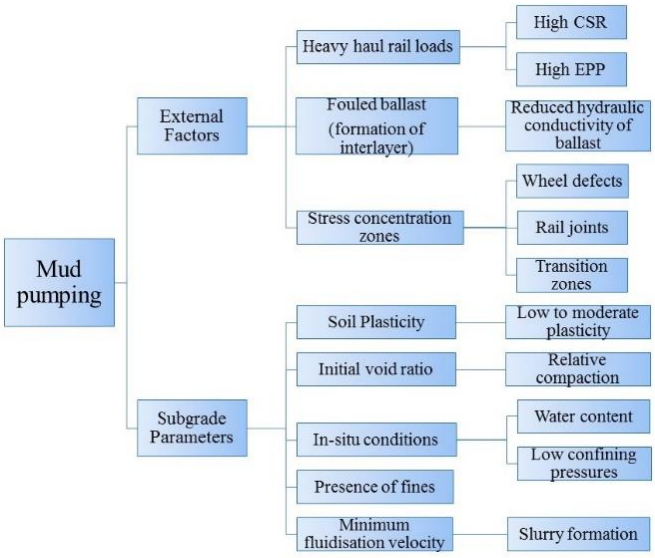

Fig. 7: Summary of the factors that influence the pumping of fines under ballasted rail tracks

Under severe cases of pumping, the subgrade fines infiltrate the voids of the ballast layer and reduces the hydraulic conductivity of the ballast. It results in the formation of an interlayer and aggravates mud pumping. The generation of excess pore pressure in the subgrade layer can be attributed to be the main reason for mud pumping. However, extensive testing involving the evaluation of fluidisation potential of soils, studying the role of stress concentration zones and investigating the feasibility of ground improvement techniques are deemed necessary to ascertain the mechanism of mud pumping and to propose appropriate mitigation measures.

ACKNOWLEDGMENTS

This research was supported by the Australian Government through the Australian Research Council's Linkage Projects funding scheme (project LP160101254) and the Industrial Transformation Training Centre for Advanced Technologies in Rail Track Infrastructure (ITTC), University of Wollongong. The financial and technical support from SMEC-Australia and ARTC (Australian Rail Track Corporation) is acknowledged. The support from the Transport Research Centre, University of Technology Sydney is also acknowledged.

REFERENCES

Alobaidi, I. and Hoare, D.J. 1994. Factors affecting the pumping of fines at the subgrade–subbase interface of highway pavements: a laboratory study. Geosynthetics International, 1(2): pp. 221-259.

Alobaidi, I. and Hoare, D.J. 1996. The development of pore water pressure at the subgrade–subbase interface of a highway pavement and its effect on pumping of fines. Geotextiles and Geomembranes, 14(2): pp. 111-135.

Alobaidi, I. and Hoare, D.J. 1999. Mechanisms of pumping at the subgrade–subbase interface of highway pavements. Geosynthetics International, 6(4): pp. 241-259.

ASTM D698-07 Standard. 2012. Standard Test Methods for Laboratory Compaction Characteristics of Soil Using Standard Effort.

Aw, E.S. 2007. Low Cost Monitoring System to Diagnose Problematic Rail Bed: Case Study at a Mud Pumping Site. Doctor of Philosophy. thesis, Massachusetts Institute of Technology.

Bhowmik, R., Shahu, J. and Datta, M. 2018. Failure analysis of a geomembrane lined reservoir embankment. Geotextiles and Geomembranes, 46(1): 52-65.

Bray, J.D. and Sancio, R.B. 2006. Assessment of the liquefaction susceptibility of fine-grained soils. Journal of Geotechnical and Geoenvironmental Engineering, 132(9): pp. 1165-1177.

Castro, G. and Poulos, S.J. 1977. Factors Affecting Liquefaction and Cyclic Mobility. Journal of the Geotechnical Engineering Division, 103(6): 501-506.

Duong, T.V., Cui, Y.-J., Tang, A.M., Dupla, J.-C., Canou, J., Calon, N., Robinet, A., Chabot, B. and De Laure, E. 2014. Physical Model for Studying the Migration of Fine Particles in the Railway Substructure. Geotechnical Testing Journal, 37(5): pp. 1-12.

Hayashi, S. and Shahu, J.T. 2000. Mud pumping problem in tunnels on erosive soil deposits. Géotechnique, 50(4): pp. 393-408.

Hudson, A., Watson, G., Le Pen, L. and Powrie, W. 2016. Remediation of Mud Pumping on a Ballasted Railway Track. In Proceedings of the The 3rd International Conference on Transportation Geotechnics Vol. 143, pp. pp. 1043-1050.

Indraratna, B., Korkitsuntornsan, W. and Nguyen, T. T. 2020a. Influence of kaolin content on the cyclic loading response of railway subgrade. Transportation Geotechnics: 100319. doi: https://doi.org/10.1016/j.trgeo.2020.100319.

Indraratna, B., Singh, M., Nguyen, T.T., Leroueil, S., Abeywickrama, A., Kelly, R. and Neville, T. 2020b. Laboratory study on subgrade fluidisation under undrained cyclic triaxial loading. Canadian Geotechnical Journal, (In Press). doi: https://doi.org/10.1139/cgj-2019-0350.

Indraratna, B., Tennakoon, N., Nimbalkar, S. and Rujikiatkamjorn, C. 2013. Behaviour of clay-fouled ballast under drained triaxial testing. Géotechnique, 63(5): 410-419. doi: 10.1680/geot.11.P.086.

Justin, J.D. 1923. The Design of Earth Dams. Transactions of the American Society of Civil Engineers, 88(1): 1-61.

Kermani, B., Xiao, M. and Stoffels, S.M. 2019. Analytical study on quantifying the magnitude and rate of subgrade fines migration into subbase under flexible pavement. Transportation Geotechnics, 18: 46-56. doi: https://doi.org/10.1016/j.trgeo.2018.11.003.

Kunii, D. and Levenspiel, O. 2013. Fluidization engineering. Elsevier.

Mamou, A., Powrie, W., Priest, J. and Clayton, C. 2017. The effects of drainage on the behaviour of railway track foundation materials during cyclic loading. Géotechnique.

Nguyen, T.T., Indraratna, B., Kelly, R., Phan, N.M. and Haryono, F. 2019. Mud pumping under railtracks: mechanisms, assessments and solutions. Australian Geomechanics Journal, 54(4): 59-80.

Powrie, W. 2014. On track: the future for rail infrastructure systems. In Proceedings of the Proceedings of the Institution of Civil Engineers-Civil Engineering. Thomas Telford Ltd Vol. 167, pp. 177-185.

Selig, E.T. and Waters, J.M. 1994. Track Geotechnology and Substructure Management.

Sheng, D., Zhang, S., Niu, F. and Cheng, G. 2014. A potential new frost heave mechanism in high-speed railway embankments. Géotechnique, 64(2): 144-154.

Singh, M., Indraratna, B. and Rujikiatkamjorn, C. 2019. Use of Geosynthetics in Mitigating the Effects of Mud Pumping: A Railway Perspective. In Geotechnics for Transportation Infrastructure. Edited. Springer. pp. 609-618.

Tennakoon, N. 2012. Geotechnical study of engineering behaviour of fouled ballast. Doctor of Philosophy. thesis, University of Wollongong.

Tennakoon, N., Indraratna, B., Rujikiatkamjorn, C., Nimbalkar, S. and Neville, T. 2012. The role of ballast-fouling characteristics on the drainage capacity of rail substructure. Geotechnical Testing Journal, 35(4): 629-640.

Yang, Z., Boogaard, A., Wei, Z., Liu, J., Dollevoet, R. and Li, Z. 2018. Numerical study of wheel-rail impact contact solutions at an insulated rail joint. International Journal of Mechanical Sciences, 138: 310-322.

Yoder, E.J. 1957. Pumping of Highway and Airfield Pavements : Technical Paper. In Joint Highway Research Project. Purdue University, Lafayette, Indiana.

Large-Scale Laboratory Testing of Ballasted Rail Track and Influence of Artificial Inclusions on Track Behaviour

S. K. Navaratnarajah
Department of Civil Engineering, Faculty of Engineering, University of Peradeniya, Peradeniya, Sri Lanka

B. Indraratna
Centre for Geomechanics and Railway Engineering, University of Wollongong, Wollongong City, NSW 2522, Australia

ABSTRACT: Transport systems play a key role to support the envisaged rapid development of the country and the development of public transport services especially the rail transport system which has been well recognized as essential for growing future demands. Therefore, the use of rail transportation systems has been increased significantly in recent years. Large size granular material (ballast) is the key element used in conventional ballasted tracks. However, deformation and degradation of ballast material and damage to other track elements are inevitable due to large dynamic forces imparted to the track substructure. This leads to periodic track maintenance and increases the cost of operating tracks. Understanding ballast mechanical behaviour and the role of artificial inclusions such as rubber elements to the track substructure leads to better design and efficient maintenance. The use of conventional tests for understanding the mechanical behaviour of ballast material produce imprecise results due to the large granular particles size relative to test sample size. This study presents the key findings of the large-scale laboratory tests conducted on track substructure to understand the ballast behaviour and the influence of artificial inclusions on the reduction of deformation and degradation of ballast. The results from this study confirm that the rubber elements used at the interface of ballast with concrete are significantly reducing the stress, strain and degradation of ballast.

Keywords: Ballast, Under Sleeper Pads, Under Ballast Mats, Degradation, Cyclic Load

1 INTRODUCTION

The strength and deformation characteristics of large size granular aggregates are greatly influenced by the shape and size of the particles (Indraratna et al., 1993, Marsal, 1967). The disparity between the actual particle size used in a track foundation and scaled-down particles used in a specimen for conventional shear and triaxial testing leads to misleading stress-strain responses in the laboratory due to the size-dependent compressibility, dilation, and crushing aspects of soil aggregates. Large scale testing apparatus with a specimen of actual particle size provides more insightful and tangible practical outcomes to geomechanical problems especially for ballast particles used in rail track substructures.

For most of the countries to have an efficient transport system, railroad transport needs to be improved with a higher load-carrying capacity and faster trains to cope up with the increasing future demands. However, the deterioration of a rail track due to large dynamic wheel loads is inevitable over the years and one that leads to more frequent high-cost maintenance. This problem is more critical where heavier concrete sleepers are used in rail tracks. One measure used to minimize track deterioration is the use of artificial inclusions such as resilient rubber elements at the hard-concrete interfaces. In recent years, the use of soft synthetic rubber pads in track foundations to alleviate track damage has become increasingly popular (Indraratna et al., 2014, Jayasuriya et al., 2020, Navaratnarajah and Indraratna, 2017, 2018, Nimbalkar et al., 2012, Sol-Sanchez et al., 2015, Zhai et al., 2004). Among the wide range of mitigation techniques, one option could be to modify the vertical stiffness of track by attaching resilient rubber pads under the sleeper called Under Sleeper Pads (USPs) especially for heavy-duty concrete sleepers and placing rubber mats called Under Ballast Mats (UBM) on top of hard subgrade such as concrete tunnel and bridges (Indraratna et al., 2012, Loy, 2008, Navaratnarajah, 2017, Navaratnarajah et al., 2016, Sol-Sanchez et al., 2015). Apart from bringing back the track resiliency, USPs and UBMs increase the contact area between ballast to the concrete interface which leads to a reduction in stress transmitted from the sleepers to the substructure layer and helps to distribute the wheel load more uniform to the underlying substructure elements and even out the differences in stiffness along transition zones and turnouts (Abadi et al., 2015, Loy, 2009, Navaratnarajah et al., 2018, Sol-Sanchez et al., 2014).

With the modern development, Railway Agencies are using concrete sleepers instead of timber sleepers because of the low durability of

timber sleepers. But the use of concrete sleepers increasingly damages the ballast layer. When soft USPs are installed under hard concrete sleepers, it reduced the ballast degradation and extended the intervals needed to tamp the ballast, and increased the service life of ballast by at least 100%, both of which resulted in enormous savings in maintenance expenditure (Marschnig and Veit, 2011). Only limited studies have been carried out to investigate geotechnical behaviours such as stress-strain and the degradation aspects of ballast under dynamic loads when the ballast is stabilised with rubber elements (Indraratna et al., 2014, Johansson et al., 2008, Navaratnarajah and Indraratna, 2020, Nimbalkar and Indraratna, 2016, Nimbalkar et al., 2012, Sol-Sanchez et al., 2014).

In this study, a series of large-scale static load tests using direct shear apparatus and large-scale cyclic load tests using the Process Simulation Prismoidal Triaxial Apparatus (PSPTA) was conducted to understand and assess the stress-strain and degradation behaviour of ballast, and how artificial inclusions such as USPs and UBMs influence these behaviours. These unique facilities were designed and built at the University of Peradeniya, Sri Lanka (Fig. 1: Large-scale direct shear apparatus), and University of Wollongong, Australia, (Fig. 2: Large-scale PSPTA) to examine the integrated behaviour of actual track materials used in a ballasted track (Indraratna et al., 2020, Navaratnarajah et al., 2020).

Fig. 1: (a) Large scale direct shear apparatus and (b) Direct shear box

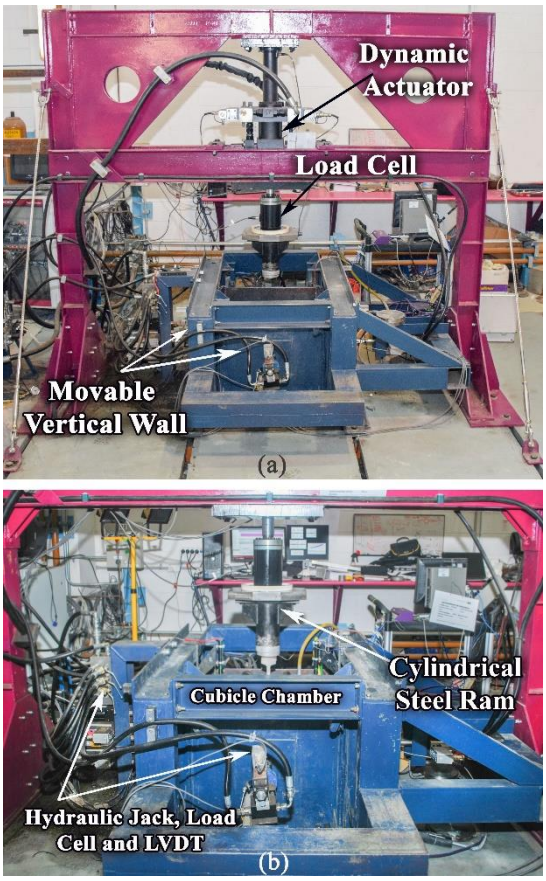

Fig. 2: (a) Large-scale Process Simulation Prismoidal Triaxial Apparatus (PSPTA) and (b) Cubicle Chamber

2 LARGE-SCALE LABORATORY TESTS

To assess the ballast behaviour and the role of rubber elements in more detail, a series of static direct shear and cyclic loading tests were conducted using the state-of-the-art large-scale direct shear and PSPTA with the full-size ballast materials. To evaluate the interface behaviour of the ballast materials with rubber and concrete sleeper, direct shear tests were conducted using the large-scale direct shear apparatus shown in Fig. 1. The shear chamber of this apparatus is 300 mm high and 400 mm in diameter. The triaxial chamber of the PSPTA which simulates the track unit cell is shown in Fig. 2b. The size of the cubical triaxial chamber is 800 mm × 600 mm × 600 mm. This apparatus can realistically simulate the stress and boundary conditions found in ballasted tracks. In a real rail track, lateral movement of the ballast is not fully restrained, particularly parallel to the sleepers (Indraratna et al, 2001). Therefore, the four vertical walls of the PSPTA chamber were built to allow free movement under applied cyclic loading. In this study, only two walls parallel to the sleeper were allowed to move under low confinement, the other two walls were locked in a position to simulate a

typical straight track (longitudinal deformation parallel to the rail is negligible). Details of the test materials used in this study and their specifications and the shear and cyclic load test procedures are discussed in the following section.

2.1 *Test Materials*

Materials used in this study are fresh ballast, subballast, concrete bases, rubber pads (USPs and UBMs). For static tests, ballast was collected from the Gampola, stockpile owned by Sri Lankan Railways, and for cyclic load test, the ballast was collected from Bambo Quarry, Wollongong, Australia. The ballast and subballast materials were prepared according to the current Sri Lankan and Australian practices for shear and cyclic tests, respectively. The particle size distribution (PSD) of fresh ballast and subballast are shown in Fig. 3 and the grain size characteristics are shown in Table 1.

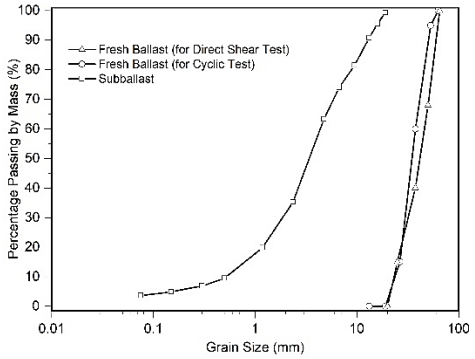

Fig. 3 Particle size distribution curve of the ballast sample and sand used in this study

Table 1: Grain size characteristics

Parameters	**Fresh Ballast (for Direct Shear Test)**	**Fresh Ballast (for Cyclic Test)**	**Subballast**
Particle Shape	Angular	Angular	Rounded to angular
Type of Gradation	Uniformly graded	Uniformly graded	Well graded
D_{max} mm	65.0	63.0	19.0
D_{min} mm	20.0	19.0	0.075
C_u	2.0	1.6	8.8
C_c	0.9	1.2	1.6

To avoid any influence of fine soil particles, the laboratory ballast samples were cleaned by water to remove any dust and clay adhering to the surface of the aggregates and dried before screening through selected sieves and then mixed in desired proportions to obtain the required particle size distribution (PSD) shown in Fig. 3. Subballast was used as the base materials when conducting cyclic load tests with and without USP placed under the concrete sleeper. To simulate a hard subgrade condition such as a rail track over a concrete bridge, a reinforced concrete base was placed underneath the ballast layer and cyclic load tests were conducted with and without UBMs placed on top of the concrete base. The properties of USPs and UBMs used in this study are shown in Table 2.

Table 2: properties of rubber elements

Rubber Element	Thickness (mm)	Weight (kg/m^2)	Bedding Modulus (N/mm^2)
USP	10	4.2	0.22
UBM	10	9.2	0.20

2.2 *Large Scale Direct Shear Tests*

The ballast to concrete interface behaviour with and without rubber elements was tested using the large-scale direct shear apparatus. The upper half of the apparatus in Fig. 1b is fixed to a frame and the lower half is free to move horizontally with the application of lateral load until shear failure occurs at the interface. Hydraulic jack connected with load cell was used to apply the lateral shear load with a shearing rate of 4 mm/min. Normal loads were applied to the top-loading plate using the lever arm technique as shown in Fig. 1. Shear and vertical displacements were measured using two displacement gauges fixed to the top-loading plate and lower half of the apparatus. Applied shear force was measured using a load cell fixed between the hydraulic jack and the lower half of the apparatus. Both the displacement gauges and the load cell were connected to a data logger to record load and deformation data. Tests were performed under three normal stresses of 30 kPa, 60 kPa and 90 kPa. Specimens were sheared until a 60 mm maximum displacement corresponding to 15% shear strain is reached. The photographs of direct shear test procedures are shown in Fig. 4.

Fig. 4 Photographs of the direct shear test (Interface of ballast-concrete with and without rubber element)

The shear behaviour of the ballast-concrete interface with and without rubber element was tested and compared with the shear resistance of the fresh ballast. Dry powder graphite lubricant was added at the steel-steel sliding interfaces to minimise frictional resistance caused by the apparatus. At the end of each test, ballast materials were screened through the standard sieves to calculate the ballast breakage index as per Indraratna et al. (2005).

2.3 *Large Scale Cyclic Load Tests*

The cyclic load tests were performed by using the PSPTA showed in Fig. 2. The test specimen consisted of a 150 mm thick subballast or concrete base overlain by a 300 mm thick layer of ballast. When testing with UBM, a rubber mat was placed on top of the concrete base and when testing with USP, the base layer was replaced with subballast material and a USP layer was placed under the concrete sleeper. The rubber materials placed in these locations will not give any disturbance to the track maintenance operations (Navaratnarajah and Indraratna, 2018). Tests were conducted with and without USPs and UBMs for each case of subballast and concrete base underneath the ballast layer, respectively. Ballast aggregates were placed on top of the subballast base/concrete base/rubber mat in three equal 100 mm thick layers, compacted by a rubber-padded vibratory hammer to a typical field density of approximately 1560 kg/m^3. The rail-sleeper assembly was placed on top of the compacted ballast, and the space around the concrete sleeper was filled with a 150 mm thick compacted crib ballast. Figure 5 shows the photographs of the cyclic load test procedure.

Fig. 5 Photographs of cyclic load test (ballast-concrete interface with and without USP and UBM)

The cyclic loading was the equivalent of a 25t axle load to simulate a passenger train and a 35t axle load for a freight train with a loading frequency of 15 and 20 Hz; this simulated a train travelling at about 110 and 145 km/h, respectively (Indraratna et al., 2014). The amplitude of cyclic loads was determined using the American Railway Engineering Association (AREA) method (Li and Selig, 1998). Lateral confinement was applied by a hydraulic jack connected to movable lateral vertical walls that simulated low confining stress of 10-15 kPa. The longitudinal walls were locked for movements in that direction to ensure plane strain conditions, while the pressure exerted on the longitudinal walls was measured. Electronic potentiometers, settlement plates, and pressure cells were used to measure the deformation and stress variation in the ballast layer. The vertical and lateral loads and associated stress and deformation were recorded by data loggers connected to computers. A total of 500,000 load cycles were applied for each cyclic load test. Ballast degradation was evaluated using the Ballast Breakage Index (BBI) method.

3 RESULTS AND DISCUSSION

Nine direct shear tests with normal loads of 30, 60 and 90 kPa by varying 2 different interfaces (ballast-concrete and ballast-rubber) were carried out and compared with that of fresh ballast to understand the ballast interface behaviours. A total of sixteen cyclic load tests were carried out with and without USP and UBM at varying frequencies (15 and 20 Hz) and axle loads (25 and 35t). The stress-strain and degradation responses of ballast observed in these tests and a comparison with and without the use of rubber elements and various interface shear resistance are explained in the following sections.

3.1 *Stress-strain and degradation behaviour under direct shear load*

Shear stress-strain behaviour of fresh ballast and the other two different types of interfaces under different normal loads are illustrated in Fig. 6. The shear resistance of the ballast and different interfaces are increasing with the applied normal stress. The highest shear resistance and ballast particle breakage occurred in fresh ballast due to the particle interlocking of highly angular fresh ballast which immensely contributed to these higher values. In the other two interfaces, the surface friction between ballast and interface material and stiffness of the interface materials are the contributing factor that affects the stress-strain and degradation behaviour. Out of the two interfaces,

the concrete interface showed the highest shear resistance due to the relatively rough and hard surface compared to the rubber interfaces. However, when rubber element is inserted at the top of the concrete surface the ballast degradation has significantly curtailed. For all the three normal stresses, the ballast degradation at the ballast-rubber interface is significantly lower (65 to 75%) than that of the concrete interface as per BBI values shown in Fig. 6.

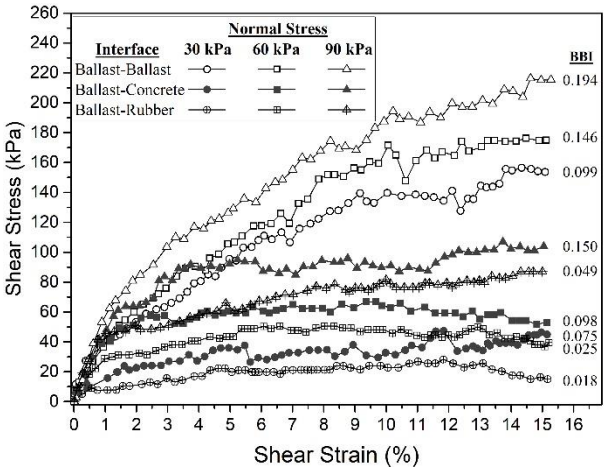

Fig. 6 Stress-strain and degradation of fresh ballast and two interfaces (ballast-concrete and ballast-rubber)

3.2 *Stress-strain and degradation behaviour under cyclic load*

The vertical (ε_1) and lateral (ε_3) plastic strains of ballast under cyclic loading were measured at a selected number of load cycles (N=1, 100, 500, 1000, 5000, 10000, 50000, 100000,…..500000) and are shown in Fig. 7 (a),(b) for ballast with and without USP and 8 (a),(b) for ballast with and without UBM. For all the different load, frequency and substructure layers cases, the results indicated that the ballast deformed rapidly up to around 10,000 cycles due to its initial densification and further packing after the corners of the sharp angular aggregates began to break, but once the ballast stabilised after around 100,000 cycles, the rate of ballast strain decreased as the load cycles increased. As expected, the plastic strain of ballast increasing with the increase of axle loads and train speeds.

The vertical and lateral plastic strain with and without USP for 25t and 35t axle loads shown in Figures 7 (a) & (b) confirmed that the ballast deformation has decreased significantly by using USP. The increased contact area of ballast by the USP at the sleeper-ballast interface reduced the induced stresses at the interface and at the particle-particle contact, allowing for a more uniform distribution of stress which in turn decreased the overall deformation. Based on the loading frequencies of 15 and 20 Hz tested in this study, the vertical strain decreased up to about 29% for a 25t axle load and up to about 21% for a 35t axle load when USP was used with the concrete sleeper. Lateral strain decreased up to about 14% for a 25t axle load and up to about 11% for a 35t axle load. The ballast degradation increased with the axle load and train speed (loading frequency) as per the BBI values shown in Fig 7. The results indicate that ballast degradation was significantly reduced by the USP used under the concrete sleeper. The increased contact area due to USP and the subsequent reduction of ballast stress is probably the main reason behind this substantial reduction of ballast breakage. On average, the USP reduced degradation by more than 50%. This shows attaching USPs at the bottom face of the concrete sleepers is an ideal technique to reduce the long-term plastic strain and degradation of ballast in a track subjected to repetitive cyclic loading.

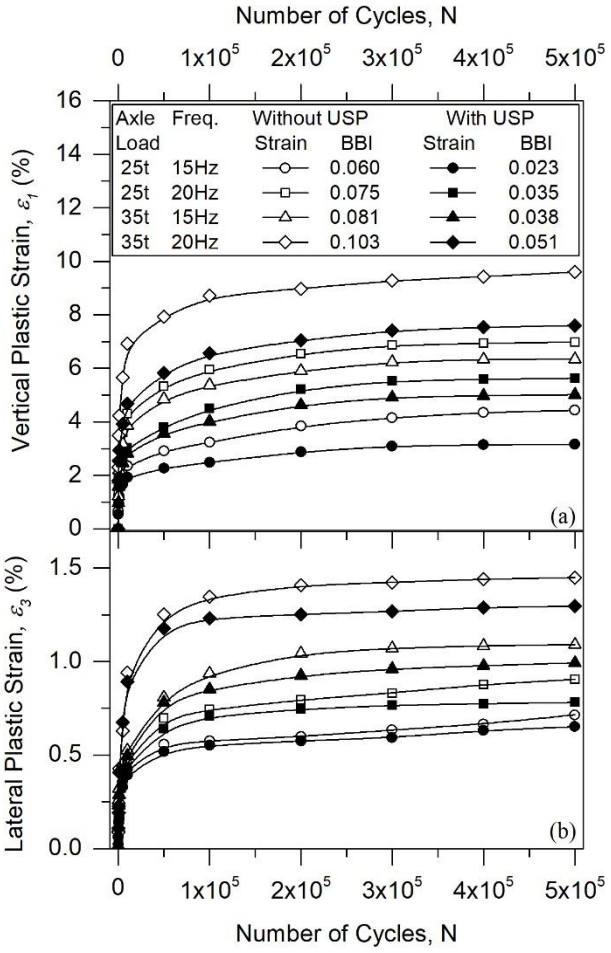

Fig. 7 Plastic strain and degradation of ballast with and without USP: (a) Vertical strain and (b) Lateral strain (data sourced from Navaratnarajah et al. (2018))

As expected, the vertical and lateral plastic strain of ballast shown in Fig. 8 (a) & (b) are high due to the stiffer concrete base at the bottom of the ballast. However, the plastic deformation of the ballast was significantly reduced using UBM on top of the concrete base. Vertical plastic deformation was reduced by 10-20% and the lateral plastic deformation was reduced by 5-10% for the loading frequencies 15 and 20 Hz and axle loads 25 and 35t tested in this study. The BBI results in Fig. 8 show that ballast degradation is reduced significantly by the use of UBM on top of the concrete base. On average the degradation of the ballast was reduced by more than 40% by the UBM.

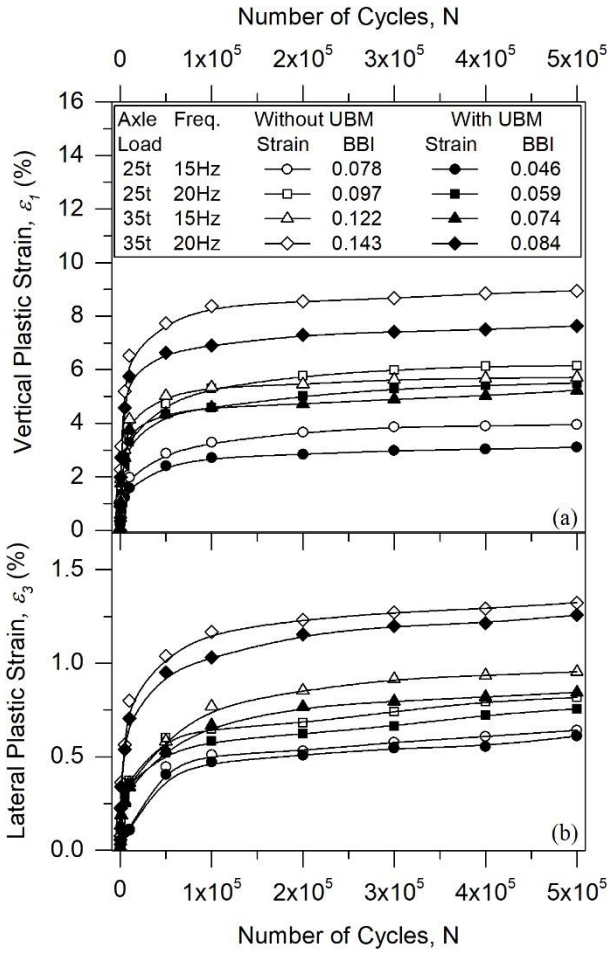

Fig. 8 Plastic strain and degradation of ballast with and without UBM: (a) Vertical strain and (b) Lateral strain (data sourced from Navaratnarajah and Indraratna (2017))

4 CONCLUSIONS

A series of direct shear tests using large-scale direct shear apparatus and cyclic loading tests using the Process Simulation Prismoidal Triaxial Apparatus (PSPTA) were carried out to study the ballast behaviour and assess the stress-strain and degradation behaviour of ballast, and to understand how artificial inclusions such as USPs and UBMs influence these behaviours. This study confirms when a harder concrete interface having rubber element at its harder interface with ballast give a significant improvement in terms of reducing ballast degradation. The cyclic load test of a regular open track simulated by placing subballast underneath the ballast layer and a USP attached on the bottom face of a concrete sleeper and a track on harder subgrade such as track on bridges and tunnels simulated by placing concrete base layer underneath the ballast and the UBM placed on top of the concrete base showed promising outcomes in terms of reducing vertical and lateral strains and degradation of ballast. Generally, concrete sleepers transmit stress to the ballast through a finite number of small discrete contacts at the sleeper-ballast interface. However, it is evident from the study that the USP attached with a concrete sleeper enhances the interface contacts and markedly reduces the vertical and lateral strain and degradation of ballast. Based on this study, using USPs on concrete sleepers is a favourable solution to reduce the stress-strain and degradation of ballast, and in a practical sense to minimize the maintenance costs of ballasted rail tracks. The test results also confirmed that UBM reduced the ballast strain and degradation quite considerably when the ballast is laid on harder subgrade in tracks.

It is evident from this study that by placing rubber elements, loads on the ballast bed can be distributed more homogeneously than by a hard base and thereby improves track stability. The benefits of reducing degradation with rubber elements potentially minimize the number of maintenance operations and reduce the life cycle costs of track foundations.

ACKNOWLEDGMENTS

The large-scale testing work carried out at the University of Peradeniya, Sri Lanka was supported by the Accelerating Higher Education Expansion and Development (AHEAD) Operation of the Ministry of Higher Education funded by the World Bank (Grant No: AHEAD/DOR/No.63) is acknowledged by the Authors. The authors also wish to acknowledge the Australian Research Council (ARC) for its financial support for the work carried out at the University of Wollongong, Australia.

REFERENCES

Abadi, T., Le Pen, L., Zervos, A. and Powrie, W. (2015). Measuring the area and number of ballast particle contacts at sleeper/ballast and ballast/subgrade interfaces, The International Journal of Railway Technology, 4(2): 45-72.

Indraratna, B., Lackenby, J. and Christie, D. (2005). Effect of confining pressure on the degradation of ballast under cyclic loading, Géotechnique, 55(4): 325-328.

Indraratna, B., Navaratnarajah, S.K., Nimbalkar, S. and Rujikiatkamjorn, C. (2014). Use of shock mats for enhanced stability of railroad track foundation, Australian Geomechanics Journal, Special Edition: ARC Centre of Excellence for Geotechnical Science and Engineering, 49(4): 101-111.

Indraratna, B., Nimbalkar, S. and Rujikiatkamjorn, C. (2012). Performance evaluation of shock mats and synthetic grids in the improvement of rail ballast, Proc., 2nd Int. Conference on Transportation Geotechnics (ICTG), pp 47-62.

Indraratna, B., Qi, Y., Tawk, M., Heitor, A., Rujikiatkamjorn, C. and Navaratnarajah, S.K. (2020). Advances in ground improvement using waste materials for transportation infrastructure, Proceedings of the Institution of Civil Engineers-Ground Improvement: 1-20.

Indraratna, B., Wijewardena, L. and Balasubramaniam, A. (1993). Large-scale triaxial testing of greywacke rockfill, Geotechnique, 43(1): 37-51.

Jayasuriya, C., Indraratna, B., Rujikiatkamjorn, C. and Navaratnarajah, S.K. (2020). Application of Elastic Inclusions to Improve the Performance of Ballasted Track, Geo-Congress 2020: Engineering, Monitoring, and Management of Geotechnical Infrastructure, pp 364-373.

Johansson, A., Nielsen, J.C.O., Bolmsvik, R., Karlström, A. and Lundén, R. (2008). Under sleeper pads-Influence on dynamic train-track interaction, Wear, 265(9-10): 1479-1487.

Li, D. and Selig, E. (1998). Method for Railroad Track Foundation Design. I: Development, Journal of Geotechnical and Geoenvironmental Engineering, 124(4): 316-322.

Loy, H. (2008). Under Sleeper Pads: improving track quality while reducing operational costs, European Railway Review, 4: 46-51.

Loy, H. (2009). Under Sleeper Pads in Turnouts, Railway Technical Review 2: 35-38.

Marsal, R.J. (1967). Large-scale testing of rockfill materials, Journal of the Soil Mechanics and Foundations Engineering, ASCE, 93(2): 27-43.

Marschnig, S. and Veit, P. (2011). Making a Case For Under-Sleeper Pads, International Railway Journal, 51(1): 27-29.

Navaratnarajah, S., Gunawardhana, K. and Gunawardhana, M. (2020). Influence of Type of Interfaces on Railway Ballast Behavior, Lecture Notes in Civil Engineering - ICSECM 2019, Springer Nature Singapore, pp 243-251.

Navaratnarajah, S.K. (2017). Application of Rubber Inclusions to Enhance the Stability of Ballasted Rail Track under Cyclic Loading. Ph.D. Thesis, University of Wollongong, Australia.

Navaratnarajah, S.K. and Indraratna, B. (2017). Use of Rubber Mats to Improve the Deformation and Degradation Behavior of Rail Ballast under Cyclic Loading, ASCE Journal of Geotechnical and Geoenvironmental Engineering, 143(6): 04017015.

Navaratnarajah, S.K. and Indraratna, B. (2018). Closure to "Use of Rubber Mats to Improve the Deformation and Degradation Behavior of Rail Ballast under Cyclic Loading" by Sinniah K. Navaratnarajah and Buddhima Indraratna, ASCE Journal of Geotechnical and Geoenvironmental Engineering, 144(7): 07018014.

Navaratnarajah, S.K. and Indraratna, B. (2020). Stabilisation of Stiffer Rail Track Substructure Using Artificial Inclusion, Indian Geotechnical Journal, 50(2): 196-203.

Navaratnarajah, S.K., Indraratna, B. and Ngo, N.T. (2018). Influence of Under Sleeper Pads on Ballast Behavior Under Cyclic Loading: Experimental and Numerical Studies, ASCE Journal of Geotechnical and Geoenvironmental Engineering, 144(9): 04018068.

Navaratnarajah, S.K., Indraratna, B. and Nimbalkar, S. (2016). Application of Shock Mats in Rail Track Foundation Subjected to Dynamic Loads, Procedia Engineering, 143: 1108-1119.

Nimbalkar, S. and Indraratna, B. (2016). Improved Performance of Ballasted Rail Track Using Geosynthetics and Rubber Shockmat, Journal of Geotechnical and Geoenvironmental Engineering, 142(8): 04016031.

Nimbalkar, S., Indraratna, B., Dash, S. and Christie, D. (2012). Improved Performance of Railway Ballast under Impact Loads Using Shock Mats, Journal of Geotechnical and Geoenvironmental Engineering, 138(3): 281-294.

Sol-Sanchez, M., Moreno-Navarro, F. and Rubio-Gámez, M.C. (2014). Viability of using end-of-life tire pads as under sleeper pads in railway, Construction and Building Materials, 64: 150-156.

Sol-Sanchez, M., Moreno-Navarro, F. and Rubio-Gámez, M.C. (2015). The use of elastic elements in railway tracks: A state of the art review, Construction and Building Materials, 75(0): 293-305.

Zhai, W.M., Wang, K.Y. and Lin, J.H. (2004). Modelling and experiment of railway ballast vibrations, Journal of Sound and Vibration, 270(4–5): 673-683.

Compaction data representation for waste materials based on void and water ratios

Ana Heitor
School of Civil Engineering, University of Leeds, LS2 9JT, United Kingdom
formerly Centre for Geomechanics and Railway Engineering, , University of Wollongong, NSW 2522, Australia

Buddhima Indraratna
ARC Industry Transformation Training Centre for Advanced Rail Track Technologies, Faculty of Engineering & Information Science, University of Wollongong, NSW 2522, Australia

Cholachat Rujikiatkamjorn
ARC Industry Transformation Training Centre for Advanced Rail Track Technologies, Faculty of Engineering & Information Science, University of Wollongong, NSW 2522, Australia

ABSTRACT: With the event of more sustainable construction practices, the potential use of unconventional industrial waste materials as structural fills has become more common in industry. The compaction characteristics of these materials are usually established for evaluating the degree of densification aligned with the end-product specifications to be adopted at the time of placement. The conventional representation of the compaction curve relies on the determination of the overall density or dry unit weight associated with a given water content. While this representation has been widely used in practice for soils it has some limitations for mixtures of unconventional waste materials having specific gravity values quite different to those of soils. Their dry unit weight represented in the conventional dry unit weight – water content plane gauges the relative contribution in weight rather than the mixture's degree of densification. In this paper the compaction data representation based on void and water ratios that cater for the different specific gravity of each source material is illustrated for waste materials. The proposed alternative representation allows for the interpretation of the compaction data and determination of compaction effectiveness for the different mixtures ratios more effectively.

1 INTRODUCTION

With the event of a more sustainable construction industry, the used of unconventional industrial waste materials (e.g. fly ash, filter cake ash, steel furnace slag, quarry tailings, coal wash, among others) have been studied for potential use as structural fills (Indraratna et al., 1991; Indraratna, 1996; Rujikiatkamjorn et al., 2013, Mir and Sridharan, 2013, Heitor et al.,2016). While the use of the materials as engineered/structural fill or as amendment agent has been accepted and regulated, the requirements in terms of specific performance criteria need to be studied on a case by case basis. Often, since individual geotechnical characteristics of the materials (e.g. excessive deformation, breakage, swelling, insufficient bearing capacity, among others) do not comply with specific performance criteria, different materials are mixed to suit the design specifications (e.g. Malasavage et al., 2012; Chiaro et al., 2014; Lee and Shang, 2014). Furthermore, the compaction characteristics are usually established for evaluating the degree of densification aligned with the end-product specifications to be adopted at the time of placement. When materials having distinct values of specific gravity (Gs) are mixed, the representation of the compaction curve in the dry unit weight (γ_d) and water content (w) plane can be misleading as it is strongly influenced by the weight proportion of the materials.

In this study, the advantages associated with the use of an alternative compaction plane representation are demonstrated for compacted granular waste materials prepared using different blends ratios.

1.1 *Compaction curve representation*

A compaction test is performed so that the variation of density a given material for different levels of moisture and under specified compaction energy can be determined. The compaction data is conventionally represented in terms of $\gamma_d - w$, which is directly computed from the laboratory standard Proctor compaction tests (e.g. AS 1289.5.1.1 - 2003). The main advantage of using these two variables (i.e. $\gamma_d - w$) lies in their simple determination based

on the experimental results. For instance, bulk unit weight (γ) can be simply calculated considering the mass over volume ratio of the soil in the mold and dry unit weight can be easily obtained considering the water content (Eq.1).

$$\gamma_d = \frac{\gamma}{(1+w)} \qquad (1)$$

However, for mixtures involving materials having different G_s values (for instance granular waste materials) the compaction data represented in the conventional $\gamma_d - w$ reflects the weight percentage of the different materials, rather than the compaction efficiency or degree of densification. Furthermore, for different blend ratios of materials having different G_s values, several zero air voids (ZAV) lines (Eq. 2) need to be plotted and the representation of additional saturation lines is cumbersome.

$$\gamma_d = \frac{G_s \gamma_w}{1+\frac{wG_s}{S_r}} \qquad (2)$$

where is γ_w is the unit weight of the water and S_r is the degree of saturation ($S_r=1$ for fully saturated conditions). To avoid these limitations, the compaction data expressed in terms $\gamma_d - w$ may be represented in terms of the equivalent variables of void ratio (e) and water ratio (e_w) determined based on the value of G_s, as follows:

$$e = \frac{\gamma_w G_s}{\gamma_d} - 1 \qquad (3)$$

$$e_w = eS_r = wG_s \qquad (4)$$

This alternative representation has significant advantages in relation to the conventional γ_d - w representation (Fig 1) since G_s is incorporated in the determination of both e and e_w. Furthermore, in this representation the different degree of saturation lines across the compaction plane (Fig. 1) are now unique lines (i.e. independent of the value of G_s) having a gradient of $1/S_r$ (Eq.5). This can be advantageous in locating the compaction states for the different blend ratios that prescribe to a given range of percentage of air voids (A_v) for instance shown in Eq. 6.

$$e = \frac{1}{S_r} e_w \qquad (5)$$

$$A_v = n(1-S_r) \qquad (6)$$

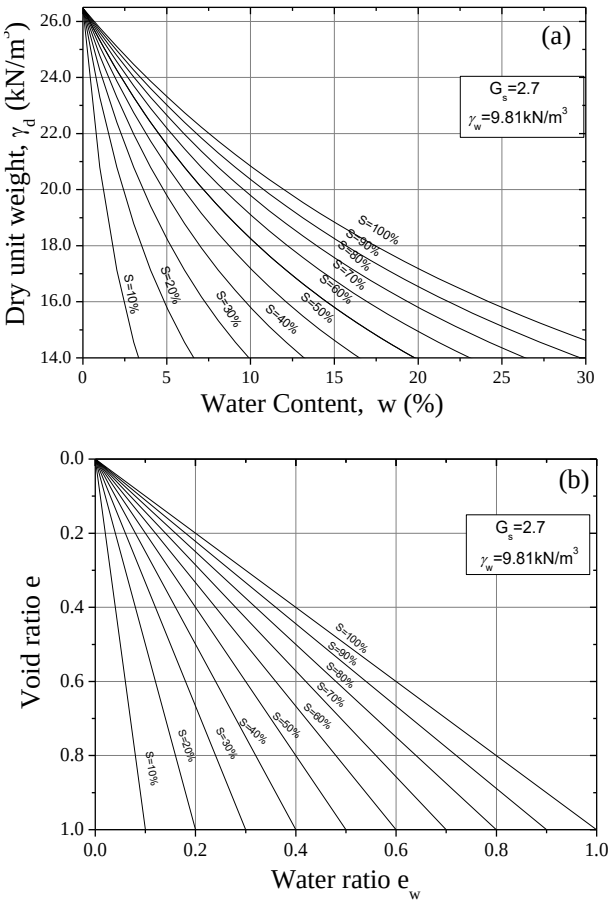

Fig1. Degree of saturation lines across the compaction plane in terms of (a) γ_d - w and (b) e - e_w.

2 UNCONVENTIONAL WASTE MATERIALS COMPACTION DATA REPRESENTATION

2.1 *Example application for coal wash and steel furnace slag blends*

The capability of the new representation is first evaluated for various blends ratios of two industrial granular by-products (i.e. steel furnace slag and coal wash) widely available in the Illawarra region (NSW, Australia). Table 1 shows the summary of the index properties of the blends analyzed.

Table 1. Summary of the properties of the CW-SFS blends (data from Tasalloti et al., 2015)

Material tested*	Specific gravity G_s	Saturated Permeability (cm/s)
100 CW	2.27	5.1×10^{-5}
75CW/25SFS	2.51	3.6×10^{-5}
50CW / 50SFS	2.73	2.1×10^{-5}
25CW / 75SFS	3.01	6.2×10^{-6}
100 SFS	3.34	5.0×10^{-7}

*CW=coalwash, SFA=Steel Furnace slag

Fig 2 shows the compaction data of the mixtures of SFS with CW plotted in terms of $\gamma_d - w$ and $e - e_w$. While larger dry unit weights were attained for those mixtures having a higher steel furnace slag content in the $\gamma_d - w$ plane this was not the case the $e - e_w$ plane. This is not surprising given that steel slag material has a specific gravity of 3.34 which is much larger than that of coal wash (i.e. G_s=2.27). Among the CW-SFS blends (Figure 2b) the coal wash source material shows the lowest void ratio which indicates that it has attained the highest degree of densification. This observation is in agreement with the lower permeability values obtained for SFS-CW mixtures tested at their optimum water content (e.g. Table 1). In this instance, owing to the granular nature of both materials, a lower void ratio is clearly reflected on a smaller permeability.

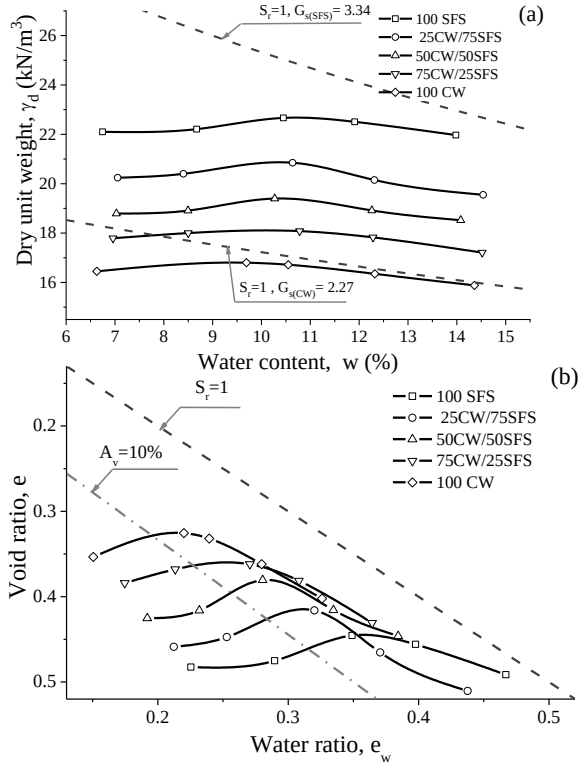

Fig 2- Compaction data of the steel slag blend materials in terms of (a) γ_d - w and (b) e - e_w.(data from Tasalloti et al, 2015)

2.2 *Applications with other materials*

Similar observations can also be made for other granular waste materials such as steel slag fines (Malasavage et al., 2012) and fly ash (Mir and Sridharan, 2013, Lee and Shang, 2014) as shown in Figure 3. Fig 3a and 3b shows the compaction data of dredge mud (DM) amended with steel slag fines represented in the conventional $\gamma_d - w$ and in $e - e_w$ plane, respectively. While the compaction data is similar in both representations the blends having 50DM/50SFF and 80DM/20SFF show a stark difference. In Figure 3a, both of these blends appear to be very distinct in the $\gamma_d - w$ plane whereas in $e - e_w$ plane they are nearly coincident which indicates that equivalent degree of densification, although other properties (i.e. friction angle and permeability) were reported to be quite distinct.

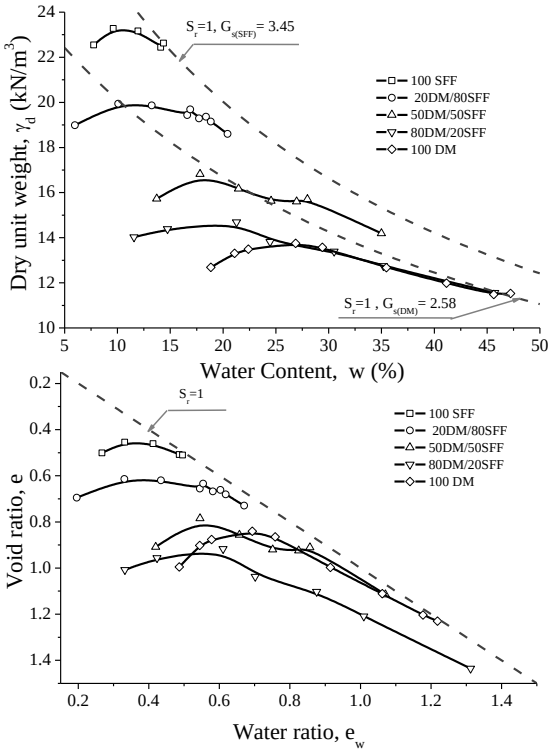

Fig 3- Compaction data of the steel slag fines(SFF) with dredged mud (DM) (Data from Malasavage et al., 2012)

The use of the representation is thus only beneficial in determining field acceptance criteria. Other interesting observation can be made for the representation of the compaction data of black cotton soil and mine tailings amended with fly ash (Mir and Sridharan, 2013) shown in Figs. 4. The most striking aspect is that most of the mixtures of fly ash with black cotton soil (Fig. 4b) attain an equivalent degree of densification ($0.83 < e_{opt} < 0.88$) despite having a relatively large range of dry unit weights (i.e. $11.5 < \gamma_{d,max} < 14.5$ kN/m^3).

3 APPLICATIONS FOR COMPACTION QUALITY CONTROL

While the incorporation of unconventional waste materials in the earthwork industry has become gradually more popular from the environmental and sustainability perspective, the use of these materials calls for a change in project delivery, particularly in defining typical end-product specifications for different blend ratios. The use of the proposed alternative compaction curve representation not only allows for the comparison between the different blend ratios and densification levels but also enables those materials to be compared with typical granular fill

materials such as clayey sands, silty sands, sandy clay.

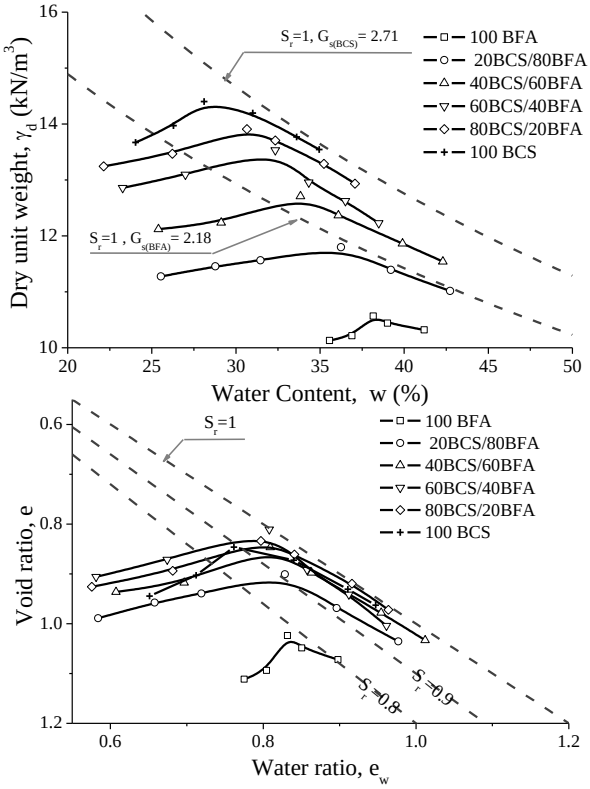

Fig 4 - Compaction data of the black cotton soil (BCS) with flyash (BFA) (data from Mir and Sridharan, 2013)

The representation can be very useful in practice as it allows the comparison of densification and the equivalence with other typical fill materials. While the compaction data (i.e. densification level) alone is not enough to judge the in service performance, it can give some indications (e.g. friction angle, bearing capacity) of the expected performance of these materials on the basis of their similarity with other fill materials, albeit a more comprehensive study should be undertaken to characterize the shear strength behaviour.

4 CONCLUSIONS

An alternative compaction data representation was proposed for waste materials mixtures having distinct values of specific gravity. The comparison between the compaction data represented in the dry unit weight (γ_d) and water content (w) and void ratio (e) and water ratio (e_w) plane showed that for the materials examined a large dry unit weight did not necessarily correspond to a large degree of densification, in fact, it rather represented the weight proportion in the mixtures. In addition, the use of the proposed representation allows for the comparison with other typical fill soils in terms of densification level that may allow practitioners engineers to gauge indicative performance on the basis of their compaction data similarity.

ACKNOWLEDGMENTS

The authors wish to acknowledge ARC for financial support under a Linkage project. The assistance from the industrial partners Port Kembla Port Corporation (PKPC), Coffey Geotechnics, Douglas Partners, Menard Bachy, BHP Billiton-Illawarra Coal and Australian Steel Mill Services is appreciated. Some of data presented here is published in more detail in other papers, we kindly acknowledge the authors contributions.

REFERENCES

Chiaro, G., Indraratna, B., Tasalloti, S. M. A. and Rujikiatkamjorn, C. (2014). Optimisation of coal wash – slag blend as a structural fill. Ground Improvement Journal, ICE (doi:10.1680/grim.13.00050).

Heitor, A., Indraratna, B. and Rujikiatkamjorn, C. (2013). Laboratory study of small-strain behavior of a compacted silty sand. Canadian Geotechnical Journal 50(2): 179-188.

Heitor, A., Indraratna, B., Kaliboullah, C. I., Rujikiatkamjorn, C. and McIntosh, G. (2016) A study on the drained and undrained shearing behaviour of compacted coal wash, Journal of Geotechnical and Geoenviromental Eng., ASCE DOI: 10.1061/(ASCE)GT.1943-5606.0001422.

Indraratna, B. (1996). Utilization of lime, slag and fly ash for improvement of a colluvial soil in New South Wales, Australia. Geotechnical and Geological Eng. 14(3): 169-191.

Indraratna, B., Nutalaya, P. and Kuganenthira, N. (1991). Stabilization of a dispersive soil by blending with fly ash. Quarterly Journal of Engineering Geology 24(3): 275-290.

Lee, J. K. and Shang, J. Q. (2014). Evolution of thermal and mechanical properties of mine tailings and fly ash mixtures during curing period. Canadian Geotechnical Journal 51(5): 570-582.

Malasavage, N. E., Jagupilla, S., Grubb, D. G., Wazne, M. and Coon, W. P. (2012). Geotechnical performance of dredged material-steel slag fines blends: Laboratory and field evaluation. Journal of Geotechnical and Geoenvironmental Engineering 138(8): 981-991.

Mir, B. A. and Sridharan, A. (2013). Physical and Compaction Behaviour of Clay Soil–Fly Ash Mixtures. Geotechnical and Geological Engineering 31(4): 1059-1072.

Rujikiatkamjorn, C., Indraratna, B. and Chiaro, G. (2013). Compaction of coal wash to optimise its utilisation as water-front reclamation fill. Geomechanics and Geoeng. 8(1): 36-45.

Tasalloti, S.M.Ali, Indraratna, B., Rujikiatkamjorn, C., Heitor, A. and Chiaro, G. (2015) A laboratory Study on the Shear Behaviour of Mixtures of Coal Wash and Steel Furnace Slag as Potential Structural Fill ASTM Geotechnical testing journal Vol. 38 (4), pp. 361-372.

Strength and Deformation Properties of Coal Wash Mixed with Rubber Crumbs

M. Tawk
Formerly, PhD Candidate, School of Civil, Mining and Environmental Engineering, and Centre for Geomechanics and Railway Engineering, University of Wollongong, Wollongong, NSW 2522, Australia

B. Indraratna
Distinguished Professor, Director, Transport Research Centre, Founding Director, ARC Industrial Transformation Training Centre for Railroad Technologies (ITTC-Rail), University of Technology Sydney, Ultimo, NSW 2007, Australia.

C. Rujikiatkamjorn
Professor, Transport Research Centre, School of Civil and Environmental Engineering, University of Technology Sydney, Ultimo, NSW 2007, Australia.

A. Heitor
Lecturer of Geotechnical Engineering, School of Civil Engineering, University of Leeds, UK. Formerly Centre for Geomechanics and Railway Engineering, University of Wollongong, Australia.

ABSTRACT: Coal wash and rubber crumbs are abundant waste materials that could potentially be used as construction fills in engineering projects. The properties of coal wash were thoroughly investigated in past studies and the material was proved to be appropriate for various applications such as port reclamation projects. In this study, rubber crumbs are mixed with coal wash to reduce its breakage potential and enhance the ductility of the mixture. This study presents the results of triaxial tests on four coal wash-rubber crumbs (CWRC) mixtures with 0%, 5%, 10% and 15% rubber content. All the mixtures were compacted to the same initial void ratio to evaluate the effect of rubber crumbs on the strength and deformation characteristics of the mixture. The tests were carried out under three confining pressures (i.e., 25, 50 and 75 kPa) to simulate different field conditions. The shear strength of the material decreased with increasing rubber content and the axial strain at failure increased due to the compressibility of rubber. However, even at 15% rubber content, the material sustained a relatively high apparent friction angle and showed a considerable increase in ductility. Also, the test results also showed that the characteristic state and the critical state of the material do not depend on rubber content. This indicates that, for low rubber contents (<15%), coal wash governs the strength properties of the mixture before and after failure while rubber is only affecting the deformations occurring at different stress states.

1 INTRODUCTION

From the small tyres of cars to those of heavy-duty machinery, hundreds of millions of used rubber tyres end up in landfills each year. The accumulation of these wastes can cause serious and detrimental environmental issues, especially if they catch fire. In the past few years, numerous studies have evaluated the properties of rubber-aggregates mixtures (Feng and Sutter 2000; Kim and Santamarina 2008; Lopera Perez et al. 2016; Youwai and Bergado 2003; Zornberg et al. 2004)and some suggested the reuse of tyre derived aggregates blended with traditional aggregates such as sand and gravel, as a construction material in engineering projects (Cho et al. 2007; Esmaeili et al. 2016; Lee et al. 1999; Signes et al. 2016). More recently, other studies suggested mixtures of rubber crumbs (RC) and other waste materials such as steel furnace slag (SFS) and recycled concrete (Indraratna et al. 2018; Qi et al. 2018; Qi et al. 2018; Saberian et al. 2018) to be used in ground engineering projects.

Coal wash (CW), a by-product of the well-established coal mining industry in Australia and other countries around the world, is another waste that occupies large areas of land that could be used for other purposes. Recent studies showed that the geotechnical properties of CW are to some extent similar to those of traditional quarried rock aggregates used in construction activities (Heitor et al. 2016; Indraratna 1994; Indraratna et al. 2012; Montgomery 1990; Rujikiatkamjorn et al. 2013). For instance, compacted CW blended with SFS has

been previously used as a structural fill in port reclamation projects (Chiaro et al. 2015; Tasalloti et al. 2015). Also, a mixture of CW and fly ash (FA) has been proposed as a subbase material in roads (Wang et al. 2019).

While the geotechnical properties of CW are sometimes comparable to those of raw quarried aggregate, CW is weaker than traditional aggregates and has a high potential for breakage when subjected to loading. Indraratna et al. (2018) showed that the degradation of a mixture of CW and SFS is significantly reduced when 10% RC are added to the mixture. However, SFS may experience swelling, a problem that was also highlighted by Chiaro et al (2015), resulting in undesirable differential settlements in practice.

In this study, a mixture of CW and RC (CWRC) is proposed as a potential construction material for transportation infrastructure projects. Rubber is added to reduce the degradation of CW particles and to improve the energy absorption capacity of the material. Strength, deformation, and energy absorption properties of four CWRC mixtures with 0%, 5%, 10% and 15% added rubber were evaluated under static conditions at three confining pressures of 25, 50 and 75 kPa to mimic filed conditions.

2 MATERIALS AND EXPERIMNTAL PLAN

CW used in this study was sourced from a colliery near Wollongong (NSW, Australia) and RC were procured from a tyre recycling company in Victoria. CW is a well graded material with a specific gravity of 2.25, while rubber shreds are much lighter having a specific gravity of 1.15. The PSD curves of CW and RC are shown in Fig. 1.

Four CWRC mixtures were considered in this study having 0%, 5%, 10% and 15% rubber added

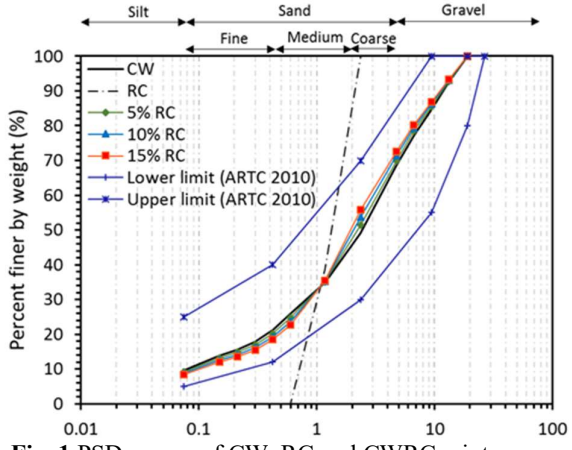

Fig. 1 PSD curves of CW, RC and CWRC mixtures.

which corresponds to 0%, 4.76%, 9.09% and 13.04% rubber content, respectively, with respect to the total weight of the mixture. Figure 1 shows that the PSD curves of all mixtures fall within the lower and upper limit for materials used in a subballast layer in railways (Austalian Rail Track Corporation 2010).

CW material was sieved using the wet and dry method (Standards Australia 2009) and each sample was prepared by mixing the exact weight of each size to reach the target PSD (Fig. 1). Then water was added to reach the target moisture content and the sample was left to cure in a sealed container under constant humidity and temperature for consistent water distribution within the sample. Static triaxial tests were performed in three stages. First the sample was saturated by increasing the back pressure until a Skempton value greater than 0.95 was achieved. Then, the sample was consolidated at the target effective confining pressure (i.e., 10, 25, 50 and 75 kPa). The sample was then sheared at a constant strain rate of 0.1 mm/min until the maximum strain limit of the equipment was reached.

3 EXPERIMENTAL RESULTS

3.1 *Stress-strain response*

The deviator stress vs. axial strain and volumetric strain vs. axial strain curves of CWRC mixtures under a confining pressure of 50 kPa are shown in Fig. 2. The maximum deviator stress representing the strength of the material decreases when rubber is added to the mixture. The same trend was observed for CW-SFS-RC mixtures (Indraratna et al. 2018) and this an expected outcome because RC have a lower frictional resistance than CW. While all mixtures exhibit a post-peak softening behaviour, the ductility of the material is significantly improved when rubber content increases marked by a reduction in the post-peak softening modulus.

The volumetric strain response shows a contractive behaviour followed by dilation for all CWRC mixtures. However, the maximum compressive strain and the axial strain at which the maximum compressive strain occurs increase with the rubber content. This behaviour is attributed to the compression and deformation of rubber particles which induce higher strains. Also, the mixture with no rubber reaches a relatively constant volumetric strain at the end of the test. For the mixtures with rubber, there is no distinct residual volumetric strain even at 20% axial strain. This is attributed to the elasticity and compressibility of rubber particles which results in a continuous deformation and volume change even at the critical state. A much higher axial strain is needed to reach a constant

volumetric stain, which exceeds the limits of the equipment used in this study.

The characteristic state is defined as the stress state at which the change in the volumetric strain is

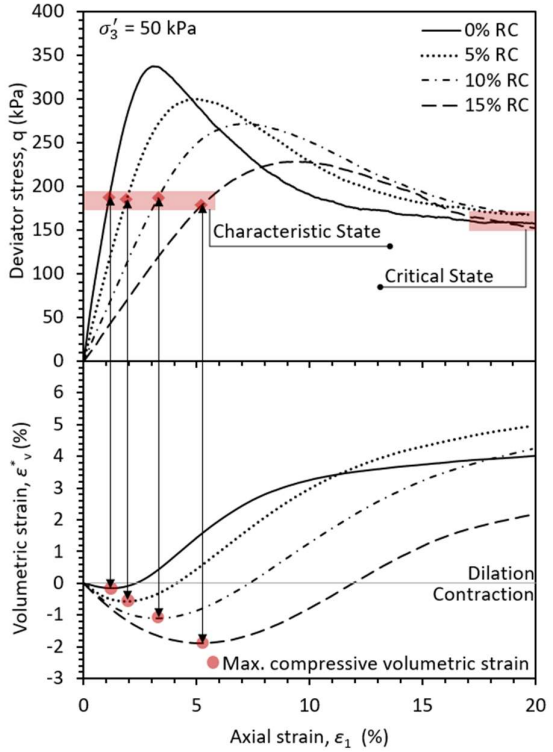

Fig. 2 Stress-strain response of CWRC mixtures (after Indraratna et al. 2019).

zero. Unlike the critical state, at the characteristic state the change in the deviator stress in not zero. In other words, the characteristic state coincides with the maximum compressive volumetric strain. While the maximum compressive strain increases with increasing rubber content, Fig. 2 shows that the stress at the characteristic state is the same for all CWRC mixtures regardless of rubber content. Also, all mixtures reach the same critical state where the change in the deviator stress becomes negligible. This indicates that the strength of the material at the characteristic state and at the critical state is governed by the frictional resistance of CW only and is not dependent on rubber content. However, this is only applicable to mixtures with a relatively low rubber content (i.e., <15%). For instance, Indraratna et al. (2018) reported a decrease in the critical stress ratio for CW-SFS-RC mixtures when the rubber content varied between 0% and 40%.

3.2 *Initial tangent modulus*

The initial tangent modulus (ITM) is an indication of the elastic deformation of the material ($E_{t,i} = \Delta q/\Delta e_1$). In this study the ITM is measured as the slope of the stress-strain curve before the characteristic state is reached. Figure 3 shows the ITM of the CWRC mixture at three confining pressures (i.e., 25. 50 and 75 kPa). It is clear that the ITM decreases with increasing rubber content while the rate of reduction decreases when the amount of rubber increases. Again, this indicates that rubber improves the ductility of the material which also implies that higher axial strains are expected for the same stress level.

3.3 *Peak friction angle*

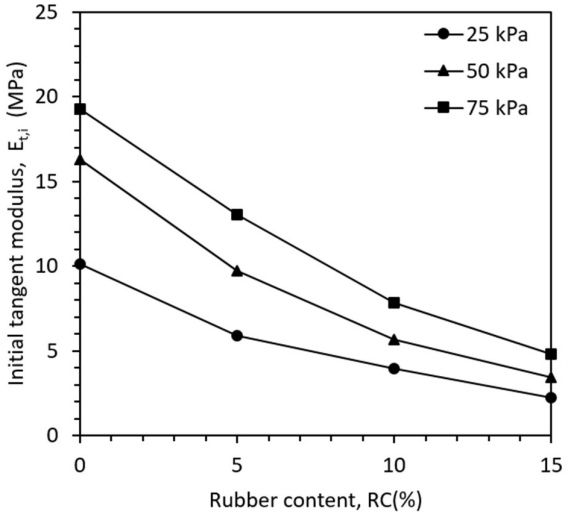

Fig. 3 Initial tangent modulus of CWRC mixtures (after Indraratna et al. 2019).

The peak friction angle is an important parameter that is often used as a criterion when selecting appropriate materials for different construction activities. For transportation sublayers that are not the main bearing layers such as a capping/subballast layer in railways, a peak friction angle of 45° in considered acceptable.

Like traditional granular materials, the peak friction angle decreases with increasing confining pressure, as shown in Fig. 4. For the small range of rubber content considered in this study, the peak friction angle of CWRC mixtures decreases almost linearly with increasing rubber content. However, for a confining pressure greater than 50 kPa, which is representative of field conditions, all the mixtures have a peak friction angle greater than 45°.

3.4 *Void ratio*

The void ratio is an important indication of the deformable space within a granular matrix. In this study, void space is not the only volume that can deform under loading. Rubber particles are highly compressible, and their deformation can significantly affect the total deformation of the

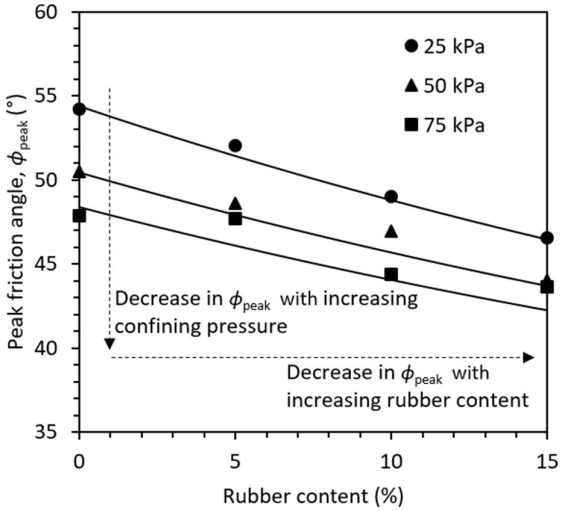

Fig. 4 Peak friction angle of CWRC mixtures (after Indraratna et al. 2019).

material. To distinguish between the total volume change, which accounts for the compression of rubber particles, and the void volume change, which accounts only for the change in the volume of voids, a modified void ratio is calculated as:

$$e^* = \frac{V_v}{V_{CW}} \quad (1)$$

where V_v is the volume of voids and V_{CW} is the volume of CW. Figure 5 shows the initial modified void ratio and the modified void ratio at the characteristic state vs. rubber content at three confining pressures (i.e., 25, 50 and 75 kPa).

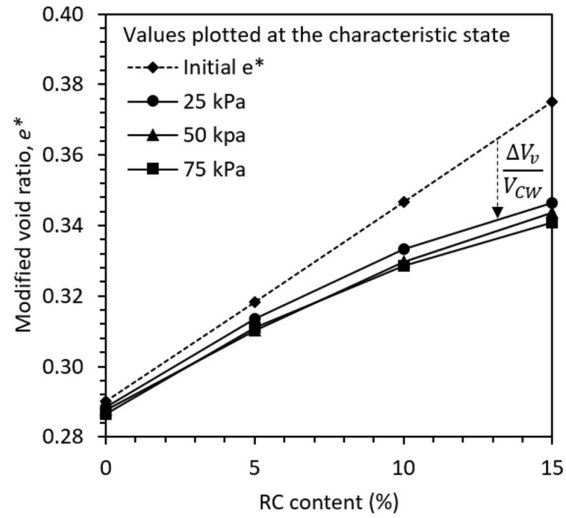

Fig. 5 Modified void ratio of CWRC mixtures at the initial state and at the characteristic state.

All the mixture were compacted to the same initial void ratio. When rubber is added, for the same total unit volume, the volume of voids remains the same, the volume of CW decreases and the volume of rubber increases. Therefore, the initial modified void ratio increases with increasing rubber content. However, it is evident that the change in the modified void ratio at the characteristic state is higher when rubber is added. This indicates that the addition of rubber facilitates the rearrangement of particle in the compression range and results in a smaller volume of voids. This is attributed to the deformation of rubber particles which provides a more compact packing of CW particles when the mixture is subjected to loading. For the same rubber content, there is a slight reduction in the modified void ratio with confining pressure because of the narrow range of confining pressures considered in this study.

3.5 *Breakage and permeability*

Rubber was blended with coal wash to reduce particle degradation because CW is weaker than traditional aggregates and can easily break under loading. Figure 6(a) shows the Breakage Index (BI) (Indraratna et al. 2005) of four CWRC blends after shearing. Although a higher compaction effort was used when rubber was added to the mixture to achieve the same initial void ratio, a reduction in breakage is still observed when rubber content increases.

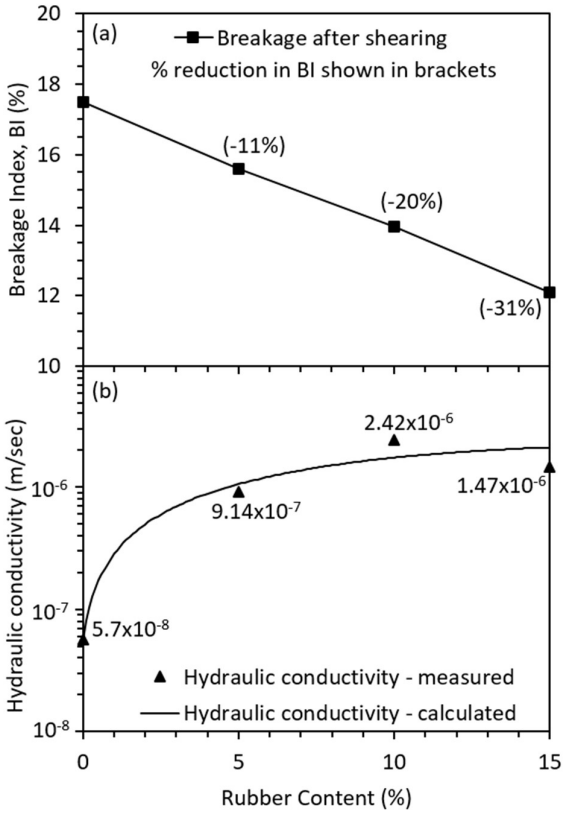

Fig. 6 (a) breakage after shearing and (b) saturated hydraulic conductivity of CWRC mixtures.

Figure 6(b) also shows the effect on rubber content on the hydraulic conductivity of the CWRC mixtures. The saturated hydraulic conductivity increases with increasing RC content. The same trend was observed by Indraratna et al. (2018) for CW-SFS-RC mixtures. However, for the range of rubber content considered in this study, the permeability is still within the acceptable limits for transportation infrastructure sublayers where semi-impermeable conditions are desired (i.e., $k<10^{-5}$ m/s). The hydraulic conductivity can be approximated by a power function of the form:

$$k_{sat}=a + (b\times RC) + \left(c\times RC^2\right) \quad (2)$$

where k_{sat} is the saturated hydraulic conductivity in m/sec, RC is the rubber content added to the mixture in % and a, b and c are fitting parameters with values of $5.706\text{x}10^{-8}$, $2.314\text{x}10^{-8}$ and $-6.322\text{x}10^{-8}$, respectively.

3.6 *Energy absorption*

Rubber is highly elastic and energy absorbing. In this regard, adding rubber to relatively incompressible aggregates like CW improves the energy absorbing potential of the material. Being energy absorbing does not only result in a reduction in breakage as shown above. An energy absorbing layer in transportation infrastructure projects may be used to reduce vibrations generated by the dynamic loads experienced in transportation corridors.

Figure 7 shows the maximum work dissipated by the CWRC mixtures up to the point of failure as a representation of the maximum energy that can be absorbed by the material during loading (Indraratna et al. 2019). As expected, the enrgy absorption capacity of the mixture increases with increasing rubber content. However, this is more evident at higher confining pressures because the compressibility of rubber increases with increasing confining pressure.

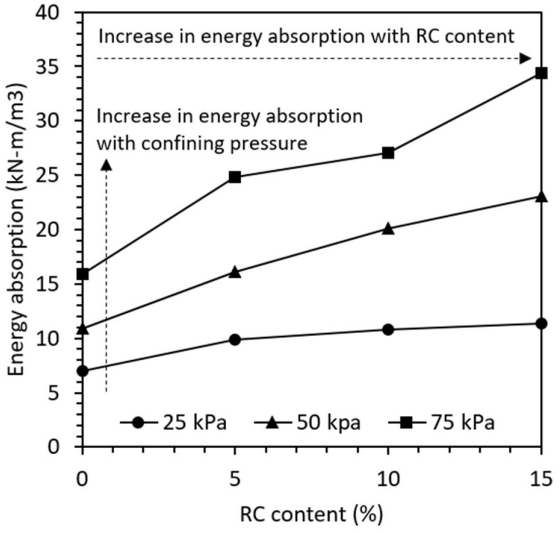

Fig. 7 Energy absorption capacity of CWRC mixtures (after Indraratna et al. 2019)

4 CONCLUSIONS

The strength and deformation properties of four mixtures of CW and RC with 0, 5, 10 and 15% rubber added were investigated under static loading conditions using monotonic triaxial tests. Based on the experimental results, the following results can be made:

- The addition of compressible rubber to a matrix of relatively incompressible material like CW improves the ductility of the mixture thus minimizing the potential for tensile cracking or sudden failure if the live loads exceed the strength of the material.
- Although the peak strength of the material decreases when rubber is added, for a confining pressure greater than 50 kPa, the mixtures have a peak friction angle greater than 45°, which is acceptable for materials used in transportation infrastructure sublayers that are not the main load bearing layers (i.e., capping/subballast layer in railways).
- The compression and deformation of RC facilitates the rearrangement of particles during loading which results in a smaller volume of void within the granular skeleton. This improves the interlocking of particles which could partly compensate for the reduction in strength when rubber is added.

While the results of the static triaxial tests showed promising results in terms of acceptable strength and deformations, the behaviour of the material must also be investigated under cyclic loading conditions, a more accurate representation of the dynamic loads experienced in practice in transportation infrastructure.

ACKNOWLEDGMENTS

The first author's PhD scholarship is supported by the Australian Research Council (ARC) Linkage Project (LP160100280). The authors would like to acknowledge the assistance provided by South 32 and Tyre Crumbs Australia in the procurement of CW material and rubber material used in this study, respectively. The assistance provided by Richard Berndt in the performance of laboratory tests is also gratefully appreciated. Some figures in this paper

have been modified, whereby the original data has been reproduced with kind permission from Transportation Geotechnics.

REFERENCES

Austalian Rail Track Corporation (2010). "Engineering (Track & Civil) Standard - Earthworks, Formation and Capping Material." Austalian Rail Track Corporation Limited.

Chiaro, G., Indraratna, B., Tasalloti, S. A., and Rujikiatkamjorn, C. (2014). "Optimisation of coal wash-slag blend as a structural fill." *Proc., Institution of Civil Engineers: Ground Improvement*, 33-44.

Cho, S. D., Kim, J. M., Kim, J. H., and Lee, K. W. (2007). "Utilization of waste tires to reduce railroad vibration." *Materials Science Forum*, 544-545, 637-640.

Esmaeili, M., Zakeri, J. A., Ebrahimi, H., and Sameni, M. K. (2016). "Experimental study on dynamic properties of railway ballast mixed with tire derived aggregate by modal shaker test." *Advances in Mechanical Engineering*, 8(5), 1-13.

Feng, Z., and Sutter, K. (2000). "Dynamic Properties of Granulated Rubber/Sand Mixtures." *Geotechnical Testing Journal*, 23(3), 338-344.

Heitor, A., Indraratna, B., Kaliboullah, C. I., Rujikiatkamjorn, C., and McIntosh, G. W. (2016). "Drained and undrained shear behavior of compacted coal wash." *Journal of Geotechnical and Geoenvironmental Engineering*, 142(5), 04016006-04016001-04016006-04016010.

Indraratna, B. (1994). "Geotechnical characterization of blended coal tailings for construction and rehabilitation work." *Quarterly Journal of Engineering Geology*, 27, Part 4, 353-361.

Indraratna, B., Lackenby, J., and Christie, D. (2005). "Effect of confining pressure on the degradation of ballast under cyclic loading." *Géotechnique*, 55(4), 325-328.

Indraratna, B., Qi, Y., and Heitor, A. (2018). "Evaluating the Properties of Mixtures of Steel Furnace Slag, Coal Wash, and Rubber Crumbs Used as Subballast." *Journal of Materials in Civil Engineering*, 30(1), 04017251.

Indraratna, B., Rujikiatkamjorn, C., and Chiaro, G. (2012). "Characterization of compacted coal wash as structural fill material." *GeoCongress 2012: State of the Art and Practice in Geotechnical Engineering*, 3826-3834.

Indraratna, B., Rujikiatkamjorn, C., Tawk, M., and Heitor, A. (2019). "Compaction, degradation and deformation characteristics of an energy absorbing matrix." *Transportation Geotechnics*, 19, 74-83.

Kim, H. K., and Santamarina, J. C. (2008). "Sand–rubber mixtures (large rubber chips)." *Canadian Geotechnical Journal*, 45(10), 1457-1466.

Lee, J. H., Salgado, R., Bernal, A., and Lovell, C. W. (1999). "Shredded Tires and Rubber-Sand as Lightweight Backfill." *Journal of Geotechnical and Geoenvironmental Engineering*, 125(2), 132-141.

Lopera Perez, J. C., Kwok, C. Y., and Senetakis, K. (2016). "Effect of rubber size on the behaviour of sand-rubber mixtures: A numerical investigation." *Computers and Geotechnics*, 80, 199-214.

Montgomery, D. G. "Utilisation of Coal Washery Wastes in Engineering Construction." *Proc., International Coal Engineering Conference*, Institution of Engineers, Australia, 79-83.

Qi, Y., Indraratna, B., Heitor, A., and Vinod, J. S. (2018). "Effect of Rubber Crumbs on the Cyclic Behavior of Steel Furnace Slag and Coal Wash Mixtures." *Journal of Geotechnical and Geoenvironmental Engineering*, 144(2), 04017107.

Qi, Y., Indraratna, B., and Vinod, J. S. (2018). "Behavior of Steel Furnace Slag, Coal Wash, and Rubber Crumb Mixtures with Special Relevance to Stress-Dilatancy Relation." *Journal of Materials in Civil Engineering*, 30(11), 04018276.

Rujikiatkamjorn, C., Indraratna, B., and Chiaro, G. (2013). "Compaction of coal wash to optimise its utilisation as water-front reclamation fill." *Geomechanics and Geoengineering*, 8(1), 36-45.

Saberian, M., Li, J., Nguyen, B., and Wang, G. (2018). "Permanent deformation behaviour of pavement base and subbase containing recycle concrete aggregate, coarse and fine crumb rubber." *Construction and Building Materials*, 178, 51-58.

Signes, C. H., Fernández, P. M., Garzón-Roca, J., and Franco, R. I. (2016). "Analysis of the bearing capacity of unbound granular mixtures with rubber particles from scrap tyres when used as sub-ballast." *Materiales de Construcción*, 66(324), e105.

Standards Australia (2009). "Methods of testing soils for engineering purposes—Soil classification tests—Determination of the particle size distribution of a soil—Standard method of analysis by sieving." Standards Australia Limited Sydney, Australia.

Tasalloti, S. A., Indraratna, B., Rujikiatkamjorn, C., Heitor, A., and Chiaro, G. (2015). "A laboratory study on the shear behavior of mixtures of coal wash and steel furnace slag as potential structural fill." *Geotechnical Testing Journal*, 38(4), 361-372.

Wang, D., Tawk, M., Indraratna, B., Heitor, A., and Rujikiatkamjorn, C. (2019). "A mixture of coal wash and fly ash as a pavement substructure material." *Transportation Geotechnics*, 21, 100265.

Youwai, S., and Bergado, D. T. (2003). "Strength and deformation characteristics of shredded rubber tire-sand mixtures." *Canadian Geotechnical Journal*, 40(2), 254-264.

Zornberg, J. G., Cabral, A. R., and Viratjandr, C. (2004). "Behaviour of tire shred-sand mixtures." *Canadian Geotechnical Journal* 41(2), 227-241.

Shear and Degradation Behaviour of Rail Ballast with Different Interfaces

S. K. Navaratnarajah
Department of Civil Engineering, University of Peradeniya, Peradeniya, Sri Lanka.

H. G. S. Mayuranga
Department of Civil Engineering, University of Peradeniya, Peradeniya, Sri Lanka.

ABSTRACT: Ballasted railway track substructure consists of different interfaces such as ballast-sleeper (concrete or timber), ballast-resilient rubber pads (under sleeper pads - USP or under ballast mats - UBM), and ballast-subballast or subgrade which influence the overall shear resistance of the rail track. Due to the importance of understanding the shear behaviour of these interfaces, this paper explores the results of large-scale direct shear tests conducted for different interfaces that are commonly available in ballasted railway tracks. The large-scale direct shear test for fresh ballast and three different interfaces including (1) Ballast-Concrete sleeper, (2) Ballast-Timber sleeper, and (3) Ballast-USP were carried out by adopting full-size ballast particles under three different normal stresses of 30, 60 and 90 kPa. Based on the results, a comparison of shear strength parameters of different interfaces with fresh ballast was made. Further, ballast degradation was quantified and compared by using Ballast Breakage Index (BBI) method.

1. INTRODUCTION

Ballasted railway track is the conventional and widely used railway track system in many countries including Sri Lanka due to its advantages compared to other railway track systems. With the increasing demand for high speed and heavy trains, lateral instability of the railway track is significant due to extreme lateral stresses imparted on the underlying formation including the ballast layer. The major load-bearing ballast layer around and underneath the sleepers provides resistance against the lateral stresses in order to maintain the track stability.

Ballast layer materials consist of loose, free-draining course-grained particles and as a result of the internal friction between particles, undue compressive stresses transmitted from the moving train loads are absorbed and distributed to the underlying formation (Esveld, 2001). According to Selig and Waters (1994) and Dahlberg (2003), the ballast materials provide adequate resistance to vertical, longitudinal and lateral forces applied on the track structure due to moving trains, maintain the proper level and alignment of the track, absorb the energy from dynamic loads, and hinder the growth of vegetation that might badly affect the track function. Open-graded distribution of particle sizes of ballast layer immediately drain out the water falling onto the top surface of the track which is leading to maintain the stability of the track bed (Dissanayake et al., 2016, Navaratnarajah, 2017, Schmidt et al., 2017, Selig and Waters, 1994).

The sleeper-ballast contact area is an important parameter that affects the effective distribution of train load to the underlying formation through the rail, sleeper, and ballast layer. Abadi et al. (2015) investigated that the use of finer gradation of ballast, use of low stiff materials for sleeper such as timber or plastic, and use of soft USPs improve the sleeper-ballast contact area and reduce the ballast layer stresses. Many recent studies have shown that the use of Under Sleeper Pads (USP) at the sleeper-ballast interface and Under Ballast Mats (UBM) at the ballast-subballast or subgrade interface, considerably improve the performance of railway tracks (Indraratna et al., 2014, Lakuši et al., 2010, Loy, 2008, Navaratnarajah and Indraratna, 2017, Navaratnarajah et al., 2018).

Structural components of a ballasted railway track such as rail, sleeper, ballast, subballast and subgrade create different types of interfaces: (1) rail-sleeper, (2) sleeper-ballast, (3) ballast-subballast and (4) subballast-subgrade. Besides this, the incorporation of Rail Pads (RP - at the rail-sleeper interface), USPs and UBMs, create various interfaces such as (1) rail-RP, (2) RP-sleeper, (3) USP-ballast, (4) ballast-UBM, (5) UBM-subballast or subgrade. The type of material used for the sleeper such as timber, steel or concrete also creates many other different interfaces and significantly changes the ballast shear and degradation behaviour. Shear strength capacity of ballast plays a major role in

maintaining the lateral stability of the railway track. At the same time, different interfaces of track significantly influence the overall shear behaviour of the ballast layer. Further, ballast particle degradation is significantly affected by the surface type of the interface such as soft interface (ballast-USP) and hard interface (ballast-concrete sleeper or ballast-timber sleeper) (Navaratnarajah and Indraratna, 2020, Navaratnarajah et al., 2015). Therefore, it is important to investigate the shear strength parameters and the degradation behaviour of rail road ballast with different interfaces of the railway track.

In this study, large-scale direct shear apparatus was used to evaluate the shear strength parameters of three different interfaces: (1) Ballast-Concrete sleeper, (2) Ballast-Timber sleeper and (3) Ballast-USP on Concrete sleeper under three different normal stresses. The shear strength and degradation of ballast under these interfaces were compared with that of fresh ballast.

2. LARGE-SCALE DIRECT SHEAR TESTING

2.1 Test materials

The materials used for this study are fresh ballast, timber sleeper, concrete sleeper, and USP. The fresh ballast collected from a stockpile at Gampola Railway Unit is identified as biotite gneiss which is commonly used in railway tracks in Sri Lanka. The collected ballast sample was washed and air-dried in order to remove fine particles that adhere to ballast aggregates. Though the moisture content influence the behaviour of ballast, in this study that was not studied due to the limited test facilities.

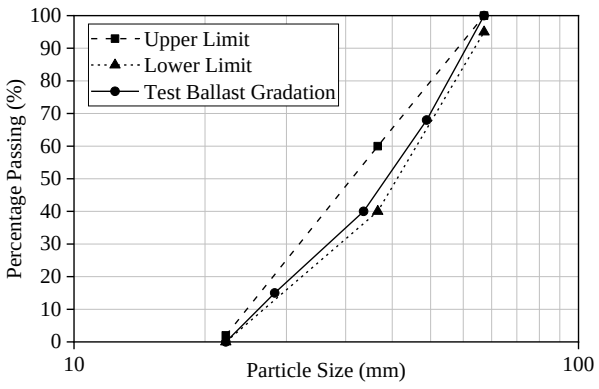

Fig. 1: Test ballast gradation with upper and lower limits of Indian standard gradation

The test sample was prepared confirming the particle size distribution according to the Indian standard gradation which is currently used for Sri Lankan railway track ballast. Particle size distribution of the prepared sample and the upper and lower limits of Indian standard gradation (IRS-GE-1, 2004) are shown in Fig. 1.

Two types of sleeper materials were used in this study: timber and concrete. A used timber sleeper was obtained from Gampola Railway Unit and in order to use it in large-scale test apparatus, it was cut to prepare a circular shape sleeper. The strength of concrete used for the concrete sleeper in this study was 60 Mpa and it was casted as a circular shape sleeper. Commercially available 10 mm thick USP was used and attached to the bottom of the concrete sleeper when testing for rubber interface. Timber sleeper, concrete sleeper and USP attached to the concrete sleeper are shown in Fig. 2.

Fig. 2: Test samples of sleeper (a) Timber; (b) Concrete; (c) USP

2.2 Large scale test apparatus

A series of direct shear tests were carried out by using large-scale direct shear apparatus design and built at the University of Peradeniya. A schematic diagram and a photograph of the test apparatus are shown in Fig. 3 a and b, respectively.

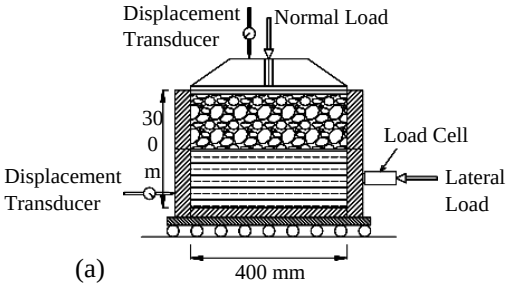

Fig. 3: Large-scale direct shear apparatus (a) Schematic diagram; (b) Photograph of test apparatus

The test apparatus can accommodate a full-size ballast aggregate specimen of 400 mm diameter and 300 mm height. The test apparatus is capable of shearing a test sample into two halves of equal portions. The top half of the apparatus is fixed into the supporting frame and the bottom half can be

moved in horizontal direction under the applied lateral force on it. The top loading plate is allowed to move freely in the vertical direction allowing for material compression/dilation. The normal load is applied to the sample through the top loading plate by using a lever technique. The lateral (shearing) force is applied to the bottom half of the test apparatus using a hydraulic jack. Vertical and shearing displacements were measured by using two displacement transducers attached vertically at the top loading plate and horizontally at the bottom half of the test apparatus, respectively.

According to ASTM standards, the ratio of maximum particle size to test apparatus diameter for direct shear test is limited to 0.1. However, Fakhimi and Hosseinpour (2008) reported that this limit could be expanded to 0.2 for cohesion-less materials when low normal stresses are used. In this study, the maximum particle size of the aggregates tested was 63 mm. Therefore, above mentioned specified ratio was 0.16 and it was within the limit explained by Fakhimi and Hosseinpour (2008).

2.3 Test procedure

Large-scale direct shear tests were conducted for fresh ballast and 3 different interfaces: Ballast-Concrete sleeper, Ballast-Timber sleeper and Ballast-USP on concrete sleeper. Each test was conducted under 3 different normal stresses of 30, 60 and 90 kPa which was applied through the top loading plate. The shear load was applied laterally at a rate of 4 mm/min and it was maintained throughout the experiment (Dissanayake et al., 2016). The shear load was applied until the specimen undergoes a lateral displacement of 60 mm which is corresponding to 15% shear strain. In order to measure the applied shear load, a load cell was placed in between the bottom half of the apparatus and the hydraulic jack. Two displacement transducers and the load cell were connected to a data logger to record the measurements of displacements and the shear load automatically. At the end of each test, the ballast breakages were calculated based on the Ballast Breakage Index (BBI) method proposed by Indraratna et al. (2005).

3. RESULTS AND DISCUSSION

3.1 Shear behaviour

Shear stress versus shear strain behaviour of each test sample is illustrated in Fig. 4. Stress-strain calculation was made considering the shear area of the interface and the full height of the sample. Based on the results, the maximum shear resistance was recorded in fresh ballast for all normal stresses compared to other interfaces. The second and third maximum values were observed in Ballast-Concrete and Ballast-USP interfaces and the minimum shear resistance was recorded for the Ballast-Timber interface. Higher interlocking behaviour of ballast aggregates can be considered as the reason for getting a higher shear resistance value for Ballast-Ballast interface. Due to the variation of surface friction of other 3 different interfaces, they exhibited relatively lower shear resistance values compared to the fresh ballast sample.

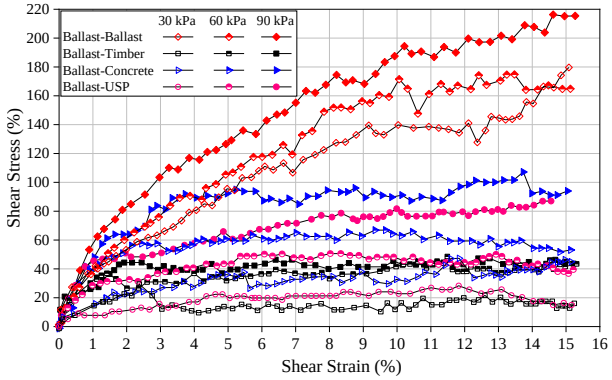

Fig. 4: Variation of shear stress with shear strain

3.2 Dilation behaviour

Fig. 5 shows the variation of the normal strain versus the shear strain. It provides evidence for the dilation behaviour of test samples, especially in fresh ballast. Maximum dilation was observed in fresh ballast sample and excluding the Ballast-Timber interface, the other two interfaces exhibited dilation behaviour. The dilation behaviour has been decreased with the increase in the normal load.

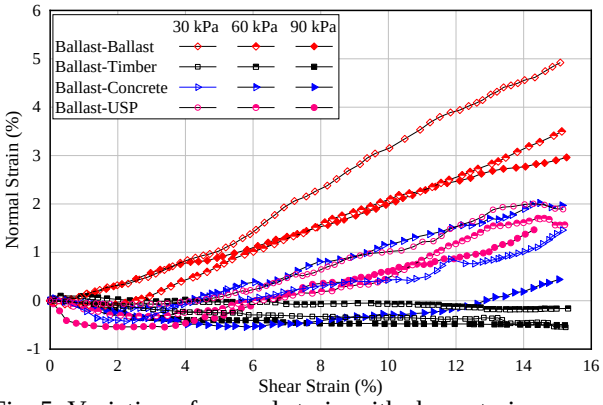

Fig. 5: Variation of normal strain with shear strain

Dilation behaviour was not observed in the Ballast-Timber interface. The reason could be the less surface roughness of the timber surface (relatively soft and smooth) which influences the ballast particles to slide on the timber surface instead of rolling compared to concrete surface. This can be

verified by comparing the surfaces of the timber sleeper before and after the testing, as shown in Fig. 6 (a) and (b) where scratch marks can be clearly observed in the sleeper surface after the test. When concrete sleeper surfaces are compared before and after the test, as shown in Fig. 6 (c) and (d), it can be justified that the particle rolling effect could be the reason for the dilation behaviour of Ballast-Concrete interface because scratch marks are not clearly visible in concrete surface compared to timber surface.

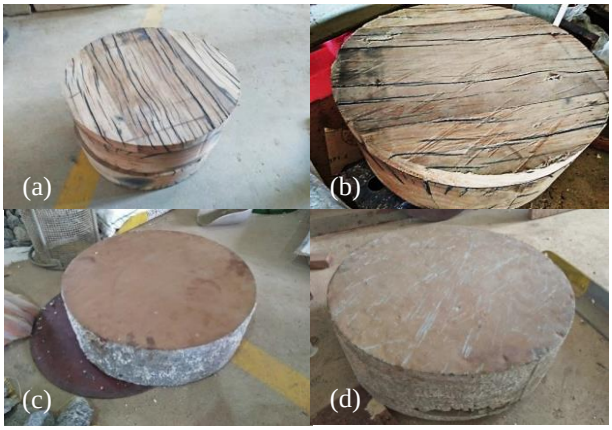

Fig. 6: Timber sleeper (a) before the test; (b) after the test; Concrete sleeper (c) before the test; (d) after the test

3.3 Friction angle

Fig. 7 illustrates the relationship of shear stress versus normal stress at peak and corresponding Mohr-Coulomb failure envelops (assuming zero cohesion). Calculated friction angle values are presented in Table 1.

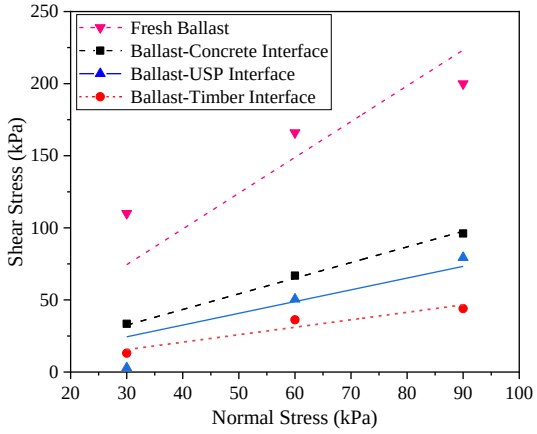

Fig. 7: Peak shear stress-normal stress relationship and corresponding Mohr-Coulomb failure envelops

Based on the results, the maximum shear resistance was observed in fresh ballast followed by Ballast-Concrete, Ballast-USP and then Ballast-Timber interfaces. Percentage reduction in friction angle value of Ballast-Concrete, Ballast-USP, and Ballast-Timber interfaces compared to that of Ballast-Ballast interface are 32%, 43%, and 48%, respectively.

Table 1: Friction angles of fresh ballast and three different types of interfaces

Interface	Friction angle (ϕ)
Fresh ballast	69
Ballast-Concrete	47
Ballast-USP	39
Ballast-Timber	36

3.4 Ballast particle breakage

At the end of each test, ballast samples were sieved and obtained the particle size distribution in order to evaluate the ballast particle breakage based on the Ballast Breakage Index (BBI) method proposed by Indraratna et al. (2005) as shown in Fig. 8. The calculated ballast breakage index values are graphically shown in Fig. 9 for each test condition.

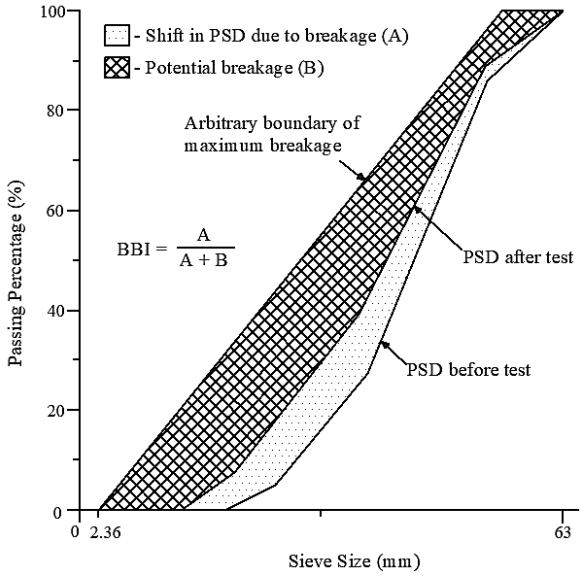

Fig. 8: Ballast Breakage Index (BBI) definition (modified after Navaratnarajah (2017))

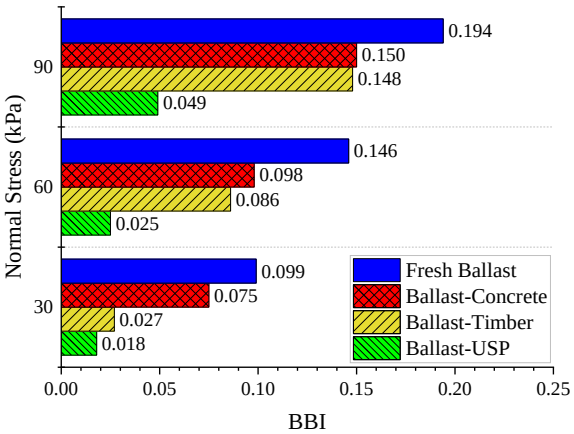

Fig. 9: Ballast Breakage Index (BBI)

According to Fig. 9, higher particle degradation can be observed in fresh ballast followed by Ballast-Concrete, Ballast-Timber, and Ballast-USP interfaces. The interlocking nature of ballast aggregates could be driven for more breakage of particles under shear loading and hence, it has exhibited a higher breakage index compared to other results. When the normal stress increases from 30 to 90 kPa, about 50-65% increase in BBI value can be observed for fresh ballast, Ballast-Concrete, and Ballast-USP interfaces. For the Ballast-Timber interface, this increment can be observed as about 82%. By using USP, about 65-75% reduction in BBI value can be achieved compared to the Ballast-Concrete interface which is commonly used interface in conventional ballasted tracks. Therefore, this study reveals that the use of USP reduces ballast degradation under different static loading conditions.

4. CONCLUSIONS

Series of large-scale direct shear tests were conducted to evaluate the shear strength parameters of fresh ballast and 3 different interfaces: Ballast-Concrete, Ballast-Timber, and Ballast-USP under static loading condition. Fresh ballast exhibited the highest shear strength due to the interlocking nature of highly angular ballast particles and also due to the high strength of parent materials. The lowest shear resistance has been observed in the Ballast-Timber interface. The shear resistance of the Ballast-USP interface was less than the Ballast-Concrete interface.

Ballast particle breakages were compared based on the Ballast Breakage Index (BBI) method proposed by Indraratna et al. (2005). The highest ballast breakage was observed in fresh ballast sample followed by Ballast-Concrete, Ballast-Timber and Ballast-USP interfaces. Even though the ballast breakage of concrete sleeper is high compared to timber sleeper, the performance of concrete sleeper in terms of lateral resistance capacity is high compared to timber sleeper. Therefore, the use of USP attached to the concrete sleeper will provide better performance of the railway track.

ACKNOWLEDGEMENTS

The support provided by the University of Peradeniya Research Grant (Grant No: URG-2017-29-E) and Accelerating Higher Education Expansion and Development (AHEAD) operation funded by the World Bank (Grant No: AHEAD/RA3/DOR/STEM/No.63) are highly appreciated by the authors. The authors would like to acknowledge the support provided by the District Engineer of Nanuoya Railway office, and the staff of Gampola Railway Unit of Department of Railways Sri Lanka for helping to collect railway ballast and timber sleeper materials.

REFERENCES

Abadi, T., Le Pen, L., Zervos, A. and Powrie, W. (2015). Measuring the area and number of ballast particle contacts at sleeper/ballast and ballast/subgrade interfaces, The International Journal of Railway Technology, 4(2): 45-72.

Dahlberg, T. (2003). Railway track settlements-a literature review, Report for the EU project SUPERTRACK. Division of Solid Mechanics, IKP. Linköping University. Linköping. Sweden.

Dissanayake, D., Kurukulasuriya, L. and Dissanayake, P. (2016). Evaluation of shear strength parameters of rail track ballast in Sri Lanka, Journal of the National Science Foundation of Sri Lanka, 44(1).

Esveld, C. (2001). Modern railway track, MRT-productions Zaltbommel.

Fakhimi, A. and Hosseinpour, H. (2008). The role of oversize particles on the shear strength and deformational behavior of rock pile material, Proc., The 42nd US Rock Mechanics Symposium (USRMS), American Rock Mechanics Association, pp 1-7.

Indraratna, B., Lackenby, J. and Christie, D. (2005). Effect of confining pressure on the degradation of ballast under cyclic loading, Géotechnique, 55(4): 325-328.

Indraratna, B., Nimbalkar, S., Navaratnarajah, S.K., Rujikiatkamjorn, C. and Neville, T. (2014). Use of shock mats for mitigating degradation of railroad ballast, Sri Lankan geotechnical journal - Special issue on ground improvement, 6(1): 32-41.

IRS-GE-1 (2004). Specifications for Track Ballast, Indian Railway Specification.

Lakuši, S., Ahac, M. and Haladin, I. (2010). Experimental investigation of railway track with under sleeper pad, 10th Slovenian road and transportation congress, pp 386-393.

Loy, H. (2008). Under sleeper pads: improving track quality while reducing operational costs, European Railway Review, 4: 46-51.

Navaratnarajah, S. and Indraratna, B. (2020). Stabilisation of Stiffer Rail Track Substructure Using Artificial Inclusion, Indian Geotechnical Journal: 1-8.

Navaratnarajah, S.K. (2017). Application of rubber inclusions to enhance the stability of ballasted rail track under cyclic loading. Ph. D. Thesis, University of Wollongong, Australia.

Navaratnarajah, S.K. and Indraratna, B. (2017). Use of rubber mats to improve the deformation and degradation behavior of rail ballast under cyclic loading, Journal of Geotechnical and Geoenvironmental Engineering, 143(6).

Navaratnarajah, S.K., Indraratna, B. and Ngo, N.T. (2018). Influence of under sleeper pads on ballast behavior under cyclic loading: experimental and numerical studies, Journal of Geotechnical and Geoenvironmental Engineering, 144(9): 1-16.

Navaratnarajah, S.K., Indraratna, B. and Nimbalkar, S. (2015). Performance of rail ballast stabilized with resilient rubber pads under cyclic and impact loading, Proceedings of the International Conference on Geotechnical Engineering, pp 617-620.

Schmidt, S., Shah, S., Moaveni, M., Landry, B.J., Tutumluer, E., Basye, C. and Li, D. (2017). Railway ballast permeability and cleaning considerations, Transportation Research Record, 2607(1): 24-32.

Selig, E.T. and Waters, J.M. (1994). Track geotechnology and substructure management, Thomas Telford.

Shear and degradation behavior of rail track ballast contaminated with fines: An experimental study

S. K. Navaratnarajah
Department of Civil Engineering, University of Peradeniya, Sri Lanka

S. Venuja
Department of Civil Engineering, University of Peradeniya, Sri Lanka

ABSTRACT: Rail transport is one of the highly demanded transport modes due to its safety, reliability and economic profits. The ballast layer, major component by weight and volume, effectively transmits the train exerted loads from sleepers to the underlying layer at a minimal level. Ballast is degraded over time because of repetitive train loads. Ballast fouling is one of the major factors that affect the load-bearing capacity of the ballast layer as well as deters the permeability. This experimental based research primarily analyzes the changes in shear and degradation behavior of rail track ballast after fouling by other foreign material. The outcomes of the laboratory tests clearly indicate that fouling by sand increases the overall density of the sample, therefore, increases the shear strength and clay fouling acts as a lubricant thus reduces the shear strength. Ballast breakage under static loading increases with the increment in vertical load and decreases with fouling agents.

1 INTRODUCTION

Currently, ballasted rail tracks and slab tracks are widely used in many countries all over the world. The ballast layer is used to transmit the loads from sleepers to the underlying layers in ballasted tracks in contrast concrete slab is used under the sleepers in slab tracks. Because of the availability of low-cost raw material of ballast, simplicity of construction and low initial construction expenditure, the ballasted tracks are the most popular compared to slab tracks (Al-Douri et al., 2016). Ballast is a highly angular granular material with high load-bearing capacity sourced from granite, quartzite, limestone, basalt, dolomite and other crushed stones, and provides highly porous medium (Chan and Johan, 2016, Navaratnarajah, 2017, Tennakoon et al., 2012). Ballast has high shear strength, high specific gravity, resistance to weathering, high toughness and hardness (Indraratna et al., 2009). Ballast gradation is the major factor that affects the stability and drainage of tracks. Various gradations of ballast are adapted in different countries based on the shear strength and permeability requirements.

The performance of ballast decreases with time due to lack of lateral confinement, ballast breakage, and ballast fouling. Ballast fouling is a phenomenon where the voids in the ballast layer are partially or fully filled with foreign materials such as sand, coal, silt, dust, clay and by its own degradation (Anbazhagan et al., 2012, Esmaeili et al., 2014). The quantification of ballast fouling is hard due to the huge variation in particle size and the specific gravity of the ballast and fouling agent. Ballast fouling reduces permeability, decreases the energy absorbing capacity and leads to vegetation growth, therefore affects the track function and longevity (Anbazhagan et al., 2012, Tennakoon et al., 2012).

The major issues of track deterioration are differential settlements, cracks in sleepers, damages on railheads, misalignments of rails and imperfections in wheel and rail contact surfaces due to the repeated heavy load and high speed of moving trains and environmental conditions (Al-Douri et al., 2016, Ataei et al., 2014, Navaratnarajah et al., 2016). This leads to regular monitoring and high-cost maintenance activities such as ballast tamping and stone blowing (Chan and Johan, 2016, Navaratnarajah and Indraratna, 2020). The insertion of geosynthetics into ballast or sub-ballast layer or at ballast and sub-ballast interface and the insertion of resilient rubber mats under the sleepers or under the ballast layer, reduce the rate of deterioration (Askarinejad et al., 2018, Navaratnarajah et al., 2015, Navaratnarajah and Indraratna, 2017, Navaratnarajah et al., 2018, Nimbalkar and Indraratna, 2016).

This study analyzed the shear stress and breakage behavior of ballast with various fouling materials such as sand and clay with different percentages under three different static normal loads by performing large scale direct shear tests. The standard direct shear apparatus is not capable to conduct the tests with these larger ballast

materials. Therefore a large-scale cylindrical direct shear apparatus was used for this study.

2 LABORATORY TESTS

2.1 *Material collection*

Materials used in this study are ballast and fouling materials such as river sand and clay. Ballast was collected from the Gampola stockpile, clay material was collected from Digana area and available river sand in Geotechnical laboratory was used. First, the ballast material was sieved using ISO 3310-1 standard sieve series and particles with various sizes were separated. Then, the ballast was washed with water and allowed to dry in order to remove any impurities like dust or other soil particles.

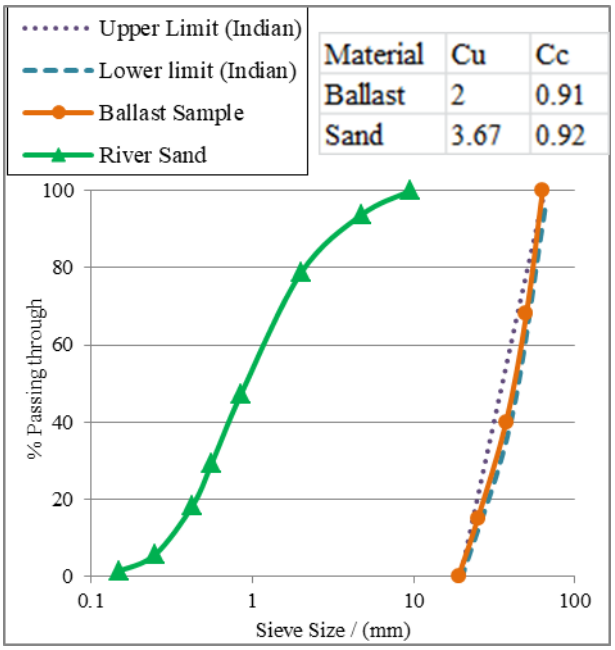

Fig. 1 Particle size distribution curve of the ballast sample and sand used in this study

The particle size distribution (PSD) is shown in Fig. 1, of the prepared ballast sample based on Indian standard which is adapted by Sri Lankan Railways. River sand was dried and sieved. Clay (LL = 37, PL = 23) was air-dried and pulverized to eliminate undesired particles.

2.2 *Large Scale Direct Shear Tests*

Large scale direct shear apparatus consists of two equal cylindrical halves with 400 mm diameter and 150 mm height each. The upper part is stationary and the lower part is movable with the application of shear load. A static load lever arm method is adapted to apply the normal load to the test material through a vertically movable top loading plate. The components of this test apparatus are illustrated in Fig. 2.

Fig. 2 Large scale direct shear test apparatus

The field unit weight of 16.1 kN/m^3 (Dissanayake et al., 2016) was maintained throughout the tests. The calculated amounts of ballast by sizes based on PSD were mixed properly before placing them into the apparatus. The ballast was placed into the apparatus in three layers, each layer was compacted using a rubber-padded hammer to attain field density. For sand fouled ballast, 10% and 15% fouling by ballast mass of sand were used. The sand was poured on top of the ballast sample and forced settled down into the voids of the ballast using a shutter vibrator.

(a) (b)

(c)

Fig. 3 Large scale direct shear test samples of (a) Fresh ballast; (b) Sand fouled ballast; (c) Clay fouled ballast

However, for clay fouled ballast 5% fouling by ballast mass of clay was coated to the ballast using the wet mixing method before placing it into the apparatus. This method incorporates with real situation where the clay fouling happens via mud pumping (intrusion of clay from subgrade) and

surface runoff (in hill countries the clay particles are moved from mountains with rainwater runoff and deposited on top of the track foundation). After drying, the clay-coated ballast was placed into the apparatus in three layers. Fig. 3 shows the various test materials in the test apparatus, as explained above.

The large scale direct shear tests were conducted under various normal stresses such as 30, 60 and 90 kPa and a constant shearing rate of 4 mm/min. All tests were carried out up to a maximum of 15% shear strain (a horizontal displacement of 60 mm). Data logger was used in obtaining the readings of horizontal and vertical displacements and the shear load with the help of dial gauges and load cells, respectively.

3 RESULTS AND DISCUSSION

3.1 *Shear and dilation behavior of ballast with various normal loads*

Shear stress-strain variation of ballast is shown in Fig. 4. Shear stress of fresh ballast gradually increased with shear displacement and after reaching peak shear stress there was a marginal change in shear stress with horizontal displacement. There was an increase in shear stress with the normal load increment as predicted for ballast, and this increment was due to high frictional resistance attained by higher interlocking between angular particles. The shear stress variations of fouled ballast samples with shear strain as well as with various normal loads were followed the similar trend of fresh ballast. At lower normal loads like 30 and 60 kPa, the shear stress of fresh ballast is significantly higher than the fouled ballast. This was due to the lubricant behavior of fouled soil particles within the ballast void spaces. But in sand fouled ballast, the shear stress is larger than the fresh ballast at 90 kPa, because of the increase in friction resistance as a result of the rise in the overall density of the sample that restricts the independent movement of ballast particles and the buildup of contact at shear plane by the intrusion of sand particles. At 90 kPa, the lubricant behavior of clay was minimal compared with interparticle contacts. Therefore, there was a marginal reduction in shear stress of clay fouled ballast at 90 kPa than that of fresh ballast.

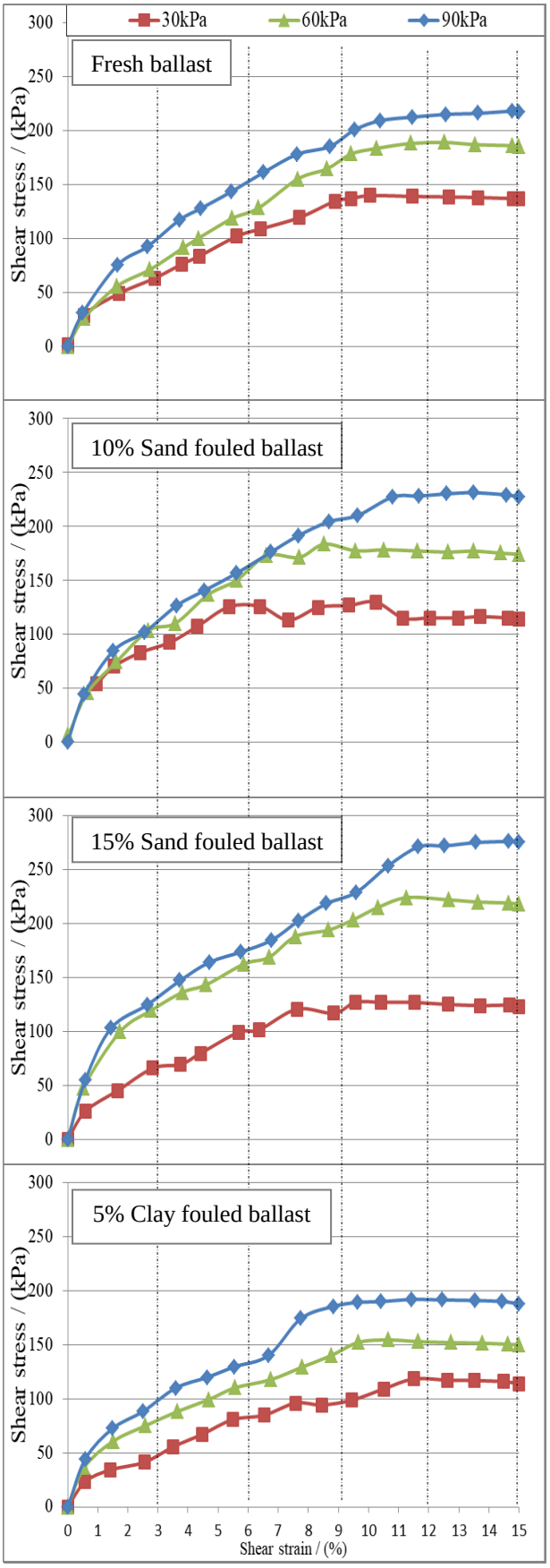

Fig. 4 Variation of shear stress with the shear strain of ballast

The peak shear stresses were obtained using shear stress vs shear strain curves. Fig. 5 exhibits the variation of peak shear stresses of fresh, 10 % sand fouled, 15 % sand fouled and 5 % clay fouled ballast samples under different normal stresses. As the cohesion of ballast is small, intercepts of trend lines were set to zero for the comparison of friction angle variation with fouling. It clearly indicates that the sand fouling increases the shear stress of ballast as the friction angle increased from 70° of fresh ballast to 71° and 73° of 10% and 15% sand fouled ballast, respectively. There is a reduction in friction angle from 70° of fresh ballast to 67° of 5% clay fouled ballast.

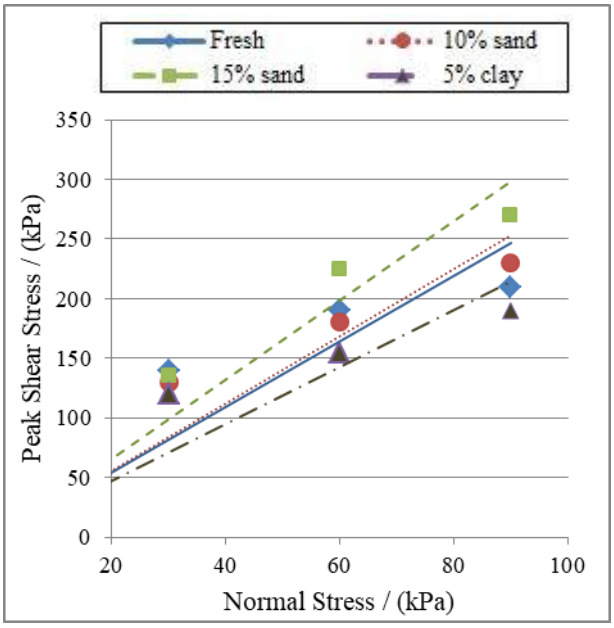

Fig. 5 Peak shear stress variation of fresh and fouled ballasts with various normal loads

Dilation of ballast particles is followed with initial compression for higher normal loads. With the continuous application of shearing, the granular ballast particles started to roll over the other ballast particles and dilated. Dilation was reduced with higher normal loads as well as with fouling. But a clear trend was not obtained from this test results.

3.2 *Degradation behavior of ballast with fouling and various normal loads*

The calculation method of Ballast Breakage Index (BBI) was proposed by Indraratna et al. (2005) and it uses the area of shifting in PSDs of each sample before and after testing with respect to an arbitrary boundary of maximum breakage as illustrated in Fig. 6.

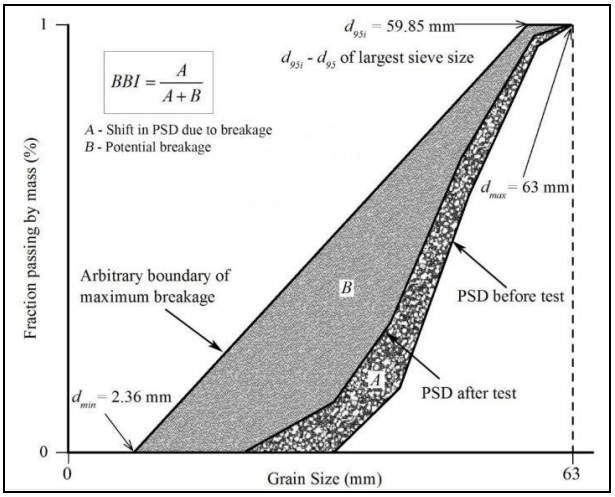

Fig. 6 Ballast Breakage Index (BBI) calculation method (Adopted from Navaratnarajah (2017))

BBIs of fresh and fouled ballasts with under different normal loadings is shown in Fig. 7. The BBI of ballast increased with the rise in normal stress, due to the compression of ballast that leads to high breakage at higher normal stresses. When the ballast is fouled with sand and clay materials, the BBI was reduced. This is because of the densification of the sample by sand intrusion and reduction in frictional resistance by clay intrusion. Moreover, the ballast breakage reduction is also resulted from the higher number of contacts in the fouled ballast compared to fresh ballast due to the accumulation of fines inside the voids in the ballast layer where fines partly transferred the contact forces (Ngo et al., 2014).

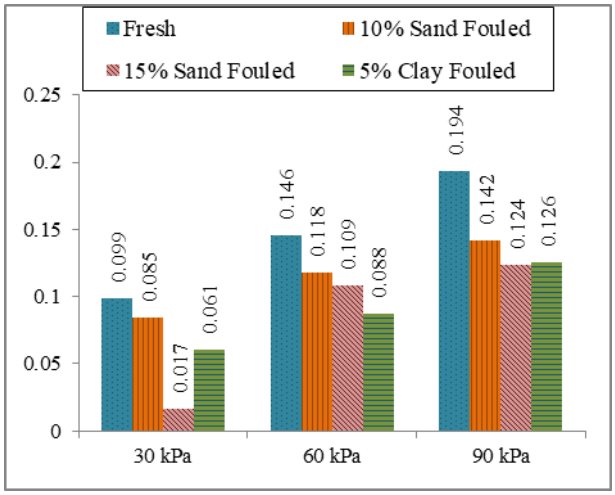

Fig. 7 Ballast breakage index with various normal loads of fresh and fouled ballast

4 CONCLUSIONS

Tests on fresh and fouled ballast under static loads clearly demonstrated that applied normal loads,

fouling material and fouling percentage have impacts on shear stress, dilation and breakage behavior of ballast. Shear stress increases with the increase in applied normal stresses. Shear stress of sand fouled ballast is higher than the fresh ballast due to the higher frictional resistance. Clay coated ballast particles slide over the other particles thus reduction in surface friction as well as a decline in shear stress than that of fresh ballast. Ballast breakage increased with normal loads and decreased with fouling agents.

Drainage property of ballast was not studied in this research. Permeability of the ballast layer has an influence on track longevity. Therefore, it is mandatory to study the variation in drainage pattern of ballast after fouling, despite the merits such as improvement in shear stress and decline in ballast breakage. As ballast is a coarse granular material, it does not show the same behavior under static and dynamic loading conditions. This research only considered the static loading condition.

ACKNOWLEDGMENTS

This research work was primarily supported by the University of Peradeniya Research Grant (Grant No: URG-2017-29-E). Accelerating Higher Education Expansion and Development (AHEAD) Operation of the Ministry of Higher Education funded by the World Bank (Grant No: AHEAD/RA3/DOR/STEM/No.63) is also acknowledged with the appreciation by the Authors. The authors convey their gratitude to the Railway District Engineer, Nanuoya and staff of Gampola Railway units of Sri Lankan Railways for their help and support in collecting the test materials.

REFERENCES

Al-Douri, Y.K., Tretten, P. and Karim, R. (2016). Improvement of railway performance: a study of Swedish railway infrastructure, Journal of Modern Transportation, 24(1): 22-37.

Anbazhagan, P., Bharatha, T. and Amarajeevi, G. (2012). Study of ballast fouling in railway track formations, Indian Geotechnical Journal, 42(2): 87-99.

Askarinejad, H., Barati, P., Dhanasekar, M. and Gallage, C. (2018). Field studies on sleeper deflection and ballast pressure in heavy haul track, Australian journal of structural engineering, 19(2): 96-104.

Ataei, S., Mohammadzadeh, S., Jadidi, H. and Miri, A. (2014). Effects of maintenance operations on railway track's mechanical behaviour by field load testing, International Journal of Pavement Engineering, 15(3): 215-227.

Chan, C.M. and Johan, S.F.S. (2016). Performance enhancement of railtrack ballast with rubber inclusions: a laboratory simulation, The 15th Asian Regional Conference on Soil Mechanics and Geotechnical Engineering, Japanese Geotechnical Society Special Publication, pp 1640-1643.

Dissanayake, D., Kurukulasuriya, L. and Dissanayake, P. (2016). Evaluation of shear strength parameters of rail track ballast in Sri Lanka, Journal of the National Science Foundation of Sri Lanka, 44(1): 61-67.

Esmaeili, M., Zakeri, J.A. and Mosayebi, S.A. (2014). Effect of sand-fouled ballast on train-induced vibration, International Journal of Pavement Engineering, 15(7): 635-644.

Indraratna, B., Lackenby, J. and Christie, D. (2005). Effect of confining pressure on the degradation of ballast under cyclic loading, Geotechnique, Institution of Civil Engineers, 55(4): 325-328.

Indraratna, B., Nimbalkar, S. and Christie, D. (2009). The performance of rail track incorporating the effects of ballast breakage, confining pressure and geosynthetic reinforcement, 8th International Conference on the Bearing Capacity of Roads, Railways, and Airfields, pp 5-24.

Navaratnarajah, S. and Indraratna, B. (2020). Stabilisation of Stiffer Rail Track Substructure Using Artificial Inclusion, Indian Geotechnical Journal: 1-8.

Navaratnarajah, S., Indraratna, B. and Nimbalkar, S. (2015). Performance of rail ballast stabilized with resilient rubber pads under cyclic and impact loading, International Conference on Geotechnical Engineering, pp 617-620.

Navaratnarajah, S.K. (2017). Application of rubber inclusions to enhance the stability of ballasted rail track under cyclic loading. Doctor of Philosophy, University of Wollongong.

Navaratnarajah, S.K. and Indraratna, B. (2017). Use of rubber mats to improve the deformation and degradation behavior of rail ballast under cyclic loading, Journal of geotechnical and geoenvironmental engineering, 143(6): 1-15.

Navaratnarajah, S.K., Indraratna, B. and Ngo, N.T. (2018). Influence of under sleeper pads on ballast behavior under cyclic loading: experimental and numerical studies, Journal of Geotechnical and Geoenvironmental Engineering, 144(9): 1-16.

Navaratnarajah, S.K., Indraratna, B. and Nimbalkar, S. (2016). Application of shock mats in rail track foundation subjected to dynamic loads, Procedia engineering, 143: 1108-1119.

Ngo, N.T., Indraratna, B. and Rujikiatkamjorn, C. (2014). DEM simulation of the behaviour of geogrid stabilised ballast fouled with coal, Computers and Geotechnics, 55: 224-231.

Nimbalkar, S. and Indraratna, B. (2016). Improved performance of ballasted rail track using geosynthetics and rubber shockmat, Journal of Geotechnical and Geoenvironmental Engineering, 142(8): 1-13.

Tennakoon, N., Indraratna, B., Rujikiatkamjorn, C. and Nimbalkar, S. (2012). Assessment of ballast fouling and its implications on track drainage, 11th Australia - New Zealand Conference on Geomechanics: Ground Engineering in a Changing World, pp 421-426.

Track Deflection At Transition Zones Of Ballasted Rail Tracks – A Field Study

R. M. D. L. Rathnayake
Department of Civil Engineering, University of Peradeniya, Peradeniya, Sri Lanka.

H. G. S. Mayuranga
Department of Civil Engineering, University of Peradeniya, Peradeniya, Sri Lanka.

C. S. Bandara
Department of Civil Engineering, University of Peradeniya, Peradeniya, Sri Lanka.

J. A. S. C. Jayasinghe
Department of Civil Engineering, University of Peradeniya, Peradeniya, Sri Lanka.

S. K. Navaratnarajah
Department of Civil Engineering, University of Peradeniya, Peradeniya, Sri Lanka.

ABSTRACT: Track deflection is a major problem in conventional ballasted railway tracks which should be controlled to provide a safe and comfortable ride. The dynamic track deflection is governed by the stiffness and damping properties of all the parts of the track system. Higher track deflections have been observed at transitions zones of bridges, culverts, and tunnels due to the change of track stiffness caused by the change of materials below the ballast layer. This problem is worst for older railway tracks with poor maintenance. Hence, the present study was carried out to investigate the track deflection of transition zones of an old ballasted railway track with an old steel bridge in Sri Lanka. This article presents and discusses the measurements made. The results highlight the variation of the deflection behavior along the track.

1. INTRODUCTION

The most economical and widely used transportation mode of many countries is the ballasted railway network. A typical ballasted railway track composes of steel rails, sleepers, ballast layer, sub-ballast layer, and subgrade. A railway network composes of many complex subsystems like bridges, culverts, tunnels, road crossings, switches, and elevated structures. The regular ballasted tracks approaching these conjunction points are called transition zones. These are the most vulnerable areas along railway lines where the vertical stiffness of the track changes significantly (Heydari-Noghabi et al., 2017, Navaratnarajah and Indraratna, 2017).

As per literature, the primary causes of track degradation near transition zones are uneven stiffness and damping between the bridge and its approach, geotechnical causes, and soil water responses. The amount of damage done due to these issues varies on secondary causes such as trainload, train speed, the height of embankment, type of abutment and bridge joints (Gallage et al., 2013).

The sudden change of the track stiffness when a train moves between the ballasted track underlain by natural ground and the track underlain by a hard structure causes increments in dynamic loads (Navaratnarajah et al., 2015). This leads to pumping ballast, ballast breakage, hanging ties, rail battering, and deterioration of track geometry (Davis and Li, 2006, Navaratnarajah, 2017). This results in high maintenance costs, reduction of ride quality, train delays, increased wear and tear of track and vehicle components and speed restrictions (Coelho et al., 2011, Indraratna et al., 2019, Li and Davis, 2005, Navaratnarajah et al., 2016, Shan et al., 2013, Wang and Markine, 2017, Woodward et al., 2014).

Many mitigation techniques for track degradation of transition zones are suggested and tested in the literature. Increasing the damping of the bridge, reducing track settlement and increasing track modulus of the ballasted track at the transition zone are the major principles followed in most of these techniques. Reducing stiffness at the stiff side using sleeper pads, ballast mats, using additional rails and transition slabs, concrete pilling, the formation of stone columns and use of geogrids are some of the mitigation techniques applied (Davis and Li, 2006,

Gallage et al., 2013, Indraratna et al., 2015, Insa et al., 2012, Navaratnarajah and Indraratna, 2020, Navaratnarajah et al., 2018).

Even though the track deterioration at the transition zones is a critical problem related to railway networks, only a little quantitative research has been undertaken in these zones. This research was done in order to quantify the existing problem and understand the mechanism behind it.

2. METHODOLOGY

To investigate the track deflection at the transition zones of old ballasted railway tracks in Sri Lanka, a study was carried out on a test stretch that contained a steel bridge structure, a transition zone with timber sleepers, and then a regular open track with concrete sleepers on the ground. Bridge location was in Colombo-Avissawella mainline in between Narahenpita and Kirulapane railway stations. The bridge was supported by two brick abutments. The total span of the bridge is 32.2 m. In this study, two 66 tons, class M7 locomotives each having four axles were coupled and used at different speeds. The deflection of three adjacent sleepers and a location on the bridge 1m away from the edge towards the bridge was measured using displacement transducers.

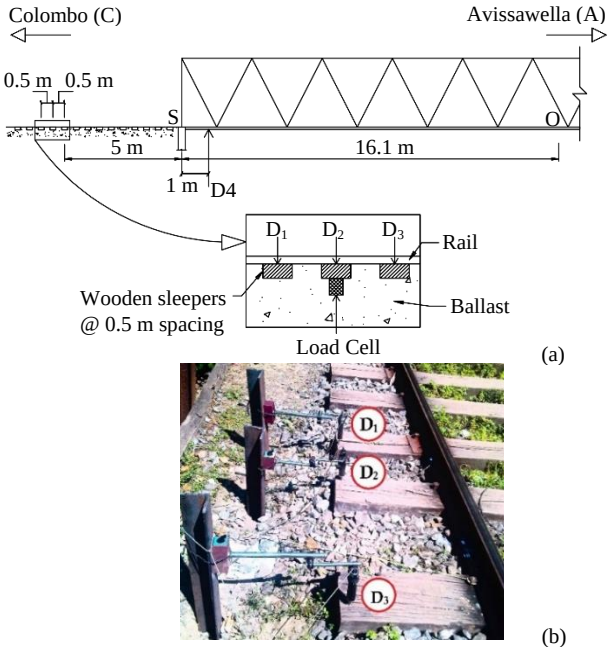

Fig. 1: Arrangement of displacement transducers and load cell (a) schematic drawing; (b) assembly in the test location

Deflection at the center of the bridge was observed using a theodolite. A load cell was used to measure the load on the ballast just below one sleeper. The arrangements of displacement transducers and the load cell are represented in Fig. 1.

Two test runs were done from A to C (bridge-embankment approach) with speeds 26 km/h and 32 km/h. Two test runs were done from C to A (embankment-bridge approach) with speeds 29 km/h and 37 km/h. The readings of the deflection transducers, D_1, D_2, and D_3 were collected against time. The negative values of data exhibit the downward displacements and positive values exhibit the upward displacements.

3. RESULTS AND DISCUSSION

Time displacement histories of D_2 displacement transducer for four speeds are presented in Fig. 2. Similar behavior was observed near D_1 and D_3. Fig. 2(a) and (b) represent the time when the train was leaving the bridge in the direction towards Colombo and Fig. 2(c) and (d) represent the time when the train was approaching the bridge in the opposite direction. On all four occasions, the displacement variation with the passing of the wheelset is clearly visible. Also, upward movements of the sleeper (positive displacement) are observed at the time when the train approaches and leaves the sleeper. When the train is travel leaving the bridge, the displacement of the sleeper when the train is leaving the sleeper is much higher than the displacement when the train is approaching the sleeper. This behavior is vise versa when the train travels in the opposite direction approaching the bridge.

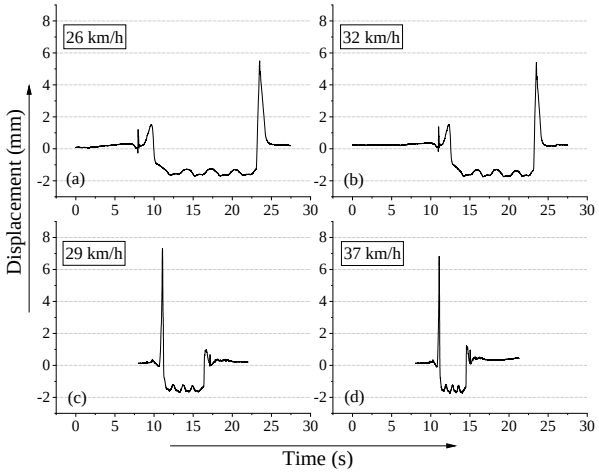

Fig. 2: Variation of displacement of sleeper with time measured by D_2 gauge (Positive [+] is upward displacement)

Variation of maximum negative and positive displacements with speed measured by the displacement transducers D_1, D_2, and D_3 are plotted in Fig. 3(a) and (b) respectively. During the two test runs with speeds, 26 km/h, and 32 km/h the train was traveling from Avissawella to Colombo. During the other two test runs, the train was traveling from Colombo to Avissawella. Regardless of the direction, maximum negative displacements

have increased in both D_1 and D_2 locations. At D_3 this trend cannot be observed. Although the displacement is increased with the speed when the train travels in the same direction, displacements are reduced when the train travels from the transition zone to the bridge. This behavior can be seen at all three points for the positive displacements when the train is leaving the bridge. Maximum displacements of D_1, D_2, and D_3 corresponding to the train speeds are tabulated in Table 1.

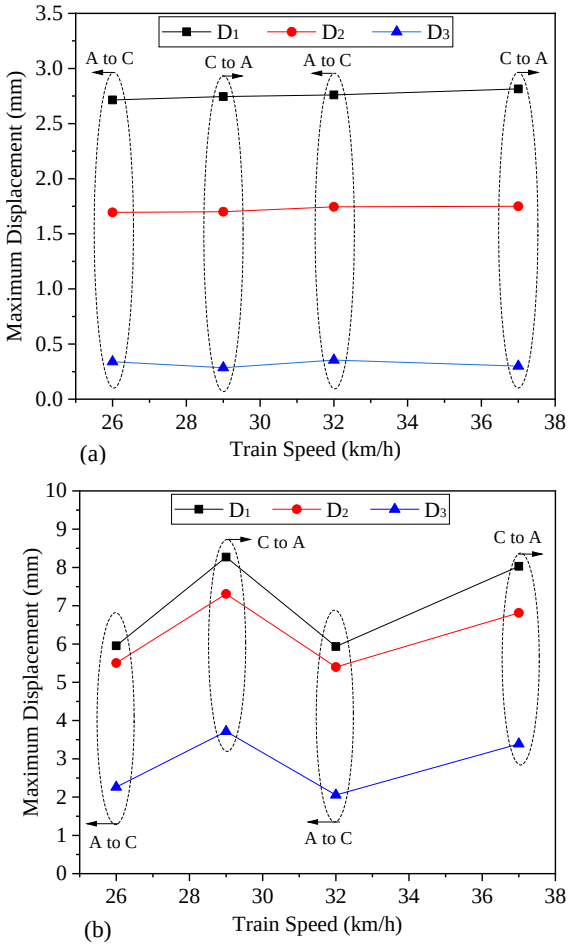

Fig. 3: Variation of maximum (a) negative and (b) positive sleeper displacement with time

Table 1: Maximum displacements correspond to train speeds

Speed (km/h)	Direction	Maximum [-] displacement(mm)		
		D_1	D_2	D_3
26	A to C	-2.715	-1.695	-0.340
29	C to A	-2.745	-1.700	-0.285
32	A to C	-2.760	-1.745	-0.355
37	C to A	-2.815	-1.750	-0.300
		Maximum [+] displacement(mm)		
		D_1	D_2	D_3
26	A to C	5.955	5.505	2.260
29	C to A	8.270	7.310	3.715
32	A to C	5.935	5.400	2.055
37	C to A	8.030	6.815	3.390

Variation of the average value of the maximum displacement for each speed along the rail track is presented in Fig. 4. The maximum displacement of the sleepers has reduced in the direction towards the bridge. At the support of the bridge a concrete sleeper rest on the brick abutment. Therefore, the deflection at that point is negligible and hence assumed to be zero. A displacement gauge attached underneath the bridge 1 m away from the support has a maximum reading of -1.445 mm. The maximum deflection at the center of the bridge is observed to be -18 mm.

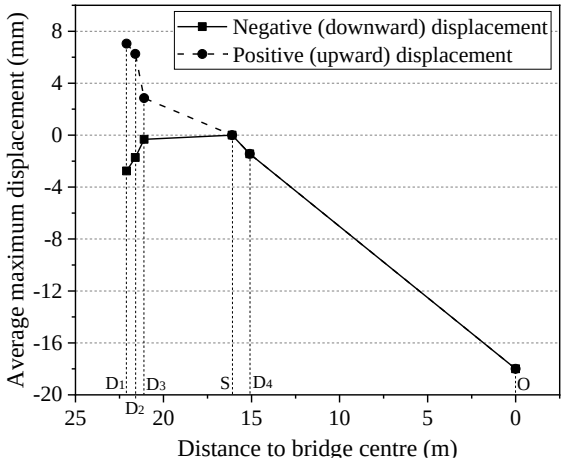

Fig. 4: Variation of average maximum displacement with the distance

The data obtained by the load cell (load versus time) is plotted in Fig. 5. The load cell was placed directly under the sleeper in which the D_2 displacement gauge is attached. It is assumed that the load cell data represents the load transferred to the ballast underneath the sleeper. Fig. 5(a) and (b) show the load vs time when the train is leaving the bridge and (c) and (d) show the time when the train is traveling in the opposite direction approaching the bridge.

Variation of the load with the passing of the wheelsets is clearly observed. The peak values of the loads correspond to an axle being directly over the load cell. A sudden downward slope occurs during the unloading of the track in between two sets of axels of a locomotive. When the train was leaving the bridge (Fig. 5(a) and (b)) the front wheelset of every axel has resulted in a higher spike than the back wheelset. Also, during the two runs in this direction, the maximum load corresponds to the front wheelset of the third axel. During the two runs in the opposite direction from the transition zone to the bridge, the back-wheel set of all the axels have obtained higher load spikes than the front-wheelsets. The highest value was recorded when the back wheelset of the second axel of the first locomotive was traveling over the load cell.

Therefore, it can be concluded that there is an influence of the direction of the train for the track deterioration of a transition zone.

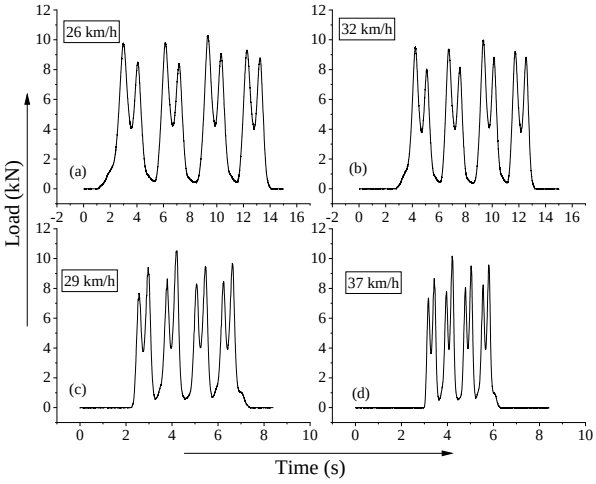

Fig. 5: Variation of load with time

The maximum load corresponding to each speed is plotted in Fig. 6. The maximum load was obtained when the train was traveling towards the bridge. When considering both directions separately, the load has been decreased with the increment in train speed.

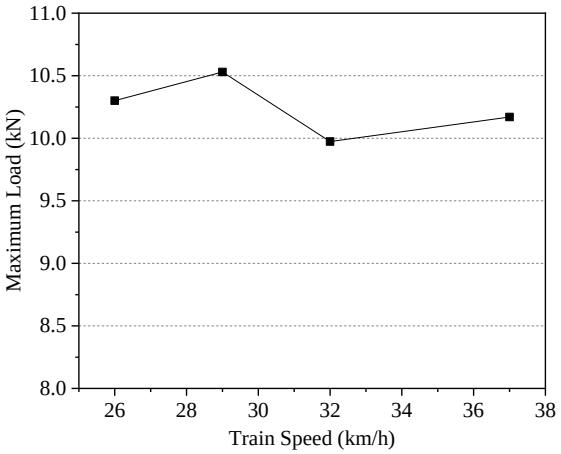

Fig. 6: Variation of maximum load with train speed

4. CONCLUSIONS

The short-term dynamic behavior when a train is traveling over a transition zone of an old steel bridge is measured, analyzed, and presented in this paper. The obtained results clearly demonstrate that there is a change in the deflection behavior on the track with the direction of the train. Steel bridge deflects in the middle due to the moving harmonic force applied by the train. The maximum deflection on the bridge was observed as -18 mm.

It can be observed that the average maximum displacement is increased along the track when measured away from the stiff edge of the bridge. When compared with the studies in literature, we can assume that this increment will be diminished when the train travels away from the transition zone leaving the bridge.

5. FUTURE WORK

Using the obtained measurements, a finite element model is to be developed and validated to have a parametric study by changing different parameters such as trainload, speed, and the properties of the test stretch including the steel bridge and the transition zone.

ACKNOWLEDGMENTS

The support provided by Accelerating Higher Education Expansion and Development (AHEAD) operation funded by the World Bank (Grant No: AHEAD/RA3/DOR/STEM/No.63) is highly appreciated by the authors. The collaboration of the Open University of Sri Lanka and the Department of Railways in this field study is greatly appreciated.

REFERENCES

Coelho, B., Hölscher, P., Priest, J., Powrie, W. and Barends, F. (2011). An assessment of transition zone performance, Proceedings of the Institution of Mechanical Engineers, Part F: Journal of Rail and Rapid Transit, 225(2): 129-139.

Davis, D. and Li, D. (2006). Design of track transitions, Research Results Digest 79. Transportation Technology Center, Inc., Pueblo, Colorado: 4-15.

Gallage, C., Dareeju, B. and Dhanasekar, M. (2013). State-of-the-art: track degradation at bridge transitions, Proc., Proceedings of the 4th international conference on structural engineering and construction management 2013, pp 40-52.

Heydari-Noghabi, H., Varandas, J., Esmaeili, M. and Zakeri, J. (2017). Investigating the influence of auxiliary rails on dynamic behavior of railway transition zone by a 3D train-track interaction model, Latin American Journal of Solids and Structures, 14(11): 2000-2018.

Indraratna, B., Navaratnarajah, S.K., Nimbalkar, S., Rujikiatkamjorn, C. and Neville, T. (2015). Performance monitoring: case studies of tracks stabilised by geosynthetic grids and prefabricated vertical drains.

Indraratna, B., Sajjad, M.B., Ngo, T., Correia, A.G. and Kelly, R. (2019). Improved performance of ballasted tracks at transition zones: A review of experimental and modelling approaches, Transportation Geotechnics: 100260.

Insa, R., Salvador, P., Inarejos, J. and Roda, A. (2012). Analysis of the influence of under sleeper pads on the railway vehicle/track dynamic interaction in transition zones,

Proceedings of the Institution of Mechanical Engineers, Part F: Journal of Rail and Rapid Transit, 226(4): 409-420.
Li, D. and Davis, D. (2005). Transition of railroad bridge approaches, Journal of geotechnical and geoenvironmental engineering, 131(11): 1392-1398.
Navaratnarajah, S. and Indraratna, B. (2020). Stabilisation of Stiffer Rail Track Substructure Using Artificial Inclusion, Indian Geotechnical Journal: 1-8.
Navaratnarajah, S., Indraratna, B. and Nimbalkar, S. (2015). Performance of rail ballast stabilized with resilient rubber pads under cyclic and impact loading.
Navaratnarajah, S.K. (2017). Application of rubber inclusions to enhance the stability of ballasted rail track under cyclic loading.Ph. D. Thesis, University of Wollongong, Austrailia.
Navaratnarajah, S.K. and Indraratna, B. (2017). Use of rubber mats to improve the deformation and degradation behavior of rail ballast under cyclic loading, Journal of geotechnical and geoenvironmental engineering, 143(6): 04017015.
Navaratnarajah, S.K., Indraratna, B. and Ngo, N.T. (2018). Influence of under sleeper pads on ballast behavior under cyclic loading: experimental and numerical studies, Journal of Geotechnical and Geoenvironmental Engineering, 144(9): 04018068.
Navaratnarajah, S.K., Indraratna, B. and Nimbalkar, S. (2016). Application of shock mats in rail track foundation subjected to dynamic loads, Procedia engineering, 143: 1108-1119.
Shan, Y., Albers, B. and Savidis, S.A. (2013). Influence of different transition zones on the dynamic response of track–subgrade systems, Computers and Geotechnics, 48: 21-28.
Wang, H. and Markine, V. (2017). Analysis and improvement of the dynamic track behaviour in transition zone, Proc., Tenth international conference on the bearing capacity of roads, railways and Airfields. Taylor & Francis Group. London: Athens, Greece, pp.
Woodward, P.K., Laghrouche, O. and El-kacimi, A. (2014). Railway track transition dynamics and reinforcement using polyurethane geocomposites, Geotechnical Engineering, 45(1): 28-38.

Large scale direct shear test on fouled ballast: a numerical study

R. M. D. L. Rathnayake
Department of Civil Engineering, University of Peradeniya, Peradeniya, Sri Lanka.

S. K. Navaratnarajah
Department of Civil Engineering, University of Peradeniya, Peradeniya, Sri Lanka.

ABSTRACT: Due to the increasing population growth, the traffic congestion of highways is increasing day by day. Hence, using ballasted railway tracks with high-speed trains having heavy axel loads has become more popular. In ballasted tracks, the ballast layer transmits the loads from sleepers to the track foundation. Also, the ballast layer absorbs energy and vibrations transferred from a moving train. Ballast breakage occurs due to repeated wheel loads. Also, due to various external factors such as washing out fines, winds, and mud pumping ballast become fouled with materials such as sand, silt, and clays. These phenomena lead the ballast layer to change its strength properties. In this study, a numerical model was developed using ABAQUS to simulate large-scale direct shear tests on the ballast. The model is validated using experimental results and a parametric study is performed to predict the change of ballast shear behavior with varying loading and varying amount of fine intrusion in ballast.

Keywords: Ballast; Fine intrusion; Large scale direct shear test; Numerical model

1. INTRODUCTION

A conventional ballasted railway track consists of a superstructure that includes sleepers, rails, and a fastening system, and a substructure that includes a ballast layer, sub-ballast layer, and subgrade Navaratnarajah and Indraratna (2020). The ballast layer transmits the trainload from sleepers to subgrade while absorbing the energy and vibration generated during train passage. Sub ballast helps to further distribute applied cyclic stress to the foundation and acts as a blanket to prevent inter-penetration of materials from the ballast and subgrade (Indraratna et al., 2020). Ballast is generally coarse angular aggregates of size between 6 mm to 64 mm (Kennedy, 2011). Sub ballast is finer aggregate than ballast and subgrade is either soil or rock formation.

Due to ballast particle degradation during the repeated trainload, and infiltration of foreign particles due to various environmental conditions such as floods, ballast tend to be fouled with fine material such as clay and sand (Navaratnarajah, 2017). These fine materials get accumulated in voids of ballast and eventually reduces the shear strength, and drainage capability of ballast (Indraratna et al., 2011, Navaratnarajah and Indraratna, 2020). Reduction of shear strength leads to more rail wear, loss of lateral stability of the superstructure components (TolouKian et al., 2018). Even though plenty of railway derailments are reported annually due to the loss of shear strength of fouled ballast, there are very few researches carried out on the effect of foul material on the shear strength of railway ballast.

The study of the effect of shear behavior with fouling material on railway ballast is important to maintain the railway tracks to function efficiently. This study focuses on the numerical modeling of large-scale direct shear test on fouled ballast. A finite element model of direct shear apparatus is developed to simulate direct shear test on railway ballast material fouled with fine particles and it is calibrated and validated using available test results from a previous study conducted by changing the applied normal stress and type of fouled materials

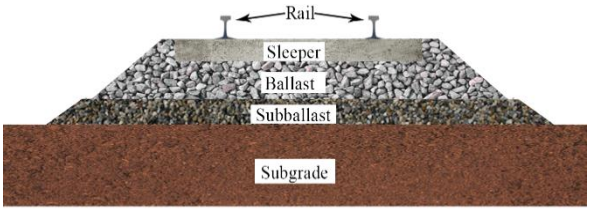

Fig. 1: Typical Geometry of Ballasted railway track

(sand and clay). The validated finite element model has been used to conduct various parametric studies by changing the foul material type and fouling percentage to predict how the shear strength of ballast varies with the foul material and fouling percentage.

2. LABORATORY TESTS

Large scale direct shear test which can be conducted using actual size ballast particles is the most effective laboratory test which can be conducted to evaluate the shear strength properties of ballast. Danesh et al. (2018) has conducted a large-scale direct shear test on fresh and degraded ballast specimens using a large direct shear box to investigate the effect of ballast degradation on its shear strength. Kharanaghi and Briaud (2020) conducted a series of large-scale direct shear tests on crushed granite to investigate the shear behavior and influence of the normal stress. Stark et al. (2014) and TolouKian et al. (2018) have designed and created Large-scale direct shear testing machines to test coarse-sized aggregates under real normal ballast loads without scaling down the ballast material. Ngo et al. (2018) has investigated the shear stress-strain behavior of geosynthetic-reinforced ballast using a large-scale direct shear test device. Dissanayake et al. (2016) and Navaratnarajah et al. (2019) have conducted laboratory tests to evaluate shear strength properties of fresh and fouled ballast in Sri Lanka using large-scale direct shear apparatus.

The experimental study done by Navaratnarajah et al. (2019) includes a series of direct shear tests conducted on fresh ballast and ballast fouled with sand and clay. Tests were conducted with varying percentages of foul materials and varying normal stresses. The large-scale direct shear apparatus used is shown in Fig. 2. This apparatus consists of a top ring that is fixed and a bottom ring that can be moved with applied lateral load. Each ring has a diameter of 400 mm and a height of 150 mm. A normal load is applied using a loading plate and a lateral load is applied to the bottom ring at a constant rate of 4 mm/min using a hydraulic loading system.

3. FINITE ELEMENT MODELING

Large scale direct shear test is modeled using finite element modeling software by few researchers. Moayed et al. (2012) has conducted a 3D finite element analysis to simulate large-scale direct shear test on sandy clay using ABAQUS software. Wang et al. (2018) have done discrete element modeling of direct shear test on granular particles

Fig. 2: Large Scale Direct Shear Apparatus.

to incorporate inter-particle contact forces. Other than these many researchers have modeled 3D finite element models of railway track components using various modeling techniques. Biabani et al. (2016), Leshchinsky and Ling (2013), and Navaratnarajah et al. (2018) have modeled railway ballast using the Drucker-Prager yield criterion. Biabani et al. (2016) and Navaratnarajah et al. (2018) have used C3D8R hexahedral elements while Leshchinsky and Ling (2013) have used C3D4R tetrahedral 4-noded elements. Finite element software such as ABAQUS and Midas/GTS is used in developing these models.

In this study, a 3D finite element model to simulate direct shear test on ballast is developed using ABAQUS finite element software. The model was developed according to the dimensions and properties found in the large-scale direct shear test apparatus used by Navaratnarajah et al. (2019). The ballast particles filled into the rings are modeled using C3D8R hexahedral elements. This element type is most used and suitable in modeling cylindrical parts.

This model is a pressure-dependent analysis and therefore Drucker-Prager yield criterion was used when modeling ballast. Ballast was modeled as a continuum using the overall properties of ballast material mixed with sand. The top ring and the bottom ring are modeled as discrete rigid elements to save computational time. The mesh size was selected after a mesh convergence study which gave a converged numerical model for displacement at mesh size 20 mm.

To simulate the experimental procedure of the direct shear test, the upper ring of the model was fixed to restrict motion to any direction and a horizontal displacement at the rate of 4 mm/min was applied to the bottom ring. The normal load was applied as pressure and the simulations were

done by changing the normal pressures from 30 kPa, to 60 kPa, and 90 kPa and changing fouling material type (sand or clay) and the fouling percentage (5%, 10%, and 15%). Fig. 3 shows the finite element discretization of the direct shear sample.

The results of the model were compared with the results of experimental studies done by Navaratnarajah et al. (2019) to validate the numerical model. The material properties used for the numerical model are tabulated in Table 1 and results of the numerical model and experimental data are plotted in Figs. 4(a), (b), (c), and (d). These results include the Shear stress-strain behavior for fresh ballast, 5% clay fouled ballast, 10% sand fouled ballast, and 15% sand fouled ballast for 30 kPa, 60 kPa, and 90 kPa normal loads, respectively.

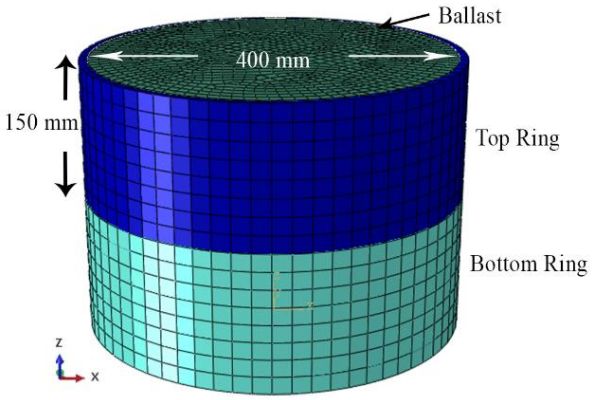

Fig. 3: Finite Element Model

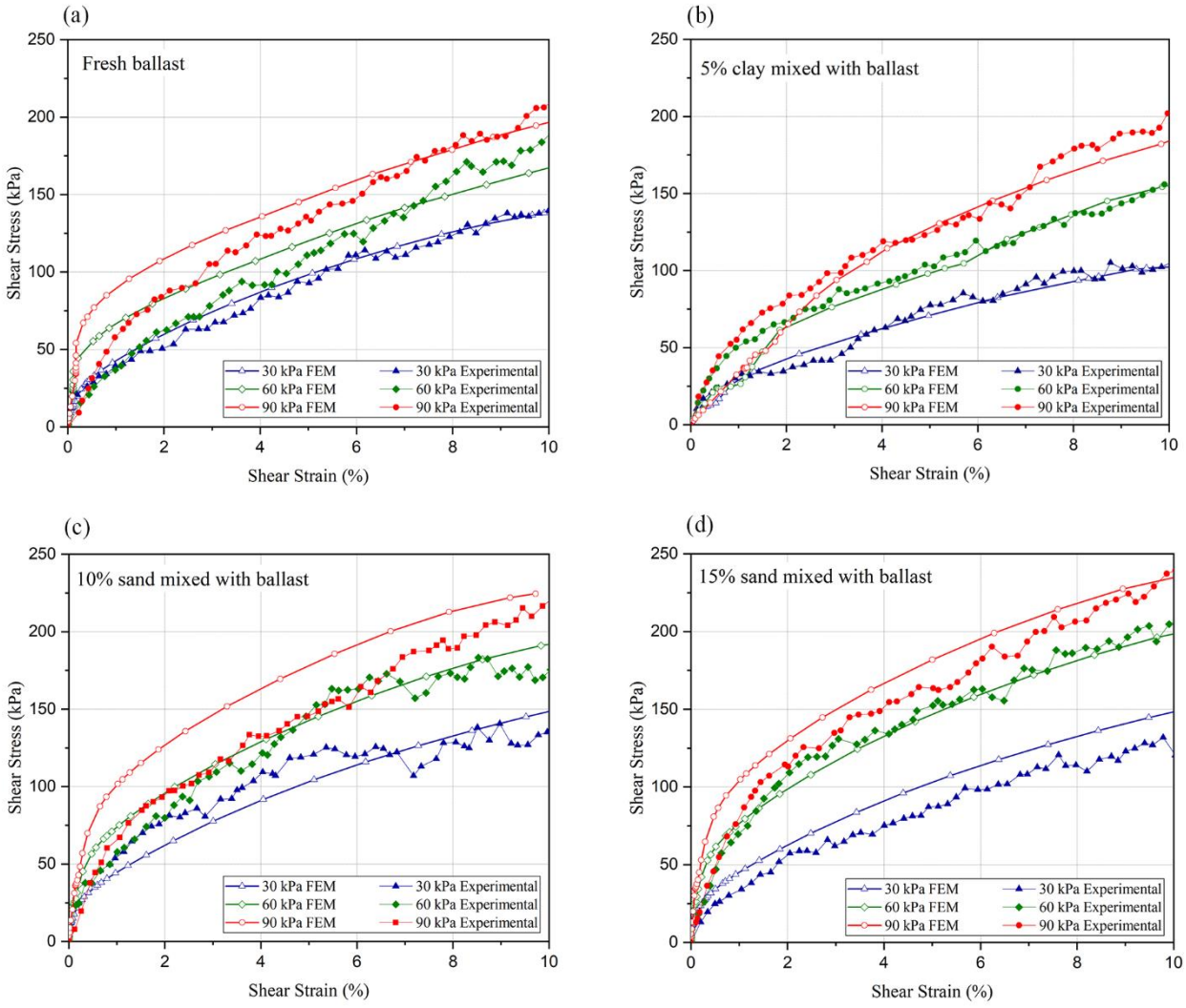

Fig. 4: Shear stress vs shear strain behavior of ballast under 30kPa, 60kPa, and 90kPa normal stress loads (a) Fresh ballast; (b) 5% clay mixed with ballast; (c) 10% sand mixed with ballast, and (d) 15% sand mixed with ballast

Table 1: Material properties used in the FEM model

Material Properties	Fresh ballast	Ballast fouled with 5% clay	Ballast fouled with 10% sand	Ballast fouled with 15% sand
Density(kg/m^3)	1640	1750	1805	1900
Young's modulus	3	1.56	6	7.5
Friction angle	40	38	43	45
Dilation angle	15	15	15	15
Poisson's ratio	0.25	0.25	0.28	0.29

4. RESULTS AND DISCUSSION

4.1. MODEL VALIDATION

Generally, it can be observed that shear stress is increasing with vertical pressure during both experimental and numerical studies. When considering fresh ballast, it can be observed from Fig. 4(a) that the experimental shear stress vs shear strain values and numerical simulation values tally with each other with a considerable accuracy during the application of 30 kPa. During the application of 60 kPa and 90kPa, the numerical analysis data come close with the experimental data only after achieving 6% of the shear strain.

When 5% clay is mixed with ballast, the shear strength of the ballast shows a reduction during both experimental study and numerical analysis as shown in Fig. 4(b). This is due to the reduction of shear friction between ballast due to clay particles. The intrusion of clay particles reduces the friction angle of the ballast material.

Fig. 4(c) and (d) show the behavior of ballast when fouled by 10% and 15% sand. The shear stress of ballast is increasing with shear stress in sand fouled ballast than in fresh ballast. This is due to the increment of ballast density and Young's modulus with increasing fines percentage. The overall deviations of numerical analysis data and experimental data can be mainly because of the discrete element behavior of real ballast which is difficult to be captured by modeling ballast as a continuum material.

4.2. PARAMETRIC STUDY

Using the validated numerical model, a parametric study was done to observe the shear stress-strain behavior of fouled ballast with 10% sand and 15% sand with normal pressures increased up to 120 kPa and 150 kPa. Figs. 5(a) and (b) shows the shear stress vs shear strain behavior of sand fouled ballast under 30 kPa, 60 kPa, 90 kPa, 120 kPa, and 150 kPa normal stress loads with 10% of sand mixed with fresh ballast and 15% of sand mixed with fresh ballast respectively. According to the

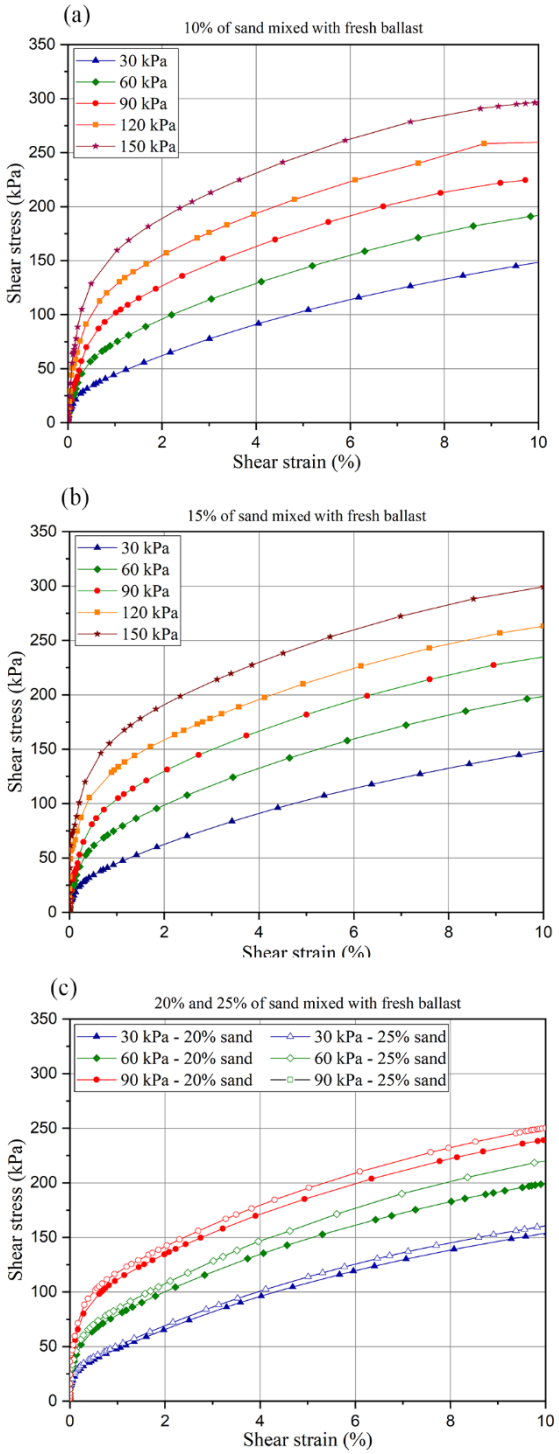

Fig. 5: Shear stress vs shear strain behavior of sand fouled ballast for varying normal stress loads (a) 10% of sand mixed with fresh ballast; (b) 15% of sand mixed with fresh ballast, and (c) 20 % and 25 % weight of sand fines mixed with fresh ballast

results, it is seen that sand mixed ballast is capable of carrying higher normal stress loads of 120 kPa and 150 kPa. This is due to the high strength of sand mixed ballast. The clay mixed ballast showed failure at the shear plane at low strain value and therefore a parametric study was not continued for the ballast fouled with clay.

By extrapolating the properties such as density, Young's modulus and friction angle of ballast material to achieve the properties of 20% and 25% sand fines another parametric study was carried out. The results are represented in Fig. 5(c). It is observed that shear strength is increased with shear strain when the fouling percentage is high.

5. CONCLUSIONS

A Numerical Model to simulate large-scale direct shear test on railway ballast material is developed using ABAQUS software and validated using experimental data. Simulations are done using the validated model by changing the material properties of ballast to achieve the properties of fouled ballast with fouling material such as clay and sand. The intrusion of clay is showing a reduction of shear strength in ballast due to the reduction between shear friction in ballast while the intrusion of sand particles has increased the shear strength of ballast. This model can be used to predict the shear behavior of fouled ballast up to a certain accuracy.

ACKNOWLEDGMENTS

The support provided by Accelerating Higher Education Expansion and Development (AHEAD) operation funded by the World Bank (Grant No: AHEAD/RA3/DOR/STEM/No.63) is highly appreciated by the authors.

REFERENCES

Biabani, M.M., Indraratna, B. and Ngo, N.T. (2016). Modelling of geocell-reinforced subballast subjected to cyclic loading, Geotextiles and Geomembranes, 44(4): 489-503.

Danesh, A., Palassi, M. and Mirghasemi, A.A. (2018). Evaluating the influence of ballast degradation on its shear behaviour, International Journal of Rail Transportation, 6(3): 145-162.

Dissanayake, D., Kurukulasuriya, L. and Dissanayake, P. (2016). Evaluation of shear strength parameters of rail track ballast in Sri Lanka, Journal of the National Science Foundation of Sri Lanka, 44(1).

Indraratna, B., Qi, Y., Tawk, M., Heitor, A., Rujikiatkamjorn, C. and Navaratnarajah, S.K. (2020). Advances in Ground Improvement Using Waste Materials for Transportation Infrastructure, Proceedings of the Institution of Civil Engineers-Ground Improvement: 1-44.

Indraratna, B., Su, L.-j. and Rujikiatkamjorn, C. (2011). A new parameter for classification and evaluation of railway ballast fouling, Canadian Geotechnical Journal, 48(2): 322-326.

Kennedy, J. (2011). A full-scale laboratory investigation into railway track substructure performance and ballast reinforcement. Heriot-Watt University.

Kharanaghi, M.M. and Briaud, J.-L. (2020). Large-scale direct shear test on railroad ballast, Proc., Geo-Congress 2020: Modeling, Geomaterials, and Site Characterization, American Society of Civil Engineers Reston, VA, pp 123-131.

Leshchinsky, B. and Ling, H. (2013). Effects of geocell confinement on strength and deformation behavior of gravel, Journal of Geotechnical and Geoenvironmental Engineering, 139(2): 340-352.

Moayed, R.Z., Tamassoki, S. and Izadi, E. (2012). Numerical modeling of direct shear tests on sandy clay, World Academy of Science, Engineering and Technology, 61: 1093-1097.

Navaratnarajah, S. and Indraratna, B. (2020). Stabilisation of Stiffer Rail Track Substructure Using Artificial Inclusion, Indian Geotechnical Journal: 1-8.

Navaratnarajah, S.K. (2017). Application of rubber inclusions to enhance the stability of ballasted rail track under cyclic loading.Phd Thesis, University of Wollongong.

Navaratnarajah, S.K., Indraratna, B. and Ngo, N.T. (2018). Influence of under sleeper pads on ballast behavior under cyclic loading: experimental and numerical studies, Journal of Geotechnical and Geoenvironmental Engineering, 144(9): 04018068.

Navaratnarajah, S.K., Venuja, S., Shahmi, N.M. and Rimas, N.M. (2019). Influence of fine materials on stress-strain and degradation behavior of railway ballast under static loading conditions, 10th International Conference on Structural Engineering and Construction Management, pp.

Ngo, N.T., Indraratna, B., Ferreira, F.B. and Rujikiatkamjorn, C. (2018). Improved performance of geosynthetics enhanced ballast: laboratory and numerical studies, Proceedings of the Institution of Civil Engineers-Ground Improvement, 171(4): 202-222.

Stark, T.D., Swan, R.H. and Yuan, Z. (2014). Ballast direct shear testing, Proc., 2014 Joint Rail Conference, American Society of Mechanical Engineers Digital Collection, pp.

TolouKian, A.R., Sadeghi, J. and Zakeri, J.-A. (2018). Large-scale direct shear tests on sand-contaminated ballast, Proceedings of the Institution of Civil Engineers-Geotechnical Engineering, 171(5): 451-461.

Wang, C., Deng, A. and Taheri, A. (2018). Three-dimensional discrete element modeling of direct shear test for granular rubber–sand, Computers and Geotechnics, 97: 204-216.

Evaluation of current approaches for determining moisture variations due to climatic effects in unbound pavements with thin seals

C.J. Maha Madakalapuge

ARC Smart Pavements Hub - SPARC, Department of Civil Engineering, Monash University, Clayton Campus, VIC 3800, Australia

T.T Dutta

ARC Smart Pavements Hub - SPARC, Department of Civil Engineering, Monash University, Clayton Campus, VIC 3800, Australia.

Didier Bodin

ARC Smart Pavements Hub SPARC, Department of Civil Engineering, Monash University, Clayton Campus, VIC 3800, & ARRB, Melbourne Australia.

Jayantha Kodikara

ARC Smart Pavements Hub - SPARC, Department of Civil Engineering, Monash University, Clayton Campus, VIC 3800, Australia.

ABSTRACT: Unbound pavements with thin sprayed seals are the most common type of roads in Australia. Both unbound granular material and subgrade properties are influenced by moisture changes. Moisture conditions beneath the pavement vary depending on the prevailing climatic conditions such as precipitation, air temperature, humidity, percentage sunshine and solar radiation. Different countries have adopted various approaches to incorporate climatic factors into pavement design. This paper critically evaluates two design methods that incorporate climatic factors into the design of flexible pavements. The significance of accurately predicting the moisture variations during the service life has been recognized. This paper explores how the degree of saturation (DOS) fluctuates in each layer at different depths under prevailing climatic conditions by analysing the results of a numerical model developed using finite element-based software HYDRUS 1D. Both long term and short-term hydraulic behaviours of flexible pavements were investigated using the model developed.

1 INTRODUCTION

Road pavement rehabilitation is a large outlay for the Federal and State governments, while billions being spent on road maintenance operations every year. Roads can fail due to various reasons. Environmental factors such as moisture and temperature have long been identified as a major reason for road failures that impact both long term and short-term pavement performance. Particularly, unbound pavements with thin seals are more susceptible to environmentally driven deterioration.

In Australia, about 90% of all surfaced roads is comprised of unbound granular pavement with sprayed seal surfacing (Austroads 2017). The main advantage of unbound pavement is having low initial cost (Austroads 2017). However, unbound granular materials are more vulnerable to performance losses due to moisture variations that occur during service life. Additionally, subgrade properties can be adversely affected by moisture changes.

Moisture conditions beneath the pavement vary depending on several prevailing climatic factors such as precipitation, air temperature, humidity, percentage sunshine and solar radiation. Different countries have adopted different approaches to incorporate these climatic factors into pavement design to better meet both short term and long-term performances. This paper extensively reviews the current approaches that incorporate climatic factors in the pavement design methods. Moreover, this

study has attempted to numerically model moisture variations in flexible pavements under prevailing climatic conditions using HYDRUS 1D. The developed model was used to analyse both short term and long-term hydraulic behavior of flexible pavements.

2 INCORPORATION OF CLIMATIC FACTORS TO PAVEMENT DESIGN

2.1 *USA Design process*

The USA pavement design method can be identified as one of the most advanced approaches that incorporate climatic effects into the pavement design. It embodies a specialist module for climate effects simulation for a candidate pavement known as the Enhanced Integrated Climatic Model (EICM) (NCHRP 2004). It can produce moisture and temperature profiles with time for the pavement considering the detailed climatic input data for a given location in the pavement. These inputs are then considered in the structural pavement design.

2.1.1 Enhanced Integrated Climatic Model (EICM)

EICM is a one-dimensional coupled heat and moisture flow program that simulates the changes in the behaviour and characteristics of pavement and subgrade materials in conjunction with climatic conditions over several years of operation (NCHRP 2004). It calculates the temperature, pore pressure (suction), moisture content and resilient modulus for each node in the profile for the entire analysis period by considering the climate during the design life.

EICM requires a set of input parameters, including weather-related information, ground water related information, drainage, surface properties, pavement structure and material information to produce the desired output. Mainly, EICM uses hourly climatic data such as air temperature, precipitation hourly wind speed, percentage sunshine and relative humidity as the main climatic inputs. Those parameters can be obtained from weather stations located close to the given project's site. EICM software includes a library of weather data for approximately 800 weather stations throughout the USA.

EICM has some limitations in applications. The validity of the output can be challenged by the accuracy of past data. Moreover, EICM does not account for vapour movements due to temperature gradient when determining the moisture profiles over time. Heat fluxes resulting from rainfall and infiltration into the pavement are not considered.

2.2 *Australian design process*

The current Australian Pavement Design Guide (Austroads 2017) has adopted a conservative approach to incorporate climatic factors into the pavement design. It has given guidance on dealing with moisture and temperature-related issues in pavements under the Section 4 Environment. In particular, it has noted "*The moisture conditions in unbound granular pavement materials can also have a major effect on performance. When the degree of saturation of unbound granular materials exceeds about 70%, the material can experience significant loss of strength/modulus"* (Austroads 2017).

Moreover, Austroads (2017) guides the designer to evaluate the subgrade strength based on climatic and drainage conditions. Since the strength of the subgrade is one of the significant factors that determine the pavement thickness, composition and performance (Austroads 2017), it has to be evaluated precisely in their design stage. California Bearing Ratio (CBR) and elastic parameters namely vertical modulus (E_v), horizontal modulus (E_h) and Poisson's ratio (ν) are commonly used to measure the subgrade strength.

Design subgrade CBR value is determined by considering the density and the moisture condition, which are expected to prevail in the service for the long term. Thus, designers have to predict the moisture condition likely to occur during the service life of the pavement based on their knowledge and experience to accurately assess the subgrade CBR value. The guidance provided by Austroads (2017) is presented in Table 1. The specification stipulates the specimen's compaction moisture content and

Table 1: Typical moisture conditions for laboratory CBR testing (Austroads, 2017)

Median annual rainfall(mm)	Specimen compaction moisture content	Testing condition	
		Excellent to good drainage	Fair to poor drainage
< 500	OMC	Un-soaked to 4-day soak	1 to 4-day soak
500-800	OMC	Un-soaked to 4-day soak	4 to 7-day soak
>800	1 to 1.15 × OMC	Un-soaked to 4-day soak	4 to 10-day soak

soaking conditions that needed to be adopted in the laboratory CBR test. The decision is made on the basis of two criteria: annual rainfall and drainage condition.

However, Australian pavement design has not been advanced to perform computations on seasonal basis to incorporate the effects of climatic conditions on the behaviour of materials. It does not account for the temporal variation of moisture or temperature that occurred due to changes in prevailing climatic conditions during the service life, in the pavement design in detail.

3 NUMERICAL MODELLING OF MOISTURE VARIATION IN PAVEMENTS

Hydrologist and geotechnical engineers use different modelling tools to simulate the moisture flow through unsaturated soils (Fayer 2000; Lee 2012; Simunek et al. 1999). Among them, HYDRUS-1D is a well-tested program by Hydrologists that incorporates hydro and thermal phenomena and their coupling effects (Saito et al. 2006; Simunek et al. 1999). This paper has attempted on developing a numerical model using Hydrus 1D to study how moisture varies under prevailing climatic conditions during the service life of the pavement.

3.1 *Methodology*

A pavement, which was constructed and monitored as a part of the doctoral research of Ryan Steven de Carteret, Faculty of Engineering and Build environment at the University of Newcastle (Carteret 2015) was modelled using HYDRUS 1D under actual climatic condition. Particularly this pavement was selected for the modelling because the required model parameters were available and the climatic data had been recorded continuously for a period of 2 years.

The test pavement was located in Dubbo, New South Wales approximately 400 km northwest of Sydney. Carteret (2015) has constructed an unbound pavement with a double/double sprayed seal as a test pavement to investigate moisture movements and salinity underneath the pavement.

This paper deals with the modelling of the above-mentioned pavement for 2 years. The moisture profiles are generated under isothermal conditions at each layer. This helps to study the short-term moisture variations in flexible pavements with thin seals. This paper also describes the simulation results for the same pavement for a period of 10 years to evaluate the long-term moisture variations.

3.1.1 Pavement geometry

The test pavement consists of basically four layers such as seal, base, subbase and subgrade as shown in Fig 1.

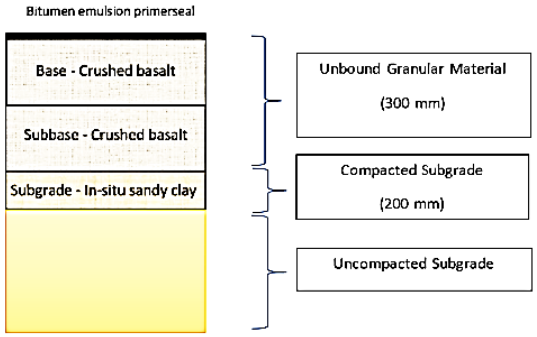

Fig 1: Unbound pavement geometry

The subgrade is the in-situ material which is natural sandy clay. Only the topmost 200 mm of the subgrade was compacted prior to pavement construction to achieve the required density. The compacted density and the gravimetric moisture content were measured as 1660 kg/m3 and 7.5% for the compacted subgrade after the compaction. Both the base and the subbase layers are unbound granular layers which are consisted of crushed basalt. The UGM layers were compacted in two layers of 150 mm to achieve a dry density of 2135 kg/m3 at 6% of gravimetric water content. Both the base and subbase layers are modelled as one layer of 300 mm thick since both layers have the same properties.

The topmost layer is a double/double sprayed bituminous emulsion primer seal (two applications each of bitumen and cover aggregate) which was sprayed on top of the base layer. The applied class of the bitumen was CRS/170-60 and the nominal size of aggregate was 7 mm pre-coated aggregates. The seal was modelled as a 10 mm thick layer.

3.1.2 Climate

The climatic data had been recorded for a period of 2 years. Annual rainfall was approximately 660 mm/year while mean monthly rainfall was relatively uniform throughout the year in this area according

to the Australian Bureau of Meteorology (http://www.bom.gov.au). This area can be classified as a semiarid region. The climatic data such as minimum and maximum temperature, precipitation and pan evaporation have been collected from nearby weather stations.

The test pavement had been monitored for the same period of time and the water content was measured at different depths underneath the pavement, data of which are collected every 6 months. The water table level has been monitored at a nearby borehole, which is located approximately 500 m away from the test site. The recorded daily precipitation (mm/day) evaporation(mm/day) and the water table depth during the monitored time period are shown in Fig 2. These data are the key input parameters that define the top and the bottom boundaries of the finite element model of the pavement.

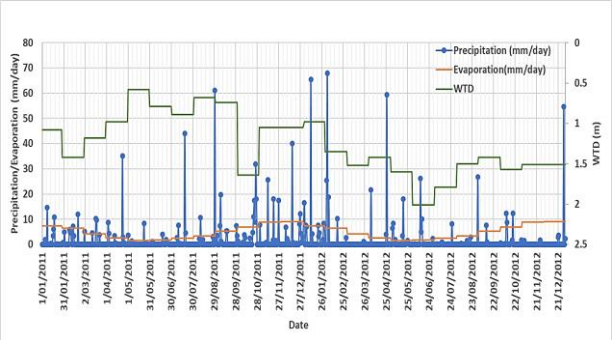

Fig 2: Daily variation of precipitation. evaporation and ground water table depth

3.1.3 Material properties

Soil water retention curve (SWRC) and the hydraulic conductivity function are the key input properties required for numerical modelling of moisture variations. Thus, both of these properties should be defined for each layer. In the current study, models developed by Van- Genuchten has been used to define both SWRC and hydraulic conductivity function of each layer (Van Genuchten 1980).

SWRCs of all materials except the seal have been determined from laboratory tests such as Tensiometer method, Thermal Conductivity Sensors (TCS), Chilled-Mirror Psychrometer (WP4) and filter paper. Fig 3 shows the SWRC of those materials which have been generated by fitting the experimental results to Van- Genuchten model. It is assumed that SWRC of seal is similar to the UGM.

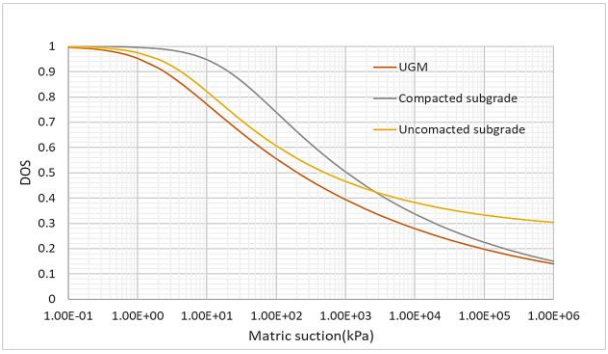

Fig 3: SWRC of each material

Saturated hydraulic conductivities of all four layers have been obtained by laboratory hydraulic conductivity tests in accordance with ASTM D5084 standard as shown in Table 2.

Table 2: Saturated hydraulic conductivity of materials

Pavement Layer	Sat. hydraulic conductivity (m/s)
Seal	2×10^{-5}
Base	4×10^{-5}
Compacted Subgrade	1.15×10^{-9}
Uncompacted subgrade	3.85×10^{-9}

4 RESULTS AND DISCUSSION

4.1 *Simulation results for two years*

At first, the test pavement was modelled in Hydrus 1D and the moisture variation is simulated for each layer for two years-time under prevailing climatic conditions.

4.1.1 DOS in base layer

As shown in Fig 4, when the DOS in the granular layer is examined, it can be seen that the bottom of the base layer has become more saturated than the top of the base layer due to water migration down through the permeable seal and base.

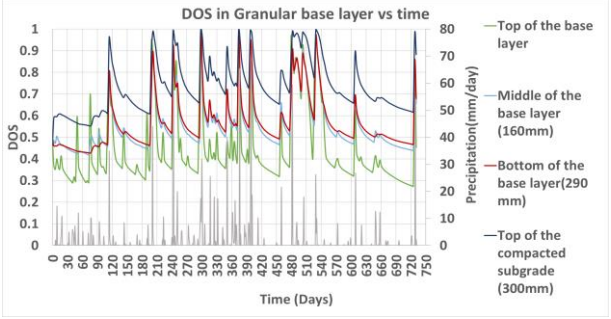

Fig 4: DOS in granular base layer vs time

Under this condition, even the bottom of the base feels the rainfall fluctuations as it varies accordingly. At some points, the bottom of the base reaches a state of full saturate condition. Generally, when the DOS reaches above 70% or more generally above the line of optimums, it is possible to expect the beginning of the poor performance, which gets exacerbated as the DOS increase further close to full saturation.

When comparing the bottom of the base layer (290 mm from the surface (red)) and the top of the compacted subgrade (300 mm from the surface (dark blue)), a significant increase of DOS can be observed. The top of the compacted subgrade reaches even DOS of 1 at some points, which is not favourable.

Since the permeability of compacted subgrade is lower than that of the granular base layer, water can accumulate at this boundary which can lead to a failure. Therefore, a drain can be placed at the boundary between the base layer and the compacted subgrade to prevent the water ingression to the subgrade from the base layer. However, it is important to evaluate "the capillary break" effect that will hinder the performance of a drain at this location. For instance, the drain will not perform properly unless the pressure at the bottom of the base is positive or the soil is saturated at the base. Fig 5 illustrates the variation of the pressure head (mm) at the boundary between the base and the compacted subgrade. Under this condition, since the pressure at the bottom of the base has not reached positive, a lateral drain will not perform well due to the capillary barrier effect.

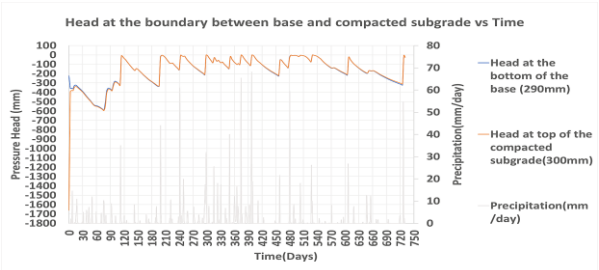

Fig 5: Head (mm) at the boundary between base and compacted subgrade vs time

4.1.2 DOS in subgrade

Fig 6 illustrates the DOS variation at different depths in the subgrade. The top of the compacted subgrade demonstrates dramatic fluctuations of the DOS while they even reach fully saturated conditions at some points. Both the middle and bottom of the compacted subgrade are not sensitive to fluctuations of rainfall. But at both levels, it gradually increases the saturation degree and reaches a value of around 90%.

The top of the uncompacted subgrade is initially drying and then slightly increasing the DOS to approximately 70%. The reason for the initial drying is that at first, it tries to reach an equilibrium depending on the initial condition that has been given as an input.

The DOS at the middle of the uncompacted subgrade remains a steady value as the initial condition but with a slight decrease apparently due to the lower permeability.

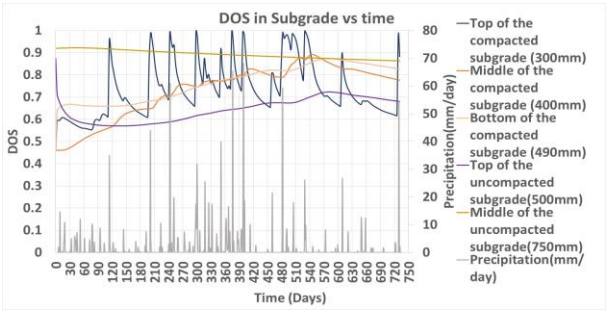

Fig 6: DOS in subgrade vs time over 2 years

4.2 *Simulation for 10 years*

The same test pavement was simulated for 10 years to obtain moisture variations in each layer by assuming that the 2-year monitored climate is repeated for the remaining years to observe the long-term behaviour of the DOS in each layer.

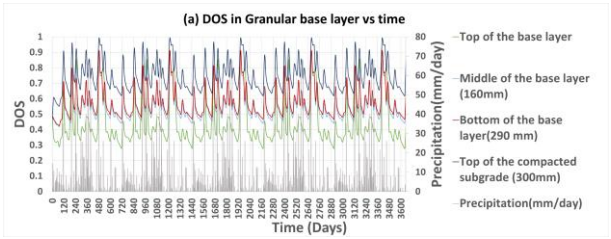

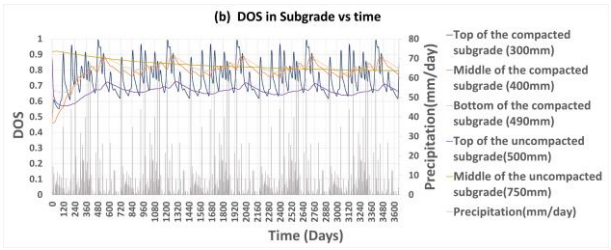

Figure 7(a) and 7(b): DOS in granular base layer vs time over 10 years, DOS in subgrade vs time over 10 years

Fig 7a and 7b illustrate the long-term behaviour of DOS variations in the base layer and the subgrade respectively. It can be observed that the moisture condition at each depth reaches a certain average DOS after either initial drying or wetting, and then it fluctuates around that value according to seasonal climatic variations.

As an example, the DOS at the bottom of the base layer reaches a value of around 60% after initial drying and wetting during approximately the first 3 months. Subsequently, it fluctuates around that value. Similar behaviour can be clearly observed in the subgrade as well. It can be also seen that the DOS at the middle of the compacted subgrade reaches a value around 80% after the initial wetting. In this instance, it takes approximately 1.5 years to reach this equilibrium position. After that, it slightly varies around 80% throughout the simulation period. Moreover, according to the results generated, it can be concluded that the time taken to reach the equilibrium condition is different from one depth to another depth.

5 CONCLUSIONS

Firstly, this paper presented an extensive literature review on how climatic factors have been incorporated into pavement design in the USA and Australian design guides. The significance of having an accurate numerical modelling approach to incorporate climatic effects and to predict moisture and temperature variation of flexible pavements has been identified. It can be concluded that the current Australian pavement design method can be improved by developing such an approach to predict moisture variations that could occur during the service life.

Secondly, this paper attempted on adopting HYDRUS 1D moisture and heat flow program to predict the actual moisture variation in flexible pavements. This paper presented simulation results for 2 years and ten years for a test pavement and analyzed both short term and long-term hydraulic behaviours in terms of DOS.

Under the given climatic conditions, moisture flows from top to bottom and results show the manner in which DOS fluctuates under the prevailing climatic conditions. It could be easily identified at which depths, and at what times DOS exceeds the acceptable limits. Thus, the designer could adapt the design by considering these expected moisture variations and improve the design. Moreover, it helps to accurately predict the pavement performance losses before hand and manage the rehabilitation process as well. Therefore, this kind of numerical modelling is essential to advance the current design process in Australia.

However, a few limitations can be identified in the current model. Since the developed model is one-dimensional, the actual three-dimensional moisture flow movements could not be captured. Hence 1d modelling may be considered valid for middle third of the pavement. It is needed to be validated under different climatic conditions and parameters to be properly calibrated.

6 REFERENCES

Austroads (2017). "Guide to pavement technology part 2." *Pavement structural design* Austroads Ltd, Sydney.

Carteret, R. S. d. (2015). "Environmental salinity and bitumen-sealed unbound granular road pavements." Doctor of Philosophy The University of New Castle Center for Geotechnical and Materials Modeling

Fayer, M. J. (2000). "UNSAT-H Version 3.0: Unsaturated Soil Water and Heat Flow Model." U.S. Department of Energy, Pacific Northwest National Laboratory, Richland, Washington 99352.

Lee, K. Y. (2012). "Continuous deterioration modelling of road pavement performance." Thesis (Ph.D.)--Monash University, 2012.

NCHRP (2004). "Guide for Mechanical Empherical Design Part 2 " *Design Inputs* NCHRP, Transport Research Board, National Research Council

Saito, H., Šimůnek, J., and Mohanty, B. P. (2006). "Numerical Analysis of Coupled Water, Vapor, and Heat Transport in the Vadose Zone." *Vadose Zone Journal*, 5(2), 784-800.

Simunek, J. J., Van Genuchten, M., and Šejna, M. (1999). "The HYDRUS-1D software package for simulating the one-dimensional movement of water, heat, and multiple solutes in variably-saturated media." 3, 1-240.

Van Genuchten, M. (1980). "A Closed-form Equation for Predicting the Hydraulic Conductivity of Unsaturated Soils1." *Soil Science Society of America Journal*, 44.

Permeability Behaviour of Clay Fouled Railway Ballast

H. G. S. Mayuranga
Department of Civil Engineering, University of Peradeniya, Peradeniya, Sri Lanka.

S. K. Navaratnarajah
Department of Civil Engineering, University of Peradeniya, Peradeniya, Sri Lanka.

ABSTRACT: Ballast fouling is a major factor leading to the instability of ballasted railway tracks because of its detrimental impact on the permeability characteristic of ballast. Fines washing out from the slopes and accumulating in rail tracks is a common problem in the mountainous region and severely affect the permeability behaviour of the track. Therefore, this study focused on investigating the permeability behaviour of fouled ballast in Sri Lankan railway tracks at different levels of fouling and estimating the stage at which the track maintenance work should be commenced. For this, the large-scale permeability apparatus was used in the laboratory to conduct a series of constant head permeability tests on fresh ballast and ballast fouled with clay material. Using experimental data, a numerical model was developed to quantify the track drainage capacity at different fouling levels. Based on the results, critical fouling levels were identified to commence the ballast cleaning work.

Keywords: Railway Ballast; Fouling; Large Scale Permeability Test; Seepage Analysis

1. INTRODUCTION

Ballasted railway networks play a vital role in railway transportation of many countries due to their numerous advantages. The ballast layer is considered to be the major structural component of a railway track which distributes the large stresses safely and uniformly to the underlying formation. A newly constructed ballast layer provides adequate void spaces and that ensures the required drainage characteristic of the railway track.

However, the ballast layer gradually gets contaminated by various sources which reduce the overall drainage capacity of the track. During the operation of the railway track, breakage of corners and edges of ballast particles is significant under repetitive loading (Navaratnarajah et al., 2018) and the fine particles generated through the ballast breakage accumulate in void spaces of the ballast layer which is known as ballast fouling and that reduces the effective permeability capacity of railway track (Li et al., 2015; Navaratnarajah, 2017). Further, the intrusion of fine particles and mud from the surface and the underlying layers enhances the ballast fouling and reduces the track drainage.

The reduced track drainage due to ballast fouling leads to track instability and that minimizes safety while increasing the maintenance frequency. Therefore, it is important to investigate the track drainage behaviour of ballast under different fouling conditions and to predict the appropriate stage to implement track maintenance without compromising safety. Therefore, this paper explores the permeability behaviour of sandy clay fouled ballast at different levels of fouling based on the Void Contamination Index (VCI). The large-scale permeability apparatus was used to conduct a series of permeability tests at the laboratory. After obtaining the hydraulic conductivity values for different levels of ballast fouling from the experimental results, a 2-D FEM model was developed and seepage analysis was carried out to obtain track drainage capacities at different conditions. According to the drainage classification proposed by Terzaghi et al. (1996), the drainage conditions were identified for different scenarios of ballast fouling. Based on the results, this paper proposes recommendations to maintain a proper drainage condition in railway tracks.

2. LARGE-SCALE LABORATORY TESTING

2.1 Preparation of test materials

The ballast materials used for the laboratory testing were collected from the Nawalapitiya railway unit of the Department of Railways, Sri Lanka. The collected samples were washed and air-dried to obtain clean ballast particles. Then the graded ballast aggregates were mixed to prepare test samples following the Indian standard gradation of

ballast which is currently being adopted in ballasted tracks in Sri Lanka. The particle size distribution of the current study and the upper and lower limits of Indian standard gradation of ballast (IRS-GE-1, 2004) are shown in Fig. 1. The specific gravity of fresh ballast was 2.68 and the void ratio of compacted ballast to achieve field density was 0.63 (Dissanayake et al., 2016). The fouling material employed in this study was identified as sandy clay with 48% fines. The particle size distribution of fouling material obtained from the hydrometer test is shown in Fig.1. The properties of Sandy Clay material are given in Table 1.

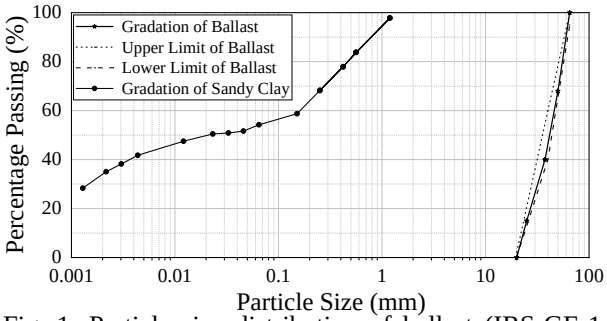

Fig. 1: Particle size distribution of ballast (IRS-GE-1, 2004) and Sandy Clay materials

Table 1: Properties of Sandy Clay material

Property	Value
Liquid limit (LL)	47%
Plastic limit (PL)	24%
Plasticity index (PI)	23%
Optimum moisture content (OMC)	16.5
Maximum dry density (MDD)	1674 kg/m^3
Specific gravity	2.64
Void ratio	0.58

2.2 Large-scale permeability apparatus

To investigate the influence of fouling materials on the permeability behaviour of railway ballast, the large-scale permeability apparatus was used which was designed and built at the Geotechnical Engineering Laboratory of the University of Peradeniya. As shown in Figs. 2 (a) and (b), the apparatus can be used to conduct constant head permeability tests on large size granular particles. The major components of the apparatus are the cylindrical chamber where the ballast specimen is placed, constant head tank, piezometer, and measuring cylinder. To avoid the impact of sample size, it is required to maintain the diameter of the cylindrical chamber greater than 6 times the mean diameter of maximum ballast particle (Indraratna et al., 1993; Tennakoon, 2012). So that the selected diameter of the cylindrical steel chamber was 400 mm and that can be used to accommodate a ballast sample up to a height of 800 mm. The ballast sample height used in this study was 400 mm and that was greater than 5 times the maximum ballast particle size (Tennakoon, 2012). Under the ballast layer, a filter layer was used to minimize the washout of sandy clay particles during the test. Below that, a 200 mm thick large size granular layer (> 63 mm) was maintained to ensure the free drainage boundary at the bottom of the cylindrical chamber.

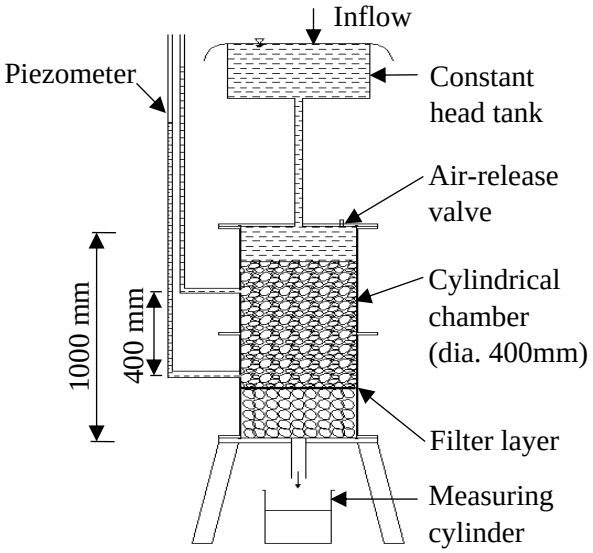

(a)

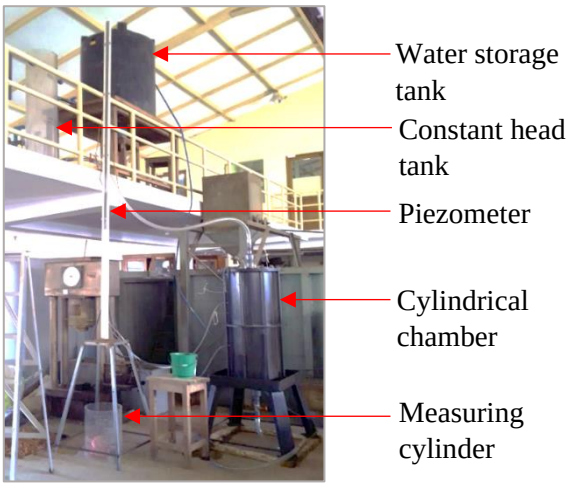

(b)

Fig. 2: Large-scale permeability test setup (a) Schematic diagram; (b) Photograph of test apparatus

2.3 Test procedure

In this study, the Void Contamination Index (VCI) (Indraratna et al., 2010) was adopted to represent the level of ballast fouling which is given by,

$$VCI = \frac{(1+e_f)}{e_b} \times \frac{G_{sb}}{G_{sf}} \times \frac{M_f}{M_b} \times 100 \qquad (1)$$

where, G_s, M, and e denote specific gravity, dry mass, and void ratio respectively, and subscripts b and f denote ballast and fouling material respectively.

To evaluate the permeability behaviour of ballast, 5 different ballast samples were prepared

including one clean ballast sample and 4 sandy clay fouled ballast samples having VCI values of 25, 50, 75, and 100%. Fouling materials were uniformly mixed with clean ballast samples according to the required VCI to obtain fouled ballast samples. At each test, the cylindrical chamber was filled with a prepared sample using 4 layers of each having 100 mm in thickness. Each layer was compacted to achieve the required field density by using a vibratory compactor with a rubber-padded base to prevent particle breakage while compacting. Before starting the test, the cylindrical chamber was filled with water and kept for one hour to saturate the sample. The water level of the air release valve at the top of the cylindrical chamber was used as a reference to ensure the saturation of the sample. Then the constant head tank was filled up to the constant level and the water was allowed to flow through the ballast sample. To maintain the laminar flow condition, the hydraulic gradient of the permeameter was maintained below 4 (Tennakoon, 2012). For each sample, head differences were recorded from the piezometer at 5 different flow rates. From the gradient of flow rate versus head difference graph, the hydraulic conductivity (k) was calculated for each case by using Equation 2 which was derived from Darcy's law.

$$k = ml/A \quad (2)$$

Where, m is the gradient of the graph, l is the height difference of the piezometer and A is the cross-sectional area of the test specimen.

2.4 Test results

The variation of flow rate with head difference for each test specimen is shown in Fig. 3. Based on that, the hydraulic conductivity values were calculated by using Equation 2 and the results are summarized in Table 2. Based on that, the fresh ballast used in railway tracks in Sri Lanka shows a hydraulic conductivity of 0.43 m/s.

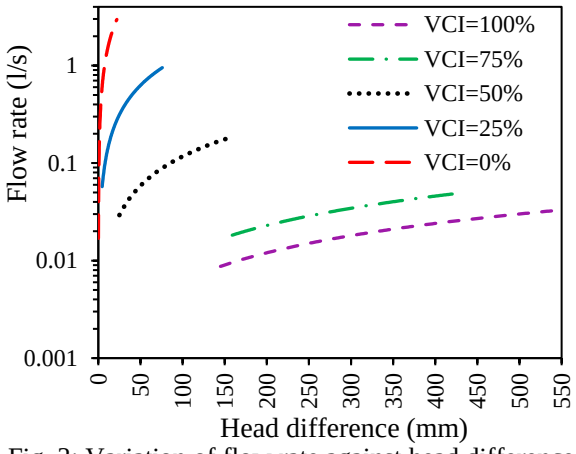

Fig. 3: Variation of flow rate against head difference for selected VCI values

Table 2: Hydraulic conductivity of ballast for different VCI

VCI (%)	Hydraulic conductivity, k (m/s)	Reduction of k with respect to clean ballast (%)
0 (Clean ballast)	4.30×10^{-1}	-
25	3.99×10^{-2}	90.72
50	3.82×10^{-3}	99.11
75	3.18×10^{-4}	99.93
100	1.91×10^{-4}	99.96

However, it is clear that the presence of fouling materials in the ballast layer dramatically reduces the hydraulic conductivity of clean ballast by more than 90%. Fig. 4 depicts the variation of hydraulic conductivity with VCI by considering the exponential behaviour of data corresponding to the correlation coefficient of $R^2 = 0.94$. The variation of the graph can be expressed by using Equation 3 and that can be used to predict the hydraulic conductivity (k) of ballast at different VCI.

$$k = 0.1784 \times e^{-0.074 \times VCI} \quad (3)$$

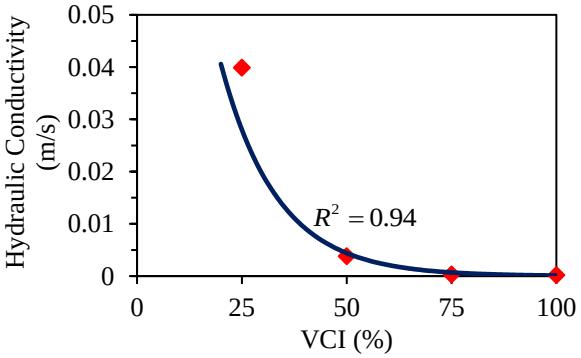

Fig. 4: Variation of hydraulic conductivity against VCI

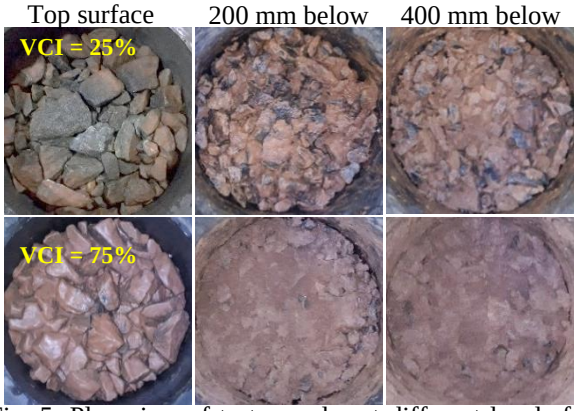

Fig. 5: Plan view of test samples at different levels for 25% and 75% VCI

The photographs of selected cross-sections of fouled ballast samples were taken while unloading the material as shown in Fig. 5. The figures clearly show that there is a higher accumulation of fine particles at bottom layers compared to top layers of

ballast specimens which can be generally found in the actual rail track.

3. 2-D NUMERICAL ANALYSIS

Under the field conditions, the flow of water through the rail track ballast can occur in both horizontal and vertical directions. Therefore, it is important to consider a 2-D seepage analysis of ballast to evaluate the track drainage capacity (Tennakoon, 2012). For that, a 2-D numerical model of the railway track was developed by using SEEP-W (GeoStudio, 2012) software. The hydraulic conductivity values obtained from the experimental investigation for different fouling levels of ballast were used as input parameters to evaluate the track drainage under different scenarios. Since the void spaces in the ballast layer are random, the hydraulic conductivity values in vertical and horizontal directions were considered as same for the numerical seepage analysis (Tennakoon, 2012).

3.1 Development of 2-D numerical models

Since the cross-section of the rail track is symmetric about the middle vertical axis, only one half of the track was considered for the numerical analysis. In the 2-D numerical model, a free-draining boundary was maintained at the top surface of shoulder ballast, an impervious boundary was maintained at the bottom of the ballast layer, and a symmetric boundary was used at the middle vertical axis of the full rail track.

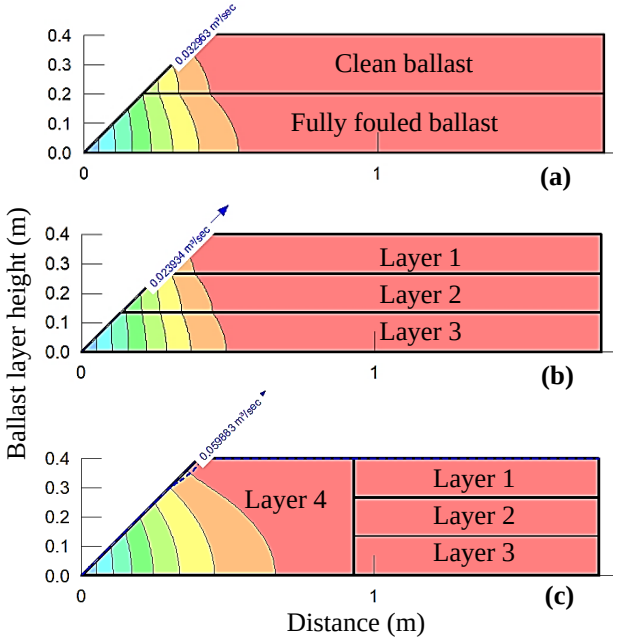

Fig. 6: Developed 2-D numerical models for seepage analysis: (a) Model 1, (b) Model 2, and (c) Model 3

In this study, 3 numerical models were developed to represent the permeability behaviour of rail track under 3 possible track conditions as described below.

Model 1: The ballast layer was divided into two horizontal layers as shown in Fig 6 (a). The top layer is filled with clean ballast and the bottom layer is filled with completely fouled ballast (VCI = 100%) representing the undercutting operation in the rail track. The track drainage capacities were obtained for different clean ballast layer thicknesses.

Model 2: As shown in Fig. 6 (b), the ballast layer was divided into three equal horizontal layers. For each layer, different VCI values were considered to obtain the track drainage capacity.

Model 3: The shoulder ballast was considered separately and the ballast layer was divided into three equal horizontal layers as shown in Fig. 6 (c). Different VCI values were considered in each portion of the ballast to evaluate the effect of shoulder ballast on track drainage capacity.

By considering the maximum rainfall intensity in Sri Lanka, the critical flow rate value (Q_c) was selected as 1×10^{-4} m^3/s. The maximum track drainage capacities (Q) were obtained for different scenarios by conducting seepage analysis using the developed numerical models. The track drainage classification was carried out for different scenarios, based on the drainage classification proposed by Terzaghi et al. (1996) as given in Table 3.

Table 3: Track drainage classification (Terzaghi et al., 1996)

Drainage category	Criteria
Free drainage	$Q/Q_c > 100$
Good drainage	$10 < Q/Q_c < 100$
Acceptable drainage	$1 < Q/Q_c < 10$
Poor drainage	$0.1 < Q/Q_c < 1$
Very poor drainage	$0.01 < Q/Q_c < 0.1$
Impervious	$Q/Q_c < 0.01$

3.2 Results of numerical simulation

Fig. 7 summarizes the drainage capacities obtained from numerical simulation for Model 1. Based on that, the track drainage reduces with the reduction of clean ballast layer thickness. However, when the clean ballast layer thickness is 10 mm, the drainage condition is still within the acceptable limit. This clearly highlights the significance of maintaining a clean ballast layer at the top of the ballast through the undercutting operation.

The track drainage behaviour for different scenarios captured from the results of Model 2 is shown in Fig. 8 and Table 4. According to the results, a significant reduction in track drainage can be remarked when the fouling level at top of the ballast layer (Layer 1) increases. Besides, a relatively higher fouling level in the top 2 layers results in poor drainage condition even though the bottom ballast layer is fairly clean. Also, similar to

the results obtained from Model 1, a good or acceptable drainage condition can be expected when the top ballast layer is relatively clean.

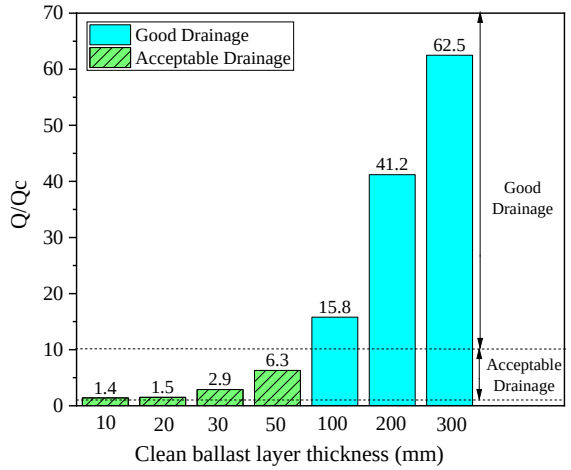

Fig. 7: Variation of Q/Q_c value with clean ballast layer thickness shown in Model 1

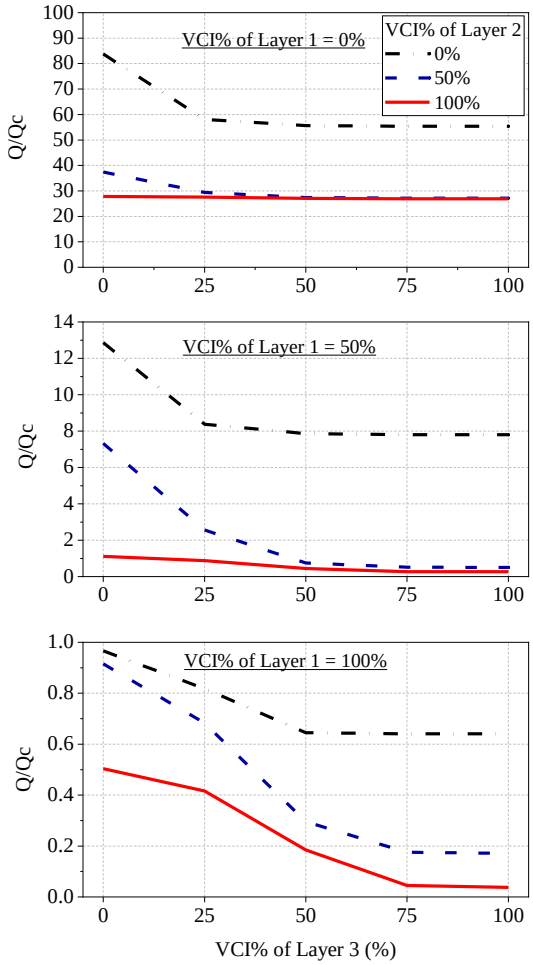

Fig. 8: Variation of Q/Q_c with different levels of fouling based on Model 2

The results obtained from Model 3 are briefed in Table 5. The results clearly show the influence of shoulder ballast on the track drainage condition. Regardless of the fouling levels in Layer 1 to 3, the track drainage varies with the fouling level in the shoulder ballast layer. When the shoulder layer is clean or fouled up to 25% VCI, a good or acceptable drainage condition can be expected. However, when the fouling level of the shoulder ballast layer is 50% VCI or more, the track drainage is poor or very poor which requires proper track maintenance.

Table 4: Numerical simulation results for Model 2

VCI (%)			Q/Qc	Drainage condition
Layer 1	Layer 2	Layer 3		
0	0	0	83.82	Good Drainage
0	0	50	55.67	
0	0	100	55.42	
0	25	25	32.45	
0	25	100	29.66	
0	50	50	27.42	
25	25	0	27.26	
0	50	100	27.16	
0	75	75	26.94	
0	100	100	26.92	
50	0	0	12.87	
25	25	25	7.78	Acceptable Drainage
50	50	0	7.32	
25	25	100	5.15	
25	100	100	2.52	
100	0	0	0.97	Poor Drainage
100	25	0	0.95	
100	50	0	0.92	
75	75	0	0.83	
100	25	25	0.75	
50	50	50	0.74	
50	50	100	0.51	
100	100	0	0.50	
100	100	25	0.42	
100	50	50	0.30	
50	100	100	0.27	
100	100	50	0.18	
75	75	75	0.06	Very Poor Drainage
75	75	100	0.05	
100	75	75	0.05	
75	100	100	0.05	
100	100	75	0.05	
100	100	100	0.04	

Based on the numerical simulation, the track drainage conditions corresponding to different fouling conditions were identified. The results clearly show that the fouling level of the top layer of ballast and the shoulder ballast have a significant impact on the track drainage. To understand the permeability level of a railway track, first, it is sufficient to check the VCI% in the top 100 mm layer of ballast and the shoulder ballast. According to that, the following two conditions in a particular railway track can be identified as critical stages to start track maintenance; (1) when the top layer of ballast exhibits VCI > 25% and (2) when the shoulder ballast layer exhibits VCI > 25%. Then, it is recommended to check the fouling condition in the bottom two layers of ballast if the above two

conditions are applicable for a particular track section to understand whether it is required only undercutting and clearing shoulder ballast operations or replacement of ballast. It is better to replace the ballast layer if the fouling level of the bottom two ballast layers exceed at least 75% VCI, which will limit the track drainage as soon as the top layer starts to foul.

Table 5: Numerical simulation results for Model 3

VCI%				Q/Qc	Drainage condition
Layer 1	Layer 2	Layer 3	Layer 4		
0	0	0	0	75.97	
0	0	100	0	75.60	
0	50	100	0	75.10	Good
100	0	0	0	74.98	Drainage
100	50	0	0	74.87	
100	100	100	0	74.85	
0	0	0	25	7.14	
0	0	100	25	7.09	
0	50	100	25	7.00	Acceptable
100	0	0	25	6.97	Drainage
100	50	0	25	6.96	
100	100	100	25	6.95	
0	0	0	50	0.68	
0	0	100	50	0.68	
0	50	100	50	0.68	Poor
100	0	0	50	0.67	Drainage
100	50	0	50	0.67	
100	100	100	50	0.67	
0	0	0	75	0.06	
0	0	100	75	0.06	
100	50	0	75	0.06	
100	100	100	75	0.06	Very Poor
0	0	0	100	0.03	Drainage
0	50	100	100	0.03	
100	0	0	100	0.03	
100	100	100	100	0.03	

4. CONCLUSIONS

Series of large-scale permeability tests were conducted to evaluate the hydraulic conductivity of ballast fouled with sandy clay material at different levels of fouling. Prominent reductions in hydraulic conductivities were observed for fouled ballast samples compared to the clean ballast sample. The obtained results were used to develop 2-D numerical models to capture the track drainage conditions under different scenarios. Then the track drainages were classified into different categories in between free drainage and impervious conditions.

The numerical results exhibited the importance of maintaining a clean ballast layer at the top of the ballast and maintaining a clean shoulder ballast layer to obtain a good drainage condition in ballasted track. It is recommended to start ballast cleaning work when a particular track reaches the acceptable drainage condition. Also, a method was discussed to decide the requirement of track maintenance based on the fouling level of a particular track section.

This study shows that a simple 2-D seepage analysis is enough to decide the level of drainage condition of a rail track rather than conducting an expensive permeability test especially for large size granular materials like ballast.

ACKNOWLEDGEMENTS

The support provided by the University of Peradeniya Research Grant (Grant No: URG-2017-29-E) and Accelerating Higher Education Expansion and Development (AHEAD) operation funded by the World Bank (Grant No: AHEAD/RA3/DOR/STEM/No.63) are highly appreciated by the authors. Also, the District Engineer of Nanuoya Railway office, and the staff of Gampola Railway Unit of Department of Railways, Sri Lanka are acknowledged for the support provided to collect ballast material.

REFERENCES

Dissanayake, D., Kurukulasuriya, L. and Dissanayake, P. (2016). Evaluation of shear strength parameters of rail track ballast in Sri Lanka, Journal of the National Science Foundation of Sri Lanka, 44(1).

Indraratna, B., Nimbalkar, S.S. and Tennakoon, N. (2010). The behaviour of ballasted track foundations: track drainage and geosynthetic reinforcement, GeoFlorida 2010: Advances in analysis, modeling & design, pp 2378-2387.

Indraratna, B., Wijewardena, L. and Balasubramaniam, A. (1993). Large-scale triaxial testing of grey wacke rockfill, Geotechnique, 43(1): 37-51.

IRS-GE-1 (2004). Specification for track ballast, Research Designs and Standards Organisation (RDSO), Ministry of Railways

Li, D., Hyslip, J., Sussmann, T. and Chrismer, S. (2015). Railway geotechnics, CRC Press, pp 585.

Navaratnarajah, S.K. (2017). Application of rubber inclusions to enhance the stability of ballasted rail track under cyclic loading. PhD Thesis, School of Civil, Mining and Environmental Engineering, University of Wollongong.

Navaratnarajah, S.K., Indraratna, B. and Ngo, N.T. (2018). Influence of under sleeper pads on ballast behavior under cyclic loading: experimental and numerical studies, Journal of Geotechnical and Geoenvironmental Engineering, 144(9): 04018068.

Tennakoon, N.C. (2012). Geotechnical study of engineering behaviour of fouled ballast. PhD Thesis, School of Civil, Mining and Environmental Engineering, University of Wollongong.

Terzaghi, K., Peck, R.B. and Mesri, G. (1996). Soil mechanics in engineering practice, John Wiley & Sons, pp 592.

Applicability of degradation prediction models for unpaved roads in Sri Lanka

J.A.N.N. Jayakody & S.K. Navaratnarajah
Department of Civil Engineering, Faculty of Engineering, University of Peradeniya, Sri Lanka

D.J. Robert*
School of Engineering (Civil & Infrastructure), RMIT University, Melbourne, Australia

M.C.M. Nasvi & L.C. Kurukulasuriya
Department of Civil Engineering, Faculty of Engineering, University of Peradeniya, Sri Lanka

F. Giustozzi, C. Gunasekara & S. Setunge
School of Engineering (Civil & Infrastructure), RMIT University, Melbourne, Australia

**corresponding author (dilan.robert@rmit.edu.au)*

ABSTRACT: Nearly 60% of the roads in Sri Lanka are unpaved of which the majority is managed by local government authorities. Lack of monitoring and maintenance practices of these gravel roads deteriorates the conditions significantly and results in costly maintenance or frequent re-graveling. This could be minimized if the deterioration is predicted with a higher degree of accuracy with local calibration and attend the maintenance and re-gravelling work at the correct time. With the unavailability of the past records of maintenance data, a field study was conducted for 'Swiss road' in Inamaluwa in the central province of Sri Lanka using field measurements. The aim of this study was to investigate the applicability of Gravel Loss (GL) prediction models to Sri Lanka and to predict the maintenance requirement of gravel roads. The GL was identified as the critical distress type and was modeled using six common prediction models, viz. HDM-4 model, TRH 20 model, Australian model, ARRB model, Brazil model and Kenyan model. The GL predictions were conducted using field calibrated models embedded within probabilistic framework using Markov analysis. From the study it was identified that HDM-4, TRH 20, ARRB and Kenyan models give a closer prediction to the actual values and that HDM-4 model is recommended for Sri Lanka with proper calibration. The study should be continued for a longer period to obtain more reliable degradation predictions.

Keywords: Gravel loss, Degradation prediction, Condition rating, Markov analysis

1 INTRODUCTION

1.1 *Unsealed roads in Sri Lanka*

In Sri Lanka, the total road network consists of 217 km of expressways, 12,220 km of national road of 'A' and 'B' categories, 15,500 km of provincial roads of 'C' and 'D' categories and more than 85,000 km of minor roads of 'E' category, of which a total of 60% of the roads are unpaved (ADB, 2013). As of the year 2001, 33% of the provincial roads and 87% of the local roads in Sri Lanka, which belong to categories C, D and E, were kept unpaved, making a total length of unpaved roads more than 51,000 km to-date. Most of the unsealed roads in Sri Lanka are connecting roads to the main road network facilitating transportation for agricultural lands and other local areas.

Unsealed roads are generally considered complex in management as their condition is often challenged by climatic factors, the material used, traffic, type of terrain, road geometry and the maintenance practices followed. Several distresses occur in unsealed roads including insufficient drainage capacity, dust, corrugation, potholes, ruts, gravel loss and exposure of oversized aggregates (Henning et al., 2006, Alzubaidi and Magnusson, 2002). Among them, gravel loss (GL) is the most critical distress from the economic point of view, as the cost for re-graveling of a gravel road is as high as 60% of the total maintenance cost (Henning et al., 2008). According to Beckemeyer and McPeak (1995), re-gravelling is the most significant factor affecting the life cycle

operating costs of an unsealed road pavement and typically a 150 mm thick unsealed wearing course will be lost within 8 to 12 years (Andrews, 2009).

1.2 *Gravel loss (GL) and different GL prediction models*

GL is defined as the change in the average gravel thickness over a period of time. The rate of GL is recorded as the vertical loss in mm of material from the road surface (Paterson, 1991). It can typically be 20 to 50 mm per year in a tropical environment with medium to high rainfall (Pardeshi et al., 2020, Rolt et al., 2020). Many studies have been conducted on monitoring gravel loss throughout the world and many models are in practice for GL prediction. These different GL models use various input parameters, which are showing different sensitivity features. The models considered in this study are HDM-4 model, TRH 20 model, ARRB model, Australian model, Brazil model and Kenyan model and they are shown in Table 1 below.

Even though different GL models are available in current practice, most of these models cannot be directly applied to the local conditions as they have been developed based on conditions applicable to a particular context. Direct application of these models without realistic calibrations for the maintenance predictions can lead to unrealistic outcomes. Limited studies and data are available for Sri Lankan unsealed roads to evaluate the applicability of different gravel loss models suit for local conditions. In this study, a selected gravel road is monitored with periodic measurements and the suitability of the available models is evaluated to support maintenance prediction which can enhance the resilience of these critical infrastructure.

2 METHODOLOGY

2.1 *Study area*

In this study "Swiss road" in Inamaluwa area in Central province of Sri Lanka which is managed by Dambulla *Pradeshiya sabha*, was considered for the field measurements and subsequent GL prediction. This area is located in the dry zone of Sri Lanka, which is having 1000-1500 mm of rainfall annually (Katupotha and Kodituwakku, 2015). The average daily traffic in both directions is 60 veh/day as obtained from the traffic survey conducted as a part of this study.

Table 1: Different GL models and their features

Model	Model Equation
HDM-4	$G_{LA} = k_{gl}(12.63 + 0.898(MMP * G) + 3.65(KT * ADT))$ (1) Where G_{LA} is gravel loss (mm); k_{gl} is the calibration factor for gravel loss; ADT is average daily traffic (total vehicles/day); MMP is mean monthly precipitation (mm/month); G is average longitudinal gradient of the road (%) and KT is traffic-induced material whip-off coefficient
TRH 20 model	$G_{LA} = 3.65(ADT(0.059 + 0.0027N - 0.0006P_{26}) - 0.367N - 0.0014PF + 0.0474AP_{26}$ (2) Where G_{LA} is gravel loss (mm); ADT is average daily traffic (vehicles/day); N is the Weinert N value; P_{26} is amount of material passing 26.5 mm sieve (%) and PF is plasticity factor
ARRB model	$G_{LA} = f\left[\frac{Ta^2}{Ta^2+50}\right][4.2 + 0.092 * Ta + 3.50 * RI^2 + 1.88 * Vc]$ (3) Where G_{LA} is GL (mm); Ta is annual traffic in both directions (thousands of vehicles); RI is annual rainfall (m); VC is gradient for uniform road length (%) and f is constant for gravels
Australian model	$G_{LA} = k_{gl*}\frac{D}{100} * (-0.00985 * ADT - 0.02991 * MMP - 0.00583 * PI * P_{075})$ (4) Where G_{LA} is gravel loss (mm); k_{gl} is the calibration factor for gravel loss, D is time period (days); ADT is average daily traffic (total vehicles/day); MMP is mean monthly precipitation (mm/month); P_{075} is the percentage of surface material passing 0.075mm sieve
Brazil model	$G_{LA} = D[1.58 + 0.366 * G + 0.083 * SV - 0.210 * PI + 0.0132 * NC + 0.0081 * NT + \frac{420.45}{R}]$ (5) Where, G_{LA} is gravel loss (mm); D is time under consideration in hundreds of days (days/100); G is absolute value of gradient (%); SV is percentage of surface material passing 0.075mm sieve; PI is plasticity index (%); NC is average daily car traffic in both directions; NT is average daily truck traffic in both directions and R is radius of horizontal curvature (m)
Kenyan model	$G_{LA} = f\left[\frac{Ta^2}{Ta^2+50}\right][4.2 + 0.092 * Ta + 3.50 * RI^2 + 1.88 * Vc]$ (6) Where G_{LA} is gravel loss (mm); Ta is annual traffic in both directions (thousands of vehicles); RI is annual rainfall (m); VC is Gradient for uniform road length (%) and f is Constant for gravels (Laterite-0.94, quartzitic-1.1, volcanic-0.7, coral gravel-1.5)

2.2 *Field data collection*

The selected road is 2.3 km in length in total out of which 0.8 km is paved with gravel surface. Three 100 m sections of the road representing the gravel length were selected for the study. First, the selected 100 m sections were established on the field using steel pegs and concrete pegs to make a temporary benchmark (TBM) for each section. After establishing the sections, the first set of surface-level measurements were obtained with reference to the established TBM. Fifteen-point measurements (1-15) were recorded for each 100 m section covering three cross-sections (CS 1, CS 2 and CS 3) and each cross section has five measuring points as shown in Fig. 1. The levels at these points (1-15) were monitored at two-month intervals using a precise level instrument and the GL value was calculated based on the difference in the level readings.

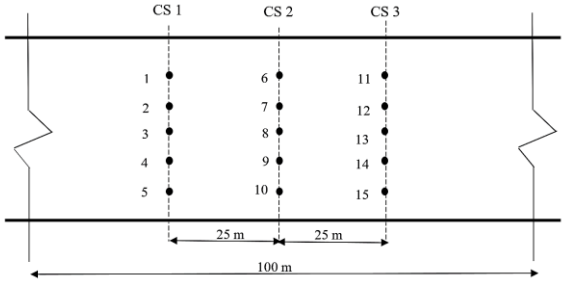

Fig. 1: Established points for GL monitoring

The surface profiles at time T1 (at time = 0) and T2 (after 2 months) along the road section 1 (100 m length) for CS 1 (points 1-5), CS 2 (points 6-10) and CS 3 (points 11-15) are shown in *Fig. 2.*

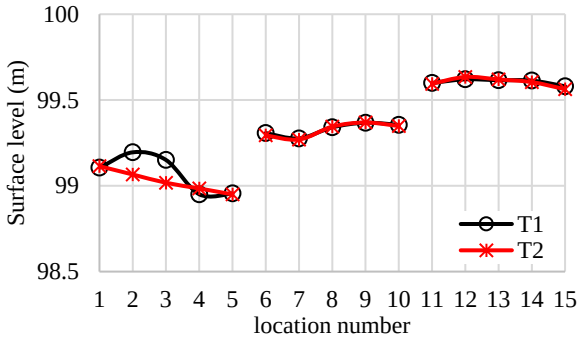

Fig.2: Surface level variation in the road

The trend of the level variation in the CS 1 was observed to highly deviate from the other two sections, it seems unrealistic, and therefore the measurements obtained from the section CS 1 were eliminated from the analysis. The observed deviation at CS 1 might be due to the gradient of the road which has accelerated erosion of surface due to heavy rain just before the T2 measurements. Therefore, the average GL values from the other two sections (CS 2 and CS 3) were used for the prediction of the GL rate.

2.3 *Markov analysis for GL prediction*

Markov analysis is one of the common probabilistic modeling techniques and it has the ability to develop a prediction model with just two sets of data unlike regression models which need data over a period of years to predict trends. It is also able to calculate the performance even if the data for some years is missing and able to capture the random nature of the pavement degradation (Aleadelat et al., 2019, Saha et al., 2017, Butt et al., 1987). In the Markov analysis, future decisions on preservation actions for roads are not fixed and it depends only on the current performance of the pavement.

Markov analysis is performed assuming the pavement is in a near-perfect condition, and with the time, the pavement condition will be deteriorated and the damage will be increased. A pavement condition rating is defined at each level to depict the overall condition of the pavement with reference to a scale such as 0-5 or 0-10. A state vector, which gives the probability of a pavement section's being in each of the given states, is developed and the corresponding transition probability matrix (TPM) is derived. In the Markov analysis, it is assumed that a pavement cannot degrade by more than a single state within the considered period of time. The same TPM is used for the entire period of analysis with homogeneous approach while a separate TPM for each year is required for the non-homogeneous approach. Through the homogeneous approach, by using the initial state vector [v (0)] and the TPM, the probability at any given year (t) is predicted by using Equations (7) to (9) (Saha et al., 2017).

$$[v(1)] = [v(0) \text{ x } [TPM] \quad (7)$$

$$[v(2)] = [v(1) \text{ x } [TPM] = [v(0)] \text{ x } [TPM]^2 \quad (8)$$

$$[v(t)] = [v(t-1) \text{ x } [TPM] = [v(0)] \text{ x } [TPM]^t \quad (9)$$

Annual GL was predicted based on the field data for geometry, material, traffic and climatic parameters as inputs using the selected GL prediction equations. Here, calibration factor for the HDM-4 model is taken as 1 due to the limitation of data for a proper calibration. The road section was rated according to the GL, adhering to 5 classes defined based on the total lost gravel thickness after each year. The 'State 5' was assigned for roads in the best condition, for which the limiting GL is 30 mm. The limiting GL values considered for states 4, 3, 2 and 1 are 60, 90, 120 and 150 mm, respectively. These values were selected depending on the general gravel thickness of

unsealed roads in Sri Lanka, which is around 6 inches (150 mm) according to the practitioners.

Based on the observed GL values, the transition probabilities were calculated using Markov analysis and the transition probability matrix was developed. The initial probability matrix was developed assuming a near-perfect condition at the start of the analysis [1 0 0 0 0] and using the Markovian probabilistic approach, the condition at the end of each year was predicted and the road condition versus time curve was developed for the section considered.

2.4 *Life cycle cost analysis*

Maintenance activities could be scheduled in an efficient and economical way, if a proper prediction of the degradation is available. This avoids both unnecessary and insufficient maintenance activities. A life cycle analysis along with a cost prediction is significant in such decisions. The study was extended to predict the lifecycle cost based on the GL behavior by applying the Markov analysis. Having obtained the TPM for GL, by incorporating the unit costs associated with the maintenance at each transition to a lower state (increase in the GL), the cost prediction curves at each state with time were produced.

3 RESULTS

3.1 *Degradation prediction – Deterministic method*

Deterministic method was used to calculate the GL values using different available GL prediction models. Input parameters for traffic, climate, geometric and material properties as required by each model as shown in the Table 2 were fed to the models using actual field conditions.

The cumulative GL values after each year were calculated using model equations and they were plotted with the time as in Fig. 3.

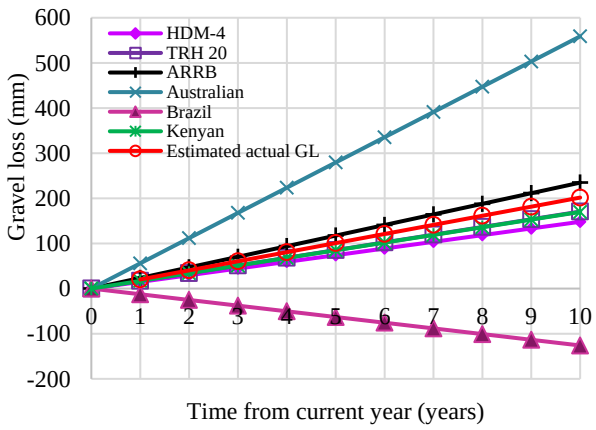

Fig. 3: GL prediction with time from different models

Table 2: Input parameters for different GL models

Input type	Input parameter	Input values	Applicable models					
			HDM-4	TRH 20	ARRB	Australian	Brazil	Kenyan
Material	Material Type -*f*	1.3, (0.94*)			✓			✓
	Plasticity index -PI	24	✓			✓	✓	
	Passing 0.075mm sieve -P075 (%)	71	✓	✓		✓	✓	
	Passing 26.0mm sieve -P26 (%)	100		✓				
Traffic	Annual average daily traffic -AADT (veh/day)	60	✓	✓		✓	✓	
	Annual traffic in both direction -Ta (veh/year)	21900			✓			✓
Climate	Mean monthly Precipitation -MMP (m/month)	0.16	✓			✓		
	Annual rainfall -RI (mm/year)	1800			✓			✓
	Weinert N-value	1		✓				
Geometry	Gradient (%) for uniform road length-Vc	0.8	✓		✓		✓	✓
	Average curvature -KVc (deg/km)	0	✓					
Calibration factor	Calibration factor for GL - k_{gl}	1	✓			✓		

* used for Kenyan model

According to Fig. 3, there are considerable differences in the GL values calculated by different models. This is due to the variation of the input parameters, and the model coefficient values developed for different regions of the world. GL predicted from models such as HDM-4, TRH 20, Kenyan and ARRB show a good agreement with the actual GL values, whereas Brazil model underpredicts the GL value while the Australian model overpredicts the GL compared to the actual GL value. Only Brazil model includes a parameter for the radius of the horizontal curvature of the road, and as the selected road sections were straight sections, the predicted GL values from Brazil model have been comparatively lower and it is not comparable with the other GL models for local site conditions investigated in this study. The Australian model is more sensitive to plasticity factor (PF = PI×P075), which was estimated as higher values, and as a result, the GL values estimated using this model are high compared to other GL models.

The rate of actual GL was calculated using the field measurements for the periods of 2 months and using that rate, actual GL curve was developed for 10 years assuming a linear behavior throughout the considered time and any growth in the ADT has not been

considered. Based on these results, ARRB, HDM-4, Kenyan and TRH 20 models have closer trends with the actual GL observed in the field. HDM-4 model is also applicable to Sri Lankan roads with a proper calibration, as it is a globally accepted model and less dependent on the sensitivity of the input parameters.

Even though the prediction was continued up to 10 years, when the cumulative GL reaches 150 mm which is the typical surface gravel layer thickness used in Sri Lanka, the road is completely out of gravel layer and it exposes to the subgrade. Accordingly, the cumulative GL exceeding 150mm indicate a complete failure in terms of GL.

3.2 *Degradation prediction – Probabilistic method*

The application of Markov analysis to different models and field data has estimated the degradation prediction for 10 years. Fig. 4 shows the prediction of the variation of road condition states using Markov analysis based on gravel thickness loss according to the actual field measurements. As the road was assumed to be at near-perfect condition at the beginning, the probability of the road section being in the condition 5 at time 0 is 100%. With the progression of GL, the condition shifts to lower values gradually making a non-linear variation and the probability of road section falling to condition 1 increase with time indicating the failure of the road.

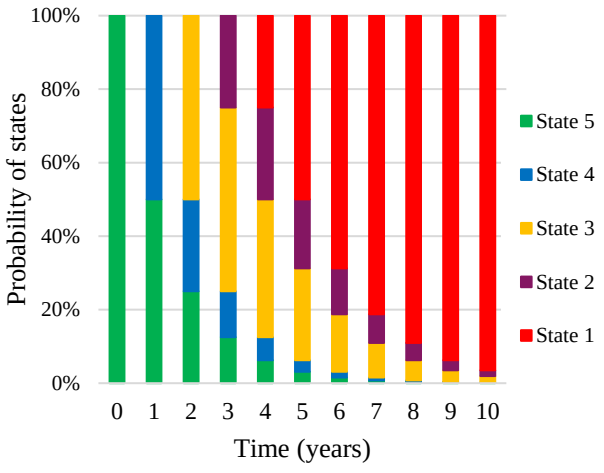

Fig. 4: Markov analysis for field data

The degradation curves from different models are shown in Fig.5. Australian model shows a higher rate of degradation than the actual while the HDM-4, TRH 20 and Kenyan models predict lower than the actual rate which is similar with their deterministic behaviors. ARRB model shows a degradation rate more similar to actual behavior.

When comparing the probabilistic prediction based on states, it is clear that the actual behavior is well matched with the ARRB model even without any calibration for this selected road. This is because the GL values result from this model fall into the same state when applying the Markov analysis as states are defined as a range of values. As the Australian model shows a higher annual GL rate, it has reached the failure condition within 3 years according to the probabilistic prediction. GL trend of HDM-4, TRH 20, Kenyan models match well with the actual behavior even though it shows comparatively somewhat lesser GL values due to the variation of model inputs. Even though the predictions are based on data collected for a period of 2 months, the data obtained from long-term monitoring of GL can improve the calibration with reliable model predictions.

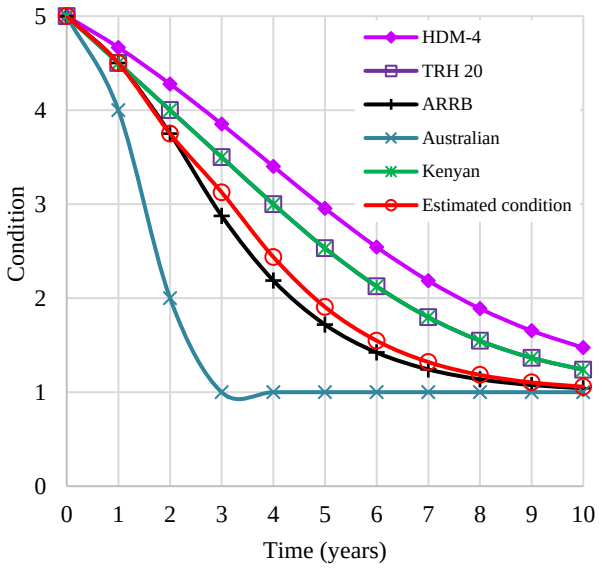

Fig. 5: Condition prediction curves

3.3 *Lifecycle cost prediction*

The maintenance cost rates used for the unsealed roads in Sri Lanka were obtained from 'Highway schedule of Rates (HSR) 2020' (MOHSL, 2019). Accordingly, re-gravelling cost for 1 km length of gravel road having a 5.0 m average width and a 150 mm gravel thickness layer is 2.7 million Sri Lankan rupees. The condition prediction from the Markov analysis was used for the calculations. Total cost required to bring a 1 km road section to a particular condition based on the gravel thickness was obtained by considering all the possible transitions and the total cost to bring to a condition 5, 4 and 3 are shown in Fig. 6.

Accordingly, the cost required to bring this road section to a higher condition increases non-linearly with time. This shows the importance of taking the

maintenance actions at the correct time to avoid unnecessary additional costs for local councils.

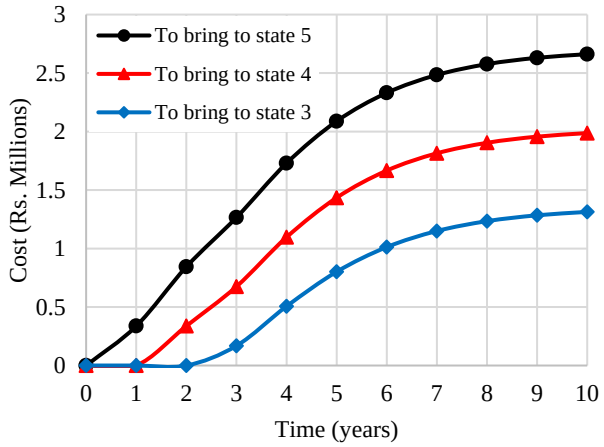

Fig. 6: Maintenance cost prediction for 1 km

4 CONCLUSIONS

This study was conducted to predict the GL and condition assessment of an unsealed road in the Central Province of Sri Lanka using Markov analysis. Based on the outcome of this study, the following conclusions are drawn;

- Among the considered models; ARRB, TRH 20, Kenyan and HDM-4 models have closely predicted the actual GL value. HDM-4 model is recommended to the Sri Lankan roads based on the current study as it widely used internationally with local calibration of the input parameters which are of less sensitive in general.
- Re-gravelling of this road section is recommended at or before nine-year intervals as it reaches failure condition after nine years.
- When the service life reaches nine years, the expected cost to bring the road to a better state is significantly high. Therefore, timely maintenance decisions should be taken considering both deterioration rate and available budget.
- With the unavailability of historical data, the study was limited to a very short period and the monitoring should be continued for a longer period across many other roads to obtain more reliable calibration parameters and corresponding degradation predictions. The field monitoring study is being continued at present for other unpaved roads in Sri Lanka to develop a maintenance prediction framework.

The current study could be used to assist the long-term sustainability of unsealed roads in Sri Lanka as this can be used to predict the maintenance requirement and the expected maintenance cost with time. The regular maintenance can reduce the burden of unexpected cost boosts in future in addition to provide better level of service for the road users.

ACKNOWLEDGMENTS

The support of Excutive Engineer's office, PRDA, Naula and the *Pradeshiya sabha* Dambulla in facilitating field data collection and partial funding of RMIT towards this research is gratefully acknowledged.

REFERENCES

ADB. 2013. *Annual report-2012*. Advancing Regional Cooperation And Integration In Asia And The Pacific, <https://www.adb.org/documents/adb-annual-report-2012> (March 18, 2021).

Aleadelat, W., Wulff, S. & Ksaibati, K. 2019. Development of performance prediction models for gravel roads using Markov chains. *American Journal of Civil Engineering*, 7**,** 73-81.

Alzubaidi, H. & Magnusson, R. 2002. Deterioration and rating of gravel roads: state of the art. *Road Materials and Pavement Design*, 3**,** 235-260.

Andrews, B. 2009. Guide to pavement technology: part 6: unsealed pavements.

Beckemeyer, C. A. & Mcpeak, T. J. 1995. Rural Road Design, Maintenance, and Rehabilitation Guide.

Butt, A. A., Shahin, M. Y., Feighan, K. J. & Carpenter, S. H. 1987. *Pavement performance prediction model using the Markov process*.

Henning, F. P., Giummarra, G. J. & Roux, D. C. 2008. The development of gravel deterioration models for adoption in a New Zealand gravel road management system.

Henning, T., Kadar, P. & Bennett, C. R. 2006. Surfacing alternatives for unsealed rural roads.

Katupotha, J. & Kodituwakku, K. 2015. Diversity of Vegetation Types of the Pidurangala Granitic Inselberg with Ancient Forest Monastery, Near Sigiriya, Sri Lanka: A Preliminary Study.

MOHSL. 2019. *Highway schedule of rates (HSR) - 2019* <https://www.mohsl.gov.lk/downloads/1565994329.pdf > (April 20, 2021).

Pardeshi, V., Nimbalkar, S. & Khabbaz, H. 2020. Field Assessment of Gravel Loss on Unsealed Roads in Australia. *Frontiers in Built Environment*, 6**,** 3.

Paterson, W. 1991. Deterioration and maintenance of unpaved roads: models of roughness and material loss. *Transportation research record*, 1291**,** 143-156.

Rolt, J., Mukura, K. & Otto, A. 2020. Development of a Simplified Agency Life-Cycle Costing Tool for Gravel Roads. *Sustainability*, 12**,** 4512.

Saha, P., Ksaibati, K. & Atadero, R. 2017. Developing pavement distress deterioration models for pavement management system using markovian probabilistic process. *Advances in Civil Engineering*, 2017.

Influence of geosynthetic and rubber inclusions on shear and breakage behavior of rail track ballast

S. Venuja
Department of Civil Engineering, Faculty of Engineering, University of Peradeniya, Sri Lanka

S. K. Navaratnarajah
Department of Civil Engineering, Faculty of Engineering, University of Peradeniya, Sri Lanka

ABSTRACT: Ballasted rail tracks and concrete slab tracks are the two major types of rail track structures all around the world. Due to the ease of construction and relatively low initial cost, ballasted tracks are popular compared to slab tracks. Ballast is a coarse and highly angular material with high shear strength and bearing capacity. Ballast is getting degraded over time due to the continuous transmission of energy by the wheel loads from freight and passenger trains, which leads to track settlement, track degradation, and high cost for maintenance. Rubber mats and geogrids are used in railways to improve the performance of ballast used in rail tracks. . In this study, several tests were conducted on fresh ballast and ballast stabilized with geosynthetic and rubber under direct shear loadings to check the performance of ballast. The outcomes in this study show that the combination of rubber mats with geogrid works well in terms of reducing ballast degradation and maintaining shear resistance of the ballast layer.

1 INTRODUCTION

Rail transport provides safer and economically beneficial passage to a large number of commuters and a large quantity of freights at once. It also has another advantage of having traffic problems faced in roadway transport. Typical conventional rail tracks consist of rails, sleepers, fasteners, ballast layer, capping layer, and formation soil (Alemu, 2011, Boler et al., 2014, Feng et al., 2019). The ballast layer is the primary load-bearing layer thus a thicker layer consists of granular aggregates with nominal size 40 - 50 mm (Claisse and Calla, 2006). It also provides easy water flow through its larger voids (Bian et al., 2016, Guo et al., 2020).

Ballast particles are undergoing corner breakage, crushing, and fouling due to either repeated train movements or operation during maintenance activities such as tamping. Aggregates become rounded as the corners are broken, thus reduction in particle interlocking within the ballast layer. This leads to excessive total and differential settlement hence discomfort and safety issues in train transport (Aursudkij, 2007, Dahal et al., 2018, Dash and Shivadas, 2012, Ebrahimi et al., 2015). Still, the ballast is more desirable to track structure compared to concrete or asphalt slabs. Therefore, it is essential to improve the performance and service life of ballast under repeated cyclic and impact loads using artificial inclusions.

This paper presents the application of artificial inclusions and the ballast performance improvement using rubber pads and geogrids. This paper also discusses the application and benefits, the experimental approach, results, and derived conclusions based on the laboratory tests carried out on ballast with rubber pads and geogrid under shearing load conditions using a large-scale direct shear test apparatus.

2 APPLICATION AND BENEFITS

2.1 *Rubber pads*

Rubber inclusions lessen the intensity of impact and cyclic loads generated by moving trains on the substructure and reduces the track degradation. It also absorbs the vibration and provides a more comfortable and less noisy travel experience to the commuters. Rail pads (RP), under sleeper pads (USP), and under ballast mats (UBM) are the commonly used different types of rubber inclusions in the track structure (Navaratnarajah et al., 2020). As shown in Fig. 1, these rubber elements are inserted in different positions.

The flexibility of USP material increases the number of load-bearing sleepers per axle and also increases the contact area between sleeper and ballast (Navaratnarajah, 2017, Navaratnarajah, 2019). This leads to a significant reduction of the stress on the ballast layer. Sleepers with USPs also improve the lateral resistance of the track (Gräbe et al., 2016, Navaratnarajah et al., 2015). UBMs are more effective on stiffer formation conditions as it reduces the faster ballast deterioration. Another advantage of the introduction of UBM is the reduced

thickness of the ballast layer is sufficient to perform well (Indraratna et al., 2014, Indraratna et al., 2020). Nowadays researchers are working on the effect of placing recycled rubber clumps into the capping layer (Indraratna et al., 2019, Indraratna et al., 2020, Sun et al., 2020).

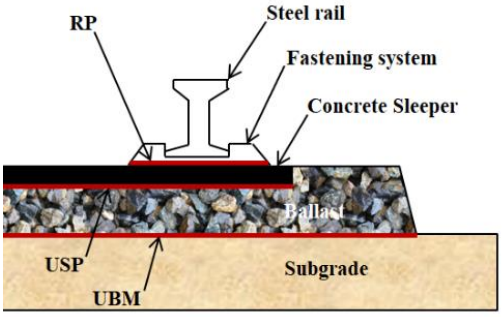

Fig. 1 Various rubber pads used in rail track structure

2.2 *Geogrids*

Geogrids are flexible, tensile elements that are strong in tension. When geogrid is inserted into the ballast layer it acts as reinforcement. It interlocks the ballast aggregates into its open apertures and resists the movement of the aggregates (see Fig. 2). Therefore, the ballast layer experiences lateral confinement after the installation of geogrid. Geogrid also facilitates quicker drainage without any hindrance. And also it leads to an increase in shear strength of the ballast layer (Biabani and Indraratna, 2015, Chen et al., 2012, Horníček et al., 2017, Sweta and Hussaini, 2018). Uniaxial, biaxial, and triaxial geogrids are commercially available but biaxial geogrids are adapted for rail track applications. Geogrid reinforcement gives optimum performance improvement to the tracks on weak subgrade as it provides more compressibility (Chawla and Shahu, 2016, Indraratna et al., 2006, Ngo et al., 2017, Venuja et al., 2020).

Fig. 2 Mechanical interlocking of ballast aggregates into the geogrid apertures

3 EXPERIMENTAL WORK

3.1 *Materials and test apparatus*

Essential materials for this experimentally based study are ballast, USP, UBM, and geogrid. Ballast was collected from the Nawalapitiya railway unit. Ballast was sieved and thoroughly cleaned with water to remove any adhered particles. The mechanical properties of USP and UBM which were used in this study can be found elsewhere (Venuja et al., 2020). Polypropylene extruded biaxial geogrid was obtained from a local supplier.

Large-scale direct shear test apparatus was used to conduct tests on ballast with and without the inclusion of USP, UBM, and geogrid. Unlike the square shear plane of standard direct shear apparatus, this test device is designed with a circular shear area. Thus, the apparatus consists of two equal hollow cylinders with dimensions of 400 mm diameter and 150 mm height each. The upper cylinder is immobile where the lower cylinder is allowed to move in the shearing direction only. Shearing can be applied using a hydraulic jack and normal load can be applied to the sample using a static lever arm system.

3.2 *Test setup*

Ballast was mixed in the mass proportions as shown in Table 1 to get the particle size distribution that satisfies the standard limits of Indian Railway ballast requirements. After mixing, ballast was filled into the apparatus in three layers and each layer was compacted using a rubber-padded hammer to achieve the field unit weight of 16.1 kN/m^3.

Table 1. The particle size distribution of test specimen

Sieve sizes / (mm)	mass retained (%)
63	0
50	32
37.5	28
25	25
20	15

Tests were conducted on fresh ballast, ballast with single artificial inclusion, and ballast with a combination of artificial inclusions. UBM was laid at the bottom of the apparatus, USP was put on top of the ballast, and geogrid was placed on top of the UBM based on the test requirement (see Fig. 3). All test specimens were tested under 30, 60, and 90 kPa normal stresses with a constant lateral shearing rate of 4 mm/min. Load cell, vertical displacement transducer, and horizontal displacement transducer were connected to the data logger to obtain the

readings of shear load, vertical displacement, and horizontal displacement with time, respectively.

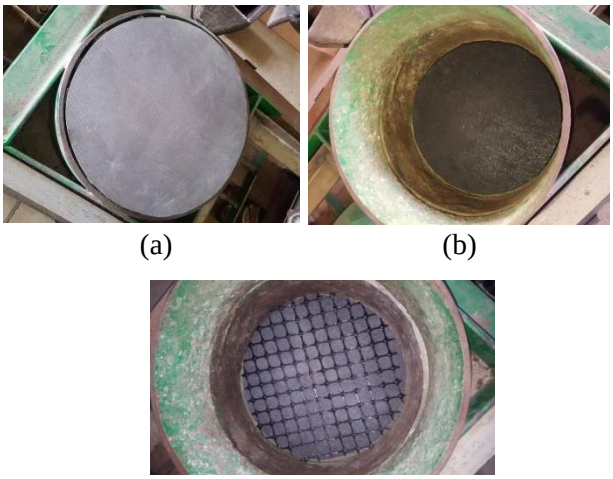

(a) (b)

(c)

Fig. 3 Type of artificial inclusions and it's insertion positions; (a) USP; (b) UBM; (c) Geogrid

4 RESULTS ANALYSIS

Shear stresses were calculated using the corrected shear area for the circular-shaped shear plane suggested by Olson and Lai (1989). Fig. 4 shows the shear stress variation with the shear strain of all types of samples under 30, 60, and 90 kPa. Shear stresses of all samples showed an increasing trend and attained maximum values near 13 to 15 % of shear strains. Shear stress increased with applied normal loads irrespective of sample type. This is due to the higher interlocking between aggregates which is induced by higher normal stresses, results improved frictional resistance. Further, as shown in Table 2, friction angles of each type of sample were calculated by developing Mohr-Coulomb failure envelopes. The rubber elements showed a reduction in shearing resistance compared to fresh ballast. This is due to the fact that the rough concrete interface is replaced with a somewhat smooth interface of rubber elements. However, ballast with (USP + UBM + geogrid) showed nearly the same values of friction angle as fresh ballast. This could be a result of the mechanical interlocking provided by geogrid which provides more resistance to shearing.

Table 2. Friction angles of various samples using Mohr-Coulomb criteria

Sample	Friction angle (°)
Fresh ballast	68
Ballast + UBM	61
Ballast + USP	59
Ballast + UBM + USP	62
Ballast + UBM + USP + Geogrid	67

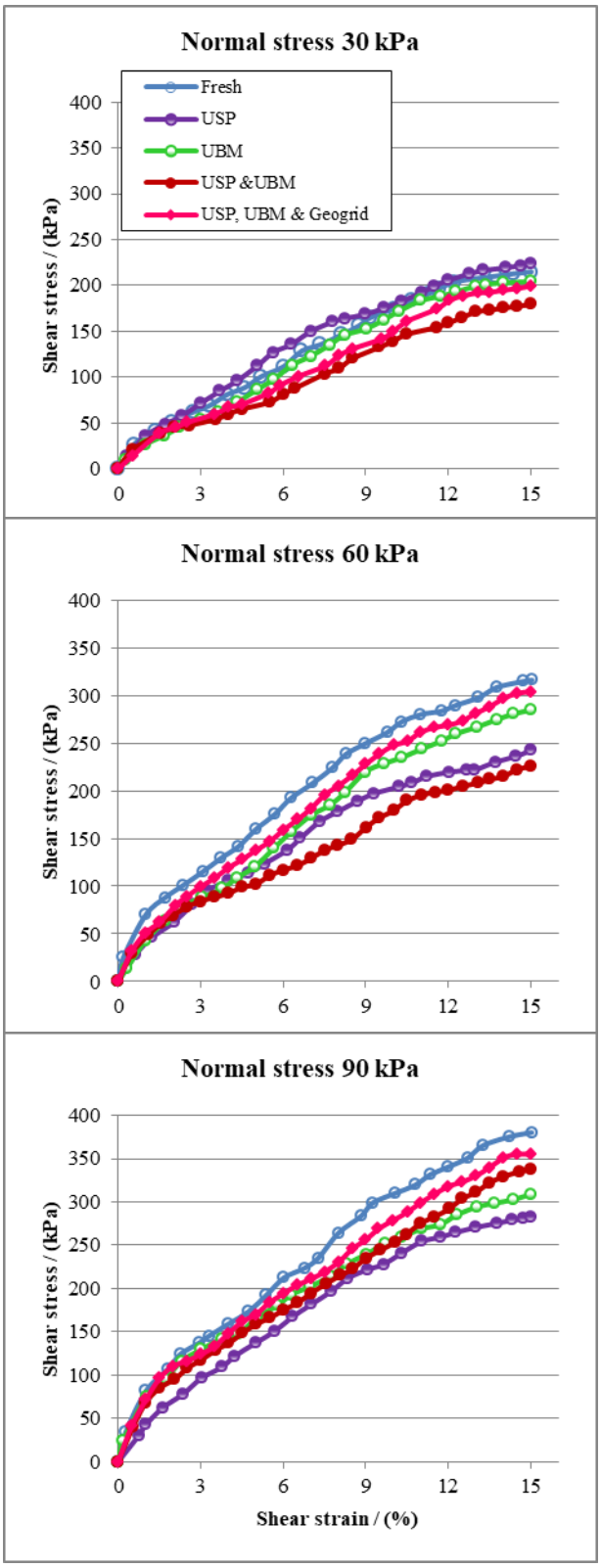

Fig. 4 Shear stress variation of different samples with shear strain under different normal stresses

Fig. 5 shows the dilation behavior of different samples under 60 kPa normal stress with shear strain. All samples showed minimal compression at the initial shear strain and started dilating after that. This is because the normal load application is

prominent at the beginning. Dilation is caused by the rolling over of ballast aggregates on top of each other during shearing. A significant change in volumetric behavior with sample types was not observed. But dilation was decreased with high normal stresses for all types of samples.

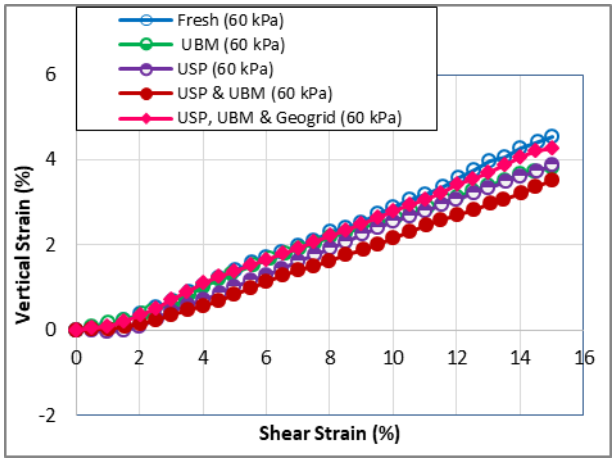

Fig. 5 Vertical strain variation of different samples with shear strain under 60 kPa normal stress

Breakage of ballast particles was observed at the end of each test. Ballast breakage is an important parameter that needs to be quantified which influences the track performance. The well-known method to quantify the breakage is the ballast breakage index (BBI) which was proposed by Indraratna et al. (2005) is used in this study. BBI values were calculated by conducting sieve analysis after each test and plotting the particle size distribution of each sample before and after the test. Calculated BBI values of different samples are tabulated in Table 3.

Table 3. BBI of various samples under different normal loads

Ballast and type of inclusions	Normal Stress		
	30 kPa	60 kPa	90 kPa
Fresh ballast (S1)	0.043	0.052	0.069
Ballast + UBM (S2)	0.033	0.034	0.059
Ballast + USP (S3)	0.024	0.030	0.037
Ballast + UBM + USP (S4)	0.023	0.029	0.035
Ballast + UBM + USP + Geogrid (S5)	0.020	0.030	0.036

When the normal stress increased from 30 kPa to 90 kPa, there is a significant increase in the BBI of each sample. This is because the higher normal stress compresses the ballast sample which leads to higher breakage. Less breakage was observed for the ballast with a combination of USP and UBM as USP distributed normal loads through an extended area and UBM created a softer interface with ballast aggregates. Also, the BBI of all samples under 90 kPa were calculated layers-wise by painting each layer. As the shear band is formed near the shear plane, particles in the shear band were undergone high breakage therefore high BBI was observed in the middle layer of each sample as shown in Fig. 6.

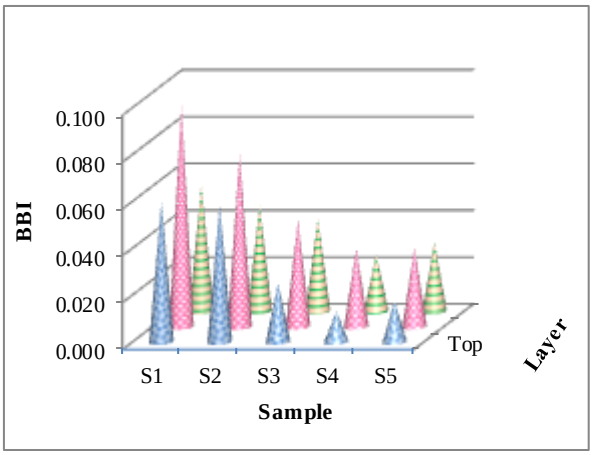

Fig. 6 Layer wise BBI of each type of sample under 90 kPa normal stress

5 CONCLUSIONS

This series of direct shear tests were conducted on ballast to analyze the shear, dilation, and breakage behavior of ballast with artificial inclusions such as USP, UBM, and geogrid. Regardless of the type of inclusions, shear stress increased with normal stress as higher frictional resistance was generated due to improved particle interlocking. Similarly, high breakage was observed with higher normal stress. Ballast with USP and UBM showed a minimum value of BBI. Further, rubber reduces the shear slightly and reduces the breakage considerably high. However, the inclusion of geogrid with the combination of rubber brings back some of the lost shear of ballast. Therefore, based on the finding from this study, it is recommended to use a combination of rubber pads and geogrid in the rail tracks to improve the performance in terms of increasing ballast shear resistance and reducing ballast particle breakage.

ACKNOWLEDGMENTS

This research work was mainly funded by the University of Peradeniya Research Grant (Grant Number: URG-2017-29-E). Accelerating Higher Education Expansion and Development (AHEAD) Operation of the Ministry of Higher Education funded by the World Bank (Grant Number: AHEAD/RA3/DOR/STEM/No.63) is also acknowledged here with the appreciation by the Authors. Further, extended thanks to the Railway District Engineer, Nanuoya and staff of Nawalapitiya Railway units of Sri Lankan Railways for their help and support in collecting the ballast materials.

REFERENCES

Alemu, A.Y. (2011). Survey of railway ballast selection and aspects of modeling techniques. Master Degree, Royal Institute of Technology.

Aursudkij, B. (2007). A laboratory study of railway ballast behavior under traffic loading and tamping maintenance. Doctor of Philosophy, University of Nottingham.

Biabani, M.M. and Indraratna, B. (2015). An evaluation of the interface behaviour of rail subballast stabilised with geogrids and geomembranes, Geotextiles and Geomembranes, 43(3): 240-249.

Bian, X., Huang, H., Tutumluer, E. and Gao, Y. (2016). "Critical particle size" and ballast gradation studied by Discrete Element Modeling, Transportation Geotechnics, 6: 38-44.

Boler, H., Qian, Y. and Tutumluer, E. (2014). Influence of Size and Shape Properties of Railroad Ballast on Aggregate Packing, Transportation Research Record: Journal of the Transportation Research Board, 2448(1): 94-104.

Chawla, S. and Shahu, J.T. (2016). Reinforcement and mud-pumping benefits of geosynthetics in railway tracks: Model tests, Geotextiles and Geomembranes, 44(3): 366-380.

Chen, C., McDowell, G.R. and Thom, N.H. (2012). Discrete element modelling of cyclic loads of geogrid-reinforced ballast under confined and unconfined conditions, Geotextiles and Geomembranes, 35: 76-86.

Claisse, P. and Calla, C. (2006). Rail ballast: conclusions from a historical perspective, Proceedings of the Institution of Civil Engineers - Transport, 159(2): 69-74.

Dahal, B., Naziur Mahmud, S.M. and Mishra, D. (2018). Simulating ballast breakage under repeated loading using the discrete element method, Proc., Proceedings of the 2018 Joint Rail Conference, pp 1-10.

Dash, S.K. and Shivadas, A.S. (2012). Performance Improvement of Railway Ballast Using Geocells, Indian Geotechnical Journal, 42(3): 186-193.

Ebrahimi, A., Tinjum, J.M. and Edil, T.B. (2015). Deformational behavior of fouled railway ballast, Canadian Geotechnical Journal, 52(3): 344-355.

Feng, B., Park, E.H., Huang, H., Li, W., Tutumluer, E., Hashash, Y.M.A. and Bian, X. (2019). Discrete Element Modeling of Full-Scale Ballasted Track Dynamic Responses from an Innovative High-Speed Rail Testing Facility, Transportation Research Record: Journal of the Transportation Research Board, 2673(9): 107-116.

Gräbe, P.J., Mtshotana, B.F., Sebati, M.M. and Thünemann, E.Q. (2016). The effects of under-sleeper pads on sleeper-ballast interaction, Journal of the South African Institution of Civil Engineering, 58(2): 35-41.

Guo, Y., Zhao, C., Markine, V., Shi, C., Jing, G. and Zhai, W. (2020). Discrete element modelling of railway ballast performance considering particle shape and rolling resistance, Railway Engineering Science, 28(4): 382-407.

Horníček, L., Břešťovský, P. and Jasanský, P. (2017). Application of geocomposite placed beneath ballast bed to improve ballast quality and track stability, IOP Conference Series: Materials Science and Engineering, 236: 012039.

Indraratna, B., Lackenby, J. and Christie, D. (2005). Effect of confining pressure on the degradation of ballast under cyclic loading, Geotechnique, 55(4): 325-328.

Indraratna, B., Nimbalkar, S., Navaratnarajah, S.K., Rujikiatkamjorn, C. and Neville, T. (2014). Use of shock mats for mitigating degradation of railroad ballast, Geotechnical journal, 6(1): 32-41.

Indraratna, B., Qi, Y., Jayasuriya, C., Heitor, A.R. and Navaratnarajah, S.K. (2019). Use of rubber tyre elements in track stabilization, Proc., 9th Asian Young Geotechnical Engineers Conference and 15th International Conference on Geotechnical Engineering, pp 1-17.

Indraratna, B., Qi, Y., Tawk, M., Heitor, A., Rujikiatkamjorn, C. and Navaratnarajah,

S.K. (2020). Advances in Ground Improvement Using Waste Materials for Transportation Infrastructure, Proceedings of the Institution of Civil Engineers - Ground Improvement: 1-44.

Indraratna, B., Shahin, M.A., Rujikiatkamjiorn, C. and Christie, D. (2006). Stabilization of Ballasted Rail Tracks and Underlying Soft Formation Soils with Geosynthetic Grids and Drains: 143-152.

Navaratnarajah, S., Indraratna, B. and Nimbalkar, S. (2015). Performance of rail ballast stabilized with resilient rubber pads under cyclic and impact loading, International Conference on Geotechnical Engineering, pp 617-620.

Navaratnarajah, S.K. (2017). Application of rubber inclusions to enhance the stability of ballasted rail track under cyclic loading. PhD thesis, University of Wollongong.

Navaratnarajah, S.K. (2019). Resilient element attached under the concrete sleepers to improve the rail track performances, Journal of the Eastern Asia Society for Transportation Studies, 13: 2506-2520.

Navaratnarajah, S.K., Gunawardhana, K.R.C.M. and Gunawardhana, M.A.S.P. (2020). Influence of type of interfaces on railway ballast behavior, ICSECM 2019, Lecture Notes in Civil Engineering, Springer, pp 243-251.

Ngo, N.T., Indraratna, B. and Rujikiatkamjorn, C. (2017). Stabilization of track substructure with geo-inclusions—experimental evidence and DEM simulation, International Journal of Rail Transportation, 5(2): 63-86.

Olson, R.E. and Lai, J. (1989). Direct shear testing, Advanced Geotechnical Laboratory, Chaoyang University of Technology.

Sun, Q., Indraratna, B. and Grant, J. (2020). Numerical Simulation of the Dynamic Response of Ballasted Track Overlying a Tire-Reinforced Capping Layer, Frontiers in Built Environment, 6: 6(1-15).

Sweta, K. and Hussaini, S.K.K. (2018). Effect of shearing rate on the behavior of geogrid-reinforced railroad ballast under direct shear conditions, Geotextiles and Geomembranes, 46(3): 251-256.

Venuja, S., Navaratnarajah, S.K., Bandara, C.S. and Jayasinghe, J.A.S.C. (2020). Review on Geosynthetic Inclusions for the Enhancement of Ballasted Rail Tracks, ICSECM 2019, Lecture Notes in Civil Engineering, Springer, pp 459-468.

Venuja, S., Navaratnarajah, S.K., Wickramasinghe, T.H.V.P. and Wanigasekara, D.S.A. (2020). A laboratory investigation on the advancement of railway ballast behavior using artificial inclusions, ICSBE 2020, Lecture Notes in Civil Engineering, Springer (Proofread submitted).

Mechanistic-Empirical (ME) Pavement Design in Arizona, USA

Y. P. Yasanayake
Maricopa County Department of Transportation (MCDOT), Engineering Division, Phoenix, Arizona, USA

ABSTRACT: The Mechanistic-Empirical Pavement Design Guide (ME Design) has been introduced since the mid-2000s in the USA. The corresponding software program is titled Pavement ME Design. The pavement design in Arizona, more specifically flexible pavement design Maricopa County, is currently performed using both 1993 AASHTO Pavement Design Guide (AASHTO 1993) and ME Design. In the 1993 guide, subgrade support, traffic, and climate were considered in layer thickness design, but omitted was the asphalt mix properties. It uses different layer coefficients to distinguish layers, is empirical, is based only on limited research, and ignores mechanistic behavior of the layers. In contrast, ME design is based on an extensive research program executed over a decade and considers mechanistic-empirical behavior of layers. Climatic factors were given a significant consideration, and traffic loads were predicted as realistic as possible. Dynamic modulus (E*) was introduced to capture the actual mechanistic behavior of bound layers. ME design outputs predicted distresses for a given pavement structure, in contrast to the 1993 guide, which outputs layer thicknesses. ME design gives flexibility of calibrating the program to local conditions: local materials, climate, and traffic. However, complex design process compared to the simple 1993 method demands a high level of expertise. Currently, Maricopa County and some other US transportation agencies are running both programs in parallel.

1 INTRODUCTION

1.1 *Recent History of Pavement Design in USA*

The *AASHTO* (American Association of State Highway and Transportation Officials) *Guide for Design of Pavement Structures* (1993) is the primary document used to design new and rehabilitated highway pavements in the United States (US). The AASHTO 1993 guide adopts empirical design methods based on field performance data measured at the "AASHO Road Test" conducted in 1958-60.

AASHTO is a standards setting body which publishes specifications, test protocols and guidelines which are used in highway design and construction throughout the US. The 1958-60 road test determined how traffic contributed to the deterioration of highway pavements. It was conducted in Ottawa, Illinois to study the performance of pavement structures of known thickness under moving loads of known magnitude and frequency. This study is quoted as a primary source of experimental data used for the purposes of road design.

Since this design is based on limited test data obtained from a single climatic location, the United States' National Cooperative Highway Research Program (NCHRP) had funded a major research project in the early 2000s to develop a mechanistic-empirical pavement design procedure. As a result, a new design software called Pavement ME Design was developed and is now available through the AASHTOWare website. Currently, some of the US transportation agencies are using the new method for pavement design in parallel with the 1993 method. Maricopa County Department of Transportation (MCDOT) has also started using the new method as of January 2020.

1.2 *Maricopa County, Arizona, USA*

Maricopa County has over 2000 miles (3300 km) of paved roadways: 1100 miles (1770 km) of arterial roads and 1000 miles (1600 km) of collector roads. Majority of paved County roadways are flexible pavements as rigid pavements are adopted rarely.

Maricopa County (see Fig. 1) lies in the semi-arid Sonoran Desert and receives about 10 inches (254 mm) of annual rainfall with no snowfall. On average, there are 296 sunny days per year in Maricopa County and the summers are sweltering, the winters are cold, and it is dry and mostly clear year-round. Temperatures typically vary from 40°F to 106°F (4°C to 41°C), but dip below 31°F (–0.6°C) during winter and reach above 111°F (44°C) during summer.

Fig. 1 Maricopa County, Arizona, USA

Most of the populated areas in Maricopa County consists of flat lands with alluvium deposits created by erosion of surrounding mountains. The alluvium deposits contain interbedded silt, sand, gravel, and clay layers. Bedrock and rock outcroppings are encountered mainly near mountains. Geotechnical investigations reveal the presence of problematic soils such as expansive soils and collapsible soils, occasionally.

2 AASHTO 1993 PAVEMENT DESIGN

MCDOT still uses the AASHTO 1993 pavement design method until the full implementation of the ME design. A description of the method is as follows.

2.1 *Design Input*

Subgrade support and traffic loads are the main inputs in the design. Climate is considered with only a seasonal variation factor based on the geographical location.

2.2 *Subgrade Support*

The resilient modulus (M_R) of subgrade soils quantifies the support provided by the subgrade. Typically, a correlated value derived from R-Value test or California Bearing Ratio (CBR) test is used since the direct measurement of resilient modulus is costly and time consuming. The computation process of M_R can be found in Chapter 10 of the MCDOT's Roadway Design Manual (RDM).

2.3 *Traffic Load*

Fig. 2 shows the 13-Vehicle Classification identified by the Federal Highway Administration (FHWA) for the purpose of traffic and pavement designs. When designing a road, the average annual daily traffic (AADT) is determined along with the truck content (T), and the vehicle class distribution (Class 1 through 13). Vehicles in Class 4 and above are considered as trucks when determining T.

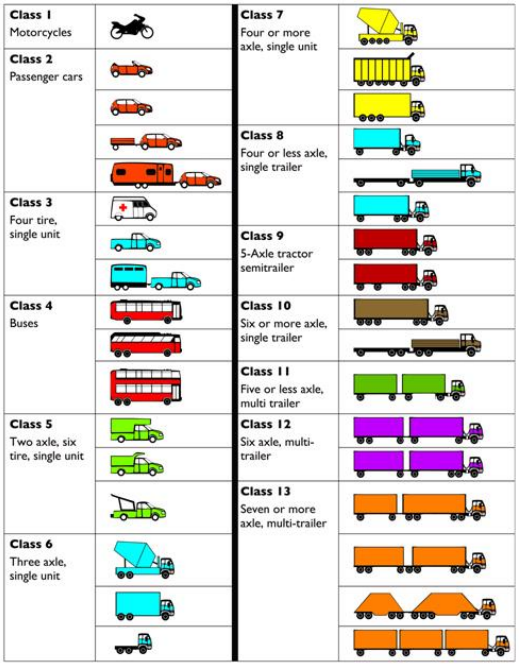

Fig. 2 FHWA 13 Vehicle Category Classification

The AASHTO 1993 design is based on cumulative 18,000 lbs. (18-kip or 80 kN) equivalent single-axle loads (ESALs). Initial 2-way daily 18-kip ESALs, $W_{0(2\text{-}18)}$, is computed using the number of vehicles in each class (N_i) and the corresponding traffic equivalent factor (TEF_i) as shown on Equation 1 where k is the number of vehicle classifications. The TEF values are listed on the MCDOT's RDM.

$$W_{0(2-18)} = \sum_{i=1}^{k} N_i TEF_i \quad (1)$$

Then, cumulative traffic load over the design life or ESALs in the design lane (W_{18}) is computed from Equation 2. The overall growth factor, OGF, is computed from Equation 3 for the design life, n, where typically n = 20 years. The traffic growth rate g is estimated from projection models or by the experience. Percent trucks in design direction (D_D) and design lane (D_L) are also required in Equation 2.

$$W_{18} = 365 \times OGF \times W_{0(2-18)} \times D_D \times D_L \quad (2)$$

$$OGF = \frac{(1+g)^n - 1}{g} \quad (3)$$

Then, the W_{18} value, standard normal deviate corresponding to the design reliability level (Z_R), overall standard deviation (S_0), allowable serviceability loss at end of design life (Δ_{PSI}), subgrade resilient

modulus (M_R) are used in the empirical design equation (Equation 4) to obtain the Structural Number (SN), which is the required structural capacity.

$$\log_{10}(W_{18}) = Z_R S_0 + 9.36 \log_{10}(SN+1) - 0.2 + \frac{\log_{10}\left(\frac{\Delta_{PSI}}{4.2-1.5}\right)}{0.40 + \frac{1094}{(SN+1)^{5.19}}} + 2.32 \log_{10}(M_R) - 8.07 \quad (4)$$

2.4 *Pavement Thickness Design from SN*

The value of SN is used to determine the required thicknesses, D_1, D_2, D_3, of layers of the pavement structure with layer coefficients, a_1, a_2, a_3, and drainage coefficients m_2, m_3. Refer to Equation 5 and Fig. 3.

$$SN = a_1 D_1 + a_2 D_2 m_2 + a_3 D_3 m_3 + \cdots \quad (5)$$

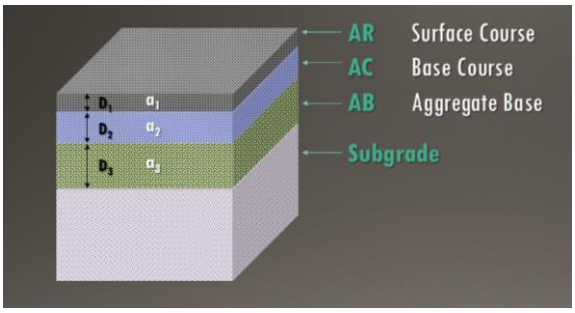

Fig. 3 Typical Pavement Structure

In this method the serviceability or performance of the pavement was considered as an input and the layer thicknesses are determined. The layered analysis adopted along with specified minimum and maximum layer thicknesses attempt to prevent any poorly designed pavement structures. However, under-designed or over-designed pavement structures cannot be fully avoided in this method.

3 ME PAVEMENT DESIGN

MCDOT has adopted the ME design as of January 2020. The ME design guide is posted on MCDOT's website for the users to access it online.

One of the main differences between the AASHTO 1993 design and the ME Design is that the 1993 guide designs the thickness of each pavement layer while the ME Design predicts the performance of the pavement corresponding to user input layer thicknesses.

3.1 *ME Design Software*

The NCHRP-funded research for the ME design was originally conducted by Arizona State University (ASU) under a subcontract with Applied Research Associates, Inc. (ARA) who developed the Pavement ME Design software. It is being continuously improved by ARA on behalf of AASHTOWare (see Fig 4). An enhanced version of the ME Design program was issued in the early 2010s replacing the old version issued in the early 2000s. At the time of this document, Version 2.6 was available for purchase on the AASHTOWare website.

Fig. 4 AASHTOWare Pavement ME Design Program

3.2 *ME Design Data Input*

The main data input areas in Pavement ME Design program include climate, traffic, and materials. The program accepts data in three hierarchical levels designated Level 1, Level 2, and Level 3. Level 1 represents the most advanced level where the designer can input site specific data from material characterization such as dynamic modulus and resilient modulus of the asphalt mix. On the other hand, Level 3 represents the lowest level where the designer can use readily available data such as sieve analysis and plasticity index along with the default data provided by the program. Level 2 can be used when some intermediate test data are available. For example, instead of inputting direct resilient modulus test data for unbound layers (aggregate base and subgrade), R-value or CBR can be input so that the program can internally generate a correlated resilient modulus value.

Performance criteria, which is to be established first, set acceptable limits for various distress types along with an assigned reliability. MCDOT has adopted the national distress criteria that comes with the program (see Table 1).

Based on input data, the program mechanistically quantifies the cumulative damage resulting from traffic loads on the pavement throughout the design life. Then, the damage is empirically correlated to each distress type and checked against the set criteria. For example, the International Roughness Index (IRI) value is set to 172, and when IRI exceeds 172, the pavement is considered "Failed".

Table 1. National Distress Criteria

Distress Type	Target
Terminal IRI (inches/mile)	172
Permanent Deformation-total (inches)	0.75
AC Bottom-Up Cracks (% lane area)	25
AC Thermal Cracks (ft/mile)	1000
AC Top-Down Cracks (% lane area)	25
Permanent Deformation-AC only (in.)	0.25

3.3 *ME Design Climate Data*

ME Design allows the user to search any desired region in the US and select a climate location. Historic climate data available for the selected location will be used by the program in the analysis. The seasonal temperature variations affect the dynamic modulus of the pavement. The program picks the corresponding dynamic modulus depending on the historical temperature values of the season from the master curve. The master curve is described in Section 3.7.

The depth to groundwater is also entered under climate data. The depth to groundwater is obtained from site specific investigations or from Arizona Department of Water Resources (ADWR).

3.4 *ME Design Traffic Data*

Average annual daily truck traffic (AADTT) is computed from the average annual daily traffic (AADT) and the percent trucks (T) for the roadway under design. Vehicle classes 4 through 13 (Fig. 2) are considered as trucks when determining the percent trucks. Number of lanes in the design direction, percent trucks in design direction (D_D), percent trucks in design lane (D_L), and operational speed are required as inputs. Operational speed is the speed at which drivers are observed operating their vehicles. The 85th percentile of the distribution of observed speeds is the most frequently used descriptive statistic for the operational speed for a location. When operational speeds are low, pavements exhibit relatively low dynamic moduli, or in other words, exhibit soft material properties. For example, low speeds at intersections result in severe rutting conditions due to low dynamic moduli response.

The traffic data shown in Table 2 are used as inputs in the ME Design program. The traffic data required for the new program is sophisticated compared to the 1993 design requirements. Fig. 5 shows some of the data for truck configuration. Basic traffic count data for Maricopa County roads are available on the MCDOT website.

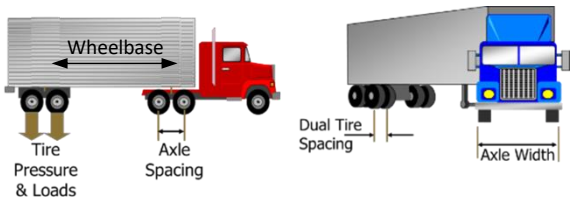

Fig. 5 Truck Configuration Data

Table 2. Pavement ME Design Traffic Data

Main Data Type	Description
AADTT	Average Annual Daily Truck Traffic
Axle Configuration	Axle width, spacing, and tire pressure
Lateral Wander	Lane width, wheel location, and standard deviation for lateral wander
Wheelbase	Spacing and % trucks corresponding to short, medium, and long truck categories
Vehicle Class Distribution and Growth	% distribution of trucks among Class 4 through Class 13, growth rate, and growth function
Monthly Adjustment	Monthly adjustment, if data is available
Axles per Truck	Average values for single, tandem, tridem, and quad axles for Class 4 through Class 13 trucks

3.5 *Material Data*

For MCDOT's flexible pavements, a substantial amount of material characterization is required. The materials used in bound layers include asphalt binder, asphalt rubber asphalt concrete (ARAC), and asphalt concrete (AC). The unbound layers include aggregate base (AB), treated subgrade (TS), and the subgrade. Typical tests carried out on various layers of the pavement are shown in Fig. 6.

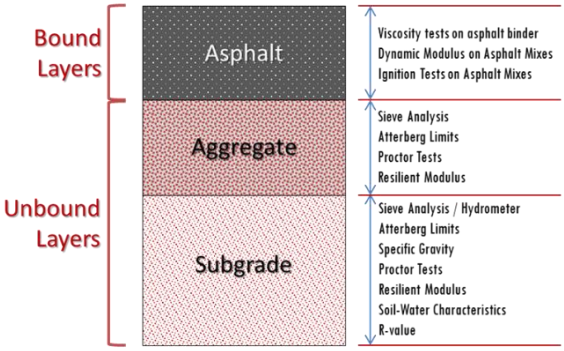

Fig. 6 Material Testing on Various Pavement Layers

3.6 *Mechanistic Principle*

The mechanistic principle adopted in ME design assumes that the pavement can be modeled as a multi-layered elastic structure system as illustrated in Fig. 7, where δ is the pavement deflection, ϵ_c is the compressive strain, and ϵ_t is the tangential strain. The damage caused by the applied loads over the design period is quantified mechanistically, and then the damage is correlated to various distress types empirically. Therefore, the design method is called mechanistic-empirical design.

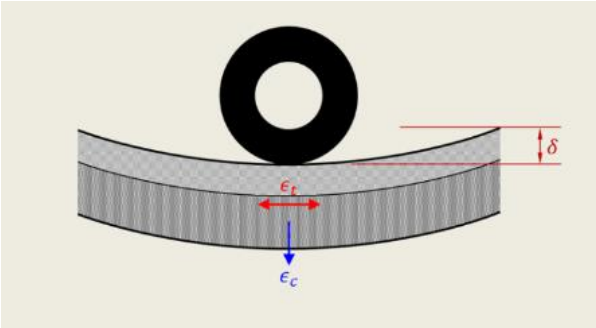

Fig. 7 Mechanistic Principle

3.7 *Material Data—Bound Layers*

The bound layers may consist of multiple asphalt layers: asphalt-rubber (ARAC) and various asphalt concrete (AC). The design process requires selecting suitable layer thicknesses for bound layers (ARAC and AC), and unbound layers (AB and TS).

ARAC and AC are made of mainly asphalt binder and aggregates. The binder properties such as viscosity, η, and mix properties such as dynamic modulus (E*) play an important role in modeling mechanistic behavior of the pavement structure. Suitable binder grade (viscosity grade) is selected based on climatic conditions. The binder input data include penetration measured at 77°F (25°C) and Brookfield viscosity measured at five different higher temperatures. The program generates the viscosity curve of the binder based on these input data as shown in Fig. 8.

Dynamic modulus (E*) of the mix is determined for several load frequencies applied to the asphalt concrete specimen at different temperatures in the laboratory. In the design, the load frequencies represent the durations of the applied traffic load, while the temperature represents the pavement temperature. The time-temperature superposition is used to obtain a single curve for the mix called the master curve. Typical test data (five curves corresponding to five temperatures) obtained from E* test are plotted as shown in Fig. 9. Keeping the 70°F (21°C) curve as reference, the other four curve segments are shifted (the top two to the left and the bottom two to the right) to obtain the master curve. Time-

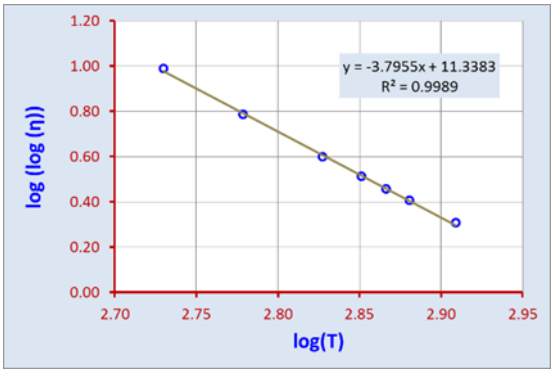

Fig 8. Temperature (T)-Viscosity (η) Relationship

temperature superposition exhibits that low temperatures correspond to short durations while high temperatures correspond to long durations.

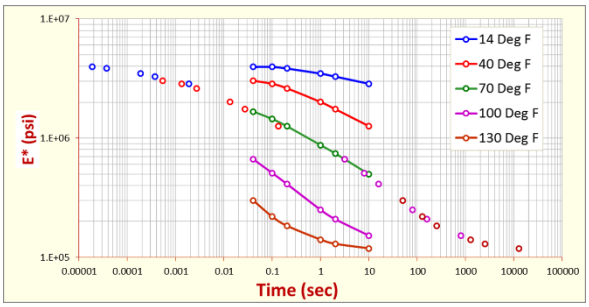

Fig. 9 Principal of Time-Temperature Superposition

Based on the distance of shift required, a shift function is plotted placing the temperature on the x-axis (see inset in Fig. 10). For a given pavement temperature, the program reads the value from the shift function corresponding to the temperature and enters the master curve to obtain the corresponding E* value.

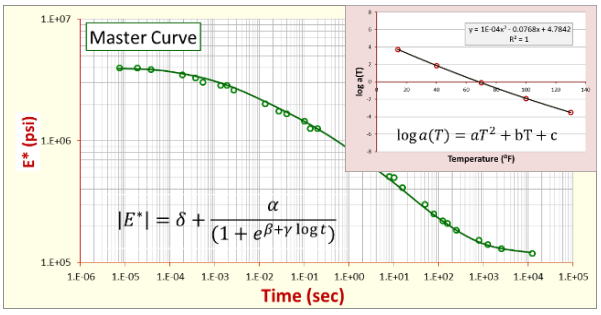

Fig. 10 The Master Curve and Shift Function

A typical master curve and the shift function are shown in Fig. 10. E* value is high (or pavement is stronger) when the load duration is short (i.e. faster moving traffic) and the weather is cold. In contrast, E* is lower (or pavement is weaker) when load duration is large (i.e. traffic is slow) and weather is hot. Note that the program uses a parameter called

Log(*reduced time*) on the x-axis of the master curve instead of actual time values.

3.8 Material Data—Unbound Layers

In addition to binder and mix properties of bound layers, the properties of unbound layers (AB and subgrade) are also entered into the program. Unbound layer properties include resilient modulus, R-Value, CBR, gradation, Atterberg limits, moisture-density relationship, specific gravity, saturated hydraulic conductivity, and soil-water characteristic curve (SWCC). The extent of data input is dependent on the hierarchical level selected for the design.

4 LOCAL CALIBRATION AND CASE STUDY

MCDOT conducted research for calibrating the ME Design program for local conditions. The research included testing locally used materials from 15 different roadway projects and monitoring the distresses over a ten-year period. The measured data were compared to predicted data from the program runs. Any observed bias was eliminated by adjusting selected calibration factors. The material data and adjusted calibration factors are published on MCDOT's website for designers to use.

MCDOT completed a pavement design for an arterial roadway using both methods in February 2020. The 1993 method resulted in a thin bound layer (6.5 in. AC) over a thick unbound layer (14 in. AB) while the ME design resulted in a thick bound layer (8.5 in. AC) over a thin unbound layer (8 in. AB). The ME design was adopted considering heavy truck content projected for the roadway.

5 RUNNING THE PROGRAM

Once all the data input is complete, the ME Design program can be run by clicking the Run tab on the menu bar. The program takes less than 10 minutes to complete a run and generates an output report that includes the summary sheet, input data, material curves, and performance of pavement over the design period. If there are any data input errors, the program will list them so that the designer can revisit those areas to make corrections.

Understanding the concepts and the program features are important before using the software. As the program is new, MCDOT was scheduling training sessions, help, and support for its consultants during the first year of use, 2020. These activities are to be rescheduled due to the prevailing COVID-19 pandemic situation.

6 PROGRAM OUTPUT

The first page of design output that gives the predicted pavement performance is shown in Fig. 11. The last column indicates if a distress has Passed or Failed with respect to the distress criteria. If there are failed distresses, the program should be rerun with a revised pavement structure until the output has no failed distresses.

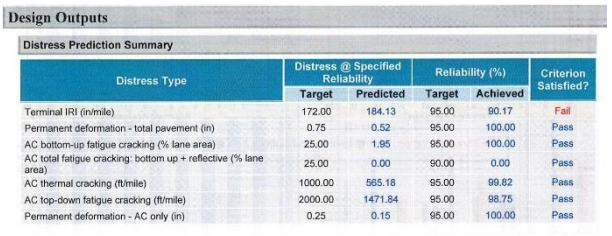

Design Outputs

Distress Prediction Summary

Distress Type	Distress @ Specified Reliability		Reliability (%)		Criterion Satisfied?
	Target	Predicted	Target	Achieved	
Terminal IRI (in/mile)	172.00	184.13	95.00	90.17	Fail
Permanent deformation - total pavement (in)	0.75	0.52	95.00	100.00	Pass
AC bottom-up fatigue cracking (% lane area)	25.00	1.95	95.00	100.00	Pass
AC total fatigue cracking: bottom up + reflective (% lane area)	25.00	0.00	90.00	0.00	Pass
AC thermal cracking (ft/mile)	1000.00	565.18	95.00	99.82	Pass
AC top-down fatigue cracking (ft/mile)	2000.00	1471.84	95.00	98.75	Pass
Permanent deformation - AC only (in)	0.25	0.15	95.00	100.00	Pass

Fig. 11 Design Output—Distress Prediction Summary

7 CONCLUSIONS

The ME design is superior to the AASHTO 1993 method as it is based on extensive testing conducted in various climatic conditions. The ME design also uses a mechanistic approach along with empirical methods and can be calibrated to local conditions by the user.

8 REFERENCES

AASHTO Guide for Design of Pavement Structures, AASHTO, 1993.

AASHTOWare Pavement ME design website: https://me-design.com/MEDesign/?AspxAutoDetectCookieSupport=1

MCDOT Interim Mechanistic-Empirical (ME) Flexible Pavement Design Guide, website: https://www.maricopa.gov/DocumentCenter/View/56244/Pavement-ME-Design-Guide-Interim-Oct-2019

MCDOT Roadway Design Manual (July 2019). Chapter 10 Pavement Design Guide, Maricopa County, Phoenix, Arizona, USA, pp 10-1 – 10-43

MCDOT Roadway Design Manual (July 2019), website: https://www.maricopa.gov/DocumentCenter/View/51399/Roadway-Design-Manual-2019

MCDOT website: https://www.maricopa.gov/5307/Transportation-MCDOT

ACKNOWLEDGMENTS

The author highly appreciates the support given by Maricopa County Department of Transportation (MCDOT), Phoenix, AZ, USA.

Resilient moduli response of PET plastic blends with demolition wastes

S. Perera, A. Arulrajah & F. Maghool
Department of Civil and Construction Engineering, Swinburne University of Technology, Australia

Y. C. Wong
Department of Mechanical Engineering and Product Design Engineering, Swinburne University of Technology, Australia

ABSTRACT: Urbanization expansion of the countries has effected on high plastic waste generation in the world as well as on the scarcity of natural resources. Replacing the traditional construction aggregates with recycled construction and demolition (C&D) waste materials is a sustainable approach which abates both landfilling concerns and the demand for virgin quarry materials. An evaluation of the resilient characteristics of Polyethylene terephthalate (PET) plastic waste and its blends with Recycled Concrete Aggregate (RCA) and Crushed Bricks (CB) in both unbound and 3% cement stabilized conditions is presented and the test results were compared with state road authority requirements to assess their performance as a pavement sub-base material. Two parameter-theta models were developed and compared for each blend and condition. The results indicated that PET blends with RCA and CB can be effectively utilized as a pavement subbase material replacing the virgin quarry materials.

Keywords: Cement stabilization; Demolition waste; PET plastic; Resilient modulus; RLT test

1 INTRODUCTION

The expansion of urban environment due to the rapid population growth have caused an increasing amount of waste production in the modern world. After the design life, many consumer goods and artificial objects usually end up in landfills. Therefore, non-renewable resources such as plastics, iron, glass, and carbon fuels are often recycled to avoid landfilling (Perera et al., 2019).

1.1 *Plastic waste*

The material "Plastic" plays a significant role in a daily life of a modern human being. The annual plastic consumption has been progressively improved over the past decades, predominantly driven by its inherited factors such as inexpensiveness, user-friendly designs, fabrication capabilities, high durability, lightweight and strength (Siddique, 2008).

Plastic wastes account for 8% to 12% of municipal waste stream with nearly 190 million metric tons generated annually in all countries in the world and there is a 20 times increase of annual plastic production in the world from 1950 to 2001 (Siddique, 2008). In Australia, annual generation of 2.24 million metric tons of plastics waste is reported and this accounts for 16% of the annual municipal solid waste generation (Bajracharya et al., 2016). Due to the speedy growth of plastic waste in the world, usage of shredded plastics as a sustainable building material has become upcoming interest in civil engineering field (Perera et al. 2019).

1.2 *Polyethylene Terephthalate plastics*

Polyethylene Terephthalate (PET) is one of the seven plastic types commonly available in the market, which is noted as number 1 in the resin identification numbering system. Most of the PET wastes collected in municipal solid waste stream are containers, which were used to store liquids such as mineral water, soft drinks, cooking oil, cleaning agents and food containers (Siddique, 2008).

Spent PET products, such as water bottles and food containers, are not direct environmental hazards , although create significant issues due to its substantial volume fraction in municipal solid waste collection, slow biodegradability and high resistance to the atmospheric conditions (Chiu and Cheng, 1999). With increasing consumption and disposal of PET artifacts, particularly for packaging and transporting mineral water, the landfill area requirement for these spent plastics is becoming significant (Siddique, 2008).

From the amount of plastic waste recycled in United States in 1996, PET plastic type formed the second highest fraction with a generation of 1700,000 metric tons and only 286,000 metric tons of them were recycled (Subramanian, 2000).

1.3 *Construction and demolition waste*

Construction and demolition (C&D) materials are considered as surplus or waste material associated with building or demolition of structures, which mostly includes common building materials. Recycled concrete aggregate (RCA) from demolition of structural elements, crushed bricks (CB), reclaimed asphalt pavement and masonry waste are predominant materials in C&D wastes, often used in pavement applications, particularly as a base/subbase material (Arulrajah et al., 2014).

RCA is a direct by-product of demolition processes of concrete structures, such as buildings. In the process of recycling the RCA, the bulk concrete from concrete elements are crushed and screened into different sizes varying on the type of end application. 8.7 million metric tons of RCA in Australia stockpiled annually and currently there are several incentives from government sustainability authorities in Australia to use recycled C&D aggregates in civil engineering infrastructure projects (Arulrajah et al., 2014).

CB is commonly found material in building sites as an excessive material after construction or after demolition of brick walls or brick columns in ancient buildings (Arulrajah et al., 2012). In general, CB is not consisted with a pure bricks but a mixture, which contains 70% of bricks and asphalt, concrete, and rock contributes to the rest. Typical sample of recycled CB has a maximum particle size around 20 mm. CB was reported as a potential substitute for pavement coarse aggregates, which can mostly conserve virgin quarry materials. Recycled CB is processed at a larger scale by the recycling industries in the state of Victoria, Australia (Arulrajah et al., 2014).

1.4 *Cement stabilization*

Cement stabilization has been investigated for increasing the strength and stiffness properties of the unbound of mixtures, reducing the structural thickness of the base and subbase, increase the durability and enhance the load distribution to the underneath layers of the pavement (Disfani et al., 2014, Taha et al., 2002). A research, performed by Taha el al. (2002) using 100% reclaimed asphalt pavement stabilized with either 3, 5, or 7% cement, reported this product to be more cost effective and less harmful approach towards the environment than when using a 100% virgin quarry aggregate with no cement. Although the added cement content enhances the strength of the unbound materials, cement dosages from 2% to 4% were only adopted in pavement base construction by the state transportation agency, the Texas Department of Transportation (TxDOT Tex-120-E, 2013). High cement stabilization using more than 4% cement for base treatments has resulted in stiffer bases, which leads to cracking in high-temperature conditions (Sebesta and Scullion, 2004).

Consequences of increasing plastic waste generation have become a significant problem for both land and marine environment (Monteiro et al. 2018). Environmental authorities and municipal councils often meet with issues when it comes to landfilling them without causing much harm to the eco-system. Limited number of studies were carried out to find out the sustainable use of C&D waste materials as construction and building materials in engineering applications particularly which use significant amount of virgin quarry materials such as road and pavement applications. A very few studies have been carried out which combines plastic and C&D waste materials together and assess their feasibility in adopting them in civil engineering applications.

2 MATERIALS AND METHODS

2.1 *Materials*

RCA and CB used in this experimental program had a maximum particle size of 20 mm and the materials were collected from a recycling factory situated in Melbourne, Australia. RCA and CB used in this research belong to upper subbase (class 3) and lower subbase (class 4) recycled materials, respectively. The maximum PET size was selected as 5 mm, based on several past works by Arulrajah et al. (2017).

PET plastic bottles were collected from an indoor sport center located at Dandenong, Melbourne. The plastic labels, plastic lids and bottleneck rings were removed before shredding. A shredding machine with 5 mm screening size was used to shred the cleaned PET bottles to produce platy flakes less than 5 mm. General Portland cement (C), commonly available in the market was used as the stabilizing binder in this research. The shredded PET and the C&D materials were oven dried at 104 °C temperature for 24 hours. The dried C&D and PET were used to prepare the blends, after adding the required amount of water during each test. The material compositions of the blends are presented in Table 1.The physical appearance and the microscopic view of the materials used in this research are presented in Fig. 1.

2.2 *Methods*

A suite of laboratory tests was undertaken to determine the engineering properties of both unbound PET/C&D blends and stabilized PET/C&D blends treated with 3% (% by mass of the dry C&D+PET) cement. The suite laboratory tests included basic

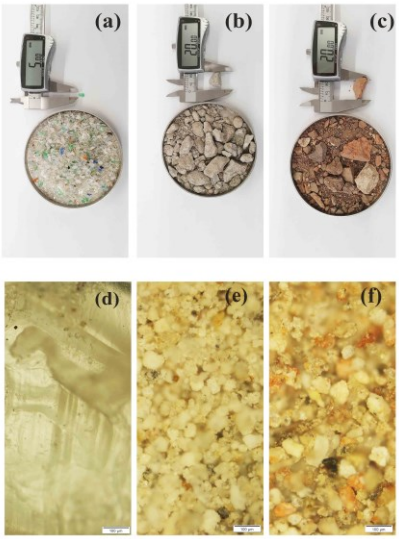

Fig. 1 The physical appearance of (a) PET, (b) RCA and (c) CB and the microscopic view of (d) PET, (e) RCA and (f) CB materials, used in this study

characterization tests such as particle size distribution, particle density and water absorption, organic material content, flakiness index, Los Angeles (LA) abrasion loss and modified Proctor compaction. The resilient responses of the unbound and 3% cement stabilized blends were evaluated by repeated load triaxial (RLT) tests and bulk stress models were developed for each sample to predict the variation of resilient modulus (M_R).

Table 1 Material composition and blend names

Materials (%)				Blend name
RCA	CB	PET	C*	
100	0	0	0	100%RCA
100	0	0	3	100%RCA + 3%C
95	0	5	0	5%PET + 95%RCA
95	0	5	3	5%PET + 95%RCA +3%C
0	100	0	0	100%CB
0	100	0	3	100%CB + 3%C
0	95	5	0	5%PET + 95%CB
0	95	5	3	5%PET + 95%CB + 3%C

*C percentage was calculated with respect to the total dry mass of RCA, CB and PET of each blend

The particle size distribution tests for the materials were conducted as per mentioned in Australian standards (AS), AS-1289.3.6.1 (2009) for each material before compaction. The blends were classified according to the AS 1726 (2017), based on the sieve analysis results. Organic material (OM) content of PET, RCA, CB and PET blends were determined according to ASTM D2974-14 (2014). Particle density and water-absorption values of the C&D materials and PET were determined in accordance with in AS 1141.5 (2000). For the evaluation of particle shape characteristics, flakiness index test was performed according to BS 812-105.1. Crushing and degradation characteristics of the materials were evaluated by Los Angeles (LA) abrasion loss test as per mentioned in ASTM C131 / C131M-14 (2014). A maximum LA abrasion loss value of 40 is usually permitted for the materials used in pavement subbases in the state of Victoria (VicRoads, 2017).

The resilient modulus of the blends was determined by the repeated load triaxial (RLT) tests in accordance with AASHTO T307-99 (2007). A triaxial cell was used to carry out the RLT tests for the samples with sizes of 100±1 mm in diameter and 200±1 mm height where a system of loads comprising of a haversine-shaped loading pulse with 0.1 s loading period and 0.9 s resting period. Single sample was prepared for each blend and a typical sample was compacted in 8 layers, by applying 25 blows per layer, compacted to achieve approximately 98% of MDD at OMC based by applying the modified Proctor compaction energy as mentioned in ASTM D1557-12 (2012) with minimal segregation of materials in compacted layers. After 7 days of curing, samples were subjected to RLT test in order to evaluate the resilient modulus values.

3 RESULTS AND DISCUSSION

When comparing the microscopic images of the three basic materials presented in Fig. 1, PET depicts a smoother surface than RCA and CB. From the two C&D materials tested, considerable amount of wooden particles were observed in RCA samples. Although, most PET flakes were transparent, the flakes derived from coloured containers added different colours to the PET sample. Three control materials including PET, RCA and CB along with PET/RCA and PET/CB blends were used for the basic characterization tests. Fig. 2 shows the particle size distribution (PSD) curves of the blends and the grading characteristics of the basic materials are presented in Table 2.

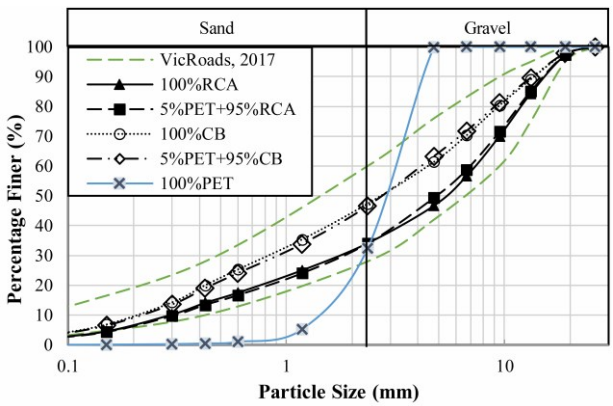

Fig. 2 Particle size distribution curves of the materials (Perera et al., 2019)

According to Fig. 2, CB blends contain higher percentage of finer particles than RCA and adding 5%PET had negligible effect on the PSD curves or grading characteristics of the PET/C&D blends.

The modified Proctor compaction curves of the unbound, 3% cement stabilized blends are presented in Fig. 3, and the optimum moisture content (OMC) and maximum dry density (MDD) values of the blends are tabulated in Table 3. MDD values of the cement-stabilized blends are higher than the respective unbound blends. The fine cement particles can fill the voids in blends and increase the MDD of the blends producing a better compaction.

Moreover, the MDD of RCA blends are lower than the CB blends. This could be due to containing high wooden particles in RCA. In addition, CB contained higher percentage of finer particles than RCA. During the process of compaction, CB can be effectively compacted than RCA by filling the voids of the sample with finer particles.

Table 2 Grading characteristics and geotechnical properties of the basic materials (Arulrajah et al., 2019)

Blend	RCA	CB	PET
Gravel content (%)	65.9	52.6	68.1
Sand content (%)	32.2	44.7	31.9
Fines content (%)	1.9	2.7	0
D max (mm)	20	20	5
D_{10} (mm)	0.3	0.21	1.3
D_{30} (mm)	1.8	0.83	2.2
D_{60} (mm)	7.3	4.3	3.1
C_u	24.3	20.5	2.4
C_c	1.5	0.8	1.2
Classification	GW	GW	GP
Specific gravity	2.65	2.62	1.37
Water absorption (%)	11.3	8.2	-
Flakiness Index	8.94	14.7	-
LA abrasion loss	30.8	33.8	-
Organic matter (%)	3.8	2.4	100

Adding 5%PET in blends has reduced the MDD values and increased the OMC values of the C&D materials. Replacing C&D particles with PET with low specific gravity could be resulted in low MDD values of PET/C&D blends.

The M_R values determined by the RLT test defines the material response to traffic loading under existing physical conditions and commonly adopted as an input parameter in designing flexible pavements. The variation of M_R of a) RCA blends and b) CB blends under 15 different combinations of confining pressures and cyclic axial stresses are presented in Fig. 4. The range of M_R values of the blends are summarized in Table 3.

The M_R values of the blends have been increased with applied confining pressure. The high confining pressure leads to high particle interlocking in soils as experienced and reported in previous studies by Arulrajah et al. (2017).

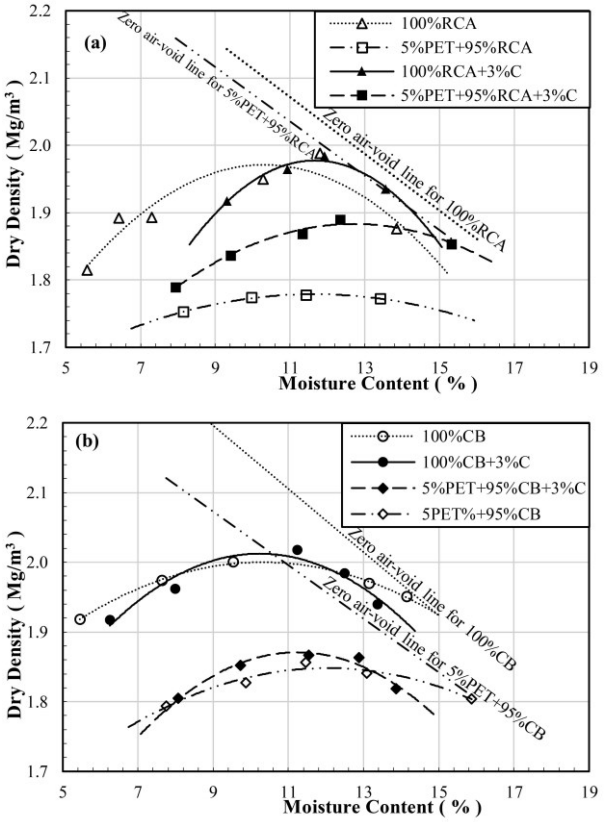

Fig. 3 Modified compaction curves a) RCA blends and b) CB blends

Table 3 Compaction characteristics and M_R values of the blends

Blend	MDD (Mg/m^3)	OMC (%)	M_R range (MPa)
100%RCA	1.91	10.3	370-1191
100%RCA+3%C	1.98	11.7	329-1420
5%PET + 95%RCA	1.78	11.8	143-618
5%PET + 95%RCA+3%C	1.88	12.9	292-1194
100%CB	2.00	10.2	281-869
100%CB+3%C	2.02	10.3	325-924
5%PET + 95%CB	1.85	12.1	67-362
5%PET + 95%CB+3%C	1.88	11.3	229-750

RCA blends show higher M_R values than CB under the same confining pressures applied at 15 stages of the RLT test. M_R values of the stabilized materials are highly governed by the LA abrasion loss value of the materials used (Disfani et al., 2014). According to Table 2, CB displays higher LA abrasion loss value than RCA and this could be affected on the RCA blends depicting greater M_R values than CB blends. According to Table 2, CB shows higher finer particle percentage and flakiness index value than RCA. Materials, which have particles with high flakiness index and high finer per-

centages, increase the surface area of the total material mixture. Such sample in stabilized conditions requires more cement volume per contact material grains for the same cement content, hence resulting in low resilient modulus values (Disfani et al., 2014).

Adding PET decreases the M_R value of the pure RCA and CB blends in both unbound and stabilized conditions. According to the Fig. 1, PET has a smooth surface when compared with C&D material particles. Blending smooth surfaced material has decreased the M_R values of the PET/C&D blends.

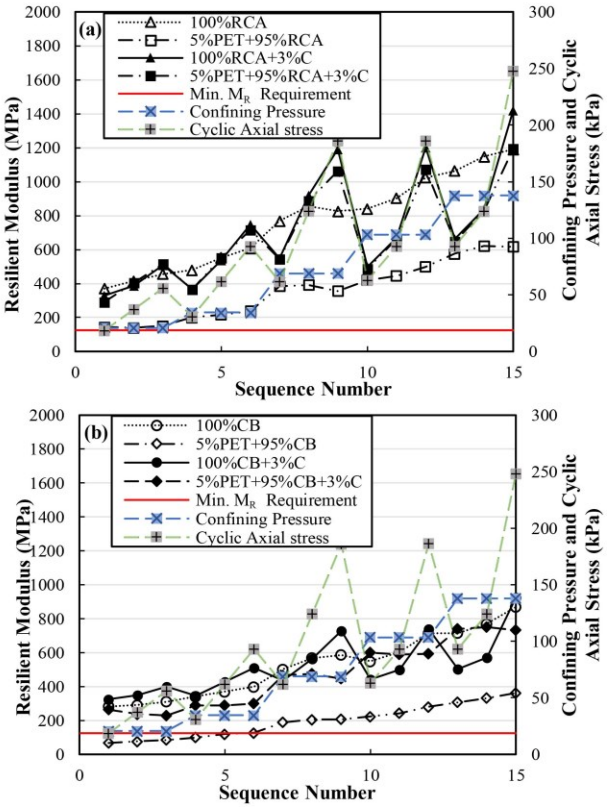

Fig. 4 Variation of M_R with confining pressure and cyclic axial stress for a) RCA blends; b) CB blends

All the unbound blends except 5%PET+95%CB blend satisfied the minimum M_R requirement of 125 MPa for pavement bases and subbases set forth by AASHTO (1993) guide for design of pavement structures. Stabilizing PET blends with 3% cement significantly improves M_R values of unbound PET blends. M_R value of the 5%PET+95%CB blend is improved from 67 MPa to 229 MPa after stabilization with cement. According to RLT test results, all 5%PET blends can be effectively utilized in pavement base/ subbase after stabilizing them with 3% cement.

AASHTO T307-99 (2007) suggests that bulk stress model which follows the Equation 1 is suitable to predict M_R of granular materials where M_R is resilient modulus, k_1 and k_2 are bulk stress model parameters and θ is bulk stress.

$$log\ M_R = log\ k_1 + k_2\ log\ \theta \quad (1)$$

The bulk stress (θ) models of the two blends (a) RCA and (b) CB are presented in Fig. 5 and the θ- model parameters log k_1 and k_2 of the blends are presented in Table 4. According to Fig. 5, the log M_R values of the blends increased with the log θ values. Bulk stress of a sample depends on applied the confining pressure. Because of the high particle interlocking in high confining pressures, the log M_R values of the blends have been increased with the *log θ*. Bulk stress models of RCA show higher k_1 and log k_2 parameters than bulk stress models of CB which suggests that RCA performs better out of the two C&D materials used in this study. Adding PET decreases the k_1 and log k_2 parameters of the bulk stress models of pure RCA and CB blends in both unbound and stabilized conditions. Furthermore, stabilizing blends with 3% cement improves the parameters of the bulk stress models of all blends.

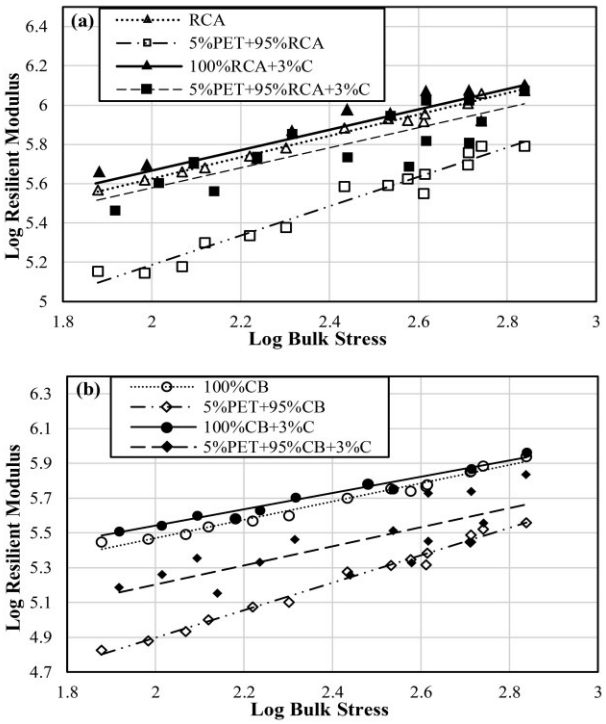

Fig. 5 Bulk stress models; a) RCA and b) CB blends

Table 4 Parameters of the bulk stress models

Blend	*log* k_1	k_2	R^2
100%RCA	4.54	0.544	0.989
100%RCA+3%C	4.63	0.519	0.761
5%PET + 95%RCA	3.69	0.747	0.961
5%PET + 95%RCA+3%C	4.56	0.511	0.697
100%CB	4.42	0.526	0.982
100%CB+3%C	4.68	0.468	0.978
5%PET + 95%CB	3.32	0.789	0.988
5%PET + 95%CB+3%C	4.10	0.549	0.689

4 CONCLUSIONS

This study includes a suite of laboratory studies to evaluate basic geotechnical parameters and resilient parameters of PET blends with RCA, CB in both unbound and lightly cement stabilized conditions.

The grading limits of RCA, CB and associated PET blends were found to be within the limits set by VicRoads for the pavement base/subbase materials and adding 5%PET had caused negligible effect on the grading curves of RCA and CB. Adding 5%PET reduced the MDD values and increased the OMC values of the C&D materials.

Adding PET has reduced the M_R values of RCA and CB due to the reduction of frictional forces between particles especially when particles with high surface frictional resistance are replaced by smooth-surfaced materials such as PET. Except 5%PET+95%CB blend, all other PET/C&D blends had higher M_R values than 125 MPa, the minimum M_R requirement for the pavement base/subbase materials. After 3% cement stabilization, all the blends including 5%PET+95%CB blend satisfied the minimum requirement for the M_R.

Bulk stress models of RCA blends showed higher k_1 and log k_2 parameters than bulk stress models of CB suggesting that RCA performs better out of the two C&D materials used in this study. Adding PET reduced the k_1 and $log\ k_2$ parameters of the bulk stress models of pure RCA and CB blends in both unbound and stabilized conditions.

Utilizing PET/C&D as pavement base/subbase material would reduce the plastic waste amount in municipal solid waste stream, the demand for virgin quarry material as a pavement construction material and the landfill requirement for both PET and C&D wastes.

REFERENCES

AASHTO (1993). Guide for design of pavement structures, 1993. Washington D.C., The American Association of State Highway and Transportation Officials

AASHTO T307-99 (2007). Standard method of test for determining the resilient modulus of soils and aggregate materials, Washington, D.C., The American Association of State Highway and Transportation Officials.

Arulrajah, A., Piratheepan, J., Bo, M. & Sivakugan, N. (2012). Geotechnical characteristics of recycled crushed brick blends for pavement sub-base applications, Canadian Geotechnical Journal, 49(7):796-811.

Arulrajah, A., Disfani, M. M., Horpibulsuk, S., Suksiripattanapong, C. & Prongmanee, N. (2014). Physical properties and shear strength responses of recycled construction and demolition materials in unbound pavement base/subbase applications, Construction and Building Materials, 58:245-257.

Arulrajah, A., Yaghoubi, E., Wong, Y. C. & Horpibulsuk, S. (2017). Recycled plastic granules and demolition wastes as construction materials: Resilient moduli and strength characteristics, Construction and Building Materials, 147:639-647.

Arulrajah, A., Perera, S., Wong, Y. C., Horpibulsuk, S. & Maghool, F. (2019). Stiffness and flexural strength evaluation of cement stabilized PET blends with demolition wastes, Construction and Building Materials, 239:117819

AS 1141.5 (2000). Particle density and water absorption of fine aggregate Australian Standard 1141.5.1., Australian Standard, Sydney, NSW, Australia.

AS 1289.3.6.1 (2009). Methods of testing soils for engineering purposes, Method 3.6.1: Particle size distribution by sieving. AS-1289.3.6.1, New South Wales, Australia.

AS 1726 (2017). Geotechnical site investigations.

ASTM C131 / C131m-14 (2014). Standard Test Method for Resistance to Degradation of Small-Size Coarse Aggregate by Abrasion and Impact in the Los Angeles Machine, ASTM International, West Conshohocken, PA, 2006, www.astm.org.

ASTM D1557-12 (2012). Standard Test Methods for Laboratory Compaction Characteristics of Soil Using Modified Effort (56,000 ft-lbf/ft^3 (2,700 kN-m/m^3)), ASTM International, West Conshohocken, PA, 2012, www.astm.org.

ASTM D2974-14 (2014). Standard Test Methods for Moisture, Ash, and Organic Matter of Peat and Other Organic Soils, ASTM International, West Conshohocken, PA, 2014, www.astm.org.

Bajracharya, R. M., Manalo, A. C., Karunasena, W. & Lau, K.-T. (2016). Characterisation of recycled mixed plastic solid wastes: Coupon and full-scale investigation, Waste Management, 48:72-80.

British Standards Institution (1989). BS 812-105.1: Method for Determination of Particle Shape; Flakiness Index,London, UK.

Chiu, S. J. & Cheng, W. H. (1999). Thermal degradation and catalytic cracking of polyethylene terephthalate, Polymer Degradation and Stability, 63(3):407-412.

Disfani, M. M., Arulrajah, A., Haghighi, H., Mohammadinia, A. & Horpibulsuk, S. (2014). Flexural beam fatigue strength evaluation of crushed brick as a supplementary material in cement stabilized recycled concrete aggregates, Construction and Building Materials, 68:667-676.

Monteiro, R. C. P., Ivar Do Sul, J. A. & Costa, M. F. (2018). Plastic pollution in islands of the Atlantic Ocean, Environmental Pollution, 238:103-110.

Perera, S., Arulrajah, A., Wong, Y. C., Horpibulsuk, S. & Maghool, F. (2019). Utilizing recycled PET blends with demolition wastes as construction materials. Construction and Building Materials 221:200-209.

Sebesta, S. & Scullion, T. (2004). Effectiveness of minimizing reflective cracking in cement-treated bases by microcracking, Report no FHWA/TX-05/0-4502-1

Siddique, R., Khatib, J. & Kaur, I. (2008). Use of recycled plastic in concrete: A review. Waste Management 28(10):1835-1852.

Subramanian, P. M. (2000). Plastics recycling and waste management in the US. Resources, Conservation & Recycling 28(3):253-263.

Taha, R., Al-Harthy, A., Al-Shamsi, K. & Al-Zubeidi, M. (2002). Cement stabilization of reclaimed asphalt pavement aggregate for road bases and subbases. Journal of Materials in Civil Engineering 14(3):239-245

TxDOT Tex-120-E (2013). Texas Department of Transportation, Tex-120-E: Test procedure for soil-cement testing. TxDOT, Austin, Texas.

VicRoads (2017). VicRoads Code of Practice RC 500.02 – Registration of Crushed Rock Mixes.

Analysing theoretical CPT and SPT correlations of soils in Kelani valley

R.D.T. Kaushalya
Climate Resilience Improvement Project (CRIP), Sri Lanka

H.A.N.D. Senarathna
Climate Resilience Improvement Project (CRIP), Sri Lanka

S.P. Hemakumara
Climate Resilience Improvement Project (CRIP), Sri Lanka

S.Widanapathirana
Climate Resilience Improvement Project (CRIP), Sri Lanka

P.A.A.P.K. Pannala
Climate Resilience Improvement Project (CRIP), Sri Lanka

ABSTRACT: The Standard Penetration Test (SPT) has been extensively used all over the world to determine soil properties and stratigraphy at various ground elevations. The Cone Penetration Test (CPT) is another in-situ test which can be used as an alternative to SPT. Multiple researches have been carried out to determine theoretical relationships between these two tests. In this research, the applicability of theoretical relationships between cone penetration tip resistance (q_c) and raw SPT N value (N) for soils in Kelani valley was analysed. The analysis is based on 05 sets of SPT and CPT tests conducted at the same location approximately within 0.1m proximity covering both banks of Kelani River from Hanwella to Kaduwela. The developed q_c/N correlation was then compared with the past literature. A linear relationship was derived for alluvium soils and the results were generally in agreement with previous correlations given in literature.

1 INTRODUCTION

Geotechnical investigations are vital to investigate soil properties and geological conditions of subsoil strata, to estimate design parameters for construction works. The Standard Penetration Test (SPT) and the Cone Penetration Test (CPT) are the main in-situ tests used in geotechnical investigations. SPT is the most common type of in situ test practiced in Sri Lanka as well as around the world (Mehtab, et al., 2018) for geotechnical investigations. The primary reason of SPT is being chosen over other methods is due to its cost effectiveness. However, the main concern regarding the SPT method for engineers and geologist worldwide is its drawbacks regarding reliability and repeatability. Thus, the main objective of the research is to develop a theoretical relationship between the SPT and CPT methods for identified soil types in Kelani river banks. The main advantages of the CPT method over the SPT method are the repeatability, simplicity, convenience, efficiency, reliability and continuous record of soil profile. However, the SPT method produces soil samples that can be tested in the laboratory unlike the CPT method. Geotechnical engineering designs are usually based on soil parameters obtained from SPT results, which takes considerable amount of time and effort. Therefore, it is important to look into the existence of a correlation between these two tests. Multiple researches have been carried out worldwide to determine theoretical relationships between these two tests. The applicability of theoretical relationships between CPT tip resistance (q_c) and raw SPT N value (N) for Sri Lankan soils in Kelani River banks between Hanwella and Kaduwela, was analysed during the study.

2 LITERATURE REVIEW

It is essential to correlate the static tip resistance (q_c) of the CPT against the raw N value of SPT with the aim of utilizing available information for field performances and correlations of N with respect to soil properties (Kara, O., 2015). A correlation between SPT & CPT was proposed by Akca

(2003), Robertson et al. (1983), Ismael and Jeragh (1986),Schmertmann (1970), Danziger and de Velloso (1995) and Mehtab Alam et al., (2018) for various types of soils. Akca (2003) suggested a correlation for the soils in United Arab Emirates (UAE) and obtained higher values for q_c over N ratio during the analysis. The study concluded that the foremost reasons for higher values are due to densification, Shelly structure and cementation in the UAE soils. Robertson et al. (1983) demonstrated the ratio of q_c/N as a function of mean grain size (D_{50}). The issues associated with SPT and how it is related to the SPT and CPT correlation were discussed in the research. Ismael and Jeragh (1986) formulated a correlation for sands of calcareous desert in Kuwait. The q_c values of CPT, and N values of SPT were correlated and compared with the values that were presented by Schmertmann (1970) for fine to medium and slightly silty sands. Numerous Brazilian soil types were interrelated to obtain CPT vs SPT relation by Danziger and de Velloso (1995). The values provided in this research were found to be in the same range that was obtained by Schmertmann (1970). De Alencar Velloso (1959) had demonstrated the relationship between q_c and N for various soil types such as clay, silty clay, sandy clay, silty sand, sandy silt and fine sand. A linear regression model was developed by Mehtab Alam et al., (2018) using 107 SPT and 49 CPT measurements across the city of Lahore, Pakistan to develop SPT vs CPT correlations for various soils.

These previous studies are used to differentiate the results in the analysis section of this study for a variety of soils. The comparison is presented in section 5.2.

3 FIELD INVESTIGATIONS

3.1 *Data Collection*

The geotechnical investigations were carried out on both banks of Kelani River from Hanwella to Kaduwela. Thirty (30) number and fifty-four (54) SPT and CPT tests were conducted at 1 km and 500 m approximate distance respectively (Climate Resilience Improvement Project, 2018). From these, 05 sets of SPT and CPT measurements were conducted approximately at the same location within 0.1m proximity. Therefore, it was vital to derive theoretical correlation using these data to interrelate results of the remaining 25 boreholes and 49 CPT measurements. Fig 1 shows spatial distribution of selected 05 sets of SPT and CPT test locations along Kelani river bank.

Fig. 1 Selected 05 SPT and CPT locations

The ground investigations revealed that the stratigraphy of the Kelani valley is generally composed of alluvial deposits made of silt, sand, clay and gravel underlain by laterite and residual soils of various thicknesses. The selected boreholes consisted of cohesive alluvium and granular alluvium soils at depths varying up to 18 m. The British Standards BS 5930:2015 - Code of Practice for Ground Investigation was followed for soil classification. The key soil categories are classified as follows. (Climate Resilience Improvement Project, 2018)

- Silty Sand
- Sandy Silt
- Silty Clay
- Clayey Sand
- Gravelly Sand

3.2 *Standard Penetration Test (SPT)*

SPT was conducted within the boreholes at every 1.0 m depth interval in accordance with the BS 5930: 2015 - Code of Practice for Ground Investigation.

The test was conducted by driving a 50 mm diameter standard split tube sampler into the soil to a depth of 45 cm using a 63.5 kg hammer falling under gravity through 760 mm. In this investigation, a Doughnut type automatic drop hammer assembly was used. It is a latch, automatically operated releasing the hammer on reaching the correct fall height. The number of blows required to penetrate the standard split tube sampler through the last 30 cm (out of 45 cm) is called the Standard Penetration Value.

3.3 *Cone Penetration Test (CPT)*

CPT is a fast and reliable geotechnical investigation method used for stratigraphic determination of subsoil profiles, soil types and its properties, water table and pore pressure etc. The CPT tests has been conducted out in general accordance to BS EN ISO 22476-1:2012: Geotechnical investigation and testing, Sampling methods and groundwater measurements; technical principles for execution.

CPT Testing was carried out using HYSON 100 kN lightweight Cone Penetrometer manufactured by A. P. Ven Den Berg machine fabric of the Netherlands. The Electric Cone (ICON: I-CFXYP20-10) with 10 cm^2 cone section area and 150 cm^2 friction sleeve area was used. In CPT, the cone penetrometer was pushed hydraulically into the ground vertically as possible at a constant rate of approximately 2 cm/sec. CPT tests were terminated when the measured Tip Resistance exceeded 37.5 MPa, the rod starts to bend or the hole reached the maximum depth of rods available (approximately 21 m). The following information were provided during the test.

- Cone resistance (q_c)
- Sleeve friction (f_s)
- Friction ratio (R_f)
- Pore pressure (u^2)
- Inclination angle of cone tip

4 METHODOLOGY

The identified main soil varieties at the selected five boreholes were compared and classified based on depth of each strata and location of borehole. The observed raw SPT N values and average q_c values with regard to each soil type was used for the calculations. The method of arithmetic average was applied for the calculation of q_c with respect to the N values at the final 30 cm of the 45 cm sample at each 1 m depth interval.

Correlations concerning SPT and CPT were derived for all the selected soil classes performing linear regression. The directly proportionate q_c=nN relationship with zero intercept was adopted. The n is defined as the gradient of q_c vs N correlation. The developed relationships were compared with past studies as described in section 5.2.

5 RESULTS AND DISCUSSION

5.1 *Results*

A correlation was developed between q_c and N for each type of soil along the Kelani river valley from Hanwella to Kaduwela. Five soil categories have been recognized along the river valley namely Silty Sand, Sandy Silt, Silty Clay, Clayey Sand and Gravelly Sand. Other types of soils were disregarded in the development of a relationship due to inconsistency and unavailability of sufficient data to develop a relationship. The average q_c and N values for each depth range were interrelated.

The Table 1 shows the correlations obtained from the selected 05 sets of SPT and CPT measurements for Silty Sand, Sandy Silt, Silty Clay, Clayey Sand and Gravelly Sand soil types in Kelani valley.

Table 1: Correlations for each soil type

Soil Type	Correlation Equation	Correlation coefficient (R^2)
Silty Sand	q_c = 0.378N	0.646
Sandy Silt	q_c = 0.361N	<0.1
Silty Clay	q_c = 0.261N	<0.1
Clayey Sand	q_c = 0.225N	0.703
Gravelly Sand	q_c = 0.608N	0.213

The q_c vs N correlation derived for each soil type is illustrated in Fig. 2 to Fig. 6 below.

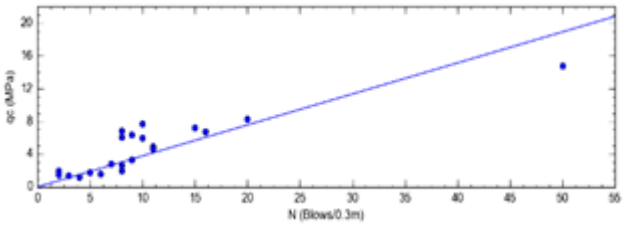

Fig. 2 q_c vs N relationship for silty sand

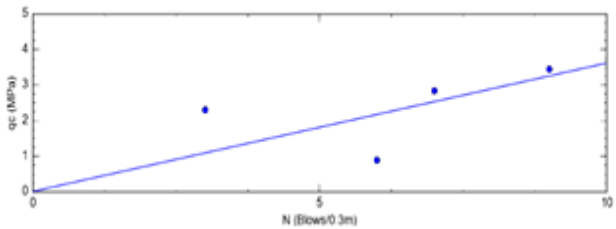

Fig. 3 q_c vs N relationship for sandy silt

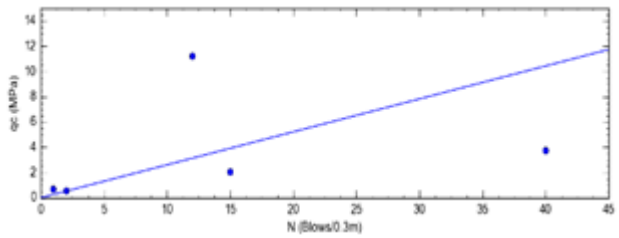

Fig. 4 q_c vs N relationship for silty clay

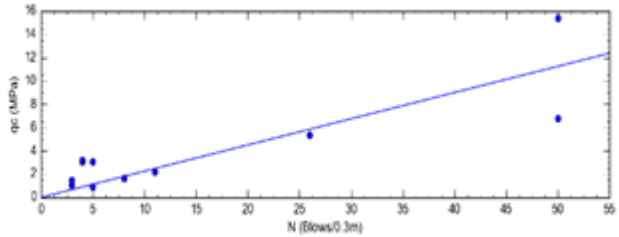

Fig. 5 q_c vs N relationship for clayey sand

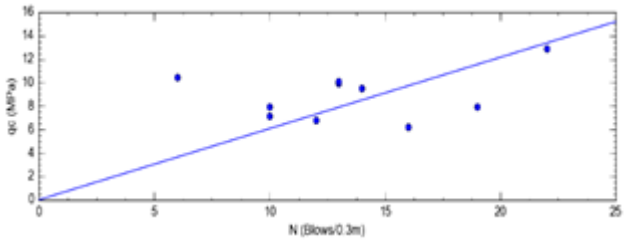

Fig. 6 q_c vs N relationship for gravelly sand

5.2 *Comparison of q_c/N with previous studies*

The preceding researches that developed correlations between tip resistance (q_c) of CPT and raw SPT blow counts (N) were used to compare q_c/N results in this study. The comparison is tabulated in the following table.

Table 2: Comparison of correlated q_c/N with past studies

Authors	Soil Type	Proposed	This Research
De Alencar Velloso (1959)	Sandy silt	0.35	0.361
Franki Piles (1960) from Akca (2003)	Silty sand	0.5	0.378
	Silty clay	0.3	0.261
Schmertmann (1970)	Fine to medium sand, silty sand	0.3-0.4	0.378
	Coarse sand, sand with gravel	0.5-0.6	0.608
Akca (2003)	Silty sand	0.702	0.378
	Sandy silt	0.58	0.361
Robertson (1983)	Silty sand	0.3-0.4	0.378
Danziger and De Valleso (1995)	Fine to medium sand, Silty sand	0.3-0.42	0.378
Barata et al., (1978)	Clayey silty sand	0.2-0.35	0.225
	Sandy silty clay	0.15-0.25	0.261
Mehtab Alam et al., (2018)	Silty Sand	0.427	0.378
	Sandy Silt	0.337	0.361
	Silty Clay	0.319	0.261
Meigh & Nixon (1961)	Gravelly Sand	0.3-0.4	0.608

The obtained q_c/N ratio for Kelani valley sandy silt soil category studied under this research is 0.361. The value was compared with respect to the q_c/N values proposed by past researches. De Alencar Velloso (1959), Akca (2003) and Mehtab Alam et al., (2018) have proposed 0.35, 0.58 and 0.337 respectively for q_c/N ratio. It can be stated that the obtained q_c/N value for sandy silt soil category is in line with values stated in De Alencar Velloso (1959) and Mehtab Alam et al., (2018) studies.

q_c/N value attained for silty sand in this research was 0.378 whilst Franki Piles (1960), Schmertmann (1970), Akca (2003), Robertson (1983), Danziger and De Valleso (1995) and Mehtab Alam et al., (2018) derived as 0.5, 0.3-0.4, 0.702, 0.3-0.4, 0.3-0.42 and 0.427 respectively. It can be noted that the q_c/N ratio obtained for silty sand soil category in Kelani valley studied under this research is in agreement with preceding researches done by Schmertmann (1970), Robertson (1983) and Danziger and De Valleso (1995).

The derived q_c/N value for silty clay soil type in Kelani valley in this analysis is 0.261. Akca (2003), Barata et al., (1978) and Mehtab Alam et al., (2018) suggested 0.3, 0.15-0.25 and 0.319 respectively for the ratio of q_c/N. It is observed that correlated q_c/N for silty clay soil variety has a proper match with regard to the values proposed in the previous studies such as Akca (2003), Barata et al., (1978) and Mehtab Alam et al., (2018).

The results of geotechnical investigations at Kelani river banks indicated 0.225 q_c/N ratio for clayey sand. Barata et al., (1978) proposed 0.2-0.35 q_c/N ratio for the same soil type in their study. It is noted that the obtained q_c/N ratio falls within the suggested range of the study done by Barata et al., (1978).

The q_c/N ratios acquired for Kelani valley gravely sand class in this study is 0.608. This value is examined with respect to the values obtained by earlier researches. Schmertmann (1970) and Meigh & Nixon (1961) recommended 0.5-0.6 and 0.3-0.4 respectively. It is clear that q_c/N for gravely sand is in alignment with the Schmertmann (1970) and Meigh & Nixon (1961).

This concludes that the study for Kelani valley soils shows a good match for q_c/N ratio with regard to the past studies for the soil types; sandy silt, silty sand, silty clay, clayey sand and gravelly sand.

5.3 *Discussion*

The results of this research is generally in agreement with the correlations given in Table 2. For most of the soil types, the q_c/N ratios are well matched with correlations given in literature. q_c/N values proposed in Franki Piles (1960) and Akca (2003) for silty sand are comparatively higher than the results of this research. However, the obtained q_c vs N correlation for silty sand is in good agreement with Robertson (1983). It can be noted that, this study underestimates the q_c/N relationship of silty clay compared with Mehtab Alam et al., (2018) and Franki Piles (1960). The q_c vs N relationships derived under this study were only limited to alluvium soils due to the availability of limited data. There are possibilities of expanding this research to investigate theoretical q_c vs N relationships of other dominant soil types in Sri Lanka.

6 CONCLUSIONS

This paper presents the applicability of theoretical CPT and SPT correlations to the Sri Lankan soils in the Kelani River banks between Hanwella and Kaduwela. The available soil types in the study area are silty sand, sandy silt, silty clay, clayey sand and gravelly sand. The developed q_c/N relationships were compared with previously proposed correlations in literature. The comparison shows that the correlations developed for Kelani valley is in a good agreement with the literature.

Table 3 represents the linear relationships obtained for tip resistance (q_c) of CPT vs raw SPT blow counts (N) for silty sand, sandy silt, silty clay, clayey sand and gravelly sand of Kelani valley soils from Hanwella to Kaduwela. These relationships can be applied to correlate the results of CPT and SPT measurements in similar geographical locations in Sri Lanka.

Table 3: Correlation of tip resistance (q_c) of CPT vs raw SPT blow counts (N) for Kelani valley soils

Soil Type	Correlation Equation
Silty Sand	$q_c = 0.378N$
Sandy Silt	$q_c = 0.361N$
Silty Clay	$q_c = 0.261N$
Clayey Sand	$q_c = 0.225N$
Gravelly Sand	$q_c = 0.608N$

7 RECOMMENDATIONS

This research only attempted to develop direct proportional linear equation between q_c and N. For further analysis it can be recommended to use multiple linear regression models, power relationships, logarithmic relationships considering soil parameters such as sleeve friction (f_s), friction ratio (R_f), and mean grain size (D_{50}) etc.

The results of this research can be improved by increasing the number of sets of CPT and SPT tests at various sites to sharpen the reliability of the relationship which is used in this study and obtain a greater accuracy in the correlation of tip resistance (q_c) in CPT and raw SPT blow counts (N) for the variety of soil categories at different geographical locations in Sri Lanka.

REFERENCES

Akca, N. (2003). Correlation of SPT–CPT data from the United Arab Emirates. *Engineering Geology 67*, 219-231.

British Standards. (2006). BS EN ISO 22475-1:2006 Geotechnical investigation and testing. Sampling methods and groundwater measurements. Technical principles for execution.

British Standards. (2012). BS EN ISO 22282-1:2012 Geotechnical investigation and testing. Geohydraulic testing. General rules.

British Standards. (2012). BS EN ISO 22476-1:2012 Geotechnical Investigation and testing – Field testing. Part 1: Electrical cone and piezocone penetration test.

British Standards. (2015). BS 5930:2015 Code of practice for ground investigations.

Climate Resilience Improvement Project. (2018). Kelani Flood Mitigation Startegy, Sri Lanka, FACTUAL REPORT - LEFT BANK Prepared for Preliminary Ground Investigation. Colombo: National Building Research Organisation.

Climate Resilience Improvement Project. (2018). Kelani Flood Mitigation Startegy, Sri Lanka, FACTUAL REPORT - RIGHT BANK Prepared for Preliminary Ground Investigation. Colombo: National Building Research Organisation.

Climate Resilience Improvement Project. (2018). Kelani Flood Mitigation Startegy, Sri Lanka, GEOTECHNICAL INTERPRETATIVE REPORT

Prepared for Preliminary Ground Investigation. Colombo: National Building Research Organisation.

Climate Resilience Improvement Project. (2018). Kelani Flood Mitigation Startegy, Sri Lanka, Preliminary Ground Investigation Scope of Works - Tranche 1. Ministry of Irrigation and Water Resources Management and Disaster Management.

Guen, O. (2014). *Correlation between SPT and CPT*. Trondheim: Norwegian University of Science and Technology.

Jarushi, F., AlKaabim, S., & Cosentino, P. (2015). A New Correlation between SPT and CPT for. *International Journal of Geological and Environmental Engineering*, 101-107.

Kara, O., & Gündüz, Z. (2010). Correlation between CPT and SPT in Adapazari, Turkey.

Mehtab, A., Muhammad , A., Shamsher, S., Saeedullah , M. J., Muhammad, A. B., Maqsood, U.-R., & Nawaz , A. (2018). Empirical SPT-CPT correlation for soils from Lahore,Pakistan. *IOP Conference Series: Materials Science and Engineering.* IOP Publishing.

Mominul, H., Ansary, M., & Abedin, M. (2014). Applicability of existing CPT, SPT and soil parameter correlations for. *3rd International Symposium on Cone Penetration Testing*, (pp. 373-381). Las Vegas,.

Robertson, P., Campanella, R., & Wightman, A. (1983). SPT-CPT Correlations. *Journal of Geotechnical Engineering*, 1449-1459.

Sayed , A. M., Sherif, A. W., & Ahmed , A.-R. H. (2014). A unified CPT–SPT correlation for non-crushable and crushable cohesionless soils. *Ain Shams Engineering Journal*, 63-73.

Schmertmann,', J. H. (1970). Static Cone to Compute Static Settlement Over Sand. *Journal of the Soil Mechanics and Foundations Division*, 1012 -1135.

Tarawneh, B. (2014). Correlation of Standard and Cone. *EJGE*, 6717-6727.

Mechanistic insights on metallic corrosion in compacted Kaolin

R.M. Azoor, R.N. Deo, B.M. Shannon & J. Kodikara
Department of Civil Engineering, Monash University VIC 3800, Australia

ABSTRACT: Underground corrosion is a significant problem concerning buried infrastructure and is influenced by many variables. This work adopted a multidisciplinary approach combining experimental observations from electrochemistry, soil mechanics and geotechnical engineering to elucidate the role of soil compaction and moisture distribution in underground corrosion. The optimum moisture content for metal corrosion in Kaolin was demonstrated and its relationship to the optimum moisture content for compaction was presented. Numerical modelling was used to examine the corrosion behavior of Kaolin compacted to different densities under field conditions. It was shown that differences in compaction and the resulting changes to moisture distribution could lead to localized, elevated levels of corrosion, which may result in rapid failure of buried infrastructure.

1 INTRODUCTION

Corrosion deterioration of metals buried in soil causes significant problems in the management of buried metallic infrastructure such as underground pipelines. With aging pipe networks around the world, failure rates are increasing and an accurate evaluation of the rates of corrosion degradation is necessary for proactive maintenance. Soil moisture and aeration and their variation in the ground are known to influence the patterns and levels of corrosion in buried assets (Romanoff 1957, Tomashov 1966, Azoor et al. 2019b).

It has been shown previously that there exists an optimum soil moisture for underground corrosion. (Tomashov 1966, Gupta and Gupta 1979, Deo et al. 2014, Akkouche et al. 2016). Experimentally it was shown that the degree of saturation corresponding to this optimum condition varies with soil type and that it can be related to the soil water retention curve and soil compaction (Azoor et al. 2019b).

Corrosion processes especially in the field can be accentuated by a mechanism known as macro-cells. Macro-cells are formed when a spatial difference in some property influencing corrosion (such as aeration) is created. When this happens, the anodes and cathodes are spatially separated resulting in intense corrosion at the anode.

Given the known influence of compaction on corrosion, variable levels of compaction may lead to changes in the moisture and aeration levels in soil and may influence the rates of corrosion through the action of macro-cells. This study was conducted to examine such influences. A numerical model for a pipeline buried in variably compacted Kaolin was developed based on previous experimental data and the patterns and levels of corrosion arising are examined and their implications discussed.

2 EXPERIMENTAL METHODS

Most experimental methods described in this paper were reported previously (Azoor et al. 2017, 2019b, 2019c, Azoor 2019). The following sections therefore only briefly summarize the steps of the experimental program.

2.1 *Soil water retention tests*

Soil water retention tests were conducted using the UMS HYPROP and WP4C (UMS GmbH 2015, METER Group Inc. 2018) equipment. The tests were conducted under drying conditions for a consolidated Kaolin clay sample. The weight of the HYPROP test equipment with the consolidated clay sample was recorded together with suction readings while the sample dried under laboratory conditions. Once the tensiometers cavitated, the test was stopped and the WP4C equipment was used to measure the soil suctions in small clay specimens extracted from the same bulk sample and dried to pre-determined moisture contents. The HYPROP and WP4C equipment assembly used for tests are shown in Fig 1.

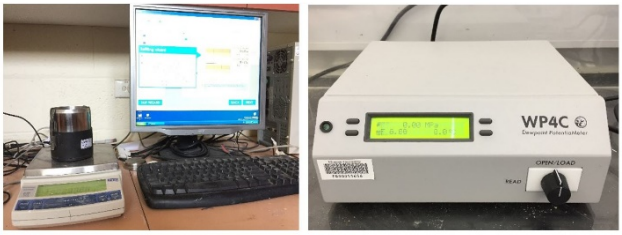

Figure 1 The HYPROP (left) and WP4C (right) equipment used for the generation of water retention curves for Kaolin

2.2 *Oxygen diffusion and standard proctor compaction tests*

Standard diffusion experiments were conducted using the diffusion chamber method (Currie 1960) using the UMS-G experimental setup (Rouf et al. 2016). The clay specimens were compacted into a specimen holder while maintaining approximately the same dry density at different degrees of saturation. The specimen holder was loaded into the UMS-G apparatus and the oxygen concentration in the diffusion chamber was measured after initially purging the chamber with nitrogen. The solution proposed by Carslaw and Jaeger (1959) was used to calculate the effective oxygen diffusion coefficient in the Kaolin samples compacted to different degrees of saturation (S_r).

The standard Proctor compaction test results reported by Islam (2015), Kodikara et al. (2016), &(2018) were used for the analysis in this work.

2.3 *Electrochemical tests*

Potentiodynamic polarization tests (Tait 1994) were carried out on clay specimens compacted to different degrees of saturation. The detailed methodology and results can be found in Azoor et al. (2019b). The corrosion current density (i_{corr}) and the corrosion potential (E_{corr}) were obtained from the potentiodynamic polarisation test using a fitting process known as Tafel fitting (Azoor et al. 2019b). The corrosion rate (i_{corr}) values were plotted against the degree of saturation (S_r) and was used for model calibration. In addition, electrical conductivity of Kaolin compacted at different degrees of saturation were measured using the experimental method detailed by Deo and Cull (2015). The electrical conductivity was also used as input to the model along with the oxygen diffusion coefficients and the water retention curve.

3 NUMERICAL MODELING

A modified version of the numerical model presented by Azoor et al. 2018 was used in the present work. In addition to the equations presented therein, equations for unsaturated moisture flow are solved for in this work. An initial 1-dimensional numerical model was created to simulate the experimental conditions of optimum soil moisture for corrosion. The numerical model was calibrated to match the experimental current densities (i_{corr}). Using calibrated values, a 3D field scale model was developed to examine the corrosion of pipeline through Kaolin soil with varying levels of compaction.

3.1 *Model setup*

The 1-D model was created to compare against the experimental corrosion rates. A domain length of 0.033 m matching the depth of the electrochemical cell (Azoor et al. 2019b) used in the experiments was used. The boundary conditions and governing equations were implemented in a similar fashion to that described by Azoor et al. (2019a). However, in the present simulation, the moisture migration including gravity effects was calculated based on the soil water retention curves, as opposed to the uniform degree of saturation assumed previously (Azoor et al. 2019a).

For the 3-D field scale simulation, a soil block with dimensions 10×3×3 m with a pipe of diameter 0.3 m buried at a depth of 1 m from the surface was created. The corrosion parameters were sourced from the experiments described above and the 1-D numerical model. The water retention curve developed for Kaolin were fitted to a van Genuchten equation and used to describe the moisture distribution within the soil block that facilitates corrosion. A simplified van Genuchten equation with the Mualem criteria, given in Eq. 1, was used for this purpose. A static S_r distribution with effects of gravity were included, and the variations in S_r due to non-uniform compaction were simulated.

$$S_r = \frac{1}{\left[1+\left(\alpha\psi\right)^n\right]^{\left(1-\frac{1}{n}\right)}} \quad (1)$$

α and n are fitting parameters and ψ is the soil suction head (m). Eq. 1 was fitted into the experimental data to extract the parameters for the simulation. The fitting parameters were modified to generate an assumed water retention curve for densely compacted Kaolin to be used for the differential aeration simulation as detailed in the following section.

3.2 *Simulating differential aeration due to varying levels of compaction*

It has been shown that for a given soil, compaction leads to a change in its water retention curves due to changes to its structure (Vanapalli et al. 2004). These changes are primarily due to changes in the structural pores in soil, and according to the data presented by Vanapalli et al. (2004), compaction results in a shift of the water retention curves primarily in the lower suction regions. This factor was used in the simulation of differently compacted Kaolin. It was assumed that a portion of the soil in the simulated soil block is compacted more densely than the surrounding soil, which may occur as the result

of a post installation activity such as a service connection or repair on a pipe. For simplicity, this densely compacted region was assumed to be hemispherical in shape and its water retention properties were described by a modified water retention curve similar to the experimental curves presented by Vanapalli et al. (2004). To simulate the dense region, the water retention curves described by Eq. 1 were varied in 3-dimensional space. Figure 2 shows the experimental water retention curve and the modified curve used to denote the compacted Kaolin.

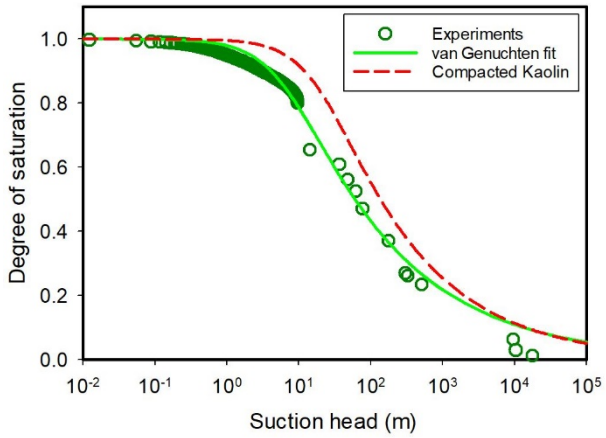

Figure 2: The water retention curve fitted to experimental data and the assumed water retention curve for compacted Kaolin, as used for input to the numerical model.

The densely compacted retention curve was implemented within a hemi-spherical region to denote the localized region (re-compacted excavation pit) with high density. The model geometry, showing the region of the densely compacted clay amidst the rest of the clay medium, the pipeline and the mesh used for simulation is given in Fig. 3. A smooth transition between the densely compacted region (red) and the surrounding clay (green) was implemented using Heaviside step functions for the water retention curve parameters α and n. A finer mesh size was used around the pipeline for better accuracy.

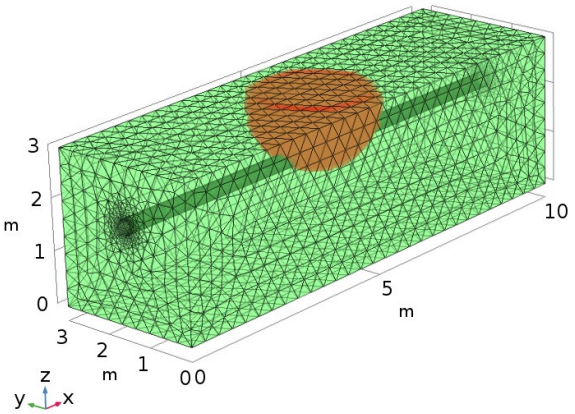

Figure 4: The model geometry, mesh and the soil domain. The denser Kaolin is denoted in red while the Kaolin compacted to OMC is denoted in green

4 RESULTS AND DISCUSSION

4.1 *The optimum level of corrosion for clay and its relationship to soil compaction*

It has been shown previously that that there exists an optimum moisture content for corrosion in soil at which the corrosion rate is maximized (Gupta and Gupta 1979, Akkouche et al. 2016, Azoor et al. 2019b). Further it was shown that the degree of saturation at this optimum moisture content, is coincident with the degree of saturation at the optimum moisture level for compaction (OMC). Based on experiments on three soil types. Azoor et al. (2019b) showed that the uniform corrosion rate is maximized at this degree of saturation, and that it is the degree of saturation at the inflection point of the water retention curve or the particular soil. The reason for this behavior was explained based on the moisture distribution regimes in soil. It was shown that corrosion is maximum under ample availability of both water and oxygen under the funicular regime, where both the air and water phases are continuous. With increasing saturation, the corrosion rate increases, with increasing water connectivity. As the air phase becomes discontinuous with further increasing saturation, the hindrance to oxygen diffusion cause a decline in corrosion rate. The entrapment of air occurs after the optimum moisture content during dynamic compaction (Kodikara 2012, Kodikara et al. 2018), and therefore affects corrosion in the same manner. Given that the usual practice when installing buried pipelines is to compact backfill to OMC, this practice needs to be revaluated in light of corrosion deterioration.

The standard compaction results for Kaolin are shown in Fig. 4.

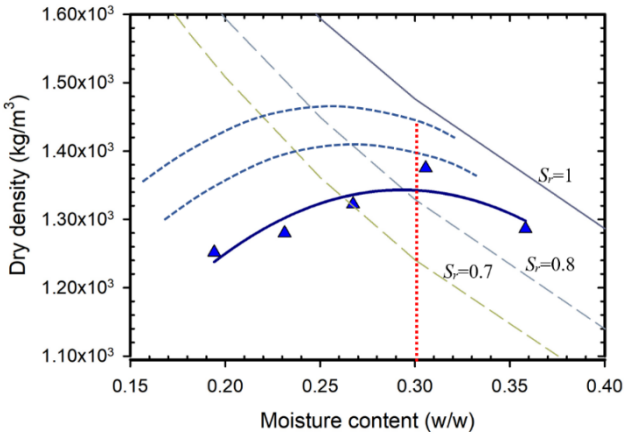

Figure 3:Standard compaction results for Kaolin with expected curves at higher compaction energies

The expected curves with higher compactive efforts are denoted in dotted lines. It is noted that with increasing compaction energy, the S_r at the optimum moisture content remains approximately the same.

For this reason, it has been argued that the degree of saturation, S_r is better parameter for controlling moisture in field compaction (Tatsuoka and Gomes Correia 2018)

In the case of the creation of a densely compacted region as examined in this study, it is likely that compaction that occurs at a later stage would be conducted at the same moisture content albeit with a higher compaction energy. This corresponds to a situation denoted by the red dotted line in Fig. 4, where the S_r of the newly compacted region becomes higher than the surrounding soil. If the surrounding soil was initially compacted to OMC, this means that the denser region will have a S_r higher than that of the surrounding soil at OMC. With the water retention curves given in Fig. 2 and a surface suction head of 10 m, the distribution of S_r in the variably compacted soil block was obtained as shown in Fig. 5.

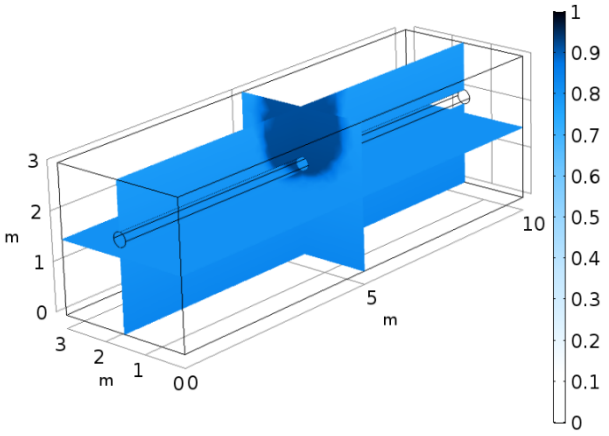

Figure 5: The S_r distribution within the soil block with densely compacted region showing a higher S_r

While the values given here are only indicative, if the compaction stress is known, the change in degree of saturation and density/void ratio can be determined mechanistically (Kodikara et al. 2020).

It can be seen in Fig 5 that, as demonstrated using Fig 4 above, the S_r in the hemi-spherical densely compacted region is higher than the surrounding S_r compacted to OMC.

4.2 *Differential aeration corrosion in a pipe in soil with varying levels of compaction*

With the above distribution of S_r (Fig. 5) the corrosion levels expected in the pipe passing through both regions were simulated. The same corrosion parameters were used as the soil type is the same. A time period of ~ 22 years was simulated with a constant suction condition leading to a static S_r distribution given in Fig 5. Variations in S_r due to effects such as climate were not considered. As discussed by Azoor et al. (2018), time dependent corrosion phenomena such as corrosion product deposition, passivation and corrosion localization were implemented and the resulting corrosion behavior was examined.

The electric potential on the pipeline, and of the surrounding soil at the end of 22 years, which indicates the level of corrosivity of the medium, is given in Fig. 6.

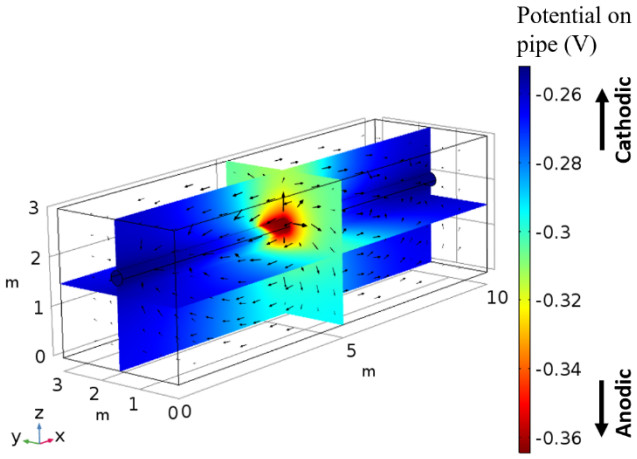

Figure 6: The electrode potential on the corroding pipeline (magnitudes in color scale) and the potential in the surrounding soil (same magnitudes but opposite in sign). Black arrow vectors denote the net current flowing through soil.

The colors denote the electrode potential on the pipeline and the surrounding soil. Note that the magnitudes in the given color scale correspond to the potential values on the pipe. The adjacent soil potential values are the same but with opposite signs. It is seen in Fig. 6 that the section of pipe under the densely compacted clay turns anodic while the rest of the pipe turns cathodic. It is also seen that a net current (denoted by the black arrow vectors) flows from the anodic portion to the cathodic portion. This net current signifies a macro-cell formation and indicates that the region under the dense clay undergoes higher levels of corrosion than the rest of the clay medium.

The mass loss due to corrosion can be converted to the metal thickness loss using the molar mass and density of the corroding material. Assuming that iron is the corroding metal, the cumulative thickness loss in the pipe was examined. The curves for two points, one within the densely compacted region and the other in the under the surrounding clay were plotted. The final mass lost on the pipe surface was also visualized. Figure 7 shows the cumulative corrosion thickness loss and the final corrosion profile on the pipeline.

It can be seen that the levels of corrosion within the dense clay lump is several times larger than that of the region under the clay compacted to OMC. It

is further seen corrosion losses on the pipeline are higher at the edge between the two regions, giving rise to a localized region of corrosion. This localization is a direct consequence of macro cell activity. The final corrosion profile, as shown in the inset in Fig. 7, shows this relatively deep "patch" of corrosion underneath the dense clay. While in this study the dense clay was an idealized region, in reality, such regions could take various sizes and shapes, and may lead to various patch configurations. In fact it has been found that the dominant reason of failure of buried pipelines occurs due to such corrosion patches (Deo et al. 2019) that occur due to many reasons.

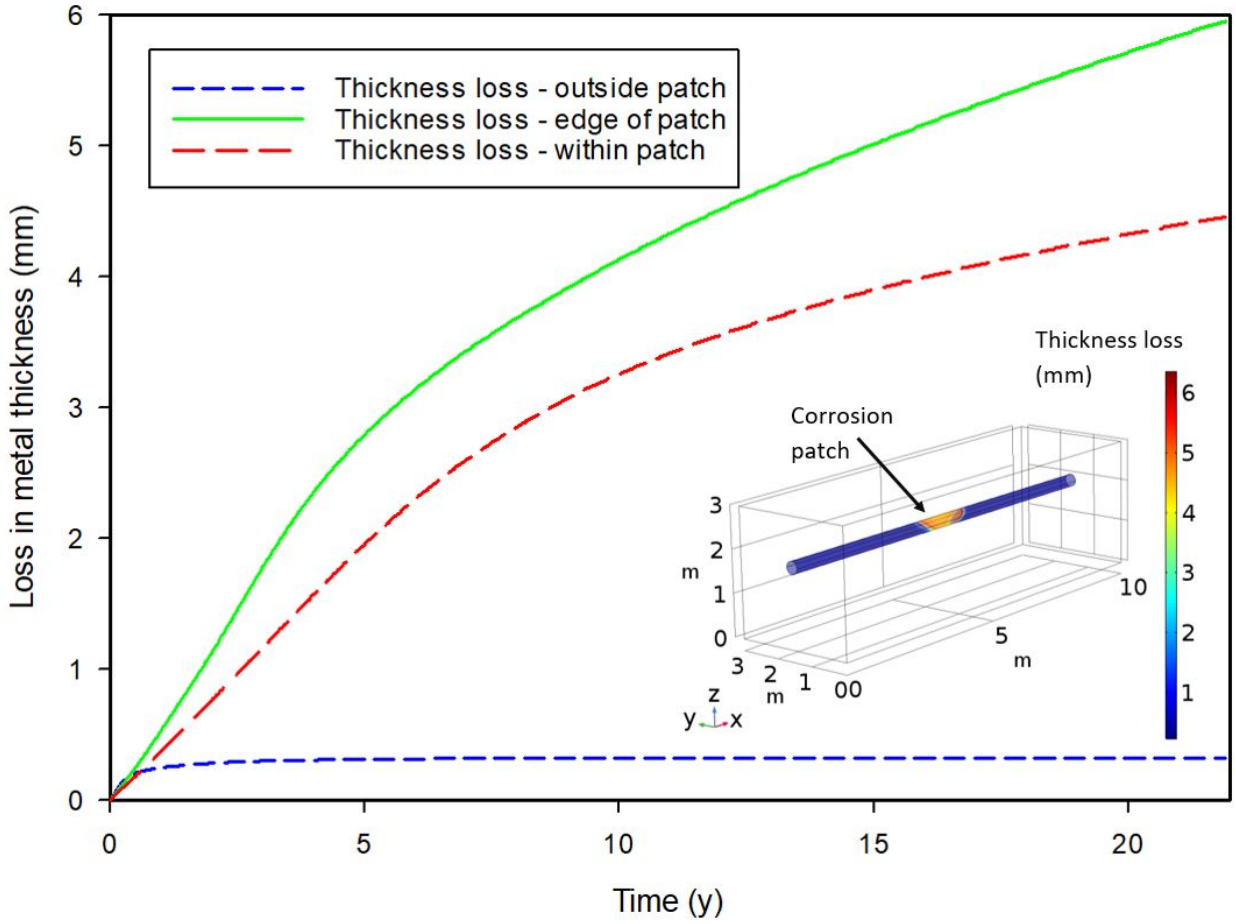

4.3 *Assumptions, limitations and future work*

It was assumed that the pipe undergoing corrosion is uncoated or that the coating is severely deteriorated. Further, the modifications such as clamping of the pipe as part of the repair were not included for simplicity. Under certain conditions such clamps may also influence corrosion. The model simulation presented involved a static S_r distribution, and the same soil type. In reality, S_r would vary with time under the influence of climatic variations and other factors. Soil types would also vary in space similar to the degree of compaction. Such variations could be captured using random fields and stochastic processes. In the case of soil type variations, the soil chemistry and their influence on the corrosion kinetics will also need to be considered.

5 CONCLUSIONS

Using results from a multidisciplinary experimental program, the relationship between corrosion rates in the field and standard compaction practice was discussed. A calibrated numerical model was developed to examine the influence of variable compaction on the corrosion behavior of a metal pipeline buried in Kaolin. It was demonstrated that a densely compacted region amidst clay soil compacted to the OMC could lead to the formation corrosion patches. These corrosion patches are the result of macro-corrosion cells which eventually lead to higher levels of localized corrosion, and are the primary reason or pipe failures. Corrosion patches may also arise due to other external factors and natural variations in soil properties.

ACKNOWLEDGMENTS

Rukshan Azoor acknowledges the Monash University International Postgraduate Research Scholarship (MIPRS), Monash Graduate Scholarship (MGS), Graduate Research International Travel Award (GRITA) and the Postgraduate Publications Award (PPA) provided for his PhD studies.

REFERENCES

Akkouche, R., Rémazeilles, C., Jeannin, M., Barbalat, M., Sabot, R., and Refait, P. 2016. Influence of soil moisture on the corrosion processes of carbon steel in artificial soil : Active area and differential aeration cells. Electrochimica Acta, **213**: 698–708. Elsevier Ltd. doi:10.1016/j.electacta.2016.07.163.

Azoor, R., Deo, R., and Kodikara, J. 2019a. Modelling and testing of optimum soil moisture levels in the corrosion of underground pipelines. *In* 7th International Symposium on Deformation Characteristics of Geomaterials. Glasgow.

Azoor, R.M. 2019. Evaluation of soil aeration as applicable to underground metal corrosion. PhD Thesis, Monash University.

Azoor, R.M., Deo, R.N., Birbilis, N., and Kodikara, J. 2019b. On the optimum soil moisture for underground corrosion in different soil types. Corrosion Science, **159**(May): 108116. Elsevier. doi:10.1016/j.corsci.2019.108116.

Azoor, R.M., Deo, R.N., Birbilis, N., and Kodikara, J.K. 2017. Modelling the Influence of Differential Aeration in Underground Corrosion. *In* Proceedings of the 2017 COMSOL Conference in Boston. *Edited by* COMSOL. Boston MA.

Azoor, R.M., Deo, R.N., Birbilis, N., and Kodikara, J.K. 2018. Coupled Electro-Chemical-Soil Model to Evaluate the Influence of Soil Aeration on Underground Metal Pipe Corrosion. Corrosion, **74**(11): 1177–1191. doi:https://doi.org/10.5006/2860.

Azoor, R.M., Deo, R.N., Shannon, B.M., and Kodikara, J.K. 2019c. Using soil moisture retention curves and corrosimetry to characterise the role of soil moisture in underground corrosion. *In* 13th Australia New Zealand Conference on Geomechanics. Perth WA.

Carslaw, H.S., and Jaeger, J.C. 1959. Conduction of Heat in Solids. Clarendon Press, Oxford UK.

Currie, J.A. 1960. Gaseous diffusion in porous media Part 1. - A non-steady state method. British Journal of Applied Physics, **11**(8): 314–317. doi:10.1088/0508-3443/11/8/302.

Deo, R.N., Birbilis, N., and Cull, J.P. 2014. Measurement of corrosion in soil using the galvanostatic pulse technique. Corrosion Science, **80**: 339–349. Elsevier Ltd. doi:10.1016/j.corsci.2013.11.058.

Deo, R.N., and Cull, J.P. 2015. Spectral induced polarization techniques in soil corrosivity assessments. Geotechnical Testing Journal, **38**(6): 965–977. doi:10.1520/GTJ20140219.

Deo, R.N., Rathnayaka, S., Zhang, C., Fu, G.Y., Shannon, B., Wong, L., and Kodikara, J.K. 2019. Characterization of corrosion morphologies from deteriorated underground cast iron water pipes. Materials and Corrosion, (March): 1–15. John Wiley & Sons, Ltd. doi:10.1002/maco.201910906.

Gupta, S.K., and Gupta, B.K. 1979. The critical soil moisture content in the underground corrosion of mild steel. Corrosion Science, **19**(3): 171–178. doi:10.1016/0010-938X(79)90015-5.

Islam, T. 2015. A study of volumetric behaviour of compacted clayey soils in the void ratio, moisture ratio and net stress space. PhD Thesis, Monash University.

Kodikara, J. 2012. New framework for volumetric constitutive behaviour of compacted unsaturated soils. Canadian Geotechnical Journal, **49**(11): 1227–1243. doi:10.1139/t2012-084.

Kodikara, J., Islam, T., and Rajeev, P. 2016. Interpretation of the loading–wetting behaviour of compacted soils within the “MPK” framework. Part II: Dynamic compaction1. Canadian Geotechnical Journal, **53**(5): 806–827.

Kodikara, J., Islam, T., and Shounthrarajah, A. 2018. Review of Soil Compaction : History and Recent Developments. Transportation Geotechnics, (September). doi:10.1016/j.trgeo.2018.09.006.

Kodikara, J., Jayasundara, C., and Zhou, A.N. 2020. A generalised constitutive model for unsaturated compacted soils considering wetting/drying cycles and environmentally-stabilised line. Computers and Geotechnics, **118**(April 2019): 103332. Elsevier. doi:10.1016/j.compgeo.2019.103332.

METER Group Inc. 2018. WP4C Dew Point PotentiaMeter-Operator’s Manual.

Romanoff, M. 1957. Underground Corrosion. United States Department of Commerce, Washington DC.

Rouf, M.A., Bouazza, A., Singh, R.M., Gates, W.P., and Rowe, R.K. 2016. Gas flow unified measurement system for sequential measurement of gas diffusion and gas permeability of partially hydrated geosynthetic clay liners. Canadian Geotechnical Journal, **53**(6): 1000–1012. doi:10.1139/cgj-2015-0123.

Tait, W.S. 1994. An Introduction to Electrochemical Corrosion Testing for Practicing Engineers and Scientists. PairODocs Publications, Wisconsin.

Tatsuoka, F., and Gomes Correia, A. 2018. Importance of controlling the degree of saturation in soil compaction linked to soil structure design. Transportation Geotechnics, **17**(April): 3–23. doi:10.1016/j.trgeo.2018.06.004.

Tomashov, N.D. 1966. Underground corrosion of metals. *In* Theory of Corrosion and Protection of Metals, 2nd edition. Macmillan, 1966, New York. pp. 399–421.

UMS GmbH. 2015. Operation Manual HYPROP. Munich Germany.

Vanapalli, S.K., Fredlund, D.G., and Pufahl, D.E. 2004. Influence of soil structure and stress history on the soil–water characteristics of a compacted till. Géotechnique, **51**(6): 573–576. doi:10.1680/geot.51.6.573.40456.

Assessment of Geogrid Reinforced Weak Subgrades using a Modified CBR Mould

Kasun Wimalasena
School of Civil and Environmental Engineering, Queensland University of Technology, Australia

Chaminda Gallage
School of Civil and Environmental Engineering, Queensland University of Technology, Australia

ABSTRACT: Geogrids can be used to reinforce/stabilise the weak subgrades and hence, the pavement service life would be extended and/or reduce thickness of the structural layers. However, performance of the geogrid reinforced subgrade is significantly affected by numbers of factors such as: the geogrid type, the geometry of geogrids, the subgrade strength, the layer thickness above the geogrid, the location of geogrids, and type of granular material above the geogrid. Therefore, it is important to understand the performance of geogrid reinforced subgrade under different conditions. Although California Bearing Ratio (CBR) test has been used to assess the geogrid reinforced weak subgrades, the results are significantly affected by the boundaries of the standard CBR mould. Therefore, this study has developed a 305 mm diameter cylindrical mould (a modified CBR mould) to investigate the effects of geogrid and the thickness of granular layer above the geogrid on the performance of geogrid reinforced subgrade. The results demonstrate that both geogrid and the granular cover contribute to the subgrade improvement.

1 INTRODUCTION

Weak subgrade is one of the main challenges that must be overcome in road construction (Jayalath and Wimalasena 2020). In fact, expansive clay soil is very common across the Australian continent (Kodikara et al. 2014, Gallage et al. 2017). As a result, significant amount of the total cost of road construction projects must be allocated for weak subgrade improvement (Wimalasena and Jayalath 2020). In order to upgrade the subgrade condition, soft subgrade treatment methods such as: backfilling with new materials, increase granular layer thickness, rock blanketing or soil stabilization could be considered (Gallage et al. 2015, Jayalath et al. 2018, Gallage et al. 2019). However, aforementioned methods significantly increase the demand for the granular materials (Jayakody et al. 2019a, Jayakody et al. 2019b, Wimalasena et al. 2019, Clark and Gallage 2020, Clark et al. 2020;) and raising environmental concerns (Rashid et al. 2017). Therefore, sustainable construction methods and techniques are required to be developed to improve the weak subgrades (Abu-Farsakh et al. 2014).

Accordingly, geosynthetics have been emerging over the past decades as one of the best alternatives to overcome the challenges in road construction (Zornberg 2015). As a result of reinforcement effect of geosynthetics, the pavement stiffness and the bearing capacity of the weak subgrades could be improved and hence, would be a sustainable method of soft subgrade improvement while reducing demand for natural gravel (Zornberg and Gupta 2010).

Geosynthetics could be found in different types such as geotextiles, geogrids and geomembranes. However, geogrids have been recognized as the best type of geosynthetics for reinforcing the weak subgrades (Ferrotti et al. 2011). The level of reinforcement has a significant impact from the type of geogrid, the type and thickness of granular cover and the location of geogrid (Al-Qadi et al. 2012). However, limited studies have been performed in Australia to assess the geogrid reinforcement under local conditions despite geogrids are widely being used across the country for weak subgrade reinforcement.

California Bearing Ratio (CBR) test is one of the methods many researchers have been used to assess the geogrid reinforced weak subgrades (Duncan-Williams and Attoh-Okine 2008, Singh et al. 2019). Koerner (2005) developed a design method for geotextile reinforced roads using standard CBR test procedure. The CBR test is conducted in a standard mould of 150mm diameter and hence, results would significantly be affected by boundary effects (Leng 2003). In order to minimize the boundary effects, Bergado et al. (2001) have proposed a modified CBR mould by increasing the size of the diameter to 300mm. In that, the diameter of the plunger and the height of the mould has been maintained at the

standard dimensions. However, increasing the loading area on the top of the test section would be beneficial to capture the geogrid reinforcement effectively.

This research aimed to evaluate the improvement of a weak subgrade due to the reinforcement with a biaxial geogrid. The variation of geogrid reinforcement under different granular cover thicknesses was investigated. The experiments were performed in a modified CBR mould of 305 mm diameter and 510 mm in height. Reinforcement ratio was defined to compare different section configurations.

2 MATERIALS

2.1 *Subgrade material*

The soil used in this research project was collected from a road rehabilitation project in Toowoomba, Australia. A bulk of soil was collected from the subgrade level that was exposed after removing the existing pavement. A series of standard geotechnical tests were performed in the laboratory in accordance with the test specifications defined by the Department of Transport and Main Roads, Queensland (TMR), to classify the material. Figure 1(a) shows the particle size distribution and Table 1 presents the basic properties of subgrade material. Subsequently, this material was classified as silt of high plastic as per the unified soil classification system.

Table 1: Properties of subgrade material

Property	Value
Soil Particle Density	2.62
Maximum Dry Density (g/cm^3)	1.3
Optimum Moisture Content (%)	33
Liquid Limit (%)	73
Plastic Index (%)	20
Shrinkage Limit (%)	13.5
USCS Classification	MH

2.2 *Granular material*

The granular material was collected from a quarry in Brisbane and a series of gradation tests were performed in the laboratory to classify the granular type based on the TMR specifications(MTRS05). Figure 1(b) shows the particle size distribution of the granular material and it was confirmed that the collected granular is in compliance with specified type 2.1 granular in (MTRS05)TMR specifications. The standard proctor compaction test was performed to determine the optimum moisture content and the maximum dry density as 7.0% and 2.3 g/cm^3, respectively.

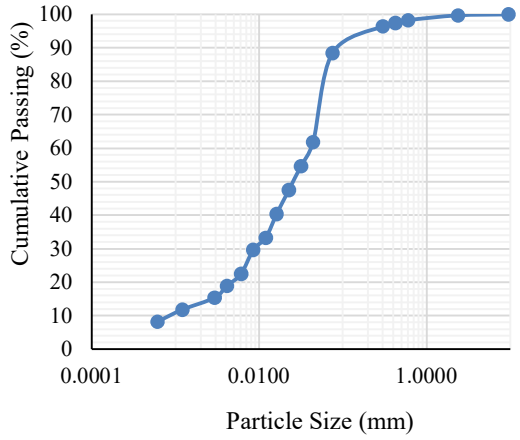

(a)

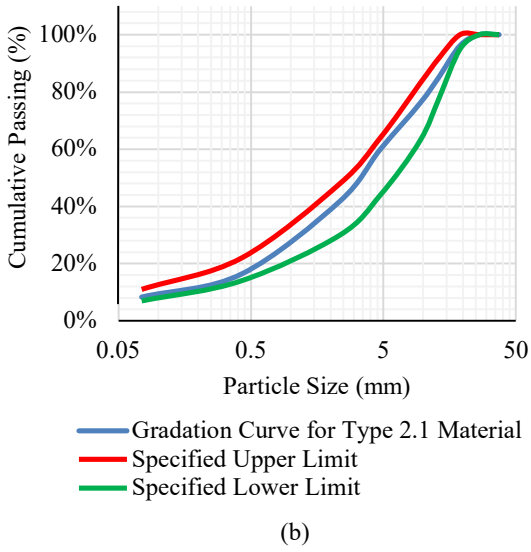

(b)

Figure 1: Particle size distribution of: (a) Subgrade material; (b) Granular material

2.3 *Reinforcement*

A biaxial geogrid made of polypropylene was used in this test series as reinforcing material. The nominal strength of the biaxial geogrid in both machine direction and cross machine direction is 40kN/m and has a square shape aperture of 31mm x 31mm.

3 EXPERIMENTAL INVESTIGATION

3.1 *Test apparatus*

A series of CBR tests were conducted in a modified CBR mould of 305 mm diameter and 510 mm in

height. Hence, it was expected to reduce the boundary effects compared to the standard CBR mould. A new plunger of 61mm diameter was proposed to be used with the modified CBR mould to achieve 1:5 ratio between the diameters of the plunger and the modified mould. An annular weight of 19.85kg was also manufactured to apply a surcharge vertical stress equal to 2.85kN/m^2 that is applied in Standard CBR test.

3.2 *Test methodology*

All test sections were constructed to a total height of 410 mm inside the modified CBR mould. The granular cover thickness was varied as 50 mm, 150mm and 200 mm and the height of the subgrade was varied as 360 mm, 260 mm and 210 mm, respectively. Both reinforced and unreinforced sections for each layer configuration were tested and the geogrid was placed at the base-subgrade interface in reinforced sections. A schematic diagram of test setup with 150 mm granular cover is shown in Figure 2.

The subgrade was created to bearing capacity of CBR 4. This was achieved by mixing the soil to specific moisture content and compacted to a decided degree of compaction. In order to decide the corresponding moisture content and the degree of compaction, a trial and error process was followed.

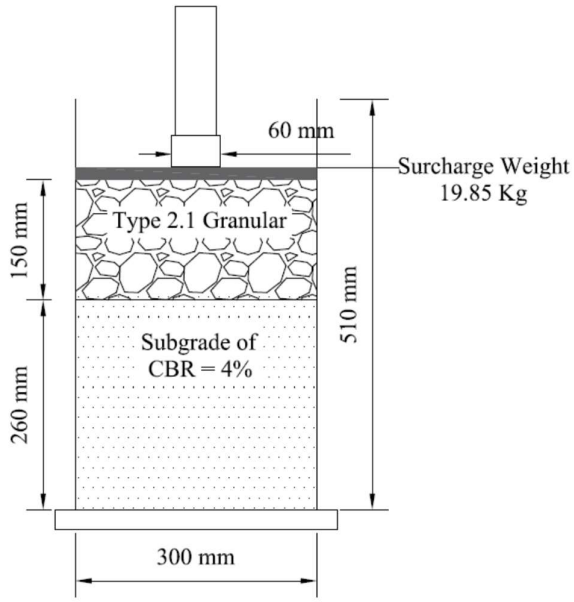

Figure 2: Schematic diagram of the test setup for 150 mm thick granular cover configuration

Initially, the soil was mixed with 5 different moisture contents, which are above the optimum moisture level, and compacted inside the standard CBR mould to achieve a predetermined degree of compaction. The degree of compaction was selected between 85% and 100% to ensure that the created subgrade will not be too soft to have higher settlements at the layers underneath when compacting the top layers of the sample. The samples were tested to determine the CBR values and subsequently, trial set of moisture contents and the corresponding degree of compactions were decided to create a subgrade of CBR 4. Thereafter, the standard CBR test was repeated for the trial values decided as above and verified that a subgrade of CBR 4 can be created by compacting soil with 44% moisture content to a 95% degree of compaction. Afterwards, the subgrade was created inside the modified CBR mould to the required height by compacting 50 mm thick equal layers.

(a) (b)

Figure 3:(a) Modified CBR mould test setup; (b) Geogrid at base subgrade interface.

On top of the subgrade layer, the granular layer was compacted to the required height in equal layers of 50mm thickness. The moisture content of the gravel layer was maintained 2% below the optimum moisture content to eliminate possible early shear failures.

The trial sections were loaded as illustrated in Figure 3(a) following the loading conditions specified for the standard CBR test procedure in TMR standard Q113A(MTM 2018). The load-deformation data were recorded and the vertical load to create a penetration of 5.00mm was considered to analyses the reinforced and unreinforced sections. The reinforcement ratio was calculated as given in equation 1.

$$\eta = \left\{ \frac{Load_{\ 5.0mm}\ of\ reinforced\ section}{Load_{\ 5.0m}\ \ of\ unreinforced\ section} \right\} \quad (1)$$

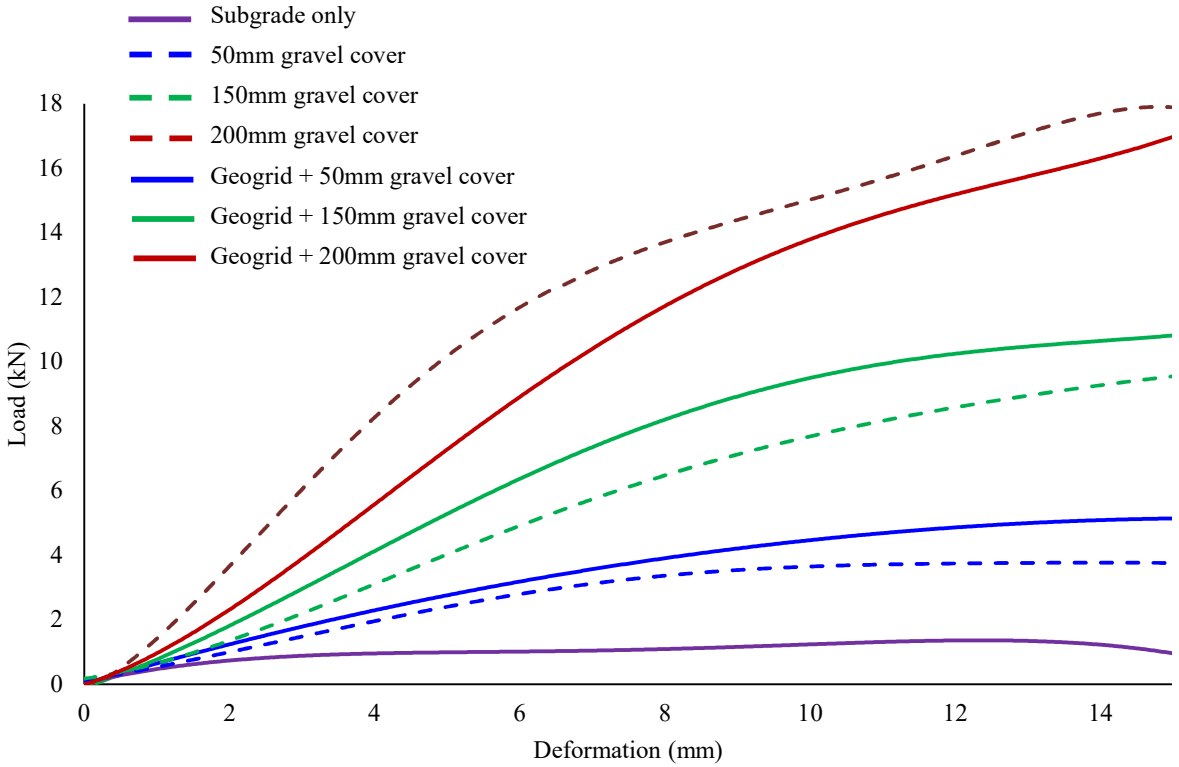

Figure 4: Load deformation curves of unreinforced, reinforced and subgrade only condition.

4 RESULTS AND DISCUSSION

The load-deformation curves obtained from modified CBR tests were compared to assess the weak subgrade improvement. Figure 4 illustrates the load-deformation relationships of subgrade only, unreinforced granular and reinforced granular section configurations. In this study, it was decided to use the load at 5.00 mm deformation to assess the subgrade improvement quantitatively and, hereafter, this load value is called the bearing capacity of the subgrade/stabilised subgrade.

As shown in Figs 5, irrespective of the use of geogrid at the interface, the bearing capacity of the stabilised subgrade increases with the increase in the thickness of the granular layer above the subgrade. The increase in the granular thickness will decrease the stress increment in clay subgrade. Therefore, the overall deformation at a given load decreases or the load capacity at a given deformation (penetration) increases.

When comparing the bearing capacities of subgrades stabilised with and without a geogrid at the interface, it can be seen (Figs 4, 5, and 6) that the bearing capacities of geogrid reinforced sections are

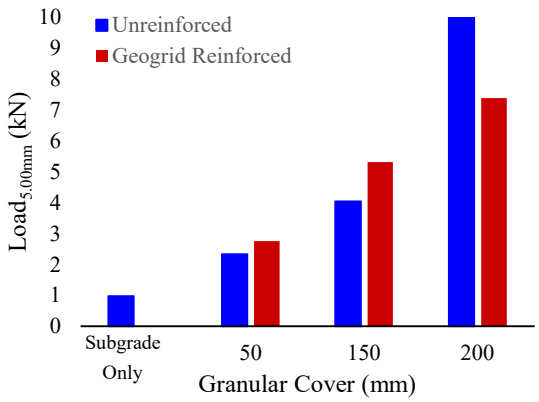

Figure 5: Load to create 5.0mm penetration.

greater than those of unreinforced sections up to the gravel cover thickness of 150 mm. This reflects the fact that geogrids contribute to the bearing capacity improvement of the overall section. Therefore, in order to achieve the bearing capacity of the unreinforced section, a reinforced section with reduced granular thickness with a geogrid placed at a base subgrade interface could be proposed as it is economical and reduces the demand for natural gravel. However, when the granular cover is 200 mm, the bearing capacity of the unreinforced section is greater than the reinforced section.

The geogrid interacts with gravel and provide self-confinement to gravel in the vicinity of the geogrid by the interlocking mechanism. The thickness of this confinement layer may depend on many parameters such as gravel type, type of geogrid and its aperture, and interface properties of gravel and geogrid. Therefore, when a geogrid layer is used for stabilising weak subgrades, a certain thickness of gravel above the geogrid acts as a stiffer layer due to the interlocking-induced confinement. As a result, the subgrade reinforced with a geogrid will exhibit a higher bearing capacity compared to the unreinforced subgrade. However, if the granular layer thickness is greater than the thickness of the gravel layer confined by the geogrid, the stress influence zone caused by the applied surface loading will locate within the layer which is above the geogrid-confined layer. Then this model will represent a scenario where a foundation is in a weak layer underlain by a stronger layer (Sharma et al. 2009). As a result, when increasing the thickness of granular layer above a certain value, in this study it is 200 mm, the bearing capacity of the unreinforced subgrade can be greater than that of the reinforced subgrade.

As per the foundation theory, the influence area of a circular footing expands to a depth of about 1.5D from the bottom of the foundation, where D is the diameter of the circular footing. If the modified CBR test setup is considered similar to a circular footing with a diameter of 61 mm, the influence zone will be 91 mm from the granular surface. Having the geogrid outside the influence zone will not make any contribution for the subgrade improvement. This could again be aligned with the recommendation made by Mousavi et al (2017) to include the geogrid layer at the upper 1/3 of the granular layer for higher granular layer thicknesses. Considering the 200mm granular cover section, which the unreinforced exhibits higher bearing capacity than reinforced, the maximum thickness of the stiff layer could be approximated as 100 mm assuming the influence zone is the upper section of the granular layer.

Comparing the load-deformation results of both reinforced and unreinforced sections with subgrade only condition, it can also be seen that it is not only the geogrid that directly contribute to the weak subgrade improvement but also the granular cover as well. For instance, both reinforced and unreinforced section configurations with 150mm granular cover demonstrated a significantly higher bearing capacity (Fig 5) compared to the subgrade only condition even though the reinforced section configuration recorded the highest among them. Hence, it is understood that when reinforcing the weak subgrade, it is not only the geogrid that contributes to the increment of the bearing capacity but also a significant contribution will be given by the granular layer on top of the geogrid. Also, this indicates that the behaviour of composite layer, which includes reinforcement and gravel, is both reinforced and gravel layer, should be considered in understanding the behaviour of geogrid reinforcement rather explicitly considering the geogrid and granular layer.

In order to assess the weak subgrade improvement due to the geogrid, the reinforcement ratio was calculated by using equation 1. Figure 6 shows the calculated reinforcement ratios for each section configurations, which provides an idea of the contribution from the geogrid reinforcement for weak subgrade improvement. The reinforcement ratio above 1 represents that the geogrid has extended a positive contribution in sections with 50mm and 150mm granular cover thicknesses in increasing the bearing capacity. However, the opposite behavior has been observed for 200mm granular section. The reinforcement ratio below 1 demonstrates that the unreinforced section is better than geogrid reinforced section in terms of bearing capacity.

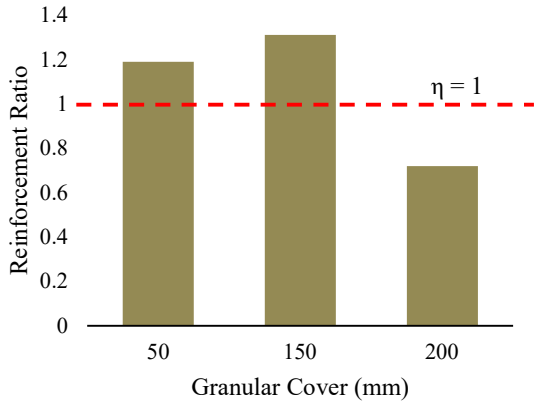

Figure 6: Reinforcement ratio of section configurations

The authors are planning to conduct a similar series of tests in a 1m x 1m x 1.4 model box using 200 mm diamater loading area to minimise the boundary effects and limitations of this modified CBR mould testing.

5 CONCLUSIONS

This study performed a series of monotonic loading tests on subgrades modeled in a modified CBR mould to assess the bearing capacity improvement of a weak subgrade stabilised with a geogrid and a gravel layer. The following conclusions can be drawn from the results:

• The bearing capacity of the stabilised subgrade increases with the increase in the thickness of granular cover over the weak subgrade irrespective of the use of a geogrid at the interface.

• The thickness of the stiff layer created by the geogrid interlocking-induced confinement is about 100 mm above the geogrid

To count the benefit of geogrid in the stabilisation of subgrades, it can be recommended to place geogrids at least (D + 100) mm depth below the loading area. Where D is the diameter of the loading area.

ACKNOWLEDGMENTS

This research work is part of a research project (Project No IH18.06.1) sponsored by the SPARC Hub:the Australian Research Council (ARC) Industrial Transformation Research Hub (ITRH) Scheme (Project ID: IH180100010). The financial and in-kind support from Department of Transport and Main Roads (Queensland), Logan City Council, Global Synthetics (Australia), Polyfabrics (Australia) and Queensland University of Technology (QUT) is gratefully acknowledged.

REFERENCES

Abu-Farsakh, M.Y., Gu, J., Voyiadjis, G.Z., and Chen, Q. (2014). Mechanistic–empirical analysis of the results of finite element analysis on flexible pavement with geogrid base reinforcement, International Journal of Pavement Engineering, 15(9):786-798.

Al-Qadi, I.L., Dessouky, S.H., Kwon, J., and Tutumluer, E. (2012). Geogrid-reinforced low-volume flexible pavements: pavement response and geogrid optimal location, Journal of Transportation Engineering, 138(9):1083-1090.

Bergado, D., Youwai, S., Hai, C., and Voottipruex, P. (2001). Interaction of nonwoven needle-punched geotextiles under axisymmetric loading conditions, Geotextiles and Geomembranes, 19(5):299-328.

Clark, B.R., Gallage, C., (2020) Superior performance benefits of multigrade bitumen asphalt with recycled asphalt pavement additive, Construction and Building Materials, 230:116963.

Clark, B. R., Gallage, C., Yeaman, J., (2020). Temperature variation through Deep Multigrade Asphalt Pavements and Proposed Method for Accounting for Fluctuations, Journal of Materials in Civil Engineering, 32(3):04020005.

Duncan-Williams, E., Attoh-Okine, N.O., (2008). Effect of geogrid in granular base strength–An experimental investigation, Construction Building Materials, 22(11):2180-2184.

Ferrotti, G., Canestrari, F., Virgili, A., and Grilli, A. (2011). A strategic laboratory approach for the performance investigation of geogrids in flexible pavements, Construction Building Materials, 25(5):2343-2348.

Gallage, C.P., Gunasekara Jayalath, C., (2019) Use of Particle Image Velocimetry (PIV) technique to measure strains in geogrids, Proceedings of the 7th International Symposium on Deformation Characteristics of Geomaterials, IS-Glasgow 2019, E3S Web of Conferences, Volume 92, p1-6.

Gallage, C., Eom, T., Barker, D., and Ramanujam, J., (2015). Falling Weight Deflectometer (FWD) tests on granular pavement reinforced with geogrids–Case study, ICGE Colombo 2015 Proceedings of the International Conference on Geotechnical Engineering, pp 597-600.

Gallage, C., Tehrani, K., and Williams, D. (2017). Instrumented large soil-column to investigate climate-induced ground deformation in expansive soil, Proceedings of the 19th International Conference on Soil Mechanics and Geotechnical Engineering, Seoul 2017, International Society for Soil Mechanics and Geotechnical Engineering, pp 1147-1150.

Jayakody, S., Gallage, C., Ramanujam, J., (2019). Effects of reclaimed asphalt materials on geotechnical characteristics of recycled concrete aggregates as a pavement material, Road Materials and Pavement Design, 20(4):754-772

Jayakody, S., Gallage, C., Ramanujam, J., (2019) Performance characteristics of recycled concrete aggregates as an unbound pavement material, Heliyon, 9 (5): e02494

Jayalath, C.P.G., Wimalasena, K.D., (2020). Measuring Strains on Geogrid Specimens Under the Laboratory Tensile Test, International Journal of GEOMATE, 18(65):86-93.

Gunasekara Jayalath, C., Gallage, C.P., Dhanasekar, M., Dareeju, B.S., Ramanujam, J.M., Lee, J., (2018). Pavement model tests to investigate the effects of geogrid as subgrade reinforcement, Proceedings of the 12th Australian and New Zealand Young Geotech Professionals Conference, p1-8.

Kodikara, J., Rajeev, P., Chan, D., Gallage, C., (2014). Soil moisture monitoring at the field scale using neutron probe, Canadian Geotechnical Journal, 51(3):332-345.

Koerner, R., (2005). Designing with Geosynthetics, Upper Saddle River, NJ 07458, Pearson Education, Inc.

Leng, J., (2003). Characteristics and behavior of geogrid-reinforced aggregate under cyclic load, Dissertation for the Degree of Doctor of Philosophy, 152 p.

Mousavi, S., Hamed, A., Roy, H., Borden, A., (2017). Optimum location of geogrid reinforcement in unpaved road, Canadian Geotechnical Journal 54 (7):1047-1054.

MTM:Materials Testing Manual (2018). Queensland Departmet of Transport and Main Roads.

MTRS05:Transport and Main Roads Specification for Unbound Pavements(2018). Queensland Departmet of Transport and Main Roads.

Rashid, A. S. A., Latifi, N., Meehan, C. L., Manahiloh, K. N., (2017). Sustainable improvement of tropical residual soil using an environmentally friendly additive, Geotechnical and Geological Engineering, 35(6):2613-2623.

Sharma, R., Chen, Q., Abu-Farsakh, M., Yoon, S., (2009). Analytical modeling of geogrid reinforced soil foundation. Geotextiles and Geomembranes, 27(1):63-72.

Singh, M., Trivedi, A., and Shukla, S. K., (2019). Strength Enhancement of the Subgrade Soil of Unpaved Road with Geosynthetic Reinforcement Layers, Transportation Geotechnics, 19:54-60.

Wimalasena, K., Pradeep, T., and Rengarasu, T., (2019). Suitability of Demolished Concrete Waste in Hot Mix Asphalt Concrete for Local Roads in Sri Lanka, Journal of the Eastern Asia Society for Transportation Studies, 13:1641-1647.

Wimalasena, K., and Jayalath, C.P.G., (2020). Effect of Geogrid Reinforcement in Weak Subgrades, International Journal of GEOMATE, 18(65):140-146.

Zornberg, J., and Gupta, R.(2010) Geosynthetics in pavements: North American contributions, Theme Speaker Lecture, Proceedings of the 9th International Conference on Geosynthetics, Guarujá, Brazil, May, Vol. 1, pp. 379-400.

Evolutionary-Based Prediction of Bearing Capacity of Shallow Footing Based on Soil Classification of Sandy Materials

A. Al Marei, R. Kilani, H. Ahmad & M. Jamal
Arab Center for Engineering Studies, Kingdom of Saudi Arabia

E. Spyropoulos
Saudi Aramco, Kingdom of Saudi Arabia

ABSTRACT: The purpose of this assessment is to find out a correlation between the soil classification of sandy materials and the angle of friction. The correlation is based on existing data considering the influences of the fine content, the particle grain size, and the SPT N values to predict the allowable bearing capacity in a straightforward manner with accuracy. Evolutionary Polynomial Regression (EPR) is utilized to find out the correlation. Statistical analysis indicates that EPR ideal models have a precision running somewhere in the range of 87% and 89%. A parametric report has been done to analyze the response of the EPR ideal models. The results indicate that the developed EPR optimum models are able to correlate the soil classification of sandy materials and the angle of friction with high accuracy. Accordingly, the ERP models can be used in geotechnical designing applications within a parametric range.

1 INTRODUCTION

The allowable bearing capacity of foundations is defined by Sitharam (2018) as "the maximum gross stress intensity to which the soil at the base of foundation can be subjected without risk of shear failure and excessive settlement". Bearing limit perspective is considered essential in geotechnical designing. Several parameters should be considered while deciding the bearing limit of the Sand including unit weight (γ), internal friction angle (φ), and footing size, and depth factors.

A foundation in which the depth of the foundation is equal to or less than the width is known as a shallow foundation. Footings are constructed to transfer the loads from columns into the soil. For a safe design, two conditions should be fulfilled. First, an adequate safety against shear failure. Second, tolerable settlements for the serviceability of structures.

In this survey, EPR is utilized to correlate the soil classification of sandy materials and the angle of friction. The data of angle of friction is collected from direct shear tests and includes 976 tests performed by experienced technicians at a laboratory. The tests are divided into two groups: 80% training and 20% testing for model verification.

2 EVOLUTIONARY POLYNOMIAL REGRESSION (EPR)

EPR was created by Savic and Giustolisi in 2006. From that point forward, EPR has been utilized in numerous geotechnical applications including earthquake and soil liquefaction, modeling soil permeability, modeling concrete degradation, settlement assessment of shallow foundations, and assessment of total sediment load of Malaysian waterways.

According to Javadi et al., (2010), EPR is an information-driven strategy dependent on a new transformative registering procedure, intended to look for polynomial constructions addressing a framework. The general formula of EPR is introduced underneath by Giustolisi and Savic (2006):

$$y = \sum_{j=1}^{m} F\left(X, f(X), a_j\right) + a_o \qquad (1)$$

Where: y is the assessed vector of the yield of the output; m is the number of terms of the objective formula; F is a function developed by the formula; X is the matrix of input variables; f is a function defined by the user; a_j is a constant.

As per Ebrahimian and Nazari (2013), EPR technique comprises of two phases. To start with, distinguishing the principle structure using a genetic algorithm (GA). Second, assessment of the boundaries utilizing least square regression. According to Javadi et al., (2012), the advantages of

utilizing the GA are easier execution of the algorithm and producing explicit expressions. EPR has the best features of conventional regression techniques with symbolic regression and with genetic programming as per Shahnazari et al. (2013). EPR is a powerful program that can be assessed utilizing few constants, develop automatic models, and perform linear and nonlinear analysis says Shahnazari et al. (2013). Figure 1 beneath shows the stream chart of the EPR strategy.

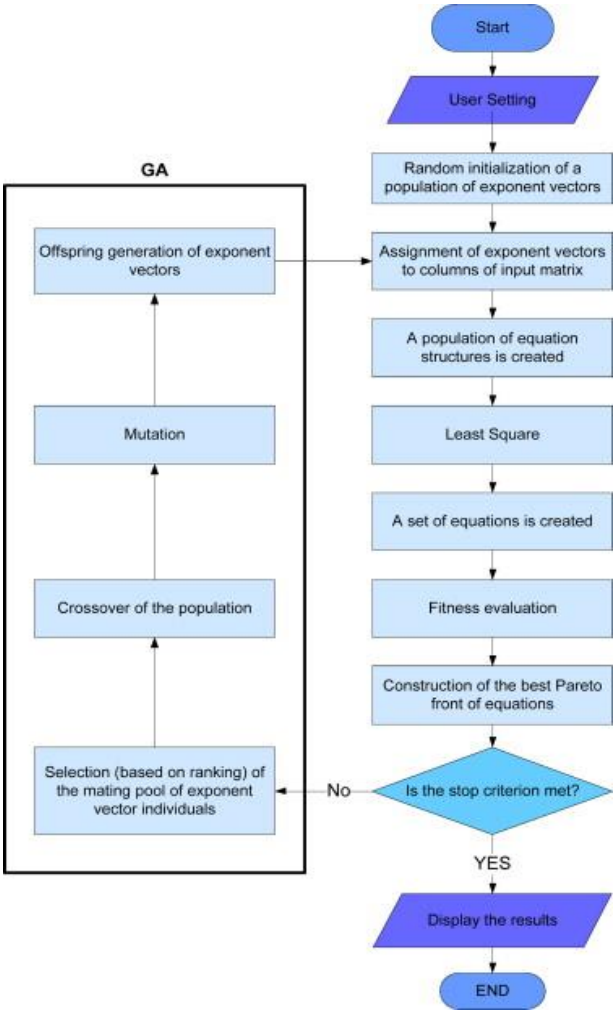

Fig.1 Flow diagram for EPR procedure by Alani and Faramarzi (2014)

3 CORRELATING SOIL CLASSIFICATION OF SANDY MATERIAL WITH FRICTION ANGLE

3.1 *Database*

The angle of friction values is obtained from the direct shear tests and include 976 laboratory tests performed by experienced technicians at a laboratory. The testing was done based on the soil classification of sandy material, listed in Table 1.

Table 1. Database details

Location	SM	SP	SP-SM	SW	SW-SM	Total
1	15	5	2	11	17	50
2	1	0	0	2	1	4
3	8	0	0	19	17	44
4	23	0	18	16	16	73
5	37	0	31	2	20	90
6	7	4	27	12	7	57
7	1	301	58	22	33	415
8	26	3	11	31	25	96
9	13	0	18	5	0	36
10	28	9	17	0	0	54
11	23	0	26	0	8	57
Total	182	322	208	120	144	976

3.2 *Model inputs and outputs*

The most effective and important parameters should be chosen as inputs to increase the accuracy of the models. According to previous studies, the main parameters used to predict friction angle are the influences of fine content, the particle grain size, and the SPT N values. The output parameter is the angle of friction (Ø). Table 2 list the range of parameters used in this study.

3.3 *Data division*

The available data are divided into a training set to generate the model and a testing set to examine the performance of the model. According to Javadi et al (2006) and Rezania and Javadi (2007), the performance of the model is significantly influenced by the way the data is divided. Table 2 list the statistical properties of the training and testing sets. In this study, 781 case histories (80% of the data) have been used for training and 195 case histories (20% of the data) have been used for testing. The two sets have been chosen in a way that they have the same statistical population by making the statistical parameters for both sets close to each other using the iteration process. The statistical parameters are mean, standard deviation, maximum and minimum. The main reason for performing a statistical analysis is to achieve a robust representation of the whole population for both sets, says Rezania et al. (2011). In the testing set, interpolation is performed to obtain friction angle.

If the values of parameters (inputs) are outside the range of the training set, the model will extrapolate to obtain friction angle as per Ahangar-Asr et al. (2012). Thus, the training set shall include the minimum and maximum values of each parameter.

Table 2. Statistical Parameters of Data used for prediction

Soil Type	Parameters	Range	Data Sets	Statistical Parameters Max	Min	Mean	σ
SM	Fine (%)	12.0-49.4	Training	49.4	12.0	22.8	8.4
			Testing	49.4	12.7	21.9	8.5
	SPT N Value	1-100	Training	100	1	36.9	27.0
			Testing	100	1	39.2	26.9
	Ø (deg)	18.6-41.0	Training	41.0	18.6	32.9	6.3
			Testing	41.0	18.9	33.6	6.2
SP-SM	Fine (%)	5.0-12.0	Training	12.0	5.0	7.9	2.0
			Testing	11.7	5.0	8.3	2.1
	SPT N Value	95-100	Training	100	3.0	35.0	24.0
			Testing	95.0	8.3	34.7	22.6
	Ø (deg)	22.7-42.0	Training	42.0	22.7	34.0	4.6
			Testing	41.0	26.0	34.1	4.4
SP	Fine (%)	0.0-5.0	Training	5.0	0.0	2.7	1.1
			Testing	5.0	0.0	2.7	1.3
	SPT N Value	3.0-95.0	Training	95.0	3.0	43.2	26.8
			Testing	95.0	5.0	42.4	25.7
	Ø (deg)	25.0-44.0	Training	44.0	25.0	37.6	4.8
			Testing	44.0	26.0	37.6	4.8
SW-SM	Fine (%)	5.0-12.0	Training	12	5	7.8	2.0
			Testing	12	5	8.2	2.1
	SPT N Value	1.0-95.0	Training	95.0	1	34.5	24.2
			Testing	95.0	2	34.3	22.4
	Ø (deg)	23.9-46.1	Training	46.1	23.9	37.5	5.3
			Testing	45.0	25.5	37.4	5.2
SW	Fine (%)	0.0-5.0	Training	5.0	0.0	2.9	1.2
			Testing	5.0	0.7	3.2	1.1
	SPT N Value	2.0-95.0	Training	95.0	2	31	21.1
			Testing	95.0	8	30	19.6
	Ø (deg)	26.0-45.6	Training	45.6	26.0	37.6	4.5
			Testing	44.0	30.9	37.5	4.1

3.4 *EPR procedure*

EPR parameters ought to be chosen to come up with the model. The main parameters in the EPR are the number of terms, polynomial structure, number of generations, regression type, function type, constant estimation method, and range of exponents. The EPR technique has been performed through cycle measure, in which the parameters have been exposed to changes until the ideal model is achieved. Table 3 list the parameters that are utilized to create the EPR ideal models.

Table 3. Parameters used to develop EPR models

Parameter	EPR setting
Regression type	Statistical
Polynomial structure	$Y = sum(a_i * X_1 * X_2 * f(X_1) * f(X_2)) + a_0$
Function type	No Function
Term	[1:5]
Range of exponents	[0 .5 2]
Generation	10
Constant estimation method	Least Square

3.5 *EPR optimum model*

The accuracy and simplicity of the models were taken into consideration during the iteration process. EPR optimum models are listed below and they are applicable for the ranges shown in Table 4.

Table 4. EPR Optimum Models

Serial Number	Soil Classification	EPR Model
1	SM	$\emptyset = 19.1465 + 2.461 * N60^{0.5}$ (2)
2	SP-SM	$\emptyset = 21.4276 + 2.2525 * N60^{0.5}$ (3)
3	SP	$\emptyset = 24.0099 + 2.169 * N60^{0.5}$ (4)
4	SW-SM	$\emptyset = 24.1767 + 2.4219 * N60^{0.5}$ (5)
5	SW	$\emptyset = 25.0406 + 2.3869 * N60^{0.5}$ (6)

Where Ø is the angle of friction (degree), and N60 is the standard penetration number for 60% energy ratio. To evaluate the EPR ideal models, a statistical analysis, and a parametric report is performed.

4 RESULTS AND DISCUSSIONS

4.1 *Predicted net allowable bearing capacity*

Table 5. Predicted Net Allowable Bearing Capacity (KPa)

Soil Type	B (m)	Very Loose N_f 4	Loose N_f 10	Medium Dense N_f 20	Medium Dense N_f 30	Dense N_f 40	Dense N_f 50
SM	1	50	75	120	165	225	290
	2	65	100	140	205	270	330
	3	45	70	95	135	180	220
	4	35	55	70	100	135	165
	5	25	40	55	80	105	130

Soil Type	B (m)	Very Loose N_f 4	Loose N_f 10	Medium Dense N_f 20	Medium Dense N_f 30	Dense N_f 40	Dense N_f 50
	1	65	95	145	200	265	335
	2	90	130	175	260	350	440
SP-SM	3	65	100	115	175	235	295
	4	50	75	85	130	175	220
	5	40	60	70	105	140	175
	1	95	135	200	275	360	455
	2	115	175	190	290	395	495
SP	3	75	115	125	195	260	330
	4	55	85	95	145	195	245
	5	45	70	75	115	155	195
	1	105	150	240	340	455	600
	2	130	200	205	320	435	550
SW-SM	3	85	130	135	210	290	365
	4	65	100	100	160	215	275
	5	50	80	80	125	170	220
	1	115	170	265	375	505	665
	2	145	220	220	350	475	605
SW	3	95	145	145	230	315	400
	4	70	110	110	175	235	300
	5	55	85	85	140	190	240

Notes and Assumptions:

- Hammer efficiency is assumed to be 60%.
- Footing is assumed to be 1m deep and overburden pressure assumed to be 17 KN/m^2
- Unit weight (ASCE 1996) $=13.503+0.2769*N_{60}+0.0023*N_{60}^2$
- N_q (Terzaghi)= $Tan^2 [45+Ø/2]*e^{(\pi*tanØ)}$.
- Nγ (Vesic)= $2*[N_q+1]*tanØ$.
- Shear Failure (Terzaghi)= 1/F $[q*N_q+0.4*\gamma'*B*N_\gamma]-\gamma'*D$.
- The factor of safety is 3.
- Modulus of elasticity if N<15 (Begemann 1974) is $100*C*(N_{60}+6)$.
- Modulus of elasticity if N>15 (Begemann 1974) is 4000+100C(N60-6).
- The selected C values are 5 for SM, 7 for SP-SM, 8 for SP, 9 for SW-SM, and 10 for SW.
- Elastic Settlement= $q_{all}*B*(1-0.33^2)*I/Es$.
- The allowable settlement is assumed to be 25mm.
- The water level is assumed to be at a deep depth and hence there is no water effect on the bearing capacity.
- For submerged or saturated conditions, half the NABC shall be considered.

4.2 *Statistical Analysis*

Statistical analysis has been done to evaluate the performance and robustness of the EPR models. The numerical definition of each statistical basis is illustrated.

Coefficient of determination (R^2)

$$\frac{\sum_N(X_m)^2-\sum_N(X_m-X_p)^2}{\sum_N(X_m)^2} \quad (7)$$

Root mean square error (RMSE)

$$\sqrt{\frac{\sum_N(X_m-X_p)^2}{N}} \quad (8)$$

Mean absolute error (MAE)

$$\frac{\sum_N|X_m-X_p|}{N} \quad (9)$$

Where N is the number of case histories and X_p and X_m are the predicted and the measured values of angle of friction, respectively.

Coefficient of determination (R^2) is utilized to estimate the overall correlation between the predicted and measured angle of friction, says Ebrahimian and Nazari (2013). It estimates the accuracy of the predicted angle of friction values in relation to the measured angle of friction values. Results show that R^2 estimates of the EPR ideal models range somewhere in the range of 87% and 89%. This level of precision is a clear sign that EPR is effectively able to predict the angle of friction. The second statistical criterion is Root Mean Square Error (RMSE) which is utilized to estimate errors, more weight is given to large errors, says Ebrahimian and Nazari (2013). RMSE ranges between 0.4 degrees and 1.13 degrees for the EPR models, which demonstrates that no huge errors have been captured. Lastly, mean Absolute Error (MAE) is utilized to predict small errors and the average difference between measured and predicted

Ø. Results show that the MAE of the EPR ideal models ranges between 1.1 degrees and 1.55 degrees. It tends to be seen from RMSE and MAE that the variety of errors is little. Based on the predicted to measured ratio and statistical criteria of testing sets, the EPR optimum models are accurate and capable to predict unseen cases, verifying the presupposition of the paper.

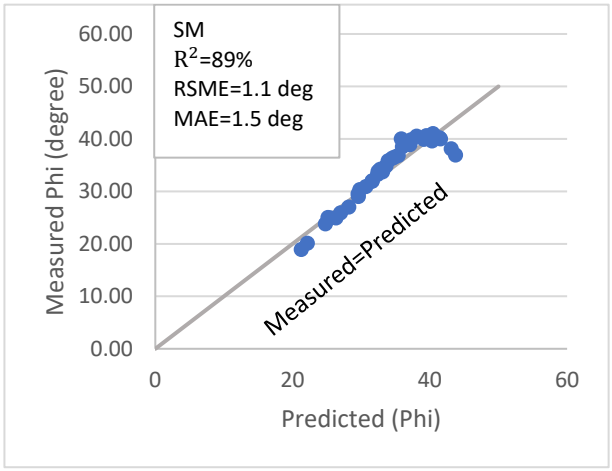

Figure 2. Measured versus predicted Ø values for the EPR model of SM

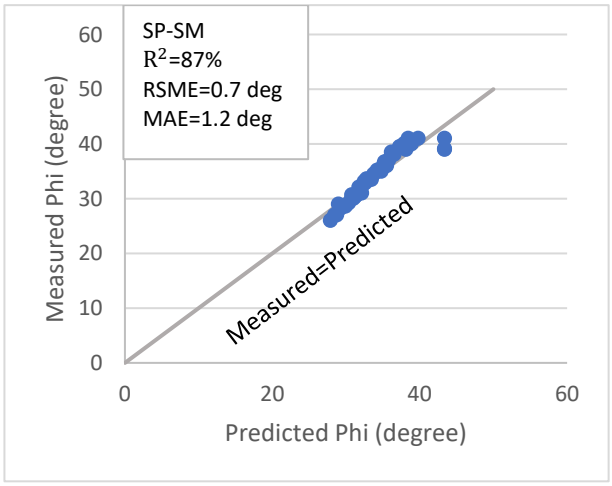

Figure 3. Measured versus predicted Ø values for the EPR model of SP-SM

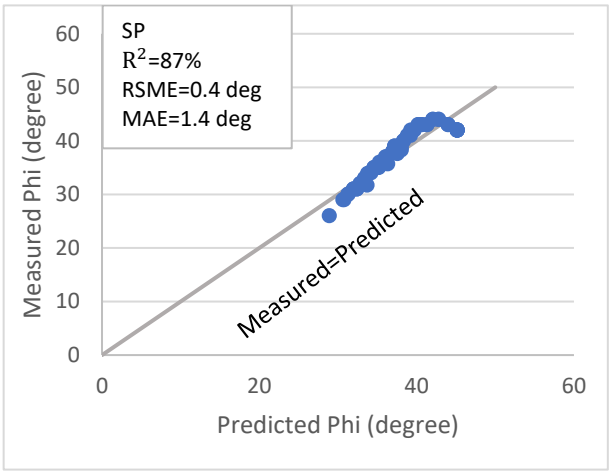

Figure 4. Measured versus predicted Ø values for the EPR model of SP

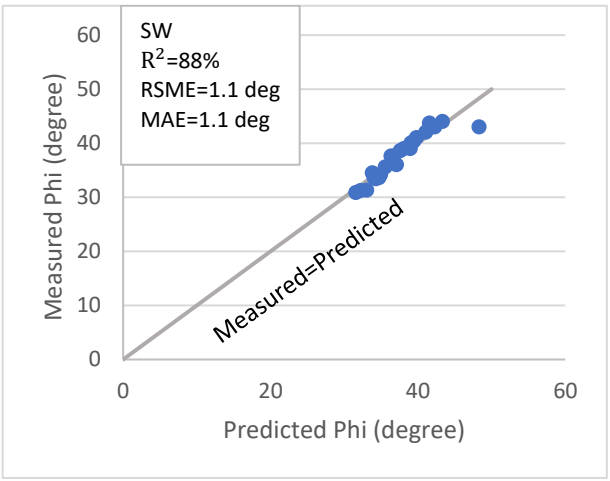

Figure 5. Measured versus predicted Ø values for the EPR model of SW

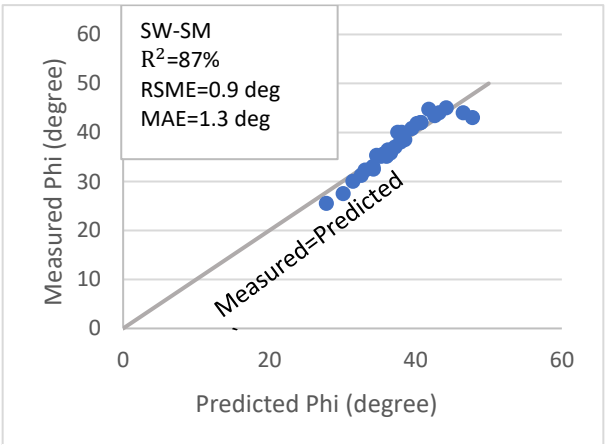

Figure 6. Measured versus predicted Ø values for the EPR model of SW-SM

The measured versus anticipated Ø and upsides of R^2, RMSE, and MAE for testing sets are illustrated from Figure 2 to Figure 6. The 45° line addresses the case wherein predicted values are equal to the measured values. The results show that predicted to measured values are satisfactory and that the EPR

models can accurately predict the angle of friction values. Moreover, the maximum measured angle of friction is 48 degrees which are aligned with Bowel's estimates that the maximum angle of friction is less than 50 degrees.

4.3 *Parametric Study*

A parametric study has been carried out to verify the response and robustness of the EPR ideal models. The parametric study is capable to confirm whether the response of the EPR models matches the conventional methods. The study has been conducted by increasing the SPT N values to measure their influence on the angle of friction. The study confirms that EPR models can capture the underlying physical meaning of friction angle.

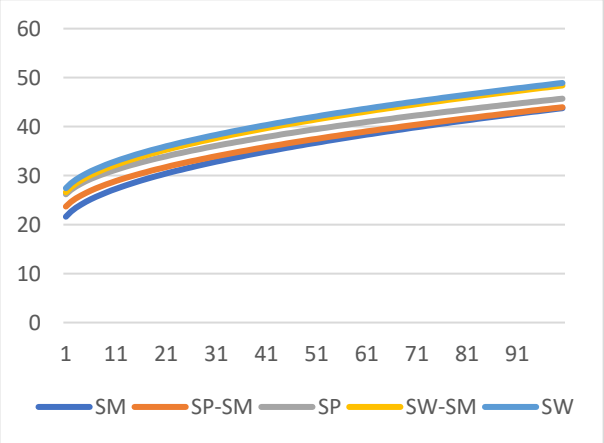

Figure 7: Parametric Study for the Optimum EPR Models

The figure 7 presents the results of the parametric study based on the soil classification of the Sandy materials. The study confirms the ability of the EPR models to capture the underlying physical meaning of friction angle.

5 CONCLUSION

Evolutionary Polynomial Regression (EPR) is utilized to correlate soil classification of sandy material and angle of friction. The data for the prediction of the angle of friction is collected from the direct shear tests at a laboratory and includes 976 tests performed by experienced technicians. The data is divided into 80% training for modeling and 20% testing for model verification. Statistical analysis has been carried out to inspect the accuracy of the EPR ideal models. Furthermore, a parametric report has been carried out to assess the response of the EPR ideal models. Based on the angle of friction equations obtained from the ERP, a predicted net allowable bearing capacity was estimated for soil classification of sandy material.

Statistical analysis confirms the accuracy of the EPR ideal models ($R^2 = 87\% - 89\%$). The parametric study confirms the ability of the EPR models to capture the friction angle physical meaning. In conclusion, the EPR ideal models can predict the friction angle based on the sandy material classification. Hence, the EPR ideal models can be used in geotechnical applications within the parametric ranges listed in Table 2.

REFERENCES

Ahangar-Asr, A., Johari, A., and Javadi, A.A. (2012). An evolutionary approach to modelling the soil–water characteristic curve in unsaturated soils. *Computers & Geosciences*, 43 (1), PP. 25-33.

Alani, Amir M., and Faramarzi, A. (2014). An evolutionary approach to modelling concrete degradation due to sulphuric acid attack. *Applied Soft Computing*, 24 (1), PP. 985-993.

Ebrahimian, B., and Nazari, A. (2013). Evolutionary-based prediction of ε50 for the lateral load- displacement behavior of piles in clay. *Acta Geotechnica Slovenica*, 10 (2), PP. 43-56.

Giustolisi, O., and Savic, D. (2006). A symbolic data-driven technique based on evolutionary polynomial regression. *Journal of Hydroinformatics*, 8 (3), PP. 207-222.

Javadi, A. A., Ahangar-Asr, A., Faramarzi, A., and Mottaghifard, N. (2012). An EPR approach to the modeling of civil and geotechnical engineering systems. *Metaheuristics in Water*, Geotechnical and Transport Engineering, 13 (1), PP.311-326.

Javadi, A.A., Faramarzi, A., Ahangar-Asr, A., and Mehravar, M. (2010). Finite element analysis of three dimensional shallow foundation using artificial intelligence based constitutive model. *Proceedings of the International Conference on Computing in Civil and Building Engineering*, 30 (1), PP. 421-426.

Javadi, A.A., Rezania, M., and Mousavi Nezhad, M. (2006). Evaluation of liquefaction induced lateral displacements using genetic programming. *Computers and Geotechnics*, 33 (4-5), pp. 222–233

Marei, A.Y. (2015) "An Evolutionary-Based Approach for Prediction of Ultimate Bearing Capacity of Shallow Foundations on Cohesionless Soils," MSc thesis, Department of Civil Engineering, University of Birmingham.

Rezania, M., and Javadi, A.A. (2007). A new genetic programming model for predicting settlement of shallow foundations. *Canadian Geotechnical Journal*, 44 (12), pp. 1462–1473.

Rezania, M., Faramarzi, A., and Javadi, A. (2011). An evolutionary based approach for assessment of earthquake-induced soil liquefaction and lateral displacement. *Engineering Application of Artificial Intelligence*, 24 (1), PP. 142-153.

Shahnazari, H., Shahin, M., and Tutunchian, M. (2013). Evolutionary-based approaches for settlement prediction of shallow foundations on cohesionless soils. *International Journal of Civil Engineering*, 12 (1), PP. 55-64.

Sitharam, T. G. (2018). Advanced foundation engineering. Boca Raton: Taylor & Francis, a CRC title, part of the Taylor & Francis imprint, a member of the Taylor & Francis Group, the academic division of T&F Informa, plc.

Correlations & Nomograph among index properties, compaction parameters, and particle size distribution of Sri Lankan Sandy Soil.

Shaluka Wijesiri
IESL College of Engineering, Sri Lanka

M.D.J.P.Wickramasooriya
Irrigation Department, Sri Lanka

ABSTRACT:
Correlations are described as statistical measures that indicates the extent to which two or more variables fluctuate together. Regression analysis is a powerful statistical method that allows to examine the correlation between two or more variables of interest. A nomograph is a two-dimensional, pictorial representation of a mathematical relationship. This relationship incorporates three or more variables which are functionally describable. A nomograph, utilizing collinear concepts, connects scales depicting these variables with straight lines which enable a value of the dependent variable to be determined for selected values of the independent variables This study mainly focuses on developing the new correlations and developing a nomograph to estimate compaction parameters of sandy soil in Sri Lanka. Correlations were developed among optimum moisture content, plasticity index, and maximum dry density using the test results from different laboratories in Sri Lanka. Laboratory tests were performed to verify the obtained correlations. A Nomograph was developed to estimate optimum moisture content by using particle size analysis and plastic limit test results.

1 INTRODUCTION

1.1 *Background*

Geotechnical engineering has grown rapidly in the recent century with the contribution from academics, researchers and practicing professionals. In situ and laboratory geotechnical testing still, remain as the two preferred methods of determining design parameters.

Soil Investigation through borehole drilling and sampling offers the most dependable value of the relevant soil properties for the purpose of geotechnical design, however it is laborious, expensive and invasive. Therefore, an alternate quick and less destructive of assessing soil properties is very crucial to enable quick and widespread measurements and calculation of ground engineering design at different conditions of soil, which is an essential factor in the predicting soil parameters. As a solution, the correlations and nomograph obtained through this research can be used to save time by reducing the different types of tests that have to be performed.

This research mainly consists of three parts.

1. Obtaining data from laboratories, analyzing the data and studying the correlation among Compaction parameters, index properties and particle size distribution for Sandy clay in Sri Lanka.
2. Performing laboratory tests to verify the equations obtained in the analysis and studying the correlation among Compaction parameters and Index properties for the test results.
3. Development of a model nomograph for an equation from the results.

1.2 *Problem statement*

When the site has less facilities and equipment to perform tests, not enough qualified technicians and suitable laboratories are the major drawbacks for soil testing in the site. As a remedial action for this situation, the relationships between soil parameters for sandy soil, will be studied from this research.

Determination of Compaction parameters by Index properties and particle size distribution is the main priority of this research. Proctor compaction test is used to determine the compaction parameters. Predicting compaction parameters from particle size distribution parameters and index properties, is a convenient method because the proctor compaction test is time consuming and requires a considerable labor. Instead compaction parameters can be predicted using the results of the tests performed in the soil classification stage.

Thus, Studying and using the correlations between soil parameters is an acceptable way to determine soil parameters. Several attempts have been made in the past to find correlations among index properties and compressibility parameters and strength because of the difficulties to find some of the soil parameters practically.

2 AIMS & OBJECTIVES

In this study, the main objective is to study the interdependency between Compaction parameters and Index properties for Sri Lankan sandy soils. Followings are the specific objectives of this study.

• Derivation of verified correlations between Compaction parameters, index properties and particle size distribution for Sandy clay in Sri Lanka.
• Developing a Nomograph to estimate OMC using Particle Size Distribution (PSD) analysis results and index properties.

It is expensive and time consuming to carry out most of the tests at the construction sites. Thus it is hoped that the outputs of this research will financially benefitted with estimations for the soil parameters considerable accuracy. Further studies can be carried out in future to enhance the accuracy of the results.

3. METHODOLOGY

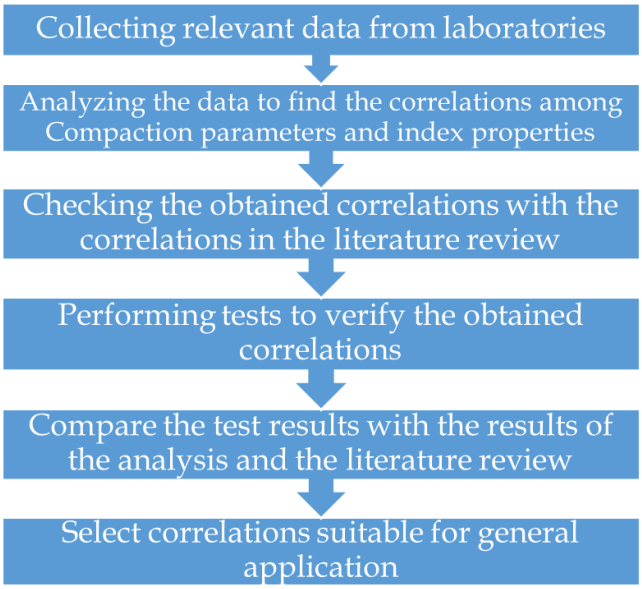

3.1 *Data collection process*

The research is conducted based on soil data obtained from different places in Sri Lanka.

- Project-Kuda oya(Uma oya) Borrow pit investigation
- Project-Mahakitula area
- Project-Kelani North Flood bund
- Project-Kaluganga (Kanthale)
- Project- Kurai reservior
- Rambukkan oya
- Moragahakanda project
- Pulugunawa tank

3.2 *Laboratory Tests*

Based on the samples retrieved from the sites, laboratory tests on the samples that were conducted at Irrigation Department Geotechnical laboratory. Accordingly, the following tests have been performed.
The test standards of obtained data for analysis in this research.

- ASTM D6913 - 04(2009) – Standard Test Methods for Particle-Size Distribution (Gradation) of Soils using Sieve Analysis
- ASTM D7928 – 17- Standard Test Method for Particle-Size Distribution (Gradation) of Fine-Grained Soils using the Sedimentation (Hydrometer) Analysis
- Specific Gravity of soil (ASTM D-854)
- ASTM D-4318 “Standard Test Method for Liquid Limit, Plastic Limit and Plasticity Index
- Standard Proctor Test (ASTM D-698)

3.3 *Linear regression analysis*

Methodology for analyzing in the SPSS application is as following.

- Defining the variables in the application
- Detecting Outliers
- Look for coefficient of correlation value and the statistical significance.
- Obtaining the scatter plot and fitting the trend line
- Obtaining an equation

3.4 Nomograph

Nomograph was developed with FA*, OMC and Index properties. As a calculating aid, Nomographs can solve very complicated formulas with amazing ease. As a curiosity, nomograms provide a satisfying, hands-on application of interesting mathematics.

*FA is defined as the summation of the percentage of particles by weight passing 2mm (No10) sieve and retained in 0.001mm sieve.

4. RESULTS AND DISCUSSION

4.1 *Analysis*

This analysis is in three segments to facilitate review. This analysis is carried out as a comparison between 3 research attempts done to estimate the correlation between Atterberg limits and Compaction parameters.

1. Reference research paper taken from the literature Review-Estimation of soil compaction parameters based on the Atterberg limits (Ksenija Đoković*, Dragoslav Rakić**, Milenko Ljubojev-2013)
2. Analysis of test results of 44 samples of Clayey sand acquired from the Irrigation Department of Sri Lanka. (SPSS Analysis graph.2019)
3. Results of tests performed in the Institute of Engineers Sri Lanka College of Engineering laboratory (IESLCE Laboratory) for the verification of the equations obtained in the analysis

4.2 *Results and Discussion*

4.2.1 Optimum Moisture Content Vs Liquid Limit

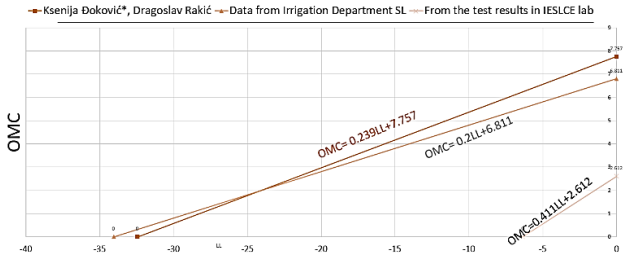

Fig 1 – OMC vs LL

The most similar relationships were found with (Ksenija Đoković*, 2013) graph and the SPSS Analysis Graph, 2019 (Analysis of test results of 44 samples of Clayey sand acquired from the Irrigation Department of Sri Lanka.). Fig 01 indicated a slight different relationship, but with a strong coefficient of correlation (0.987) and high level of significance. And from graphically observing it can be said that the (Verification Graph) has a slightly equal gradient just as the other two graphs. That might be due to many reasons that will be discussed next in the conclusions section. According to the graphical representation above, (Ksenija Đoković*, 2013) have used data with liquid limits ranging from 28 to 71. The (SPSS Analysis Graph, 2019) data showed a range of 23 to 51. The (Verification Graph) data only shows a range of 22 to 28.

4.2.2 Optimum Moisture Content Vs Plastic Limt

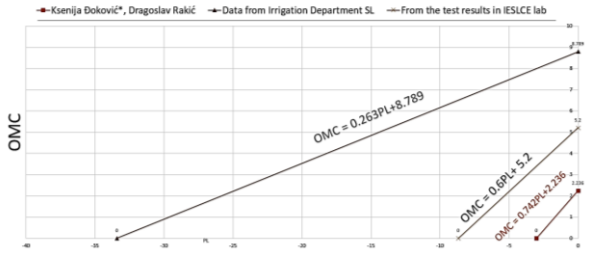

Fig 2 – OMC vs PL

SPSS Analysis Graph, 2019 revealed good coefficient of correlation and a good level of significance of the optimum moisture content and Plastic limit. Fig 02 shows a strong coefficient of correlation and the level of significance is a high value. Visually it can be said that the shape of the graph is almost equal for all 3 graphs. It could therefore be used to estimate the optimum moisture content with a high degree of accuracy. (Ksenija Đoković*, 2013) Used PL data ranging from 17 to 28. The (SPSS Analysis Graph, 2019) data showed a range of 14 to 28. And the data shows a range of 10 to 15. That might also have affected the above deviation

However, Fig 02 and the (SPSS Analysis Graph, 2019) can also be recommended for further research since they show a good coefficient of correlation and a good level of significance.

4.2.3 Optimum Moisture Content Vs Plasticity Index

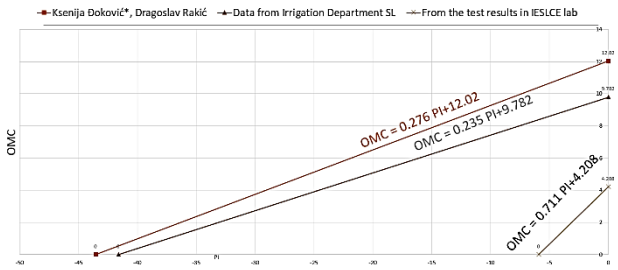

Fig 3 – OMC vs PI

The Plasticity index was found to be strong related to Optimum moisture content with a good level of significance in the Fig 03 And (SPSS Analysis Graph, 2019) and (Ksenija Đoković*, 2013) graph looks to be in almost equal gradients and the shapes of the graphs. (Ksenija Đoković*, 2013) PI data ranges from 11-40. And the (SPSS Analysis Graph, 2019) data range is 12-35. Those ranges are a little bit close so that might have affected the similarity of the two graphs. The correlation coefficients and the level of significance of the developed regression equations indicative of a more linear relationship between the optimum moisture content and plastic limit than in the regression analysis considering all data collectively. So the OMC and the PI correlation should be recommended for discussion in the future.

4.2.4 Maximum Dry Density Vs Liquid Limit

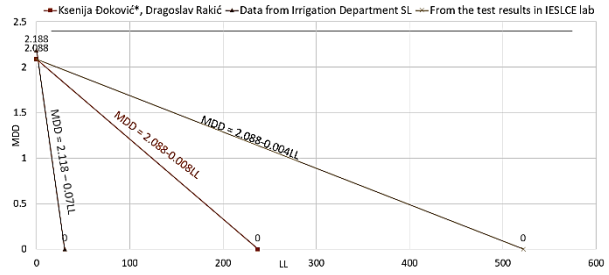

Fig 4 – MDD Vs LL

The graphs of maximum dry density versus the liquid limit considering all 3 research attempts on one ·graph indicated good coefficient of correlation but shows a slight deviation of gradient from one another.

(Ksenija Đoković*, 2013) Used PL data ranging from 17 to 28. The (SPSS Analysis Graph, 2019) data showed a range of 14 to 28. And the Fig 04 data shows a range of 10 to 15. That might also have affected the above deviation

The best coefficient of correlation was with liquid limit, as can be seen by (Ksenija Đoković*, 2013). With a regression value of 0.73 and a good level of significance. The least significant graph was based upon the results of the Fig 04. It has a slightly good regression value but the level of significance is a lower value. The graphs relating the (SPSS Analysis Graph, 2019) data also revealed a strong linear relationship. The strength of the relationship appeared to be slightly better than the graphs utilizing data from all the Fig 04 and has a good level of significance. (P=0). So the Eq (3) can be recommended for further discussion for the general use.

It can be said that the equation from the Irrigation department graph can be used to predict the maximum density with a good accuracy.

4.2.5 Maximum Dry Density Vs Plastic Limit

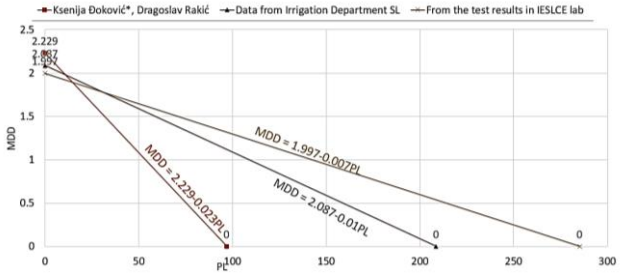

Fig 5 – MDD Vs PL

Again, the most direct relationship for PL with maximum dry density is from the (Ksenija Đoković*, 2013) With a coefficient of correlation of 0.53 and a good level of significance. (SPSS Analysis Graph, 2019) and the Fig 05 data have relatively similar and slightly good coefficient of correlations. But when we look at the level of significance, the Irrigation department graph shows a good significance. (Ksenija Đoković*, 2013) Used PL data ranging from 17 to 28. The Irrigation department data showed a range of 14 to 28. And the Fig 05 data shows a range of 10 to 15. That might also have affected the above deviation.

4.2.6 Maximum Dry Density Vs Plasticity Index

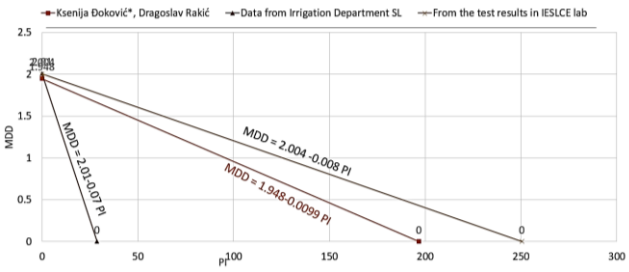

Fig 6 – MDD Vs PI

For the correlation between MDD and PI (Ksenija Đoković*, 2013) graph and the (Verification Graph) seems a little bit similar. (Ksenija Đoković*, 2013) PI data ranges from 11-40. And the (SPSS Analysis Graph, 2019) data range is 12-35. Those ranges are a little bit close so that

might have affected the similarity of the two graphs. But we should keep in mind, the (Ksenija Đoković*, 2013) analysis has used a lot of different types of soil including clayey soil. And the Fig 06 is based upon a very limited number of data and the level of significance is not acceptable. So the graph based upon (SPSS Analysis Graph, 2019) data will be most suitable and should have more attention in putting to use for Sri Lankan soil.

5 CONCLUSION AND FUTURE DEVELOPMENTS

Regression analysis was obtained by statistical models that defined the relationship between the Atterberg limits (liquid limit, the plastic limit, plasticity index) and soil compaction parameters (maximum dry density and optimum moisture content). Statistical analysis was carried out using 44 representative samples of clayey sands in Mahakitula, Rambukkan oya, kelaniya and few other areas.

The results of the regression analysis are,

1) OMC = 0.2 LL + 6.811 (R^2=0.658, p= 0 < 0.05)
2) OMC = 0.263PL+8.789 (R^2=0.429, p= 0.004 < 0.05)
3) OMC = 0.235 PI+9.782 (R^2=0.587, p= 0 <0.05)
4) MDD = 2.118 – 0.07LL (R^2=0.578, p= 0 < 0.05)
5) MDD = 2.087-0.01PL (R^2=0.419, p= 0.005)
6) MDD = 2.01-0.07 PI (R^2=0.488, p= 0.01 < 0.05)

- The results of the tests performed to verify the results of the regression analysis are as follows.
  1) OMC=0.411LL+2.612 (R^2=0.987, p= 0.004 < 0.05)
  2) OMC = 0.6PL+ 5.2 (R^2=0.869, p= 0.05 < 0.05)
  3) OMC = 0.711 PI+4.208 (R^2=0.869, p=0.05 < 0.05)
  4) MDD = 2.088-0.004LL (R^2=0.469, p = 0.426 > 0.05)
  5) MDD = 1.997-0.007PL (R^2=0.425, p= 0.476 > 0.05)
  6) MDD = 2.004 -0.008 PI (R^2=0.408, p= 0.476 > 0.05)

- To be considered successful in a regression analysis, the coefficient of correlation should be at least over 0.5 and the level of significance should be less than 0.05. Thus following equations can be considered successful in regression analysis. Here, the equations were selected from the regression analysis that used 44 data samples because it is highly reliable.

  1) OMC = 0.2 LL + 6.811 (R^2=0.658, p= 0 < 0.05)
     - The range of data selected for LL value is 23-51. Thus this equation would show a high accuracy for this range.
  2) OMC = 0.235 PI+9.782 (R2=0.587, p= 0 <0.05)
     - The range of data selected for PI value is 12-35. Thus this equation would show a high accuracy for this range.
  3) MDD = 2.118 – 0.07LL (R^2=0.578, p= 0 < 0.05)
     - The range of data selected for LL value is 23-51. Thus this equation would show a high accuracy for this range.

- It must be emphasized that use of the equations developed in this study should be limited to clayey sands of consideration for which they were developed, and only then after the validity of the equations has been established through check procedures.
- To index properties. It appears that considerably better correlation can be achieved by limiting the soil categories used for this study. It is therefore concluded that future efforts to find the correlations should be concentrated on the soils of the individual soil groups. Useful equations and prediction procedures have been developed in this study to achieve the maximum correlation. These equations can be tested furthermore and can be adjusted until sufficiently accurate apply their use in many prediction situations.

- The ranges of index properties seem to be low in both Analysis data and verification data. If the data samples were selected with a wide range of index properties, the results would be closer to the actual value.
- The number of test sessions performed to verify the obtained results was low due to the time scope of this project. Verifying should be done with more number of tests.

6. RECOMMENDATIONS FOR THE NOMOGRAPH

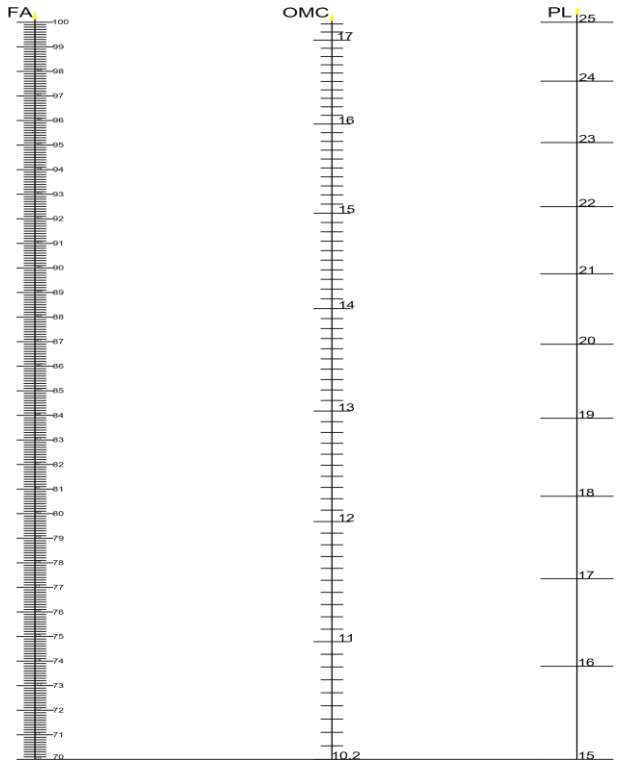

The Nomograph design to determine the Optimum Moisture Content was a successful effort. The Optimum moisture content can be determined with a good accuracy within the given limits. But this nomography design is done in a limited time frame and with a limited number of data. There are a few recommendations to develop this nomograph further.

1. More number of data can be used to improve the accuracy of the nomograph.
2. The FA parameter limits were 70-100 and the Plastic limit limits were 15- 25. With these limitations, the range that shows OMC varies as well. Data can be used with a bigger range. And then the OMC can be calculated within a bigger range at the given accuracy.
3. There are number of complex nomograph types (N-Z Charts, Proportional nomographs, Concurrent-Scale Nomograms, Compound Nomographs etc). Some of nomographs with a higher accuracy need a lot of time designing. This nomograph is designed with a limited time. This parallel scale nomograph can be converted into a more accurate nomograph in the future.
4. This nomograph will be accurate only for sandy soil. If we use more number of data of different number of soils, a nomograph for the universal soil can be designed.

7. REFERENCES

Marvin Tartt Harris -A study of the correlation potential of the optimum moisture content, maximum dry density, and consolidated drained shear strength of plastic fine grained soils with index properties- -1969

NG K.S.*, Chew Y.M., Osman M.H., Mohamad Ghazali S.K.-Estimating maximum dry density and optimum moisture content of compacted soils

Tesfamichael Tsegaye, Dr.Henok Fikre, Tadesse Abebe- Correlation Between Compaction Characteristics and Atterberg Limits of Fine Grained Soil found in Addis Ababa

Sridharan and H. B. agaraj- Plastic limit and compaction characteristics of fine grained soils

I.I.I. Inan, W.K. Mampearachchi and P.A.S. Udayanga-2016- Effect of Fine Percentage on the Properties of Sub-base Material

Ksenija Đoković*, Dragoslav Rakić**, Milenko Ljubojev-2013- Estimation of soil compaction parameters Based on the Atterberg limits

Engineering Properties of Soils in Sri Lanka

Eng. (Mrs) B.B. Mayadunna
Department of irrigation, Sri Lanka

Dr. Eng. (Mrs) M.A. Pallewatta
Department of irrigation, Sri Lanka

Eng. S. Kokularamanan
Department of irrigation, Sri Lanka

ABSTRACT: Engineering properties of soils are important in geotechnical designs. In Sri Lanka, numerous soil investigations have carried out for various foundation and other geotechnical designs by different organizations. Geotechnical investigations always involve with high cost and considerable amount of time. Therefore, a necessity has identified to develop a common source of detailed soil properties that would match the local conditions to address this current issue and to facilitate in preliminary designs as well as quick engineering decision-making. This paper describes a process of adopting an engineering soil map for Sri Lanka with core engineering properties and a local soil classification system to identify the ground condition. In this study, different engineering properties such as consistency limits, particle size analysis, specific gravity, compaction and tri axial properties have considered and nearly 2000 samples were tested relevant to above parameters which were obtained from the Irrigation Department, covering all the regions around Sri Lanka. Finally, Engineering properties of soil of Sri Lanka were mapped with the aid of ArcGIS software through a comprehensive analysis of basic statistical parameters.

1 INTRODUCTION

Stability of civil engineering structures such as buildings, bridges, highways, tunnels, dams, towers, etc. depend on their foundations. Geotechnical properties of foundation soil and soil which are used as construction materials, are very important in analyzing and designing the structures. Determination of engineering properties of soil is carried out using geotechnical or soil investigations, which consume extensive amount of time, money and many resources such as labors, machinery and equipment. Hence, the preliminary geotechnical designs were always very difficult due to lack of details. Therefore, in this study, analysis of spatial distribution of existing ground condition and correlations of soil properties, were carried out for the soil records already available at Irrigation department, Sri Lanka. Finally, engineering soil property map for existing ground condition and summaries of the results with mean and standard deviations were generated with this paper as it can be utilized for preliminary geotechnical designs.

1.1 *Engineering Properties of Soils*

Different engineering properties of soil have different influences on the civil engineering structures. Particle size analysis of soil is important to identify the distribution of particles of different sizes in the soil mass and it provides an idea regarding the gradation of the soil. Soil particles coarser than 75 µm is determined by sieve analysis whereas less than 75 µm are determined by hydrometer analysis. This parameter help in designing of filters for earth dams and determining suitability of soil for different constructions such as roads, airfield, levee, dam, and other embankment construction (Roy & Bhalla , 2017).

Plasticity limit and liquid limit are important to understand the consistency or plasticity of fine-grained soils. Soil behaves as solid with low moisture and becomes plastic with increasing moisture. Atterberg Limits represent the moisture contents at which a specific soil's behavior changes from solid to plastic (Plastic Limit) and from plastic to liquid (Liquid Limit). This information is used as an indication of settlement or consolidation of soils under load as soil settlement is high at the liquid limit and the opposite is true when soil is near or below the plastic limit (GeoSciences, 2017).

Specific Gravity is an important index property of soils that is closely associated with chemical composition and reflects the history of weathering (Oyediran & Durojaiye, 2011). It gives an idea about

suitability of the soil as a construction material. Higher value of specific gravity gives more strength for roads and foundations (Roy & Bhalla , 2017).

Soil Compaction provides an indication on rearrangement of soil particles by reducing the void ratio (Balasubramanian, 2017). Soil is compacted to improve the shear strength of the material and makes more stable by increasing the maximum dry density, which results in low permeability (Davison & Springman, 2000). Compaction is monitored by the optimum moisture content at which the soils are compacted in the field and the maximum dry density determined by the laboratory proctor compaction test.

The shear strength parameters of soil are defined by cohesion and the friction angle. The shear strength of soil depends on the effective stress, drainage conditions, density of the particles, rate of strain, and direction of the strain (Roy & Bhalla , 2017). The shear strength of a soil is prime important for foundation design, earth and rock fill dam design, highway design, retaining wall designs and backfilling designs as shear strength governs slope equilibrium, load-bearing capability of soils (Roy & Bhalla , 2017). Triaxial test is used to simulate these confining pressures using internal friction angle and cohesion. For short-term stability of foundations, dams and slopes, shear strength parameters for unconsolidated undrained or consolidated undrained conditions are used; while for long-term stability shear parameters corresponding to consolidated drained conditions give more reliable results (Roy & Bhalla , 2017). Considering the interactions among different Engineering properties of soils and their influences on civil engineering structures, this paper discuss the spatial variations of engineering properties of soil in Sri Lanka.

2 MATERIALS AND METHODS

During this study, different engineering properties such as consistency limits, particle size analysis, specific gravity, compaction and tri axial properties were considered. A total of 1905 soil samples collected through soil augering and test pits during the soil investigations which have already tested relevant to above parameters, were obtained from the Irrigation Department, covering all the regions of Sri Lanka.

The methodology used in this study was in three phases. The first stage was, development of study area map in ArcGIS and analyzing spatial distribution of soil types along with subsurface variations, using Microsoft Excel by graphical representation method. 1905 soil samples were scattered among 75 locations in Sri Lanka by covering all the regions. Engineering properties of soils along with the test pit or auger hole number and depths of sampling were considered for this analysis. Data were sorted according to the location and then analyzed the availability of soils. 75% probability was considered in analyzing the availability of soil categories and subsurface variations were plotted to depict the general ground variations of available soil groups separately. Borehole data, recorded through drilling during the sub surface investigations, were collected to analyze the distribution of rock layer of the country. Rock depths were considered of different investigated locations and 3D model was developed to illustrate the variation of rock depths around the country. Inverse Distance Weighted (IDW) interpolation technique was used to generate raster layers from point data. Then ArcScene interface was used to develop 3D model.

The second stage was the analysis of variations of engineering properties of most prominent soil groups among the Districts. As the initial step, materials were basically categorized into the different groups such as fine grained plastic soils (High plastic clay (CH), Low plastic clay (CL), High plastic silt (MH), Low plastic silt (ML), coarse grained plastic and non-plastic soils (Silty sand (SM), Clayey Sand (SC), Silty sand with clay (SM-SC), Silty gravel (GM), Clayey gravel (GC), Well graded gravel with clay (GW-GC), Well graded sand (SW), Poorly graded sand (SP), Well graded sand with silt (SW-SM), Well graded sand with clay (SW-SC), Poorly graded sand with silt (SP-SM)) and fine grained organic soils. Then the data collected locations were grouped Districts wise. Engineering properties; consistency limits, particle size distribution, specific gravity, optimum moisture content, maximum dry density, angle of friction and cohesion were compared in relation to the districts. This detailed analysis and comparisons were done only for the CL, CH, ML, MH, SC, SM and SC-SM soil categories.

Finally, the database creation and analysis of results with soil database introduced by U.S. Bureau of Reclamation were carried out. The consideration was given for statistical summarizing of engineering properties of soils in Sri Lanka. Basic statistical parameters; mean, minimum, maximum, standard deviations and variance of soil properties such as liquid limit, plastic limit, specific gravity, optimum moisture content, maximum dry density, cohesion and angle of friction were calculated for all the categories of soils and results were tabulated. This database was generated by representing all the tested soil samples covering entire country. Then it was compared with the database produced by United States to analyze the variation of soil properties in locally and internationally.

3 RESULTS AND DISCUSSION

3.1 *Spatial Distribution of Soil Types*

Figure 1 shows the spatial distribution of soil investigations carried out and data collected locations for this study.

Graphical representation of soil properties of all the samples collected at a particular location during the investigation is challenging. Therefore, a measure of the soil properties of the representative samples at selected locations were used to illustrate the spatial distribution of soil types among the selected locations and subsurface variations of the soils along the depth.

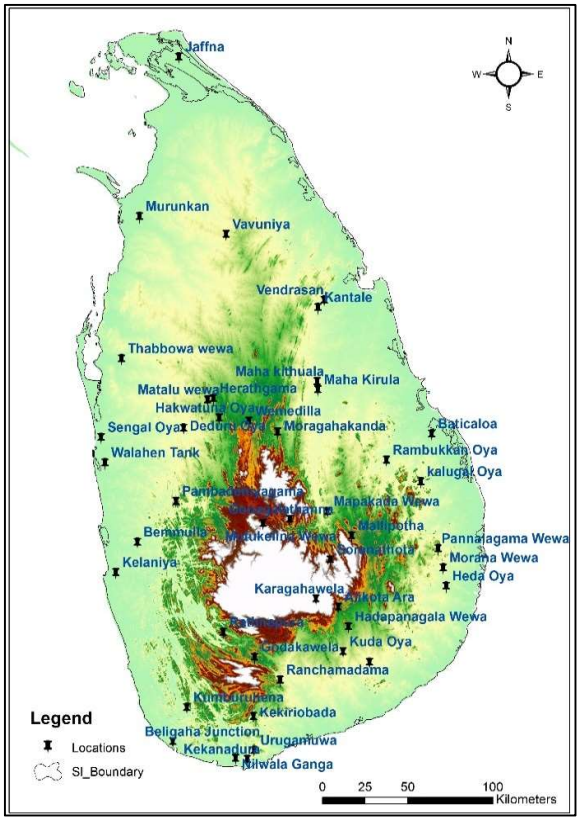

Figure 1: Distribution of data collected locations

Appendix A represents the variation of soil types in each location used to collect data. In some locations, more than one soil type could be identified. This represents only the soil types having more than 75% probability of occurrence and average sub surface variations of soil strata. Irrigation Department is more concerned on Clayey Sand (SC) and Lean Clay (CL) as construction materials. Clayey Sand (SC) is the most prominent soil in all the regions and mostly it expands to a depth below 1 meter. Variation of vertical horizons of SC and CL are tabulated in Table1.

Table 1:Variation of soil profile in Sri Lanka

Soil Type	Max. Depth (m)	Average Depth (m)	Min. Depth (m)
SC	2.15	1.25	0.45
CL	1.85	1.10	0.50

In most cases, soil investigations have to stop due to ground water ingress and appearance of rock or boulders. Above analysis depends on the investigation results. Other than SC and CL, SM and SC-SM could found in Ampara, Anuradhapura, Baticaloa, Gampaha, Kurunegala, Matale, Colombo and Puttalam areas. CH was found at Anuradhapura, Kurunegala and Matale regions.

Borehole details scattered around the country were used to plot the rock profile in 3D (Figure 2) using ArcGIS and ArcScene. With the aid of this map, ground surface elevation and rock depth can be easily identified of a particular location. This is extremely useful for better understanding of overall subsurface conditions over a wide spread area.

3.2 *Spatial Distribution of Engineering Properties of Soil*

Spatial variations of different engineering properties of soil are described under this section (Appendix B). Average specific gravity of selected soil types among the districts are shown in Appendix B, Figure B1. It gives a clear idea about the variation of chemical composition of the same soil type in different districts. By referring to the figure plotted with collected data, it can be observed that specific gravity of SC are comparatively ow in Baticaloa (2.64 g/cm3) and high in Rathnapura 2.69 g/cm3). Variation of specific gravity of clay is ranged from 2.61 g/cm3 at Kurunegala to 2.68 g/cm3 at Badulla.

Spatial distribution of consistency limits illustrate in Figure B2. This is largely influenced by water content of the soil which changes the soil state from semi solid to plastic and then plastic to liquid state. The plasticity index (PI) is defined as the difference between the liquid limit and the plastic limit of a soil and represents the moisture content of the soil, which behaves as a plastic solid. According to the Figure B2, comparatively low value has been observed for Plasticity index of clay in Colombo area (13.5%). This implies that degree of plasticity of clay in Colombo is medium. Figure B2 implies that SC in Galle is high plastic with PI of 27%. SC in Kurunegala and Rathnapura also having high plasticity and SC in other areas are having medium plasticity.

Distribution of particles of different sizes in the soil mass is discussed in Figure B3-B6. There is no

significant Variation of average clay percentage of SC in investigated regions. However, in Kandy and Trincomalee average clay percentage of SC is below 15% where average is 20.33% (Figure B3). Maximum of 24.75% clay in SC was observed in Anuradhapura area. Average clay percentage of CL is varying between 23.75% (Baticaloa) to 40.71% (Trincomalee) with a mean of 32.32%.

Higher silt percentage in soil samples could be observed in both Matara and Baticaloa for both SC and CL and lower silt percentage in SC could observed in Kandy and Polonnaruwa (Figure B4).

Considering the sand percentage of the tested soil samples, no significant variations were observed in both SC and CL (Figure B5).

Gravel percentage in SC is high in Galle (22.50%) and Colombo (15.48%) and average of 4.47% of gravel is available in other regions (Figure B6). Presence of gravel in CL is below 1.75% and in some areas (Baticaloa, Galle, Hambanthota, Jaffna, Kandy, Monaragala and Rathnapura) gravel was not observed at all.

Degree of compaction of soil is determine by maximum dry density and optimum moisture content of soil. More water need to be added in order to get the maximum dry density of soils in Badulla,

Gampaha, Matara and Rathnapura. Soils in Baticaloa, Monaragala, Kurunegala and Ampara reach their maximum dry density with lesser requirement of water. Both SC and CL follow this pattern. With this moisture content effect, there is no significant variation was observed in maximum dry density of soils (Figure B7). 2.03 g/cm^3 of maximum dry density was observed in Kandy while minimum of 1.64 g/cm^3 was observed in Gampaha (Figure B8). Lowest value of 1.52 g/cm^3 of maximum dry density was

recorded from Gampaha area for CL material.1.82 g/cm^3 is the maximum observation made for maximum dry density for the same material in Ampara District.

Figure B9 & B10 illustrate the variation of shear strength parameters. Maximum of average cohesion is observed in Badulla (12.55 kPa) in SC and lower values were obtained in Mannar, Jaffna, Kurunegala, Ampara and Monaragala. For CL highest value was observed at Matale and lowest at Ampara (Figure B9). Internal friction angle of SC is varying from 23^0 to 38^0 at Jaffna and Ampara respectively (Figure B10). Few samples were tested for cohesion and friction angle due to the time constraints.

3.3 *Database for Sri Lankan Soil*

Basic statistical parameters were tested for all the available soil types with tested samples. Summary of the results were tabulated and shown in Appendix C. Eighteen types of soil groups were identified after the laboratory testing. They are: CH, CL, CL-ML, GC, GC-SC, GC-GM, GM, GW-GC, MH, ML, OH, OL, SC, SC-SM, SM, SM-GM, SW-SC and SW-SM.

Irrigation Department is more concerned on SC and CL out of above listed as construction materials and therefore, some soil groups were collected at rarely for the analysis as majority of the test results were related to soil of SC and CL. "N" number of samples clearly emphasize the availability of top soils in Sri Lanka. Higher N value for SC implies that mostly existence top soil strata of Sri Lanka is SC.

Maximum, Minimum, Average, Standard Deviation and Variance of Engineering properties of soil; Liquid Limit, Plastic Limit, Plasticity Index,. Specific Gravity, Optimum Moisture Content, Maximum Dry Density, Cohesion and Friction Angle were analyzed for all the soil groups.

Variations of the parameters except Specific Gravity and Maximum Dry Density is significant within the country. Standard Deviation implies how

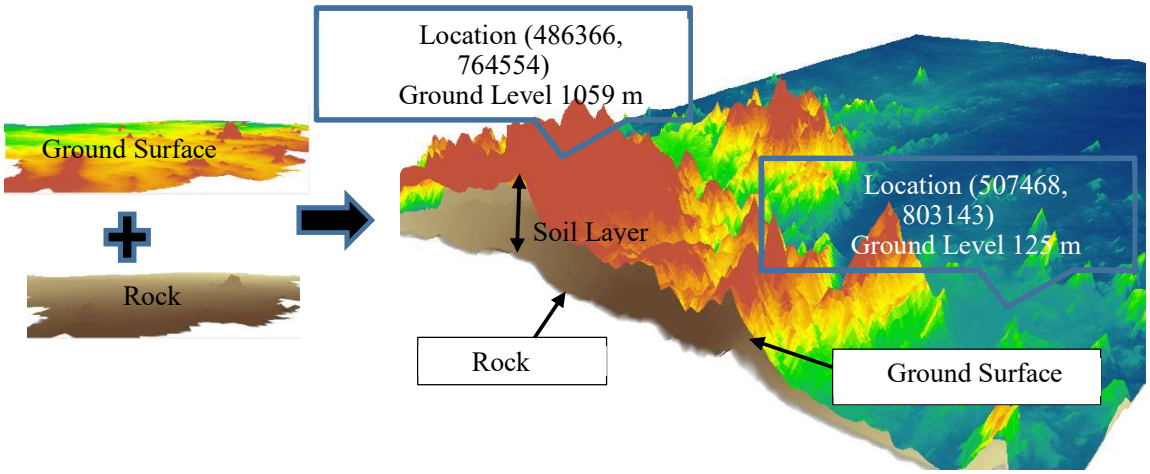

Figure 2: 3D representation of cross section of ground profile in Sri Lanka

far the data scatter from its mean. Higher the variance lower the accuracy of getting average for analysis.
Results were compared with the database produced by United States and following observations were made (Table 2). Specific Gravity of Sri Lankan soils are lower than that of US soils. Max. Dry Density of GC and CH in Sri Lanka is high, compared to US soils and Optimum Moisture Content follows opposite pattern to Max. Dry Density. Variation of values observed for cohesion for SL and US is significant.

Table 2: Comparison of Engineering properties of soils in SL and US

Soil Group	Specific Gravity	Max Dry Density (g/cm^3)	Optimum Moisture Content (%)	Friction Angle (Degrees)	Cohesion (kPa)	
GC	2.73	1.85	14.2			US
	2.69	2.04	10.75			SL
SM	2.68	1.88	12.3	34	20.7	US
	2.65	1.76	16.37	29.61	4.51	SL
SC	2.69	1.91	12.4	32.7	19.3	US
	2.66	1.84	13.84	33.14	8.35	SL
CL	2.7	1.77	16.4	28.1	15.2	US
	2.65	1.71	17.62	25.91	11.53	SL
CH	2.73	1.53	24.8	20.5	32.4	US
	2.63	1.55	22.84			SL

4 CONCLUSIONS

This study described the variation of soil profile in Sri Lanka. It was determined the goal of the study as to create a soil map with a geodatabase organizing the engineering properties of soil.

According to the analysis, it could be observed high variations of engineering properties of a same soil catogory in some locations. Subsurface variations of soil profile in some nearby areas also subject to drastic fluctuation. Therefore, it can be concluded that averaging of parameters with the available data will not be matched the exact local condition as well as US data also does not perfectly match the Sri Lankan pedology.
Consequently, it would be very useful to expand this geodatabase with collaboration of other institutes, doing soil investigations to include more soil investigation details from locations in a grid pattern. The evaluation of geotechnical investigations through SPT reports has enabled further improvements to geotechnical mapping by interpreting shear strength parameters. This would improve the accuracy of the generalized parameters with lower standard deviation.

A 3D representation of soil profile along with the bedrock variation in Sri Lanka will facilitate preliminary geotechnical designs for future projects without performing costly subsurface explorations. It should be emphasized that this study may contribute to implementation of civil engineering projects as it encompasses information regarding spatial distribution of soil properties along with bed rock variations.

ACKNOWLEDGMENTS

The authors wish to present their appreciations upon technical staff in Engineering Materials Division and Geology Division of Irrigation Department. The authors would like to acknowledge the support provided by Eng. Herath, Ms. W.H.S.Madushani, Ms. M.H.M.K.Ranaweera, Ms. K.K.Sandamini and Mr. G.M.S.Perera.

Appendices can be viewed at https://drive.google.com/file/d/1W1QONXG7yKmjo34ttRSqj_3CqtFnqS0Z/view?usp=sharing

REFERENCES

Balasubramanian, A. (2017). *Engineering Properties of Soils.*

Davison, D., & Springman, P. (2000, May). *Soil Mechanics*. Retrieved from University of the West of England: http://environment.uwe.ac.uk/geocal/SoilMech/compaction/compaction.htm

Earth Manual. (1998). Colorado: U.S. Department of the interior, Bureau of Reclamation.

GeoSciences, H. (2017, March 29). *Why should you care about Atterberg Limits?* Retrieved from HWA GeoSciences: https://www.hwageo.com/single-post/2017/03/09/Why-you-should-care-about-Atterberg-Limits

Oyediran, I., & Durojaiye, H. (2011, September). Variability in the Geotechnical properties of some residual clay soils from southwestern Nigeria. *International Journal of Scientific & Engineering Research, 2*(9), 235-239.

Roy, S., & Bhalla , S. K. (2017). Role of Geotechnical Properties of Soil on Civil. *Resources and Environment*, 103-109.

Effect of wet-dry cycles on soil moisture and void ratio of a silty clay

B.M. Shannon & J.K. Kodikara
Department of Civil Engineering, Monash University, Australia

ABSTRACT: Compacted clay soils can become problematic when used under infrastructure such as roads, buildings, landfill caps, etc. and subjected to wet-dry cycles. Environmental wet-dry cycles will tend to change densities and moisture contents and may cause differential soil movements. This paper examines a silty clay soil compacted to three different energy levels. The soil specimens were subjected to wet-dry cycles with large changes water content changes (~3 to 33%). The subsequent soil volume changes were recorded at different intervals along the wet-dry curves (void ratio, ~0.3 to 1). The results showed that after wet-dry cycling the different compaction energy levels shifted to new wet-dry cycle curves, however not enough soil damage or redistribution of grains occurred for all compaction energies to converge to one environmentally stabilized soil wet-dry curve.

1 INTRODUCTION

1.1 *Soil wet-dry cycles*

Soil experiences changes in density and moisture content due to shrinkage and swelling caused by seasonal variations in climate. During periods of wetter months, soil volume increases as higher water contents are held between the clay particles. In summer months the soil shrinks, decreasing the moisture content and hence increasing the density. This seasonal movement can have an effect when infrastructure is placed in the soil medium or on top of the soil medium. This can become a problem if soils are compacted to a dense state and wet-dry cycles cause the associated soil to swell. In the case of external infrastructure, extra stress caused by soil swelling can cause differential movements, causing damage to the surface structure.

Wetting and drying of soil has an influence on many soil properties, such as void ratio, water content, mean stress (Sivakumar *et al.* 2006), compressive/tensile strength (Guérif 1990; Shannon *et al.* 2015), suction, hydraulic conductivity (Benson *et al.* 1999), area of cracking (Yesiller *et al.* 2000), and fracture energy (Costa *et al.* 2013). Therefore, it is important to know what may happen to a soil after compaction.

1.2 *Previous research on soil wet-dry cycles*

Albrecht and Benson (2001) subjected natural clays to wet-dry cycles and found that soils compacted close to optimum water content showed small volumetric strains and soils with low compaction effort shrank the most. Wijesooriya and Kodikara (2012) examined shrinkage and swelling using the wax method (D4943-08 2008) on numerous test specimens to determine wet-dry cycle curves using a destructive method. A stable region of shrink/swelling was present after a sufficient number of wet-dry cycles. Another destructive method of wet-dry cycle testing was conducted by Rayhani *et al.* (2007), where desiccation cracking cycles were examined. Soils with high plasticity were found to exhibit higher hydraulic conductivity after drying. Chen and Ng (2013) found that wet cycles caused irreversible swelling that reduced the preconsolidation stress. Sivakumar *et al.* (2006) varied suction (up to 800 kPa) on wet-dry specimens and the results showed significant hysteresis differences between the wet-dry curves. The MPK method (Kodikara 2012) uses void ratio (e), moisture ratio (wGs – gravimetric water content multiplied by specific gravity) and net stress (p) with the traditional compaction curve.

Most research conducted in the previous papers used destructive methods (removing and damaging specimen) or small wet-dry range to control suctions. Less research has focused on soil movement, soil water content, and soil void ratio a long time after compaction, when soil movement has reached an equilibrium or the soil's natural state.

1.3 *Paper summary*

This paper examines a compacted backfill silty clay soil used under a road and examines the various shrink-swell properties of the clay soil under numerous wet-dry cycles. The data was compared to see whether soil removed from the field after 8 months followed a similar wet-dry cycle curve as what was tested in the laboratory. The idea was to determine if an environmentally stabilized curve, predicted by Kodikara (2012), where soil will tend to shrink or swell towards after numerous wet and dry cycles, could be found for different soil compaction efforts.

2 METHODS

2.1 *Field methodology*

The soil examined was located in Strathfield, Sydney Australia. The soil was a natural silty clay soil backfill used around a pipe buried in the 1920s. The surrounding soil around the pipe was excavated (Fig. 1) so that instrumentation could be installed on the pipe (Chan *et al.* 2016). The same soil was backfilled and soil sampling of the backfill density was conducted after compaction in the field in March 2013. Soil samples were removed after compaction and assessed for the density/void ratio, gravimetric water content/moisture ratio and Atterberg limits. The road was coated in bitumen and reopened to traffic.

In November 2013 (eight months later), subsequent testing of the compacted soil occurred, where borehole cores were taken down past the pipe depth (1-1.5 m depth). The soil density/void ratio and gravimetric water content/moisture ratio were examined from the borehole soil cores. The core soil was also used for wet-dry cycle testing.

Fig. 1 Location of the soil sampled after excavation to expose a large water pipe.

2.2 *Soil information*

The silty clay soil from Strathfield, NSW, Australia was examined for soil properties (the soil will be referred to as Strathfield soil throughout this paper). The following properties from the soil can be found in Table 1 tested to Australian Standard (AS1289 2009) by the Authors and an outside geotechnical company. Proctor compaction tests, Atterberg limits, consolidated undrained triaxial tests and consolidation tests were conducted.

Table 1. Properties of Strathfield soil

Properties	Strathfield soil
Color	light brown/orange
Specific gravity, Gs	2.66–2.70
Max standard dry density (g/cm^3)	1.83
Standard OMC (%)	14.4
Liquid limit (%)	46.6
Plastic limit (%)	14.6
Linear shrinkage (%)	13.8 (nil to slight curling)
Plastic index (%)	32.4
Shrink-swell index (Iss)	3.8
Average compression index, c_c	0.169
Compressibility parameter, λ	0.073
Average swelling index, c_s	0.018
Unload/reload parameter, κ	0.0078
Average coefficient of consolidation, c_v (m^2/sec)	6.62×10^{-8}
Average permeability (m/s)	4.86×10^{-10}
Drained friction angle, φ' (°)	33.7
Drained cohesion, c' (kPa)	8
Critical state line, M	1.36

2.3 *Wet-dry cycle soil preparation*

The soil was dried, crushed and sieved to remove any large particles that may influence the small specimen size (<425 μm) for wet-dry cycling. Specimens were mixed to an initial moisture content of 16.2 % (just wet of optimum water content). Soil was left for 24 hours to reach an equilibrium. Samples were compacted using a Loadtrac III static compaction/consolidation machine in a 50 mm diameter mold to three different compaction energies (500 kPa, 2000 kPa and 8000 kPa), to simulate loose compaction, optimum compaction and dense compaction. Soil samples were removed from the mold and cut into smaller specimens of approximately 10 g. Specimens were coated using hand-spray elastomer plaster (Liu and Buzzi 2014). The hand-spray plaster acted as a coating to allow water movement into and out of the soil specimens at reduced rates throughout wet-dry cycles, whereas containing the soils shape (providing small confining stress).

A precision balance (0.01 g accuracy) was used to measure specimen weight. Specimens were weighed before and after spraying to determine the weight of the hand-spray plaster, soil weight and

water weight. A glass beaker, filled with deaired and demineralized water, was used to measure the bulk volume of the soil. The beaker was placed on top of the balance and a specimen was carefully hung from a piece of string and immersed into the beaker filled with water (Fig. 2). The new weight was recorded after equilibrium (approximately 2 seconds) and the specimen was removed and excess water was dried using a paper towel. The specimens were re-weighed after removal to see if weight had increased due to immersion. All stages were done as quickly as possible to limit water evaporation or water ingress. Water was used instead of silicon oil to avoid contamination of the sample if the coating had split open. If a large amount of water ingress had occurred, the sample was recoated and the extra weight of the coating was recorded.

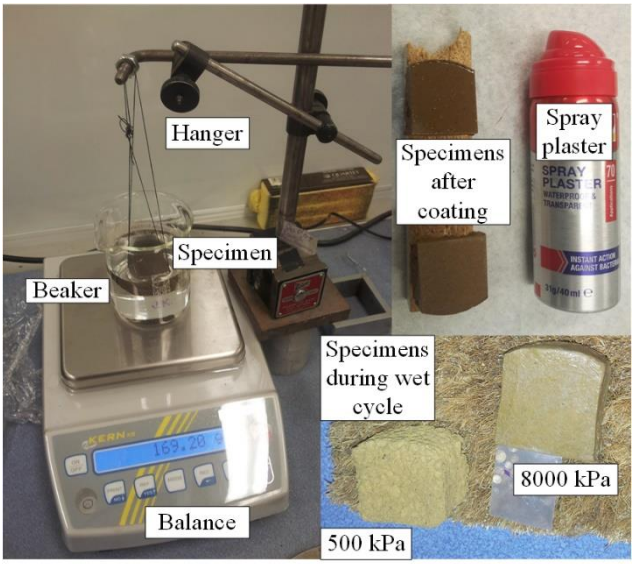

Fig. 2 Testing setup.

The immersion mass of water displaced by the specimen (m_{water}) was used to calculate the bulk volume of the specimen (V) (Eq. 1).

$$V = \frac{m_{water}}{\rho_{water}} \quad (1)$$

Where V is the bulk volume of the specimen, m_{water} is the mass recorded from the displacement of the deaired water caused by immersion of the soil specimen (g), and ρ_{water} is the density of the de-aired water (1 g/cm^3).

Specimens were then wetted in a humidity chamber (100% humidity) or in direct water and taken out periodically after water uptake. Subsequently, specimens were dried in a constant temperature (20-22°C) and humidity (40-60%) room and measured periodically. At each point the buoyancy and hence volume was recorded. Specimens were subjected to at least 4 wet-dry cycles. Cyclic testing was conducted up to a period of 1 year (July 2014–2015). Some specimen testing was halted earlier due to damaging of the specimen (e.g. dropped or broken).

The benefit of the hand-spray method for shrink swelling cycles is that multiple cycles can be conducted on the same specimen. The method is an accurate way to measure soil water volume without destructive sampling.

3 RESULTS

3.1 *Field results*

Fig. 3 shows the results of samples taken from the compacted site. Note that some of the compacted specimens (soil report data) were tested by a geotechnical contractor and may have contained a percentage of gravel, as the void ratio is below the saturation line. This may also be due to an error in the specific gravity value (skewing the saturation values), or error in testing. The results show all the points are compacted wet of optimum (0.39 moisture ratio, gravimetric water content 14.4%). However, when the sample testing was conducted 8 months later (by the authors) all the compaction points occur at a much higher void ratio and higher moisture ratio (see Fig.3), indicating swelling had occurred. The optimum moisture ratio (OMR) is plotted in Fig.3 and correlates to the optimum water content (for a dry density vs. water content plot), however uses moisture ratio, e_w, instead of water content, w (Eq. 2).

$$e_w = G_s \times w/100 \quad (2)$$

Where G_s is the specific gravity, w is the water content (%).

Table 2 gives the average properties from after compaction and the average properties from bore hole cores 8 months later. The soil exhibited significantly lower dry densities (higher void ratio) and higher gravimetric water content after 8 months. As winter occurs during June to August, it could be assumed a wet cycle occurred.

Table 2. Average properties after compaction and 8 months after compaction of Strathfield soil

Average properties	After compaction	8 months later
Gravimetric water content (%)	19.35	26.35
Bulk density (g/cm^3)	2.07	1.93
Dry density (g/cm^3)	1.74	1.52
Saturation (%)	95.0	94.5

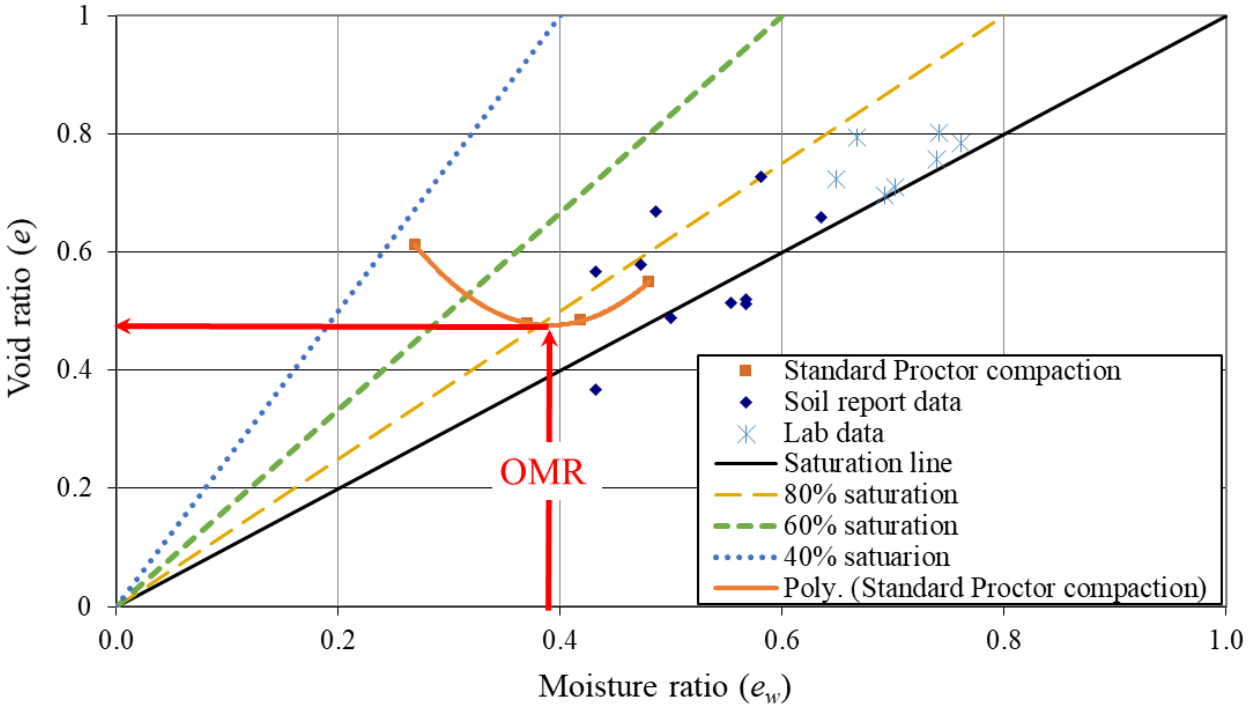

Fig. 3 Void ratio vs. moisture ratio for the soil samples taken after initial compaction and soil samples taken 8 months later from the same site.

3.2 *Wet-dry cycle results*

Fig. 4 shows the results for three of the soil specimens compacted to different initial pressures. The initial point and subsequent points are shown, and the final wet-dry curves are plotted. The compaction curve is also shown for reference. The specimens show significant soil movement in the first few cycles, then come to an equilibrium. This can be seen by the scatter points above the wet-dry cycle lines. The first few cycles show soil expanded to higher void ratios than the further cycles. The loosely (500 kPa) compacted specimen shows high movement from initial compaction level, whereas the higher energy compacted specimens (2000 and 8000 kPa) do not show this level of movement. The 2000 kPa compacted specimen shows a slight increase in void ratio from initial compaction level, however the 8000 kPa specimen only showed minimal change in void ratio wet-dry path. Note that results below the saturation line may be due to variations/errors in the specific gravity and measuring equipment. It can be assumed that the 800 kPa specimen remains close to saturation throughout a range of 0.35 to 0.8 moisture ratio.

The drying curves of the 500 kPa compaction and 2000 kPa compaction energies follow that explained by Kodikara *et al.* (1999), where three shrinkage phases are seen. The soil shrinks from saturation level (water removed from soil only), then experiences normal shrinkage (air enters the soil and water removed from soil at uniform rate), residual shrinkage (more air enters the soil than water removed) and zero shrinkage (soil particles do not move while water is removed and air enters soil). The highly compacted specimen (8000 kPa) only showed primary shrinkage, residual shrinkage and zero shrinkage.

The gravimetric water content change was from around 1% (dry cycle minimum) to 40% (wet cycle maximum, for low initial compaction pressure). After repeated wet-dry cycles the maximum water content, in which the specimens could achieve seemed to reduce. The highest compaction effort resulted in the more consistent wet-dry cycle paths with less reduction or increase in initial compaction point movement.

It is clear that the smaller compaction energies (500 kPa) have decreased in the void ratio after wet-dry cycles. Once the initial peak was reached the next cycle did not reach the same high void ratio peak even after being wetted for a month (points above void ratio of 0.9). The soil is inelastic and would not rebound to the previous state.

Results of the soil compacted to 2000 kPa show that the soil maintains its wet-dry paths through the original cycles. After numerous cycles the highest swelling point is reduced (points above void ratio of 0.7) as the soil begins to follow a new drying and wetting path. The soil particles in this state is still rearranging when the desaturation begins, however before complete desaturation begins soil has been moved further from complete saturation. The influence of initial compaction had started to reduce by the sixth cycle.

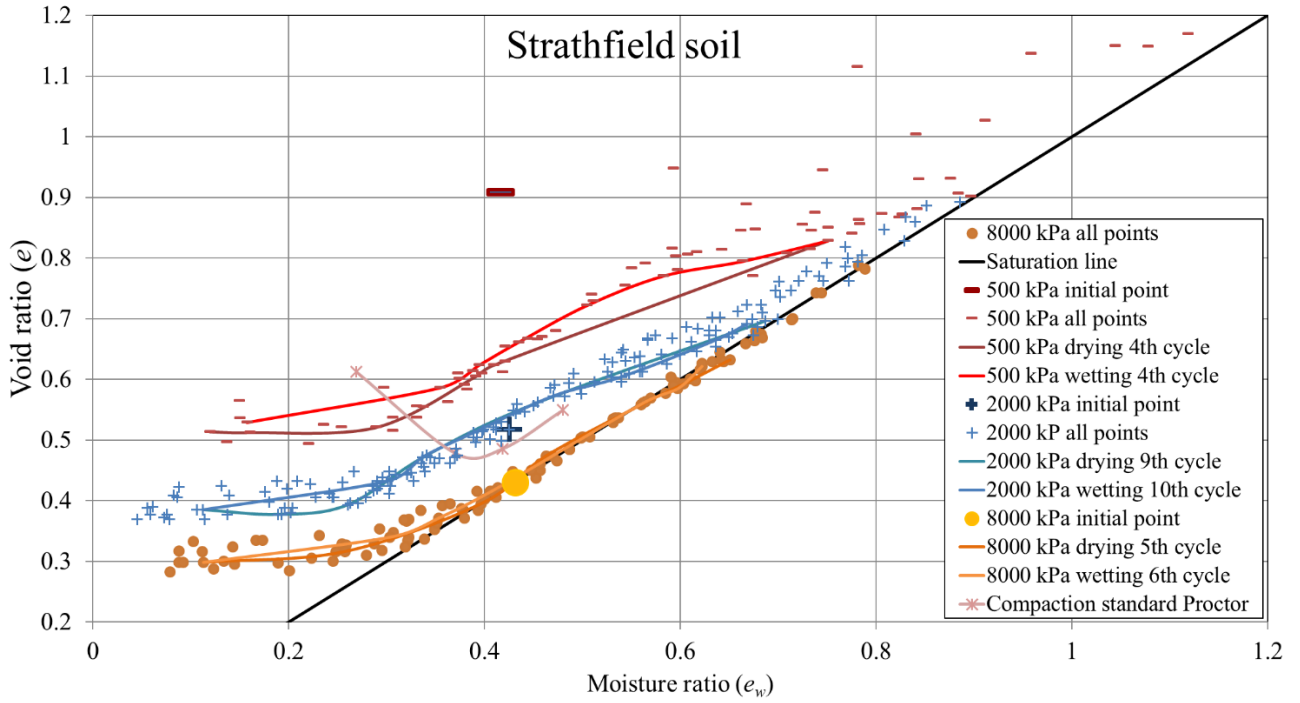

Fig. 4 Void ratio vs. moisture ratio for the three different static compaction energies. Initial staring points for each compaction level are shown. Proctor standard compaction curve is also shown.

3.3 *Comparison with field data*

Comparison with field data and wet-dry cycle testing show that the soil compacted to wet of optimum may have experienced swelling to a higher void ratio (0.7 to 0.8) and moisture ratio (0.65 to 0.75). Comparing the soil statically compacted to 2000 kPa or 8000 kPa shows a good comparison with the field data, in that soil would be close to the saturation line at higher void ratio at a moisture ratio above 0.7 (gravimetric water content of >26%).

Therefore, it could be expected that if the soil has undergone a wet cycle in this case that the void ratio may have increased to 0.7 to 0.8 from the initial compaction level void ratio of 0.4 to 0.7.

4 CONCLUSIONS AND RECOMMENDATIONS

4.1 *Conclusions*

Soil wet-dry cycles were examined for a natural silty-clay soil located in Strathfield, NSW, Australia and compared with compacted soil data from the field. The results for three different static compaction energies were examined (500 kPa, 2000 kPa and 8000 kPa). A loosely compacted specimen reduced in void ratio significantly to find an environmentally stabilized region of wet-dry cycles. The higher compacted specimens (2000 and 8000 kPa) did not experience a high void ratio change after wet-dry cycles. The gravimetric water content change was from around 3% (dry cycle minimum) to 40% (wet cycle maximum). After repeated wet-dry cycles the maximum water content reached seemed to reduce. The highest compaction effort resulted in the more consistent wet-dry cycles with less reduction or increase in initial compaction point movement.

The results from the field, where compacted soil was at a lower void ratio and lower moisture content, compare well with the data collected from wet-dry cycles. It could be assumed that a wet cycle caused the change in density and moisture content of the soil in the field.

Therefore, when compacting soils, a higher level of compaction may result in less void ratio movement or uptake/decrease of water, provided soil is not disturbed by external effects. A unique line wet-dry line seems to be experienced from each of the compaction levels tested.

A line of optimums for all levels of soil compaction was not found. This may be only seen if soil was disturbed or experiences extreme wetting (placed in water) or drying (dried in an oven to promote cracking).

4.2 *Recommendations*

The following points are recommended for further wet-dry cycle examination:

- Testing is required to determine the wet-dry curve trend for different soil types.
- Changing the initial compaction point should be examined on the change in wet-dry curves.
- Extreme wetting and drying cycles simulating high rainfall or drought to see the variation in soil void ratio.
- Increasing the number of tests could also be beneficial, as well as measuring soil suction throughout testing.
- Disturbance of the soil in reaching a stabilized curve would be beneficial to validate soil shrink-swell theory.

ACKNOWLEDGMENTS

The Authors would like to thank Sydney Water for the use of the pipe and soil. Funding was provided by Sydney Water and the Advanced condition assessment and pipe failure prediction project (Critical pipes project) as well as all project partners.

REFERENCES

Albrecht, B.A., and Benson, C.H. (2001). Effect of desiccation on compacted natural clays. Journal of Geotechnical and Geoenvironmental Engineering, 127(1): 67–75.

AS1289 (2009). Methods of testing soils for engineering purposes. Standards Australia, Sydney, Australia.

Benson, C.H., Daniel, D.E., and Boutwell, G.P. (1999). Field performance of compacted clay liners. Journal of Geotechnical and Geoenvironmental Engineering, 125(5): 390–403.

Chan, D., Shannon, B., and Kodikara, J. (2016). Relative importance of external factors on pipe performance. In OzWater 2016, Melbourne, Australia.

Chen, R., and Ng, C.W.W. (2013). Impact of wetting-drying cycles on hydro-mechanical behavior of an unsaturated compacted clay. Applied Clay Science, 86: 38–46.

Costa, S., Kodikara, J., and Shannon, B. (2013). Salient factors controlling desiccation cracking in laboratory experiments. Géotechnique, 63(1): 18-29.

D4943-08, A. (2008). Standard test method for shrinkage factors of soils by the wax method. ASTM International, West Conshohocken, PA, USA.

Guérif, J. (1990). Factors influencing compaction-induced increases in soil strength. Soil and Tillage Research, 16(1-2): 167–178.

Kodikara, J. (2012). New framework for volumetric constitutive behaviour of compacted unsaturated soils. Canadian Geotechnical Journal, 49(11): 1227–1243.

Kodikara, J., Barbour, S.L., and Fredlund, D.G. (1999). Changes in clay structure and behaviour due to wetting and drying. In Proc. 8th Australian–New Zealand Conference on Geomechanics, Hobart, pp. 179–185.

Liu, X., and Buzzi, O. (2014). Use of hand-spray plaster as a coating for soil bulk volume measurement. Geotechnical Testing Journal, 37(3): 1–7.

Rayhani, M.H., Yanful, E.K., and Fakher, A. (2007). Desiccation-induced cracking and its effect on the hydraulic conductivity of clayey soils from Iran. Canadian Geotechnical Journal, 44(3): 276–283.

Shannon, B., Kodikara, J., and Rajeev, P. (2015). The use of restrained ring test method for soil desiccation studies. Geotechnical Testing Journal, 38(1): 98–112.

Sivakumar, V., Tan, W.C., Murray, E.J., and McKinley, J.D. (2006). Wetting, drying and compression characteristics of compacted clay. Géotechnique, 56(1): 57–62.

Wijesooriya, S.D., and Kodikara, J.K. (Year) Published. Experimental study of shrinkage and swelling behaviour of a compacted expansive clay soil. In ANZ 2012, Melbourne, Australia2012, pp. 25–30.

Yesiller, N., Miller, C.J., Inci, G., and Yaldo, K. (2000). Desiccation and cracking behavior of three compacted landfill liner soils. Engineering Geology, 57: 105–121.

Geotechnical Assessment for Alignment Selection in the Australian High Speed Rail Study

A. Lander
EDG Consulting, Australia (formerly AECOM Australia)

ABSTRACT: The High Speed Rail Study Phase 2 was a strategic study on the implementation of a High Speed Rail (HSR) network on the east coast of Australia, examining potential corridors, alignments and station locations. As part of the alignment study, the ground conditions for the 2000km long by 200km wide Brisbane to Melbourne study area needed to be identified, assessed, categorised and compiled as GIS data for comparative alignment evaluation within a short time period, requiring innovative use of digital information and engineering geology principles to successfully complete the assessment.

1 INTRODUCTION

1.1 *High Speed Rail Study Phase 2*

The High Speed Rail Study Phase 2 was a strategic study on the implementation of a High Speed Rail (HSR) network on the east coast of Australia, examining potential corridors, alignments and station locations (AECOM, 2012). The Phase 2 study defined an optimal alignment and assessed the financial feasibility of an HSR network, building on a short list of city locations and inter-city corridors that were identified in the Phase 1 study.

The study covered an area approximately 2000km long by 200km wide, stretching from Melbourne in the south to Brisbane in the north. The proposed alignment is shown in Figure 1.

Fig. 1 Proposed HSR alignment from Phase 2 study

1.2 *High Speed Rail Alignment Evaluation*

HSR is typically defined as a purpose-built rail system that travels in excess of 250km/h, often covering long distances between cities. At the high speeds involved the curve radii are usually large. This requires careful consideration of competing constraints to achieve a functional and economical alignment.

A comparative alignment evaluation methodology was developed for the study that enabled a large number of constraints to be considered simultaneously. The Trimble Quantm alignment planning package was used to generate numerous regional alignments based on entry/exit nodes and rail track geometric criteria, assess the alignments against different constraints (e.g. environmentally sensitive areas). These were then used to assess the likely cost and present the lowest cost options for further review and refinement. The software used attributed GIS shapefiles as inputs with each GIS layer representing a separate constraint.

1.3 *Cost Estimation*

The estimate of cost for a particular generated alignment was calculated automatically based on a set of rules developed for each constraint. Simple relationships were developed for cut and embankment geometry, threshold heights for switching from embankments to bridges and other typical civil engineering earthworks and structures. Cost relationships were then linked to the civil engineering works and could be by length (e.g. track formation subgrade preparation), by area (e.g. face area of retaining walls) or by volume (e.g. embankment volumes).

1.4 *Study Timeframe*

To allow sufficient time for the alignment modelling, the timeframe for developing the dataset inputs for the full 2000km long study area was a little over two weeks. This necessitated a digital approach to compiling the datasets.

2 GEOTECHNICAL ASSESSMENT

2.1 *Geotechnical Constraints*

Two primary geotechnical constraint datasets were identified for inclusion in the alignment modelling; Geology, and Mining. Geology was used to group the engineering nature of the geological materials. Mining was used to identify past, present and future mining activity.

A third geotechnical constraint dataset, Slope, was initially proposed, to account for landslide risk and construction in steep terrain. Alignment planners, to simplify the overall alignment model, chose to exclude this dataset based on initial results..

2.2 *Geology Data Set*

Geological units present across the study area number in the thousands and encompass the full range of geological materials from soft, recent estuarine and alluvial deposits to high strength igneous and metamorphic rock.

With the size of the study area, the range of material types and the scope of the study, it was necessary to simplify the geology into several broad groups that captured the key impact of the geological materials on the works. To achieve this, the geology was separated into three domains, namely Rock, Soil and Soft Soil. These domains broadly separated the ground conditions by their engineering performance:

- Rock – comprising all types of rock materials in the engineering sense. These were typically materials that support steep slopes in cuttings and may be excavated using hard rock tunnelling techniques.
- Soil (other than soft) – comprising all soil strength materials that do not need extensive treatment to form the subgrade to the track formation. They can form only moderate slopes in cuttings without additional support and are readily excavatable.
- Soft soil – comprising all deep compressible soils that will require extensive ground treatment to allow construction of the HSR infrastructure. It was not intended to include shallow alluvial deposits that occur locally around minor watercourses or other alluvial deposits that are unlikely to require extensive ground treatment to depth. Soft soils in coastal areas also represent Acid Sulphate Soil risks.

2.3 *Classification Using Digital Geological Data*

Available digital data sources comprise a nationwide digital elevation model and seamless geology map data for each relevant state; Victoria, New South Wales (NSW) and Queensland. Geology maps were available in 1:250,000 scale for NSW and Victoria and 1:100,000 scale in Queensland and around some mining districts in Victoria and NSW.
1:25,000 geology maps were also available for coastal areas in northern NSW. All the information was obtained as fully attributed GIS metadata files. An example of the GIS geological map covering less than 1% of the study area is shown in Figure 2.

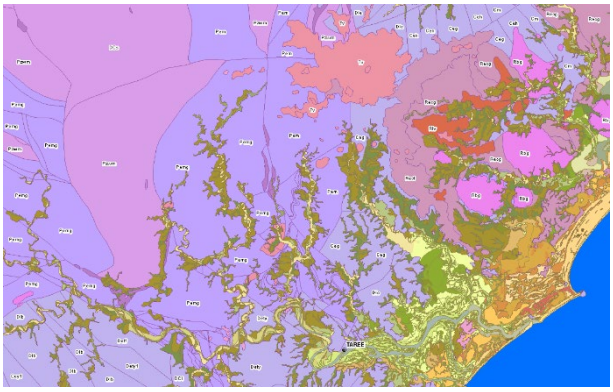

Fig. 2 Geological map data from GIS

To rapidly classify the geology of the whole study area into the three domains, automated processes were developed to search the geological attributes in the GIS data and identify key terms. From the wide range of information available, the following key attributes were found to best represent the engineering nature of the geology:

- Geological age
- Dominant lithology
- Description.

The classification then proceeded along the following lines:

- Rock – was identified as all Quaternary and Tertiary geological units where the dominant lithology is clearly defined as rock (e.g. basalt) and all pre-Tertiary geological units.
- Soft Soil – was identified as all Quaternary (Holocene) geological units. These units were well delineated on the coastal geology maps and in major cities. Where detailed mapping of the Quaternary geology is available, the description of the materials and depositional environment (e.g. marine/alluvial) was also used in assessing the classification, particularly where detailed information was available (e.g. Troedson A.L. and Hashimoto T.R. (2008)).

- Soil - was identified as remaining Tertiary and Quaternary (Pleistocene) geological units.

The classified Geology shapefile output for the same area from Figure 2 is shown in Figure 3.

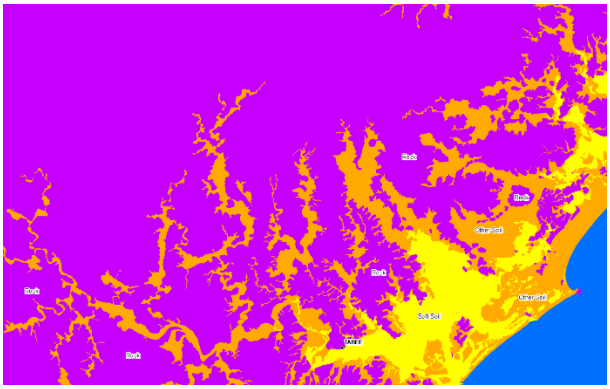

Fig. 3 Geology shapefile

2.4 *Challenges with the Data*

There were frequent inconsistencies within the data sets based on the original geological mapping, mostly associated with mapping of similar units in separate phases of mapping or across state borders.

Of significance to the classification of Soil and Soft Soil, the geological age and lithology were sometimes inconsistent between adjacent map sheets.

The geological age attributes in the GIS data for units within these domains could appear as:

- Quaternary, Tertiary.
- Quaternary (Holocene), Quaternary (Pleistocene), Neogene (Pliocene), Neogene (Miocene), Palaeogene (Oligocene).
- Quaternary to Tertiary.
- Cainozoic.

This raised some difficulty in classification as some of the broader descriptions may or may not include soft soils. It was often not possible to assess whether these were recent, compressible soils or older, more competent soils. Further, most of these units were described as 'undifferentiated' and 'unnamed' within the Description or Formation attributes.

Much of the inland alluvial sediments (i.e. Murray Basin), which were also described in these terms, are deep Late Tertiary to Quaternary soils that are not soft soils in an engineering sense, but may contain local inclusions of soft soils. It was then difficult to separate out the soft soils from the other soils.

In some cases, the formation name could assist in assessing the soil conditions based on information available elsewhere in the public domain. This approach was only used on units covering large areas where other attributes had proven inconclusive in classifying the ground conditions.

In the coastal areas, where deep soft soils have been deposited through the infilling of valleys submerged during the last sea level rise, an attempt was made to correlate the presence of soft soils with surface slope and elevation from the digital elevation model. The surface slope criterion completely overlapped the whole of the areas identified by elevation and was subsequently excluded from further assessment. The elevation appeared to provide a reasonable approximation to the extent of soft soils noted in other sources.

Where areas were described as Quaternary alluvium but had higher local elevations, this often represented more substantial materials (e.g. barrier sands, high level terraces, etc) or materials that were likely to have experienced loading from subsequent processes (e.g. dune deposits). In each of these cases, the likelihood that these materials represented deep soft soils of high compressibility and requiring extensive ground treatment was low.

2.5 *Site Specific Assessments*

Much of the automated processes described above were used to classify the vast areas of land between major towns and cities in Australia. Site specific desk studies were carried out at key locations identified from the initial alignment selection and geological sections developed. These included:

- Approaches to major cities, where tunnels would be required to pass under built-up areas.
- Major river crossings (e.g. Hawkesbury River to north of Sydney.
- Alignments through coal measures.
- Alignments through major topographic features with history of landslides (e.g. Wollongong Escarpment).

2.6 *Mining Data Set*

The identification of mining constraints was limited by the available information. Initial considerations included a separation by mining methods (e.g. longwall) and the depth of workings to assess the risk of settlement impact to the HSR. However, in reviewing the available information, it was evident that there was insufficient detailed information readily available to assess all of these factors consistently throughout the study area. Further, the information on potential future mining areas (e.g. mining tenements) was considered likely to overstate the extent of workings and gives no indication as to the type of works or the likelihood of proceeding to actual production.

It was decided to categorise the mining sets simply as two sets:

- Past mining – these are known past workings, taken from the Mine Subsidence Board data.
- Future mining – these are potential areas for future mine workings and are taken from the Mine Subsidence District boundaries and from mining lease boundaries.

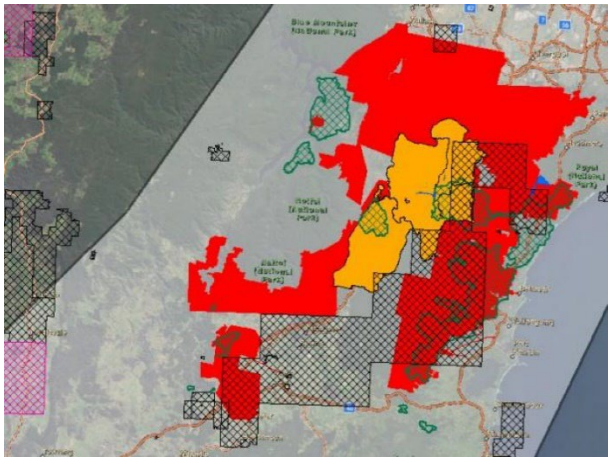

Fig. 4 Mining shapefile

3 LINKING ALIGNMENT SELECTION AND COST TO THE DATA SETS

3.1 *Typical Track Formation and Support – Geology Data Set*

The geology data sets formed a major input to the alignment development and cost estimation as they dictated the form and extent of the earthworks for the track formation. The broad relationships for typical ground profiles and earthworks in the geology domains shown in Table 1 were developed for use in the alignment planning.

Table 1. Typical ground profiles and earthworks

Item	Rock	Soil	Soft Soil
Soil depth over rock	3m	10m	20m
Cut batters	2V:1H	1V:2H	-
Subgrade support	-	-	Viaduct

Differentiation of bridge foundation types for the different geology domains was excluded to simplify the alignment selection procedure

3.2 *Typical Track Formation for Cost Estimation – Mining Data Set*

Past mining areas represented areas with increased risk associated with settlement. A nominal cost per linear metre for ground treatment was provided for alignments that passed over past mine workings based on the costs of grouting programs and percentages of alignment requiring grouting from past projects.

Future mining areas are extremely difficult to quantify on a consistent basis for the entire range of mining types and methods. Costs associated with sterilisation of resources would vary dramatically with the minerals involved. Potential alignments crossing future mining areas were set to automatically raise flags for further investigation on a case-by-case basis once the concept alignment was identified.

4 CONCLUSIONS

The use of digital data and engineering geological principles enabled a large study area to be rapidly assessed and classified to aid in alignment selection and cost estimation in planning for an Australian HSR network.

Delineation of soft soils presented the major challenge for the study, particularly with inconsistent geological mapping, and this was achieved through assessing a combination of geological origin, age and local elevation.

The exclusion of the Slope dataset was also potentially problematic and required follow-up site specific assessment of areas with increased landslide risk.

REFERENCES

AECOM (2012). HSR Phase 2 Report, <https://www.infrastructure.gov.au/rail/publications/high-speed-rail-study-reports/> (Jan, 2020).

Troedson A.L. and Hashimoto T.R. (2008). Coastal Quaternary geology — north and south coast of NSW. Geological Survey of New South Wales, Bulletin 34.

ACKNOWLEDGMENTS

The author recognizes the exceptional GIS work done for this assessment by Llewellyn Cain, who sadly passed away in 2017.

Figures presented in this paper are taken from the AECOM (2012) High Speed Rail Study Phase 2 report.

Flow characteristics of supercritical carbon dioxide-stimulated fractures in granite under in-situ stress conditions

B. L. Avanthi Isaka and P.G. Ranjith
Department of Civil Engineering, Monash University, Building 60, Melbourne, Victoria, 3800, Australia

ABSTRACT: The substantial increase of the world's energy demand in recent years is challenging world energy production and the extraction of energy resources, resulting the over-use of naturally occurring resources such as fossil fuels. Hence, the use of renewable resources for energy production is seen as a viable option to address the emerging energy demand around the world. The development of technically-sound enhanced geothermal systems (EGSs) for geothermal energy extraction has been identified as a viable solution for this emerging energy demand. The use of supercritical carbon dioxide ($ScCO_2$) as the working fluid in EGSs as a replacement for the traditional water-based method is promising due to the multiple advantages of $ScCO_2$-injection for underground reservoir stimulation. The evolution of reservoir stimulation using $ScCO_2$ and the understanding of the flow behaviour of a $ScCO_2$-stimulated geothermal reservoir is vital for the application of $ScCO_2$-EGSs as a replacement for water-based EGSs. Therefore, the aim of this study is to investigate the flow characteristics of ScCO2-induced fractures under high-temperature and high-pressure conditions. A series of experiments was conducted to investigate the flow characteristics of $ScCO_2$-induced fractures in Harcourt granite and the results were compared with those for water-induced fractures to investigate the effectiveness of $ScCO_2$ for fracture stimulation compared to the traditional water-based method. The studies revealed that $ScCO_2$ has the potential to induce more complex fracture patterns in Harcourt granite under high-temperature and high-pressure conditions, compared with the single plain fractures induced by the water-based method. The flow characteristics of these induced fractures show complex variations with the increase of in-situ stresses which leads to 90% aperture closure at 50 MPa confining stress.

1 INTRODUCTION

According to the International Renewable Energy Agency (IRENA, 2019a) that the global renewable energy capacity increased to 2351 GW at the end of 2018 with a 50% share (1172 GW) from hydropower. In addition, wind and solar energy accounted for 24% and 20% capacities, respectively. At the same time, geothermal energy contributed to global renewable energy production with an addition of 13 GW. 7.9% growth in global renewable energy production was experienced in 2018 with a 61% share of new renewable capacity installed in Asia (IRENA, 2019a). The key goal of the transition of energy production from fossils to renewables is to ensure clean greener energy production with minimum environmental impact and material extraction.

Deep geothermal energy extraction from hot dry rocks (HDRs) located deep underground (beyond 4 km) is promising due to its immense potential. High-temperature rock masses with no or negligible pore fluid and permeability can be accessed for heat extraction with the advances in technology. Furthermore, HDR geothermal resources are considered to be a breakthrough solution to emerging energy demands (Blackwell et al., 2006; MIT, 2006). Enhanced geothermal systems (EGSs), which consist of two major parts: a surface power generation system and an underground heat exchange system have been developed to extract heat from hot dry rock (HDR) geothermal resources. Major steps in the development of EGSs to extract heat stored in low-permeable, high-temperature rock formations include the exploration and assessment of geothermal sites, well-drilling (injection and production), reservoir creation, completion of a closed-loop for heat extraction via fluid circulation, operation of the power plant at ground level and maintenance of reservoirs for long-term operation (Lu, 2018).

The working fluid used in EGSs plays an important role and needs to be effective in heat extraction, high in flowability, rich in abundance, low in chemical reactivity, and high in proppant carrying capacity, in order to be productive in long-term operation. Predominantly, water-based fracturing is used in the industry since it is the most cost-effective and simplest technique identified to date. Although a number of "waterless" fracking methods have been proposed for use in unconventional reservoirs like tight gas, shale gas and coal beds, the use of these methods in EGS is limited due to the high-temperatures prevalent deep underground.

The use of carbon dioxide as the working fluid in EGSs for both reservoir stimulation and heat

mining purposes was first proposed by Brown (2000), based on research conducted by the Los Alamos National Laboratory, Fenton Hill, New Mexico. Carbon dioxide behaves as a supercritical fluid above its critical point (31.1 °C and 7.39 MPa), causing it to act as a fluid but flows like a gas. Under the extreme environmental conditions prevailing deep underground at 3-5 km depths with in-situ stresses in the range of 50-125 MPa and at high temperatures 100-400 °C (Breede et al., 2013), carbon dioxide is in the supercritical phase ($ScCO_2$). Therefore, recent studies have identified that $ScCO_2$ exhibits favourable properties for usedas the working fluid in EGS replacing traditional water-based fluids.

In order to use CO_2 as the working fluid in EGSs, the performance of CO_2 in deep underground geothermal reservoir stimulation needs to be investigated. The connectivity of CO_2-induced induced fracture networks, aperture sizes and the distribution of fracture networks in hot rock influence the performance of the geothermal reservoir in multiple respects, including heat extraction and mass flowrate. The coupled hydro-thermo-mechanical behaviour of a CO_2-based geothermal reservoir is poorly understood at present. The flow characteristics of fractured media depend upon detailed properties of the fractures, such as aperture distribution, tortuosity, effective stresses and the temperature of the rock media (Darot and Reuschlé, 2000; Chen et al., 2014; Chen et al., 2017). Therefore, it is important to have a detailed understanding of the evolution of the flow characteristics such as permeability and outlet flowrate under the different environmental conditions prevalent deep underground. Hence, the flow characteristics of $ScCO_2$-induced fractures in granite under high-temperature and high-pressure conditions were evaluated experimentally in this study.

2 METHODOLOGY

2.1 *Testing material and specimen preparation*

Harcourt granite sourced from Mount Alexander, Victoria, which has a mineralogical composition of 40% feldspar, 27% quartz, 30% biotite and minor percentages of other minerals, was selected as the testing material. The average bulk density, uniaxial compressive strength, elastic modulus and Poisson's ratio of Harcourt granite are 2630 kg/m^3, 250 MPa, 17 GPa and 0.22, respectively.

Cylindrical rock specimens 22.5 mm in diameter and 45 mm high were cored from a single block of Harcourt granite for testing. The standards of the American Society for Testing and Measurement (ASTM D7012, 2014) were followed during specimen preparation. A 3 mm diameter borehole was drilled up to the mid-depth of the rock specimens prior to testing to facilitate fluid injection. A rock specimen prepared for the testing is shown in Fig. 1(a).

2.2 *Testing apparatus and test method*

The high-temperature and high-pressure triaxial test apparatus available in the Deep Earth Energy Research Laboratory (DEERL) at Monash University was used for both fracturing and permeability testing (see Fig. 1(b)). First, the rock specimen was placed inside the pressure cell on top of a pedestal with a fluid flow line inside it. The rock specimen was covered with a copper sleeve to avoid the contamination of confining media with the specimen and injection fluid. A separate pedestal was placed on top of the rock specimen to connect the rock specimen to the fluid flowline, as shown in Fig. 1(c).

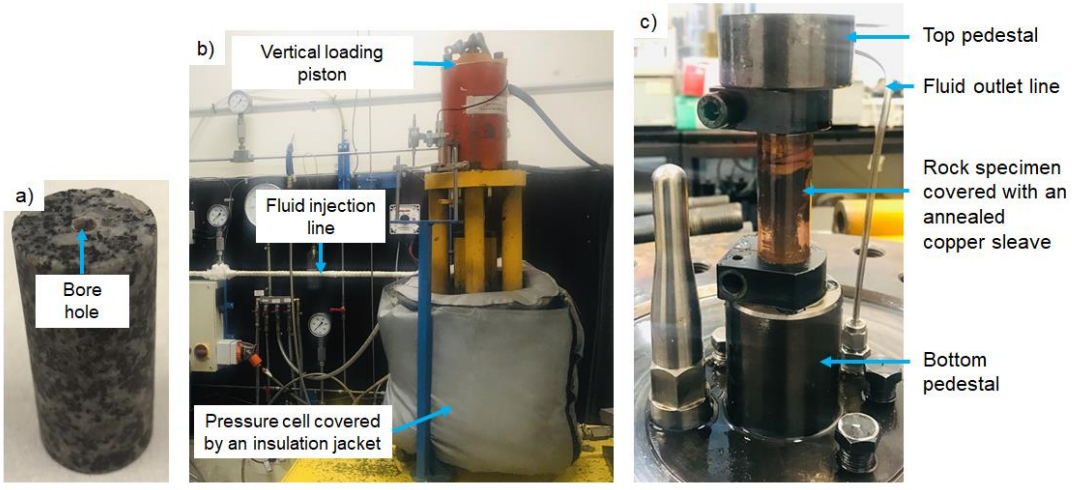

Fig. 1 a) Cylindrical Harcourt granite specimen, b) high-temperature and high-pressure tri-axial test apparatus, and c) specimen arrangement for the testing

Temperature was applied to the pressure cell using a heating band, and the temperature was monitored using a thermocouple fixed inside the pressure cell. Once the target temperature was achieved, the confining pressure was applied using a syringe pump attached to the plumbing system. The whole system was maintained for 4 hours to stabilise the desired temperature and pressure inside the sample. The injection of $ScCO_2$ was then started, and the gaseous CO_2 was allowed to transfer into supercritical phase above its critical point (31.10°C and 7.39 MPa) inside the fluid flowline.
The injection line was heated to 60°C using a heating element attached to the insulated flow line in order to allow phase transition during CO_2 pressurisation. For the fracturing tests, $ScCO_2$ was continuously injected into the rock specimen along the drilled borehole at a constant injection rate of 30 ml/min until fracture initiation. Two fracturing tests were conducted at a constant confining pressure of 40 MPa and at two different temperatures of 100°C and 200°C. The fractured rock specimens were CT-scanned at a resolution of 11.5 µm in order to characterise the morphology of the induced fractures. A series of permeability tests was conducted to evaluate the fracture permeability and flow characteristics of $ScCO_2$ induced fractures at 40 MPa confining pressure and at 100°C. A similar specimen arrangement was used to measure fracture permeability using the high-temperature and high-pressure triaxial set-up.

3 RESULTS AND DISCUSSION

3.1 *Breakdown pressure during $ScCO_2$ fracturing*

The pressure-time plots for two rock specimens during $ScCO_2$ fracturing under 40 MPa confining pressure, and at 100°C and 200°C are shown in Fig. 2. The figure shows a slight pressure development at the initial stage of injection, and the phase transition of CO_2 from the gas state to the supercritical state takes place at this stage. Thereafter, wellbore pressurisation takes place gradually with a significant increase in the inlet pressure.

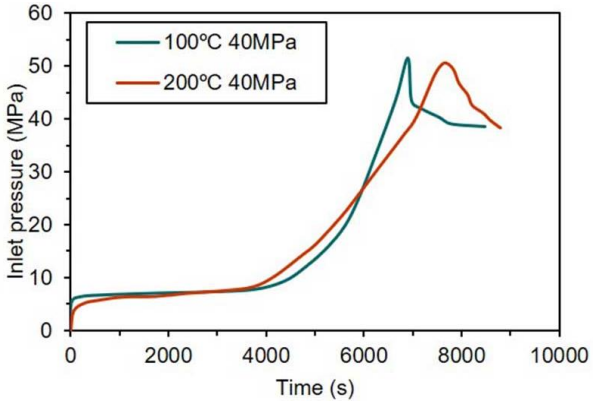

Fig. 3 : Pressure-time plot during $ScCO_2$ fracturing under 40 MPa confining pressure and at 100°C and 200°C

Rock breakdown and fracture initiation occur with the continuous injection of $ScCO_2$, characterised by a significant pressure drop at the inlet with a surge of the outlet pressure. Breakdown pressures of 52 MPa and 51 MPa resulted for fracture initiation under 40 MPa confining pressure at two different temperatures of 100°C and 200°C, respectively. A slight reduction in the breakdown pressure was observed with the increase of temperature from 100°C to 200°C due to the thermally-induced deterioration to the rock specimen caused by microcracking. Percolation of $ScCO_2$ into these microcracks due to its higher flowability followed by pressurisation induces fracture initiation under low breakdown pressures at high temperatures.

3.2 *Morphology of $ScCO_2$ induced fractures at high temperatures and pressures*

The CT images of the $ScCO_2$-fractured rock specimens were analysed to evaluate the morphology of the fractures induced during $ScCO_2$ injection. CT images of the cross-sections at the bottom of the rock specimens fractured under 40 MPa confining pressure and at two different temperatures of 100°C and 200°C are shown in Fig. 3(a) and Fig. 3(b), respectively. Moreover, a CT image of a rock specimen fractured by water injection under 40 MPa confining pressure and at 100°C is shown in Fig. 3(c) for comparison, from a previous study by Kumari, Ranjith et al. (2018). The light colour regions of the CT images represent biotite grains with density around 3090 kg/m^3 whereas the grey regions show both feldspar and quartz grains with average densities of around 2560 kg/m^3 and 2650 kg/m^3, respectively.

Predominantly, diametrical fractures are induced during fracturing when the circumferential stress at the wellbore exceeds the tensile strength of the rock specimen. Fig. 3 shows diametrical fractures in the rock specimens fractured using both water and $ScCO_2$.

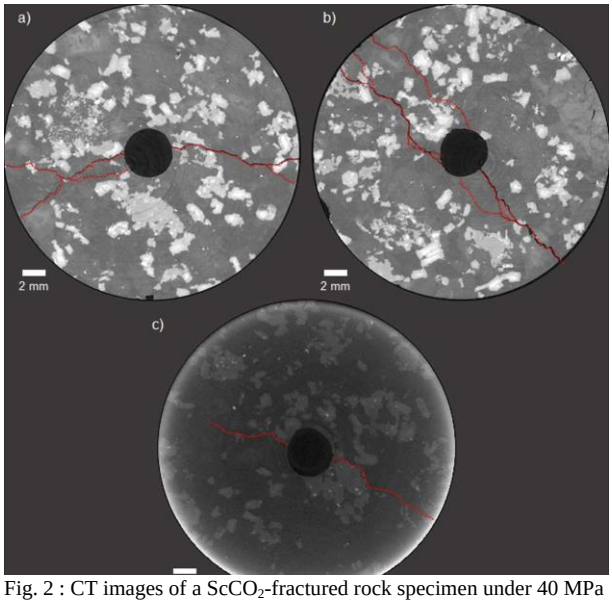

Fig. 2 : CT images of a $ScCO_2$-fractured rock specimen under 40 MPa confining pressure, and at (a) 100°C and (b) 200°C, and (c) water-fractured rock specimen under 40 MPa confining pressure and at 100°C.

Interestingly, multiple secondary branches connected to the main diametrical fracture were observed in the two rock specimens fractured using $ScCO_2$ making the fracture pattern more complex. Furthermore, the complexity of the fracture induced at 200°C is more complex than the fracture induced at 100°C. However, the water-induced fracture is only a plain diametrical fracture, as shown in Fig. 3(c). Since $ScCO_2$ is a low-viscous fluid with density similar to water, it has the ability to percolate into the grain boundaries and microcracks in the defect regions of the rock specimen. Therefore, the pressurisation of these defect regions with microcracks makes them interconnected, resulting in more complex fracture patterns with low energy. With the increase of the extent of microcracking, the percolation potential of $ScCO_2$ is enhanced and the complexity of the fracture pattern increases. Therefore, $ScCO_2$ has greater ability than water to generate extensive fracture patterns with multiple interconnected secondary branches under high-temperature conditions.

The CT images of the rock specimens (shown in Fig. 3) indicate that the fractures mainly propagate through the grain boundaries and rarely through grains. In addition, the biotite grains exhibit moderate resistivity to cracking compared to quartz and feldspar grains. Therefore, grain boundary cracks through biotite grains are predominantly observed in the CT images.

3.3 *Flow behaviour of $ScCO_2$-fractured rock specimens*

3.3.1 *Darcy's flow characteristics through fractures*

A series of permeability tests was conducted at a constant temperature of 95°C and at varying confining pressures from 5-60 MPa for the rock specimen fractured under 40 MPa confining pressure and at 100°C. The steady-state flowrate was plotted against the injection pressure at each confining pressure for the rock specimen to evaluate the applicability of using Darcy's law to determine the permeability characteristics of the fracture. Fig. 4 shows the steady-state flowrate vs.injection pressure for the fractured rock specimens. As indicated in Fig. 4, the steady-state flowrate exhibits a proportional linear relationship with the injection pressure for each confining pressure. Therefore, the flow regime through the fracture is characterised as a Darcy's flow regime, and Darcy's law coupled with cubic law was incorporated to calculate the fracture permeability of the fractured rock specimens.

3.3.2 *Variation of hydraulic aperture and fracture permeability with confining pressure*

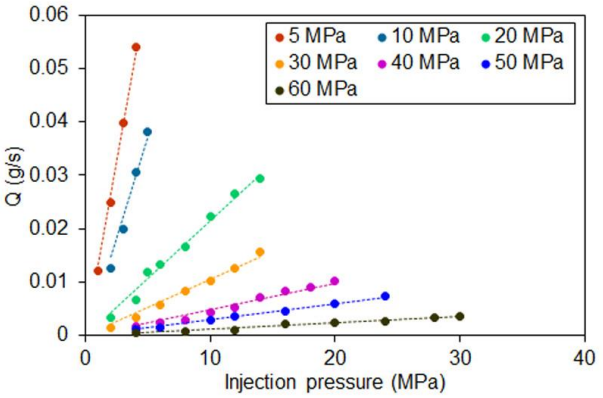

Fig. 4 : Steady-state flowrate vs. injection pressure at each confining pressure for rock specimens fractured under 40 MPa confining pressure and at 100°C.

The permeability of a fracture, which can be idealised as two smooth parallel plates with a narrow opening, can be calculated using Darcy's law coupled with the cubic law as stated in Eqs. 1-3, where Q is the steady-state flowrate, w is the width of the fracture, e is the hydraulic fracture aperture, ΔP is the pressure gradient along the fracture, μ is the fluid viscosity, l is the length of the fracture, A is the cross-sectional area of the rock specimen, and k is the fracture permeability. Temperature- and pressure-dependent density and viscosity values for water were taken from the database of the NIST REFPROP program (Lemmon, Huber et al. 2007).

$$Q = \frac{we^3\Delta P}{12\mu l} \tag{1}$$

$$\frac{dP}{dx} = \frac{Q}{A}\frac{\mu}{k} \tag{2}$$

$$k = \frac{e^2}{12} \tag{3}$$

Hydraulic apertures were calculated for every steady-state flowrate under each injection pressure and confining pressure to evaluate the effect of injection pressure and confining pressure on fracture permeability. The evolution of hydraulic aperture with injection pressure is shown in **Error! Reference source not found.**(a) for each confining pressure. As the figure shows, the hydraulic aperture remains unchanged with the increase of injection pressure at each confining pressure and this behaviour further verifies the assumption of a Darcy's flow regime in the fracture. Importantly, a significant reduction in hydraulic aperture results with the increase of confining pressure, as shown in **Error! Reference source not found.**(a). Moreover, the calculated average fracture permeabilities are plotted against the confining pressure in **Error!**

Reference source not found.(b). A non-linear reduction in fracture permeability is observed with the increase of confining pressure from 5 MPa to 60 MPa due to stress-induced fracture closure. A 96% reduction in permeability is observed with the increase of confining pressure from 5 MPa to 60 MPa due to fracture closure under high effective stresses. This phenomenon indicates the importance of the use of proppants in order to retain fractures open under the t high in-situ stress conditions prevalent deep underground.

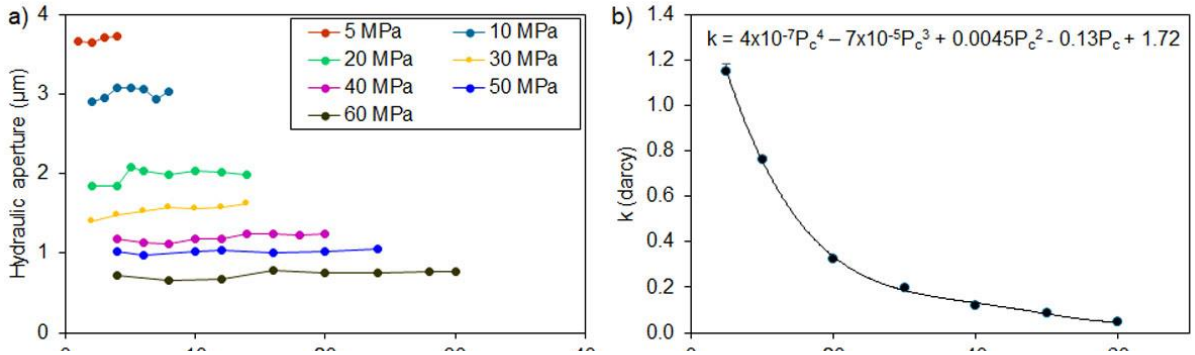

Fig. 5 a) Evolution of hydraulic aperture with the injection pressure for different confining pressures, and b) variation of average fracture permeability with confining pressure for the $ScCO_2$ fractured rock specimen.

It is worthwhile to compare the permeability of $ScCO_2$-fractured rock specimens with that of intact rock specimens to evaluate the effectiveness of using $ScCO_2$ as the working fluid in EGSs, replacing water in order to maximise the energy harvest by creating a well-interconnected fracture network. Harcourt granite is a crystalline rock with intact permeability varying in the range of 0.01–0.10 μD. The permeability of $ScCO_2$ fractured rock specimens is greater than 0.1D even under high confining pressures up to 60 MPa. Therefore, fracture stimulation by $ScCO_2$ injection enhances the matrix permeability of rock specimens under extreme environmental conditions.

4 CONCLUSIONS

A series of experiments was conducted to evaluate the fracturing performance of $ScCO_2$ and the flow behaviour of fractured rock specimens under extreme geological conditions to evaluate the performance of $ScCO_2$ for use as a working fluid in EGSs. Based on the experimental results, the following conclusions can be drawn:

- $ScCO_2$ has the potential to induce fractures in rock specimens under high-temperature and high-pressure conditions with prolonged pressurisation.
- The breakdown pressure for fracture initiation decreases with increasing temperature due to the thermally-induced deterioration of the rock specimens with increasing temperature
- $ScCO_2$ generates complex fracture patterns in rock specimens at high temperatures since it has the ability to percolate into thermally-induced microcracks and the pressurisation of the microcracks makes them interconnected by the development of a complex fracture network.
- $ScCO_2$ fracturing enhances the permeability of rock specimens over 0.1D even under high confining pressure of 60 MPa compared to the intact permeability of 0.01-0.10 μD.
- Therefore, $ScCO_2$ can be effectively used as the working fluid in EGSs and has multiple favourable characteristics for reservoir stimulation and mass flowrates in order to achieve enhanced energy recovery.

REFERENCES

Blackwell David, Petru T Negraru & Maria C Richards 2006. Assessment of the enhanced geothermal system resource base of the United States. Natural Resources Research, 15, 283-308.

Breede Katrin, Khatia Dzebisashvili, Xiaolei Liu & Gioia Falcone 2013. A systematic review of enhanced (or engineered) geothermal systems: past, present and future. *Geothermal Energy*, 1**,** 4.

Brown Donald W., 2000, A hot dry rock geothermal energy concept utilizing supercritical CO_2 instead of water. Proceedings of the Twenty-Fifth Workshop on Geothermal-Reeservoir Engineering, Stanford University, Citeseer, 233-238.

Chen Shiwan, Chunhe Yang & Guibin Wang 2017. Evolution of thermal damage and permeability of Beishan granite. *Applied Thermal Engineering*, 110**,** 1533-1542.

Chen L, JF Liu, CP Wang, J Liu, R Su & J Wang 2014. Characterization of damage evolution in granite under compressive stress condition and its effect on permeability. International Journal of Rock Mechanics and Mining Sciences, 71, 340-349.

IRENA 2019a. Renewable capacity statistics 2019. Abu Dhabi: International Renewable Energy Agency (IRENA).

MIT-led Interdisciplinary Panel 2006. The future of geothermal energy: Impact of enhanced geothermal systems (EGS)

on the United States in the 21st century. Geothermics, 17, 881-882.

M Darot & T Reuschlé 2000. Acoustic wave velocity and permeability evolution during pressure cycles on a thermally cracked granite. *International Journal of Rock Mechanics and Mining Sciences,* 37**,** 1019-1026.

Lu Shyi-Min 2018. A global review of enhanced geothermal system (EGS). Renewable and Sustainable Energy Reviews, 81, 2902-2921.

Correlations for undrained shear strength and Over Consolidation Ratio for cohesive alluvial deposit at Kelani valley using laboratory tests and piezocone tests

S.H.S Jayakody & R.M.S. Fernando
National Building Research Organisation, Sri Lanka

ABSTRACT: Finding reliable parameters for undrained shear strength and consolidation parameters is a challenge for the geotechnical engineers worldwide. Although laboratory and in situ tests are the most common method of obtaining design parameters for soils, one cannot overlook the fact that significant amounts of cost and time are associated with carrying out such tests. Hence, it is quite common to adopt correlations to obtain design parameters. A significant amount of field and laboratory testing data are available for alluvial soils along the Kelani River in Sri Lanka. The available data includes results of borehole SPT testing, piezocones, and extensive laboratory testing. The aim of this study is to evaluate and discuss the applicability of the existing correlations on undrained shear strength parameters and Over Consolidation Ratio (OCR) for cohesive soils in this region. This may provide assistance on geotechnical designing work in the Kelani Riverbanks or sites which comprise similar alluvial profiles.

1 INTRODUCTION

Finding appropriate undrained shear strength and consolidation parameters for cohesive soils for a particular site is a major challenge for any geotechnical engineer. In terms of achieving the above objective, generally engineers are faced with the following difficulties:

(a) Laboratory testing of undisturbed samples
- Variability of sample quality i.e., soil disturbance during sampling (LaRochelle et al., 1981), which causes results to be erroneous and scattered.
- Differences in values obtained from different types of laboratory tests (Leroueil et al., 1983), which are not always representative of in-situ soil behavior.

(b) Limited number of tests
- Limited number of laboratory tests and/or in situ tests carried out for a given project because of cost and time constraints.

(c) Applicability of in-situ tests

Very few in-situ tests can directly provide undrained shear strength and consolidation parameters. Therefore, correlations are adopted to provide such parameters but generally they are found to give a wide range because of uncertainties involved in such tests (Lunne et al., 1997). Therefore, there is a need for continuous feedback of data from local experience to confirm, validate, and even modify the existing correlations.

The aim of this study is to evaluate and modify the available cone penetration tests with pore pressure measurement (CPTu) correlations on undrained shear strength (c_u) parameters and one-dimensional consolidation parameter, viz. Over Consolidation Ratio (OCR) for saturated cohesive soils found in a particular area, viz., the alluvial soils in the Kelani Riverbanks. Findings of this study should provide assistance to future designers who may work in the Kelani Riverbanks or similar sites which comprise similar alluvial profiles. In this regard, authors discuss the results obtained from SPT testing, CPTu, and extensive laboratory testing. As such, with the comparison of above results, the best approach to use CPTu correlations is determined using available correlations in the literature. Further, if any modifications are to be needed for the existing correlations to be applicable to other sites of similar nature, are also discussed.

2 INVESTIGATED SITE

Detailed investigations were carried out along the river alignment, on both banks of the Kelani River, between Kaduwela and Hanwella in Sri Lanka. The ground investigation revealed that general stratigraphy of the river alignment is alluvial and composed of cohesive and granular materials or a mixture of silt, clay, sand and gravel, underlain by a variable thickness of residual soils, which in turn is underlain by bedrock. Further, cohesive

alluvium consisting of varying amounts of decomposed and partially decomposed organic matter and undecomposed wood/timber of blackish dark grey colour were also seen. It is distinct that the formation of most of the cohesive alluvial deposit was due to the suspended fine clay, silt and organic material in high energy water flows during heavy rainy seasons.

3 FINDING OF THE STUDY

The study included the following tests:

- Unconsolidated Undrained (UU) triaxial tests
- 1D Consolidation tests
- Piezocone tests with porewater pressure measurement (CPTu)
- Natural Moisture Content
- Liquid Limit (LL) and Plastic Limit (PL)

3.1 Undrained shear strength from UU triaxial tests

The results of 16 UU triaxial tests and index property tests were used in this study. Table 1 summarizes the results obtained. The tests were carried out on "undisturbed" cohesive soil samples from the alluvial profile. All tests were carried out on 70 mm diameter specimens. Accuracy of the results obtained from the UU triaxial tests to ascertain the maximum past pressure or pre-consolidation pressure (p_c') was checked with the correlation of $c_u/\sigma'_v = 0.22$ for Normally Consolidated (NC) and $c_u/p'_c = 0.22$ for over consolidated (OC), respectively, as reported by Mesri (1989), for confirmation, where σ'_v is the effective overburden pressure.

Most of the results shows that (Table 1), soil behaves as NC or slightly over consolidated (SOC) generally confirms to what Mesri (1989) proposed while the results of soil behaving as over consolidated (OC) differ greatly from what Mesri (1989) proposed (i.e., 0.22 p'_c). It might be that the p'_c values obtained from oedometer are influenced by sample disturbance. As the sample disturbance increases, the p'_c value decreases due to de-structuring of the samples during sampling and preparation. Generally, one possible sample disturbance that could occur in organic soils for NC/SOC or OC is due to gas exsolution in the pore water which result in the reduction of the p'_c value (Hight et al., 2000).

3.2 Undrained shear strength from CPTu

Several CPTu tests have been performed at the site using a l0 cm^2 probe. The value of c_u estimated using corrected cone resistance (q_t) is one of the most important empirical approaches in the interpretation of CPTu results (Lunne et al., 1997). Hence, in this study, the authors' focussed on the above empirical approach to estimate c_u i.e., using the following equation (1):

$$c_u = \frac{q_t - \sigma_{vo}}{N_{kt}} \quad (1)$$

where N_{kt} is an empirical cone factor

As per the above equation, the use of an appropriate cone factor is vita. In this study, the UU triaxial test was used as the reference test to calibrate N_{kt} value.

Apart from the above approach, the authors also considered estimating C_U using pore pressure response in CPTu test results. This aspect had been developed based on cavity expansion theory. A number of relationships have been proposed between excess pore pressure Δu and c_u (Vesic 1972; Campenella et al., 1985). The equation (2) has the form of

$$c_u = \frac{\Delta u}{N_{\Delta u}} \quad (2)$$

where $\Delta u = u_2 - u_0$

3.3 Calibration of cone factor with UU triaxial test

The results of UU triaxial tests were used together with CPTu records from the site to calculate values of N_{kt} (hereinafter it is referred to as N_{Ktuu}) for very soft to stiff cohesive alluvium deposit at Kelani Valley region. The values of N_{ktuu} are plotted on the correlation suggested by Stark and Delashaw (1990) for non-fissured, NC to SOC clay, in Fig. 1. It shows that the cone factor ranges from 10 to 24 with decreasing OCR and also has an average value of approximately 17. However, in the study carried out by Stark and Delashaw (1990), it shows that the cone factor ranges from 8.5 to 16.5, with an average value of approximately 12. Also, the resulting cone factor (N_{ktuu}) appears to be independent of plasticity index (PI) except for OC deposits, even though a clear trend is observed of increasing cone factor with PI in the correlation suggested by Stark and Delashaw (1990) as shown in Fig.1.

Table 1. Summary of the results

No	MC/LL/PI	Soil type	State	SPT-N	σ'_v (kPa)	p'_c (kPa)	c_u (kPa)	
							UU triaxial test	Mesri (1989)
1	64/59/25	CM	OC	5-50	69	100	57	22
2	59/50/18	MC	NC/SOC	2	99	-	20	22
3	63/-/NP	CM	OC/ Dense	2-6	87	90	65	20
4	44/-/NP	CS	NC/SOC	1-5	162	140	56	36
5	45/49/20	CM	NC/SOC	2-4	109	90	21	24
6	43/-/NP	CM	NC/SOC	0-1	92	58	15	20
7	31/-/-	CG	OC	8-50	132	-	106	-
8	47/49/15	CM	NC/SOC	3-4	112	130	54	29
9	46/56/15	CM	NC/SOC	3-11	124	-	26	27
10	58/76/34	CM	NC/SOC	3-10	180	-	38	40
11	31/50/22	CM	OC	3-10	193	-	91	-
12	46/52/23	MC	NC/SOC	2-3	107	82	24	24
13	34/50/14	CM	OC	3-10	121	-	170	-
14	33/-/-	CM	OC	6-16	161	-	79	-
15	22/37/18	CM	NC/SOC	4-5	90	82	17	19
16	32/44/15	CS	OC	8-10	82	130	110	30

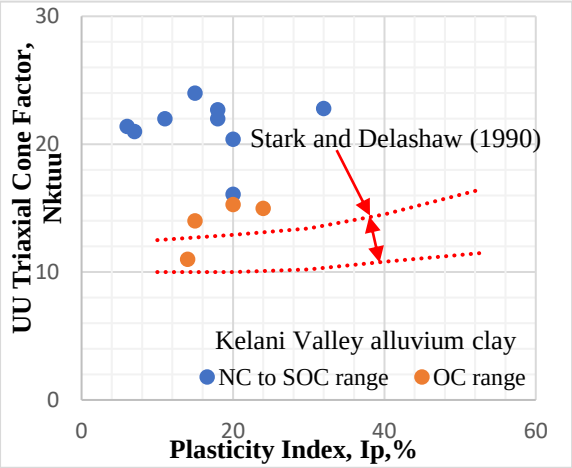

Fig. 1. Cone factor N_{ktuu} versus plasticity index

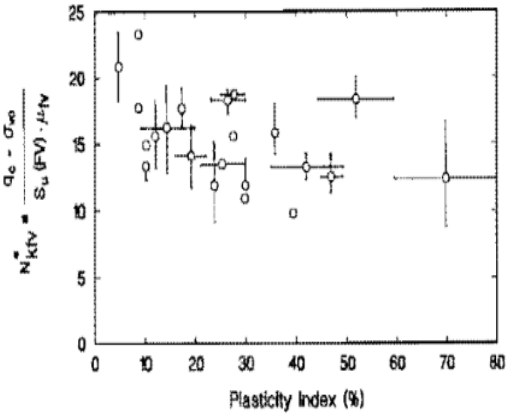

Fig. 2. Previously published corrected field vane - cone factors (after Lunne and Kleven, 1981 and Meigh, 1987)

This reason could be attributed to the fact that the correction factor between the measured UU triaxial test result and mobilized c_u could be unity. For instance, the authors calibrated the measured UU triaxial results, except for OC and highly OC soil, with the method proposed by Mesri (1989) and as a result the authors found the UU triaxial results to be reliable for the NC and SOC deposits.

The results of the above study fit well with the study carry out by Lunne and Kleven (1981) and Jamiolkowski et al. (I982) for very soft to medium clays where the cone factor was based on c_u measured using a field vane shear test. They found that, if the vane shear strength values are corrected using the correction factor as proposed by Bjerrum's (1972), the cone factor is independent of PI.

As shown in Fig. 2, the cone factor values are between 8 and 24, with an average of approximately 15. It is found that , even though the upper limit is similar, the lower limit is somewhat varies in both studies. The lower limit is generally considered as OC behaviour and hence it could be influenced by the uncertainty in interpreting cone measurements in them (Lunne et al., 1997). According to these facts, the average value could be similar in both studies. However, it should be noted that, the cone factor increased with PI, even when vane shear correction factor was applied in some of the previous studies, (Aas et al., 1986; Hamza et al., 2005). Hence, further studies are recommended to make a strong conclusion in this regard. OC soil was discarded due to uncertainty in interpreting cone measurements. If only NC to SOC results are selected, the cone

factor ranges between 15 and 24 with an average value of approximately 19.

It is understood that there is uncertainty with the accuracy in q_t in a few tests for the very soft clays. For instance, one example is where q_t was relatively high, even though in soft clay. Hence, in these circumstances, the authors used the Equation (2) with the excess pore water pressure as recommended by Lunne et al. (1997) to estimate the cone factor. Further, the authors used this equation for NC or SOC deposits where the excess porewater pressure was greater than its static porewater pressure. It was found that the cone factor, $N_{\Delta u,}$ is in the range of 5–12 which is different to the range of 7–10 proposed by Lunne et al. (1997). The possible reason for this lower limit could be the reduction of CPTu saturation ascribed to the cone passing through a non-cohesive layer, or over consolidated layer (Lunne et al., 1997).

3.4 Pre consolidation pressure from laboratory consolidation tests

The results of about 20 consolidation tests in alluvial soils were used in this study. Also, index property tests have been carried out each "undisturbed" sample. However, due to uncertainties in the recovered laboratory test results and other reasons pointing to their validity, only 12 tests were selected for the current study.

It is noted that both σ'_v is the effective vertical stress and σ_v is the total vertical stress, could be estimated from the soil profile assuming soil unit weight. OCR is the ratio of σ'_v/p'_c which indicates the state of consolidation. This assessed value could be checked against values obtained using empirical relationships with MC (moisture content) and LL (liquid limit) obtained from the investigation. For instance, for specimen No 1, OCR is assessed to be almost 1 and the soil state therefore would be NC or SOC. Further, with the MC (65%) and LL (58%) values, it can be decided whether the soil will behave as NC or SOC soil. The results of the consolidation tests, index property tests and more discussion can be found in Jayakody and Fernando (2021).

3.5 Pre consolidation pressure (p'c) from CPTu Tests

To estimate p'_c or OCR using CPTu, the most common and widely used correlations are $p'_c=k(q_t-\sigma_{v0})$ or $OCR=k(q_t-\sigma_{v0})/\sigma'_{v0}$ (Lunne et al., 1997). Hence, in this study, the authors' focused on finding a reliable k value which could be applicable to these soils. According to Robertson (2012), k could vary widely, in the range of 0.14 to 0.50 for the normalized cone resistance (Q_t) of the range of 5 to 20. Hence, it is understood that k is dependent on Q_t. As suggested by Lunne et al. (1997), it can be assigned an approximate estimate of OCR using the following equation:

$$Q_t = \frac{(q_t-\sigma_{v0})}{\sigma'_{v0}} \quad (3)$$

Where Q_t is in the range of 2.5–5.0 depending on PI.

For NC clay, Q_t ranges in the order of 2.5 to 5.0 while if a deposit has a Q_t larger than this range, the deposit is like to be over consolidated. Majority of the results is found to be NC to SOC state. Hence, a reliable correlation for NC to SOC range is more appropriate for this study. In confirmation of the NC to SOC state with CPTu results the normalized cone resistance suggested by Lunne et al. (1997) is very useful. Accordingly, the soil state of each specimen as found based on laboratory tests, have been confirmed as per the approximate evaluation of OCR as suggested by Lunne et al. (1997). Also, Robertson (2012) suggested that, k is dependent on sleeve friction ratio, F_r *where* $F_r=f_s/(q_t-\sigma_{v0})$. The empirical constant (k) calculated based on the data from the laboratory and CPTu tests in this study are plotted versus F_r which is calculated using the data from CPTu in Fig.3 (Jayakody and Fernando (2021)). It is noted that, OC range in the graph has been considered for the normalized resistance of specimens (Q_t)>6.6 for this study.

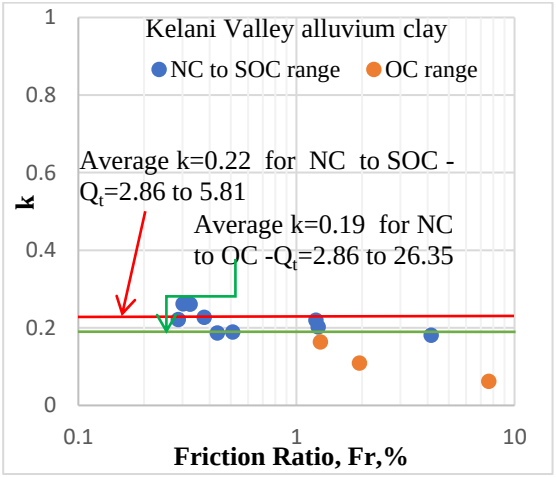

Fig. 3. Calculated empirical constant k, for the data in laboratory and CPTu tests in this study

It shows that the average *k* is about 0.22 for soil which behaves as NC to SOC range or very soft to stiff cohesive soil (i.e., *Qt* of the order of 2.86 to 5.81) while *k* is about 0.19 for all soil (i.e., NC to OC). It seems that generally *k* slightly increases with decreasing F_r as predicted by Robertson (2012). However, according to the study carried out by Hamza and Shahien (2013), *k* slightly increases with F_r. Hence, further studies need to be carried out to make a strong conclusion in this regard as well. More detailed discussion can be found in Jayakody and Fernando (2021).

The pore pressure measured during cone penetration tests could be used to find the stress history or OCR of a cohesive soil deposit. Finding a reliable OCR value based on pore pressure is very useful particularly, in a very soft soil deposit. For instance, it would be a difficult task to find OCR with the use of q_t, as uncertainty of finding q_t in soft soil deposit (Lunne et al. 1997). However, there are many disadvantages such as:

- Low pore pressure readings due to the reduction of CPTu saturation as a result of passing through a non–cohesive layer or over consolidated layer (Lunne et al. 1997)
- Pore pressure (u_2) value could be zero or negative in some very stiff and heavily fissured clay

These disparities could lead to erroneous values of OCR. Therefore, even though a number of relationships between OCR and various forms of normalized pore pressure have been proposed, none of them appears to be valid for all soils. Also, Campanella and Robertson (1988) stated that "a review of published correlations shows that no unique relationship exists between pore pressure ratio and OCR, because the pore pressure measured at any location is also influenced by clay sensitivity, pre-consolidation mechanism, soil type and local heterogeneity".

The common correlation provided in literature is (Mayne and Holtz,1988)

$$\sigma'_p = k_{epp}\,(u_2 - u_0) \qquad (4)$$

where k_{epp} is the excess pore pressure constant.

Based on worldwide data, Larson and Mulabdic (1991) obtained values ranging from 0.3 to 0.4 for k_{epp}. They also stated that k_{epp} varies with LL and OCR. Mayne and Kulhaway (1995) proposed a k_{epp} value of 0.40 only for "champlain" clays and 0.54 for worldwide data. Demers and Leroueil (2002) showed that average k_{epp} is about 0.49.

The empirical constant (k_{epp}) calculated from laboratory data and the pore pressure (u_2) from CPTu tests in this study are plotted against LL obtained from index tests in Fig.4. It is noted that the specimens which include NP (non-plastic fines) are ignored from the plot as they show low u_2 values. Fig. 4 shows that the average k_{epp} is about 0.42 for Kelani Valley very soft to stiff cohesive soil (i.e., Q_t of the order of 2.86 to 26.4) (Jayakody and Fernando (2021)).

The correlation factor of 0.42 is very close to what Mayne and Kulhaway (1995) suggested only for "Champlain" clays and the upper limit of what Larson and Mulabdic (1991) found for the worldwide data in their study. However, the statement made Larson and Mulabdic (1991) has to be further studied as this plot does not show a clear trend that k_{epp} varies with LL.

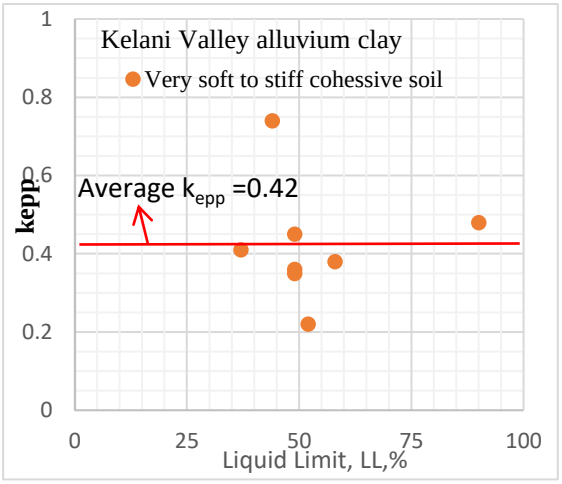

Fig. 4. Calculated empirical constant k_{epp}, for the data in laboratory and CPTu tests in this study

4 CONCLUSIONS

The following conclusions are made based on the study.

- The cone factor, N_{kuu}, relating the UU triaxial test to the cone tip resistance of the CPTu, ranges from 10 to 24 with decreasing OCR and also has an average value of approximately 17 for Kelani Valley very soft to stiff, saturated clays. If only NC to SOC soil is selected, the cone factor is within the range of 15 to 24 with an average value of approximately 19.

- The cone factor, N_{kuu}, appears to be independent of PI except for soil having considerably high OCR.
- Calibration of c_u with UU triaxial tests is possible using the method proposed by Mesri (1989) for NC to SOC deposit.
- The range of cone factor, using excess pore water pressure ($N_{\Delta u}$), is of the order of 5 to 12 for the NC or SOC deposit where the excess porewater pressure indicates to be greater than its static pore water pressure.
- The average k in the mostly used correlation in $p'_c=k(q_t-\sigma_{v0})$ or OCR= $k(q_t-\sigma_{v0})/\sigma'_{v0}$, could be taken to be about 0.22 for soil which behave as NC to SOC range or very soft to stiff cohesive soil (i.e., Q_t of the order of 2.86 to 5.81) while k is about 0.19 for all soils (i.e., NC to OC) found in Kelani Valley.
- The value k slightly increases with decreasing F_r as predicted by Robertson (2012). However, according to the study carried out by Hamza and Shahien (2013), k slightly increases with F_r. Hence, further studies need to be carried out to make a strong conclusion in this regard as well.
- The average empirical constant of (k_{epp}) 0.42 in correlation $\sigma'_p= k_{epp}\,(u_2- u_0)$, could be used for soil which behaves as Kelani Valley very soft to stiff cohesive soil (i.e., Q_t of the order of 2.86 to 26.4). However, the statement made by Larson and Mulabdic (1991), needs to be further studied as the plot of k_{epp} versus LL does not show a clear trend that k_{epp} varies with LL.

ACKNOWLEDGEMENTS

The authors acknowledge officials of National Building Research Organisation and Engineering Laboratory Services for their support on this study.

REFERENCES

Aas, G., Lacasse, S., Lunne, T. & Hoeg, K. (1986), Use of in situ tests for foundation design on clay, Proc. of ASCE Specialty Conference, In Situ '86: Use of In Situ Tests in Geotech. Eng., pp. 1-30.

Bjerrum L. (1972), Embankments on soft ground state-of-the-report, Proceedings of the ASCE specialty conference on performance of earth and earth-supported structures. Lafayette, Vol. 2: 1-54.

Campenella RG et al. (1985), Recent developments in in situ testing of soils, In: Proceedings of the XI international conference on soil mechanics and foundation engineering, San Francisco, pp 849–854

Campanella, R.G. and Robertson, P.K. (1988), Current status of the piezocone test, Proceedings of the International Symposium on Penetration Testing, ISOPT-1, Orlando, 1, 93-116, Balkema Pub., Rotterdam.

Demers, D. and Leroueil, S. (2002), Evaluation of pre-consolidation pressure and the over-consolidation ratio from piezocone tests of clay deposits in Quebec. Canadian Geotechnical Journal 39: 174-192.

Hamza, M., Shahien, M., Ibrahim, M.H.Z. (2005), Characterization and undrained shear strength of Nile delta soft deposits using piezocone, Proc. 16th International Conference on soil mechanics and geotechnical engineering, Osaka, Japan.

Hamza, M. and Shahien, M. (2013), Compressibility parameters of cohesive soils from piezocone, Proc. 18th International Conference on soil mechanics and geotechnical engineering, Paris.

Hight, D. W., Hamza, M. M. & El Sayed, A. S. (2000), Engineering characterization of the Nile Delta clays, Proc. of Intern. Symposiam. Yokohama.

Jamiolkowski, M, Lancellotta, R., Tordella, L., and Battaglio, M. (1982), Undrained strength from CPT, Proceeding of 2nd European Symposium on Penetration Testing, Amsterdam, pp. 599-606.

Jayakody, S.H.S. & Fernando, R.M.S. (2021), Correlations for over consolidation ratio for cohesive alluvial deposit at Kelani Valley (Kaduwela to Hanwella) using laboratory tests and piezocone tests, Proceedings of Annual Sessions of Institute of Engineers, Sri Lanka.

LaRochelle, P., Sarrailh, J., Tavenas, F., Roy, M., & Leroueil, S. (1981), Causes of sampling disturbance and design of a new sampler for sensitive soils, Canadian Geotechnical Journal, 18(1), 52-66.

Larson, R., & Mulabdic, M. (1991), Piezocone tests in clays, Swedish Geotechnical Insititute report no.42, Linkoping, 240p.

Leroueil, S., Tavenas, F., & Le Bihan, J.P. (1983), Propriétés caractéristiques des argiles de l'est du Canada, Canadian Geotechnical Journal, 20(4): 681-705.

Lunne, T., P.K. Robertson, P. K. & Powell, J. J. M. (1997, Cone Penetration Testing. Blackie Academic and Professional- London, 312 p.

Mayne, P.W. and Holtz, R.D. (1988), Profiling stress history from piezocone soundings, Soils and Foundations, 28(1), 16-28.

Mayne, P.W. and Kulhaway, F.H. (1995), First order estimate of yield stresses in clays by cone and piezocone - CPT' 95, International Symposium on Cone Penetration Testing, Linkoping, 4-5 October 1995, Swedish Geotechnical Society, Report 3:95; pp 221-226.

Mesri, G. (1989), A re-evaluation of su(mob)=0.22 σ'_p using laboratory shear tests, Canadian Geotech. J., Vol. 26, No. 1, pp. 162-164.

Robertson P.K. (2012) "Interpretation of in-situ tests-some insights". Proc.4th Int. Conf. Geot. & Geoph. Site Characterization, ISC'4, Brazil, 1, pp 1-22.

Stark, T.D. & Delashaw, J.E. (1990), Correlations of unconsolidated-undrained triaxial tests and cone penetration tests, Transportation Research Record Proceeding No. 1278: 96-102.

Vesic, A. S. (1972), Expansion of Cavities in Infinite Soil Mass, Journal of the Soil Mechanics and Foundations Division, ASCE, 98, 265-290.

Use of a novel graphene-based geotextile under hydro-thermo-mechanical loading in pavement applications

H.T. Senadheera
Department of Civil Engineering, Monash University, Clayton Campus, VIC 3800, Australia

Prof. A. Bouazza
Department of Civil Engineering, Monash University, Clayton Campus, VIC 3800, Australia

Prof. J. Kodikara
Department of Civil Engineering, Monash University, Clayton Campus, VIC 3800, Australia

D. Gibbs
Technical, Research and Innovation, Geofabrics Centre for Geosynthetic Research, Innovation & Development, QLD 4214, Australia

ABSTRACT: Pavement reliability modelling and maintenance operations are mostly dependent on information provided by in-situ monitoring methods integrating sensors within the road. Additionally, vehicle volume, mass and speed surveys are also crucial for effective traffic management and to prevent fatigue damage caused by vehicle overloading. However, most of the existing methods can only provide information on discrete locations in the pavement, while also being destructive to the pavement being monitored. In the current research, a novel graphene-coated geotextile is explored for potential use as a distributed sensor for applications involving hydro, thermal and mechanical loading in pavements. Currently used for leak detection purposes in containment facilities, this project will extend its use, by investigating its feasibility to detect pavement response and damage, especially in relation to excessive deformation and moisture.

1 INTRODUCTION

Various pavement distresses such as cracking, rutting, wear and deflection are important indicators of pavement performance. These distresses can occur in pavements due to vehicle and environmental loading, which includes temperature and moisture effects. Therefore, monitoring pavement hydro, thermal and mechanical loading is crucial in pavement reliability modelling and maintenance operations. In-situ monitoring methods integrating sensors within the road are being used to measure real-time pavement response such as stress, strain, deflection, temperature and moisture content. In addition, the monitoring of mechanical loading is important for vehicle management procedures to ensure pavement longevity by controlling increased distress caused by vehicle overloading. Traffic volume, vehicle mass and speed surveys are thus important for effective management of traffic and to prevent fatigue damage caused by vehicle overloading as well. However, the current methods in practice lack the capability of providing spatially-continuous information on pavement hydro, thermal and mechanical loading.

Geotextiles have various applications in geotechnical structures such as filtration, separation, reinforcement and drainage in landfills, embankments and roads. A typical road formation structure has several components where geotextiles play an important role i.e., separation of the in-situ material and imported road base, reinforcement of pavement layers, subsurface and road-side drainage and in geotextile reinforced seals (GRS). In the current project, a novel graphene-based geotextile is evaluated for use in road infrastructure. Graphene has high electrical conductivity and to make the geotextile conductive, a layer of graphene has been applied on one side of a geotextile. Manufactured by the industry partner Geofabrics, this geotextile is currently used in double lined systems in waste, containment and landfill applications for leak detection purposes. The current project will extend its use to applications involving hydro, mechanical and thermal loading, focused on detecting pavement response and damage, especially in relation to excessive moisture (such as in flooding) and excessive deformation (such as rutting and sinkhole detection) in pavements. One of the potential advantages of this is that geotextiles are already used in pavements and if it can also be used as a sensor, then its use is significantly enhanced.

2 CURRENT PAVEMENT MONITORING METHODS IN PRACTICE

2.1 *In-situ Monitoring Methods*

In contrast to pavement evaluation methods, in-situ monitoring methods allow continuous examination of the road health condition by integrating sensors within the road. These sensors enable real-time measurement of pavement response such as stress, strain, deflection, temperature and moisture content at different pavement layers.

Horizontal asphalt strain gauges (H-gauges) and vertical strain gauges are two types of strain sensors that are usually embedded at the bottom of the bituminous layer, where large strains occur. Vertical asphalt strain gauges require drilling a hole for installation to keep the sensor in place. Vertical asphalt strain gauges have lower survival rate during installation compared to that of H-gauges, due to high temperatures and vibrations during compaction (Wang et al., 2012). Fiber optics (FO) is an emerging technique for strain measurement that has properties of small size, flexibility and resistance to electromagnetic interference. There are three main types of sensing arrangements in FO; discrete, quasi-distributed and distributed. Fiber Bragg Grating (FBGs) are used for quasi-distributed measurements while Distributed Fiber Optics (DFO) allow continuous and real-time measurements at each point along the length of the fiber optic cable. Since FBG technologies can only provide local strain measurements, they are only appropriate for monitoring specific road sections, while DFOs can monitor across a larger portion of the structure. However, FOs are expensive while also the installation is strenuous and delicate (Li et al., 2004).

The distresses and delamination occurred in the pavement are strongly dependent on excessive temperature and moisture content effects. Therefore, it is important to continuously monitor moisture and temperature within the pavement for accurate representation of its mechanical behaviour. Thermocouples and TDR probes respectively are the most commonly utilized means of temperature and moisture measurement.

2.2 *Monitoring Mechanical Loading on Pavements*

In particular, monitoring of mechanical loading on pavements, is crucial for establishing vehicle management procedures to prevent structural overloading and for effective traffic management. In other words, according to the fourth power law in pavements, an overloaded heavy vehicle can cause several times greater damage to the pavement than a properly loaded vehicle. Thus, traffic surveys that include vehicle volume, vehicle mass and speed surveys provide important information for traffic management and control.

To carry out traffic volume surveys, manual and automatic counting methods are used by Australian road agencies. Pneumatic tubes and piezoelectric cables laid on the pavement surface as axle detectors for automatic axle counts. Pneumatic tubes are susceptible to damage and have shorter life spans, thus are used primarily for short-term traffic surveys. In contrast, piezoelectric cables are more durable, however, they are more expensive. The most accepted and widely used vehicle count technology by Australian road agencies is inductive loop. In general, inductive loops are less-costly and reliable since they are well-developed and also well-known to engineers. However, they are destructive to the pavement and thus their installation deteriorates the pavement (Peeta & Zhang, 2020).

Weigh-in-Motion (WIM) systems are being used for unbiased estimates of vehicle weights as they allow for the weighing of vehicles in motion without the need to stop them or any additional constraints on speed. The reliability of WIM systems is highly dependent on the accuracy and low cost of the axle detection sensors and their installation (Austroads, 2020). WIM systems are able to provide detailed vehicle information such as weight and speed while the vehicle is in motion, which is considered to be its most promising feature. However, they are currently unable to provide sufficient accuracy in vehicle weight measurements for tolling and fee payment purposes (Koniditsiotis, 2000). There is no standard Australian specification or method to evaluate the accuracy of WIM systems, which adds to the difficulties in its installation, calibration, operation and maintenance (Austroads, 2020).

3 GRAPHENE

Graphene defined by its atomic structure, is a quasi-two-dimensional monolayer of Carbon atoms which are arranged in a hexagonal lattice, forming a 2D honeycomb lattice plane. Graphene has three strong sigma-bonds in each lattice and one pi-bond which provides electron that move freely with little interference, resulting in high electrical conductivity. Although the thickness is only around 0.35 nm, the carbon structure of graphene is very stable, thus having a very high mechanical strength, which is about 100 times the strength of steel of same thickness (Zhen & Zhu, 2018).

Due to the aforementioned attractive properties, graphene becomes a promising material for the function of sensing in high-sensitivity sensing systems. For example, under mechanical strain, the electronic structure of graphene would be altered

such that a bandgap is introduced into the material, resulting in significant electro-mechanical behaviour, i.e. piezo-resistive effect (Yang et al., 2018). Due to high flexibility, sensitivity and working range of graphene-based strain sensors compared to that of traditional metal-based or silicon-based strain sensors, many strain sensors have been fabricated for graphene transferred onto flexible polymer substrate (Li et al.,2012).

4 GEOTEXTILES

Geosynthetics are synthetic materials used in civil engineering problems, which have different types such as, geogrids, geotextiles, geomembranes, geonets, geosynthetic clay liners (GCL), geocells and geocomposites. Geotextiles fall into the group of permeable fabrics and are used in different geotechnical applications such as filtration, separation, drainage and reinforcement. The most common types of synthetic fibers used for manufacture of geotextiles are polypropylene, polyester and polyethylene (Austroads, 2009). Geotextiles have two main categories named woven or non-woven, which are further divided according to the manufacturing method and synthetic fibers used etc. Woven geotextiles are manufactured by weaving warp threads in the direction of production with weft threads at right angles, which are usually yarns, filaments or tapes. In contrast, non-woven geotextiles are made of randomly-oriented fibers that are bonded by mechanical, thermal or chemical methods. Nonwoven geotextiles are typically used for filtration, separation and drainage purposes whilst woven geotextiles are generally used for reinforcement.

With the identified scope of this project, only non-woven geotextiles have been further explained.

4.1 *Non-woven Geotextiles*

A nonwoven geotextile is produced by linking filaments together using one of the bonding processes i.e., heat bonding, needle punching or resin bonding. Since the fibers are not bonded together by weaving, non-woven geotextiles have random fiber orientation, which is its most prominent feature. However, the direction in the fabric parallel to the direction which the textile followed in the manufacturing process is called the 'Machine Direction' (MD), whilst the direction perpendicular to the MD is called the 'Cross-Machine Direction' (CMD). Pertaining to its random fiber orientation, nonwoven geotextiles have lower tensile strength but higher elongation, thus higher damage resistance, compared to woven geotextiles. The three main functions of nonwoven geotextiles are separation, filtration and drainage in geotechnical structures such as pavements, embankments, retaining walls, drainage systems and landfills.

4.2 *Geotextiles in a Road Formation*

As shown in Fig. 1, non-woven geotextiles can be used to separate the in-situ subgrade and the imported road base, so that the strength of the base material is not deteriorated by the mixing of subgrade fines into the base aggregates. Thus, the structural integrity of the pavement can be maintained with the use of geotextiles as a separator. As the aggregate layers are laid to create the road formation, geosynthetic reinforcement layers can be used to increase strength of the road and to reduce the thickness of aggregate layers required.

Geotextiles can provide functions of filtration and drainage in subsurface and roadside drainage systems using its permeability properties. Nonwoven geotextiles can be used where it needs to allow the passage of water but not fine soil particles across its plane, to prevent the migration of fines into water transmitting drains and also in situations where it needs a carrier to transmit excess water from the pavement (Austroads, 2009). Needle-punched, nonwoven geotextiles are used in strain alleviating membrane (SAM) and strain alleviating membrane interlayer (SAMI) applications, which are used to treat cracked pavements by slowing down the progress of reflective crack propagation to the surface of HMA layers.

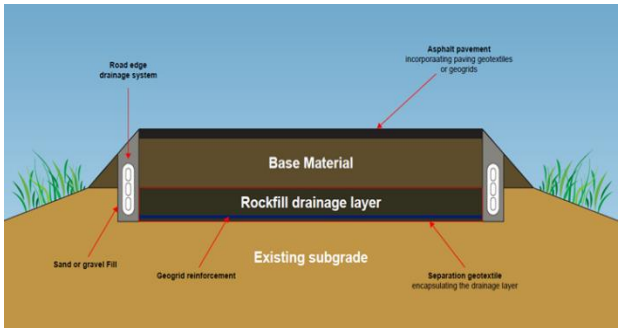

Fig. 1 Functions of geotextiles in a road formation

4.3 *Smart Geotextiles*

Recently, new technologies have been developed to incorporate sensing ability to geosynthetics themselves. Fiber optic sensor based on FBG is the first sensor to be integrated with geotextiles for strain measurement and it was commercialized as 'Geodetect' by Tencate. Originally developed in the 1990s as an early warning system for the French Railway Service (SNCF) to detect sinkholes in train circulating areas, the 'Geodetect' system was then used to monitor strains of geosynthetic structures such as embankments, railways and roads (Robinet, Voet,

Nancey, & Briançon, 2006). The optical technology of FBGs is used in this system and the optical fibers are attached with the geotextile fibers in the fabrication process itself, which eliminated the issue of installation in traditional strain sensors. Nevertheless, this technique can only provide strain information at finite number of points on a fiber optical cable, which is not suitable for monitoring large areas. In addition, the high cost of FBGs and the fragile nature of fiber optics have limited vast application of 'Geodetect' for monitoring (Wu et al., 2020).

Conductive textiles using the same principle in strain gauges, i.e. piezoresistivity, have been developed as pressure or strain sensors, that are capable of measuring strains over large areas. (Hui et al., 2006). 'Velostat' is one such commercially available pressure-sensitive conductive textile made with polyolefin incorporated with Carbon Black (CB) to make it electrically conductive. Taking advantage of the sensing capacity within geosynthetics, Hatami, Grady, and Ulmer (2009) pioneered in developing a 'sensor-enabled' or 'self-instrumented' geogrids, using electrically conductive fillers in geosynthetic materials that exhibit piezoresistivity. They used polymer composites filled with Carbon Black (CB) and Carbon Nanotubes (CNT) to fabricate a novel sensor-enabled geogrid (SEG), which can measure strain in geosynthetics without the use of strain gauges. Cui et al. (2018) carried out both in-isolation and in-soil laboratory tests, on sensor-enabled geobelts (SEGB) filled with CB, to study its mechanical properties and strain-sensitive conductivity. Geoconduct, Conductive Sensom Layer (CSL) and Geovolt are such commercially available conductive geomembranes, but only used in monitoring systems to detect and locate leaks in geomembrane-lined containment facilities and not for strain monitoring.

Graphene is an excellent electrical conductor and when deformed, its electronic structure would be altered leading to a resistance change i.e. indicating a piezo-resistive behaviour. Highly sensitive graphene-based layered percolative film (LPF) strain gauges by spray-deposition of a graphene solution, were fabricated by Hempel et al. (2012). These strain gauges presented reliable performance with low cost production and easy scalability, showing potential for structural monitoring applications. Graphene woven fabric (GWF) were embedded into polymers and were used as strain gauges on the surface of structures; these showed promising results as an economical sensing method for micro-control applications (Li et al., 2012).

A graphene coated nonwoven geotextile was fabricated and characterized for large-scale applications such as Electrokinetic Geosynthetics (EKG) in leak detection surveys and as a heating component for residential and industrial use (Kongahge et al., 2016). Geofabrics Australasia has manufactured world's first commercial conductive geotextile, utilizing IMGNE® X3 graphene technology to provide surface resistivity across the geotextile (details in Section 4.4). It has been successfully employed in integrity surveys of waste, containment and landfill lining systems for leakage location detection (Aitchison et al., 2019). Harwood et al. (2018) carried out a proof-of-concept research to examine the piezoresistive response of a graphene-coated geotextile through laboratory tests, which provided favourable results in identifying this behaviour to be used in practical Structural Health Monitoring (SHM) applications.

4.4 *Graphene-based Nonwoven Geotextile by Geofabrics*

Geofabrics Australasia has manufactured a graphene-based geotextile by coating graphene on one side of a non-woven PET geotextile, making it highly conductive. It is currently being used for liner integrity surveys i.e., electrical leak location surveys, which are an integral part of quality assurance in landfills, tailings dams and water storage facilities.

There are several methods of leak location surveys in barriers using electrical inspection, where a voltage is applied to the surface of the barrier, and if present, leaks can be detected via a closed electrical circuit forming at the leak location. To assist with the current flow, a sufficient electrolyte is needed on the opposite side of the barrier to which the voltage is supplied. Thus, water is often used when the sub-graded soil is dry or non-conductive to facilitate the inspection process (water lance/water puddle method). However, using water to wet the liner can lead to false records of the presence of leaks due to the presence of water and also can incur high installation, transport and storage costs (Aitchison et al., 2019). Therefore, as an alternative approach, conductive geotextiles have been introduced for use as a layer in multi-layer construction to test covered and uncovered geomembranes for defects. A voltage is supplied to the barrier layer, close to the conductive geotextile, and when the inspection probe is close to a defect, current will flow through the defect into the electrically conducting geotextile to form a closed circuit (Fig. 2). The graphene-based geotextile, has thus been successfully applied in several mining and waste applications as a leak detection layer due to its high conductivity achieved through the incorporation of graphene.

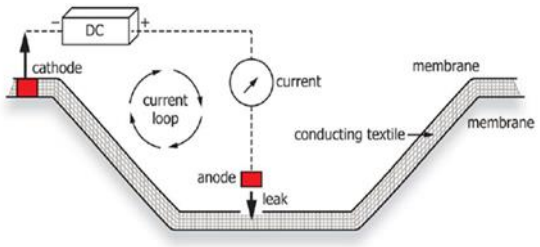

Fig.2 Schematic of leak detection with conductive geotextile (ASTM D7852-13)

5 APPLICATION OF THE GRAPHENE-BASED GEOTEXTILE IN PAVEMENTS

As explained in Section 2, there is still a lack of a monitoring method that enables determination of measurands such as strains, moisture contents etc. in a spatially continuous capacity, within the context of smart road infrastructure. Thus, the research is aimed at investigating the feasibility of the graphene-based geotextile to provide spatially continuous information on hydro-thermo-mechanical loading, when embedded in a pavement structure (Fig. 3).

5.1 *Sensing Principle in the Graphene-based Geotextile*

When an external influence, in terms of mechanical stress, temperature or moisture content, is applied on the graphene-coated geotextile, the conductive path network formed by the graphene coating undergoes deformation and distortion. This manifests as a change in electrical resistance and since graphene has high electrical conductivity, the resistance can be measured using an appropriate measurement technique. When the resistance change and the applied influence are reliably related, the graphene-coated geotextile can provide indications of the imposed influence. An appropriate field measuring technique can be employed to capture these changes in resistance in the geotextile, taking advantage of its distributed sensing capability.

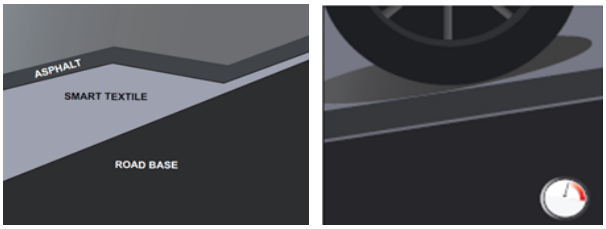

Fig. 3 Graphene- based geotextile embedded smart pavement

5.2 *Response of the Graphene-based Geotextile under Mechanical Loading*

To understand the behaviour of the graphene-based geotextile under traffic loads, the geotextile was subjected to tensile loading. Microscopic images using a digital microscope were obtained before and after deformation to explain the behaviour of the graphene connections with applied strain

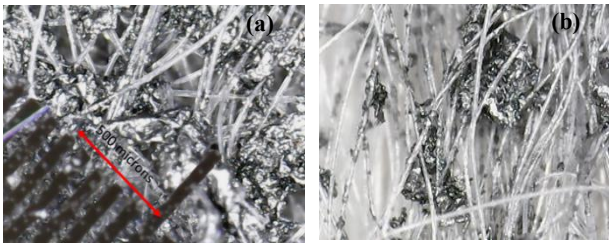

Fig. 4 Microscopic images of the graphene-based geotextile obtained from Dino-lite (200x) digital microscope. (a) Before deformation (unstrained state) (b) After failure of the geotextile specimen

As seen from Fig. 4a, the graphene coating on the geotextile is not uniform and the network of conductive paths formed by the graphene coating on the synthetic fibers of the geotextile portrays tortuosity. Pertaining to this tortuosity in the conductive paths, the conductivity/resistivity of the graphene-coated geotextile depends on the arrangement of the graphene paths through which the current flows. The conductive network of graphene is stretched, distorted and then broken with increasing induced load, which manifests as an increased resistance in the macroscopic scale (Fig. 4b). The resistance changes linearly at initial strains since the deformation of graphene connections shows a linear response (stretching only) with the applied mechanical strain. However, with further applied strain, the graphene connections start to fracture, making the resistance response non-linear and highly sensitive to strain (Park et al., 2002).

In order to investigate the material's electrical sensitivity to damage accumulation, the geotextile specimens can be subjected to cyclic tensile loading (Ku-Herrera et al., 2016). This is important to understand the reversibility of the $\Delta R/R_0$ response with applied strain, since it will be used in pavements under cyclic vehicle loading. Thus, any residual resistance after an unloading curve, might give an indication of the workability of the geotextile, particularly in a pavement scenario (Fig. 5).

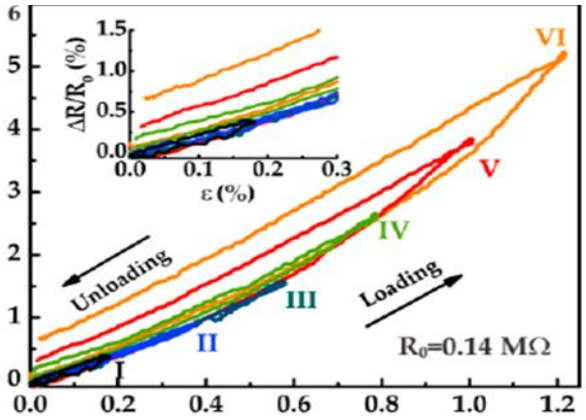

Fig. 5 Electro-mechanical response of the CFRPSs under incrementally-increasing cyclic tensile loading (Ku-Herrera et al, 2016)

6 CONCLUSIONS AND FUTURE WORK

As explained in Section 5, the graphene-based geotextile has potential to be utilized as a distributed sensor in smart road monitoring, by capturing its electrical resistance response under hydro-thermo-mechanical loading. In order to achieve this, future work is planned to be carried out to,

1. Experimentally characterize the electro-hydro-thermo-mechanical behaviour of the graphene-based geotextile and to develop preliminary analytics
2. Capture the response of the graphene-based geotextile in smart pavements using an experimentally-validated numerical model
3. Develop an appropriate field monitoring tool and to establish proof of concept for practical applications of the geotextile sensor.

It is anticipated that the outcomes from this research will provide significant benefits towards developing tools and techniques for pavement monitoring and assessment, and vehicle management of smart road infrastructure using novel sensing materials.

ACKNOWLEDGEMENTS

This research work is part of a research project (Project No IH18.07.1) sponsored by the SPARC Hub (https://sparchub.org.au) at Department of Civil Engineering, Monash University funded by the Australian Research Council (ARC) Industrial Transformation Research Hub (ITRH) Scheme (Project ID: IH180100010). The financial and in-kind support from Geofabrics, Australasia is gratefully acknowledged. Also, the financial support from ARC is highly acknowledged.

REFERENCES

Aitchison, P., Giorgio, V. and Mathieson, G., Imagine Intelligent Materials Pty Ltd, (2019). Geotextile with conductive properties. U.S. Patent Application 16/075,126.

Austroads (2009). 'Guide to Pavement Technology Part 4G: geotextiles and geogrids', Edition 1.1, AGPT04G-09, Austroads, Sydney, NSW.

Austroads (2020), 'Guide to traffic management part 3: transport and analysis methods', 4th edn, AGTM03-20, Austroads, Sydney, NSW.

Cui, X.Z., Cui, S.Q., Jin, Q., Wang, Y.L., Zhang, L. and Wang, Z.X. (2018). Laboratory tests on the engineering properties of sensor-enabled geobelts (SEGB). Geotextiles and Geomembranes, 46(1):66-76.

Harwood, C., Shepard, J. and Weishaar, A. (2018). Graphene Coated Geotextiles: A Proof of Concept. 2018 NCUR.

Hatami, K., Grady, B.P. and Ulmer, M.C. (2009). Sensor-enabled geosynthetics: use of conducting carbon networks as geosynthetic sensors. Journal of geotechnical and geoenvironmental engineering, 135(7):863-874.

Hempel, M., Nezich, D., Kong, J. and Hofmann, M. (2012). A novel class of strain gauges based on layered percolative films of 2D materials. Nano letters, 12(11):5714-5718.

Koniditsiotis C. (2000). 'Weigh-In-Motion Technology', Technical Report AP-R168, Austroads, Sydney, NSW.

Ku-Herrera, J.J., Pacheco-Salazar, O.F., Ríos-Soberanis, C.R., Domínguez-Rodríguez, G. and Avilés, F. (2016). Self-sensing of damage progression in unidirectional multiscale hierarchical composites subjected to cyclic tensile loading. Sensors, 16(3):400.

Li, H.N., Li, D.S. and Song, G.B. (2004). Recent applications of fiber optic sensors to health monitoring in civil engineering. Engineering structures, 26(11):1647-1657.

Li, X., Zhang, R., Yu, W., Wang, K., Wei, J., Wu, D., Cao, A., Li, Z., Cheng, Y., Zheng, Q. and Ruoff, R.S. (2012). Stretchable and highly sensitive graphene-on-polymer strain sensors. Scientific reports, 2(1), pp 1-6.

Park, J.B., Okabe, T., Takeda, N. and Curtin, W.A. (2002). Electromechanical modeling of unidirectional CFRP composites under tensile loading condition. Composites Part A: Applied Science and Manufacturing, 33(2):267-275.

Peeta, S., and Zhang, P. (2020). Counting Device Selection and Reliability: Synthesis Study. Joint Transportation Research Program.

Robinet, F., Voet, F., Nancey, A., and Briançon, L. (2006). Set up of a warning system integrated inside a reinforced geotextile for the survey of railway.

Wang, L., Wenjing, X., Druta, C., and Wang, D. (2012). Integration of structural health monitoring and asset management.

Wu, H., Yao, C., Li, C., Miao, M., Zhong, Y., Lu, Y. and Liu, T. (2020). Review of application and innovation of geotextiles in geotechnical engineering. Materials, 13(7):1774.

Yang, T., Zhao, X., He, Y. and Zhu, H. (2018). Graphene-based sensors, Graphene, pp 157-174.

Zhen, Z., and Zhu, H. (2018). Structure and properties of graphene, Graphene, pp 1-12.

Comparison of Different Philosophies on Design of Geosynthetic Reinforced Piled Embankment (GRPE)

H.D.S. Mithila and N.H. Priyankara
Department of Civil and Environmental Engineering, University of Ruhuna, Sri Lanka

ABSTRACT: Designing structures such as highway embankments over soft compressible soil or weak foundation soil results in many issues such as intolerable settlement, potential bearing failure and global and local instability. In order to face these issues, many ground improvement methods are in use such as wick drains, surcharge loading and gravel column etc. But among these methods Geosynthetic Reinforced Piled Embankment (GRPE) stands out due to its efficient load transfer mechanism and less construction time. In terms of design of GRPE, though there are various analytical methods, most feasible method is not yet established. Thus, this research presents a justification to obtain the best analytical method to design GRPE by performing parametric study between most commonly used analytical methods BS 8006 and New German method (EBGEO) and their results were compared with PLAXIS-2D FEM plain strain numerical simulation. Based on the analysis, it was revealed that EBGEO method is the most suitable analytical method to design GRPE since it approaches PLAXIS 2D design outputs better than that of BS 8006.

1 INTRODUCTION

Geosynthetic reinforced piled embankment (GRPE) utilizes geosynthetic reinforcement with high tensile properties, to span the clear distance between adjacent piles resulting in in-crease of efficiency of load transfer from soil to pile. The embankment load is transferred through geosynthetic reinforcement to piles ensuring negligible load is transmitted to soft soil between piles avoiding any excessive differential settlement. (kempfert et al.,1997).

Embankment load is transferred to underlying piles mainly through mechanisms of soil arching and tension membrane developed in geotextile as illustrated in Fig.1. Fluet et al.(1986), studied the effect of geogrid on the base of embankment. This study concluded that geogrid layer promoted arching process whereas if geogrid was removed no significant arching could be observed. In terms of designing GRPE, different analytical methods would provide different values for load transferred to pile, geosynthetic tension and embankment settlement when varying input parameters such as stiffness of geosynthetic reinforcement, embankment height, pile spacing, pile width stiffness soft soil directly below geogrid. Based on these contradictions, it is uncertain to state which design method is ideal for designing GRPE.

Therefore, the aim of the study is to analyze GRPE using most commonly used analytical methods BS 8006 and EBGEO and compare its results with analysis results of FEM software PLAXIS 2D.

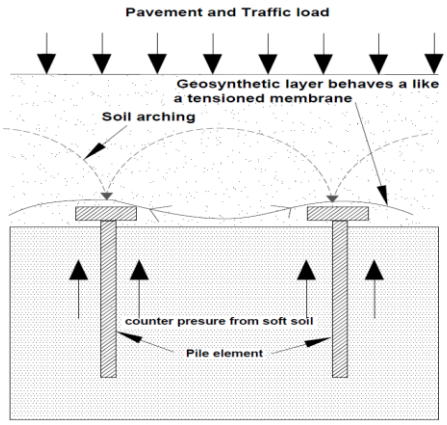

Fig. 1 Load transfer mechanism of GRPE

2 METHODOLOGY

This research is focused on analyzing and comparing the behavior of GRPE based on different design methods. Basically, two types of models were used for analysis which were axisymmetric model and plain strain model.

2.1 Axisymmetric Study

Axisymmetric model was used to model a single pile and its results were compared with Pile Dynamic Analysis (PDA) and analytical calculations. It was performed to justify the applicability of PLAXIS 2D FEM to verify analytical design methods of GRPE to validate PLAXIS 2D model for pile capacity calculations.

0+332.5 R1 pile of Matara-Beliatta section of southern express-way was modelled as reference pile as shown in Fig.2. Subsurface soil profile and relevant in-put data was obtained from boreholes and soil test reports from southern expressway project.

As illustrated in Fig.2, Precast Pile with 20.9m length and 0.5m diameter was positioned along the axis of symmetry. Bottom boundary was assumed rigid and standard fixities were used at side boundaries. Since pile diameter was 0.5m, it was defined as a column with 0.25m width. Along the pile length, interface was modelled and it was extended 0.5m below pile tip to avoid stress oscillation at the stiff corner.

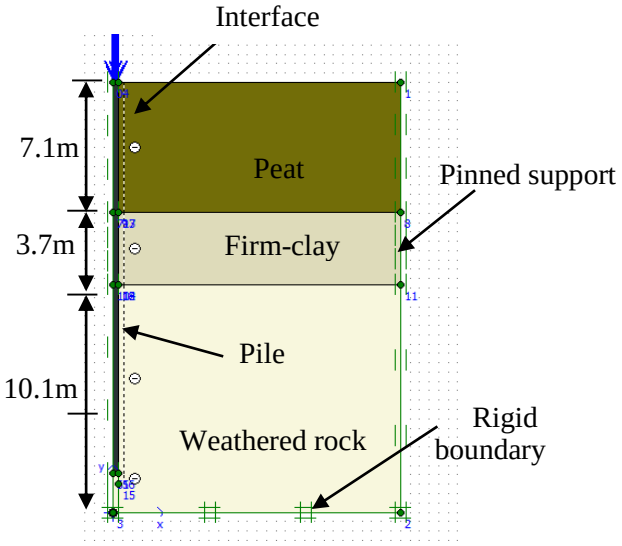

Fig. 2 Axisymmetric model of single pile analysis

Then, mesh was generated for finite element analysis. Ultimately, loading was applied iteratively until failure occurs and bearing capacity and load settlement curve were obtained as outputs. Similarly, using PDA test reports and analytical calculations load settlement curve and bearing capacity of pile was obtained for same geometry.

2.2 Plain strain Study

Plain strain model was used to model entire GRPE and perform parametric study comparing with results of analytical methods of BS 8006 and EBGEO. In terms of procedure of parametric study, input parameters such as pile width , embankment height, surcharge,geogrid and softsoil stiffness were varied to observe common output parameters of geosynthetic tension and total load transferred to pile. Ultimately, by comparing proximity of results of analytical codes to that of PLAXIS 2D outputs the most suitable method was to be identified.

2.2.1 PLAXIS 2D (FEM) – Plain strain condition

In terms of PLAXIS 2D model, considering symmetry only half from the center of geometry was modelled as illustrated in Fig. 3.

In the calculation phase staged construction procedure was used for simulation of the realistic process of construction as follows.
Phase 01- Piles and geogrid installation
Phase 02-Placing first embankment layer (plastic state)
Phase 03-Allowing for consolidation (14 days)
Phase 04-Placing second embankment layer(Plastic state)
Phase 05-Allowing for consolidation (14 days)
Phase 06-Surcharge application (365 days)

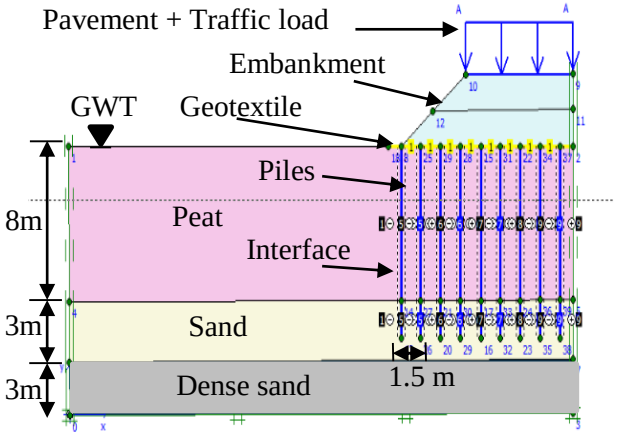

Fig. 3 Plainstrain model of GRPE in Plaxis 2D

2.2.2 BS 8006 method

<u>Case 01: Total load on pile</u>
Total stress developed on pile is obtained as,

Total stress on pile top (σ_v) =γH +P (1)

Where,
γ is Unit weight of embankment soil, *H* is embankment height and *P* is Traffic load (Surcharge)

Since, BS8006 method neglects the support from soft soil. It considers total load induced on equivalent pile grid is ultimately transferred to pile.

Therefore,

Total load on pile = σ_v x S^2(2)
Where,
S is center to center pile spacing

Case 02: Geosynthetic tension

Equation 3 is used to obtain the line load on the strips of reinforcement between adjacent piles (W_T) and Equation 4 is used to obtain tensile stress in geosynthetic reinforcement (T_{rp})which depends on W_T.

$$W_T = \frac{1.4\,S\gamma\,(S-a)}{S2-a2} \times \left(S^2 - a^2\left(\frac{P_c}{\sigma_v}\right)\right) \quad (3)$$

Where,
a is Pile width

$$T_{rp} = \frac{W_T\,x(s-a)}{2a} \times \sqrt{1+\frac{1}{6\xi}} \quad (4)$$

Where,
ξ is Estimated strain in geogrid

2.2.3 EBGEO method

Case01: Load on pile

Fig. 4 is used to obtain the the normal stress developed on geosynthetic between piles ($\sigma_{Z0,k}$) due to embankment loading condition.

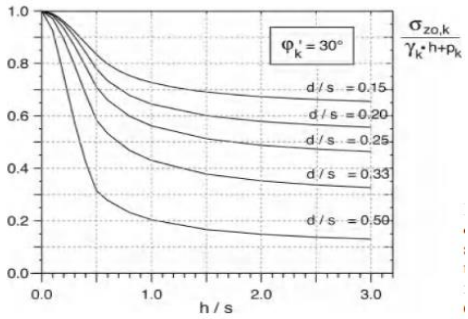

Fig. 4 Graph for obtaining Normal stress between piles(EBGEO,2011)

Where,
h is Embankment height ,s is Maximum spacing between piles and d is Equivalent pile width

Equation 5 is used to obtain stress developed on piles due to arching.

$$\sigma_{ZS,G+Q,K} = ((\gamma h + P_{,K}) - \sigma_{ZO,G+Q,K}) \times A_E/A_S + \sigma_{ZO,G+Q,K} \quad (5)$$

Where,
$\sigma_{ZS,G+Q,K}$ is stress developed on piles due to arching , A_E is Equivalent area for single pile grid and A_S is Cross sectional area of a single pile

So, Direct load on piles due to arching,

$$= \sigma_{ZS,G+Q,K} \times A_S \quad (6)$$

Case02: Geosynthetic tension

Unlike in BS 8006 , EBGEO integrates the support from soft subsoil into calculation of geogrid tension.

$$K_{s,k} = \frac{E_{S1}\,x\,E_{S2}}{E_{S1}\,x\,t1 + E_{S2}\,x\,t2} \quad (7)$$

Where,
$K_{s,k}$ is mean modulus of subgrade reaction , E_s is constrained modulus of stratum and t_w is thickness of considered stratum

Fig. 5 is used to calculate the maximum strain developed in the geogrid.

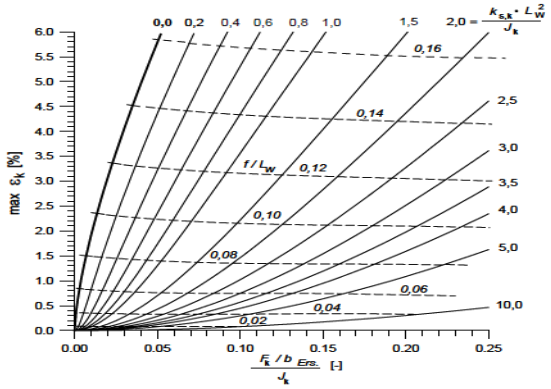

Fig. 5 Maximum strain in geogrid (EBGEO,2011)

Where,
J_k is Tensile stiffness of geogrid.,L_w is clear distance between two piles ,b_{Ers} is Pile width, F_k is resultant vertical strip load on geogrid and ξ_k is Maximum strain in geogrid

Ultimately, from equation 8 mobilized geosynthetic tension on geogrid ($E_{M,k}$) can be obtained.

$$E_{M,k} = \xi_k \times J_k \quad (8)$$

3 RESULTS AND DISCUSSION

3.1 *Axisymmetric study*

Load-settlement graph obtained by Pile Dynamic Analysis (PDA) test report of considered and PLAXIS 2D FEM analysis results is shown in Fig.6.

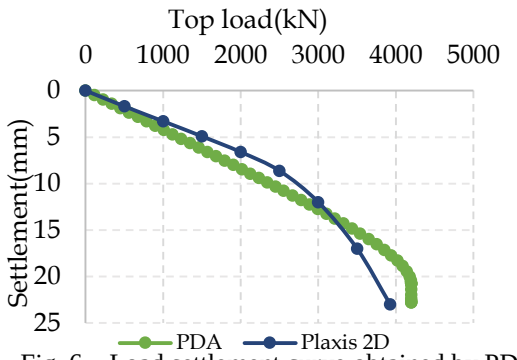

Fig. 6 Load settlement curve obtained by PDA and PLAXIS 2D results

Total bearing capacity obtained by PLAXIS 2D model PDA test report and analytical calculations is illustrated in Fig.7.

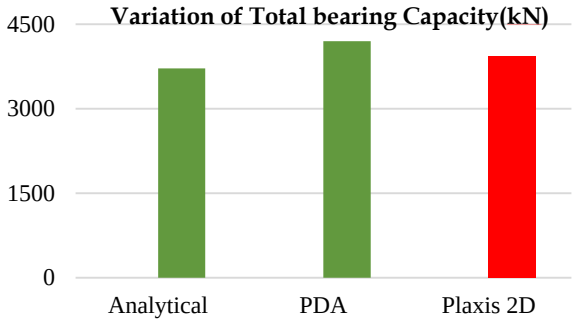

Fig. 7 Variation of total bearing capacity

When observing the above results it is quite clear that PLAXIS 2D simulation result are quite close to in situ test results of PDA and analytical calculations. Therefore, PLAXIS 2D is applicable for modelling pile behavior and it is justifiable to be used as base of validation for plain strain GRPE modelling.

3.2 Plain Strain Study

Fig.8 depicts the variation of total load when varying input parameters of surcharge and pile width. It can be noted that BS 8006 results are significantly conservative compared with other methods.Also, BS 8006 results suggest total load on pile is independent from pile width which is not agreed by PLAXIS 2D and EBGEO.

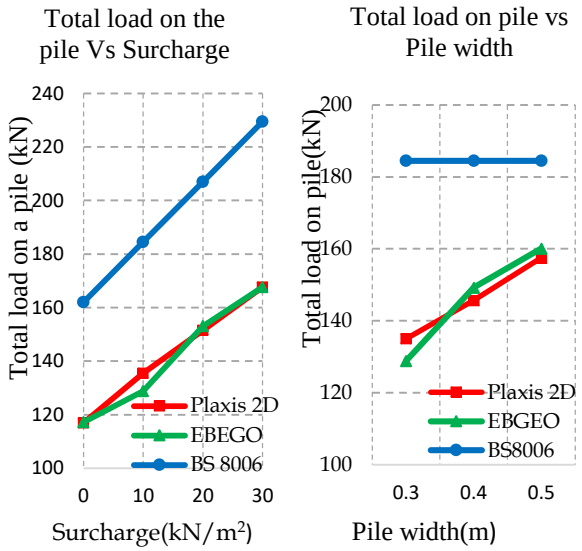

(a) (b)

Fig. 8 Variation of Total load on pile with (a) Surcharge and (b) Pile width

Fig. 9 depicts the variation of geogrid tension when varying input parameters of peat layer stiffness (soft soil layer directly below geogrid), geogrid stiffness, and surcharge and embankment height. Similarly as shown with total load on pile, BS 8006 provides conservative values for geogrid tension when varying above input parameters.

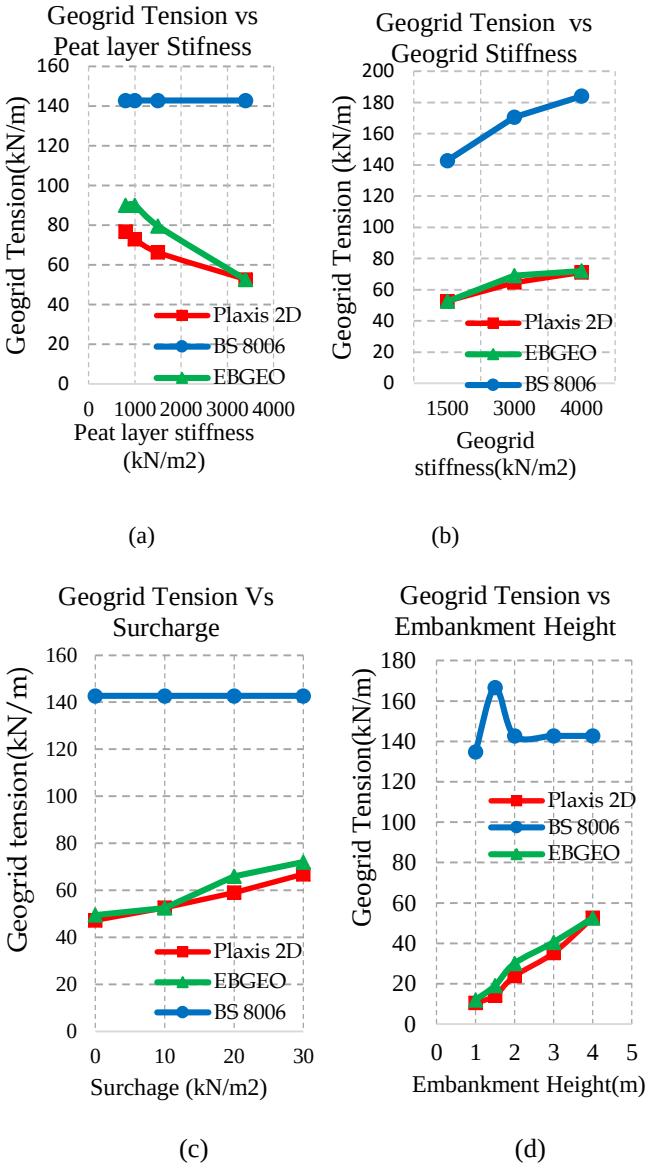

Fig.9 Variation of Geogrid tension with (a) peat layer stiffness ,(b) Geogrid stiffness (c) surcharge and (d) Embankment height

4 CONCLUSIONS

This study was carried out to verify and obtain the most suitable analytical method to design GRPE.In the process, parametric study was performed using BS 8006, ,EBGEO and PLAXIS 2D to identify most suitable design method between BS 8006 and EBEO. The main results drawn from the study are summarized as follows.

1. Total load on the pile is dependent upon the pile width. Higher the pile width, higher the total load transferred to pile width.
2. BS 8006 is much more conservative than other methods. Therefore, designing in compliance with BS8006 is not economical.
3. Stiffness of soft soil layer directly below geogrid was found to be an influential parameter in designing of GRPE which is neglected by BS 8006. It assumes total embankment load is ultimately transferred to piles due to negligence of support from soft soil.
4. Parametric study clearly depicted that EBGEO complies considerably well PLAXIS 2D results. Thus, it can be concluded that EBGEO is the best and most economical method to design GRPE considering its compliance with PLAXIS 2D results.

REFERENCES

British Standards BS 8006 (1995). Code of practice for strength ened/Reinforced /Reinforced Soils and other fills",Section 8.3.3 ,British Standard Institution.

EBGEO(2011). Recommendations for Design and Analysis of Earth Structures Using Geosynthetic Reinforcements, Translation of the 2nd German edition,German Geotechnical Society.

Fluet, J.E., Christopher, B.R., and Slaters, A.R. (1986). Geosynthetic stress-strain response under embankment Loading conditions .Proc.3rd Int. Conf. on Geotextiles, Vienna , Vol.1, pp 175-180.

Kempfert, H.G., Goel, C., Alexiew ,D. and Heitz,C.(2004). German recommendations for reinforced embankments on pile-similar elements, Geotechnical Engineering with Geosynthetics, pp 279-284.

Impact of new tunnels on the performance of existing tunnel and tunnel liners: A study based in Sydney region

Manasi Wijerathna, Ashok Peiris, Kim Chan

GHD Pty Ltd, 29 Christie Street, St Leonards, NSW, 2065, Australia

ABSTRACT: Interaction of new tunnels with existing tunnels has been studied in literature to investigate the impact on tunnel support systems, surface deformations and tunnel deformations. However, not many such studies investigated the stresses and bending moments induced in an existing tunnel liner due to a new tunnel construction. This paper studies the impact of construction of road tunnels in Sydney region, crossing above a historical utility tunnel, on the tunnel liner performance. When a new tunnel is constructed with a narrow separation to an existing tunnel, additional stresses and bending moments are induced on the existing tunnel steel liner. As the steel liner may not have initially designed for these additional stresses, understanding the impact of proposed road tunnel on the utility tunnel liners is crucial to ensure its functionality, during and after the proposed road tunnel construction. In this study, the steel liner response to the excavation of road tunnels was investigated using a 3D numerical model developed in ABAQUS finite element program.

Key words: Crossing tunnels, 3D numerical modelling, tunnel liner integrity, Sydney geology

1 INTRODUCTION

New developments of infrastructure such as transport network, water and sewerage, transmission, power and communication systems are essential in growing cites. Yet, the modern cities are already congested, and acquisition of land for mass developments such as roads and railways is nearly impossible. Underground construction and elevated construction are other solutions for the land scarcity. In the case of underground construction, the impact of a tunnel excavation may extend to a far greater distance than of a deep foundation or a basement excavation. For example, the effect of a tunnel at 30 m depth may trigger deformations/settlements at the ground surface.

Tunnel construction induced ground deformations have been studied extensively in literature, using numerical models, centrifuge model tests and case histories (Al-Taee *et al.* (2017), Novozhenin and Vystrchil (2016), Shi *et al.* (2013), Mair (2008)). Most investigations on tunnel to tunnel interactions, reported in literature are based on clayey ground (Kim (1996), Ng *et al.* (2013), Addenbrooke and Potts (2001)). Only few studies are available on the tunnel to tunnel interaction in rock (Liu *et al* (2008), Liu *et al.* (2009)). However, literature review revealed that no study to date has investigated the impact on steel liners due to new tunnel construction in rock.

This study investigates the behaviour of a steel liner of a utility tunnel in Sydney rock, during and after the construction of two new road tunnels crossing above the existing tunnel. Sydney rock consists of a high horizontal in-situ stress regime, making the interactive behaviour between an existing tunnel and a new tunnel difficult to predict based on the available knowledge. Therefore, a 3D finite element model was developed to investigate the steel liner response to the excavation of proposed road tunnels. ABAQUS finite element programme was used to develop the model as it facilitates the featuring of important details of the utility tunnel. The joints of the steel pipes, concrete liner, the fractured rock around the utility tunnel due to drill and blast construction etc. have been modelled. Steel pipe was modeled as a shell element so that pipe actions and deformations could be readily extracted.

The structural integrity of the utility tunnel was interpreted in terms of sensible parameters such as circumferential bending of the steel liner, radial cracking of concrete liner, separation of steel liner joints, longitudinal bending of the pipe and deformation of the pipe cross section.

2 DESCRIPTION OF THE MODEL

The example problem investigated in this study is based in Sydney region. The existing utility tunnel is locate at 65 m below the ground surface. Two parallel road tunnels are newly constructed crossing above the utility tunnel with a clearance of 9 m between the crown of the utility tunnel and invert of

the road tunnels. The new road tunnels are inclined to the utility tunnel, at an angle of 52^0, in the horizontal plane as shown in Figure 1. The section view shown in Figure 2 indicates the arrangement of existing and new tunnels within the site stratigraphy. As shown in Figure 2, the subsurface geology consists of four soil/rock strata. The top most soil layer is a 5.6 m thick residual soil layer underlain by 6 m thick extremely to very low strength shale layer, 30 m thick medium strength shale layer and 42 m thick high strength Sandstone layer, respectively.

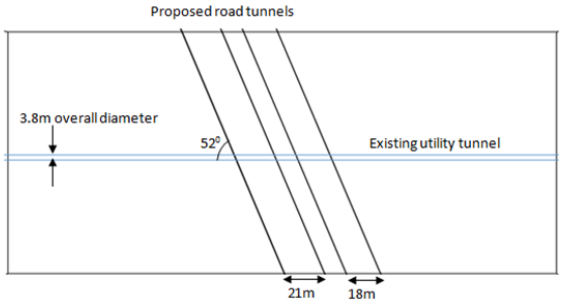

Fig 1: Layout of the existing and new tunnels: Plan view

Figure 3 shows a typical cross section of the utility tunnel. As shown in the figure, the utility tunnel has a circular cross section of 3.8 m overall diameter. The rock tunnel is internally lined with two concrete liners; 400 mm thick sprayed concrete liner and 200 mm thick aggregate concrete liner, and thirdly a steel liner. The inner steel liner is of 2.475 m diameter and 16 mm thickness. The steel liner comprises of 2.7 m long tubular segments joined by non-welded joints. A hydraulic drain is calved at the crown of the aggregate concrete liner, as depicted in Figure 3. Under the operational conditions, the utility tunnel is subjected to 700 kPa internal water pressure.

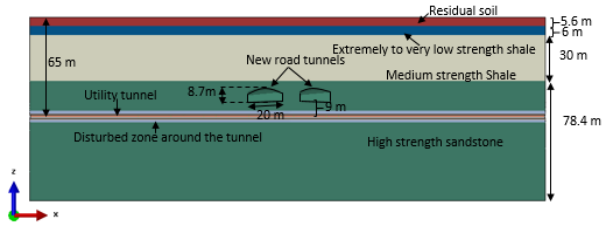

Fig 2: Section view of the ground profile

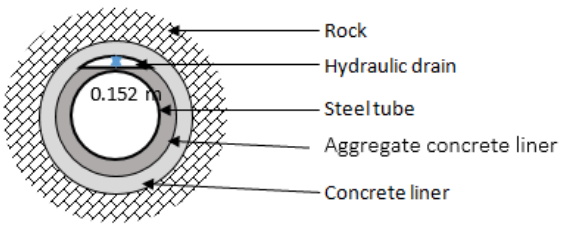

Fig 3: Typical cross section of the utility tunnel

3 FINITE ELEMENT MODEL

The finite element model was 120 m deep, 340 m long in the direction parallel to the utility tunnel and 150 m wide in the direction perpendicular to the utility tunnel. A relatively long longitudinal dimension was used in the model, to reduce the influence of boundary conditions on the behaviour of the utility tunnel steel liner, near the proposed road tunnel excavation.

Table 1: Material properties used in the numerical analysis

Material	Elastic modulus (MPa)	Poisson's ratio - ν	Unit weight (kN/m^3)
Residual soil	40	0.3	20
Shale extremely to very low strength	150	0.3	24
Shale medium strength	300	0.15	24
Sandstone high strength	3000	0.15	24
Sandstone – Disturbed zone	1500	0.15	24
Concrete liner	15000	0.2	24
Aggregate concrete liner	18000	0.2	24
Steel pipe	205000	0.3	77.2
Steel pipe joints	102500	0.3	77.2

The mechanical properties of soil/rock material used in the model were selected based on the properties reported in the literature (Chan *et al*, 2005, Bertuzzi, 2014, Pells, 2004). Table 1 shows the mechanical properties of the soil/rock units used in the model. Linear elastic behavior was assumed for the soil and rock layers. Linear elastic model is considered to be adequate to represent the mechanical behavior in this model since the rock strengths are large in the region where excavation is taking place. Therefore, the rock should not reach plastic state.

Joints in the steel tube were introduced as bands with low stiffness. Centre to centre spacing between joints was 2.7 m and the width of a joint was 0.075 m. Both steel pipe and the joints were modelled as fully elastic material. The material properties used for steel pipe and joints are also given in Table 1. The concrete was assumed to be low grade concrete (Grade 15), since the construction was carried out some 80 years ago. The material properties adopted for concrete and aggregate concrete are also shown in Table 1.

Table 2: Horizontal in-situ stress profile adopted in the study

Depth	Soil type	Major horizontal stress component	Minor horizontal stress component
0	-	$\sigma_H = \sigma_v$	$\sigma_h = 0.7\sigma_H$
5.6	Residual soil	$\sigma_H = \sigma_v$	$\sigma_h = 0.7\sigma_H$
11.6	Shale extremely to very low strength	$\sigma_H = \sigma_v$	$\sigma_h = 0.7\sigma_H$
41.6	Shale medium strength	$\sigma_H = 2\sigma_v + 1.5$ MPa	$\sigma_h = 0.7\sigma_H$
120	Sandstone high strength	$\sigma_H = 2\sigma_v + 2.5$ MPa	$\sigma_h = 0.7\sigma_H$

Sydney region is known to have large locked in horizontal stresses in the underground rock layers. Therefore, in situ stresses in the ground were incorporated in the model based on published data for Sydney geology (Chan *et al.*, 2005, Bertuzzi, 2014). The adopted horizontal in-situ stress profile is given in Table 2. The in-situ stress profile was pre-defined in the numerical model as geostatic stresses. The major and minor components of the horizontal, locked-in stresses were defined by lateral coefficient, K, in perpendicular directions on a horizontal plane. The major horizontal stress direction was considered as approximately perpendicular to the road tunnel.

3.1 *Analysis sequence*

After establishing the initial geostatic conditions, the excavation of the existing utility tunnel was carried out by deactivating the corresponding rock volume. In the subsequent step, the disturbance to the surrounding rock due to drill and blast construction of the utility tunnel was simulated by reducing the elastic modulus of rock by 50%. The two layers of concrete tunnel liners were then installed, with the hydraulic drain integrated into the aggregate concrete liner. The steel pipe was installed afterwards. The rock/concrete liner interface and liner/liner interfaces were considered fully bonded. A 700 kPa pressure was applied inside the tunnel to replicate the operational water pressure. The excavation of the road tunnels was simulated progressively with 10 m long excavation steps. There was a 20 m construction lag between the excavation faces of the two road tunnels.

4 BEHAVIOUR OF ROCK UNIT AROUND THE UTILITY TUNNEL

Behaviour of the rock unit surrounding the utility tunnel was investigated using the deformations and changes of horizontal stress in the rock. Figure 4 shows displacement vectors in rock around the utility tunnel at the end of road tunnel construction. The lengths of the arrows are proportionate to the magnitude of displacement. As shown in Figure 4, the initially circular cross section of the tunnel deforms into an oval shape, with shorter width and longer height. This is because the tunnel is being laterally compressed, due to high horizontal stresses in rock compared to vertical stresses. As a result of the aforementioned non-uniform deformation, a larger horizontal stress is released at the two sides of the utility tunnel, compared to the crown and the invert.

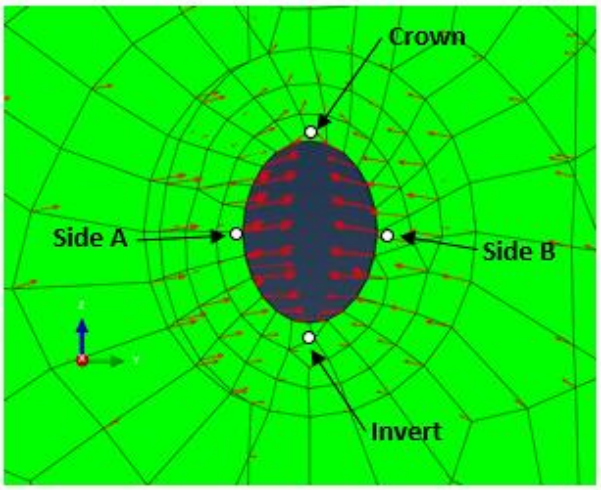

Fig 4: Displacement vectors in the rock around the utility tunnel directly beneath the road tunnels (Deformation scale factor 100)

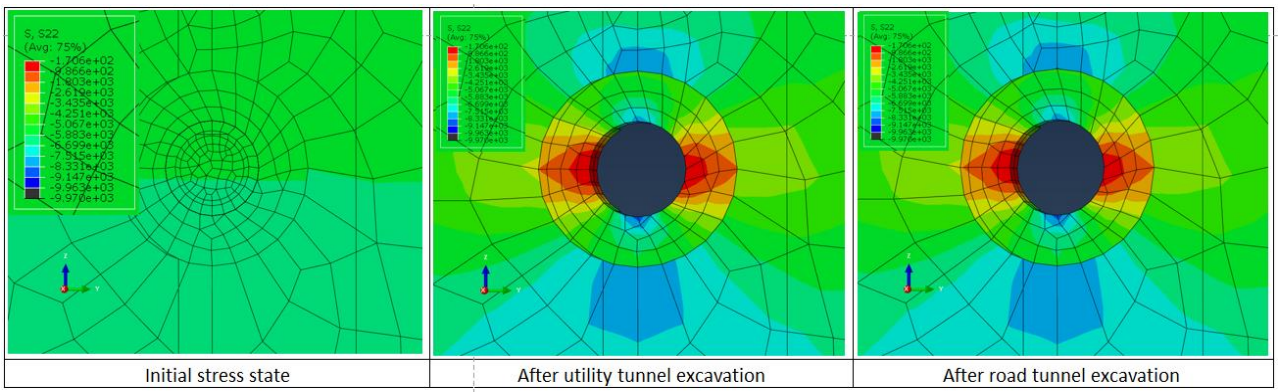

Fig 5: Changes in horizontal stresses in the rock around the utility tunnel at different construction stages

Figure 5 shows the change of horizontal stresses around the utility tunnel, at different construction stages. As discussed in Table 2, the horizontal stresses were proportionate to the vertical stresses at the initial state. Therefore at the initial stage in Figure 5, highest stress is observed at the invert, equal and intermediate stresses were observed at the sides and lowest stresses were observed at the crown. After the excavation of the utility tunnel, the horizontal stresses change due the movements of the tunnel surface as well as stress release through rock fracture during drill and blast construction. The stress release at the sides of the tunnel is higher due to the inward movement at the sides of the tunnel. The construction of the new road tunnel 9m above the utility tunnel did not create large stress changes near the utility tunnel.

5 PERFORMANCE OF THE UTILITY TUNNEL

The deformations, stresses and bending moments in the pipe before and after the road tunnel excavation were investigated using the numerical model results. The structural integrity of the steel pipe was assessed for differential settlements of the pipe, excessive bending moments and joint separation. Further, the radial cracking of the internal cement liner that may cause long term corrosion was also assessed. There was also a concern that cracking of the cement liner could induce excessive leaking of water through the joints of the steel pipe, potentially flooding the road tunnels.

5.1 *Deformations*

Figure 6 shows the deformed shape and a contour plot of deformations in the steel pipe after the road tunnel excavation. Figure 7 shows the deformed shape of the utility tunnel cross section across the location of the maximum displacement in the pipe, shown in Figure 6. The arrows in Figure 7 indicate the magnitude and the direction of movements in the pipe relative to its original form. The deformation scale is exaggerated in Figures 6 and 7 to clearly view the variations in the deformations.

As observed in Figure 6, the steel pipe mainly deforms in the vertical direction. The primary cause of this deformation is the relaxation of the locked in stresses due to the excavation of road tunnels. As a result, the pipe directly below the road tunnels move upwards when the excavation face passes the utility tunnel. The maximum net vertical movement of the pipe due to the road tunnel excavation was about 4 mm. The angular distortion of the pipe along the longitudinal direction was predicted as 1: 5000, vertical: horizontal. The estimated limits for the vertical displacement and the angular distortion of the pipe to not to cause any structural and functional damage were 10 mm and 1: 2000 V: H, respectively. Accordingly, the expected vertical movements of the pipe are within the acceptable limits.

The crown and invert radial displacements shown in Figure 7 are +3.83 mm and +2.61 mm, respectively. This is an increment of pipe diameter, by 1.22 mm which is equal to 0.05% of the pipe diameter. The left and right radial displacements of the pipe are +1.49 mm and +0.87 mm, respectively. This equates to a reduction in pipe diameter by 0.62 mm or 0.03% of the pipe diameter. The change in ovality that can cause radial cracking in the cement liner and damage corrosion protection to the steel pipe is 4% of the pipe diameter according to Australian Standard AS2566.1 design guide. The predicted change in ovality of the pipe is much less than the limiting 4%. Therefore, it can be concluded that the radial cracking of the cement liner will not occur in the utility tunnel.

The observed maximum longitudinal deformation of the utility tunnel due to construction of the road tunnels is relatively insignificant with a maximum of 0.25 mm. This magnitude of longitudinal deformation is not sufficient to damage the joints of the steel pipe. Further, this longitudinal deformation is too small to cause any significant cement liner crack openings or compression that may lead to localised cement liner crushing.

5.2 *Stresses*

Figure 8 shows the variation of hoop stresses along the tunnel at the crown, invert, left side and the right side, in comparison to the stresses at current operating conditions. The hoop stresses prior to the road tunnels are uniform along the pipe length at approximately 44MPa, 14MPa, 20MPa and 20MPa at the pipe crown, invert, left and right respectively. The excavation of the road tunnels causes an increase of hoop stresses on the sides of the steel pipe and decrease of hoop stresses on the crown and invert of the pipe. The maximum effect occurs directly below the two road tunnels. The hoop stresses are mostly positive which suggests that the pipe membrane is in tension. The compressive stresses are localised on the pipe and the maximum compressive stress is 5MPa. Therefore local buckling of the pipe due to compression is highly unlikely.

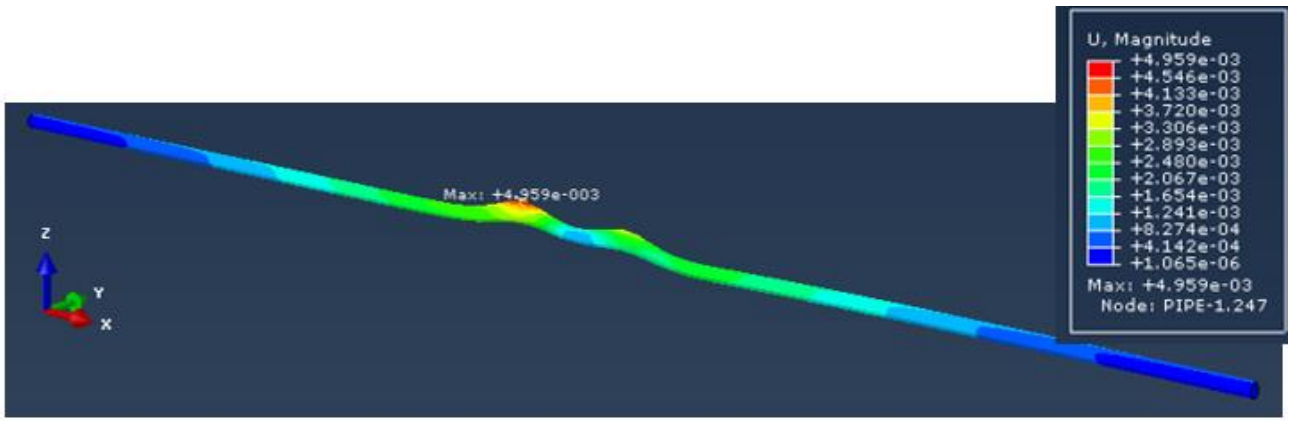

Fig 6: Deformed shape of the pipe, after road tunnel (Deformation scale factor = 1000)

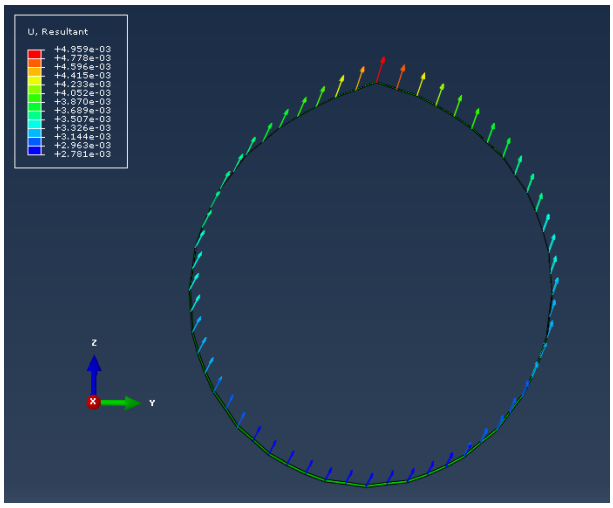

Fig 7: Deformed shape of the pipe cross section (Deformation scale factor = 100)

5.3 *Bending moments*

Figures 9(a) and (b) show the plots of bending moments about longitudinal axis and bending moments about hoop direction at the crown and the invert of the pipe for both final and current conditions. The bending moments about the longitudinal axes are indicative of overall bucking of the pipe and the bending moments about hoop direction are indicative of local buckling of the pipe. As shown in the figures, the bending moments in the pipe have not changed significantly except at the crown. The reason for higher bending stresses at the crown is the thin cover to the pipe due to hydraulic drain at the crown. Therefore, the plausibility of local buckling of pipe due to the increased bending moments should be assessed, structurally.

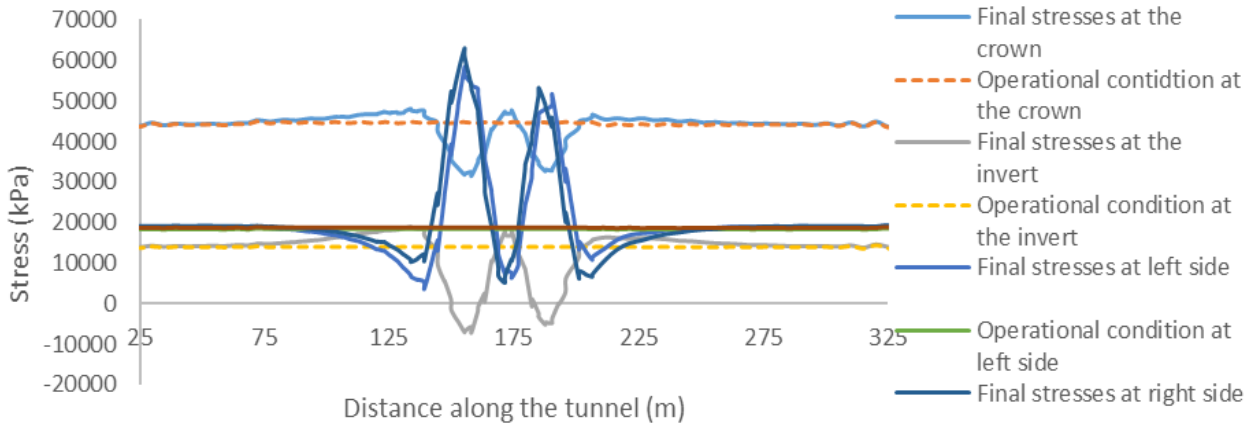

Fig 8: Variation of hoop stresses along the tunnel

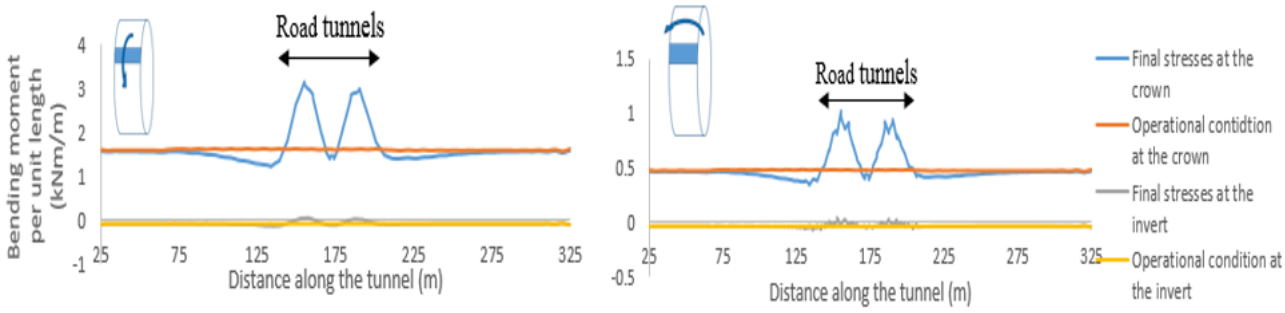

(a) (b)

Fig 9: Bending moments about longitudinal axis

6 CONCLUSIONS

The behavior of an existing steel tunnel liner, during the excavation of two new road tunnels was investigated in this study. The structural integrity of the tunnel was assessed using a detailed numerical model developed in ABAQUS/Standard finite element software. The key criteria considered in assessing structural integrity of the steel pipe were differential settlements of the pipe, direct stresses in the pipe, excessive bending moments large enough to cause local or global buckling, separation of the joints, and the radial cracking of the internal cement liner. The results indicate that the maximum vertical movement and angular distortion of the pipe are 4 mm and 1: 5000 V: H, respectively. These vertical deformations and the gradient are not large enough to cause significant differential settlements. The change in ovality of the pipe is less than 0.05% which is within the acceptable limits. The maximum longitudinal displacement of the pipe was 0.25 mm only. This suggests that the pipe is safe against joint separation and long term corrosion due to cracking of concrete liner. The hoop stresses in the pipe are mostly in tension and the bending moments were generally small. Therefore, the pipe should not fail in direct compression. However, some localized bending moments were observed at the crown of the steel pipe directly below the road tunnels. This indicates a possibility of local buckling at the crown of the pipe, and it should be assessed on a structural viewpoint.

7 REFERENCES

ABAQUS/Standard. (2014). ABAQUS Version 6.14 – Computer Software. Providence, RI: Dassault Systèmes Simulia Corp.

Addenbrooke, T.I. and Potts, D.M., (2001)., Twin tunnel interaction: surface and subsurface effects. Int J Geomech 1(2):249–71

Al-Taee, M.M.H., Al-Adilli, A. and Sivakugan, N., (2017)., Analysis of behavior of soil surrounding around Baghdad metro at Baghdad city center during and after tunnel excavation using the finite element method, International Journal of Civil Engineering and Technology (IJCIET), 8(10)

AS/NZS 2566.1:1998, Buried flexible pipelines Part 1: Structural design, Joint Standards Australia/Standards New Zealand Committee WS/28.

Bertuzzi, R., (2014)., Sydney sandstone and shale parameters for tunnel design. Australian Geomechanics, 49(1):1-40

Chan, K.F., Kotze, G.P. and Stone, P.C., 2005, Geotechnical modelling of station caverns for the Epping to Chatswood rail line project: Sydney, October 2005, AGS-AUCTA Mini-symposium: Geotechnical Aspects of Tunnelling for Infrastructure Projects.

Kim, S.H., Model testing and analysis of interactions between tunnels in clay. PhD thesis, Department of Engineering Science, University of Oxford; 1996.

Liu, H.Y., Small, J.C. and Carter, J.P., (2008)., Full 3D modelling for effects of tunnelling on existing support systems in the Sydney region, Tunnelling and Underground Space Technology, 23(4):399-420.

Liu, H.Y., Small, J.C., Carter, J.P. and Williams, D.J., (2009)., Effects of tunnelling on existing support systems of perpendicularly crossing tunnels, Computers and Geotechnics, 36(5):880-894.

Mair, R.J., (2008)., Tunnelling and geotechnics: new horizons. Géotechnique, 58(9):695-736.

Ng, C.W., Boonyarak, T. and Mašín, D., (2013)., Three-dimensional centrifuge and numerical modeling of the interaction between perpendicularly crossing tunnels, Canadian Geotechnical Journal, 50(9):935-946.

Novozhenin, S.U. and Vystrchil, M.G., (2016)., New method of surface settlement prediction for saint-petersburg metro escalator tunnels excavated by EPB TBM, Procedia Engineering, 150:2266-2271.

Pells, P.J.N., (2004)., Substance and mass properties for the design of engineering structures in the Hawkesbury sandstone, Aust Geomech, 39(3):1-21.

Shi, J., Ng, C.W. and Chen, Y., (2015)., Three-dimensional numerical parametric study of the influence of basement excavation on existing tunnel, Computers and Geotechnics, 63:146-158.

Laboratory Modelling of Stresses within the Minefills and Loads on Barricades

J.D.S.U. Jayakodi, R.J. Bennett, A.J. Reddicliffe, N. Sivakugan & Peter To
Department of Civil and Environmental Engineering, James Cook University, Australia

ABSTRACT: Mine backfilling is a widely used method to fill the large voids created as a result of mining to ensure the regional stability of the mining area. Conventionally, the backfills are mainly mine tailings in the form of hydraulic fills or paste fills. Prior to backfilling, the horizontal drives of the mine are essentially barricaded with competent retaining walls to prevent backfill material entering other areas of the mine. The stresses developed within an underground mine during backfilling are largely influenced by soil arching. This paper describes an investigation of the stress distribution within backfilled mine stopes and drives, and determine the loadings on drive barricades through an experimental program. The laboratory models clearly verified the reduction in the stresses due to soil arching. The results are also compared with analytical and numerical solutions. The extensive laboratory test program and the conclusions reported herein will be very valuable to the mining industry.

1 INTRODUCTION

Mining is a complex process of extracting mineral resources from ore deposits. Brazil, South Africa, Canada, USA and Australia are the most leading countries in the mining industry. The major minerals produced by these countries include Iron ore, Manganese, Aluminium, Gold, Tin, Nickel, Chromium, Beryllium, oil sands, etc. Australia, by any standards, is well endowed with most minerals even though it has barely scratched the surface of its mineral resources. The nation holds the world's largest known economic resources of Bauxite, Lead, Zinc, Silver, Gold, Uranium, Diamonds and Mineral Sands. Mining contributes a substantial proportion to the country's Gross Domestic Product (GDP) and is the backbone of Australian economy. Mining of all resources contributes about 8% to Australia's GDP and around 60% of exports. The continued economic performance, community involvement and workplace health and safety in the mining industry are imperative to a strong national economy and the quality of life in Australia.

Mining can be classified into two categories based on the location of the deposit as open pit mining and underground mining. Open pit mining extracts the mineral ore from earth by removal of ore from an open pit where the overburden is relatively thin. In contrast, underground mining extracts the valuable ore from deep ore bodies and the ore body is accessed through ramps, shafts and tunnels. The removal of ore in underground mining creates large cavities, known as stopes. The stopes are accessed through horizontal drives that allow machinery to remove the ore. Once the rock has been removed and processed, the stope requires backfill for surrounding stability and continued production. The backfilling of stopes can represent up to 20% of underground mining costs (Grice, 2001). The horizontal drives need to be barricaded or capped to allow for the backfill process to take place. The construction and performance of these barricades is a major topic in the mining industry today. The correct calculation of the stress state in the backfill and the associated pressures exerted on the barricade is a critical engineering challenge (Li and Aubertin, 2009a). The objectives of this research are to investigate the stress distribution within backfilled mine stopes and drives, and determine the loadings on drive barricades through a laboratory model tests.

2 BACKGROUND

2.1 *Mine tailings disposal and mine backfilling*

The mining industry in Australia is also the largest generator of solid wastes (Boger, 1998), making the backfilling of voids and the disposal of tailings an integral part of the mining process (Rankine et al. 2007). The mine tailings are waste material generated during mining process which should be disposed by constructing tailing dams and/or used to backfill the underground voids. The underground voids created annually in Australia can reach 10 million cubic metres (Grice, 2001). Though the backfill system is often expensive, typically covering about 30% of total mining costs, reliability and flexibility of the backfill system greatly support the mining operation (Bloss 2014). An efficient backfill

process can lead to ensuring regional stability, maximizing ore extraction, minimizing ore dilution, controlling ground subsidence, providing a working floor and facilitating subsequent excavation and ore removal nearby (Sivakugan et al. 2015).

2.2 *Types of minefills*

The choice of materials that are utilized for backfill operation depends on the location of backfilling, availability of materials for a particular fill and prevailing ground conditions (Grice, 1998a). Therefore, a classified or total stream of tailings is processed and directed to mined out stopes. Different types of minefills and their properties are extensively discussed in Rankine et al. (2006). Hydraulic Fills (HF) and Paste Fills (PF) are the two most common minefills used worldwide.

2.3 *Typical structure of a backfilled stope*

Stopes are underground voids which have been created by the ore removal during a systematic process and that are backfilled with minefills. Stopes can be approximated as rectangular prisms with vertical walls and having a plan of 40 m by 50 m and heights exceeding 100-200 m. Height (H) to Breadth (B) ratio can be high as 6-10 (Sivakugan et al. 2014). Backfilled or non-backfilled stopes are interconnected by horizontal access drives with typical cross section of more than 5 m, located at different sublevels of the stope, which allow trucks and other machinery. These drives are generally barricaded with strong retaining walls before backfilling the stope. The barricades are designed to be free draining such that they allow the water in the fill to seep through while retaining the fill. Realistic determination of the vertical stresses within the mine stope can pave the way to improving the design of barricades. Fig. 1 shows an idealized stope with HF system.

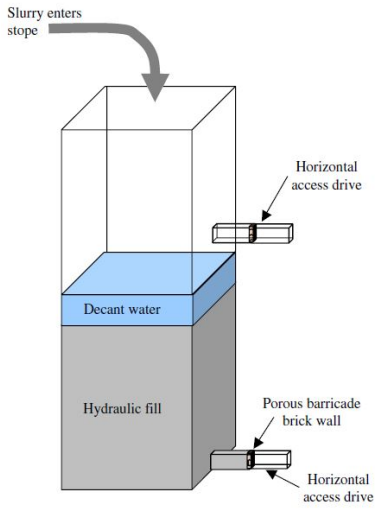

Fig. 1 Schematic diagram of a backfilled stope

2.4 *Soil arching*

Arching is a well-known phenomenon which has been identified in many geotechnical and mining applications. Among them, arching within backfilled mine stopes has been researched extensively. During filling, the vertical shear stresses acting on the stope walls reach the maximum value. Accordingly, the vertical normal stresses at any point within the fill stope can be substantially less than the expected overburden pressure. Therefore, a significant fraction of the fill weight is carried by the rock walls in the form of shear stresses.

3 STRESSES WITHIN THE BACKFILLED MINE STOPE

There have been few studies reported with field measurements of vertical stress in backfilled mine stopes such as Belem et al. (2004) and Thompson et al. (2012). Because of limited field measurements, there had been attempts to investigate the stress behavior within backfilled stopes, taking into account the arching effect by three independent approaches namely analytical, experimental and numerical modelling.

Analytical methods predict the variation of average vertical normal stress with the height of the stope with no consideration to the variation in lateral direction. Analytical closed form solutions include the ones proposed by Marston (1930), Terzaghi (1943), Aubertin et al. (2003), and Sivakugan and Widisinghe (2013) for 2-D and 3-D mine stopes and trenches.

Marston's (1930) equation for a trench backfilled by granular material is given by:

$$\sigma_v = \frac{\gamma w}{2\mu K_a}\left[1-\exp\left(-\frac{2K_a\mu h}{w}\right)\right] \quad (1)$$

where, σ_v the vertical normal stress at the fill height h, w the stope width, γ the unit weight of the fill, K_a the Rankine's active earth pressure coefficient, and $\mu=\tan\delta$ where δ is interfacial friction angle of the fill-wall.

Use of numerical models in geotechnical applications has increased in popularity compared to analytical and physical models. Numerical modelling is important for large scale underground mines, where in-situ measurements and monitoring of stresses, strains, displacements and pore pressures is often very difficult, expensive or not feasible.

3.1 *Lateral earth pressure coefficient*

The lateral earth pressure coefficient (K) is the ratio of effective horizontal stress to effective vertical stress. Depending on the lateral strain, and whether the soil is at active, at-rest, or passive state, K is of-

ten assumed as K_a, K_0, or K_p in geotechnical applications. In the case of backfilled mine stopes, K has been assumed as K_a or K_0 in the previous studies.

3.2 *Laboratory modelling*

The physical properties of the experimental material that were investigated included the grain size distribution, specific gravity and maximum, minimum densities to find relative density (Table 1). Furthermore, direct shear tests to calculate soil friction angle *(φ)* and soil/wall interfacial friction angle *(δ)* were conducted. These tests were done in accordance with Australian Standards.

Table 1. Properties of fill the material

Property	Value
Maximum void ratio (e_{max})	1.003
Minimum void ratio (e_{min})	0.633
Specific gravity (G_s)	2.6
D_{10} (mm)	0.12
D_{30} (mm)	0.18
D_{60} (mm)	0.26
Friction angle ($\varphi°$)	40.2
Interfacial friction angle ($\delta°$)	38.5
Average unit weight (kN/m^3)	13.3

The grain size distribution curve of the test material and that of the Australian hydraulic fills determined using 25 separate Australian hydraulic fills by Sivakugan et al. (2006b) and Rankine et al. (2006) gives confidence that the tested material will appropriately simulate an Australian dry hydraulic fill.

A simple laboratory model stope test setup was used to study the effects of wall friction and hence arching on the stresses within the granular fill. Fig. 2(a) shows the photograph of the laboratory model stope set up and a schematic diagram is shown in Fig. 2(b). The model is suspended from steel wires connected to a load cell hanging from the top of the frame. The model is lowered until it is just touching the balance, without registering any load on the balance. When the model is filled with a granular fill of weight (m+n), the fill load is shared by the balance at the bottom and the load cell reflecting the load carried by the wall. The load cell reads the fill load transferred to the wall (m) and the balance reads the fill load transferred to the bottom (n). At any stage of filing, m and n can be measured separately through this setup. A square shape stope with breath=150 mm and height=900 mm was tested and the wall condition was varied from rough to smooth to simulate underground mine wall roughness or a grain silo. Since the stope walls are very rough after blasting, the interfacial friction angle can be taken as the friction angle of the fill as the failure occurs on the fill-fill interface, not the fill-wall interface. Hence, a similar condition was created using a very rough sandpaper attached to the stope walls of the model and perspex was used as the smooth wall to represent the condition of a grain silo.

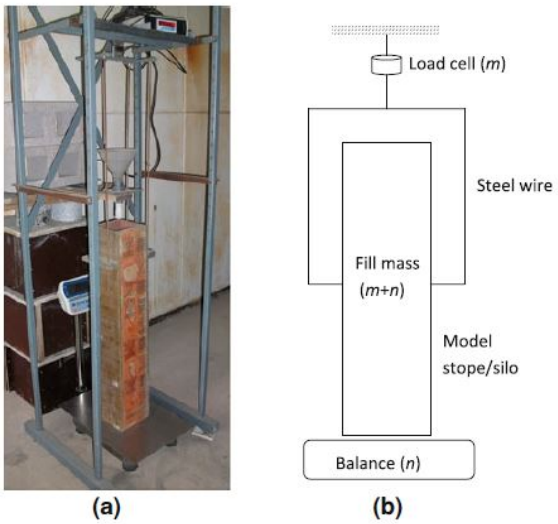

Fig. 2 Laboratory model stope setup (a) photograph (b) schematic diagram

The experimental results from Fig. 3 clearly show that the vertical normal stress at the bottom of the filled stope is considerably less than the theoretical overburden pressure at each fill height given the fact that certain fraction of the fill load is carried by the walls as shear stresses and thus soil arching is evident in the simulated mine stope.

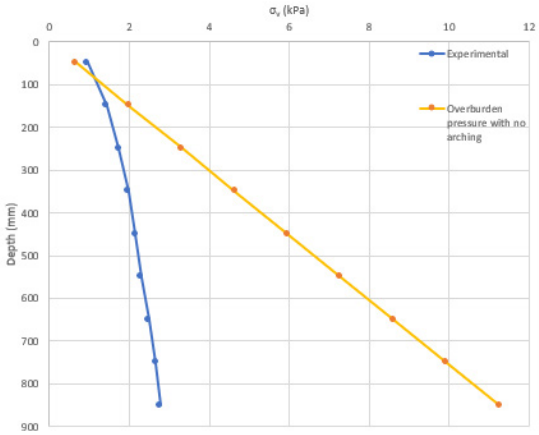

Fig. 3 Variation of vertical normal stress with stope depth

The Rankine's active earth pressure coefficient (K_a) used in this study is 0.2153 and the At-rest earth pressure coefficient (K_0) from Jaky's (1944) equation is 0.3543. The Marston's analytical equation was used to express the stress variation for both K_a and K_0 cases separately. Fig. 4 shows a dimensionless analysis to compare the laboratory result to that of the Marston's equation (1). The ratio of vertical stress to the product of unit weight and the stope

width (i.e., $\sigma/\gamma B$) is plotted against the depth and stope width ratio (i.e., z/B). The dimensionless analysis allows for the comparison of varying stope sizes and soils properties. Fig. 4 depicts that the Marston's equation with $K=K_a$ largely overestimate the stresses whereas $K=K_0$, $\delta=\phi$ condition gives more reasonable approximation to the laboratory results. Hence, the at-rest lateral earth pressure coefficient (K_o) is most reliable in Marston's equation (1) to predict the stress at a depth approaching $6B$, and this is reiterated by Pirapakaran and Sivakugan (2007a), however $\delta=0.67\phi$ was applied. The mine stope walls are generally more competent and hence the wall movement is not expected in a backfill system. Therefore, the backfill can be considered more stable suggesting that K_0 is more accurate to use in the Marston's equation. Laboratory results from both rough and smooth wall conditions confirmed that the vertical stress is continuously increasing through to $6B$ depth, however the analytical solutions suggested an asymptotic value for the stress at a depth as low as $4B$.

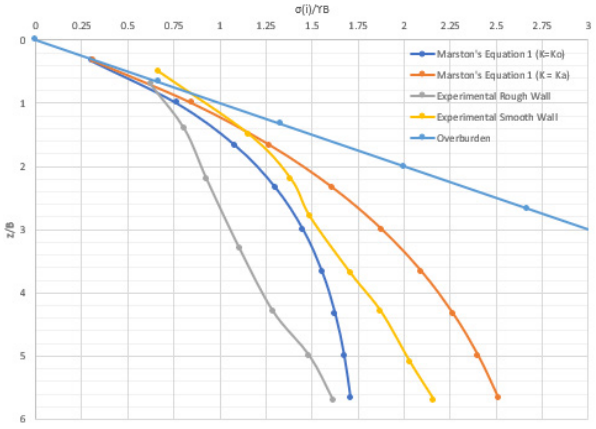

Fig. 4 Comparison of laboratory and Marston's analytical results

4 OPERATIONAL STRESSES AT DRIVE BARRICADES

The horizontal drives that access the stope for ore removal need to be barricaded or capped to allow for the backfill process to take place. Barricade failures in underground mines lead to serious consequences including damage to machinery, flooding and in some cases injury or death. A barricade failure in 2000 at the Bronzewing mine in Western Australia resulted in 18000 m^3 of hydraulic fill being released into the working area, claiming three lives (Rankine et al. 2007). Hence, the correct calculation of the pressures exerted on the barricade is immensely important to design the barricade safe.

A barricade laboratory model comprising 310 mm diameter vertical stope and several drive attachments was used in these experiments. The granular soil mass in the model was subjected to surcharge loads (q) ranging from 30 kPa to 900 kPa and the soil pressures were recorded at the stope center, stope edge and on the barricade face using three Earth Pressure Cells (EPC) attached in the model. A schematic diagram of the testing apparatus is shown in Fig. 5.

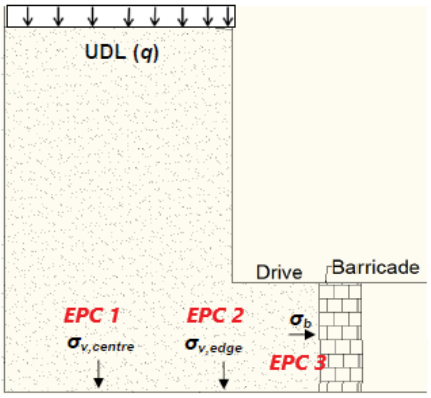

Fig. 5 Schematic diagram of the barricade testing apparatus

The lateral variation of the vertical normal stress at the stope base and across the stope width for all surcharges as recorded by EPC1 and EPC2 is shown in Fig. 6 below. It can be clearly seen that the reduction of vertical stresses towards the stope edge is attributed to the shear stresses developed at the stope walls reflecting the arching effect and this behaviour was confirmed with the numerical analysis done for the laboratory model stope tests carried out in section 3.2 using a FLAC code (Fast Lagrangian Analysis of Continua) as shown in Fig. 7. In contrast, Marston's analytical equation does not account for the lateral variation of vertical stresses and hence, the stress values remains constant across the full stope width at any depth of the fill.

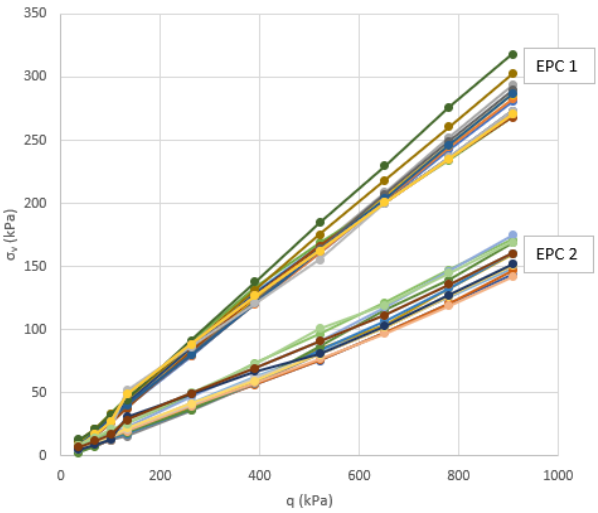

Fig. 6 Lateral variation of vertical stress at the stope base-experimental results

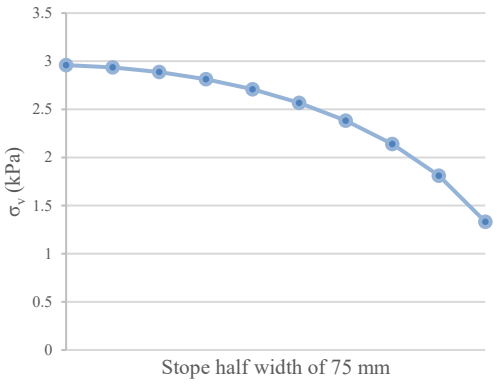

Fig. 7 Lateral variation of vertical stress at the stope base from center to edge-FLAC simulation

(a) (b)

Fig. 8 (a) Drive barricade model apparatus (b) EPCs attached to the stope base

Square (SD) and circle (CD) cross section drives of two separate dimensions (100 mm and 150 mm) were tested using the apparatus shown in Fig. 8 to determine the effect of drive shape and size on vertical and horizontal stress distribution. The barricade offset or setback distance was set at 4 different positions (0, 25, 50, 75 mm) for each drive size and shape to determine the stress function as offset increases.

Fig. 9 displays the recorded barricade pressure at each offset tested for the 100 mm drive with circular cross-section (CD100). The plot displays a definite correlation between barricade pressure and offset distance. As the barricade is constructed at an increasing distance from the stope brow the stress reduces. This relationship was apparent for all four offsets and confirms that reduction of lateral load acting on the barricade with increasing offset distance, encouraging miners to install the barricade as far as possible from the stope brow. However, the common industry practice is to keep the barricade offset distance equal to the drive height to reduce the drainage time of the fill (Li and Aubertin, 2009a).

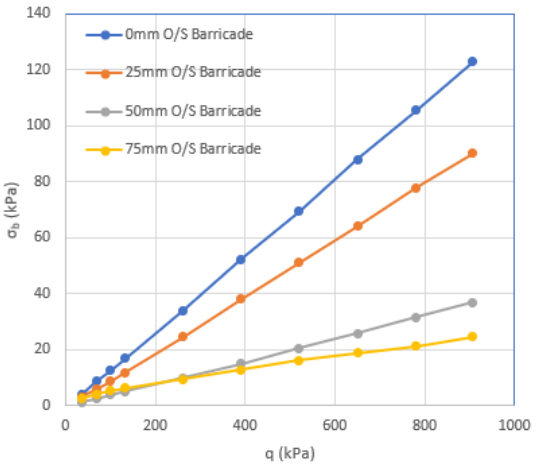

Fig. 9 Barricade stress variation with offset in CD100

The dimensionless analysis using the parameters (i.e. stress at barricade /stress at drive entrance vs barricade offset (x)/drive height (d) in Fig. 10 shows that the barricade stress is larger for small drive sizes at each offset distance, however, the barricade stress is not largely influenced by the shape of the drive. It can be seen that the barricade stress is reduced to approximately 20% of the stress at the drive entrance when the offset distance is half of the drive height or more.

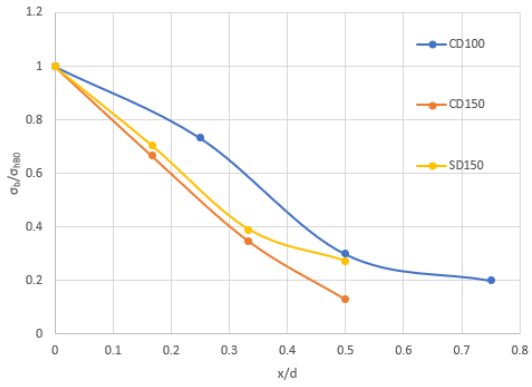

Fig. 10 Dimensionless comparison of drive shape/size with barricade offset distance

The above results were well compared with the analytical solutions reported in Li and Aubertin (2009a), confirming the non-linear progression of the barricade stress with offset and the use of higher friction angle soils to be advantageous when attempting to reduce stress with offset.

Kuganathan (2002) expresses an analytical equation to determine the barricade stress as below.

$$\sigma_b=\sigma_o\times\exp\left(-\frac{PK_0\tan\delta}{A}L\right) \quad (2)$$

where, σ_b the horizontal stress at the barricade, σ_0 the horizontal stress at the drive entrance, P the drive perimeter, A the barricade cross sectional area and L the barricade offset distance.

Laboratory results were compared with the Kuganathan's equation in a dimensionless analysis as shown in Fig. 11. The analytical solutions show an overestimation of barricade stresses at an offset approaching the drive height for both active and at-rest earth pressure coefficients however the at-rest condition is more comparable with the experimental results justifying the same behavior as in Fig. 4. Furthermore, Kuganathan solutions also verified that the trend of barricade stress reduction with offset distance is non-linear.

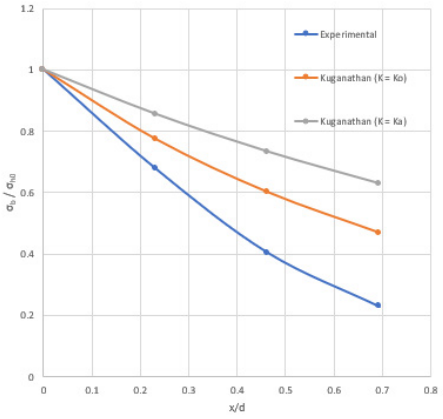

Fig.11 Analytical and experimental comparison of barricade stresses

5 SUMMARY AND CONCLUSIONS

To better understand the stresses within the mine stopes and drives, two separate laboratory models were developed. They were filled with fine sand and a series of tests was carried out to clearly demonstrate the reduction in σ_v within the stope due to arching, and the decay in σ_h within the drive. The model test results were then compared with analytical solutions and it was shown that the Marston's equation gives realistic predictions of σ_v within a vertical stope, provided $K = K_0$ and $\delta = \phi$. Laboratory results and numerical simulations with FLAC verify the reduction of vertical normal stresses laterally across the stope width with the lowest recorded at the stope walls. However, the analytical solutions give an average vertical stress across the entire stope width at any depth of the fill without considering the lateral variation.

The barricade model tests confirm that within the σ_h decays with horizontal distance rapidly, confirming the analytical solutions presented in Li and Aubertin (2009a) and Kuganathan (2002). The comparison also verifies the advantage of using a backfill with higher friction angle to reduce the barricade stresses with offset. The Kuganathan's expression overestimates the barricade stresses when compared with experimental results however, it was again confirmed that K_0 is more reliable to predict the barricade stresses at each offset distance.

6 REFERENCES

Aubertin, M., Li, L., Arnoldi, S., Belem, T., Bussière, B., Benzaazoua, M. and Simon, R. (2003). Interaction between backfill and rock mass in narrow stopes, 12th Pan American Conference on Soil Mechanics and Geotechnical Engineering, pp 1157-1164.

Belem, T., Harvey, A., Simon, R. and Aubertin, M. (2004). Measurement and prediction of internal stresses in an underground opening during its filling with cemented fill, 5th International Symposium on Ground Support in Mining and Underground Construction, pp 619 – 630.

Bloss, M.L. (2014). An operational perspective of mine backfill. Minefill 2014: 11th International Symposium on Mining with Backfill, pp 15-30.

Boger, D.V. (1998). Environmental rheology and the mining industry, 7th International Symposium on Mining with Backfill: Minefill '98, Australia, pp 15–17.

Grice, T. (1998a). Underground mining with backfill, 2nd Annual Summit-Mine Tailings Disposal Systems, pp 1-14.

Grice, T. (2001). Recent minefill developments in Australia, 7th International Symposium on mining with backfill, Seattle, Washington.

Jaky, J. (1944). The coefficient of earth pressure at rest, Journal of the Society of Hungarian Architects and Engineers, 7(2), 355-358.

Kuganathan, K. (2002). A method to design efficient mine backfill drainage systems to improve safety and stability of backfill bulkheads and fills, 8th AusIMM Underground Operators Conference: Growing our Underground Operations, pp 181-188.

Li, L. and Aubertin, M. (2009a). Horizontal pressure on barricades for backfilled stopes. Part I: Fully drained conditions, Canadian Geotechnical Journal, 46(1), 37-46.

Marston, A. (1930). The theory of external loads on closed conduits in the light of the latest experiments, 9th Annual Meeting of the Highway Research Board Held at Washington, D.C., Vol 9, pp 138-170.

Pirapakaran, K. and Sivakugan, N. (2007a). Arching within hydraulic fill stopes, Geotechnical and Geological Engineering, 25(1), 25-35.

Rankine, R., Pacheco, M. and Sivakugan, N. (2007). Underground mining with backfills. Soils and Rocks, 30(2), 93-101.

Rankine, K., Sivakugan, N. and Cowling, R. (2006). Emplaced geotechnical characteristics of hydraulic fills in a number of Australian mines, Geotechnical and Geological Engineering, 24(1), 1-14.

Sivakugan, N., Rankine, R.M., Rankine, K.J. and Rankine, K.S. (2006b). Geotechnical considerations in mine backfilling in Australia, Journal of Cleaner Production, 14(12-13), 1168-1175.

Sivakugan, N., Veenstra, R. and Naguleswaran, N. (2015). Underground mine backfilling in Australia using paste fills and hydraulic fills, International Journal of Geosynthetics and Ground Engineering, 18(1), 1-7.

Sivakugan, N. and Widisinghe, S. (2013). Stresses within granular materials contained between vertical walls, Indian Geotechnical Journal, 43(1), 30-38.

Sivakugan, N., Widisinghe, S. and Wang, V.Z. (2014). Vertical stress determination within backfilled mine stopes, International Journal of Geomechanics, 14(5), 06014011.

Terzaghi, K. (1943). Theoretical Soil Mechanics, John Wiley and Sons, New York, pp 66-99.

Thompson, B.D., Bawden, W.F. and Grabinsky, M.W. (2012). In situ measurements of cemented paste backfill at the Cayeli Mine, Canadian Geotechnical Journal, 49(7), 755-772.

Integral Bridge Abutment-soil Interaction Analysis Using PIV Technique

L.D. Sigdel, C. Leo, S. Liyanapathirana & P. Hu
School of Computing, Engineering and Mathematics, Western Sydney University, Australia

ABSTRACT: Integral abutment bridges(IABs) are bridges designed without the use of expansion joints. Hence, the superstructure and substructure of IABs translate or rotate in unison to accommodate alternate cycles of expansion and contraction due to temperature changes. IABs are less expensive to construct and easier to maintain, compared to traditional bridges with joints. However, IABs also result in complex soil-structure interactions problem created by thermally induced cyclic movements imposed on the approach embankments to integral bridge abutments. As a consequence, the wall movements create more uncertainty in predicting the lateral earth pressure distributions, and the soil settlement and heaving behind the abutment wall. This paper presents a study of the soil-abutment interaction of an IAB during translational active and passive movements of the abutment. Particle image velocimetry(PIV) technique has been used to observe the soil deformation, and to explain the ratcheting of the lateral earth pressure distribution and the development of settlement trough and surface heave at the back of the abutment.

1 INTRODUCTION

A traditional bridge includes the expansion joints and bearings to accommodate the bridge expansion and contraction due to the temperature variations. The 'Integral Abutment Bridge (IAB)' is a bridge structure constructed by eliminating the bearing and joints between the deck and abutment (Biddle et al. 1997). In forgoing the use of bridge joints, IABs also avoid the costs and issues associated with their installation, and subsequent maintenance and repair. Hence, IABs have become the primary choice of design over traditional bridges. However, there is a complex soil-structure interaction mechanism between the retained soil and bridge abutment during expansion and contraction of the bridge deck due to diurnal and seasonal temperature changes. Consequently, IABs have some practical limitations.

Since the superstructure and sub-structure (abutment wall) of an IAB are integrally connected, cyclic loading due to seasonal thermal variations cause the wall to move into and away from the retained soil. Consequently, these wall movements cause the densification and loosening of the backfill soil behind the abutment wall. Also, it is evident that an increase in the lateral earth pressure on the abutments occurs during repeated cyclic movements of the bridge deck (CIRCIA 1976 and England 1994). Knowledge of complex soil-structure interaction to correctly estimate the lateral stress is therefore necessary to design the IABs subjected to cyclically imposed movements.

Based on the type and design of abutments and its foundation, abutments either rotate and, or translate without rotation to accommodate the thermal expansion and contraction of the bridge superstructure. The magnitude of the translation and, or rotation of the abutments due to the seasonal temperature variations is larger than the daily temperature changes, and it can significantly mobilise the retained soil than due to the daily temperature variations. Neither Australian nor Eurocode provides design guideline of integral abutment bridges; however, BA 42/96 (2003) has brief design guidelines of IABs, which is later updated as PD6694 (2004).

BA 42/96 (2003) limits the maximum overall length of IABs to 60 m and recommends to design where the induced cyclic movement of abutments is equal, or below ± 20 mm. Later the recent design guideline PD6694 limits the maximum movement to 40 mm. The lateral earth pressure distribution at the soil-abutment boundary during cyclic loading cannot be predicted from monotonic stress-strain data of soil (BA 42/96 2003). Also, the estimation of the passive earth pressure distribution on the abutments with relation to the wall movements in PD6694 is significantly larger than those given by Hambly (1991). In addition, it does not explain the soil deformations behind the abutments and consequent effects on the lateral earth pressure distribution. Hence, it is necessary to understand the complex soil-structure interactions mechanism at

monotonic and cyclic loading conditions to correctly estimate the lateral earth pressure distribution for the design of IABs. The study at different wall movement conditions will benefit the future design and help to investigate the inadequacies in current design approach, which is based on the monotonic soil-structure interactions.

It is inherently essential to capture and understand the complex soil-structure interaction of an IAB in order to accommodate the effects of different thermal conditions on lateral soil pressure. Particle image velocimetry (PIV) technique Stanier et al. (2016) has been widely used for measuring deformations in geotechnical models, also known as digital image correlation (DIC) (Peters et al. 1983). The DIC is an image-based deformation measurement technique by analysing the sequences of digital images captured during geotechnical model tests. GeoPIV-RG software is an improved image-based analysis program using the normalised cross-correlation framework developed by Stanier et al. (2015), and White et al. (2003). This research used the GeoPIV-RG software implemented in MATLAB to study the soil-abutment interactions. The brief description of the GeoPIV algorithm and detailed description of the software is given by White et al. (2001), White et al. (2003), and Stanier et al. (2015).

The principle of PIV analysis is graphically presented in Fig. 1. The PIV algorithm tracks the texture (i.e. the spatial variation of brightness) between the test patch taken from an initial image and the best match patch from the following image within the area of interest. The highest degree of match between the patch from an initial image 1(time = t1) and patch from the following image 2 (time = t2) gives the displaced position of the same patch (u2, v2). The analysis is continued for all the sequential images to obtain the complete trajectories of each test patch.

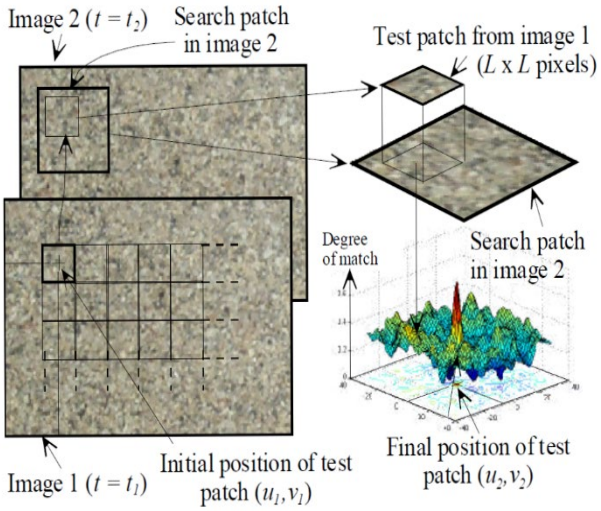

Fig. 1 Overview of PIV-DIC analysis principles (White & Take 2002)

This paper briefly explains the soil structure interaction of an IAB by tracking the localised shearing and volumetric changes, which are obtained during the movement of an abutment wall within a geotechnical model tank. The model wall was translated horizontally in an active or passive mode simulating the bridge deck contraction and expansion during temperature decrease and increase, respectively. The results from contraction and expansion soil-abutment interactions are observed. The deformations tracked by the DIC technique are used to determine the volumetric and shear strain changes in the retained soil mass. Differences observed in the active and passive wall movements concerning soil deformation, volumetric and shear strain changes are analysed and discussed.

2 EXPERIMENTAL PROGRAMME

Since the contrasting nature of the material texture influences the precision of the GeoPIV results, White and Take (2005) suggested that any material with contrasting grain structure can be used to maximise the quality of the tracking mechanism of particles during the model tests. Previous studies by Lam et al. (2012), White and Take (2005) and Zhang et al. (2005) did not mention any specific scatter method and focused on randomly scattering materials with a different texture. In this study, the dry siliceous sand was mixed randomly with the black sand and applied to the exposed face of the model tank to achieve an image texture with sufficient contrast. Sieve analysis showed that sand was of uniform size, with a particle size starting from 300 to 425 µm. The sand was loosely placed in the test chamber by maintaining the constant falling height, and the obtained dry density was 1.596 g/cm^3. The friction angle of siliceous sand was 30°. The measurement of two subset texture quality parameters: (a) the standard deviation of subset pixel intensities (σ_{Is}) > 15 (Stanier & White 2013) and (b)r the sum of the square of subset intensity gradients (SSSIG)> 10^5 (Pan et al. 2008) indicated the images with mixed of normal and black sands have sufficient contrast and adequate texture distribution.

2.1 PIV model tank

The laboratory model tank of dimensions 700× 250 × 300 mm (length, breadth, height) contains a transparent perspex window of 50mm thickness at the front panel to capture the images for the PIV analysis. The model contains the retained soil of 660× 248 × 230 mm (length, breadth, height), and the movable wall of 300mm height, 248mm width and 13mm thickness. The movable vertical

wall is connected with two supporting rods to prevent any rotational movement during translational wall movement, and one movable bar, as shown in Fig. 2.

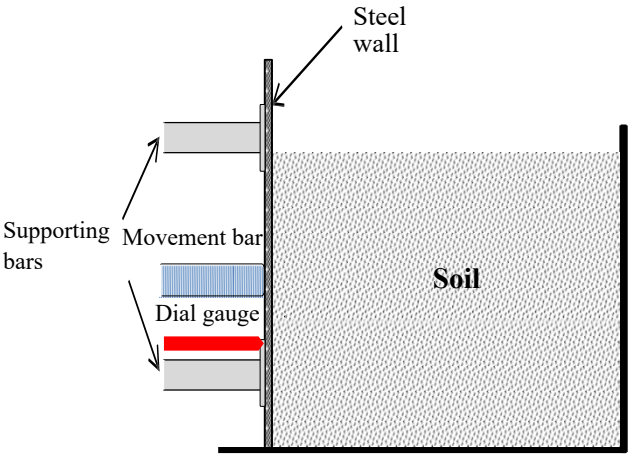

Fig. 2 The experimental model set-up (Al-Qarawai 2016)

All three bars are connected to the rigid frame, and the movement of the wall is controlled by the external screw connected to the centre of the rigid frame. The wall was freely sitting on the bottom of the model tank, and the configuration of the rods and wall was set-up in such a way that the movement is truly translational.

2.2 Camera

An 18- megapixel digital camera (Canon EOS 550D) with the maximum frame rate of 30 fps at 1080p HD video recording was used for the experiment. The camera was closely set up with the tripod at the distance of 500 mm away from the front side of the transparent window to obtain clear photographs, and the position was maintained throughout the tests such that the image resolution is sufficient for the PIV analysis.

2.3 Lighting

Two white LED lights of 20W are placed at two sides of the model tank to provide uniform illumination at the exposed face of the model tank. An artificial light dispersing method was applied on the surface of the light to enhance the uniform distribution of the emitting light.

2.4 Control points

Six control points with known object-space coordinates were positioned at the transparent window to calibrate the image space coordinates to the object space coordinates using the subroutine provided in GeoPIV-RG. Calibration parameters also assist in quantifying the precision of the deformation measurement technique physically.

2.5 Model testing

The steel wall representing the bridge abutment is supported on and translates along the rigidly held bottom surface of the model tank (Figure 1). The supporting walls of the tank are rigidly fixed and do not move with the abutment. The movement of the abutment (steel wall) is leveraged against one face of the rigid supporting walls of the tank. Therefore, the model set up represents the IAB configuration, as described in the BA 42/96 (2003). The wall was moved 20 mm horizontally at the rate of 0.125 mm/sec and 0.167 mm/sec for the active and passive movements, respectively. A video was recorded during both experiments, and images were extracted from the video for the PIV analysis to maintain uniformity among these images. The texture quality, apparatus set-up, and granular material were the same for monotonic active and passive movement tests.

2.6 PIV analysis

PIV technique was employed using GeoPIV-RG software to analyse soil deformations and to calculate the volumetric strain and the maximum shear strain. The area of interest (AOI) was selected, corresponding to the adjacent boundaries of the retained soil for the analysis. Both analyses were conducted using the same analysis parameters. The tolerance value of seed correlation coefficient ($CC_{ZNCC\text{-}seed\text{-}tol}$) (Stanier et al. 2015) was 0.9 for both analyses, and the diameter of the subset (D_s) was set as 64-pixel with 32-pixel subset spacing.

3 RESULTS AND DISCUSSION

The soil rearrangement and shear band formation behind the abutment wall were observed during 20 mm active and 20 mm passive wall movements. The volume changes due to shear deformations were also observed from the image analysis. The total maximum shear strain (i.e. summation of maximum principal strain difference), and the total volumetric strain (the change in volume with respect to the original volume) is expressed as a percentage.

Fig. 3 shows the vectors of total displacement and Fig. 4 shows the contours of total soil displacement after 20 mm of active translation. As expected, Fig. 3 and Fig. 4 shows that the significant deformation was concentrated near the wall, forming a somewhat active wedge-shaped region, and no significant deformation was observed outside this active wedge.

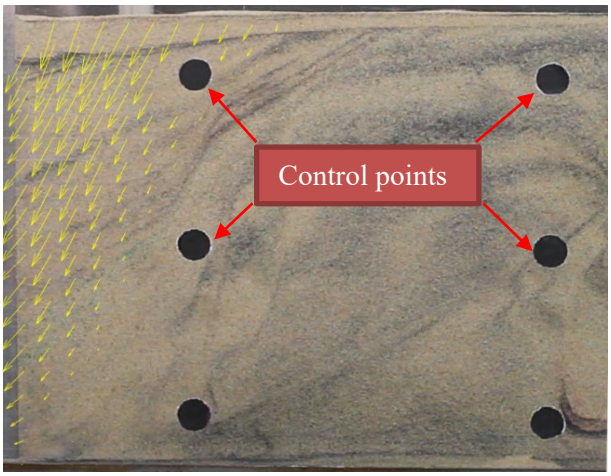

Fig. 3 Soil displacement vectors after 20 mm of active translational movement

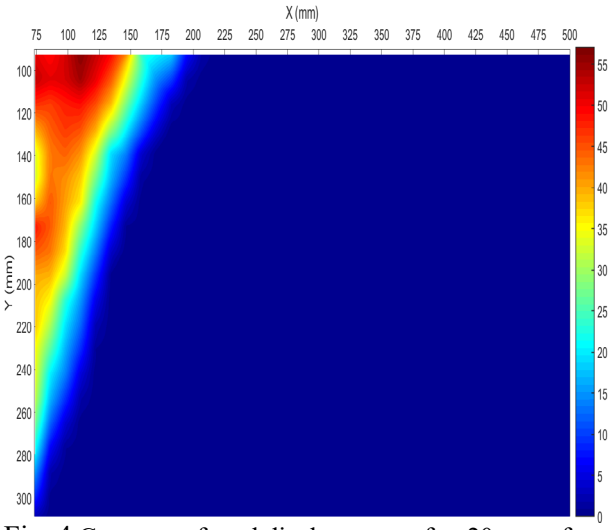

Fig. 4 Contours of total displacement after 20 mm of active translational movement

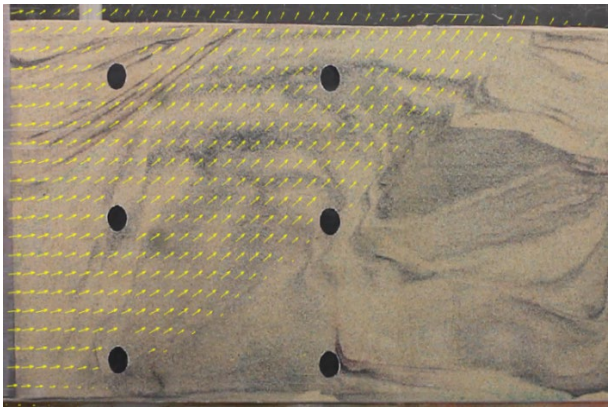

Fig. 5 Soil displacement vectors plot after 20 mm of passive translational movement

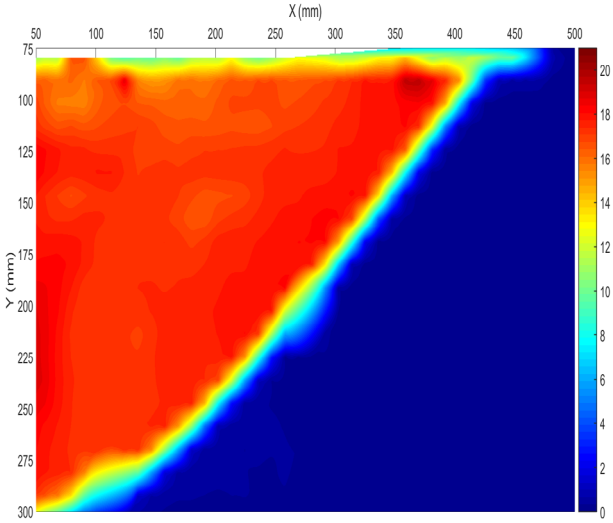

Fig. 6 Contours of total displacement after 20 mm of passive translational movement

Similarly, total displacement vectors and the contours of soil deformation after 20 mm of passive displacement are shown in Fig. 5, and Fig. 6, respectively. The magnitude of total displacements observed in the passive case is more than double the active case for the same magnitude (i.e. 20 mm) of wall movement towards and away from the neutral position of the wall. The area of deformation is approximately 350% higher in the passive translation compared to the active case. These deformations indicate that the formation of a settlement trough behind the abutment wall is significantly high for the active case. It also shows that the maximum displacement occurred behind the wall and the deformations forming a passive wedge-shaped region.

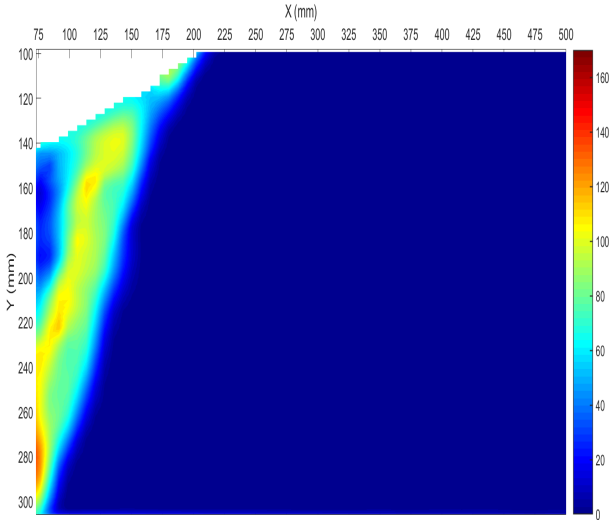

Fig. 7 Shear strain after 20 mm of active translational movement

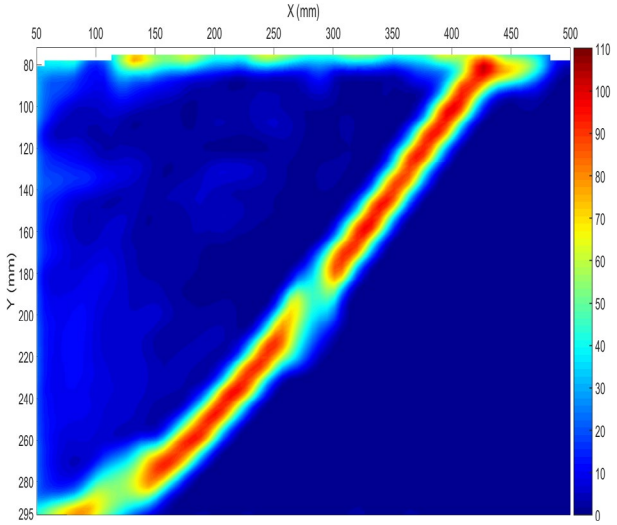

Fig. 8 Shear strain after 20 mm of passive translational movement

Fig. 7 and Fig. 8 shows that the total maximum shear strains levels are 45% higher in the active translation than those observed for the passive translation. The observed shear strain is highly concentrated near the toe of the wall and moving up to the surface in the active case. Also in passive case, shear strain contour shows the same amount of concentration near the toe and a 35° plane extending to the surface, which indicates that mostly the granular particles are moving upwards along the shear plane. A wider shear band was observed during the active displacement, while a narrower shear band of curvilinear shape appeared during the passive wall movement. However, the wider shear band is approximately a straight line. The wider shear band in active wedge failure indicates the region where rearrangement of soil grains happened.

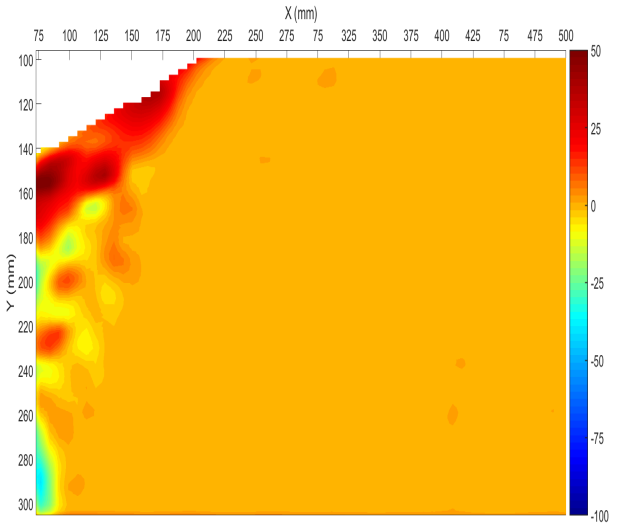

Fig. 9 Volumetric strain after 20 mm of active translational movement

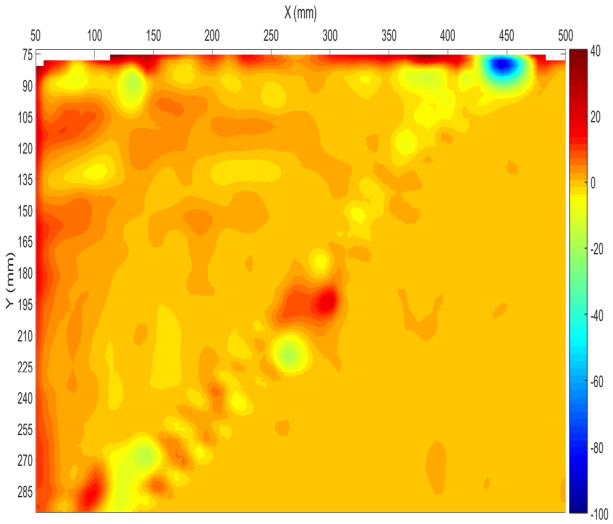

Fig. 10 Volumetric strain after 20 mm of passive translational movement

As shown in Fig. 9 and Fig. 10, the volumetric strain pattern for the active wall movement shows both densification (positive volumetric strain) and loosening (negative volumetric strain) of soil behind the abutment wall. Loosening occurred at the surface of the settlement trough; densification occurred along the back of the abutment wall because of soil slumping in the downward direction, which was seen below the settlement trough. It is the same region where the gradient of deformation is quite high and also the predominant region of strain localisation.

A clear pattern of soil dilation can also be seen in both active and passive displacement profiles shown in Fig. 9 and Fig. 10. The dilation mostly happened near the abutment wall in the active case, whereas dilating material is observed inside the sliding mass in the passive wall movement, and mostly mobilised within the shear band. A thin band of dilating material could also be observed in Fig. 8 and Fig. 10, which represents soil heaving at the top surface of sliding mass within the passive zone.

The maximum volumetric strain is 15% higher in active deformation. However, soil ratcheting is higher in the case of passive displacement than that for the same amount of active displacement. It can be seen that the soil densification is happening near the abutment wall to a larger extent in the passive movement than the active movement, which is in agreement with the previous findings.

4 CONCLUSIONS

The results presented in this paper have shown the complex soil-structure interaction mechanism between bridge abutments and retained soil. A small

model tank with a movable abutment wall and granular retaining soil were subjected to monotonic active and passive movements. The GeoPIV technique was employed to analyse the soil deformations and to study the development of shear bands along the failure surface.

The corresponding densification and loosening of granular soil due to the movement of the wall imply that the soil properties change continuously during the wall movement. Although the amount of heave is significantly lower for 20 mm of passive displacement, it can accumulate increasingly with the time and will change the backfill conditions. Also, the precise observations of the soil deformations illustrated that GeoPIV-RG has the capability to indicate the densification and loosening zone.

The temperature difference has a notable effect on the earth pressure acting on the wall, but for the same amount of wall movement during expansion and contraction develop different effects on the wall. Results show that soil densification is mostly happening near the abutment wall during the passive displacement, which can increase the lateral stress on the abutment. Also, the dilation area below the approach slab (top surface of retained soil) indicates that the integral bridge abutment and approach slab connection needs to provide adequate lateral clearance for the approach slab and also the design consideration to resist the lateral build-up stress at different temperature conditions.

Both monotonic wall movements started from the at-rest earth pressure conditions. However, practically, the temperature variations are cyclic with or without constant cyclic magnitude. Also, the pressure distribution can be different from the initial at-rest condition when the wall moves back to the at-rest position after an active cycle or a passive cycle. The complex soil-structure interactions suggest that there is a need to develop new models of lateral earth pressure coefficients for cyclic soil-wall movements not covered by classical active and passive pressure theories which are based on monotonic soil-wall interactions. Therefore, the ongoing investigation on the cyclic wall movements will help to perform the comparative studies on lateral earth pressure ratcheting during the significant yearly and minor daily temperature variations.

ACKNOWLEDGMENTS

The authors are grateful to laboratory technical staff at the Western Sydney University for their continuous assistance during the experiments and, to Western Sydney University for the Graduate student research fund. Also, the authors wish to acknowledge the support provided by Ahmed Al-Qarawi and Minghao Lu in carrying out the experiments.

REFERENCES

Al-Qarawi, A. (2016). The application of EPS geofoam in mitigating the approach problems in integral abutment bridges. ME thesis, Western Sydney Uni., Sydney, NSW.

BA 42/96. (2003). Amendment No. 1, highway structures: Approved procedures and general design, Section 3.5. The Stationary Office, London

Biddle, A., Iles, D., and Yandzio, E. (1997). Integral steel bridges: Design guidance, Publication No. P163. Ascot: Steel Construction Institute.

England, G. (1994). Shakedown solutions for soil containing structures as influenced by cyclic temperatures-Integrated bridge and biological filter. Proc. of the 3rd Int. Conf. on Structural Engineering, pp 1-11.

Hambly, EC (1991), Bridge deck behaviour, CRC Press.

Hayward, C., and Gross, T. (1976). Design and construction of circular biological-filter walls. Construction Industry Research and Information Association. London, Report No. *58*(26652), 26.

Lam, S. Y., Elshafie, M. Z., Haigh, S. K., and Bolton, M. D. (2012). A new apparatus for modelling excavations. International Journal of Physical Modelling in Geotechnics, 12:24-38.

Pan, B., Xie, H., Wang, Z., Qian, K., and Wang, Z. (2008). Study on subset size selection in digital image correlation for speckle patterns. Optics express, 16:7037-7048.

Peters, W. H., Ranson, W. F., Sutton, M. A., Chu, T. C., and Anderson, J. (1983). Application Of Digital Correlation Methods To Rigid Body Mechanics. Optical Engineering, 22:738-742.

Stanier, S. A., Blaber, J., Take, W. A., and White, D. (2015). Improved image-based deformation measurement for geotechnical applications.Canadian Geotechnical Journal, 53:727-739.

Stanier, S. A., and White, D. (2013). Improved Image-Based Deformation Measurement in the Centrifuge Environment. Geotechnical Testing Journal, 36:915-928.

White, D., and Take, W. (2002). Particle Image Velocimetry (PIV) software for use in geotechnical testing, University of Cambridge, Department of Engineering.

White, D. J., Take, W. A., and Bolton, M. D. (2005). Discussion of "Accuracy of digital image correlation for measuring deformations in transparent media" by Samer Sadek, Magued G. Iskander, and Jinyuan Liu. Journal of computing in civil engineering, 19(2), pp 217-219.

White, D., Take, W., and Bolton, M. (2003). Soil deformation measurement using particle image velocimetry (PIV) and photogrammetry. Geotechnique, 53:619-631.

White, D., Take, W., Bolton, M., and Munachen, S. (2001). A deformation measurement system for geotechnical testing based on digital imaging, closed-range photogrammetry, and PIV image analysis. ICSMGE lisse 2001, Proceedings of the 15th International Conference on Soil Mechanics and Geotechnical Engineering, pp 539-542.

Zhang, Y., Tan, T., and Leung, C. (2005). Application of particle imaging velocimetry (PIV) in centrifuge testing of uniform clay. International Journal of Physical Modelling in Geotechnics, 5:15-26.

Critical review of the use of Crosshole Sonic Logging (CSL®) method as a tool to investigate the integrity of bored and cast in-situ piles

A.G.K.P. Niwunhella, K.C.Waduge and H.S.Thilakasiri
Department of Civil Engineering, Sri Lanka Institute of Information Technology

ABSTRACT: Integrity of bored and cast in-situ piles should be assessed thoroughly as tendency of occurring defects in such piles is higher due to improper construction methodologies. Crosshole Sonic Logging (CSL®) test is widely used in the industry to identify potential anomalies in order to ensure the quality and integrity of bored piles. In this paper, several classification systems of bored piles based on CSL test results are identified and the effectiveness of each classification system is assessed towards the critical evaluation of pile integrity. The impact of the classification on the performance of piles using Tomographic Analysis is identified towards the acceptability of piles and potential reasons for the occurrence of defects are studied in Sri Lankan context. Moreover, the shortcomings of CSL test have been identified and evaluated the adaptability of alternative tests such as Thermal Integrity Profiling (TIP®) method to overcome the inherent shortcomings of CSL method.

1 INTRODUCTION

1.1 Crosshole Sonic Logging (CSL®) test and Tomography

Cross Hole Sonic Logging (CSL®) test is a non-destructive pile integrity testing method based on transmission of an ultrasonic wave through concrete between two probes moved in pre-installed access tubes along the pile shaft. First Arrival Time (FAT) and the Energy of the received signal are considered for the identification of the suspicious areas where the anomalies may be present in the pile shaft. Based on the delay of FAT and reduction in energy of the received signal, pile profiles are categorized according to the following universal pile profile categorization scale.

Table 1: Universal pile profile categorization scale

Category	FAT increase	AND / OR	Signal reduction	Comment
G	Up to 10%	AND	< 6 dB	Good
Q	10 to 20%	AND	< 9 dB	Questionable
P/F	21 to 30%	OR	9 to 12dB	Poor/ Flaw
P/D	>30%	OR	>12 dB	Poor/ Defect

Though, CSL test reveals the existence of defects at a certain depth of bored piles, the capability is not sufficient to provide a comprehensive detail of the defect along the shaft in terms of its lateral extent and the exact location. Hence, the severity of the identified defect and its physical properties can be assessed using the Tomography Analysis. Tomography is generally defined as a mathematical simulation which provides 2-dimensional and 3-dimensional visual images of the defect along the pile based on the wave speeds obtained from CSL test results. Basically, the pile is modelled and simulated as a grid with an assigned wave speed for each node determined from a mathematical solving algorithm of FAT along the pile depth. Tomography interprets the areas with less wave speeds in different colour schemes for easy identification of the lateral extent. The severity in terms of effective area of the anomalies can be quantified as a threshold to assess the overall acceptability of pile.

Based on the CSL test results, piles can be classified into several acceptance levels from worst to good condition implicating the pile integrity. Classification systems with different acceptance criterion based on the CSL test can be identified in the industry, from the expertise literature and the several standards around the world. It is important to study the effectiveness of different pile classification systems used in the industry based on CSL test. Huang (2018) identified a criterion for the classification of piles using CSL test under several standards around the world. Brown et al. (2010) proposed a methodology for the evaluation of defects and acceptance criteria on piles with a graphically illustrated approach.

Likins et al. (2007) carried out a study using a pile shaft with intentionally built defects and it was shown that the defects were successfully identified with CSL and Tomography analysis. Paikowsky et al. (2000) conduted a successful programme to identify the integrity of four piles with intentionally built defects using Pile Integrity Sonic Analyzer (PISA) along with the Tomography analysis.

The integrity of abutment foundation of Jacu-Pêsego viaduct in Brazil was thoroughly assessed using the fruitful collaboration of CSL and Tomography by Beim et al. (2005). However, it is widely known fact that the CSL measures the integrity of the pile inside of the reinforcement cage.

1.2 Thermal Integrity Profiling (TIP) method

Thermal Integrity Profiling is a standard (ASTM D7949) non-destructive pile integrity testing method which was developed at University of South Florida. It is based on the heat generation during the curing of concrete to evaluate the integrity of deep foundations including bored piles, drilled shaft, micro piles, Auger Cast In-situ Piles (ACIP) and Continuous Flight Auger (CFA) piles. According to Mullins & Piscsalko (2012), TIP method measures the temperature at the radial location of reinforcement cage where the gradient is highest. TIP is capable of determining the integrity of entire pile cross section including the area outside the rebar cage.

According to Fig. 1, relatively low temperatures represent the absence of concrete caused by necking, soil intrusion or low concrete content. However, the presence of excess concrete is indicated by the relatively higher temperatures. Therefore, measured temperature indicates the cage alignment as well as the effective cover. Using the received data, investigations are required to be done in order to identify defects or cage alignment. Followings are the indications of anomalies of pile.

- Low temperature relative to the average temperature at that depth.
- Average temperature significantly lower than the average temperature of other depths.

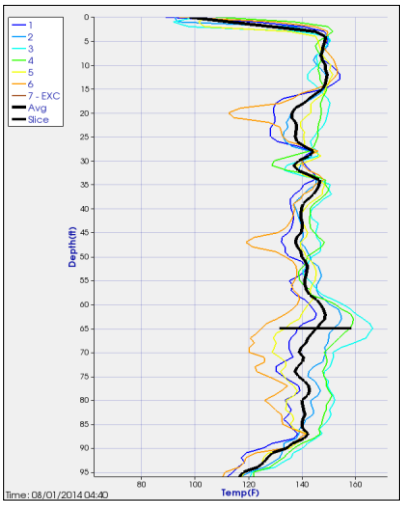

Fig. 1 Depth vs Temperature variation

2 METHODOLOGY

CSL test and Tomography analysis reports of twenty five bored and cast in-situ piles in Sri Lanka were collected for the interpretation. From test report sample and expertise publications, three classification systems which are integrated with pile acceptance criterion were identified. Key differences of the classification systems and their potential impact towards the pile acceptability were assessed.

The data interpretation was carried out by classifying the collected pile sample under the different classification systems. Thereafter, the acceptability of the pile was determined in accordance with the outcome of Tomography Analysis. A quantitative and qualitative analytical approach were used to determine the most accurate classification system which provided the reliable prediction on the acceptability of piles according to the Tomographic analysis of the CSL profiles. Impact of the anomaly distribution along the pile shaft on the acceptability of pile was investigated. Moreover, the impact and contribution of the Tomographic analysis towards the acceptability of the piles were determined. Also, the accuracy, shortcomings and limitations of CSL test were identified by comparing the integrity from CSL test with the actual field observations of several bored and cast in-situ piles. The adaptability of TIP method to overcome the identified shortcomings of CSL test was assessed along with a comparison of the financial feasibility of both test methods in Sri Lankan context.

3 RESULTS

3.1 Identified classification systems

In this study, the classification systems which were used to classify the piles using CSL test results were mainly based on technical expertise of the professionals and industrial institutions. Three classification systems of piles were identified and adapted from the test report sample and expertise publications for result interpretation.

According to Webster et al. (2011) and several test reports in the sample, Classification system 01 can be identified and presented in Table 2 as follows.

Table 2 : Classification system 01

Rating/ Class	Criteria
A	Acceptable piles, majority of profiles falls to Category G.
B	Questionable (Q) profiles require no further action but may be considered when P/F or P/D also occurs in the same cross section.
C	Flaws (P/F) should be addressed if they are indicated in more than 50% of the profiles.
D	Defects (P/D) must be addressed if they are indicated in more than one profile and involving at least 3 tubes.

In addition, two different classification systems were identified and adapted from the test report sample, tabulated in Table 3 and 4 as follows.

Table 3: Classification system 02

Rating/ Class	Criteria
1	Piles with majority of good profiles (G) and Q, P/F or P/D will be classified as acceptable.
2	Piles with a majority of doubtful (Q) profiles will be classified as acceptable. But they will be recommended for further analysis and remedial action if required when P/F or P/D also occurs in the same transverse direction.
3	Piles with flaws (P/F) in the same transverse cross section in more than 50% of the profiles will be recommended for further analysis and will require remedial action.
4	Piles with defects (P/D) indicated in more than one profiles involving at least three tubes will be recommended for remedial actions.

Table 4: Classification system 03

Rating/ Class	Criteria
1	Piles with majority of good profiles (G) and Q, P/F or P/D will be classified as acceptable. (Acceptance Level 01)
2	Piles with majority of doubtful (Q) profiles will be recommended for further analysis and remedial action if required. (Otherwise this category is an acceptable category). (Acceptance Level 02)
3	Piles with flaws (P/F) in more than 33% of the profiles will be recommended for further analysis and will require remedial action. (Acceptance Level 03)
4	Piles with defect (P/D) indicated in more than 33% of the profiles in will be recommended for remedial action. (Acceptance Level 04)

3.2 Classification of piles

Refer Table A-1 in Appendix A for the summarized data interpretation of sample of twenty five piles.

Classification of the piles in the sample was based on the integrity of area within the rebar cage of the pile.

3.3 Identification of shortcomings in CSL test

CSL test report indicated that a bored pile (Pile A) with 1200mm diameter and 13.5m in length was considered acceptable below its cutoff level. Only one pile profile at 1.57m of depth was identified as questionable (Q) out of all six profiles as shown in Table 5.

But, according to the waterfall diagrams shown in Fig. 3, CSL test indicated an anomalous region about 3.25m depth around tube combination 4-1. It was a considerable anomaly as FAT delay is about 18%.

As shown in Fig. 2, surrounding excavation of the above pile revealed an exposure of rebar cage to outside in all directions indicating the non-existence of concrete cover outside of rebar cage. Hence, CSL test result and actual field observations have showed contradictory outcomes where CSL test has failed to identify the exposure of rebar cage. It further verifies the ability of CSL test to identify anomalies is only limited to the area within the rebar cage. This type of defect is very critical for piles used to carry both axial forces and moments as the moment carrying capacity of piles without the required cover is minimal due to the corrosion of the exposed rebars.

Fig. 2 Surrounding excavation of pile A

Table 5: CSL test results of pile A

Profile No	Depth (m)	FAT delay (%)	Energy decrease (dB)	Pile category
1-2	Full depth	<10	<6	G
2-3	Full depth	<10	<6	G
4-1	1.57	18	<6	Q
4-3	Full depth	<10	<6	G
1-3	Full depth	<10	<6	G
2-4	Full depth	<10	<6	G

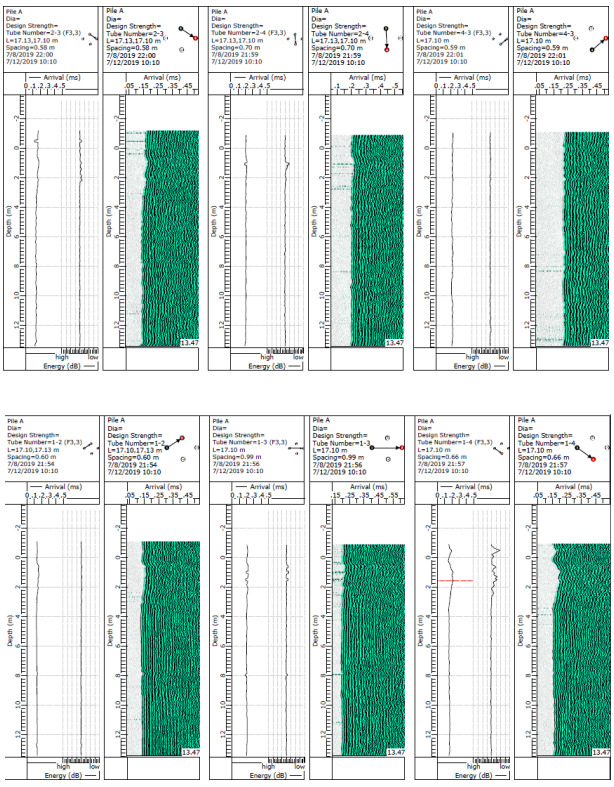

Fig. 3 Waterfall diagrams of pile A

3.4 Financial feasibility of TIP test in Sri Lanka

All the cost related details relevant to both CSL and TIP tests were collected through Pile Dynamics Inc. (PDI) which is the manufacturer of both CSL and TIP test kits. The initial cost of TIP test including entire test apparatus and software is USD 42,600.00 excluding the GST and shipping charges from USA. The cost of thermal wire is around USD 5.00 per feet with the capability of manufacturing custom lengths as per the request. Each thermal wire should be enclosed with a connector and a terminator which are USD 25.00 and USD 20.00 each respectively. Table 6 shows the detailed cost comparison of CSL test and TIP method to evaluate integrity of 20m long bored pile in Sri Lanka. It included the cost of materials transportation and installation.

Table 6: Cost comparison of CSL and TIP tests

No	Pile type	Total cost to conduct CSL test (LKR)	Total cost to conduct TIP method (LKR)
01	A 1000 mm dia. bored pile with four access tubes / thermal wire cables.	70,000.00*	322,721.62**
02	A 1500 mm dia. bored pile with six access tubes / thermal wire cables	85,000.00*	457,074.93**

* Please note that these prices are excluding tax. At present, Value Added Tax (VAT) will be 8% in Sri Lanka.
** Values can vary with the exchange rates. Here, it is considered as USD 1.00 = LKR 180.05

4 DISCUSSION AND ANALYSIS

In classification system 01 as shown in Table 2, the localization of P/D anomalies in the same cross section is considered for the acceptance criterion on class D which is critical. Piles are classified as class C when more than 50% of the profiles fall into P/F category indicating that it is based on the distribution of anomalies.

According to Table 3, the criterion for class D of classification system 02 is identical to the criterion of classification system 01. Also, it can be identified that the localization of anomalies in cross sections is considered for class C criterion. Moreover, piles are classified as class B, when majority of profiles fall into Q category. And, further actions will be recommended if P/F or P/D profiles exists

on the same cross section which is more critical for the integrity.

Acceptance criteria of classification system 03 comprises with considerably different considerations compared to classification systems 01 and 02. According to Table 4, piles are classified as class D, when P/D profiles are indicated in more than 33% of the profiles. The distributed presence of P/D profiles along the shaft is considered which is critical during the evaluation, as the severity of P/D profiles are fairly high. Also, piles are classified into class C, when P/F profiles are indicated in more than 33% of the profiles which indicates the distributed presence of P/F profiles. It is more conservative than other systems, as it allows 33% of profiles with flaws (P/F) for the consideration where other two systems are based on 50% of profiles.

It can be identified that classification system 03 is comparably conservative than the other classification systems. In classification system 03, the acceptability of the piles in both level 3 and 4 are critical, due to the consideration of less P/D and P/F profiles in the acceptable criteria.

88% of the piles in the sample are determined unacceptable where anomalies are localized within the same transverse cross sections. It reflects that localized presence of the anomalies within cross sections enhances its severity and results an overall unacceptability of the pile. According to Table A-1 in Appendix A, it can be identified that 64% of piles in the sample are considered unacceptable based on the effective areas of anomalies from Tomography. The class wise allocation of twenty five piles of the sample for each classification system can be identified as follows.

Table 7: Class wise allocation of pile sample

Classification system	Class wise allocation			
	Class A/ 1	Class B / 2	Class C/ 3	Class D/ 4
Classification system 01	-	01	04	20
Classification system 02	01	01	04	19
Classification system 03	02	03	01	19

According to Table 7, it can be identified that majority of twenty five piles are classified as class D under all three classification systems.

In accordance with Table 7 and Table A-1, overall integrity of 25% of piles in class C and D of classification system 01 is determined as acceptable, based on the effective area from Tomography analysis. 30 % of piles in class 3 and 4 are considered acceptable in classification system 02. Also, in classification system 03, 20% of piles in class 3 and 4 are determined as acceptable from Tomography. It indicates that classification system 03 has a lower percentage on predicting inaccurate acceptance using CSL test results.

Severity and extent of the identified anomalies were evaluated from Tomography analysis by using 2D and 3D images of both longitudinal and transverse sections. Final acceptability of each pile was concluded based on the effective area of anomalies. Piles which are initially considered as unacceptable in classification systems were considered as acceptable based on the effective areas of anomalies from Tomography analysis. It reflects the significance of Tomography analysis towards the mitigation of the unnecessary further analysis and remedial actions. Fig. 4 shows the accurate contribution of each classification system on predicting the overall acceptability of the piles in the sample.

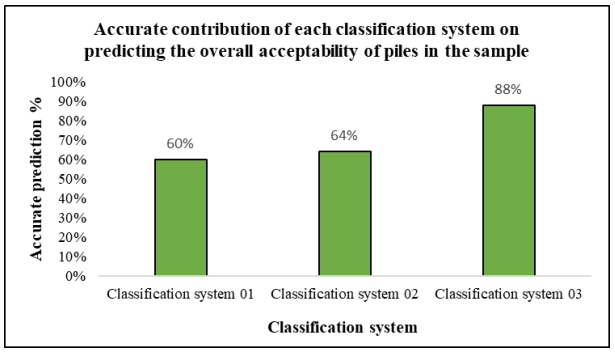

Fig. 4 Accurate contribution of each classification system on predicting the overall acceptability

According to Fig. 4, classification system 03 has a considerable accuracy and effectiveness on predicting the overall acceptability of piles. The use of the conservative approach during the evaluation of anomalous profiles in classification system 03, may have increased the potential of predicting the pile integrity accurately.

Though the accuracy of CSL test is fairly higher than the other conventional pile integrity testing methods according to Sanjula (2019), there can be several shortcomings which influence on the effectiveness of the test. According to Section 3.3, it was observed that CSL test is only capable of identifying the defects in the area within the rebar cage as access tubes are installed along the rebar cage of pile. It basically allows the transmission of the ultrasonic wave within the rebar cage region and defects inside the region will only be detected. Defects in the outside of rebar cage will not be identified and its potential to the pile integrity will not be considered as well. Hence, several situations as mentioned in the Section 3.3 can be occurred where the integrity of pile is doubtful, even if it is

acceptable by CSL test. It can be considered as a major shortcoming of CSL test which directly affects on the pile integrity. Moreover, following can be considered as other shortcomings of CSL test.

- Debonding and inclination of access tubes can influence on the overall result.
- Access tubes should be installed prior to the concrete work. Hence, preselection of the pile is required.

TIP method can be suggested as an alternative for CSL test to overcome its inherent shortcomings. Capability of determining the pile integrity of entire cross section including area outside the rebar cage can be considered as the main advantage of TIP method over CSL test. Also, TIP can measure the shape of shaft and estimate the rebar cage alignment. Test can be performed during the curing process of concrete, thus results can be obtained within 12 to 24 hours.

According to Table 6, the average cost of TIP method is considerably higher than the cost of CSL test. Hence, TIP is not economically feasible compared to the CSL test. However, TIP provides a valuable return for such investments due to its ability to scan entire pile cross section with higher accurate results with less consumption of time. But, in situations where number of piles are limited and applied loads are higher, TIP method would be ideal during the integrity evaluation.

5 CONCLUSIONS

Classification system 03 in Table 4 has provided more accurate and reliable interpretation on predicting the acceptability of the piles using CSL test results. The application of conservative acceptance criteria based on the severity, distribution and frequency of anomalies has increased the potential accuracy of classification system 03.

Tomography analysis has imposed a major impact on the performance of pile by accepting the piles which are initially considered unacceptable from classification systems. Such piles are evaluated to ensure the presence of adequate integrity using the effective areas of anomalies. It mitigates the potential of taking the unnecessary remedial actions and the additional cost regarding the further analysis.

Distributive and localizing behavior of anomalies impose a certain impact on the severity of the anomalies. Piles with localized anomalies within the cross sections are likely to be unacceptable as it enhances the severity. Also, the distributed presence of anomalies along the shaft imposes a less influence on the severity. And, those pile are likely to be acceptable except the considerable distribution of Poor/Defect (P/D) anomalies which denotes a severe condition.

Major shortcoming of CSL test is the inability to detect anomalies outside of rebar cage. TIP method can be suggested as an alternative for the inherent shortcomings of CSL test due to its higher accuracy. But TIP method is considerably expensive than CSL test. However, TIP can be very useful and ideal to evaluate the integrity of most critical, important and sensitive pile shafts in the structures as integrity of such piles are extremely vital.

ACKNOWLEDGMENTS

The authors would like to convey their sincere gratitude to Piletest Consultants (Pvt) Ltd. for the provision of the field data and the assistance to carry out the study successfully.

REFERENCES

Beim, J.W., Debas, L.F., Kormann, A.C.M., Martinati, L.R. and Neto, L.A. (2005). Tomography: A New Technology for Quality Control of Deep Foundations, GEO3 Construction Quality Assurance/Quality Control Technical Conference: Dallas/Ft. Worth, TX, pp.323-328

Brown, D., Turner, J. and Castelli, R. (2010). Drilled Shafts: Construction Procedures and LRFD Design Methods, NHI Course No. 132014, Geotechnical Engineering Circular No. 10, Report No. FHWA-NHI-10-016, Federal Highway Administration, Washington, DC.

Huang, K., (2018). A research for Class II defect Bored Pile's Accept Criteria; A case of Penang Second Marine Bridge, IOP Conference Series: Earth and Environmental Science, Volume 128, p. 012080.

Likins, G., Rausche, F., Webster, K. and Klesney, A. (2007). Defect analysis for CSL testing, Geotechnical Special Publication No. 158, American Society of Civil Engineers: Reston, VA.

Mullins, G. and Piscsalko, G. (2012). Thermal Integrity Profiling: An Innovative Technique for Drilled Shafts, The Magazine of Deep Foundation Institute, pp. 51-54.

Paikowsky, S. G., Chernauskas, L. R., Hart, L. J., Ealy, C. D., and DiMillio, A. F. (2000). Examination of a New Cross-Hole Sonic Logging System for Integrity testing of drilled shafts, Proceedings of Sixth International Conference on the Application of Stress-Wave Theory to Piles, Niyama S. and Beim J. edt, pp. 223-230.

Sanjula, T.V. (2019). Investigation of the accuracy of the commonly used pile integrity determination methods in Sri Lanka. UG thesis, Sri Lanka Institute of Information Technology, Malabe, Sri Lanka.

Webster, K., Rausche, F. and Webster, S. (2011). Pile and shaft integrity test results classification, mitigation, acceptance, and/or rejection, TRB Annual Meeting 2011 Washington, D.C, No.11-2619

Accuracy of the commonly used pile integrity testing methods

T. V. Sanjula
Department of Civil Engineering, Sri Lanka Institute of Information Technology

H. S. Thilakasiri
Department of Civil Engineering, Sri Lanka Institute of Information Technology

R. M. Abeysinghe
PileTest Consultants (Pvt) Ltd., Sri Lanka

ABSTRACT: In Sri Lanka, the use of pile foundations has amplified, with the rapid construction of high-rise structures. Construction difficulties and improper quality control measures cause anomalies in pile shaft which reduces the load-carrying capacity. Among various integrity determination methods available, Pile Integrity Test (PIT®), Pile Driving Analyzer (PDA®), Cross-hole Sonic Logging (CSL®) and pile coring are the most commonly used procedures in Sri Lanka. In this paper, test results of bored and cast-in-situ piles in different development projects in Sri Lanka were collected and analyzed to identify the capabilities and accuracy levels of different testing methods. In this respect, the accuracy of identifying the defect, severity and location of the defect of CSL tests were investigated by comparing with tomographic analysis and coring results. Limitations of PIT and PDA were identified by comparing with CSL, tomographic and/or coring of piles. Finally, reliability of the different testing methods was summarized.

1 INTRODUCTION

At present, pile foundations which are in the category of deep foundations have achieved a wide utilization in the industry, as it provides high bearing capacities and in need of less earthmoving than shallow foundations. Generally bored and cast-in-situ piles have the tendency of containing anomalies due to complications in the construction process. Hence it is vital to carry out necessary testing procedures to identify the defects present in the pile shaft. There is a wide range of available testing methods to evaluate the integrity of the piles. Among various non-destructive testing methods available, small strain dynamic testing using Pile Integrity Test (PIT), Cross-hole Sonic Logging (CSL) test, Tomographic Analysis and large strain dynamic testing using Pile Driving Analyzer (PDA) are most common in Sri Lanka as they are economical, user-friendly and time saving when compared to other similar methods. The conventional method of coring of the pile shaft, which is a destructive method of testing is also conducted to confirm the defects. Proper apprehension of prerequisites, limitations and thorough planning for conductance of these tests are important to obtain accurate evaluation on the pile integrity.

It is the common practice in the industry to conduct different integrity determination methods for the same pile profile when the obtained results are of unsatisfactory levels. The results of some of the considered tests subject to variation in different situations. Hence it is important to identify the causes for the deviations in order to evaluate the accuracy in the output result.

White et al. (2008) have tested 66 friction pile shafts using the CSL and PIT where they have indicated both similar and contradictory results. Likins et al. (2007) have also presented a case where the accuracy of CSL and effectiveness of tomography analysis has been confirmed by testing of a pile with purposely designed defects. Rausche (2004) has identified that pulse-echo method of PIT has disregarded the small defects in piles which are between 1% to 5% of the pile cross sectional area and that the CSL has identified the defects more precisely but is only limited to the area between the two access tubes. A study done by Massoudi and Teferra (2004) has appraised three case histories where PIT has been conducted to identify the anomalies present in different types of pile shafts and has concluded that PIT successfully matches with results of static load test in one of the cases. These various interpretations in the literature denote the unpredictable nature of the integrity determination methods, in different situations.

A more comprehensive analysis based on the potential capability of the PIT, PDA, CSL, Tomog-

raphy Analysis and pile coring to identify the anomalies in the pile shaft is presented through this paper.

2 METHODOLOGY

Field data on piles subjected to different testing methods were collected and the data were sorted and arranged. Velocity records of the piles from the PIT, CASE method and CAPWAP method results of PDA, the waterfall diagram records from the CSL, Tomographic analysis results of corresponding CSL and the coring data were acquired for analytical purposes, as available. The obtained data were sorted, arranged and compiled for concise data presentation, and overall data on thirty piles were obtained. Then, the test results of different integrity determination methods conducted to the same pile were compared and analyzed to identify the similarities, diversions and possible causes for variations in the results. Through the interpretations of the analysis, the accuracy levels of each integrity tests were evaluated. The limitations of the tests were identified through the analyzed data samples.

3 RESULTS

Field data on piles which have been subjected to two or more integrity determination methods has been obtained and the indicated data were evaluated to identify the similarities and differences in the results. The piles were categorized as follows,

i. Category A : Piles with confirmed defects
   - Combination 1 : Coring and CSL®
   - Combination 2 : Coring and PIT®

ii. Category B : Piles with semi verified defects
   - Combination 3 : CSL® and PIT®
   - Combination 4 : CSL® and PDA®

For the Category A, piles which have been subjected to coring were considered, as it provides clear visualization and confirmation of the defects present in the pile shaft.

For Category B, piles which have been subjected to CSL were considered, as the results interpreted from the CSL does not provide direct confirmation of the anomalies in the pile shaft. The interpretations from CSL results may have some uncertainty.

4 DISCUSSION

Field data on thirty piles which have been subjected to two or more of integrity evaluation methods from Pile Integrity test, Pile Driving Analyzer, Cross hole Sonic Logging test, Tomographic Analysis and pile coring have been evaluated. In most of the piles, the obtained data has denoted some contradiction in the final result. The quantity of piles regarded for each category and combination are presented in Table 1.

Table 1. Percentage of piles considered for each category and combination

Category	Combination	Percentage of piles in each combination	Percentage of piles in each category
A	Coring and CSL®	6.67%	10%
	Coring and PIT®	3.33%	
B	CSL® and PIT®	40%	90%
	CSL® and PDA®	50%	

By evaluating the obtained data of the pile sample, it could be observed that majority of the piles indicate the defective zone in or near the toe region of the pile. This confirms that proper cleaning and concreting of the pile toe is critical in the initial stage of pile construction. Hence, implementation of necessary quality control measures is highly recommended during construction.

The destructive method of pile coring can infer inaccurate interpretations on pile integrity when the drilled hole is not kept vertical. Even a small tilting can result misinterpretation of depths of the defects. The PIT identifies defects by the response of the pile to an impact on the pile head. To obtain accurate results and depths, it is important to receive a clear toe response in velocity records. But due to various site conditions there could be a contrast in depths to defects in different testing methods. Hence, when comparing test results of integrity tests conducted to the same pile profile, if the anomalies present in the pile shaft indicates within ±1.25m in length of one another, it was considered as “similar interpretations” in results. This allowance was adapted to consider the above-mentioned errors that can occur in the tests.

Defect interpretation ability of pile coring can be considered as a more precise approach of integrity determination if the verticality of the drilled hole is maintained. As the length of the drilled holes of piles in Category A have matched with the pile length, it can be interpreted that the output data from coring are precise.

Considering Category A - Combination 01, the two piles subjected to both coring and CSL have shown similar interpretations of the anomalies present in the pile shaft. The precision in the data interpretation ability of CSL has been confirmed by the pile coring as visualization on the defects at the indicated depth has been obtained. This proves that the accuracy of CSL and tomography are fairly high. But the evaluation of the pile integrity is limited to the concrete between the access tubes of the pile.

Conferring to the above case, it could be observed that the CSL interpretations of the considered piles are accurate. Hence, for further evaluation of test results of other integrity determination methods, it could be regarded that CSL provide considerably accurate data interpretations. But the certainty of the precision of CSL test results are lower than coring data.

In regard to Category A - Combination 02, the coring and PIT data have provided contradictory interpretations. This case opposes the ability of PIT on accurate data interpretations.

The Piles in Category B - Combination 03, has shown both similar and contradictory interpretations of PIT test results as illustrated in Fig. 1.

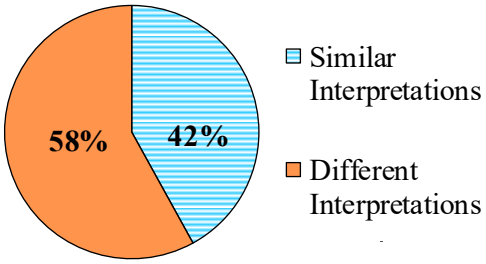

Fig. 1 Comparison of test results from PIT and CSL

As it is regarded that the CSL data provide more accurate interpretations, this demonstrates the inability of PIT to properly identify the defects in the pile shaft in certain cases.

Fig. 2 demonstrates that out of 58% piles where PIT have shown different interpretations to the corresponding CSL test results, 57% have not indicated a clear toe response in the velocity record of the pile. These data support that the precision of data interpretation in PIT is affected by the inability of the stress wave to reach the toe level of the pile.

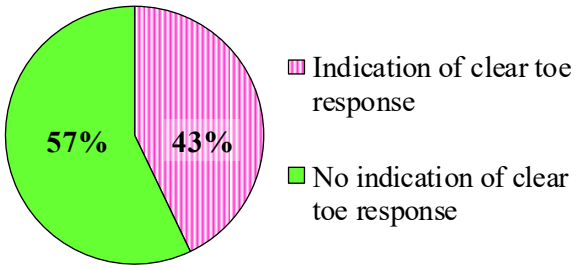

Fig. 2 Effect of toe response in contradictory data interpretations of PIT

This phenomenon mainly occurs when the soil resistance along the pile shaft and the length of the pile is fairly high. Also, when a large anomaly in the shaft is present following with a considerably small defect, the reflection of the stress pulse due to the large anomaly might mask the reflection due to the small defect. Moreover, in some cases, the defects near the pile top have not been indicated in the velocity record, which may occur due to the masking effect, where the anomaly contains within the impact pulse. As a remedial action for these cases, selection of a suitable hammer which will generate an adequate stress wave could be recommended.

Considering the fifteen piles belonging to Category B, Combination 04, the PDA test results have indicated some contradictory results than CSL by both case method and CAPWAP method or by one of the methods.

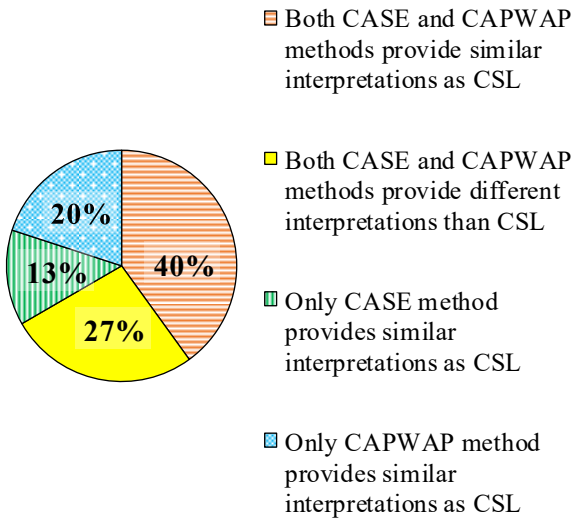

Fig. 3 Comparison of test results from PDA and CSL

Regarding Fig. 3, 73% of the piles have shown similar results to CSL by either one of CASE method or CAPWAP method, or by both methods. Hence, it could be interpreted that PDA shows considerably high accurate levels with respect to

the considered pile sample. From Fig. 3 it is clear that,

- Probability of CASE method in defect identification = 53%
- Probability of CAPWAP method in defect identification = 60%

Hence, from the considered sample it can be evaluated that in PDA, CAPWAP method has higher probabilities in defect identification than CASE method.

When comparing data interpretation ability of PIT and PDA in Figs 1 and 3, it could be observed that PDA has presented high percentage of similar interpretations than PIT when compared with CSL data. Hence it can be regarded that the PDA have shown more accuracy than PIT.

Accordingly, from the evaluation of the above field data, an understanding of the accuracy of the tests in some of the circumstances could be obtained.

5 CONCLUSION

The piles analysed in the research demonstrate cases where each considered testing methods have presented both similar and contradictory results which represent its accuracy.

As majority of the piles indicate defects near the pile toe region, it can be considered that proper pile toe construction is critical in the initial stage.

With respect to the considered pile sample, it could be regarded that CSL along with tomography analysis has provided more accurate interpretations of the anomalies present in pile shaft. The accuracy of CSL results has been confirmed by coring data.

Where PIT and coring has been conducted to the same pile, PIT has been unable to confirm the defect, resulting in uncertainty on the accuracy of PIT in certain cases.

From the evaluated test results, it is evident that PDA has shown high accuracy levels in results interpretation than PIT when compared with CSL data.

In cases where PIT has indicated contradiction to the corresponding CSL, it could be observed that majority of the piles have not shown a clear toe response.

When considering CASE method and CAPWAP method of PDA, the CAPWAP method has exhibited high probabilities of accuracy when compared with corresponding CSL data.

Consequently, it is clear that a better understanding of the defects present in the pile shaft can be obtained by utilizing a combination of integrity determination methods, rather than conducting an individual test for a pile. For the selection of a suitable testing method and result interpretation, the limitations of each test should be properly recognized.

ACKNOWLEDGMENTS

The authors would like to thank PileTest Consultants (PVT) Ltd. that supported by providing necessary field data for this study. In particular, authors wish to acknowledge Manager; Mr. R. M. Wijesinghe of the organization, for the support.

REFERENCES

Likins, G., Rausche, F., Webster, K. and Klesney, A. (2007). Defect analysis for CSL testing. In Contemporary Issues In Deep Foundations, pp. 1-10.

Massoudi, N. and Teferra, W. (2004). Non-Destructive Testing of Piles Using the Low Strain Integrity Method. Proceedings of the Fifth International Conference on Case Histories in Geotechnical Engineering: New York, NY; 1–6.

Rausche, F. (2004) Non-destructive evaluation of deep foundations (CD-ROM), Proceedings of the Fifth International Conference on Case Histories in Geotechnical Engineering, New York, NY.

White, B., Nagy, M., & Allin, R. (2008). Comparing cross-hole sonic logging and low-strain integrity testing results. In Proceedings of the Eighth International Conference on the Application of Stress Wave Theory to Piles (pp. 471-476).

Observations on Non-uniform Deformations in Laboratory Shear Test Soil Specimens using Digital Image Correlation

A. Soysa & D. Wijewickreme
Department of Civil Engineering, University of British Columbia, Canada

ABSTRACT: The level of uniformity of the deformations in soil specimens during monotonic triaxial compression and extension tests was assessed using simplified digital image correlation (DIC) analysis. Photographs of the specimens taken during and at the termination of the loading were compared with respect to the initial stage using an open-source subset-based 2-dimensional DIC package. Approximate qualitative DIC analysis considering a simplified two-dimensional image allowed assessing the development of vertical and horizontal displacements during triaxial tests conducted on specimens of silt-alone, sand-alone, and sand-silt homogeneous mixtures. It was found that this simple analysis approach could trace "barreling" and "necking" type deformations that take place during triaxial shear tests with reasonable acceptability for qualitative comparative assessments. The displacement contours of sand-silt layered specimens revealed similar type of variations with compared to that of uniform sand-alone and silt-alone specimens, thus no especially notable confined or local deformation were observed in sand-silt layered specimens.

1 INTRODUCTION

Axial or shear displacements of soil specimens are generally measured using a Linear Variable Differential Transformer (LVDT) in typical geotechnical laboratory shear tests. However, the LVDT measurements only provide total (global) displacement of the test specimen and are not able to capture distribution of deformation along the test specimen, leaving the effects of possible and inevitable non-uniform and localized deformations not addressed in the calculation of strains. Gaining satisfactory observations on the displacement distribution of the test specimen would enhance the insight and the interpretation of the soil response and shear failure mechanism. For an example, strain localization - including shear banding - is one of the most important consideration in understanding the pre- and post-failure deformations in geomaterials.

Digital image correlation (DIC) - an optical metrology based numerical computing technology - (Chu et al. 1985; Peters eta l. 1983) is a popular contactless, high-accurate measuring system in solid mechanics. In recent years, DIC methods have been significantly improved achieving high accuracy and reducing the computation complexity with the advancement of technology and it is widely used in many applications such as surface displacement analysis, particle image velocimetry (PIV) and material stress analysis (Bay, 2008). DIC methods have also been used in geotechnical laboratory application by many researchers (White et al. 2003; Higo et al. 2013; Takano et al. 2015) to study the localized deformation and development of strains in soil specimens.

DIC analysis incorporates a correlation function to track the translation of the locations those are arbitrarily specified in the reference image against a later image, in which solid body movements are of interest. In cases where deformations or displacement are to be traced (unlike the rigid body movements), the translations in the area of interest are determined by optimizing the cross-correlation coefficient calculated in the correlation. When an image analysis is performed using single fixed digital camera images, such as two-dimensional DIC and PIV, it is limited to the displacement in the two-dimensional surface; whereas DIC analysis on images from multiple coordinated camera unit or with computed tomography (CT) images is capable of tracking a three-dimensional displacement field which is often referred as digital volume correlation (DVC). As DVC comprises of displacement–rotation–strain degrees of freedom in the global spatial domain (unlike the displacement only in surface domain during DIC), it inherits more complexities and computational challenges.

The incorporation of two-dimensional DIC in geotechnical laboratory applications faces numerous challenges due to many factors such as: (i) the cylindrical surface typical to most element testing specimens – difficulty in tracking in or out of plane deformation in the two-dimensional surface of the selected image; (ii) rubber membranes enclosing the soil specimens masking the direct visibility of soil particles - it is only possible to trace the speckle on the rubber membrane that encloses the soil; (iii) refraction issues arising from the pressurized water and the acrylic confining chamber in conventional triaxial tests; and etc. Although many research

works (Chaney et al. 1997; Alshibli and Al-Hamdan, 2001; Sachan and Penumadu, 2007; Bhandari et al. 2012) have being carried out to address these challenges and adopt DIC algorithms in the measurement of deformation in specimens, due to the complexity of the challenges, a standard procedure or guideline for using DIC in the geotechnical laboratory shear tests is yet to be formulated. Reliable deformations measurements from geotechnical laboratory shear tests are crucial and essential in obtaining high quality data for characterizing geo-material behavior. Nevertheless, it was found that, with reasonable assumptions and simplifications, results from simple two-dimensional DIC can be effectively used for a qualitative assessment of the shear loading response of soil.

This paper intends to present some initial observations from DIC analysis performed on the images captured during triaxial shear tests conducted on specimens of sand-alone, silt-alone, and sand-silt mixtures with appropriate simplifications and reasonable assumptions. The limitations and drawbacks of simple two-dimensional DIC analysis are also identified.

2 EXPERIMENTAL SET-UP

2.1 *Camera set up*

A digital camera was set up placing it on a tri pod that was approximately 2m in front of the triaxial cell; the camera angle and the location were adjusted such that: (i) the mid-point of the image is aligned with the center of the cylindrical specimen; and (ii) image plane is parallel to the vertical axis (see Fig. 1) to avoid perspective distortion. Sufficient distance from the camera and the specimen was maintained to minimize camera lens-based distortions.

When a photo of a specimen in the triaxial cell is captured, a light ray passes through water medium (in the cell) to acrylic medium (cell wall) and then to air medium (in the atmosphere) resulting refractions in each cases of change in mediums as shown in Fig. 2. The images were captured at a resolution of 3456 x 5185 pixels, later the photos were cropped to a resolution of 1291 x 2365 pixel to feed to the DIC analysis when the region of interest was defined.

The complex algorithms on ray tracing-based corrections (three-dimensional refraction models) to account the deviations due to refractions were not practiced in here; however, initial calibrations were performed to ensure sufficient accuracy in measuring displacements was obtained along the vertical axis that passes through the mid-height of specimen (Note: Vertical axis passing through the midpoint of the specimen can be considered least affected by the refractions). In this regard, a photo of a specimen in a water-filled acrylic cell [see Fig. 3-(C)] was used as the reference image for the initial calibration instead of a photo of just a specimen before it is enclosed with the acrylic cell and water [see Fig. 3-(A)], and total axial displacement derived from the DIC process was compared with the computed axial displacement from a data set obtained from a LVDT. However, horizontal displacement (projection of the radial displacement into two-dimensional surface) was not calibrated. A close match between LVDT and DIC in axial displacement measurements indicated the system reliably to trace the surface deformation characteristics of triaxial specimens to a satisfactory level with a focus of only qualitative assessment of the distribution of displacement characteristics.

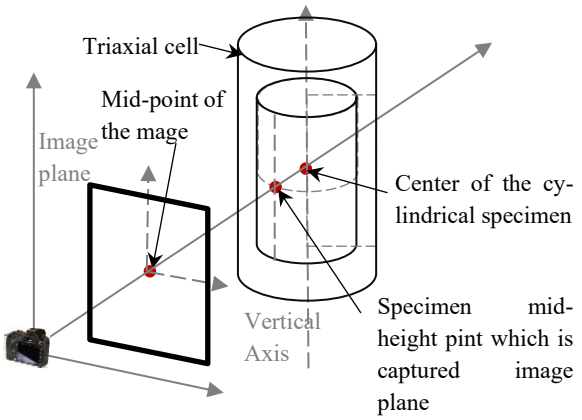

Fig. 1 Schematic of specimen in the triaxial cell and the image plane with respect to the camera

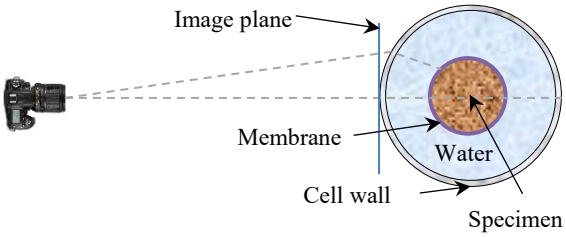

Fig. 2 Schematic of ray refraction in three different mediums (air/atmosphere, acrylic wall and water)

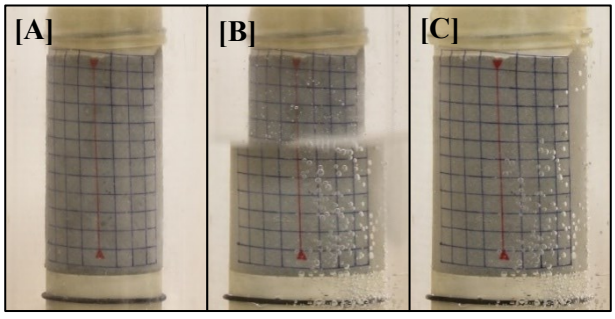

Fig. 3 Photographs of: [A] a typical soil specimen; [B] the specimen partially filled with water in the acrylic cell; and [C] the specimen in the fully water-filled acrylic cell

The above does not preclude the need for the use of ray-tracking techniques (to account for refraction in three-dimensional space and advance calibration/validation of camera images with the measurement points of the specimen) when accurate quantitative assessment of displacement distribution of a triaxial specimen is desired.

2.2 *Digital Image Correlation*

Ncorr (an open-source subset based 2-dimensional DIC package) by Blaber et al. (2015) was used for the DIC analysis presented in this paper. Ncorr allows the user to define multiple regions of interests, multiple sequence image analysis, subset radius, subset spacing, multiple threads and visual interfaces in both in Lagrangian and Eulerian view options.

2.3 *Simplifications and assumptions*

For an approximate qualitative analysis from DIC, the following assumptions are made with respect to imaging of triaxial specimens:
(i) externally measured displacements of the rubber membrane are an accurate representation of the displacements experienced by the soil particles of the specimen located immediately behind the membrane;
(ii) displacements in three-dimensional space of the specimen with ~72 mm diameter can be approximately represented in 2-dimensional space from the photographs taken using a single camera;
(iii) deviations of the actual locations in the reference image with respect to the specimen due to refractions and associated distortions are considered negligible for the approximate qualitative analysis conducted herein.

2.4 *Soil used in triaxial specimens*

Fraser River sand and silt obtained from Lower Mainland British Columbia, Canada were processed to obtain samples of sand and silt. The digital images of homogeneous specimens containing sand-alone (100C), silt-alone (100F), 50% sand - 50% silt mixture (50C50F) and some layered sand-silt specimens (50C50F-FC and 50C50F-CFC), which were captured during triaxial compression and extension tests, were used in DIC analysis for qualitative assessment of the spatial distribution of displacement and localized deformations.

3 SPATIAL DISTRIBUTION OF DISPLACEMENTS IN TRIAXIAL SPECIMENS FROM DIC ANALYSIS

The approximate height and radius of a triaxial test specimen considered herein were about ~145 mm and ~72 mm respectively. The test specimens were isotropically consolidated to 100 kPa, prior to the application of displacement-controlled shearing (i.e., compression or extension). DIC results obtained from six tests (referred to herein as A, B, C, D, E and F) are summarized and presented in Fig. 4 and Fig. 5. For each test, the two photographs (in the left two columns in Fig. 4 and Fig. 5) show the initial reference frame (Case I) and final deformed frame (Case III), respectively. The total axial displacement (TAD) in the Case I is 0 mm as it refers to the post-consolidated state just before the commencement of shearing (for both the cases of compression and extension). An intermediate state during the shearing was also used in the DIC analysis and referred as Case II in each test. Spatial distributions of the horizontal and vertical displacement are presented as color coded contour plots for Case II and Case III in each test. The middle two columns in Fig. 4 and Fig. 5 refer to the contour plots of horizontal displacements, whereas right two columns show vertical displacement plots. The following sections intend to detail the DIC analysis results and to discuss the observed spatial distributions of displacement of each test.

A – 100C-Com
This refers to a triaxial compression test performed on a specimen comprised 100% Fraser River sand.

Photographs showing Case I and Case III in Fig. 4-A indicate a “barrel-shaped” deformation that has taken place during the compression loading. A careful visual observation would reveal slightly more barreling deformation at the right side of the specimen compared to that at left side. DIC analysis results shows very uniform development of horizontal and vertical displacement for the intermediate state of Case II. The minimum vertical displacement occurred at the bottom base, whereas the top base indicated maximum vertical displacement and the progress from that minimum to maximum values shows a very uniform pattern in the plot. The vertical displacement progress for Case III seems to be very uniform. Although horizontal displacement plot indicated a slightly more displacement at the mid height on right edge, comparative to the left edge, in an overall sense, this test can be considered as a case of uniform development of axial displacement along the specimen.

B – 100C-Ext
The series of photos in Fig. 4-B refers to triaxial extension test performed on a specimen comprised 100% Fraser River sand. Contrary to barreling type observed in *A – 100C-Com*, necking type deformation can be observed in *B – 100C-Ext* - as expected in an extension test.

In general, uniform progress of displacement can be seen for both horizontal and vertical directions in Case II. However, as the TAD increased in Case III, slight local progress of vertical displacement, at the mid height of the specimen (where necking was developed) can be observed. Horizontal displacements indicated a minor deviation from the symmetricity in the contour plot.

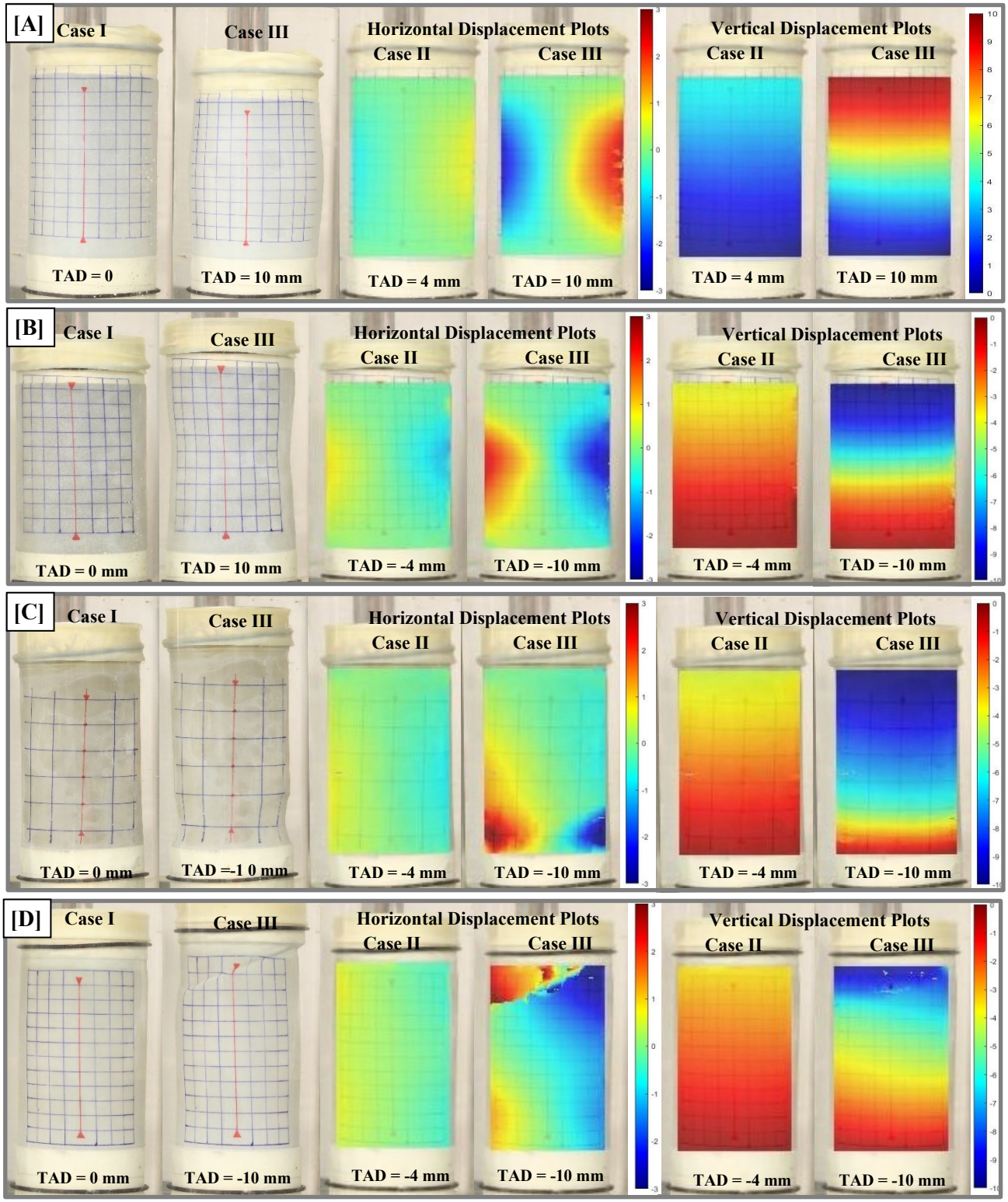

Fig. 4 Results of DIC analysis showing Case I (Initial reference case), Case 2 (Intermediate case with a TAD of 4 mm) and Case III (final case with a TAD of 10 mm) [TAD – Total axial displacement, A: 100C-Com, B: 100C-Ext, C: 100F-Ext, D: 50C50F-Ext]

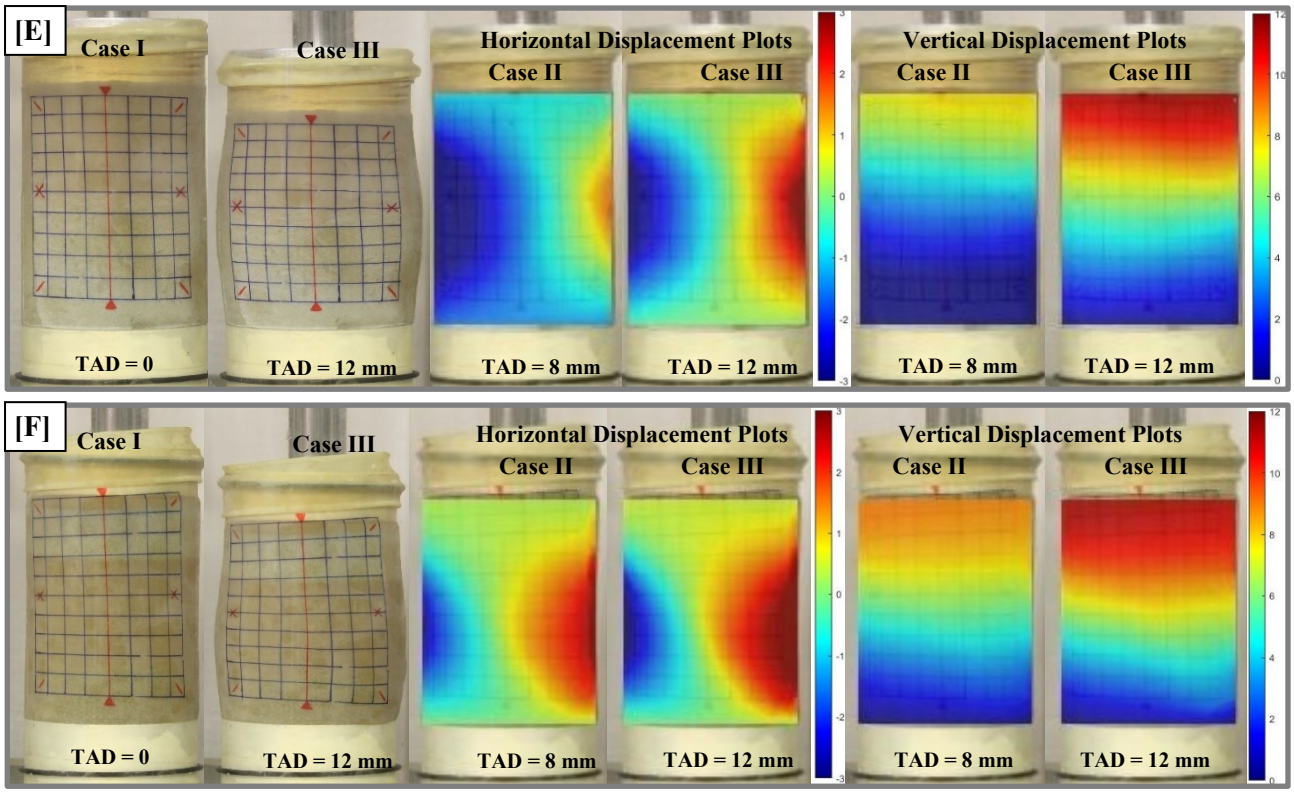

Fig. 5 Results of DIC analysis showing Case I (Initial reference case), Case 2 (Intermediate case with a TAD of 8 mm) and Case III (final case with a TAD of 12 mm) [TAD – Total axial displacement, E: 50C50F-FC-Com, F: 50C50F-CFC--Com]

C – 100F-Ext

This set of images in Fig. 4-C refers to triaxial extension test performed on a specimen comprised 100% Fraser River silt. The clearly visible localized necking type deformation was seemed to have been satisfactorily traced in DIC analysis.

In Case II, both horizontal and vertical contour plots indicate a uniform progress in accumulation of displacement. However, in Case III, contour plot for horizontal displacement shows that higher magnitudes of displacements are confined to the bottom region of the specimen. Further, vertical displacement contour plots show non-uniformity in the progress of displacements along the specimen, especially at the bottom portion of the specimen. The clearly observable confined contours in the contour plots in Case III at the bottom of the specimen indicated the significant local displacement.

D – 50C50F-Ext

A triaxial extension test performed on a specimen with a composition of 50% Fraser River sand and 50% silt mixture and the specimen comprised a uniform sand-silt mixture. Fig. 4-D presents the photographs and contour plots related to this test.

Photographs showing Case I and Case III in Fig. 4-D clearly indicated the developed shear failure plane at the top portion of the specimen. DIC analysis implied smooth progress of displacement at the stage of Case II, and also satisfactorily traced the local shear failure at the top portion in Case III. However, it is noticeable the contours specially around the shear failure plane are cluttered, showing the inefficiency of simple two-dimensional surface DIC analysis in tracking the shear band with possible membrane wrinkles.

E – 50C50C-CF-Com

Fig. 5-E refers to the DIC analysis results of triaxial compression test performed on a sand-silt specimen which had two layers (top silt layer and bottom sand layer). The test specimen possessed an overall composition of 50% Fraser River sand and 50% silt.

Vertical displacement plots indicated very uniform progress in accumulation of displacement along the specimen and the pattern is very similar to that of *A – 100C-Com*. However, notable deviation of symmetricity in horizontal displacement contours can be observed.

F – 50C50F-CFC-Com

The photographs and results of DIC analysis for the triaxial compression test performed on a sand-silt specimen which had three layers (middle silt layer sandwiched by the top and bottom sand layers) are

shown in Fig. 5-F. The test specimen possessed an overall composition of 50% Fraser River sand and 50% silt.

Similar to the results observed in *E – 50C50C-CF-Com* fairly uniform progress in vertical displacement and deviation from symmetricity in horizontal displacement contours can be observed. Despite being layered specimens (in test E and F), no significant confined/local displacement could be observed.

4 SUMMARY AND CONCLUSIONS

A DIC analysis, with several assumptions to simplify the computation, was performed focusing approximate qualitative assessments on displacement distribution of triaxial specimens. It was found the simple two-dimensional DIC analysis could capture barrel and necking type deformations and associated non-uniformities during triaxial compression and extension tests with a reasonable manner for qualitative comparative assessments.

The displacement contours of sand-silt layered specimens revealed similar type of variations with compared to that of uniform sand-alone and silt-alone specimens. No notable confined or local deformation were observed in layered specimens. It was identified that a simple two-dimensional DIC is inefficient in tracing shear band development with membrane wrinkles in triaxial soil specimen.

It is noteworthy that simple two-dimensional DIC analysis allows qualitative assessment on the non-uniformity in the progress of displacement accumulation of soil specimens during geotechnical laboratory test, enabling some enhancement to the insight and the interpretation of the soil response and shear failure mechanism. Having said this, it is important to note that the assessment of displacement and strains in triaxial soil specimen through DIC analysis raises challenges due to three-dimensional surface, light ray refraction in air, acrylic and water, rubber membrane covering soil particles and etc.

Despite the capability of the simple two-dimensional DIC analysis in capturing the non-uniformities of the deformations in geotechnical laboratory test specimens for qualitative assessment, authors recognize the use of X-ray or micro CT coupled DIC analysis (DVC) and consideration of three-dimensional geometry, light ray refraction for higher degree of accuracy in a quantitative assessment for displacements and strains.

ACKNOWLEDGMENTS

The research was conducted with the financial support provided by the Natural Sciences and Engineering Research Council of Canada (NSERC) Discovery Grant program. The writers sincerely acknowledge the contribution of technical assistance of the UBC Civil engineering Workshop personnel.

REFERENCES

Alshibli, K. A., and Al-Hamdan, M. Z. (2001). Estimating volume change of triaxial soil specimens from planar images. Computer-Aided Civil and Infrastructure Engineering, 16(6), 415–421.

Bay, B. K. (2008). Methods and applications of digital volume correlation. Journal of Strain Analysis for Engineering Design, 43(8), 745–760.

Bhandari, A. R., Powrie, W., and Harkness, R. M. (2012). A digital image-based deformation measurement system for triaxial tests. Geotechnical Testing Journal, 35(2), 209–226.

Blaber, J., Adair, B., and Antoniou, A. (2015). Ncorr: Open-Source 2D Digital Image Correlation Matlab Software. Experimental Mechanics, 55(6), 1105–1122.

Chaney, R. C., Demars, K. R., Macari, E. J., Parker, J. K., and Costes, N. C. (1997). Measurement of volume changes in Ttriaxial tests using digital imaging techniques. Geotechnical Testing Journal, 20(1), 103-109.

Chu, T. C., Ranson, W. F., Sutton, M. A., and Peters, W. H. (1985). Applications of digital-image-correlation techniques to experimental mechanics. Experimental Mechanics, 25(3), 232–244.

Higo, Y., Oka, F., Sato, T., Matsushima, Y., and Kimoto, S. (2013). Investigation of localized deformation in partially saturated sand under triaxial compression using microfocus X-ray CT with digital image correlation. Soils and Foundations, 53(2), 181–198.

Peters, W. H., Ranson, W. F., Sutton, M. A., Chu, T. C., and Anderson, J. (1983). Application of digital correlation methods to rigid body mechanics. Optical Engineering, 22(6), 738–742.

Sachan, A., and Penumadu, D. (2007). Strain localization in solid cylindrical clay specimens using Digital Image Analysis (DIA) technique. Soils and Foundations, 47(1), 67–78.

Takano, D., Lenoir, N., Otani, J., and Hall, S. A. (2015). Localized deformation in a wide-grained sand under triaxial compression revealed by X-ray tomography and digital image correlation. Soils and Foundations, 55(4), 906–915.

White, D. J., Take, W. A., and Bolton, M. D. (2003). Soil deformation measurement using particle image velocimetry (PIV) and photogrammetry. Geotechnique, 53(7), 619–631.

Numerical Simulation of a DCM Column-Supported Embankment: A Case Study

D.S. Liyanapathirana, H. Samuel, C. Leo & P. Hu
School of Engineering, Western Sydney University, Australia

ABSTRACT: In this paper, a case study of a highway embankment in Thailand constructed over Deep Cement Mixed (DCM) column improved ground was investigated. The case study was simulated using the RS2 (2019) finite element program. A 2D plane-strain model was created adopting the equivalent area approach for DCM columns. The field measurements for settlements, excess pore water pressures and lateral deformation of the embankment are compared with the finite element results to verify the numerical model, and to understand the load transfer mechanism. The most likely failure mode of the embankment was investigated by computing the Factor of Safety (FOS) against the bearing failure and bending failure of individual DCM columns, and the overall stability of the embankment. Results show that the most likely failure mode for this embankment is the bending failure of attached columns underneath side slopes of the embankment.

1 INTRODUCTION

Embankments are widely used to provide an elevated platform for roads, railways and runways. When they are constructed over soft clays or organic type weak soils with high compressibility and low shear strength characteristics, extremely large settlements and instability problems are inevitable. To overcome these problems, a wide range of ground improvement technologies have been developed aiming to improve the bearing capacity and settlement characteristics of the soft ground. Although methods based on consolidation are available for the soil to gain strength and stiffness over a long period of time, it is often not economical due to the uncertainties associated with soil conditions, time restrictions associated with the delivery of projects and considerable settlement around the operational area, which may cause damages to adjacent facilities. Consequently, Deep Cement Mixed (DCM) columns are introduced as a fast track and an economical ground stabilisation method to bypass the disadvantages associated with conventional consolidation based ground improvement techniques.

In recent years, ground improvement using in situ DCM columns has been growing steadily in popularity due to efficiency in terms of time and cost, as well as reliability in terms of strength gain compared to many other available ground improvement techniques. DCM columns have been used in many field projects (e.g., Huang and Han, 2009; Jamsawang et al., 2011; Yapage et al., 2014; Chai et al., 2015;) over the last two decades. The DCM columns are always constructed under the embankments or structures to transfer the embankment, traffic and superstructure loads through soft soil to the deep firm strata.

To investigate the complex behaviour of embankments constructed over DCM columns, 2D and 3D numerical modelling based on the finite element method has been used extensively in the past (Yapage et al., 2015). However, not much research effort has been expended to understand the failure modes of column-supported embankments. According to Yapage et al. (2015), progressive failure due to bending failure of individual columns is typical for DCM-column supported embankments because of low bending capacity of DCM columns. However, the failure mode for an embankment may vary based on the design considerations such as the diameter and spacing of columns and other measures, such as geosynthetic reinforcement or large diameter columns near side slopes, adopted to control lateral deformations.

In this paper, a case study of an embankment supported over DCM columns reported by Jamsawang et al. (2016) is considered. The columns in this case are resting on a medium stiff clay layer. During the embankment construction and subsequent consolidation over a period of 130 days, settlement, lateral deformation, pore pressures, and vertical stresses acting on a column near the centre of the embankment and soft clay in between columns closer to the centre

were measured. A two-dimensional plane-strain numerical model created using RS2 (2019) was used to simulate the observed embankment behaviour. Finally, Factor of Safety (FOS) against bearing and bending failure modes of individual columns and overall stability of the embankment were assessed to identify the most likely failure mode for the embankment.

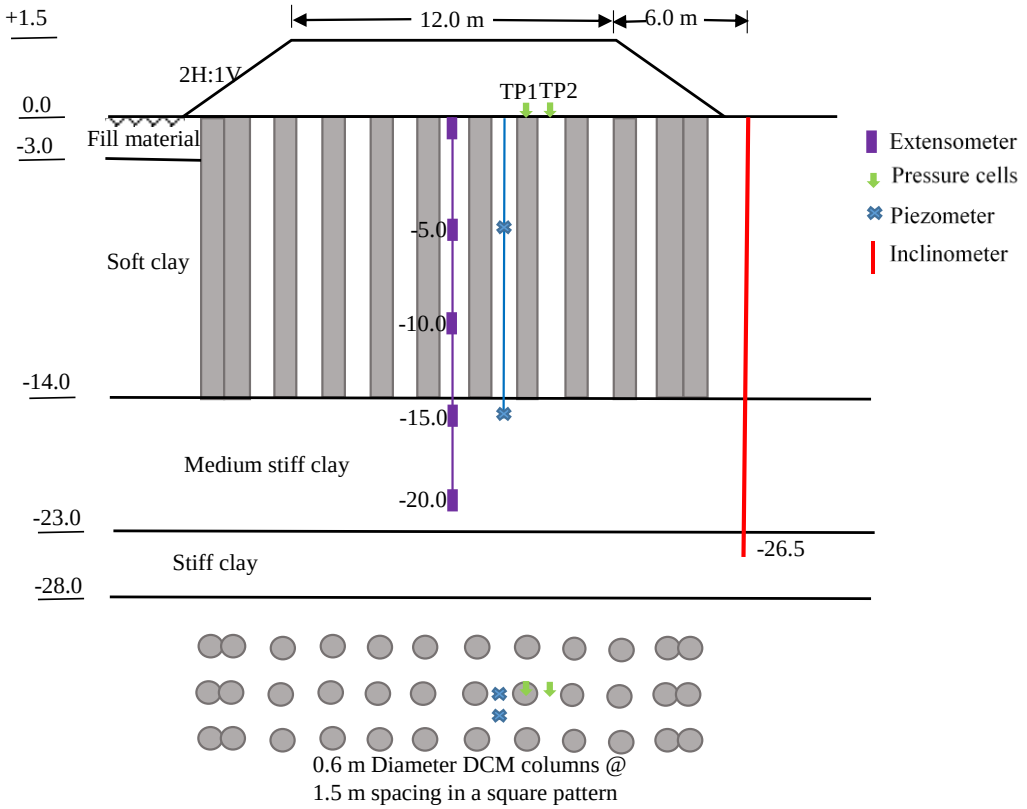

Fig. 1 DCM column-supported embankment with instrumentation (a) Cross-section and (b) Plan views

2 NUMERICAL MODEL

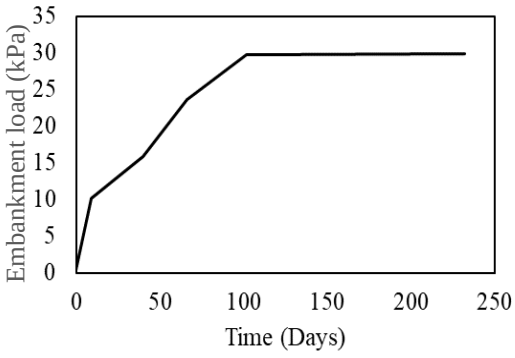

Fig. 2 Embankment construction stages

The highway embankment case study described in this paper is located in the Bangbo district of Samutprakan province, Thailand (Jamsawang et al., 2016). The geometry of the embankment and locations where field measurements were recorded using earth pressure cells, a piezometer, an extensometer and an inclinometer are shown in Fig. 1. The 0.6 m diameter DCM columns were constructed in a square pattern with centre to centre spacing of 1.5 m. Attached double columns were used near the sloping sides of the embankment, as shown in Fig. 1. The natural ground at the site consists of an 11 m soft clay layer overlain by a 3 m fill layer. Below the soft clay there is a 9 m thick medium stiff clay layer underlain by a 5 m thick stiff clay layer. DCM columns were extended through the fill material and soft clay, and hence have a length of 14 m.

The groundwater table is at a depth of 3 m below the ground surface, which is also the boundary between the fill material and soft clay. The embankment construction was carried out in four stages over 102 days as shown in Fig. 2. The first fill layer of the embankment was 0.5 m thick and placed over 9 days. The second lift was 0.3 m and placed over 31 days. The third and fourth lifts were 0.4 m and 0.3 m, respectively and they were placed over 26 days and 36 days, respectively.

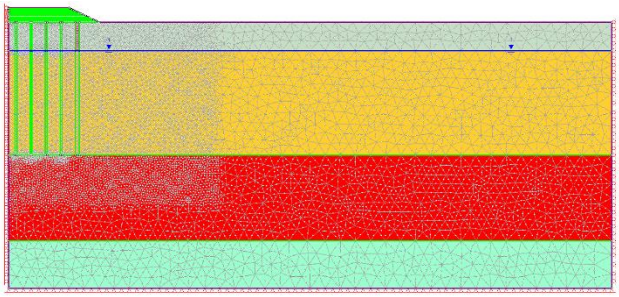

Fig. 3 Finite element model

When the two-dimensional numerical model is developed in RS2 (2019) finite element program, columns were converted into column walls considering the equivalent area approach.

Table 1. Material properties: Mohr-Coulomb model

	Embankment	Fill material	DCM columns	Stiff clay
Unit weight, γ (kN/m^3)	20	20	15	20
Elastic Modulus *E* (MPa)	20	30	80	50
Poisson's ratio, *v*	0.33	0.33	0.33	0.2
Cohesion, c' (kPa)	1	1	450	18
Friction angle, ϕ' (°)	30	32	0	25
Permeability coefficient, *k* (m/d)	N/A	N/A	5×10^{-4}	2.5×10^{-4}

Table 2. Material properties: Modified Cam Clay

	Soft clay	Medium stiff clay
Unit weight, γ (KN/m^3)	14	16
Modified compression index, λ	0.18	0.12
Modified swelling index, κ	0.04	0.06
Poisson's ratio, *v*	0.35	0.15
Friction angle, ϕ (°)	23	25
Over-consolidation ratio (OCR)	1.5	2
Permeability coefficient, *k* (m/d)	5×10^{-4}	2.5×10^{-4}

In the finite element model, all soil layers, DCM columns and embankment are modelled using six-node triangular elements. Below the water table, pore pressure degrees of freedom were included for the corner nodes of the six-node triangular elements. Due to symmetry of the problem, only half of the geometry is considered in the finite element model as shown in Fig. 3. Bottom of the finite element mesh is restrained in both X and Y directions and the two vertical boundaries are restrained in only X direction. The RHS vertical boundary was kept far away from the embankment to avoid any boundary effects. A zero pore pressure boundary is set at the top of the soft clay layer to simulate the ground water table.

The embankment, fill material above soft clay, DCM columns and the stiff clay layer were modelled using the Mohr-Coulomb (MC) model. The soft clay and the medium stiff clay layers were modelled using the Modified Cam Clay (MCC) model. Tables 1 and 2 show the material properties for MC and MCC models, respectively, derived based on the field test data provided by Jamsawang et al. (2016).

3 NUMERICAL MODELLING RESULTS

3.1 *Settlements*

Settlement at the center of the embankment at the level of the column heads was measured during construction and continued until 235 days. The maximum settlement was 77.4 mm based on field measurement and 73.7 mm based on finite element analysis, as shown in Fig. 4. The difference between measured and predicted settlement is less than 5%, which indicates the capability of RS2 program in simulating the consolidation analysis.

In Australia, there is no design guideline for the design of embankments. Instead, the design should be conformed to the British Standard 8006. The Geotechnical Design Standard (2015) – Minimum Requirements published by Transport and Main Roads, Queensland, Australia sets limitations for maximum in-service settlement of 50 mm after construction. The standard also specifies allowable differential settlement at the time of design and handover, which is 0.5% over 5 m for sprayed seal granular asphalt over granular and full depth asphalt pavements. At any time, settlement should not be larger than 5 mm for any step. For this embankment, the rate of embankment settlement after construction, during the consolidation is 23.7 mm/year. If this embankment is assessed based on the Geotechnical Design Standard (2015), after few years it may not meet the total maximum in-service settlement requirement, if the rate of settlement continued at the same rate. Differential settlement over the embankment surface from the center to the edge over 6 m is 3.1 mm, which is equivalent to 0.05%. Therefore, differential settlements may not be a problem for this embankment.

Fig. 5 shows the field measured and predicted settlement variation over depth at a point 3 m away from the embankment toe. Finite element model has captured the overall settlement profile well but underestimated the settlement profile within the

stiff clay layer. Based on these results, 43% of the surface settlement occurred within the soft clay layer and 50% of the settlement occurred in the medium stiff clay layer. The reduced settlement observed in the soft clay compared to the medium stiff clay layer is due to the stiffer fill material layer above the soft clay.

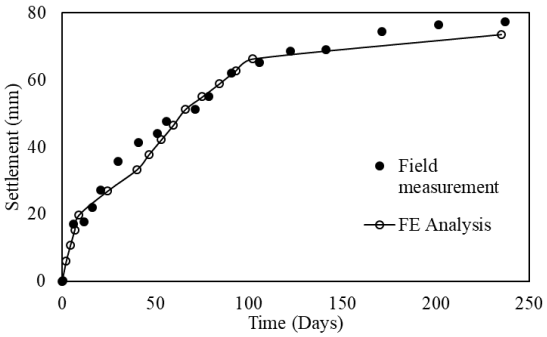

Fig. 4 Observed and predicted settlement variation for clay with time at the center of the embankment

3.2 *Excess pore pressures*

Fig. 6 shows the excess pore pressure generation during the embankment construction and subsequent dissipation during consolidation at two points, directly under the embankment, closer to the top of soft clay and medium stiff clay layers. For the former, the generated excess pore pressures are very low because of its proximity to the water table, which was defined using a zero pore pressure boundary, where the generated excess pore pressures are quickly dissipated. The maximum excess pore pressure generated in the soft clay layer, 2 m below the fill material with very high permeability, is 2 kPa. Another reason for the low excess pore pressure generation is much less embankment load transferred to the soft clay closer

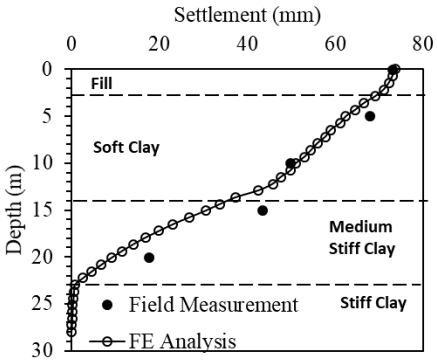

to the column heads due to soil arching.

Fig. 5 Settlement variation with depth at 3 m away from the toe after 235 days

In the medium stiff clay layer and the stiff clay layer underneath it, permeability is half of that for soft clay. Hence drainage of excess pore pressures within the lower two layers of clay is poor. Also, DCM columns are sitting on top of the medium stiff clay layer. The loads carried by columns are transferred to the medium stiff clay layer. Hence excess pore pressures recorded within the medium stiff clay layer, 1 m below the soft clay is much higher than those recorded near the top of the soft clay layer. The measured maximum pore pressure generated at 1 m below the soft clay is 15.6 kPa. The predicted maximum excess pore pressure at the same location is about 14 kPa, which is about 10% lower than the field measurement. However, the field measured and predicted excess pore pres-

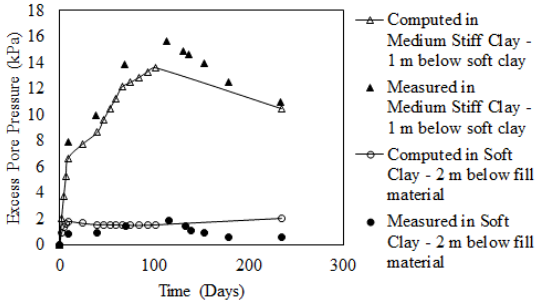

sures show similar trend and there is a good agreement between them.

Fig. 6 Excess pore pressure dissipation with time in soft and medium stiff clay layers

3.3 *Loads applied over DCM columns and soil in-between*

Fig. 7 shows the vertical stress transferred to the DCM column closest to the centre and the soil in-between 1st and 2nd columns. Finite element predictions agree well with the filed measurements recorded by earth pressure cells. At the end of embankment construction, the total embankment load transferred over the improved ground is 30 kPa. However, according to Fig. 7, the predicted and measured vertical stresses transferred to the column heads are 36.58 and 34.38 kPa, respectively, which are higher than the 30 kPa embankment load. If the RS2 (2019) predictions for columns are compared, the loads transferred to the column closest to the centre is 1.22 times the embankment load but the load transferred to the soil in-between 1st and 2nd columns is 0.62 times the embankment load. These values confirm that there is soil arching above the columns.

The stress concentration ratio, which is the ratio between stress over columns to stress over surrounding soil, calculated for this embankment is about 2. This value is less than the stress concentration ratio for semi-rigid foundations such as DCM columns, given by Han and Wayne (2000), which is 5 to 10. According to their study, for flexible foundations such as lime stabilised columns or stone columns, stress concentration ratio is between 1 and 5. In this case study, a lower stress concentration ratio may have been achieved due to

the fill material with higher stiffness than soft clay around column heads.

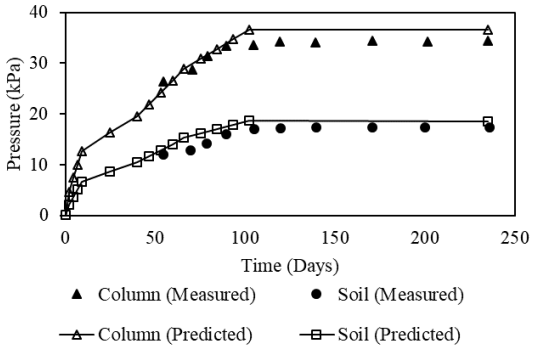

Fig. 7 Vertical stress measured at the center of the 1st column and soil between 1st and 2nd columns, from the embankment center

According to the field test data for individual DCM columns reported by Jamsawang et al., (2016), the ultimate load carrying capacity of individual columns is about 300 kN. Based on the measured and computed vertical stress over the column closest to the centre, the applied load is about 10 kN. Based on this value, if the FOS against failure of a column exceeding vertical load carrying capacity is calculated, it is 30. Therefore, the FOS against vertical load carrying capacity is not a critical parameter for this embankment.

3.4 *Lateral deformation of ground*

In the field study, the lateral deformation of the ground 3 m away from the toe of the embankment was measured at the end of 235 days. Fig. 8 shows the measured and computed deformations.

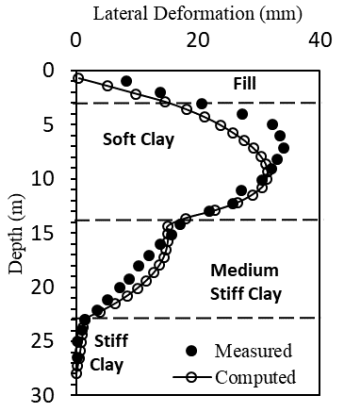

Fig. 8 Measured and computed lateral deformations.

The maximum lateral deformation measured 3 m away from the toe of the embankment is 34 mm and the corresponding predicted deformation is 7% less than the measured deformation. However, this deformation is much higher than the lateral deformation of the DCM column closer to the toe, which is 21 mm. These results clearly indicate that, although lateral deformations are controlled underneath the embankment due to ground improvement using DCM columns, away from the improved area substantial lateral deformations may still occur. If any sensitive structures are nearby, the additional loads applied on those structures must be taken into account due to embankment construction.

According to Liu et al. (2007) and Jamsawang et al. (2016), the overall stability of an embankment can be determined based on the deformation ratio, which is the ratio between maximum lateral deformation at the toe and the maximum settlement at the center of the embankment. In this case study, the lateral deformation computed at the toe is 5.38 mm and the maximum settlement at the center is 10.9 mm, which gives a deformation ratio of 0.5. Based on the deformation ratios published by Buggy (2013) for embankments in Limerick Tunnel project, Ireland, a deformation ratio of 0.6 was considered to provide acceptable stability and satisfactory performance. Therefore, in the current case study, based on the deformation ratio of 0.5, overall stability of this embankment can be considered as marginally safe. However, this ratio may not be a good indication of stability when the overall embankment deformations are small but with slightly larger lateral deformations at the toe compared to the surface settlement. Another aspect is that the lateral deformations can be significant at few metres away from the toe of the embankment, as shown in Fig. 8.

3.5 *Bending moment*

Fig. 9 shows the bending moment variation along the double column underneath the slope. In this case, bending moment was calculated using the following equation:

$$BM = EI\frac{d^2x}{dy^2} \quad (1)$$

where x is the lateral deformation of the column, y is the distance measured along the column, E is the Young's modulus of the column material and I is the second moment of area for the column cross section. It can be seen that the maximum bending moment was developed at the interface between the fill and the soft clay layers and it is about 2.2 kNm.

Jamsawang et al. (2016) reported field tests carried out for two DCM columns, investigating the lateral load carrying capacity of single columns. For the two columns tested, they observed lateral load carrying capacities of 16 kN and 12 kN, giving an average capacity of 14 kN. Also, they observed cracks appearing approximately 0.1 m below the ground surface, which indicate failure of columns. Based on this information, yield moment (M_{yield}) can be calculated as 1.4 kN·m for a single column and 2.8 kNm for double columns. If this value is used to compute the FOS against bending failure of the double columns, it is 1.3.

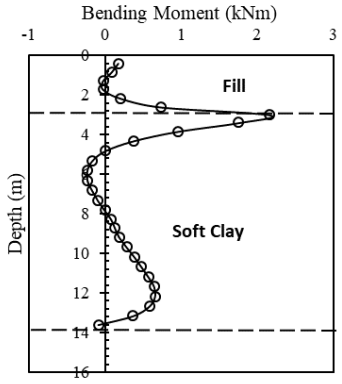

Fig. 9 Bending moment distribution within the double column near embankment toe.

3.6 *Overall Stability*

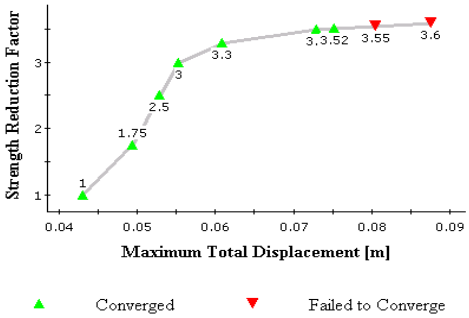

Fig. 10 FOS for global stability of the embankment

In RS2 (2019), the global FOS for the embankment can be calculated factoring the shear strength parameters, i.e., cohesion and friction angle, for the soil and columns. Since strength reduction approach is available only for MC model, MCC parameters were converted to cohesion and friction angle. In RS2, FOS against global stability is indicated by rapid increase in deformations as shown in Fig. 10. For this embankment, the FOS against global stability is 3.54 as indicated in Fig. 10.

Table 3 shows the three values of FOS obtained for three different failure modes considered for this embankment. It is clear that the most critical failure mode for this embankment is the bending failure of columns due to excessive lateral deformation of columns near the side slopes of the embankment.

Table 3. FOS against different failure modes

Failure mode	FOS
Bearing failure of columns	30
Bending failure	1.3
Global stability	3.54

4 CONCLUSIONS

In this paper, a case study of a DCM column-supported embankment was presented. Numerical simulations were carried out using the RS2 (2019) finite element program. Based on the rate of settlement calculated after embankment construction, in-service settlement can be a problem for this embankment although the differential settlements are very low. The investigation of the lateral deformations show that the maximum value occurs away from the toe. Hence, during and after embankment construction, additional loads may be transmitted on foundations of nearby structures. The most likely failure mode for the embankment was investigated by calculating the FOS for failure of individual columns as well as overall stability. Results show that failure is likely to happen due to bending failure of double columns near the side slopes of the embankment.

REFERENCES

Buggy, F.J. (2013). Deformation performance and stability control of multi-stage embankments in Ireland, 18th Int. Conf. Soil Mech. & Geot.. Eng., France, pp. 1241-1244.

Chai, J.C., Shrestha, S., Hino, T., Wo, D., Kamo, Y. and Carter, J.P. (2015). 2D and 3D analyses of an embankment on clay improved by soil-cement columns, Computers and Geotechnics Vol. 68, pp. 28-37.

Han, J. and Wayne, M.H. (2000). Pile-soil-geosynthetics Interactions in geosynthetic reinforced platform/piled embankments over soft soil. 79th Annual Transport Research Board Meeting, Washington DC, USA, Paper No. 000777.

Huang, J. and Han, J. (2009). 3D coupled mechanical and hydraulic modelling of a geosynthetic reinforced deep mixed column-supported embankment. Geotextiles and Geomembranes, Vol. 27, pp. 272-280.

Jamsawang, P., Bergado, D.T. and Voottipruex, P. (2011). Field behavior of stiffened DCM piles. Proc. Inst. Civil Eng. Ground Improvement, Vol. 164, No. 1, pp. 33-49.

Jamsawang, P., Yoobanpot, N., Thanasisathit, N., Voottipruex, P. and Jongpradist, P. (2016). Three-dimensional numerical analysis of a DCM column-supported highway embankment, Computers and Geotechnics, Vol. 72, pp. 42-56.

Liu, H.L., Ng, C.W.W. and Fei, K. (2007). Performance of a geogrid-reinforced and pile-supported highway embankment over soft clay: case study. Journal of Geotechnical and Geoenvi. Eng., Vol. 113, No. 12, pp. 1483-1493.

RS2 (2019). A two-dimensional finite element analysis of soil and rock for underground and excavated slopes, Rocscience Inc., Toronto, Canada.

Yapage, N.N.S., Liyanapathirana, D.S., Kelly, R.B., Poulos, H.G. and Leo, C.J. (2014). Numerical modelling of an embankment over soft ground improved with deep cement mixed columns: case history, Journal of Geotechnical and Geoenvironmetal Engineering, Vol 140, No. 11, pp. 1-10.

Yapage, N.N.S., Liyanapathirana, D.S., Kelly, R.B., Poulos, H.G. and Leo, C.J. (2015). Numerical modelling of geotextile-reinforced embankment over deep cement mixed columns incorporating strain-softening behavior of columns, International Journal of Geomechanics, Vol. 15, No. 2, pp. 1-18.

Use of High Strength Geotextiles in Underwater Construction – Case Study at Port of Brisbane

J. Ameratunga
Independent Consultant, Formerly at Coffey Geotechnics Pty Ltd

P Boyle
Formerly at Port of Brisbane Pty Ltd

N Honeyfield
Formerly at Port of Brisbane Pty Ltd

ABSTRACT: At Port of Brisbane, high strength geotextiles were used to support a 4.6km rockfill embankment/seawall up to about 8m high in Moreton Bay as a perimeter containment which was subsequently lined to create a Future Port Expansion (FPE) area, able to store materials from channel maintenance dredging operations for future land development. The water depth along the embankment alignment ranged from about 1m to 6m depending on the tidal heights and location offshore. High strength geotextiles were adopted to improve the stability of the rock bunds which were to be constructed on very soft clay. Transporting, handling, and laying of the geotextiles across a 70m wide embankment was complex. The difficulties were more related to geotextile placement underwater without significant damage and folds, which could have drastically reduced the strength of the geotextiles. The paper discusses the project in detail and how high strength geotextiles were placed under water to ensure no folds in the geotextiles. Further, when folds did occur, what measures were taken to rectify the situation either by removing the folds and/or changing the design of the upper part of the bund.

1 INTRODUCTION

High strength geotextiles are widely used in geotechnical projects and are a welcome addition to innovative ideas that come up in engineering design and construction. While the design of high strength geotextiles is fairly well covered in technical literature (e.g. Shukla, 2002), construction is not.

High strength geotextiles provide resistance only when they strain. Generally, the maximum strain of a high strength geotextile is less than 15%, and more likely to be 10 to 12%. Designs are typically based on limiting the strain to 5% or less. As geotextiles have to strain to offer design resistance, placement of geotextiles during construction becomes extremely important and critical for the safe execution of the project. A good example is the occurrence of wrinkles or folds when a geotextile is placed. As the soil above and below the geotextile deforms, the strain in the geotextile will be absorbed by the folds/wrinkles and therefore the geotextile will not be strained, defeating the purpose of the design. This could lead to catastrophic consequences such as failures. Therefore, it is imperative that geotextiles are stretched on placement. Although it seems easy, stretching a geotextile after placement to get rid of folds is a very difficult exercise. This becomes more difficult when the geotextiles need to be placed under water because of visibility issues.

In this paper, a case study is presented where high strength geotextiles had to be placed under water in the sea. A 4.6km long seawall was built in Moreton bay in Queensland, Australia and high strength geotextiles were placed under water throughout the length of the perimeter seawall alignment.

2 PROJECT DESCRIPTION

Fig. 1 Site Location

The Port of Brisbane (PoB), the main container port of the State of Queensland on the east coast of Australia, is located in the lower reaches of the Brisbane River on reclaimed land at the river mouth. (See Fig. 1)

Reclamation activities commenced in the 1970's to establish and gradually increase the Port's footprint to meet growth with land development occurring across the existing land masses of Fisherman Islands and adjacent Bishop Island.

During the 1980's and 1990's, PoB had experienced a steady increase in its development footprint, catering for a steady increasing trade growth. However, a significant growth period was identified for the South East Queensland region post 2000, demanding the need for an increase in growth of port facilities and therefore port land. As trade growth was forecast to accelerate, it was felt necessary to increase land available for port activities.

PoB embarked on a project in 1999 to expand port land by 235ha, immediately adjacent to and northeast of the existing developed land, using progressive reclamation. In order to carry out the land reclamation, wholly in Moreton Bay, as a first step, a 4.6km long Future Port Expansion (FPE) perimeter seawall (Fig. 2) was proposed to be constructed to be the containment wall.

Fig. 2 FPE Seawall - 2004

The design and construction of the 4.6km long seawall and future reclamation alerted to several key issues:

1) Weak subsoils below the footprint, extending to 30m or more below the seabed.
2) The additional soft clay thickness as high as 9m once reclamation is carried out using dredged mud from the Brisbane river navigational channel.
3) Expected settlements as high as 2m during construction of the seawall.
4) Depth of water, shallow over a significant length of the alignment, hence draft insufficient for the use of barges for construction.
5) High depth of water over the rest of the alignment during high tide, hence land based construction not feasible.
6) Existence of the Marine Park near the footprint of the proposed seawall and therefore disturbance to fauna/flora not acceptable.

3 LOCAL GEOLOGY

According to the published geology map of Brisbane (1:100,000 scale), the site is underlain by Quaternary marine deposits consisting of "fluvial lithofeldspathic sublabile sand and muddy sand". The main geological formations in the area are Holocene deposits overlying Pleistocene deposits which in turn overlie the Petrie Formation.

The Holocene alluvial deposit consists of the following two sub-layers:

Upper Layer: Mainly sand with inter-layered soft clays and silts. The thickness varies across the site to a maximum of about 4m but is relatively thin or absent along the East Bund (see Fig. 2).

Lower Layer: Very soft to firm compressible clay, generally normally consolidated, from about 3m depth below the seabed. The clay thickness along the proposed seawall alignment varies from about 6m to 30m. The majority of the East Bund is underlain by about 25m to 30m of soft clay.

The Pleistocene deposit which underlies the Holocene comprises mainly over consolidated, very stiff to hard clays and medium dense to dense sands. As the compressibility of these materials is low, its contribution to overall wall settlement is minimal.

4 PROPOSED DESIGN

At the earliest stages of the design, it was confirmed that the Holocene clay at shallow depth was generally too weak to support high embankments unless ground improvement was carried out. Although the feasibility of several ground improvement methods was assessed, they were found to be either costly, high risk and/or constrained by time available. It was decided in discussion with the Client that no limitation be imposed on the seawall settlement as it could be topped up as and when necessary. This allowed less attention to control settlement but manage stability. For the latter, the use of high strength geotextile was assessed to be the preferred option as it was the most cost effective and least risk solution.

The seawall was delineated into three parts for ease of design and construction (See Fig. 2):

- North Bund – Extends the line of the existing wharves along the Brisbane River. It is 1.8km long and located in water depth <1m (at low tide) for ~1.6km of its length.
- East Bund - Curved section between the North and South bunds, ~1.8km long, representing the deepest water on the project.

Water depths range from 2.5m to 4m (at low tide). This section of the project also included the weakest foundation conditions on the project and consequently was one of the highest risk areas on the project.

- South Bund - Extends the South-Eastern extent of the existing reclamation of the Fisherman Islands and connects the landfall to the end of the East bund over a length less than 0.9km. The bund is located in water depths ranging from 0m to 2.5m.

Two types of embankments were selected for the design and construction of the seawall:

- Where the seabed was shallow (i.e. North & South bunds), the design was a simple rock embankment on a high strength geotextile, which in turn was to be laid on the seabed by a purpose-built shallow draft barge.
- A wide pancake of sand on a high strength geotextile (up to 700kN/m) was adopted for the deeper water (i.e. East Bund) on which a rock bund was placed (see Fig. 3). The sand pancake was constructed by hydraulic means utilizing a purpose-built sand spreading barge connected to a cutter suction dredger. The barge, mainly operating during high tides when placing the upper layers, placed sand to a level just above the low tide level, which allowed the rock bund construction using land-based machinery. Hydrographic survey was carried out as the sand was placed and the final profile was used to reanalyze stability along the alignment (every 10m). Where necessary, additional sand was placed using the barge prior to placement of the filtration geotextile and the rock berm.

Details of stability analyses including parameters used are presented in Ameratunga et al. (2010).

5 CONSTRUCTION

The construction, including laying technique of the high strength geotextile, was one of the key innovations of the project which helped the safe construction of the seawall and its completion on time.

The barge used for construction had the dimensions 56m (length) x 17m (width) x 3.6m (depth) and was modified for laying the two types of geotextiles, and spreading the sand to form the sand pancake. High strength geotextiles were supplied by Maccaferri Brisbane from Polyfelt Geosynthetics in Malaysia. The delivery was in 5.3m wide rolls. The length of each roll varied to suit the panel sizes as required by the design along the alignment.

1. Once delivered at the Port of Brisbane, the rolls were sent to a tarpaulin manufacturer in Toowoomba (about 150km away) for stitching into panels up to 42m wide (machine direction) and 100m long and weighing up to 6.5t. After several trials, a single J Seam (i.e. one-fold), with a double chain stitch using Metric 6 gauge yarn was used. The webbing sewn on each end of the panel was seat belt strapping with a loop every 300mm, to allow for easier handling on site.
2. Once sewn into the panels, they were flaked (folded) to be 2.2m wide with the length remaining as 100m. Each flaked panel was then rolled onto a steel core 2.4m long. The 2.4m width was adopted to cater for transporting each panel on truck from Toowoomba to the Port of Brisbane site. Plastic was used to wrap the rolls to avoid damage and prevent the geotextile becoming wet prior to placement (weight of geotextile could double when wet).
3. The geotextile rolls were placed on the barge using a Franna crane which placed the rolls on the table under the gantry in the order for laying. Approximately 200t of 75 to 300mm rock was also loaded onto the barge to use for ballasting the panels once laid on the seabed.
4. The geotextile was laid off the port side of the barge (see Fig. 4). As the barge moved (to the right on Fig. 4), the geotextile passed under the barge. The guide frames installed to the port side of the barge were designed to prevent the geotextile from snagging on the barge and help to push the geotextile to the seabed (see Fig. 4).

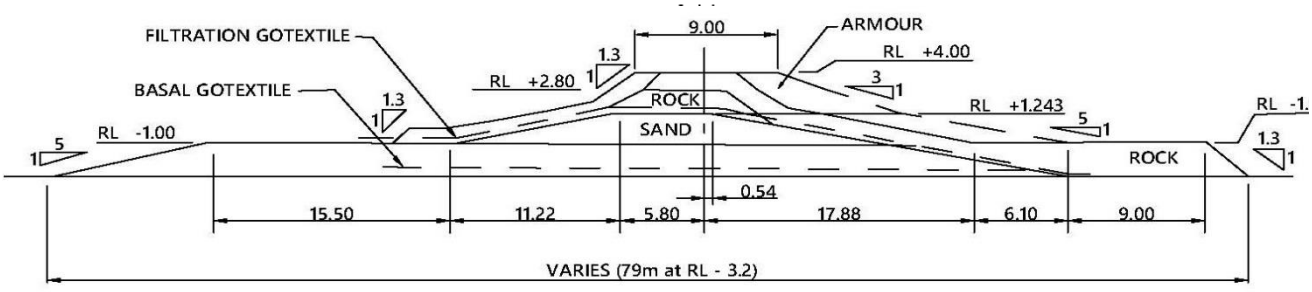

Fig. 3 East Bund Cross Section

5. Ballast rock was then dropped over the side onto the laid geotextile using a 22t excavator as the geotextile was exposed as the barge moved. The ballast prevented the movement of the geotextile under the action of currents and waves (Fig. 5 shows a view from above of a barge model constructed during the design phase
6. After one panel is placed the laying of the next panel commenced. A detailed description of how each panel was connected to the next is described by Strevens et al. (2005).

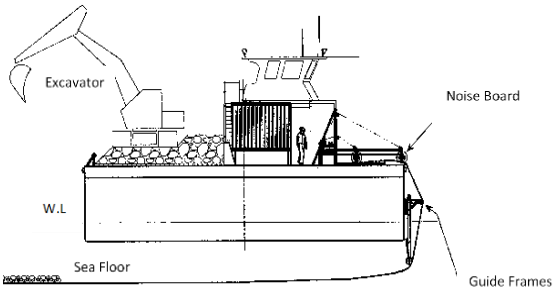

Fig. 4 Barge section during geotextile placement

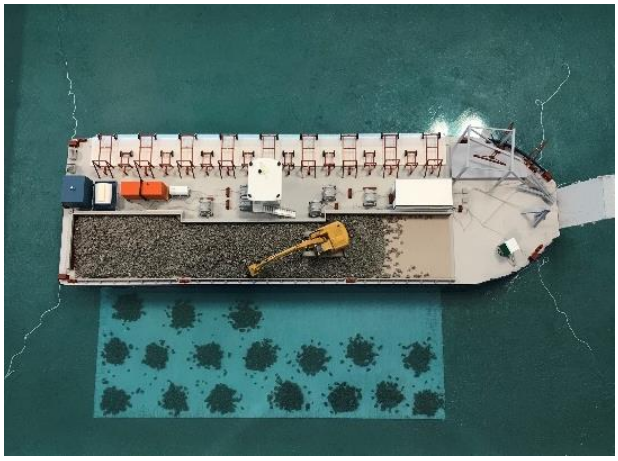

Fig. 5 Model showing the geotextile placement

Significant risks were identified for each operation and risk assessments were carried out and measures were proposed to reduce or avoid such risks. Two of the significant risks were:

1) Incorrect positioning of the geotextile. Depending on how far it is out of position, the design stability could be affected. Although the placement was carried out by GPS control from the barge, a survey was done after placement to figure out whether construction tolerance of 2m has been achieved.

2) As previously mentioned, if folds occur during placement the effectiveness of the geotextile could drop to zero and assumed to be equivalent to a no geotextile case. This was a very high risk as the stability of the whole embankment could be affected. A steel reinforcement bar was tied onto the geotextile over the full width of the panel (every 5m advance of the barge) to assist in reducing the folds as the geotextile was placed. In addition, divers were sent after placement to identify any folds and report to the design team of the locations where folds were visible.

On occasions where either case above occurred, attempts were made to pull the geotextile out using a tug. This was not always feasible because of the resistance offered by the geotextile moving against the seabed. Where pulling out failed, the upper part of the design geometry was modified to achieve an adequate factor of safety. This generally ended up widening the sand pancake using the barge and/or changing the rock berm profile.

6 CONCLUSIONS

The paper describes the construction aspects of the high strength geotextiles at the FPE Seawall project. Placement of geotextiles under water is described. Also, measures that were taken to ensure correct positioning without folds described. When this was not possible, what measures were taken to provide a safe modified design are discussed.

ACKNOWLEDGEMENTS

The seawall project was designed and constructed by an Alliance comprising Leighton Contractors, WBM Oceanics, Coffey Geotechnics, Parsons Brinckerhoff Australia and Port of Brisbane Corporation. Our gratitude also goes to Jarreau Alinur for reviewing the paper.

REFERENCES

Ameratunga, J., Boyle, P., De Bok, C. and Berthier, D. (2010). "Ground Improvement in Port of Brisbane (PoB) clay". ISSMGE Bulletin, Vol 4, Issue 2, June 2010, pp 28-54

Shukla, S.K. (2002). Geosynthetics and Their Applications. Thomas Telford Publishing, London, UK, 430 p.,

Strevens, M. Ameratunga, J., Boyle, P. and Fokes, G. (2005). Innovative techniques deliver the foundation for construction of a 4.6km Seawall in Brisbane. PIANC 2005 conference, Adelaide, Australia.

Assessment of Influence of Oxides Composition on Consistency and Compaction Properties of Red Mud Waste

P. Sreekanth Reddy
Department of Civil Engineering, NIT Mizoram, Aizawl-796012, India. E-mail: psreddy.civil.phd@nitmz.ac.in

Bijayananda Mohanty
Department of Civil Engineering, NIT Mizoram, Aizawl-796012, India. E-mail: bijayananda.ce@nitmz.ac.in

B. Hanumantha Rao
School of Infrastructure, IIT Bhubaneswar, Argul-752050, India. E-mail: bhrao@gmail.com (Corresponding Author)

ABSTRACT: Many geotechnical properties of soils and waste materials are influenced by mineralogical and oxides compositions of these materials. Therefore, knowledge on these compositions is necessary for better understanding about engineering behaviour of soils and waste materials. Among several industrial wastes, red mud (RM) is a unique material as it possesses diverse oxides and mineralogical compositions. RM, though, is a by-product material, it exhibits the geotechnical behaviour that resembles clay and sandy soils. Such behaviour is beneficial in a sense it can be utilized as a geomaterial. The varying oxides composition with respect to the origin of ore, high alkalinity of RM and necessity for stabilization, makes the material render not acceptable as a potential resource material towards practical applications. Additionally, pH and water content can also influence the oxides composition. In this regard, an effort is made to provide information on oxides composition and its influence on various properties such as consistency limits, compaction characteristics etc. Compaction parameters and oxides composition of RM samples are determined by adopting standard Proctor test and Energy Dispersive Spectrum analysis. The results revealed that the compaction characteristics are influenced by low crystalline goethite mineral and amorphous alumina. The results further portrayed that, contents of Al_2O_3, Na_2O and CaO present in RM can have significant effect on the plastic behaviour. The presence of high quantity of Na_2O leads to poor compaction.

KEYWORDS: Red Mud; Expansive soils; Oxide composition; Physical properties

1 INTRODUCTION

The ability of soil to withstand the applied pressure by the external load is influenced by the proportion and composition of different solids fraction, as well as by the variation in soil water content, which alters the cohesion and adhesion between the particles. Therefore, it is important to investigate the susceptibility of a material to compaction, specifically when its composition of solids fraction is distinct in itself and as compared to conventional materials. Generally, waste materials are constituted with metallic oxide compositions in disproportionate contents, making them susceptible to compaction in contrary to natural soils. The presence of aluminum and iron oxide minerals in soils has a favourable effect on soil physical properties, increasing aggregate stability, friability, porosity, and hydraulic conductivity, and reducing swelling, clay dispersion, bulk density, and modulus of rupture.

Approximately, half the composition of RM is in the form of iron oxide (35-50%). Other major oxides components are aluminium (15-20%), silica (5-12%), titanium, calcium, and sodium. Therefore, the role of these oxides composition cannot be subverted on stabilization and the compaction properties. Moreover, knowledge on oxides composition is of great importance in getting the insight on properties such as strength attainment, aggregate stability, dispersion, etc. It has been well recognized that these properties are influenced by type of iron oxide precipitate formed as well as the extent of oxide interaction with the surface, which is a pH dependent (Fordham, 1969, 1970. 1973; Greenland and Oades, 1968; Greenland, 1975; Saleh and Jones. 1984; Yong and Ohtsubo, 1987). In light of promoting increased utilization of wastes in geotechnical engineering applications, studies pertinent to evaluating the impact of oxides on compaction characteristics become necessary.

In this paper, an effort is made to establish compaction characteristics of RM and undersand the influences of oxides composition on compaction and plasticity behavior of RM. As

such, an important fact that when dealing with wastes or by-products, it is essential to establish their oxides composition and understand the possible consequences of disparity in these compositions on geotechnical properties of waste or by-products. Such comprehensive appraisal is necessary, especially in promoting utilization of wastes or by-products in a sustainable and environmentally acceptable manner.

2 MATERIALS

Red mud, RM, used in the study was collected from the disposal impoundment of National Aluminium Company Limited (NALCO), Damanjodi, Koraput, Odisha, India. The RM is directly collected from the pond area in a disturbed state. The collected sample was in wet state and it is oven-dried at a temperature of 105 ± 5°C for a period of 24 hours. The samples were pulverized for separation of agglomerated particles for proper mixing prior to testing for physical and chemical characterization. The plastic behaviour and dry density of the soil sample were determined as per the standards of ASTM D4318-17e1 and ASTM D698-12e2 respectively. The chemical composition of RM used in the study as well as data collected from literature was shown in Table 1. In addition, the average of different oxides composition was considered and represented in the form of pie diagram as shown in Fig. 1. From Table 1 and Fig. 1, it is clear that RM comprise of Fe_2O_3 and Al_2O_3 as major oxides contents.

Table 1. Oxides composition of RM used in the study and data collected from literature

Reference	Oxide Composition					
	Fe_2O_3	Al_2O_3	SiO_2	CaO	Na_2O	TiO_2
Present Study	49.36	20.82	10.65	1.32	13.53	2.8
Bhumij (2015)	29.54	10.53	4.97	1.5	5.4	-
Sridevi et al. (2016)	51	18	9.8	1.8	5.3	4.6
Rao et al. (2012)	39.32	22.84	19.84	1.24	7.75	7.87
Singh et al. (2017)	53.75	16.07	8.25	1.48	3.82	4.24
Kalkan (2006)	35.04	20.2	13.5	5.3	9.4	4
Li et al. (2018)	6.44	20.4	20.76	17.56	17.33	2.08
Kushwaha et al. (2018)	34.21	12.4	7.8	3.99	5	15.5
Rubinos et al. (2015)	37.22	20.82	3.81	6.3	4.64	20.1
Gore (2015)	40	16.3	9.6	8.6	4.5	8.8

3 RESULTS AND DISCUSSION

3.1 Influence on Plastic Behaviour

The presence of caustic content (NaOH) and associated mineralogical chemistry of the RM will affect its mechanical behaviour. The presence of Fe_2O_3 in a material reported to be contributed to colour, aggregation, and adsorptive properties (Grafe et al. 2011). While the presence of oxides such as aluminum and iron in soils or waste materials, reported to have a favourable effect on physical properties, increasing aggregate stability etc (Reddy et al. 2018; Alam et al. 2017). To understand the influence of oxides composition on plastic behaviour of RM, a histogram is drawn with the data obtained from present study as well as the literature, as depicted in Fig. 2. From the visual observation, it can be observed that there is a definite influence of oxides content on plastic behaviour.

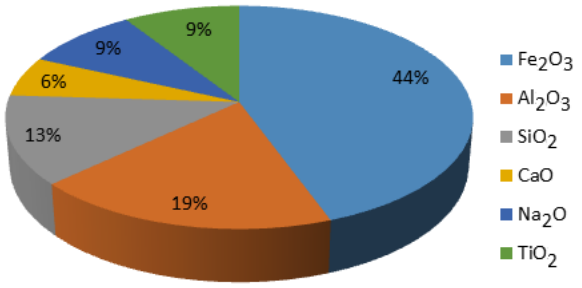

Fig. 1 Graphical representation of different oxides composition in RM from diverse origin

From Fig. 2 it can be observed that the plastic behaviour of RM increased with the oxide content of CaO, SiO_2 and Al_2O_3 up to 17%, 21% and 20% respectively and later, it decreased. On the other hand, decrease in the plasticity can be seen with an increase in Fe_2O_3 content. This is attribute to the fact that RM consists of Na^+ element in sodalite (belong to Na_2O and Fe_2O_3 family) form, which generally holds more water (common to Na-bentonite) and presence of high percentage of Na^+ causes dispersion in material, which decreases the plasticity.

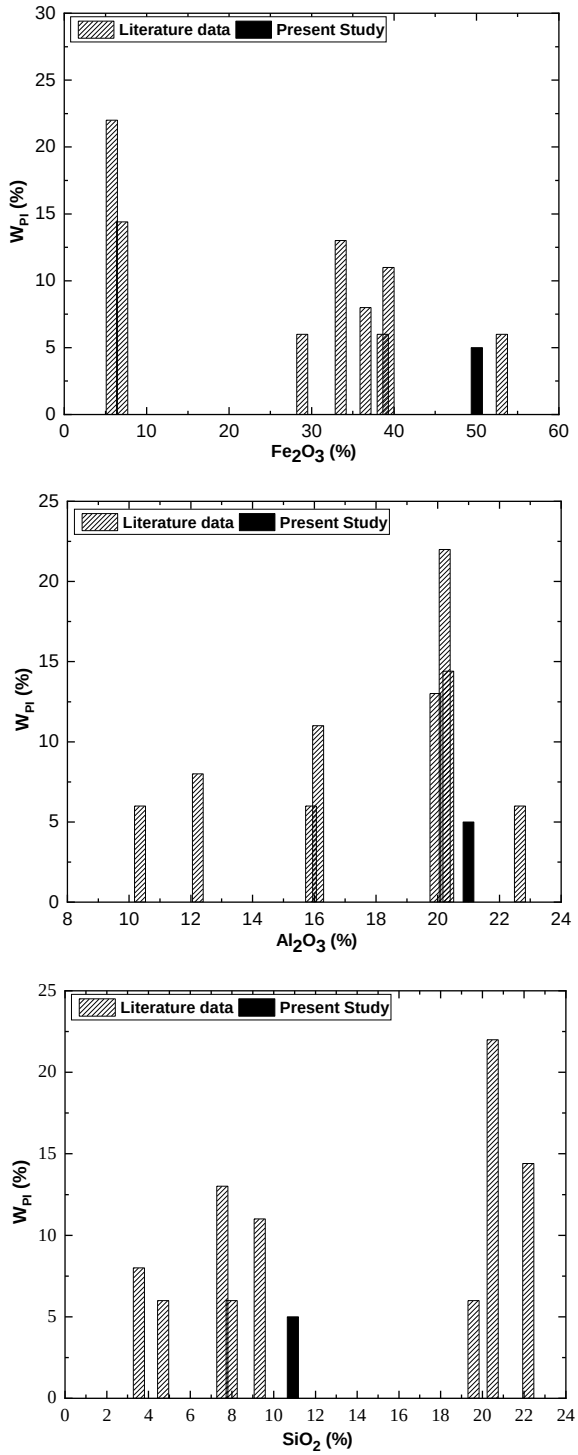

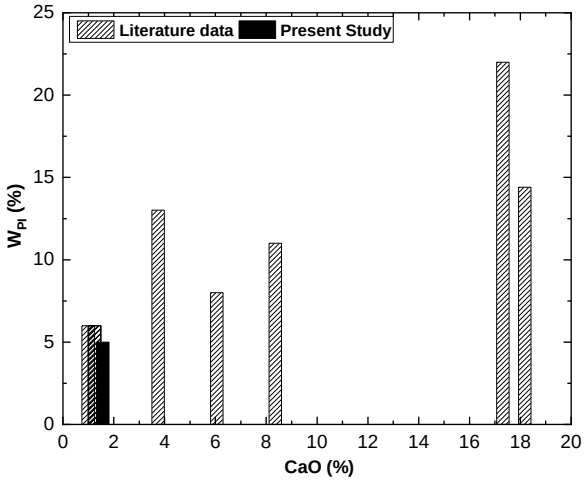

Fig. 2 Plastic behaviour of RM with varying chemical composition (Bhumij 2015;Rao et al. 2012;Feng and Yang 2018; Singh et al. 2017;Kalkan 2006;Li et al. 2018;Kushwaha et al. 2018;Rubinos et al. 2015;Gore 2015)

3.2 Influence on Compaction Behaviour

The presence of crystalline and amorphous particles in the form of iron and alumina oxides can influence the compaction characteristics of the RM. The micrographs displayed in Fig. 3 confirm the presence of crystalline and amorphous particles in the RM. The increase in iron oxide leads to increase in low crystalline particles (goethite), which are fine and sphere shaped. The higher densities in RM are due to the combination of these spherical particles of iron and flaty particles of alumina. Further for deriving better understanding on oxides influence, data of different oxides composition (i.e. Fe_2O_3, Al_2O_3, SiO_2 and CaO) with relevant reported compaction parameters pertinent to the RMs of different origin were collected from the literature. Using the assimilated data, correlations were developed between oxide compositions (Fe_2O_3, Al_2O_3, SiO_2 and CaO) and dry unit weight, as depicted in Fig. 4.

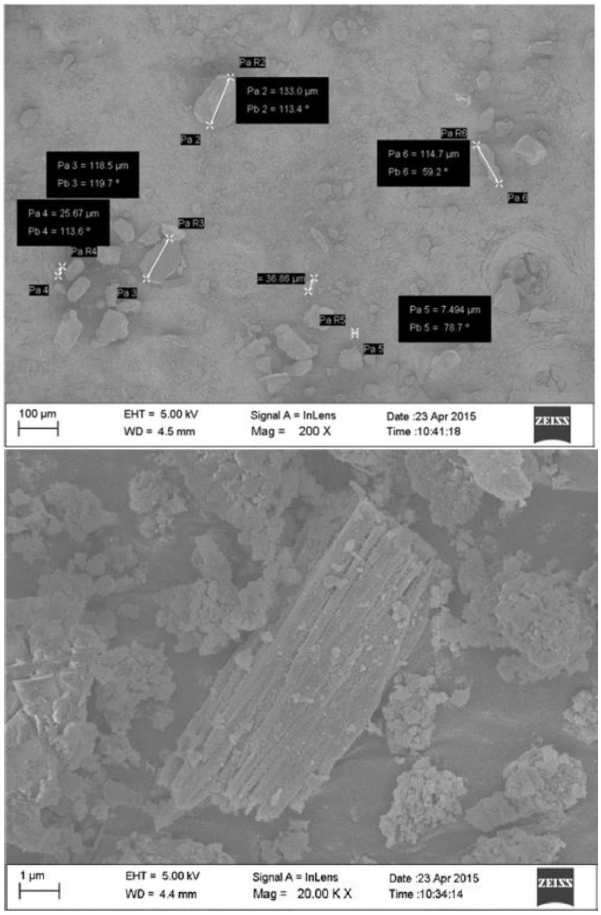

Fig. 3 Micrographs of RM displaying particle different particle sizes (Rao and Reddy 2017)

A simple observation of the figure reveals that oxides composition can have a definite influence on compaction characteristics of the RM. As depicted in Fig. 4, it can be observed that γ_{dmax} decreased with an increase in Fe_2O_3 content and increased with an increase in Al_2O_3 content. There seems to be no definite variation with CaO and SiO_2 content, indicating a fact that these oxide compositions are passive to water retention. The w_{opt} content is observed to be 40 % for γ_{dmax} obtained in the current study. But the w_{opt} corresponding to the literature data is in the range of 22-32.2 %, which is lesser than the prior one. This is due to the dominance of Fe_2O_3 content, which is active towards water retention. Supporting this, Reddy et al. (2020) reported an increment in OMC with greater content of Fe_2O_3.

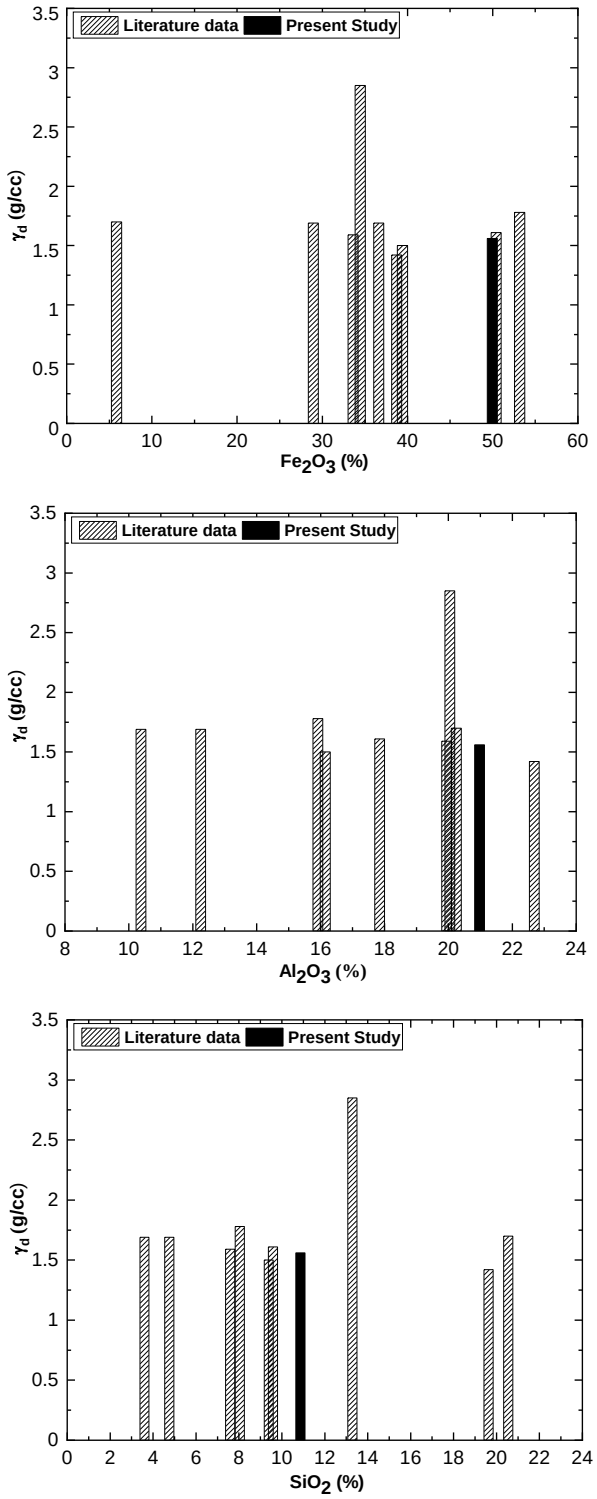

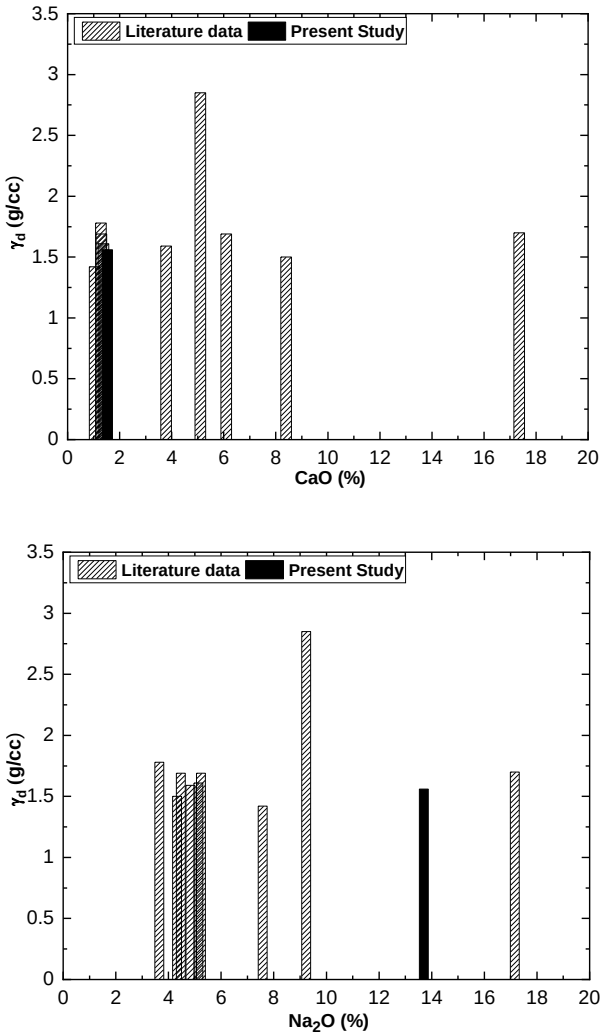

Fig. 4 Variation of γ_{dmax} of RMs with oxides composition (Bhumij 2015; Sridevi et al. 2019; Rao et al. 2012; Singh et al. 2017; Kalkan 2006; Li et al. 2018; Kushwaha et al. 2018; Rubinos et al. 2015; Gore 2015)

As Fe_2O_3 content vary with the RM from different locations, so does the $w_{opt.}$ The decrease in dry density may be due to the increase in low crystalline minerals (goethite), which are of fine and spherical shape fractions. This statement is well correlates that the quantity of fines increased to a value more than that required to fill the voids of the coarse-grained soils, the maximum dry density decreases (Terzaghi et al.1996). On the other hand, the increment in dry density is observed in case of Al_2O_3, due to the presence of significant amount of alumina oxide, which are of flat shaped fractions. It is a fact that the combination of fines and coarser particles will attain higher dry density for the same compactive effort (Terzaghi 1931).

It is obvious from the graph that the excess presence of Na_2O caused discrepancy in the compaction parameters, which however is pronounced in the case of RM. Generally, the presence of Na^+ causes repulsion behaviour between the particles, apart from enhancing the affinity to attract large amount of water as compared to conventional soils.

Since, compaction properties have strong interrelations with other properties of a given geomaterial, presence of any oxide content beyond certain percentage does not fetch any advantage in the real-life scenario. It is stimulating to note the pronounced effect of Fe_2O_3 and Na_2O on compaction parameters as compared with its counterpart of Al_2O_3.

4 CONCLUSIONS

Extensive literature data has been collected for drawing the relationships for oxides composition of RM with plasticity and compaction behaviour. From the study the following conclusions are drawn:

1). RM contains Fe_2O_3, Al_2O_3, SiO_2, Na_2O and CaO as its major oxides composition in which iron and alumina oxides are in majority proportion.
2). It is found that the contents of Al_2O_3, Na_2O and CaO can have an influence on the plastic behaviour of RM.
3). The high alkalinity of RM hinders the binding property, resulting in dispersion behaviour when water comes in contact with it.
4). The compaction characteristics are influenced by the low crystalline goethite mineral and amorphous alumina. The presence of high quantity of Na_2O leads to poor compaction.

REFERENCES:

Alam, S., Das, S.K., Rao, B.H. (2017). Characterization of coarse fraction of red mud as civil engineering construction material. Journal of Cleaner Production, 168:679–691.

ASTM D4318-17e1 (2017). Standard test methods for liquid limit, plastic limit, and plasticity index of soils, ASTM International, West Conshohocken, PA, USA.

ASTM D698-12e2 (2012). Standard test methods for laboratory compaction characteristics of soil using standard effort (12 400 ft-lbf/ft^3 (600 kN-m/m^3)), ASTM International, West Conshohocken, PA, USA.

Bhumij, R.K. (2015). *Compaction Characteristics of Red Mud and Pond Ash Mix as Filling and Embankment Material*, Doctoral dissertation.

Feng, Y. and Yang, C. (2018). Analysis on physical and mechanical properties of red mud materials and stockpile stability after dilatation, Advances in Materials Science and Engineering.

Fordham, A. W. (1969). Sorption and precipitation of iron on kaolinite: Sorption isotherms and their interpretation in terms of iron(III) ionic equilibria, Australian Journal of Soil Research, 7:199–212.

Fordham, A. W. (1970). Sorption and precipitation of iron on kaolinite: the solubility of iron (III) hydroxides precipitated in the presence of kaolinite, Australian Journal of Soil Research,8:107-122.

Fordham, A. W. (1973). Sorption and precipitation of iron on kaolinite. IV. Further characteristics of sorption from 0.15 M solutions, Australian Journal of Soil Research, 11:185–195.

Gore, M.S. (2005). *Geotechnical characterization of bauxite residue (red mud)*, Doctoral Thesis, The University of Texas, Austin, USA.

Gräfe, M., Power, G. and Klauber, C. (2011). Bauxite residue issues: III. Alkalinity and associated chemistry, Hydrometallurgy, 108(1–2):60–79.

Greenland, D. J., and J. M. Oades. (1968). Iron hydroxides and clay surfaces. Trans. 9th Int. Congress of Soil Science Adelaide I, pp.657–668.

Greenland, D. J. (1975). Charge characteristics of some kaolinite-iron hydroxide complexes, Clay Minerals, 10:407–416.

Kalkan, E. (2006). Utilization of red mud as a stabilization material for the preparation of clay liners. Engineering Geology,87:220–229

Kushwaha, S.S., Kishan, D., Chauhan, M.S. and Khetawath, S. (2018). Stabilization of red mud using EKO soil enzyme for highway embankment. Materials Today: Proceedings, 5(9):20500–20512.

Li, J., Feng, S.J., Chen, H.X. and Wang, H. (2018). Chemical and geotechnical properties of red mud at Liulin, China. In Geo Shanghai International Conference, Springer, Singapore, pp. 405–414

Rao, C.V.H., Ganapati, N.P., Satyanayarana, P.V.V. and Adiseshu, S. (2012). Application of GGBS stabilized red mud in road construction. IOSR Journal of Engineering, 2 (8):14–20.

Rao, B. H. and Reddy, N. G. (2017). Zeta potential and particle size characteristics of red mud waste. In Geoenvironmental practices and sustainability, Springer, pp. 69–89.

Reddy, N.G., and Rao, B.H. (2018). Compaction and consolidation behaviour of untreated and treated red mud waste. Geotechnical Research, 5(2):105–121.

Rubinos, D., Spagnoli, G. and Barral, M.T. (2015). Assessment of bauxite refining residue (red mud) as a liner for waste disposal facilities. International Journal of Mining, Reclamation and Environment,29(6): 433–452.

Saleh, A.M. and Jones, A.A. (1984). The crystallinity and surface characteristics of synthetic ferrihydrite and its relationshipto kaolinite surfaces, Clay Minerals, 19:745–755.

Singh, S.P., Samantasinghar, S. and Sindhuja, D. (2017). Stabilization of red mud using ground granulated blast furnace slag by geopolymerization technique. In International Congress and Exhibition Sustainable Civil Infrastructures: Innovative Infrastructure Geotechnology, Springer, pp. 338–350.

Sridevi, G., Sahoo, S. and Sen, S. (2019). Stabilization of expansive soil with red mud and lime. In Ground Improvement Techniques and Geosynthetics, Springer, Singapore, pp. 259–268

Terzaghi, K., (1931). *Construction Soil Mechanics*. ONTI Publishing House

Compressibility characteristics of solid waste in Meethotamulla waste site

G.D.W.N.Galhena

National Building Research Organisation, Sri Lanka

S. A. S. Kulathilaka

Department of Civil Engineering, University of Moratuwa, Sri Lanka

U. P.Nawagamuwa

Department of Civil Engineering, University of Moratuwa, Sri Lanka

ABSTRACT: Municipal Solid Waste (MSW) Management became a growing concern in Sri Lanka with the landfill failures occurred at Meethotamulla. The need to ensure the stability of existing landfills which are mostly uncontrolled through appropriate engineering designs is a major task at present. MSW forms the largest portion of the landfill and its strength and stiffness characteristics controls all aspects of landfill designs. In this research compressibility characteristics of MSW at different stages of decomposition were evaluated under both saturated and unsaturated conditions. Considering the highly heterogeneous state of MSW, larger samples were tested using a Rowe Cell of diameter 150mm with loading, unloading and reloading increments. Characteristics were determined based on the conventional Terzaghi consolidation theory to assess the improvement achievable through preloading. The test results revealed that MSW experienced high primary and secondary consolidation settlements. These could be significantly reduced by preloading. The coefficient of consolidation values were quite high.

Key words: MSW, Compressibility characteristics, Meethotamulla, Rowe cell

1 INTRODUCTION

Municipal solid waste (MSW) is a type of solid waste generated from community, commercial and agricultural operations. This includes wastes from households, offices, stores, industries and other non-manufacturing activities. Management of municipal solid waste is a major problem all over the world. Sri Lanka is facing a severe problem of Municipal Solid Waste (MSW) management. As developing nation, the currently adopted predominant method in Sri Lanka is open dumping due to low cost and less processing involved.

Recently, Municipal solid waste management became a growing concern in Sri Lanka with the catastrophic landfill failures occurred at Meeethotamulla. Accordingly, it has been decided that on site closure and rehabilitation is the most viable economical solution for the Meethotamulla abandoned site. Geotechnical risk such as stability and settlement issues in landfills need to be addressed in such rehabilitation work. Determination of stiffness properties of solid waste is useful for assessing the deformation of waste dumps and the effect on structures built on landfill with post-closure plans.

Over the last two decades or so, dedicated efforts were made by several researchers in understanding various factors influencing the stress strain and volume change behavior, stiffness and shear strength of MSW. Relevant studies for MSW at landfills/dump sites in Sri Lanka are very limited. It is widely reported that the MSW is highly heterogeneous and its engineering properties may vary from landfill to another. Hence, site-specific evaluation of these properties is very essential. Due to extreme heterogeneity and anisotropy of MSW, determination of parameters is much more difficult compared to that of soils. Hence, with many limitations the conventional theories of soil mechanics related to compressibility are to be tested with MSW.

Accordingly, this study is conducted to identify the consolidation behavior of MSW by conducting laboratory tests and determining compressibility characteristics of MSW.

2 SETTLEMENT BEHAVIOUR OF MSW AND COMPRESSIBILITY CHRCTERISTICS

Generally, landfill settlement is a combination of short-term load-related settlement and long-term settlement under constant load due to biodegradation phenomena. Short term settlement occurs rapidly (i.e. during the filling process) and significant

amount of long-term settlement remains for a longer period. Prevailing compression models can exhibit load-related settlement and but not suitable for the displacement due to biodegradation. Magnitude of settlement and duration have direct impact on the design aspects, operational activities, termination of landfills and usage after closure of landfills [Dixon and Jones (2005)].

Kavazanjian et al. (1999) conducted several oedometer tests using oedometer ring having inner diameter of 460mm and height of 460mm. In all cases, there was a relatively rapid immediate compression response upon load application followed by a time-dependent delayed compression response.

Fig. 1 shows the obtained compression results. Obtained Compression index (C_c) is between 0.121 and 0.247 and recompression index (C_r) is between 0.003 and 0.017. Also, secondary compression index (C_α) has a range of 0.01 to 6.6 x 10^{-6}.

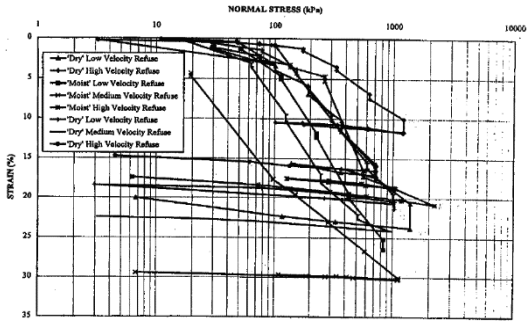

Fig. 1 Large scale laboratory compression data from Kavasanjian et al. (1999)

Further, Imre et al. (2014) conducted oedometer tests using box of 50cmx 50cm (thickness of sample = 7cm, depth of box = 40cm). Hydraulic loading system was used and test was performed under vertical single drainage through bottom of sample. Fig. 2 compares the obtained compression curves for waste sample with behavior of a soft lacustrine Szeged clay. Curve 1, 2, 3 represented three different degradation levels (i.e. phase 1, phase 2, phase 3).

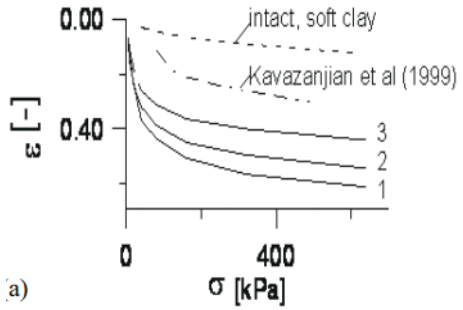

Fig. 2 Compression curves for three samples in semi-logarithmic plot (after Imre et al., 2014)

The maximum volumetric strain for the waste samples is equal to 61%, 44% and 54%, for samples 1, 2 and 3 respectively.

Also, Naveen et al (2018) conducted several one-dimensional consolidation tests for dry and dumped specimen collected form Mavallipura landfill in India. Cell with diameter of 76mm and depth of 40mm is used for the experiment. Data of each loading stages were used to develop the e vs log (σ) curves for MSW and obtained graph is presented in Fig. 3. Obtained values of compression index (C_c) were found to be 0.47 for the dry MSW and 0.15 for dumped MSW. Secondary compression coefficient (C_α) values were 0.071 and 0.005 for dry MSW and dumped MSW respectively.

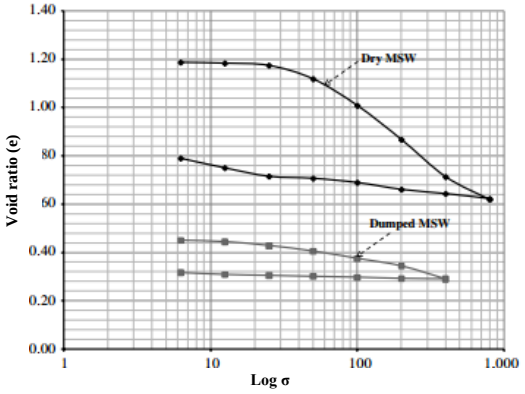

Fig. 3 Void ratio vs pressure graph (after Naveen et al., 2018)

3 EXPERIMENTAL STUDIES

The samples representing two degradation levels from Meethotamulla dump site were used in this study to determine the compressibility characteristics through consolidation test. These sample are more than 15 years old and the primary bio degradation is completed. One sample is obtained from the bottom of waste dump (Location 01) and another sample is from middle of the waste dump (Location 02) (Fig. 4 and Fig. 5).

Hereinafter sample which is obtained from location 01 is referred as sample 1 and sample which is obtained from location 2 is referred as sample 2.

Fig. 4 Location selected for sample collection

Fig. 5 Obtained sample for experiments.

3.1 *Waste Classification*

According to Waste classification framework proposed by Dixon and Langer (2006) classification and sorting were performed and composition of the tested solid waste are presented in Table 1.

Table 1. Composition of tested municipal solid waste

Material type	Location 1 (%)	Location 2 (%)
Soil like	54.47	43.66
Paper/cardboard	0	0
Flexible plastics	13.27	19.90
Rigid plastics, rubber	0	0
Metals	0	0
Glass, Minerals	12.80	13.15
Wood, Textiles	16.90	20.13
Miscellaneous	2.56	3.16

As the identifiable paper, cardboard or any organic material were not encountered from samples, it can be stated that all degradable components were fully degraded in both samples. Further, sample 1 contain more degraded materials and sample 2 contains more polythene and textiles.

3.2 *Test Method*

There are many difficulties in obtaining intact waste samples due to the inconsistency, presence of large fragments, etc. Hence, researchers used recompacted samples to overcome the deficiencies in sampling and sample preparation process (Landva & Clark, 1990). In this study, remolded waste samples were used. Fragments that were too large to fit inside the cell were either broken by hand / cut into small pieces or discarded where it is not possible to processed to reduce the size of component.

Considering the highly heterogeneous state of MSW, larger samples were tested using a Rowe Cell of diameter 150mm with loading, unloading and reloading increments (Fig. 6).

Head (1994) stated that test with equal strain loading condition and vertical single drainage can be considered as the most related test to traditional oedometer tests and settlement reading and volume change measurement taken form the drainage line can be directly correlated under above condition. Hence, vertical single drainage with equal strain test method is selected for the testing programme.

The loading sequence used was 25-50-100-200kPa. Then unloaded through 100-50-25kPa Thereafter sample was reloaded through 50, 100, 200 and 400kPa. Finally, again sample was unloaded to 25kPa. Two tests were performed using sample of each location under saturated and unsaturated condition.

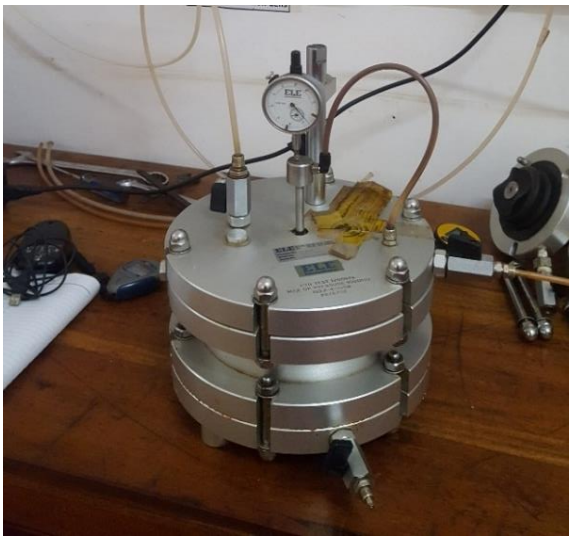

Fig. 6 Rowe cell apparatus used for the study

3.3 *Determination of Basic Properties of MSW*

In situ densities were measured in sampling location in order to achieve conditions close to site conditions in remolded samples. Water replacement method in a test pit was used to determine the in-situ densities of samples. Air dried method was adopted to determine the moisture content of MSW samples. Further, specific gravity is determined using large pycnometer having a volume of 1000ml following the procedure recommended in the ASTM D854. The summary of obtained basic properties of MSW are presented in Table 2.

Table 2.Basic Properties of test specimens (MSW)

Properties	Location 1		Location 2	
	Test 1	Test 2	Test 3	Test 4
Bulk unit Weight (kN/m^3)	12.7		11.2	
Specific gravity	2.34		1.92	
Moisture content (%)	74.3	55.2	41.5	66.9

Note: Test 1 and test 4 – under saturated condition
Test 2 and test 3 – under unsaturated condition

4 RESULT AND DISCUSSION

4.1 *Settlement behavior*

Settlement vs log (time) plots were done for all loading and reloading increments in testing done with both saturated samples and unsaturated samples. The results of loading increments 50-100 kPa of samples 1 (Saturated and unsaturated) are presented in Fig. 7.

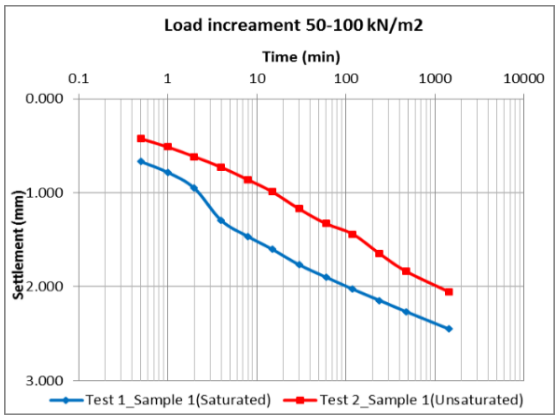

Fig. 7 Settlement vs log (time) for Loading stage of Sample 1 (Saturated and Unsaturated condition)

The settlement plots do not show a reduction in gradient with time as seen with inorganic clays. The plot of similar gradient as seen in peaty clay clearly indicate that MSW samples have high secondary consolidation settlement. Settlement in the saturated samples are much larger than those in unsaturated samples.

The e vs log (σ) plots obtained for both saturated and unsaturated sample 1 and sample 2 are presented in Fig. 8 and Fig. 9 e vs log (σ) curves for MSW exhibit similar behavior as the e vs log (σ) for conventional engineering soil.

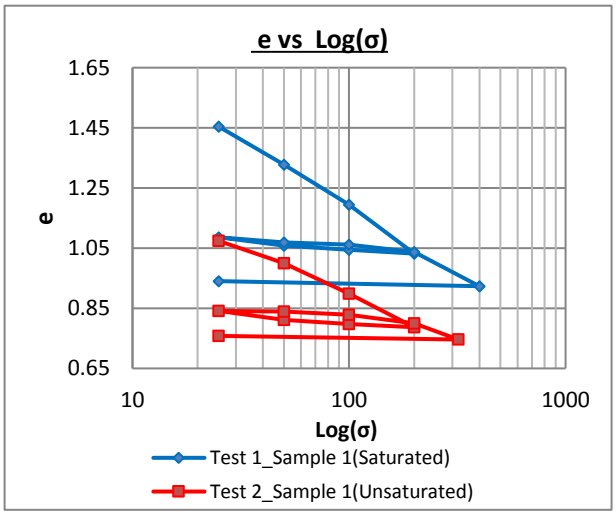

Fig. 8 e vs log (σ) curve for sample 1 under saturated and unsaturated conditions

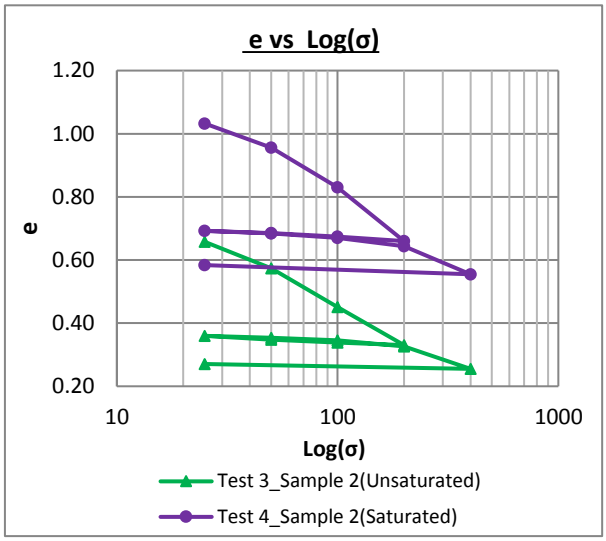

Fig. 9 e vs log (σ) curve for sample 2 under saturated and unsaturated conditions

4.2 *Variation of Compression Index (Cc) and Recompression Index (Cr)*

Compression index and recompression index values were determined using e vs log (σ) and obtained results are presented in Table 3.

Table 3. Compression index and Recompression index values

Test Set	Values of compression index (C_C)	Values of recompression index (C_r)
Test 1_Sample 1 (Saturated)	0.5421	0.0438
Test 2_Sample 1 (Unsaturated)	0.3707	0.0352
Test 3_Sample 2 (Unsaturated)	0.4010	0.0296
Test 4_Sample 2 (Saturated)	0.5647	0.0472

The value of the compressibility index C_c and recompression index for the MSW specimens under saturated condition have higher value than the specimen under unsaturated condition. Further, above results clearly shows significant reduction in C_r to the respective values of C_c. The C_r values are less than 10% of C_c values.

The C_r values represent the primary consolidation behavior of a preloaded MSW. The much reduced C_r values indicate that the primary consolidation settlement of MSW can be significantly reduced by preloading.

4.3 *Variation of Coefficient of Volume Compressibility (m_v)*

Coefficient of volume compressibility for both loading and reloading increment were determined and variation is presented in Fig. 10.

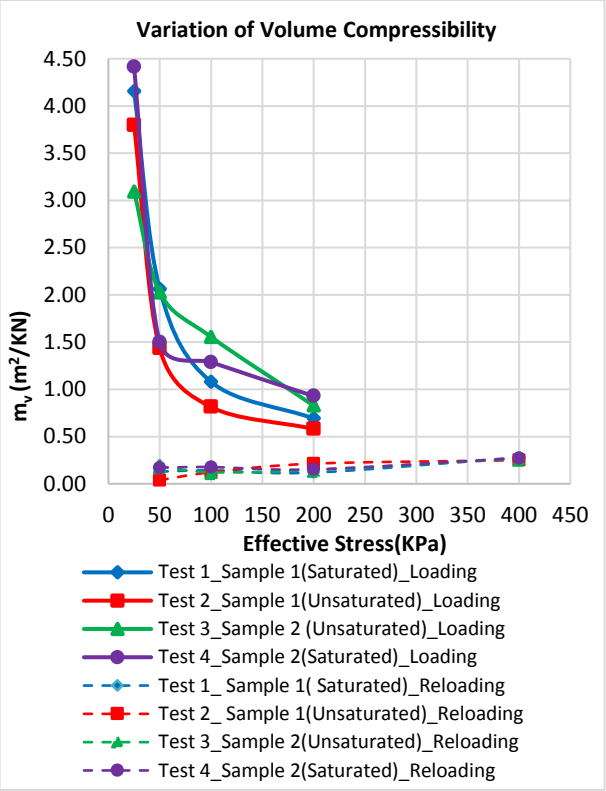

Fig. 10 Variation of m_v for Sample 1 and Sample 2 (under saturated and unsaturated condition)

The coefficient of volume compressibility values of all samples decrease as the effective stress increases and they followed the same trend. Further, m_v values of unsaturated sample are less than the values of saturated samples. The m_v values in reloading increments were much smaller compared to that of loading increment. This confirms the effectiveness of preloading technique in reducing the primary consolidation.

4.4 *Variation of Coefficient of Secondary Consolidation (C_α)*

Variation of coefficient of secondary consolidation in loading and reloading stages are presented in Fig. 11. The C_α values of unsaturated and saturated samples were of the same order. There is no notable difference due to the saturation. In general C_α values has increased with the stress level in the loading increments. The coefficient of volume compressibility values in reloading increments were much smaller compared to that of loading increment. This shows that the secondary consolidation characteristics of MSW can be significantly improved by preloading.

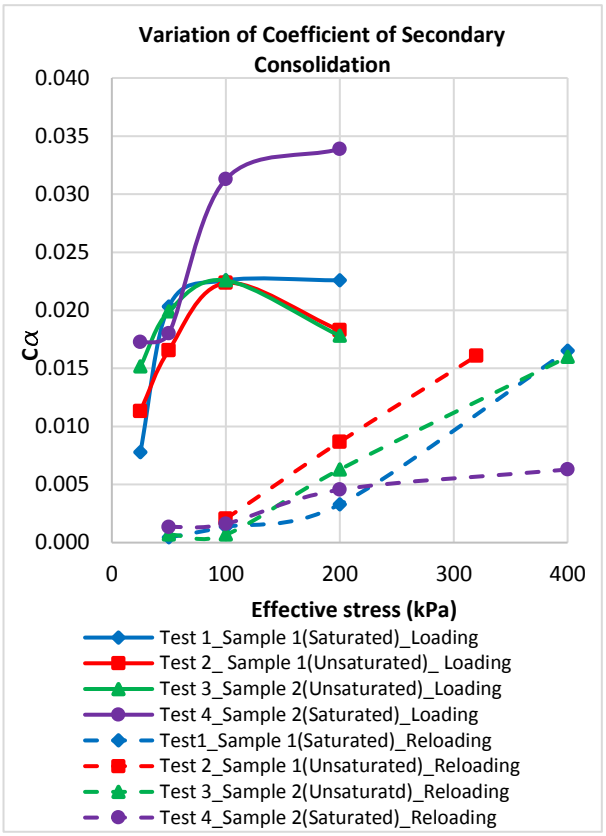

Fig. 11 Variation of C_α for Sample 1 and Sample 2 for loading and reloading stages

Further, C_α'/C_α was plotted against the over consolidation ratio achieved during the loading stages to identify the reduction of C_α by the loading process (Fig. 12).

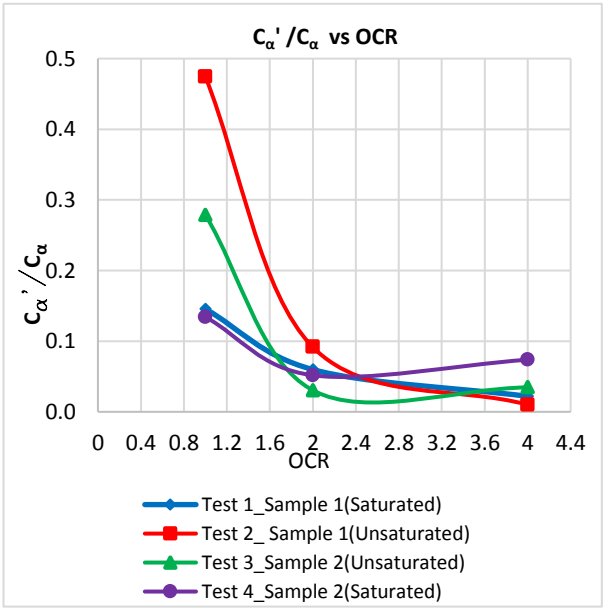

Fig. 12 Variation of C_α'/C_α with over consolidation ratio

All curves shows that the reduction of C_α achieved is larger with the larger OCR. The results confirms that significant reduction of C_α can be

achieved with preloading of that extent. Considerable reduction of C_α would be achieved with OCR values in the range of 1.2 to 2.0.

4.5 *Variation of Coefficient of Consolidation (C_v)*

The coefficient of consolidation C_v is essential to predict the rate of settlement of municipal solid waste sites. The value of the coefficient of consolidation (C_v) is estimated here using rectangular hyperbola method and presented in Fig. 13.

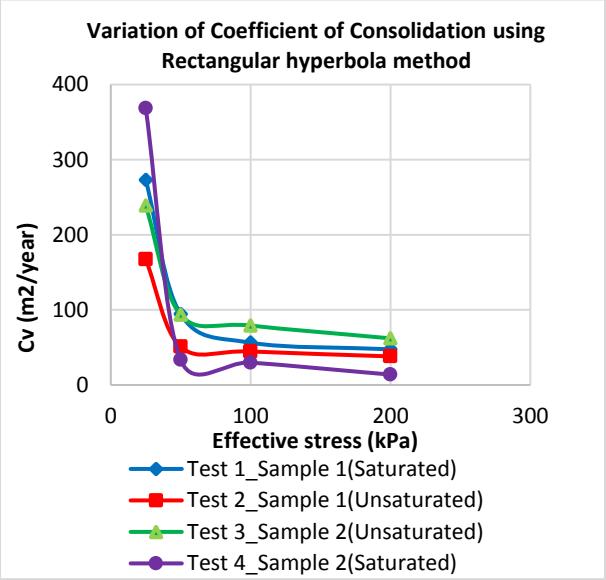

Fig. 13 variation of C_v using rectangular hyperbola method

Apart from the initial increment of 0–25 kN/m^2 the coefficient of consolidation values were of the same order in other higher stress levels. C_v values are much greater than those observed for soils. Further, there is no clear difference in C_v values of saturated and unsaturated samples.

5 CONCLUSION

Municipal Solid Waste Management was an ignored problem but is became a growing concern in Sri Lanka with the Catastrophic landfill failures occurred at Meethotamulla. In order to minimize the future risk of failure, it is necessary to establish a proper assessment of stability and deformation of municipal solid waste landfill in Sri Lanka. These landfills will have to be restored into safe useful land by appropriate geometric modification. Hence, site-specific evaluation of shear strength and stiffness properties is very essential, and this study is mainly focused on compressibility characteristics. The following conclusion can be drawn;

- Coefficient of volume compressibility values of all samples tend to decrease as the effective stress increases and m_v values for saturated sample shows higher compressibility values at each stress levels.
- The values of the Compressibility index and Recompression index for the MSW specimens under saturated condition are higher than under the unsaturated condition. Further, there was a significant reduction in C_r compared to value of C_c.
- There was a considerable reduction of coefficient of secondary compression during reloading stage compared to loading stage. This revealed that the secondary consolidation characteristic of MSW can be significantly improved by Preloading.
- Coefficient of Consolidation values are much greater than those observed for soils.
- These results indicate that the compressibility characteristics of MSW can be improved by preloading. In recent times the preloading was very effectively used in construction of roads through sites underlain by peaty clay. Hence, in the rehabilitation of MSW landfill and converting them to useful lands, preloading process can be adopted to ensure that the settlements of these improved grounds are well within acceptable limits during the service time. Due to high coefficient of consolidation, technology such as Prefabricated Vertical Drains (PVD) may not be necessary to accelerate the consolidation.

REFERENCES

ASTM D854-Standard Test Methods for Specific Gravity of Soil Solids by Water Pycnometer (1984). Annual Book of Standards, Soil and Rock, 04.08: 210-213.

Dixon, N., Jones, D.R.V. (2005). Engineering properties of municipal solid waste. Geotextile and Geomembranes, 23(No 3):205-223.

Dixon, N., Langer, U. (2006). Development of a MSW classification system for the evaluation of mechanical properties, Waste Management, 26: 220-232.

Head, K. (1994). Manual of Soil Laboratory Testing (Permeability, Shear Strength and Compressibility Tests).

Imre, E., Firgi, T., Telekes, G. (2014). Evaluation of the Oedometer Tests of Municipal Landfill Wate Material, YBL Journal of Built Environment, 2(1).

Kavazanjian, E., Matasovic, N., Bachus, R.C. (1999). Large-diameter static and cyclic laboratory testing of municipal solid waste, Environmental Sanitary Engineering Centre,pp 437-444.

Landva, A., Clark, J. (1990). Geotechnics of waste fill - Theory and practice, ASTM International, pp. 86-103.

Naveen, B., Sivapullaiah, P., Sitharam, T. (2018). Appropriate Method of Determination of Coefficient of Consolidation for Municipal Solid Waste. Geotechnical Testing Journal, 41(6): 1026-1039.

Waste characterization for settlement assessment for surcharge over waste foundation

T.A. Peiris, F.R. Siahaan
GHD Pty Ltd, Australia

P.K. Wong
Coffey Services Australia Pty Ltd, Australia

T. Muttuvel
SMEC Pty Ltd, Australia

ABSTRACT: Municipal Solid Waste (MSW) placed in the landfill are highly compressible and variable with significant organic content. As ground improvement is required to limit the post construction settlements of embankment built over landfill, the ability to estimate the primary settlement is necessary to assess the performance of improved ground and predict the secondary settlement. This paper presents a basic methodology for waste characterization to enable the assessment of geotechnical properties and derivation of Waste Compressibility Index (WCI). WCI can be correlated with compression ratio for the prediction of primary settlement. A case study is presented where railway embankment was built over a landfill foundation treated by means of surcharging. The abovementioned methodology has been used in the design to characterize MSW and assess primary settlement. The back-analysis carried out to verify the above methodology indicated a reasonable agreement between the back-analyzed CR and CR estimated by using WCI.

1 INTRODUCTION

The scarcity of land and route requirement warrant the need for the new highway and roadway infrastructures to be constructed over the foundation with poor subgrade condition. This includes the increasing number of landfill facility where waste materials are typically placed within subdivided cells. The majority of landfill facility are typically used as the dumping ground for Municipal Solid Waste (MSW) which has heterogeneous content and relatively high compressibility. Consequently, ground improvement is usually required to limit the post construction settlements to which the abovementioned infrastructures are subjected (Van Impe and Bouazza, 1997). In some conditions, ground improvement by means of surcharging is preferred as other intrusive technique can induce a risk of potential adverse impact to landfill features or nearby structures as well as environmental damage. For the design of surcharge ground improvement and subsequent monitoring, it is essential to predict primary settlement by means of compression ratio (CR).

Prior to the estimate of CR, the MSW materials will need to be characterized to allow for their treatment as equivalent geomaterials. Conventional laboratory testing is not usually practical due to large size and irregular shape of the samples, limited availability of equipment to measure large strain due to large void collapse (Landva et al., 2000), as well as health and safety issue. In-situ testing such as cone penetration testing, pressuremeter or dilatometer may not be sufficient if they are not undertaken in large quantity and in conjunction with investigations which involve sample recovery. The undertaking field trial is useful to assess the settlement characteristics but the design of such trial will require an understanding on the MSW properties.

Various literatures have presented a unique relationship between CR and various geomaterial properties (organic content, moisture content and density) of MSW materials. CR has been reported to decrease with the reduction in the organic content (Sower 1973; Chen et al. 2009). CR has also been observed to increase with the increase in moisture content (Reddy et al. 2009; Wall and Zeiss 1995). On the other hand, an increase in MSW density has been reported to have an influence in the decrease in the compression index (C_c) of MSW materials (Landva et al. 2000; Chen et al. 2009). It is worth noting that the primary settlement assessed by using CR is related to the physical and mechanical process involving the reorientation of particles, movement of the fine materials into larger voids and collapse of void spaces (Sharma and De 2007) under a given load. Generally, the primary compression of MSW materials is not a result of dissipation of excess pore water pressure due to relatively high permeability and unsaturated condition of MSW materials (Wall and Zeiss 1995; Bareither et al. 2012). As organic

solids are more compressible than other MSW constituents and consequently tend to form weaker structures around voids, the relative influence of organic solid content to the primary settlement is significantly more in comparison to other constituents.

This paper presents a basic methodology for the waste characterization for the purpose of estimating the primary settlements. A discussion is presented on the proposed basic investigation scope to allow for a good recovery, identification and assessment of MSW constituents. The assessed constituents can be used to calculate a dimensionless index suggested by Bareither et al. (2012) which has been correlated with compression ratio (CR). To demonstrate the aforementioned technique, a case study involving the construction of railway embankment in the east coast of Australia is presented. Back-analyses were undertaken on selected monitoring points to verify the abovementioned technique.

2 WASTE CHARACTERIZATION AND ESTIMATE OF PRIMARY SETTLEMENT

2.1 *Waste characterization*

The fieldwork investigation should be preceded by a desktop study undertaken as part of the planning process. This study may comprise review of historical aerial photographs, waste placement records, survey record and operational records (i.e. gas monitoring, groundwater monitoring, etc). It is useful to obtain information regarding the landfill cell design, type/volume of MSW constituents, landfill depth, thickness/interval of cover layers and landfill age. Details are given in Landva and Clark (1990).

The majority of landfill comprise highly variable MSW materials with varying degree of placement compaction (Zekkos et al., 2006). As the MSW characterization requires a continuous exposure of MSW sample, a suitable investigation technique should be employed. An open excavation pit may be suitable for relatively shallow landfill formation which is usually no more than 3 m to 5 m deep.

As most of landfill can be expected to be thicker than 5 m, and obstructions within landfills may cause difficulties to conventional drilling, it may be necessary to adopt suitable techniques such as sonic drilling where continuous sampling can be obtained. An unsuitable drilling technique may result in poor sample recovery, increased in fieldwork duration or difficulty in locally penetrating obstructions.

Physical measurements should be taken on each sample run to obtain total length, sample diameter and approximate sample weight (with or without water). Detailed inspection on the sample should then be carried out to allow for classification of MSW materials. This includes the constituent material type, proportion (i.e. measured by thickness or area and weight), odor and color. Where possible, notes should also be recorded on the material density, moisture condition and state of decomposition. High resolution photographs of MSW samples with a ruler should be taken to allow for further analysis.

Landva and Clark (1990) proposed the a classification of MSW materials based on the degradation potential where the MSW are divided into 4 groups: Organic Putrescible (OP) comprising readily biodegradable materials such as food waste, garden waste; Organic Non-putrescible (ON) comprising slowly biodegradable materials such as paper, wood, textiles; Inorganic Degradable (ID) comprising metal with potential degradation due to corrosion; Inorganic Non-degradable (IN) comprising typical inert materials such as construction rubbles, soil, ash, glass, ceramics. It is imperative that the quantity and properties of OP materials are sufficiently obtained from the investigation as these and their associated changes over time will affect the compressibility and strength characteristics of MSW materials. While the OP content can be estimated by means of laboratory testing for organic content, such testing has been typically applied to soil-like materials and can be impractical for other shapes (e.g. tree trunk, books, etc). A large number of tests may be needed to get representative results.

For the primary settlement assessment, it would be necessary to obtain several geomaterial properties including bulk unit weight (γ_b). With the characterized MSW, the dry density (γ_d) can be obtained (Landva and Clark, 1990):

$$\gamma_d = \frac{1}{\sum_1^n \frac{w_{si}}{w_{sc}} \times \frac{1}{\gamma_{di}}} \quad (1)$$

Where γ_d = average dry density of landfill (kN/m^3); w_{si} = solid weight of waste constituent (kg); w_{ci} = total solid weight of waste samples (kg); γ_{di} = typical dry density of waste constituent (kN/m^3). Depending on condition of recovered materials, it could be more practical to estimate the volume of waste constituent or the volume of whole sample. This can be done by physical measurement with or without the use of water as the displacing medium. The dry density can be estimated:

$$\gamma_d = \frac{1}{v_t} \sum_1^n v_{si} \times \gamma_{di} \quad (2)$$

$$\gamma_b = \gamma_d\,(1 + m_d) = \gamma_d \left(1 + \sum_1^n \frac{w_{si}}{w_{sc}} \times \frac{\Delta\gamma_{di}}{\gamma_{di}}\right) \quad (3)$$

Where v_{si} = approximate volume of waste constituent (m^3 or liter); v_t = approximate total volume of assessed sample (m^3 or liter). For practical purpose, γ_{di} for a specific material type can either be obtained from published data or representative laboratory testing. The second component of the sum in the bracket in the equation (3) essentially describes the average of moisture content of various waste constituents.

Moisture content of sample (m_d) is typically needed to estimate γ_b for a typical geomaterial. Such estimate in the field could potentially be challenging due to the use of drilling fluid and the varying absorption capacity of various waste constituents. It is possible to estimate moisture content for each waste constituent which is capable of absorbing water. Alternatively, it is possible to estimate moisture content (by dry weight) on the basis of its correlation with organic content which typically has a high capacity of water absorbance. This correlation, which was developed based on field observation, was originally presented Landva and Clark, 1990 and Park et al. 2011. In this study, additional data from published literatures were added as shown in Figure 1 below. The uncertainty and variability in the estimate should be noted in the selection of appropriate value of moisture content. A comparison against available literature (Zekkos et al., 2006) presenting comprehensive database of landfill unit weight is also worthwhile.

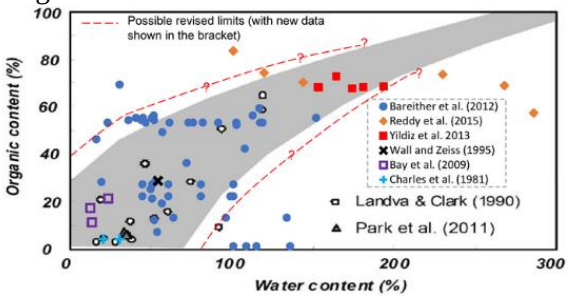

Figure 1: Extended relationship between organic content and moisture content

2.2 *Estimate of Primary Settlement*

Bareither et al. (2012) proposed a dimensionless Waste Compressibility Index (WCI) based on the percentage of biodegradable materials, moisture content and MSW density.

$$WCI = m_d \left(\frac{\gamma_w}{\gamma_d}\right)\left(\frac{OP}{100 - OP}\right) \qquad (4)$$

Where OP is the percentage of biodegradable materials (taken as organic materials); m_d is dry weight moisture content; γ_w is unit weight of water. Dry weight moisture content is equivalent to the moisture content where solid weight excludes water. Bareither et al. (2012) developed a relationship to estimate CR from WCI.

$$CR = 0.26 + 0.058 \log_{10} WCI \qquad (5)$$

Where CR = compression ratio ($C_c/(1 + e_0)$); C_c = compression index. It should be noted that the estimate of CR can be carried out with a range of ± 0.087 for each value of WCI. Similar to the variation in the correlation between organic content and moisture content, the estimate of CR will require a judgement and, if warranted, may involve sensitivity or reliability study. The above estimate is proposed for MSW layers where organic content is present and governs the primary compression of the MSW materials. The use of WCI considers the variation in the organic content due to the decomposition of MSW materials. Where organic content reduces (i.e. WCI approaches 0 %), the corresponding CR becomes relatively smaller. In the absence of organic content, the WCI is no longer applicable.

The compression ratio (CR) can then be used to analyze the primary settlement due to the void ratio reduction by using the following equation:

$$S_{prim} = S_{prim\,(non-waste)} + S_{prim\,(waste\,WCI)} = \Delta\sigma_v \frac{H_{nw}}{D} + CR\ H_{w-WCI} \log_{10} \frac{\sigma_v' + \Delta\sigma_v}{\sigma_v'} \qquad (6)$$

Where D = constrained modulus (kPa), $\Delta\sigma_v$ = additional pressure (kPa) due to surcharge embankment, H_{nw} = thickness (m) of non-waste layers not considered in the WCI, H_{w-WCI} = thickness of waste layers considered in WCI calculation, σ_v' = initial effective stress (kPa).

3 CASE STUDY – RAILWAY PROJECT IN EAST COAST OF AUSTRALIA

3.1 *Design Overview*

A new rail embankment was proposed to be built in the eastern coast. A section of the alignment with an approximate length of 295 m had to be built over buried landfill cells (Fig. 2) where MSW has been placed. The area from Ch 445 to Ch 560 is located within the relatively new landfill (about 15 years in age at the time of design) while the area from Ch 560 to Ch 720 is located within relatively old landfill (about 30 years in age at the time of design).

As part of site investigation, several boreholes were drilled within the old landfill. Due to relatively shallow and variable liner depths, test pits investigation was employed within the new landfill area to reduce risk of liner damage. Based on investigation and survey data, it was inferred that the thickness of landfill generally varied (ref. Table 1) along the proposed alignment which was roughly parallel to the existing landfill cell batter. A portion of old landfill area between Ch 540 to Ch 660 was underlain by full thickness of landfill cell (about 13 – 15 m).

Three boreholes (BH7, BH8 and BH9a) within the old landfill and test pits within the new landfill were used to characterize MSW materials. Boreholes BH7 and BH8 were drilled using sonic technique with excellent sample recovery. Borehole BH9a was drilled by using conventional rotary drilling technique with Standard Penetration Test (SPT) at every 1.5 m interval. Only partial sample recovery was achieved in borehole BH9a. The majority of SPT testing resulted in refusal or blow count of over 50 per 300 mm penetration. Locations of BH7, BH8 and BH9a are shown in Figure 2. Assessed

MSW composition from these investigation locations are given in Figure 3.

The settlement monitoring of a field trial conducted earlier in 1985 was also considered. This field trial was conducted for other purpose in nearby area. Prior to the field trial, the investigation was undertaken by means of a test pit excavated to 5 m deep below the then ground surface. A circular trial embankment was built by using uncompacted crushed sandstone to a total height of 3 m with a top diameter of about 3 m.

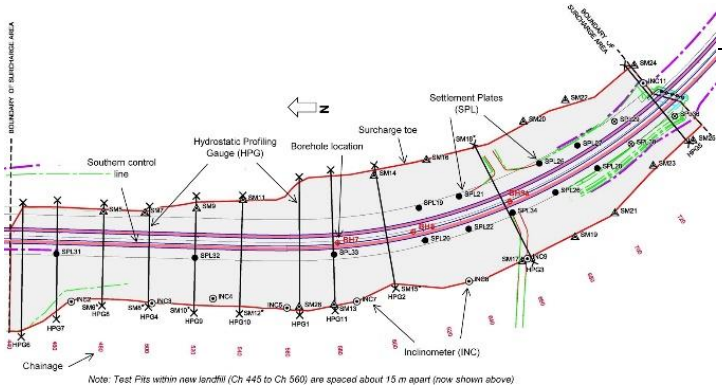

Figure 2: Plan showing treated section of proposed railway embankment, monitoring instrumentations

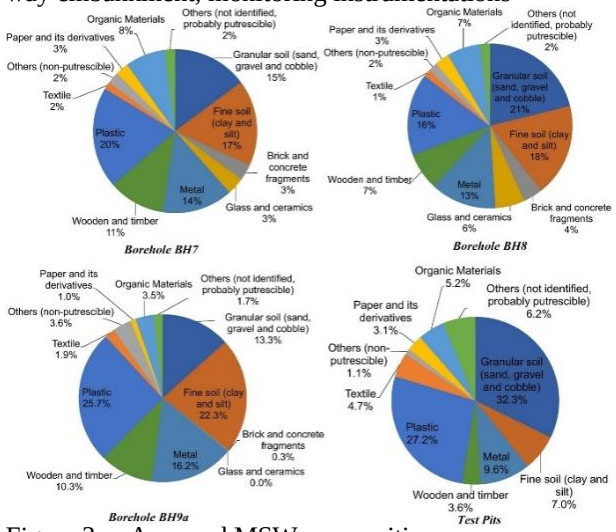

Figure 3: Assessed MSW composition

Subsequent to the characterization of MSW materials, an average dry density (γ_d) was obtained for the entire MSW depth of each borehole. The γ_d value was calculated by using equation (2) and typical dry density values of individual MSW constituent (Landva and Clark, 1990). These values are consistent with those presented in Zekkos et al. (2006). Then, moisture content values of MSW were assessed based on the approximate organic content (Figure 3). As this correlation yields a range of moisture content values for a given value of organic content (OP), a range of WCI was consequently estimated for each respective borehole. The assessed WCI values are given in Table 1.

Due to remaining risk of remaining variability and uncertainty, WCI value of 0.063 was adopted based on the upper range of variation in the investigation results. This gave CR of 0.2 for the design.

Table 1. Summary of parameters for estimate of CR

Borehole (Chainage)	Inferred MSW thickness (m)	OP (%)	γ_d (kN/m^3)	Range of assessed WCI[#]
BH7 (Ch 580)	12	12.5	11	0.0065 – 0.052
BH8 (Ch 620)	11.5	11.3	12.2	0.0052 – 0.042
BH9a (Ch 660)	12.5	6.3	11.5	0.0029 – 0.023
Test Pits*	Up to 8	14.5	10.9	0.0077 – 0.062
1985 Trial[+]	10^	30^	8.5	0.063 – 0.32[+]

*Based on 8 test pits spaced at about 15 m within the new landfill area; +The 1985 Trial embankment was located about 100 m to the south of Ch 745; ^Based on limited investigation. Thickness including up to 3 m of non-waste materials excluded in WCI; [#]Range of assessed WCI based on range of possible moisture content (5%-40%) with 20% being the most likely value.

Ground improvement in the form of surcharging was employed to reduce the post construction settlements. The ground improvements in the forms of rigid/semi-rigid inclusions and dynamic compaction were not selected due to a risk of damage to the existing landfill features including the liner. The high surcharge embankment and waiting period were designed to induce the primary settlement (reduction in void ratio) and consequently reduce the post construction settlement via the decrease of creep strain rate ($C_{\alpha\epsilon}$). It is shown that the decrease in $C_{\alpha\epsilon}$ has a distinct correlation with the reduction in void ratio (Siddiqui et al., 2013).

3.2 *Construction Monitoring*

As part of the design, it was necessary to adopt an observational approach to assess the performance of ground improvement and reduce risk of uncertainty with regards to the prediction of post construction settlement. This was carried out by monitoring the settlements due to the surcharge loading. Ground settlement were monitored by using Settlement Plates (SPL) and Hydrostatic Profiling Gauges (HPG) as shown in Fig. 3. Lateral movements were monitored by using inclinometers (INC).

Results of construction settlement monitoring are shown in Figs. 4 and 5 along the southern control line of the alignment. Two mechanisms of primary consolidation were considered to assess the end of primary consolidation. The first involves the void ratio decrease due to particle rearrangement while the second involves the collapse of larger voids held up by weak structure. As MSW is highly permeable, the completion of first mechanism is typically immediate. However, the completion of second mechanism may take longer than the first mechanism due to progressive weakening of the void structure under given load. In general, various

literatures have reported that both mechanisms were completed within 1 to 4 months (Wall and Zeiss 1995, Sharma and De 2007). Secondary settlements are not shown in Fig. 5 for clarity purpose.

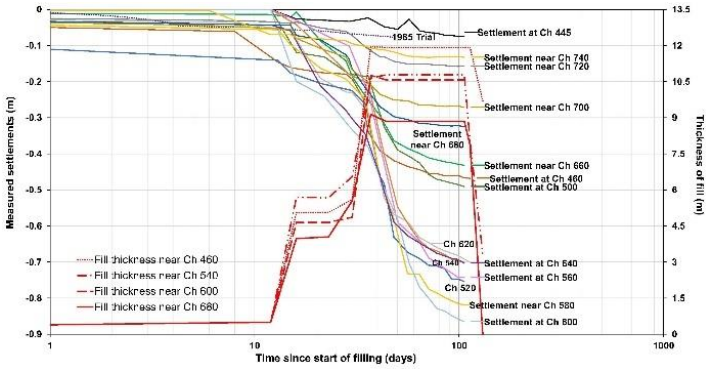

Figure 4: Plots of measured settlements and fill thickness

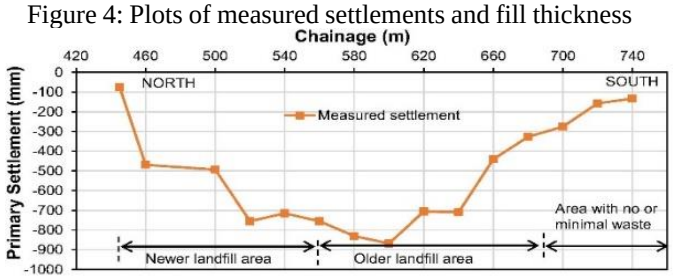

Figure 5: Plots of total primary settlements

As the primary consolidation of MSW materials under the surcharge load was not induced by the dissipation of excess pore pressure (i.e. time-dependent behavior), the end of primary consolidation was deemed to have finished by observing that the secondary settlement has become apparent in semi log plot (i.e. no noticeable change in general curvature). This observation includes the absence of localized changed in settlement curvature due to sudden void collapse. Such monitoring of void collapse was improved by adopting line measurement of settlements by using HPG. The assessed end of primary consolidation was generally about 3 months from the start of monitoring (i.e. about day 100 in Fig. 4) or about 2.5 months from the reference time which took into consideration the staged placement of fill materials.

For the 1985 Trial, the completion of primary condition could not be readily assessed particularly with respect to the end of void collapse. Due to the shallow embankment with smaller dimension and uncompacted fill, the collapse of larger and stronger voids under given load possibly have not occurred until the end of monitoring. As a result, the settlement value was extrapolated to about 3 months from the end of filling which is consistent with those observed in BH7, BH8 and BH9a.

3.3 *Discussion on Primary Settlement*

In Fig. 5, measured settlements were relatively smaller within the northern end (Ch 445 to Ch 460) and southern end (Ch 680 to Ch 740) where the presence of MSW materials was negligible.

By using equation (6) above and settlement monitoring data, the CR value was back-analyzed for the purpose of this study. To reduce the uncertainty in relation to localized variation in the MSW properties, the back-analyses were undertaken for settlement plates in the vicinity of boreholes BH7, BH8, BH9a as well as the location of 1985 Trial. The back-analyzed CR values for BH7, BH8, BH9a and 1985 Trial are 0.14, 0.13, 0.0875 and 0.12, respectively. Each of CR value was then plotted against the range of WCI for respective location which were previously assessed by considering a range of possible moisture content. These plots are shown in Figure 6 along with a range of relationship between CR and WCI given in Bereither et al. (2012). The back-analyzed CR appear to be higher with the higher content of organic materials (OP) with the exception of the 1985 Trial. Such observation for the 1985 Trial was possibly related to the inadequacy of data used for the assessment of WCI. As the information from 1985 Trial was obtained from a 5-m deep test pit, limitations in the investigation depth and sampling quality would have applied in the assessment of the MSW properties. This suggests the significance of a selection of appropriate investigation technique to obtain good quality MSW samples from most or entire depth.

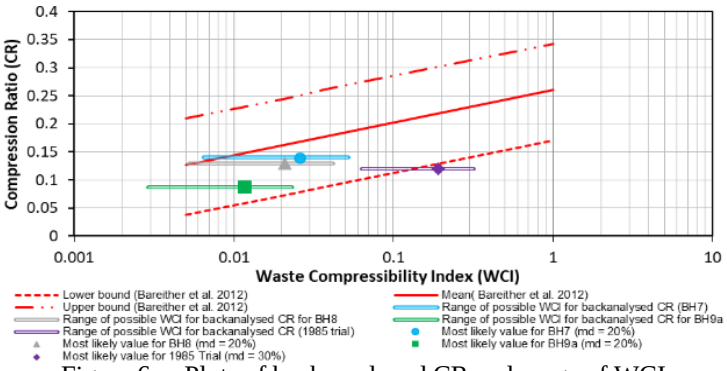

Figure 6: Plots of back-analyzed CR and range of WCI (CR-WCI relationship from Bareither et al., 2012)

Fig. 6 also shows that the range of WCI for back-analyzed compression ratio generally fall within the relationship given by Bareither et al (2012). It can also be seen from that back-analyzed compression ratio for BH7 and BH8 are generally closer to and have proportional gradient to the mean line. As previously mentioned, the quality of recovered samples from BH7 and BH8 was generally higher than that of borehole BH9a and the test pit in 1985 Trial. This implies that a good sample recovery is beneficial for MSW characterizations. Despite its practicality, the relationship was developed by Bareither et al. (2012) by using available database of compressibility parameters at the time of publication. Therefore,

it is a good practice that this relationship is used carefully especially for the range of WCI where less available data were used in regression analysis.

As indicated in Figure 4, primary settlement is generally completed within 2.5 months from the reference time which takes into consideration the staged placement of fill materials. This period is consistent with times observed in literatures (Edil et al. 1990, Walls and Zeiss 1995, Andersen et al. 2004, Sharma and De 2007). This timing is consistent with the observed lateral movement (ref. Fig. 7) which stabilizes with the measured settlements. From Fig. 7, it also can be noted that ratios between lateral movement measured at surcharge toe to the maximum settlement under embankment during the waiting period vary from 8% to 18% with the majority being in the range of 10% to 15%. These ratios are less than the typical ratio for embankment over soft clay (Tavenas and Leroueil, 1980). This infers relatively high shear strength of MSW despite the presence of over 9-m thick fill (including up to 9 m thick of surcharge) built over short period.

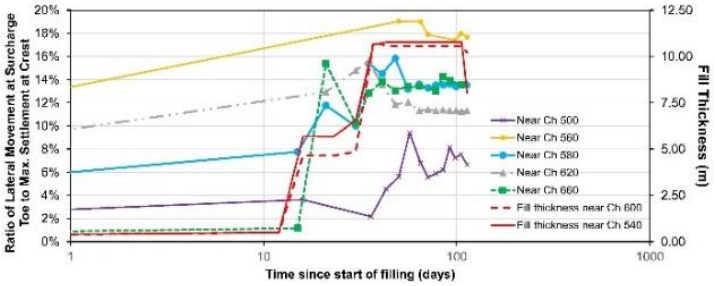

Figure 7: Plots of ratios of lateral movement at the toe to the maximum settlements

4 CONCLUSION

This paper presents an overview of a basic investigation methodology which can be adopted for the (MSW) characterization and subsequent assessment of the compression ratio (CR) required for the estimate of primary consolidation settlement of highly compressible MSW. The estimate of primary settlement is useful for the assessment of construction settlement as well as the design of ground improvement extent to achieve required reduction in void ratio and collapse of large critical voids.

A case study involving a railway embankment built over buried landfill cells is presented. The ground improvement in the form of surcharging was adopted due to project constraint. In-situ waste characterization was carried out. The back-analyzed compression ratio were found to be consistent with the published relationship between Waste Compressibility Index and CR.

Given the variability in waste properties and a range of parameters assessed from the discussed correlations, it is imperative that the basic investigation is carried out with suitable technique and in sufficient quantity. Additional assessments, such as sensitivity, reliability and risk assessments, should also be considered during the design. It is a good practice to conduct an observational technique where waste settlements can be monitored during the construction or earlier operational period of a typical infrastructure to refine the prediction.

5 REFERENCES

Andersen, E. O., Balanko, L. A., Lem, J. M. and Davis, D. H. (2004). Field Monitoring of the Compressibility of Municipal Solid Waste and Soft Alluvium, Proc. of Fifth Int. Conference on Case Histories in Geotechnical Engineering.

Bareither, C. A., Benson, C. H. and Edil, T. B. (2012). Compression Behavior of Municipal Solid Waste: Immediate Compression, ASCE Jnl of Geotechnical Engineering, 138 (9): 1047 – 1062.

Chen, Y. M., Zhan, L. T., Wei, H. Y. and Ke. H. (2009). Aging and compressibility of municipal solid wastes. Waste Management, 29 (1): 86 – 95.

Park, H. I., Borinara, P. and Hong, K. D. (2011). Geotechnical Considerations for End-Use of Old Municipal Solid Waste Landfills, Int. Jnl. Environmental Research, 5 (3): 573 – 584.

Landva, A. O. and Clark, J. I. (1990). Geotechnics of waste fill—Theory and practice, ASTM STP 1070, West Conshohocken, Pa. 86–103.

Landva, A. O., Valsangkar, A. J. and Pelkey, S. G. (2000). Lateral earth pressure at rest and compressibility of municipal solid waste, Canadian Geot. Journal, 37 (6): 1157 – 1165.

Reddy, K. R., Hettiarachchi, H., Gangathulasi, J., Bogner, J. E. and Lagier, T. (2015). Geotechnical properties of synthetic municipal solid waste, Int. J. of Geot. Eng., 3(3):429–438.

Reddy, K. R., Hettiarachchi, H. and Giri, R. K. (2015). Effects of degradation on geotechnical properties of Municipal Solid Waste from Orchard Hills, Landfill, USA. Int. J. of Geosynth. and Ground Eng. 1:24.

Siahaan, F., Muttuvel, T. and Peiris, A. (2017). Characterization of Municipal Solid Waste Materials for the purpose of engineering design in transport infra project. Aust. Geo. Jnl., 52 (3): 67 – 75.

Siddiqui, A. A., Powrie, W. and Richards, D. J. (2013). Settlement characteristics of mechanically biologically treated wastes, ASCE Jnl of Geotechnical Engineering, 139 (10): 1676 – 1689.

Sharma, H. D. and De, A. (2007). Municipal Solid Waste landfill settlement: Postclosure Perspectives, ASCE Journal of Geotech. and Geoenv. Engineering, 133 (6): 619 – 629.

Sowers, G. (1973). Settlement of waste disposal fills. Proc., 8th Int. Conf. on Soil Mechanics and Foundation Engineering, Vol. 22, Balkema, Rotterdam, Netherlands, 207 – 210.

Tavenas, F. and Leroueil, S (1980). The behavior of embankments on clay foundations. Canadian Geo. J,17(2),236-260.

Van Impe, W. F. and Bouazza, A. (1996). Densification of domestic waste fills by Dynamic Compaction, Canadian Geotechnical Journal, 33: 879 – 887.

Wall, D. K., and Zeiss, C. (1995). Municipal landfill biodegradation and settlement, ASCE Jnl of Env Eng, 121 (3): 214 – 224.

Yildiz, S., Yaman, C., Demir, G., Ozcan, H. K., Coba, A., Okten, H. E., Sezer, K. and Goren, S. (2013). Characterization of Municipal Solid Waste in Istanbul Turkey. Environmental Progress and Sustainable Energy, 23 (3): 734 – 639.

Zekkos. D., Bray, J.D, Kavazanjian Jr, E., Matasovic, N., Rathje, E. M., Riemer, M. F. and Stokoe II, K. H. (2006). Unit weight of Municipal Solid Waste, ASCE Jnl. of Geotech. and Geoenv. Engineering, 132 (10): 1250 – 1261.

Role of Waste Glass Powder in Fly ash/slag-based Alkali-activated Binders

M.H. Samarakoon and P.G. Ranjith
Department of Civil Engineering, Monash University, Building 60, Melbourne, Victoria, 3800, Australia

ABSTRACT: Generation of waste is rapidly increasing due to extensive resources consumption of emerging industries causing harmful environmental impacts. Among them, glass waste contributes to a considerable portion of the municipal waste stream due to the practical difficulties in glass recycling. This paper investigates the applicability of waste glass powder in conventional fly ash/blast furnace slag-based alkali-activated binders (AABs). Both strength and microstructure of the hardened AAB paste were improved with the addition of waste glass powder up to 30% by weight as a replacement of fly ash, by keeping a fixed slag content of 50% in the mixture. The inclusion of glass powder produces calcium-based hydration products altering the geopolymer network of conventional pure fly ash-based systems. This study reveals the potential use of waste glass powder as a precursor and its effect on AABs in terms of mechanical and microstructural aspects of the hardened paste.

1 INTRODUCTION

1.1 *Alkali-activated binders (AABs)*

Alkali-activated binders (AABs), also named as non-Portland cement binders mainly consisted of solid precursors and alkali activator. Waste materials or industry by-products with relatively high contents of silicon, calcium, and aluminium can be successfully utilized as the solid precursor in AABs, alone or with appropriate combinations. Based on the recent studies, alkali activators can be either in liquid or solid forms and create a primary medium to dissolve Al, Si, and Ca-based raw materials. Subsequently, it helps to generate geopolymer or alkali-activated materials in the reaction phase.

According to the reaction chemistry in the binder phase based on the mineral composition of the solid precursors, AABs are mainly divided into three major categories: 1) Low calcium-based, 2) High calcium-based and 3) Hybrid binders (Garcia-Lodeiro et al., 2015). Low-calcium binders mainly consist of 3-dimensional aluminosilicate polymer reaction products which called geopolymers, synthesized by silicon and aluminium-rich materials such as metakaolin, fly ash and mine wastes. High calcium-based materials such as ground granulated blast furnace slag (GGBFS) and cement kiln dust (CKD) mainly serve for high calcium systems, generally called as AAMs. Inclusion of ordinary Portland cement (OPC), replacing aluminosilicate precursors produces hybrid or blended binders which result in a series of complex hydration products. These binders can be further classified into two types depending on the addition of OPC clinker: low-Portland cement and non-Portland cement blends. However, non-Portland AABs show favourable results over Portland cement binders not only in strength properties but also in cost and emission aspects.

1.2 *Waste materials for AABs*

To date, various studies have been conducted to introduce industrial by-products or waste materials for the solid precursors of AABs. Most widely used solid precursors include but not limited to coal ashes (fly ash and bottom ash), municipal solid waste incinerator ash, palm oil fuel ash, metal slags (blast furnace slag, nickel slag, red mud, aluminium sludge), mine waste (copper, gold, vanadium, tungsten, phosphate), cement kiln dust and waste glass (Samarakoon et al., 2019).

Among them, the inclusion of glass waste in AABs is feasible due to its high pozzolanic properties and considerable alkali content. The glass production rates are increasing in the glass industry by producing millions of tons of waste glass, especially in the municipal solid waste stream (Ling et al., 2013). Recycling of waste glass to produce new glass is becoming limited due to the failure of achieving reuse requirements such as purity and same colour codes (Jani and Hogland, 2014). Therefore, more studies may need to seek novel methods to consume glass waste efficiently as a result of the serious environmental problems caused due to the disposal of such wastes. Although there are studies regarding waste glass inclusion in OPC (Lu et al., 2017), limited studies are available to find the effects of including waste glass in AABs. This study mainly focuses on the inclusion of waste glass powder as a precursor, and its influence on strength and microstructure of fly ash/GGBFS-based AABs activated by low concentrated alkaline solution.

2 EXPERIMENTAL WORK

2.1 *Materials*

Class F fly ash (FA) and slag (GGBFS) were sourced from Independent Cement & Lime Pty Ltd, Australia. Soda-lime type crushed glass (CG) were purchased from Let's Clean Pty Ltd, Australia and was further crushed by a standard ring-mill to make it finer. Analytical grade NaOH pellets (purity ≥ 98%) from Merck Pty Ltd, Australia was used as the alkali activator. The chemical compositions (by x-ray fluorescence method) of FA, GGBFS, and CG are shown in Table 1. Particle size analysis (by Malvern laser technique) results showed that the mean diameter (d_{50}) of FA, GGBFS, and CG were 17.6, 15.3 and 11.5 µm respectively.

Table 1. Chemical composition of raw materials (wt. %)

	FA	GGBFS	CG
SiO_2	62.7	32.7	72.43
Al_2O_3	27.1	13.0	1.24
Fe_2O_3	2.6	0.3	0.43
CaO	2.1	43.0	13.43
MgO	0.4	5.8	0.69
K_2O	1.26	-	0.45
Na_2O	0.59	0.4	10.81
SO_3	< 0.1	1.4	0.11
P_2O_5	0.3	-	-
TiO_2	1.0	-	-
*LOI	2.5	0.7	0.03

* Loss on ignition

2.2 *Mix design*

The reference mixture of 50% FA and 50% GGBS was used without CG (named CG0) as the starting point. To study the effect of adding CG in AABs, FA was partially replaced by CG with 10%, 20%, and 30% by weight (named CG10, CG20, and CG30 respectively). The 4M alkaline solution was prepared by dissolving NaOH pellets in distilled water, one day prior to casting samples. Table 2 shows the mix design details of the paste mixtures. The solid precursors were firstly dry mixed for 5 minutes using a HOBART® 5L mixer at a low speed. Then the NaOH solution was added gradually, and the batches were mixed for an additional 5 minutes at a medium speed. The fresh pastes mixtures were cast in cylindrical PVC moulds (38 mm× 76 mm, aspect ratio = 2.0) and then compacted with a vibration table for 3 layers (each layer for 30s). The top surface of the samples was sealed with a plastic foil to reduce moisture loss and then cured at 60 °C in a laboratory oven for 24h. After 24 h, the specimens were de-moulded, sealed with polythene and then kept in ambient conditions (21-23 °C and 50 ± 5% relative humidity) until the testing age of 1, 7 and 28 days.

2.3 *Testing methods*

Uniaxial compressive strength (UCS) tests were conducted to evaluate the strength of the hardened paste, using the Shimadzu 300 kN testing machine with a 0.1 mm/min displacement rate. ARAMIS photogrammetry was incorporated to capture the lateral deformations, strains development, and failure stages during loading (Nasvi et al., 2014). All the samples were face-ground by a grinding machine to ensure purely axial loading during compression testing.

XRD analysis was conducted using D8 Cobalt diffractometer (0.6 mm slit, 0.02° step interval, 40 kV and 25 mA tube setting, Co Kα1 (1.7889 Å) radiation and 10° – 90° 2θ range) to identify the mineralogy of the hardened AABs after 28 days of curing.

Scanning electron microscopy (SEM) was conducted to evaluate the microstructure of hardened paste using Quanta FEI scanning electron microscope.

3 RESULTS AND DISCUSSION

3.1 *Effect of CG on strength properties*

The effect of CG content on AABs at different curing ages was investigated to find the optimum substitution percentage of CG. Fig. 1 shows the strength development of AABs up to 28 days for 4M NaOH solution.

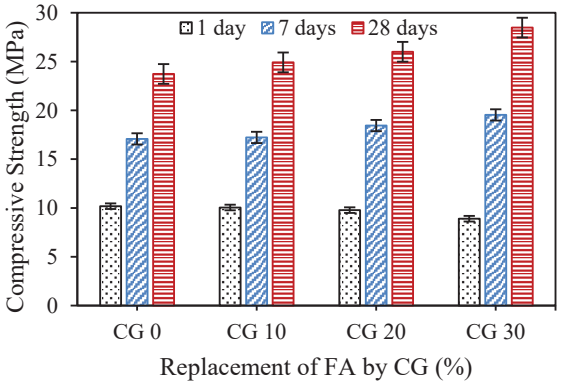

Fig. 1 Variation of UCS of AABs with the CG addition

Irrespective to the CG content, the compressive strength is increased with the curing age for all mixtures. It is also expected that the strength would be further increased after 28 days. However, the strength was slightly reduced with the CG inclusion at the early age of 1 day. This is mainly related to the lower dissolution rates of silica of CG and slower activation of precursors in mild NaOH concentration of 4M. Furthermore, the weaker bond between glass particles and the cement matrix due to

smooth surface of glass particles, agglomeration of random large size glass particles inside the matrix and micro-cracks inside the glass particles induced by further crushing process may also affect for the slight reduction of early strength (Lu and Poon, 2018). However,

Table 2. Mix design details of AABs

Sample ID	* L/S ratio	Alkali activator	GGBFS (wt %)	FA (wt%)	CG (wt %)
CG0	0.45	4M NaOH solution	50	50	0
CG10				40	10
CG20				30	20
CG30				20	30

*Alkaline liquid to solid ratio

AABs at 28 days of curing showed strength improvement with the addition of CG. CG30 mixtures showed around 20% increment compared to CG0 mixtures. This is related to the reduced porosity caused by the formation of hydration products as well as the agglomeration of unreacted glass particles as a filler in the cement matrix (see Section 3.2.1).

ARAMIS camera was used during the compression loading to monitor the effect of CG addition on strain variation of the AABs at 28 days curing age. According to Fig. 2, both strain distribution and volumetric strain decrease with the incorporation of CG. Moreover, a diagonal failure is observed at samples without CG while the samples with 30% CG showed split tensile failure. This implies the transformation from ductile to brittle behaviour of waste glass replaced AABs with the curing age (Nasvi et al., 2014). This also relates to the improved interlocking between glass particles and the cement matrix due to angular particle morphology of crushed glass.

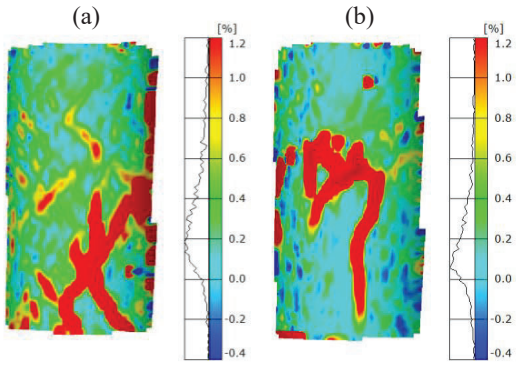

Fig. 2 Strain distribution by ARAMIS photogrammetry at 28 days of curing (a) CG0 and (b) CG30

3.2 *Effect of CG on microstructure*

3.2.1 *SEM/EDS analysis*

Fig. 3(a) and (b) show the microstructure of CG0 and CG30 AAB paste cured at 28 days, respectively. According to Fig. 3(b), it is clear that, with the increasing CG content, the agglomeration of unreacted CG particles is higher. However, those particles were bonded well into the matrix with the curing time by the hydration products around them. Therefore, these micro-particles finally precipitate as a filler by reducing the porosity of the hardened binder.

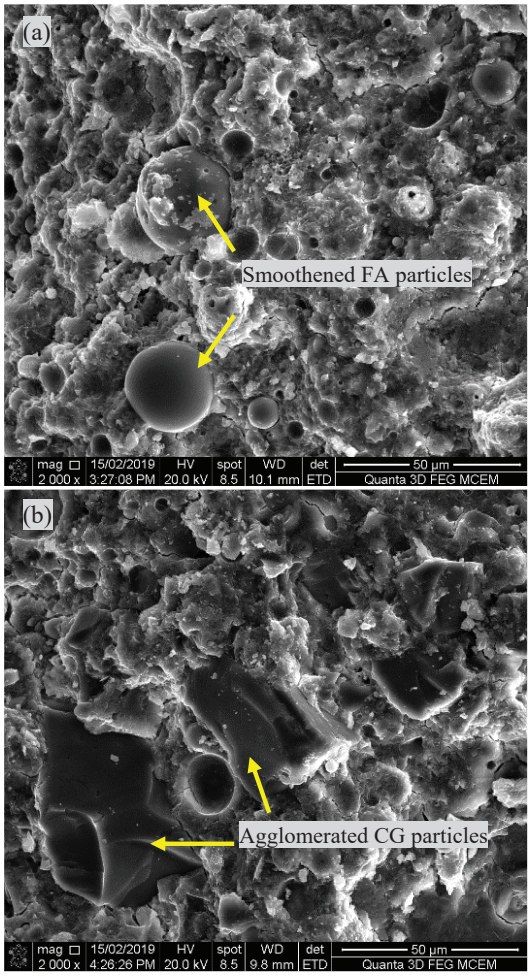

Fig. 3 SEM images of AAB paste at 28 days (a) CG0 and (b) CG30

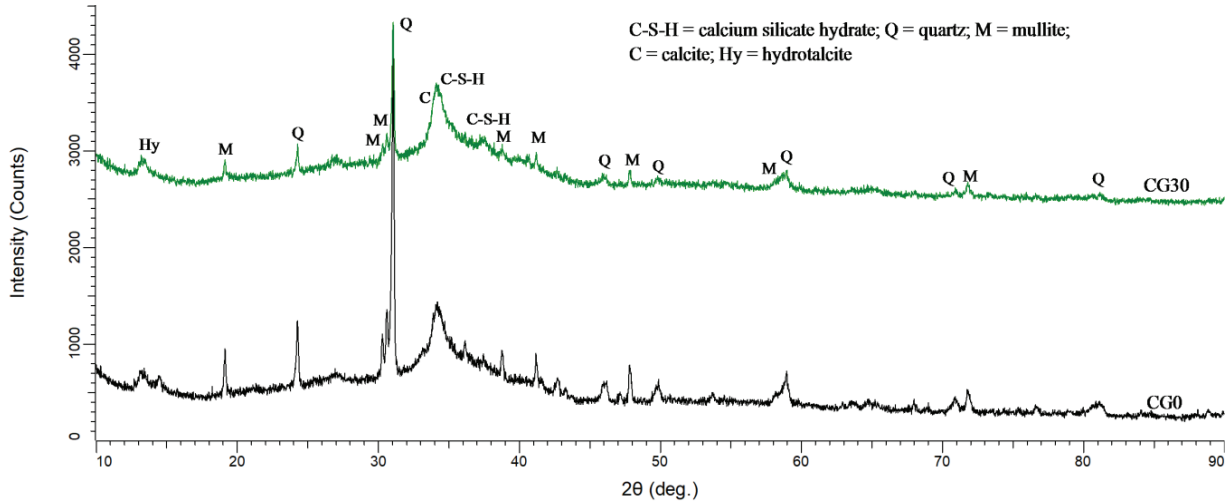

Fig. 4 XRD patterns of CG0 and CG30 AAB paste at 28 days

3.2.2 *XRD analysis*

The effect of CG addition on the mineralogy of the hardened AAB paste was analyzed using XRD technique, and the results after 28 days curing age are showed in Fig. 4. Results show the crystalline peaks of unreacted minerals such as quartz and mullite and the semi-crystalline peaks of the reacted binder such as calcium silicate hydrate (C-S-H), calcite, and hydrotalcite. The production of C-S-H is relatively higher for CG30 compared to CG0 and showed lower peaks of unreacted quartz and mullite with the CG addition.

4 CONCLUSIONS

The inclusion of waste glass in AABs offers promising solutions including but not limited to a reduction in both waste generation and extensive land area for disposal, saving costs, energy, and virgin raw materials in production, and the inertization of hazardous materials with lower emissions to the environment. This study shows that waste glass powder can be successfully utilized in FA/GGBFS AABs under the low alkaline concentration of 4M. Both strength and microstructure of the hardened AABs improved with the CG addition up to 30% of the weight as a replacement of fly ash, by keeping a fixed slag content of 50%. According to the mineralogy and microstructure analysis, it was found that the inclusion of glass powder produces calcium-based hydration products altering the geopolymer network of conventional pure fly ash-based systems. This sustainable alkali-activated binder can be used for masonry and architectural mortar applications in the pre-cast industry. However, further studies specified for the field applications are suggested before using.

ACKNOWLEDGEMENTS

The authors would like to acknowledge the use of facilities within the Monash X-ray Platform and the Monash Centre for Electron Microscopy. The authors are also grateful to Independent Cement & Lime Pty Ltd, Australia for providing fly ash and slag.

REFERENCES

Garcia-Lodeiro, I., Palomo, A. & Fernández-Jiménez, A. 2015. An overview of the chemistry of alkali-activated cement-based binders. *Handbook of alkali-activated cements, mortars and concretes.* Elsevier.

Jani, Y. & Hogland, W. 2014. Waste glass in the production of cement and concrete–A review. *Journal of environmental chemical engineering,* 2**,** 1767-1775.

Ling, T.-C., Poon, C.-S. & Wong, H.-W. 2013. Management and recycling of waste glass in concrete products: Current situations in Hong Kong. *Resources, Conservation and Recycling,* 70**,** 25-31.

Lu, J.-x., Duan, Z.-h. & Poon, C.S. 2017. Fresh properties of cement pastes or mortars incorporating waste glass powder and cullet. *Construction and Building Materials,* 131**,** 793-799.

Lu, J.-X. & Poon, C.S. 2018. Use of waste glass in alkali activated cement mortar. *Construction and Building Materials,* 160**,** 399-407.

Nasvi, M.C., Ranjith, P.G., Sanjayan, J., Haque, A. & Li, X. 2014. Mechanical behaviour of wellbore materials saturated in brine water with different salinity levels. *Energy,* 66**,** 239-249.

Samarakoon, M., Ranjith, P., Rathnaweera, T. & Perera, M. 2019. Recent Advances in Alkaline Cement Binders: A Review. *Journal of Cleaner Production,* 227**,** 70-87.

Large Scale In-Situ direct shear testing on Waste Material at Meethotamulla Open Dump Site

S.H.S. Jayakody
National Building Research Organisation, Sri Lanka

S.A.S. Kulathilaka & U.P. Nawagamuwa
Department of Civil Engineering, University of Moratuwa, Sri Lanka

ABSTRACT: The catastrophic slope failure at the infamous Meethotamulla landfill claiming 34 lives and destroying infrastructure became one of the hot topics in Sri Lanka in 2017. Although municipal solid waste (MSW) is a difficult material to test, many comprehensive studies have been conducted to determine the likely ranges of Engineering properties that are necessary in the design of landfills. In this study, in-situ direct shear tests were performed to assess and develop an insight into the shear strength properties of MSW. A large-scale direct shear apparatus which has dimensions of 300 mm×300 mm in plan view and 150 mm in height was fabricated to conduct in-situ tests. One of the main objectives was to test the MSW at differently aged locations in the abandoned Meethotamulla waste fill site. In-situ density and moisture content test along with composition analysis were also conducted. As stated by many researchers, a peak failure state was not observed during the direct shear tests. There was no significant variation in the shear stress parameters of the differently aged samples all of them were significantly degraded. The results obtained from the tests were analyzed and compared with the published data in literature. Recommendations were made regarding the further studies needed in the direction of developing a relationship between the differently aged MSW and their shear strength properties.

1 INTRODUCTION

1.1 *Background*

Municipal Solid Waste (MSW) is a typical term used for a heterogeneous collection of wastes produced in urban areas, the nature of which varies from region to region (United Nations Environment Program, 2005). There are numerous MSW landfills in Sri Lanka that are mostly unregulated and uncontrolled. Meethotamulla waste fill is such an open dump which collapsed in 2017 claiming 34 lives of people and destroying infrastructure. The closure and reclamation of Meethotamulla waste fill found to be the most effective approach for resolution after analyzing several alternatives.

Slope instability is one of the major concerns in the process of developing a landscaped landfill. Therefore, it is vital to understand shear strength properties of MSW considering a wide range of values published by many researchers (Jones et al. (1997), Manassero et al.(1996), Kavazanjian (2001), Reddy et al. (2009), Miyamoto, et al., (2012) etc). The determination of geotechnical properties of MSW is a very difficult task due to; its heterogeneity, changing significantly with time and not being easily amenable to direct measurement. Laboratory testing, in-situ testing and back analysis of failure were different methods used to determine the shear strength of MSW. Each method has its own pros and cons.

In the Sri Lankan context, little or no studies have been carried out to determine the shear strength properties of MSW. This paper presents in-situ shear tests carried out to investigate the shear properties of MSW by fabricating a large-scale direct shear apparatus (300 mm x 300 mm). The results obtained were compared with published literature.

2 EXPERIMENTAL PROGRAM

2.1 *Fabrication of large-scale direct shear apparatus*

Large-scale direct shear apparatus (shear box, mechanisms for applying normal load and shear load) was fabricated after some modification to the original design by Miyamoto, et al., (2012). Shear box has dimensions of 300 mm × 300 mm in the plan view and 150 mm in height as shown in Fig. 1. Fig.2 shows the fabricated shear box. A simple screw jack attachment was fixed to the shear box apparatus to apply a manually controlled shear force. The load transmitted to the top half of the sample is measured using an electronic load cell which was calibrated in the range of 0 - 100 kN to an accuracy of 0.1 kN. Horizontal and vertical displacement are measured using transducers.

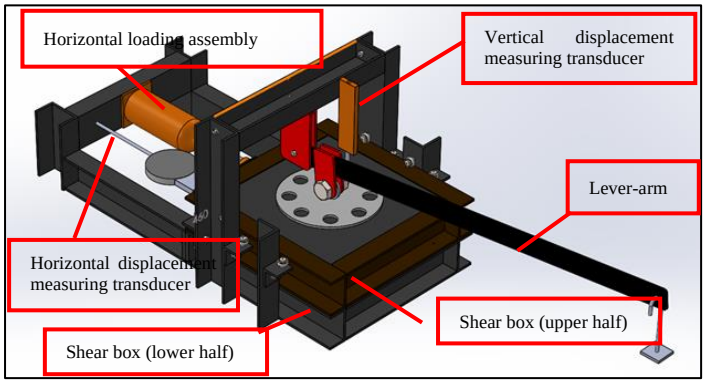

Fig. 1 Schematic diagram of the direct shear test apparatus

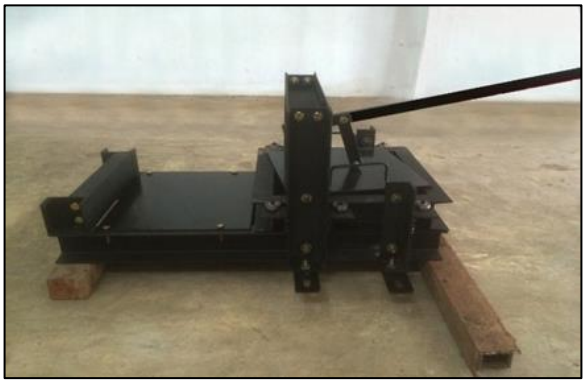

Fig. 2. Fabricated shear box

Normal load is applied through a lever-arm system. The lever-arm system enables a 10 times increase of the normal stress. A calibration was done to establish the relationship between the normal stress and the applied load. The maximum normal load that can be applied from this arrangement is 25 kN/m^2. A data acquisition system(data logger) was developed and coded to collect the data. Then the collected data were read by an open-source platform "HTerm". Before the testing was carried out at the waste fill, a pilot test was conducted to confirm that different components of the shear apparatus function in the expected manner and to verify that the data acquiring system functions well. Further, practical issues which could be faced at the Meethotamulla site were also identified. The results of the pilot test confirmed that all the components in the large-scale system functioned as expected.

2.2 *In-situ direct shear testing at Meethotamulla*

The locations for the testing were selected at four different heights such that these locations will represent waste dumping at different timescales as shown in Fig 3.

Fig. 3 Locations selected for the in-situ testing

In the absence of proper data on dumping stages these different testing heights were selected (26 m, 22 m, 14 m, and 7 m) to represent the different degradation assuming the depths will be proportional to the age of MSW. Three specimens have to be prepared per location. In this regard, it was assumed that all three samples would have the similar age and will be of same waste composition. Fig. 4 shows the specimen prepared for testing. Shear tests at the site were performed (Fig. 5) under condition of three normal stresses (10, 20 and 25 kN/m^2) and rate of shearing was maintained at 1 mm/min. However, the shear rate could not be kept exactly at 1 mm/ min as a consequence of the manual controlling system.

Fig. 4 Specimen prepared for the in-situ testing

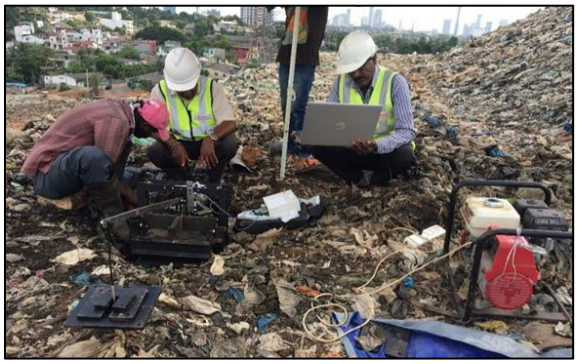

Fig. 5 Conducting the in-situ shear test on waste

2.3 *Waste composition analysis at Meethotamulla*

In this study, the classification framework proposed by Dixon and Langer (2006) is followed. This can be identified as the most rigorous waste composition analysis proposed so far. Samples were collected from the same locations where the shear tests conducted. Table 1 shows that there are no significant variations of materials at different locations and this may be due to the ad-hoc nature of waste dumping system which was practiced at the site. Further, bio-degradable items were not found at the time of the tests were carried out. Table 2 demonstrates the composition of MSW based on shape-related, size-related and type of material by weight existed at site.

2.4 *Laboratory testing*

An attempt was made to observe the shear be-

-havior under laboratory conditions after removing the waste particles greater than 10 mm (which could contribute to shear strength of MSW through their tensile strength), i.e shear test was carried out on remolded samples in large-scale shear apparatus.

2.5 *In-situ density and moisture content*

In-situ waste density was determined by simple water replacement method. Moisture content of the waste material was also obtained by air drying taking the waste from same locations where shear tests were carried out at the site. The results are given in the Table 3.

Table 1. Material Composition at each location (%)

Material (Dry)	Location 01	Location 02	Location 03	Location 04	Average
Soil like	40.5	35.7	48.3	53	44.4
Paper like	0.5	0	0	1	0.4
Flexible plastics	19	25	24.2	17.8	21.5
Rigid Plastics	12.5	9.4	12	5.2	9.8
Metals	0	0.5	0.5	0	0.3
Glass, Minerals	11	8.8	6	8.2	8.5
Wood, Textiles	14.5	19.1	8	13.3	13.7
Miscellaneous	2	1.5	1	1.5	1.5
Total	100	100	100	100	100

Table 2. Mass distribution within the relevant size ranges of the shape related subdivisions

Shape Related	In- compressible/ Low- compressible					High compressible					Reinforcing					Sum
Size Range (mm)	<10	10-40	40-120	120-500	>500	<10	10-40	40-120	120-500	>500	<10	10-40	40-120	120-500	>500	
Material	Dry Mass (%)															
Paper/ Cardboard	-	-	-	-	-	-	-	-	-	-	-	0.38	0.33	-	-	0.72
Flexible plastics	-	-	-	-	-	0.42	2.70	3.51	0.90	0.79	-	8.61	7.92	12.16	1.71	38.71
Rigid Plastics, rubber	-	4.12	8.48	2.63	2.26	-	-	-	-	-	-	-	-	-	-	17.49
Metals	-	-	0.44	-	-	-	-	-	-	-	-	-	-	-	-	0.44
Glass, Minerals	-	6.54	7.04	1.75	-	-	-	-	-	-	-	-	-	-	-	15.33
Wood, Textiles	-	-	4.41	8.31	5.26	-	-	-	-	-	-	2.35	3.11	1.16	-	24.61
Miscellaneous	1.50	-	-	-	-	0.46	-	-	-	-	-	0.75	-	-	-	2.71
Sum	1.50	10.66	20.37	12.69	7.52	0.88	2.70	3.51	0.90	0.79	0.00	12.09	11.37	13.33	1.71	100

3 RESULTS AND DISCUSSION

3.1 *Interpretation of in-situ test results*

Relationship between shear stress vs strain and shear stress vs normal stress are plotted for the large-scale shear tests carried out at the four locations at Meethotamulla site. Results of the laboratory test are not included in this comparison. Moisture content and unit weight of each sample could not be kept constant since the tests have been carried out under in-situ conditions. Shearing rate could have been slightly different because of the manual shearing arrangement. A peak shear stress is not noticeable in every shear stress vs strain graph as observed by many researchers (Siegel et al. (1990); Oweis &Khera (1990) Gottelandet *al.* (1995)). Typically, shear strength of MSW has been defined in the literature as the mobilized shear stress at 5–25% axial strain. To define the Mohr- Coulomb envelope, shear stress obtained after 10% strain was considered in this study. Fig. 6, Fig. 7 and Fig. 8 present the shear stress variations with strain for three normal stresses of 10 kPa, 20 kPa and 25 kPa respectively. Mohr-Coulomb envelope for the mobilized shear stresses and laboratory test are shown in Fig. 9. Table 3 presents the summary of the test results.

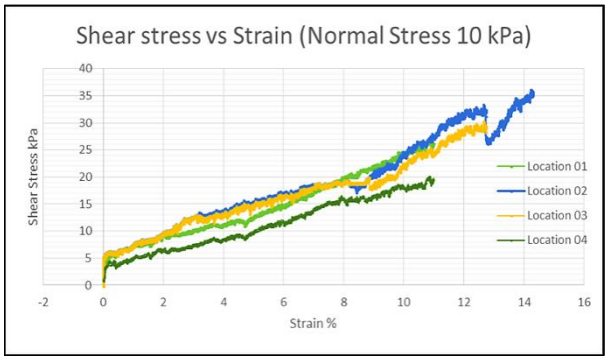

Fig. 6 Comparison of Shear Stress vs Strain (Normal stress 10 kPa)

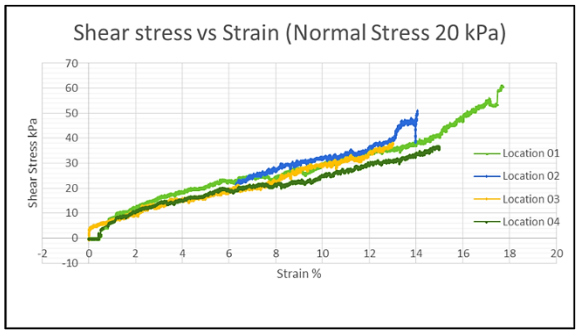

Fig. 7 Comparison of Shear Stress vs Strain (Normal stress 20 kPa)

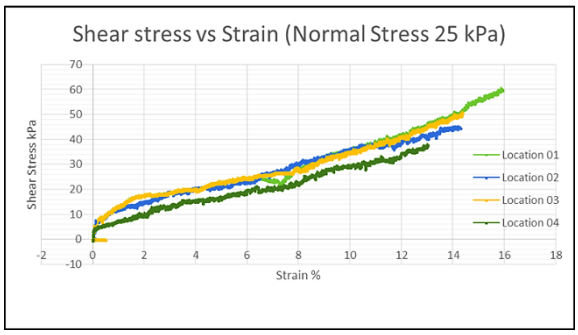

Fig. 8 Comparison of Shear Stress vs Strain (Normal stress 25 kPa)

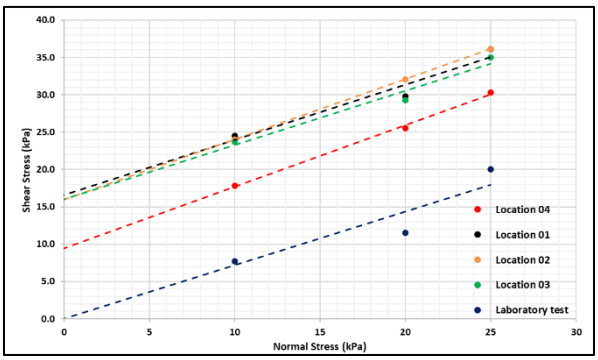

Fig. 9 Comparison of Mohr – Coulomb envelopes for 10% strain

Table 3. Summary of the results

Normal Stress σ (kPa)	Location 01 26 m	Location 02 22 m	Location 03 14 m	Location 04 07 m	Laboratory test
	Shear Stress τ (kPa) at 10% shear strain				
10	24.5	24.0	23.7	17.8	7.7
20	29.8	32.1	29.3	25.5	11.50
25	36.1	36.1	35.0	30.3	20.0
Cohesion (kPa)	16	16	16	09	0
Friction angle	ϕ=37˚	ϕ=38˚	ϕ=36˚	ϕ=39˚	ϕ=36˚
Unit weight(kN/m^3)	14.4	13.4	12.1	15.5	-
Moisture content	59.2%	55.3%	50.8%	60.2%	-

The results obtained from the laboratory testing after the removal of lengthy fibrous materials (with tensile strength) showed that the friction angle is of the same order as the in-situ condition while the cohesion has become zero. However, to build up a relationship between the presence of lengthy and reinforcing particles to the shear strength of waste, more testing must be done and compared.

3.2 *Comparison between past studies and results of this study*

Results from in-situ shear tests conducted on MSW are compared with the shear parameters recommended for design and to general shear testing results on waste from the literature to assess and validate the representativeness of the ranges of shear properties of MSW. The design parameters and the shear test results in the literature were presented in many ways, i.e. in normal and shear stress diagrams (Mohr-Coulomb envelope) and in pairs of cohesion and friction angles. Pelkey et al. (2001) and many researchers interpreted that, the MSW friction angle decreased considerably as the applied normal stress increases. In this study, the maximum normal stress applied is limited to 25 kPa due to the structural and practical limitation of the shearing apparatus. Therefore, application of range of normal stresses and the influence towards the friction angle variation were not illustrated.

It is clear that, the mobilized shear stress increases with increasing displacement subsequently, the mobilized friction angle increases significantly as with the shear displacement. The mobilized friction angle ranged between 12˚ and 45˚ at shearing displacements between 18 mm to 36 mm as illustrated in Fig. 10. However, the use of the Mohr-Coulomb envelope with mobilized values may result in a conservative design. Therefore, the evaluation of mobilized shear parameters is only meaningful, if a similar displacement for the mobilized shear parameters is chosen.

Manassero et al. (1996) separated the failure envelope into three different zones, Zone A, B and C. The results obtained from the in-situ tests were plotted on the graph suggested by Manassero et al. (1996) (Fig. 11). The results obtained in this study did not match with the trendline in Zone A which represents the applied normal stress below 20 kPa. As 25 kPa was the maximum applied normal stress used in the in-situ tests, a validated prediction cannot be done for the Zones B and C. However, the values for the shear strength observed at 10% strain in the shear tests on MSW lie above the trend line in Zone B suggested by Manassero *et al.*, (1996).

The large-scale shear test results on the MSW from this research are plotted in the Fig. 12, which presents a summary of proposed design lines and a

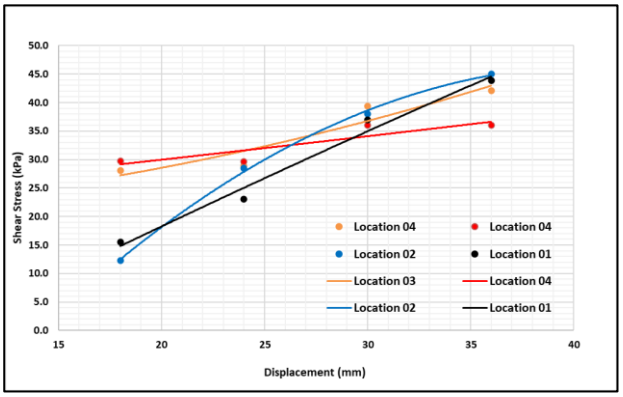

Fig. 10 Variation of mobilized friction angle vs shear displacement

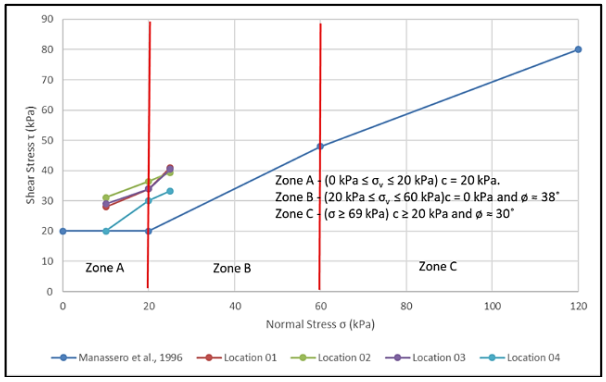

Fig. 11 Shear- normal-stress diagram after Manassero et al. (1996) including large scale shear test results from Meethotamulla site

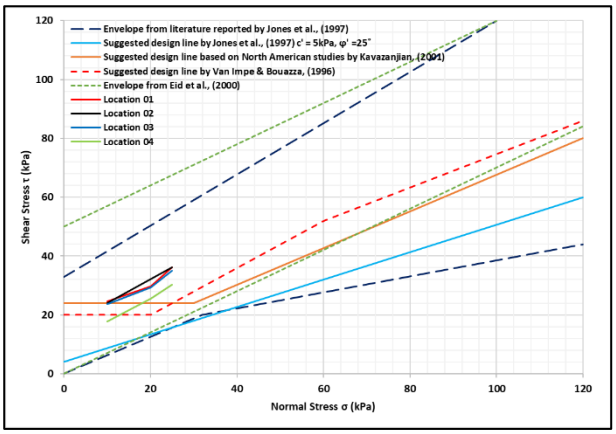

Fig. 12 Detail of the shear- normal-stress diagram after Jones et al. (1997)including envelope from Eid et al. (2000) and large shear test results from Meethotamulla

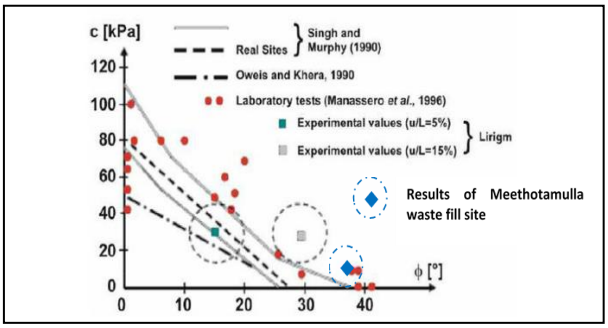

Fig. 13 Modified graph with recommended design shear parameters after Gotteland et al. (2000)

design envelope suggested and combined by Jones *et al.* (1997), and updated by Eid *et al.* (2000) and Kavezerjian (2001). This is an extended version of design values for shear parameter similar to the suggestion from Manassero *et al.* (1996). It can be seen that the results are fitted inside of the proposed envelope from Jones *et al.* (1997) and from Eid *et al.* (2000).

Gabr and Valero (1995) suggested design shear parameter by means of zoning the results of previous studies with pairs of cohesion and friction angle and it was updated by Gotteland et al. (2000). The results from in-situ shear testing conducted in Meethotamulla site were also added and demonstrated in Fig. 13. Sánchez-Alciturri et al. (1993), recommended the overlapping area of laboratory tests and field tests analyses as the area for choosing the design parameters. From these results it can be stated that a fixation of a design area or even a design line is not sensible. The results from the large shear tests carried out on in-situ MSW samples ranged without exception within the zone of laboratory tests.

4 CONCLUSIONS AND FURTHER STUDIES

During this study, the shear properties of MSW at abandoned Meethotamulla site were determined through in-situ testing and the test results were compared with the relevant published studies. In this regard, a large-scale direct shear apparatus was fabricated following the design done by a Japanese expert team on MSW management (Miyamotoa 2012). To assess the shear behavior, samples were selected at four different heights corresponding to different ages in the Meethotamulla site and tested using the large-scale shear device. Material composition of each location is different to each other.

Mobilized friction angle ranged from 36˚-39˚ and cohesion ranged from 09-16 kPa. A significant change in the shear parameters were not resulted even for differently aged locations. Nevertheless, the mobilized shear parameters derived from the shear tests were within the zones found in literature. Comparing data with the literature, especially to design lines or areas has to be done with care. Density of the MSW was in the range of 12 – 15.5kN/m^3 and moisture content at different locations in the same range of 50-60 % at the in-situ condition. According to the composition analysis it can be concluded that most probably, organic matter has already 100% degraded and mixed with soil. Apart from soil like material all other are non-degradable material. However, a relationship between the shear stress parameters and the degradation potential could not be cleared identified with the results.

It is a much-needed requirement to do the shear tests for higher normal stress values (at least up to 120 kPa based on the past studies) with a mechanism to measure the normal stress applied to the system. In this regard, an automatic/hydraulic system to increase the normal stress with load cells to optimize the testing condition rather the lever arm method would be required. Further, to assess a relationship between shear stress properties and degradation potential, more tests have to be carried out in different waste dumps. More importantly, it was identified that guidelines have to be developed to derive the design parameters from the mobilized shear stress parameters especially due to heterogeneity nature of MSW.

REFERENCES

Dixon, N. & Langer, U., 2006. Development of a MSW classification system for the evaluation of mechanical properties. s.l., s.n., pp. 220-232.

Eid, H., Stark, T., Evans, D. & Sherry, P.,Vilar 2000. Municipal Solid Waste Slope Failure. Journal of Geotechnical and Geoenvironmental Engineering

Gotteland , P., Lemarechal, D. & Richard, P., 1995. Analysis and Monitoring of the Stability of a Domestic Waste Landfill. In: 5th International Landfill Symposium. Cagliari, Italy: S. Margherita di Pula, pp. 777-787

Gotteland, P., Gourc, J., Aboura& A., T., 2000. On Site Determination of Geomechanical Characteristics of Waste". International Conference on Geotechnical and Geological Engineering. Melbourne, Australia, ICMS.

Gabr, M. & Valero, S., 1995. Geotechnical properties of municipal solid waste. s.l., ASTM, Vol.18, pp. 241-254

Jones, D., Taylor, D. & Dixon, N., 1997. Shear strength of waste and its use in landfill stability analysis. s.l., Thomas Telford, p. 343–350

Kavazanjian, E., 2001. Mechanical properties of municipal solid waste. Cagliari, Italy, s.n., pp. 415-424

Manassero, M., Van Impe, W. & Bouazza, A., 1996. Waste disposal and containment. Osaka, s.n., pp. 193-242.

Miyamoto, S., Omine, K., Yasufuku, N., Yamawaki, A., Doi, Y., & Kawasaki, M., 2012. Shear property of solid waste materials by in-situ direct shear test. Los Angeles, CA, s.n

Oweis, I. &Khera, R., 1990. Geotechnology of Waste Management. 2 ed. s.l.:Butterworth-Heinemann

Pelkey, S., ValsangkarA., & Landva. A., 2001. Shear displacement dependent strength of municipal solid waste and its major constituents. Geotechnical Testing Journal, pp. 381-390

Reddy, K. R. et al., 2009. Geotechnical properties of fresh municipal solid waste at Orchard Hills landfill, USA. s.l., s.n., pp. 952-959

Sanchez-Alciturri, J.M., Palma, J., Sagaseta, C., Canizal, J., 1993. Mechanicalproperties of wastes in a sanitary landfill. In: Proceedings of the Green '93, Waste Disposal by Landfill, Bolton, UK, pp. 357–363

Siegel, R. A., Robertson, R. J. & Anderson, D. G., 1990. Slope stability investigations at a landfill in southern California. In: Special Technical Publication. STP 1070. s.l.:American Society for Testing and Materials, ASTM, pp. 259-284

United Nations Environment Program, 2005

Numerical Modelling of a GCL Overlap Hydraulic Performance

Isuri Weerasinghe
PhD candidate in Geotechnical Engineering, School of Civil and Environmental Engineering, Science and Engineering Faculty, Queensland University of Technology, Brisbane, QLD, Australia

Chaminda Gallage
Senior Lecturer, School of Civil and Environmental Engineering, Science and Engineering Faculty, Queensland University of Technology, Brisbane, QLD, Australia

Les Dawes
Professor, School of Civil and Environmental Engineering, Science and Engineering Faculty, Queensland University of Technology, Brisbane, QLD, Australia

Preston Kendall
Business Development Manager- Water and Coastal, Geofabrics Australasia, Molendinar QLD 4214, Australia

ABSTRACT: Geosynthetic clay liners are of interest to the geo-environmental industry throughout the recent decades for its significant barrier performance. Constant challenges encountered by its users have resulted in numerous research on improving its hydraulic performance. The geosynthetic clay liner overlap plays a critical role in a barrier design where the system is prone to failure with the effect of various factors such as overlap length, temperature, effective confining stress and hydraulic head acting on it. However, the limited ability to test GCL overlaps in laboratory scale has resulted in limited research on addressing the overall effect of these field conditions. This study proposes a numerical method to model the flow box apparatus which could be used to analyze the factors affecting the hydraulic performance of the GCL overlap as an alternative solution to long term laboratory testing conducted. This FE model is recommended to be further developed to improve the hydraulic performance of liner systems through comprehensive research.

1 INTRODUCTION

The application of geosynthetics in the geo-environmental industry is increasing rapidly due to its vast number of related uses (Cheah, et al., 2016, 2017; Gallage, et al., 2019; Garcia, et al., 2007; Jayalath, et al., 2018; Weerasinghe, et al., 2019a). Geosynthetic clay liners have been extensively used as hydraulic barriers for the past few decades due to their ability to limit the transfer of fluids such as water, leachates or gases. GCLs are constantly being used in landfills, mines and other containment facilities mainly to reduce ground contamination or liquid transfer depending on the specific application.

Continuous research is being conducted to enhance the hydraulic performance of the GCLs, and as a result, a high-quality barrier product having a hydraulic conductivity ranging from 1×10^{-11} to 1×10^{-12} m/s is being produced by industry today. However, instances occur where the product has struggled to maintain the developed optimum level of hydraulic conductivity where the GCL panels are overlapped. Extensive research has identified that the GCL is not able to retain its expected performance at the overlap due to effects such as the shrinkage, confinement applied on the liner, insufficient overlap length etc. (Cooley, et al., 1995; Rowe, et al., 2016; Rowe, et al., 1997; Thiel, et al., 2005; Weerasinghe, et al., 2019b, 2020; Yang, et al., 2015).

Cooley and Daniel are considered pioneers who researched the GCL overlap performance developing a large 1 m ×1 m tank named the "Flow box" in the laboratory model test scale to observe large flow rates passing through the overlaps compared to the non-overlapped portions of the GCL (Daniel, et al., 1997b). Researchers such as Estornel and Daniel (1997a) and Mazzieri, et al. (2015) further made several attempts to replicate this overlapping condition in the element scale permeameter cells specified in the standard ASTM D5887 (ASTM, 2009) used for GCL hydraulic performance testing. These attempts were not quite successful due to the edge effects that were encountered due to the small

circular cross-section which could not incorporate a full overlap seam width (Kendall, et al., 2014).

The challenges faced in testing the GCL overlap and its time-consuming nature has restricted laboratory scale research in this area. Further investigation on field observations are hindered due to these shortcomings. This study proposes a numerical modelling technique to replicate the GCL overlap laboratory conditions as a solution / alternative to laboratory testing.

2 MATERIALS AND METHODS

2.1 *Geosynthetic clay liner (GCL)*

A commercially available needle punched GCL was used for the experimentation. The Geosynthetic clay liner samples contain powdered bentonite sandwiched between a non-woven cover geotextile (270g/m^2) and a woven carrier geotextile (110 g/m^2), made from polypropylene and are bonded by needle-punching. The minerology of the bentonite material extracted from the GCL was analyzed using X-ray diffraction (XRD) in QUT CARF laboratory facilities and identified the material comprised of 72% montmorillonite, 14% quartz, 8% albite and 4% cristobalite (all estimated within 1% error).

2.2 *Flow box apparatus*

The concept of "Flow box apparatus" developed by Daniel (1997b) was used in this study to measure the hydraulic performance of GCL overlaps. The flow box designed was a large-scale model box of 0.5m × 1m × 0.3m, width, length and height respectively. A hydraulic head of 3.5 m was applied on to the sample using a water tank placed above the flow box. A 0.3 m height gravel load provided the necessary overburden confining stress on to the specimen. Figure 1 shows a schematic representation of the model scale flow box apparatus used for this study.

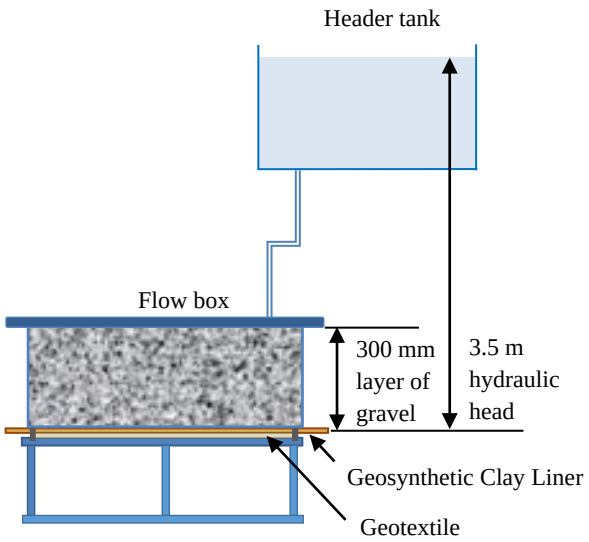

Figure 1 Large scale Flow box test

2.3 *Sample Preparation*

A specimen of the suitable sample size: the size of the cross-section of the flow box, was sampled from the GCL roll in order to conduct a flow box test for a single GCL layer. A specimen of dimensions 600 mm × 1100 mm was sampled from a roll using a mechanical cutter allowing minimum disturbance to the powder bentonite in the GCL roll. The additional 100 mm (than the actual cross-section) was sampled from the perimeter of the specimen to allow the sample to be bolted to the flow box without any leakages.

Sampling a GCL overlap specimen for the flow box tests, was slightly different to the above. The procedure followed to prepare a 300 mm overlap with 0.5 kg/m2 of supplemental bentonite is as follows. The overlap area/ roll ends along the width of the GCL roll used in this research study is impregnated with a 300 mm strip of supplemental powder bentonite in its manufacturing process. Two pieces of 600 mm × 1100 m samples were cut from these transverse roll ends in such a way that they could be placed in the flow box, overlapping the 300 mm strip with supplemental bentonite upon each other. Figure 2 illustrates a schematic diagram of an overlap specimen sampled from the GCL roll for the flow box tests.

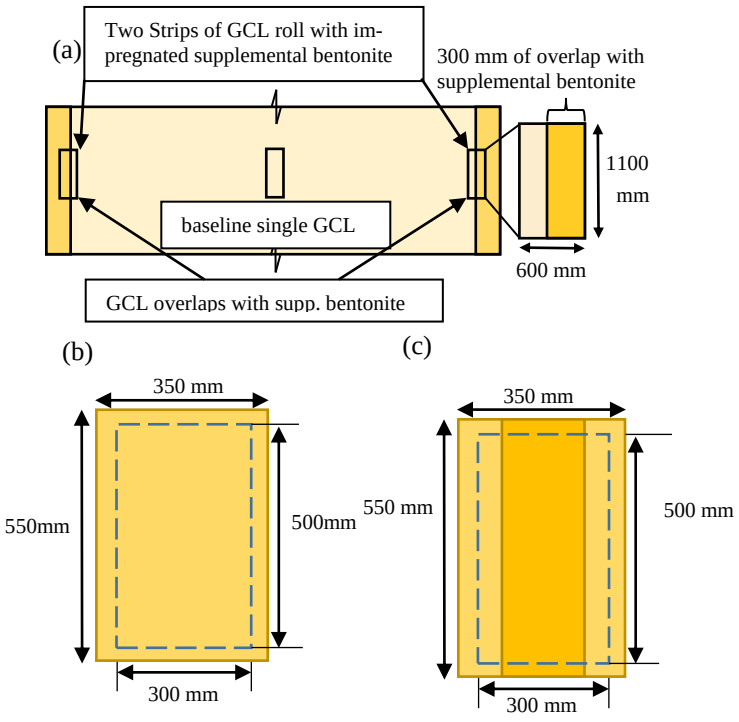

Figure 2 (a) GCLs sampled from the GCL roll (b) Plan view of the single GCL (c) Plan view of the GCL overlap

2.4 *Test Setup*

The flow box apparatus was set up with the GCL specimen as follows. A geotextile was placed on the base plate of the flow box apparatus to create a uniform flow condition. The GCL specimen was placed on top of it. Rubber gaskets were then placed along the perimeter of the box in order to reduce side wall leakages along the walls of the box. Then the flow box was kept on top of the sample, bolted to the base of the box which clamped the GCL sample tightly in between. Then the sample was prehydrated using municipal tap water. This reduced the delay in the unhydrated GCL specimen establishing a steady state condition by a considerable amount of time. A 0.3 m height of gravel was laid on top of the sample and enclosed using the lid on the top. The water tank filled with municipal tap water was placed at 3.5 m above the flow box to create the necessary hydraulic head. The water tank supplied continuous flow through the specimen throughout the experiment.

Usually, it took approximately 3 weeks for the GCL to saturate and commence flow. Once the water started flowing, the flow rate was recorded at regular time intervals.

2.5 *Calculating the flux*

The average steady state flow rate (Q) was divided by the cross-sectional area of the flow box (A) to give the total overlap system flux (J).

Total Flux;

$$J = \frac{Q}{A} \tag{1}$$

The hydraulic flux obtained from the flow box tests were used to be compared with the output of the numerical model developed in this research study.

The GCL hydraulic conductivity was also calculated using Darcy's Law equation as follows. The hydraulic conductivity was calculated using the constant head method provided in the ASTM D5887. The equation used is as follows;

$$k_T = \frac{QT}{Ath} \tag{3}$$

where,
k_T = hydraulic conductivity at temperature T, m/s,
Q = quantity of flow, taken as the average of inflow and outflow, m^3
T = thickness of specimen, m,
A = cross-sectional area of clay component, m^2,
t = interval of time, s, and
h= difference in hydraulic head across the specimen, m, of water.

The hydraulic conductivity calculated was used as an input parameter for the FE model developed.

2.6 *Test program*

Three flow box tests were carried out for GCL/GCL overlap samples using the procedure described. The experimental period for each test varied between 2-3 months.

1. Test 1 – single layer GCL
2. Test 2 – 300 mm GCL overlap
3. Test 3 – 150 mm GCL overlap

2.7 *Numerical Model*

The numerical modelling software GEOSLOPE used for numerous geotechnical applications in the industry was selected as most appropriate for this study. A FE model was developed using the Seep/w analysis in the software to measure the hydraulic performance of a GCL/GCL overlap. The cross-section of 0.5 m width of the flow box was illustrated in the model where the GCL single layer or overlap of given thickness was modelled using the data obtained from the actual flow box test results. The thickness of the GCL was dependent on the experimental conditions of each test carried out.

A single layer GCL experiment was conducted as the baseline test for the analysis. The hydraulic conductivity obtained from the actual flow box experiment was used as the material input property of GCL. Once the model is developed for a single GCL, the hydraulic flux obtained from the model was compared with the hydraulic flux obtained from the experiment for validation.

Next, the 300 mm GCL overlap with supplemental bentonite is simulated in the FE model. An additional interface layer was introduced in between the two GCL layers overlapped, to replicate the supplemental bentonite layer impregnated in the overlapping area. The 150mm GCL overlap is then modelled to highlight the ability of the numerical model to analyze different experimental conditions.

3 RESULTS AND DISCUSSION

3.1 *Experimental results*

The three model tests were carried out in the laboratory "flow box" setup for geosynthetic clay liner/

overlaps in order to gather experimental data to be used for the development of the numerical model.

The results obtained from the single layer flow box test is presented in Table 1 as follows;

Table 1 Laboratory flow box test results

GCL specimen used	Hydraulic Flux ($m^3/s/m^2$)
Single layer	5.64×10^{-9}
300 mm overlap	4.13×10^{-9}
150 mm overlap	6.26×10^{-9}

The method followed in ASTM D5887(ASTM, 2009) was used to calculate the hydraulic conductivity of the GCL material using the flow rate recorded for the single GCL sample. The hydraulic conductivity of a geosynthetic clay liner was observed to be 1.9×10^{-11} m/s.

3.2 *FE model*

An attempt was made to replicate the actual experimental condition of the flow box test in SEEP/W analysis in GEOSLOPE software. The flow box cross-section was developed in the numerical model scaling it at the same dimensions of the actual flow box as described. The GCL single layer was then modelled as illustrated in Figure 3.

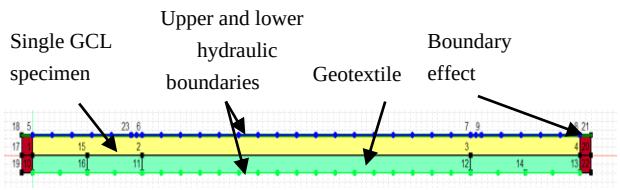

Figure 3 Numerical model of a single layer GCL

The GCL was assigned as a composite material property where the hydraulic conductivity of the material was provided using the experimental data. A geotextile material was added underneath the GCL as per the actual experiment for the purpose of uniform liquid flow filtered through the GCL. The hydraulic head difference was assigned as top and bottom boundary conditions to the specimen. Impermeable boundary materials were assigned to replicate the flow box with no leakages.

Once the model is run, the hydraulic flux passing through the material was obtained from the software. The flux obtained was 5.64×10^{-9} m^3/s $/m^2$ and was an exact match for the experimental results.
The next step of the numerical analysis was to improve this existing FE model to replicate a GCL overlap criterion which was more complicated. Figure 4 shows the cross-sections of the 300 mm and 150 mm GCL overlaps developed using the software. In this preliminary analysis, the actual thickness of each GCL layer was used to develop the cross-section of the model for each test. An additional material named "air" with a higher hydraulic conductivity was introduced to replicate the open spaces trapped with air when overlapping the two GCL sheets on top of each other. The supplemental bentonite in the overlapping area was introduced as an interface property between the two GCL layers.

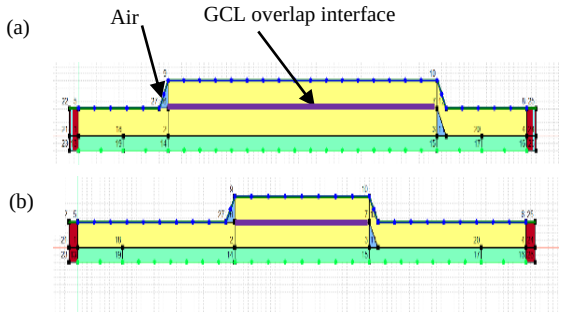

Figure 4 GCL overlap cross-section modelled in GEOSLOPE SEEP/w analysis (a) 300mm overlap (b) 150 mm overlap

The hydraulic conductivity of the single layer GCL was input as the material property for the GCL, for both layers and the other experimental conditions were also maintained the same. The hydraulic conductivity input parameter for the interface material was varied considering the horizontal flow through the interface to achieve the flux rates obtained from the laboratory flow box results.

The hydraulic flux results obtained from both overlap tests were observed to result in a similar behavior as expected from literature. The model results presented in Figure 5 clearly replicated the additional flow passing through the overlap area in the analysis.

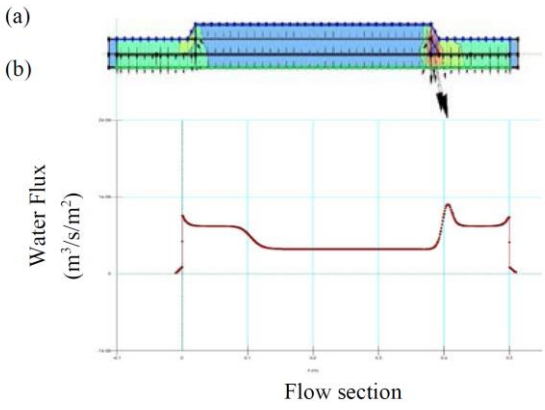

Figure 5 (a) Cross-section of the flow box in FE model (b) Graphical representation of the flow through the GCL overlap in the FE model

The GCL overlap interface hydraulic conductivity values that were obtained from the two FE models for 150mm and 300mm overlap lengths achieving the experimental hydraulic flux values were as follows (Table 2);

Table 2 GCL overlap interface hydraulic conductivity obtained from the GEOSLOPE Seep/W model

GCL overlap	GCL overlap interface hydraulic conductivity (m/s)
300 mm overlap	2.23×10^{-7}
150 mm overlap	2.96×10^{-7}

The hydraulic conductivity of the two interface layers highlight the fact that the lower the overlap length, the higher the conductivity through the interface would be. It was also identified that the flux passing through the 150 mm overlap was even higher than the flux through the single layer due to the higher horizontal flow through the interface in the overlap. The optimum hydraulic conductivity expected from a GCL is hence not achieved by the 150 mm overlap. The results confirm the conclusions obtained in literature through laboratory work that the 300 mm overlap length is a more appropriate choice (Brachman, et al., 2018; Egloffstein, et al., 2012). The analysis could further be broadened by modelling a series of overlap lengths to observe how the interface hydraulic performance is varied.

However, one challenge of the developed model was the variation of thickness that was to be incorporated in every FE model test run in the software. Each manufacturer is able to develop a relationship of their GCL thickness to each experimental condition in the laboratory scale to estimate the thickness of the GCL in the field condition.

Authors also suggest using a normalized hydraulic conductivity using a specific thickness, as the material parameter when modelling the laboratory tests in the software. A simple relationship such as the following (Equation 4) could be used to normalize the material input parameter as a solution.

$$K_{eff} = K_{flowbox} \times \frac{t_{eff}}{t_{flow\ box}} \quad (4)$$

Likewise, the other experimental conditions such as the hydraulic head or the overburden confining stress that affects the hydraulic performance of a GCL overlap in the field condition could also be modelled and varied using the FE model following a similar approach. This endorses the fact that the numerical model, if further improved, could be an effective alternative in modelling the challenging long term GCL overlap tests.

4 CONCLUSION

Research on geosynthetic clay liner overlaps have been a constant challenge due to the limitations in laboratory tests due to the lack of a standard element scale method to test GCL overlaps. Insufficient space in element scale tests to replicate a full width overlap and the time-consuming nature of large-scale model tests have decelerated the rate of research conducted to address and overcome the challenges faced by the GCL overlapping condition. This study proposes a numerical model to replicate a geosynthetic clay liner overlap in a FE model using GEO SLOPE software. The research results present how the single layer GCL hydraulic performance results obtained from the flow box are used to develop the initial FE model. Two 150 mm and 300 mm overlap tests are then used to improve the model for a GCL overlap.

The study identifies the ability of the FE model to replicate the changes in overlap length of a GCL instead of conducting several long-term flow box tests for analysis. The results present how the liquid flow through the 150 mm overlap is higher than the 300 mm overlap. The ability of the model to capture the variation of flow with the variation of GCL overlap is highlighted in this study. The necessity for a series of long-term laboratory tests is addressed through this FE model.

The numerical model can be further modified by varying different experimental conditions such as hydraulic head, overburden confining stress etc. to observe its effect on the hydraulic performance of the GCL overlap. This clearly highlights the value of the FE model to replicate different field conditions by varying different factors affecting the GCL overlap performance. Authors recommend further improvements to the model in order to account for analysis on more factors affecting the GCL overlap hydraulic performance to be used by practitioners to improve GCL liner systems.

5 CONFLICT OF INTEREST STATEMENT

No conflict of interest among the authors to be disclosed.

ACKNOWLEDGMENTS

Authors gratefully acknowledge Geofabrics Australasia for providing the laboratory facilities and in-kind support to conduct the test series for the research project. The first author extends her gratitude to the Australian Government Research Training Program (RTP) Stipend for awarding the scholarship for her doctoral degree at Queensland University of Technology, Australia.

REFERENCES

ASTM. (2009). *D5887 - Standard Test Method for Measurement of Index Flux Through Saturated Geosynthetic Clay Liner Specimens Using a Flexible Wall Permeameter*.

Brachman, R. W. I., Rowe, R. K., and Take, W. A. (2018). Reductions in GCL Overlap Beneath an Exposed Geomembrane. *Journal of Geotechnical and Geoenvironmental Engineering, 144*(12), 04018094.

Cheah, C., Gallage, C., Dawes, L., and Kendall, P. (2016). Impact resistance and evaluation of retained strength on geotextiles. *Geotextiles and Geomembranes, 44*(4), 549-556.

Cheah, C., Gallage, C., Dawes, L., and Kendall, P. (2017). Measuring hydraulic properties of geotextiles after installation damage. *Geotextiles and Geomembranes, 45*(5), 462-470.

Cooley, B., and Daniel, D. (1995). Seam performance of overlapped geosynthetic clay liners.

Daniel, D., Bowders, J., and Gilbert, R. (1997a). Laboratory Hydraulic Conductivity Testing of GCLs in Flexible-Wall Permeameters. *Testing and Acceptance Criteria for Geosynthetic Clay Liners*.

Daniel, D. E., Trautwein, S. J., and Goswami, P. K. (1997b, 1997). Measurement of hydraulic properties of geosynthetic clay liners using a flow box. In (Vol. 1308, pp. 196-207).

Egloffstein, T. A., Kalsow, J., Von Maubeuge, K. P., and Ehrenberg, H. (2012, June 29, 2012). Multi-component geosynthetic clay liners: A product with new possibilities. In *ASTM 3rd Symposium on Current and Future Practices for the Testing of Multi-component Geosynthetic Clay Liners* (Vol. 1562, pp. 1-14): ASTM International.

Gallage, C., and Jayalath, C. (2019). Use of Particle Image Velocimetry (PIV) technique to measure strains in geogrids. In *E3S Web of Conferences*.

Garcia, E. F., Gallage, C. P. K., and Uchimura, T. (2007). Function of permeable geosynthetics in unsaturated embankments subjected to rainfall infiltration. *Geosynthetics International, 14*(2), 89-99.

Jayalath, C. P., Gallage, C., Dhanasekar, M., Dareeju, B. S., Ramanujam, J., and Lee, J. (2018, 6-9 November 2018). Pavement model tests to investigate the effects of geogrid as subgrade reinforcement. In *12th Australian and New Zealand Young Geotechnical Professionals Conference*.

Kendall, P. M., and Austin, R. A. (2014). Investigation of GCL Overlap Techniques using a large scale Flow Box. In *7th International Congress on Environmental Geotechnics* (pp. 746-753): International Society of Soil mechanics and Geotechnical Engineering.

Mazzieri, F., and Di Emidio, G. (2015). Hydraulic conductivity of a dense prehydrated geosynthetic clay liner. *Geosynthetics International, 22*(1), 138-148.

Rowe, R. K., Brachman, R. W. I., and Joshi, P. (2016). Hydraulic Performance of Overlapped Geosynthetic Clay Liner Seams Requiring Field-Applied Supplemental Bentonite. *Journal of Geotechnical and Geoenvironmental Engineering, 142*(12), 4016067.

Rowe, R. K., Quigley, R. M., and Petrov, R. J. (1997). Selected Factors Influencing GCL Hydraulic Conductivity. *Journal of Geotechnical and Geoenvironmental Engineering, 123*(8), 683-695.

Thiel, R., and Richardson, G. N. (2005). *Concern for GCL Shrinkage when Installed on Slopes*.

Weerasinghe, I. A., Gallage, C., and Dawes, L. (2019a). Optimising Geosynthetic Clay Liner Overlaps: Implications on Hydraulic Performance. *Environmental Geotechnics, 0*(0), 1-11.

Weerasinghe, I. A., Gallage, C., Dawes, L., and Kendall, P. (2019b, 11 February). Liquid flow mechanism of a geosynthetic clay liner overlap. In *Geosynthetics 2019*.

Weerasinghe, I. A., Gallage, C., Dawes, L., and Kendall, P. (2020). Factors affecting the hydraulic performance of a geosynthetic clay liner overlap. *Journal of Environmental Management, 271*, 110978.

Yang, X., Sheng, J.-C., Zheng, Z.-W., Sun, Y.-J., Yang, H., Zhan, M.-L., and Gu, Y. (2015). Experimental study on seepage properties of GCL with different overlap methods. *Yantu Gongcheng Xuebao/Chinese Journal of Geotechnical Engineering, 37*(9), 1668-1673.

Sewer effluent discharge trends in Colombo Regional Centre (CRC) area

W.G.D. Nadeeshan
Natural Resources Management and Laboratory Services, Central Engineering Consultancy Bureau, Sri Lanka

H.G.P.A. Ratnaweera
Department of Civil Engineering, The Open University of Sri Lanka

ABSTRACT: The CRC area of the Open University of Sri Lanka sits on a reclaimed land adjoining the Kirullapona Canal. The on-site sewage disposal systems service buildings spanning over 75% of the land area. Leakage of untreated effluent to the surface and the surrounding soil is observed during wet weather periods. The groundwater levels in the area resonates well with the fluctuating canal water levels, hence migration of effluents to the water body is expected. This study ascertains the variations in groundwater flow gradients and the spread of discharge water quality parameters, the percolation rates near effluent discharge points, during wet and dry weather periods. The results were compared with effluent discharge parameters prescribed in the National Environmental Act and the standard SLS745 (2004). The results indicate that on-site sewer disposal has impacted the groundwater near discharge points, however, showed little or no impact on the canal water quality.

1 INTRODUCTION

Sri Lanka's Greater Colombo region is undergoing rapid development with several multi-story apartment complexes and business offices. However, due to the lack of a centralized municipal waste management system many such entities depend on on-site sewage disposal systems (OSDS). A few developers use small scale waste treatment facilities to discharge treated effluent. The Colombo Regional Centre (CRC) of the Open University of Sri Lanka still uses a septic tank-soakage pit system to discharge its sewage. Such systems rely on soil's capacity to retain and delay the effluent movement.

Effluent from on-site wastewater treatment systems may have elevated levels of nutrients and microbial contaminants which have the potential to affect discharge water quality (Anderson & Belanger, 1991). Such microbial contaminants may also affect borehole extraction wells and groundwater wells supplying potable water to the community. The National Environmental Act, as amended (NEA, 1988), prohibits the discharge of untreated sewage. The design of on-site disposal systems requires large open spaces to retain and treat effluents, and to facilitate soakage. Low infiltration rates in poorly drained soils may cause saturation near ground surface and surface ponding. Effluent collected on the surface may pour into surface drains causing a health hazard or may move laterally through the soil to be discharged to surface water bodies (Ogilvie et al., 2013). Greater infiltration rates with a high hydraulic gradient tend to move partially treated effluents rapidly to groundwater and surface water bodies. Rising groundwater table during the wet weather periods also hinders the effluent movement.

The soil in CRC area becomes saturated during prolonged rainy periods and with the rise in groundwater table. This causes the septic tank – soakage pit systems to become water-logged. It also causes backing-up of discharge effluent in the drainage lines in the ground-floor hampering the use of ground floor toilets.

This study intends to capture the seasonal variations in groundwater and surface water levels and hydraulic gradients by performing water level measurements at eight (8) boreholes and five (5) canal locations. It also intends to obtain the seasonal variation in effluent water quality parameters: Chemical Oxygen Demand, Bio-chemical Oxygen Demand, Faecal Coliform, Electrical Conductivity, pH and Turbidity. The seasonal variations in percolation rates near ground surface, closer to three effluent discharge locations is also determined.

2 METHODS AND MATERIALS

2.1 *Measurement of groundwater levels*

The reduced level at the monitoring borehole casing cover block, was established relative to a temporary benchmark. These reduced levels and the

dip-meter readings were used to establish seasonal variations in groundwater levels spanning over the study period. The seasonal variations in the canal water levels were obtained relative to the same temporary benchmark.

2.2 *Effluent discharge quality parameters*

Groundwater samples were collected from each monitoring borehole, during wet (July 2018), dry (October 2018) and intermediate (January 2019) weather periods. The dip-meter was inserted to measure the groundwater level; then the boreholes were purged up to a height of 300mm and allowed to recover prior to sampling. Samples for the chemical analysis were stored in sterile Dissolved Oxygen (DO) sample bottles. These bottles were tightly sealed to minimize oxidization; then were transferred to the Environmental Laboratory within a 2-hour period. Water samples for the microbiological analysis were collected in sterile glass bottles, and they were stored and transported in crushed ice; then refrigerated at 4^0C and analysed within a period of 24 hours since sampling (APHA, 2005).

The Electrical Conductivity (EC) was measured using a Jenway Model 4520 conductivity meter, duly calibrated. pH was measured using Model 601A pH meter, calibrated using pH4 an pH6 buffer solutions. These probes were rinsed with distilled water prior to placing in each sample container.

Colour was determined by first filtering the samples using a regular filter paper and tested using the Nessleriser comparator. Turbidity was measured using a HACH 2100P Turbidimeter. The Turbidimeter was calibrated during each sampling run with prepared standard solutions. Samples were also analysed for Faecal Coliform (FC), using CPCB Standard, as per APHA (2005).

2.3 *The Percolation Test*

Percolation tests were performed at selected locations, during the months July, August, September, October 2018, as per SLS 745 (2004). Fig. 1 shows the locations P1, P2, P3 and P4, where the percolation tests were carried out.

3 RESULTS AND DISCUSSION

3.1 *Ground Water Table and Flow Gradients*

Fig. 1 shows the groundwater contours obtained during, dry, intermediate, and wet weather periods. The values indicated are based on a Temporary Benchmark level of 100m taken at borehole BH1. The highest groundwater level was observed at borehole BH1. The effluent discharge point closer to BH1 has the highest water usage while P4 (refer Fig. 1 and Table 1) shows that it has a low percolation rate. These two factors may have contributed to the formation of the effluent mound. The lowest groundwater level and a steeper hydraulic gradient are observed at borehole BH8, located near Kirillapone Main Canal embankment. This may cause partially treated affluent to seep to the main canal. Fig. 1 also shows that the flow gradients during all weather periods are oriented towards the Main Canal and the upper reach of the Tributary Canal that bound two sides of the CRC area. No significant flow gradient is observed towards the property boundary along BH3, BH4 and BH7.

The observations also show a variation in groundwater levels ranging from 99.800m (BH1) to 97.650m (BH8) during the dry weather period; and 99.915m (BH1) to 98.685m (BH8) during the wet weather period. The above data also show a 1m drop in the groundwater level during dry weather periods.

The depth of partial saturation at BH1 closer to the effluent discharge point, during the wet weather period is 0.185m. This depth does not meet the 2.5m requirement stipulated in the standard SLS745 (2004). During the dry weather period, the said requirement is observed at boreholes BH6 and BH8, which are located near the canal embankments.

3.2 *Discharge effluent quality parameters*

Figures 2 through 7 show the observed variations in parameters BOD, COD, Faecal Coliform count, Electrical Conductivity, pH and Turbidity in water samples obtained during the three weather periods and compares these numbers with the threshold values stated in SL Gazette (2008). Many boreholes yielded low concentrations of the parameters measured during the wet weather period, showing significant dilution. Frequent emptying of the septic tank near BH1 and BH2 during the wet weather period and the removal of contaminants via surface runoff during overflowing may also have reduced groundwater contamination. Water samples obtained from the canal gave low contaminant concentrations due to dilution.

The Chemical oxygen demand (COD) of water samples ranged between 80 to 335mg/L, with boreholes BH1, BH2, BH5 and BH7 exceeding the threshold value of 250mg/L. Dissolved Oxygen (DO) content of water samples ranged between 0.8 to 2.7 mg/L, and all water samples were found to be below the permissible limit. The Biochemical Oxygen Demand (BOD) of water samples ranged between 48 to 222mg/L, and boreholes BH1, BH4, BH6 and BH8 exceeding 100mg/L. Faecal Coliform counts ranged between 19 to

320MPN/100ml, and boreholes BH1, BH2, BH3, BH4, BH7 and BH8 have exceeded 60MPN/100ml.

Measured EC values were between 711µs/cm to 1273µs/cm. Boreholes BH1, BH2, BH5, BH7 and BH8 exceeded 1000µs threshold. The variation in pH determines the treatment process. The observed pH values range between 5.02 to 6.94 and are within the prescribed range of 6 to 8.

3.3 *Percolation Test Results*

Table 1 shows the variations in the infiltration rates measured at locations P1, P2, P3, and P4 (Fig. 1) during the wet, intermediate, and dry weather periods. Locations P1, P2, and P3 are in the vicinity of the soakage pits, which overflow during the wet weather period. The above values do not fall within the range of 25–125 mm/h, as recommended in SLS745 (2004). The said standard further requires maintaining a 2.5m high partially saturated zone above the seasonal groundwater table to maintain efficient decontamination and soakage.

4 CONCLUSIONS

The fluctuations in groundwater levels resonates with the water levels in both canals. The groundwater flow gradients are towards the Kirillapone Main Canal and the upper reach of the Tributary Canal.

Groundwater levels during the wet weather period do not provide a partially saturated zone of 2.5m as required in SLS745 (2004) to maintain effective seepage.

Measured infiltration rates do not fall within the range specified in SLS745 (2004) to maintain effective seepage.

The measured discharge effluent quality parameters show significant dilution during the wet weather period. This may be attributed to high groundwater levels and effluent migration towards the two canals.

Effluent parameters measured during the dry weather period exceed stipulated values in SL Gazette (2008) for efficient on-site sewer disposal.

Table 1: Variations in percolation rates observed (locations shown in Fig. 1)

Location	Percolation rate (mm/h)			
	Wet	Intermediate		Dry
	July	August	September	October
P1	224	230	198	205
P2	14	18	8	10
P3	20	22	6	6
P4	24	24	2	2

ACKNOWLEDGMENTS

The authors wish to acknowledge the support rendered by Ms. N.P.M. Rajaguru, Senior Staff Technical Officer, Department of Civil Engineering, during this study.

REFERENCES

APHA (2005), Standard Methods for the Determination of Water and Wastewater, American Public Health Association, 21st Edition.

Anderson, D.L. and Belanger, T.V. (1991), The Potential for Surface Water Contamination from On-site Sewage Disposal Systems (OSDS) in the Indian River Lagoon Basin. St. Johns River Water Management District SWIM Project (lR-1-100-D), Phase I Report

NEA (1988), The National Environmental Act (Amended), 56.

SL Gazette (2008) The Gazette of the Democratic Socialist Republic of Sri Lanka, No. 1534/18 Part I, 01.02.2008.

SLS745 (2004) Sri Lanka Standard code of practice for the design and construction of septic tanks and associated effluent disposal systems, Part II, Sri Lanka Standards Institute.

Ogilvie, H., Rissmann, C., Hughes, B. and Ledgard, G. (2013) On-site Wastewater Groundwater Quality Risk, Technical Report, https://www.researchgate.net/publication/271770330.

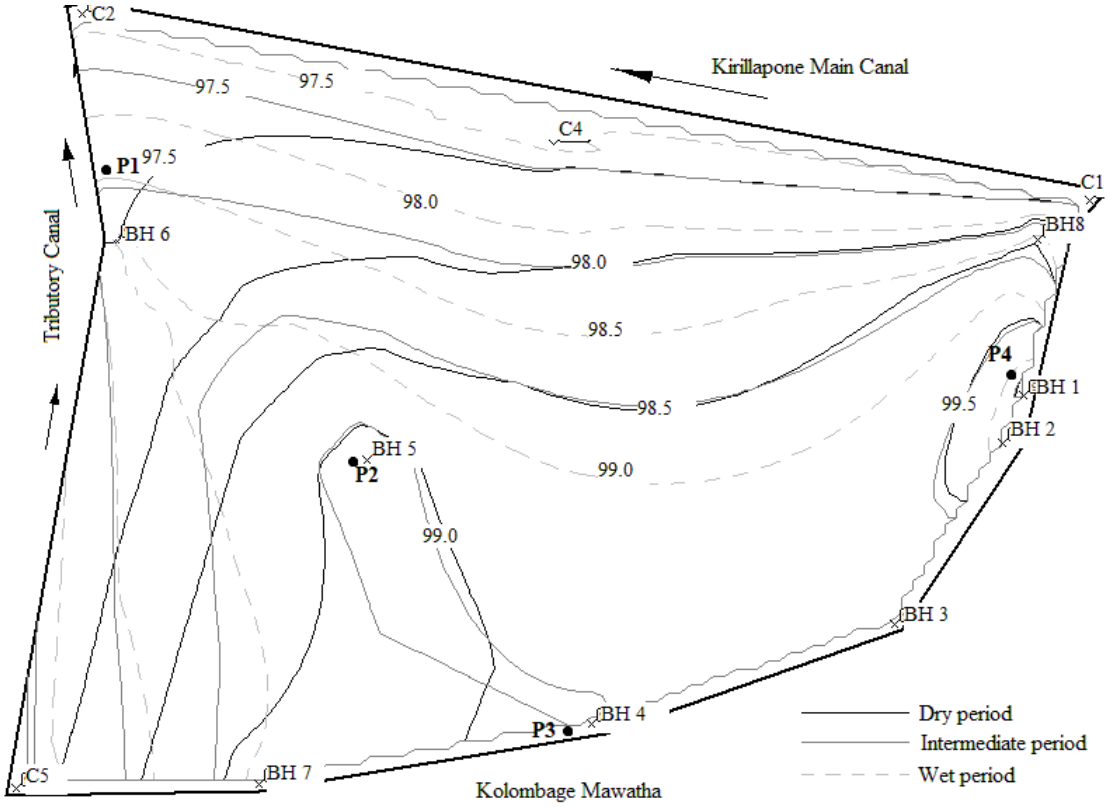

Fig. 1: Groundwater and surface water contours during changing weather periods.

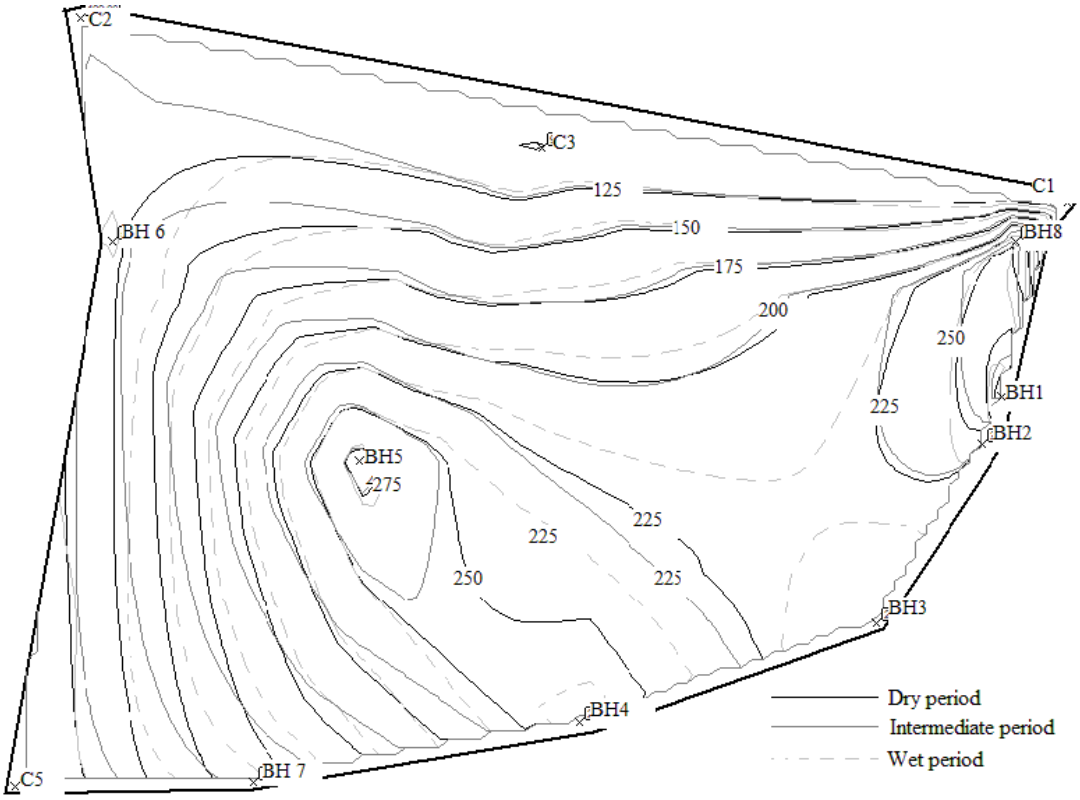

Fig. 2: Observed variations in COD (Prescribed range <250ppm, SL Gazette, 2008)

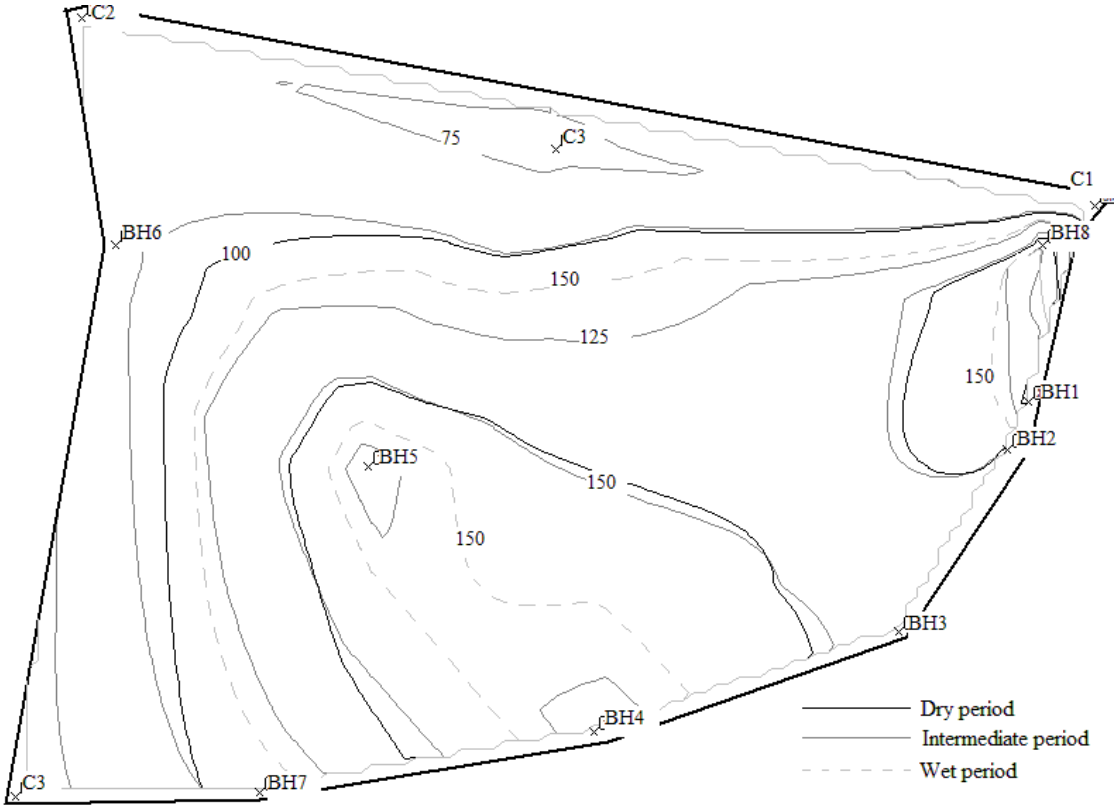

Fig. 3: Observed variations in BOD (Prescribed range <100ppm, SL Gazette, 2008)

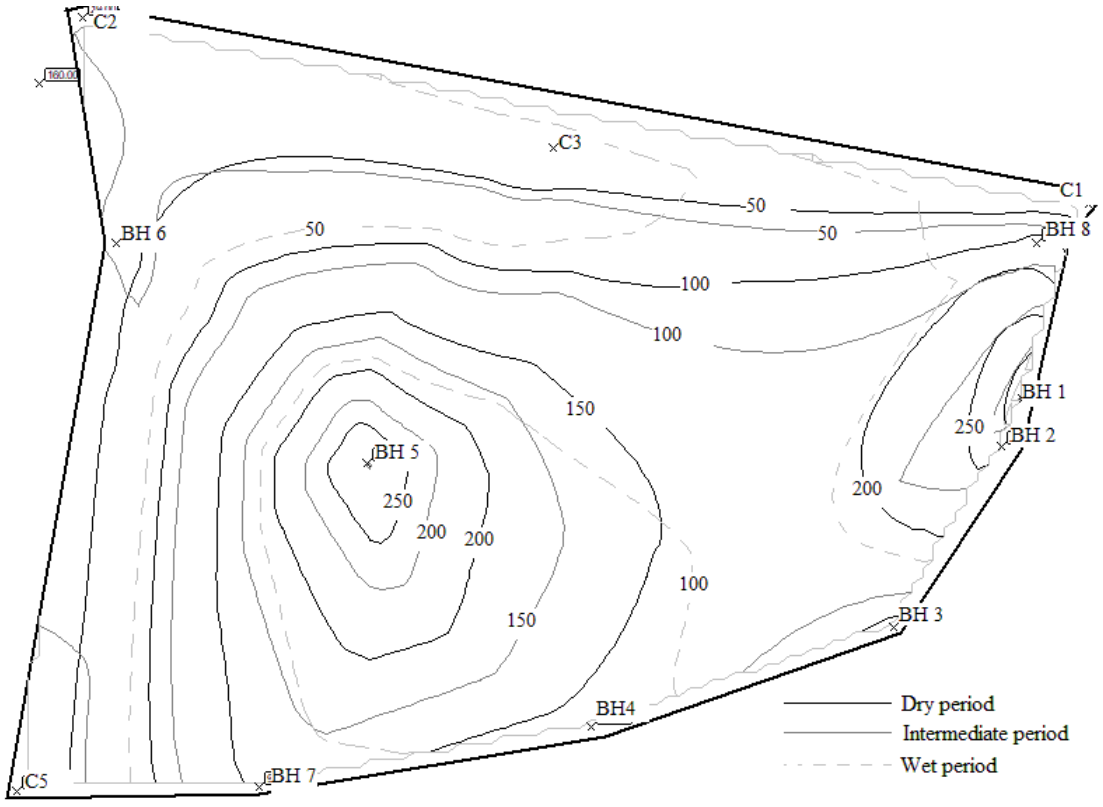

Fig. 4: Observed variations in Faecal Coliform (Prescribed range <60MPN/100ml, SL Gazette, 2008)

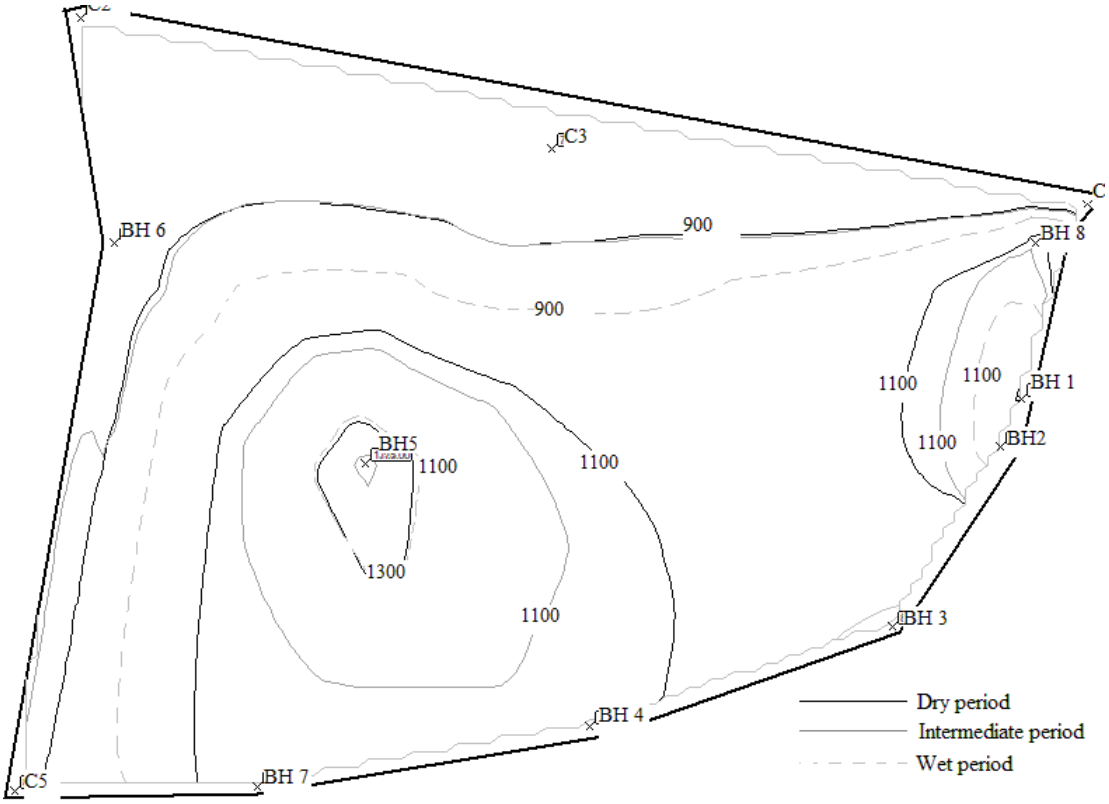

Fig. 5: observed variations in Electrical Conductivity (Prescribed range <1000µs, SL Gazette, 2008)

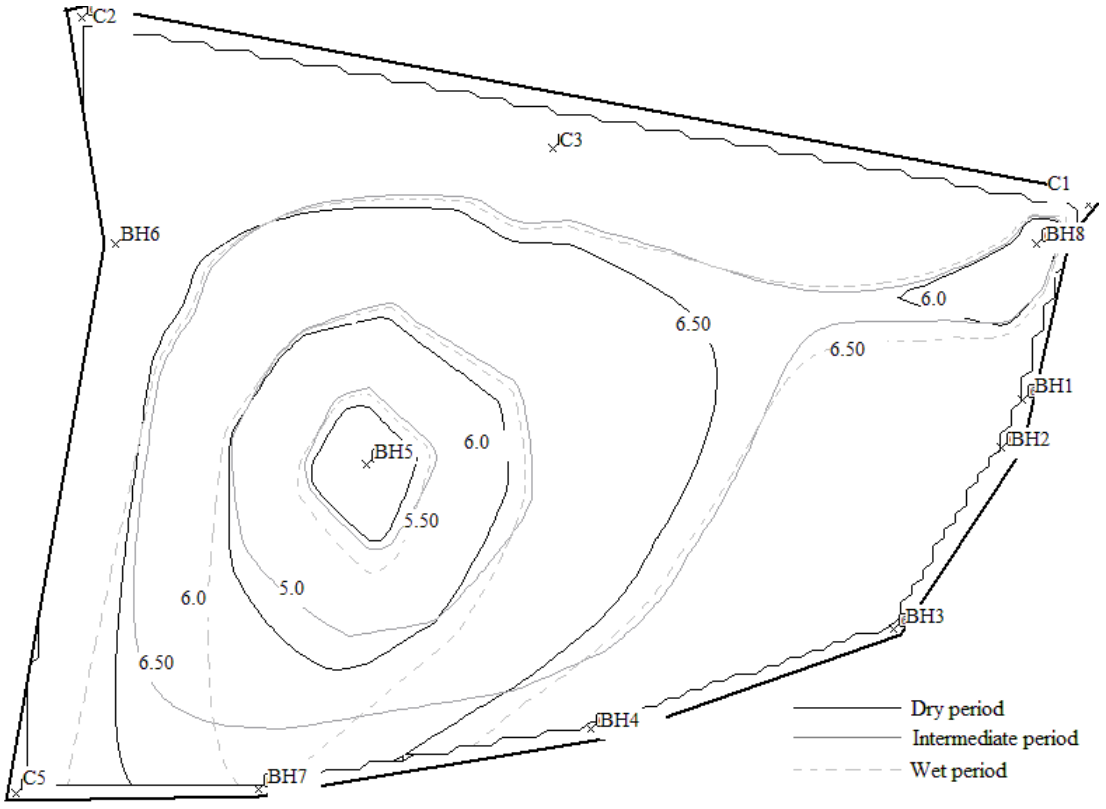

Fig. 6: Observed variations in pH (Prescribed range 6-8, SL Gazette, 2008)

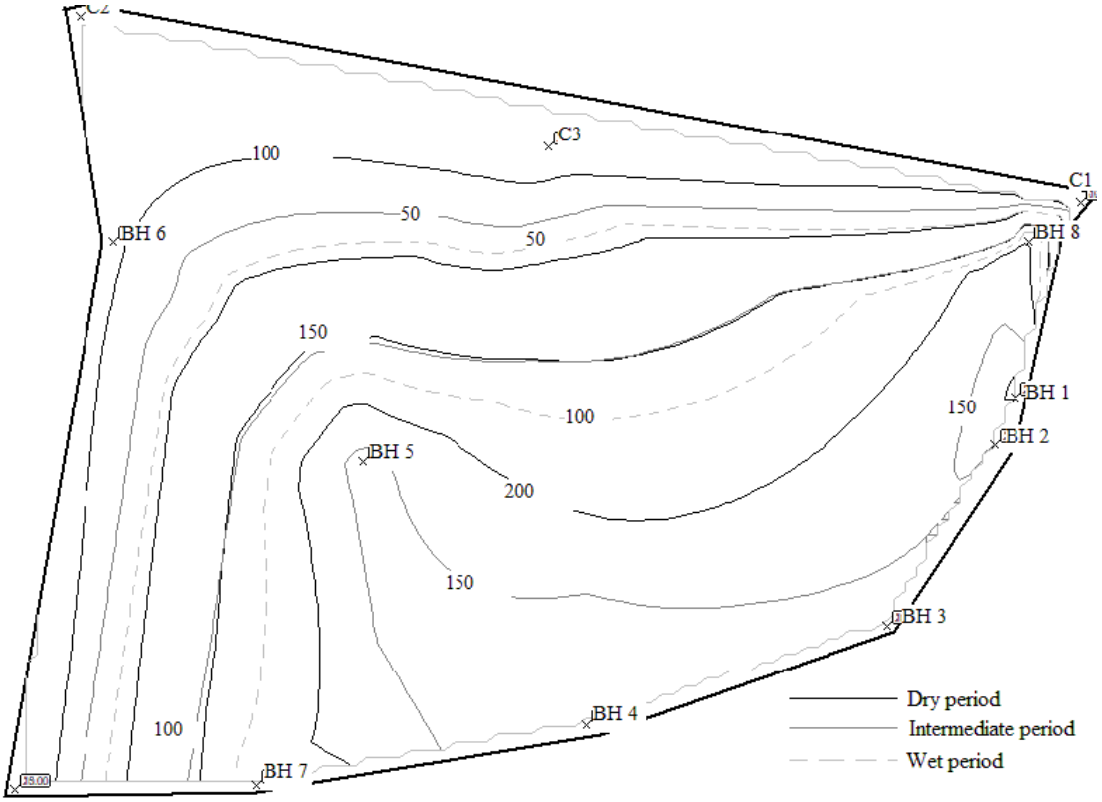

Fig. 7: Observed variations in Turbidity (Prescribed range <50NTU, SL Gazette, 2008)

Investigation into strength and rheology of cemented paste fill using pozzolanic waste products and plasticizer as partial cement replacement

G.G. Yowa, N. Sivakugan, & R. Tuladhar

Civil Engineering, James Cook University, Townsville, Australia

ABSTRACT: When ore is extracted underground, voids are created which are backfilled with waste rocks or tailings to stabilise the voids. Cemented paste fill, one of the popular backfill types that use mill tailings contains cement dosage ranging from 3-7% to increase the strength. Even this small cement dosage adds significantly to the cost of backfilling. Therefore, this study investigated the possibilities of partially replacing cement with supplementary cementitious materials (SCMs) like slag, fly ash, and pitchstone. Results indicated that the unconfined compressive strength (UCS) of samples that used blended pitchstone, slag, and fly ash exceeded 1 MPa after 28 days curing and were comparable to control mixes that used 100% Portland cement. The use of admixture polycarboxylate plasticizer improved the workability of paste significantly. Partial replacement of cement with SCMs in mine backfilling can result in significant cost savings, and make backfilling more environmentally friendly. The findings are useful for mining industry.

Key words: cemented paste fill, pozzolans, supplementary cementitious material, pitchstone fines, polycarboxylate plasticizer

1 INTRODUCTION

1.1 *Background*

Minerals are extracted using either surface or underground mining methods. Underground methods are categorized under unsupported, supported, caving, and combination methods. Mine backfilling is applied only in underground mines that utilise either the supported methods such as the cut and fill or the combination methods such as the primary-secondary stoping. Backfilling is not required in caving and unsupported methods. When ore is extracted underground, large voids are created which are then backfilled with mined waste rocks or mill tailings to stabilise the voids prior to extracting ore from the adjacent stopes. The type of backfill used depends on the method applied to extract the ore. Common backfill types are the hydraulic fill, waste rock fill, cemented rock or aggregate fill, and cemented paste fill.

1.2 *Scope, significance, and objective*

This research focuses on the mix designs of cemented paste fill (CPF), one of the most popular backfill types that use mill tailings. Tailings are mixed with binder and water and transported as slurry through pipelines and are placed in stope voids. Tailings have substantial clay content and a small dosage of cement binder (3-7%) is added to increase the strength. Even this small cement dosage adds significantly to the cost of backfill operation. Partial replacement of cement binder with pozzolanic waste products such as slag, fly ash or pitchstone can result in significant cost savings, and disposing of waste mill tailings into underground voids can make backfilling more environmentally friendly.

Minimising cost and optimising production are essential for the survival of mines during periods of low commodity prices. CPF is a major cost driver and accounts for 10-20% of mine operating cost, while cement binder accounts for up to 75% of filling cost (Belem et al., 2008, Xu et al., 2018). CPF is expensive compared to other types of backfills and requires a more cost saving approach to be continually used for wall support and establishing working level. CPF slurry requires high water content (30-40% of solid mass) to prevent blockages along pipelines. Strength development of CPF is slower at low cement dosage (<4%) and high-water content. Liquefaction can occur when the UCS of CPF is less than 100kPa during adjacent stope blasting (Belem et al., 2008). These challenges have prompted research into the application of pozzolans and admixtures to minimise the usage of clinker cement and water and still attain the desired strength and rheology of CPF for mine backfilling. Common pozzolans like slag and fly ash have been widely researched and used in the industries. Natural

pozzolans like pitchstone has been studied in concrete application (Tuladhar et al., 2018) and its viability for usage in mine backfilling remains a promising area for further investigation.

Therefore, this research aims to use blends of fly ash, slag, and pitchstone with Portland cement as binders to investigate the possibility of partially replacing Portland cement with these SCMs through an extensive laboratory test program. Admixture polycarboxylate plasticizer is used in this study to enhance the slurry workability. Laboratory tests were done on strength, microstructure, and rheology of the different mixes.

2 MATERIALS

2.1 *Tailings*

Tailings from George Fisher Mine (GFM) in Australia were used in this study. Tailings were oven tried at 105˚C for a day, sieved and sizes passing 4.75 mm were used.

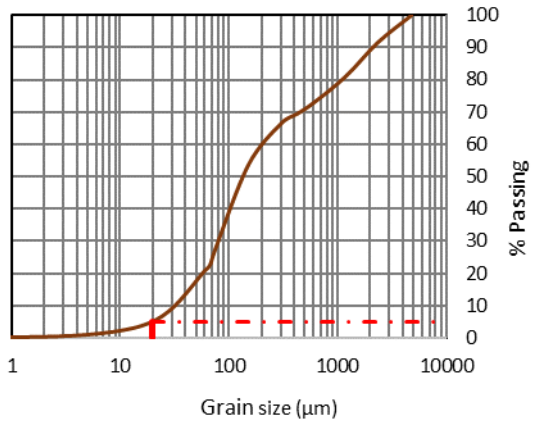

Fig. 1 Particle size distribution of tailings

Particle size distribution was done using mechanical sieving with openings from 75 µm to 4.75 mm as per AS 1289.3.6.1 standard. The fines (<75 µm) collected from the pan were further analysed using Malvern laser analyser. As a generic rule of thumb, tailings should have a minimum of 15% finer than 20 µm for water retention and lubricating effect (Sivakugan et al., 2006). Grain size distribution for GFM tailings (Fig.1) showed approximately 5% by mass of particles were less than 20 µm which indicated less fines.

2.2 *Binder and admixture*

General purpose cement (GPC), and blends of fly ash, slag, and pitchstone fines were used as binders. Class F fly ash and grade 100 slag was used. Fly ash is a waste product from coal burning. Slag is a waste product from metal smelting, and pitchstone fines (<75 µm) is a waste product from perlite production at Nychum in North Queensland. Admixture polycarboxylate plasticizer was used to improve the rheology.

3 EXPERIMENTAL STUDIES

3.1 *Mix design*

Mix ingredients were determined using the following equations;

Solid content:

$$SC\ (\%) = \frac{(M_{ds}+M_b)}{(M_{ds}+M_b+M_w)} \times 100 \qquad (1)$$

Binder content:

$$BC\ (\%) = \frac{M_b}{(M_{ds}+M_b)} \times 100 \qquad (2)$$

Water content:

$$w\ (\%) = \frac{M_w}{(M_{ds}+M_b)} \times 100 \qquad (3)$$

Admixture dosage:

$$AD\ (\%) = \frac{M_a}{M_b} \times 100 \qquad (4)$$

where, M_{ds} is the mass of dry solid, M_b is the mass of binder, and M_w is the mass of water, and M_a is the mass of admixture.

Increasing the solid content enables more tailings to be placed but makes it difficult for slurry to flow without pipe blockages. Through a series of trials, it was found that the solid content of 74%, giving 260 mm slump is the optimum mix. With these threshold values, mix designs were carried out. The test program is summarized in Fig. 2.

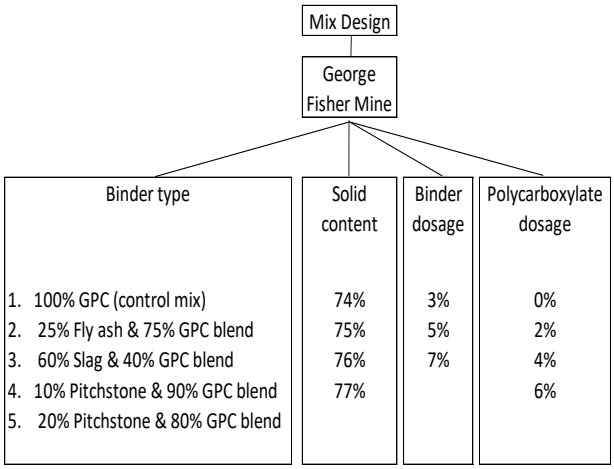

Fig. 2 Combination of different mix design

Control mixes are referred to mixes that contained 100% GPC binder. For each mix, 2 samples were

cast for each of the curing periods (7, 14, 28, 56 and 112 days) for strength testing.

3.2 *Strength measurements*

Cylindrical PVC moulds of 50 mm diameter by 120 mm height were used to cast the mixes and tested at different curing periods. ASTM D2166 standard was used for unconfined compressive strength (UCS) test. Samples were trimmed to diameter to height ratio of 1:2 and loaded to failure. Load and deformation data from the triaxial data logger were analysed for the strength properties.

3.3 *Rheology measurements*

Brookfield DV3T rheometer with V73 and V75 spindles were used to measure yield stress at low (0.05-0.5) RPM and between torque range of 10-100%. Yield stress was determined at the maximum torque value. Slump test was done using standard truncated cone of 100 mm top diameter, 200 mm bottom diameter, and 300 mm height as per ASTM C143 standard.

4 RESULTS AND DISCUSSIONS

4.1 *Effect of pozzolans on UCS*

UCS strength comparisons were made for the 5 binder types used. The 5 charts in Fig. 3 compares the UCS of the 5 binder types used at 4% polycarboxylate dosage and at 74% solid content and for curing periods from 7 to112 days.

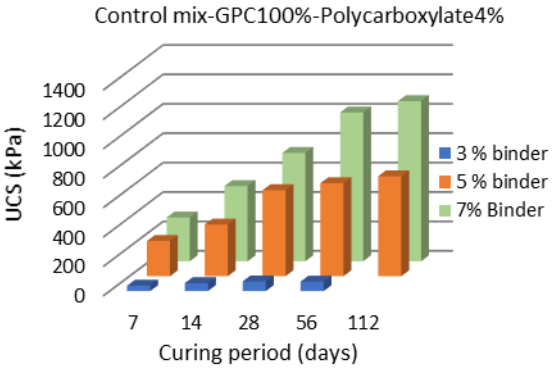

a)

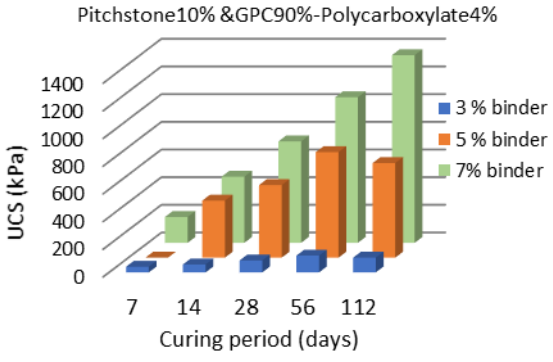

b)

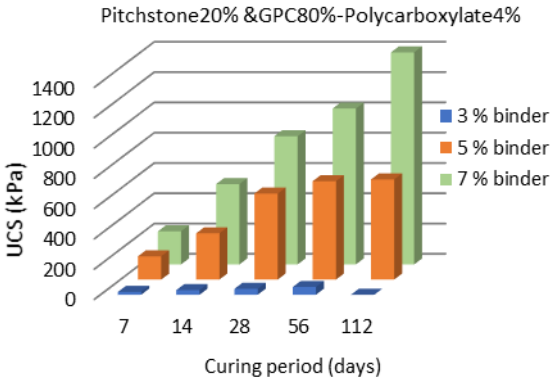

c)

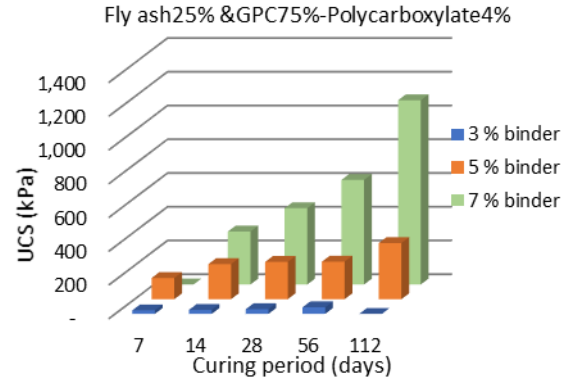

d)

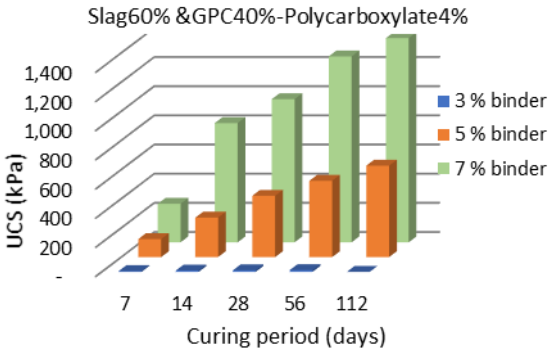

e)

Fig. 3 UCS for (a) GPC control mix; (b &c) Pitchstone blend; (d) fly ash blend; (e) slag blend

Results (Fig. 3) indicated that UCS for 5 binders at lower dosage (3%) was below 150kPa, which is considered as incompetent and can liquefy when subjected to blasting. Binder dosage at 5% and curing over 28-112 days reached 500-800kPa, which can serve as competent fill for adjacent ore blasting, however, may not be desirable for pillar support. Binder dosage at 7% and curing over 56 days attained strength above 1MPa which can serve as crown, sill, or rib pillar support when mining adjacent stopes.

4.2 *UCS and ground support limits*

UCS limits for paste fill have been adapted in mines for different strength requirements. A minimum UCS target of 100kPa is maintained to

prevent liquefaction from blasting or seismic magnitude of 7.5 on Richter scale and is adapted from the work of Clough et al. (1989). A free-standing paste requires UCS less than 1MPa, and for ground support requires UCS higher than 1MPa (Belem et al, 2008).

Comparisons were made for binder dosage of 5% and 7% at 74% solid content, and curing up to 56 days. Results (Fig. 4 and Fig. 5) indicated that the pozzolans attained unconfined compressive strength (UCS) comparable to control mix with 100% GPC binder. Apart from the popular SCMs like fly ash (FA) and slag (SL), pitchstone fines (PF) of both 10% and 20% blend with GPC have attained meaningful strength for application in mine filling.

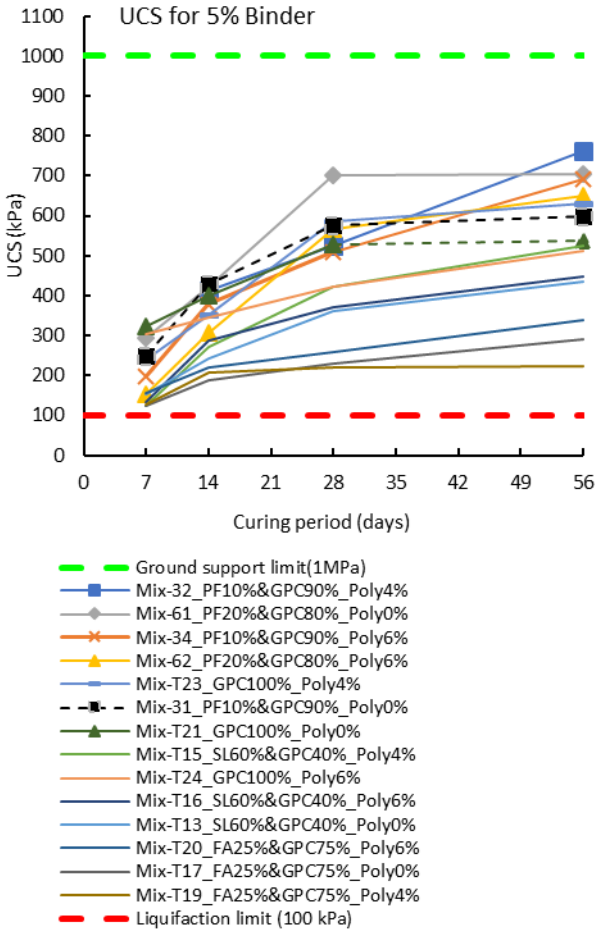

Fig. 4 Strength of 5% binder mixes

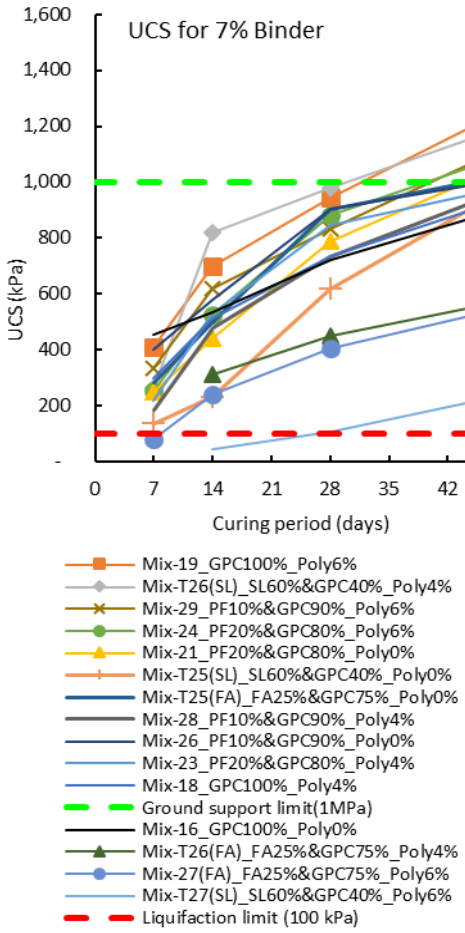

Fig. 5 Strength of 7% binder mixes

4.3 *Pozzolans and strength activity index*

Strength activity index (SAI) is a measure of reactivity of pozzolan with cement and is defined as the UCS of pozzolanic mix relative to the control mix (100% GPC) over the same curing period and is expressed as percentage. ASTM C618 requires that pozzolanic materials must attain SAI above 75% of control mix at 7 to 28 days.

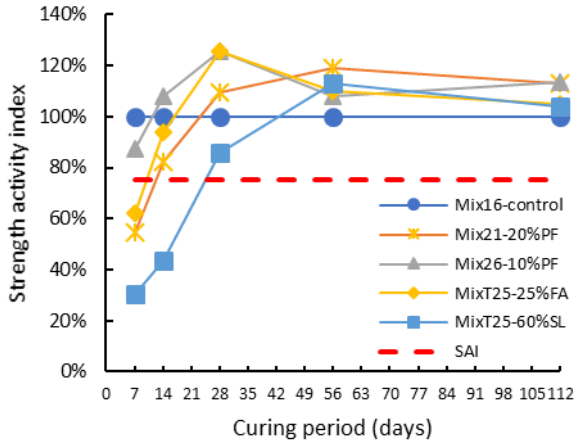

Fig. 6 SAI comparison over curing periods

Results (Fig. 6) indicated that for all 5 binders at 7% binder dosage, 75% SAI was attained at 28 days curing and in compliance with strength requirements as per ASTM C618 for concrete and paste fill application.

4.4 *Effect of polycarboxylate dosage on yield stress*

Typical yield stress of CPF is around 250Pa while the operating yield stress is site specific and can range from 50 to 500Pa depending on the pumping, reticulation, and paste properties (Sivakugan et al., 2015). Paste fill slurry behaves like a Bingham fluid and the rheological model is expressed as:

Shear stress: $\tau = \tau_0 + \eta\gamma$ (5)

where τ_0 is the yield stress, η is the plastic viscosity and γ is the shear rate.

Polycarboxylate plasticizer is an admixture that reduces the yield stress and increases the slump. Comparisons were made with several binder and polycarboxylate dosages on 74% solid content mixes as shown in Fig. 7.

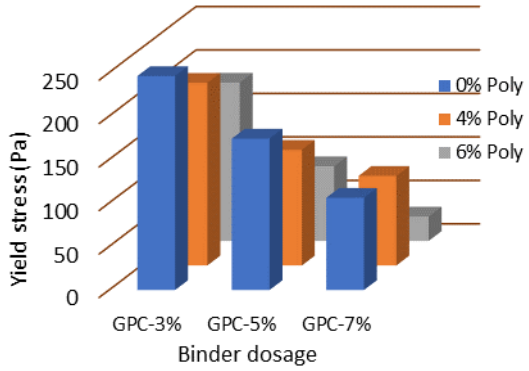

Fig. 7 Yield stress and polycarboxylate

Results (Fig.7) indicated that polycarboxylate plasticizer reduces yield stress with increase in dosages.

Slump ranges from 235 to 275 mm (Sivakugan et al., 2015). Slump cone is the quickest and conventional mode of relating slump to yield stress. Slump of 150 to 250 mm is optimum for pumping through reticulation lines (Belem et al., 2008). Comparisons were made with increasing polycarboxylate dosage on several solid contents as shown in Fig. 8.

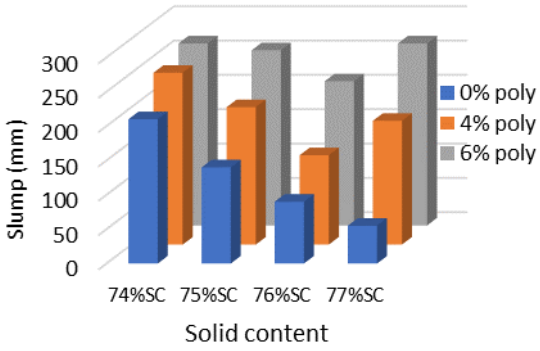

Fig. 8 Polycarboxylate, slump, and solid content

Results (Fig 8) indicated that with increase solid content (>74%), polycarboxylate dosage of 6% significantly increased the slump ranging from 200 to 260 mm. The slump range (200-260 mm) is optimum for paste filling.

4.5 *Relevance of UCS and yield stress*

Optimum mix of CPF should maintain flow through pipelines and attain strength that can withstand blasting. Based on general practice, UCS of 1000 kPa and yield stress of 150 Pa were used as limits to identify the optimum mixes. Comparison was made for 56 days cure for 7% binder dosage as shown in Fig.9.

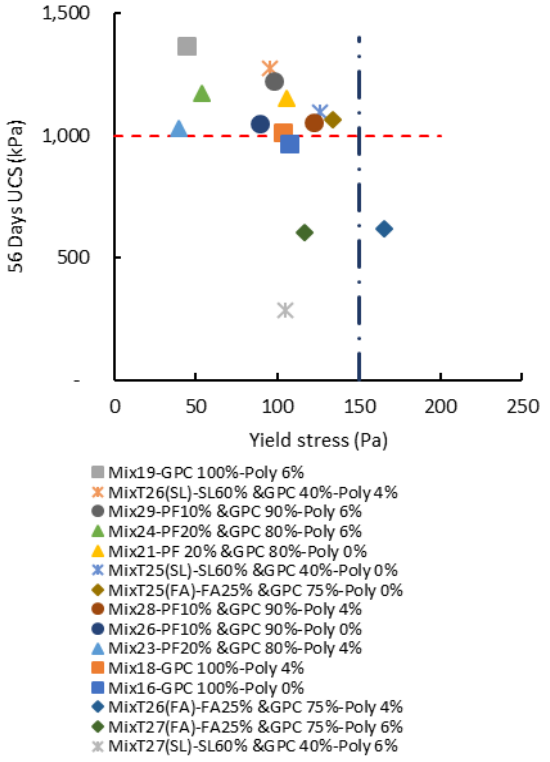

Fig. 9 Yield stress and 56 days UCS

Results (Fig.9) indicated that majority of the mixes have reached 1MPa and above except 3 mixes of fly ash and slag blend with 4-6% polycarboxylate

dosage. Interestingly, all the mixes with pitchstone fines were within the optimum mix zone.

4.6 *SEM over curing periods*

SEM comparisons were done on 7% binder dosage of control mix 16 (100% GPC) and pitchstone blend, mix 24 (20% PF & 80% GPC) to identify the development of hydration products over different curing periods (7, 14, and 28 days) at 5 µm magnification as shown in Fig. 10.

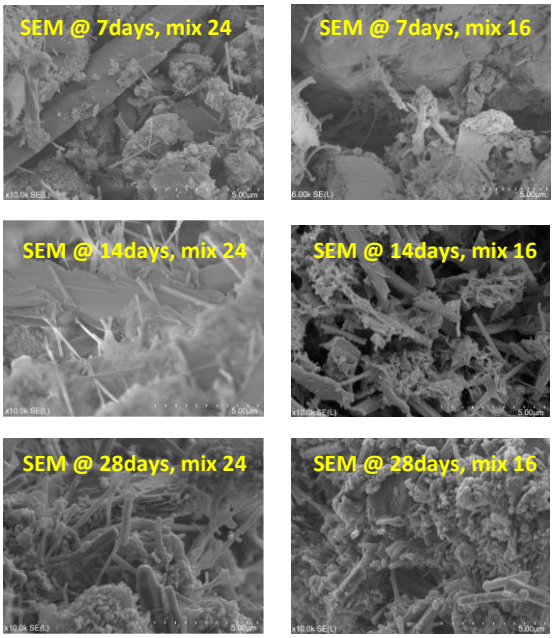

Fig. 10 SEM comparisons of mix 16 & 24

Results of microstructure development indicated growth of ettringite crystals (needle like) at earlier stages (7-14 days), while calcium silicates (C-S-H) developed later and occupied most of the voids and contributed to the increase in the strength of CPF.

5 CONCLUSION

The overall goal of this research was to optimise the cemented paste fill (CPF). Strength results indicated that the blends of SCMs used attained strength activity index above the threshold of 75 % compared to the control mix (100% GPC). The pozzolans used complied with the strength requirements as per ASTM C618 standard and can be utilised in concrete and paste filling. UCS of the blends of pozzolans at 7% binder dosage reached 1MPa after 28 days curing and can be used in ground support in underground mines. Interestingly, blends of pitchstone fines which have never been trialled in mine backfilling before have produced comparable strength results that are useful. Results from the rheological measurements indicated that the polycarboxylate plasticizer had a significant influence on the workability of the cemented paste slurry. As the dosage of the polycarboxylate increased, the slump increased, and the yield stress decreased for slurries with high solids (>74%). Overall, the use of SCMs can reduce backfilling cost, and the use of polycarboxylate plasticizer can reduce water requirements. Moreover, disposing of waste mill tailings into underground voids can minimize the surface footprint and make backfilling more environmentally friendly.

ACKNOWLEDGMENTS

The authors are grateful to several individuals who have assisted throughout the research. Shaun Robinson and Troy Poole assisted with laboratory tests, Shaun Askew and Ruilan Liu with SEM and rheology, Tayla Dinnison and Lucy Bombardieri for assisting with the fly ash and slag tests.

REFERENCES

AS 1289.3.6.1 Methods of testing soils for engineering purposes determination of the particle size distribution of a soil by sieving, Australia Standard.

ASTM C143- Standard test method for slump of hydraulic cement concrete, ASTM International.

ASTM C618- Standard specification for coal fly ash and row or calcined natural pozzolan for use in concrete, ASTM International.

ASTM D2166- Standard test method for unconfined compressive strength of cohesive soil, ASTM International.

Belem, T., & Benzaazoua, M. (2008). Design and application of underground mine paste backfill technology, Journal of Geotechnical and Geological Engineering, 26(2), 147-174.

Clough, G W; Sitar, N; Bachus, R C J. (1989).Cemented sands under static loading, Journal of Geotechnical Engineering Division, ASCE 1981,107(6), 799-817.

Niroshan, N., Sivakugan, N., & Veenstra, R. L. (2017). Laboratory study on strength development in cemented paste backfills, Journal of Materials in Civil Engineering, 29(7), 4017027.

Sivakugan, N., Rankine, R. M., Rankine, K. J., & Rankine, K. S. (2006). Geotechnical considerations in mine backfilling in Australia, Journal of Cleaner Production, 14(12), 1168-1175.

Sivakugan, N., Veenstra, R., & Niroshan, N. (2015). Underground mine backfilling in Australia using paste fills and hydraulic fills,Journal of Geosynthetics and Ground Engineering, 1(2), 18.

Tuladhar, R., Sexton, A., & Joyce, P. (2013). Durability of concrete with pitchstone fines as a partial cement replacement, Conference proceedings, Concrete Institue of Australia.

Xu, W., Cao, P., & Tian, M. (2018). Strength development and microstructure evolution of cemented tailings backfill containing different binder types and contents, Journal of Minerals, 8(4).

Polymer modified microbial induced carbonate precipitation: Novel approach to densify the loose sand

T.H.K. Nawarathna
Faculty of Technology, University of Jaffna, Sri Lanka
K. Nakashima
Faculty of Engineering, Hokkaido University, Japan
S. Kawasaki
Faculty of Engineering, Hokkaido University, Japan

Microbial induced carbonate precipitation (MICP) has gained much attention recently as an ecofriendly approach to treat the problematic grounds. In MICP, calcium carbonate ($CaCO_3$) is produced artificially by hydrolysis of urea using enzyme urease. In the current research, the effect of the cationic polysaccharide, chitosan on the MICP process was investigated. $CaCO_3$ precipitation experiment was conducted with and without chitosan by the hydrolysis of urea using ureolytic bacteria *Pararhodobacter* sp. SO1 in the presence of $CaCl_2$. Morphology and the polymorphism of the samples were analyzed by scanning electron microscopy and X-ray diffraction. In the presence of chitosan, higher amount of precipitate was obtained than that of without chitosan. Without chitosan, rhombohedral crystals were dominant while with chitosan distorted crystal agglomerations combined with the chitosan hydrogel were observed. Further, sand solidification experiments were conducted in the presence and absence of chitosan. With chitosan, strongly cemented sand specimen could be obtained.

1 INTRODUCTION

Bio grouting has been recognized as an efficient and environmentally friendly technique to treat the weak soils in contrast to the other grouting methods which are harmful for the environment. Further, most interesting point is bio-grouts have a possibility to increase the cohesion with the nearby materials, then increase the mechanical strength of the whole system (Li et al., 2015). Among the bio grouting methods, microbial induced carbonate precipitation (MICP) has gained much attention recently as an ecofriendly and sustainable approach to treat the problematic weak grounds.

MICP is a bio-geochemical process which is driven by enzyme urease. Urease is a multi-subunit, nickel containing enzyme and can be found in some bacterial species and plants (Maroney and Ciurli, 2014). Urease enzyme has a capability of hydrolysis of urea and produce ammonium and carbamate ions. Carbamate ions spontaneously transferred into ammonia and carbonic acid and then in the presence of calcium ions (Ca^{2+}), $CaCO_3$ is formed (Amarakoon and Kawasaki, 2017; Fujita et al., 2017; Mortensen et al., 2011; Dejong et al, 2010) as given in the equations (1-3).

$$CO(NH_2)_2 + H_2O \longrightarrow H_2NCOO^- + NH_4^+ \quad (1)$$

$$H_2NCOO^- + H_2O \longrightarrow HCO_3^- + NH_3 \quad (2)$$

$$Ca^{2+} + HCO_3^- + NH_3 \longrightarrow CaCO_3 + NH_4^+ \quad (3)$$

It has been proven that MICP method has capability to improve the soil properties very effectively and efficiently. Remarkable increment of the strength and stiffness have been reported for the MICP treated sand (Montoya and DeJong, 2015; Cheng et al., 2013). Also, interestingly MICP has capability to increase the soil strength while maintaining the sufficient permeability which is required during the biocementation process (Paassen, 2009; Ivanov et al., 2010).

Due to the higher performance of the MICP process, researchers are now looking for the possible techniques to improve the efficiency of the MICP process further. Use of organic materials is one of the most interesting approach and could increase the efficiency of the MICP process more effectively. The concept is called as the polymer modified MICP. Since it is a recently identified trend, only little number of previous research works can be seen under the polymer modified MICP (Wang and Tao, 2018; Nawarathna et al., 2018). This study is the first to address the effects of chitosan on the $CaCO_3$ crystallization and MICP process using the ureolytic bacterium *Pararhodobacter sp.* SO1. The *Pararhodobacter sp.* SO1 is a gram-negative bacterium which is locally isolated from the beach sand in Nago, Okinawa, Japan (Danjo and Kawasaki, 2013). Chitosan is one of the most abundant and inexpensive cationic natural polysaccharides.

2 METHODOLOGY

2.1 *Preparation of bacterial cell culture*

The bacterial cells were pre-cultured in Zobell 2216E medium (polypeptone 5.0 g/L, yeast extract 1.0 g/L, $FePO_4$ 0.1 g/L in artificial seawater, pH 7.6–7.8; 5 mL) by shaking at 30 °C and 160 rpm for 24 h. Then, main culture was prepared by adding 1 mL of pre-culture into 100 mL of fresh Zobell 2216E medium and kept in the shaking incubator under the same conditions as those used for the pre-culturing, for 48 h. By centrifugation of the bacteria culture (10 °C, 6300 ×g, 5 min), cells were collected and resuspended in sterilized water to adjust the cell concentration (OD600 =1). Bacteria cell concentration was measured as an optical density value measured at 600 nm wave length (OD600) by using UV-visible spectroscopy.

2.2 *$CaCO_3$ precipitation*

$CaCO_3$ precipitation was achieved by adding bacteria into the substrate solution containing urea (0.3 mol/L) and $CaCl_2$ (0.3 mol/L). Reaction mixture (10 mL) was kept in shaking incubator under 30 °C and 160 rpm for 24 h. $CaCO_3$ precipitation was separated from the supernatant by centrifugation (24 °C, 14200 ×g, 10 min) and after oven drying (90 °C, 24 h) dry weight of the precipitate was measured. Experiments were conducted with (0.03 %) and without chitosan under two different bacteria concentrations (OD_{600} = 0 – 0.05). Chitosan solution (1%) was prepared by completely dissolving the chitosan powder in 1% acetic acid solution and neutralizing to pH 6.8 by using 0.1 M NaOH solution. Morphology of the $CaCO_3$ precipitate was analyzed for uncoated samples by scanning electron microscopy (SEM; acceleration voltage – 5 kV).

2.3 *Sand Solidification in syringe*

Laboratory scale model experiments were conducted using 35 mL syringe (mean diameter = 2.5 cm and height 7 cm) in-order to check the effect of the chitosan on sand solidification. Commercially available Mikawa sand was used for the experiment and it is a uniformly graded sand with the mean diameter of D_{50} = 0.6 mm and particle density is equal to 2.66 g/cm^3. oven dried (110 °C, 48 h) sand (40 g) was filled into the syringe as 3 layers and 20 hammer blows were given to each layer. After initial setup, bacteria suspension (16 mL, OD600 = 1) was injected into the syringe and leave it 5-10 min for the addiction of the bacteria to sand particles. Then drained out from the outlet, maintaining 2 mL of the solution above the surface.

After that, cementation solution (20 mL; 0.3 M urea, 0.3 M $CaCl_2$, 0.02 M sodium hydrogen carbonate, 0.2 M ammonium chloride, and 3 g/L nutrient broth) was added into the syringe and solution drained out from the outlet, keeping 2 mL of the solution above the surface to maintain the sand in saturated condition.

Experiments were conducted with and without addition of chitosan and curing time was 14 days. Bacteria were injected on the first day and again after the 7 days while cementation solution was injected daily. In the case of experiment with chitosan, chitosan was injected to the syringe on the 11th day. After 14 days, sand samples were recovered from the syringe and unconfined compressive strength (UCS) of the samples were measured using needle penetration device.

All experiments were done in triplicate and mean value was plotted. Standard deviation was used to represent the error bars.

3 RESULTS AND DISCUSSION

3.1 *Effects of chitosan on $CaCO_3$ precipitation*

Variation of the amount of precipitate with and without chitosan under different bacteria concentration is given in Fig. 1. It can be seen that, the amount of the precipitate has increased with the bacteria concentration. In MICP, $CaCO_3$ formation efficiency is directly proportional to the urease activity of the bacteria (Qabany et al, 2012). Fujita et al. (2017) found that urease activity of the *Pararhodobacter* sp. SO1 increase with the increase of cell concentration. Increase of the urease activity with the cell concentration led to the formation of higher amount of precipitate at higher cell concentration.

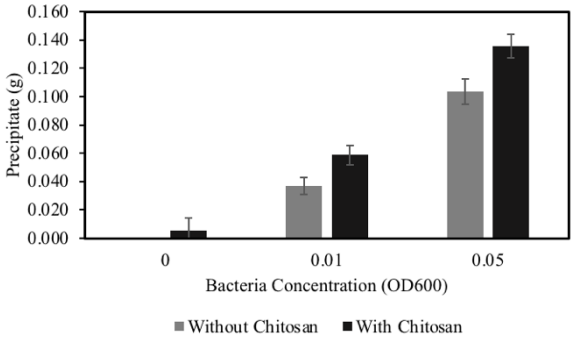

Fig. 1 Variation of the amount of precipitate with the bacteria concentration (OD600), with and without chitosan

The most interesting point is higher amount of precipitate could be obtained with the addition of chitosan. Precipitate with chitosan mainly has two components, precipitated $CaCO_3$ and the precipitated chitosan hydrogel. Chitosan forms its hydrogel under the alkaline conditions since the dissolution coefficient of the chitosan is approximately 6.5 (Liu et al, 2015; Kumirska et al, 2015). In the current reaction mixture, pH is around 7.1 due to formation of

the ammonia as a byproduct of the urea hydrolysis. This weak alkaline environment forms a favorable condition for the chitosan to form its hydrogel by hydrophobic interactions (Rami et al, 2014). Further, chitosan upgrades the $CaCO_3$ nucleation and growth. Ca^{2+} ions are embedded into the chitosan hydrogel and produce nucleation sites for the $CaCO_3$ crystals to nucleate and growth by following acid-base interaction (Greer et al, 2017).

Morphology of the $CaCO_3$ crystals in the presence of the chitosan was analyzed by SEM and given in Fig. 2. With the increase of the bacteria concentration morphology of the crystals has changed from rhombohedral crystals to distorted shape crystal agglomerations. Chitosan hydrogel can be seen clearly in lower bacteria cell concentrations due to the lower rate of $CaCO_3$ formation. However, in higher cell concentrations, due to higher rate of $CaCO_3$ formation crystal agglomerations were formed. Also, due to adsorption of the chitosan into the growing crystal faces distorted crystal faces were created. Nawarathna et al (2018) found that, without any additives fewer number of good rhombohedral crystals are formed under lower bacteria cell concentrations and at higher bacteria cell concentrations larger number of smaller crystals are formed due to the presence of larger number of nucleation sites. In the MICP process bacteria cells themselves act as nucleation site for $CaCO_3$ crystals to nucleate and growth.

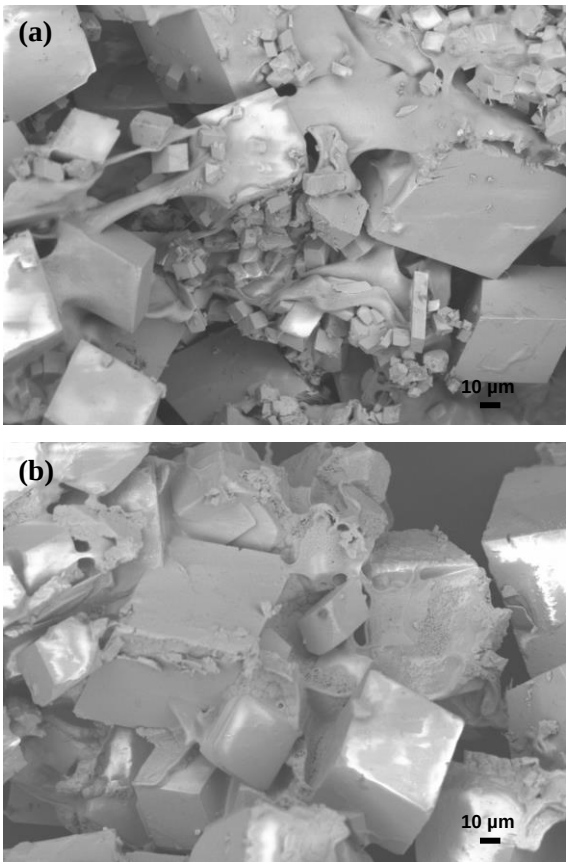

Fig. 2 SEM images of the precipitate with chitosan under different bacteria concentrations (OD600) (a) 0.01 (b) 0.05

3.2 *Effect of chitosan on sand densification*

Laboratory scale sand solidification experiments were conducted with and without chitosan and after 14 days of curing, UCS values of the top, middle and bottom of the sample were measured. Fig. 3 shows the obtained UCS values for the samples with and without chitosan.

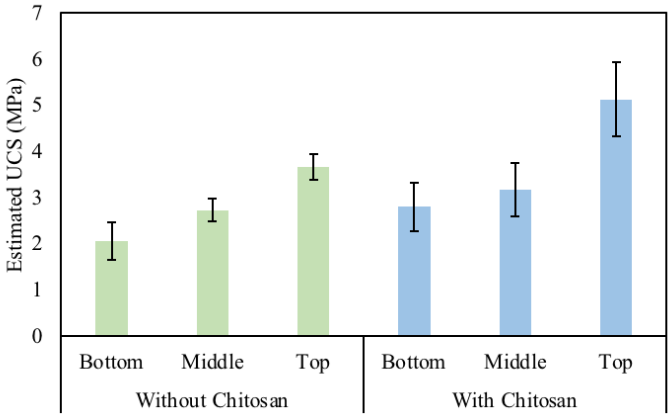

Fig. 3 Estimated UCS values of the sand specimens with and without chitosan

In both of the cases, UCS value decrease from top to bottom due to the accumulation of bacteria at the top of the sample compare with the bottom of the sample. Higher urease activity at the top of the sample led to higher precipitation and higher cementation at the top of the specimen and gradually decrease along the length of the sample. Also, *Pararhodobacter* sp. SO1 is an aerobic bacterium (Khan et al, 2015) and bacterial activity of aerobic bacteria mainly depend on the oxygen concentration of the surrounding environment. Therefore, lack of the oxygen at the bottom of the sample would be a reason for the lower precipitation and cementation at the bottom of the sand column. By adding chitosan, well cemented sand column with higher UCS value could be obtained compared with the case of without chitosan. 40 % of strength increment could be achieved at the top of the sample by adding chitosan than without chitosan.

As mentioned earlier, chitosan forms its hydrogel under the alkaline condition. This hydrogel assisted to form a better bridge between sand particles and filled the pore spaces efficiently. Therefore, better cementation and strength was achieved. Efficient filling of pore spaces and formation of the bridge between the sand particles are essential to have a better cementation and efficient solidification of the loose sand (Harkes et al, 2009). During the experiment, 11th day was selected to inject chitosan in-order to prevent the early formation of chitosan hydrogel. Introduction of chitosan at the begging will be led to formation of hydrogel initially and prevent the further penetration of the cementation solution

through the sand specimen. Therefore, it will reduce the efficient formation of $CaCO_3$ as well as cementation between the sand particles. Fig. 4 shows, how chitosan hydrogel helps to achieve a better cementation.

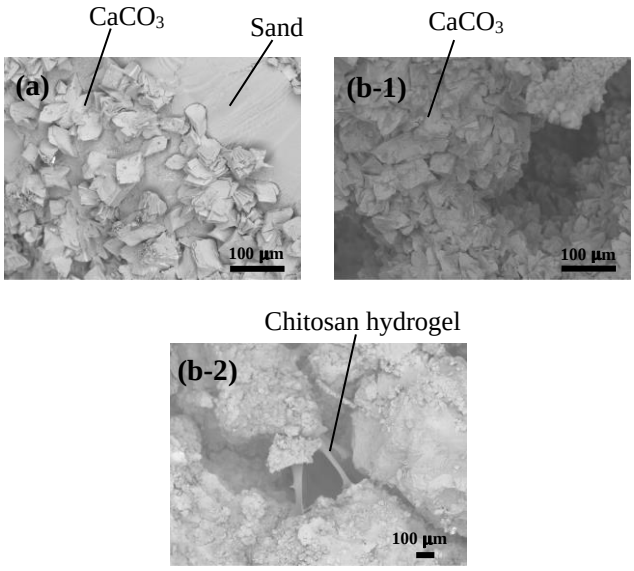

Fig. 4 SEM images of the solidified sand specimens (a) with chitosan (b-1,2) without chitosan

4 CONCLUSION

Effects of the chitosan on the sand densification and the $CaCO_3$ formation was investigated by using the MICP process. Higher amount of precipitate could be obtained by adding chitosan than that of without chitosan. Chitosan upgrade the $CaCO_3$ formation by providing more nucleation sites. Due to the acid-base reaction, Ca^{2+} ions are attached into the chitosan hydrogel and produced nucleation sites for the $CaCO_3$ crystals to nucleate and growth. Further in the presence of chitosan, chitosan hydrogel also precipitated with the $CaCO_3$. Distorted shape crystal agglomerations were formed in the presence of chitosan while without chitosan rhombohedral crystals were dominant. Most interestingly, strongly cemented sand column could be obtained by adding chitosan than the conventional method. Formed chitosan hydrogel assisted to create a better bridge between the sand particles and led to achieve a better strength.

ACKNOWLEDGMENTS

This work was partly supported by JSPS KAKENHI Grant Number JP15K18273 and JP16H04404.

REFERENCES

Amarakoon, G.G.N.N. and Kawasaki, S. (2017). Factors affecting sand solidification using MICP with Pararhodobacter sp., Materials Transactions, 59:72−81.

Cheng, L., Cord-Ruwisch, R. and Shahin, M.A. (2013). Cementation of sand soil by microbially induced calcite precipitation at various degrees of saturation, Canadian Geotechnical Journal, 50:81–90.

Danjo, T. and Kawasaki, S. (2013) A study of the formation mechanism of beach rock in Okinawa, Japan: toward making artificial rock, International Journal of GEOMATE 5:634–639.

DeJong, J.T., Mortensen, B.M., Martinez, B.C. and Nelson, D.C. (2010). Bio-mediated soil improvement, Ecological Engineering, 36:197–210.

Fujita, M., Nakashima, K., Achal, V. and Kawasaki, S. (2017). Whole-cell evaluation of urease activity of Pararhodobacter sp. isolated from peripheral beach rock, Biochemical Engineering Journal, 124:1−5.

Greer, H.F., Zhou, W. and Guo, L. (2017) Reversed crystal growth of calcite in naturally occurring travertine crust, Crystals, 7: 36-54.

Harkes, M.P., Paassen, L.A.V., Booster, J.L., Whiffin, V.S. and Loosdrechta, M.C.M.V. (2010). Fixation and distribution of bacterial activity in sand to induce carbonate precipitation for ground reinforcement, Ecological Engineering, 36:112−117.

Ivanov, V., Chu, J., Stabnikov, V., He, J. and Naeimi, M. (2010). Iron-based bio-grout for soil improvement and land reclamation, Ancona Italy, 2010. Second international conference on substantiable constructional materials technologies, pp415-420.

Khan, M.N.H., Amarakoon, G.G.N.N., Shimazaki, S. and Kawasaki, S. (2015). Coral sand solidification test based on microbially induced carbonate precipitation using ureolytic bacteria, Materials Transactins, 56:1725−1732.

Kumirska, J., Weinhold, M.X., Thoming, J. and Stepnowski, P. (2011). Biomedical activity of chitin/chitosan-based materials-influence of physicochemical properties apart from molecular weight and degree of N-acetylation, Polymers, 3:1875−1901.

Li, M., Fu, Q.L., Zhang, Q., Achal, V. and Kawasaki, S. (2015). Bio-grout based on microbially induced sand solidification by means of asparaginase activity. Scientific Report, 5:16128.

Liu, H., Ojha, B., Morris, C., Jiang, M., Wojcikiewicz, E.P., Rao, P.P.N. and Du, D. (2015). Positively charged chitosan and N-trimethyl chitosan inhibit Aβ40 fibrillogenesis, Biomacromolecules, 16:2363−2373.

Maroney, M.J. and Ciurli, S. (2014). Nonredox nickel enzymes, Chemical Reviews, 114: 4206−4228.

Montoya, B.M. and DeJong, J.T. (2015). Stress-strain behavior of sands cemented by microbially induced calcite precipitation, Journal of Geotechnical and Geoenvironmental Engineering, 141: 04015019– 04015029.

Mortensen, B.M., Haber, M.J., DeJong, J.T., Caslake, L.F. and Nelson, D.C. (2011). Effects of environmental factors on microbial induced calcium carbonate precipitation, Journal of Applied Microbiology, 111: 338−349.

Nawarathna, T.H.K., Nakashima, K., Fujita, Takatsu., M and Kawasaki, S. (2018). Effects of cationic polypeptide on $CaCO_3$ crystallization and sand solidification by microbial-induced carbonate precipitation, ACS Sustainable Chemistry and Engineering, 6:10315–10322.

Qabany, A.A., Soga,K. and Santamarina, C. (2012) Factors affecting efficiency of microbially induced calcite precipitation, Journal of Geotechnical and Geoenvironmental Engineering, 138:992−1001.

Rami, L., Malaise, S., Delmond, S., Fricain, J.C., Siadous, R., Schlaubitz, S., Laurichesse, E., Amedee, J., Montembault, A., David, L. and Bordenave, L. (2014). Physicochemical modulation of chitosan-based hydrogels induces different biological responses: Interest for tissue engineering, Journal of Biomedical Material Research, 102:3666−3676.

Van Paassen, L.A., Harkes, M.P., Van Zwieten, G.A., Cander Zon, W.H., Van Der Star, W.R.L. and Van Loosdrecht, M.C.M. (2009). Scale up of BioGrout: a biological ground reinforcement method. Alecandrina Egypt, 2009. Proceedings of the 17th International Conference on Soil Mechanics and Geotechnical Engineering. pp2328–2333.

Wang, X. and Tao, J. (2017). Polymer-modified microbially induced carbonate precipitation for one shot targeted and localized soil improvement, Acta Geotechnica, 14:1-15.

The approach of assessing time of preload and surcharge removal during the construction of embankment over soft soils

Bosco Poon
GHD, Sydney, Australia

Kim Chan
GHD, Sydney, Australia

Ashok Peiris
GHD, Sydney, Australia

ABSTRACT: The process of preload release involves a review of the instrumentation and monitoring data. Back analysis is carried out to match field measurements with numerical predictions by adjusting relevant geotechnical model, parameters and construction sequence. Once a match is achieved, the calibrated geotechnical model is used for the prediction of long-term settlement. The removal of preload and surcharge fill is only allowed via the release of a Hold Point, when the predicted long term settlement satisfies the design criteria. This paper provides technical advice and guidance to undertake geotechnical review of preload performance as part of the Hold Point release process.

1 INTRODUCTION

Preload and surcharge with or without prefabricated vertical drains is a commonly adopted soft ground treatment method. In order to confirm that the soft ground has been suitably treated, a process of preload and surcharge release is in place during construction.

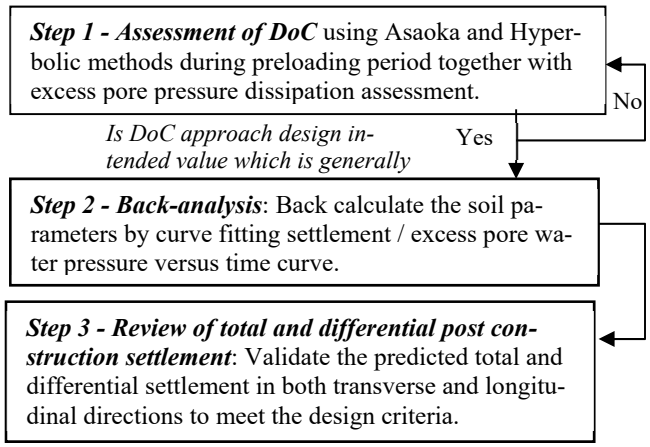

Fig. 1 Three main steps involved in the preload performance assessment

The removal of preload and surcharge is only allowed via the release of a Hold Point by a nominated verified, certifying that the validated predicted total and differential post construction settlements meet the design criteria. The process of preload performance assessment involves three main steps that can be outlined in Fig. 1. By way of showing some examples cited from two soft ground projects, namely, Harwood Bridge project and Warrell Creek to Nambucca Heads (WC2NH) project, this paper provides technical guidance to geotechnical practitioner on the three aspects of Hold Point release process outlined in Fig. 1.

2 ASSESSMENT OF DOC

The instrumentation data should be closely monitored during the preloading period. The objective is to assess the Degree of Consolidation (DoC) prior to carrying out more rigorous back-analysis of the soil properties. Two observational methods, namely, Asaoka (1978) method and Hyperbolic method proposed by Tan *et al*. (1991) can be used to assess DoC, which are then compared with other DoC values assessed based on pore water pressure measured from the vibrating wire piezometers (VWP).

Asaoka (1978) method is a commonly used graphical method to estimate final total primary consolidation settlement from the settlement data obtained during a certain time period after fill placement. The disadvantage with this method is that it is strongly affected by the choice of time interval Δt used in constructing the Asaoka diagram. The use of a small Δt should be avoided. Fig. 2a shows an Asaoka plot constructed using $\Delta t = 5$ days, with the initial settlement data taken as the settlement at $t_0 =$

105 days, which was the beginning of the full load. Due to the relatively small Δt adopted, the plotted data are almost sub-parallel to the 45° line. The assessment of the total primary settlement has become very sensitivity to the subjectivity in fitting a line through these points, leading to the uncertainty of the estimated DoC value ranging from 90% to 98%. Edil *et al*. (1991) proposed a parameter j_{95} and recommended that Δt to be chosen to give a j_{95} value between 10 and 30. The j_{95} is essentially the number of samples to reach a 95% DoC and is defined as:

$$j_{95} = \frac{\ln(0.05 s_p/(s_p - s_0))}{\ln \beta_1} \qquad (1)$$

where s_0 is the settlement at the end of the fill placement after which the embankment load is constant. s_p is defined as $s_p = \beta_o / (1- \beta_1)$. β_o is the intercept and β_1 is the slope of the straight line in the s_t vs. s_{t-1} plot. The use of Δt = 5 days in Fig. 2a gives j_{95} = 60, which exceeds the range suggested by Edil *et al*. (1991). By adopting Δt =20 days, the calculated j_{95} = 20 is within the recommended range of 10 – 30, and the Asaoka plot shown in Fig. 2b shows a more oblique trend to the 45° line than that of using a smaller Δt value. The assessed DoC = 91% based on Δt =20 days is therefore a more reliable prediction than that using Δt =5 days.

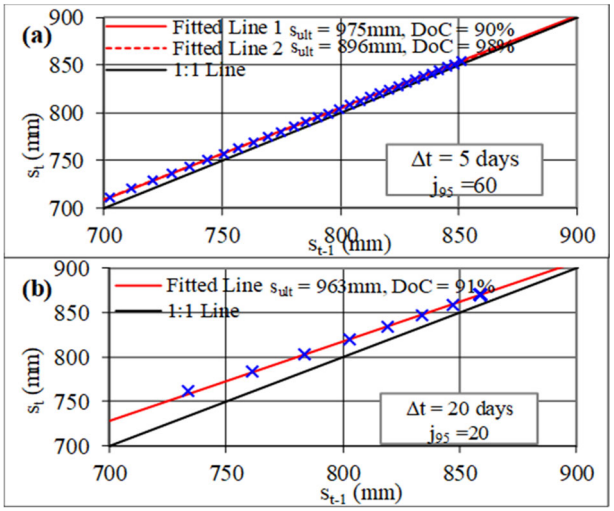

Fig. 2 Asaoka with (a))Δt=5 days, (b)Δt = 20 days (from SP101 at northern abutment of Harwood Bridge

Tan *et al*. (1991) proposed a hyperbolic relationship between monitored settlement, s, and consolidation time, t, given by $t/s = \alpha + \beta t$. Tan *et al*. have shown that when time tends to infinity, the inverse of the slope of the graph at linear segment will give the ultimate settlement. The main attraction of the hyperbolic method is its simplicity without the need to consider Δt value. Unlike the Asaoka's method that is based on a governing partial differential equation that considers only the primary consolidation, the hyperbolic method is based on actual data, which intrinsically includes creep settlement. As a result, the settlements obtained from hyperbolic method are usually slightly larger than those obtained from Asaoka's method. The SP101 data from Harwood Bridge project was assessed in Fig. 3 using hyperbolic method. The estimated settlement is compared with those assessed using Asaoka (1978) method as show in Table 1 (also including other settlement plate data at the northern abutment of Harwood Bridge). It can be seen that the settlements obtained from hyperbolic method are slightly larger than those from Asaoka's method.

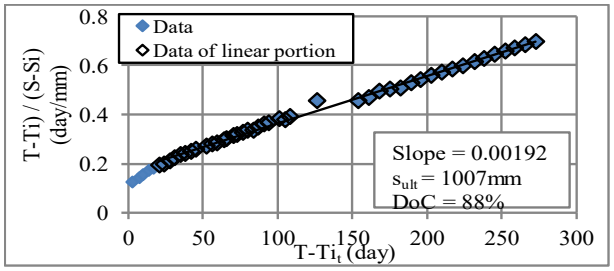

Fig. 3 Hyperbolic analysis (SP101 at the northern abutment of Harwood Bridge)

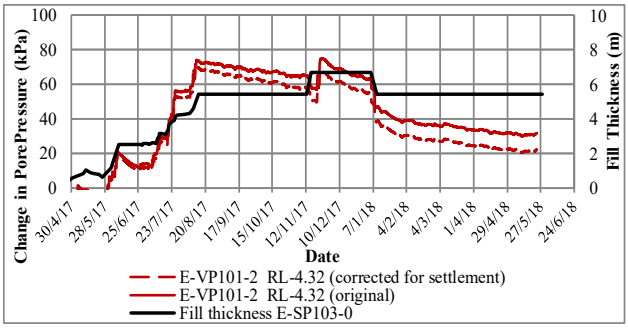

Fig. 4 Excess pore pressure from piezometer at RL-4.32m in VP101 with and without settlement correction

Table 1 Summary of DoC (Harwood Bridge)

Settlement plate ID	**Predicted *s* (mm)**		**Assessed DoC (%)**	
	Asaoka	*Hyperbolic*	*Asaoka*	*Hyperbolic*
E-SP101	963	1007	91	88
E-SP102	950	995	93	90
E-SP103	997	1060	91	89
E-EM101	1000	1065	92	89

The assessment of DoC should also considered the excess pore water pressure measured from the vibrating wire piezometers (VWP). In the interpretation of excess pore water pressure, it is important to correct the measured total pore water pressure for the increase in pressure head due to the settlement of piezometer under load. The settlement of the piezometer with time can be estimated from the registered settlement of the magnet in the nearby extensometer. Fig. 4 shows a higher excess pore water pressure inferred from a piezometer at RL-4.32m in VP101 (from Harwood Bridge project) than if it is correctly interpreted with the consideration of settlement correction.

3 BACK ANALYSIS PROCESS

Back analysis is usually carried out towards the end of the preload waiting period or when the assessed DoC values have reached the intended DoC as per design, which is in general 90% or greater. The objective of carrying out the back analysis is to verify/adjust the consolidation and compressibility parameters by curve-fitting the recorded settlement-time curves and the excess pore pressure measurements. This is followed by the review of the long term creep settlement predictions based on the actual final effective stress after the preloading and surcharging in order to validate the predicted total and differential settlement in both transverse and longitudinal directions to meet the design criteria. The discussion of post surcharge creep settlement is provided in Section 5. This section focuses on the back-analysis of engineering parameters. The analysis aspects involved in the back-analysis are provided in Section 4. In the curve fitting process as part of the back-analysis, the adjusted engineering properties shall always be reviewed by comparing with laboratory and in-situ test data, as well as published correlations. A methodological approach is outlined herein in order to provide guidance for undertaking the back-analysis.

Step 1 – Review the soil stratigraphy and total soil depth In the back-analysis of the settlement plate and extensometer data, the soil layer thicknesses of the adopted geotechnical model shall be accurately defined based on the nearest CPTs, even though they may be different to those of the original design model. The soil model adopted in the detailed design was for an area whereby the soil depth could be the deepest or the average within the area. There is no guarantee that the soil layer thicknesses or total soil depth used in the design are representative of those at the monitoring locations. For the case of Harwood Bridge Project, the soil stratigraphy has been reviewed during the back-analysis of settlement plate SP103 based on the nearby ACPT010. It can be seen that the upper and the lower clay thicknesses are 5.5 m and 3.6 m, respectively (see Fig. 5a), which are greater than the adopted design thicknesses of 4.5 m and 3 m.

Step 2– Adjust the over consolidation ratio (OCR) and review of ground water level OCR is one of the most influential parameter affecting the predicted total settlement. During the detailed design stage of Harwood Bridge Project, the OCR values of the clay layers were assessed using a numerical "aging" technique in conjunction with the sophisticated Soft Soil Creep Model embedded in the commercially available FEA software program PLAXIS 2D. For the case of WC2NH project, the design OCR values were derived based on SHANSEP equation (Eq. 2) and using the SHANSEP parameters of m = 0.8 and S = 0.22. In both design cases, it was found that using the design OCR values underestimate the measured total settlements. During the construction stage of both projects, the OCR values were correlated with the S_u inferred from the nearest CPT via SHANSEP while adopting m = 0.95 and S = 0.22 (Fig. 5b and 5c). This set of SHANSEP parameters has been used in many soft soil projects along east coast of Australia with success. It has also been used by the Authors to predict the behavior of a well-known trial embankment in Ballina (Chan et al. 2018). The back-analyzed OCR values via SHANSEP approach is strongly influenced by the ground water level since the vertical effective stress σ'_v is used in Eq. 2. It is therefore imperative to review the ground water level via monitoring data as part of the back-analysis process.

$$S_u/\sigma'_v = S \times OCR^m \qquad (2)$$

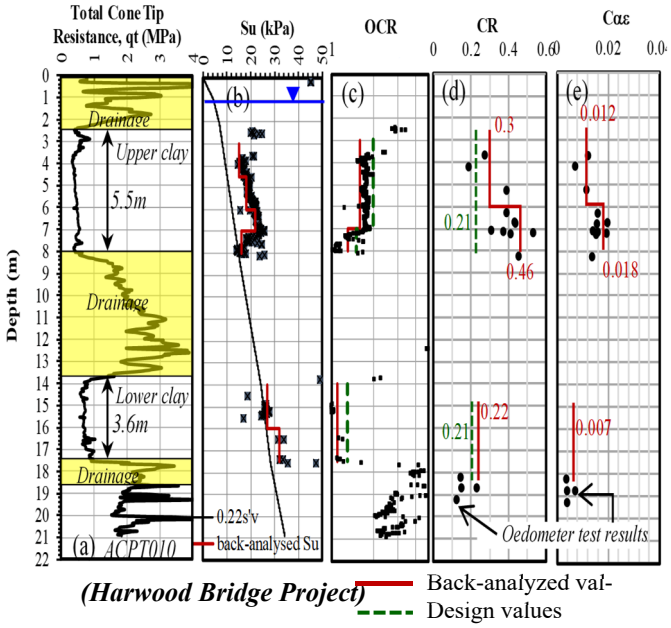

Fig. 5 (a) ACPT010 at (b) CPT inferred S_u, (c) CPT inferred OCR, (d) CR, (e) $c_{\alpha\varepsilon}$

Step 3 – Review the compression Ratio (CR) and recompression Ratio (RR) While OCR and water level are the major parameters influencing the predicted total settlement. The CR (= $cc/(1+e_0)$) and RR (= $c_r/(1+e_0)$) should also be reviewed (or adjusted if required) for their consistency with oedometer test data as part of the back-analysis process. It is not unusual to adopt a higher compressibility values than the laboratory results that are derived from disturbed soil samples. Take Harwood Bridge Project as an example, the adopted CR value in the design was 0.21, which lies close to the lower bound of the oedometer test results (Fig. 5d). For back-analysis, the CR value was increased to be slightly higher than the upper bound of the test results.

Moreover, the upper clay layer was divided into two sub-layers, with the lower layer having a higher back-analyzed CR value. This is consistent with the high compressibility identified by the oedometer test data, as well as the high water content exhibited within this sub-layer (up to 95%). The RR value may need to be adjusted in order to better fit the proportion of settlement occurred before and after OCR =1. RR can be correlated with CR. Typical RR/CR ratio is about 0.14 and with a likely range of 0.1-0.2.

Step 4 – Review the normally consolidated creep strain rate $c_{\alpha\varepsilon(NC)}$ Unless otherwise suggested by laboratory test data, the normally consolidated creep strain rate $c_{\alpha\varepsilon(NC)}$ can be taken as 4% of the back-calculated CR in accordance with the c_α/cc law of compressibility for inorganic clay proposed by Mesri and Godlwski (1977). Fig. 5e shows that the back-analyzed $c_{\alpha\varepsilon(NC)}$ values based on the correlation are consistent with the oedometer test results on Harwood Bridge project. In the case where the tail end of the settlement vs. time curve is interpolated to derive a straight line. This linear line shall not be misrepresented as the pure creep settlement behavior since it may comprise a large proportion of residual primary settlement. It is the authors' opinion that using the observed settlement rate at the tail end to assess the creep rate is likely to result in excessive post construction settlement prediction. The $c_{\alpha\varepsilon(NC)}$ should more appropriately be assessed from the back-analyzed CR value, and compared with the laboratory test data.

Step 5 – Refine the shape of the fitted curve – The shape of the fitted curve is largely influenced by (i) drainage boundary of the clay layers, (ii) load history and (iii) adopted coefficient of consolidation values c_v. With regard to the drainage boundary, it is imperative to review the sand-clay boundaries based on the area specific CPTs such as that outlined in Fig. 5a. The applied fill load in the back-analysis should also follow closely the loading history. Examples of which are shown in Figs. 9 and 10. In relation to c_v, the back analysis should consider firstly the normally consolidated $c_{v(NC)}$ by comparing the back-analyzed values with piezocone measurements as well as published correlation, followed by using appropriate over-consolidated $c_{v(OC)}$ values. Fig. 6b presents c_v values assessed from piezocones on WC2NH project. The c_v values were assessed based on $c_v = c_h/2$ (based on Beales and O'Kelly, 2008 and our experience in the region), where c_h is the coefficient in the horizontal direction inferred from the dissipation test results. The c_v values in Fig. 6b are plotted side by side with the OCR profiles (Fig. 6a) inferred from the corresponding piezocones. If the inferred c_v within the same soil unit (Unit 2a) are plotted against the corresponding OCR on a log-log plot as shown in Fig. 7, a prominent linear trend can be seen and the intersection of the median line of this trend line with OCR = 1 gives an estimated $c_{v(NC)}$ of about 12 m^2/yr. NAVFAC (1971) developed correlations of c_v of remoulded, normally consolidated and over-consolidated clays with their liquid limits (LL) as shown in Fig. 8. The Unit 2a on WC2NH project has a LL range of 35% – 50%. By using a mean LL of 42%, the correlated $c_{v(NC)}$ is about 8 m^2/yr, which is consistent with that inferred from field measurements in Fig. 7.

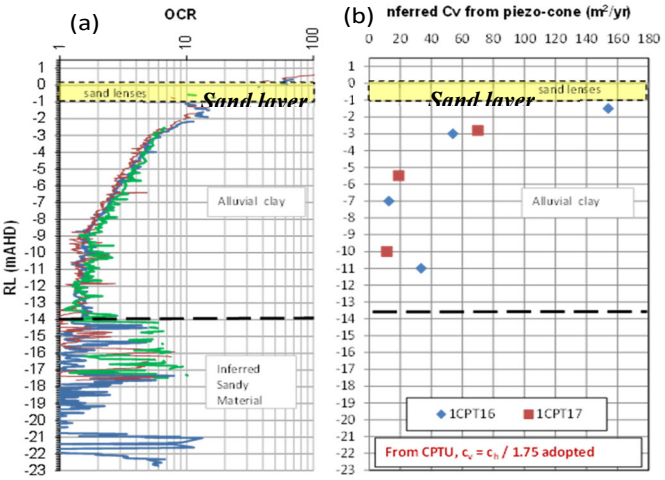

Fig. 6. Typical profiles of (a) OCR and (b) cv vs. RL inferred from piezocones on WC2NH project

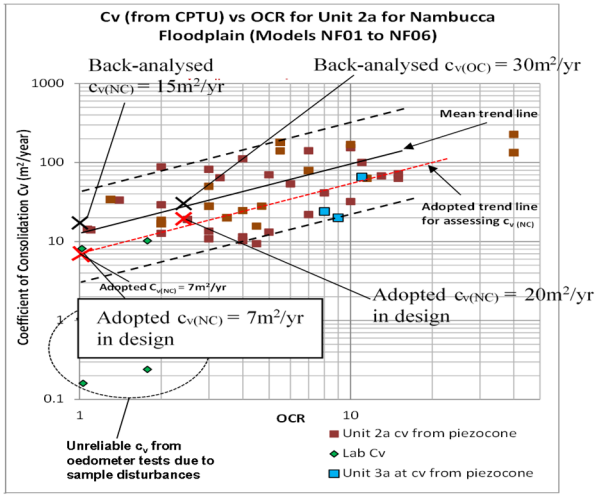

Fig. 7 – c_v vs. OCR for Unit 2a from WC2NH project

During the design stage, a conservative design trend line of c_v vs. OCR was adopted (on the safe side of the median line) and the adopted design $c_{v(NC)}$ and $c_{v(OC)}$ values were 7 m^2/yr and 20 m^2/yr, respectively. During construction, the back-analyzed $c_{v(NC)}$ and $c_{v(OC)}$ were 15 m^2/yr and 30 m^2/yr. These back-analyzed values, while greater than the design values, are more aligned with the median trend line as. The linear c_v vs. OCR trend shown in Fig. 7 is material type specific. Poon and Chan (2015) have shown that similar linear trends can be created for

other soil types on the double log space. But the slope and y-intercept (i.e. $c_{v(NC)}$ at OCR = 1) would be different and are dependent on LL.

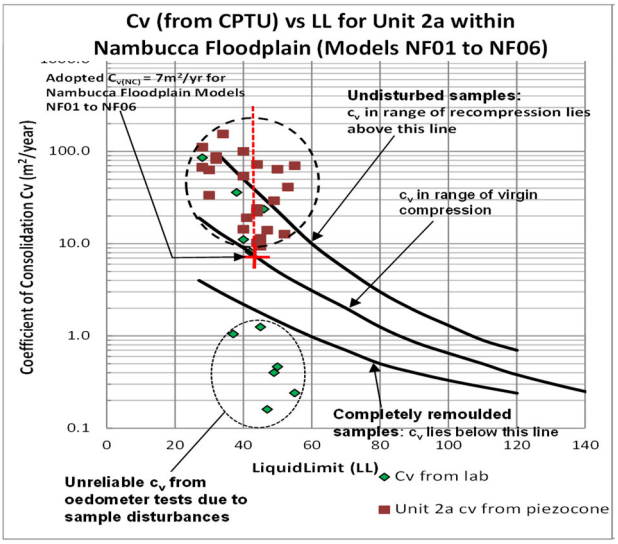

Fig. 8 – c_v vs. LL

For ground treatment using prefabricated vertical drains, the smear zone characteristic such as the smear radius ratio and the permeability ratio should also be considered. For design and back-analysis purposes, the smear radius ratio of 11 and permeability ratio of 2 based on the research works by Indraratna et al. (2015) may be applied.

4 ANALYTICAL TECHNIQUES

For back-analysis purposes, it is the Authors' preference to deploy simple 1D consolidation model in which creep settlement is assumed to commence at the end of the primary consolidation. Notwithstanding this, a more sophisticated Soft Soil Creep (SSC) model that is embedded in the software program PLAXIS 2D has gained much popularity in recent years. This model utilizes a form of time-dependent concepts of Modified Cam-Clay and visco-plasticity, thus taking into account of the simultaneous nature of primary consolidation and creep. This section provides some remarks on the use of SSC for back-analysis.

Permeability – In the FEA model, c_v is not a direct input, but is a composite parameter that depends on both the coefficient of permeability, k, and the coefficient of volume compressibility of the soil, m_v. The m_v value is calculated within the FEA program based on the input parameters of CR and RR, whereas k is related to the void ratio, e, in accordance with the permeability function: $e = e_0 + c_k \log(k/k_0)$, where e_0 is the initial void ratio, k_0 is the initial permeability value and c_k is the permeability index. k_0 and c_k are the input parameters to FEA to define the permeability function. For clays, k_0 is typically about 1e-4 m/day. k_0 can be also be converted from c_v using the following equation:

$$k_0 = k_v = 0.434 \times CR \times c_v \times \gamma_w/\sigma'_v \quad (3)$$

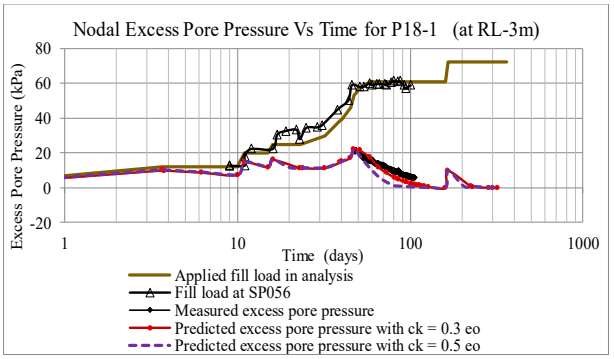

Fig. 9 – Comparison of large strain SSC using $c_k = 0.3\ e_0$ and $c_k = 0.5e_0$ with measured excess pore pressure

The permeability index c_k is an influential parameter that affects most of the post peak excess pore pressure dissipation rate. The smaller the c_k value, the slower is the rate of excess pore pressure dissipation, and the flatter is the slope of the predicted excess pore pressure vs. log time curve after fill placement as demonstrated by an example presented in Fig.9. Tavenas *et al.* (1983) proposed a correlation of $c_k = 0.5e_0$, but can be as low as $c_k = 0.25e_0$ as pointed out by Chan *et al.* 2018.

Buoyancy effect – Fig. 10 shows a fitted settlement-time curve for a settlement plate on WC2NH project. Using the same set of back-analyzed parameters from 1D analysis, it can be seen that the prediction given by the 2D FEA with SSC model overestimate the measured settlement. Noted that the FEA undertaken was a small strain analysis applying a constant load with time after fill placement. However, the embankment has settled a maximum of 1.1m during the preloading period. Part of the fill material that was originally above the ground water table (GWT) has settled below the GWT (GWT near ground surface). This entailed a load reduction of about 10kPa ≈ (1.1-0.1)×10kN/m^3. To investigate the buoyancy effect, a large strain 2D FEA with SSC model was conducted with updating mesh and pore water pressure. As can be seen in Fig. 10, the buoyancy effect has compensated the creep settlement accumulated during primary consolidation, leading to relatively reasonable estimate of the settlement compared to the measurements. The settlement prediction shown in Fig. 10 has demonstrated an important point that while the simple 1D analysis gives a similar predicted settlement-time curve compared to that given by the sophisticated large strain SSC FEA, its theoretical considerations were far less rigorous than the latter. Simple soil model could be used more consistently with simple numerical method (e.g. updating mesh or buoyancy effect

may not be necessary), whereas complex soil model is best to be used in conjunction with sophisticated computational approaches (e.g. large strain analysis with updating mesh and pore water pressure). Mixing complex soil models with simplified computational approaches, or vice versa, may not give desirable outcomes

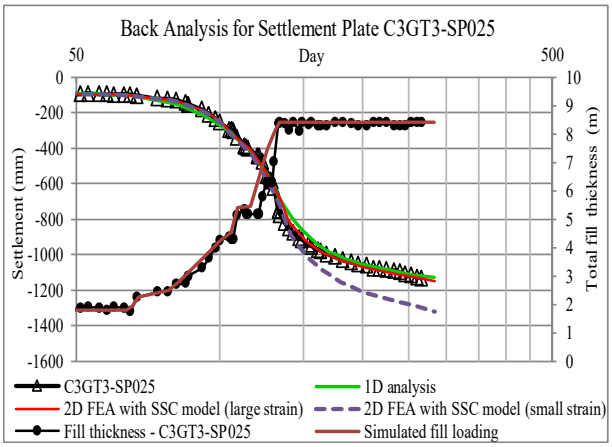

Fig. 10 – Numerical analysis results with measured settlement plate data (from WC2NH project)

5 CONCLUSION

The following points can be made regarding the preload and surcharge release process:

- For the assessment of DoC using Asaoka's method, the use of small time interval Δt should be avoided. Edil *et al*. (1991) proposed a parameter j_{95} and recommended that Δt to be chosen to give a j_{95} value between 10 and 30. The use of hyperbolic method to assess DoC is attractive due to its simplicity without the need to consider Δt. The settlements predicted by hyperbolic method are usually slightly larger than those from Asaoka's method. The assessment of DoC should also consider the excess pore water pressure measured from the VWP. It is important to correct the measured total pore water pressure from VWP data for the increase in pressure head due to the settlement of piezometer under load.
- The main factors affecting the predicted total settlement in the back-analysis are (i) soil stratigraphy and soil depth, (ii) adopted OCR values and (iii) ground water level. These elements should be reviewed based on the nearest CPTs to the monitoring location as opposed to relying on the original design model.
- SHANSEP equation with parameters m = 0.95 and S = 0.22 has been used to back-analyzed OCR by the Authors on numerous soft ground projects with success. The $c_{\alpha\varepsilon\,(NC)}$ is best to be correlated with CR based on the law of Mesri.
- c_v is usually used as input 1D consolidation analysis. The back-analyzed c_v values should be compared with field piezocone measurements as well as published correlation. For 2D FEA, the input permeability k is linked to e via c_k, which has a great influence on the post peak excess pore pressure dissipation rate.
- For design and back-analysis purposes, the smear radius ratio of 11 and permeability ratio of 2 based on the research works by Indraratna *et al*. (2015) may be applied.
- For back analysis, simple soil model could be used more consistently with simple numerical method whereas complex soil model is best to be used in conjunction with sophisticated computational approaches (e.g. large strain analysis with updating mesh and pore water pressure). Mixing complex soil models with simplified computational approaches, or vice versa, may not give desirable outcomes

REFERENCES

Asaoka, A. Observational procedure of settlement prediction. Soil Found., 1978. 18 (4), 87–101.

Chan, K., Poon, B. and Darshana P. (2018) Prediction of embankment performance using numerical analyses – Practitioner's approach. Computers and Geotechnics, 93, 163 – 177.

Edil,T.B.,Fox,P.J., Lan,L.T. (1991). Observational procedure for settlement of peat. Proc., Int. Conf. on Geotech. Eng. for Coastal Development Theory and Practice on Soft Ground,'91, Yokohama, Japan, 165–170.

Indraratna, B., Perera, D., Rujikiatkamjorn, C. & Kelly, R. (2015). Soil disturbance analysis due to vertical drain installation. Proc. of the Inst. of Civil Engers: Geotech. Engng, 168 (3) 236-246.

Mesri, G., and Godlewski, P.M. (1977). Time and Stress-Compressibility Interrelationship, Journal of the Geotechnical Engineering Division, ASCE,. 103, No. GT5, pp. 417-430.

Poon B. and Chan, K. (2015) Assessment of the Coeff. of Consolidation for Staged Preloading Operations, 12th Austr. NZ Conference on Geomechanics (ANZ 2015), Wellington, NZ.

Tan, T. S., Inoue, T., and Lee, S. L. (1991) Hyperbolic method for consolidation analysis. J. Geotech. Engrg, 117 (11), 1723–1737.

Tavenas, F., Leblond, P., Jean, P. & Leroueil, S. (1983). The permeability of natural soft clays, Part 2: Permeability characteristics. Canadian Geotech. Journal, 20: 645-660.

Improvement of compressibility characteristics of waste material by dynamic compaction

R.I.A Rathnayaka
Department of Civil Engineering, University of Moratuwa, Sri Lanka

S.A.S. Kulathilaka
Department of Civil Engineering, University of Moratuwa, Sri Lanka

ABSTRACT: Open dumping is the most prevalent method of waste disposal in Sri Lanka. These sites, which are currently used as waste dump yards in urban areas, will have to be rehabilitated to be converted to be used as parks, roads or for other different construction projects. Establishing the strength and stiffness characteristics of these waste materials at different levels of degradation and how these characteristics can be enhanced to suit the proposed developments is a major challenge. This paper presents a study of the effectiveness of dynamic compaction as a technique of enhancing the compressibility characteristics of waste dumps. MSW was subjected to dynamic compaction in a laboratory test setup, and the compressibility characteristics were assessed by conducting the consolidation tests on compacted MSW using the Rowe cell. The effectiveness of the process is compared with that of preloading. Dynamic compaction has improved the compressibility characteristics of MSW but less effective than preloading.

1 INTRODUCTION

1.1 *Background*

Municipal solid waste (MSW) is solid waste resulting from, or incidental to, municipal, community, commercial, institutional, and recreational activities, but not including industrial hazardous or 'special wastes'. According to the Environmental Foundation Limited (EFL)(2021), Sri Lanka generates about 7000MT of solid waste per day with the Western Province accounting for nearly 60% of waste generation. Each person generates an average of 0.4-1kg of waste per day.

For the last 20-30 years, government institutions have attempted to figure out the best waste management strategy for the country. Nevertheless, open dumping still remains to be the most common method of disposal of municipal solid waste (MSW) due to low cost and less processing involved.

Rapid development in urban areas in the past decades has created a high demand for lands. The lands, which were use as open dumping yards in the past, can be consider as valuable sources that are capable of fulfilling this demand to some extent. Therefore, the sites, which are currently used as waste dumping yards, will have to be rehabilitated in order to be converted to be used as parks, roads or many other construction projects.

The strength and stiffness characteristics of these waste materials are in different levels of degradation and how these characteristics can be enhanced to suit the proposed development is a major challenge. This study was done to assess the effectiveness of dynamic compaction as a viable and economical technique of enhancing the compressibility characteristics of waste dumps.

1.2 *Background knowledge*

According to Naveen et al (2018), determination of the geotechnical properties of waste is challenging because of the heterogeneity of the material. Durmusoglu et al. (2006) reported that, although principles of the general soil mechanics are usually applied because of high deformability and microbial decomposition of waste, application of the principles of the soil mechanics to waste is problematic.

The mechanisms of settlement that govern the solid waste material are numerous and complex. Bowders et al (2001) reported that there are many reasons behind this behaviour of waste such as extreme heterogeneity of the wastes, their own particle deformability, the large voids present in the initial waste fill, and their biodegradability. Settlements of MSW are not as well understood as those for soils and are more difficult to estimate

According to Watts and Charles (1990) and Manassero et al. (1996), the settlement behaviour of MSW is often classified as occurring in several distinct phases.

1.2.1 *Primary compression of waste*

Primary consolidation of solid waste occurs due to the self-weight of the waste or application of surcharges such as fill over the time. Bajarngard et al (1990) and Stulgis et al. (1995) reported that previous data on waste settlements have indicated that

primary compression of waste fills complete in 10 to 90 days after dumping.

1.2.2 *Secondary compression of waste*

Primary compression is then followed by the secondary compression. Secondary compression occurs due to biodegradation process in waste fill, and it can take years for this settlement to complete depending upon varies phases of waste that it consists as mentioned above. Wall and Zeiss (1995), reported that the biodegradation components of long term (secondary) compression or bio consolidation is due to a process by which solid organic particles in the waste are solubilized and converted to methane and carbon dioxide.

1.2.3 *Dynamic compaction*

Late French engineer Louis Menard invented dynamic compaction in 1969. Dynamic compaction (DC) is a ground improvement technique by transmitting high-energy impacts to the ground. A conventional crane may be used to repeatedly raise and drop a tamper from a predetermined height in a grid to achieve a target maximum depth of improvement.

According to Van Impe and Bouazza (1996), use of dynamic compaction for the densification of MSW can be considered as a challenging task due to many reasons such as:

- Moisture condition of waste fills mainly depend on rain and cannot be expected to have optimum conditions for compaction.
- Secondary compression of solid waste occurs due to biodegradation, and it can take up to 20-25 years after the dumping for it to complete.
- The composition of solid waste varied significantly and a uniform composition (such as in a soil) cannot be expected.

The effect of the dynamic compaction depends on the saturated and unsaturated conditions of the waste fill. Usually, a waste fill is designed to be above the phreatic line and can be considered as unsaturated. If the fill is unsaturated, the dynamic energy will directly transfer to the waste material and compaction will occur in a quick manner.

2 METHODOLOGY

2.1 *Overview*

The following steps were followed in order to achieve the objectives of the study.

I. A detailed literature review was carried out to identify results of other research done regarding compressibility characteristics of waste material.
II. MSW samples were collected and prepared in order to carry out the testing.
III. A dynamic compaction apparatus was fabricated in order to simulate the field conditions in the laboratory.
IV. Prepared waste samples were compacted using the dynamic compaction apparatus and compacted waste sample was extruded using a cutter.
V. MSW samples in both compacted as well as in un-compacted state subjected to loading in a Rowe Cell of diameter 150 mm and height 50 mm.
VI. Results were analyzed to establish the characteristics related to compressibility such as; coefficient of volume compressibility (m_v), compressibility index (C_c), coefficient of consolidation (C_v) and coefficient of secondary compression ($C\alpha$).
VII. Results were compared to assess the effect of dynamic compaction on compressibility characteristics of MSW.

2.2 *Collection and preparation of MSW samples*

Municipal solid waste used in this study was collected from Meethotamulla landfill site that had been used for waste dumping for more than 20 years.

There are some limitations on the maximum particle size, which can be used for specimen preparation. Typically, the largest particle size should be 1/6 of the specimen diameter. As the Rowe cell diameter is 150 mm, largest particle size should be about 25mm. Hence, fragments greater than 25mm of MSW either were discarded or, where possible, were broken/cut to make them fit inside the cell.

2.3 *Determination of basic parameters of MSW*

Density of the MSW sample before and after the compaction were measured using the water replacement method in the prepared test pit.

In order to determine the specific gravity, laboratory specific gravity tests were conducted using a pycnometer with a volume of 1000ml and generally followed the procedure used for soil testing as per the ASTM D854.

In order to determine the moisture content air-dried method was adopted for specimens obtained from tested samples.

The basic parameters of MSW are presented in table 01.

The density values observed in this study can be considered as low for MSW compared to the values reported in the literature. This is most likely due to the difference in the composition of MSW used in this study.

Table 1. Basic Parameters of MSW

Test Set	Sample Condition	Bulk Unit weight (kg/m^3)	Specific Gravity	Moisture Content (%)
1	Compacted	873.45	1.41	21.4
2	Non-compacted	493.41		20.2

2.4 *Determination of waste composition*

Waste classification framework proposed by Dixon and Langer (2006) is used in this study based on the relevancy to nature of MSW in Sri Lanka. Composition of MSW is presented in table 2.

Table 2. Composition of MSW sample

Material Type	%
Soil like	36.2
Paper/ Cardboard	0.00
Flexible plastics/ Rigid plastics	24.5
Rubber	0.00
Metals	0.00
Glass, Minerals	14
Wood, Textiles	20.3
Miscellaneous	5
Total	100

As fragments greater than 25mm of MSW specimen used in this study were broken/cut to make them fit inside the cell, subdivision of component in each material group based on shape related properties was not carried out in this study.

2.5 *Aspects of dynamic compaction apparatus*

To simulate the field dynamic compaction in the laboratory, a dynamic compaction mechanism was prepared. A hume pipe of a diameter of 4 ft and a height of 4 ft was installed on the ground. Soil was placed inside to a height of 300mm in two layers and compacted.

A hole of plan dimensions 400 mm x 400 mm and depth of 200mm was made within the compacted soil in the Hume pipe to fill/compact the waste samples. Fig. 1 and fig. 2 presents the arrangement for the dynamic compaction.

Dynamic compaction through free falling of the weight was achieved using an electromagnet and a pulley mechanism (Fig 3). A weight of 31.8 kg was dropped from a height of 1 m on the waste. The weight was dropped 20 times on the same location in order to achieve the compaction. Weight was lifted to the top again by a rope. In a field operation the weight would be dropped appropriate number of times in a grid pattern covering the area to be improved. Several cycles of dropping will be done by increasing the weight and height in later stages.

According to Van Impe and Bouazza (1996) depth of improvement of MSW by dynamic compaction is given by;

$$D = n\sqrt{WH} (1)$$

Where D is the depth of influence (m), W is the weight of the pounder (tons), H is the drop height (m) and n is a coefficient that accounts for soil type, type of pounder, etc.

Zekkos et al. (2013) has suggested an n value of 0.4 ± 0.05 for MSW regardless of the age. Using this value the achieved depth of improvement is 84 mm. As a sample thickness about 50mm was to be used inside the Rowe cell, this depth of improvement was adequate.

After the dynamic compaction, samples were extruded using a cutter with a diameter of 150 mm.

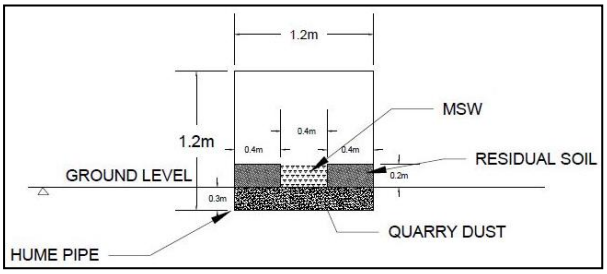

Fig.1 Cross section of the dynamic compaction arrangement

Fig.2 Arrangement for dynamic compaction

2.6 *Testing of MSW samples*

Rowe Cell of diameter 150 mm was used for performing compressibility tests. Head (1997) stated that vertical single drainage with equal strain test method is the test closely related to traditional Oedometer tests and settlement reading can be directly related to volume change measurement in the

drainage line. Hence, vertical single drainage with equal strain test method is selected for the testing.

Two MSW samples were tested using the Rowe cell (Fig. 4) One sample was from the MSW subjected dynamic compaction and the second sample was from the non-compacted MSW.

For the two samples, two different loading sequences were implemented. Compacted MSW sample was subjected to only loading and unloading increments. The non-compacted MSW sample was subjected to loading, unloading and reloading increments. Reloading increments in the non-compacted sample would represent the behaviour of the MSW subjected to preloading. Compacted sample was not taken through reloading increments.

Fig. 3 Free falling of the weight and lifting up by rope

Fig.4 Sample loaded in the Rowe cell

3 RESULTS AND DISCUSSION

3.1 *Variation of compression index (c_c) and recompression index (c_r)*

Void ratio was evaluated with the average specific gravity obtained and plots were done to compute compressibility indices. Fig.5 presents the e vs. log (σ) curves for compacted and non-compacted samples.

The indices computed using e vs. log (σ) graph are presented in Table 3.

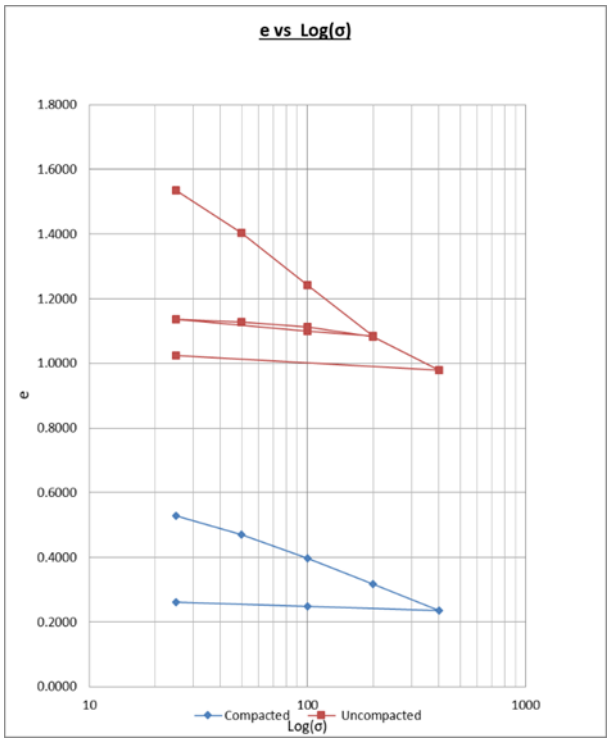

Fig. 5 e vs log (σ) curve for compacted and non-compacted MSW samples

Table 3. Compression index and recompression index values

Test Set	Values of compression index (C_c)	Values of recompression index (C_r)
Sample 1 (Compacted)	0.2373	-
Sample 2 (non-compacted)	0.4906	0.0537

The compression index of MSW that was subjected to dynamic compaction has reduced to about 50 % of that of the non-compacted MSW. But the recompression index of non-compacted sample was only about 10% of its compression index.

The C_r values represent the primary consolidation behaviour of a preloaded MSW. The much-reduced C_r values indicate that the reduction of primary consolidation settlement of MSW achievable by preloading is much greater than that achievable through the dynamic compaction.

3.2 *Variation of coefficient of volume compressibility (m_v)*

The coefficient of volume compressibility, m_v values decreased as the effective stress increases in

both compacted and non-compacted samples (Fig 6). The m_v value of non-compacted sample during reloading increments were much smaller than those of compacted samples. As the over consolidation ratio approached unity those values approached the values of compacted sample.

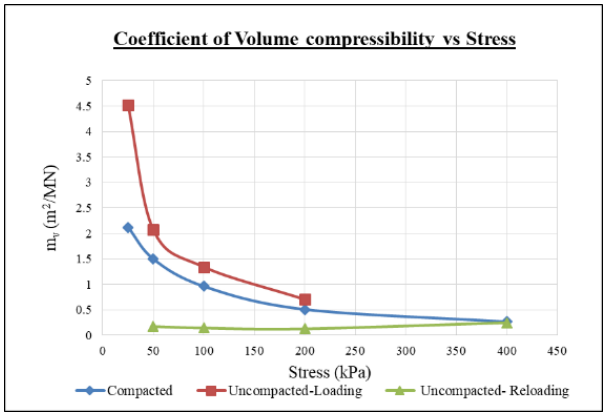

Fig. 6 Variation of volume compressibility

These results indicate that the compressibility of MSW can be reduced more by preloading as compared to the dynamic compaction.

3.3 *Variation of coefficient of secondary consolidation (c_α)*

The settlement curves of MSW are similar to those of peaty clay and a reduction of gradient could not be identified with time (Fig.7). This is an indication that MSW exhibit high secondary consolidation. Coefficient of secondary consolidation C_α values for different loading and reloading stages are presented in Fig 8. However, these magnitudes are lower than that of peaty clay.

In general, $C_\alpha$values increased with the stress level in the loading increments. The dynamic compaction process has caused a significant reduction of coefficient of C_α. The preloading process has also caused a significant reduction of C_α.The $C_\alpha$values in reloading increments with higher over consolidation ratios were much smaller compared to those of compacted sample. In reloading increments $C_\alpha$values increased as the over consolidation ratio approached unity.

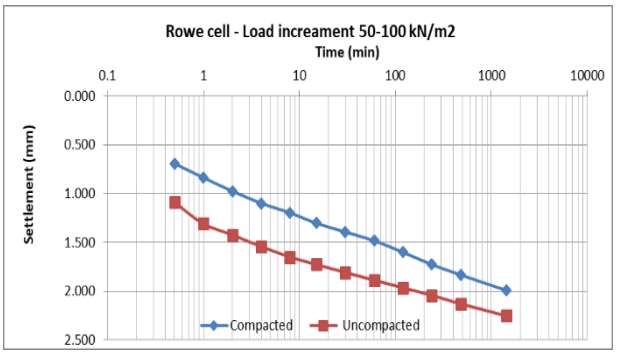

Fig.7 Settlement vs log (time) curve for compacted and non-compacted samples

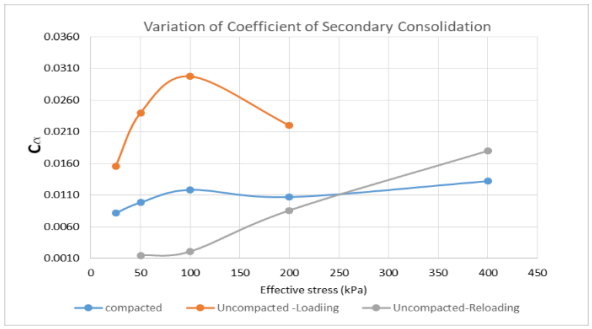

Fig. 8 Variation of coefficient of secondary consolidation

According to the Lewis et al. (2004), dynamic compaction was more effective in reducing the rate of secondary settlement of landfill as compared to the preloading. According to them C_α ranges from 0.0153 to 0.0513 with an average value of 0.0313 for the landfill material treated by dynamic compaction and C_α ranges from 0.0529 to 0.0817 with an average value of 0.0657 for the landfill material treated by preloading. These values are higher than the values observed during this study. Difference in the results may be due to the difference of the degradation stages and composition of the MSW.

3.4 *Variation of coefficient of consolidation (c_v)*

The coefficient of consolidation C_v is essential to predict the rate of settlement of MSW sites. The value of the coefficient of consolidation (C_v) is estimated here using laboratory consolidation test results.

In the soil, engineering practices Taylor's square root of time fitting method and Casagrande's logarithm of time fitting method are the two widely used methods to find coefficient of consolidation. However, when the shape of the settlement curves do not confirm the standard shapes proposed by the Casagrande and Taylor. Rectangular hyperbola method (Sridaran 1981, Selig et al 1985) and velocity method (Parkin 1978) can be used as better alternative methods. Hence, these two methods were considered to find the coefficient of consolidation for each loading step in order to identify the settlement characteristics of MSW.

Fig. 9 and fig.10 presents the variation of C_v values obtained. Values of coefficient of consolidation obtained by both methods are showing the same trend on increasing stress level. Apart from the initial increment of 0–25 kN/m^2 the coefficient of consolidation values were of the same order at higher stress levels. These values are quite high as compared to those of conventional soils.

C_v values obtained by both methods were of the same order at higher stress levels. The dynamic compaction process has caused a reduction of the value. The higher C_v values indicate that the pore

pressure dissipation during an improvement process would be quite rapid.

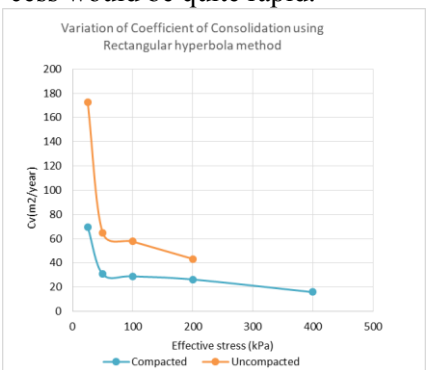

Fig.9 Variation of C_V(Rectangular hyperbola method)

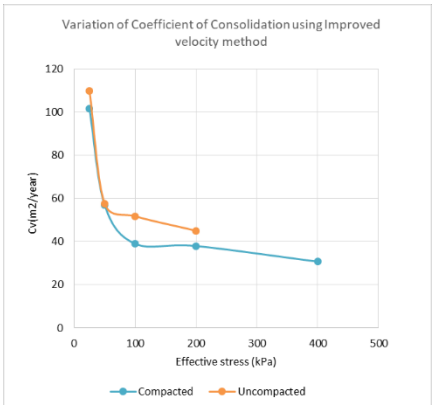

Fig.10 Variation of C_V (Improved velocity method)

4 CONCLUSION

Open dumping is the predominant method of MSW management in Sri Lanka. The failure to address issues in open dumping of MSW in a timely manner has resulted in unsanitary eyesores in Karadiyana, Bluemendhal, Meethotamulla, Kolonnawa etc. These sites, which are currently used as waste dump yards in urban areas, will have to be rehabilitated for various construction projects. It is important to understand the compressibility characteristics of waste material before embarking on these development projects.

Preloading and dynamic compaction both are possible methods in reducing the compressibility of waste material and in this study effectiveness of both methods were evaluated and compared.

Compression index of MSW that was subjected to dynamic compaction was reduced about 50 % of the compression index of the non-compacted MSW. Recompression index values of non-compacted MSW values are less than about 10% of compression index values of non-compacted MSW samples. Similarly, results obtained for coefficient of volume compressibility shows greater reduction by preloading compared to the dynamic compaction. Both preloading and dynamic compaction shows significant effectiveness in reducing the coefficient of secondary consolidation.

Compressibility characteristics of MSW can be improved significantly using both preloading and dynamic compaction. According to results observed in this study preloading can be considered as the more effective method. However, considering the time it takes to achieve the required compressibility reductions by preloading, dynamic compaction can be considered as another advantageous option.

REFERENCES

Bjarngard, A., and Edgers, L. (1990). "Settlement of Municipal Solid Waste Landfills". The thirteenth Annual Madison Waste Conference, 192-205.

Bowders, J., Roth, N., Loehr, E., Russell, M., Klouzek, A., and Bouazza, M. (2001). "Municipal solid waste settlement". Missouri Waste Control Coalition Conference, Columbia Missouri.

Dixon, N., and Langer, U. (2006). "Development of a MSW classification system for the evaluation of mechanical properties". Waste Management, 26(3), 220-232.

Durmusoglu, E., Sanchez, I., and Corapcioglu, M. (2006). "Permeability and compression characteristics of municipal solid waste samples". Environmental Geology, 50(6), 773-786.

Environment Foundation (Guarantee) Limited."Status of Waste Management in Sri Lanka." (2021).<https://efl.lk/status-waste-management-sri-lanka.> (May 27, 2021).

Head, K. (1980). Manual of soil laboratory testing. Pentech Press, London.

Manassero, M., Van Impe, W. and Bouazza, A., 1996. Waste disposal and containment. In: International Congress on Environmental Geotechnics. A.A. Balkema, Rotterdam, pp.1425-1474.

Naveen, B., Sivapullaiah, P., and Sitharam, T. (2018). "Appropriate Method of Determination of Coefficient of Consolidation for Municipal Solid Waste". Geotechnical Testing Journal, 41(6).

Parkin, A. (1978). "Coeffcient of consolidation by the velocity method". Géotechnique, 28(4), 472-474.

Selig, E., Sridharan, A., and Prakash, K. (1985). "Improved Rectangular Hyperbola Method for the Determination of Coefficient of Consolidation". Geotechnical Testing Journal, 8(1), 37.

Sridharan, A., and Rao, A. (1981). "Rectangular Hyperbola Fitting Method for One Dimensional Consolidation". Geotechnical Testing Journal, 4(4), 161.

Stulgis, R., Soydemir, C. and Telgener, R., 1995. Predicting landfill settlement. In: Geoenvironment 2000: Characterization, Containment, Remediation, and Performance in Environmental Geotechnics. Pp.980–994.

Van Impe, W., and Bouazza, A. (1996). "Densification of domestic waste fills by dynamic compaction". Canadian Geotechnical Journal, 33(6), 879-887.

Wall, D., and Zeiss, C. (1995). "Municipal Landfill Biodegradation and Settlement". Journal of Environmental Engineering, 121(3), 214-224.

Watts, K., and Charles, J. (1990). "Settlement of recently placed domestic refuse landfill.". Proceedings of the Institution of Civil Engineers, 88(6), 971-993.

Zekkos, D., Kabalan, M. and Flanagan, M., 2013. Lessons Learned from Case Histories of Dynamic Compaction at Municipal Solid Waste Sites. Journal of Geotechnical and Geoenvironmental Engineering, 139(5), pp.738-751.

Strength Analysis of Improved-Soil Pertinent to Shallow Ground Stabilization: A Meta-Analysis

C. M. Malalathunga

Faculty of Engineering and Technology, University of Wolverhampton, Sri Lanka

K. H. S. M. Sampath

Department of Civil Engineering, University of Moratuwa, Sri Lanka

ABSTRACT: Due to the increasing pace of urbanization in Sri Lanka, the necessity for rapid and stable construction has arisen. Ground improvement is one of the most crucial stages of construction which ensures the stability and the safety of the structure. Among multiple options, quarry dust is mainly used as a low-cost, eco-friendly stabilizer to increase the strength and to achieve low settlements underneath foundations. Through several experimental analyses conducted on assessing the superiority of quarry dust as an admixture, it is already established that quarry dust is a viable solution for ground improvement. However, rather than sticking to experimental-based results, it is better to conduct meta-analyses using already available experimental data to predict the strength characteristics under different conditions. This research is focused on using statistical tools to predict the strength parameters pertinent to shallow ground improvement – i.e., cohesion and friction angle, using three influential input parameters. The analysis is carried out using linear regression analysis (LRA) and a machine learning technique called artificial neural network (ANN) modelling. The results indicate that although the general statistical tools like LRA fails to capture the complex inter-relationships between input and output parameters, more advanced ANN models can accurately predict the strength variations under given conditions. Hence, the ANN models can be used to partially replace the experimental analyses and expedite the determination of strength parameters using already available experimental data.

1 INTRODUCTION

Soil problems are a regular occurrence in the construction industry. In fact, the poorer soil present in most construction sites may limit the ability of intended structures, as the earth can readily fail when loaded. Hence, a suitable ground improvement technique should be adopted to improve the ground profile prior to the construction. Mixing the in-situ soil with aggregate material which are already available in the industry would improve the strength, which in turn significantly improve the bearing capacity of the soil.

Despite the fact that sand-soil mixes can improve strength, quarry dust is an excellent substitute for sand because it is inexpensive and has adequate strength characteristics. The rising expense of soil stabilizers, along with the need to save waste disposal costs have prompted a worldwide focus on the beneficial use of wastes in engineering applications. Due to the harmful effects of these materials on environment and the health risks they pose, the safe disposal of industrial wastes necessitates quick and cost-effective solutions. Quarry dust is a waste product created during the stone crushing process and using it for ground improvement is an advantageous method to put it to good use. In fact, in each crusher, quarry dust is left out as a waste material of about 20-25% of total production (Soosan et al., 2005).

There are numerous experimental data available on assessing the use of quarry dust for shallow ground improvement under different in-situ conditions and under different construction sequences (Sabat, 2012, Thirumalai, 2017). These include the analysis of different soil types, applied loads, ground conditions, etc. The availability of large amount of experimental data triggers the possibility of conducting meta-analyses or statistical analyses that contributes to strengthen the knowledge on this aspect. The use of statistical tools like linear regression analysis (LRA) and machine learning techniques like artificial neural networks (ANN) are becoming popular in analyzing these types of problems because of their proven higher accuracy (Bong et al. 2020). Use of statistical tools and soft computing models to intelligently predict the strength variations of stabilized soil will be a game changer in this field.

Therefore, the main focus of this research is to determine the behavior of shear strength parameters (i.e., cohesion and friction angle) of weak in-situ soil mixed with different proportions of quarry dust through a rigorous meta-analysis – which will be achieved using conventional statistical tools as well as advanced soft computing models. Number of data

sets are collected from various studies and statistical models are developed to assess the viability of predicting strength parameters of stabilized soil. The accuracy of the developed models is tested with several statistical indices.

2 COLLECTION OF DATA AND SELECTION OF INPUT AND OUTPUT PARAMETERS

Data for the statistical analyses have been collected from several previous research (Sridharan et al, 2006, Banerji et al, 2017, Nayak et al, 2012, Pradeep et al, 2016). In fact, Sridharan et at. (2006) used five soil types (i.e., red earth, red earth II, laterite, kaolinite, wet marine clay and dry marine clay) and quarry dust from different locations and analyzed variation of soil strength with quarry dust percentage (QDP), optimum moisture content (OMC) and maximum dry density (MDD). Banerji et at. (2017) used sub grade soil and analyzed soil characteristics such as Atterberg limits, OMC, MDD, soaked CBR, dry CBR, cohesion and friction angle. Nayak et al. (2012) performed experiments on lithomarge clay and assessed geotechnical parameters like Atterberg limits, MDD, OMM, UCS, friction angle, cohesion, and coefficient of permeability. Pradeep et al. (2016) collected laterite soil with low bearing capacity and analyzed the Atterberg limits, MDD, OMC, friction angle and cohesion.

Although, numerous parameters are collected from previous experimental analyses, all the parameters are not consistent throughout all the studies. Hence, the statistical analysis is carried out by selecting specific parameters that are common to all the studies. Therefore, by considering the availability of experimental data and their consistency, this statistical analysis utilizes three input parameters, which are optimum moisture content (OMC), maximum dry density (MDD) and Quarry dust percentage (QDP). Cohesion and friction angle are selected as the output parameters because the focus of this study is to predict the variation of strength parameters of quarry dust-mixed soil under given conditions. The summary of the selected input and output parameters and their respective data range are summarized in Table 1.

Table 1. Input and output parameter ranges utilized in the statistical models

	Parameters	Range
Input	OMC (%)	11 – 32.5
	MDD (kN/m^3)	12.9 – 20.5
	QDP (%)	0 - 100
Output	Cohesion (kPa)	6 - 42
	Friction Angle (°)	9 - 43

The models are trained with 41 data sets collected from previous research and the model is tested using 10 independent data sets to confirm their accuracy on predicting the output parameters.

3 META-ANALYSIS

3.1 *Linear Regression Analysis (LRA)*

Linear Regression Analysis (LRA) solves data sets using least square fit by generating a regression matrix, solving simultaneous equations, and determining coefficients using the backslash operator. The generalized equation between independent (x_i) and dependent (y) variables can be given in the form of equation (1).

$$y_t = b_0 + b_1 x_{1t} + b_2 x_{2t} + \cdots + b_n x_{nt} \quad (1)$$

According to this formula, the forecast for "y" is a straight-line function of each of the "x" variables, maintaining the rest constant, and the contributions of distinct "x" variables to the predictions are additives. The constants $b_1, b_2 \ldots . b_n$ – the so-called coefficients of the variables, are the slopes of their unique straight-line interactions with "y". The coefficients and intercept are calculated using least squares, which means they are set to the unique values that minimize the sum of squared errors within the data sample to which the model is fitted. The model's prediction errors are regularly distributed, independently and identically measured.

3.2 *Artificial Neural Network (ANN) Modelling*

The utilized artificial neural network (ANN) consists of three layers: 1) input layer, 2) hidden layer and 3) output layer (see Figure 1). Performance of the model is dependent on the number of hidden layers. Although higher number of data sets yield accurate predictions, that will increase computational burden. Each layer has a number of processing units known as neurons. Overfitting/underfitting of the data can happen when there are too many/less neurons, respectively (Sampath et al, 2019). The network response is deduced from the activity of these neurons. The formal neurons will calculate the sum of its inputs $(x_1, x_2 \ldots . x_n)$ for any integer $j = 1$ and any number n.

$$x_i = (x_1, x_2, x_3 \ldots \ldots, x_n) \quad (2)$$

Hidden layer of net input values will be:

$$Net_j = \sum_{j=1}^{n} x_i w_{ij} + \theta_j \quad (3)$$

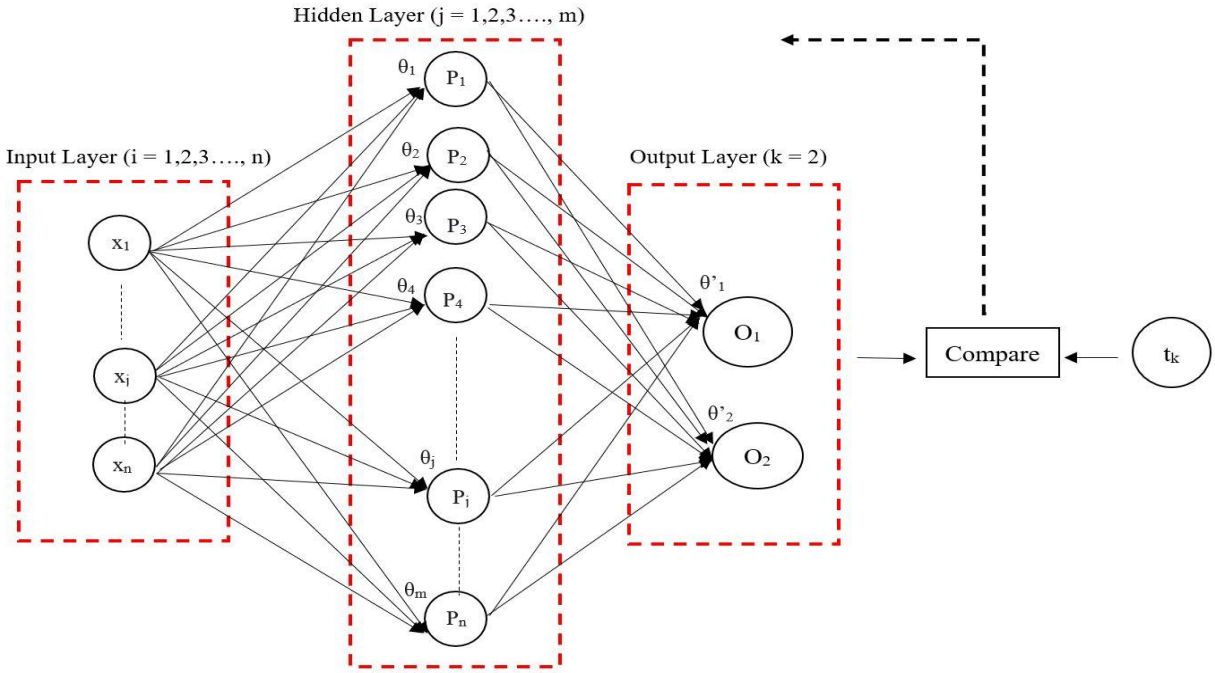

Fig. 1 - Network architecture of ANN model

Where, input unit is x_i, w_{ij} denotes the weight on the link between j^{th} neuron and i^{th} input and θ_j is bias in the j^{th} neuron.

Calculation of the net output from the hidden layer is done using activation function $(f_{(n)})$ as in the equation (4). For the activation function also known as transfer function, "hyperbolic tangent sigmoid transfer function (TRANSIG)" is used as mentioned in the equation (5).

$$P_j = f(Net_j) \tag{4}$$

$$f(n) = \frac{2}{1+e^{-2n}} - 1 \tag{5}$$

For the output layer (i.e., for 3rd layer), the net input is,

$$Net_k = \sum_{j=1}^{m} P_j W_{jk} + \theta'_k \tag{6}$$

The result of the output layer (i.e., the anticipated value from the ANN model) is,

$$O_k = f(Net_k) \tag{7}$$

The predicted outputs are then compared with the desired output. k^{th} output error in output layer is given by,

$$e_k = t_k - O_k \tag{8}$$

Where desired output is t_k while ANN predicted output is O_k. The mean squared error function (MSE) determines the overall error function.

$$E = \frac{1}{n}\sum_{j=1}^{m}(t_k - O_k)^2 \tag{9}$$

Once the error for a forward pass has been calculated, the training of the network is essentially a process of minimizing the error to identify the best weights and biases. The TRAINGDX function, which combines adaptive learning rate and momentum training is used to lower the error surface, whereas adaptive learning function LEARNGDM is used to calculate the weights.

An epoch is a pass through all the training patterns. This approach is repeated for a user specified number with each data set allocated for network training, until the error becomes minimal. Table 2 lists the model parameters utilized in this research. The parameters are selected through a trial-and-error process, in which a careful attention is paid to optimize the model by increasing the accuracy, while minimizing the computational burden.

Table 2. Parameters of ANN model

Parameter	Value
Number of input parameters	3
Number of output parameters	2
Number of hidden layers	1
Number of hidden neurons	8
Number of training epochs	1000
Number of training data sets	41
Number of validation data sets	10
Network type	Feed-forward back-propagation
Transfer function	TANSIG
Error (Performance) function	MSE
Training function	TRAINGDX
Adaptation learning function	LEARNGDM

4 RESULTS AND DISCUSSION

4.1 *Linear Regression Analysis (LRA)*

Linear Regression Analysis (LRA) was executed with 41 data sets and validated using 10 independent data sets for both cohesion and friction angle separately. The results of LRA at both training and validation stages are given in figure 2 and figure 3, respectively. It is noticeable that in both cases the scattered data deviate from 1:1 line, confirming that the LRA fails to give accurate predictions for the cohesion, based on the available data. This is further confirmed by the R^2 value, which is only 0.7171 and 0.8695 at both training and validation stages, respectively. This confirms that the developed model is not capable of predicting the cohesion values in a precise manner. However, based on the LRA results, a linear relationship between the output parameters (i.e., cohesion (C)) and the input parameters (i.e., $QDP\ \%, OMC\ and\ MDD$) is given in equation 10. This equation may be used to roughly predict the cohesion value of a soil sample based on the given input parameters.

$$C = 0.75(OMC) + 4.42(MDD) - 0.33(QDP) - 55.1 \quad (10)$$

Where, C is the cohesion, OMC is the optimum moisture content in %, MDD is maximum dry density in kN/m^3 and QDP is quarry dust percentage.

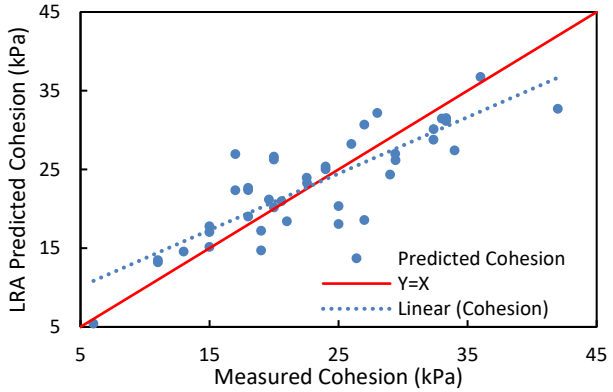

Fig. 2 - Relationship between measured and LRA-predicted cohesion at training stage.

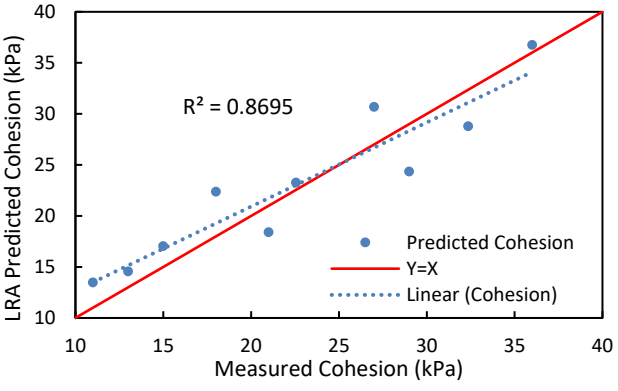

Fig. 3 - Relationship between measured and LRA-predicted cohesion at validation stage.

LRA analysis was done for friction angle prediction using the same input data sets and validated with 10 data sets similar to cohesion analysis. The scattered plots of the friction angle prediction at both training and validation stages are given in figure 4 and figure 5, respectively. It is noticeable that at the training phase, the dispersed data deviates from the 1:1 line, indicating that the LRA fails to provide reliable predictions for the friction angle based on the existing data. This is further supported by the lower R^2 value of just 0.8196. However, the R^2 at the validation stage yields somewhat moderate value of 0.9212, indicating a better relationship compared to cohesion model. Based on the LRA results, a linear relationship between output parameter (i.e., friction angle) and the input parameters is developed as presented in equation 11. If the given input values are known, this equation can be used to predict the friction angle of a soil sample improved with different quarry dust mix proportions.

$$FA = 1.72(OMC) + 7.82(MDD) + 0.03(QDP) - 137.5 \quad (11)$$

Where, FA is the friction angle.

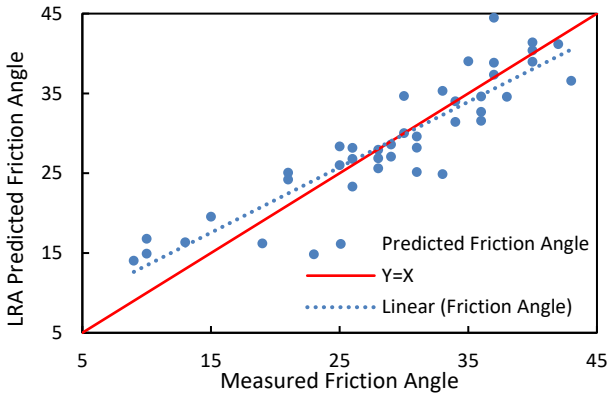

Fig. 4 - Relationship between measured and LRA-predicted friction angle at training stage

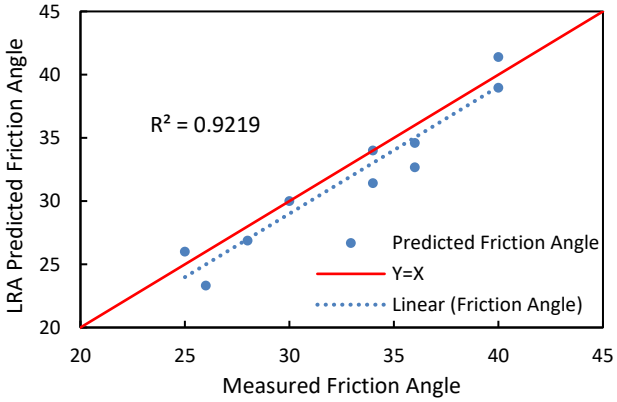

Fig. 5 - Relationship between measured and LRA-predicted friction angle at validation stage

4.2 *Artificial Neural Network (ANN) Modelling*

The relationship between input and output parameters determines the efficiency of input data and their capacity to effectively predict the output (target) (Mikaeil et al., 2017). A rial and error method was used to select the optimum artificial neural network structure as explained in section 3.2. ANN model consists of three input parameters (OMC, MDD and QDP%) that have a direct effect on two output parameters (C and FA). Optimum model parameters are as in the Table 2. The results of ANN modeling for cohesion at both learning and validation stages are given in figure 6 and figure 7, respectively. It is noticeable that data does not deviate from 1:1 line as much as LRA, confirming that the ANN modelling gives accurate predictions for the cohesion, based on the available data. This is further confirmed by the higher R^2 value of 0.9841. The validation data set was selected, such that it is distributed over the whole output range, so that the model can be tested more accurately, covering the entire data range. The higher R^2 value closer to one, confirms the accuracy; therefore, the cohesion can be predicted more precisely using the developed ANN model.

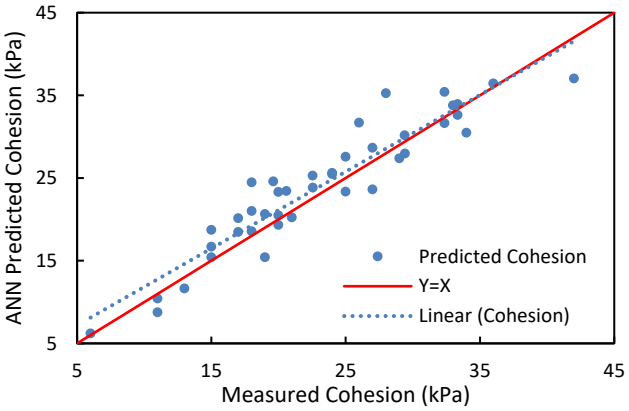

Fig. 6 - Relationship between measured and ANN-predicted cohesion at training stage.

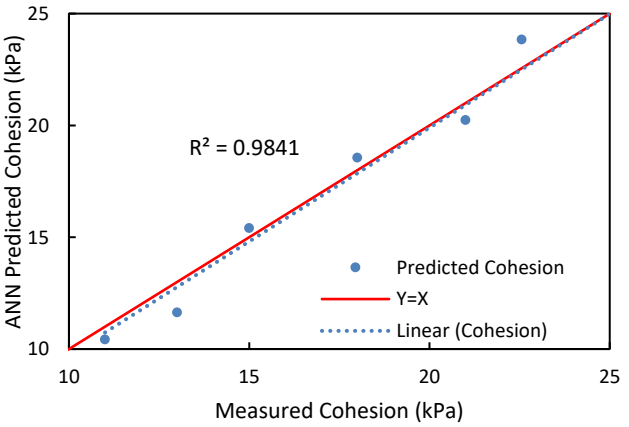

Fig. 7 - Relationship between measured and ANN-predicted cohesion at validation stage.

Similar to cohesion analysis, explained previously, the ANN model was developed for friction angle prediction as well, by using the same input and output parameters. The results of ANN modeling at both learning and validation stages are given in figure 8 and figure 9, respectively. It is noticeable that at both stages, the predicted and measured data points do not deviate much from 1:1 line, in contrast to the observation in LRA. This is further confirmed by the R^2 value which is as high as 0.98499. This confirms that ANN model can predict the friction angle with high accuracy with the given input data, and within the given data range.

Cohesion and friction angle are two of the important shear strength parameters, in determining the soil strength and construction stability. Being able to predict the resultant shear strength parameters of improved soil accurately, anyone can easily assess the soil stability after improving the soil with quarry dust mixing. Importantly, this can be done without additional experimental investigations thus, the cost for the analysis is quite low compared to other methods.

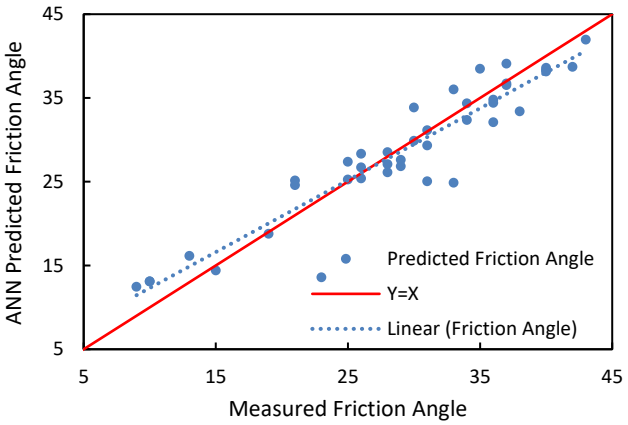

Fig. 8 - Relationship between measured and ANN-predicted friction angle at training stage.

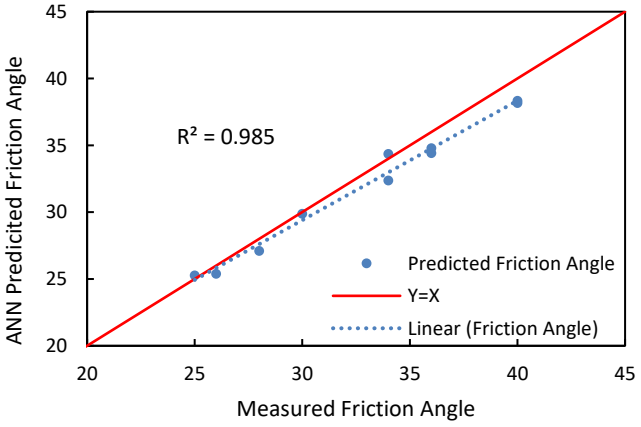

Fig. 9 - Relationship between measured and ANN-predicted friction angle at validation stage.

4.3 *Model Performance Evaluation*

The model performance is evaluated by comparing the validation results. In fact, residual error is calculated by comparing both LRA and ANN model predicted values to the experimental value and then subtracting predicted value from experimental value separately for both cohesion and friction angle. This gives a clear image on how the predicted output values deviate from the actual output values in each tested data point. For the cohesion analysis, the residual error of ANN tested data set is way less than that of LRA for all the tested data sets. Figure 10 depicts that LRA predicted values are not in line with measured cohesion. For instance, in tested data set no. 05, the LRA predicted value is way off compared to measured cohesion indicating 4.65 kPa difference. Since the cohesion only ranges between 6 MPa and 42 MPa, such a wide range of variations is unacceptably large. In friction angle analysis, the LRA predicted value in test no. 02 deviates largely from measured friction angle indicating a 3.33° difference. Since the friction angle only ranges between 9° and 43°, such large deviations are unacceptable. However, the maximum deviation shown by ANN predicted data is only 1.85°, which is only a half of the LRA analysis error. This confirms the higher predictability of ANN model over LRA model.

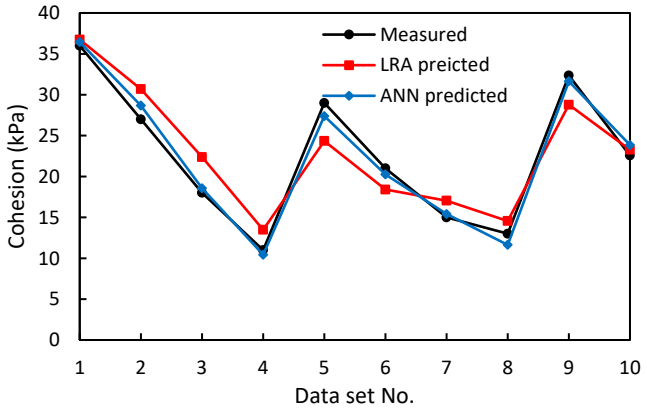

Fig. 10 – Comparison of measured and predicted cohesion

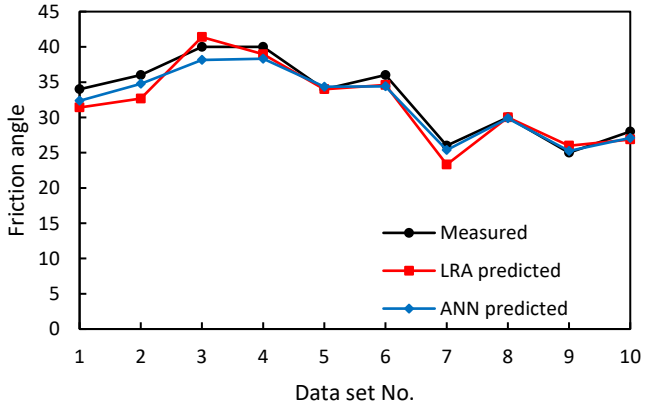

Fig. 11 – Comparison of measured and predicted friction angle

Further, the detailed performance evaluation using various statistical indices such as the coefficient of determination (R^2), root mean square error (RMSE), mean absolute percentage error (MAPE), Nash-Sutcliffe model efficiency coefficient (E_f) and variance accounted for (VAF) also confirmed that ANN model has a higher prediction capacity over LRA model for both cohesion and friction angle.

5 CONCLUSIONS

- Although the general statistical tools like LRA fails to capture the complex inter-relationships between input and output parameters, more advanced ANN models can accurately predict the strength variations under given conditions.
- Hence, the ANN models can be used to partially replace the experimental analyses and expedite the determination of strength parameters using already available experimental data.
- The method can therefore be considered as an effective way of determining strength parameters when certain in-situ parameters related to the specific situation are known.
- In general, if the quarry dust % that to be mixed with natural soil and OMC and MDD of the stabilized soil are known, it is possible to predict the resultant strength parameters (i.e., cohesion and friction angle) of the improved soil, by using the developed ANN model.

REFERENCES

Bong, T., Kim, S.R. and Kim, B.I., 2020. Prediction of ultimate bearing capacity of aggregate pier reinforced clay using multiple regression analysis and deep learning. Applied Sciences, 10(13), p.4580.

Mikaeil, R., Shaffiee Haghshenas, S., Ozcelik, Y. and Shaffiee Haghshenas, S., 2017. Development of intelligent systems to predict diamond wire saw performance. Journal of Soft Computing in Civil Engineering, 1(2), pp.52-69.

Sabat, A.K., 2012. A study on some geotechnical properties of lime stabilised expansive soil–quarry dust mixes. International Journal of emerging trends in engineering and development, 1(2), pp.42-49.

Sampath, K.H.S.M., Perera, M.S.A., Ranjith, P.G., Matthai, S.K., Tao, X. and Wu, B., 2019. Application of neural networks and fuzzy systems for the intelligent prediction of CO2-induced strength alteration of coal. Measurement, 135, pp.47-60.

Soosan, T.G., Sridharan, A., Jose, B.T. and Abraham, B.M., 2005. Utilization of quarry dust to improve the geotechnical properties of soils in highway construction. Geotechnical Testing Journal, 28(4), pp.391-400.

Thirumalai, R., Babu, S.S., Naveennayak, V., Ragavendra, B. and Praveenkumar, G., 2017. Stabilization of black cotton soil using granite waste and quarry dust. International Research Journal of Engineering and Technology, 4(8), pp.226-229.

T-shaped DCM columns in preventing excessive deformations in embankments

Manasi Wijerathna
GHD Pty Ltd, St. Leonards, Australia

D.S. Liyanapathirana
School of Engineering, Western Sydney University, Australia

ABSTRACT: T-shaped Deep Cement Mixed (DCM) columns are recently proposed as an alternative to conventional DCM columns with uniform area replacement ratios (ARR). They alleviate the requirement of a Load Transfer Platform (LTP) and have the capacity to reduce the ARR significantly compared to conventional DCM columns. Therefore, T-shaped columns are gaining popularity as a cost effective alternative for conventional columns. However, the performance of T-shaped DCM columns has not been received much attention in the literature. Hence, in this paper, the suitability of T-shaped DCM columns and three other design options (geosynthetic or wall panels underneath side slopes) used in practice in reducing lateral deformations is investigated. Although DCM wall panels are generally considered as efficient in reducing lateral deformations, results show that T-shaped DCM columns are the most efficient in reducing both lateral and vertical deformations. Also, the results show that the geosynthetic reinforcement is not an efficient solution in reducing lateral deformations when combined with T-shaped columns.

1 INTRODUCTION

Deep cement mixing technique is widely used to stabilise soft ground underneath embankments to reduce deformations and to increase the overall stability. Although deep cement mixing approach is originated in Nordic countries and in Japan, currently it is widely being used in many other countries including Australia. When the ground is improved with Deep Cement Mixing (DCM), differential settlement between native soft ground and DCM columns is a common problem. In conventional DCM column-supported embankments, the DCM columns are closely spaced and a load transfer platform (LTP) in the form of compacted gravel combined with geosynthetic is placed above the level of column heads, to reduce excessive differential settlements (King et al. 2017; Liu et al. 2007; Wu et al. 2017; Yapage and Liyanapathirana 2014; Zhang et al. 2016).

In recent years, different column configurations have emerged to improve the efficiency of DCM column-supported embankments. Recently, a T-shaped DCM column configuration is adopted for the Husuzhe Highway project in the Jiangsu Province of China (Liu et al. 2012). In these columns, the top few meters have a larger diameter than the rest of the DCM column. It is expected that T-shaped columns have the capacity to carry more loads than conventional DCM columns with uniform cross-section. After conducting physical model tests and numerical analyses, Yi et al. (2010, 2017, 2016) concluded that T-shaped DCM columns have a higher bearing capacity compared to conventional DCM columns with uniform cross section.

During the Pacific Highway upgrade project in NSW, Australia, a combination of individual DCM columns beneath the crest and DCM wall panels beneath the slopes were used to reduce settlement and lateral deformations in the embankment. However, the settlements were not reduced to desirable levels using the proposed column configuration, due to low bearing capacity of the improved ground. Hence, in this paper, the role of T-shaped DCM columns in resisting excessive deformations and preventing post peak softening of DCM columns is investigated using the aforementioned embankment case history. In addition to the soil improvement configuration proposed in the case history, four alternative design approaches including T-shaped DCM columns are numerically simulated in this study. The overall performance of the embankment with the proposed design approaches is compared with the case history to identify the efficiency of T-shaped columns in ground improvement.

2 DESCRIPTION OF THE EMBANKMENT CASE STUDY

The geometry and ground improvement details used in the case history of deep cement mixed column-supported embankment, which is a part of the Ballina Bypass section of the Pacific Highway up-

grade project in NSW, Australia, is shown in Figure 1. The embankment is 5.57 m high and 18.95 m wide at the crest level. The subsoil profile down to 25 m depth from the ground level (Yapage et al. 2014) is shown in Figure 1. The embankment is located over an 8.5 m deep weak soil deposit and it is improved with individual DCM columns beneath the crest and DCM wall panels beneath the side slopes. The diameter of DCM columns was 0.8 m.

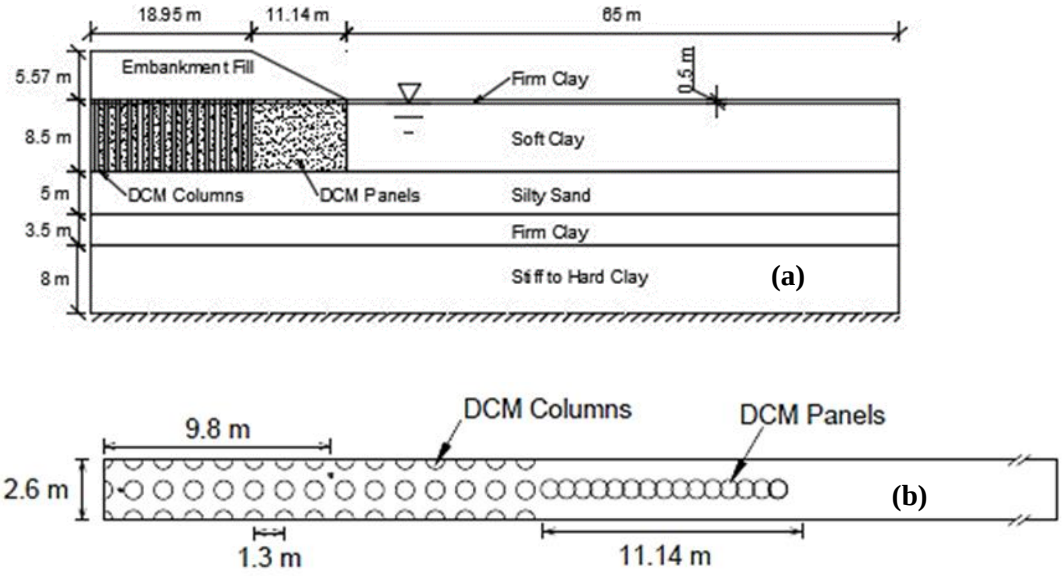

Figure 1: Geometry of the improved embankment and ground conditions (a) Section view (b) Plan view (enlarged to improve clarity of column configuration)

Table 1: Material properties for clay layers

Parameter	Top firm clay	Soft clay
γ (kN/m^3)	18	14.5
k_0	0.6	0.9 (0.5-4.5) 0.64 (4.5-8.5)
e_0	2.0	3.0
λ	0.5	0.5
κ	0.053	0.053
M	0.98	0.98
ν	0.3	0.3
k (m/s)	9.1×10^{-8}	6.0×10^{-8}

Note: γ, unit weight; k_0, coefficient of lateral earth pressure; e_0, void ratio; λ, slope of isotropic normal compression line; κ, slope of isotropic unload line; M, stress ratio; ν, Poisson's ratio; k, permeability

The physical and mechanical properties for the embankment, DCM columns and the subsoil, shown in Tables 1, 2 and 3, which were initially reported by Yapage et al. (2014) were used for the numerical analyses in this study. The construction rate of the embankment during the first construction stage was 0.125 m/day. In the first construction stage, 5.27 m height of the embankment was constructed over 42 days. In the actual construction sequence, the remaining 0.3 m height of the embankment was constructed within 21 days after a 30 days waiting period. However, for the numerical modelling, the remaining 0.3 m height was constructed over 50.9 days, during the second construction stage, which started immediately after the end of the construction of the first stage.

Table 2: Material properties for sand, firm and hard clays, and embankment fill

Parameter	Silty sand	Firm clay	Stiff-hard Clay	Fill
γ (kN/m^3)	18	16.5	16.5	19
k_0	0.55	0.55	0.55	-
e_0	2.23	2.0	2.0	-
ϕ' (degrees)	30	25	25	30
c' (kPa)	0	0	0	2
ν	0.3	0.3	0.3	0.3
E (MPa)	15	9	17	15
k (m/s)	8.3×10^{-7}	6.0×10^{-10}	5.3×10^{-10}	-

Note: ϕ', effective friction angle; c', effective cohesion; E, elastic modulus

Table 3: Properties of DCM columns

Parameter	Value
Unit weight, γ (kN/m^3)	18
Coefficient of lateral earth pressure, k_0	0.55
Void ratio, e_0	2.0
Effective friction angle, ϕ' (degrees)	27 (Peak) 13.5 (residual)
Effective cohesion, c' (kPa)	57.5 (Peak) 28.5 (residual)
Poisson's ratio, ν	0.3
Elastic modulus, E (MPa)	27.1
Permeability, k (m/s)	6.0×10^{-8}

3 PROPOSED DESIGN OPTIONS

The case history of the embankment used for this study is improved with individual DCM columns beneath the crest and DCM wall panels beneath the slopes. The panels were used to limit the lateral deformations and the design team came to the conclusion that the panels are the most efficient approach to control lateral deformations. However, the design failed to meet the design criteria due to yielding of DCM columns. The objective of this study is to investigate alternative design options that yield better performance of the embankment. The alternative design options proposed in this study are described in Table 4. A design option with uniform DCM columns beneath the crest and slopes (Option 1) was also analysed in this study to facilitate understanding the role of DCM wall panels, T-shaped DCM columns and geosynthetic reinforcement, distinctively, in reducing settlement and lateral deformations.

Table 4: Description of the suggested design options

Design option	Description	Remarks
Case history	DCM columns beneath the crest and DCM column walls beneath the slopes	S_c = 1.3 m, S_w = 3 m
Option 1	DCM columns beneath the crest and slopes	S_c = 1.3 m
Option 2	DCM columns beneath the crest and slopes + geosynthetic reinforcement	
Option 3	T-shaped DCM columns beneath the crest and slopes	S_c = 1.3 m, D_T = 1.1 m, L_T = 3m
Option 4	T-shaped DCM columns beneath the crest and slopes + geosynthetic reinforcement	

Note: S_c - spacing between columns, S_w – Spacing between column walls, D_T – Diameter of the T-shaped column head, L_T – Length of the T-shaped column head

4 NUMERICAL MODELLING

The case history of the embankment and the proposed design options for the highway embankment described in the previous section were simulated using 2D plane-strain models developed in the ABAQUS/Standard (2014) finite element programme. The 3D embankment problem was converted into a 2D plane-strain model based on the equivalent area (2D-EA) approach. The individual DCM columns are converted into continuous plane-strain walls in the 2D-EA model using Equation (1) (Ariyarathne et al. 2013).

$$t_{eq} = \frac{\pi D^2}{4s} \quad (1)$$

where t_{eq} is the thickness of the equivalent column wall, D is the diameter of DCM columns and s is the spacing between DCM columns in the column grid arranged in a square pattern. The material properties of the equivalent column walls are same as the properties shown in Table 3.

The DCM wall panels used in the case history were converted into a 2D plane-strain model based on the equivalent properties approach (2D-EP), without changing its original width. The equivalent properties of the DCM wall panels were calculated using Equations (2) to (5). Elastic moduli of the top firm clay and soft clay, required for Equation (2) were calculated using the equations: $E = 3K(1-2\nu)$ and $K = (1+e_0)p'/\kappa$, where K is the bulk modulus and p' is the mean effective vertical stress in the soil layer (Rani et al. 2014). The effective cohesion of top firm clay and soft clay, in Equation 3, were assigned as zero. Effective friction angle for soft clay and top firm clay was taken as 25^0 (Yapage et al. 2014), when calculating equivalent effective friction angle (φ'_{eq}) in Equation (5). The stress concentration ratio (n) was assumed as 6.5 (Yapage et al. 2014).

$$E_{eq} = E_c.a_r + E_s.(1-a_r) \quad (2)$$

$$c'_{eq} = c'_c.a_r + c'_s.(1-a_r) \quad (3)$$

$$\gamma_{eq} = \gamma_c.a_r + \gamma_s.(1-a_r) \quad (4)$$

$$\varphi'_{eq} = \tan^{-1}\left[\frac{(1-a_r)\tan\varphi'_s + n a_r \tan\varphi'_c}{(1-a_r) + n a_r}\right] \quad (5)$$

where E_{eq}, E_c and E_s are the elastic moduli of the equivalent column wall, DCM column and surrounding soil respectively; a_r is the area re-

placement ratio of DCM columns; c'_{eq}, c'_c and c'_s are the effective cohesion of the equivalent column wall, DCM column and surrounding soil, respectively; γ_{eq}, γ_c and γ_s are the unit weights of the equivalent column wall, DCM column and surrounding soil, respectively; and φ'_{eq}, φ'_c and φ'_s are the effective friction angles of the equivalent column wall, DCM column and surrounding soil, respectively.

Since the embankment was symmetrical over the centreline, only half of the embankment was modelled. The vertical boundary at the centreline of the embankment was assigned with a symmetrical boundary condition. The vertical boundary at 95 m away from the centreline was assigned zero lateral deformation. The movements of the bottom boundary at 25 m depth from the ground surface were restricted in both vertical and horizontal directions. The ground water table is located at 0.5 m depth from the ground surface and zero pore water pressure was assigned along this surface to allow pore water pressure dissipation.

The modified cam clay model was used for the top firm clay layer and the soft clay layer. Elasto-plastic Mohr Coulomb model was used to simulate the silty sand layer, firm clay layer, stiff to hard clay layer and embankment fill material. The soil layers and DCM columns below the ground water table were modelled using eight-node quadrilateral elements with reduced integration and pore pressure degrees of freedom at the corner nodes (CPE8RP). Eight-node quadrilateral elements with reduced integration and without pore pressure degrees of freedom (CPE8R) were used to model soils and DCM columns above the ground water table. The mechanical behaviour of DCM columns was modelled using an extended version of the Mohr-Coulomb model incorporating the strain softening behaviour shown by cement mixed soils beyond yield.

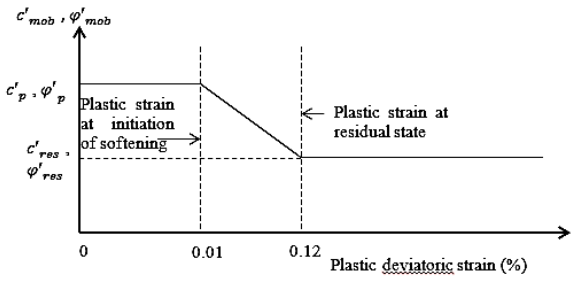

Figure 2: Variation of mobilized cohesion and friction angle with plastic deviatoric strain

shows the variation of cohesion and friction angle with increasing plastic deviatoric strain, in the extended Mohr-Coulomb model (Yapage et al. 2015). The strain softening of DCM columns was initiated at the plastic strain of 1%, in this model. At the plastic strain of 12%, the columns subjected to complete softening and the cohesion and friction angle reached their residual values. The ratio of residual to peak strength properties (c'_{res}/c'_p and $\varphi'_{res}/\varphi'_p$) was taken as 0.5. These values are based on the parameters reported by Yapage et al. (2014 and 2015) for the extended Mohr-Coulomb model based on the triaxial data for cement mixed soils.

The geosynthetic layer introduced in Option 2 and Option 4 was modelled using an elastic perfectly plastic material model. Three-node quadratic displacement truss elements (T2D3) were used to model the geosynthetic layer. The tensile stiffness of the geosynthetic was 2000 kN/m and the thickness was 4 mm. The tensile strength of the geosynthetic was taken as 300 kN/m. The interaction between the geosynthetic layer and the embankment fill material was modelled as a surface to surface contact with an interface friction coefficient of 0.8. Figure 3 shows the finite element mesh used for the case study.

Figure 3: Finite element model of the case study

5 RESULTS AND DISCUSSION

The performance of the embankment with different soil improvement options are compared in this section using ground deformations.

5.1 *Ground deformations*

Figure 4 shows the final settlement profiles along the base of the embankment and Figure 5 shows the lateral displacement profiles below the toe of the embankment, with different design options. Among the five design options considered, the case history shows the largest settlements. Settlements in the case history are large near the centreline of the embankment. Settlements close to the centreline of the embankment in Option 1 are lower than in the case history. However, settlements close to the slope of the embankment are large in Option 1

compared to the case history. The maximum settlement in Option 1 occurred at 7.15 m away from the centreline of the embankment. This is because of the reduced lateral load resistance in Option 1 after replacing the DCM wall with individual DCM columns. The lateral deformation profile also shows large deformations close to the toe of the embankment in Option 1.

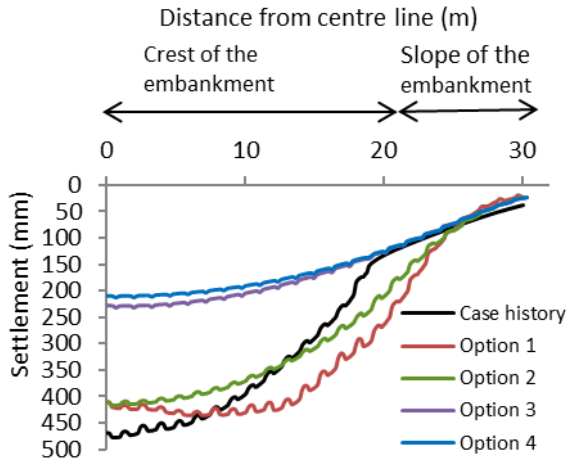

Figure 4: Final settlement profiles along the base of the embankment

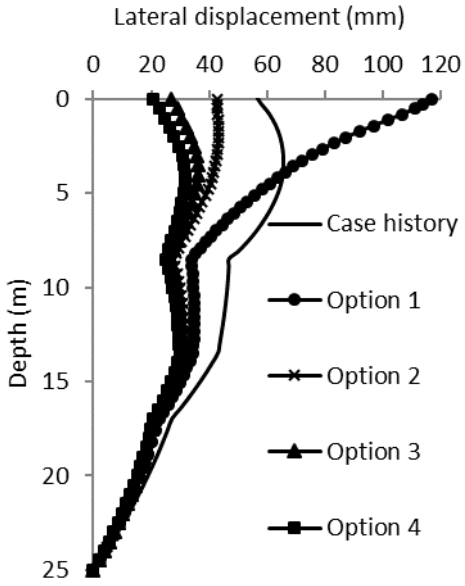

Figure 5: Lateral displacement profiles beneath the toe of the embankment

Both settlements and lateral deformations reduced in Option 2 compared to Option 1, due to the effect of geosynthetic reinforcement. The maximum settlement was reduced by 7% after introducing the geosynthetic reinforcement. When a geosynthetic reinforcement layer is incorporated into the column-supported embankment in Option 2, the maximum lateral deformation was reduced from 117.7 mm (in Option 1) to 43.2 mm. Although this reduction is only about 30% compared to the case history, the improvement is very significant compared to Option 1, where only individual DCM columns are used underneath the side slopes and the centre of the embankment. The differential settlement between soil and DCM columns is also reduced slightly in Option 2 compared to Option 1. The lateral displacement profile observed for Option 1 indicates a column-tilting type deformation beneath the toe (Figure 4). When it comes to Option 2, the displacement profile has changed to a bending type deformation, due to the effect of the geosynthetic reinforcement. The maximum tensile stress in the geosynthetic layer in Option 2 is 183 kPa. This clearly indicates the influence of geosynthetic reinforcement in reducing deformations in conventional uniform DCM column improved ground.

When the ground is improved with T-shaped DCM columns the settlements at the base of the embankment reduced significantly. The reduction of maximum settlement in the T-shaped DCM column improved ground in Option 3 and Option 4, respectively, are 51% and 56% compared to the case history. Differential settlements are also small in T-shaped DCM column improved ground compared to the ground improved with uniform DCM columns and the case history. Furthermore, the settlements beneath the slope of the embankment are slightly lower in Option 3 and Option 4 than in the case history where DCM walls were used beneath the slopes. The reduction in maximum lateral displacement in Option 3 and Option 4, compared to the case history, are 45% and 52% respectively. It shows that the T-shaped DCM columns improved the lateral stiffness and bearing capacity of the subsoil layer better than the combination of individual DCM columns and DCM column walls used in the Case history. However, the yielding of DCM columns could not be completely avoided by using T-shaped DCM columns. In Option 3 and Option 4, the T-shaped DCM columns indicated yielding below the length of the column head (L_T), at a depth of 3.75 m. However, the plastic strains in the T-shaped DCM columns were not large enough to cause post yield strain softening.

In Option 4, the T-shaped DCM column improved embankment is reinforced with a geosynthetic layer. As observed in Figure 3 and Figure 4, the lowest settlement and lateral deformation are given by Option 4. However, compared to Option 3, the performance of the embankment has improved only marginally in the Option 4. The maximum tensile stress observed in the geosynthetic

layer in Option 4 is 81 kPa. This shows that the geosynthetic layer is not significantly contributing to resist the lateral deformations in the embankment, in Option 4. Therefore, among the suggested options, Option 3 is the most effective solution. However, it should be noted here, that the area replacement ratio of soil improvement is not the same in the design options considered in this study.

6 CONCLUSIONS

The efficiency of T-shaped DCM columns used in DCM column supported embankments was investigated in this paper, while considering the post-yield strain softening behaviour of DCM columns. The study was carried out using 2D plane-strain finite element models. A case history of an embankment improved with individual DCM columns beneath the crest and DCM walls beneath the slopes is used for the study. The design options considered for the embankment, in this study are; (1) only individual DCM columns (Option 1), (2) individual DCM columns and geosynthetic reinforcement (Option 2), (3) T-shaped DCM columns (Option 3) and (4) T-shaped DCM columns and geosynthetic reinforcement (Option 4). The performances were evaluated in terms of ground deformations. The uniform DCM column improved embankment (Option 1) showed further improvement in lateral deformations and settlements when a geosynthetic reinforcement layer is incorporated, which is the Option 2 considered in this paper. Also, these results show that the geosynthetic layer has contributed significantly in reducing deferential settlements. The embankment improved with T-shaped DCM columns showed significantly lower settlements, differential settlements and lateral deformations compared to the case study, the Option 1 and the Option 2. When geosynthetic reinforcement is used along with T-shaped DCM columns (Option 4), the reductions in lateral deformations, settlements and differential settlements, compared to Option 3, are very small. This indicates that the geosynthetic layer is less effective when used with T-shaped DCM columns.

REFERENCES

ABAQUS/Standard. (2014). *ABAQUS version 6.14 - Computer software*, Dassault Systèmes Simulia Corp., Providence, Rhode Island, USA.

Ariyarathne, P., Liyanapathirana, D.S., and Leo, C.J. (2013). "Comparison of different two-dimensional idealizations for a geosynthetic-reinforced pile-supported embankment." *International Journal of Geomechanics*, 13(6), 754-768.

King, D.J., Bouazza, A., Gniel, J.R., Rowe, R.K., and Bui, H.H. (2017). "Load-transfer platform behaviour in embankments supported on semi-rigid columns: implications of the ground reaction curve." *Canadian Geotechnical Journal*, 54, 1158-1175.

Liu, H.L., Ng, C.W.W., and Fei, K. (2007). "Performance of a geogrid-reinforced and pile-supported highway embankment over soft clay: case study." *Journal of Geotechnical and Geoenvironmental Engineering*, 133(12), 1483-1493.

Liu, S.-Y., Du, Y.-J., Yi, Y.-L., and Puppala, A.J. (2012). "Field investigations on performance of T-shaped deep mixed soil cement column–supported embankments over soft ground." *Journal of Geotechnical and Geoenvironmental Engineering*, 138(6), 718-727.

Rani, R. S., Prasad, K. N., and Krishna, T. S. (2014). "Applicability of Mohr-Coulomb & Drucker-Prager models for assessment of undrained shear behaviour of clayey soils." *International Journal of Civil Engineering and Technology*, 5(10), 104-123.

Wu, L., Jiang, G., Liu, X., Xiao, H., and Sheng, D. (2017). "Performance of geogrid-reinforced pile-supported embankments over decomposed granite soil." *Proceedings of the Institution of Civil Engineers-Geotechnical Engineering*, 1-15.

Yapage, N.N.S., and Liyanapathirana, D.S. (2014). "A parametric study of geosynthetic-reinforced column-supported embankments." *Geosynthetics International*, 21(3), 213-232.

Yapage, N.N.S., Liyanapathirana, D.S., Kelly, R.B., Poulos, H.G., and Leo, C.J. (2014). "Numerical modeling of an embankment over soft ground improved with deep cement mixed columns: Case history." *Journal of Geotechnical and Geoenvironmental Engineering*, 140(11), 04014062.

Yapage, N.N.S., Liyanapathirana, D.S., Poulos, H.G., Kelly, R.B., and Leo, C.J. (2015). "Numerical modeling of geotextile-reinforced embankments over deep cement mixed columns incorporating strain-softening behavior of columns." *International Journal of Geomechanics*, 15(2), 04014047.

Yi, Y., Liu, S., and Puppala, A.J. (2016). "Laboratory modelling of T-shaped soil–cement column for soft ground treatment under embankment." *Géotechnique*, 66(1), 85-89.

Yi, Y., Liu, S., Puppala, A.J., and Xi, P. (2017). "Vertical bearing capacity behaviour of single T-shaped soil–cement column in soft ground: laboratory modelling, field test, and calculation." *Acta Geotechnica*, 12, 1077-1088.

Yi, Y., Liu, S., and Zhu, Z. (2010). "Bearing capacity of T-shaped soil-cement deep mixed column composite foundation." *Journal of Building Structures*, 31(9), 119.

Zhang, C., Jiang, G., Liu, X., and Buzzi, O. (2016). "Arching in geogrid-reinforced pile-supported embankments over silty clay of medium compressibility: Field data and analytical solution." *Computers and Geotechnics*, 77, 11-25.

A soil improvement method based on plant-derived urease-induced carbonate precipitation

R. A. N. Dilrukshi
Faculty of Technology, Wayamba University of Sri Lanka, Sri Lanka
K. Nakashima
Faculty of Engineering, Hokkaido University, Sapporo 060-8628, Japan
S. Kawasaki
Faculty of Engineering, Hokkaido University, Sapporo 060-8628, Japan

ABSTRACT: The plant-derived urease-induced calcium carbonate (CC) precipitation (PDUICCP) was studied to use as a soil improvement technique. Test specimens (Diameter, ϕ = 2.3 cm and Height, h = 7.1 cm) made from Mikawa sand (Mean diameter, D_{50} = 870 μm) were cemented with CC using a crude extract of crushed watermelon (*Citrullus lanatus*) seeds as the urease source and calcium chloride ($CaCl_2$) as the calcium source and using urea ($CO(NH_2)_2$). A significant strength improvement ranging from estimated unconfined compressive strength (UCS) of 0.5 MPa to 3.0 MPa was observed in urea-urease treated sand specimens by changing the concentration of $CaCl_2$- urea, urease activity and curing time. The carbonate ions (CO_3^{2-}) resulting from urea hydrolysis play a major role to precipitate CC within the test specimens. By using different concentrations of $CaCl_2$- urea, urease activity and different curing time, there is a tendency to increase the precipitated CC and hence to increase estimated UCS. Therefore, this method has potential to use as a strength improvement method for loose sand and to replace commercially available urease by crude urease from watermelon seeds for precipitating carbonates. Hence, this method is a soil improvement method that has a less impact to the environment.

1 INTRODUCTION

The concept of biotechnology for soil improvement has spread in the field of geotechnical engineering in 2005 and National Re-search Council has identified, as biogeotechnical engineering is an important research area (Dejong et al. 2013). Different biogrout formation mechanisms have been identified and the most widely used carbonate precipitation method is using urea and ureolytic bacteria (Harkes et al. 2010)/ purified/crude extracts of plant urease enzyme (Park et al. 2014; Nam et al. 2015; Neupane et al. 2013). Out of them, microbially induced carbonate precipitation (MICP) method is the most widely explored carbonate precipitation method. Therefore, the urease enzyme activity in most bacteria metabolism processes has been used extensively as tool to precipitate calcium carbonate (CC) at the presence of Ca^{2+} and urea within a system by following the reactions in Eqs. (1)– (6) (Mobley and Hausinger, 1989, De Muynck et al. 2010).

$$CO(NH_2)_2 + H_2O \rightarrow NH_2COOH + NH_3 \quad (1)$$

$$NH_2COOH + H_2O \rightarrow H_2CO_3 + NH_3 \quad (2)$$

$$2NH_3 + 2H_2O \rightarrow 2NH_4^+ + 2OH^- (pK_a = 9.3) \quad (3)$$

$$H_2CO_3 \rightarrow H^+ + HCO_3^- (pK_1 = 6.3) \quad (4)$$

Total reaction:

$$CO(NH_2)_2 + 2H_2O \rightarrow 2NH_4^+ + CO_3^{2-} \quad (5)$$

$$Ca^{2+} + CO_3^{2-} \rightarrow CaCO_3 \quad (6)$$

However, because of some advantages of plant-derived urease over microbial urease, this study focused on the use of plant-derived urease induced CC precipitation (PDUICCP) as a novel soil improvement method. The limitation of bacterial growth and movement in deep, fine grained soils (van Paassen et al., 2009; van Paassen et al., 2010) is one weakness of MICP method. Further, the government approvals and licenses are required to use microbial urease and, monitoring of microbial ecology for safety is required (Akiyama et al. 2011). The cultivation of bacteria as well as the fixation of bacteria are not required for plant urease (Yasuhara et al. 2012). The urease enzyme that extract from plant species is expensive when purchased from a commercial supplier. However, lab-grade enzyme is very effective (Knorr, 2014). Furthermore, crude extract of plant urease has a potential to use as a replacement for commercially available purified urease (Nam et al., 2015). The objective of this study was to strengthen the small-scale sand specimens to an estimated unconfined compressive strength (UCS) ranging from several kPa to MPa using crude

extract of watermelon seeds urease induced CC precipitation technique and to identify the range of applicability of this method using obtained results such as liquefaction mitigation and artificial soft rocks formations.

2 MATERIALS AND METHODS

For this study, finely ground watermelon seeds were taken and 0.5 g of crushed seeds were stirred at 500 rpm with 10 mL of distilled water (concentration was represented as 50 g/L) for 1 h. The crude extract was obtained after filtering and collecting the filtrate. One part of the collected crude extract directly used to measure the urease activity; the other part was centrifuged at 10,000 rpm for 3 min at 25 °C and the supernatant was used to measure the urease activity. A quantitative value for urease activity was obtained using the indophenol method (Natarajan, 1995).

The rate of precipitation of CC under various combinations of $CaCl_2$-urea and urease was evaluated in transparent polypropylene test tubes (Height, h_1 = 9.0 cm and Diameter, $ø_1$ = 1.4 cm) by measuring Ca^{2+} concentration with time. The purpose of doing test tube experiment above was to understand the temporal behavior within the sand specimen placed in syringe when solidification take place. A total 10 mL of equimolar solutions of $CaCl_2$-urea, with concentrations of 0.3 mol/L (hereafter M), 0.5 M, and 0.7 M were prepared separately in watermelon seed extract with known concentrations. The initial seed extract (crude extract) concentrations were 5 g/L ,10 g/L, 50 g/L and 100 g/L and, the urease activity values obtained after centrifuging each extract at 25 °C were 0.459 U/mL, 0.877 U/mL, 3.917 U/mL and 7.151 U/mL respectively. At the preparation of 10 mL of equimolar solution of $CaCl_2$-urea in the test tubes, required amount of $CaCl_2$ was dissolved in 10 mL of centrifuged crude extract and mixed well. The reaction was initiated after mixing required amount of urea into the $CaCl_2$-urease solution and, all test tubes were capped and placed at a stable location under required temperature. Sampling at about 2 cm below the top surface level of the solution in the test tubes was done at different time intervals for the determination of Ca^{2+} concentration. At the same time, sampling was done from two control samples prepared using (i) $CaCl_2$ and urea without urease and, (ii) $CaCl_2$ and urease without urea. The control samples were also tested at 25 °C.

Mikawa sand No. 4 that can be obtained commercially in Japan with mean diameter D_{50} = 870 μm, particle density ρ_s = 2.66 g/cm^3, minimum void ratio e_{min} = 0.802 and maximum void ratio e_{max} = 1.118 was used for the syringe solidification test. A total 43.5 g of oven-dried Mikawa sand (Poorly graded sand (SP) according to Unified Soil Classification System) was compacted into a 35-mL syringe (Diameter, ϕ = 2.3 cm, Height h = 7.1 cm) to attain the final density of the specimen to the maximum density of sand (1.476 g/cm^3). Then the syringe was placed in an incubator to maintain a constant temperature throughout the experiment. Further, a drainage valve was connected to the bottom of the syringe and kept as closed. The total void volume of 13.1 mL of the specimen was filled by $CaCl_2$-urea-urease solution which was prepared by dissolving $CaCl_2$-anhydrous and urea into centrifuged crude extract and, the top level of the solution in the syringe was set as the top surface level of the sand in the syringe. Desiccation of the syringe test specimen was avoided by covering the top of the syringe using Parafilm M (Structure Probe, Inc., West Chester, PA). A new solution of $CaCl_2$-urea-urease with the same concentration and volume was added daily into the syringe test specimen until required curing time (days) was attained. While adding new solution, previously injected solution was slowly drained out through the drainage valve. The temporal variation of Ca^{2+} concentration (ppm) and pH of the drainage solution were measured once every 2 days using a calcium ion meter (HORIBA LAQUA twin, Model B 751) and pH Spear by dipping the electrode of pH Spear (Eutech Instruments Pte., Ltd., Singapore) respectively. Similarly, two control test specimens were prepared with (a) 0.7 M $CaCl_2$ + urea, no urease (b) 0.7 M $CaCl_2$ + urease = 3.912 U/mL, no urea. After reaching the curing time, (7, 14, 21, and 28 days in this study), the specimen was carefully removed from the syringe and the needle penetration (NP) test was conducted by using NP device (SH-70; Maruto Testing Machine Company, Tokyo, Japan) to determine the estimated UCS . Estimated UCS was read directly from the chart on the NP device prepared based on the regression equation (Eq. (7) (correlation coefficient: chart 0.941, x: NP (N/mm), y: UCS (MPa)),

$$\text{Log}\,(y) = 0.978\log(x) + 2.621 \qquad (7)$$

After finishing needle penetration test, a segment of each test specimen was observed by scanning electron microscopy (SEM) (TM 3000 Miniscope; Hitachi Ltd., Tokyo, Japan).

3 RESULTS AND DISCUSSIONS

3.1 *Urease activity test*

According to the urease activity test results obtained, activity increased with the concentration of

seed extract (Fig. 1). Moreover, urease activity before centrifuging was slightly higher than the urease activity after centrifuging (Fig. 2). The reaction temperature was also affect for the urease activity.

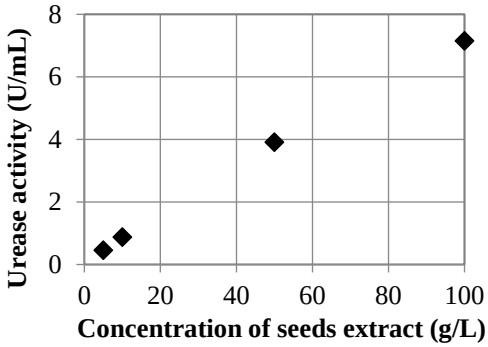

Fig. 1 Urease activity for different concentrations of watermelon seed extracts at 25 ℃ reaction temperature.

After examining urease activity values at different reaction temperatures ranging from 25 °C to 70 °C, the maximum activity was obtained around 50 °C (Fig. 2). Subsequently, the activity abruptly declined with further increase in temperature.

3.2 *Test tube experiment*

The temporal variation of Ca^{2+} concentrations in polypropylene test tubes with different urease activities are shown in Fig. 3. The rate of decrease of Ca^{2+} in the solution increased with the increase of urease activity at each concentration of $CaCl_2$-urea. This can be explained by the increase in the rate of urea hydrolysis with the increase of urease activity. The urea hydrolysis reaction shown in Eq. 5 is catalyzed by urease enzyme and hence, the CO_3^{2-} release to the system. When more CO_3^{2-} release to the system, the CO_3^{2-} react with Ca^{2+} and finally leads to rapid precipitation of CC.

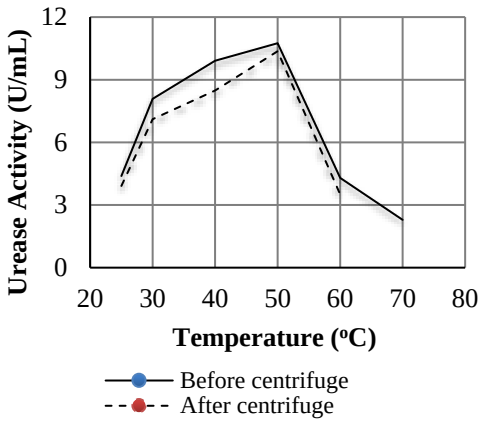

Fig. 2 Variation of urease activity with different reaction temperatures.

Moreover, when the amount of urea in the solution is small, that small amount of urea is hydrolyzed more rapidly rather than high amount of urea by a given amount of enzyme for a given enzymatic activity. Therefore, when the $CaCl_2$-urea concentration decreases, the urease with low urease activity can be used to hydrolyze the urea and hence to precipitate CC.

3.3 *Syringe solidification test*

3.3.1. *Relationship between $CaCl_2$- urea concentration and estimated UCS*

Estimated UCS values achieved for different concentrations of $CaCl_2$-urea are shown in Fig. 4 for two test cases with constant urease activity. The minimum estimated UCS value that could be measured from the NP device was 200 kPa. Therefore, estimated UCS values less than 200 kPa were reported as 0 kPa, for ease of graphical representation. The estimated UCS values increased with $CaCl_2$-urea concentrations ranging from 0.3 M to 0.7 M

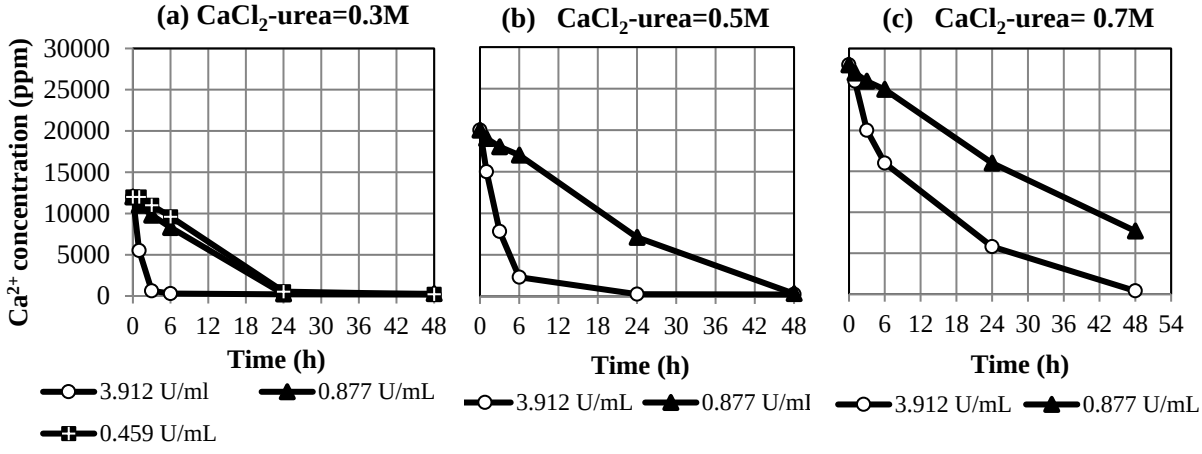

Fig. 3 Change in Ca^{2+} with urease activity.

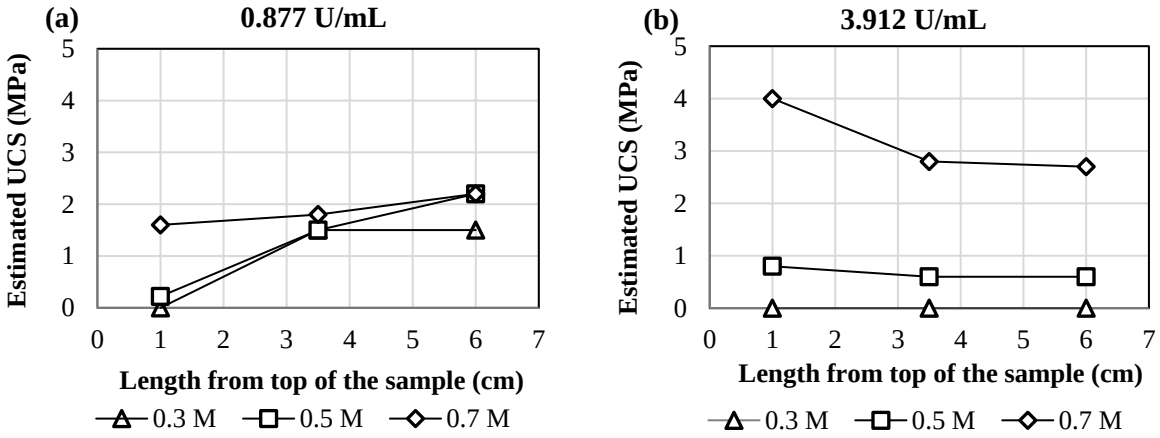

Fig. 4. Effect of $CaCl_2$- urea concentration on estimated UCS after 14 days of curing time. (a) Urease activity = 0.877 U/mL; (b) Urease activity = 3.912 U/mL.

under constant urease activity. According to Eqs. (5) and (6), 1 mol of urea react with 1 mol of $CaCl_2$ to form 1 mol of CC. Hence, when we increase the equimolar concentrations of $CaCl_2$- urea from 0.3 M to 0.7 M, the amount of precipitated CC within the void spaces increases and it helps to reduce the voids between sand grains. Finally, it affected to increase estimated UCS. However, the theoretical amounts calculated from reaction stoichiometry are not necessarily giving the actual experimental amounts of CC. In future, the measurement of experimental amount of CC instead of getting theoretical amount is considered.

3.3.2. *Relationship between urease activity and estimated UCS*

As shown in Fig. 5, the estimated UCS increased with the increase of urease activity up to a certain level and further increments of urease activity caused to a decrease in the estimated UCS values for the test cases with 0.5 M and 0.3 M $CaCl_2$- urea. However, in case of 0.7 M $CaCl_2$-urea, the estimated UCS increased with the increase of urease activity. The low concentration of urea (0.3 M and 0.5 M) was rapidly hydrolyzed by the urease with urease activity of 3.912 U/mL compared with the higher concentration of urea (0.7 M). Therefore, CC started to precipitate before injecting the 0.3 M $CaCl_2$- urea solution into the syringe specimen. As a result, the voids between sand particles filled with pre-precipitated CC (PPCC) rather than precipitating within the specimen. This may not be favorable to form an effective bond between sand particles. Therefore, a higher estimated UCS obtained at low urease activity than for high urease activity for 0.5 M and 0.3 M $CaCl_2$-urea. However, further decreases in urease activity caused to decreases in the estimated UCS value. The reason may be the low rate of urea hydrolysis of the urease with low urease activity to hydrolyze 0.3 M and 0.5 M urea within 1 day and hence, an insufficient amount of CO_3^{2-} to precipitate

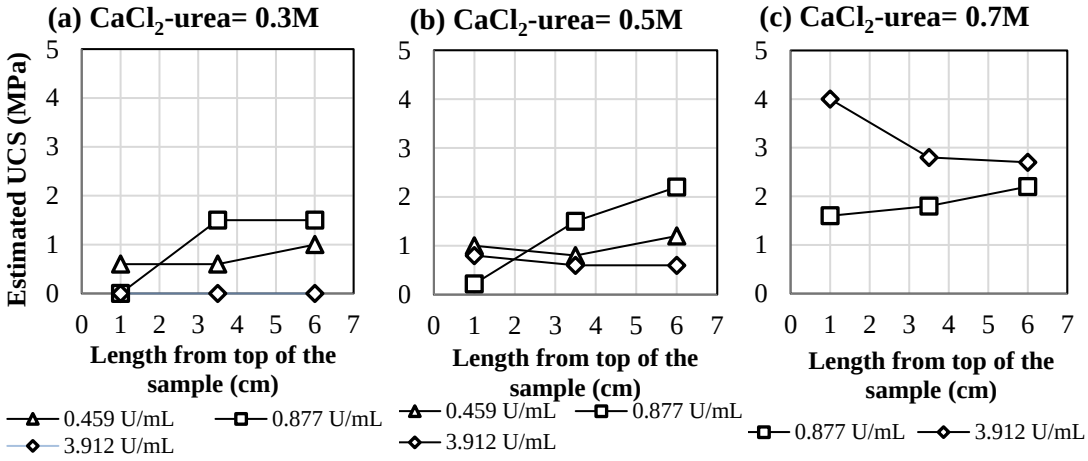

Fig.5. Effect of urease activity on estimated UCS after 14 days of curing time.

CC. Similar observations detected in test cases with 0.7 M $CaCl_2$- urea. The estimated UCS has decreased with decreasing urease activity in test case with 0.7 M $CaCl_2$- urea. As mentioned above, the reason may be due to the low rate of urea hydrolysis of the urease with low urease activity to hydrolyze 0.7 M urea within 1 day. This can be clearly understood using the Ca^{2+} concentrations in the outlet solutions. The Ca^{2+} concentration in the outlet was higher at low urease activity than high urease activity. The rate of urea hydrolysis is low at low urease activity and hence, the produced CO_3^{2-} due to urea hydrolysis are not sufficient to bind with free Ca^{2+} in the solution. This is a possible reason for obtaining low estimated UCS for urease activity of 0.877 U/mL compared with 3.912 U/mL, as in Fig. 6 (c). Therefore, selecting most appropriate urease concentration for each concentration of $CaCl_2$-urea solution is important for an effective CC precipitation.

3.3.3 *Relationship between curing time and estimated UCS*

According to Fig. 6, regardless of the $CaCl_2$-urea concentration and urease activity, the estimated UCS values increased with curing time (days). The reason may be due to increase of precipitated CC with curing time. The total CC precipitated within the syringe specimen was calculated using the method described by Danjo and Kawasaki (2016). The total CC precipitated within the syringe specimen relevant to Fig. 6 (a) was 0.11, 0.21, and 0.23 g/g sand after 7, 14, and 21 days of curing time, respectively. The amount of precipitated CC after 7 days' curing time with 0.7 M $CaCl_2$- urea is nearly same as that after 14 days' curing time with 0.3 M $CaCl_2$- urea. However, estimated UCS values were different in those two test cases, as shown in Fig. 6 (a) and (c).Because of rapid urea hydrolysis, CC precipitation takes place before injecting the solution into the sand specimen. Therefore, some PPCC remained at the top surface of the specimen and hence, the total amount of calculated CC was not effectively precipitated within the specimen in the 0.3 M $CaCl_2$- urea–urease solution. This is a possible reason for the change in estimated UCS, even at the same amount of calculated precipitated CC. Furthermore, calcite polymorph was clearly observed for all test cases after magnifying the SEM images regardless of the urease activity and $CaCl_2$- urea concentration.

4 CONCLUSION

This study describes the use of the PDUICCP method as an alternative method for MICP by using crude extracts of crushed watermelon seeds as urease enzyme. Small-scale test specimens made from commercially available Mikawa sand were cemented and satisfactory estimated UCS values were achieved. According to the results obtained, following conclusions were made.

- Several kPa to MPa values of estimated UCS were obtained by changing the concentration of $CaCl_2$-urea, urease, and curing time. The increase of the curing time caused to increase the estimated UCS value. The increase of $CaCl_2$-urea concentration from 0.3 M to 0.7 M also caused to increase the estimated UCS value. Conversely, the effect of urease activity on estimated UCS is different for different concentrations of $CaCl_2$-urea solution. According to the results, it is good to maintain low urease activity for low concentrations of $CaCl_2$-urea sol-

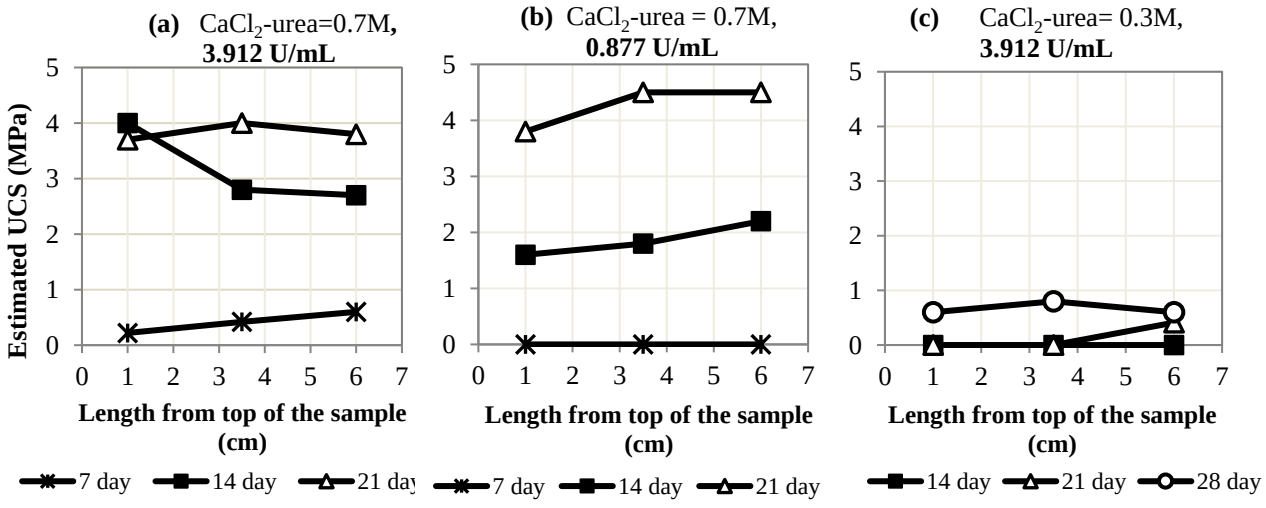

Fig. 6. Effect of curing time on estimated UCS with different concentrations of $CaCl_2$-urea and urease activities.

-tions and high urease activity for solutions with high concentrations of $CaCl_2$-urea, to maintain the rate of urea hydrolysis and finally to maintain the rate of CC precipitation. Otherwise, CC starts to precipitate before injecting the solution into the syringe specimen. Then the voids between sand particles, especially in the upper portion of the sand specimen, filled with PPCC instead of precipitating within the specimen, which may not be favorable to create effective bonds between sand particles. According to the results of this study, the urease activity of 3.912 U/mL is suitable for 0.7 M $CaCl_2$-urea solutions and 0.877 U/mL for 0.3 M and 0.5 M $CaCl_2$- urea solutions. The average estimated UCS obtained after 14 days of curing time for 0.7 M $CaCl_2$-urea and 3.912 U/mL urease was around 3.0 MPa and this was around 1.5–2.0 MPa for 0.3 M and 0.5 M $CaCl_2$-urea and 0.877 U/mL urease, at 25 °C.

By altering the values of each parameter discussed above, there is a possibility to apply this method to improve the strength of saturated loose sand and hence to mitigate the liquefaction and to form artificial stones like sandstone. In conclusion, the crude extract of crushed watermelon seeds is a potential urease source instead of commercially available urease, for carbonate precipitation. However, it is required to further investigate the properties such as durability, longevity, and reversibility of the carbonate precipitation process and, a thorough investigation of this novel area must be done, to bring it to an environmental friendly, cost effective method when develop this technology from bench scale to pilot scales.

ACKNOWLEDGMENTS

This work was partly supported by JSPS KAKENHI [grant number JP16H04404]. We thank Edanz Group for editing a draft of this manuscript.

REFERENCES

Akiyama, M., Kawasaki, S. and Aoi, S. (2011). Fundamental study on new grouting material using calcium phosphate compounds – effect of addition of ammonia sources and soil microorganisms on unconfined compression strength. Jpn. Geotech. J. 6, 513–524.

Danjo, T. and Kawasaki, S. (2016). Microbially induced sand cementation method using Pararhodobacter sp. strain SO1, inspired by beachrock formation mechanism. Mater. Trans. 57 (3), 428–437.

De Muynck, W., De Belie, N. and Verstraete, W. (2010). Microbial carbonate precipitation in construction materials: A review. Ecol Eng 36: 118-136.

DeJong, J.T., Soga, K., Kavazanjian, E., Burns, S., van Paassen, L., AL Qabany, A., …Weaver, T. (2013). Biogeochemical processes and geotechnical applications: progress, opportunities, and challenges. Geotechnique 63 (4): 287-301.

Harkes, M.P., van Paassen, L.E., Booster, J.L., Whiffin, V.S. and van Loosdrecht, M.C.M. (2010). Fixation and distribution of bacterial activity in sand to induce carbonate precipitation for ground reinforcement. Ecol. Eng. 36, 112–117.

Knorr, B. (2014). Enzyme-induced carbonate precipitation for the mitigation of fugitive dust. A thesis for the degree Master of Science. Arizona State University.

Mobley, H.L.T. and Hausinger, R.P. (1989). Microbial ureases: significance, regulation, and molecular characterization. Microbiol. Mol. Biol. Rev. 53: 85–108.

Nam, I.H., Chon, C.M., Jung, K.Y., Choi, S.G., Choi, H. and Park, S.S. (2015). Calcite precipitation by ureolytic plant (*Canavalia ensiformis*) extracts as effective biomaterials. KSCE J. Civ. Eng. 19 (6): 1620–1625.

Natarajan, K.R. (1995). Kinetic study of the enzyme urease from Dolichos biflorus. J. Chem. Edu. 72 (6): 556–557.

Neupane, D., Yasuhara, H., Kinoshita, N. and Unno, T. (2013). Applicability of enzymatic calcium carbonate precipitation as a soil-strengthening technique. Journal of Geotechnical Geoenvironmental Engineering. 139: 2201-2211.

Park, S.S., Choi, S.G. and Nam, I.H. (2014). Effect of plant induced calcite precipitation on the strength of sand. J. Mater. Civ. Eng. 06014017: 1–5.

Van Paassen, L.A., Ghose, R., Van der Linden, T., Van der Star, W. and Van Loosdrecht, M. (2010). Quantifying biomediated ground improvement by ureolysis: largescale biogrout experiment. J. Geotech. Geoenv. Eng. 136: 1721–1728.

Van Paassen, L.A., Harkes, M.P., Van Zwieten, G.A., Van der Zon, W. H., Van der Star, W.R.L. and Van Loosdrecht, M.C.M. (2009). Scale up of BioGrout: a biological ground improvement method. In: 17th International conference on Soil Mechanics and Geotechnical Engineering. pp. 2328–2333.

Yasuhara, H., Neupane, D., Hayashi, K. and Okamura, M. (2012). Experiments and predictions of physical properties of sand cemented by enzymatically-induced carbonate precipitation. Jpn. Geotechn. Soc. Soils Found. 52: 539–549.

Ground Improvement Works & Implementation of Observational Approach

Satha. Iyathurai
Associate Director – Ground Engineering and Tunnelling, AECOM, Brisbane, Australia
Thayalan. Nall
Technical Director – Ground Engineering and Tunnelling, AECOM, Brisbane, Australia
Jay. Ameratunga
Technical Executive, WSP, Brisbane, Australia
Beng. Cheah
Principal Geotechnical Engineer, Tetra Tech Coffey, Brisbane, Australia

ABSTRACT: The construction of the $2.2 billion Gateway Upgrade Project in Brisbane, Australia was successfully completed in 2011. The project included the construction of 20km of road embankments with close to 40% of the alignment constructed over soft, near normally consolidated, soil deposits. Due to the presence of these compressible layers, extensive ground improvement methods and instrumentation were used. This paper covers some of the ground improvement works carried out, difficulties encountered during the construction of the embankments and how instrumentation was useful in mitigating adverse behavior.

1 INTRODUCTION

The Gateway Upgrade Project (GUP) is one of the major road infrastructure projects constructed in Queensland, Australia. The project alignment passes through a significant extent of estuarine and marine deposits consisting of very soft silts and clays. They are prominent to the north of the River, which is the area of works this paper is concentrated on.

Due to the presence of compressible layers and paleo-channels, extensive ground improvement (GI) methods and instrumentation were used. Various construction methods were used due to differing ground conditions across the project, and constantly reviewed to ensure optimum outcomes. Wherever possible, cost effective GI options such as preloading, with and without wick drains, were utilised to meet the post construction settlement (PCS) criteria. Where constraints such as physical site limitations, deeper weak soils, available construction time, or unexpected conditions were evident, alternative methods were adopted. At some interchanges, it was necessary to adopt several different types of GI as presented in Fig. 1 to cater for many variables.

The Observational Approach was specifically selected because of the variable and complex ground conditions and the merging of different GI types across the project.

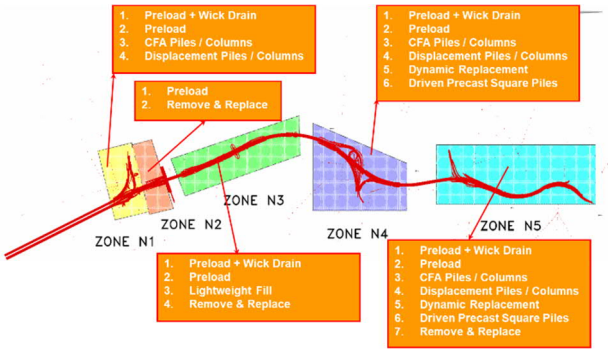

Fig. 1 Adopted ground improvement Methods in GUP

2 GEOLOGICAL CONDITIONS

The predominant geological units along the alignment are Quaternary Alluvium, Triassic aged rocks of Tingalpa/Aspley Formations, Eocene aged Petrie Formations and Brisbane Tuff outcrops.

2.1 *Geological formations*

Alluvial deposits, generally comprising sands, silts, muds, clays, gravels and peats, are found along the entire length of the alignment on the north side of the Brisbane River. Deposits are saturated, deep (10m to 35m thick), and overlie Petrie Formation Rock. On the southern side of the river, the alluvial deposits are dominant along major tributaries.

Tertiary aged rocks of the Petrie Formation lie along the alignment to the North of the Brisbane River, at depth, below Holocene and Pleistocene alluvial deposits.

2.2 *Local geology*

In general, the site area is part of a deltaic plain formed by the Brisbane River. The growth of the Brisbane delta then progressed slowly to its present form as sediments supplied by the Brisbane River built up. The quaternary age alluvium/coastal sediments of the plain can be divided into the following geological units in terms of their relative age:

- Holocene sediments (Young alluvium) – highly compressible; and
- Pleistocene sediments (Old alluvium).

2.3 *Geotechnical investigations and laboratory testing*

The geotechnical component of the overall construction risk is directly related to the ground variability and how accurately the ground conditions could be predicted. Hence, an extensive field investigation comprising boreholes, cone penetration testing with pore pressure measurements (CPTu), test pits, in-situ shear vane (SV) testing and dissipation testing, was carried out to establish the geological and geotechnical models. Selected samples were subjected to laboratory testing to obtain physical properties, and strength and compressibility properties.

3 GEOTECHNICAL MODEL

3.1 *Undrained shear strength*

Undrained shear strength, s_u, is important for cohesive soils in the assessment of short-term embankment stability and design of GI techniques.

The parameter s_u is best assessed using in-situ tests such as SV tests or laboratory tests such as triaxial tests. While CPTu provides another method of assessing s_u, it is an indirect method and therefore calibration with other tests such as SV or Unconsolidated Undrained (UU) tests is necessary.

3.2 *Compression and recompression ratio*

The magnitude of primary settlement of a normally consolidated clay layer subjected to external loading is proportional to the Compression Ratio (*CR*). The laboratory test results indicate that *CR* value varies between 0.1 and 0.35 with a design value of 0.3.

The magnitude of recompression settlement of an over-consolidated clay layer subjected to external loading is directly proportional to the Re-Compression Ratio (*RR*). The laboratory results indicate that a *RR/CR* ratio of 0.1 is appropriate for this site.

3.3 *Coefficient of secondary consolidation*

The coefficient of secondary compression, $C\alpha\varepsilon$, was evaluated using empirical relationships with *CR* and results of one dimensional consolidation tests. The laboratory results indicate that $C_{\alpha\varepsilon}$ could be taken as 4% to 6% of *CR* which is within the range proposed by Mesri (1991). Other published literature (Wong, 2007; Alonso et al., 2000) also suggests that the creep strain decreases with increasing OCR in an exponential pattern, which was adopted in the design.

3.4 *Coefficient of consolidation*

The rate of consolidation is controlled by the coefficient of vertical (c_v) / horizontal (c_h) consolidation. It is generally accepted that laboratory tests do not provide reliable results because of the sample size, and therefore emphasis was given to the CPTu dissipation tests results. These results indicate higher coefficients than those derived from oedometer tests and a value of c_v=2.5m^2/yr was adopted in the design for lower Holocene clay (LHC) with a c_h/c_v ratio of 2.

3.5 *Summary of design parameters*

A summary of design parameters adopted in the GI designs is presented in Table 1.

Table 1 Basic geotechnical design parameters

Unit	γ (kN/m^3)	c_v (m^2/yr)	*CR*	*OCR*
Crust	18.5	6.0	0.15	2.5 - 6.0
Upper Holocene Clay (UHC)	16.5	6.0	0.30	1.65 - 2.0
Lower Holocene Clay (LHC)	16.5	2.5	0.30	1.3 - 1.5
Pleistocene	17.0	3.8	0.15	>>3.0

Note: γ - Saturated Unit Weight

4 GROUND IMPROVEMENT WORKS

The settlement of soft soils due to loading arises from a combination of immediate settlement, primary and secondary consolidation. For infrastructure projects, immediate settlement is not a major concern as most of it occurs before the completion of pavement construction. Hence, GI is generally critical only to control the primary and secondary settlements.

The main function of GI is to increase the bearing capacity/density/strength/lateral stability/ liquefaction resistance, and to control deformation, accelerate consolidation, decrease imposed load and form seepage cut-offs or fill voids.

4.1 *Types of ground treatment used in GUP*

The following GI methods were used to control PCS:

- Flexible Solutions
  - Remove and Replace (R&R)
  - Preloading/Surcharging without wick drains (PL)
  - Preloading/Surcharging with wick drains (WD)
  - Lightweight fill such as bottom ash
- Rigid Solutions
  - Contiguous Flight Auger Piles/Columns
  - Displacement Auger Piles/Columns
  - Piled Embankment/Piled Raft
  - Dynamic Replacement (DR)

To improve the stability, additional measures such as high strength geotextiles, temporary berms etc., were also used.

4.1.1 *Preloading/Surcharging with or without wick drains*

The PCS of embankments constructed on soft ground can be reduced by preloading or surcharging. The time settlement curves at selected locations are shown in Figs 2 and 3 (Coffey, 2007) to represent different GI options as discussed above and the design is summarised in Table 2.

Table 2. Details of GI options at selected locations

Location (M5AN)	Fill Height	Total Settlement Without GI	Proposed GI Option	PCS in 10 years with GI
Ch 19275	7.6m	135mm	No GI	45mm
Ch 21480	5.7m	370mm	PL	100mm
Ch 21730	2.9m	515mm	PL + Surcharge (No WD)	195mm
M510-960	5.4m	990mm	WD @1.4m and PL	185mm
Ch 22080	4.4m	925mm	WD @1.4m+ Surcharge	195mm

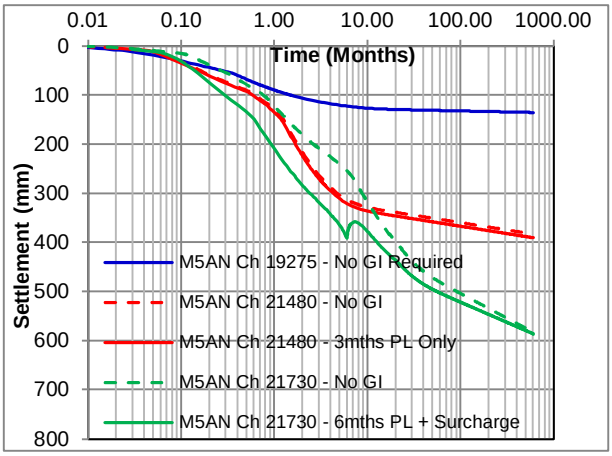

Fig. 2 Ground improvement options – PL + Surcharge

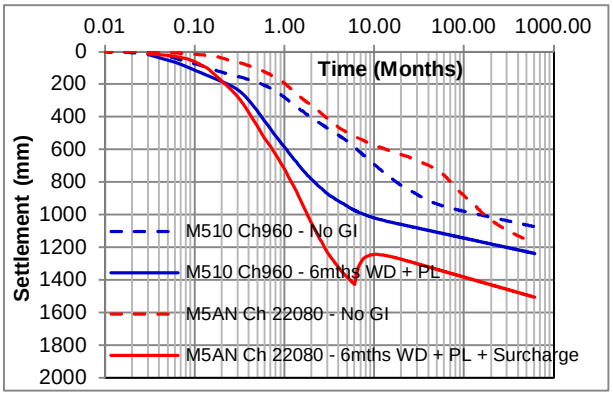

Fig. 3 GI options – WD + PL + Surcharge

4.1.2 *Remove and replace*

The R&R method is one of the simplest forms of GI and suitable when soft soil is shallow. However, site constraints and/or acid sulphate soils render this option economically less attractive at some locations. These are some of the areas where the R&R options were used:

- The subgrade does not meet CBR requirement for the pavement for low embankments.
- The alignment passes below an Air Train: Reduce induced settlement by maintaining the final stress below the pre-consolidation pressure; R&R with bottom ash was adopted.

4.1.3 *Lightweight fill (LWF)*

LWF was used at a number of locations along the GUP alignment due to various reasons: (i) to reduce the lateral load on the piles; (ii) to reduce the preloading time / amount of surcharge; and (iii) near services - to limit the additional stress on them.

4.1.4 *Contiguous flight auger piles/ columns*

Contiguous flight auger (CFA) is a non-displacement method used where fast, vibration free installation is required. CFA Piles are structurally designed as piles with reinforcement, whereas CFA Columns are specifically designed as inclusions for GI to limit settlement and they are not reinforced and not considered as piles.

CFA's were used at several locations, mainly at the bridge abutments, to meet tight PCS criteria, and near services to control ground movement.

4.1.5 *Displacement auger piles /columns*

Displacement auger columns are specifically designed for GI to limit settlement and not governed by the piling code, whereas displacement auger piles are structurally designed as piles with reinforcement and need to be designed in accordance with the piling code.

4.1.6 *Piled embankment (PE)/piled raft*

For high embankments constructed over thick deposits of soft soils where excessive PCS are anticipated, the use of a PE is considered to be one of the most effective options to reduce PCS and avoid potential failure during construction. In most cases, where PE is used adjacent to structures and PCS is to be limited to not more than 25mm, the piles are likely to be required to be founded on a hard stratum.

4.1.7 *Dynamic replacement (DR)*

In addition to the above GI options, DR technique was considered a viable option for GI works within a landfill area, and in areas of high embankments where the depth of the soft soil layer was limited to about 6m. The limitations on DR columns include:
(i) DR Columns deeper than 6 m tend to cause the surface heave rather than pushed downwards;
(ii) Method of construction may not be deemed suitable for areas where sensitive structures are present due to vibration;
(iii) unable to penetrate stiffer layers; and
(iv) column yielding.

DR method was used in the GUP project in several areas, including in the vicinity of a 110kV power line. The installation of DR could cause significant lateral movement and construction vibration that might have an impact on the performance integrity of the cable. Due to lack of available vibration data, site specific methods were used to limit the vibration (peak particle velocity – ppv) in the cable to 20mm/s. Prior to DR installation works near the high voltage power line, a trial was carried out to measure the vibrations due to DR installation. The monitoring involved measurement of ppv in three orthogonal axes using an Instantel DS-677 Minimate Plus vibration monitor with one triaxial geophone. The monitoring results are presented in Fig. 4. As shown in Fig. 4, a safe working area of 25m from the 100kV cable line was proposed for the installation of DR columns.

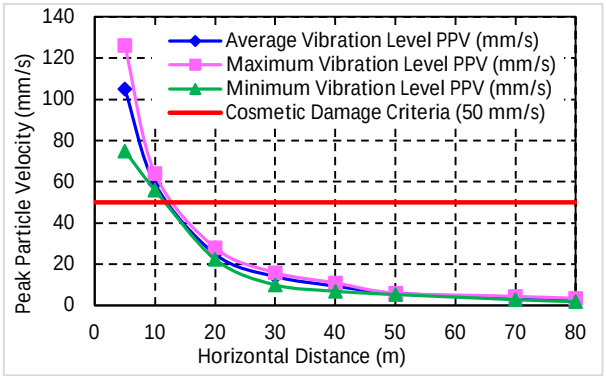

Fig. 4 Site-specific vibration vs distance

4.1.8 *Design of Load Transfer Platform (LTP)*

The rigid inclusions generally consist of vertical piles or columns that are designed to transfer the embankment load through the soft soil units to the underlying strata. In order to prevent punching of the columns through the embankment fill and creating differential settlements at the surface of the embankment, the load from the embankment must be effectively transferred to the columns via a geosynthetic reinforced LTP.

Single layer basal reinforcement

LTP with single layer basal reinforcement was designed using catenary design approach. There are several methods available in the literature for the design of basal r/f: BS8006, Terzaghi's theory, Guido's theory, Nordic handbook (Swedish method) and German method.

All the above design methods ignore the resistance from the soil. Comparisons of above methods for a 400mm square pile spaced at 1.8m c/c spacing is shown in Fig. 5. In addition, numerical analysis using PLAXIS was carried out and the results are shown in Fig. 5, which shows that most of the methods yield higher tensile forces except the Guido (1987) method which is independent of fill height. Hence, we have adopted numerical methods to design the basal reinforcements rather than using the methods published in literature.

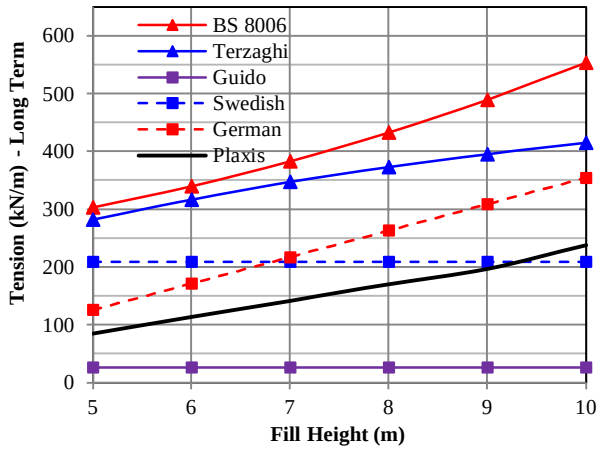

Fig. 5 Comparison of basal reinforcement requirements

Multi-layered reinforcement

The design of a multi-layered LTP is based on the use of multiple layers of reinforcement to create a stiff reinforced soil mass/beam (known as a soil raft). The beam design approach, Collin Method (ref. Collin et al., 2005), is a refinement of the Guido (1987) Method and assumes that the reinforced soil mass acts as a beam to transfer the load from the embankment above the platform to the columns below.

Method adopted in GUP

The project scope technical requirements required that the PE has to be designed based on BS8006. As discussed in the above sections, we demonstrated that the BS8006 is conservative and a single layer basal reinforcement could be replaced with a soil raft and consequently adopted.

5 OBSERVATIONAL METHOD (OM)

Due to uncertainties and the inevitable variability in the ground conditions, it is a good industry practice to adopt the Observational Method (OM) (Nicholson et al., 1999) to assess the embankment performance during construction. A typical OM can be seen in Fig. 6. The types of instruments that were used in GUP includes: Settlement plates; Surface settlement pegs/ markers; Magnetic extensometers; Horizontal Profile Gauges; Lateral displacement markers; Inclinometers; Piezometers & Standpipes.

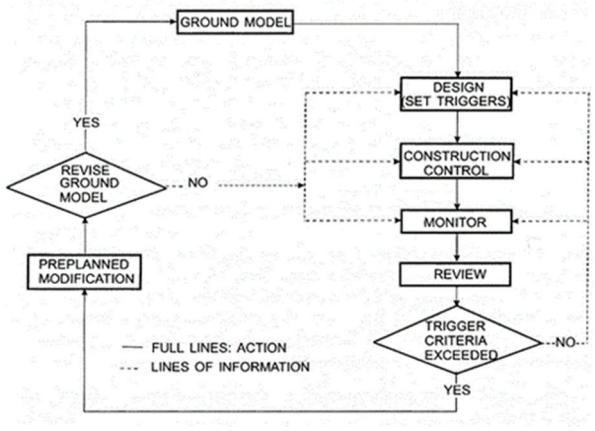

Fig. 6 Typical OM – Flow chart

6 CONSTRUCTION ISSUES & REMEDIAL

Some of the construction issues encountered during construction along with remedial solutions adopted are discussed in this section:

Landfill Area - DR was selected as the preferred GI option due to durability and constructability. At selected DR locations, the depth of DR columns was measured using air drilling techniques and noted that DR columns had not reached the design depth due to the likely presence of undesired material in the waste such as large logs/car bodies/tyres in the landfill. PCS was re-assessed based on the measured penetration depth and it was found that the residual settlement exceeds project requirements. As part of the OM, remedial measures, which included the use of higher surcharge with PL/WD, were implemented to reduce the PCS.

Bridge 26A - The transition zone at the bridge BR26 Abutment A was designed as a PE, with 26m long 400mm square precast driven piles. Due to construction programming, the abutment piles had been installed prior to the driven piles of the PE. During the installation of the driven piles, it was observed that the bridge piles moved laterally, greater than anticipated. As a remedial option, relief holes were drilled in the vicinity of the abutment piles to release the stresses from the abutment piles.

Bridge 23A (wrap-around wall, refer to Cheah et al., 2013) - The ground conditions at this location were interpreted to be 1m of crust overlying 5m thick Holocene soft clay, overlying Pleistocene Sand/Clay. The fill height was about 13m and due to physical site constraints associated with property boundaries, the slope had to be locally steepened over a 100m length, from a 1V:2H to 1V:1.3H. Such steep batter required strengthening of the batter. In addition, it required the improvement of the soft clay below ground to reduce risk of deep failures. To provide stability to the steepened embankment batter, wrap-around geosynthetic reinforcements were adopted while DR columns were proposed to improve the ground below to improve bearing capacity and to reduce long term settlement and lateral movement.

During construction, significant heave occurred, about 2m. Although this heave was not unexpected, the magnitude was. Due to this significant heave, the wrap-around wall was redesigned. However, during fill placement, up to 380mm of lateral soil movement was measured at the toe when the fill height reached 13.4m RL, 3.6m short of the final level. As shown in Fig. 7, between 8 and 12 Sep 2008, the fill height increased from 12.4mRL to 13.4mRL and lateral displacement increased from 210mm to 380mm whereas the settlement increased only from 300mm to 350mm only. The ratio of lateral to vertical movement increase was >1 indicating extremely high shear strains.

To avoid potential instability, planned actions were implemented, including the immediate removal of the last lift, cessation of construction activities and more frequent monitoring. Back analysis was carried out to recalibrate the geotechnical model by assuming the FOS to be 1.0. This involved progressively reducing the overall s_u of the DR column reinforced clay layer in the design until the calculated FOS approached 1.0. A strength reduction of about 40 to 45% from design value was required to reduce the FOS to 1.0. Using the back analysed s_u, a 20 m wide 3 m high berm was calculated as necessary to increase the calculated FOS from 1.0 to 1.2 as shown in Fig. 8 (a). With the

berm in place it was further calculated that when the full surcharge height was reached the FOS would drop to about 1.05 as shown in Fig. 8 (a) and the inferred failure profile is presented in Fig. 8 (b). This means that the theoretical FOS would be just 5% higher than that during the imminent failure stage. As the performance of the embankment during construction would be instrumented the lower FOS was considered acceptable.

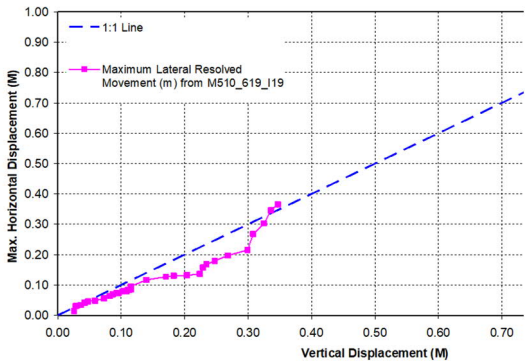

Fig. 7 Variation of maximum displacement with settlement (adopted from Cheah et al., 2013)

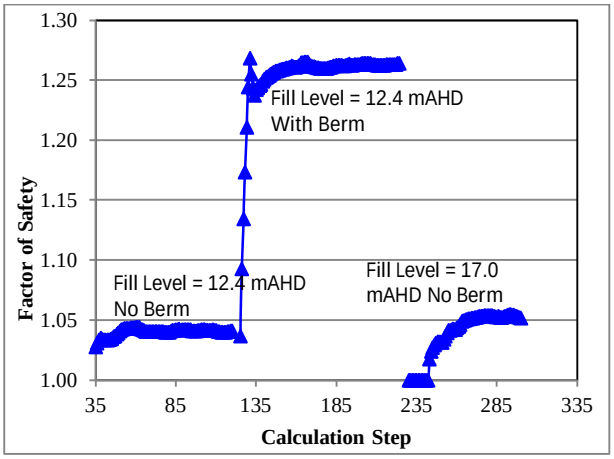

(a)

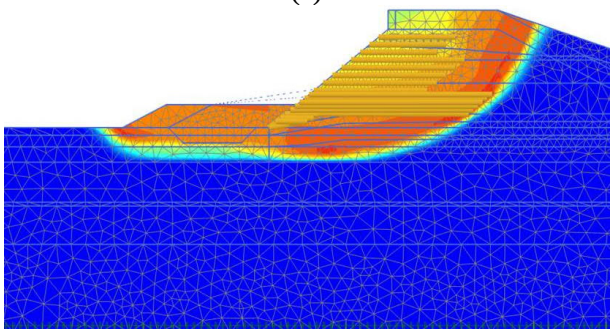

(b)

Fig. 8 (a) Variation of FOS with Calculation Step; and (b) stability plot at end of fill placement (adopted from Cheah et al., 2013)

7 CONCLUSIONS

The ground improvement methods and monitoring regime/observational approach implemented in the GUP have been discussed in this paper. Although the design and construction of the GUP project involved more challenges and difficulties, the project has been successfully completed. The complex design has been managed via better control of the construction planning/activities and use of the observational approach. The Observational Method has been successfully used to provide early warning of an imminent failure during the construction and it had allowed timely actions to be taken to reduce further risk.

ACKNOWLEDGEMENTS

The views expressed in the manuscript are solely those of the authors. Permission by the Queensland Motorways Limited (QML), Leighton Abigroup Joint Venture, Department of Transport and Main Roads and Coffey to publish this paper is gratefully acknowledged. The authors also acknowledge Coffey's GUP team members for their support.

REFERENCES

Alonso, E.E., Gens, A., and Lloret, A. (2000), "Precompression design for secondary settlement reduction" Geotechnique, 50, No. 6, pp. 645-656.

BS 8006 (1995). "Strengthened / reinforced soils and other fills, Section 8.

Cheah, B.H., Iyathurai, S., Nallarulananthan, T. and Hackney, G.A. (2013). "Successful Implementation of Design Changes during Construction of an Embankment". 18th Southeast Asian Geotechnical & Inaugural AGSSEA Conference, Singapore, Leung, Goh & Shen (eds).

Coffey (2007). "Gateway Upgrade Project, Separable Portion B, Stage 3 – Final Design".

Collin, J.G., Han, J. and Huang, J. (2005). "Geosynthetic-Reinforced Column-Supported Embankment Design Guidelines". North American Geosynthetics Society/Geosynthetics Institute Conference, Las Vegas.

Guido, V.A., Knueppel, J.D., Sweeny, M.A. (1987). "Plate loading tests on geogrid-reinforced earth slabs". Proceedings Geosynthetic '87 Conference, New Orleans, USA, pp. 216-225.

Mesri, G. (1991). "Prediction and Performance of Earth Structures on Soft Clay – General Reporter". Proceedings, International Conference on Geotechnical Engineering for Coastal Development – Theory to Practice, Vol. 2, Yokohama, Japan.

Nicholson, D, Tse, C and Penny, C. (1999). "The Observational Method in ground engineering – principles and applications". Report 185, CIRIA, London.

Wong, P.K. (2007). "Preload Design to Reduce Post-construction Creep Settlement". ANZ Geomechanics Soft Soil Workshop, Brisbane.

Ground Improvement with Timber Columns & Associated Durability Issues

Thayalan. Nall
Technical Director, Geotechnical, AECOM, Brisbane

Satha. Iyathurai
Associate Director, Geotechnical, AECOM, Brisbane

Jay. Ameratunga
Technical Executive, Geotechnical, WSP, Brisbane

ABSTRACT: Timber piles are sometimes preferred over conventional piles as they prove to be economical and easy to transport/handle. They are also used as ground improvement columns/piles to limit settlement and enhance stability. It is also known that timber pile sections within tidal zone are prone to decay and exposed to marine borer attack. Recently, in a highway upgrade project, the existing highway needed to be widened into the nearshore reclamation. In this project, ground improvement at a bridge approaches was designed using timber columns. Since the bridge is designed for 100 years, the bridge approaches also needed to be designed for 100 years to reduce the risk of any instability associated with durability of timber columns leading to collapse of asphalt or failure of road embankment. This paper outlines the design approach adopted to limit settlement and the assessments undertaken to address the durability issues of the timber column sections within the tidal zone.

1 INTRODUCTION

For many structures, timber piles are chosen as a preferred foundation type compared to conventional piles made of concrete and steel. They prove to be economical, easy to transport and handle on site. They also exhibit greater durability in chemically aggressive soils and ground water conditions with high free CO_2 and chloride levels which can be extremely detrimental to both concrete and steel. They are also driven into weak grounds as ground improvement columns or piles to limit settlement and enhance stability.

It is also known that timber pile sections within tidal zone are subject to decay and exposed to marine borer attack. In many countries timber piles are therefore recommended to be used only below the water table, where they are known to be less vulnerable to decay and foundation members are extended above permanent water level, using concrete sections.

In the recent past authors have been involved in a highway upgrade project where the existing highway widen into the nearshore reclamation, over very soft marine sediments that are prone to excessive settlement and instability during embankment fill placement. In this project, the ground improvement at the bridge approaches (Transition Zone) were undertaken with timber poles as rigid inclusions to limit long term settlement and to improve stability. Although post construction settlements (PCS) of the road embankments were designed for 25-year design life with respect to settlement (1% change in grade in both directions) the bridge has been constructed for a design life of 100 years. Therefore, from a safety perspective the bridge approaches were designed to reduce the risk of any instability associated with durability of timber column such as collapse of asphalt or failure of road embankment for a design life of 100 years. Gradual changes resulting from differential settlement and lateral displacements beyond design life (25 years) have not been of great concern, as they will be picked up during regularly maintenance and rectified. Hence the evaluation of the performance of the timber poles over 100 years became an integral part of the design. The design philosophy adopted and risks assessed are described in this paper.

2 GEOTECHNICAL MODEL

The subsoil layers encountered at the bridge transition is described below in Fig.1

The topsoil is composed of younger recent marine alluvium (Unit A) is of early Holocene age and comprised of clays and silts with traces of sand. This marine mud being poor in strength and near normally consolidated; they were very compressible and contributed to major portion of the PCS and issues associated with embankment stability.

The sediments (Unit B), underlies Unit A, are of Pleistocene in age and are characteristically stiff fine-grained soils interbedded with silty sand layers.

Although they are slightly over consolidated, under the embankment loading some sections of this layer will turn normally consolidated and expected to undergo virgin compression.

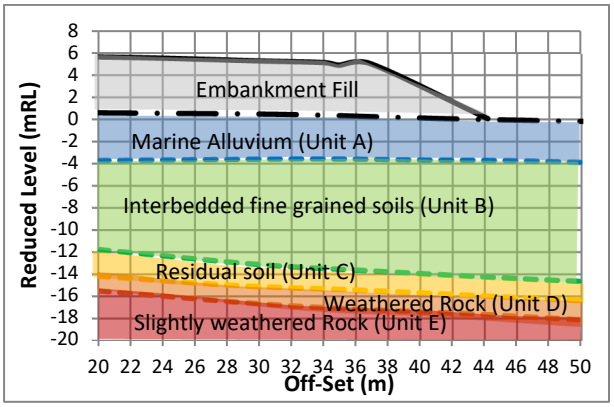

Fig. 1 Inferred ground model at transition zone

Weathered sandstone and mudstone materials form the basement layer that underlies Unit B sediments. They are composed of very stiff to hard residual soil (Unit C) down to weak sandstone and mudstone layers with a strength profile that generally increases with depth. From the settlement point of view, they were considered incompressible under the proposed embankment loading. The basement layer has been divided into three sub layers for the purpose of design based on strength defined by Standard Penetration Test (SPT) 'N' Values. They are:

- Unit C - Residual Soils with SPT 'N' values less than 30;
- Unit D - Completely weathered Rock; with SPT 'N' values between 30 and 50;
- Unit E – Highly to moderately weathered Rock with SPT 'N' values greater than 50 or refusal.

Being located next to the shoreline the water level was subjected to fluctuation of tides between +1mRL and -2mRL.

3 DESIGN CRITERIA

The design of ground improvement was primarily driven by two design criterions on PCS and stability. The section of the carriageway being a transition zone from a bridge abutment, the adopted design criteria on PCS included: (a) to limit the PCS to a specified magnitude next to the abutment, (b) maintain a vertical change in grade (VCG) of 0.5% for the 1st 10m from the abutment and at 1% thereafter over design life. Since a 6m long relieving slab being incorporated to the abutment, and the ground treatment design targeted to limit PCS to 30mm at the end of the relieving slab. The VCG was assessed at 5m intervals for compliance. The typical allowable PCS with distance is presented in Fig. 2.

To achieve such a tight settlement criterion, it became necessary to undertake ground improvement using rigid inclusions.

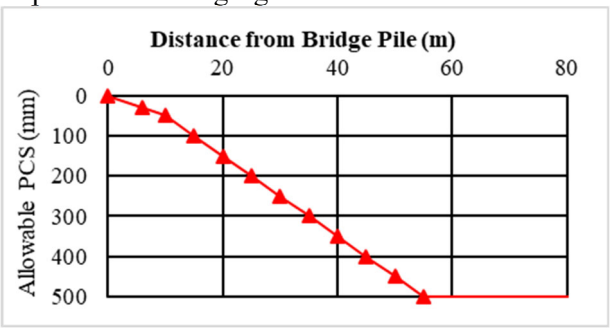

Fig. 2 Design settlement criteria

4 GROUND TREATMENT

To improve bearing capacity, limit PCS and maintain VCG, at design stages number of ground improvement methods with rigid and semi-rigid control modulus columns including dynamic replacement (DR), vibro concrete columns (VCC), continuous flight auger (CFA) columns and stone columns have been considered and workshopped during design phase. At the end timber piles were preferred since for CFA piles it would have required staging of the works allowing time for the piles to cure before walking on them or additional temporary stabilisation works. Since, both of which would have resulted in significant cost to the project and program delays, timber columns were adopted as rigid inclusions and the design philosophy adopted is discussed below.

4.1 *Design philosophy*

The timber columns of 250mm SED (small end diameter) with H6 treated have been considered. They were constructed at regular centres to improve the mass modulus and strength of weak soil layers and were founded on the residual soils (unit B, medium dense sand or stiff to very stiff/hard clay) in the area immediately adjacent to the bridge approach and were gradually reduce in depth moving away from the bridge abutments to achieve the required transition into the surrounding ground.

4.1.2 Equivalent strength and deformation properties of treated area

From a design viewpoint, if timber columns are to be installed in a regular pattern, at close spacing (3D to 4D) over a relatively large area, the reinforced soil can be defined by equivalent strength and deformation properties. The following expression for the equivalent strength and deformation

properties of the soil treated with timber columns shall be adopted (Poulos, 2002).

$$N_{eq} = a_r N_{Col} + (1 - a_r) N_S \quad (1)$$

$$N_i = tan^2\left(45 + \frac{\varphi_i}{2}\right) \quad (2)$$

$$C_{eq} = \frac{C_{Col} a_r \sqrt{N_{Col}} + C_S (1 - a_r)\sqrt{N_S}}{\sqrt{[a_r N_{Col} + (1 - a_r) N_S]}} \quad (3)$$

$$\gamma_{eq} = a_r \gamma_{Col} + (1 - a_r)\gamma_S \quad (4)$$

$$E_{eq} = E_{Col}\left[a_r^2 + \frac{E_S}{E_{Col}}(1 - a_r^2)\right] \quad (5)$$

Where N_i is passive earth pressure coefficient of material i (i.e., N_{col}, N_s and N_{eq} are passive earth pressure coefficients of column, soil and equivalent block, respectively); a_r = area ratio = $f_1(d/s)^2$, f_1 = 0.78 and 0.91 for a square and triangular pattern, respectively; d = column diameter; s = column spacing; $E_i, c_i, \varphi_i, \gamma_i$= Young's modulus, cohesion, friction angle, and unit weight of material i (i.e., i = *col* - column, *s* - soil and *eq* - equivalent block).

4.2 *Timber pile properties*

The piles are designed to have the following properties for bearing and settlement assessment:

- Unconfined Compressive Strength = 21 MPa
- Allowable compressible stress = 10.5 MPa)
- Modulus of Timber column (Ec) =8.7MPa.

A slightly reduced Ec value of 8.0 MPa has been adopted in the design.

4.3 *Design settlement and spacing*

Total settlement is a combination of immediate settlement (S_i), primary (S_P) and secondary (S_{creep}) consolidation settlement. For road projects, immediate settlements are not of a great concern as they generally occur before pavement construction. The S_p and S_{creep} are estimated using the expressions outlined below.

$$S_p = \sum SRF \times \Delta H\left(RRlog(OCR) + CRlog\left(\frac{\sigma'_{vf}}{p'_c}\right)\right) \quad (6)$$

The settlement reduction factor (*SRF*) has been defined as the ratio between E_S and E_{eq} (i.e., $SRF = E_s / E_{eq}$). Where RR, CR, OCR, P'$_c$, σ'$_{vf}$ and ΔH are defined as; recompression ratio, compression ratio, overconsolidation ratio, preconsolidation pressure, vertical final effective stress and layer thickness respectively.

$$S_{creep} = \sum \Delta H \times SRF \times c_\alpha \times log\left[\frac{t_2}{t_1}\right] \quad (7)$$

Where Cα is creep strain, while t1 and t2 are time for 90% consolidation and design life respectively.

In order to meet the minimum settlement criteria, the required spacing of timber piles has been found to vary between 0.9 m and 1.2 m (i.e., 3 to 4 times pile diameter) in a square pattern. The design settlement along the alignment is presented in Fig.3.

To efficiently manage differential settlements not reflecting at the embankment surface, (to avoid mushroom effects), the load from the embankment must be effectively transferred to the columns. This was facilitated via a geosynthetic reinforced load transfer platform (LTP).

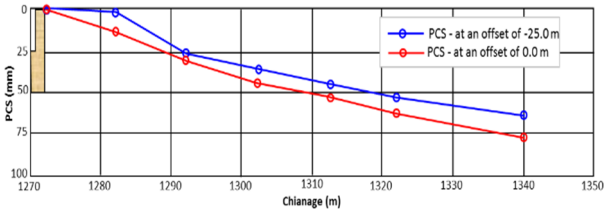

Fig. 3 Design post construction settlement

4.4 *Load transfer platform*

The design of LTP is based on the use of multiple layers of reinforcement to create a stiff reinforced soil mass was designed using the method proposed by Collin, Collin 2004). The Collin Method assumes that the reinforced soil mass acts as a beam to transfer the load from the embankment above the platform to the columns below.

This LTP design approach is discussed in detail in the US Federal Highway Administration (FHWA) report, "FHWA-NHI-16-028 Ground Modification Methods Reference Manual – Volume II". The configuration of the adopted LTP for this project is given below:

- Number of reinforcement Layer = 3 layers of Miragrid GX 60 / 60 at 250 mm Spacing
- Platform thickness = 1.0 m
- Long term geogrid strain = 3.7%
- Also, an added precaution a catenary layer of geogrid has been incorporated.

5 DURABILITY CONCERNS

The timber piles were installed through a granular working platform formed at 2.0mRL and into the existing alluvial materials beneath the working platform existed between -4mRL and +1mRL.

Due to the fluctuation of the tide, the upper section of the timber column happened to be within

the tidal zone (above -2mRL), while the lower section was expected to remain fully submerged beneath standing waters and completely encased in alluvial materials.

There are number of publications based on case studies indicate timber piles those remained submerged with reduced supply of oxygen do not undergo decay and have been preserved for over 100 years (Tomlinson 2009, and the Timber Pile Design Manual by FHWA).

At bridge approaches the sections of the column below the low tide level will be encased predominantly within materials Units A and B. Though they are subject to groundwater conditions from the tide variation, the low permeability of these materials, are expected to limit the constant fresh supply of oxygenated seawater. As a result, the activity of aerobic marine borers will be curtailed. Hence, the design assumed the durability of the lower section of the column will not be of concern.

However, the section of the timber column within the tidal zone, had been of concern with respect to durability since this will be susceptible to biodegradation from soft rot and marine bores (ref Fig.4 for typical bore attack details). Hence it became necessary to address this issue.

However, it was known that the process of bores attack will be a very slow event which leads only to a gradual reduction in material stiffness and loss of section. Hence, it may not bring about a catastrophic failure, as the timber columns will not reduce to peat or complete disappearance sooner, they are being subjected to biodegradation. However, the potential risk of columns yielding during design life was considered important and became necessary to address in the design.

In this context. for inspirations the design team turned to published literature in particular to "Manual 7 Marine borer attack on timber structures" a publication by Forest and Wood Products of Australia.

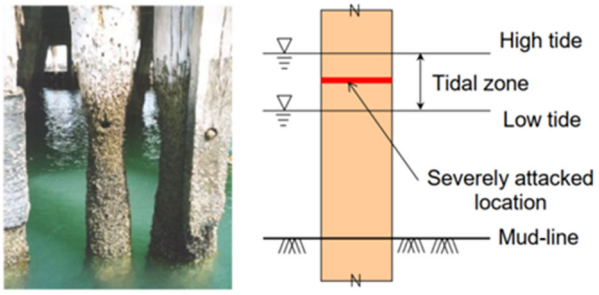

Fig. 4 Marine borer attack within tidal zone

6 ASSESSMENT OF MARINE BORE ATTACK

The model presented is summarised in Fig.5, and it takes into account factors that influence rate of marine borers attack, including location, salinity class, timber class & type of wood, preservative treatment, surface conditions and maintenance measures etc.

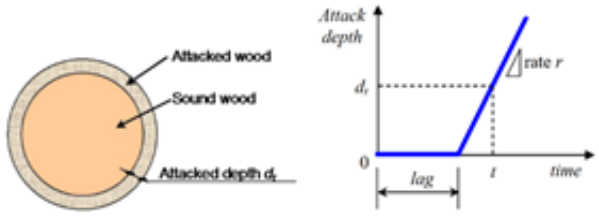

Fig. 5 Basic Model of timber attack by marine borers

The guidelines developed were based on field observations of timber piles and controlled environment laboratory studies. They propose the following expressions to estimate the rate of marine borer attack (r).

$$r = K_w K_0 \quad (8)$$

$$K_w = 0.1\, e^{0.13T} \quad (9)$$

$$K_0 = K_1 K_2 K_3 K_4 K_5 K_6 \quad (10)$$

Where:

T – Mean summer water temperature;

Kw – Location;

K_1 – Type and class of the timber;

K_2 – Salinity of water;

K_3 – Strong current and surf conditions;

K_4 – Type pf protection measure;

K_5 – Contact with other timber members; and

K_6 – Big knots with / without protective plates.

The design depth of bore attack (D_d) is expressed as:

$$D_d = D(1+\alpha V_d) \quad (11)$$

$$D = (T_d - T_{Lag})\, r \quad (12)$$

Where:

T_{Lag} = 2.0-0.1r for single treated timber;

T_{Lag} = 12-0.1r for double treated timer;

D – estimated attack depth;

V_d – coefficient of variation of D;

α - factor related to target reliability level;

T_d – design life in years; and

T_{Lag} – Lag period in years.

V_d varies between 0.7 and 0.9 depending on the timber class and type. For the timber type considered in the design V_d of 0.7 has been adopted;

- α, varies between 0.4 and 0.8 for low and normal consequence of failure. In the design α of 0.8 has been considered.

Making allowances for local conditions (such as a mean summer water temperature of 20 degrees and a salinity of 35ppt), estimated that the timber columns will be subject to an attack rate of 1.25mm/year, followed by the lag period (T_{Lag}) of 11 years. Further these estimates had been for timber piles in open water, considered conservative since, at the project site, even the section of the timber columns within the tidal zone will be embedded in fill.

With respect to strength when timber columns are encased in soil, published literatures indicate, even the attacked section of the timber column carry a portion of the axial load. For columns under axial loading the total load carrying capacity is expressed by the following expression (Kuilen and Gard 2012).

$$F_u = f_{c0} A_R + f_{cd} A_d \quad (13)$$

Where:

F_u – Total axial load;

f_{c0} – characteristic compressive strength of timber;
f_{cd} – strength of decayed timber (refer Fig. 6);

AR – area of non-attacked section of the timber;

A_d – area of attacked section of the timber

Studies also indicate that the strength of the decayed section timber drops to nothing within 5 years (Liese and Stamer, 1934). Hence in the design few considerations have been incorporated to minimise the risk of pavement/embankment instability and they are described in the section below.

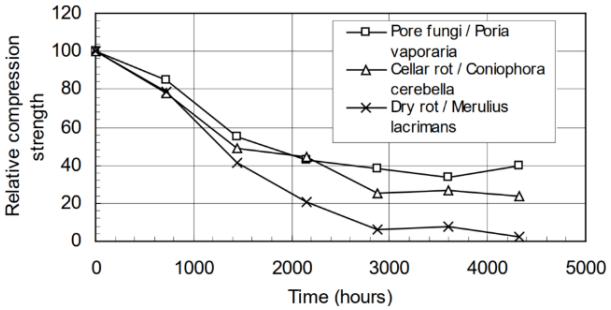

Fig. 6 Compressive strength after decay initiation

7 MEASURE TO MINIMISE RISK

Based on the above evaluation and understanding of the decay processes associated with soft rot and marine bores attacks, few design measures were incorporated to minimise potential risks. They include:

- In the assessment of embankment stability in the long term and under seismic loading, potential strength contribution from the section of the timber columns above -2mRL has been discounted. Only in the short-term loading scenarios, (i.e. during and immediately following construction) full contribution of the timber columns has been considered.
- In the assessment of PCS, the following decay model as presented in Fig. 7 has been considered for the section of the pile within the tidal zone:

- For the first 11 years the properties of the timber will not be affected (Lag Time);
- Column will lose 2.5mm of its diameter per year beyond the lag time; and
- Timber will reduce in stiffness at a yearly rate of 0.5%.

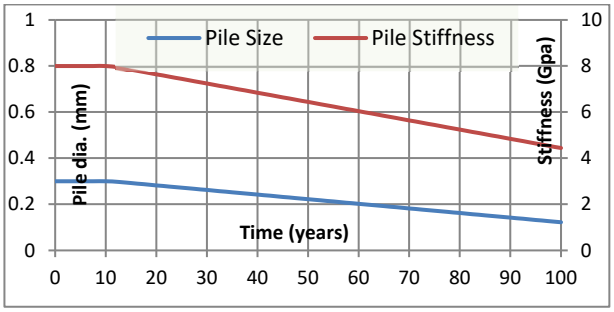

Fig. 7 Model considered for section loss

Considering the above, estimated changes to geotechnical pile capacity and mobilised compressive stress over design life are summarised in Figs 8 and 9. This clearly indicated that:

- The geotechnical capacity of the timber piles will be adequate to carry the embankment load on the column (estimated based on the column tributary area) during the design life and beyond; and

- The compressive stress at the critical section of column increases over design life, yet it would not exceed compressive strength of the timber during the 100-year design life.

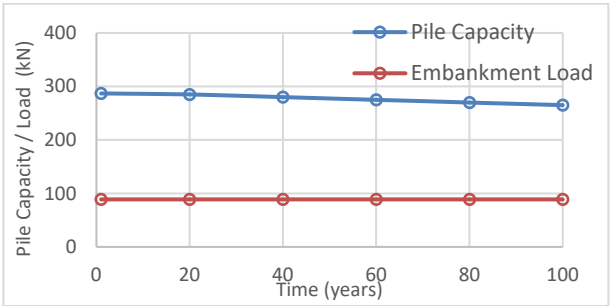

Fig. 8 Axial pile performance over design life

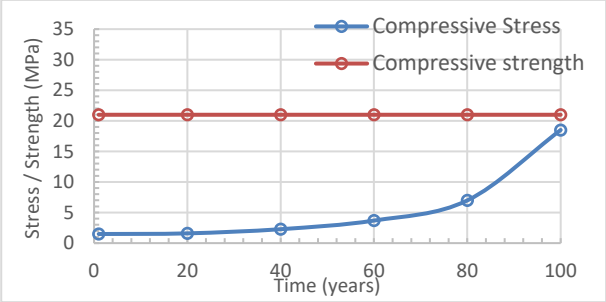

Fig. 9 Axial compressive stress and strength of the pile

The post construction settlement of the approach embankment too was assessed. The critical area being the section immediately next to the relieving slab, the variation of PCS at the edge of reliving slab over design life was evaluated and this is presented in Fig. 9. For comparison, the estimated post construction settlement ignoring potential pile decay is also presented in Fig 10.

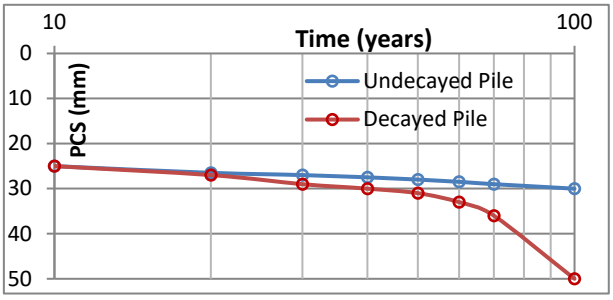

Fig. 10 Predicted post construction settlement

The outcomes of the above assessment indicate:

- The decay induced potential increase in PCS with in the first 50 years is very gradual and the increase is limited around 11%;

- However, during the 2nd half of the design life, due to timber decay the PCS increases is more pronounce and the estimated increase in settlement was found to be around 67%.

These outcomes helped convinced the client that the, timber column is a suitable alternate:

- Impact due to predicted post construction settlements are not significant and could well be managed as part of the maintenance regime (periodic asphalt surfacing);

- Gradual settlement will not undermine the performance of road surface and will not hinder the traffic flow.

- Further the load transfer platform (reinforced soil raft) which extends across the top of the timber could help smoothen settlement across the embankment, even if localised voids are formed as a result of the reduced diameter and not contribute towards any localised settlement.

8 CONCLUSIONS

Timber columns are known to be economical and easy to transport/handle, compared to other pile types. In the foundation industry their applications are largely limited to as foundation elements where the timber piles are maintained fully submerged below the standing water table. This is primarily because, as well known that timber piles located within tidal zone are prone to a rapid rate of decay and exposed to marine borer attack. Hence in soft ground engineering, timber pile usage within tidal zones is largely limited to short term or temporary support such as enhancing stability, settlement under short term loading etc.

This paper describes a case history where a design has been implemented at a bridge approach, and timber columns have been used as ground treatment columns, without compromising stringent design requirements for settlement and stability. At this project site, the road embankment supported by timber columns, widened into the nearshore reclamation that was subjected to tidal fluctuation. Further, the bridge approaches were designed for 100 years with reduced risk of any instability associated with durability of timber columns leading to collapse of asphalt or failure of road embankment.

Adopting appropriate design philosophy, good understanding on; timber behaviour, site tidal fluctuation, ground water conditions and considerations of risks associated with pavement performance, jointly contributed towards the successful completion of this design.

ACKNOWLEDGEMENTS

The authors would like to acknowledge the contribution of Dustin Tookey of Coffey International Auckland, who served as the Geotech team lead during this phase of the project and other Coffey team members contributed in many other ways toward the success of is project.

REFERENCES

Forest and Wood products Australia, Manual 7 Marine borer attack on timber structures 2007.

Poulos, H.G. (2002). Research Report on Foundation Design For Very Soft Clays, Coffey's Technical Innovation Group.

Jan-Willem van de Kuilen1,2, Wolfgang Gard, Residual Service Life Estimation Using Damage Accumulation Models, World conference on Timber Engineering, 2012.

FHWA Timber Pile Design Manual

The design of the load transfer platform for controlled modulus columns – an evaluation of two published methods

J. Thayalan
Geotechnical Engineer, WSP Australia Pty Limited, Brisbane

S. Iyathurai
Associate Technical Director, AECOM, Brisbane

ABSTRACT: Controlled Modulus Columns (CMC) are used as a viable ground improvement technique in many civil engineering works and are widely used on highway projects to support tall embankments over thick compressible layers. The load transfer platform (LTP) is an integral part of the CMC foundation system, made of geosynthetic reinforced granular fill installed between the embankment and the columns. There are several published methods that outline the design of the LTP. This paper compares two methods, these are BS8006-1:2010 and Collin's Beam Method. Comparisons are made as to the settlement mitigation capabilities of each design method, and how the empirical calculations are compared with those obtained from numerical modelling. The results of this study found that embankments with LTPs designed using BS8006-1:2010 experience less settlement and negative bending stress than those with LTPs designed using Collin's Beam Method.

1 INTRODUCTION

Road and rail embankments are an important aspect of transport infrastructure projects. An issue arises when embankments are constructed over soft, compressible soils, as settlement problems become apparent due to the low bearing capacity of the ground. To remedy this, ground improvement techniques, such as Controlled Modulus Columns (CMC), are utilized. A major component of the CMC system is the load transfer platform (LTP), which helps to transfer a major portion of the loads from the embankment onto the columns.

There are numerous design methods for LTPs, such as that of BS8006-1:2010, Kempfert (2004), Hewlett and Randolph (1988), and Collin's Beam Method (Collin, et al, 2005). The two methods focused on in this paper are that of BS8006-1:2010 and Collin's Beam Method, due to their popularity in Australia. For both of these methods, the main aspect of the LTP design process is estimating the tensile requirement of geosynthetic reinforcement. A LTP designed as per BS8006-1:2010 features a single layer of geosynthetic reinforcement at the base of the embankment; whilst Collin's Beam Method prescribes multiple layers of reinforcement in-between layers of granular fill.

This research aims to provide a comparison between BS8006-1:2010 and Collin's Beam Method; regarding their agreement with numerical outcomes, settlement mitigation performance, strain in the geosynthetic, and bending stresses in the CMC. Numerical modelling using PLAXIS 2D software was utilized to achieve these aims.

2 ADOPTED GROUND MODEL

A simple ground model was adopted to represent typical south-east Queensland soft soil conditions. The ground model features an 8m thick layer of soft clay overlying a 6m thick layer of very stiff (VSt) clay. The design parameters adopted for these clay layers are summarised below in Table 1. The ground water table is considered at 1m below ground surface.

Table 1. Adopted ground model and Design Parameters

Parameter	Soft Clay	VSt Clay
Depth (m)	0-8	8-14
Unit Weight, γ (kN/m^3)	16.5	19
Effective Cohesion, c' (kPa)	3	10
Effective Friction angle, ϕ'	26	30
Undrained Shear Strength, s_u (kPa)	25	150
Young's Modulus, E (MPa)	6.25	37.5
Poisson's ratio, v	0.3	0.3
Coefficient of vertical consolidation, c_v (m^2/yr)	2.5	N/A

These parameters have been adopted based on experience with similar material and engineering judgment.

3 EMBANKMENT PROPERTIES

3.1 *Embankment geometry*

The embankments presented in this study represent standard road/rail earth fill embankments and satisfy the requirements of the Queensland Department of Transport and Main Roads (TMR)

Geotechnical Design Standard (GDS) – Minimum Requirements (2020). The crest width of the embankments is 10m, and the batter slopes have a gradient of 1V:2H. The height of the embankment is one of the independent variables of this study, two heights of 3m and 6m are used.

3.2 *Fill material*

The material parameters of the embankment fill are presented below in Table 2, and they are in compliance with TMR's GDS. Note that the granular fill is only used for LTPs designed using Collin's Beam Method.

Table 2. Material parameters for embankment fill

Fill Type	ɣ (kN/m^3)	E (MPa)	c' (kPa)	ϕ'	v
Embankment Fill	20	30	5	30	0.3
Granular Fill	20	75	0	36	0.3

3.3 *Surcharge loading*

Surcharge loading was applied across the width of the embankments. As per TMR's GDS 10 kPa and 20 kPa surcharge loads were applied during the construction stage and service stage, respectively.

4 CMC PROPERTIES

4.1 *Section properties and spacing*

The CMC used in this study are 450mm in diameter. Section properties of the CMC are provided below in Table 3. The CMC are to be 10m in length, i.e., embedded 2m into the very stiff clay.

Table 3. CMC section properties

Diameter, D (m)	Area (m^2)	Second Moment of Inertia (m^4)
0.45	0.159	0.002013

The CMC spacing is an independent variable in this study; two centre-to-centre spacings of 3*D and 4*D are to be used.

4.2 *Concrete parameters*

The CMC used in this study are to be unreinforced and made of relatively low strength concrete. The concrete parameters, as per AS3600: 2009, are provided below in Table 4.

Table 4. CMC concrete parameters

Concrete Strength, f'c (MPa)	E (MPa)	v
20	24,000	0.2

5 LTP DESIGN

5.1 *Embankment Configurations*

Taking into consideration the two independent variables of embankment height and CMC spacing, a total of 4 embankment configurations per LTP design method are analysed as given in Table 5.

Table 5. Details of Analyses

Embankment Height (m)	Spacing	Reference
3	3D	3m_3D
3	4D	3m_4D
6	3D	6m_3D
6	4D	6m_4D

5.2 *Summary of LTP design*

For both design methods, the LTP design primarily concerns calculating the tensile requirement of the geosynthetic reinforcement. The LTPs designed using BS8006-1:2010 feature a single layer of reinforcement at the base of the embankment, whilst the LTPs designed using Collin's Beam Method feature min. three layers of reinforcement in between granular fill. The calculated tension in the geosynthetic for all embankment configurations is presented below in Fig. 1.

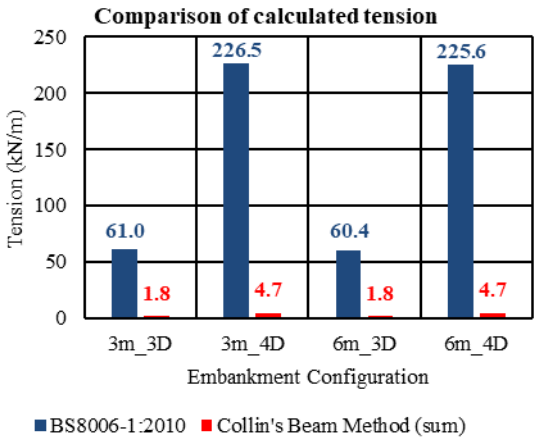

Fig. 1 Comparison of calculated tension

It is evident from Fig. 1 that the tensile requirement for the BS8006-1:2010 method is significantly higher than that of Collin's Beam Method. A likely reason for this is that, unlike BS8006-1:2010, Collin's Beam Method does not take into consideration the height of the embankment or the surcharge load at the embankment crest when assessing the geosynthetic requirements for the LTP; only column clear spacing is considered for Collin's Beam Method. For both design methods, the calculated geosynthetic tensile requirement is the almost identical for both 3m and 6m high embankments. This is attributed to embankment critical height in

the case of BS8006-1:2010, i.e., the height of embankment considered in this study is greater than critical height of 1.4* CMC clear spacing; and hence embankment loads above this critical height do not influence the tension mobilised. For the LTPs designed using Collin's Beam Method, this is because the embankment height and surcharge loading are not taken into consideration during the design process, i.e., the LTP thickness, number of geogrid layers and strength of the geogrid is only dependent on the clear spacing between the CMCs.

6 PLAXIS 2D

6.1 *Material models*

6.1.1 *Soil models and drainage behaviour*

The material models and drainage behaviour used for each soil type in PLAXIS 2D are presented below in Table 6. The Mohr – Coulomb (MC) material model was chosen for the soft clay as it is considered sufficient for this study. Undrained A behaviour is used for the soft clay to better facilitate consolidation behaviour. The embankment fill, granular fill, and very stiff clay were also modelled as MC material, under drained behavior.

Table 6. PLAXIS 2D soil models and drainage

Soil Type	Material Model	Drainage Behaviour
Embankment Fill	MC	Drained
Granular Fill	MC	Drained
Soft Clay	MC	Undrained A
Very Stiff Clay	MC	Drained

6.1.2 *Plates*

The CMC were modelled as individual plate elements in PLAXIS 2D, and the surrounding soil was modelled with in-situ soil parameters. The equivalent plate properties used in the analyses are presented below in Table 7.

Table 7. PLAXIS 2D plate properties

Spacing	Stiffness, EA (kN/m)	Flexural Rigidity, EI (kNm2/m)	Weight, w (kN/m/m)	v
3*D (1.35m)	2827433	35785	0.766	0.2
4*D (1.8m)	2120575	26839	0.574	0.2

6.1.3 *Geogrid elements*

The geosynthetic reinforcement layers were modelled using Geogrid elements in PLAXIS 2D. The input parameter for Geogrid elements is 'EA', which can be calculated as:

$$EA = \frac{T_{rp}}{\varepsilon} \quad (1)$$

Where 'T_{rp}' is tensile capacity of geotextile, and ε is corresponding strain.

6.2 *Model geometry and Construction staging*

An example of the full PLAXIS 2D model geometry for the 3m_3D embankment is provided below in Fig. 2.

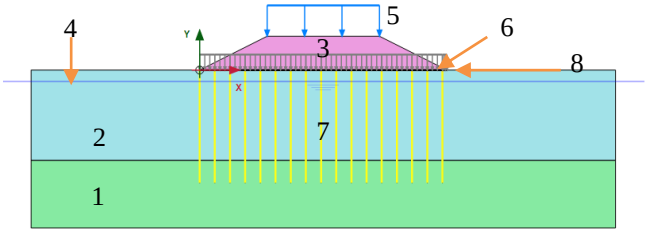

Fig. 2 Model geometry

Each element of the model is numbered:

1. Very stiff clay layer
2. Soft clay layer
3. Embankment fill
4. Ground water table level
5. Surcharge loading at crest
6. Surcharge loading at base
7. CMC plates
8. LTP (geosynthetic reinforcement and/or granular fill)

The construction stages used in the PLAXIS analyses are presented below in Table 8. The updated finite element mesh option was used to increase the accuracy of the analyses. Consolidation calculation type was used for all stages except for the initial stage, where the K0 procedure was used.

Table 8. Time stages adopted in PLAXIS 2D

Stage ID	Stage No.	Cumulative time for 3m embankment (days)	Cumulative time for 6m embankment (days)
Initial Stage	1	-	-
CMC Installation	2	30	30
End of Construction	3	51	72
2.5 Yrs Post Construction	4	963	984
End of Design Life	5	14651	14672

During the initial stage, only the ground model is present. At the CMC installation stage, the CMC plate elements and base surcharge load of 10kPa are included. At end of construction, 2.5 years post construction, and end of design life stages, the embankment fill, LTP, and traffic surcharge of 20kPa are present.

6.3 *Obtaining results*

6.3.1 *Outputs from PLAXIS 2D*

Settlement at the base of the embankment, mobilized tension in the geosynthetic, and CMC load effects were obtained from the PLAXIS outputs. Settlement at the base of the embankment was recorded at each of the stages specified in Table 8. The mobilised tension in the geosynthetic is taken as the axial load in the geogrid element. The CMC load effects (axial load and bending moment) were obtained from the plate elements. For each model, load effects were obtained for the central CMC and the CMC at the toe of the embankment.

6.3.2 *CMC bending stress*

To check whether the CMC has adequate structural capacity, the bending stress in the column must be checked. In order for an unreinforced column to remain structurally adequate, it must not experience negative bending stress (Wong and Muttuvel, 2011). The negative bending stress can occur when the CMC is subjected to large bending moments. Typically, large bending moments are present at the toe of the embankment.

The bending stress in the CMC is calculated using the no negative stress condition provided by Plomteaux and Lazacedieu (2007):

$$\sigma_N + \sigma_{M-} > 0 \text{ ; (2)}$$

$$\sigma_N = \frac{R_i}{\pi D^2/4} \text{ ; (3)}$$

$$\sigma_{M-} = -\frac{M_i}{\pi D^2/32} \text{ (4)}$$

Where:

- R_i = computed axial load
- M_i = computed bending moment
- D = CMC diameter

7 RESULTS OF ANALYSES

7.1 *Settlement*

A typical deformed mesh (scaled up 20 times) from stage no. 5 of the PLAXIS analyses is presented below in Fig. 3.

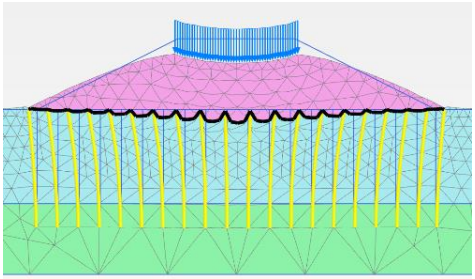

Fig. 3 Typical deformed mesh from PLAXIS analyses

The obtained settlements at the base of the embankments from PLAXIS 2D for each design stage is presented below in Fig. 4. Outcomes with the BS8006-1:2010 LTPs are plotted as solid lines, whilst Collin's Beam Method LTPs are represented as dashed lines.

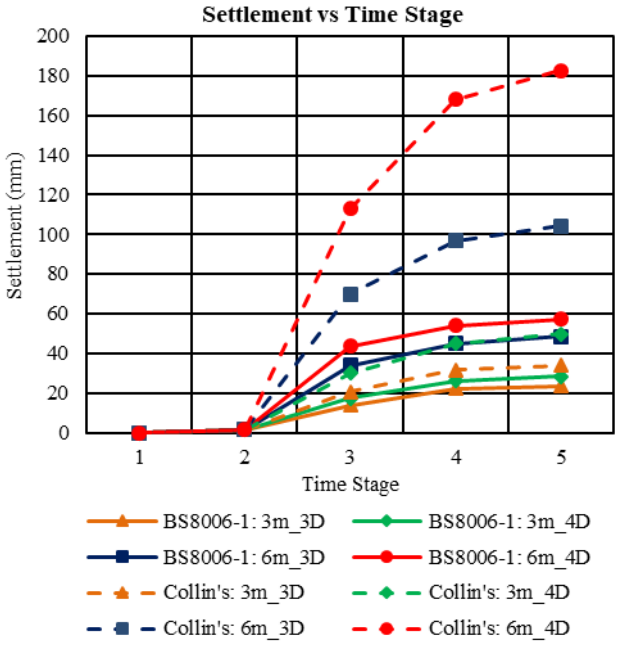

Fig. 4 Comparison of settlement at each time stage

As can be seen from Fig. 4, the embankments with LTPs designed using BS8006-1:2010 undergo significantly less settlement than their corresponding embankments with LTPs designed with Collin's Beam Method.

The 6m embankment with 4*D spacing with the LTP designed using Collin's Beam Method experiences substantially higher settlements than any other embankment. This drastic increase in settlement is likely due to the fact that, using

Collin's Beam Method, the 6m embankment uses the same LTP as the 3m embankment. This indicates a limitation with Collin's Beam Method; that it is ineffective for taller embankments as the LTP design calculations do not take into consideration the height of the embankment and surcharge loading. The BS8006-1:2010 design method also prescribes similar geosynthetic tensile strength for both 3m and 6m embankments, but the design procedure is robust enough that the reinforcement is still as effective for the 6m embankment.

To test the validity of this limitation, the 6m_4D model was rerun in PLAXIS 2D with higher (three-fold) tensile strength for each reinforcement layer. This was done to check whether adopting a stronger geosynthetic would influence the settlement performance of the embankment. The total settlement for the increased strength model is presented below in Fig. 5, compared to the original strength model.

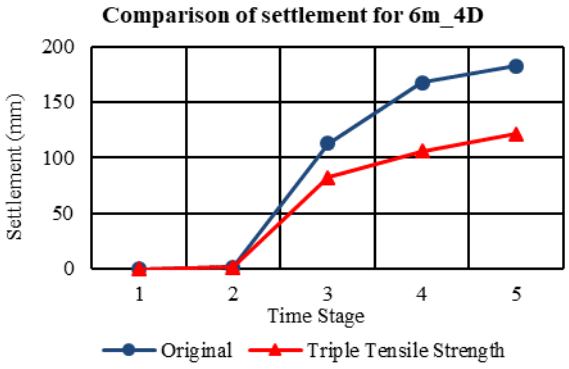

Fig. 5 Comparison between original and three-fold tensile strength reinforcement

It is evident from Fig. 5 that there is a noticeable reduction in settlement using the higher strength geosynthetic. Hence, it can be reasonably considered that Collin's Beam Method is not as effective for taller embankments, as the design of the geosynthetic reinforcement does not take into consideration the embankment height.

The results of this study indicate that, concerning settlement mitigation, the strength of the geosynthetic reinforcement plays a more vital role than the layers of granular fill within the LTP.

7.2 *Agreement with numerical outcomes*

Fig. 6 below compares the tension in the geosynthetic obtained from PLAXIS compared to the calculated value for the LTPs designed using BS8006-1:2010. As can be seen from Fig. 6, BS8006-1:2010 substantially overestimates the

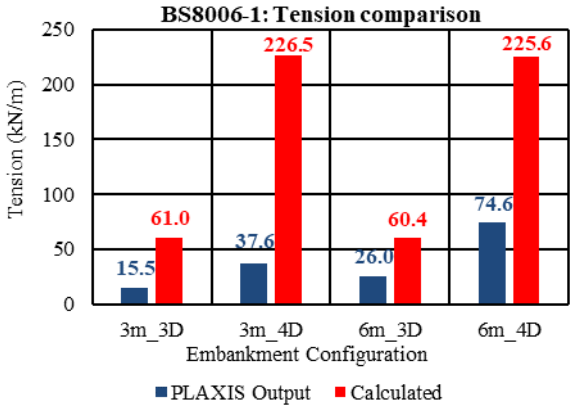

tension in the geosynthetic for all embankment configurations as expected.

Fig. 6 Comparison of tension from PLAXIS output and design calculation for BS8006-1:2010

The comparisons between calculated tension and PLAXIS obtained tension in the geosynthetic for LTPs designed using Collin's Beam Method is provided in Fig. 7 below. As can be seen from the below graph, it is apparent that Collin's Beam Method consistently underestimates the tension in the geosynthetic reinforcement. Once again, this is likely a limitation associated with the fact that Collin's Beam Method does not fully account for

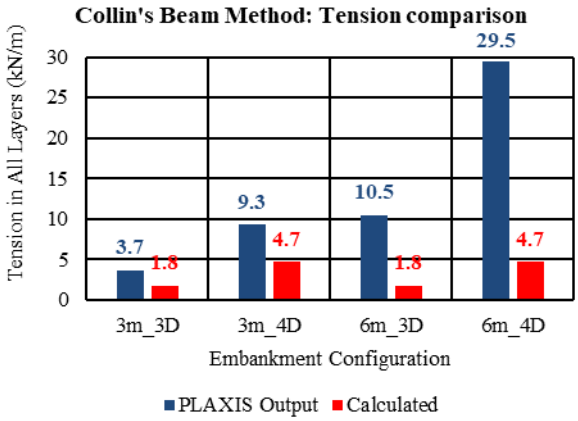

all influencing factors that contribute to the estimation of geosynthetic tensile strength.

Fig. 7 Comparison of tension from PLAXIS output and design calculation for Collin's Beam Method

7.3 *CMC bending stress*

The bending moments and axial forces applied to the CMC were obtained from PLAXIS 2D, and the bending stress was calculated using the equations provided by Plomteaux and Lazacedieu (2007). The bending stresses for the CMC at the toe of the embankment and central CMC are presented below in Fig. 8 and Fig. 9 respectively.

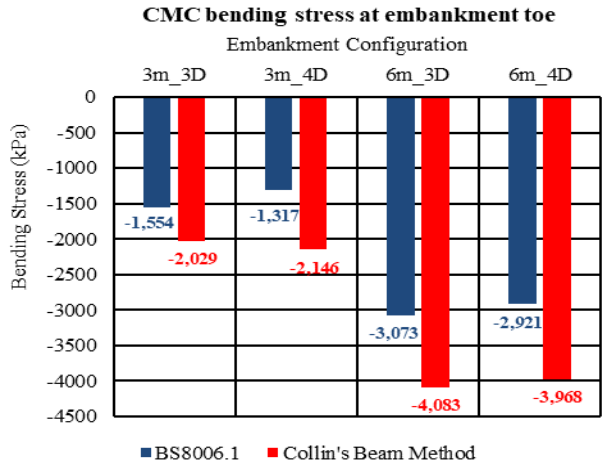

Fig. 8 CMC bending stress – embankment toe

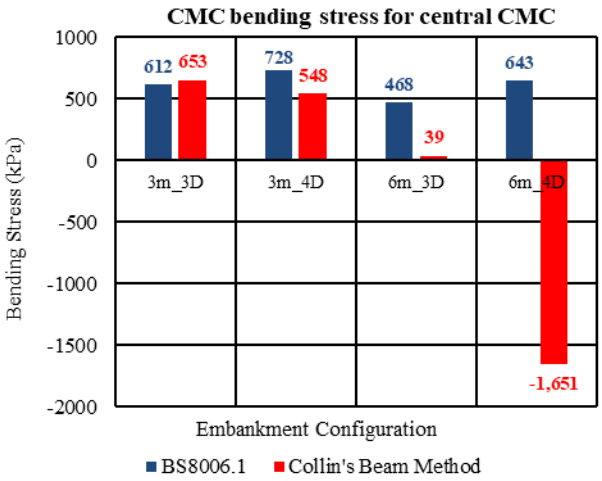

Fig. 9 CMC bending stress – central CMC

As can be seen from the above graphs, all CMC at the toe of the embankments experience negative bending stress, and thus will require steel reinforcement. This is normal practice for CMC at the embankment toe, as it is expected that bending moments will be high in these regions. All of the central CMC, based on BS8006-1:2010 geotextile, experience positive bending stress. However, this is not the case for the embankments with LTPs designed using Collin's Beam Method, where substantial negative bending stress is experienced by the central CMC in the 6m_4D embankment. In such a case, where all CMC require reinforcement, driven piles or continuous flight auger piles would be a more suitable ground improvement option.

8 CONCLUSIONS

The results of this study indicate that the performance of the LTP is largely influenced by the capacity of the reinforcement, rather than the presence of granular fill within the LTP. Based on the PLAXIS outcomes, it can be inferred that there is scope for optimisation for BS8006-1:2010, whilst Collin's method has scope for modification to more accurately evaluate the reinforcement capacity. Furthermore, the results indicate that the tensile strength of the geosynthetic reinforcement also influences the settlement performance of an embankment when analysed in PLAXIS.

To ensure a safe design approach, it is recommended that the estimated tensile requirements of the reinforcement be compared to the mobilized tension using a finite element program such as PLAXIS, and the higher value be used for design. Further work can be done in this study area by obtaining field performance data of instrumented CMC supported embankments to compare with and calibrate the numerical outcomes.

ACKNOWLEDGEMENTS

The authors would like to acknowledge Dr Chaminda Gallage of the Queensland University of Technology (QUT) for supervising the undertaking of this study as an undergraduate thesis throughout 2019.

REFERENCES

British Standards Institution. (2010). *BS8006-1: Code of practice for strengthened/reinforced soils and other fills.* BSI Standards Limited.

Collin, J. G., Han, J., & Huang, J. (2005). Geosynthetic-Reinforced Column-Support Embankment Design Guidelines. *North America Geosynthetics Society Conference.* Las Vegas.

Department of Transport and Main Roads. (December 2020). *Geotechnical desgn standard: minimum requirements.* Department of Transport and Main Roads.

Hewlett, W. J., & Randolph, M. F. (1988). Analysis of piled embankments. *Ground Engineering, 21*(3), 12-18.

Jones, C. J., Lawson, C. R., & Ayres, D. J. (1990). Geotextile reinforced piled embankments. *Proceedings, 5th International Conference on Geotextiles, Geomembranes, and Related Products*, (pp. 155-160).

Kempfert, H. G., Gobel, C., Alexiew, D., & Heitz, C. (2004). German recommendations for reinforced embankments on pile-similar elements. *Proceedings of the EuroGeo3*, (pp. 279-284). Munich DGGT.

Plomteux, C., & Lazacedieu, M. (2007). Embankment Construction on Extremely Soft Soils using Controlled Modulus Columns for Highway 2000 Project in Jamaica. *16th Southeast Asian Geotechnical Conference.* Kuala Lumpur.

Standards Australia. (2009). *AS3600: Design of Concrete Structures.* Standards Australia.

Wong, P., & Muttuvel, T. (2011). Support of Road Embankments on Soft Ground using Controlled Modulus Columns. *International Conference on Advances in Geotechnical Engineering*, (pp. 621-626). Perth.

Improving the performance of Badulusirigama Landslide using subsurface drains: A numerical study

Lilanka Kankanamge
National Building Research Organization, Sri Lanka

S. A. S. Kulathilaka
Department of Civil Engineering, University of Moratuwa, Sri Lanka

G. A. C. Ganepola
Asian Disaster Preparedness Center, Thailand - Sri Lanka Country Office

U. P. Nawagamuwa
Department of Civil Engineering, University of Moratuwa, Sri Lanka

ABSTRACT: Improvement of subsurface drainage is a commonly used slope stabilization technique all over the world. The role of subsurface drainage in keeping the phreatic surface at lower levels is vital to maintain a higher Factor of Safety of a given slope. This paper studies the impact of subsurface drainage in stabilizing an inferred landslide slope at Badulusirigama village in Badulla District, Sri Lanka. The deep-seated slip plane at Badulusirigama landslide was stabilized using a fan type subsurface drainage system. Effectiveness of the implemented measures were evaluated by means of two-dimensional slope stability analysis using Spencer method. The numerical model was first validated using monitoring data acquired from different instrumentations. Parametric studies were then conducted to assess the performance of the stabilized slope during anticipated extreme weather conditions in future. Numerical analyses demonstrated that the role of subsurface drains was important in drawing down initial high water tables and in avoiding formation of perched water table conditions in confined aquifers. The subsequent analysis showed that it is also important to actively limit rainfall infiltrations during prolonged precipitation events by means of surface drainage improvements and impermeable barriers such as vegetation, to eliminate perched water table conditions.

Key words:slope stability, deep seated failure, subsurface drainage, infiltration analysis

1 INTRODUCTION

Stability of a slope is directly connected with thermo – hydro – mechanical processes taking place in the soil and in the surrounding environment. The outcome of different interactions between these factors, alter the natural equilibrium condition of the slope. In Sri Lanka, excessive rainfall is the main triggering factor for slope instability (Abhayarathne, 2017). Ingress of water into the soil mass during heavy rainfall events leads to generation of excess pore water pressures inside the slope. This excess pore water pressure will cause reduction in effective stresses and lead to slope instability. Hence, it is vital to apply measures to control these rising ground water tables caused by prolonged infiltrations. Removal of excess or additional ground water pressures from the slopes has become the most popular economic and efficient measure of slope rectification or stabilization. The objective of using sub surface drains is lowering of ground water table. Subsurface drains are also used in emergency situations in highways where local instabilities are occurred due to the effect of perched water conditions during excessive rainfalls. The performance of a proposed subsurface drainage system may depend on number of factors such as the position of drains in the landslide, inclination, length and configuration (Cook et al. 2007; Pathmanathan 2009).

It is always vital to evaluate the performance of a proposed sub surface drainage system in stabilizing a slope failure, before the installation at site. This study investigated the performance of a subsurface drainage network implemented at a site for mitigation of landslide risk, in Badulla district, Sri Lanka. Its performance was evaluated by carrying out numerical analysis to investigate the stability of the slope corresponding to different rainfall events and ground water conditions. This paper presents the results and findings of the analyses conducted.

2 STUDY AREA

The site under study is located at Badulusirigama-village in Badulla administrative district of Sri Lanka (Fig 1(a)).The landslide affected area is situated within the premises of the Uva-Wellassa University. The width of the landslide is approximately 120 m and length is about 500 m. The slope angle of the moving area is about 10 – 15 degrees. Movements had occurred during the rainy seasons of 2007, 2011 and 2012. Local retrogressive collapses had been observed in the crown and flank slopes during heavy rainfall events. The slip surface had developed between the boundary of topmost colluvium layer and underlying completely to highly weathered rock layer. The failure type was rotational and the slip surface was encountered at a depth of around 10 -12 m on average, from the existing ground level. Mitigation of the landslide risk in the area was carried out by constructing a network of surface and subsurface drains with the technical support of the Government of Japan (Japan International Cooperation Agency, 2015).

3 SURFACE & SUBSURFACE INVESTIGATIONS

Prior to implementation of mitigation measures, a comprehensive investigation programme was conducted at the site. Initial investigation programme was comprised of a geological and a geomorphological survey, a borehole investigation, a resistivity survey and a seismic survey.

4 MONITORING PROGRAMME

The monitoring program included the acquisition of data related to ground movements.

4.1 *Potential Sliding Plane*

Monitoring data acquired from different instrumentations revealed that the potential sliding plane had developed in between the zones of colluvium and the completely weathered rock zone. Results of the monitoring programme indicated slight ground movements when excessive rainfall events were present. The extensometers installed at the upper slope area had indicated that the slide was actively moving during the heavy rain falls in December 2014. Meanwhile, extensometers at the toe of the slope had indicated compression displacements which denoted that the slide was rotational in nature. In addition to this, inclinometer and the pipe strain gauge which were installed in the slope had shown significant displacements corresponding to rainfall events. The inclinometer data showed relative displacements at a depth of around 9 – 10 m from the ground surface and strain gauge indicated displacements at a depth of 12- 13 m from the existing ground level. These evidence confirm the occurrence of active ground movements causing slope instabilities in response to excessive rainfall events along the inferred failure plane. Assembling the aforementioned information with the geophysical survey data and tension cracks observed on the ground surface, the sliding plane had been established as shown in Fig. 1(b). The whole sliding mass was divided into three slides namely, upper, middle and lower.

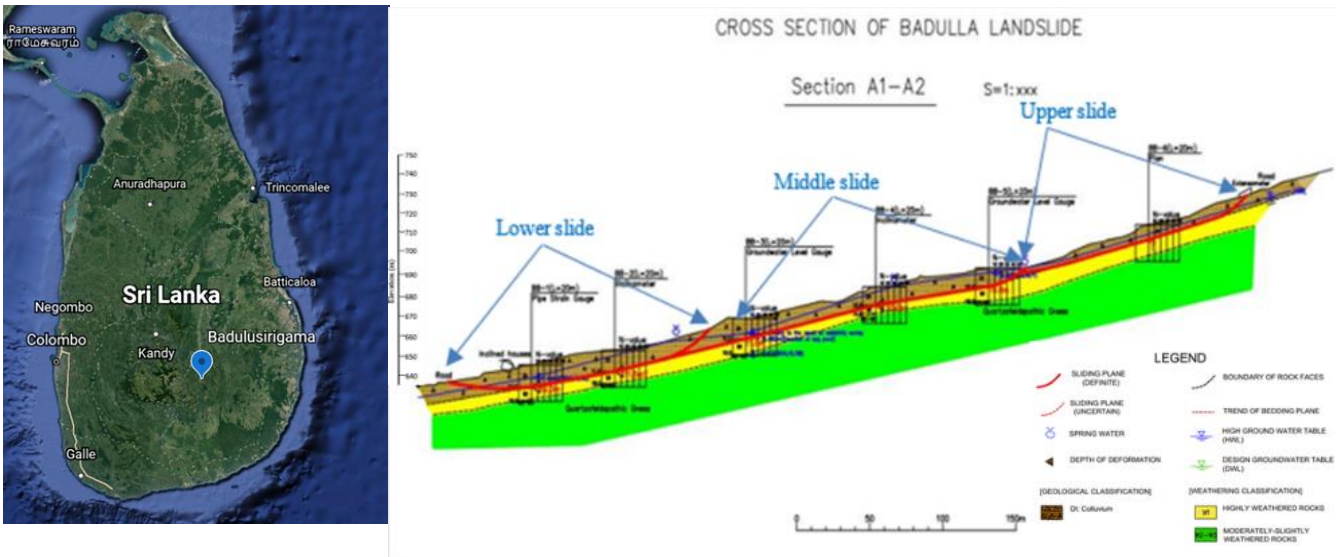

Fig.1: (a) Location of the Badulusirigama village in Sri Lanka, (b) Potential Slip surfaces defined based on the field investigations (Japan International Cooperation Agency, 2015)

Table 1: Properties used in SLOPE/W and SEEP/W formulations

	SLOPE/W module			SEEP/W module		
Formation	Cohesion (kPa)	Friction angle (deg)	Unit weight (kN /m^3)	Saturated Per-meability (m/day)	SWCC	Permeability function
1.Colluvium	2	22	15	0.0860	Silty Sand*	Estimation based on VG**
2.Completely to highly weathered rock	8	35	16	0.0860	Silt*	Estimation based on VG**
3.Highly to moderately weathered rock	20	40	17	8.6E - 10	Saturated only material	

*Built in function available in SEEP/W module

**Based on the estimation method by Van Genuchten (VG) (1980) available in SEEP/W module

5 ASSESMENT OF SLOPE STABILITY

5.1 *Development of the geotechnical model*

The geotechnical model of the site was developed based on the information obtained from the site investigation programme. The topmost soil layer was formed of colluvium materials in which the thickness was about 12 – 15 m. Thickness of the underlying completely to highly weathered layer was around 15 – 20 m. Highly to moderately weathered rock layer was encountered at a depth of around 25 m from the existing ground level at the investigated locations. Accordingly, the parameters given in Table 1 were assigned for subsoil layers for the analysis.

5.2 *Numerical analysis of the stability of existing slope*

Stability assessment was carried out using SLOPE/W and SEEP/W modules available in GEO STUDIO 2012 software (GEO-SLOPE International Ltd., 2012a; GEO-SLOPE International Ltd., 2012b). Information obtained from the monitoring programme were directly incorporated into the stability analysis. Accordingly, the slip surfaces specified in the cross section A1- A2 (Fig. 1b) were used in the analysis. The phreatic level was assumed to be present more or less at the ground surface level. This is to account for the very high ground water table and the stagnant water bodies existed by the time of significant movements occurred. Fig.2 indicates the fully specified slip surfaces used in SLOPE/W module, inferred based on the ground investigations.

Initial pore water pressure profile of the model was generated using SEEP/W module of GEO-SLOPE software. The calculated pore water pressures were then used in SLOPE/W module to conduct the stability analysis in terms of effective stresses. The factor of safety values for each of the three slides obtained from the model are presented in Table 2, Fig.3 (a), Fig. 3(b) & Fig.3(c), respectively.

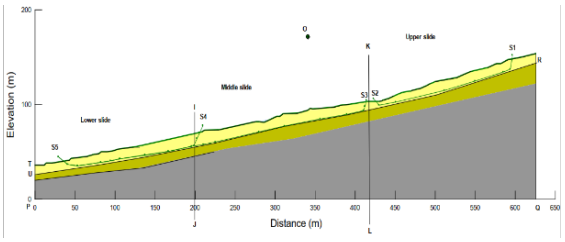

Fig.2: Fully specified slip surfaces in the SLOPE/W module

Table 2: Summary of the factor of safety values for existing slope conditions

Slide	Factor of safety
Upper	1.03
Middle	1.08
Lower	1.10

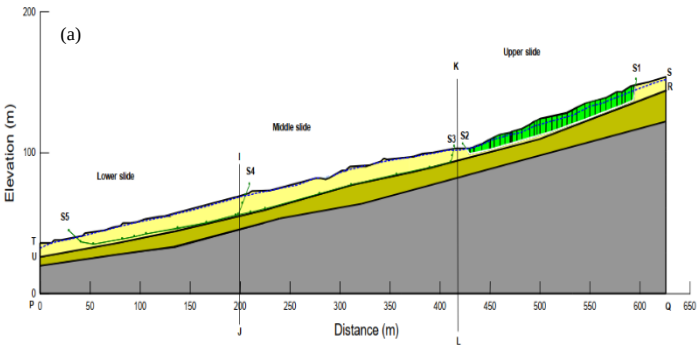

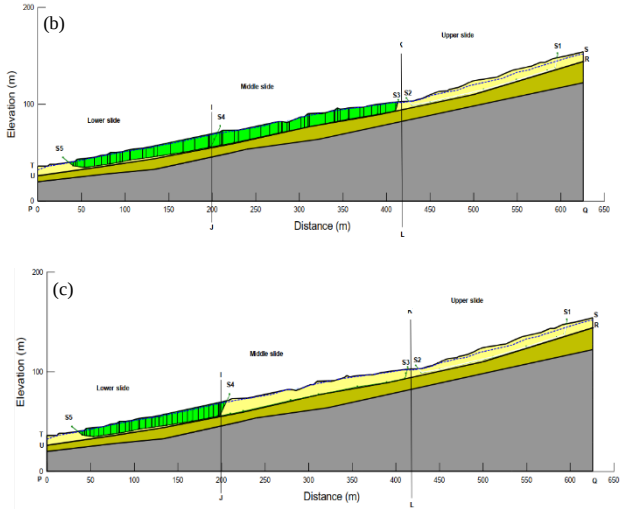

Fig.3: Critical slip surfaces with corresponding factor of safety values for: (a) upper slide, (b) middle slide, (c) lower slide

5.3 *Rectification design*

According to the information obtained from the field investigation surveys and monitoring programme, it was apparent that the Badulusirigama landslide was a slow moving (creep) deep seated landslide in which the movements were accelerated during the periods of heavy rainfall. The main triggering factor is the prolonged rainfall and consequent rise of the phreatic surface. Apart from this, development of perched water table conditions and increase of loading above the failure surface as a result of stagnant water bodies, were the main causative factors leading to ground movements. Therefore, the foremost focus when designing the mitigation measures was to control the rise of ground water table during heavy precipitation events and direct the surface water paths away from the slope.

5.4 *Subsurface Drainage Measures*

The main objective of introducing subsurface drainage was to lower the rising ground water table during infiltration events. In this context, altogether fifty one (51) number of subsurface drains had been installed at the site. The drains had been grouped in fans named from "A" to "F". "A" corresponds to the drainage fan at the highest elevation and F corresponds to the drainage fan at the lowest elevation of the slope (Fig.4). The first three fans (A, B and C) composed of eight (8) drains and each measuring 45m in length. The rest of the fans (D, E and F) has nine (9) drains in each. The length of a drain in Fans "D" and "E" is 60m, whereas in Fan "F" is 55m. The horizontal angle of the subsurface drains varybetween5 and10 degrees upwards in order to facilitate gravity flow. Fig. 5 presents a cross section of the subsurface drainage arrangement.

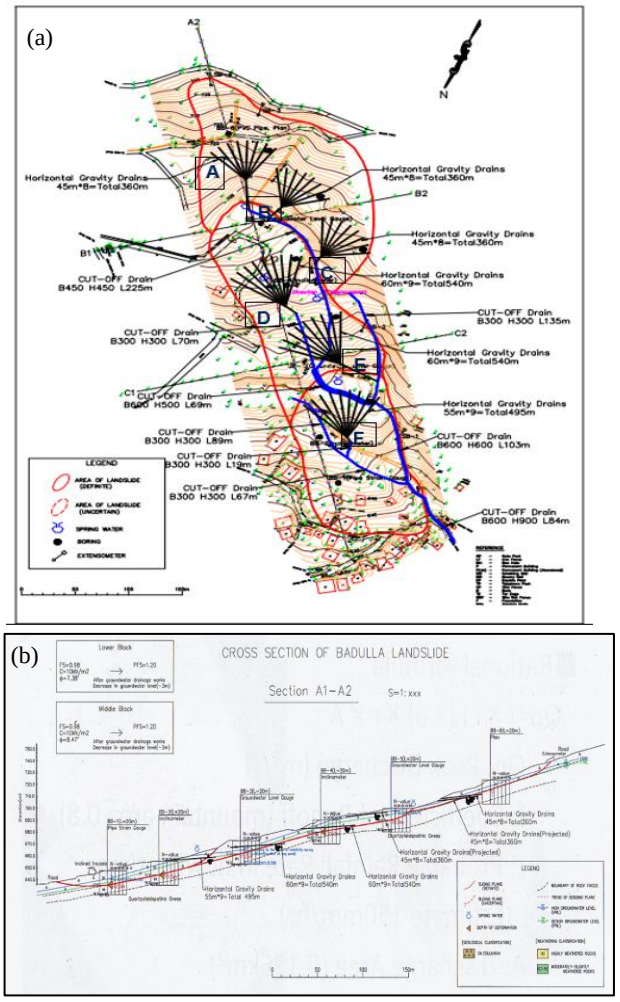

Fig.4: (a) Drainage arrangement in plan view, (b) Cross section of the subsurface drainage arrangement (JICA report on Proposal for rectification on landslide, slope failure and rock fall in pilot sites, 2015)

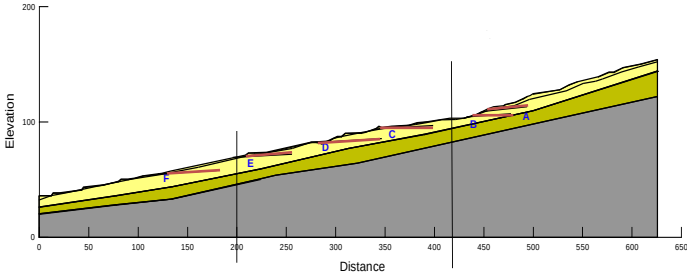

Fig. 5 Cross section showing the subsurface drainage arrangement

5.5 *Numerical analysis of slope stability after introduction of subsurface drains*

Subsurface drainage arrangement was modelled in SEEP/W in 2D plane strain conditions (Fig. 6). The drains were simulated as thin elements having a specified thickness. This region was then assigned the potential seepage face boundary condition (Total flux = 0). To simulate the impact of bottom up construction sequence, drains were activated starting from Drain F to A (DF to DA), while maintaining a 3 day elapsed time. The boundary condition

ensured that there was no outflow from the drains when the surrounding soil was unsaturated. The initial seepage condition of the slope was established using a steady state seepage analysis. It was followed by a transient analysis to investigate the behaviour of the slope corresponding to a rainfall event. Results from the transient seepage analysis was then imported to SLOPE/W module to assess the stability of the slope.

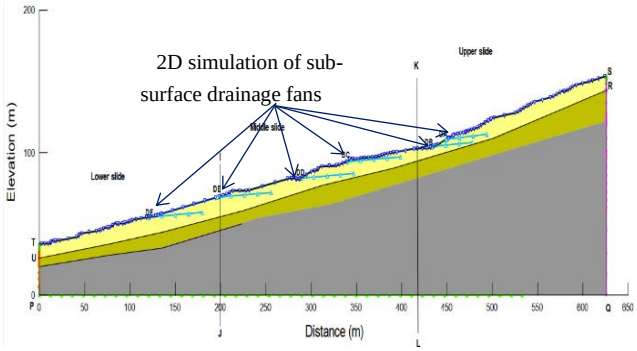

Fig.6: Subsurface drains simulated in SEEP /W module

Fig. 7 indicates the improvement of factor of safety of the slope corresponding to each of the three sliding surface after the subsurface drainage improvement. Lower slide has gained a factor of safety improvement of about 19% since the installation of DF. Thereon, factor of safety of the lower slide increases at a uniform rate with the installation of rest of the drains. However, a factor of safety value of above 1.4 was obtained since the installation of DC. Meantime installation of drain DF caused a 10% enhancement of the factor of safety of middle slide. Rapid improvements of the factor of safety values are noticeable in the middle slide, soon after the installation of DE and DD. Factor of safety has been improved from 1.2 to almost 1.31 and to 1.46 after the installation of DE and DD, respectively. The factor of safety value of the upper slide has gained a significant improvement only after the installation of DB. During the installation of four previous drains DF, DE, DD and DC, factor of safety of the upper slide has increased only slightly. The dates of activation of drains DF to DA are indicated below the time axis.

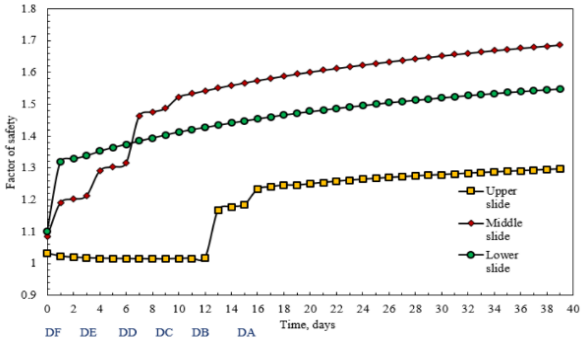

Fig.7: Variation of factor of safety of three slides after subsurface drainage improvement

The above transient analysis was continued until there were no significant variations occurred in the pore water pressure profile in between subsequent time steps. Results were saved after each time step and pore water pressure information of each time step were used to decide the termination criteria. The phreatic surface after 30 days was indicated below the effective reach of the bottom most drain. Subsequently, the shallow depths of the slope had become unsaturated and presence of negative pore water pressures were shown in the analysis.

6 PERFOMANCE OF THE SUBSURFACE DRAINAGE SYSTEM UNDER CRITICAL RAINFALL EVENTS

Afterwards, an actual rainfall event of 30 days duration with a maximum value of 216mm/day experienced by the slope during December 2014 (Fig. 8) was simulated on the slope to investigate the behaviour of the slope to the same rainfall events with improved subsurface drainage measures.

It was observed that a significant drop of the factor of safety of the three slides was noticed after the heavy rainfall of 216 mm (Fig.8). The pore water pressure contours indicated a reduction in matric suction after two days of heavy rainfall event of 216 mm. It further showed the formation of near surface saturated zones at some locations of the slope. Such situations would be more prominent in the field due to the variation of field permeability of soil resulting from heterogeneity. The recorded minimum factor of safety during the rainfall event was 1.16, 1.38 and 1.58 for upper, middle and lower slides respectively. The value is still greater than the previous (before improvement) factor of safety value obtained with more or less fully saturated conditions. However, in the actual scenario, surface drainage measures too had been introduced to drain the water away from the slope body, which was not accounted in the numerical analysis conducted.

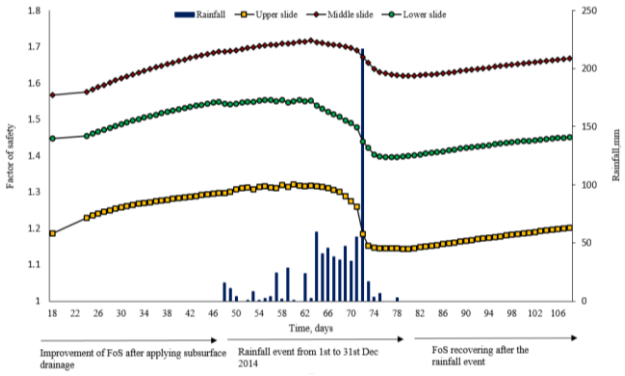

Fig.8: Variation of factor of safety of three slides after subsurface drainage improvement corresponding to rainfall event from 01st to 31st December 2014

The rate of factor of safety gain after the total rainfall event of 30 days was slower (Fig. 8) when compared to the rate of factor of safety improvement immediately after the application of subsurface drainage measures (Fig.7). This could be mainly due to the different levels of saturation of the soil. The permeability of the soil would have been much higher prior to the installation of the subsurface drains due to the presence of saturated conditions. With the drawdown of the phreatic surface the permeability of the upper soil layers would have been decreased and this demanded a longer time duration to drain away the water. After the improvement of the subsurface drainage measures, no significant rise of the water table was observed even after the rainfall event of 216 mm. The water infiltrated into the soil has followed the rapid drainage path through the installed drains without causing a pore water pressure increase. Rahardjo et al., (2002) have also reported similar findings on a parametric analysis conducted.

7 CONCLUSIONS

The case study discusses the applicability of the subsurface drainage to mitigate a deep-seated landslide in the hill country of Sri Lanka. Radial type drainage arrangement looked after a wider area of the slope and also was easy to construct in uneven morphologies causing minimum disturbance to the potential moving mass. The results of the numerical analysis conducted shows that the subsurface drainage measures are effective in drawing down high initial water tables. With the installation of drains in a bottom up sequence the safety margins of the identified slip surfaces in the respective regions increased gradually. The FoS values of the potential failure zones were increasing further for sometime even after the completion of the installation of drains.

There was a reduction of the FoS on all three potential failure surfaces when the critical design rainfall was applied on the rectified slope. A significant reduction was noted only after the day of the 216mm/day rainfall. In the preceding days the reduction of FoS was minimal due the drainage of the infiltrated water through the system of installed drains. No significant rise of ground water table was recorded during this rainfall due to the same reasons. The reduced FoS values of all three potential failure surfaces recovered rapidly after the cessation of the rainfall. The effectiveness of a system of sub surface drains in maintaining adequate safety margins in a slope during prolonged high intensity rainfall events is illustrated by these findings.

8 REFERENCES

Abhayarathna, L. R. (2017) Rainfall thresholds for initiation of landslides in Ratnapura district. In The Institution of Engineers, Sri Lanka (Ed.) Transactions – 2017. Part B. Technical Papers (pp. 1-9)

Cook, D.I., Santi, P.M. and Higgins, J.D., 2008. 2007 AEG Student ProfessionalPaper: Graduate Division: Horizontal Landslide Drain Design: State of the Art andSuggested Improvements. Environmental & Engineering Geoscience, 14(4), pp.241-250

Geo-Slope International Ltd.(2012a). Seepage modelling with SEEP/W.

Geo-Slope, International Ltd.(2012b). Stability modelling with SLOPE/W.

Japan International Cooperation Agency,(2015), “Proposal for rectification on landslide, slope failure and rock fall in pilot sites”.

Pathmanathan, M.L., 2009. Numerical Simulation of the Performance of HorizontalDrains for Subsurface Slope Stabilization (Doctoral dissertation, Washington StateUniversity)

Rahardjo, H., Hritzuk, K.J., Leong, E.C. and Rezaur, R.B., (2002). Effectiveness of horizontal drains for slope stability. Engineering Geology, 69(3-4), pp.295-308.

Effect of temperature increase for the occurrence of natural landslides

G. A. C. Ganepola
Asian Disaster Preparedness Center, Thailand – Sri Lanka Country Office

U. de S. Jayawardena
Department of Civil Engineering, Faculty of Engineering, University of Peradeniya, Peradeniya, Sri Lanka

ABSTRACT: Earth's climate shows a warming trend. Many regions in the world are experiencing higher temperatures including Sri Lanka. The effect of rising temperatures could be another catalyst for creation of slope instabilities. The aim of this study is to evaluate whether there is an effect of the increase of surface temperature on the occurrence of natural landslides in Sri Lanka. The warmer and drier atmospheric conditions could conduce to form desiccation cracks at failure initiation areas. These cracks serve as avenues for water infiltration during the wet spell and can accelerate development of pore water pressure leading to a reduction in shear strength parameters. Successive cycles of healing/ reopening of cracks and increased permeability of soils, which is brought about by seasonal variation of rainfall combined with rising temperatures can lead to areas of reduced strength, which can cause failure to occur progressively and eventually leading to a major landslide.

1 INTRODUCTION

Landslides are one of the major disasters, Sri Lanka experiences, which result in loss of human lives and considerable damages to economy. Rathnaweera and Nawagamuwa (2011) indicated that the most devastating landslide events tend to occur as a result of comparatively shorter duration, high intense rainfall compared to the lower intense rainfalls for a longer period.

Globally averaged combine land and ocean temperature show a warming trend of 0.85°C over the period 1880 – 2012 (IPCC, 2014). Sri Lanka's average temperature is increasing at a rate of 0.01°C to 0.03°C per year (Basnayake et al. 2019). Rathnayake and Herath (2005) indicated that the lengths of dry spells are increasing all over Sri Lanka.

In this context, the effect of rising temperatures, which has not yet been considered, could be another causative factor to accelerate the driving force of unstable landmass in hilly areas.

Long dry climatic condition prior to the occurrence of landslide could create physical changes such as opening of desiccation cracks on soils of the ground surface. These cracks serve as avenues for water infiltration during the wet spell and can cause increases in pore water pressure leading to a reduction in strength of the ground mass.

Thus, the increase of atmospheric temperature could be another factor to create unstable landmasses in hilly areas. This study is focused on evaluating the effect of increasing temperature on natural landslides in soil in some of the districts prone to landslides in Sri Lanka.

2 EFFECTS OF INCREASE OF TEMPERATURE ON SLOPE STABILITY

Bo, Fabius and Fabius (2008) indicated in their study that global warming has an increasing impact on many factors that relate directly to the stability of natural slopes.

Firstly, changes in temperature can cause changes in vegetation cover, for example, previously healthy vegetation can die. These impacts cause loss of root reinforcement, loss of soil suction in the soil and shallow erosion with the associated increases in water infiltration.

Secondly, increases in temperature can desiccate the soil. In some cases the lower moisture content will increase soil strength parameters and beneficial for soil suction. However, it can conversely result in losses of soil cohesion, for example as a result of fissuring of a clay deposit. These fissures or cracks accelerate water infiltration into the slope with the associated loss of factor of safety.

3 METHODOLOGY ADOPTED

This study was carried out by implementing a historical data approach. That is by comparing catalogues of historical landslide occurrences with climatic records, rainfall and temperature, covering

the last two decades (From year 1997 to year 2017).

Firstly, a landslide database was composed using historical records of landslides, which occurred in May 2017 on natural soil slopes in the Wet Zone districts of Sri Lanka namely Ratnapura, Kalutara and Matara. The study was limited to first time landslide events where the failure material was soil and initiated by natural causes. Fig. 1 presents the locations of selected landslides considered under this study.

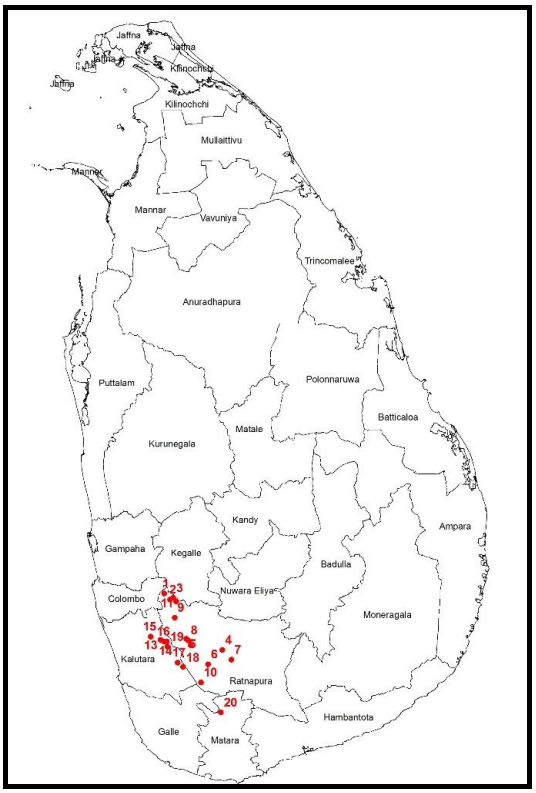

Fig. 1 Location map of selected landslides in soil

Afterwards, a climatic database was created with respect to spatial distribution of collected landslide events. The database included monthly precipitation and monthly temperature records. Climatic data were collected for a maximum period of twenty years prior to the occurrence of the failure.

The changing groundwater conditions due to particular patterns of temperature and rainfall has a great influence in the landslide activity which take place mainly in soils. Hence, by evaluating the temporal variability of water deficits at the landslide initiation location prior to the failure, it would be possible to derive whether there is an effect of increasing temperature on natural landslides in soil frequencies.

Therefore, a standard water balance equation was applied at each location to estimate monthly water deficits. The water balance equation adopted in this study is,

$$P - PET = \Delta S + G + R \quad (1)$$

Where P = precipitation, PET = Potential Evapotranspiration, ΔS= change in storage G = net ground water flow out of the catchment and R = surface runoff.

The term $\Delta S + G + R$ represents **remaining water** availability. When the term is negative, it can be considered as a water deficit condition. When the term is positive, it can be considered as a water surplus condition.

Finally, a time series analysis was carried out to study the effect of water deficits and dry climatic conditions prior to the occurrence of the landslide event.

4 CALCULATION OF REMAINING WATER

In order to determine remaining water at each failure location, precipitation (P) and potential evapotranspiration (PET) needed to be known.

4.1 *Estimation of monthly precipitation at the failure location*

Rain gauge stations of the Department of Meteorology, Sri Lanka were rarely located close to landslide locations. Therefore, in this study it was decided to use gridded rainfall data for Sri Lanka which were acquired from global gauge-satellite precipitation estimates such as CHIRPS (Climate Hazards group Infrared Precipitation with Stations). This enabled the extraction of rainfall data at the location of the occurrence of the landslide.

4.2 *Estimation of monthly temperature at the failure location*

Department of Meteorology has one weather station measuring Temperature per district. Statistical Abstract (2017) indicated that temperature decreases by 6.5^0 C for every 1000 m rise in elevation. Hence, by knowing the altitude of the failure location and that of the weather station, temperature at the failure location could be estimated. Equation (2) was used to calculate the temperature change (t_c) which needs to be corrected at each location;

$$t_c = (6.5/1000)*(\text{Elevation of weather station} - \text{Elevation of landslide location}) \quad (2)$$

4.3 *Estimation of monthly Potential Evapotranspiration*

Lu et al. (2005) mentioned that potential evapotranspiration (PET) could be defined as the amount of water that could evaporate and transpire from a vegetated landscape without restrictions other than

the atmospheric demand. It provides a convenient index to represent or estimate the maximum water loss to the atmosphere.

Various methods of calculating Potential Evapotranspiration are available in the literature. Among them "Thornthwaite's empirical formula" can be used for locations at which daily maximum and minimum temperatures are recorded (Palmer & Havens, 1958). Abundant data on temperature records are available in the Sri Lankan context.

There are research studies where "Thornthwaite method" had been used to estimate potential evapotranspiration in Sri Lanka. Thus, "Thornthwaite method" was selected in this study in calculating monthly potential evapotranspiration.

4.3.1 Thornthwaite method

The calculation steps as elaborated by Lu et al. (2005) are as follows:

Step 1

The annual value of the heat index (I) is calculated by summing monthly indices over a 12 month period. The monthly heat index (i) is obtained using equation (3).

$$i = \left[\frac{T_a}{5}\right]^{1.514} \quad (3)$$

The annual heat index is calculated using equation (4).

$$I = \sum_{j=1}^{12} i_j \quad (4)$$

i_j - Monthly heat index for the month j
T_a - Mean monthly air temperature
j – No. of months (1-12)

Step 2

Unadjusted monthly values of potential evapotranspiration (PET') in mm based on a standard month of 30 days, with 12 h of sunlight per day is given by:

$$PET' = C\left[\frac{10T}{I}\right]^{a} \text{ (mm)} \quad (5)$$

In which C = 16 (a constant) and

$a = [6.75*10^{-7}*I^3] - [7.71*10^{-5}*I^2] + [0.0179*I] + [0.4929]$ (6)

The unadjusted monthly evapotranspiration values (PET') are adjusted depending on the number of days N in a month ($1 \leq N \leq 31$) and the duration of average monthly or daily sunlight d (h), which is a function of season and latitude:

$$PET = PET' \frac{d}{12}\frac{N}{30} \quad (7)$$

In which PET (mm) is the adjusted monthly potential evapotranspiration.

5 ANALYSIS OF DATA

After calculation of remaining water values at each failure location as described above, a time series analysis was carried out to explore the variation of monthly negative remaining water values (water deficit conditions) twenty years prior to the occurrence of failures.

The variation pattern of water deficit conditions at each failure location suggested that the locations were water stressed before its failures.

According to Fig. 2, first three months (January, February and March) of the year recorded the highest frequency of water deficits during the period of investigation which was twenty years prior to the occurrence of failure. In addition, water deficits were observed in the months from July to August with a lower frequency.

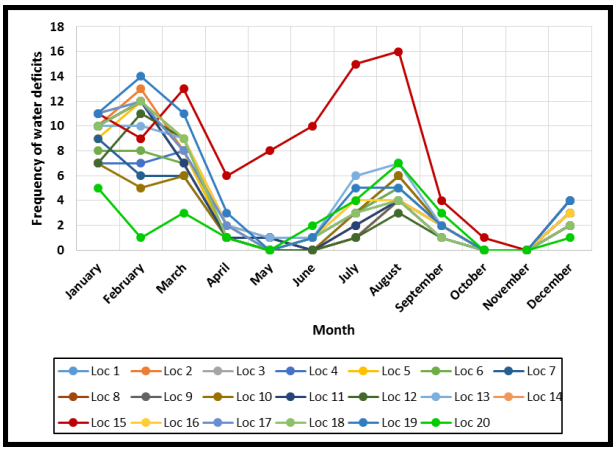

Fig. 2 Frequency of water deficit conditions recorded at each landslide location

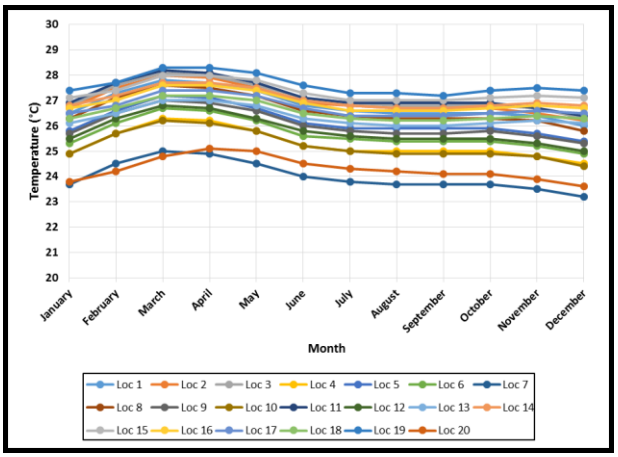

Fig. 3 Variation of average monthly temperature at landslide locations

Fig. 3 presents the values of monthly average temperature recorded at each landslide location.

Average temperatures were higher in the months from January to May and was lesser in rest of the months at all locations.

These results imply that the failure locations had experienced a dry period with high temperature almost continuously for every year prior to the major failure.

6 RESULTS INTERPRETATION

Warmer and drier atmospheric conditions are conducive to increased desiccation cracking and there is a possible environmental condition for formation of cracks on the ground surface at the failure initiation area. Due to dryness of the atmosphere, water stored in the soils loses through evapotranspiration and may lead to formation of above mentioned desiccation cracks on the ground surface. Such cracks might had newly formed or reopened during the months from January to March.

Fig. 4 shows typical desiccation cracks that could have formed on the ground surface under above mentioned environmental conditions.

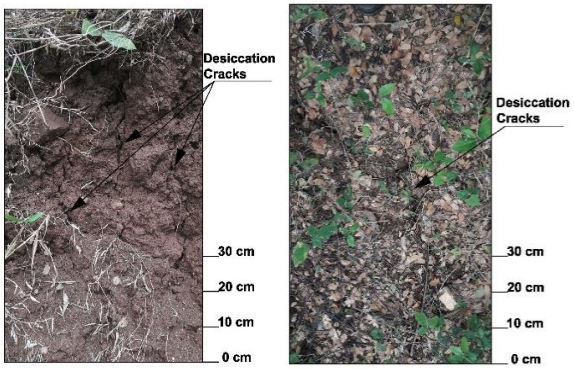

Fig. 4 Typical desiccation cracks that could be formed under dry environmental conditions

Once these cracks open in one occasion of the year, a series of rainfall events occur during the monsoon months and result in reduction in crack aperture due to swelling of clayey soils associated with infiltration of rainwater and infill materials (silt or lose particles). Healing of cracks may occur generally in the months April to June and October to November. This is primarily the result of seasonal fluctuation of precipitation/ evaporation conditions.

Those types of cracks in hilly areas can act as avenues and micro discontinuities for rainwater infiltration and thereby increase the permeability of soils. The water entering through the cracks would accelerate the development of porewater pressure and as a result, the strength parameters of soil would decrease. This rise in pore water pressure, which follow storms, could contribute to trigger landslides in soils.

7 CONCLUSIONS

These actions, namely, healing of cracks, reopening of cracks and increased permeability of soils are brought about by seasonal variation of rainfall combined with rising temperatures. Successive cycles of above actions on a slope could lead to areas of reduced strength, which could cause failure to occur progressively and eventually leading to a major failure. Present rate of rise of temperature could increase the magnitude of such cycles and could have the potential to lead to major landslides in soil in shorter times.

ACKNOWLEGEMENTS

Department of Meteorology and National Building Research Organization are acknowledged for providing necessary data to carry out the study.

REFERENCES

Basnayake, S, Punyawardena, BVR, Jayasinghe, S, Gupta, N, Shrestha, ML & Premalal, KHMS (2019), 'Climate Smart Disaster Risk Reduction Interventions in Agriculture Sector – Flood Hazard – A Practitioner's Handbook, Asian Disaster Preparedness Center, Thailand.

Bo, MW, Fabius, M & Fabius, K (2008), 'Impact of global warming on stability of natural slopes', Fourth Canadian Conference on Geohazards, Quebec. <http://www.geohazard.ggl.ulaval.ca/Processus/bo.pdf> (Jun. 20, 2018)

CHIRPS, Climate Hazards Group. <ftp://ftp.chg.ucsb.edu/pub/org/chg/products/CHIRPS-2.0/global_monthly/tifs/> (Sep. 20, 2018)

IPCC, 2014: Climate Change 2014: Synthesis Report. Contribution of Working Groups I, II and III to the Fifth Assessment Report of the Intergovernmental Panel on Climate Change [Core Writing Team, R.K. Pachauri and L.A. Meyer (eds.)]. IPCC, Geneva, Switzerland, 151 pp.

Lu, J, Sun, G, McNulty, SG, & Amataya, DM 2005, 'A comparison of six potential evapotranspiration methods for regional use in the southeastern United States', Journal of the American Water Resources Association, pp. 621-633.

Palmer, WC & Havens, AV 1958, 'A Graphical Technique for Determining Evapotranspiration by the Thornthwaite Method', Monthly Weather Review, pp. 123-128

Rathnaweera, TD and Nawagamuwa UP 2011, 'Effects of global warming on landslide frequencies in Ratnapura District, Sri Lanka. <http://kutarr.lib.kochi-tech.ac.jp/dspace/bitstream/10173/806/1/sms11-0815.pdf> (Dec. 15, 2017)

Rathnayake, U, and Herath, S 2005, 'Changing rainfall and its impact on landslides in Sri Lanka', Journal of Mountain Science, vol. 2, no. 3, pp. 218-224.

Statistical Abstract, 2017. < http://www.statistics.gov.lk/Abstract2017/index.asp?page=chap1> (Sep. 25, 2018)

A study of applicability of different facing types in soil nailing

B.I. Kumarage
National Building Research Organisation, Sri Lanka

S.A.S. Kulathilaka
Department of Civil Engineering, University of Moratuwa, Sri Lanka

ABSTRACT: Soil nailing has been used in Sri Lanka lately, as a cost-effective slope stabilization technique. However, detailed analyses with rigor, for facings/ nailheads are not often performed in the local practice. Full-face shotcrete, grid-beams, isolated nailheads, metallic meshes, and combinations of all these facings types are currently in use. The manner in which and how the basic functions such as anchoring the soil nails at slope-face, resisting local-failures, and erosion control differ with facing type. In this study, design guidelines for various facing types are critically reviewed to assess the performance of soil nails and the surface slope stability. Further, a cost comparison of each facings type is presented. Some guidelines are developed for making the decisions on the most appropriate facing type depending on the prevailing conditions.

keywords; slope rectification, soil nailing, facing types for soil nailing

1 INTRODUCTION

1.1 *Background*

Soil nailing is a technique used to reinforce the existing sloping grounds to enhance stability. The function of Soil Nails is to use the tensile capacity of reinforcement bars to enhance the overall shear strength of soils.

1.2 *Soil nail facings*

Soil nails do not stabilize the exposed surface soil when used to stabilize existing slopes or excavations. Hence, a system of soil nails generally consists of head plates and/or facings of some form that connects the installed soil nails at the surface of the slope. In addition to the function of stabilizing the surface soil, the reaction forces produced by soil-nailheads/facing provide confinement and contribute to developing tensile forces along the soil nails.

1.3 *Failures of soil nail systems*

Occasionally, failures of soil-nailed walls occur even though not many public records are available. Several failures that can be attributed to matters related to facings such as inferior facing design, lack of attention towards the interrelationship between nail spacing and type of facing, and inferior construction practices have been reported (Phear et al. 2005). Hong Kong GEO Report No. 222 (Ng et al. 2007) presents several reported cases of failures involving soil nailing.

1.4 *Use of soil nail facings in Sri Lanka*

In Sri Lanka, different types of facings are being used. Facing designs are mostly adopted from Hong Kong publications. However, detailed designs for nailhead/ facing are not often carried out. Currently, the selection of the facing type is mainly based on three major factors; observed nature of the surface slope and soil, ease of construction, and aesthetics.

During the short history of adopting soil nailing in Sri Lanka, a few failures that relate to facings have occurred. The major failure reported in a mitigation site at Diyagala – Ginigathhena in 2018, could be considered as a typical example of soil mass in the front face sliding off in between the soil nails, as described in FHWA (Byrne et al. 1998).

2 TENSILE FORCE AT THE NAILHEAD

2.1 *The behavior of soil nail forces*

With the transfer of shear stresses from the sloping ground, the actual soil nail (rebar) inside the grout body is placed under a loading condition similar to getting pulled from the two ends. As such, the tensile force along the soil nail has a distribution as shown in Fig. 1. This distribution indicates how the nailhead load, T_o is related to the maximum tensile force, T_{max} of the soil nail. Many studies and guidelines have discussed this relationship in the context of the performance of facings.

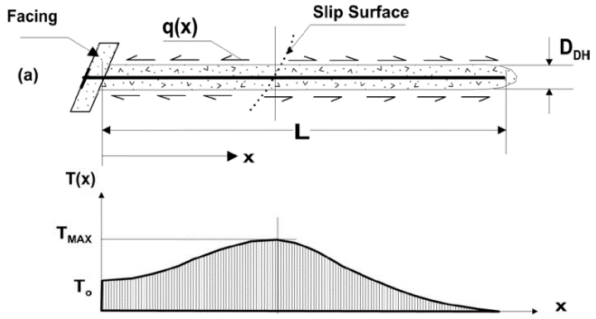

T_{max}= Maximum nail force
T_0 = Tensile force at the nailhead

Fig. 1 Distribution tensile force along the soil nail (Lazarte et al. 2015)

2.2 *Design guides for obtaining nailhead force*

FHWA (Byrne et al. 1998) present the results of a series of tests carried out on instrumented full-scale soil nail walls at different sites (Fig. 2) with which they propose a method for obtaining the nailhead load.

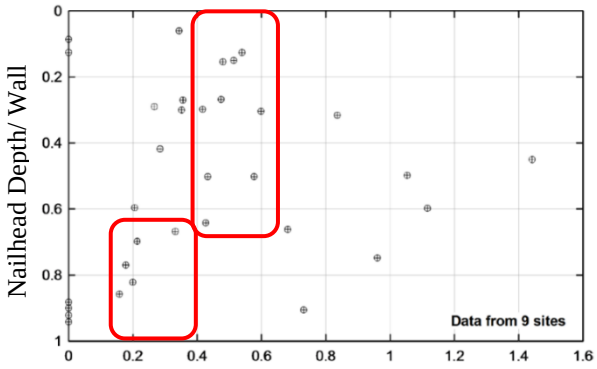

Fig. 2 Normalized Nailhead Load (FF) Distribution (FHWA 1998)

The average normalized nailhead loads vary approximately from 0.50 to 0.60. Accordingly, equation(1)can be used for estimating the nailhead load:

$$T_0 = F_F K_A \gamma H S_H S_V \quad (1)$$

Where,T_0 is the nailhead load. F_F is the normalized nailhead load,γ_s is the unit weight of soil, H is the slope height, S_H, S_V are horizontal and vertical nail spacing, and K_A is active earth pressure coefficient obtained by the Coulomb method.

FHWA (Byrne et al. 1998) recommends using $F_F = 0.5$ in equation (1) for obtaining T_o. Full-scale tests by Gaessler and Gudehus (1981) on shotcrete facings, field studies by Stocker and Riedinger (1990), Clouterre (1991), and the results of instrumented soil nail walls by Holman and Tuozzolo (2009) justifies this recommendation.

Finite element analysis with FLAC (Shiu and Chang 2005) showed values of T_0 / T_{max} varying around 0.55 to 0.7

Clouterre (1991), proposed an alternative method for calculating the T_0 / T_{max} ratio for shotcrete facings. This method has been recommended in CIRIA report c637 (Phear et al. 2005) as well and the expression presented is in equation (2).

$$T_o = T_{max}[0.6 + 0.2(S_v - 1)] \quad (2)$$

Where $T_{max}$is the maximum nail force, and $S_V$is vertical soil nail spacing

2.3 *Determining the suitable method for obtaining the nailhead load*

A summary of methods published is in Table 1.

Table 1. Methods for obtaining nailhead load

Publication	Calculation method
FHWA, 1998	Recommends 50% of the Coulomb earth pressure ($F_F = 0.5$)
CIRIA c637	Refers to FHWA
Clouterre, 1991	Calculates T_0/T_{max} based on nail spacing. Varies 0.6 to 1
GEO Report175	Calculates T_0/T_{max}via FLAC isolated nailheads. Varies from 0.55 to 0.7.

Accordingly, the discussed approaches could be utilized in the designs as follows.

Case 1:

In cases where precise analysis data are not available, the method given in equation (1) can be directly used for estimating the nailhead loads.

Case 2:

In cases where an analysis of stability is carried out, T_{max} can be obtained via the analysis and used to obtain T_0 using equation (2).

2.4 *Application for a case history - landslide rectification at Hakgala*

Methods discussed were applied for the soil nail system at the rectification of Landslide at Hakgala (Kumarage 2021).

The rectification design of section CS5 (Slope height H = 13 m, Slope angle = 66º) is illustrated in this study. The escarpment section at CS5 had a FOS of 0.811 with the limit equilibrium analysis done using Slope/W software by Spencer method.

A nailing arrangement in the form of three 16m long and three 12m long 32mm diameter soil nails at an angle of 15° was used in this analysis. Resultant spacing arrangement S_H = S_V = 2.0 m increased the Factor of Safety (FOS) up to 1.335 (Fig. 3).

The method described in "Case 02" was adopted to obtain the nailhead load. The values obtained for nails at each level were obtained from Slope/W output. The value from the bottom-most level (T_{max}=145.34 kN) became the most critical. This T_{max} value and S_V=2 m were used in equation (2) to obtain the nailhead load, T_0=116.27 kN.

The Slope/W analysis and calculations were repeated to evaluate the nailhead load under different nail spacing. Although the minimum acceptable FOS = 1.324 was achieved by the S_V = 2.5 m and S_H = 2 m arrangement, it was seen that the nailhead load of this arrangement is 32% higher than that of S_V = S_H =2.0 m spacing arrangement. As such S_V = S_H =2.0 m was preferred to economize the facing design. Nailhead load value obtained (T_0=116.27 kN) will be used for facing designs in the later sections.

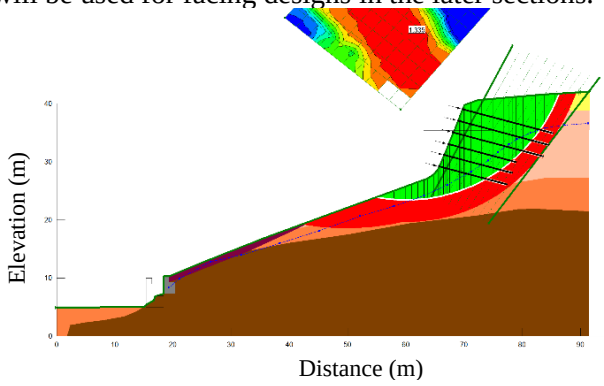

Fig. 3. Stability analysis soil nailing - CS5 – Hakgala

3 DESIGN OF SHOTCRETE FACINGS

3.1 *The behavior of forces on shotcrete facings*

Shotcrete facing is essentially a reinforced concrete slab (wall) that connects the nailheads and is constructed on the slope surface. The nailhead loads resulting from the soil movements are distributed across the surface starting from the nail head plate.

The two most critical failure mechanisms are the flexure and the punching shear around the nailhead that result from the nailhead load. To obtain the earth pressure behind the facing, force equilibrium of the facing in the nail direction is considered (Fig. 4).To account for the non-uniform earth pressure, the factor, C_F is generally used.

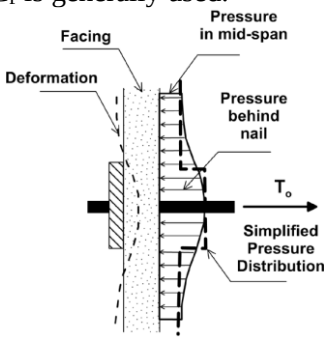

Fig. 4. Soil pressure behind the facing (FHWA 1998)

3.2 *Guides for designing shotcrete facings*

Both FHWA (Byrne et al. 1998) and CIRIA c637 (Phear et al. 2005) present expressions for obtaining flexural resistance and punching shear resistance of full shotcrete facing modeling it as a non-uniformly loaded 2-way spanning continuous slab.

The design guides presented in the Clouterre (1991) also have similar fundamentals to the FHWA (Byrne et al. 1998), although Clouterre recommends considering the soil pressure behind the facing as a uniformly distributed load (udl).

A summary of the methods for shotcrete design proposed in publications is shown in Table 2.

Table 2. Approaches for shotcrete design

Publication	Calculation approach
FHWA, (1998)	Non-uniformly loaded 2-way continuous slab. Allowable limit design.
CIRIA c637 (2005)	Non-uniformly loaded 2-way continuous slab (refers to BS 5400 part 4). Allowable limit design.
Clouterre, (1991)	Uniformly loaded continuous 2-way spanning slab. Refers to BAEL83

All 3 approaches rely on the same basic principle. Nevertheless, the method used to calculate the ultimate resistance moment and ultimate shear strength of concrete in CIRIA c637 (Phear et al. 2005) isn't based on BS 8110. As such, as a part of this study, a new set of calculations for the structural design of shotcrete based on Clause. 3.7, Design of flat slabs in BS 8110:1997: Part 1 was presented. This closely resembles the loading mechanism of shotcrete facings. With this the designer can obtain the reinforcement requirements based on the nailhead loads.

3.3 *Application of shotcrete design approaches for a case history*

Continuing from nailhead load calculations in section 2.4, analysis was done to assess the applicability and requirements of shotcrete facing for section CS5 in the Hakgala Landslide mitigation project. Accordingly, the method recommended in CIRIA c637 (Phear et al. 2005) was used to determine the structural requirements against flexure and punching. The facing requirement for alternative nail spacing obtained is tabulated in Table 3.

Table 3. Shotcrete designs for alternative nail spacing

S_V (m)	S_H (m)	T_{oULT} (kN)	Facing thickness (mm)	Main R/F	Bearing plate size (mm)
2	2	116.27	150	2Y16	200x200
1.5	2	115.23	150	2Y16	150x150

This proved that a shotcrete facing of practicable structural requirement can be used at the CS5 area. The maximum nail spacing (either vertical or horizontal) was found to govern the structural requirement of the spacing. As such, using S_V =S_H arrangement could be recommended as stated in section 2.4.

The FHWA (Byrne et al. 1998), and the CIRIA c637 (Phear et al. 2005) based methods were also used to calculate nailhead resistance, R_n (lower of flexural, R_{FF} and punching, R_{FP} resistance values) at each $S_V = S_H$ nail spacing arrangement from 1 m to 3 m. The three methods produced similar R_n values throughout the spectrum. It was seen that the punching shear resistance is governing the structural requirement and the punching resistance is more sensitive to the thickness and around the nailhead. Thus, shotcrete facing that has increased thickness at the nailhead area could be highly efficient.

4 DESIGN OF GRID BEAM FACINGS

4.1 *The behavior of forces on grid beam facings*

Grid beams are systems of reinforced concrete beams constructed across the surface of the slope and connects the nailheads. The main difference between shotcrete and grid beam is that shotcrete is transferring the loads throughout the whole slope face whereas grid beam limits the load transfer to the beam width. Therefore, steel meshes are typically installed along with the grid beam systems to prevent local instabilities between the grids.

Flexure or shear resulting from the nailhead load are the most critical failure mechanisms. As in shotcrete, the equilibrium of facing in the nail direction is considered to obtain earth pressure behind facing.

4.2 *Guides for designing grid beam facings*

HKIE report (HKIE and GEO 2013) presents a method where the beam is treated as a simply supported beam with a UDL for the structural design. However, the HKIE method is based on the Hong Kong code of practice (Building Department HK 2013). Accordingly, in this study, procedures for calculating the structural design of grid beams have been presented based on BS 8110:1997: Part 1, Clause. 3.4, Design of Beams.

Grid beams design methods have been developed in this study by modifying the Shotcrete design methods in FHWA (Byrne et al. 1998) and CRIA c637 (Phear et al. 2005). The accuracy of these methods was compared against HKIE (HKIE and GEO 2013) method.

4.3 *Application of grid beam design approaches for the case history*

Analyses were carried out to assess the applicability of a grid beam facing for the Hakgala Landslide mitigation project's CS5 area using the modified method which is based on the BS 8110:1997: Part 1. The same method was used to assess the grid beam design at different nail spacing and an extract of the results is presented in Table 4.

Table 4. Grid beam designs for alternative nail spacings

S_V(m)	S_H(m)	T_{oULT} (kN)	Beam size(mm)	Main R/F	Shear R/F
2	2	116.27	250x250	4Y12	R10@150mm
1.5	2	115.23	250x250	4Y12	R10@150mm

The structural arrangement suggests that a grid beam system is applicable. As in shotcrete facings, it is highly recommended to use a $S_V = S_H$ arrangement to economize facing requirememt. To account for local instabilities, the requirements of a flexible steel mesh facing along with the grid beams will be also assessed.

5 ISOLATED NAILHEAD SYSTEMS

Isolated nailheads (Pillows) are essentially concrete pads that distribute nailhead load onto the slope surface. The load transfer of pillows could be analogized to pad footings of a building. Bearing failure of the slope becomes the critical failure mode. Design of isolated nailheads has been extensively discussed in GEO report 175 (Shiu and Chang 2005) using finite element modeling, as well as in CIRIA c637 (Phear et al. 2005) which proposes an empirical formula called the lower-bound method. Both methods produce comparable results.

The calculation carried out using the lower bound method for the case history at Hakgala revealed a pillow size requirement of 800 mm x 800 mm to resist the obtained nailhead load. This size requirement makes pillows less appealing due to the excess weight induced by the facing on to the nail.

6 DESIGN OF FLEXIBLE STRUCTURAL FACINGS

6.1 *The behavior of forces on flexible facings*

In all cases where a hard facing such as concrete blocks (pillow method), or grid beams are used with the flexible facing, the nailhead load will not influence flexible facing design. Instead, flexible mesh-facing must resist the out-of-balance force exerted from the soil in-between the nailheads/ beams and transfer it onto the nail head plates. However, in cases where the bearing plate is used as the nailhead, the mesh must resist both the punching force from the nailhead load as well as the local instabilities because the smaller-sized plates do not generate adequate bearing resistance against the slope.

The mesh product must be chosen based on its resistance against shearing at the nailhead/ plate (dependent on wire diameter, strength, opening size). In addition, proper sizing of head-plate is equally important when designing flexible facings.

6.2 *Guides for designing flexible facings*

CIRIA report c637 (Phear et al. 2005) briefly presented a method for designing flexible meshes. To obtain the out-of-balance force, in the case of shallow slopes, a two-part wedge failure mechanism (Fig. 5) based on HA 68/94 (The Highways Agency 1994) is used. In the case of steeper slopes, a single-wedge failure mechanism based on Ruegger and Flum (2000) is used. The pore water pressure ratio, r_u taken as 0.5 to address the worst case. In these analyses, angles θ_1 and θ_2 must be varied to obtain the maximum force on the mesh, iteratively.

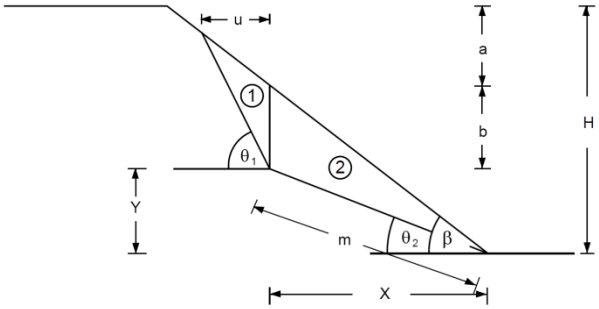

Fig. 5. Mechanism of two-part-wedge failure

Cala et al. (2020) also present methods to obtain the out-of-balanced forces using two failure modes (One-body and Two body), which are more complicated than the CIRIA c637 (Phear et al. 2005) methods. Groundwater flow parallel to the slope is idealized in these methods instead of using r_u. Features such as pre-tensioning are also included. These have been omitted from the steps developed in this study because such applications are not adopted locally.

6.3 *Application of flexible facing design approaches for the case history*

Analyses were carried out in this study to assess the applicability of a flexible facing over the grid beams for the case study; cross-section CS5 in the Hakgala Landslide mitigation project.

6.3.1 *Obtaining the out of balance force*

Spreadsheets were developed in this study to obtain the out-of-balance forces using the four proposed methods and the results are given in Table 5.

Table 5. Summary of out of balance force results

CIRIA c637		Cala, et al. 2020	
Two-part wedge	Single wedge	Two body	One body
40.69 *kN*	15.91 *kN*	26.17 *kN*	24.97 *kN*

The pore water pressure condition used, r_u = 0.5 which is an extreme scenario seems to have caused this approach to produce a larger force (40.69 kN) which will be conservatively considered for evaluating the appropriate mesh for this application.

6.3.2 *Mesh product required to be used with Grid Beams*

The tests carried out on the metallic meshes have revealed higher puncturing resistance than the theoretical values derived from tensile capacity. As such, where testing cannot be done locally, the designers could use the manufacturer-tested puncturing resistance values in the designs. However, the products must carry a reliable product certification such as ETA (European Technical Assessment).

Accordingly, with modifications, the tested strength parameters of the mesh product 3STUTOR Plus 100/2.7 was used to assess adequacy. The head plate was assumed to be of 200 x 200 mm size which intersects 14 nos of wires of the proposed mesh. The design value of punching resistance, S_m for this combination was 42 kN which is higher than the out-of-balance force, 40.69 kN. As such, it was concluded that the proposed product or equivalent could be used for the protection of local instabilities in-between the proposed grid beam facing.

6.3.3 *Mesh product required to be used with Isolated nailheads (pillows)*

The punching resistance required of a mesh to be used with an isolated nailhead system was also assessed. Although the nail spacing is the same, because of the zig-zag nailing pattern used in pillow systems, the height of the two-part-wedge model (H) is twice the vertical nail spacing. For the case history, the out-of-balance force from local instabilities where each facing type is used with the same nail spacing is compared in Table 6.

Table 6. Out of balance forces for pillows and grid beams

Facing Type	Nail spacing (S_V=S_H)	Height of failure model (m)	Punching force on the mesh (kN)
Pillows	2	4	**95.19**
Grid Beams	2	2	40.69

The mesh used with grid beams was inadequate to be used with isolated nailheads. Mesh type 3STUTOR Plus 100/4.0, that produces a higher punching resistance $S_m = 99.17\ kN$or an equivalent mesh could be used in this application. High tensile options such as TECCO G65/3 with wire strength 1770 N/mm^2, wire diameter $3\ mm$, opening size 65 *mm* could also be a viable alternative for this.

6.3.4 *Mesh product required to be used with Isolated nailheads (Bearing plates)*

The adequacy of the mesh and plate to withstand the nailhead load was assessed. The 3STUTOR Plus 100/4.0 with design punching resistance, S_m = $99.17\ kN$ or equivalents were found to be inadequate for bearing plate method. A high tensile option, TECCO G65/3 with $S_m = 120\ kN$ or equivalents were needed for this application.

High-capacity mesh requirement makes the bearing plate facing method a more expensive option compared to other facing types.

7 COST COMPARISON OF FACING TYPES

Construction cost is a key factor for choosing the applicable facing type. Comparison in Table 7 was carried out based on the current market prices extracted from contractors' proposals of recent slope mitigation projects in Sri Lanka. Percentiles of the rates for each component of facing, quoted by 8 bidders were used to compute the overall cost.

Table 7. Cost per unit area of slope of each facing type

Facing Type	Cost (LKR/m^2)
Isolated Nailheads (Pillows) with steel mesh & vegetation	**11,500.00**
Grid beams with steel mesh& vegetation of the slope	**12,736.00**
Full face Shotcrete	**14,795.00**
Bearing plate with high tensile wire facing& vegetation	**20,050.00**

Full face shotcrete is considerably expensive compared to the pillow and grid beam methods. The metal-bearing plate method which utilizes high tensile wire meshes is the most expensive due to the higher cost of the mesh.

8 CONCLUSION

Choosing the most appropriate soil nail facing meeting the requirements in a given mitigation project is an extremely important task.

Grid beams and full-face shotcrete facings offer the most freedom to achieve a higher value of nailhead resistance as well as to more effectively connect the nailheads as a statically indeterminate system. Full-face shotcrete is superior to grid beams particularly in terms of the ability to resist both nailhead loads as well as local instabilities without having to resort to other components. A full-face shotcrete facing must be the preferred choice on slopes where the surface soil is showing a sandy, blocky, or crumbly nature. These slopes are susceptible to erosion and collapsible in the event of water flowing on the slope. The confinement provided by shotcrete throughout the slope face is extremely effective in such circumstances. This should be the first choice for slopes with angles steeper than 65^o.

However, the cost of shotcrete is relatively high compared to grid beam and pillow options. If the short drains provided at the facing are not effective pore-water pressure could build up behind the facing. On the other hand, shotcrete may be less appealing aesthetically. The designer must be cautious in this aspect in opting for full-face shotcrete.

Alternatively, using isolated concrete nailhead systems with, planting, sodding, or hydroseeding would blend with natural landscape. However, where nailhead loads are larger and the out-of-balance force from local instabilities is high, the required high tensile metallic mesh products would make it uneconomical. For residual soil formations in Sri Lanka, grid beams coupled with non-high tensile mesh systems could be preferred as a cost-effective, structurally superior solution that is aesthetically pleasing.

REFERENCES

Building Department HK. (2013). "Code of Practice for Structural Use of Concrete 2013."

Byrne, R. J., Cotton, D., Porterfield, J., Wolschlag, C., and Ueblacker, G. (1998). Manual for Design & Construction Monitoring of Soil Nail Walls. FHWA.

Cala, M., Flum, D., Rüegger, R., Roduner, A., and Wartmann, S. (2020). TECCO® slope stabilization system and RUVOLUM® dimensioning method. AGH University of Science and Technology.

Clouterre. (1991). Recommendations CLOUTERRE 1991. Project National Clouterre.

Gaessler, G., and Gudehus, G. (1981). "Soil Nailing - Some aspects of a new technique." Proceedings of the International Conference on Soil Mechanics and Foundation Engineering, A. A. Balkema.

HKIE, and GEO. (2013). Design Illustrations on the Use of Soil Nails to Upgrade Loose Fill Slopes.

Holman, T. P., and Tuozzolo, T. J. (2009). "Load Development in Soil Nails from a Strain-Gauge Instrumented Wall." ASCE, 25–32.

Kumarage, B. I. (2021). "A Study of Applicability of Different Facing Types in Soil Nailing." MEng Thesis Submitted to University of Moratuwa.

Lazarte, C. A., Robinson, H., Gómez, J. E., Baxter, A., Cadden, A., and Berg, R. (2015). Soil Nail Walls - Reference Manual. FHWA.

Ng, F., Lau, M., Shum, K., and Cheung, W. (2007). GEO Report No. 222 - Review of Selected Landslides Involving Soil-Nailed Slopes. Geotechnical Engineering Office, Hong Kong.

Phear, A., C Dew, B Ozsoy, NJ Wharmby, J Judge, and AD Barley. (2005). CIRIA C637 - Soil nailing : best practice guidance.

Ruegger, R., and Flum, D. (2000). Slope stabilization with high-performance steel wire meshes in combination with nails and anchors. Proceedings of the Korean Geotechical Society Conference, Korean Geotechnical Society.

Shiu, Y. K., and Chang, G. W. K. (2005). "GEO Report No.175 - Soil nail head review." Geotechnical Engineering Office, Hong Kong.

Stocker, M. F., and Riedinger, G. (1990). "The bearing behaviour of nailed retaining structures." Design and Performance of Earth Retaining Structures, ASCE, 612–628.

The Highways Agency. (1994). HA 68/94 - Design Methods for the Reinforcement of Highway Slopes by Reinforced Soil and Soil Nailing Techniques.

Influence of Cementation Level on the Mechanical Behavior of Bio-cemented Slope Soil Treated by Surface Injection

S. Gowthaman
Department of Engineering Technology, University of Jaffna, Ariviyal Nagar, Kilinochchi 44000, Sri Lanka

M. Chen
Graduate School of Engineering, Hokkaido University, Kita 13, Nishi 8, Kita-Ku, Sapporo, Hokkaido 060-8628, Japan

H. Nakamura
Hokkaido office, East Nippon Expressway Company Limited, Atsubetsu-ku, Sapporo, Hokkaido 004-8512, Japan

K. Nakashima & S. Kawasaki
Faculty of Engineering, Hokkaido University, Kita 13, Nishi 8, Kita-ku, Sapporo, Hokkaido 060-8628, Japan

ABSTRACT: Bio-cementation has recently emerged as a novel soil stabilization technique that can improve mechanical behaviors of soil in a sustainable way. The contact cementation is induced by ureolytic soil bacteria through a set of bio-geochemical processes, leading to the formation of a stiff soil skeleton. The objective of this paper is to study the mechanical behavior of slope soil treated to varying cementation levels ranging from uncemented soil to heavily cemented sandstone like conditions. The unconfined compression test results suggest that the strength and stiffness of the soil increase with the increase in cementation level. As the cementation increased, the peak state was reached at lower axial strains, suggesting the increase in brittleness. Permeability results shows a linear decrease with the increase in cementation level. The bio-clogging mechanism also has been well demonstrated by SEM (Scanning Electron Microscopy). The outcomes of this study have deepened the understanding in specifying the desired treatment level for slope soil stabilization purpose.

1 INTRODUCTION

Bio-cementation is relatively a novel ground improvement method which shows great promise for various geotechnical engineering challenges. Bio-cementation can also be referred as microbial induced carbonate precipitation (MICP), in which the urease active bacteria could biochemically induce the calcium carbonate precipitates within soil matrix, preferentially at particle contacts. The crystallization results the contact cementation, surface coating and bridging through pore spaces (matrix supporting) (DeJong et al. 2010; Lin et al. 2016), leading to the increase in several engineering properties of soil such as stiffness, dilation, shear strength parameters, shear wave velocity and etc.

Up to now, several studies were performed to investigate the efficiency of this method for various geotechnical problems. Mitigation of liquefaction potential (Montoya et al. 2013), coastal protection (Nayanthara et al. 2019), settlement reduction (van Paassen et al. 2010), dust control (Meyer et al. 2011) and erosion control (Jiang et al. 2019) are some of the potential studies investigated. Recently, studies have demonstrated that the technique can be potentially applied for stabilization of slopes and embankments against surface degradation. Simulating the slope surface by column, Gowthaman et al. (2019a) demonstrated the feasibility of stabilizing natural slope soil by locally-isolated bacteria through surface injections. Following that, researchers performed the slope model tests to evaluate the cemented profile, suggesting that the particle distribution of residual soils drastically filter the bacteria cells at near-surface, limiting their transport to deeper zones (Gowthaman et al. 2019b). Through erodibility tests, few other researchers showed that the MICP could enhance the erosion resistance by several times compared to that of untreated slopes (Jiang et al. 2019; Salifu et al. 2016). It is therefore clear that the bio-cementation can be nondestructively applied by surface injection method for enhancing the cover condition of the slope.

Ordinary Portland Cement (OPC) is the widely used grouting material in stabilizing the slope soils, wherein the surface is sealed to immobilize the aggregates. It is the fact that bio-cementation (notionally the calcium carbonate) cannot be achieved to the strength levels of OPC; however, the technique can be a promising alternative with several unique merits such as environmental sustainability, retained permeability, cost effectiveness and revivability of strength.

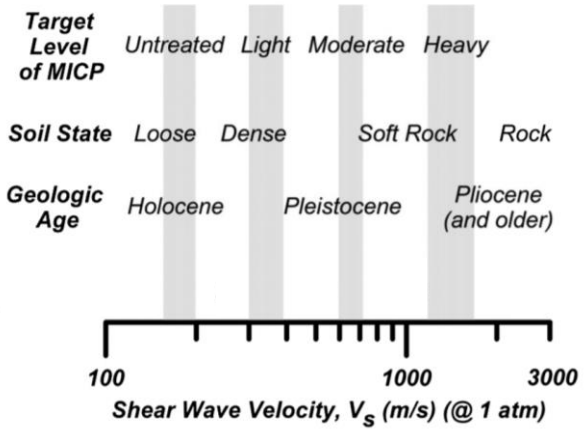

Fig. 1 Level of MICP, soil state and geologic age with shear wave velocity range (Montoya and DeJong 2015)

As previously defined by Montoya and DeJong (2015) (see Fig. 1), the bio-cementation could be achieved at various cementation levels from light to heavy, transforming the state of the soil respectively from loose to rocklike material. As per the states, the cementation levels can also be related to a broad range of geologic age, i.e., from young hydraulic fill to Pleistocene sand. It is worth noting that attentions should be carefully given in specifying the appropriate cementation level among the broad range based on the application purpose and requirement. Overtreatment as like hard rock material ($V_s \geq 1600$ m/s, see Fig. 1) leads not only to the increase in treatment cost, but also to the overburden pressure, resulting adverse effects on the stability of structure. For an effective design and implementation, a deeper understanding on the evolution of mechanical parameters with varying cementation levels is highly essential. Therefore, the objective of the study presented herein is to evaluate the mechanical properties of cemented slope soil across a range of cementation levels. The physical state of the soil is well elucidated within the chosen cementation levels. The UCS and permeability characteristics are also studied and discussed extensively herein.

2 TESTING METHODS

2.1 *Material and preparation of specimen*

The slope soil investigated herein was collected from the target erosion prone expressway slope in Hakodate (Hokkaido, Japan). The geotechnical properties of the soil are given in Table 1. G_s, D_{50}, C_u, C_c, *USCS*, *SP* and $D_{R,ini}$ are respectively specific gravity, mean particle size, coefficient of uniformity, coefficient of curvature, unified soil classification system, poorly graded sand and initial relative density. All the column specimens were prepared with similar relative density. The dimensions of the specimens were measured as approximately 30 mm in diameter and 60 mm in height.

2.2 *Soil bacteria and treatment*

The soil bacteria, *Lysinibacillus xylanilyticus*, isolated from the native soil were augmented to treat the soil. The isolation process of the bacteria can be found in the previous study (Gowthaman et al. 2019a). The bacteria were cultivated in ATCC 1376 (NH_4-YE) media at shaking incubation (25°C, 160 rpm). The bacteria were then harvested when the turbidity of the bacteria culture at the wave length of 600 nm, OD_{600}, is ranged between 4-4.5 (takes typically around 48 hours). Further detail on the biological response of the above soil bacteria can be acquired from Gowthaman et al. (2019b).

A two-phase surface injection strategy was used for the treatment. The harvested bacteria culture was injected at first, followed by the multiple number of cementation injections. The cementation media recipe consisted of $CaCl_2$, Urea and nutrient broth, at the concentration of 1 mol/L. All the solutions were simply applied at the flow rate of 4 mL/min and allowed to percolate under gravity and capillary effects. After the biological injection, few hours of retention were given prior to the cementation injections for the fixation of bacteria cells with soil particles. The cementation injections were performed every 24 hours. It should be noted that the volume of each injection was approximately equivalent to the pore volume of the specimen.

2.3 *Methods of assessment*

Different number of cementation injections (N) were performed to achieve different cementation levels. After the treatment, samples were flushed well using tap water to remove the soluble salts and chemicals. The molds were then cut carefully, and the samples were taken out for assessing the mechanical properties. Two different sets of specimens were prepared and treated identically for the (i) unconfined compression and (ii) permeability tests.

To study the strength characteristics, the unconfined compression tests using automated INSTRON 2511-308 load cell (USA), were performed on a set of specimens cemented to various levels, in accordance with the ASTM D7012 (2014). The samples were compressed at the rate of 0.036 mm/min until the critical state was achieved.

Table 1. Material properties

G_s	D_{50}	C_u	C_c	USCS	$D_{R,ini.}$	pH
2.71	0.23 mm	2.5	0.8	SP	60±2%	6.99

The effect of cementation level on permeability characteristics of cemented specimens were also studied. The falling head permeability tests were performed using DIK 4000 system (Daiki Rika Kogyo Co., Ltd., Saitama, Japan), in accordance with the ASTM D5084-03 (2003). The specimens were saturated for 48 hours prior to the analysis.

Finally, the spatial distribution of precipitated $CaCO_3$ in all the tested specimens were measured by gauging the pressure of CO_2(g) released when the samples were reacted with HCl (2 mol/L) in a closed system, as suggested by (Fukue et al. 2011). For that, the specimens were equally divided into three sections across the depth and were separately reacted with HCl. Using the calibration curve, the mass of the calcium carbonate (w_c) is estimated and expressed as percentage (in terms of mass of the calcium carbonate divided by the mass of the uncemented soil).

3 RESULTS AND DISCUSSION

3.1 *Physical state of soil with varying cementation levels*

In this study, the evolution of physical and mechanical characteristics was studied across a range of cementation levels. The changes in the physical state of the soil were continuously monitored with the treatment quantity, i.e., across the varying cementation levels. Initially, the untreated slope soil is in loose state as young and fresh. When the treatment is applied, the $CaCO_3$ forms within soil matrix, cementing the particle contacts, eventually converting the separate soil particles to aggregated larger clusters as depicted in Fig. 2. Treatment levels (representing the number of cementation injections) were chosen arbitrarily within the target shear wave velocity range (from loose to soft rock ($V_s \leq 1600$), refer Fig. 1).

At the low treatment levels (N=1 and N=3), the particles are not well aggregated; lightly cemented clusters are clearly observed together with loose material (refer Figs 2-a and 2-b, respectively), suggesting that the quantity of precipitated carbonate is not adequate to provide strong connections. When the number of treatments is increased to 5 (Fig. 2-c), a moderately cemented soil structure is achieved, and the precipitated carbonate could be able to retain its initial shape under its self-weight. However, the sample bottom is not stable as top, and the soil particles appears to be easily detachable from the bottom specimen.

When the number of treatments is increased to 7, an entirely cemented stable skeleton could be achieved (Fig. 2-d). It is worth noting, that the shear-wave velocity of the specimen (N=7) is around 1000 ± 50 m/s.

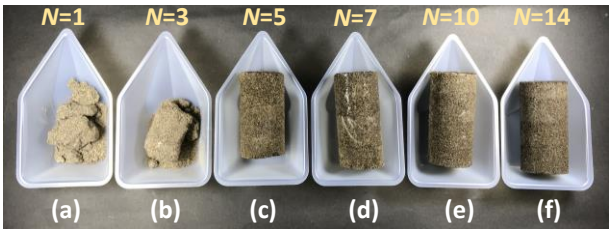

Fig. 2 Physical state of the soil with varying cementation levels

The specimens become more stable and stiffer, when the number of treatments is increased further (N=10 and N=14) (refer Figs 2-e and 2-f, respectively). Within this heavy treatment zone ($N \geq 7$), the quantity of precipitated carbonate appears to be facilitating strong bridges among particles, leading to a stiff soil skeleton. Aggregate stability is the most serious concern in slope soil preservation, and the physical states at these heavy cementation levels are likely to be more suitable and effective.

3.2 *Distribution of calcium carbonate in surface injection method*

As the bio-cementation is achieved by the surface injection method, it is very necessary to assess the distribution of the calcium carbonate and the homogeneity of treatment with depth. The slope soil is found to be consisting of negligible quantity of calcium carbonate material (less than around 0.2%).

Fig. 3 presents the distribution of calcium carbonate in all the cemented specimens, plotted against the normalized height. As expected, the average precipitated mass shows a general increase with the increase in treatment number (N). It is worth noting that all the specimens show a similar tendency that the precipitated calcium carbonate reveals a heterogeneity in the vertical distribution.

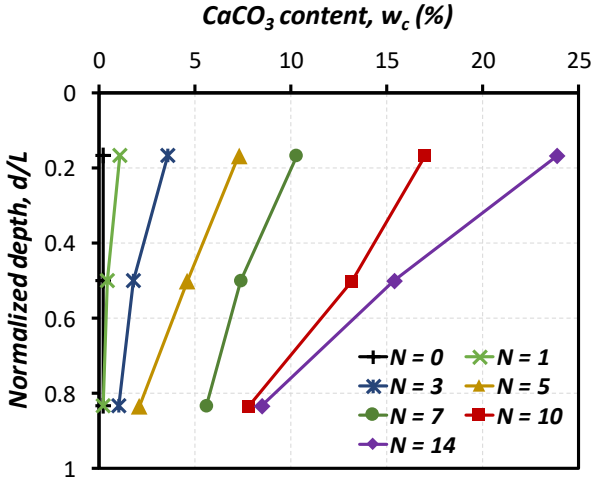

Fig. 3 Distribution of $CaCO_3$ with normalized depth (d/L) (d is the depth measured from surface; L is the total length of the specimen)

The highest mass of calcium carbonate is observed closer to the injection top for all the specimens, and this observation is in a good agreement with previous work (Cheng and Cord-Ruwisch 2014).

Fig. 3 also demonstrates that with the increase in the treatment number, the deposition rate of the calcium carbonate is higher at the top compared to that at bottom. As proved in the literatures (Gowthaman et al. 2019b; Martinez et al. 2013), the prime reason for this less uniformity is the distribution pattern of the bacteria. Transport of the bacteria is significantly determined by flow paths facilitated by soil pores. During the surface injection, more bacteria cells are filtered near the injection point due to the less pores in slope soil (fine sand consisting silt particles). As the liquid resources are supplied to the soil, reactions are induced rapidly at the zones with high bacteria concentration, leading to form the carbonates at high rates. At the time the solutions reach the specimen bottom, the resource concentration becomes less, resulting a less formation of calcium carbonate.

3.3 *Response of varying cementation levels to uniaxial compression*

A series of unconfined compression tests were performed to the treated samples. Fig. 4 presents the stress-strain behaviors of the specimens treated to varying average cementation levels ($w_{c,\,avg}$). $w_{c,\,avg}$ indicated herein represents the average of the three calcium carbonate measurements across the depths. As shown, specimens cemented to higher levels exhibit higher strength and stiffness compared to that of lightly cemented and uncemented soils of similar initial relative density. The response of untreated specimen is plotted as reference to compare the behavior of cemented slope soils. The peak and residual strengths increase with the increase in cementation level. However, the increase in the peak and residual strengths are not very significant up to the cementation level of 4.7% (up to around 1.4 times); particularly, the residual strength is found to be very close to that of untreated soil. Therefore, it is clearly understood that at lower cementation levels, the stress-strain behavior of slope soils is quite similar to the uncemented specimens.

On the other hand, when the average cementation level is increased to 7.8%, 12.7% and 16%, the peak strength increases, respectively by around 5.2, 17.6 and 58.5 times higher than that of uncemented one. Also, the higher the cementation level, the larger the initial modulus of the stress-strain response is observed, which is similar to several previous observations (Feng and Montoya 2016; Gowthaman et al. 2020).

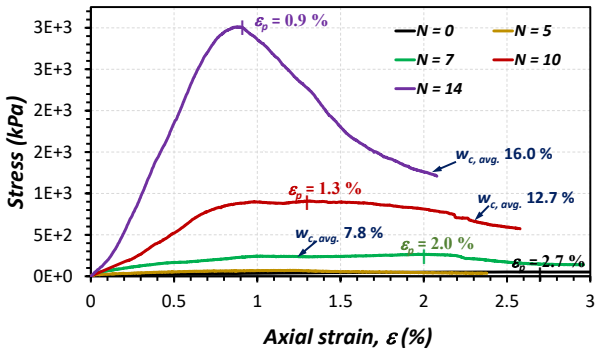

Fig. 4 Stress-strain behaviors of the slope soil treated to various average cementation levels

At higher cementation levels, there is a considerable increase in the residual strength also. Gowthaman et al. (2020) have observed the increase in effective friction angle during the shearing tests, demonstrated that residual strength is primarily attributed to surface roughness of the bio-cemented soil particles. Therefore, the increase in the critical state stress observed herein is probably due to the increase in the coated calcium carbonate.

The cementation appears to have a large influence not only the peak and residual strength but also the localization of corresponding axial strain (i.e., failure strain). The samples cemented to 7.8%, 12.7% and 16%, the peak was reached at the axial strains of 2.0%, 1.3% and 0.9%, respectively (Fig. 4), perceiving that the peak strength reaches at low axial strains as the cementation increases. This behavior is likely due to the stiffening effect i.e., the densified initial state of the specimen corresponding to the level of cementation.

The stress-strain response of uncemented slope soil exhibits the strain-hardening behavior. It is worth noting that as the cementation level increases, the behavior of slope soil transitioned from strain-hardening to strain-softening. Similar observations are also reported to bio-cemented sands in previous studies (Feng and Montoya 2016; Montoya and DeJong 2015).

3.4 *Hydraulic conductivity*

The hydraulic conductivity of the untreated specimen is around 2×10^{-2} cm/s, which falls under the category of the clean sand (Craig 1983). Fig. 5 presents the variation of hydraulic conductivity with the magnitude of maximum and average precipitated calcium carbonate contents ($w_{c,max}$ and $w_{c,avg}$, respectively). It can be seen that the hydraulic conductivity of the slope soil linearly decreases (in log scale) with the increase in the precipitated carbonate content. Basically, the hydraulic conductivity of soil is largely determined by its void space (Martinez et al. 2013); the precipitated carbonate content increases as the number of treatment in-

creases, resulting the void filling. When the soil is treated slightly ($w_{c,avg}$ of 0-3%), the reduction in hydraulic conductivity is negligible (1-2×10^{-2} cm/s), which is consistent with the observation reported by Do et al. (2017) for lightly cemented sand material.

When the soils are heavily treated ($w_{c,avg}$ of above 7%), reduction in hydraulic conductivity is significant; for example, the samples cemented to around 8% (N=5) and 13% (N=10), the reduction of hydraulic conductivity is about 70% and 85%, respectively. Also, up to around 90% of permeability reduction is observed when the sample is cemented to $w_{c,avg}$ of about 16%. Similar permeability observations are also reported by Achal and Mukherjee (2015).

As explained in the previous section, there is a non-uniformity of carbonate distribution in the treated slope soil. It is worth noting that in one-dimensional column specimen, the bulk hydraulic conductivity is controlled by the zone where the deposition of calcium carbonate is the highest, and therefore, the hydraulic conductivity is also plotted against $w_{c,max}$ (Fig. 5). When the permeability of the specimens reaches 10^{-3} cm/s, the flow of the resource liquids is significantly inhibited, leading to the retainment of the solutions on the specimens for many hours, sometimes to bio-clogging stage.

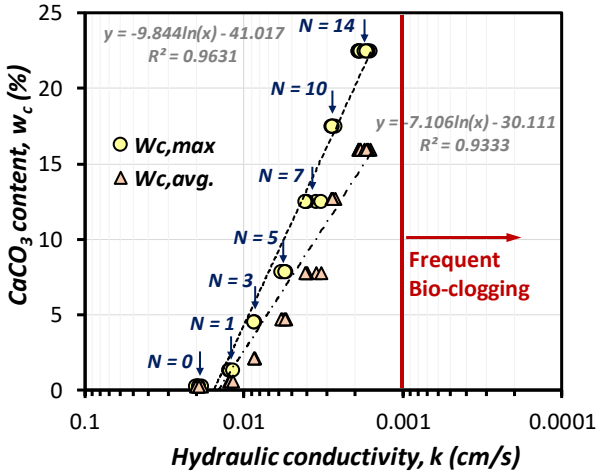

Fig. 5 Relationship between k and w_c ($w_{c,max}$ and $w_{c,avg}$ are the highest and average of the three measurements across the depths of the specimens, respectively)

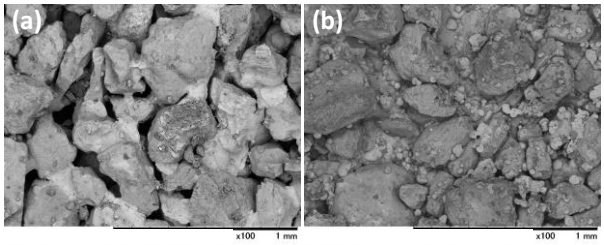

Fig. 6 Bio-cementation with (a) retained permeability (achieved typically) and (b) bio-clogged surface of the specimen (achieved during overtreatment)

3.5 *Bio-clogging in slope soil*

When the samples are treated by more than 15 injections of cementation solution, bio-clogging is frequently experienced. It should be noted that bio-clogging does not literally means that the entire voids in soil are filled by calcium carbonate. As observed earlier, the surface zone of the treated soil shows high carbonate content, revealing as the probable zone of bio-clogging. The continuous deposition in the above zone results the inhibition of flow paths, leading to bio-clogging stage.

Fig. 6 presents the SEM images of bio-cemented specimens' surface. It is clearly perceived that bio-cementation has the unique merit, the retained permeability (Fig. 6-a) even at heavy cementation levels (Fig. 6-a corresponds to N=14). In the surface injection method, filtration of bacteria at particle contacts leads to the preferential deposition of calcium carbonate at contact points. Unlike the sealings by conventional grouts like OPC, this mechanism holds the soil pores relatively open, and which are clearly visible at micro-scale (Fig. 6-a). On the other hand, overtreatment results sometimes bio-clogging (refer Fig. 6-b). It can be seen that the surface pores are almost filled by carbonate bio-cement. In this case, the infiltration of further liquid media is impossible, acting as an impermeable bio-crust as reported by Stabnikov et al. (2011). Considering the real field applications, sealing the slope surface by an impermeable bio-crust (bio-clogged surface) causes some adverse effects. Inhibiting the infiltration of storm water possibly results the water buildup on the treated slope surface, leading to additional overburden and sheet flow with high energy. Therefore, this study recommends a surface treatment with retained permeability, allowing certain quantity of storm water infiltration to control the water buildups.

4 CONCLUSIONS

The present study demonstrates that the bio-cementation technique has a large influence on improving the mechanical characteristics of slope soil. The physical and mechanical behaviors of slope soil cemented to varying cementation levels are studied herein, and the following conclusions are drawn.

- As the cementation level increases from light to heavy, the state of the soil transitions from loose to dense (i.e., soft-rocklike material).
- The increase in the bio-cementation level in slope soil results in high stiffness, peak and residual strength. However, the light cementation ($w_{c,avg}$ < 4.7%) shows only a limited improvement in strength, whereas the improvement is significant beyond the $w_{c,avg}$ of around 8%.

- As the cementation increases, the peak stress is reached at lower axial strains.
- The strain-hardening behavior is observed during the compression of uncemented slope soil, and as the cementation increases, the strain-hardening behavior transitions to strain-softening.
- The increase in cementation, the decrease in the permeability is observed. However, in surface injection method, bio-cement is preferentially deposited at particle contacts, which tends to retain the permeability.

REFERENCES

Achal, V., and Mukherjee, A. (2015). A review of microbial precipitation for sustainable construction. Construction and Building Materials, 93:1224–1235.

ASTM D5084-03 (2003). Standard Test Methods for Measurement of Hydraulic Conductivity of Saturated Porous Materials Using a Flexible Wall Permeameter, ASTM International, West Conshohocken, PA.

ASTM D7012 (2014). Standard Test Methods for Compressive Strength and Elastic Moduli of Intact Rock Core Specimens under Varying States of Stress and Temperatures, ASTM International, West Conshohocken, PA.

Cheng, L., and Cord-Ruwisch, R. (2014). Upscaling Effects of Soil Improvement by Microbially Induced Calcite Precipitation by Surface Percolation. Geomicrobiology Journal, 31(5):396–406.

Craig, R. F. (1983). Soil Mechanics. Dictionary Geotechnical Engineering/Wörterbuch GeoTechnik, Springer US, Boston, MA.

DeJong, J. T., Mortensen, B. M., Martinez, B. C., and Nelson, D. C. (2010). Bio-mediated soil improvement. Ecological Engineering, 36(2):197–210.

Do, J., Montoya, B., and Gabr, M. (2017). Mechanical behavior of sands treated by microbial induced calcite precipitation at low confining stress. ICSMGE 2017 - 19th International Conference on Soil Mechanics and Geotechnical Engineering, pp 353–356.

Feng, K., and Montoya, B. M. (2016). Influence of Confinement and Cementation Level on the Behavior of Microbial-Induced Calcite Precipitated Sands under Monotonic Drained Loading. Journal of Geotechnical and Geoenvironmental Engineering, 142(1):04015057.

Fukue, M., Ono, S.-I., and Sato, Y. (2011). Cementation of Sands Due To Microbiologically-Induced Carbonate Precipitation. Soils and Foundations, 51(1):83–93.

Gowthaman, S., Mitsuyama, S., Nakashima, K., Komatsu, M., and Kawasaki, S. (2019a). Biogeotechnical approach for slope soil stabilization using locally isolated bacteria and inexpensive low-grade chemicals: A feasibility study on Hokkaido expressway soil, Japan. Soils and Foundations, 59(2):484–499.

Gowthaman, S., Iki, T., Nakashima, K., Ebina, K., and Kawasaki, S. (2019b). Feasibility study for slope soil stabilization by microbial induced carbonate precipitation (MICP) using indigenous bacteria isolated from cold subarctic region. SN Applied Sciences, 1(11):1480.

Gowthaman, S., Nakashima, K., and Kawasaki, S. (2020). Freeze-Thaw Durability and Shear Responses of Cemented Slope Soil Treated by Microbial Induced Carbonate Precipitation. Soils and Foundations, 60(4): 484-499.

Jiang, N.-J., Tang, C.-S., Yin, L.-Y., Xie, Y.-H., and Shi, B. (2019). Applicability of Microbial Calcification Method for Sandy-Slope Surface Erosion Control. Journal of Materials in Civil Engineering, 31(11):04019250.

Lin, H., Suleiman, M. T., Brown, D. G., and Kavazanjian, E. (2016). Mechanical Behavior of Sands Treated by Microbially Induced Carbonate Precipitation. Journal of Geotechnical and Geoenvironmental Engineering, 142(2):04015066-1–13.

Martinez, B. C., DeJong, J. T., Ginn, T. R., Montoya, B. M., Barkouki, T. H., Hunt, C., Tanyu, B., and Major, D. (2013). Experimental Optimization of Microbial-Induced Carbonate Precipitation for Soil Improvement. Journal of Geotechnical and Geoenvironmental Engineering, 139(4):587–598.

Meyer, F. D., Bang, S., Min, S., Stetler, L. D., and Bang, S. S. (2011). Microbiologically-Induced Soil Stabilization: Application of *Sporosarcina pasteurii* for Fugitive Dust Control. Geo-Frontiers 2011, American Society of Civil Engineers, Reston, VA, pp 4002–4011.

Montoya, B. M., and DeJong, J. T. (2015). Stress-Strain Behavior of Sands Cemented by Microbially Induced Calcite Precipitation. J. Geotech. Geoenviron. Eng. 141(6):04015019

Montoya, B. M., DeJong, J. T., and Boulanger, R. W. (2013). Dynamic response of liquefiable sand improved by microbial-induced calcite precipitation. Géotechnique, 63(4):302–312.

Nayanthara, P. G. N., Dassanayake, A. B. N., Nakashima, K., and Kawasaki, S. (2019). Microbial Induced Carbonate Precipitation Using a Native Inland Bacterium for Beach Sand Stabilization in Nearshore Areas. Applied Sciences, 9(15):3201.

van Paassen, L. A., Ghose, R., van der Linden, T. J. M., van der Star, W. R. L., and van Loosdrecht, M. C. M. (2010). Quantifying Biomediated Ground Improvement by Ureolysis: Large-Scale Biogrout Experiment. Journal of Geotechnical and Geoenvironmental Engineering, 136(12):1721–1728.

Salifu, E., MacLachlan, E., Iyer, K. R., Knapp, C. W., and Tarantino, A. (2016). Application of microbially induced calcite precipitation in erosion mitigation and stabilisation of sandy soil foreshore slopes: A preliminary investigation. Engineering Geology, 201:96–105.

Stabnikov, V., Naeimi, M., Ivanov, V., and Chu, J. (2011). Formation of water-impermeable crust on sand surface using biocement. Cement and Concrete Research, 41(11):1143–1149.

Effects of root tensile strength of vegetation on slope stability

G. A. C. Ganepola
Asian Disaster Preparedness Center, Bangkok, Thailand, Sri Lanka Country Office

Lilanka Kankanamge
National Building Research Organization, Sri Lanka

U. P. Nawagamuwa
Department of Civil Engineering, University of Moratuwa, Sri Lanka

A. K. Karunarathna
Department of Agricultural Engineering, University of Peradeniya, Sri Lanka

N. M. S. I. Arambepola
Asian Disaster Preparedness Center, Bangkok, Thailand

ABSTRACT: Plants play an important role in stabilizing unstable slopes. Environmentally friendly and sustainable mitigation measures can be developed by combining geo-engineering techniques with soil bioengineering methods where live plants are utilized. Studies on bioengineering properties of plants found in Sri Lanka are rare; hence there is a need for comprehensive laboratory, field and modelling studies. This study investigated root tensile strength, a mechanical property, of few Sri Lankan plants found in hill country and its contribution to improve slope stability. Different existing correlations in literature between root tensile strength and apparent cohesion increase were adopted in the analysis. Among the tested roots, *Syzygium aromaticum* (Clove) showed highest tensile strength followed by *Eucaliptus grandis* (Eucaliptus). These outcomes were applied on a case study in Badulusirigama slope failure rehabilitation work and found to be very positively contributing to its stability.

1 INTRODUCTION

In ancient times, the use of plants in protecting soil slopes and earthen covers for landfill was well recognized, and it is still well known that the effect of plants will play an important role in increasing soil slope stability (Eab et al. 2015). Soil bioengineering is the use of live plant materials to serve as soil reinforcements, hydraulic wicks (or drains) and barriers to earth movement. (Gray and Sotir, 1996). In addition, according to Fatahi et al. (2010), tree roots provide three stabilizing functions: (a) reinforcement of the soil, (b) dissipation of excess pore pressures and (c) establishment of sufficient matric suction to increase the shear strength. Coppin and Richards (2007) mentioned other influences of plants on soil, such as, interception of rainfall, reduction of surface water runoff, protection against erosion by surface water flow and protection against wind erosion.

This technique of soil bioengineering has been recognized as an ecologically and environmentally friendly technique that can positively affect the stability of infrastructure such as man-made or engineered slopes. To increase the ecological values and biodiversity, it is common to have multiple types of species, such as trees, shrubs, herbs and grasses, grown on these engineered structures (Ni et al. 2016).

However, application of soil bioengineering techniques is still limited in the Sri Lankan context. Unavailability of proper records on bioengineering properties of native and common plants of Sri Lanka is one of the major limitations for application of such techniques.

This study investigated root tensile properties of fifteen plant species commonly found in Sri Lankan hill country. Consequently, a method from literature to deduce root cohesion values which is useful in ranking plant species according to their slope stability improvement potential is adopted.

2 ROOT TENSILE STRENGTH

Soil reinforcement is one of the main stabilizing functions offered by plants which contribute to mitigate slope instabilities. This function is fulfilled by plant roots and its tensile strength.

Gray and Sotir (1996) mentioned that tensile strength of roots show variations depending on species type, growing environment, season, root diameter and method of testing (eg. in a moist or air-dry state). According to them, root tensile strengths of most plant species remain in the range of 10 to 40 MPa. They further had indicated that shrubs appear to have root tensile strengths comparable to that of trees. Hence, an equivalent reinforcement from shrubs can be expected overcoming the negative effects from trees such as greater weight, rigidity and tendency for wind throwing.

Previous studies have shown that there exists an inversely proportional relationship between the root diameter and its tensile strength (Gray and Sotir, 1996; De Baets et al. 2008; Capilleri et al. 2019).

3 MODELLING ROOT TENSILE STRENGTH IN SLOPE STABILITY ANALYSIS

It is essential to assess the effect of soil reinforcement provided by root tensile strength in order to determine the contribution of plant roots to the Factor of Safety of a slope.

Wu et al. (1979), Waldron and Dakessian (1981) and Docker and Hubble (2009) incorporated additional soil reinforcement by plant roots as an increase to the shear strength. According to Waldron and Dakessian (1981), the soil reinforcement due to plant roots can be directly added to the Coulomb equation as given in Eq. (1).

$$S = c + \Delta S + \sigma_N \tan\phi \quad (1)$$

Where
S = soil shearing resistance
c = cohesion
σ_N = normal stress on the shear plane
ϕ = soil friction angle
ΔS = shear strength increase due to roots

Eq. (1) can be applied assuming a flexible, elastic root extending vertically across a horizontal shear zone of thickness z as shown in Fig. 1. It is also assumed that the soil friction angle (ϕ) is unaffected by roots and the tensile strain in the roots is not large, so that the stressed length approximates the unstressed root length. Further it is presumed that the soil loads the root in tension by tangential stress (τ) at the soil-root interface and all longitudinal displacements of the soil relative to the root, including elastic tensile strain and slippage, mobilize the maximum tangential stress τ'.

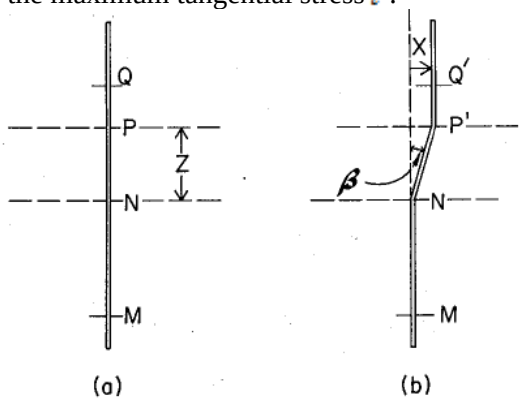

Fig.1 Model of a flexible, elastic root extending vertically through a horizontal shear zone of thickness Z. (a) Undisturbed soil. (b) Soil above N displaced horizontally a distance x with root segment MNPQ extended to length MNP'Q' (Waldron and Dakessian, 1981).

Wu et al. (1979) and Gray and Sotir (1996) elaborated on a force equilibrium model to calculate the additional shear strength provided by the roots (Eq. 2) from full mobilization of root tensile strength.

$$\Delta S = T_R \left(\frac{A_R}{A}\right)[\sin\theta + \cos\theta \tan\phi] \quad (2)$$

Where
T_R = average tensile strength of the root
$\frac{A_R}{A}$ = the fraction of soil cross section occupied by roots or the root area ratio
θ = the angle of shear distortion in the shear zone
ϕ = the angle of internal friction of the soil

$$T_R = \frac{\sum T_i n_i a_i}{\sum n_i a_i} \quad (3)$$

Where
T_i = the strength of roots in size class i
n_i = the number of roots in size class i
a_i = the mean cross-sectional area of roots in size class i

$$\frac{A_R}{A} = \frac{\sum n_i a_i}{A} \quad (4)$$

Where
A = Total area of soil

Further they said that the value of $[\sin\theta + \cos\theta \tan\phi]$ is relatively insensitive to normal variations in (θ) and (ϕ). An average value of 1.2 was proposed for the term (Eq. 5).

$$\Delta S = 1.2 T_R \left(\frac{A_R}{A}\right) \quad (5)$$

Wu et al. 1979 stated that ΔS is nearly constant and would have the characteristics of cohesion.

However, Schwarz et al. (2010) mentioned that experimental studies had revealed an overestimation of the role of root reinforcement in soils based on the above model (Eq. 5). They indicated a correction factor of around 0.4 would be needed to revert them to experimental values. Hence Eq. (5) can be simplified to:

$$\Delta S = 0.48 T_R \left(\frac{A_R}{A}\right) \quad (6)$$

Eq. (6) was used by Mahannopkul and Jotisankasa (2019) in their study in evaluating *Chrysopogon zizanioides* (Vetiver) roots for bio-slope stabilization.

4 METHOD OF STUDY

4.1 *Collection of root specimen*

The sampling locations were identified as landslide prone areas in the hill country. A set of root samples were collected from natural landscapes in hill country districts as well as from Kandyan home gardens. Root samples from fifteen plant species were collected ensuring that at least several specimen of roots for each species having different diameters for each selected plant species. Undamaged roots with an average diameter varied from 2 to 10 mm, and a minimum root length of 150 mm were selected for testing. To collect the roots, a few individual, medium-size plants, growing in the same microenvironment (same habitat, similar landscape position), were exposed using the dry excavation method. The roots were manually collected by careful excavation, or by cutting the roots on exposed profiles (Fig. 2). After excavation, the roots were individually stored in a plastic bag to preserve their moisture content. The collected root samples were immediately transported to the laboratory and tested the tensile strength at the next possible time before they lose much moisture.

Fig. 2 Root sample collection for laboratory tests

4.2 *Determination of root tensile strength*

Root tensile strength tests were conducted in the laboratory using Dynamometer universal tensile and compression test machine (Model LW 6527, WC DILLON & Co Inc, USA) (Fig 3). This device combines three functions: (1) traction force generation, (2) measuring load and displacement, and (3) data acquisition. Clamping is the most critical issue when measuring root strength. Roots with fleshy root epithelia could not be tested due to clamping problems, as the samples slipped without breaking. Also, direct mounting of roots causes grip damage in the roots. In this experiment, cotton textile bandage was wrapped around the griping ends of the roots to increase the grip and to minimize the damage to the roots.

Fig. 3 Root tensile strength testing using Dynamometer

The initial root length was set to 150 mm. The root diameter was measured at both ends and the middle was measured using a Vernier caliper. The maximum force at the breaking point was recorded. Eq. (7) was used to calculate the tensile strength.

$$T_i = \frac{F_{max}}{\pi\left(\frac{D^2}{4}\right)} \quad (7)$$

Where F_{max} is the maximum force (N) needed to break the root and D is the mean root diameter (mm).

4.3 *Modelling the effect of root tensile strength*

The increase in shear strength or the root cohesion was calculated using Eq. (6) for the tested plant species. Considering a planting configuration of species parallel to slope contours, a two-dimensional (2D) slope stability analysis was carried out. An average value of root cohesion for the entire slope, ($\bar{c}_r$) was calculated considering the spacing between each plant row as suggested by Mahannopkul & Jotisankasa (2019) (Eq. 8). They

had applied this formula for evaluating the effectiveness of Vetiver plants.

$$\bar{c}_r = \frac{c_r l_r}{l_r + l_s} \quad (8)$$

Where
c_r = Root cohesion of the plant species
l_r = width of the plant row
l_s = spacing between each plant row (width of the non-reinforced zone)

This root cohesion was incorporated into conventional limit equilibrium analysis as an increase in effective cohesion, in order to determine the Factor of Safety of the vegetated slope.

5 RESULTS AND DISCUSSIONS

5.1 *Root tensile strength results*

Forty-four root specimen from fifteen different plant species which included some from Kandyan Home Garden system, were tested as described in order to investigate its root tensile strength. At the time of testing some root specimen experienced slippages without rupturing. Only root specimen where rupturing occurred were considered in this study. Table 1 summarizes the results from remaining twenty-seven root specimen.

The inversely proportional relationship between root tensile strength and root diameter was observed in Theobroma cacao (Cocoa), Camellia sinensis (Tea) and Coffea (Cofee). Other plant species did not appear to show the inverse relationship which was discussed in literature. It is noted that the frequency of root specimen needed to be increased in order to verify the relationship.

5.2 *Modelling of root tensile strength*

For a pilot analysis to quantify the effect from plant species, site at Uva Wellassa University, in Badulusirigama, Badulla district was chosen. The approximate dimensions of the unstable area constitute a width of 120m, a length of 500m and a depth of 9m~13m. There had been slow ground movements in the rainy seasons of 2007, 2011 and 2012 posing a threat to the community living near the toe of the landslide.

A network of surface and subsurface drains was constructed at site in order to improve surface drainage of water, minimize infiltration of storm water and lower the ground water level in order to arrest any further ground movements. After the implementation of said countermeasures there has been a reduction in slope movement as indicated by the data received from slope monitoring equipment.

However at present, the site has areas with exposed bare soil formations and there is a potential for gullying in areas in between where surface drains have been built. *Panicum maximum* (a local invasive grass) bushes have grown up naturally and in an uncontrolled manner covering up a major portion of the site. There could be a risk of soil erosion occurring in some slope segments.

Table 1: Results of root tensile testing

No.	Species Name	Diameter Range (mm)	Tensile strength range (MPa)
1	*Syzygium aromaticum* (Clove)	1.37 – 2.30	40.08 – 165.01
2	*Theobroma cacao* (Cocoa)	2.03 – 2.78	48.29 – 25.77
3	*Trema orientalis* (Gaduma)	4.15 – 4.52	10.14 – 12.23
4	*Macaranga peltata* (Kanda)	2.20 – 2.60	10.31 – 11.07
5	*Cinnamomum verum* (Cinnaman)	4.42 – 5.48	21.75 – 22.41
6	*Myristica fragans* (Nutmeg)	2.28	27.19
7	*Calliandra calothyrsus*	8.70	9.89
8	*Eucaliptus grandis*	5.97 – 8.37	10.51 – 42.78
9	*Bauhinia racemosa* (Maila)	5.12 – 6.79	9.53 – 10.84
10	*Camellia sinensis* (Tea)	8.77 – 10.077	3.25 – 2.46
11	*Azadirachta indica* (Neem)	5.35	17.44
12	*Clidermia hirta* (Kata-kalu bowitiya)	5.14	9.44
13	*Osbeckia octandra.* (Heen-bowitiya)	5.08	9.66
14	*Lantana camara* (Hinguru)	6.80	5.40
15	*Coffea Arabica* (Cofee)	2.63 – 9.00	14.69 – 28.67

This in turn could pose a threat to the population of 320 people living near the toe area of the landslide. Therefore, an engineered vegetation cover is of utmost importance in this site to minimize soil erosion and rainwater infiltration into the unstable soil mass.

For the pilot analysis in this study, it was decided to use *Syzygium aromaticum* species which is commonly known as Clove as a possible vegetation cover and determine its effectiveness in arresting shallow mass movements. It is a species which offer economic benefits without the need for uprooting. Its properties were given in the Table 2.

Average root cohesion was calculated presuming a planting configuration parallel to slope contour using Eq. (8) varying spaces between lines from 0.5m to 2m. It was noted that root cohesion was greater when the spacing between lines were minimum. A root area ratio [$\frac{A_R}{A}$] of 0.25% was assumed for clove for an effective depth of 2m with roots based on field experience in calculating the average root cohesion.

Fig 4: Aerial view of the site at Uva Wellassa University

Table 2. Properties of *Syzygium aromaticum* (Clove) root

Width of plant row (l_r) (m)	Average root cohesion (MPa) for different spacing between each plant row (l_s) (m)			
	2.0	1.5	1.0	0.5
0.5	0.010	0.012	0.016	0.020

Information on subsurface profile present at site is summarized in Fig. 5 and Table 3. The same subsurface soil/ rock parameters used by Japanese International Construction Agency (JICA), (2015), during their study, were directly adopted in this analysis.

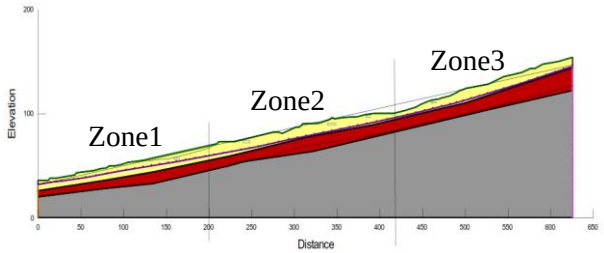

Fig. 5: Idealized subsurface profile

Table 3: Geotechnical parameters assigned for each subsurface layer

Layer	c' (kPa)	φ' (deg)	φ^b (deg)	γ (kN/m^2)
Colluvium	7	11	10	15
Completely weathered rock (soil)	7	14	-	16
Moderately weathered Rock	20	40	-	19

Where
c' = Effective cohesion
φ' = Effective angle of friction
φ^b = Angle of friction with respect to suction
γ = Unit weight

The subsurface profile shown in Fig. 5 was divided into three zones based on available geophysical investigation information. Phreatic surface of the natural slope is indicated with a blue line in Fig. 5. In the stability analysis, each zone was modelled separately.

In order to simulate unsaturated conditions in the slope, (φ^b) value of 10° was assumed as per the study done by Kankanamge et al. (2018).

In the analysis, a separate layer was introduced namely, "Colluvium after vegetation" which is about 2 m of thickness (the average root depth zone of clove tree). This layer was assigned the modified shear strength parameters given in Table 4. A spacing of 2m was considered between plant rows.

Table 4: Revised soil parameters upon application of vegetation (Clove)

Layer	c' (kPa)	φ' (deg)	φ^b (deg)	γ (kN/m^2)
Soil layer with Vegetation	10	12	10	15
Colluvium	7	12	10	15
Completely weathered rock (soil)	7	14	-	16
Mod. Weathered Rock	20	40	-	19

The conditions of the slope were then simulated in Geo Studio modules considering Limit Equilibrium approaches to check possible shallow failures. Spencer method was adopted to calculate the factor of safety with a fully specified slip surface method. The shallow slip surface was assumed to be varied between 1.5 - 2.0 m. A safety margin of 3 was applied on root cohesion values derived based on laboratory tests and empirical relationships to account for possible variations experimental studies and uncertainty.

Afterwards, variation of factor of safety was analyzed upon introduction of vegetation. The results are given in Table 5.

Table 5: Variation of factor of safety (FoS) after applying subsurface drainages with vegetation

Zone	FoS before introducing vegetation for shallow slip surfaces	FoS after introducing vegetation for shallow slip surfaces
01	1.18	1.38
02	1.13	1.41
03	1.14	1.23

This analysis shows that the factor of safety values could be increased further by introducing proper vegetation. These results can be further filtered out with a greater number of data from different samples.

6 CONCLUSIONS AND RECOMMENDATIONS

This study investigated the influence of root tensile strength on slope stability by computing the shear strength increase or the root cohesion offered by different plant species. The approach adopted in finding root cohesion values could be regarded as straight forward yet extensive way of ranking plant species as per their potential to improve slope stability. The analysis showed that the factor of safety values could be further increased by introducing appropriate vegetation. However, it is recommended to carry out detailed studies with more number of root tensile tests together with their root moisture contents on individual plant species in order to arrive at more representative values of its root cohesion.

ACKNOWLEDGMENTS

The authors wish to acknowledge the invaluable inputs and guidance by: Prof. Gehan Jayasuriya (University of Peradeniya), Eng. (Dr.) Asiri Karunawardena (Director General NBRO) and Dr. Senaka Basnayake (Director ADPC). Authors would also like to thank the team member Ms. Nayani Dayarathna (NBRO) as well for her contribution on this study. Further, they wish to convey sincere thanks to the World Bank for providing financial support (World Bank Grant No.7191576) for the study.

REFERENCES

Capilleri, P.P., Cuomo, M. & Todara, M. (2019). Experimental investigation of root tensile strength for slope stabilization, Indian Geotechnical Journal, https://doi.org/10.1007/s40098-019-00394-2.

Coppin N.J., Richards I.G., (2007). Use of vegetation in civil engineering. CIRIA London. (ISBN_0-86017-711-4)

De Baets, S., Poesen, J., Reubens, B., Wemans, K., Baerdemaeker, J.D., and Muys, B. (2008). Root tensile strength and root distribution of typical Mediterranean plant species and their contribution to soil shear strength, Plant Soil (305): 207-226

Docker, B.B. and Hubble, T.T.C. (2009). Modelling the distribution of enhanced soil shear strength beneath riparian trees of south-eastern Australia, Ecological engineering 35: 921-924

Eab K.H., Likitlersuang, S., Takahashi, A. (2015). Laboratory and modelling investigation of root-reinforced system for slope stabilization, Soils and Foundations, 55(5): 1270-1281.

Fatahi, B., Khabbaz, H., Indraratna, B. (2010). Bioengineering ground improvement considering root water uptake model, Ecological Engineering, 36: 222-229.

Gray, D.H. and Sotir, R.B. (1996). Biotechnical and soil bioengineering slope stabilization – A practical guide for erosion control. Wiley India Pvt. Ltd.

Japanese International Cooperation Agency (JICA). (2015). "Proposal for rectification on landslide, slope failure and rock fall in pilot sites

Kankanamge, L., Jotisankasa, A., Hunsachainan, N., and Kulathilaka, A. (2018). Unsaturated shear strength of a Sri Lankan residual soil from a landslide-prone slope and its relationship with soil-water retention curve, International Journal of Geosynthetics and Ground Engineering, 4:20. https://doi.org/10.1007/s40891-018-0137-7.

Mahannopkul, K, and Jotisankasa, A. (2019). Influence of root suction on tensile strength of *Chrysopogon zizanioides* roots and its implication on bio-slope stabilization, Journal of Mountain Science, 16(2): 275-284.

Ni J.J., Leung, A.K., Ng, C.W.W. and So, P.S. (2017). Investigation of plant growth and transpiration-induced matric suction under mixed grass-tree conditions, Canadian Geotechnical Journal, 54: 561-573.

Schwarz, M., Preti, F., Giadrossich, F., Lehmann, P. and Or, D. (2010). Quantifying the role of vegetation in slope stability. A case study in Tuscany (Italy), Ecological Engineering, 36(3):285-291.

Waldron, L.J. and Dakessian, S. (1981). Soil Reinforcement by Roots: Calculation of increased soil shear resistance from root properties, Soil Science, 132: 427-435.

Wu, T.H., McKinnell III, W.P. and Swanston, D. N. (1979). Strength of tree roots and landslides on Prince of Wales Island, Alaska, Canadian Geotechnical Journal 16: 19-33.

.

Pore-Water Pressure and Suction Regime in a Clay Dyke

S. Pramusandi
Department of Civil Engineering, Kasetsart University, Bangkok, Thailand

A. Jotisankasa & S. Chaiprakaikeow
Department of Civil Engineering, Kasetsart University, Bangkok, Thailand

S. Nishimura
Division of Field Engineering for the Environment, Hokkaido University, Sapporo, Japan

ABSTRACT: A field study was undertaken of an instrumented dyke on soft Bangkok clay in Pathumthani, Thailand. A 3-meter high dyke was instrumented with 2 flushable piezometers, 13 low-capacity and 2 high capacity tensiometers, automatic rain gauge, 3 of time domain reflectometry moisture sensors, as well as interval camera to monitor the slope behavior during a rainy season. The pore-water pressure, suction, moisture content and rainfall were continuously monitored over the rainy season in 2017. The in-situ tests such as dynamic cone penetrometer test, field vane shear test and spectral analysis of surface wave were also conducted to charactize the site. The upper 0.5 m of dyke fill material made up of silty and clayey soils were found to experience drastic suction changes, reaching 1800 kPa towards the end of a drought and abruptly reducing to 20-40 kPa within a day upon the onset of the rainy season. Such large and abrupt changes of the suction are likely to have aggravated the surface cracking and hence the dyke movements. Vertical movement of the dyke surface showed compression-swelling phenomena, probably due to the combined effects of drying, collapse-on-wetting and swelling and suggested that some movement is recoverable. This was not the case for horizontal movements, which exhibited constant outwards cumulative displacement.

Keywords: dyke, tensiometer, pore-water pressure, soil suction

1 INTRODUCTION

Many geotechnical and geo-environmental challenges in Thailand related to unsaturated soils, for example, rainfall induced-landslide, construction and maintenance of dams or embankment, landfills as well as shallow foundations and pavements located in areas of problematic soils such as shrink-swell clay and collapsible loess, etc. There are also needs to ensure infrastructure serviceability and integrity in future, especially with the apparent adverse effect of climate change that results in more intense rainfall and prolonged drought.

The climate change effect such as extreme cycles of drying and wetting could influence to dyke excessive movement and failure. This event occurred at Asian Institute of Technology (AIT) dyke that recently failured in dry season after raining for 3 days. Number of studies also aimed at better understanding dyke behaviour and their response to climatic factors (Van Baars , 2005, Karl et al., 2008, Nishimura et al., 2015, Vahedifard et al., 2017, Fern et al., 2017, Jasim & Vahedifard, 2017).

This paper presents the pore-water pressure and dyke movement measurement on a clay dyke due to its response to climate change effect such as rainfall. The results of this paper were also futher measurement from the previous paper (Jotisankasa et al., 2019)

2 STUDIED SITE AND GROUND PROFILE

Asian Institute of Technology (AIT) dyke on the northern side was chosen as the studied site for 10 m long section which had been constructed to create a polder, consisting of AIT, National Science and Technology Development Agency (NSTDA) and Thammasat University (TU) as shown in Figure 1. The studied section of the dyke was about 3m above the original ground level with a side slope of about 1:1.7 (V: H) as measured in 2017. Disturbed samples were collected from the AIT side of the dyke using hand-augers and test pits from the surface to 2 m depth for basic property tests as shown in Table 1. The undisturbed samples also were collected in 3 different places (top,

middle and toe of the dyke) with depth of 0.5m. The in-situ tests such as dynamic cone penetrometer test, field vane shear test and spectral analysis of surface wave were also conducted to charactize the ground profile which shown in Figure 2.

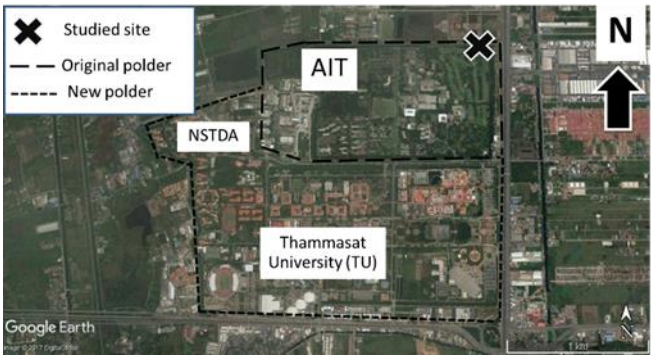

Fig. 1 Location of the studied site at Asian Institute of Technology (AIT) dyke (Jotisankasa et al., 2019)

Table 1. Summary of basic soil properties (Jotisankasa et al., 2019)

Soil unit	% Gravel, >4.75 mm	% Sand, 0.075 - 2 mm	% Silt, 0.075 -5μm	% Clay, <5μm	LL, %	PI	USCS
1-Road surface	16.6-34.7	62-80	3.2-7.3	0.8-1.2	31.9-52.2	11.5-24.0	SP, SW-SC
2-Upper clay fill	12.1	22.8	23.9	41.3	43.8	22.4	CL
3-Upper silty clay fill	2.3-4.24	13.6-17.6	37.8-50.3	29.7-44.3	48.6-50.3	19-24.4	CL/CH, ML
4-Lower silty fill	4.8-11.4	48.4-75.7	13.0-46.8	2.3-3.4	47.4-48.0	14.5-20.6	ML, SM
5-Upper crust	0.0	2.7-5.0	49.1-53.5	43.8-45.9	48-52.5	17.1-21.4	ML, MH
6-Lower crust	0.0	1.1-2.1	45.8-54.8	43.2-53.1	47.7-53.4	15.6-21.8	ML, MH
7-Soft clay*	-	10-30	20-30	50-70	60-75	30-40	CH

*Source: Horpibulsuk et al. (2007)

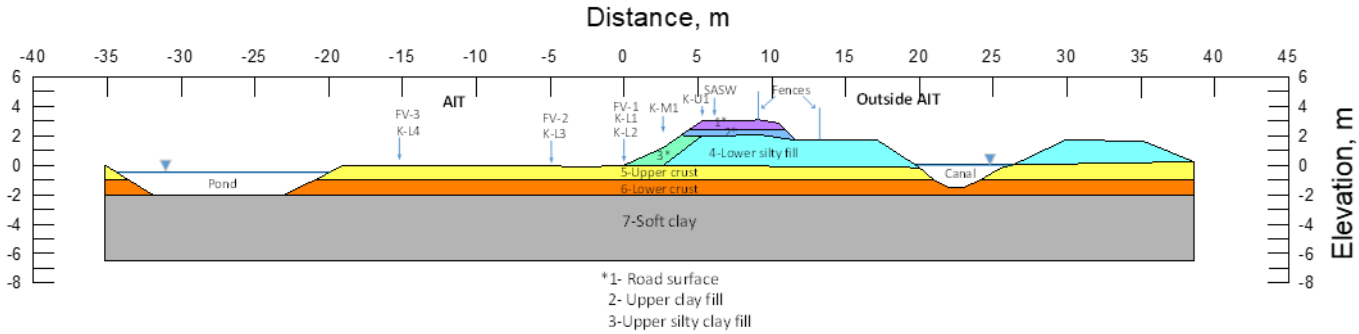

Fig. 2 Cross-section of the instrumented AIT dyke (water level in pond at 9 May 2017) (Jotisankasa et al., 2019)

3 INSTRUMENTATIONS

The instruments installed at the site are shown in Figure 8, including 13 tensiometers (Kasetsart University or KU-type), 2 flushable tensiometers (UNSUC), 3 MPS suction sensors, 3 Time Domain Reflectometry moisture sensors (TDR), 1 tipping bucket rain gauge, and 1 interval camera. Settlement plates have been installed on the slope at 7 locations (SP1 to SP7). The details of these instruments regarding installation depth and location are summarized in Table 2.

Kasetsart University (KU)-type tensiometer was developed by Jotisankasa et al., (2007) using MEMs pressure sensors and 1-bar air-entry ceramic filter, and its installation as shown in Figure 4. The KU tensiometers were complemented by another type of tensiometers, flushable UNSUC ML-2400AEL, which placed at 2 m and 3 m depths from the top of the dyke. The other type of device, Decagon MPS6 uses a ceramic specifically designed with a wide pore size distribution for wider measurement range of suction. Three MPS6 were installed at 0.5 m depth, each of which at the shoulder, middle and toe of the slope as described in Figure 3. The surface moisture condition was monitored by TDR (Time Domain Reflectometry) soil moisture sensors (Campbell C-CS655-9.9) with a 120 mm probe length, measuring the volumetric water content over the same thickness of the surface soil.

Table 2. Summary of instrumentation (Jotisankasa et al., 2019)

Instrument	Instrument code	Depth of installation, m, or location	Measurement working range
Tensiometer (KU-type)	A1, A2, A3 B1, B2, B3 C1, C2, C3 D, E, F, G	0.5, 1, 2 0.5, 1, 1.7 0.5, 1, 2 1	Pore-water pressure -80 to 600 kPa
Tensiometer (Flushable)	UNSUC1 UNSUC2	2 3	Pore-water pressure -80 to 80 kPa
MPS suction sensor	MPS1, MPS2, MPS3	0.5	Pore-water pressure -9 to -1,000,000 kPa
TDR moisture sensor	TDR1, TDR2, TDR3	0.1	-
Tipping bucket rain-gauge	RG	Top of dyke	-
Interval camera	I-cam	Top of dyke	-

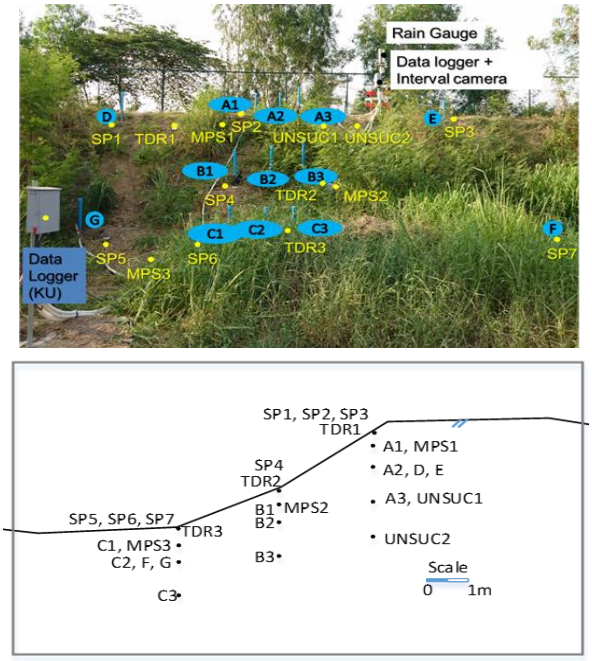

Fig. 3 Location of instruments and survey points (Jotisankasa et al., 2019)

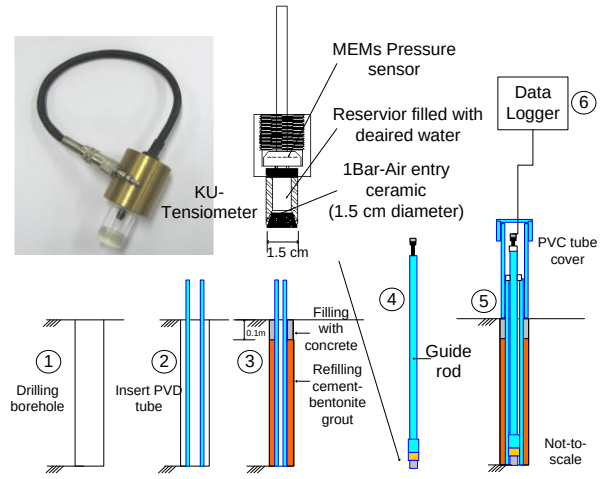

Fig. 4 KU-tensiometer and the installation method (Jotisankasa et al., 2019)

4 PORE-WATER PRESSURE AND SUCTION REGIME

4.1 *Rainfall pattern*

The instrumentation was completely installed inApril 2017, which was near the end of the dry season in Bangkok, up until September 2019. In this paper, the monitoring results up until August 2017 are presented which encompassed the rain season. The daily rainfall and cumulative rain during the measurement period are presented in Figure 5 which shows two and a half cycles of the rainy and dry season. The daily rainfall was plotted together with the 3-day antecedent rain and compared with a critical rainfall envelope (100 mm) in Figure 6 which is the commonly used criterion for rainfall-induced slope instability warning in Thailand (Mairaing et al., 2012). No major failure, however, was observed at the studied site despite there were 10 rainfall data crossing the 100 mm rainfall envelope.

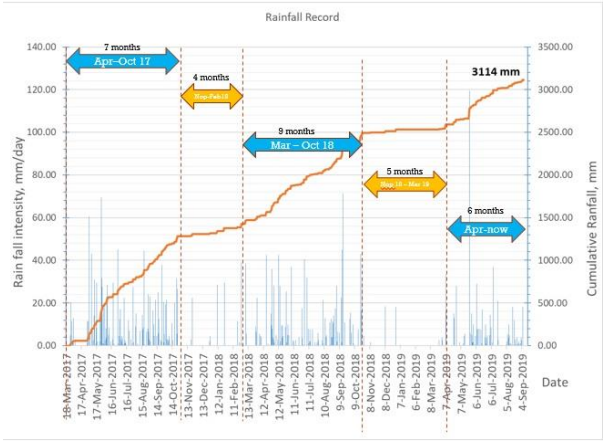

Fig. 5 Daily rainfall and cumulative rain during the monitoring period

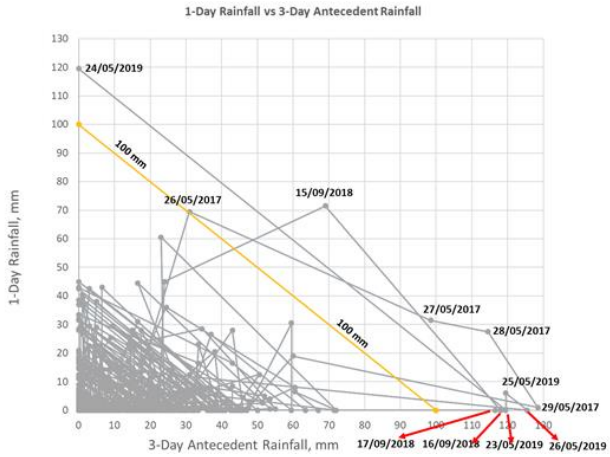

Fig. 6 Three-days antecedent rain and compared with a critical rainfall envelope (100 mm)

4.2 *Pore-water pressure and suction regime*

The variations of pore-water pressure with time at crest, middle part, and toe of the dyke are shown in Figures 7, 8 and 9 respectively. Highly negative pore-water pressure (high suction) could be observed from April until the beginning of May 2017 which was the drought period. This deviation varied from 5 to 15 kPa and was believed to be caused by hysteresis in MPS suction measurement.

A comparison between UNSUC- and KU-tensiometers was also made for measurement at 2 m depth in the crest of the dyke (UNSUC1 and A3 in Figure 7c). During the drought period in April 2017, both devices could not measure the suction reliably since the value exceeded 100 kPa and both sensors were prone to cavitation. Nevertheless, there was a discrepancy between the pore-water

pressure readings of the two kinds of tensiometer during the rain period (May until August 2017). While the KU-tensiometer indicated negative pore-water pressure gradually increasing from -70 to -60 kPa during the rain, the UNSUC-tensiometer suggested near-zero pore-water pressure which was quickly responsive to the raining event. The locations of two sensors (UNSUC1 and A3) were only about 1 m apart and the difference in ground condition was unlikely. It was thought that the UNSUC's fast response was not indicative of the likely low permeable of the fill and could be caused by imperfect sealing around the borehole and sensor rod at the time of installation. The UNSUC2 measurement at 3 m suggested a relatively constant negative pore pressure (-10 kPa), which was slowly increasing with time, a similar behaviour to A3 tensiometer.

By comparing readings from tensiometers installed at the same depth of 1 m but different locations (i.e. between D, E, and A2 in Figure 7; and F, G, and C2 in Figure 9), in general, a consistent measurement of pore-water pressure could be observed with a deviation of about 5 kPa. Point E tensiometer appeared to dry faster than Point D and A2 tensiometers from 17 until 27 May 2017. This could be due to inherent non-uniformity of the evapotranspiration process, and still could not be fully explained at the moment. The overall trend in Figure 7a suggests that the upper layer (surface to 1 m depth) of the dyke crest had a faster response to pore-water pressure change due to rain event. The readings from the lower silty fill (A3) and the crust zone (UNSUC2) appeared to have a slower response in pore-water pressure (Figure 7c). The pore-water pressure behaviour in the middle and toe of the dyke (Figures 8 and 9 respectively) also showed a slower response.

The pore-water pressures contours of the dyke were drawn based on measurements on 27 April, 27 May, 27 June, 27 July and 27 August 2017, as shown in Figure 10. In preparing these contour plots, unreliable measurements (i.e. readings when cavitation occurred, or borehole sealing was not perfect) were excluded. Apparently, the drought period in the year 2017 brought about highly negative pore-water pressure (suction) in the dyke, especially the upper 2 m where the suction reached values between 100 and 1800 kPa in late April (Figure 10a). The subsequent rainfall in May 2017 caused the dyke to become wetter with suction ranging between 10 to zero kPa (Figure 10b) near the surface, as a result of infiltration and groundwater rising. value of 60 kPa, indicating the gradual infiltration and seepage process due to relatively low permeability of the soil.

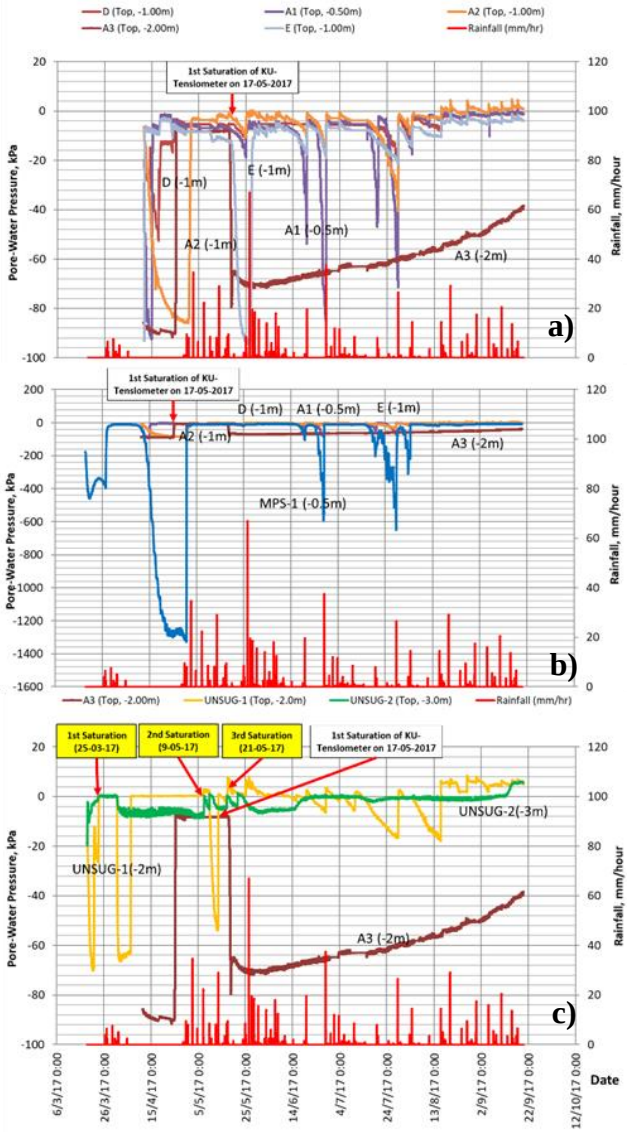

Fig. 7 Pore-water pressure along the vertical line from the upper part of dyke: Plot a) and b) pore-water pressure at depths of 0.5 and 1 meter; Plot b) is a reproduction of Plot a) in wider vertical axis range; Plot c) pore-water pressure at depths of 2 and 3 meter

Further rainfall events in June and August 2017 caused the groundwater level to rise (Figure 10c and 10e). The groundwater in the centre was slightly higher than at the toe, perhaps in response to the infiltration water recharging the groundwater table or due to the external water from outside of AIT. It can be seen that the upper part of dyke crest was drier now with the suction of nearly 600 kPa in response to the no-rain period from 20 until 27 June 2017. This indicated that the drying process took place first at the crest of the dyke as a result of gravimetric drainage. In addition to this, there was no ground cover and evaporation would have taken place more quickly. Meanwhile, the rainfall

events that happened in July 2017 made the dyke drier than the condition in June and August 2017.

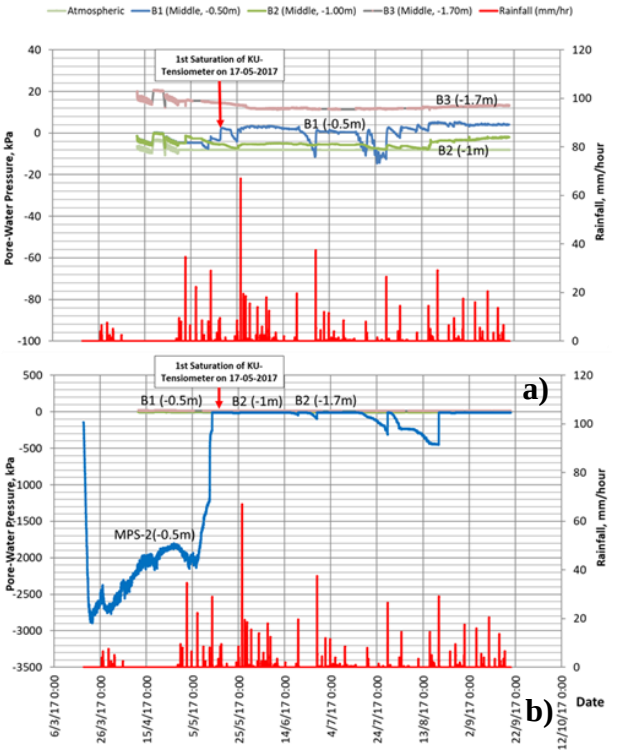

Fig. 8 Pore-water pressure along the vertical line from the middle slope part of dyke: Plot b) is a reproduction of Plot a) in wider vertical axis range

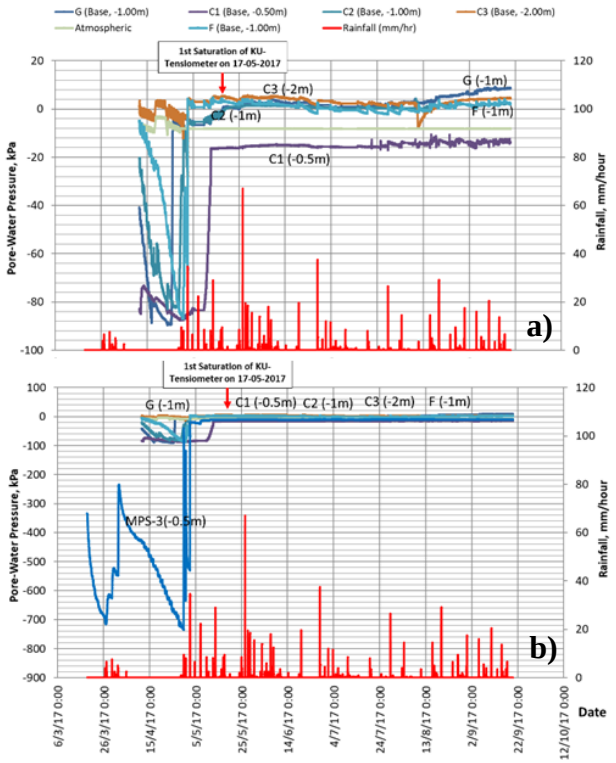

Fig. 9 Pore-water pressure at the toe of dyke: Plot b) is a reproduction of Plot a) in wider vertical axis range

4.3 *Dyke surface movement*

Surface movement of the dyke was monitored by means of Total Station surveying. Two permanent benchmarks were constructed on the piers of the nearby bridge which were assumed to be stationary. These benchmarks were used as reference points for the Total Station device. The measured coordinates (x, y, z) of all the settlement points (SP1 to SP7) were then used to calculate the vertical and horizontal movements as shown in Figure 11.

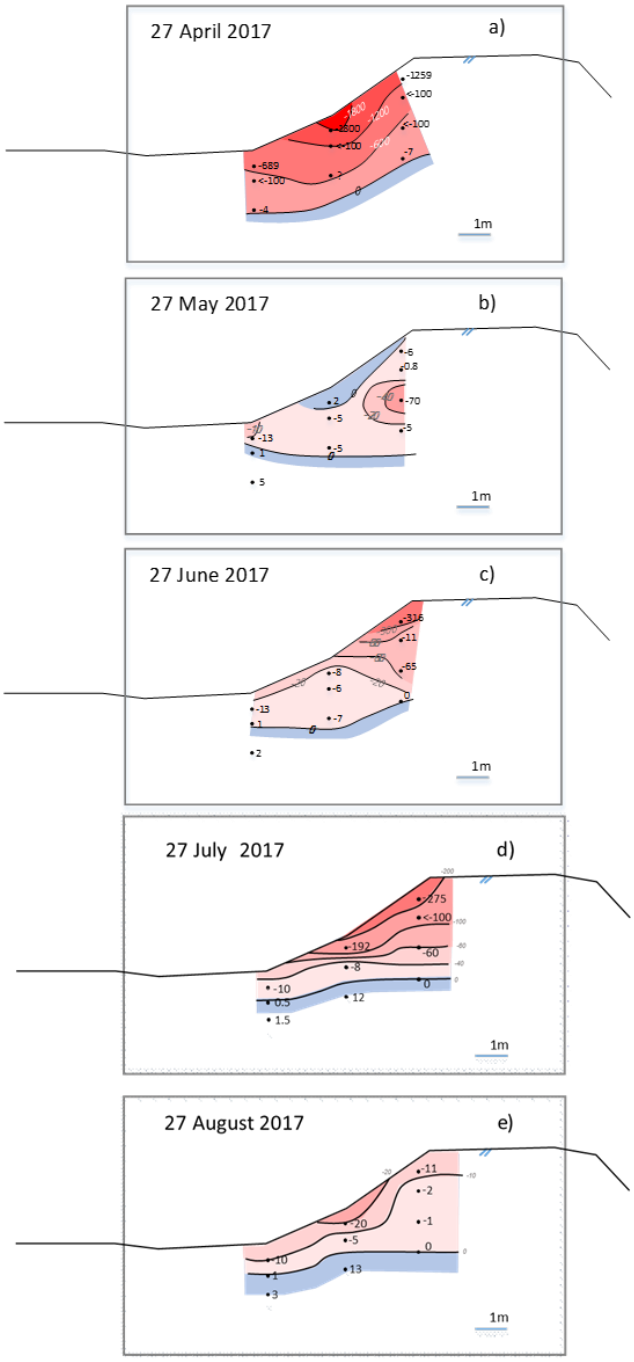

Fig. 10 Pore-water pressure contours at three selected dates (the scales are in meter and the contour values are in kPa)

The toe surface showed some heaving of less than 0.5 cm while the crest of dyke appeared to settle by about 0.5 to 1.5 cm. The middle part of the dyke experienced negligible settlement. Since the first measurement period (from 18 April to 9 May 2017) involved both drying and wetting, the first settlement could be related to both desiccation compression as well as collapse-on-wetting phenomena.

The second vector increments of movement, however, show that nearly all settlement points along the dyke swelled by about 0.5 to 1 cm during the wetting period from 9th May until 27th July. It is noteworthy that the horizontal movements were constantly outwards and their magnitude appeared to be considerable, ranging from 3 to 6 cm. This magnitude of movement seemed excessive and perhaps be affected by the accuracy of horizontal movement from the Total Station survey itself. The first increments of Vectors SP1, SP2 and SP3 nevertheless appeared to be downwards at an angle similar to the boundary between upper and lower fills. The movement at the toe (SP5, SP6 and SP7) also seemed to be mainly horizontal. Although not conclusive, this trend seems to indicate that the movement may primarily take place in the upper fill. This upper fill was also the zone of smaller shear resistance and where pore-water pressure changed to a greater extent. However, the surface movement could also be attributed to the creeping movement of the soft clay foundation soil, though this cannot be fully proven at the moment. Yet, it was quite difficult to confirm the movement based on the interval camera photo alone since the vegetation became thicker during the rainy season. All in all, the movement of the dyke appeared to be related to the change in pore-water pressure and likely be related to the upper part of fill that was recently placed.

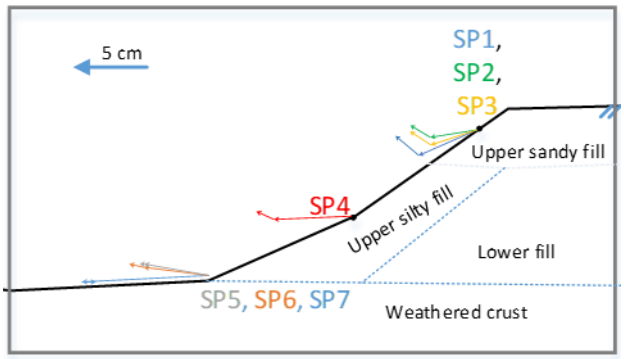

Fig. 11 Dyke surface movement

5 CONCLUSIONS

The MPS soil moisture sensor appeared to be suitable for high suction (>100kPa), while KU-tensiometer have more accurate measurement during rainy season, yet not possible to measure the suction of the dyke during dry season due to the cavitation problem. And the trend of dyke surface movement may have primarily taken place in the recently upper fill.

ACKNOWLEDGEMENTS

The authors are grateful to the financial support provided by JSPS KAKENHI Grant Number 16H04405, and Kasetsart University Research and Development Institute (KURDI). The authors also would like to thank Dr Noppadol Phienwej for providing information and comments on AIT dyke. The first authors is grateful to the Ministry of Research, Technology and Higher Education, the Republic of Indonesia and the Indonesia Endowment Fund for Education (LPDP) scholarship which supports his PhD study.

REFERENCES

Jotisankasa, A., Mahannopkul, K. & Sawangsuriya, A. (2015) "Slope stability and pore-water pressure regime in response to rainfall: A case study of granitic fill slope in northern Thailand", Geotechnical Engineering, vol. 46, no. 1, pp. 45-54.

Jotisankasa, A., Pramusandi, S., Nishimura, S., & Chaiprakaikeow, S. (2019). Field response of an instrumented dyke subjected to rainfall. *Geotechnical Engineering*, *50*(1), 81–91.

Mairaing, W. & Amonkul, C. (2010) "Soft Bangkok clay zoning" EIT-Japan Symposium on Engineering for Geo-Hazards: Earthquakes and Landslides-Surface and Subsurface Structures, Bangkok, Thailand, September 6-7, 2010.

Mairaing, W. & Thaiyuenwong, S. (2010) "Dynamic landslide warning from rainfall and soil suction measurement" Proceedings of the International Conference on Slope 2010 : Geotechnique and Geosynthetics for Slopes, 27-30 July, 2010 Chiangmai, Thailand.

Nishimura, S., Tokoro, T., Yamada, T., Izumi, N. and Rivas, M. F. (2015). "A case study of long- and short-term hydraulic state changes in embankment in Hokkaido", Proceedings of 6th Japan-China Geotechnical Symposium, JGS Special Publication, vol.1, no.7, pp.34-39.

Tsaparas, I., H. Rahardjo, D.G. Toll and E.C. Leong (2003). "Infiltration Characteristics of Two Instrumented Residual Soil Slopes". Canadian Geotechnical Journal, October, Vol. 40, No.5, pp. 1012 – 1032.

Vahedifard, F., Sehat, S. & Aanstoos, J.V. (2017) "Effects of rainfall, geomorphological and geometrical variables on vulnerability of the lower Mississippi River levee system to slump slides", Georisk, vol. 11, no. 3, pp. 257-271.

Interoperability between 3D Slope Stability Models and Interferometric Radar Data

N. Bar
Gecko Geotechnics Pty Ltd, Australia

A. McQuillan & T.E. Yacoub
Rocscience, Inc., Canada

N. Coli & L. Leoni
IDS Georadar, Italy

S.A. Rea & J. Bu
Newcrest Mining Limited, Papua New Guinea

ABSTRACT: Slope stability modelling by practicing geotechnical engineers has mostly been limited to 2D cross-sections. Faster computers and improved user interfaces of 3D software are now facilitating the routine application of 3D limit equilibrium and finite element analysis for slopes in complex ground conditions. Deformation monitoring technology has rapidly developed with real-time interferometric radar now capable of providing updates every minute across an entire slope. This is a step-change in risk management compared with manual surveying of prisms going back as little as 10-15 years. Radars are geo-referenced to the same coordinate system used in stability models. This paper presents a case study to illustrate the effectiveness of integration and interoperability between 3D stability models with interferometric radar data for understanding ground behavior and managing landslide risk.

1 INTRODUCTION

Slope stability modelling and hazard management using deformation monitoring until recently have been separate tasks, often undertaken by different geotechnical engineers or companies for a single project. For example, in a typical open pit mine, the slope could be designed (modelled) by an external consultant and the hazard management and deformation monitoring performed by the client or mining company. This usually results in a disconnect between the predicted and actual ground behavior.

In the last decade several efforts were made to reconcile or validate slope designs and models with excavation progression with varying degrees of success (Baczynski et al. 2008; Dixon et al. 2011; Bar, 2012). At the same time, slope stability modelling techniques have evolved and increased in complexity with improvements in computing capability and available software. As we approach the 2020's, three-dimensional (3D) limit equilibrium and finite element analysis software are readily available and offer a range of options to model complex failure mechanisms (McQuillan et al. 2018; Bar & McQuillan, 2018; Bar et al. 2019).

Slope deformation monitoring systems exist in a range of forms from rudimentary one-dimensional wire extensometers to highly sophisticated electronic equipment including slope stability radars (Baczynski & Bar, 2017). Ground-based radar technology has been used in open pit mines to measure displacements of pit slopes for over a decade (Coli et al. 2018). The use of radar aims at providing near-real time, high accuracy displacement and velocity information over a large slope area. This provides a high resolution and even full area coverage of a slope from a completely remote monitoring tool. That is, it removes the requirement for personnel to access various locations on a slope to install individual monitoring or reference points such as survey prisms, extensometers or GPS monitoring points, all of which also remain useful and can be integrated with the radar data (Bar et al. 2018).

With continuously improving technology and connectivity, an opportunity exists for improving slope designs and safety for personnel working near slopes with the integration of modelling and

monitoring software and interoperability between them.

The integration of radar sensor deformation monitoring data with numerical stability modelling through a streamlined workflow enables users to visualize and interrogate radar monitoring data alongside the 3D numerical model. The improved usage of radar data provided by the radar map overlays will enable advanced calibration and refinement of model input parameters, enabling a higher reliability of numerical models.

2 3D SLOPE STABILITY MODELS

Limit equilibrium analysis (LEA) has become a preferred method for routine slope stability analysis since its introduction in the early twentieth century. Its popularity stems from its ease of use, relatively fast calculation time and calibration from years of application, observations and calibration case studies using 2D cross-sections (McQuillan et al. 2018). Finite element analysis (FEA) is also widely used and is particularly useful for understanding the behavior of complex ground conditions and failure mechanisms. Until recently, limitations in computing capacity and available, user-friendly software have not facilitated the routine application of 3D stability analysis, including limit equilibrium and finite element analysis (Bar & Weekes, 2017).

Limit equilibrium analysis can be undertaken in two and three dimensions using Slide and Slide3 software by Rocscience, Inc. (Bar & McQuillan, 2018). Similarly, finite element analysis can be undertaken in 2D and 3D using RS2 and RS3 software. In fact, it has become possible to routinely develop, analyze and interpret a full 3D pit scale model in less time than that required to develop a series of 3-5 2D LEA models (Bar et al. 2019). The 3D model can subsequently be used to instantly develop 2D cross-sections which can then be analyzed and interpreted, again, faster than the traditional 2D approach.

The limit equilibrium method of slices (2D) or columns (3D) is based on the principle of statics, where the summation of forces acting on a failure surface (i.e. mobilized stress) are compared with the sum of the forces available to resist failure (i.e. available shear resistance). The ratio between these two sums is defined as the factor of safety (FoS) (Krahn, 2007). In 3D limit equilibrium analysis, the sliding mass in the form of part of a sphere, ellipsoid or complex surface, is discretized into vertical columns (Cheng & Yip, 2007). Forces are analogous to the vertical slice method used in 2D. In 3D, each column forces and moments are solved in two orthogonal directions. Vertical forces determine the normal and shear force acting on the base of each column (McQuillan et al. 2018).

Finite element models can enhance the modelling process by allowing the geotechnical engineer to calculate stresses, displacements and pore pressures using a variety of linear and non-linear constitutive relationships.

An advantage of finite element models is that they do not require an assumption to be made in advance above the shape or location of the slip or failure plane. The rock mass is divided up into a finite number of elements. Each element is assigned an idealized stress-strain relation and properties that describe how each material behaves. The elements are then connected in a continuum model which assumes materials behave isotropically and as a continuous body. Large scale structures can be explicitly modelled as interfaces, and smaller scale structures can be implicitly modelled using a ubiquitous joint model. Finite element modelling software can be used to estimate the location and shape of potential slip surfaces, as predicted by the concentration of shear strain in the model.

3 RADAR MONITORING

The SAR (synthetic aperture radar) technique uses a broad fan-beam to illuminate the same target multiple times within the same acquisition (scan). For each pixel of a SAR image, a phase value is measured along the line-of-sight of the radar. By comparing phase differences of subsequent acquisitions, it is possible to detect small variations that account for sub-millimeter deformations of the target.

The unique feature of the SAR technique is that, by moving the sensor along a linear (LinearSAR) or circular path (ArcSAR) as illustrated in Figure 1, the achieved spatial resolution is much finer or higher than what can be achieved by real aperture radar (RAR) with a dish-antenna of the same size of the SAR's travel path. This also reduces data acquisition time, which is usually less than 2 minutes irrespective of the spatial area coverage (Coli et al. 2018).

The high-resolution capability of LinearSAR and ArcSAR facilitate long range monitoring up to 5km from the target while maintaining the ability to detect sub-bench scale failures and a constant scan time. Because of the long-range capability, SAR are typically installed on the crests of open pits, which generally allow them to monitoring deformation of almost half of an open pit. IBIS radars are synthetic aperture radars used for safety-critical monitoring in mining through the provision of real-time multiple alarm criteria based on user-defined deformation and/or velocity inputs (Farina et al. 2011, 2013; Sakari et al. 2016, 2018).

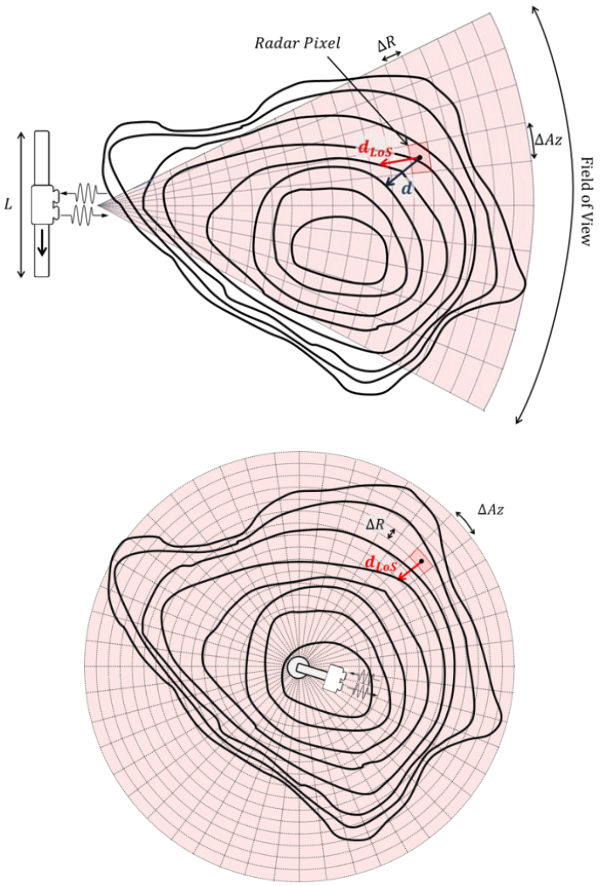

Fig. 1 Example of LinearSAR (top) and ArcSAR (bottom) monitoring configurations.

Fast scan times coupled with high spatial resolution facilitate alerting for rapid, small failures at a sub-bench scale as well as large scale slope movements. These features make the IBIS radars suitable for both tactical and strategic monitoring of pit slopes without the need for investing in multiple radar technologies (Figure 2).

SAR technology integrates critical monitoring capabilities with other monitoring instrumentation and advanced capabilities for geotechnical analysis. The continuous data storage can be utilized for long-term deformation tracking and the back-analysis or review of slope failure events (Ramsden et al. 2015; Vorster et al. 2015; Bar et al. 2016).

The slow movement detection feature of the IBIS radar data processing engine, called 'multi-scale engineer' also has the capability of identifying up to four orders of movement magnitudes (from tenths of millimeters per hour to only a few millimeters per month) simultaneously (Michelini et al. 2015).

In 2009, *IDS GeoRadar (part of Hexagon)* introduced the first interferometric radar based on synthetic aperture radar (SAR) technology to the mining industry (Farina et al. 2011). The IBIS-M and IBIS-FM (GbSAR) comprised of a radar sensor, performing both the transmission and reception of microwave signals, and a motorized mechanical axis that moved the radar sensor along a linear track to create the synthetic aperture. The radar performs multiple data acquisitions while traversing the linear track. The radar sensor itself is capable of resolving the scenario in range and the SAR technique is achieved by combining the signal acquired from various positions on the track to provide angular resolution. As a result, the entire scenario is resolved in a radar image (Figure 1) where each radar pixel (resolution cell) represents a measuring point.

Typical spatial resolution for a GbSAR moving along a 2m linear rail is 0.75m in range and 4.3m$_{rad}$ in cross-range (0.75m x 4.3m$_{rad}$ resolution at 1km scanning distance), with a maximum range of 4.5 kilometers. Like any interferometric radar, it measures line-of-sight distance, d_{LoS}, of each radar pixel, corresponding to the projection of the displacement, d, vector along the line-of-sight. With every linear scan, the GbSAR provides a new deformation measurement for all the radar pixels with sub-millimetric accuracy using the interferometric technique.

The horizontal field of view of a GbSAR is given by the antenna beam width, which is typically between 60° and 80°.

The horizontal field of view of GbSAR can be efficiently increased up to 360° by modifying the SAR acquisition from a linear path to a circular path (ArcSAR). The radar performs SAR acquisition while it is rotating on a circular track, and the acquisitions that are done at different angular positions are combined to provide angular resolution of the monitored scenario.

The IBIS-ArcSAR has the same resolution, accuracy and long-range performance as the standard linear SAR but with the additional benefit of adding a 360° field of view and reducing acquisition time to less than a minute.

4 CASE STUDY – LIHIR GOLD MINE

During the early stages of excavating a +250 meter high cutback, a double-bench slope instability was identified with the IBIS-FM radar (yellow circle in Figure 2). The instability area had increased deformation and deformation rates, was ductile, and was initiated by several days of high rainfall. The deformation rate periodically increased (and subsequently decreased) in response to high intensity and prolonged rainfall.

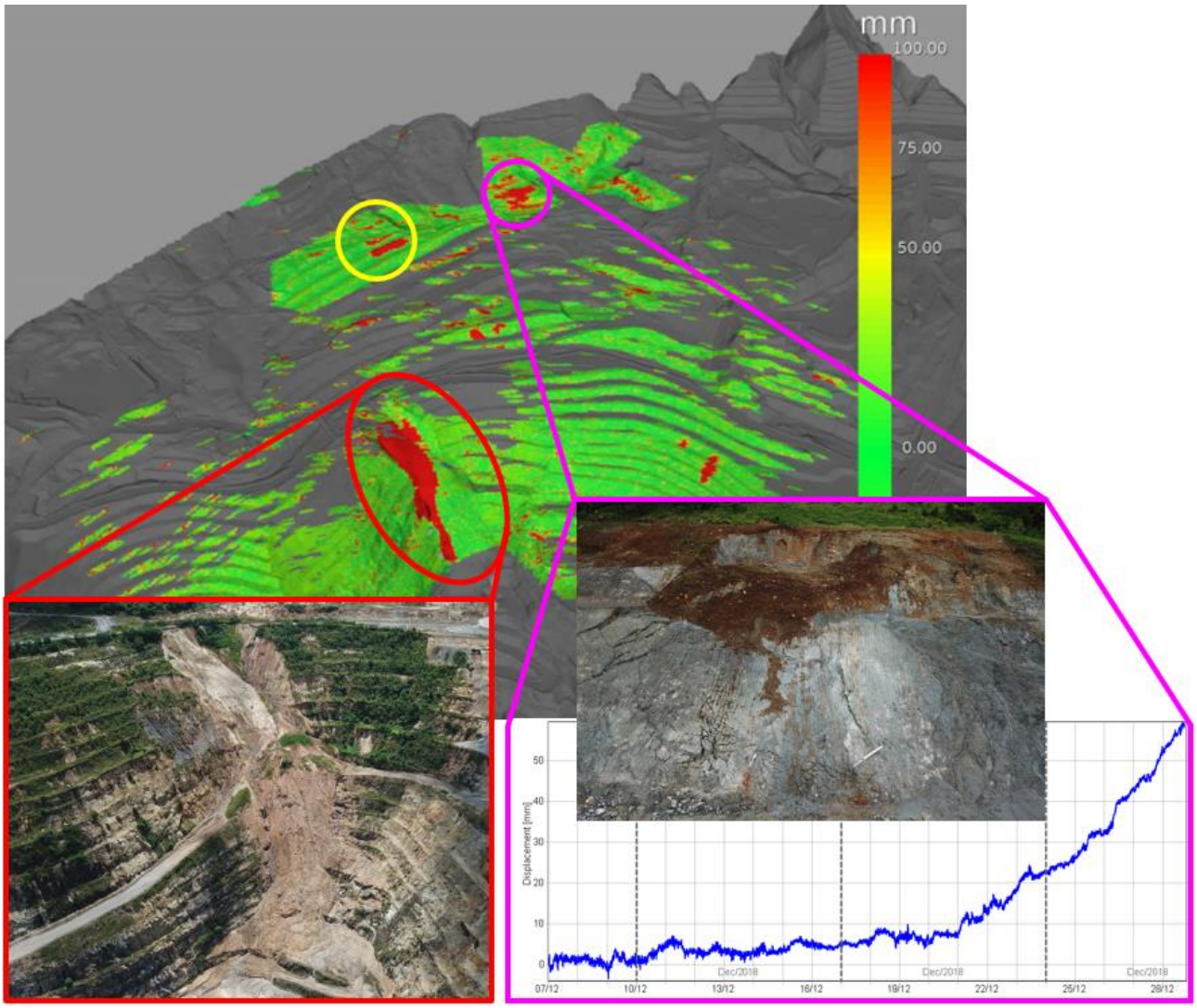

Fig. 2 IBIS-FM radar data relative to bench scale movement (pink) with rapid development on relic geological faults in argillic-altered rock overlain with colluvium & slow creep on historic landslide (red). Yellow circle demarcates the area investigated in the case study.

A walkover inspection and subsequent UAV (unmanned aerial vehicle) photogrammetry identified 20-50 centimeter wide cracks outlining the instability and established that the failure mechanism was related to a low-angle, in-pit dipping relic fault within the argillic-altered rock mass with colluvium situated above.

Pore pressures were obtained from a nearby vibrating wire piezometer that indicated the slope was likely to be fully saturated. The geotechnical model was revised to reflect this, and a three-dimensional limit equilibrium model was developed, again back-analyzing the instability, and attaining a factor of safety of 1.03 as shown in Figure 3. Three-dimensional finite element analysis confirmed the analysis, identifying areas of high deformation in the same region (Figure 4).

Subsequent models were developed to investigate remediation options including, unloading or buttressing the slope along with depressurization using deep horizontal drains. Models using depressurization and unloading indicated that the factor of safety could be improved by 15-30%.

Over 50 horizontal drains, 150 meters deep, spaced approximately 3-5 meters apart were drilled from the cutback floor with the aim of depressurizing the rock mass and low-angle fault. As illustrated in Figure 5, the deformation rates in the area of instability reduced significantly after the first series of horizontal drains were drilled directly targeting the low-angle fault. Approximately 30 additional horizontal drains of similar length and spacing were also drilled on the bench below, after the recommencement of cutback mining. One 12 meter high bench of colluvium was removed from the top of the slope as part of the unloading strategy and repair work was undertaken on the surface water diversion drain above the pit crest. This drain will soon be lined using welded HDPE (high density polyethylene) liners to minimize surface water

seeping back into the colluvium potentially causing further destabilization.

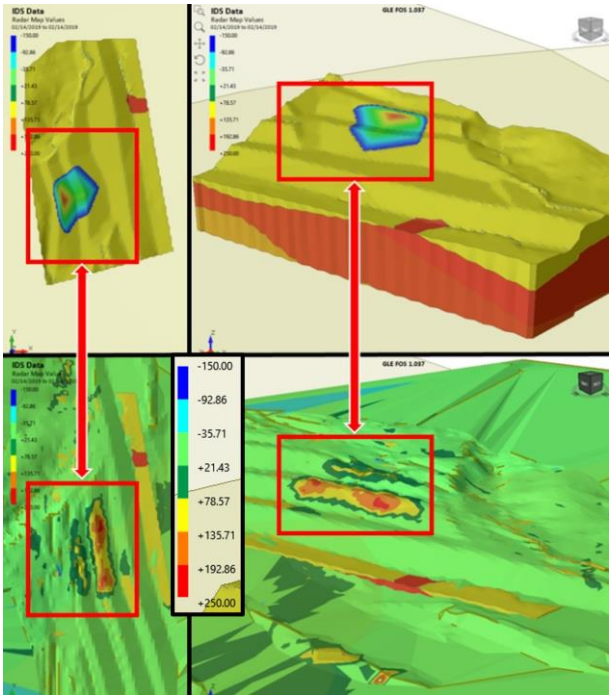

Fig. 3 Top: 3D LEA model predicting low factor of safety (FoS≈1.03) involving sliding on low-angle fault; Bottom: IBIS-FM radar data overlying 3D LEA model showing increased slope deformation in the low FoS area.

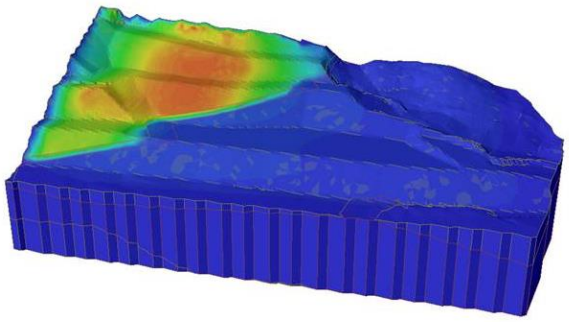

Fig. 4 3D FEA showing deformation hotspot coinciding with low FoS area and radar monitoring from Figure 3.

The IBIS-FM radar was used as a safety-critical monitoring tool to slope failure (landslide) risks while horizontal drilling was taking place below the instability and when excavating to unload the slope. A trigger-action-response-plan (TARP) linked to deformation rate alarms was used to assist the site geotechnical engineers and mine supervisors managing the hazard.

5 DISCUSSION

The amalgamation of, and interoperability between 3D limit equilibrium and finite element models and interferometric radar data has brought predictive models and live monitoring data together. It offers geotechnical engineers an additional means of reconciling design and actual slope performance. This has been illustrated through the presented case studies, where a good correlation was found between low factor of safety areas in predictive models and areas where actual movement was detected during and after excavation by the slope monitoring radar. The correlation between the models and monitoring can be further refined with a better understanding of ground conditions, particularly geological structures.

The user friendliness and ease of development enables a client or mining company to routinely undertake both tasks, which is also expected to remove some of the disconnect between the predicted and actual ground behavior. As a direct result, significant improvements can be made in relation to geotechnical hazard management by utilizing models to better understand failure mechanisms when potential instabilities are identified by radar. This allows a swift and robust response that

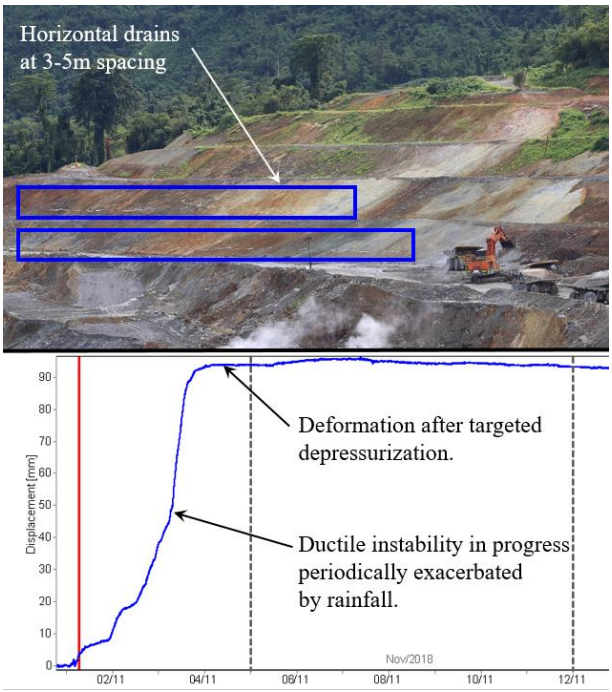

can, and has, enabled the prevention of an instability from turning into a slope failure or landslide with the introduction of engineered remedial actions.

Fig. 5 Photograph of slope illustrating the location of closely spaced horizontal drains. IBIS-FM radar cumulative displacement before and after depressurization targeting the low-angle fault.

The economic benefit of slope design optimization through reconciling model assumptions from slope performance information cannot be denied. The amalgamation of the predictive models with actual slope performance facilitates ongoing or continuous optimization of slope designs to either reduce overburden removal, increase ore recovery, or both in open pit mines.

Countless authors have been quoted stating ‘all models are wrong’. While we agree with this type

of statement in principle, we do not believe this should be, or will be, the case forever.

As technology continues to improve with connectivity (cloud-based or internet-of-things technology), artificial intelligence, and machine learning, future work in the geotechnical engineering sector will likely involve the development of an 'intelligent geotechnical management system' that facilitates data collection and validation, data analysis, geotechnical model, stability modelling and interpretation of monitoring results. Each of the components will likely be linked with interoperable applications. Examples of this would include the automatic refinement of numerical models with live updates from deformation or groundwater monitoring systems or the automatic identification of emerging risks and updates on known risks through the initiation of alarms or other action-protocols. Similarly, numerical models could automatically update as new data is collected and geotechnical models updated.

REFERENCES

Baczynski, N.R.P. & Bar, N., (2017). Landslide Monitoring and Management Challenge in Remote Papua New Guinea: Advancing Culture of Living with Landslides; 4th World Landslide Forum WLF4, pp 343-354.

Baczynski, N.R.P., Sheppard, I.K., Smith, K.J., Simbina, P. and Sakail, R., (2008). Toppling slope failure: predicted versus actual – Ok Tedi, PNG: 1st Southern Hemisphere Int. Rock Mechanics Symposium., Perth.

Bar, N., (2012). Performance driven slope management, design & optimization at Brockman Operation, Rio Tinto Iron Ore: 9th Young Geotechnical Professionals Conference, St Kilda.

Bar, N. & McQuillan, A., (2018). 3D Limit Equilibrium Slope Stability Analysis for Anisotropic and Faulted Rock Masses in Australian Coal and Iron Ore Mines: ARMS10 (10th Asian Rock Mechanics Symposium): The ISRM Int. Symp. for 2018, Singapore.

Bar, N., Parker, R. and Thomas, S.J., (2016). Managing landslide risks associated with erosion-driven slope instabilities using near real-time deformation monitoring systems: Rock Mechanics and Rock Engineering: From the Past to the Future; Int. Rock Mech. Symp.: Eurock 2016, Cappadocia.

Bar, N., Reynolds, M., Nicoll, S. and Bran, D., (2018). Geotechnical data management and visualization systems: meeting the data challenge of the 21st century and maximizing value for open pit mines: Geomechanics and Geodynamics of Rock Masses; European Rock Mechanics Symposium: Eurock 2018, St Petersburg.

Bar, N. and Weekes, G.J., (2017). Directional shear strength models in 2D and 3D limit equilibrium analysis to assess the stability of anisotropic rock slopes in the Pilbara Region of Western Australia. Australian Geomechanics Journal, 52(4):91-104.

Bar, N., Yacoub, T.E. and McQuillan, A., (2019). Analysis of a large open pit mine in Western Australia using finite element and limit equilibrium methods: ARMA 2019 – 53rd US Rock Mechanics / Geomechanics Symposium, New York.

Cheng, Y. and Yip, C., (2007). Three-dimensional asymmetrical slope stability analysis extension of Bishop's, Janbu's and Morgenstern-Prices' techniques, Jounral of Geotech. Geoenv. Eng., 133(12):1544-1555.

Coli, N., Leoni, L. Coppi, F., and Preston, C., (2018). Evolution of Synthetic Aperture Radar Technology for safety-critical monitoring in open pit mines: XIV Congreso Int. de Energía y Recursos Minerales / Slope Stability 2018, Seville.

Dixon, R.A., Johnson, T.M., de Graaf, P.J.H., Wessels, S.D.N. and Venter, J., (2011). Risk Based Geotechnical Slope Reconciliation at Rio Tinto Iron Ore, Pilbara Operations: Slope Stability 2011: Int. Symp. on Rock Slope Stability in Open Pit Mining and Civil Engineering, Vancouver.

Farina, P., Leoni, L., Babboni, F., Coppi, F., Mayer, L. and Ricci, P., (2011). IBIS-M, Innovative Radar for Monitoring Slopes in Open-Pit Mines: Slope Stability 2011: Int. Symp. on Rock Slope Stability in Open Pit Mining and Civil Engineering, Vancouver.

Farina, P., Coli, N., Yon, R., Eken, G. and Ketizman, H., (2013). Efficient real time stability monitoring of mine walls: the Cöllolar Mine case study: 23rd International Mining Congress & Exhibition of Turkey, Antalya.

Kranh, J., (2007). Limited equilibrium, strength summation and strength reduction methods for assessing slope stability: 1st Canadian-US Rock Mechanics Symp. Vancouver, pp 311-318.

McQuillan, A., Canbulat, I., Oh, J., Gale, S. and Yacoub, T.E., (2018). Geotechnical Review of an Open Cut Coal Mine Slope using 3D LEM and New Empirical Run Out Chart Predictions: XIV Congreso Internacional de Energía y Recursos Minerales / Slope Stability 2018, Seville.

Michelini, A., Coli, N., Coppi, F., Farina, P., Leoni, L., Costa, F., Costa, T.A. and Costa, T., (2015). Advanced data processing of ground-based Synthetic Aperture Radar for slope monitoring in Open Pit Mines: IMCET 2015 – 23rd International Mining Congress & Exhibition of Turkey, Antalya.

Ramsden, F., Coli, N., Benedetti, A.I., Falomi, A., Leoni, L. & Michelini, A. 2015. Effective use of slope monitoring radar to predict a slope failure at Jwaneng Mine, Botswana. In *Proc. Slope Stability 2015, The Southern African Institute of Mining and Metallurgy, Cape Town, 12-14 October 2015*.

Sakari, M., Suikkanen, M., Coli, N., Funaioli, G. and Meloni, F., (2016). Critical Real Time Radar Monitoring of Subbench Failures at Yara Suomi Oy Siilinjärvi Open Pit Mine (Finland): Rock Mechanics and Rock Engineering: From the Past to the Future; Int. Rock Mechanics Symp.: Eurock 2016, Cappadocia.

Sakari, M., Suikkanen, M., Coli, N. and Meloni, F., (2018). Use of radar system for real-time safety-critical slope monitoring at Yara Siilinjarvi mine, Finland: XIV Congreso Internacional de Energía y Recursos Minerales / Slope Stability 2018, Seville.

Vorster, J., Seidu, M., Coli, N. and Funaioli, F., (2015). Using radar technology to assess the effect of dewatering on slope stability: Slope Stability 2015, The Southern African Institute of Mining and Metallurgy, Cape Town.

Numerical analysis of seepage conditions in ancient Kalawewa dam

S.P.M. Jayathilaka
Department of Civil Engineering, University of Peradeniya, Sri Lanka
L.C.Kurukulasuriya
Department of Civil Engineering, University of Peradeniya, SriLanka

ABSTRACT: Seepage condition of the ancient Kalawewa dam was evaluated by utilizing geotechnical and monitoring data, and field tests conducted parallel to the study. Numerical analyses of seepage conditions were carried out using Finite Element Method (FEM) based techniques incorporated in Seep/W software. Two dimensional (2D) seepage analyses were carried out at Ch.2+713 m section under steady state conditions incorporating the variation of reservoir levels and the results were compared with the seepage rates obtained through the field measurement at a V-notch. The analysis was extended as an attempt to establish the hydraulic conductivity that would correspond with the piezometric data obtained in the downstream slope of the dam by introducing a central core of low permeability. A similar seepage analyses were performed based on this established hydraulic conductivity values for comparison with field seepage observations.The study revealed that by considering homogeneous hydraulic properties for the dam based on the laboratory value of coefficient of permeability, the seepage rate is over-predicted. Based on the concept of incorporating a central low permeable core for the dam, it was possible to establish a range of values for the coefficients of permeability for the core and outer region, which resulted in an improved prediction of total head and seepage rate.

Keywords:Ancient dams, Seepage Analysis, Hydraulic conductivity, Field monitoring, Seep/W

1 INTRODUCTION

Ancient dams have been built primarily for the purpose of flood control and irrigation, whereas modern dams serve hydroelectric power generation as well. Out of many dam types in the world embankment dams are more common which usenatural materials (Abhilasha et al., 2015). These dams represent about 85% of all dams built in the world (Elshemy et al., 2002).

The oldest functional dam in the world dating back to 1304 BC is reported to be the Quatinah barrage in Syria. According to history of Sri Lanka, the oldest dam was built by King Pandukabhaya who reigned from 437 to 367 BC.In ancient earth dams, shear strength and hydraulic properties of the dam materials are very much likely to have changed over thelong service life, affecting the seepage characteristics in particular.

Seepage analysis is an important tool to assess the susceptibility of slope failures associated with seepage in dams (Chen and Zhang, 2006). Further, seepage analyses of embankment dams provide measures to be adopted in the designs to mitigate seepage related failures. Recently, Finite Element Method (FEM) has been used for the seepage analysis of embankment dams. Kirra et al. (2015) used GeoStudio software to analyse the seepage of the Mandali earth fill dam in Iraq. Hasani et al. (2013) studied the seepage condition using SEEP/W software for the Ilam earth dam in Iran for four mesh sizes in order to assess the effect of meshing on accuracy of results. Kamanbedast et al. (2012) also investigated seepage condition and flow of water through the soil in the Maroon dam in Iran.

For the earth fill dams in Sri Lanka, Venuja (2018) analysed the seepage characteristics of the Iranamadu dam to estimate the seepage rate with the determination of the phreatic surface and investigated the influence of anisotropy of hydraulic conductivity of core material on seepage. Kumara (2017) evaluated the seepage flow through the Randenigala dam by establishing best-fit seepage parameters obtained through a back analysis.

Kalawewa dam which is situated north-west of Dambulla (Fig 1.) holds two conjugate bodies of water “Kalawewa and Balaluwewa twin-reservoirs” combined when the storage level of the original scheme was raised in the 19th century. Kalawewa was built during the reign of Great King Dhathusena (459-477 CE) and Balaluwewa had already been built by that time by King Kutakanna Thissa (44-22 BC) (Poyry,2012[a]).

The dam impounded a reservoir with a capacity of approximately 104 MCM at full supply level in 2018 and has a length of approximately 6,500 m and a maximum height of about 14.5 m with a base width of more than 60 m. It comprises of six sluices installed over a period of one hundred years, namely the Left Bank, Balaluwewa Goda Ela, Kalawewa Goda Ela, Kalawewa Yoda Ela, Nawa Jayaganga

sluice (Right Bank Sluice) and high level right bank sluice(Poyry,2012[a]).

Fig.1 : Location Map ofKalawewa

Kalawewa tank is known to have breached on three occasions in the past. As a result, the dam went through several stages of rehabilitation, the first being a partial restoration in 1885 and other restorations in 1959 and from 1975 to 1979 (Poyry, 2012[b]).

Even after several restoration works a proper seepage analysis has not been conducted for the assessment of safety of the Kalawewa Dam. However, such a seepage analysis is highly challenging in the absence of construction drawings, construction methodology and material properties of the dam.

In this study the seepage characteristics in Kalawewa dam at section 2+713 was evaluated using GeoStudio Seep/W software and compared with the existing instrumentation data of the dam.

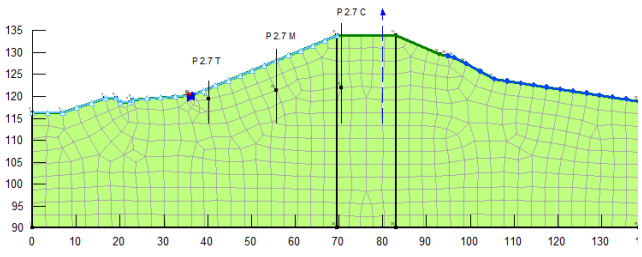

Fig.2 : Cross section ofKalawewa(Ch. 2+713)

This study was carried out with the following objectives.

(1) Comparison of seepage observations with the results of numerical analyses under steady state, using Seep/W software.

(2) Investigate the effect of permeability coefficient and non-homogeneity on seepage through the dam by numerical analysis.

(3) Establish a hydraulic conductivity value that would correspond with the piezometric data obtained in the downstream slope of the dam and the seepage flow rate.

2 MATERIALS AND DATA COLLECTION

2.1 *Material Properties*

A Geotechnical investigation has been carried out under the Dam safety & water resources planning projectunder which the dam body and foundation material properties were evaluated. Results obtained from two exploratory boreholes in section 2+713are given in Table 1 (Poyry, 2012[b]).In this study, laboratory tests were carried out on undisturbed samples obtained at locations near the middle and toe levels at section 2+713 to determine the dry density and coefficients of permeability (Table 2). It is seen that the particle size distributions and coefficients of permeability evaluated in this study are very much different to those reported by Poyry (2012[b]).

Table 1 : Soil properties at section 2+713 (Poyry, 2012[b])

Location /Depth (m)	Soil type	Particle size distribution (%)		Specific Gravity	k (cm/s)
Crest /12.5	SP	Fine Sand Gravel	-5.1 -87.3 -7.6	2.53	1.04
d/s slope / 11.5	SP	Fine Sand Gravel	- 3.1 -94.8 - 2.1	2.57	-

Table 2 : Laboratory test results at section 2+713

Location in d/s slope	Direction/ Depth	Particle size distribution (%)		Dry density (Mg/m^3)	k (cm/s)
Middle	Vertical /1 m	Clay Silt	- 20 - 10	1.72	4.38E-08
	Horizontal /1 m	Sand Gravel	- 55 - 15	1.66	7.79E-06
Toe	Vertical /GL	Clay Silt	- 20 -15	1.71	4.28E-06
	Horizontal /GL	Sand Gravel	-60 -5	1.70	1.12E-06

2.2 *Instrumentation Data*

Reservoir water level (RWL), rainfall and other hydrological data such as inflow, outflow from sluices and spillway etc, are recorded daily at Kalawewa dam. Variation of RWL from 2015 to 2019 is depicted in Fig.3.

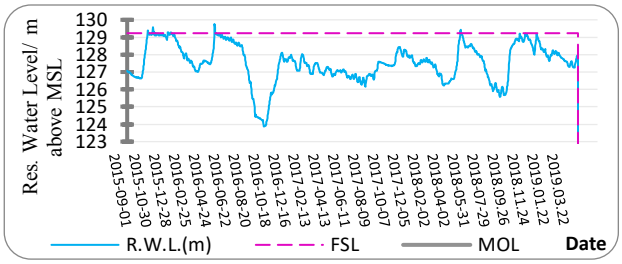

Fig.3 : Variation of RWL in Kalawewa reservoir

Data from twenty piezometers and nine V- notches are recorded twice a week and on a daily basis when RWL is near full supply level. Variation of the piezometer data obtained near crest, mid-section and toe (Fig.2) at section 2+713 is given in Fig.4.

2.2.1 *Total head and pore water pressure measurements*

In order to monitor the pore water pressure variation in the dam, piezometers are installed in the downstream side of the dam. In most of the sections only one or two piezometers have been installed which makes it difficult to estimate the shape of the phreatic surface. There are only three sections available having three piezometers installed at each sectionfor better understanding of the phreatic surface, out of which only two sections are in the main dam. Although, there are nine V-notches, none of them could measure the seepage corresponding tothese two sections.Therefore,the section at 2+713 was selected for thisstudy where the seepage flow rate can be measured on the toe drain.

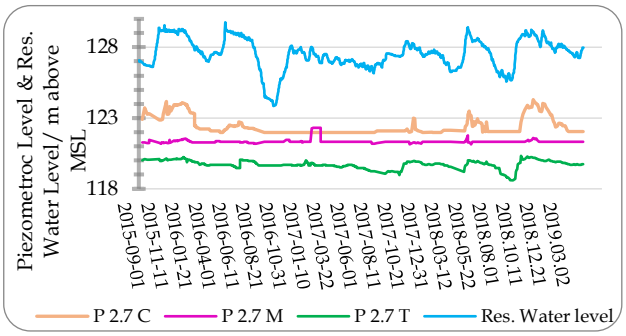

Fig.4 : Variation of piezometer level at Section 2+713 with RWL

Fig.4 shows the variation of piezometric level at section 2+713 and RWL with time for last three years. Variation of piezometer 2.7C indicates that its bottom level is not adequately deep to respond under low reservoir levels. Hence, below RWL of 127m AMSL, the piezometer gives a reading ofapproximately 122 m. Piezometer 2.7M has not responded well with the variation ofRWL. Thus,this piezometer was not considered as suitableto verify Seep/W analysis results. However, the variation of Piezometer 2.7T with reservoir water level showed good correlationfor the given time period.

2.2.2 *Toe drain flow measurement in study area*

Since there were no v-notches available to measure the seepage rate covering the section near 2+713, manual measurements werecarried out to measure the discharge through the toe drain for this section (Fig.5). This toe drain collected seepage water corresponding to 170 m length of the dam. Time was measured to fill up 5 litres of seepage water. Discharge at full supply level (i.e. 129.23m AMSL) is observed to be about 1.4 m^3/day/m.

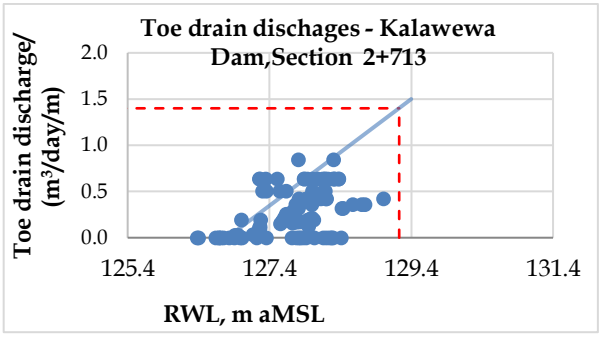

Fig.5 : Toe drain discharge- Kalawewa Dam, at Section 2+713

3 ANALYSIS, RESULTS AND DISCUSSION

3.1 *Defining of the control body of Dam*

Kalawewa dam has no cross sectional informationavailable in the form of construction drawings. In order to define the control body for the Seep/W analysis, the sectional details were established through a leveling process for the section at 2+713. The cross section of the dam used for the numerical analyses is given in Fig.2. The elevation of the base level of the dam foundation was arbitrarily selected as 90 m AMSL as the steady state Seep/W analysis at full supply level (129.23 m AMSL) yielded very close values of the total head to those observed at piezometer locations (Table 3).

Table 3 : The effect of base level of the dam on the total head at piezometers (at FSL)

Base level (m)	Head in Piezometers (m AMSL)			Total flux at toe drain (m^3/day/m)
	P 2.7 C (121.98)	P 2.7 M (121.32)	P 2.7 T (119.32)	
110	125.67	123.65	121.12	0.00162
105	125.44	123.47	121.09	0.00155
100	125.30	123.37	121.07	0.00160
90	125.15	123.31	121.09	0.00170
80	125.12	123.34	121.15	0.00187
70	125.17	123.42	121.22	0.00200
50	125.34	123.63	121.40	0.00232

3.2 *The effect of kx on the distribution of total head along the dam body & flux*

The effect of coefficient of permeability (k_x) on the development of total head was investigated with the same material properties and boundary conditions (Table 4) by varying the saturated hydraulic conductivity. The pressure distribution at the control points and flux were obtained from the analyses and compared with field data.

The saturated hydraulic conductivity had no effect on the total head developed at a point in the dam body except on the toe drain flux. In order to match up with the observed seepage rate of 1.4 m^3/day/m, the coefficient of permeability was estimated to be 1.8 x 10^{-3} cm/s (Fig.6).

Table 4: Material properties and boundary conditions used in Seep/W analysis

Inputs for Seep W	Value / Description
Material type	Silty Sand
Saturated WC	0.467 m^3/m^3
Residual WC	0.04 m^3/m^3
k_x/k_y	1
Base level	90 m AMSL
Material Model:	Saturated/Unsaturated
U/S	129.23 m
Toe drain & D/S	Potential Seepage face

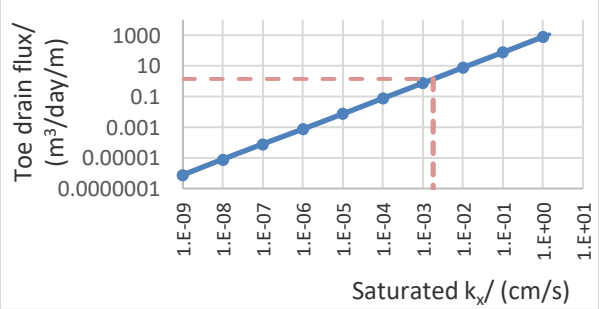

Fig.6: Variation of toe drain flux with coefficient of permeability

3.3 *Steady state seepage analysis considering homogeneous behavior*

In this analysis, the dam was considered to be of homogenous material. The upstream reservoir level was varied from 125 m to 129 m at 1 m intervals and the coefficient of permeability was varied from 0.1 cm/s to 1.8x10^{-3} cm/s, a range selected between the two contrasting values given in Tables 1 and 2. The other parameters are as given in Table 4.

The results of the Seep/W analysis obtained for the total head at the three piezometer locations were compared with the field piezometer observations. Accordingly, it can be seen that the Piezometer 2.7 C and Seep/W results give similar variation with reservoir water level (Fig.7) with Seep/W result giving about 1m higher value for the total head than the average observed value for 2019, in particular for reservoir level greater than 128 m AMSL.

However, comparison of field observations and Seep/W results for Piezometer 2.7 M does not show a good relationship (Fig.8). It appears that the piezometer had not responded well to the variation of reservoir water level.

In the case of piezometer 2.7T, Seep/W and field observations show a better relationship throughout the period of observation from 2015 to 2019 (Fig.9). However, about 1m difference between Seep/W results and observed data exists in this case too.

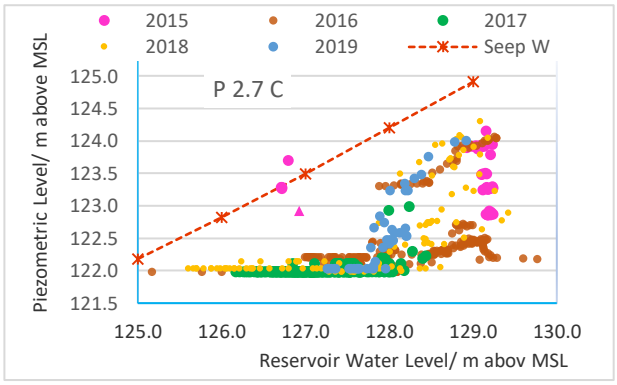

Fig.7: Variation of observed and Seep/W total head values at P2.7C with RWL

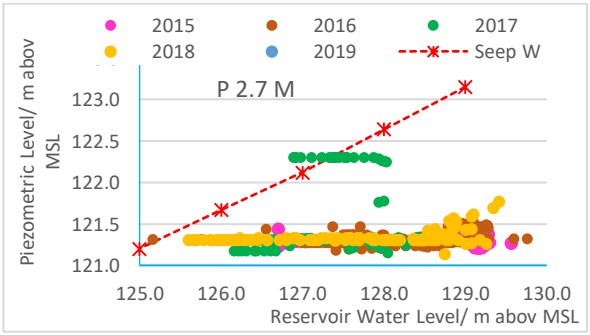

Fig.8: Variation of observed and Seep/W total head values at P2.7M with RWL

Toe drain flow rate directly relates with the RWL. Variation of toe drain flow obtained from Seep/W with the coefficient of permeability varying from 0.1 to 1.8 x 10^{-3} cm/s is shown in Fig.10.

Based on the Seep/W analyses, it can be seen that seepage into the toe drain becomes almost zero when the reservoir water level is below 125 m. According to the observations made, the seepage rate became zero when the reservoir level reaches 127 m. The observed rate of seepage is comparable with the Seep/W results when the saturated hydraulic conductivity is between

$8x10^{-4}$ cm/s and $1.5x10^{-3}$ cm/s.

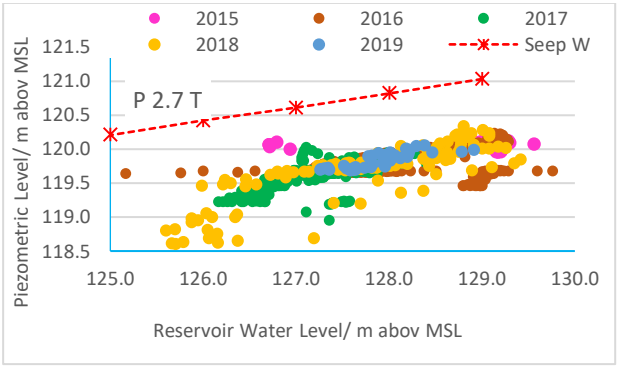

Fig.9: Variation of observed and Seep/W total head values at P2.7T with RWL

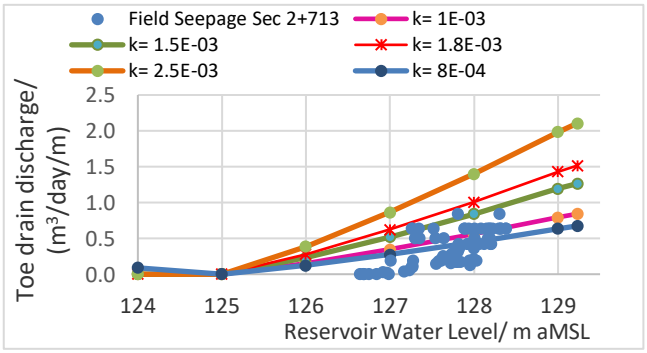

Fig.10: Observed variation of toe drain discharge with reservoir level and results of Seep/W for varying values of coefficient of permeability

3.4 *Steady state analysis of the dam with a central low permeable core*

In previous analyses, material of the dam was assumed homogeneous throughout the entire cross-section. However, the predicted total head values are higher than the observed. The reservoir level at which the flow into the toe drain becomes almost zero differed with field observations. Hence, the seepage characteristics of the dam with the presence of a low permeable central core of typical dimensions were investigated as shown in Fig.11.

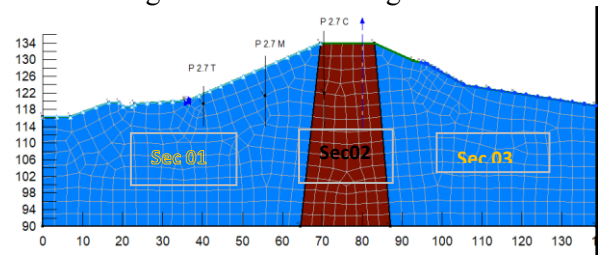

Fig.11 : Configuration of the dam section with an assumed central core of low permeability

In these analyses the coefficient of permeability of the core was varied from 8 x 10^{-4} cm/s to 5 x 10^{-3} cm/s and that of the outer region was varied from 1 x 10^{-2} cm/s to 1 x 10^{-4} cm/s.

From these analyses, it was possible to identify several combinations of values for the coefficient of permeability of core and outer regions, which provides a far better agreement with the field observations of total head values at piezometer locations and flux into the toe drain.

One such combination of values for the coefficient of permeability can be identified as 5.0 x 10^{-3} cm/s for the core and 2.35 x 10^{-2} cm/s for the other regions. For this combination, the variation of total head values from Seep/W analyses and the observations at Piezometer locations 2.7C, 2.7T and 2.7M with RWL are shown in Fig.12 to Fig.14 respectively and Fig.15 gives the comparison of Seep/W analyses and observations on the flux into the toe drain.

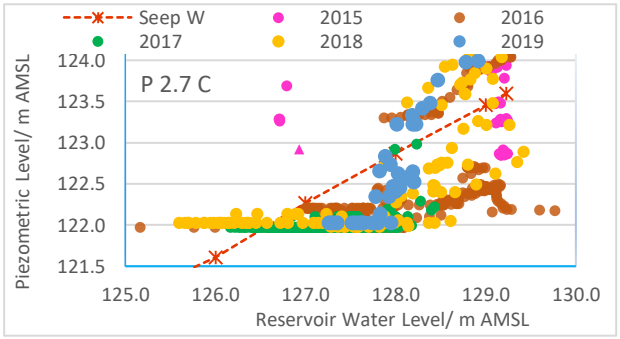

Fig.12: Variation of Seep/W and observed and total head values at P2.7C with reservoir water level, for the dam with central core

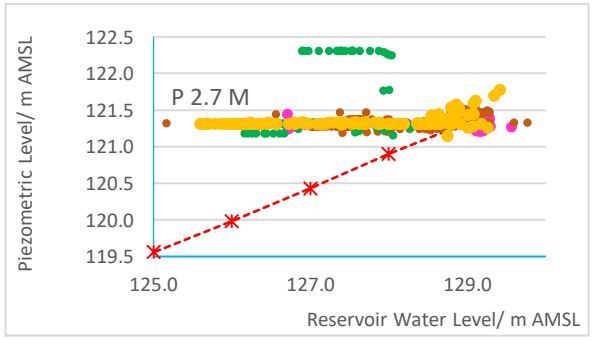

Fig.13: Variation of Seep/W and observed and total head values at P2.7M with RWL, for the dam with central core

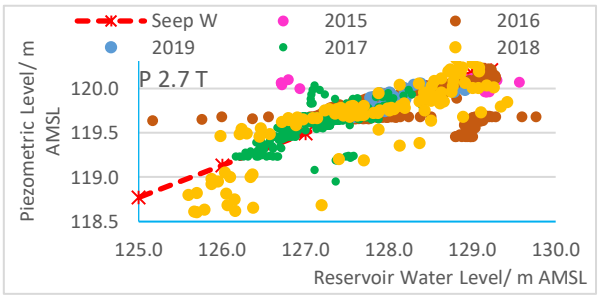

Fig.14 : Variation of Seep/W and observed and total head values at P2.7T with reservoir water level, for the dam with central core

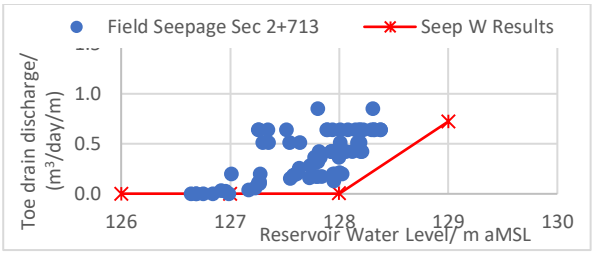

Fig.15: Seep/W and observed variation of toe drain discharge with reservoir level, for the dam with central core

The major drawback in the interpretation of observations is the non-responsiveness of piezometers to the variation of RWL (Fig.12 and Fig.13). Further, unlike in a recently constructed dam an ancient dam exhibits non-homogeneities due to changes that have taken place over many centuries. This may be the reason for having a wide range of values for the coefficient of permeability. Therefore, prediction of seepage through the dam based on data from very limited number of functional piezometers has the same degree of variation. However, in this case, introduction of a typical low permeable core appears to be a method to reduce the margin of variation of total head and seepage rate. However, this case study points out the importance of having a comprehensive instrumentation scheme to capture the non-homogeneity of hydraulic characteristics supplemented by undisturbed sampling of materials to develop a geometric and material model that is capable of representing the spatial variation of non-homogeneities for better prediction of seepage characteristics of ancient earth dams.

4 CONCLUSIONS

Following conclusions can be made from the study carried out based on existing instrumentation data and limited amount of field and laboratory tests performed on Kalawewa dam downstream slope.

1) Considering homogeneous hydraulic properties, the laboratory value of coefficient of permeability under predicted the seepage rate.
2) It was possible to estimate a value for the coefficient of permeability that can predict the seepage flow rate accurately which however, over predicted the total head values by about 1m.
3) Based on the concept of having a central core for the dam, it was possible to find a range of values for the coefficients of permeability for the core and outer region that predicts the total head and seepage rate well. This can be used as a tool to calibrate the seepage in ancient dams and for prediction of seepage as well.

ACKNOWLEDGEMENTS

Director (Major dams), Engineer in charge (Bowatenna) and Engineering Assistant (Kalawewa) of Mahaweli Authority of Sri Lanka are gratefully acknowledged for granting permission for use of the data related to the Kalawewa dam.

REFERENCES

Elshemy, M., Nasr, R.I., Bahloul, M.M. and Rashwan, I.M. (2002). 'The effect of blockages through earth dams on the-seepage characteristics', Faculty of Engineering, Tanta University, Egypt.

Hasani,H., Mamizadeh, J. and Karimi, H. (2013). 'Stability of slope and seepage analysis in earthfill dams using numerical models (case study: Ilam dam - Iran)', World Applied Sciences Journal, vol. 21, issue 9, pp. 1398-1402.

Kamanbedast, A. and Delvari, A. (2012). 'Analysis of earth dam, seepage and stability using ANSYS and GeoStudio software', World Applied Sciences Journal, vol. 17, issue 9,pp.1087-1094.

Kirra, M.S., Shahien, M., Elshelmy, M. and Zeidan, B.A. (2015a). 'Seepage and slope stability analysis of Mandaliearth dam', Iraq: Case study, International Conference on Advances in Structural and Geotechnical Engineering.

Kirra, M.S., Zeidan, B.A.,Shahien, M. and Elshelmy, M. (2015b). 'Seepage analysis of Walter F.GeogeDam, USA: A case study', International Conference on Advances in Structural and Geotechnical Engineering, pp.1-13.

Kumara W.D.J.V.(2017), Evaluation of seepage condition of Randenigala dam, MScEng thesis, University of Peradeniya, Sri Lanka.

Poyry (2012[a]), Operation and Maintenance Manual, Kalawewa Dam, Dam safety and water resource management.

Poyry (2012[b]), Detail design report, Kalawewa Dam, Dam safety and water resource management.

Seepage modelling with SEEP/W, (2012). GEO-SLOPE International Ltd.

Uromeihy, A. and Barzegari, G. (2007). 'Evaluation and treatment of seepage problems at capar-abad dam', Iran, Engineering Geology, vol. 91, pp.219-228.

Venuja T.(2018), Seepage analysis in Iranamadu dam by numerical modelling, MScEng thesis, University of Peradeniya, Sri Lanka.

Coal Bottom Ash as an Anthropogenic Soil to Prevent Soil Erosion during Post Mine Rehabilitation in Sri Lanka

S. Suloshini, A.S. Ranathunga, S.A.S. Kulathilaka & W.B. Gunawardana
Department of Civil Engineering, University of Moratuwa, Sri Lanka

ABSTRACT: The clay mines are abandoned due to the higher cost and non-availability of suitable fill material creating severe environmental issues. Coal bottom ash (CBA) is an industrial waste by-product generated in coal power plants and open dumped which causes soil and water pollution. Hence, CBA is a potential anthropogenic soil for post mine rehabilitation. Soil erosion is one of the major environmental problems in post mine land with the change in soil conditions, mainly in the tropical countries like Sri Lanka. Therefore, main objective of this study is to evaluate the potential of CBA to prevent soil erosion in the post mine land. The engineering properties of the samples were evaluated, and annual soil loss due to rainfall was measured by artificial rainfall test for six different CBA and soil mixtures. CBA exhibits high potential to prevent soil erosion with higher permeability and water holding capacity values. The annual soil loss is very low when the fine fraction of the CBA-soil mixture is lesser than 20%. Further, soil erosion can be significantly reduced when CBA fraction of the CBA-soil mixture is greater than 75%. Interestingly, the micropore structure of CBA is significantly influential on the soil erodibility.

1 INTRODUCTION AND BACKGROUND

1.1 *Clay mining*

Clay is used in the manufacturing of clay bricks, roof tiles and ceramics and the clay mining is mechanized to achieve the increasing demands. According to the US geological survey report (2021), around sixty-four million metric tons of clay was extracted in the year of 2020 globally. And it is increased by 9% when comparing the extraction of clay in the year of 2017. In Sri Lanka, mining of clay is vastly carried out in the downstream area of Maha Oya river, Dankotuwa and border of Kelani (Ranasinghe 1996). With respect to the US geological survey department's mineral report on Sri Lanka, 70,500 metric tons of clay was extracted in the year of 2015 (Renaud, 2018).

According to, Mines and Minerals Act No. 33 of 1992, "the holder of the license shall restore and rehabilitate the land on which such exploration or mining had been carried out, in the manner prescribed by this Act". However, miners tend to abandon the clay pits without any rehabilitation due to higher cost and the non-availability of suitable fill materials. This has generated larger areas of abandoned deep clay pits with average depth of 8 – 24 feet left along river basins. Accordingly, this leads to many problems like environmental issues, soil erosion, health issues, and slope instability. Due to the degradation of the environment with this massive extraction of clay which is going on all over the world, an adequate and feasible precaution should be taken as soon as possible for the rehabilitation of the abandoned clay mines.

1.2 *Coal bottom ash (CBA)*

1.2.1 *Generation of CBA*

CBA and fly ash are generated in the coal combustion process as main industrial waste materials in coal thermal power plants at a ratio of about 20:80 (Kim et al. 2005). CBA is a coarse particular material which is accumulated at the bottom of the combustion furnace. As a result of increasing demand for energy, the production of CBA has also increased. According to the study of World of Coal Ash (WOCA), approximately about 730 million metric tons of CBA is generated as an industrial waste by-product in the world annually (Singh et al. 2020). Gimhan et al. (2019) reported that it is around 50,000 metric tons per annum in Sri Lanka. Disposal of this waste product warrants effective and ecofriendly mechanisms due to the adverse environmental effects.

1.2.2 *Characteristics of CBA*

CBA predominantly contains coarse grained particles within the range of sand to fine gravel as reported by Jayaranjan et al. (2014). According to study of Yuksel and Genc (2007) and Jayaranjan et al. (2014), CBA exhibits as a good geotechnical material because of its, well graded particle distribution, lower specific gravity, low density, higher permeability, low compressibility and higher shear

strength. These characteristics make CBA to function as an anthropogenic soil effectively and economically.

According to Kumar et al. (2014) and Jayaranjan et al. (2014), CBA has the chemical composition which is similar to fly ash with higher carbon content and it might depend on the burner properties such as burner type and size, the operation procedure and the type and quality of the source material (coal). Based on the studies of Kim et al. (2005) and Singh and Siddique (2015), a significant percentage of silica (SiO_2), alumina (Al_2O_3), ferric oxide (Fe_2O_3) and calcium oxide (CaO) has been observed in CBA samples with small amounts sulfur trioxide (SO_3), sodium oxide (Na_2O), magnesium oxide (MgO), titanium dioxide (TiO_2), potassium oxide (K_2O) and loss of ignition (LOI).

1.2.3 *Present applications of CBA*

In recent years, studies were made to utilize CBA in different applications mainly in geotechnical engineering and construction industry. These studies are based on CBA with different fractions of fly ash or soil. The main geotechnical related applications of CBA are as a fill material (Kim and Lee 2015, Chrishanthi 2019), to prevent soil erosion (Matsumoto et al., 2016), as a soil stabilizer (Dissanayake et al. 2017) and as a soil amendment material (Wearing 2008). Further, CBA is used as a substitute for different construction materials like fine and coarse aggregates (Kim and Lee 2011, Sadon and Naganathan 2017). In addition, Jayaranjan et al. (2014) discussed the applications of CBA in wastewater treatment, and for making value-added products like telescope mirrors, and fireproof products.

In Sri Lankan context, CBA has been researched for preparation of light weight concrete blocks (Dassanayake & Nanayakkara 2018) and as a lightweight fill material in embankment construction (Chrishanthi 2019).

1.3 *Prevention of soil erosion by CBA*

Soil erosion is a natural process of movement and transport of the soil particles from the surface. It is caused by water, wind and mass movement. When comparing these different agents of soil erosion, water plays a significant role, which occurs after a heavy rain. Even though soil erosion is important for the formation of soil, it is drastically increased at present due to the human activities and causes severe damages to the environment and living beings. Rainfall intensity, erodability of soil, particle size, slope of the surface and vegetation are some of the decisive parameters of soil erosion.

According to literature, few studies reported on utilization of CBA to prevent soil erosion. However, several cases published on application of fly ash against soil erosion. Gorman et al. (2000) conducted field experiments to check the ability of fly ash-wood waste mixtures to prevent soil erosion at different slope angles using linear erosion measuring instrument. They revealed application of fly ash for mine reclamation reduced infiltration and increased surface run off and soil erosion. Hence, they suggested to apply fly ash-wood waste mixtures to top surface as it reduced soil erosion by one-half times.

Lehrsch and Baker (1989) revealed variations in porosity is the main influencing factor in soil erosion. CBA is more porous material than fly ash. Therefore, performance of CBA against soil erosion might be much better than fly ash. Interestingly, Matsumuto et al. (2016) conducted artificial rainfall tests for fly ash and CBA samples and concluded as the risk of soil erosion was reduced from the class of high to low when using more than 30% of fly ash or CBA.

A high rainfall intensity may cause soil erosion with the change in the soil conditions. The soil erosion leads to unsuccessful rehabilitation of mines due to topsoil losses. Therefore, it is necessary to assess the performance of CBA against soil erosion for the purpose of mine rehabilitation. The present study explores the ability of CBA to prevent soil erosion using artificial rainfall tests.

2 MATERIALS AND METHODS

2.1 *Sample preparation*

For the present study, CBA was collected from Lakvijaya power plant, Norochcholai, Sri Lanka. CBA was used as a mixture with gravely lateritic soil and selected mix proportions are shown in Table 1.

Table 1. Mix proportions of samples

	100BA	90BA	75BA	60BA	50BA	Soil
CBA (%)	100	90	75	60	50	0
Soil (%)	0	10	25	40	50	100

2.2 *Properties of CBA*

First, the physical properties of CBA-soil mixtures were found with respect to the ASTM standards. The Particle size distribution was determined by dry sieve analysis for 100BA sample and wet sieve analysis was used for the other samples in accordance with ASTM C136. Specific gravity was measured by pycnometer with respect to ASTM D854. The coefficient of permeability was tested using constant head method (ASTM D2434-19) for all the samples except soil sample and it was tested by falling head method due to the higher fine content based on ASTM D5084-03.

Water holding capacity was measured based on the retention percentage of water in the samples (ASTM D2980-17). A filter paper was placed at the

bottom of a funnel. Then, 50g of air-dried sample was placed in the funnel and 100 ml water were added. Sample was kept for 1-2 hours of time duration until there was no more visible drainage. After that, the weight of the saturated sample and oven dried sample was measured and water holding capacity was calculated. In addition, the micro structural morphology of samples was determined through Scanning Electron Microscope (SEM) to verify the porous structure.

2.3 *Determination of annual soil loss from artificial rainfall tests*

Generally, Universal Soil Loss Equation (USLE) has been considered as a well-known technique to assess the annual of soil erosion. As stated by Pathirana et al. (2009), one of the main drawbacks of this equation is to determine the appropriate values for the influencing parameters due to the lack of guidelines. In addition, Naipal et al. (2015) explained that the performance accuracy of USLE model might be reduced to the regions outside United States as it was developed based on the soil and agriculture conditions of United States. Further, soil erosion can be evaluated by artificial rainfall test. It gives the amount of soil eroded directly and it has the flexibility for arranging different rainfall precipitation. In addition, Matsumoto et al. (2016) used artificial rainfall test to investigate the annual soil loss for fly ash and CBA mixtures successfully and hence, was used for the present study as well.

A sample container with a plot area of 60 cm x 60 cm with 25 cm depth which was made of Polyvinyl chloride (PVC) board was used. It was further divided into two parts by a board which contains percolation holes (refer Fig. 1). The upper part has a depth of 20 cm. Out of 20 cm, 15 cm from the bottom was used for CBA-soil sample preparation and the rest was reserved for runoff generation. The bottom part of the sample container was used as infiltration collection zone. This facilitates to collect both surface runoff and infiltration separately and simultaneously. The surface runoff collection unit was shielded to prevent the collection of direct rain.

The CBA-soil samples saturated and filled in the container under modified Proctor compaction effort. The container is removable, and it is placed over the table at 35° with horizontal because it is the maximum for mine rehabilitation slope angle according to the standard of mines (refer Fig. 1). A single full cone spray nozzle was attached at centre as rainfall simulator which is mounted on a height of 2 m from the sample to supply water at desired intensities. The artificial precipitation was given for one hour continuously. The rainfall intensities were set to 5, 10, 20 and 40 mm/hr. The soil beds were refilled before every rainfall to regain the original condition of the bed and to overcome the soil loss from previous rainfall. After collecting the surface water, they were oven dried and weight of the eroded material was measured. The rainfall intensity in different locations of the soil bed (four corners, centre & three random places) were measured to ensure the uniform precipitation through the entire plot area using rain gauges prior to the test. It was assumed as uniform precipitation to entire plot area due to the minor variations observed (<0.5 mm/hr).

The annual soil loss was calculated using the equation proposed by Matsumoto et al (2016), expressed as (1),

$$H = (R \times E)/(A \times G \times I) \quad (1)$$

Where, H is annual soil erosion (cm/year), R is annual rainfall (mm/year), E is soil erosion (g/hour), A is area of the plot (cm^2), G is dry density of the sample (g/cm^3) and I is rainfall intensity (mm/hour).

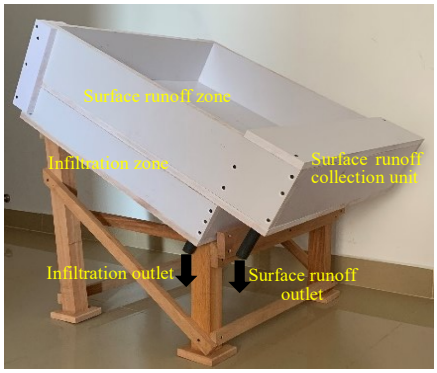

Fig. 1 Experimental set-up used for artificial rainfall test

3 RESULTS AND DISCUSSIONS

3.1 *Properties of CBA – soil samples*

The properties of CBA-soil samples are listed in Table 2.

Table 2. Properties of CBA-soil mixtures

Properties	100BA	90BA	75BA	60BA	50BA	Soil
Classification	SP	SP-SC	SC	SC	SM	MH
Specific gravity	1.88	1.89	1.99	2.18	2.23	2.50
Liquid limit (%)	20	27	33	40	43	58
Plastic limit (%)	-	10.5	20.5	25.0	27.5	33.5
Maximum dry density (kg/m^3)	975	1082	1215	1350	1462	1715
Optimum moisture content (%)	37	34	31	28	25	18
Coefficient of permeability ($x10^{-5}m/s$)	9.9	4.04	3.04	0.303	0.253	0.0287
Cohesion (kPa)	0	3.3	5.6	12.7	19.0	20.0
Friction angle (°)	35	32	29	27	26	18
Water holding capacity (%)	66.0	63.0	48.5	46.0	40.5	30.5

CBA exhibits lower specific gravity, lower dry density, higher permeability, higher shear strength and therefore, can be considered as a light weight fill material which is suitable to fill soft grounds like abandoned clay mines. The properties further improved with the addition of soil and hence, CBA-soil mixtures would perform better as a backfill material.

The composition of the CBA-soil samples is presented in Fig. 2. CBA contains more than 90% of sand particles which is decreasing with the introduction of soil. All samples have very low gravel content (< 5%). The fractions of sand and gravel reduced and that of fine increased with the decrease in the mixing ratio of CBA. More than 50% of fine content is observed for soil only sample. The variation in permeability values agreed with the change in soil composition, where increasing fine content results a reduction in permeability (refer Fig. 2 and Table 2).

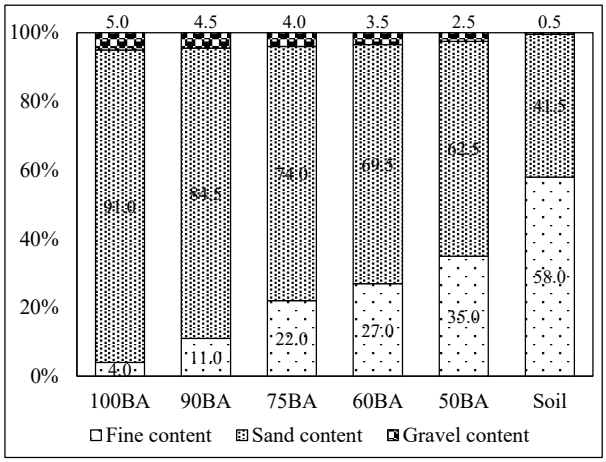

Fig. 2 Soil composition of CBA-soil mixtures

CBA has a low specific gravity and increases with the addition of soil. This lower value is due to the porous structure of CBA. The micro structural morphology of CBA and soil samples is presented in Fig. 3. CBA's highly vascular nature (average pore size ~ 1.95 µm) is clear from the SEM images where soil has very fine pores (average pore size ~ 0.70 µm) compared to CBA (refer Fig. 3). This further confirms the higher permeability observed for CBA. Further, water holding capacity is increased with the CBA fraction of the mixture. Generally, higher fine content causes higher water holding capacity of a sample. However, the microporous structure of CBA has positively influenced the water holding capacity values in the CBA-soil mixtures. Hence, not only fine content of the sample but the microstructure of CBA also plays a vital role in determining the water holding capacity of the sample. However, these parameters can be varied based on the chemical composition of the samples as well (Lovell et al. 1991).

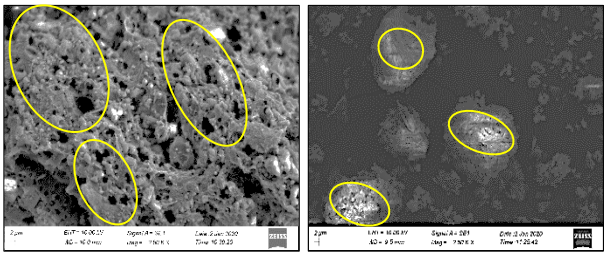

(a) CBA (b) Soil

Fig. 3 SEM images of CBA and soil samples (2500X)

3.2 *Annual soil loss (ASL)*

There are no standard guidelines reported for the risk assessment of soil erosion in Sri Lanka. In present study, the risk assessment guidelines of Indonesia are followed as Indonesia is also a tropical country like Sri Lanka. The results of performed artificial rainfall test is demonstrated in Fig. 4, following the guidelines in Table 3. The potential of CBA against soil erosion is very high even in the heavy precipitation (refer Fig. 4) where the soil erosion category is changed to "very low" from "high" with the application of CBA. For example, at 40 mm/hr rainfall intensity, ASL of CBA sample is 0.083 cm/year (very low) and for soil sample it is about 3 cm/year (high). The risk of soil erosion is reduced with the increment in CBA fraction (refer Fig. 4).

Table 3. Risk assessment of soil erosion in Indonesia

Class	ASL (cm/year)
Very high	> 4.8
High	1.8 – 4.8
Moderate	0.9 – 1.8
Low	0.15 – 0.9
Very low	< 0.15

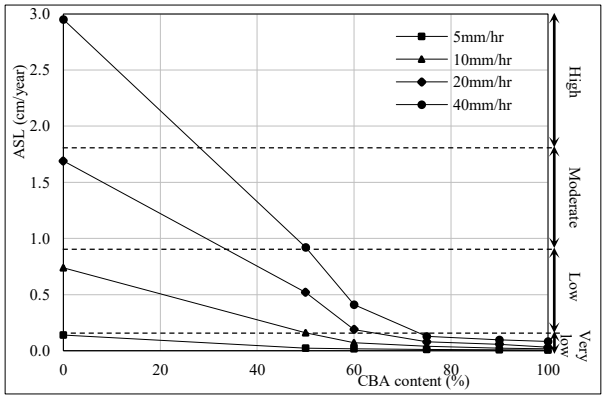

Fig. 4 ASL of samples with CBA content

The volume percentage of collected surface runoff and infiltration water is given in Fig. 5. The volume of surface run off decreased with CBA content refer to Fig. 5(a)) while it causes an increased volume of infiltration water (refer to Fig. 5(b)). Moreover, these observations agreed with the coefficient of permeability values of the samples, where higher the permeability values higher the infiltration water.

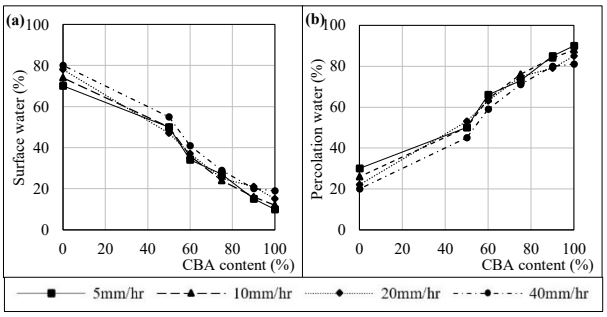

Fig. 5 (a) – Ratio of surface water, (b) – Ratio of percolation water with CBA content

Interestingly, the variation of ASL can be well represented by an exponential function with fine content while it follows a power variation with coefficient of permeability and water holding capacity as demonstrated in Fig. 6 for CBA used for the present study. ASL has gradually increased with fine content up to 40% and it is followed by an increase with a steep gradient. According to Fig. 6(a), fine content of the sample should be less than 20% to fall under the soil erosion category of "very low" (refer Fig. 6(a)). In addition, ASL shows a sudden decrease for permeability values less than $1x10^{-5}$ m/s and showcased a gradual declination afterwards (refer to Fig. 6(b)).

The highly porous structure of CBA is further advantageous leading to the prevention of soil erosion which is indicted by higher water holding capacity of CBA. Consequently, the samples able to capture more water in the porous structure and results in reduction of surface stream water and hence, the ASL is also reduced (refer to Fig. 6(c)).

In all three cases demonstrated in the Fig. 6 show a significant variation of ASL up to 75% of CBA fraction and a more gradual variation for lower CBA fractions in the CBA-soil mixture. Further, the samples with more than 75% of CBA, fall under the risk assessment category of "very low" for the CBA used in the present study.

Due to the high heterogeneity of CBA, some deviations might be observed with other CBA samples. A comparison of CBA properties between Matsumoto et al. (2016) and the present study is listed in Table 4. It clearly shows the influence of the heterogeneity of the CBA on its properties and ASL. Even though the permeability values are almost similar for both cases despite the fine content (11% higher) in Indonesian CBA, the water holding capacity is lesser than the Sri Lankan CBA. It might be due to the microporous structure of the samples where the micropores were not visible for Indonesian CBA. The non-availability of micropores has increased the specific gravity of Indonesian CBA while the higher fine fraction has ruled the water holding capacity (Matsumoto et al. 2016) unlike for Sri Lankan CBA, where it is influenced by the micropore structure.

Table 4. Comparison of results with literature

Properties of CBA	Present study	Matsumoto et al. (2016)
Source of CBA	Sri Lanka	Indonesia
Fine content of CBA	4 %	15 %
Coefficient of permeability	9.9×10^{-5} m/s	1×10^{-4} m/s
Specific gravity	1.88	1.96
Water holding capacity	66 %	60 %
Average micropore size	1.95 µm	Not visible
Rainfall intensity	40 mm/hr	80 mm/hr
Risk assessment category	Very low	Very low

Therefore, suitable CBA samples and its mixing fractions with soil must be decided with consideration of the effects of microporous structures and soil composition which affect permeability and water retention capacity values for the purpose of prevention of soil erosion. Further, the ability of CBA to prevent soil erosion during post mine rehabilitation will benefit for other types of mines and quarries as well.

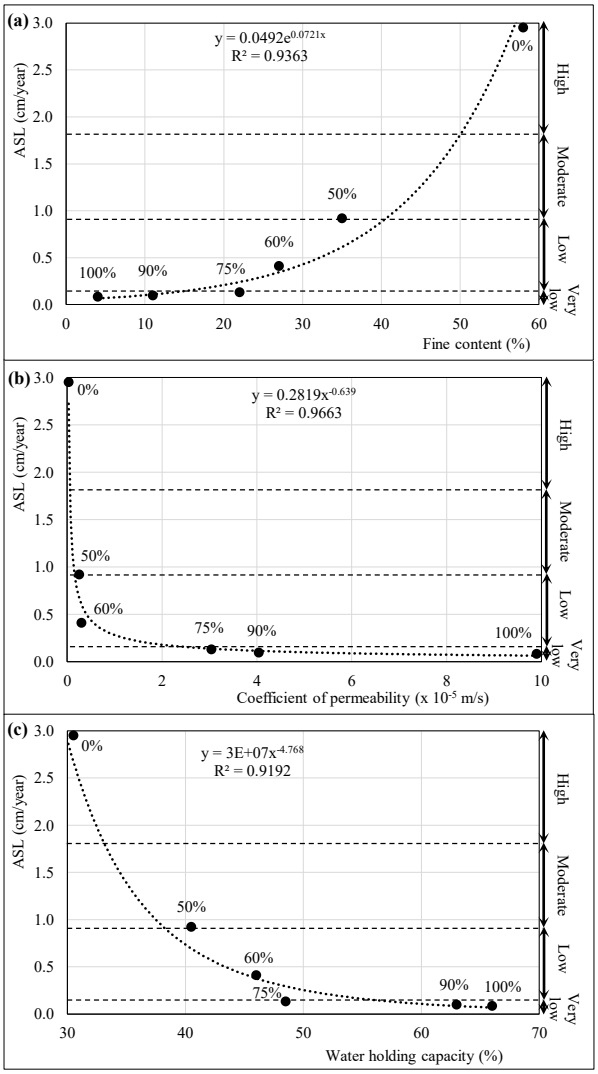

Fig. 6 Variations of ASL with (a)-fine content, (b)-coefficient of permeability, (c)- water holding capacity

4 CONCLUSIONS

The present study investigates the ability of CBA to prevent soil erosion using artificial rainfall tests. CBA with a proper soil fraction will be more economically conservative material for post mine rehabilitation. The findings of the present study are as follows:

- CBA has a higher potential to prevent soil erosion for even at very high rainfall precipitation.
- For the CBA and soil samples used in the present study, the ASL can be maintained within the "very low" risk assessment class when the CBA fraction is more than 75% in the mixture.
- The coefficient of permeability, water holding capacity and fine content are the decisive parameters in the selection of suitable CBA and appropriate mix proportion according to the field requirements.
- Variation of ASL with these decisive parameters can be well represented by exponential and power functions for the CBA-soil mixtures used for the present study.

5 RECOMMENDATIONS FOR FUTURE STUDIES

- It is recommended to evaluate the performance of CBA samples prior to the application even though they are from same power plant due to its heterogeneity nature as the porous structure of CBA plays a vital role for the reduction of ASL.
- The trace metal leachability of CBA needs to be investigated as it causes negative perceptions in the usability of CBA.
- It is advised to introduce vegetation with suitable crops that can be planted in the CBA- soil mixtures as it is one of the most effective measure to reduce the soil loss.
- It is recommended to investigate the long-term effect on utilizing CBA for safer application in the field without any threat for health and environment.

ACKNOWLEDGMENTS

This research study is funded by Senate Research Committee Long-term grant (SRC/LT/2019/14) offered by University of Moratuwa, Sri Lanka.

REFERENCES

Chrishanthi, J. A. C. (2019). Possible use of bottom ash in embankment construction, MSc Dissertation, University of Moratuwa, Sri Lanka.

Dissanayake, T.B.C.H., Senanayake, S.M.C.U. and Nasvi, M.C.M. (2017). Comparison of the stabilization behavior of fly ash and bottom ash treated expansive soil, Engineer Journal of the Institution of Engineers, Sri Lanka, 50(1):11-19.

Gorman, J.M., Sencindiver, J.C., Horvath, D.J., Singh, R.N. and Keefer, R.F. (2000). Erodibility of fly ash used as a topsoil substitute in mineland reclamation, Journal of Environmental Quality, 29:805-811.

Jayaranjan, M.L.D., Hullebusch, E.D., and Annachhatre, A.P. (2014). Reuse options for coal fired power plant bottom ash and fly ash, Reviews in Environmental Science and Biotechnology, 13:467–486.

Kim, B., Prezzi, M. and Salgado, R. (2005). Geotechnical properties of fly and bottom ash mixtures for use in highway embankments, Journal of Geotechnical and Geoenvironmental Engineering, 131(7):914–924.

Kim, H.K. and Lee, H.K. (2011). Use of power plant bottom ash as fine and coarse aggregates in high-strength concrete, Construction and Building Materials, 25(2):1115-1122.

Kim, H.K. and Lee, H.K. (2015). Coal bottom ash in field of civil engineering: A review of advanced applications and environmental considerations, Journal of Civil Engineering, 19(6):1802-1818.

Kumar, D., Kumar, N. and Gupta, A. (2014) Geotechnical properties of fly ash and bottom ash mixtures in different proportions, International Journal of Science, 3(9):1487-1494.

Lehrsch, G.A. and. Baker, D.E. (1989). Fly ash erodibility, Journal of Soil and Water Conservation, 44(6).

Lovell, C.W., W.H. Huang, W.H. and Lovell, J.E. (1991) Bottom ash as highway material, The 70th Annual Meeting of the Transportation Research Board, Washington, D.C.

Matsumoto, S., Ogata, S., Shimada, H., Sasaoka, T., Kusuma, G.J. and Gautama, R.S. (2016). Application of coal ash to postmine land for prevention of soil erosion in coal mine in Indonesia: Utilization of fly ash and bottom ash, Advances in Materials Science and Engineering, 2016:1–8.

Naipal, V., Reick, C., Pongratz, J. and Van Oost, K. (2015) Improving the global applicability of the RUSLE model – adjustment of the topographical and rainfall erosivity factors, Geoscientific Model Development Discussions., 8:2893–2913.

Pathirana, K.P.P., Asmer, T.M., Fahim S.M. and Hyther, A.L.A. (2009). Estimation of rainfall induced soil erosion an experimental study. Engineer Journal of the Institution of Engineers, Sri Lanka, 42(1):1-10.

Ranasinghe M. 1996. Mine restoration bond for clay mining and its impact on the prices of building materials in Sri Lanka. Construction Management and Economics, 14(2):165–174.

Renaud, K. M. (2018). "The mineral industry of Sri Lanka." US Geological Survey, USA.

Sadon, S. N. and Naganathan, S. (2017). Coal bottom ash as sustainable material in concrete - A review, Indian Journal of Science and Technology, 10(36):1–10.

Singh, M. and Siddique, R. (2015). Properties of concrete containing high volumes of coal bottom ash as fine aggregate. Journal of Cleaner Production, 91:269–278.

Singh, N., Shehnazdeep, & Bhardwaj, A. (2020). Reviewing the role of coal bottom ash as an alternative of cement, Construction and Building Materials, 233.

Wearing, C., Birch, C. J. and Nairn, J. D. (2008). An assessment of Tarong bottom ash for use on agricultural soils, Developments in Chemical Engineering and Mineral Processing, 12(5–6):531–543.

Yuksel, I. and Genç, A. (2007). Properties of concrete containing non ground ash and slag as fine aggregate, ACI materials journal, 104(4).

Soil Water Characteristic Curves for two landslides prone areas in Sri Lanka

S.A.G.M. Pemarathna
Department of Civil Engineering, The Open University of Sri Lanka, Sri Lanka

H.G.P.A. Ratnaweera
Department of Civil Engineering, The Open University of Sri Lanka, Sri Lanka

ABSTRACT: Rain induced shallow landslides are a common occurrence in Sri Lanka. This study describes the development of Soil Water Characteristic Curves (SWCCs) for compacted soil specimens obtained from two shallow landslide locations in the Ratnapura District. The Rowe Consolidation Cell was modified to measure the matric suction, based on the Axis Translation Method, with the change in Volumetric Water Content obtained using a capillary tube. The specimens were subjected to a maximum matric suction of 500kPa. Combined Sieve-Hydrometer Analysis, Liquid and Plastic Limit, and Specific Gravity tests were performed as per BS1377 (1990). The boundary drying and wetting curves were generated based on the improved Feng and Fredlund (1999) model explained in Pham et al. (2005).

1 INTRODUCTION

Rain-induced landslides of medium to shallow depths are a common occurrence in Sri Lanka. In partially saturated formations they are often triggered by rain infiltration, causing a reduction in matric suction, ψ, i.e., the difference between the pore air pressure, u_a and the pore water pressure, u_w, thus reducing the shear resistance of the formation. Rising water levels increase the positive static or seepage pore water pressures causing a reduction in the effective stress.

The Soil Water Characteristic Curve (SWCC) relates soil matric suction to the amount of water present in soil pores through its gravimetric water content, w, volumetric water content, θ or to its degree of saturation, S. The SWCC is considered unique for a given soil fabric (i.e., for a given pore size distribution) and the state of stress. The curve shows three distinct zones with increasing matric suction, namely the Boundary Effect Zone [1], the Transition Zone [2] and the Residual Zone [3]. Air-entry value ψ_a is the matric suction at which air enters the largest pores during transition from zones 1 to 2. The residual water content, θ_r, is the water content at residual state at which water phase becomes discontinuous at residual suction, ψ_r. (Fredlund and Rahardjo, 1993)

The SWCC shows hysteresis during drying (i.e., with increasing ψ) and wetting cycles. For a given matric suction, the volumetric water content, θ is greater during drying than when wetting. Klausner (1991) discusses the reasons for the dependency of θ on initial drying and subsequent wetting and drying cycles. The initial drying and wetting curves (Fig. 1) are established experimentally using the Axis Translation Technique. The maximum pore air pressure attained depends on the capacities of the apparatus and the high air-entry value of the ceramic porous disc. Researchers have developed equations for best fit curves based on several fitting parameters for ψ and θ, for the pressure range 0 – 500kPa. Subsequent drying and wetting occur within the two boundary curves (Fig. 1), hence it is important to predict these two curves.

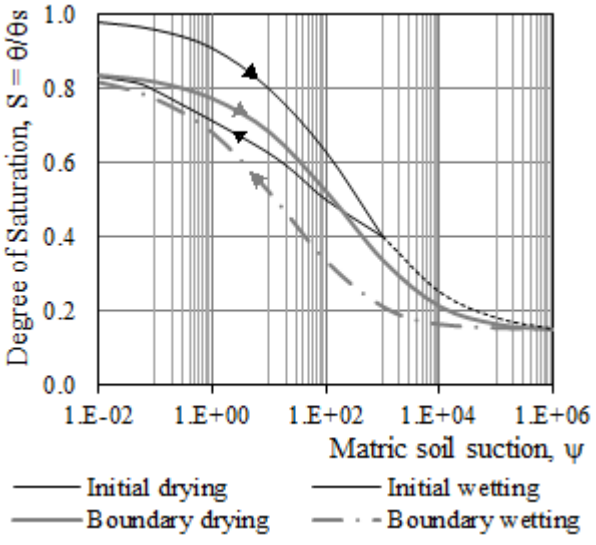

Fig. 1: Soil water hysteresis

The number of experimental data points determines the accuracy of the prediction. Zhai (2013) reports that data obtained for the range 0 – 100kPa is insufficient to generate an accurate SWCC while the range 0 – 500kPa gives better accuracy for

most soil types. Feng and Fredlund (1999) relates degree of saturation $S(\psi)$ to soil matric suction, ψ as:

$$S(\psi) = \frac{\theta}{\theta_s} = \frac{S_u b + c\psi^d}{b + \psi^d} \quad (1)$$

where S_u being the degree of saturation on the boundary curves at zero soil suction; *b*, *c* and *d* the curve fitting parameters. Eqn. (1) is used to generate the boundary drying and wetting curves. The boundary drying curve is obtained by scaling the initial drying curve to pass through S_u, which is the initial wetting curve value at zero soil suction. The boundary wetting curve is obtained using two additional parameters considering the ratio of the gradients, R_{SL} and the distance D_{SL} between the two inflection points on the respective two curves (Pham et al., 2005). Pham et al. (2005) derived the following curve-fit parameters for the boundary wetting curve:

$$R_{SL} = \frac{d_d}{d_w}; \quad D_{SL} = \log\left(b_d^{1/d_d}\right) - \log\left(b_w^{1/d_w}\right)$$

$$c_w = c_d;\ b_w = \left[\frac{b_d}{(10^{D_{SL}})^{d_d}}\right]^{\frac{1}{R_{SL}}}$$

Suffixes *d* and *w* of parameters *b*, *c* and *d* refer to the respective drying and wetting curves. Fredlund and Xing, (1994) suggests the correction factor $C(\psi)$ to force $S(\psi)$ to zero at a ψ of 10^6 kPa:

$$C(\psi) = 1 - \frac{\ln[1 + \psi/\psi_r]}{\ln[1 + 10^6/\psi_r]} \quad (2)$$

where ψ_r is the metric suction at residual degree of saturation S_r. Feng and Fredlund (1999) had used this correction factor with Eqn. (1). Pham et al., (2005) expresses ψ_r as $\psi_r = (2.7b)^{1/d}$

2 METHODS AND MATERIALS

2.1 *Sampling and classification*

Soil samples in this study were obtained from a relatively undisturbed residual formation, at a depth of 300mm, in the vicinity of recent shallow landslides at Erapola and Dikdeniya. Samples were oven dried at 60^0C and soil particles were separated using a rubber mallet, and then quartered. A combined sieve-hydrometer tests and Liquid and Plastic Limit tests were performed as per BS1377 Part 2, 1990. Miao (2001) notes that pore size and pore geometrical distribution correlates with the shape of the SWCC.

2.2 *SWCC test*

SWCCs were obtained for three specimens, two from Erapola and one from Dikdeniya. The tests were performed on the fraction passing 425μm sieve. Soil specimens were compacted into a ring (Padilla et al., 2005) and were kept submerged for 24hrs. to achieve maximum saturation. Remoulded specimens, however, may not properly represent in-situ conditions during the analysis and when proposing countermeasures against unsaturated soil-related Geo-disasters (Alowaisy et al., 2020). This may influence specimens with a significant clay content. A PVC ring of 22.45mm height and 49.63mm diameter was used since a greater contact area compared to the specimen height significantly shortens the equilibrium time. Wang (2015) finds that the specimen dimensions and shapes have little effect on the shape of the SWCC.

Specific Gravity of the soil fraction passing 0.425mm sieve size was determined as per BS1377 Part 2, 1990. The test was performed on three specimens to obtain a representative value.

Fig. 2 is a schematic diagram of the test apparatus used to measure matric suction, ψ, with volumetric water contents, θ_d and θ_w. A regulated air pressure supply expelled the water from the specimen via a 5-bar low air entry porous disc fixed to the pedestal of the modified Rowe Consolidation cell. The matric suction $u_a - u_w$ at a constant manometric water height was obtained based on the difference between the regulated inlet air pressure and the manometric head measured from the bottom level of the soil specimen. The change in volumetric water content during drying and wetting processes are computed at the equilibrium water height of the manometer. The manometer glass tube was calibrated at room temperature prior to its use.

The initial drying and wetting curves were generated by fitting the observed data to Eqn. (1). The best-fits were obtained using an iterative process based on the Monti-Carlo Simulation Technique. The degree of saturation at zero matric suction on the wetting curve, S_u was determined. The initial drying curve was scaled to determine the data points on the boundary drying curve. These points with S_u were curve-fitted to Eqn. (1) to generate the boundary drying curves. Parameters R_{SL} and D_{SL}, were selected while maintaining the hysteresis loop of the boundary drying and wetting curves. The correction factor $C(\psi)$ given in Eqn. (2) was applied to the boundary drying and wetting curves.

3 RESULTS AND DISCUSSION

3.1 *Sampling and Classification*

Figs. 3 to 5 show the combined grain size distribution curves obtained for samples obtained from the three locations.

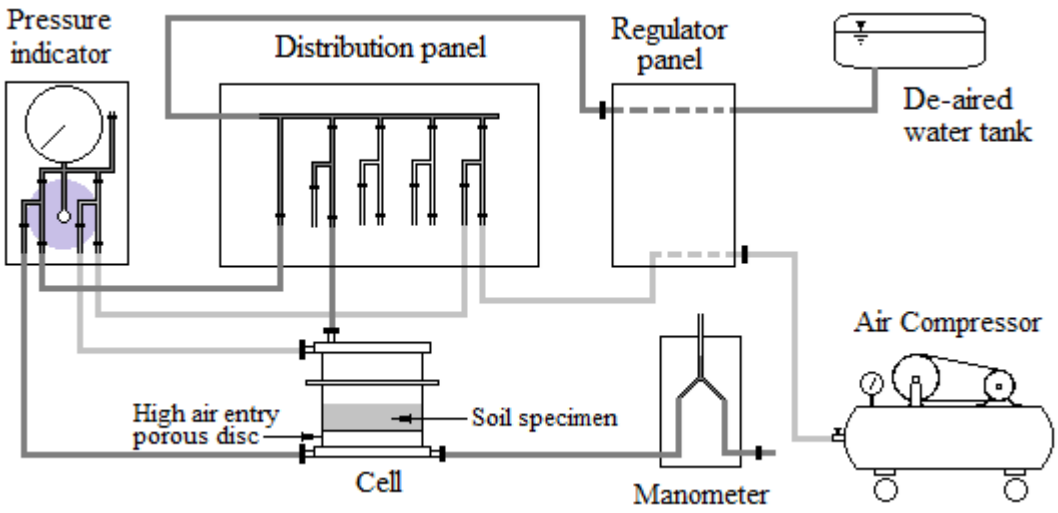

Fig. 2 Schematic diagram of the test apparatus.

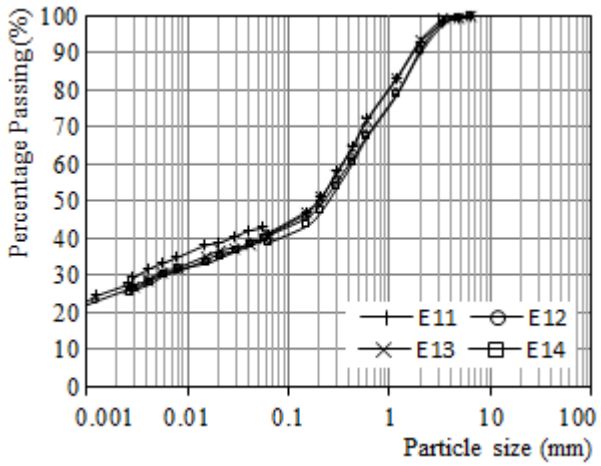

Fig. 3: Grain size distribution for Erapola [1] samples.

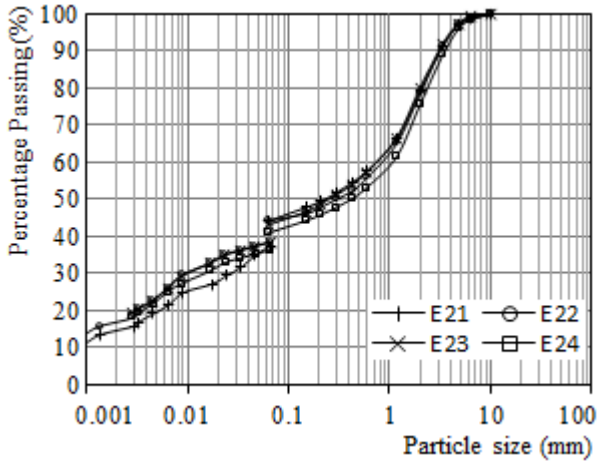

Fig. 4: Grain size distribution for Erapola [2] samples.

Figures show that consistency in grain-size distributions among quartered soil samples. Table 1 summarises the per centage of each soil group based on grain size, their index properties and the classification symbols based on MIT Soil Classification System. The specimens tested are identified as silty-clayey Sand (SM), with a low clay content, which may reduce the physico-chemical effects of using remoulded specimens.

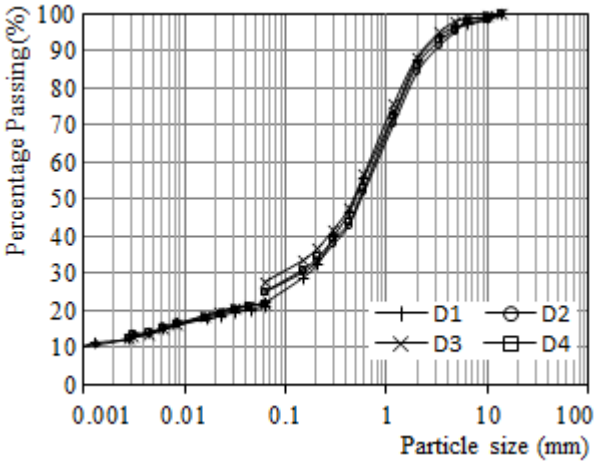

Fig. 5: Grain size distribution for Dikdeniya samples.

3.2 *Soil Water Characteristic Curves*

Table 2 lists the mechanical properties of the soil specimens tested, and their textural classification (TIN037, 2008). For sand, the per centage fraction passing 425μm sieve size was used for the textural classification since the SWCCs were based on soil passing the said sieve size.

Figs. 6 through 8 show the SWCCs generated. Though the said curves correlate well with Eqn. (1), the reliability could be enhanced by having additional scanning curves, to determine their positions relative to the established boundary drying and wetting curves. The scaled initial drying curves used to establish the boundary drying curves also show consistency with Eqn. (1).

Fig. 9 summarises the boundary curves obtained for the three locations, after applying the correction factor, $C(\psi)$ given in Eqn. (2). Tables 3 through 5 tabulates the fitting parameters obtained for each location.

Table 1: Soil classification based on grain-size and index properties.

No.	Per centage value of each soil group[1]						Index Properties			MIT
	C	M	S<425µm	S	G	<63µm	w_L (%)	w_P (%)	PI	
Erapola [1]										
E11	26.0	15.2	23.5	51.8	7.0	41.2	40.4	34.4	6	
E12	25.0	15.9	20.5	49.2	9.9	40.9	40.1	33.9	6	
E13	25.0	16.2	23.1	52.3	6.5	41.2	40.0	33.6	6	SM
E14	24.5	14.5	21.3	52.0	9.0	39.0	40.4	34.8	6	
Average	25.1	15.5	22.1	51.3	8.1	40.6	40	34	6	
Erapola [2]										
E21	15.0	29.2	10.4	35.3	20.5	44.2	46.2	33.9	12	
E22	17.0	27.3	8.0	34.3	21.4	44.3	44.9	33.8	11	
E23	18.0	25.0	10.9	37.1	19.9	43.0	45.5	31.5	14	SM
E24	18.0	22.8	9.3	34.8	24.4	40.8	46.3	32.1	14	
Average	17.0	26.1	9.65	35.4	21.6	43.1	46	33	13	
Dikdeniya										
D1	11.5	10.5	24.2	65.5	12.5	22.0	42.5	40.4	2	
D2	11.0	14.0	17.8	59.1	15.9	25.0	43.0	41.0	2	
D3	11.0	16.7	19.7	60.5	11.8	27.7	42.8	40.6	2	SM
D4	11.0	14.1	18.5	60.9	14.0	25.1	43.4	40.4	3	
Average	11.1	13.8	20.1	61.5	13.6	25.0	43	41	2	

[1] C – Clay, M – Silt, S – Sand, G – Gravel

Table 2: Soil parameters and textural classification of SWCC test specimens.

Location	G_s	ρ_d g/cm^3	θ_s	Textural classification
Erapola [1]	2.545	1.220	0.521	Clay (C)
Erapola [2]	2.597	1.224	0.529	Silty clay loam (ZCL)
Dikdeniya	2.563	1.140	0.552	Clay loam (CL)

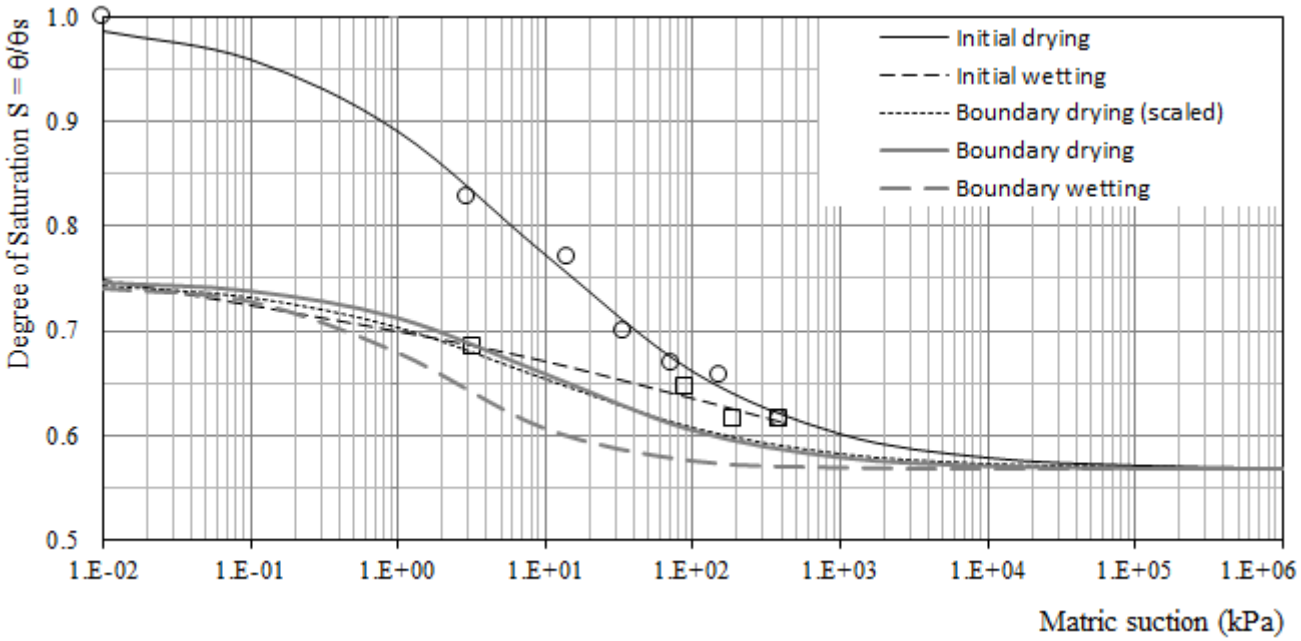

Fig. 6: Soil Water Characteristic Curve obtained for Erapola [1] specimen.

Table 3: Fitting parameters for SWCCs for Erapola [1]

Curve	S_u	b	c	d	ψ_r	R_{SL}	D_{SL}
Initial drying	-	2.960	0.568	0.516	56	-	-
Initial wetting	0.748	3.527	0.246	0.123	-	-	-
Boundary drying	0.748	3.971	0.568	0.593	55	-	-
Boundary wetting	0.748	1.757	0.568	0.791	7	0.75	0.7

Table 4: Fitting parameters for SWCCs for Erapola [2]

Curve	S_u	b	c	d	ψ_r	R_{SL}	D_{SL}
Initial drying	-	7.920	0.475	0.342	7755	-	-
Initial wetting	0.849	3.625	0.456	0.149	-	-	-
Boundary drying	0.849	8.457	0.477	0.353	7052	-	-
Boundary wetting	0.849	11.769	0.477	0.441	2535	0.8	0.2

Table 5: Fitting parameters for SWCCs for Dikdeniya

Curve	S_u	b	c	d	ψ_r	R_{SL}	D_{SL}
Initial drying	-	3.705	0.681	0.437	194	-	-
Initial wetting	0.847	3.735	0.445	0.118	-	-	-
Boundary drying	0.847	6.292	0.682	0.560	157	-	-
Boundary wetting	0.847	4.450	0.682	0.700	35	0.8	0.5

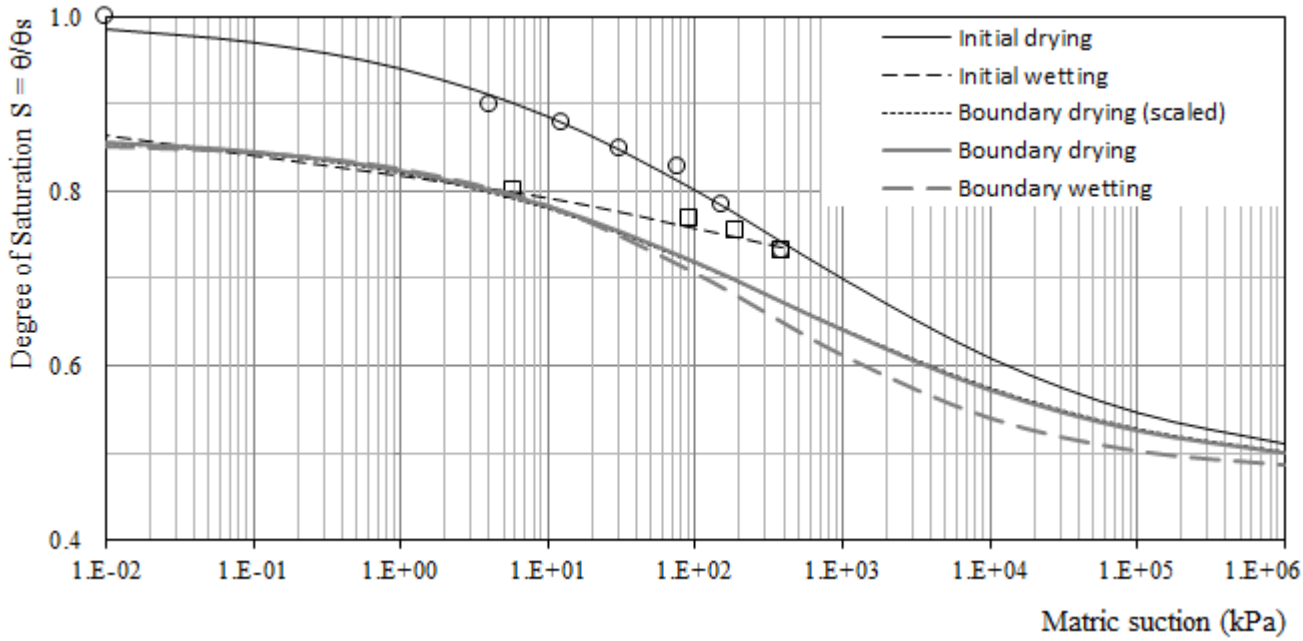

Fig. 7: Soil Water Characteristic Curve obtained for Erapola [2] specimen.

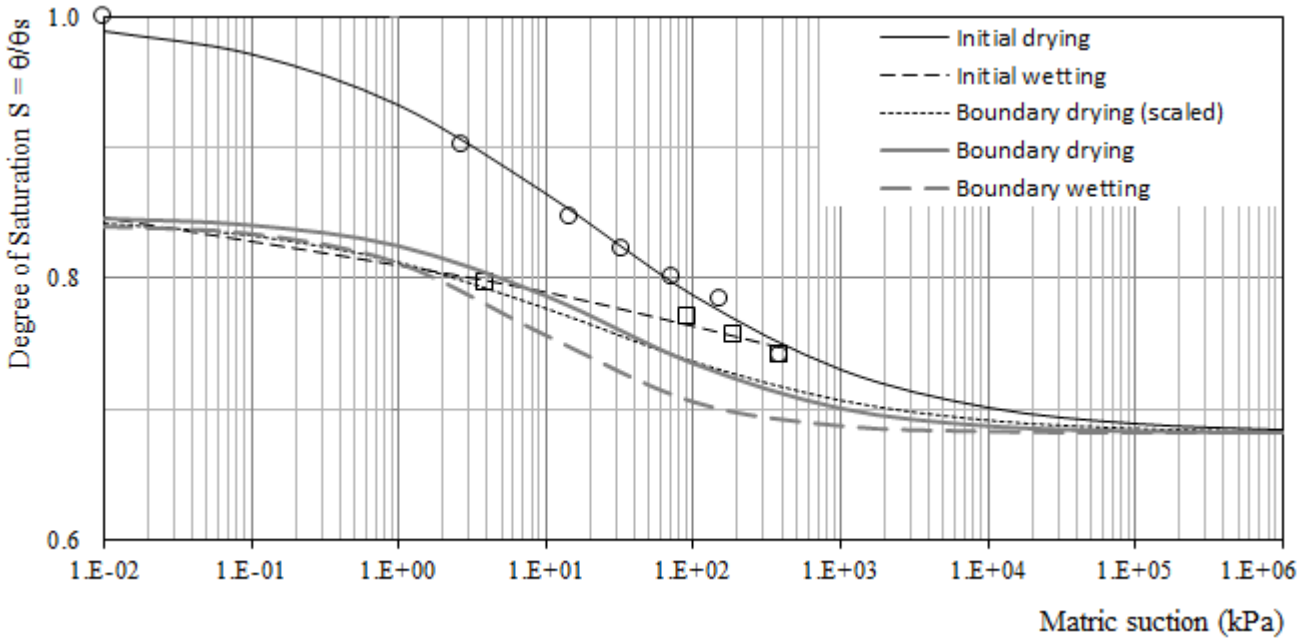

Fig. 8: Soil Water Characteristic Curve obtained for Dikdeniya specimen.

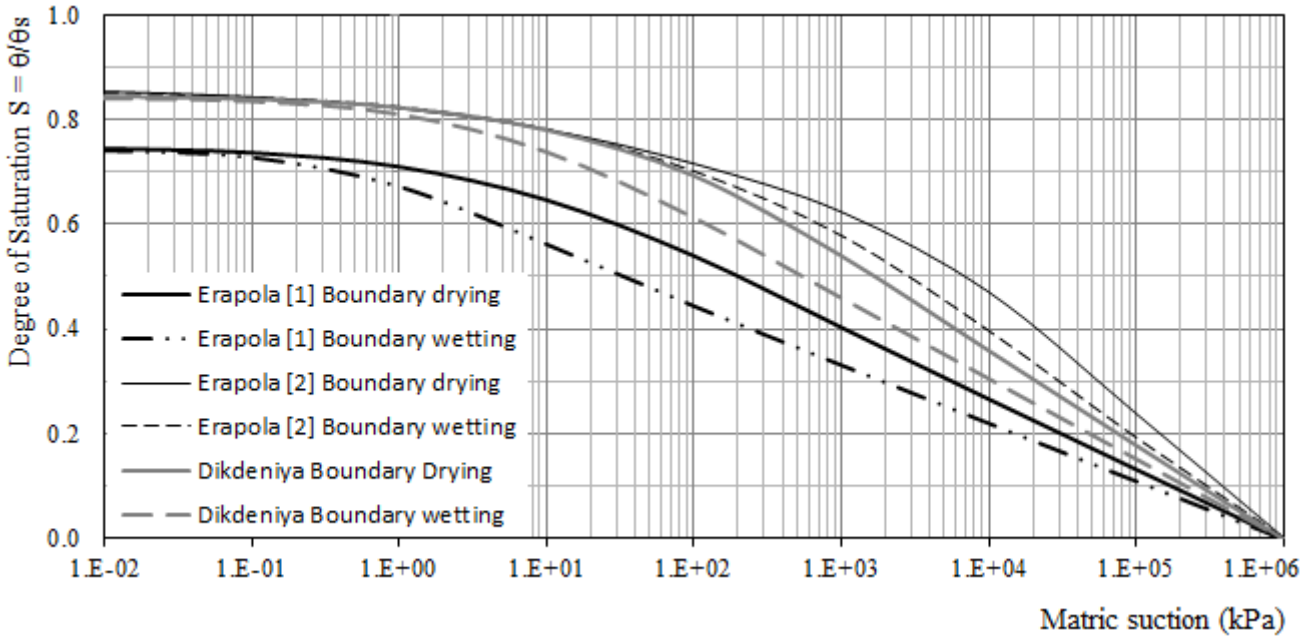

Fig. 9: Boundary curves obtained for the three specimens.

4 CONCLUSIONS

This study presents SWCCs obtained for compacted soil specimens from two shallow landslide locations. The results of the experimental study were used to generate the respective boundary drying and wetting curves.

ACKNOWLEDGMENTS

The authors wish to acknowledge the commitment and support rendered by Ms. N.P.M. Rajaguru, Senior Staff Technical Officer, Department of Civil Engineering, during the experimental phase of this study.

REFERENCES

Alowaisy, A., Yasufuku, N., Ishikura, R., Hatakeyama, M., and Kyono, S. (2020) Continuous pressurization method for a rapid determination of the soil water characteristics curve for remolded and undisturbed cohesionless soils, Soils and Foundations, https://doi.org/10.1016/j.sandf.2020.03.014.

Feng, M. and Fredlund, D.G. (1999) Hysteretic influence associated with thermal conductivity sensor measurements, In Proceedings from Theory to the Practice of Unsaturated Soil Mechanics in association with the 52nd Canadian Geotechnical Conference and the Unsaturated Soil Group, Regina, Sask., 23–24 October 1999. pp. 14:2:14-14:2:20.

Fredlund, D.G. and Xing, A. (1994) Equation for the soil water characteristic curve, Canadian Geotechnical Journal, *31(4), pp. 521-532.*

Fredlund, D.G. and Rahardjo, H. (1993). *Soil Mechanics for Unsaturated Soils*, John Wiley and Sons Inc., New York.

Klausner,Y (1991) Fundamentals of continuum mechanics of soils, Springer- Verlag Publishers, London.

Miao, L., Liu, S. and Lai, Y. (2001) Research of soil–water characteristics and shear strength features of Nanyang expansive soil, Engineering Geology, 65(4), pp. 261-267.

Pham,H.Q. Fredlund,D.G, and Barbour,S.L. (2005) A study of hysteresis models for soil-water characteristic curves, *Canadian Geotechnical Journal*, 42, pp. 1548-1568.

TIN037 (2004) Natural England Technical Information Note, http://publications.naturalengland.org.uk/file/83081, downloaded on 23.02.2020.

Wang, M., Kong, L. and Zang, M. (2015) Effects of sample dimensions and shapes on measuring soil-water characteristic curves using pressure plate, Journal of Rock Mechanics and Geotechnical Engineering, 7(4), pp. 463-468.

Zhai, Q. and Rahardjo, H., (2013), Quantification of uncertainties in soil–water characteristic curve associated with fitting parameters, *Engineering Geology*, June, 163, 144-152.

Padilla J.J., Perera Y.Y., Houston W.N., and Fredlund D.G. (2005) A new soil water characteristic curve device. Proceedings of Advanced Experimental Unsaturated Soil Mechanics, International symposium, Trento, Italy, pp. 15-22.

Characteristics of landslides induced by the 2004 Mid -Niigata Prefecture Earthquake

Surangani Bandara
Department of Remote Sensing and GIS, Sabaragamuwa University of Sri Lanka, Sri Lanka

Satoru Ohtsuka
Department of Civil and Environmental Engineering, Nagaoka University of Technology, Japan

ABSTRACT: The 2004 Mid-Niigata Prefecture earthquake of Japan triggered many landslides in the Chuetsu area of Niigata Prefecture. The main shock together with severe aftershocks triggered many landslides in the upland village of Yamakoshi while destroying the entire village. This paper examines the correlation between the earthquake induced landslide with geologic and geomorphologic factors. The earthquake induced landslides include 4504 surficial slides, 141 deep slides, and 609 shallow slides. Landslide occurrence ratio (LOR) defined as an index to analyze the relation between the landslide distribution and causative factors, including slope angle, slope aspect, distance from epicenter fault line, distance from water bodies, and bedding plane. The most common type of landslides recorded in the study area was surficial slide on steep slopes. Deep slides are influenced mainly by the bedding plane (parallel bedding slopes are more susceptible to collapse) and pre-existing landslide deposits.

1 INTRODUCTION

The 2004 Mid-Niigata Prefecture Earthquake sequence occurred in Niigata prefecture, central Japan on October 23, 2004. It caused many landslides and slope failures in the Chuetsu region of Niigata Prefecture. Figure 1 shows the location map of the Mid Niigata Prefecture Earthquake. The hypocenter of the main shock was located at relatively shallow depth and the magnitude is 6.8. In addition to the main shock, it was followed by several large aftershocks and three of them had magnitudes larger than 6. The strong ground motion, which is triggered by the earthquake, caused a vast damage in and around of epicenter including Ojiya city, Nagaoka city and Yamakoshi village due to the occurrence of several landslides (Fig. 2). According to the Niigata Prefectural Government report (2009) the earthquake and its aftershocks claimed more than 60 lives and approximately 103,000 people sought refuge, and 16,000 houses were destroyed.

The common factors that affect landslides distribution during the strong earthquake can be identified as slope angle, seismic intensity, earthquake magnitude, distance from epicenter or fault, rock types slope aspect. Relationship between seismically induced landslide and geological and geomorphological factors have been studies by Keefer (2000), Parise et al. (2000), Khazai et al. (2003), Sato et al. (2009), Qi et al. (2010), Papathanassiou et al. (2013), Basharat et al. (2014), Xu et al. (2014), and Xiaoli et al. (2015). Chigira and Yagi (2006) recognized over 1000 landslides in areas underlain by Miocene to Quaternary aged sedimentary rocks. Among them, the most common type was shallow disrupted landslides on steep slopes, but deep landslides also occurred in many locations. Therefore, detail analysis was carried out for deep landslides by the field investigation and by interpretation of aerial photographs. It concluded that many landslides occurred because of reactivation of pre-existing landslides and mobilization of valley bottom sediments, probably due to the saturation and partial liquefaction. Wang et al. (2007) analyzed 1212 landslides with 641 reactivated from pre-existing landslides in a selected study area near the epicenter. These landslides studied to clarify the correlation between geology, slope gradient, and earthquake motion. This found that landslides mostly occurred on slopes in the 20°–35° range, that the maximum distance from the epicenter to the landslides was 18 km, that the Wanazu Formation had the most concentrated landslide activity, and that the area affected by landslides was correlated with the earthquake magnitude. Sato et al. (2005) digitally mapped 1553 landslides as polygons that included the travel paths and accumulation areas. According to their findings, most of the landslides were concentrated

in the hanging wall side. Kieffer et al. (2006) has identified that a thrust fault caused more landslides in a wider area and the greatest concentration of landslides is on the hanging wall side rather than the foot side by analyzing the same earthquake.

Fig. 1 Location of the Mid-Niigata Prefecture earthquake

In this paper spatial distribution of the landslides triggered by the earthquake was obtained by correlating the Landslide Occurrence Ratio (LOR), collapse area with the impact factors that control earthquake triggered landslides. The LOR is defined as the ratio of the collapse area to the total area, where the collapse area is the surface area of landslide scars for a given class of a given predisposing factor and the total area is the total surface area for a given class of a given pre disposing factor. ArcGIS 10.7 was used to analyze the correlation of landslides with respect to the distance from the epicenter fault line, topographic parameters (slope angle, slope aspect), distance from water bodies, distance from epicenter fault line, and bedding plane.

(a)

(b)

(c)

Fig. 2 (a): Buildings and road damage due to the slope failures in the Yamakoshi village (taken by Ohtsuka S), (b): The retaining wall block the general route 291 in the Takezawa tunnel Nagaoka side entrance (taken by Sanko Consultant Co., Ltd), (c): Submerged residential building by river channel obstruction in the Higashitakezawa area, Yamakoshi village (taken by Saito H)

2 EARTHQUAKE INDUCED LANDSLIDES

The 2004 Mid-Niigata Prefecture earthquake triggered many landslides in and around of epicentral area. Oyagi et al. (2008) identified locations and areas of landslides by comparing aerial photographs before and after the earthquake and verified them with field investigation. They have classified these landslides according to the depth of the slip surface, failure type, and materials of the moving body. The following three major landslide types were identified according to the depth of the slip surface: surficial slides (depth ≤1 m), shallow slides (depth between 1 and 10 m), and deep slides (depth ≥10 m). These three types of landslides were further classified in detail as rotational and

translational. In this paper, 141 deep slides, 609 shallow slides, and 4504 surficial slides triggered by the 2004 Mid-Niigata Prefecture earthquake analyze in detail.

2.1 *Correlation of landslides and slope angle*

The slope angle was extracted based on the Digital Elevation Model (DEM) at 10 m × 10 m resolution. Figure 3 shows the landslide occurrence ratio and total collapse area with respect to the slope angle. Almost 54.45% of the surficial slide has occurred within the 40°-45° category. However, the LOR shows an increasing trend until the slope angle reaches its maximum in the category of 50. This result implies that the slope angle is strongly correlated with a surficial slide induced by the earthquake. Most of the shallow slides occurred in the slope angle category 25°-35°. According to the results, almost all the deep slides occurred at steep slopes with the slope angle of ≥ 20°. Meanwhile, more than 58% of the deep slides have an original slope angle of ≥ 30° (Bandara et al. 2017).

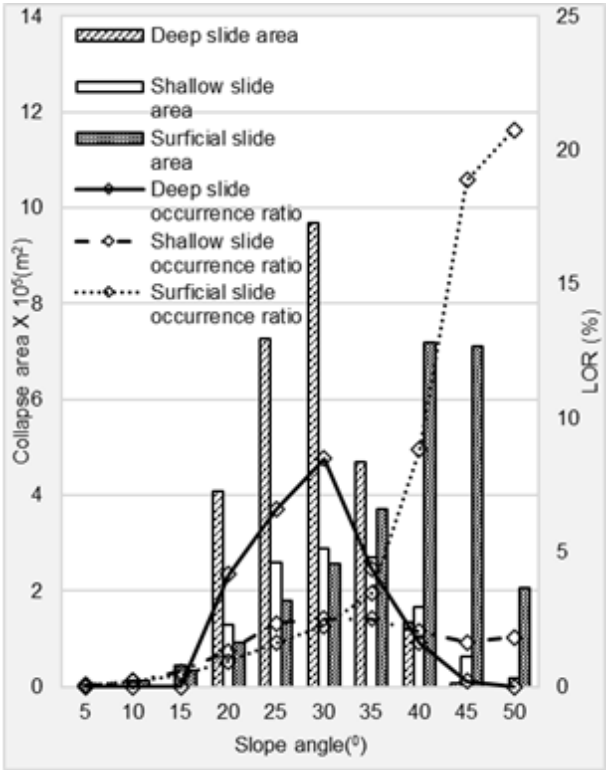

Fig. 3 Landslide collapse area and LOR according to the slope angle

2.2 *Correlation of landslides and slope aspect*

Slope direction is also an important influencing factor because it is related to factors such as the directional peak ground acceleration Dai et al. (2011). Therefore, in this paper we analyze slope facing direction influence for the stability of the slope. The relationship between LORs and slope aspect classes can be seen in Fig. 4. The occurrence ratio of the surficial slide was highest on southwest, south, and southeast facing slopes. LOR of the shallow landslide was highest on a southwest facing slopes and lowest on northeast facing slopes. LOR of the deep slide was highest on east facing slopes and lowest on North west facing slopes.

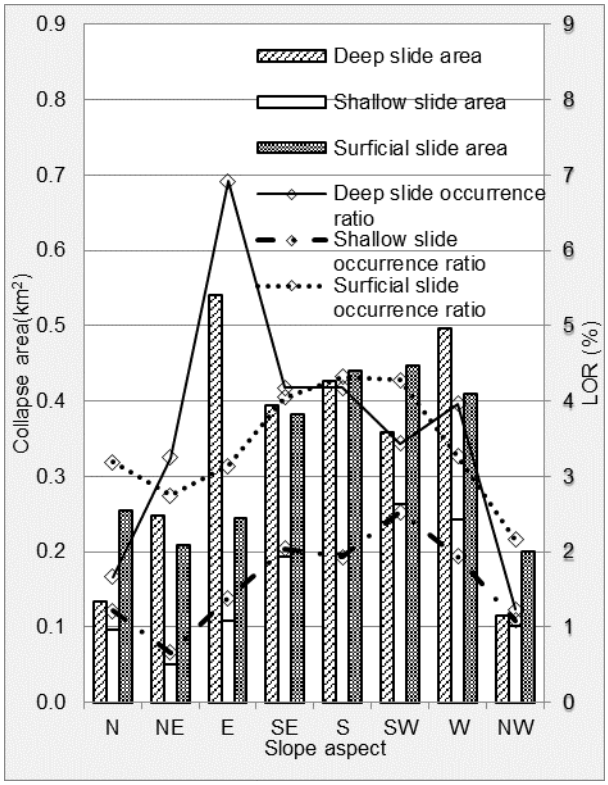

Fig. 4 Landslide collapse area and LOR according to slope aspect

2.3 *Correlation of landslides and distance from the epicenter fault line*

Causative fault and epicenter are an important factor that can influence the distribution of landslides during a strong shaking event. Hence, in this paper, the distance from the epicenter fault line is used to analyze the landslide variation. Landslide distributions were obtained as a function of distance from the epicenter fault line. Figure 5 shows the variation of LOR with epicentral distance. Shallow slide and surficial slide occurrence ratio monotonically decrease with epicenter fault line distance. This shows that the shaking motion is declining in gen-

eral with increasing distance from the epicenter fault line. However, deep slide occurrence ratio is higher even far away from the epicenter. This shows that the distance from epicenter fault line is not much impact to occur deep slides. That may possibly depend on other factors such as pre-existing landslides and lithology. Therefore, further analysis needs to explain this aspect.

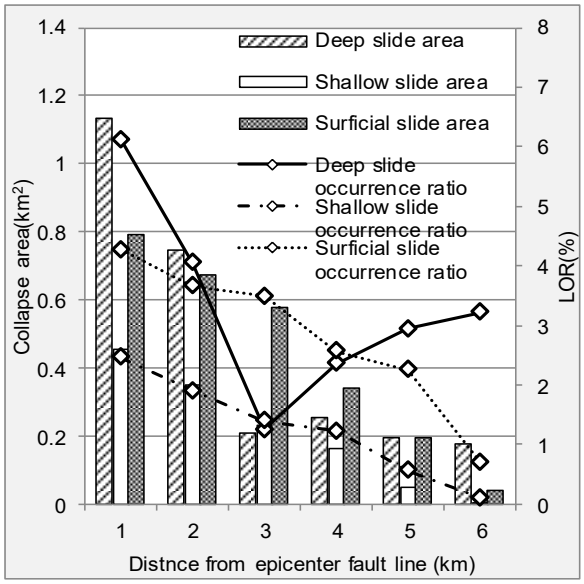

Fig. 5 Landslide collapse area and LOR according to distance from epicenter fault line

2.4 *Correlation of landslides and distance from water bodies*

It is well known that water is one of the major triggers of landslides. Numerous landslide studies discuss different effects that water may have on slope stability: decreasing suction, rising groundwater table and subsequent increasing pore water pressure, groundwater exfiltration from the bedrock, seepage erosion, hydraulic uplift pressure from below the landslide. To examine the effect of ground water level for occurrences of landslides we assumed ground water level was very high near water bodies such as rivers and ponds. Figure 6 shows the variation in LOR and collapse area with distance to water bodies. It is very clear most of the landslides located very near to rivers and ponds, among them 70.98% of the total area concentrated with in the distance of 100m from the rivers and ponds and 0.39% concentrated in the 400m distance from the water bodies.

2.5 *Correlation of landslides and bedding plane*

This study area can be identified as an earthquake active region therefore pre-existing landslides are predominant geological characteristics of the area. Historically many landslides have been occurred and ground has deformed in many ways. Hence, pre-existing landslides also considered when obtaining the correlation between slope types (dip slopes, horizontal dip slopes, reverse dip slope) and landslide occurrences. The LOR and collapse area according to the bedding orientation are shown in Fig. 7. Deep slides show high occurrence ratio in dip slopes. Furthermore, the total sliding area of pre-existing landslides is slightly greater than that of dip slopes. Even though surficial slide shows higher LOR in dip slopes the difference between dip slopes and horizontal dip slopes is very small. Shallow slides occur independently of the structure of the slope. According to the results macroscopic slope structure does not significantly affect the occurrence of shallow slides and surficial slides (Bandara et al. 2017).

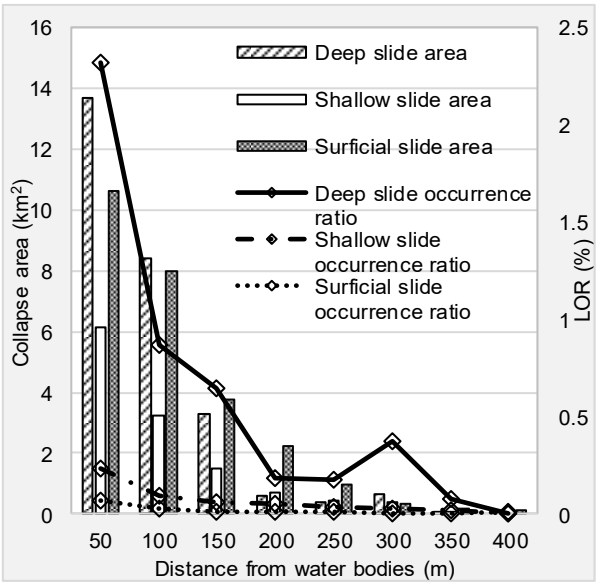

Fig. 6 Landslide collapse area and LOR according to distance from water bodies

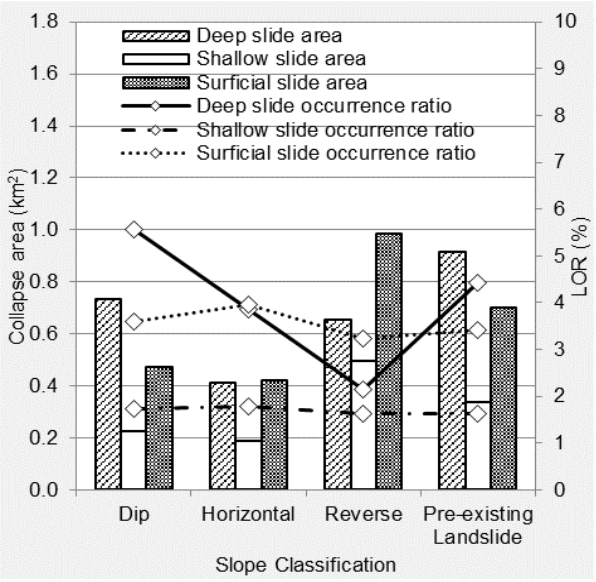

Fig. 7 Landslide collapse area and LOR according to slope morphology and slope classification

3 CONCLUSION

Analysis of landslides triggered by the 2004 Mid-Niigata Prefecture earthquake provides important characteristics of seismically triggered landslides in Niigata prefecture. The most common type of landslides recorded in the study area was surficial slide on steep slopes. In addition to that this, event has triggered 141 deep slides and 609 shallow slides. Shallow slides and surficial slides show the monotonical decrease trend with epicenter fault line. However deep slide relationship with distance from epicenter fault line is not clear. According to the obtained results, surficial slide occurrence ratio is increasing with slope angle. This result implies that the slope angle is strongly correlated with the occurrence of surficial slides induced by the earthquake. Subsurface geology and topography of the study area has significantly modified by the pre-existing landslide deposit. It is found that most of the deep slides occur in the pre-existing landslide deposits and dip slopes. Most of the collapse occurred very close to the rivers and ponds. Shallow and surficial slides occurred independently of bedding planes.

4 REFERENCES

Bandara, S., & Ohtsuka, S. (2017). Spatial distribution of landslides induced by the 2004 Mid-Niigata prefecture earthquake, Japan. Landslides, 14(6), 1877-1886.

Basharat, M., Rohn, J., Baig, M. S., & Khan, M. R. (2014). Spatial distribution analysis of mass movements triggered by the 2005 Kashmir earthquake in the Northeast Himalayas of Pakistan. Geomorphology, 206, 203-214.

Chigira, M., & Yagi, H. (2006). Geological and geomorphological characteristics of landslides triggered by the 2004 Mid Niigta prefecture earthquake in Japan. Engineering Geology, 82(4), 202-221.

Dai, F. C., Xu, C., Yao, X., Xu, L., Tu, X. B., & Gong, Q. M. (2011). Spatial distribution of landslides triggered by the 2008 Ms 8.0 Wenchuan earthquake, China. Journal of Asian Earth Sciences, 40(4), 883-895.

Keefer, D. K. (2000). Statistical analysis of an earthquake-induced landslide distribution—the 1989 Loma Prieta, California event. Engineering geology, 58(3-4), 231-249.

Khazai, B., & Sitar, N. (2004). Evaluation of factors controlling earthquake-induced landslides caused by Chi-Chi earthquake and comparison with the Northridge and Loma Prieta events. Engineering geology, 71(1-2), 79-95.

Kieffer, D. S., Jibson, R., Rathje, E. M., & Kelson, K. (2006). Landslides triggered by the 2004 Niigata Ken Chuetsu, Japan, earthquake. Earthquake Spectra, 22(S1), 47-73.

Niigata Prefectural Government, Niigata prefecture report on damage in the 2004 Niigata-Chuetsu earthquake. (2009). No. 174, final report, Niigata.

Oyagi, N., Uchiyama, S., & Inokuchi, T. (2008). Map of landslides caused by the 2004 Niigata-ken Chuetsu (Mid Niigata) earthquake (MJMA= 6.8). Technical Note of the National Research Institute for Earth Science and Disaster Prevention, 317, 1-37.

Parise, M., & Jibson, R. W. (2000). A seismic landslide susceptibility rating of geologic units based on analysis of characteristics of landslides triggered by the 17 January, 1994 Northridge, California earthquake. Engineering geology, 58(3-4), 251-270.

Papathanassiou, G., Valkaniotis, S., Ganas, A., & Pavlides, S. (2013). GIS-based statistical analysis of the spatial distribution of earthquake-induced landslides in the island of Lefkada, Ionian Islands, Greece. Landslides, 10(6), 771-783.

Sato, H. P., & Harp, E. L. (2009). Interpretation of earthquake-induced landslides triggered by the 12 May 2008, M7. 9 Wenchuan earthquake in the Beichuan area, Sichuan Province, China using satellite imagery and Google Earth. Landslides, 6(2), 153-159.

Sato, H. P., Sekiguchi, T., Kojiroi, R., Suzuki, Y., & Iida, M. (2005). Overlaying landslides distribution on the earthquake source, geological and topographical data: the Mid Niigata prefecture earthquake in 2004, Japan. Landslides, 2(2), 143-152.

Qi, S., Xu, Q., Lan, H., Zhang, B., & Liu, J. (2010). Spatial distribution analysis of landslides triggered by 2008.5. 12 Wenchuan Earthquake, China. Engineering geology, 116(1-2), 95-108.

Wang, H. B., Sassa, K., & Xu, W. Y. (2007). Analysis of a spatial distribution of landslides triggered by the 2004 Chuetsu earthquakes of Niigata Prefecture, Japan. Natural Hazards, 41(1), 43.

Xu, C., Xu, X., Yao, X., & Dai, F. (2014). Three (nearly) complete inventories of landslides triggered by the May 12, 2008 Wenchuan Mw 7.9 earthquake of China and their spatial distribution statistical analysis. Landslides, 11(3), 441-461.

Xiaoli, C., Qing, Z., & Chunguo, L. (2015). Distribution pattern of coseismic landslides triggered by the 2014 Ludian, Yunnan, China Mw6. 1 earthquake: special controlling conditions of local topography. Landslides, 12(6), 1159-1168.

Estimating the stability of a vertical cut considering tension cracks

G. Yanamandra
Department of Civil Engineering, University of New Brunswick, Canada

W. T. Oh
Department of Civil Engineering, University of New Brunswick, Canada

ABSTRACT: Tension cracks typically occur behind the crests of slopes and cuts in the case where tensile stress exceeds tensile strength. The influence of tension crack is commonly overlooked in the design process although it is a primary contributor to the instability of slopes and cuts. In the present study, a series of numerical analysis was carried out using commercial finite element software (GeoStudio 2019 R2) to analyze the stability of unsupported vertical cut excavated in an unsaturated soil considering the influence of matric suction. The results showed that factor of safety of an unsupported vertical cut can be more reliable when estimated taking account of both location and depth of tension crack. It also turned out that an unsupported vertical cut can fail before a tension crack reaches the depth calculated using the approaches available in literature.

1 INTRODUCTION

Tension cracks are found near the crest of slopes and unsupported cuts when tensile stress exceeds tensile strength (Bagge 1985). Desiccation, differential settlement and temperature changes are considered to be main reasons for the tension cracks (Li and Zhang, 2018). Tension crack is one of the governing factors that affect the stability of slopes and unsupported cuts since tension crack forms a part of slip surface and acts as a pathway for rainfall to seep through the soil. In practice, however, this aspect is often overlooked in the design of unsupported cuts. Unsupported cuts are typically made into an unsaturated soil. In this case, rainfall infiltration into a tension crack can be detrimental since it leads to significant decrease in shear strength of the soil, which is attributed to the decrease in matric suction (Gofar et al. 2006). During rainfall, pre-existing cracks are highly influential towards the deep failures (Hu 2000, Wang et al. 2012). Therefore, it is important to estimate the critical location and depth of tension cracks. Several approaches are available in literature to estimate the location and/or depth of a tension crack (Taylor 1984, Janbu 1968, Spencer 1968, Bagge 1985, Michalowski 2013, Li et al. 2018). However, limited studies were undertaken to estimate the location and depth of a tension crack in an unsaturated unsupported vertical cut.

In the present study, an approach is proposed that can be used to estimate the location and depth of a tension crack with most adverse effect on the stability of an unsupported vertical cut in an unsaturated soil. The results are then compared with those estimated using the approaches available in literature (Baker 1981, Kutschke and Vallejo 2011, Richard 2018, OSHA 2019). Geotechnical modeling software, GeoStudio (SIGMA/W and SLOPE/W; ver. 2019 R2, GeoSlope Int. Ltd.) was used for the numerical analysis throughout this study.

2 TENSION CRACK IN UNSUPPORTED VERTICAL CUTS

Baker (1981) proposed an approach that can be used to determine both location and depth of tension crack in unsupported cuts for both drained and undrained conditions. According to Baker (1981), maximum depth of tension crack takes place for vertical cut and it never exceeds one quarter of the slope height. Baker and Leshchinsky (2003) studied the spatial distribution of safety factors in a cohesive vertical cut by utilizing the safety map notion originally proposed by Baker and Leshchinsky (2001). Michalowski (2013) proposed a method to estimate the maximum depth of tension crack based on limit analysis. The location of tension crack was determined as the one with the most adverse influence on the stability. Based on the observations from the finite element analysis for an unsupported vertical cut in stiff clay, Kutschke and Vallejo (2011) concluded that the depth of tension crack ranges between 0.45 and 0.57 times the excavation height. OSHA (2019) indicates that tension cracks usually form at distance ratio of 0.5 to 0.7 to the height of the excavation. Numerical analyses were also carried out to study the influence of tension crack on the stability

of vertical cut (Lee et al. 1988; Kutschke and Vallejo 2011). The main advantage of numerical analysis is that progress failure mechanism can be taken into account during analysis.

These conventional analytical solutions can be more effectively used for saturated homogeneous soils. However, in reality, shear strength of soil is governed by the location of water table and varies with respect to matric suction. Pufahl et al. (1983) investigated lateral earth pressure for a vertical cut extending the unsaturated soil mechanics considering the influence of matric suction on the shear strength of soil. Based on the conventional Rankin earth pressure theory, the active earth pressure, σ_a, for unsaturated condition can be written as Eq. (1) assuming air-pressure is atmospheric pressure.

$$\sigma_a = \gamma z K_a - 2\left[c' + (u_a - u_w)\tan\phi^b\right]\sqrt{K_a} \quad (1)$$

where γ is unit weight, z is depth from the ground surface, K_a is earth pressure coefficient at rest, c' is effective cohesion, $(u_a - u_w)$ is matric suction, and ϕ^b is angle indicating the rate of increase in shear strength with respect to a change in matric suction

Eq. (1) can be rewritten as Eq. (2) considering the nonlinear variation of unit weight and shear strength of a soil adopting the shear strength model proposed by Vanapalli et al. (1996).

$$\sigma_a = \left[\frac{G_s + \theta(1+e)}{(1+e)}\right]\gamma_w z K_a - 2\left[c' + (u_a - u_w)S^{\kappa}\tan\phi'\right]\sqrt{K_a} \quad (2)$$

where σ_a is lateral earth pressure, G_s is specific gravity, θ is volumetric water content, e is void ratio, γ_w is unit weight of water, S is degree of saturation, and κ is fitting parameter (function of plasticity index)

Hence, the depth of tension crack is can be calculated using Eq. (3).

$$z_t = \frac{2\left[c' + (u_a - u_w)S^{\kappa}\tan\phi'\right]}{\left[\frac{G_s + \theta(1+e)}{(1+e)}\gamma_w\right]\sqrt{K_a}} \quad (3)$$

In the present study, Eq. (3) was used to estimate the depth of tension crack analytically. Richard et al. (2018) showed that there was good agreement between the observed critical height and the estimated one using Eq. (2) for a large scale temporary instrumented vertical cut (Whenham et al. 2007) in an unsaturated soil taking account of rainfall infiltration. It should be noted that Eq. (3) can only be used to determine theoretical maximum depth of a tension crack, not the location.

3 METHODOLOGY

3.1 *Soil Properties*

In the present study, it was assumed that an unsupported vertical cut was made into a glacial till (Indian Head till, IHT) that is widely spread across Canada. Basic soil properties are summarized in Table 1. The grain size distribution curve of IHT is shown in Figure 1. Figure 2 and Figure 3 show Soil-Water Characteristic Curve, and hydraulic conductivity functions of IHT used in the numerical analyses.

Table 1. Basic soil properties of IHT (Vanapalli 1996)

Properties	Value
Plasticity Index, I_p (%)	15.5
Saturated unit weight, γ_{sat} (kN/m^3)	20.7
Void ratio, e	0.55
Specific gravity, G_s	2.72
Effective cohesion, c' (kPa)	5
Effective internal friction angle, ϕ'	23.1
Saturated volumetric water content, θ_s	0.47

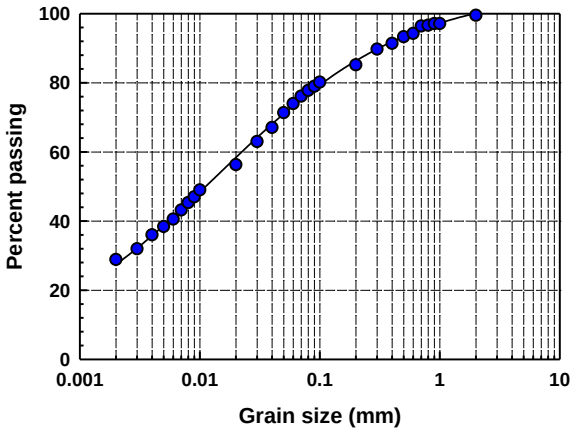

Figure 1. Grain size distribution of IHT

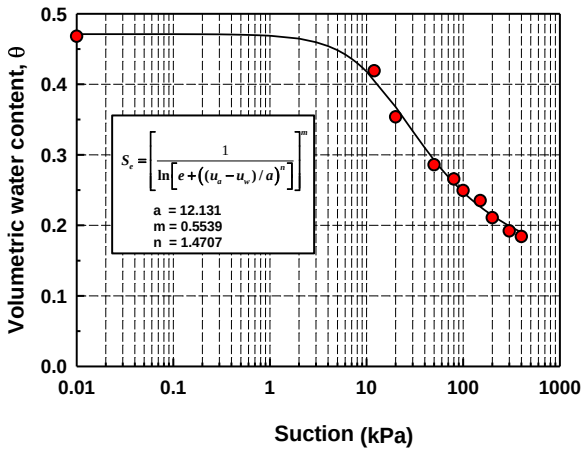

Figure 2. Soil-water characteristic curve of IHT

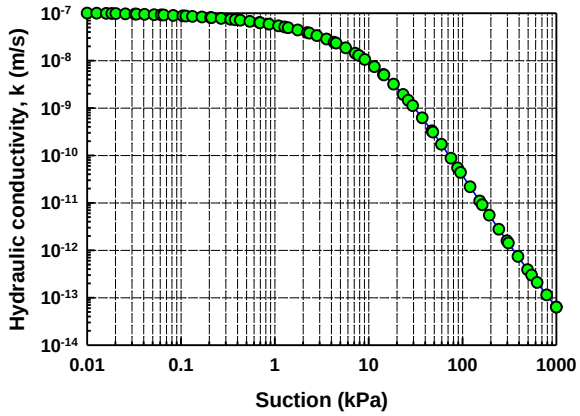

Figure 3. Hydraulic conductivity function of IHT

3.2 *Numerical Analysis*

SIGMA/W and SLOPE/W (product of GeoStudio 2019 R2) were jointly used to simulate excavation, tension crack and to conduct stability analysis of unsupported vertical cut, respectively. To consider the change in water table and subsequent redistribution of pore-water pressure due to excavation, coupled stress-pore pressure analysis option was chosen in SIGMA/W. Figure 4 shows mesh, tension crack and boundary conditions defined in SIGMA/W. Initial stress condition was established using 'Insitu' analysis type by applying body load to the elements. Initial pore-water pressures were specified by drawing an initial water table, which distributes hydrostatic positive and negative pore-water pressures below and above the water table, respectively. Water total head hydraulic boundary condition equals to the elevation of initial water table was placed along the lateral extents of the soil region on the right side (i.e. solid circles). This boundary condition was used to maintain a constant hydraulic total head along the right edges of the domain regardless of the fluctuation of water table due to excavation. Staged excavated was simulated by deactivating regions in 0.15 m increments. Excavation resulted in the drop of water table, which induced increase in negative pore-water pressure. Enough time was allowed between the staged excavations until the pore-water pressure reaches equilibrium condition. Stability analysis was carried out based on stress-strain relationships from finite element analysis from SIGMA/W results as the parent analysis. In SLOPE/W, Mohr-Coulomb strength model was assigned to the material. Tension crack was simulated as a material with zero-unit weight and strength rather than as a boundary condition (Wang et al. 2012).

The stability analyses were performed for various depths and distances from the face of cut with the level of GWT at 3 m. The depth (DP_{tc}) and distance (DS_{tc}) of a tension crack was normalized by safe height (H_{safe}), which are denoted as tension crack depth and distance ratios, respectively. Figure 5 shows positive, negative and net earth pressure distribution based on Eq. (2). The depth of tension crack was estimated to be 1.34m. The critical height can be obtained by locating the depth that equates 'Area I' and 'Area II', where the net horizontal thrust is zero (i.e. 2.5m).

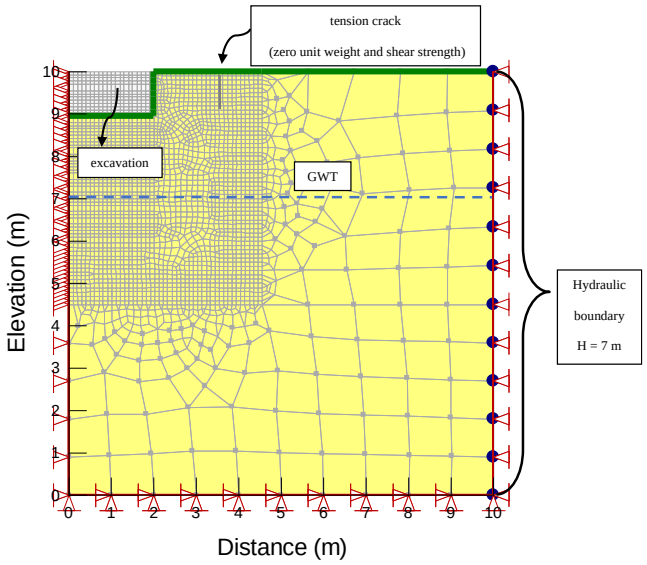

Figure 4. Meshes and boundary conditions used in SIGMA/W

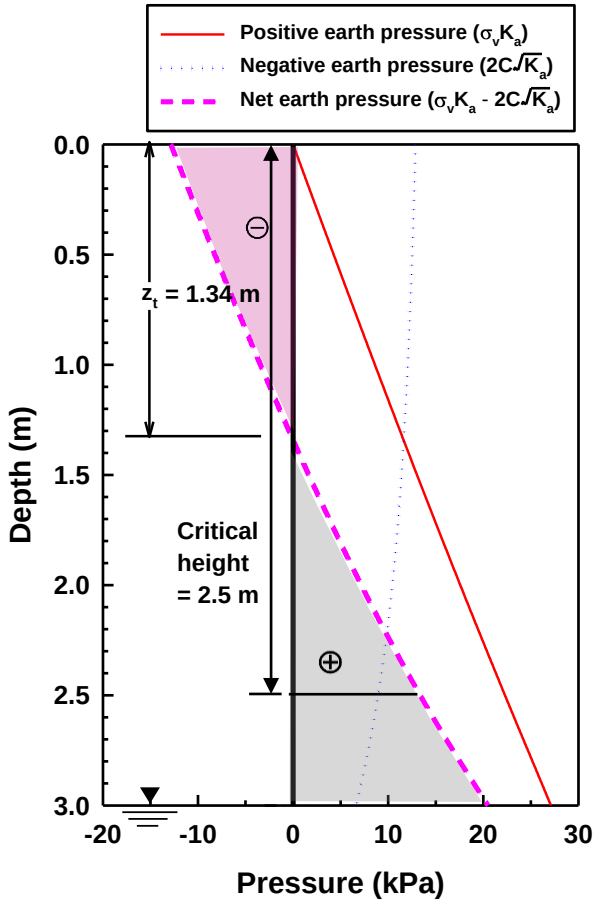

Figure 5. Estimation of depth of tension crack and critical depth of an unsupported vertical cut in IHT with GWT at 3m based on net active earth pressure (Eq. (2))

4 ANALYSIS RESULTS

Figure 6 shows the variation of factor of safety for different combination of tension crack distance and depth ratios with GWT at 3 m. The critical height based on Figure 5 was 2.5 m; therefore, safe height equals to 2.08 m (FOS = 1.2) was used in plotting Figure 6. The depths of tension crack estimated using Eq. (3) leads to the depth ratio of 0.64 (= 1.34/2.08). This tension crack depth ratio is greater than the range proposed by Kutschke and Vallejo (2011) (i.e. 0.45 – 0.57). As expected, FOS decreases with increasing the tension crack depth ratio. In case where tension crack distance ratio is less than 0.2, FOS is greater than unity up to the depth of tension crack ratio less than 0.5. In other words, if a tension crack is developed at tension crack distance ratio greater than 0.2 failure can take place before the tension crack can reach the depth estimated by Eq. (3) or proposed by Kutschke and Vallejo (2011). It can also be seen that unsupported vertical cut can remain stable unless tension crack depth ratio exceeds 0.37 for the level of GWT used in the analysis. OSHA (2019)'s guideline states that tension cracks usually form at distance ratio of 0.5 to 0.7 (Information of tension crack depth is not available in OSHA 2019). If this guideline is implemented in practice, the tension crack depth ratio of 0.37 can be used as a maximum ratio to avoid failure due to tension crack. Baker (1981) suggested that that the maximum depth of tension crack is 25% of vertical slopes. This indicates that a tension crack does not affect the stability of unsupported vertical cut for the scenario considered in the present study.

5 CONCLUSIONS

Tension cracks have an adverse impact on the stability of slopes. The location and depth of a tension crack can be estimated using empirical, semi-empirical, or numerical approaches available in literature. According to the present study, FOS of an unsupported vertical cut in an unsaturated glacial till does not drop below unity if a tension crack opens at the tension crack distance ratio less than 0.2 with GWT at 3 m. However, an unsupported vertical cut can fail before the tension crack reaches the depths estimated using Eq. (3) and the approach proposed by Kutschke and Vallejo (2011). If the guideline proposed by OSHA (2019) is implemented in practice, the depth and distance ratio should not exceed approximately 0.37 and 0.2 respectively to avoid failure due to a tension crack.

Present study was carried out for a one type of soil (i.e. glacial till) with GWT at 3 m. Therefore, more extensive study is necessary for various types of soils and the levels of GWT to justify the findings obtained in this study.

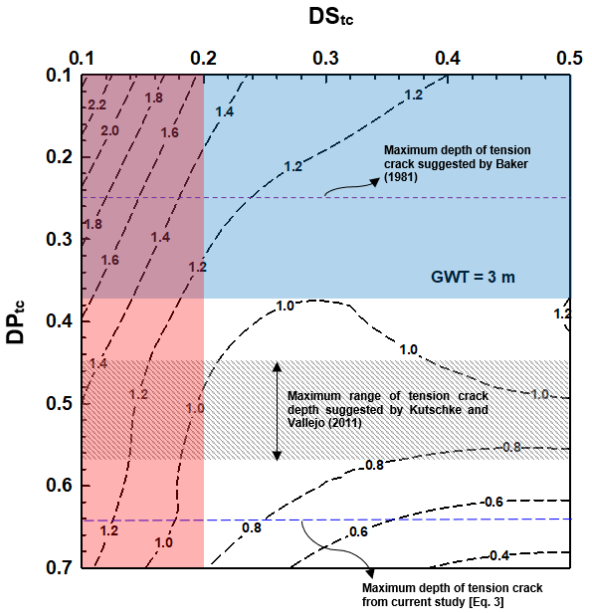

Figure 6. Variation of factor of safety for different combination of tension crack distance and depth ratios with GWT at 3 m

REFERENCES

Bagge, G. (1985). Tension cracks in saturated clay cuttings, Proceeding of the 11th international conference on Soil Mechanics and Foundation Engineering, San Francisco, (Balkema): 393-395.

Baker, R., and Leshchinsky, D. (2001). Spatial distribution of safety factors, Journal of Geotechnical and Geoenvironmental Engineering, ASCE, 127(2): 135-145.

Baker, R., and Leshchinsky, D. (2003). Spatial distribution of safety factor: Cohesive vertical cut, International Journal for Numerical and Analytical Methods in Geomechanics, 27:1057-1078.

Baker. R. (1981). Tensile strength, tension cracks, and stability of slopes, Soils and Foundations, 21(2): 1-17.

Gofar, N., Min, L. L., and Asof, M. (2006). Transient seepage and slope stability analysis for rainfall-induced landslide: a case study, Malaysian Journal of Civil Engineering, 18(1): 1-13.

Hu, S. (2000). Reliability of slope stability considering infiltration through surface cracks, Master's Thesis, Hong Kong University of Science and Technology.

Janbu, N. (1968). Slope stability computations, Soil Mechanics and Foundation Engineering Report, Technical University of Norway, Trondheim.

Kutschke, W.G., and Vallejo, L. (2011). Stability and impacts of unsupported vertical cuts in stiff clay, Geo-Frontiers Congress 2011: 3619-3628.

Lee, F.-H., Lo, K.-W., and Lee, S-L. (1988). Tension crack development in soils, Journal of Geotechnical Engineering, 114(8): 915-929.

Li, B., Zhang, F., and Want, D. (2018). Impact of crack on stability of slope with linearly increasing undrained strength, Mathematical Problems in Engineering, 2018(1096513): 1-11.

Michalowski, R.L. (2013). Stability assessment of slopes with cracks using limit analysis, Canadian Geotechnical Journal, 50(10): 1011-1021.

OSHA. Excavations: Hazard Recognition in Trenching and Shoring. OSHA Technical Manual, Section V, Chapter 2, Washington, DC: U.S. Department of Labor, Occupational Safety and Health Administration, https://www.osha.gov/dts/osta/otm/otm_v/otm_v_2.html (Accessed in July 26, 2019).

Pufahl, D.E., Fredlund, D.G., and Rahardjo, H. (1983). Lateral earth pressures in expansive clay soils, Canadian Geotechnical Journal, 20(2): 228–241.

Richard, A. (2018). Estimating the critical height of unsupported trenches in unsaturated soil, Master's thesis, University of New Brunswick, Canada.

Spencer, E. (1968). Effect of tension on stability of embankment, ASCE, 94 SM 5: 1159-1173.

Taylor, D.W. (1948). Fundamental of soil mechanics, Wiley and Sons, New York.

Vanapalli, S.K., Fredlund, D.G., Pufahl, D.E. and Clifton, A.W. (1996). Model for the prediction of shear strength with respect to soil suction, Canadian Geotechnical Journal, 33(3): 379-392.

Wang, Z.F., Li, J.H., and Zhang, L.M. (2012). Influence of cracks on the stability of a cracked soil slope, In Proceeding of the 5th Asia-Pacific Conference on Unsaturated Soils, Pattaya, Thailand, 2: 594-600.

Whenham, V., Vos, M.D., Legrand, C., Charlier, R., Maertens, J., and Verbrugge, J.C. (2007). Influence of Soil Suction on Trench Stability, In Experimental Unsaturated Soil Mechanics, Springer Berlin Heidelberg: 495-501.

The Relationship of Landslide Initiation and Rainfall Thresholds in South-East Queensland

T. Abeykoon, C. Gallage, J. Murray
School of Civil and Environmental Engineering, Faculty of Engineering, Queensland University of Technology, Australia

J. Trofimovs
School of Earth and Atmospheric Sciences, Faculty of Science, Queensland University of Technology, Australia

ABSTRACT: Empirical rainfall thresholds are used to predict the possible occurrences of rainfall-induced shallow landslides. However, the reliability and the accuracy of thresholds need to be adequately validated prior to adopting them in operational warning systems. This study aims to develop empirical rainfall thresholds for the initiation of shallow landslides in South-East Queensland (SEQ), Australia, as the rainfall causes sediment-related disasters annually in SEQ. This paper presents an examination of 104 rainfall-induced shallow landslides that occurred during 1974-2018. The corresponding rainfall conditions were analysed objectively from rainfall data to derive the thresholds using the quantile regression method separating rainfall events by the absence of rainfall for 24 h. Further, the developed I-D threshold is validated using the physical-based real-time monitoring system at Maleny, Queensland.

1 INTRODUCTION

Rainfall is considered one of the most significant extrinsic triggers of landslides, especially due to the high frequency of occurrence and the severe threats imposed on lives and properties. Rainfall attributes to the slope instabilities by raising the soil moisture, reducing soil's matric suction and increasing pore water pressure. Therefore, rainfall thresholds are commonly used in predicting potential slope failures, utilising the aforementioned interrelation between rainfall and slope instabilities. (e.g. Aleotti (2004); Baum et al. (2010); Keefer et al. (1987)). Fundamentally rainfall thresholds are defined as the minimum rainfall conditions or parameters potent with initiating a landslide (Guzzetti et al. 2008). In this regard, intensity - duration (I-D), event rainfall - duration (E-D) and antecedent rainfall parameters are widely adopted in predicting rainfall-induced slope failures.

Rainfall-induced landslides are common in South-East Queensland (SEQ). SEQ experience approximately 1050 mm annual rainfall, including around 415 mm average reliable summer rainfall (December - February). Thus most of the extreme rainfall events occurred during the summer period, leading to landslides. Notably, the majority of the Queensland state was declared a disaster zone following torrential rains during the summer of 2010 - 2011(Abbot and Marohasy 2012). Therefore the prediction of rainfall-induced landslides is quite significant for SEQ. However, the relationship between landslide occurrence and rainfall, either in empirical models or in known physical interactions of slope conditions, is still not compellingly studied, and rainfall thresholds are yet to be established. The current study attempts to portray the regional aspect of rainfall threshold for landslide initiation in the SEQ, accounting for previous landslide occurrences in the area. In this regard, 104 landslide events during the period 1974 - 2018 were considered for this study to propose empirical rainfall I-D and antecedent thresholds along with the normalised thresholds for the landslides initiation in SEQ.

2 STUDY AREA

The current study area for the analyses includes the South-East region of the Queensland state. SEQ incorporates eleven (11) local government councils including, the City of Brisbane, City of Gold Coast, Sunshine Coast Region, Moreton Bay Region, Logan City, City of Toowoomba and City of Ipswich (Queensland Government, 2020). Additionally, the Shire of Noosa local government area (870 km^2) was also accounted for the study, which was de-amalgamated from the Sunshine Coast Region on 1st January 2014. SEQ is the most urbanised region in Queensland as it comprises the three largest cities in the state; Brisbane, Gold Coast and Sunshine Coast. SEQ extends for more than 35 000 km^2 and stretches 240 km north-south and 140 km

east-west, accommodating over 3.6 million people, almost 75% of the Queensland state's population. Furthermore, the population density of SEQ is more than 180 times the population density of the remaining parts of Queensland (Queensland Government, 2020). Fig. 1 shows the local government area distribution for the current study.

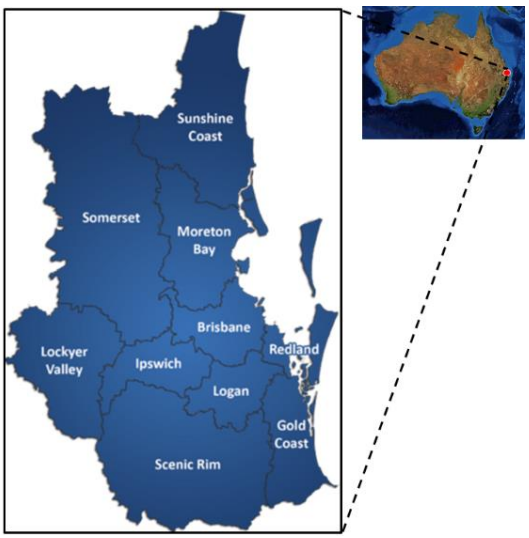

Fig. 1 Study area - SEQ region

3 DATA COLLECTION

3.1 *Landslide data*

Landslides during the period of 1842 - 2018 have been retrieved from the Geoscience Australia landslide dataset, which includes 1974 landslide events across Australia. The database comprises records for each landslide event, including the causes and impacts, event description, date, location, and the source reference. However, since the last update of the dataset in 2018, the database is no longer maintained by Geoscience Australia. The landslide dataset includes 156 landslide events in SEQ. However, certain landslide event records were discarded due to the unavailability of appropriate weather stations nearby and the unavailability of rainfall information. Hence, the number of SEQ landslide events were reduced to 104 events and are depicted as red dots on the map below in Fig. 2.

3.2 *Rainfall data*

The rainfall data were obtained from the Bureau of Meteorology (BOM), Australia, for the analyses. BOM rainfall data include rainfall recordings for every minute, every half-hour and pluviographic information (6-minute recordings).

In order to determine the BOM weather stations corresponding to a particular landslide event, spatial distributions of landslide locations and weather stations were analysed in a geographic information system (GIS). Initially, the distance between each landslide event and each weather station was calculated using Haversine's method. Generally, Haversine method is used to compute the great circle distances between two pairs of coordinates on a sphere, employing corresponding latitude and longitude as the input parameters. However, the use of Haversine approach neglects the effect of ellipsoidal, as the earth can be relatively approximated to an oblate spheroid and also neglects the altitudes of hills and deep valleys on the surface of the earth. In this regard, previous researches highlighted that even with the aforementioned assumptions, Haversine approach produced accurate results (Arifin et al. 2016; Winarno et al. 2017). Hence, based on the above assumptions, the earth was considered a perfect sphere with a mean radius of 6371 km for the calculations.

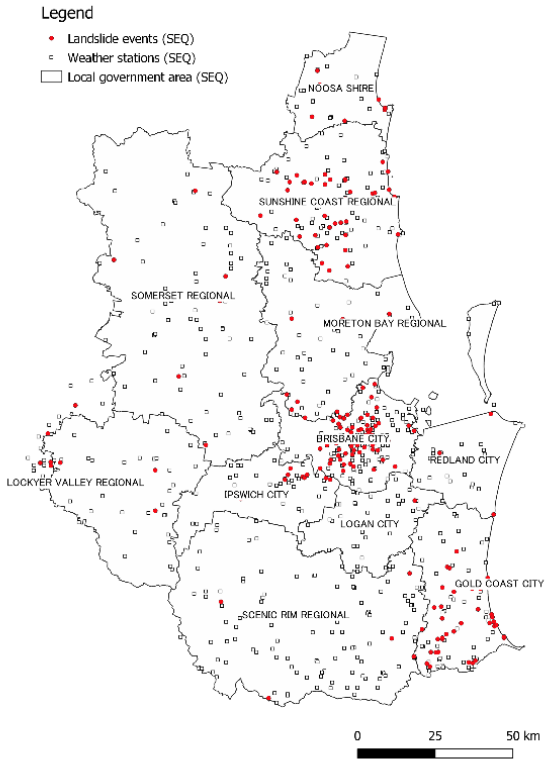

Fig. 2 Map of SEQ landslide event locations

A MATLAB script was employed to determine distances between each landslide event and weather station, correlating all the landslide events with the entire set of weather stations in SEQ that generated a database of over 23 million calculations. Moreover, a logical function was utilised to examine if the landslide event date falls within the weather station operation time period. If there are

weather stations within a 5 km radius from the landslide event, the nearest station was selected for the rainfall threshold calculations. Secondly, if no weather stations are available within a 5 km radius from the event, then the closest three weather stations were selected within a 10 km radius from the event, and data from those three stations were adopted to determine rainfall data corresponds to the event based on an Inverse Distance Weighting (IDW) interpolation, where the distances are inversely weighted relative to the prediction location (Lu & Wong, 2008). As mentioned previously, in the case of the nonexistence of an appropriate weather station within a 10 km radius from the landslide event, the record was discarded from the rainfall threshold calculations.

3.3 *Determination of rainfall I-D thresholds for SEQ*

Based on the collected rainfall and landslides datasets, the average rainfall intensity (mm/h) and the duration from the beginning of the rainfall event to the initiation of the landslide were defined. Additionally, a rainfall event was defined as the rainfall period delimited by a non-rainfall period of 24 h or more. In order to determine the rainfall I-D thresholds objectively, a quantile regression method was used in the form of: $I = a + bD^{-c}$, where I is the intensity measured in millimetres per hour and D is the duration measured in hours (Aleotti 2004; Caine 1980; Guzzetti et al. 2007). The thresholds were determined for the different quantiles (i.e. 2nd, 10th, 50th and 90th). The 2nd percentile quantile was used to determine the rainfall I-D threshold for the SEQ region based on Guzzetti et al. (2007) and Guzzetti et al. (2008). The normalised I-D threshold was be established by dividing the rainfall intensity by the mean annual precipitation (MAP), with the following equation: $I_{MAP} = a + bD^{-c}$. I_{MAP} is the rescaled average per-hour intensity.

For the curve fitting of I-D threshold equations, numerous researchers adopted different methods, including linear or logistic regressions. However, quantile regressions are identified as one of the best curve fitting options in this regard due to the increased accuracy (Saito et al. 2010). Quantile regression provides higher accuracy for cases where the variance may not be uniform within a dataset, as the approach considers the median for each quadrant (Koenker and Hallock 2001). Hence, the quantile regression varies from linear regression, as methods are based on median and mean, respectively (Ford 2015). Therefore, quantile regression is well suited for the current study because the historical rainfall and landslides data might contain some errors. The approach employs quantiles, which are resistant against the outliers and the errors. Further, it produces a better understanding of the relationship between the rainfall intensity and duration values and the occurrence of landslides than compared to other regression models, providing results with greater confidence intervals (Ford, 2015).

The data were analysed utilising the quantile regression package 'quantreg' in RStudio (Koenker and Hallock 2001). As mentioned, 2nd, 10th, 50th and 90th percentiles were determined, and the 50th percentile was employed to determine the general trend of rainfall I-D conditions associated with shallow landslides. The rainfall threshold was determined based on the 2nd percentile. The analyses produced the thresholds equations along with the graphs for rainfall I-D and also for the rescaled I_{MAP} models. The I-D values were plotted on a double logarithmic scale.

4 RESULTS

Fig. 3 presents the rainfall I-D conditions that resulted in shallow landslides in SEQ (circles) and the quantile regression lines for 2nd, 10th, 50th and 90th percentiles in double logarithmic scale. The average intensity values for the related storm event duration ranged from approximately 0.15 mm/h to 13.7 mm/h. The duration considered was approximately 0.3 hours to 383 hours to encompass the rainfall storms for all events.

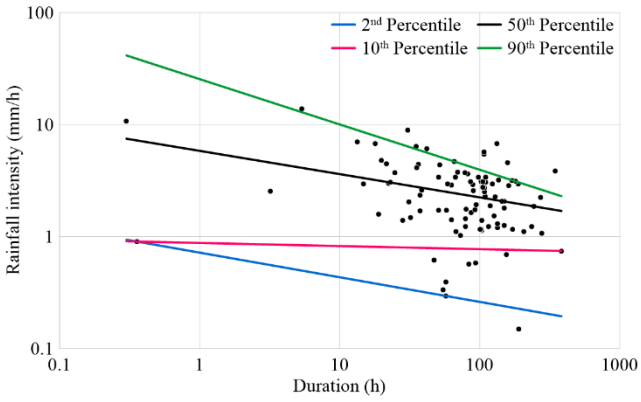

Fig. 3 Rainfall I-D conditions for shallow landslides in SEQ and the quantile regression lines for 2nd, 10th, 50th and 90th percentiles

The thresholds obtained for SEQ are summarised in Table 1 below, presenting the equations of the 2nd,10th, 50th, and 90th percentile regression lines:

Table 1. Rainfall I-D conditions for landslides initiation in SEQ

Quantile	I-D threshold equation
2nd	$I = 0.71940\ D^{-0.22001}$
10th	$I = 0.87787\ D^{-0.02771}$
50th	$I = 5.83257\ D^{-0.20771}$

90th	$I = 25.49060\ D^{-0.40462}$

The 50th percentile regression line shows the trend of the rainfall conditions and landslide initiations in SEQ. The trend is such that with the increasing rainfall duration, the rainfall intensity potential to trigger a slope failure decreases. A similar trend applies to other quantile regression lines, as the exponent (c) ranges from (-0.028) to (-0.405). The I-D threshold for SEQ (2nd percentile regression line) shows that even with rainfall events with shorter durations (i.e. around 5 h) with a rainfall intensity of 13.7 mm/h can initiate a shallow slope failure, while smaller intensities of 0.15 mm/h for longer rainfall durations (i.e. approximately 8 days) also capable of triggering a slope failure.

Similarly, Fig. 4 illustrates the I_{MAP}-D conditions in SEQ, in which the rescaled normalised rainfall intensity ranges from 1.31×10^{-4} to 0.012 h^{-1}. The rescaling has significantly reduced the variations of rainfall intensity leading to lower quantile regression lines.

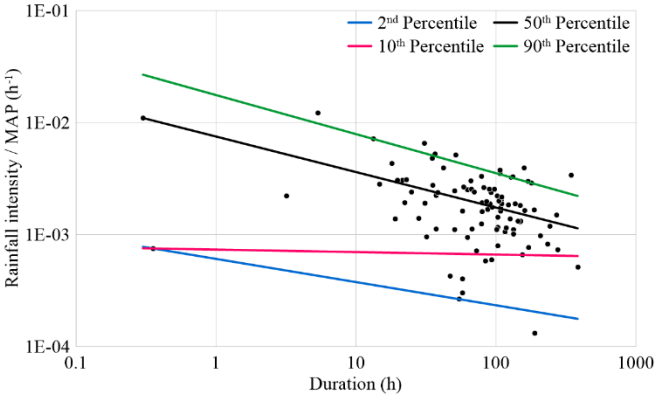

Fig. 4 Rainfall I_{MAP}-D conditions for shallow landslides in SEQ and the quantile regression lines for 2nd, 10th, 50th and 90th percentiles

The rescaled model results are presented in Table 2:

Table 2. Rescaled rainfall I-D conditions for landslides initiation in SEQ

Quantile	I-D threshold equation
2nd	$I_{MAP} = 6.070 \times 10^{-4}\ D^{-0.20713}$
10th	$I_{MAP} = 7.351 \times 10^{-4}\ D^{-0.02215}$
50th	$I_{MAP} = 7.514 \times 10^{-3}\ D^{-0.31719}$
90th	$I_{MAP} = 1.763 \times 10^{-2}\ D^{-0.34876}$

As in rainfall I-D thresholds, considering the 50th percentile regression line, the general trend is that with the increase in rainfall duration, the I_{MAP} decreases. The same trend is followed by the other I_{MAP}-D regression lines as well, ranging the exponent (c) from (-0.222) to (-0.349). Moreover, the I_{MAP} threshold depicts that the rescaled rainfall intensities of 5.22×10^{-5} h^{-1} has the potential of initiating a shallow slope failure.

5 DISCUSSION

Table 3 and 4 show the existing global and regional I-D and I_{MAP}-D thresholds. Fig. 5 and 6 depict the comparison of the SEQ thresholds with the aforementioned existing thresholds.

Table 3. Existing I-D thresholds

Reference	Equation	Duration range (h)
Caine (1980)	$I = 14.82\ D^{-0.39}$	$0.167 < D < 500$
Guzzetti et al. (2008)	$I = 2.20\ D^{-0.44}$	$0.1 < D < 1000$
	$I = 2.28\ D^{-0.20}$	$0.1 < D < 48$
	$I = 0.48\ D^{-0.11}$	$48 \leq D < 1000$
Saito et al. (2010)	$I = 2.18\ D^{-0.26}$	$3 < D < 537$
Ravindran et al. (2019)	$I = 22.6\ D^{-0.554}$	$48 < D < 432$

Note - Caine (1980) and Guzzetti et al. (2008) present global thresholds. Saito et al. (2010) and Ravindran et al. (2019) present the regional thresholds for Japan and Northern New South Wales (NSW), respectively

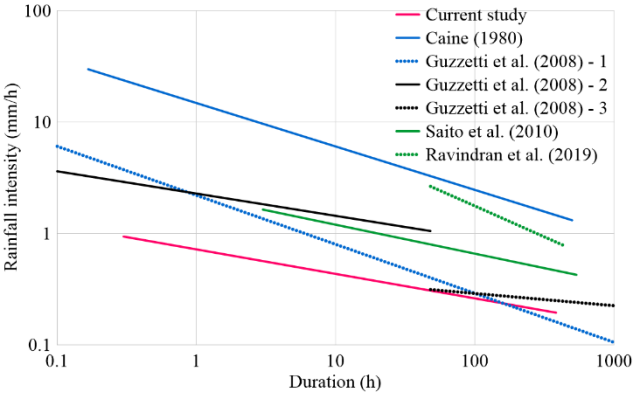

Fig. 5 Comparison of Rainfall I-D conditions for shallow landslides in SEQ with existing thresholds

Table 4. Existing I-D thresholds

Reference	Equation	Duration range (h)
Jibson (1989)	$I_{MAP} = 0.02\ D^{-0.65}$	$0.5 < D < 12$
Guzzetti et al. (2008)	$I_{MAP} = 0.0016\ D^{-0.40}$	$0.1 < D < 1000$
	$I_{MAP} = 0.0017\ D^{-0.13}$	$0.1 < D < 48$
	$I_{MAP} = 0.0005\ D^{-0.13}$	$48 \leq D < 1000$
Saito et al. (2010)	$I_{MAP} = 0.0007\ D^{-0.21}$	$3 < D < 537$

Note - Jibson (1989) and Guzzetti et al. (2008) presented global thresholds. Saito et al. (2010) presents the regional thresholds for Japan

Fig. 5 depicts that the developed I-D threshold for SEQ is lower than the other global and regional I-D thresholds for smaller rainfall durations, especially lower than the threshold of northern NSW of Australia. The difference is more significant for the

shorter rainfall duration and decreases with increasing duration. This is primarily due to the larger dataset used for the study, which includes both small and large-scale rainfall-induced shallow landslides.

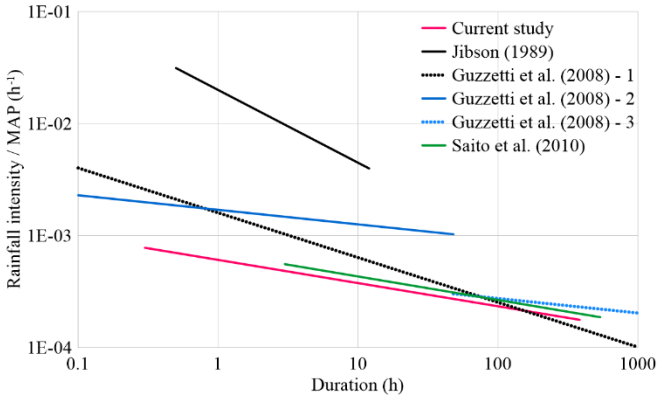

Fig. 6 Comparison of Rainfall I_{MAP}-D conditions for shallow landslides in SEQ with existing thresholds

Similarly, the I_{MAP}-D threshold developed by the study is also lower than the existing normalised thresholds, as illustrated in Fig. 6. The results presented in Fig. 5 and 6 highlight that the rainfall intensity with a potential to trigger a slope failure in SEQ is lower than the general global thresholds for smaller rainfall duration (i.e. < 100 h). Additionally, the stand out fact is that the I_{MAP}-D presented by Saito et al. (2010) for Japan depicts similar behaviour to the I_{MAP}-D threshold developed by the current study. The use of larger datasets and alike climatic setting of Japan and SEQ (i.e. humid and subtropical) may lead to similar rainfall-induced slope failure triggering characteristics.

Initially, it was anticipated that the SEQ threshold of the current study would be similar to the northern NSW study due to the close proximity of the regions. The study in northern NSW yielded a higher threshold of $I = 22.6 \times D^{-0.554}$ than compared to the SEQ result of $I = 5.83 \times D^{-0.208}$. The threshold for the NSW study provides the threshold corresponding to a 50% chance of landslide occurring, and therefore, is compared to the 50th quantile from the SEQ thresholds. The comparison of SEQ and northern NSW thresholds demonstrates the importance of separate models for local regions. Further, the sample size may have been an influencing factor as the northern NSW study considered a small number of events, compared to 100+ events from SEQ.

The methods vary considerably for different studies; therefore, caution needs to be taken when comparing the results. Factors such as quality of landslide and rainfall data should come into consideration as well. Various sources were utilised to compile the landslide database in Australia and may not necessarily be accurate or consistent. The rainfall data had to be carefully reviewed as many weather stations lacked rainfall measurements for some time periods and different rainfall measurement types.

Due to Australia being a sizeable flat continent, it proved difficult to find weather stations near many of the landslide events, even though there are almost 18,000 weather stations in Australia. Many of the landslide events were discarded where stations were not close enough. The optimal method for using rainfall data should be explored in the future.

6 CONCLUSIONS

The empirical I–D thresholds for initiating shallow landslides in SEQ were determined and compared with previously proposed global and regional thresholds. Initially, 156 landslide events in SEQ were considered, but due to the unavailability of the proximate weather stations, the study was limited to 104 rainfall-induced shallow landslides that occurred during 1842-2018. The I–D thresholds were identified quantitatively using the quantile-regression method, which is robust and resistant to errors and outliers. To compare the developed I–D threshold with those of other studies, the threshold was rescaled by dividing rainfall intensity by MAP. The results indicate that rainfall intensity of 0.15 mm/h has the potential to initiate shallow landslides in SEQ, with rainfall duration ranging from 0.3 to 383 h. The developed thresholds were lower than those reported in almost all previous studies, signifying the higher potential of rainfall-induced landslides in SEQ. The low threshold reflects geologic conditions, human interference, and short-intense or gentle-long rainfall events that occur during the summer.

ACKNOWLEDGMENTS

Authors gratefully acknowledge the BOM, Australia, especially Mr Lesley Rowland from Climate Data Services, for kind support in providing required rainfall data for the study. Further, gratitude should be extended to Geoscience Australia for maintaining the landslide database of Australia. The first author acknowledges the scholarship for the doctoral degree received from QUT, Australia.

REFERENCES

Abbot, J., and Marohasy, J. (2012). Application of artificial neural networks to rainfall forecasting in Queensland, Australia. *Advances in Atmospheric Sciences*, 29(4): 717-730.

Aleotti, P. (2004). A warning system for rainfall-induced shallow failures. *Engineering Geology*, 73(3): 247-265.

Arifin, Z., Ibrahim, M. R., and Hatta, H. R. "Nearest tourism site searching using Haversine method." *Proc., 2016 3rd International Conference on Information Technology, Computer, and Electrical Engineering (ICITACEE)*, IEEE, 293-296.

Baum, R. L., Godt, J. W., and Savage, W. Z. (2010). Estimating the timing and location of shallow rainfall-induced landslides using a model for transient, unsaturated infiltration. *Journal of Geophysical Research. Earth Surface*, 115(3).

Caine, N. (1980). The Rainfall Intensity: Duration Control of Shallow Landslides and Debris Flows. *Geografiska Annaler. Series A, Physical Geography*, 62(1/2): 23-27.

Ford, C. (2015). Getting Started with Quantile Regression. *Statistical Research Consultant,'Research Data Services*.

Guzzetti, F., Peruccacci, S., Rossi, M., and Stark, C. P. (2007). Rainfall thresholds for the initiation of landslides in central and southern Europe. *Meteorology and Atmospheric Physics*, 98(3): 239-267.

Guzzetti, F., Peruccacci, S., Rossi, M., and Stark, C. P. (2008). The rainfall intensity-duration control of shallow landslides and debris flows: an update. *Landslides*, 5(1): 3-17.

Jibson, R. W. (1989). Debris flows in southern Puerto Rico. *Landslide processes of the eastern United States and Puerto Rico, Geological Society of America special paper*, 236: 29-55.

Keefer, D. K., Wilson, R. C., Mark, R. K., Brabb, E. E., Brown, W. M., Ellen, S. D., Harp, E. L., Wieczorek, G. F., Alger, C. S., and Zatkin, R. S. (1987). Real-time landslide warning during heavy rainfall. *Science*, 238(4829): 921-925.

Koenker, R., and Hallock, K. F. (2001). Quantile regression. *Journal of economic perspectives*, 15(4): 143-156.

Ravindran, S., Gratchev, I., and Jeng, D.-S. (2019). Analysis of rainfall-induced landslides in northern New South Wales, Australia. *Australian Geomechanics*, 54(4): 85-99.

Saito, H., Nakayama, D., and Matsuyama, H. (2010). Relationship between the initiation of a shallow landslide and rainfall intensity—duration thresholds in Japan. *Geomorphology*, 118(1): 167-175.

Winarno, E., Hadikurniawati, W., and Rosso, R. N. "Location based service for presence system using haversine method." *Proc., 2017 International Conference on Innovative and Creative Information Technology (ICITech)*, IEEE, 1-4.

Evaluation of the Performance of Landslide Mitigation Measures at Ginigahthena

S.O.A.D. Mihira Lakruwan
Graduate School of Engineering, Tohoku University, Japan
National Building Research Organisation, Sri Lanka

S.A.S. Kulathilaka
Department of Civil Engineering, University of Moratuwa, Sri Lanka

ABSTRACT: The extensive road network in the central hilly terrain of Sri Lanka experiences significant variations in elevations leading to criticalroad side slopes. Continuous increase in traffic flow demands the widening of existing roads. Such wideningof roads in hilly terrain requires cutting into the slopes, leading to new landslides or reactivation of ancient landslides. Ancient landslide at bridge no.48/2 on Avissavella – Hatton – Nuwaraeliya road was reactivated with an attempt to cut into the slope at the toefor proposed road widening and propagated further with heavy rainfallthat occurred later. Mitigation of this landslide was done by slope modification, drainage improvement and soil nailing. This paper presents the effectiveness of mitigation measures under a critical rainfall event and highlights the importance of following the correct construction sequence in landslide mitigation works.

1 INTRODUCTION

1.1 *Background*

As a tropical country that experiences two monsoons with heavy precipitation, rainfall is identified as the major triggering factor for landslides in Sri Lanka. Rain-induced landslidesare asignificant challenge faced by the Engineers in infrastructure developments in the hilly terrain of the country, which has a highly variable topography. Road network that traverses through hilly terrain experience significant elevation variations. In order to cater to the demand of increasing traffic due to the economic development and population growth, it is necessary to widen the existing roads. Those road wideningrequires excavation into the slope in the hilly terrain.

Avissawella – Hatton - Nuwaraeliyaroad near Ginigathhenaneeds to be widened at the bridge no. 48/2. The critically stable ancient landslide,which was on the upper slope of the bridge,got reactivated with the attempt to excavate into the slope at the toe for the said widening. This landslide was stabilized by extensive mitigation measuresconsidering the social, economic and environmental importance.

Drainage improvement, slope modification and reinforcement by soil nailing were used as the mitigation measures. This study was done to illustrate the importance & effectiveness of the drainage improvement, requirement of combined mitigation measures and necessity of adopting staged construction with appropriate construction sequence.

1.2 *Background Knowledge*

Ratnayake &Herath(2005) reported thatduring the past few decades, rain-induced landslides have become a major natural disaster in Sri Lanka.

Slopes in Sri Lanka are formed of residual soils,rocks of different levels of weathering and parent metamorphic rock. Colluvial soils-the product of ancient landslide are also present. Response of those slopes to rainfall is very complicated due highly heterogeneous nature with abrupt variations.

Careful idealization of those slopes preceded by a detailed investigation is required to evaluate the response of such slopes to rainfall. Many changes to the initial subsurface model may have to be implemented with new evidence found during the construction stages. The thrust of the analysis is in modelling the infiltration of rainfall and effects of drainage measures in a soil profile with contrasting permeability characteristics.

Mitigation measures are to be applied on slopeswhen the required safety margins cannot be maintained during critical conditions. Since the loss of matric suction and increase of pore water pressures is the major issue in rain-induced landslides, drainage improvementsare used as the primary mitigation measure. When the required

safety margins cannot be maintained by drainage improvementalone other structural mitigation measures such as;toe gravity retaining structures, embedded retaining structures, slope reinforcements etc are used. Slope reinforcing by soil nailing is most widely adopted for steep high slopes speciallywhen there are restrictions in space.

Target Factor of Safety (FoS) values are recommended for slopes considering various risk factors. GEO Hong Kong (1984) recommended a FoS 1.2 for low risk and 1.4 for high risk slopes. Federal Highway Administration (2006) recommended the lowest FoS of 1.25 for highway embankments. Considering the critical condition and devastating impact of failure following values were established as the targetFoS values in the design for the rectification of this Ginigathhena landslide.

- Short term stability during construction– 1.1
- Long term stability in-service condition– 1.3

This paper presents the construction sequence adopted ensuring that a sufficient safety margin prevailsat all stages of construction. It also illustrates that the rectified slope can withstand a critical design rainfall that is likely to occur in the area ensuring that target safety margins prevail at all times.

2 GINIGATHHENA LANDSLIDE

2.1 *Background*

Sri Lanka has an extensive road network connecting regional cities to the capital Colombo and to each other. Avissavella – Hatton – NuwaraEliya road is a major connection road to the central region of the country. Bridge No. 48/2 on this road atGinigathhenaat an elevation of 470 m above MSL, is very narrow where two vehicles cannot be passed by. The traffic demand on the said road is increasing rapidly with economic and population growth in the area. Based on that high demand, the bridge and the road were proposed to be widened. Some excavation was done at the toe of the upper slope of the bridge to initiate the widening the bridge. Ancient landslide above the bridge got reactivated with this toe excavation, and the failure propagated to the upper slope. It was reported that there was no rain at the time of the initial failure. With the occurrence of rainfall in the area later, failure propagated further. Fig. 1&Fig. 2show the location map of the area and failure just after the rainfall event, respectively.

Fig. 1 Location map of the area

Fig. 2 Failure just after the rainfall event

2.2 *Preliminary investigation*

During the preliminary investigation, it was identified that the area under consideration is covered with a thick Colluvium deposits with boulders, which had been transported from an ancient landslide. Colluviumsoil mass is underlain by highly crystalline metamorphic bedrock.The waterlogged marshy area located at the top of the landslide mass is identified as the main reason for the prevailing high water table in the area. Water collected in the upper slope is flowing through the water stream by a side of the landslide.

With the high groundwater table of the area, the slope was already in a critical stable condition, and with the removal of the toe support by the excavation, the slope became unstable reactivating the ancient landslide. After the failure, the unstable soil mass was supported by the bridge structure and there was a possibility of further activation of this landslide as a deep-seated failure with further rainfall. This could have lead to a catastrophic failure damaging the bridge and the road. Also, there was the need for widening the bridge and the road. Therefore, it was decided to mitigate this landslide while accommodating the requirement of road and bridge widening.

2.3 *Detail investigation*

Followed by the decision to mitigate the landslide, a detailed investigation comprising a topographical survey and a geotechnical investigation was conducted. The topographical survey produced a contour map of 1 m interval and slope cross-sections. Under the geotechnical investigation, three boreholes were advanced with SPT at regular intervals and laboratory testing on recovered undisturbed samples. The survey map with contours and the subsoil profile from the geotechnical investigation are presented inFig. 3 and Fig. 4,respectively.

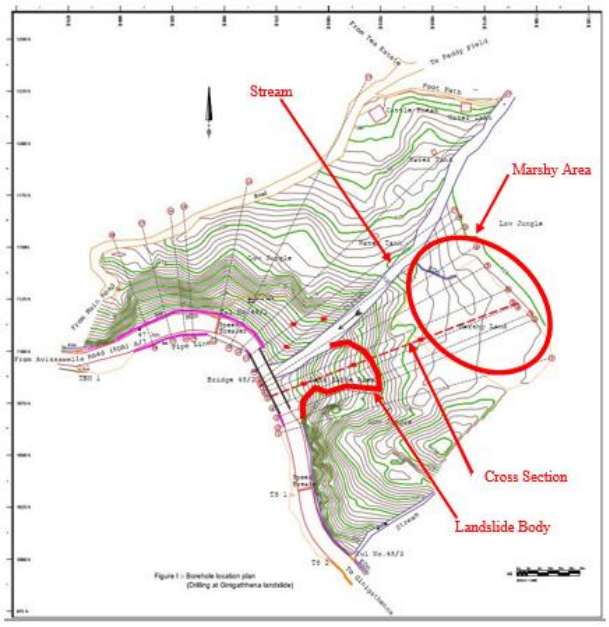

Fig. 3 Survey map of the area

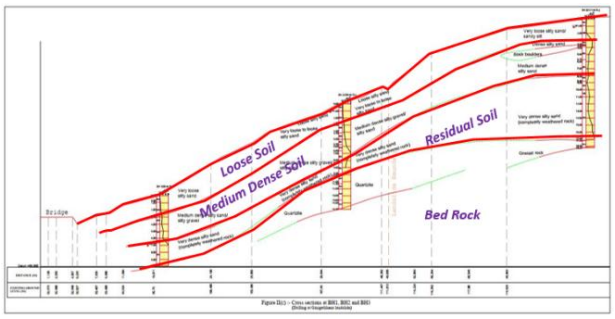

Fig. 4 Subsoil profile

2.4 *Mitigation measures*

Based on the investigation results, mitigation measures for the Ginigathhena landslide were designed focusing on three main categories as; drainage improvement, ground modifications and reinforcement. Surface drainage improvement was achieved by the cut-off drains, berm drains, trench drains & slope covering by vegetation. The subsurface drainage improvement was achieved by sub horizontal gravity drains.

The proposed road widening requires cutting into the slope at the toe region. Since the required safety margin of this reshaped slope couldn`t be achieved only by the drainage improvement, reinforcements in the form of soil nailing were used to maintain an adequate safety margin of the slope. After several trials, stability of the slope was achieved by the nailing pattern presented inFig. 5 whichincludes;

- 5 nos. of 16 m long soil nails
- 2 nos. of 12 m long soil nails
- 4 nos. of 8 m long soil nails

All soil nails were installed in 2.0 m spacing in the horizontal direction and 2.5 m spacing in the vertical direction.

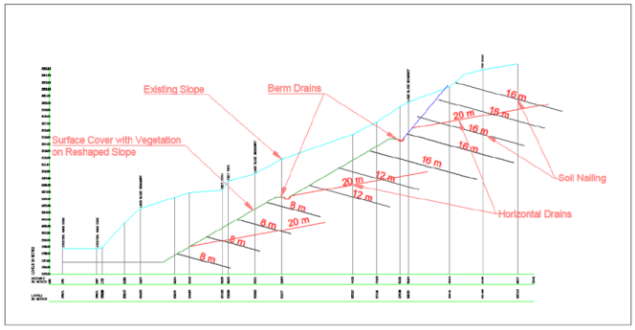

Fig. 5 Cross-section of mitigation measures

2.5 *Monitoring*

During the application of mitigation measures, a field monitoring scheme was established to monitor the behavior of the slope with mitigation measures. This monitoring system consisted of;

- Rainfall monitoring,
- Groundwater level monitoring and,
- Slope movement monitoring.

A manual rain gauge was used for monitoring the rainfall, and it was checked twice a day. Two observation wells were installed at the crest area of the slope to monitor the groundwater level. Slope movement monitoring was done by a number of fixed points established on the slope surface.

3 METHODOLOGY

3.1 *Overview*

The following steps were followed to achieve the objectives of the study.

I. Development of computer models
II. Defining critical rainfall event
III. Defining construction stages
IV. Analysis against critical rainfall
V. Evaluate stability of the slope in different construction stages

3.2 *Development of computer model*

GeoStudio software package was used for the analysis. SEEP/W (GEO-SLOPE International Ltd., 2017a)& SLOPE/W (GEO-SLOPE International Ltd., 2017b)modelsdeveloped based on the results of the geotechnical investigation were used for seepage and stability analyses, respectively. Verification of the SLOPE/W model was done by simulating the failure occurred after toe excavation. SEEP/W model was verified by simulating an actual rainfall event of 20 days on the model and comparing the resultant groundwater level from the model with actual groundwater levels obtained from the monitoring. Verification of the models are not discussed in detailed in this paper.

Surface drainage improvement was modeled on the SEEP/W analysis by applying a thin soil layer of very low permeability onto the slope surface. In the modeling of subsurface drains, horizontal drains installed at some horizontal spacing were idealized into plain strain condition by a zero pressure boundary condition applied on to a line of the same length, location and orientation as the actual drain.Fig. 6 presents the SEEP/W model with hydraulic boundary conditions, material properties and initial ground water table obtained from monitoring.

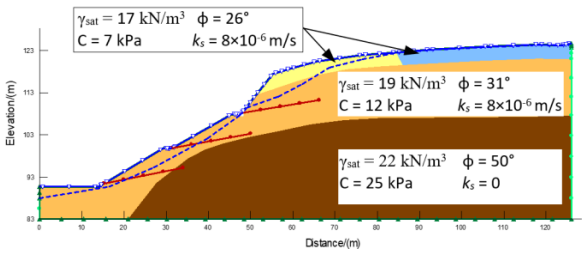

Fig. 6 Slope model with material properties and initial water table (for construction stage 3)

3.3 *Design critical rainfall event*

Since the peak rainfall observed during the monitoring period is 300 mm/day, two days of 300 mm/day rainfall was selected as the critical design rainfall and followed it by a 50 mm/day residual rainfall forseven days. A five day long dry period precededthe rainfall event (Fig. 7).

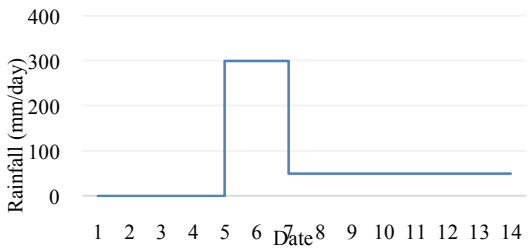

Fig. 7 Design critical rainfall event

3.4 *Construction stages*

To ensure stability at all stages a top down construction sequence has to be adopted with following construction stages.

- Stage 1 – excavation up to top berm level, soil nailing and application of drainage measures (Fig. 8)
- Stage 2 – excavation up to middle berm level, soil nailing and application of drainage measures (Fig. 9)
- Stage 3 – fully excavation, soil nailing and application of drainage measures (Fig. 10)

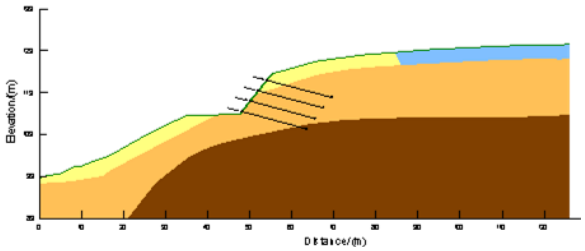

Fig. 8 Construction Stage 1

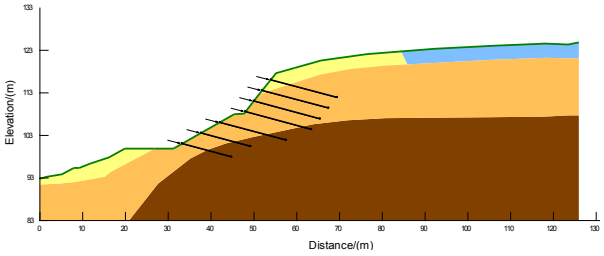

Fig. 9 Construction Stage 2

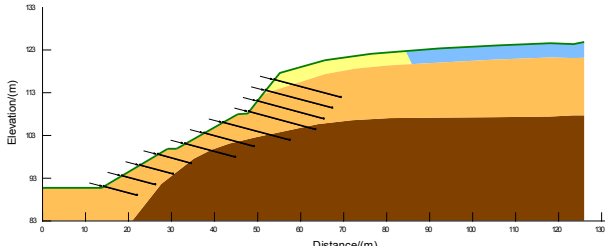

Fig. 10 Construction Stage 3

3.5 *Analysis against critical rainfall*

The implemented rectification comprised of; surface drains, sub surface drains and soil nailing. To illustrate the importance of these different measures, the effect of their different combinations was analyzed.

Accordingly, three alternative drainage improvement conditionsnamely;*"No Drains"*, *"Only Surface Drains"*and*"Both Surface and Subsurface Drains"* were analyzed for *"With Nails"* and *"Without Nails"* conditions. The ability of the slope to withstand the critical design rainfall under different rectification combinations stated above was analyzed. Results of SEEP/W analysis for the

threedrainage conditions were incorporated into the SLOPE/W analysis for the two reinforcement conditions. Consequently, daily variation of the minimum FoS value under the design rainfall event was calculated. Effective shear strength parameters shown in the Fig. 6 were used for the analysis.

4 RESULTS AND DISCUSSION

4.1 *Stability against critical rainfall*

Fig. 11 presents the variation of FoS value under thedesign rainfall event for different rectification measuresat Construction Stage 3.

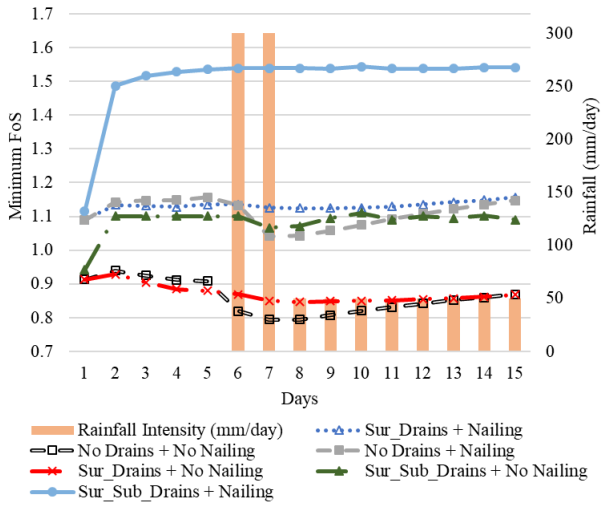

Fig. 11FoS with design critical rainfall

During the first four days, which is the dry period, FoS has slightly increased in both *"No Drains"* and *"Only Surface Drains"* conditions with the presence of soil nailing. Variation is almost similar for both cases. Surface drains are effective in directing the rainwater away from the slope minimizing the infiltration. As such, surface drains will not have any influence without rainfall. When the subsurface drainage improvement is applied,FoS has rapidly increased and maintained at a higher value. This is due to the effect of subsurface drains to drain out the water already in the slope. When nails are not applied,FoS slightly reduces after an initial increment, during the dry period in *"No Drains"* and *"Only Surface Drains"* conditions. Increase in the pore pressures close to the toe region due to the downward seepage within the soil, even during the dry period, maybe the reason for this.

When the peak rainfall is applied, FoS is significantly reduced in the *"No Drains"* condition. For *"Only Surface Drains"* condition, FoS gradually reduced when nails are not applied, and FoS maintained at the same value when nails are applied. The reduction of FoS is significantly lesser when subsurface drains are also in place.

FoS again increases with the residual rainfall for *"No Drains"* and *"Only Surface Drains"* condition. When subsurface drains are in place, only a slight increase in the FoS is observed during residual rainfall as there is not much reduction of FoS during peak rainfall.

These results imply that the surface drainage improvement slightly increases the FoS of the slope, and with the combination of surface and subsurface drainage, there is a considerable improvement of the FoS. Further, the application of reinforcement has significantly improved the FoS of all drainage conditions.

It should be noted that without nailing,FoS is less than unity at the initial stage, and it increases above the unity only when subsurface drains are applied.Also, the long term stability requirement (FoS> 1.3) is maintained only when surface and subsurface drainage improvements are applied with the soil nails. Also, the short term stability requirement (FoS> 1.1) can only be achieved by the combination of soil nailing with any drainage improvement.

The most significant feature is that the minimum FoS is in the same range for both "nailing with surface drain only" and "surface and subsurface drainage improvement without nailing" conditions. That highlights the importance of the subsurface drainage improvement when the soil nailing technique is applied. Two techniques are complimentary.However, range of FoSvalues corresponding to these two cases (1.05-1.15) is not acceptable.

4.2 *Importance of construction sequence*

The stability of the slope at each construction stage was analyzed for alternative drainage and nailing conditions under design rainfall, and minimum FoS values were obtained. Fig. 12 presents the variation of the minimumFoS values at each stage, corresponding to different drainage and reinforcement conditions under design rainfall event.The minimum FoS values have been obtained omitting theFoS value of Day 1, because the effect of the respective drainage measures had not been accounted by the SEEP/W analysis on Day 1.

The minimum FoS values are always less than 1.1 when the soil nails are not applied. Also, it is less than unity for the *"No Drains"* and *"Only Surface Drains"* conditions.Since at least a FoS value of 1.1 is required in short term stability, soil nails are required to maintain the stability of the slope during construction. Therefore, soil nails should be applied with the excavation adopting top down approach. If the slope is soil nailed in Stage 1, minimum FoS is always above 1.3.

At Stage 2,theminimum FoS is lowered below 1.1 when nails are applied without drainage measures. Therefore, top down approach along with drainage measures must be adopted in excavation and soil nailing in order to maintain the stability of the slope at Stage 2 during construction.

At Stage 3, the minimum FoS is below 1.1, implying an unstable slope when nails are not being applied and nails are being applied without drainage measures. Therefore, top down approach along with drainage improvement must be adopted in excavation and soil nailing in order to maintain the stability of the slope at Stage 3.

Therefore, the short term stability requirement can be achieved only through applying soil nails together with drainage improvement adopting the top down approach in stage construction.

The complementary nature of the two stabilization techniques was well illustrated by the analysis. The combination of two techniques to achieve the most economical rectification design was discussed in Lakruwan & Kulathilaka (2021)

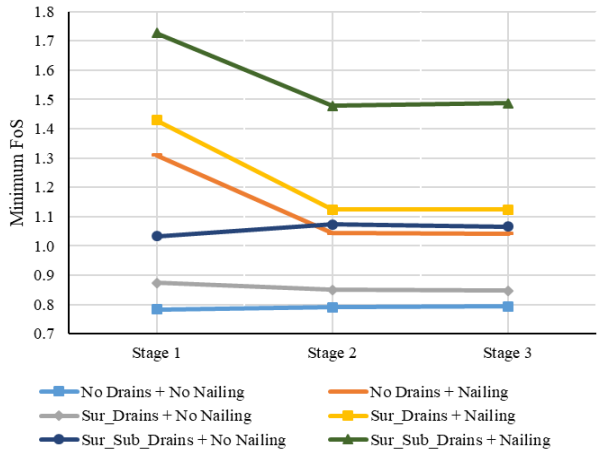

Fig. 12 Minimum FoS values at each stage

5 CONCLUSIONS

During the past few decades, rain-induced landslides have become a major natural disaster in Sri Lanka. It is a major challenge faced by the Engineers in infrastructure developments in the central hilly terrain of the country. Road widening to accommodate the increasing traffichas lead to many slope instabilities including reactivation of ancient landslides.

The failure that occurred at bridge no. 48/2 on Avissavella – Hatton – Nuwaraeliya road near Ginigathhena area was a reactivation of an ancient landslide due to excavation at the toe. This propagated further with subsequent rainfall. The landslide was mitigated using extensive measures.As in any rain-induced landslide, drainage improvement was done as the primary mitigation measure. Slope modification was done to accommodate required road widening. Since the required safety margins of the reshaped slope couldn't be achieved only by drainage improvements, soil nailing was done to enhance the stability of the slope up to the required level.

Evaluation of the performance of the design mitigation measure against critical rainfall is very important. Performance of the mitigation measures of the Ginigathhena landslide was evaluated against a design critical rainfall, which was derived based on the monitoring data.

Results showed that surface drainage improvement enhanced the stability of the slope slightly. Subsurface drainage improvement gave a significant improvement to the slope stability. However, to maintain the long term stability requirement, soil nailing had to be applied together with surface and subsurface drainage improvements.

Adopting the correct construction sequence is very important in landslide mitigation projects to ensure that no failures will take place during construction. Stage construction and adopting top down approach together with drainage improvement is vital in soil nailing constructions.

6 REFERENCES

Cruden, D., 1991. A simple definition of a landslide. Bulletin of the International Association of Engineering Geology, Volume 43, pp. 27-29.

Federal Highway Administration, 2006. Soils and Foundations, Reference Manual.. Washington, D.C.: National Highway Institute, U.S. Department of Transportation, Federal Highwal Administration.

GEO, Hong Kong, 1984. Geotechnical Manual for Slopes. Hong Kong: Civil Engineering and Development Department, The Government of the Hong Kong Special Administrative Region.

GEO-SLOPE International Ltd., 2017. Heat and mass transfer modeling with GeoStudio 2018, Calgary, Alberta, Canada: GEOSLOPE International Ltd..

GEO-SLOPE International Ltd., 2017. Stability Modeling with GeoStudio, Calgary, Alberta, Canada: GEO-SLOPE International Ltd..

Mihira Lakruwan S O A D, Kulathilaka S A S, (2021) Economizing Soil Nailing Design by Drainage Improvement - Case History at Ginigathhena, *World Landslide Forum5 (Understanding and Reducing Landslide Disaster Risk)* pp 331-340

Ratnayake, U. & Herath, S., 2005. Changing rainfall and its impact on landslides in Sri Lanka. Journal of Mountain Science, 2(3), pp. 218-224.

Stability Assessment of a Bio-Engineered Slope in Western Thailand

K. Rajamanthri
Department of Civil Engineering, Kasetsart University, Bangkok, Thailand

A. Jotisankasa
Department of Civil Engineering, Kasetsart University, Bangkok, Thailand

ABSTRACT: This paper aims to investigate the influence of vetiver grass (*Chrysopogon zizanioides*) on bio-engineered soil slope in Thailand. Slope stability and seepage analysis have been conducted to study the behavior of the vegetated slope using the data obtained from samples collected from the site. Results of the laboratory experiments are incorporated into numerical models to evaluate the response of the slope under different climatic conditions. In this study, finite element approach was used to analyze the infiltration behavior of the slope and limit equilibrium method was used for slope stability assessment. Further a parametric study was carried out to identify the most effective location of the slope to have vegetation in order to enhance the stability. When slope area was covered by vegetation, it maintained the highest safety margin and it was about 33 % increase compared to the bare slope. Further, after the four-day infiltration event the slope with its entire slope surface area protected with vegetation possessed the highest safety margins and the percentage variation of the safety margins was observed to be only 24%.

Keywords: slope stabilization, vetiver, root zone, root reinforcement, slope stability, infiltration analysis

1 INTRODUCTION

Rain induced shallow slope instabilities and soil erosion caused by runoff are frequent geotechnical problems that the engineers have to confront with especially in tropical climatic regions (Jotisankasa et al., 2014; Rahardjo et al., 2017; Rajamanthri et al., 2021). Thus, geotechnical experts have developed different structural measures to rectify such problems. Nowadays, use of soil bioengineering approaches for slope rectification are becoming popular due to its comparatively low cost, aesthetic beauty it adds to the slope, minimum disturbance to the slope, less maintenance in the long term, as well as sustainability when compared with commonly used structural mitigation methods (Wu et al., 1979; Coppin and Richards, 1990; Jotisankasa et al., 2014).

When selecting vegetation for slope rectification measures due consideration should be paid to their properties as they have a direct impact on the slope-behaviour in both short and long run (Coppin and Richards, 1990). As a result in Thailand extensive researches have been conducted on Vetiver grass (*Chrysopogon zizanioides*) to understand its different impacts on soil properties, when used as a slope stabilization and erosion control measure (Jotisankasa et al., 2014; Nguyen et al., 2018; Rajamanthri et al., 2021). Normally vetiver planted as hedgerows along slope contours and vetiver system has wide range of applications in soil bio engineering such as soil water conservation, slope stabilization by root reinforcement, erosion control and sediment trap since vetiver roots penetrate as deep as 3-4 meter. (Truong et al., 2008). However, contribution of vetiver grass towards different soil bio engineering applications is essentially a function of its properties, namely plant age and root biomass (Leung et al., 2018; Rajamanthri et al., 2021).

In this study, effectiveness of vetiver grass in maintaining the stability of a slope has been investigated. Further an infiltration analysis has been coupled with a stability analysis to study the response of bio-engineered slope to an infiltration event, with incorporating the soil properties obtained from undisturbed samples collected from the site. Numerical analysis was further extended to study the spatial distribution of the vegetation in a slope in enhancing stability.

2 STUDY AREA AND SOIL PROFILE

The study area is located in Kanchanaburi province, in Western Thailand (Fig. 1). The slope of interest (Ithong 1) suffered from a mass movement and erosion in 2006. This slope was rectified using geosynthetic reinforced soil (GRS) wall together with vetiver vegetation (Fig. 2) nearly two years ago. Accordingly, the plant age of the vetiver at the time of sampling was about 600 days. The average inclination angle of the slope was about 35°.

Sampling was carried out in both disturbed (using hand augers) and undisturbed (using a thin-wall tube sampler) form.

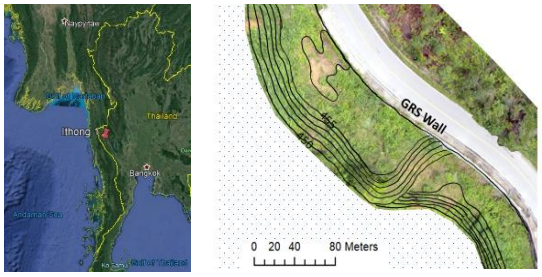

Fig. 1: Location of Ithong 1 site (contours are shown only in soil bio-engineered slope area) (Rajamanthri et al., 2021)

Undisturbed samples were collected from two different depths as shown in the Fig. 2, (Upper layer (U): 0-15 cm and lower layer (L): 15-25 cm) and three samples were obtained from each layer. One sample was collected underneath the root zone (R) and two samples were collected 20 cm away from the vetiver plant in upslope (A) and downslope (B) direction from both upper and lower layers (Fig. 2). The locations of undisturbed samples were selected in order to represent the differently grown root conditions. Further, disturbed samples were used to determine the basic soil properties (Table 1) and according to the unified soil classification system (USCS), the soil at Ithong 1 site was classified as poorly graded silty sand (SP-SM).

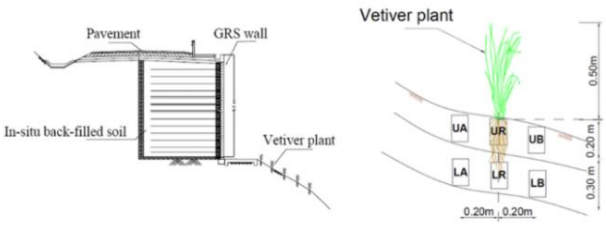

Fig. 2: Schematic diagram for sampling location (Rajamanthri et al., 2021)

2.1 *Derivation of surface and subsoil properties*

The modeled slope cross section was derived based on the ground survey data and UAV photogrammetry (Fig. 3). As per the basic soil property tests conducted subsoil profile was formed of sandy soils (Table 1), which further sub-divided into three layers, namely top soil, soil 1 and soil 2 considering the results of the in-situ Kunzelstab test.

Table 2 summarizes the material properties assigned for different soil layers. Shear strength parameters were assigned based on the in-situ Kunzelstab test results (KPT-N values). The shear strength properties of vetiver root zones were determined based on the findings of Mahannopkul and Jotisankasa, 2019. Further, unsaturated soil strength parameter (i.e. ϕ^b) was assigned for each layer as a function from soil water retention curves (SWRCs) which will be explained in forthcoming section.

Table 1. Summary of basic soil properties (Rajamanthri et al., 2021)

Soil Properties		Ithong 1
Grain size distribution (%)		
Gravel (%)	(>4.75 mm)	27.90
Sand (%)	(4.75-0.074 mm)	63.60
Silt (%)	(0.075-0.002 mm)	5.47
Clay (%)	(<0.002 mm)	3.00
Specific gravity, G_s		2.72
Atterberg's limits		
Liquid Limit (%)		22.90
Plasticity Index (PI)		2.91
Shrinkage limit (SL) %		2.65
USCS		SP-SM

Table 2. Assigned material properties for slope stability

Material	γ_{moist} (kN/m^3)	$c' + c^r$ (kPa)	ø' deg.
Top soil	17.6	0.1	29.7
Soil 1	18.4	2.5	31.9
Soil 2	20.4	4.0	33.0
Vetiver root zone	18.0**	51.4*	32.0**

Source * Mahannopkul and Jotisankasa, 2019
** Jotisankasa et al., 2014

2.2 *Assessment of the stability of the slopes*

Stability of the slope was assessed using the cross sections obtained with using the soil properties determined from laboratory experiments conducted and data reported in the literature for similar studies. During the stability analysis, the actual slope conditions were simulated under case 4 and the analysis was further extended to three other cases (Fig. 4) distinguished based on the location of the vegetation in the slope, to investigate the different responses of the slope in terms of stability. The results obtained for the actual case (i.e. case 4) and for three other parametric cases are presented in the subsequent sections. The general limit equilibrium approach in Slope/W module was used to obtain the factor of safety (FoS) values as shown in Table 3. In this case, initial ground water table is

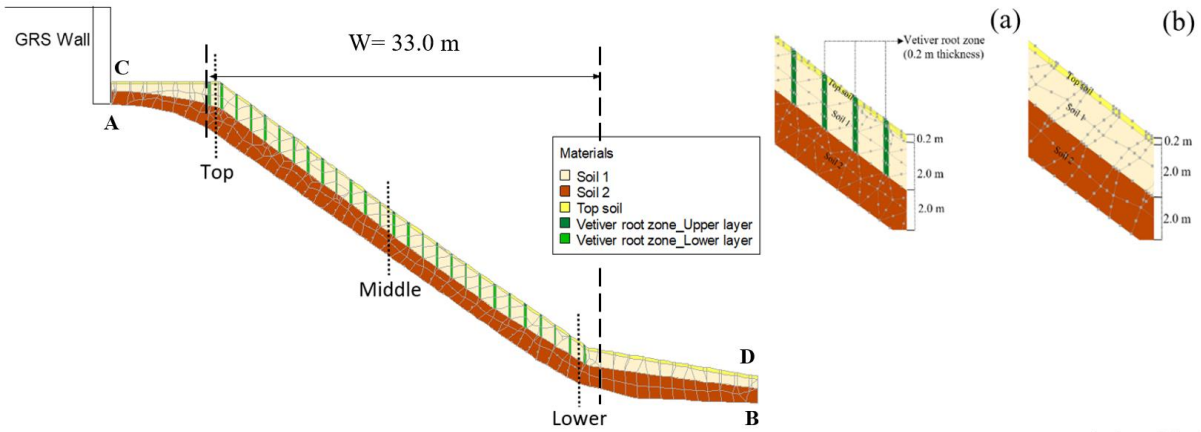

Fig 3. Geometry of the slope idealized for stability analysis (a) with vetiver (b) without vetiver

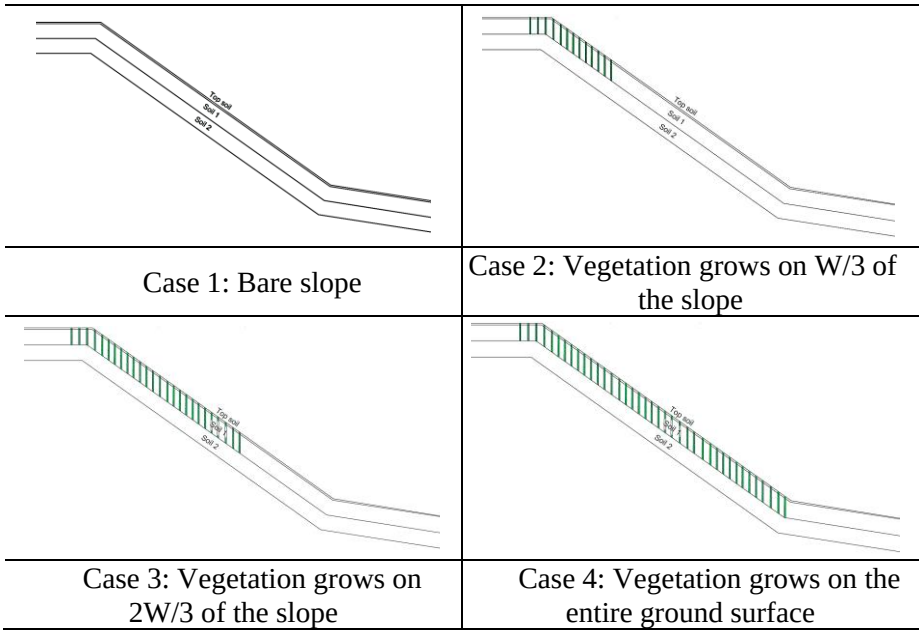

Fig 4. Vegetated slopes with different locations of root zone

assumed to be present at the bottom boundary of soil 2 (along A-B) (Fig. 3).

Table 3. Percentage variation of FoS values

Case	FoS	Variation of FoS (%)
1	1.36	-
2	1.74	20.11
3	2.03	31.53
4	2.06	32.52

It is noted that, the slope without vetiver grass has the lowest FoS value of 1.36. The highest FoS values were observed when the entire slope surface was grown by vetiver (i.e. case 4). The FoS values for case 3 and case 4 were in close agreement where 2.03 and 2.06 have been recorded (32% increase compared to the bare slope). Variation of the FoS under different cases

Variation of FoS = (1)

$$\frac{F_{i+1} - F_1}{F_1}$$

Where F_1 is the FoS value for the bare slope and F_{i+1} is the FoS value for cases considered (i=1, 2 and 3).

As per the analysis slope has a minimum positive impact by the vegetation in terms of stability when the vegetation is at the top (case 2) of the slope. The FoS value for case 2 is 1.74 which is only a 20% increase compared to that of the bare slope. Despite the vegetation coverage of only one-third the entire slope length (case 2), the increase in factor of safety due to vegetation becomes as high as 20% as compared to the bare slope case. This range of increase in FoS could be enough to prevent slope failure near the toe of GRS wall that could jeopardize its overall stability.

3 TWO-DIMENSIONAL INFILTRATION AND STABILITY ANALYSIS

In this section, variation of the pore water pressure regime of the actual bio-engineered soil slope and the parametric slopes with respect to an infiltration event of 86.4 mm/day for continuous four days, were investigated. Finite element seepage analysis of bio-engineered slope was conducted using Seep/W module in GeoStudio software, which was based on Richard's and continuity equation as described by Eq. 2.

$$\frac{\partial}{\partial x}\left[k_x \frac{\partial h}{\partial x}\right] + \frac{\partial}{\partial x}\left[k_y \frac{\partial h}{\partial x}\right] + Q = m_w \left[\frac{\partial u_w}{\partial x}\right] \quad (2)$$

Where, k_x and k_y are the permeability in x and y direction respectively, h defines as total hydraulic head, Q is the applied boundary flux or rainfall, u_w is the pore water pressure, and m_w is gradient of the soil-water characteristic curve.

3.1 *Soil properties used in seepage analysis*

Basic soil properties and functions required for seepage analysis were established through laboratory experiments and using the relationships proposed in the literature.

3.1.1 Soil water retention curves (SWRCs)

SWRCs were obtained from the undisturbed soil samples obtained from the bio-engineered soil slopes. Fig. 5 shows the experimental setup and testing procedure for measurement of SWRC which is based on the finding of Jotisankasa et al., 2010.

The soil samples were gradually wetted and their weights and suction values were measured to acquire the data points of wetting SWRCs. These SWRCs were then curve fitted using Eq. 3 proposed by van Genutchen, 1980 for suction range of 0 to 100 kPa. The curve fitting parameters are shown in Table 4.

$$\theta = \theta_r + \frac{\theta_s - \theta_r}{\left[1 + (\alpha S)^n\right]^m} \quad (3)$$

Where θ is volumetric water content, θ_r is the residual volumetric water content, θ_s is the saturated volumetric water content, S is the matric suction and α, n and m are curve fitting parameters.

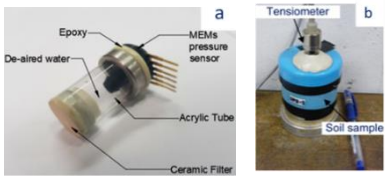

Fig 5. Experimental setup for SWRCs (a) KU miniature tensiometer (Jotisankasa et al., 2010) (b) Suction measurement using KU tensiometers (Rajamanthri et al., 2021)

Figs. 6 and 7 show the wetting SWRCs obtained from the point-wise method for both upper and lower layer samples, respectively.

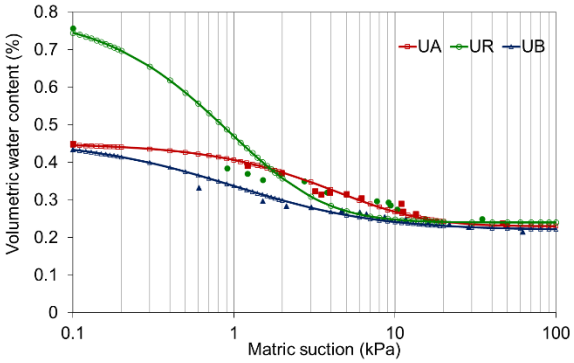

Fig 6. Soil water retention curve for upper layer samples

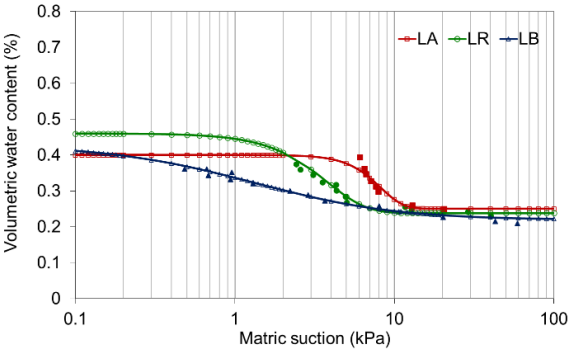

Fig 7. Soil water retention curve for lower layer samples

Table 4. Curve fitting parameters (van Genutchen, 1980)

Sample location	θ_s (%)	θ_r (%)	α (kpa^{-1})	n	m
Upper layer					
UA	45	23	0.07	1.0	3.3
UR	80	24	0.40	1.0	2.7
UB	46	22	0.80	0.9	1.2
Lower layer					
LA	40	25	0.07	3.5	7.0
LR	46	24	0.10	2.0	7.0
LB	43	22	0.60	0.9	1.2

3.1.2 Hydraulic conductivity function

Once the specimen achieved a soil suction of less than 0.5 kPa, samples were soaked for 7-10 days to obtain fully saturated soil samples (where the degree of saturation is greater than 95%) to determine saturated permeability using both constant and falling head testing method (Jotisankasa and Sirirattanachat, 2017; Rajamanthri et al., 2021).

In this study, hydraulic conductivity functions were derived, using SWRC data, based on the Genutchen-Mualem constitutive model proposed by van Genutchen, 1980 as shown in Eq. 4.

$$k_w = k_s \frac{\{1-(\alpha s)^{n-1}[1+(\alpha s)^n]^{-m}\}^2}{[1+(\alpha s)^n]^{\frac{m}{2}}} \quad (4)$$

Where k_s is the saturated hydraulic conductivity, α, m and n are parameters derived from curve fitting SWRC data.

Fig. 8 shows the permeability functions predicted from the Genutchen-Mualem constitutive model.

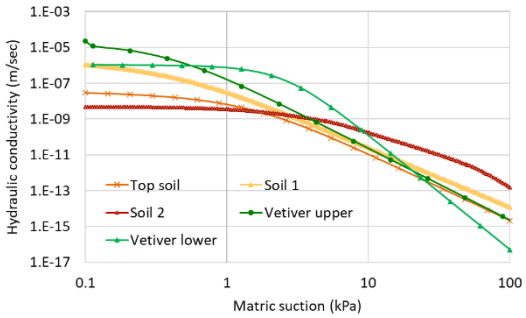

Fig. 8 Predicted permeability functions for different soil layers

3.2 *Infiltration and slope stability analysis*

3.2.1 Infiltration analysis

Infiltration analysis was simulated for steady state and transient conditions. For initial conditions, the steady state analysis was performed with a zero pressure head at the bottom boundary of the soil 2 (Jotisankasa et al., 2015). During transient seepage analysis, the upper boundary (along C-D) (Fig. 3) was specified using an infiltration of 86.4 mm/day for continuous four days (Jotisankasa et al., 2014). Further, other boundaries (left side: A-C, right side: B-D of the slope) (Fig. 3) were assigned with no flow (Q=0 m^3/sec) condition (Jotisankasa et al., 2015).

Fig. 9 shows the pore water pressure variations of the slope captured at three different locations (i.e top, middle and the lower) corresponding to the infiltration event simulated. According to the results obtained at the top of the slope (Fig. 9a), within the depth of 0 – 1.0 m highest negative pore water pressure values are maintained when the entire slope is covered by vegetation. Beyond this depth, a loss of matric suction is observed to the depth of 2.5 m, when the two third of the slope are (2W/3) is covered by the vegetation. The comparatively higher permeability in the vegetated layer compared to the bottom layer and adjacent layer in the downslope direction might distract the water flow and result in accumulation of water at the boundary. This can lead to increase of pore water pressures. Below the depth of 3.0 m (Fig 9a), highest pore water pressures are shown when the entire slope area is covered by vegetation. Therefore, once the layer is fully saturated the water will tend to enter the below soil layer, causing higher pore water pressures at deeper depths.

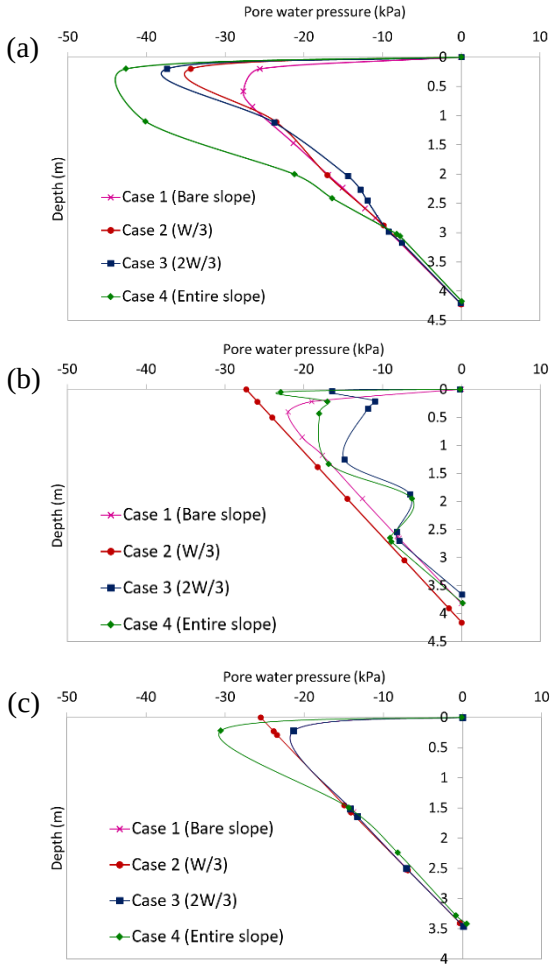

Fig. 9 Pore water pressure distribution after four-day infiltration event (a) at top region of the slope (b) middle region of the slope (c) at the lower region of the slope

As per the Fig. 9b, the highest pore water pressures at the middle of the slope are recorded by the slopes which have more vegetation zones (i.e. slope with two third of vegetation and with entirely covered by vegetation). The higher permeability may promote the infiltration into these slopes and increase the positive pore water pressures. Presence of vegetation has resulted in increasing the pore water pressures in the middle region of the slope.

When observed the pore water pressure variation at the lower region (Fig. 9c), slope entirely covered with vegetation has the lowest negative pore water pressures. Slope with a two third of the area covered by vegetation has recorded the highest pore water pressures up to a depth of 1.5 m from the ground surface. Beyond this depth, slope covered entirely by vegetation shows the highest pore water pressures. Due to the high permeability

in the root zone of entirely vegetated slope, the amount of water entering in to the slope is higher. This could generate significant head differences and encourage the subsided flow towards the downslope direction. This can be the reason for higher positive pore water pressures recorded beneath the depth of 1.5 m, when the entire slope is covered by vegetation.

3.2.2 Assessment of the slope stability after the four-day infiltration event

The pore water pressure profiles obtained from the infiltration analysis were incorporated into a stability assessment to determine the variation of FoS for the four different cases investigated. The results are summarized in Table 5. It can be seen that case 3 and case 4 still possess FoS values of 1.65 and 1.72, which indicate existence of safety margins of 20% and 23% respectively, compared to the bare slope. However, case 4 has the highest FoS value and this can be due to the effect of the support provided from the root zone at the toe region. It can be stated that, the increased cohesion due to the roots is one of the influential factors in maintaining the stability of the slopes during the infiltration event.

Table 5. Percentage variation of FoS values after four-day infiltration event

Case	FoS	Variation of FoS (%)
1	1.31	-
2	1.55	15.48
3	1.65	20.61
4	1.72	23.84

4 CONCLUSIONS

The spatial distribution of the vegetation in a slope is vital factor in governing slope stability. This paper focuses on a numerical study of infiltration and stability of a bio-engineered soil slope with different spatial distribution of vegetation. The study reveals that, there is a significant influence of vetiver grass on the stability of the slope when two-third or entire slope surface area is covered by the vetiver grass. The presence of roots increases the pore water pressure during an infiltration event in the root zone due to the increase of permeability. However, the increase of shear strength due to the root reinforcement is important in maintaining the slope stability as indicated by existence of higher safety margins in the slope during the infiltration event.

ACKNOWLEDGMENTS

The authors gratefully acknowledge the financial support by the Department of Civil Engineering of Faculty of Engineering, Kasetsart University. Also thankfully acknowledged the Geotechnical Engineering Research and Development Center of Kasetsart University for providing access to the GeoStudio software. Green Ground Solutions, Co. Ltd is also gratefully acknowledged and Departments of Rural Roads is also thanked for allowing the access to their bio-engineered sites.

REFERENCES

Coppin, N.J. and I.G. Richards. (1990). Use of vegetation in civil engineering. Ciria Butterworths

Jotisankasa, A., Tapparnich, J., Booncharoenpanich, P., Hunsachainan, N. and Soralump, S. (2010). Unsaturated soil testing for slope studies. In Proc. Int. Conf. on Slope. Thailand.

Jotisankasa A, Mairaing W. and Tansamrit S. (2014) Infiltration and stability of soil slope with vetiver grass subjected to rainfall from numerical modeling. In: Proceedings of the 6th international conference on unsaturated soils. UNSAT: 1241–1247.

Jotisankasa, A., Mahannopkul, K. and Sawangsuriya, A. (2015). Slope stability and pore-water pressure regime in response to rainfall: A case study of granitic fill slope in northern Thailand. Geotechnical Engineering Journal of the SEAGS & AGSSEA, 46(1), 45-54.

Jotisankasa, A. and Sirirattanachat, T. (2017) Effects of grass roots on soil-water retention curve and permeability function. Can GeotechJ 54(11):1612–1622

Leung, A. K., Boldrin, D., Liang, T., Wu, Z. Y., Kamchoom, V. and Bengough AG (2018) Plant age effects on soil infiltration rate during early plant establishment. Geotechnique 68(7):646–652

Mahannopkul, K. and Jotisankasa, A. (2019). Influences of root concentration and suction on Chrysopogon zizanioides reinforcement of soil. Soils and Foundations, 59(2): 500-516.

Rahardjo, H., Satyanaga, A., Hoon K., Sham, W. L., Aaron Ong, C. L., Huat, B. B. K., Fasihnikoutalab, M. H., Asadi, A., Rahardjo, P. P., Jotisankasa, A., Thu T. M. and Viet, T.T. (2017). Slope safety preparedness in southeast Asia for effects of climate change. Slope Saf Preparedness Impact Clim Change. https:// doi. org/ 10. 1201/ 9781315387789

Rajamanthri, K., Jotisankasa, A. and Aramrak, S. (2021). Effects of Chrysopogon zizanioides root biomass and plant age on hydro-mechanical behavior of root-permeated soils. International Journal of Geosynthetics and Ground Engineering, 7(2), 1-13.

Truong, P., Van T. T. and Pinners, E. (2008). Vetiver system applications technical reference manual. The Vetiver Network International.

van Genuchten, M. T. (1980). A closed-form equation for predicting the hydraulic conductivity of unsaturated soils. Soil science society of America journal, 44(5): 892-898.

Wu, T.H., McKinnell III, W.P. and Swanston D.N.J.C.G.J. (1979). Strength of tree roots and landslides on prince of wales island, alaska. 16: 19-33.

Effect of Degree of Saturation on Pullout Resistance

K.A.S.N. Fernando and N.H. Priyankara
Department of Civil and Environmental Engineering, University of Ruhuna, Sri Lanka

ABSTRACT: Soil nailing is a technique which is used to reinforce and strengthen the existing ground conditions. Among the factors influencing the soil-nail pullout resistance, the degree of saturation of the soil is an important factor, especially for permanent soil-nail structures. As such, in this research study, the effect of de-gree of saturation on pullout resistance was studied by conducting a series of laboratory pullout tests using a laboratory pullout box. Especially designed water proof cap was used to apply back pressure to saturate the soil within the pullout box. Variation of earth pressures close to the grouted nail were observed during the tests. It was evident from test results that higher the degree of saturation of soil, lower the pullout resistance. Maximum pullout resistance was observed when the degree of saturation was near the optimum moisture of the soil. When the soil is sufficiently dry, lower pullout resistance was observed.

1 INTRODUCTION

Soil nailing is a technique used for stabilizing soil masses, such as cut and fill slopes, deep excavations, retaining structures and tunnels etc by means of reinforcing the soil. The technique used in soil nailing is the soil reinforced with slender elements such as reinforcing bars which are called as nails and these reinforcing bars are installed into pre-drilled holes and then grouted. At present, soil nailing has been widely used to stabilize the existing slopes in Sri Lanka.

In the design of a soil nailing system, both internal and external failure modes have to be considered. The internal failure modes consist of pullout failure, tensile failure and facing failure. Out of that, pullout resistance is a key factor in the current soil-nailing design (Su et al. 2007). Usually, field pullout tests are carried out during the construction stage to verify the design values. There are many factors affecting the soil-nail pullout resistance and which depends on the shear strength between grouted soil-nail and surrounding soil. Among the factors influencing the soil-nail pullout resistance, the degree of saturation of the soil is an important factor, especially for permanent soil-nailed structures due to the fact that the degree of saturation of the soil mass changes with the variation of ground water level and weather conditions, and the pullout resistance may drop to a low level during intense rainfalls. However, verification of field pullout tests are very hardly be conducted under the worst condition, i.e. saturated condition. As such, the measured pullout resistance in the field is overestimated the design value.

Only very limited researches has been conducted related to soil-nailing under the Sri Lankan context. Generally, peak shear strength parameters of soil are used for the soil nailing design. On the other hand, the effect of soil saturation on soil nailing design is neglected. As such, in this research study, the effect of degree of saturation of soil on the pullout resistance was studied using especially fabricated laboratory model setup. Especially designed water proof front cap and special tubing arrangement was used to apply the back water pressure to achieve the required degree of saturation. In addition, the variation of earth pressure near the grouted nail during soil-nail installation and during pullout test was analyzed.

2 MATERIALS AND METHODS

2.1 *Pullout Box*

The research was conducted using a laboratory model set up as shown in Fig. 1. One nail was tested at a time to avoid the effect of soil disturbance during the pullout of other nails (Harshani & Priyankara 2018). Internal dimensions of the model set up used for the research study were 600 mm in length, 460 mm in width and 600 mm in height and these dimensions were enough to avoid the boundary effect. Additional extension chamber with 280 mm in length, 130 mm in width and 130 mm in height was attached to the end of the box, covering tail of the soil-nail as illustrated in Fig. 2. With this chamber, no cavity is developed at the nail tip and test length of soil-nail would remain constant during the pulling out. A water proof front cap was provided by means of a triaxial cell at the nail head for saturation process.

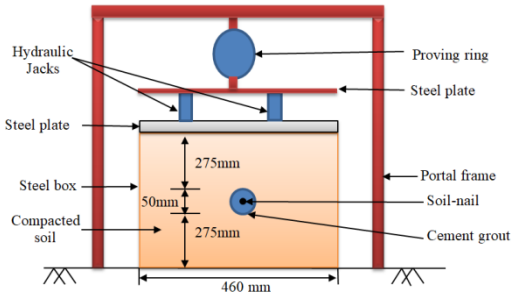

Fig. 1 A schematic diagram of model setup.

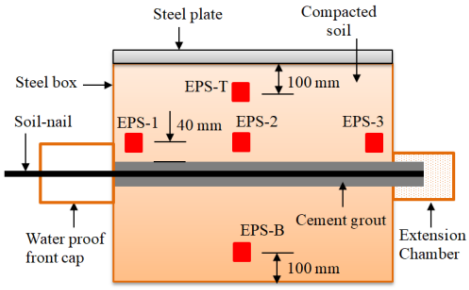

Fig. 2 Pullout box and instrumentation.

2.2 *Instrumentation and Calibration*

Five Earth Pressure Sensors (EPS) were installed in the pullout box to monitor the variation of earth pressure around the soil-nail as shown in Fig. 2. EPS were used to evaluate the effect of dilation on soil-nail pullout resistance. The EPS were calibrated using an Arduino circuit and a bread board as shown in Fig. 3. Known weights were applied on the pressure pad and the corresponding analog reading was recorded for each pressure sensor separately. The five sensors depicted a similar variation, hence the average fitted curve was used to obtain the pressure value.

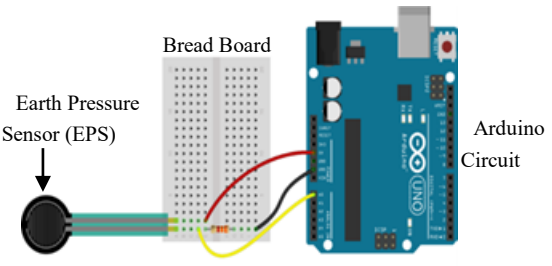

Fig. 3 Arduino Circuit arrangement used for calibration.

Application of Overburden pressure was done by using a portal frame with 2 nos. of hydraulic jacks. It was measured by using a loading cell attached to the portal frame. A steel plate was placed above the top soil surface to achieve uniform deformation of the soil across the pullout box and 2 nos. of dial gauges were used to measure the vertical deformation.

A hydraulic pullout jack was used to apply pullout force on the grouted soil-nail and jack was connected to the nail at the nail head. Hydraulic pressure was applied to the nail in the form of suction so that the nail was pulled out by the jack. A dial gauge fixed at the nail head was used to measure the horizontal displacement of the nail when the pullout force was applied.

2.3 *Material*

The material used for the experiments was commonly available lateritic soil. Engineering properties of the lateritic soil is illustrated in Table 1.

Table 1. Engineering properties of Lateritic soil

Property	Value
Saturated moisture content (%)	39.5
Gravel content (%)	0
Sand content (%)	29.0
Fine content (%)	71.0

2.4 *Test procedure*

The General test procedure for soil filling, installation of EPS, applying vertical stress, drilling, grouting, saturation and nail pullout can be listed as follows;

- Initially the soil was compacted in the pullout box using a rammer to a 90% of the maximum dry unit weight. The soil was compacted in layers with thickness of 50 mm. The amount of soil required for compaction was calculated and the corresponding amount of water was added to the soil.
- Five earth pressure sensors were installed at different levels during the compaction as indicated in Fig.1. A constant overburden stress of about 48 kPa was applied by means of 2 nos. of hydraulic jacks. Proving ring which was attached to the portal frame was used to measure the applied force. Steel plate above the hydraulic jack distributes the load uniformly to the jacks. After jacking, the overburden stress was kept constant throughout the experiment.
- Then the setup was kept for 24 hours from the application of overburden stress until the soil achieved equilibrium (until the EPS readings became constant). Afterwards, a horizontal hole of diameter 50 mm was drilled using a hand auger. Arduino setup and a computer were used for real time recording of EPS data. Steel nail of diameter 10 mm was installed at the center of the drilled hole with the use of centralizers.

- After placement of nail within the drilled hole, grouting was done using a pressure grouting cylinder as stated in Harshani & Priyankara 2019. The water:cement ratio of 0.5 by weight was used to prepare the cement grout and an admixture was used to made flowable and non-shrinkage cement slurry. Grouting pressure was kept constant as 60 kPa throughout all the laboratory experiments and it was applied using a compressor.
- Saturation was started three days after the grouting, once the grouted nail had acquired adequate strength. The nail head was covered with waterproof front cap. The water proof front cap was fixed to a steel plate and that plate was connected to the pullout box using bolts. In order to saturate soil, water flowed in to the pullout box by means of plastic tubes connected to a hole in the side plate. This inlet was divided into 4 lines using T-joints and 7 openings were provided around the soil-nail to facilitate the saturation process. Openings of the tubes were covered with filter papers to avoid clogging of openings with fine particles. A vacuum pump was used to pump out air from the voids. Vacuum was applied by connecting the vacuum pump to the valve at the front of the pullout box (near nail head). Under this suction pressure, water rose to top and filled the water proof front cap. Then using the air compressor, back-water pressure of about 30 kN/m^2 was applied to the water proof front cap which helped to saturating the soil as shown in Fig. 5. The same procedure was repeated but for different time intervals to achieve different degrees of saturation.
- After the saturation procedure was completed pullout test was conducted to determine the pullout resistance of soil- nail. The water proof front cap was removed and pulling-out was done with controlled rate of displacement method and, force and displacement of nail head was recorded. All EPS data during pullout were recorded by computer and dial gauge readings were recorded manually.

Fig. 4 Saturation of pullout box after the application of back water pressure

Fig. 5 Complete Modal Setup

3 RESULTS AND DISCUSSION

3.1 *Variation of Earth Pressure*

In this section the variation of earth pressure during the application of overburden stress, drilling, grouting, saturation and nail pullout is discussed. The earth pressure response against time during the installation of EPS and application of overburden pressure is depicted in Fig.6. The EPS indicates the total stress of the soil above it. Since observed responses being typical for all the experiments, only the tests with S_r = 82% is presented. Small fluctuations of the readings can be seen during the installation of earth pressure sensors due to soil filling in the pullout box. A significant increment in earth pressure was observed during the application of overburden stress. After application of the overburden stress, there is a large fluctuation of earth pressure readings at the initial stage. This fluctuation is caused by the movement of soil particles which contact with the EPS and due to the application of different soil weights above the EPS. After about 21 hours, there was a negligible change in the measured earth pressures indicating that the vertical stress in the soil is constant and which reflects the applied overburden stress.

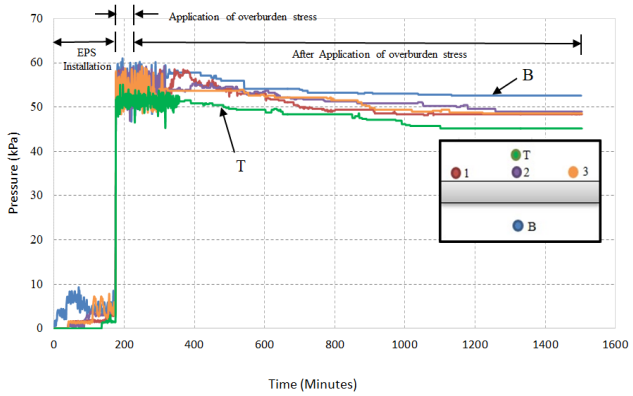

Fig. 6 Variation of earth pressure during installation and application of overburden pressure (S_r = 82%)

Soil stress increases due to outward pushing of the soil by the drill bit during drilling a hole to install soil-nail. Fig.7 clearly illustrates this behavior. It can be seen that when the drill bit reached the section with EPS, earth pressure has slightly increased. Earth pressure at Point 1 (i.e. nail head) increased prior to Point 2 (i.e. middle) and Point 3 (i.e. nail tail), and when the drilling was progressed further the earth pressure at Point 2 and Point 3 increased as depicted in Fig. 7. After drill bit has passed the section of EPS, earth pressure has significantly dropped due to release of surrounding stress. There is no significant change in the earth pressure at Point 'B' and Point 'T' as both sensors are away from the drill hole, which clearly indicates that soil disturbance during drilling is limited to a narrow region.

While installing the nail significant variation of earth pressure in any of the sensors were not observed. Grouting was done for about 6 minutes and during that period the earth pressure was again increased by about 15 kPa, but once the grouting process was completed, earth pressure has been again dropped to about 30 kPa which means the earth pressure release after grouting was about 15 kPa.

The grout had significant amount of water since water: cement ratio of the grout is 0.5. Hence during pressure grouting, water inside of the grout is absorbed by the surrounding soil, as a result hardening of the grout occurs rapidly.

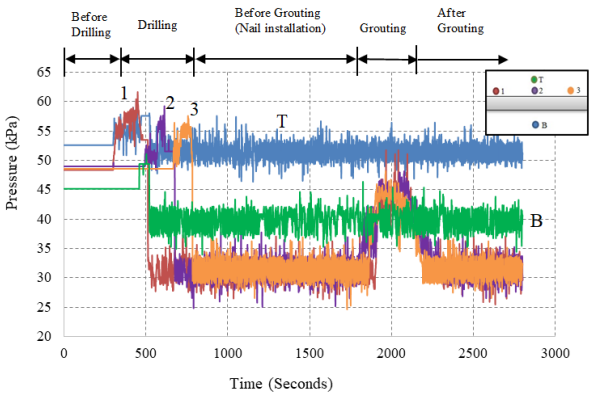

Fig.7 Variation of earth pressure during drilling the hole, nail installation and pressure grouting (S_r = 82%)

Before initiating the grout was allowed to harden so that the nail may have acquired sufficient strength. Hence the saturation was started 3 days after grouting. The variation of earth pressure during saturation process is illustrated in Fig. 8. Immediately after saturation started, the earth pressure values of all the sensors show a gradual increment. The earth pressure in EPS-B and EPS-T showed a sudden increment initially and then continued to increase slowly throughout the saturation period. The earth pressure near the soil-nail (EPS-1, EPS-2 and EPS-3) indicated a significant increment in earth pressure when the water flow passed the sensors. Due to the application of back water pressure when the water proof front cap was filled with water, there was a sudden slight increment in earth pressure near the soil-nail. It can be noted that increment in earth pressure near the nail head (EPS-1) was slightly higher than that of other two sensors as it is closest to the back flow of water from the nail head. After three days of saturation, the water was starting to fill the water proof front cap continuously, thus the back pressure was applied for a longer interval than the previous occasions. This made the earth pressure values of the EPS-1, EPS-2 and EPS-3 to significantly increase due to the continuous back water flow around the nail.

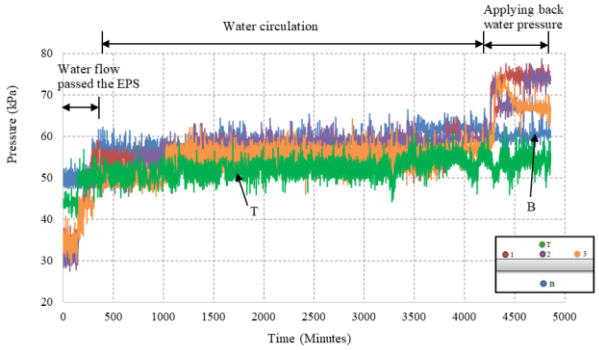

Fig. 8 Variation of earth pressure during saturation (S_r = 82%)

The readings of EPS-1, EPS-2 and EPS-3 were increased to the peak values and then decreased with the displacement of soil-nail during pullout as shown in Fig. 9. Peak value of EPS-1 was higher than EPS-2 and EPS-3. This was due to the stress transfer from nail surface to soil from head of the nail to tail. It can be noted that largest shear displacement mobilized near to the nail head and that reduced towards the nail tail. Earth pressure at EPS-B and EPS-T were not significantly changed during the pullout of nail. Hence, it is evident that earth pressure was significantly changed at or near the soil-grouted nail interface during the pullout test. This behaviour can be identified as dilation of soil as earth pressure increases during shearing and which depends on soil suction, soil density and interface roughness. Since soil density and interface roughness remain constant during the pullout, it is evident that soil suction may cause an increase in soil dilatancy. Similar relationship between soil suction and dilatancy was reported by the Ng & Zhou (2005). Therefore, it can be concluded that soil dilation is one of the key influencing parameters in pullout resistance of soil-nail.

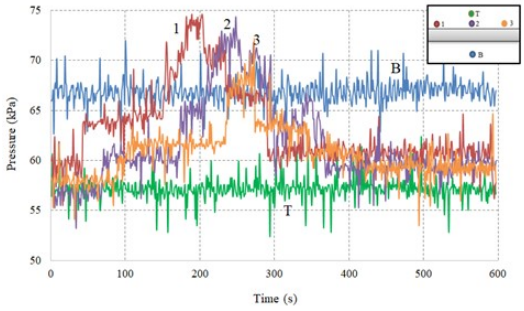

Fig. 9 Variation of earth pressure during pullout test (S_r = 82%)

3.2 *Pullout force-Displacement Behaviour*

Fig. 10 depicts the relationship between pullout force and pullout displacement for different degree of saturation under constant overburden pressure. All curves show the same pullout force-displacement behaviour irrespective of the degree of saturation. As shown in the pullout force-displacement curves, the average pullout force has been increased rapidly until it reached to the peak value and then it was decreased gradually with the displacement.

It can be seen that the displacement at the peak pullout force is less than 12 mm in all experiments. When the soil moisture content is less than optimum moisture content (ω_{opt}<17.6%), displacement rate per pullout force up to the peak value is 1.0 mm/force. When the soil moisture content is more than the optimum moisture content, displacement rate per pullout force up to the peak value is about 0.5 mm/force. As such, it can be concluded that rate of displacement per force decreases when the moisture content is greater than the optimum moisture content.

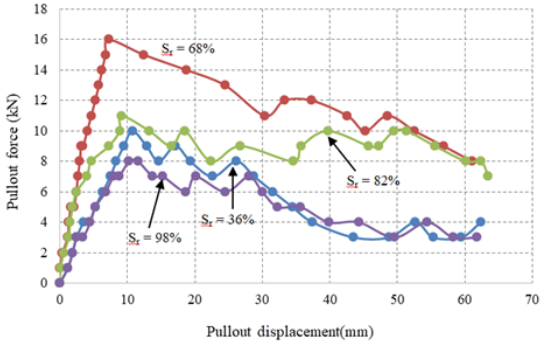

Fig. 10 Relationship between pullout force and pullout displacement under different degree of saturation of soil.

However, when the degree of saturation is more than 80%, pullout force initially increased at a rapid rate of 0.5 mm/force with pullout displacement to about 90% of the peak pullout value, and then it continued to increase at a slower rate of 1.5 mm/force until it reached the peak pullout force. In contrary to the above behaviour can be observed when the soil is fully saturated. Pullout force initially increased at a rate of 0.6 mm/force until 50% of the peak pullout value, and then it continued to increase at a slower rate of 1.2 mm/force until the peak pullout force was reached. The above explanation clearly illustrates that rate of displacement per pullout force is highly dependent on the degree of saturation. Further, it can be noted that maximum displacement of about 63 mm was achieved due to the limitations of the apparatus.

3.3 *Variation of peak pullout force with degree of saturation*

The variation of peak pullout force over degree of saturation is illustrated in Fig. 11. Shape of the peak pullout force versus degree of saturation is very similar to compaction curve where peak pullout force increases with the degree of saturation until it reaches to optimum moisture content and then decreases when the moisture content is greater than optimum moisture content. On the contrary, displacement at peak pullout force decreases until maximum peak pullout force. It can be noted that peak pullout force reaches to the maximum value when the moisture content is near the optimum moisture content i.e. S_r = 49%. However, it was observed that when S_r =36%, soil has lower pullout resistance than that of others. When the soil is at the dry side of optimum moisture content, water is absorbed by the soil due to higher matric suction. This may cause more contraction of the cement grout, thus reducing the bond strength between grouted nail surface and surrounding soil. As such peak pullout force is less at dry side than that of optimum moisture content.

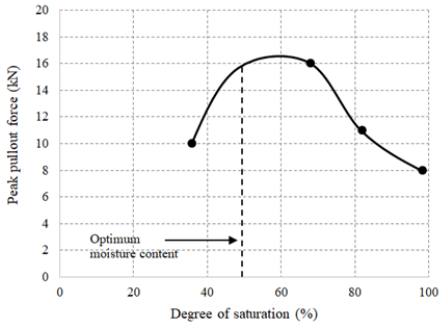

Fig. 11 Variation peak pullout force versus degree of saturation.

When the moisture content of soil is more than the optimum moisture content, apparent cohesion of soil decreases. As a result, pullout resistance de-

creases with the increase of moisture content more than the optimum.

3.4 *Failure Mechanism*

Surface of grouted nails were investigated after the tests in order to study the failure mechanism of grouted nail during pullout,. Fig. 12, illustrates the photographs of grouted nails after the pullout tests. Even though, hole diameter is only 50 mm, it can be seen that grouted nail average diameter is more than the hole diameter, indicating the effect of grouting pressure. Harshani & Priyankara 2018 illustrated that pullout resistance increases with the increase of grouting pressure due to increase of grouted nail diameter under higher grouting pressure. Further, it was observed that grouted nail diameter at the center was more than that of nail head and nail tail irrespective of degree of saturation. This implies more grouting pressure is concentrated at the center than head and tail. However, average grouted nail diameter was same irrespective of degree of saturation.

According to the shearing planes illustrated in Fig. 12 at different degree of saturation, it can be seen that shearing plane has been migrated from the interface between grouted nail and surrounding soil to further into the soil when the soil become saturated. When the soil is fully saturated, a noticeable thickness of the soil has been adhered to the grouted nail surface. This implies the migration of shearing plane from grouted nail-soil interface to soil due to decrease of soil matric suction.

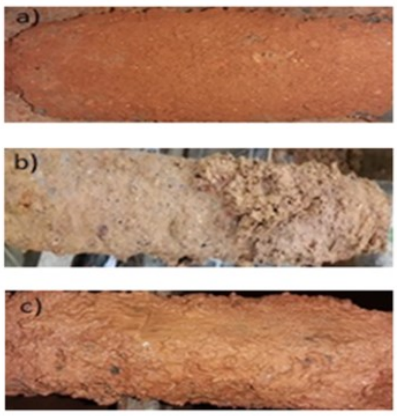

Fig. 12 Nail surfaces after pullout test for different degrees of saturation at (a) $S_r = 36\%$ (b) $S_r = 82\%$ (c) $S_r = 98\%$.

4 CONCLUSIONS

In order to study the effect of degree of saturation of soil on pullout resistance, a series of laboratory tests were conducted using pullout box by varying the moisture content. Especially designed waterproof front cap was used to apply back water pressure to saturate the soil within the pullout box. Variation of earth pressures near the grouted nail surface were observed during the experiments.

Based on the laboratory experimental results discussed above, following conclusions can be made.

1. The peak pullout force is highly dependent on the degree of saturation of soil.
2. Higher the degree of saturation (wet side of optimum moisture content), lower the pullout resistance.
3. When soil is sufficiently dry (dry side of optimum moisture content), water within cement grout is absorbed by the soil due to higher matric suction, thus reducing the bond strength between grout surface and surrounding soil resulting low pullout resistance.
4. The highest peak pullout force is occurred when the moisture content of the soil is close to the optimum moisture content. Similarly, it can be concluded that the highest peak pullout force is within the degree of saturation of soil between 45% and 70%.
5. The shearing plane is migrated further into the soil from grouted nail-soil interface when the degree of saturation is high, i.e. more than the optimum moisture content.
6. The stresses within the soil medium near the soil-nail interface significantly vary during the grouted nail installation process and during the pullout test. The earth pressure variation near the soil-nail interface during the pullout tests indicated that there is a significant effect of soil dilatancy on the pullout resistance of soil-nails. Further, soil-dilatancy depends on the matric suction of the soil.

It should be noted that number of tests were limited in this research study and more soil-nail pullout tests with more degree of saturation should be performed to examine the effect of degree of saturation on pullout resistance accurately.

REFERENCES

Harshani, R.G.F. (2018). “The Effect of Grouting Pressure on Pullout Resistance of Soil Nails.” BS Thesis, Ruhuna Univ.,Galle,Sri Lanka.

Ng, C. W.W., and Zhou R. Z. B., (2005)., Effect of soil suction on Dilatancy of an Unsaturated soil, Proceedings of 16th International Conference on Soil Mechnaics and Geotechnical Engineering: Geotechnology in Harmony with the Global Environment, ICSMGE 2005, Osaka, Japan, v.2, 559-562.

Su, L., Chan, T., Shiu, Y., Cheung T., and Yin, J., (2007)., Influence of degree of saturation on soil nail pull-out resistance in compacted completely decomposed granite fill, Canadian Geotechnical Journal,44: 1314-1328

Field monitoring of moisture-suction regime of a geosynthetic-reinforced soil wall with geo-composite side-drain

A. Jotisankasa & W. Praphatsorn
Department of Civil Engineering, Kasetsart University, Thailand

S. Cheento
Green Ground Solutions, co. Ltd, Thailand

P. Chaisri
Department of Rural Roads, Thailand

ABSTRACT: This paper reports on the slope stabilization work using a geosynthetic-reinforced soil (GRS) wall incorporated with geo-composite side drain on a hillslope in Kanchanaburi province, western Thailand. This study investigates the moisture-suction regime of the wall whereby an array of soil moisture sensors and tensiometers were installed in the fill material of a 6.5m-high geogrid reinforced soil wall. The performance of three layers of geotextile also placed in the middle of the fill, intentionally to function as a capillary barrier was demonstrated. The response of moisture and suction in the fill over one year indicated the wettest part of the fill were near the base of side drain. The knowledge of water and pore pressure regime in the GRS wall can be used for proper maintenance and more effective design in the future.

1 INTRODUCTION

1.1 *Background*

Numerous slope failures and erosion in old road fill occurred frequently in hilly terrains after prolonged and heavy rainfall in Thailand (Mairaing et al., 2012). The situation of climate change means more extreme rainfall will only exacerbate this problem. Commonly, geosynthetic reinforced soil (GRS) walls are used in Thailand to stabilize road embankment failure (Fowze et al., 2012). Yet, it has been recognized the performance of such reinforced structure largely depends on the weather and pore-water pressure condition (Yoo, 2012).

Figure 1 shows a failed slope along the rural road Kanchanaburi-4088 in Thongphapoom district, Kanchanaburi province, western Thailand, which is the location of this current study. The slide was characterized with failure depth of 3-5 meter whose upper scarp reached half of the road surface. This paper reports on stabilization of this slope using geosynthetic reinforced soil wall with instrumentation installed to monitor the pore-water pressure and moisture regime in the wall. The performance of three layers of geotextile placed in the middle of the fill, intentionally to function as a capillary barrier was demonstrated.

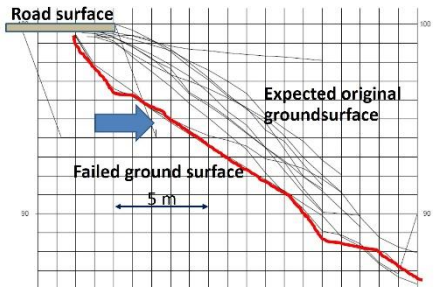

Fig. 1 The failure area prior to stabilization work

1.2 *Site investigation*

The results of site investigation by means of standard penetration test and boring log are shown in Figure 2. The depth of bedrock was found to be about 6 meter below the ground surface. The geology of

the area was that of sedimentary rocks consisting of shale, sandstone interbedded with limestone. The material encountered up to 6 meter depth was expected to be residual soil derived from sandstone as well as colluvium soil from past slide. The material was classified as silty sand or SM according to the unified soil classification system.

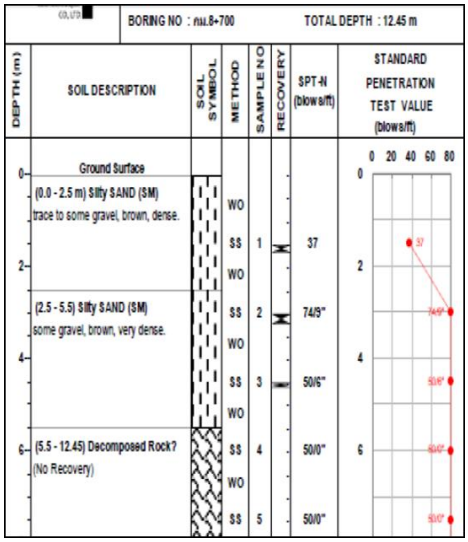

Fig. 2 Site investigation results

In addition, groundwater aeration sound (GAS) survey technique (Jotisankasa et al., 2015) was performed at the site to locate the area with high seepage. The survey was carried out prior to the stabilization work. The technique involves using very high sensitivity accelerometer to pick up vibration or "sounds" of water seepage through unsaturated soil pores that generates air bubble bursting sounds. The device measures the sound in the manufacturer's representative index known as D value. Figure 3 shows results of D value measured along the road above the slide. The D value was plotted along with the contour map of the failure zone, suggesting that the failure zone corresponds well with the zone that generated higher level of groundwater aeration sound.

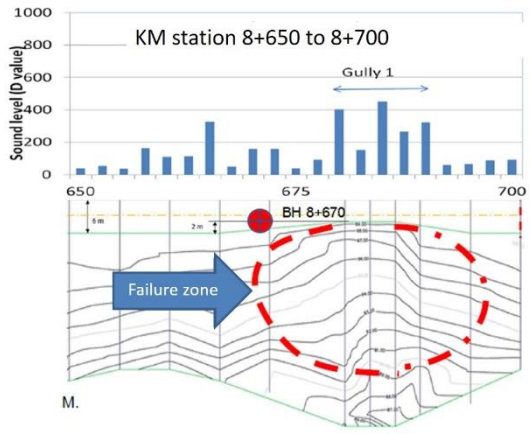

Fig. 3 Ground-water aeration survey result

Subsequent measurement of pore-water pressure at the slope crest (prior to stabilization work) using Kasetsart University (KU)-tensiometer (Jotisankasa et al., 2007; 2010) was then carried out which confirmed the presence of perched ground water above the bedrock (Figure 4).

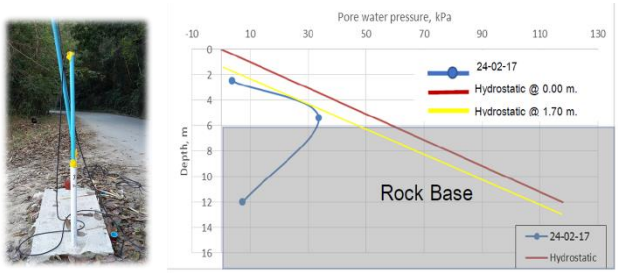

Fig. 4 Ground-water aeration survey result

2 GEOSYNTHETICS REINFORCED SOIL WALL

2.1 *Design of the wall*

The design of the wall was carried out according to FHWA-NHI-10-024. The wall is 6.5m in height. Geogrids TT045 and TT090 (Tenax), having the long term design tensile strength of 21.2 kN/m and 42.4 kN/m respectively were used as reinforcement with embedment length of 4.5m. The vertical spacing and layout of the GRS wall are shown in Figure 5. A drainage board (30cm in thickness) covered with geotextile was laid sub-vertically against the excavated face at the back of the reinforced fill, in order to divert the seepage water away from the fill. In addition, three layers of non-woven geotextile were placed around mid-height of the fill in order to act as capillary barrier and drainage in case there is still any seepage into the fill. The back-filled soil was compacted at 95% modified Proctor. Modular concrete blocks were used as facings with drainage gravel provided at the back of the modular blocks. Figure 6 shows the construction and the wall upon completion.

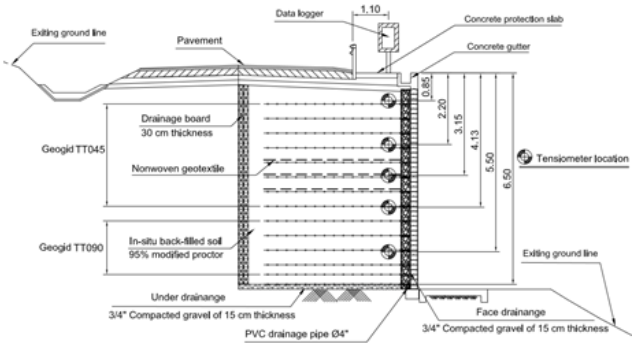

Fig. 5 Cross-section of the studied geosynthetic-reinforced soil wall

Fig. 6 The studied geosynthetic-reinforced soil wall; a) during construction; b) completed wall (viewed from a different angle)

3 FIELD INSTRUMENTATION

3.1 *Tensiometer*

Pore water pressures, both in positive and negative (i.e. matric suction) range, in the compacted fill were measured using Kasetsart University (KU) tensiometer, developed by Jotisankasa et al., (2007) using MEMs pressure sensors and 1-bar air-entry ceramic filter, as shown in Figure 7. The device has a service range of pore water pressure between -80 to 700 kPa. The installation procedure involved placing an open-ended PVC tube casing vertically during compaction work. This PVC tube was used later as an access hole, down which tensiometer would be inserted once the construction of the wall was finished. A good contact between the tensiometer's ceramic tip and the soil was ensured by checking response by a gentle push in the field. A thin layer of clay paste was also applied to the ceramic tip to improve contact condition. Five tensiometers were installed near the modular concrete block facing of the wall at depths of 0.85 m, 2.2 m, 3.15 m, 4.13 m and 5.5 m as shown in Fig. 5.

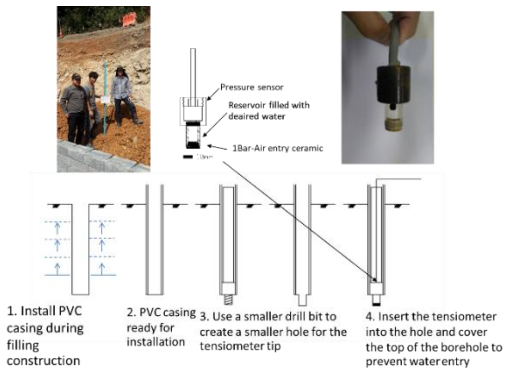

Fig. 7 KU-tensiometer and its installation

3.2 *Moisture sensor*

The moisture sensor used in this study is shown in Figure 8. The device makes use of the time domain reflectometry principle, by which the dielectric constant of the soil was measured via two rods and expressed as voltage signal. The device was calibrated as embedded in the center of a strong acrylic box (measuring 16.2x18.2x20.1 cm^3) in which the same material as in the field was compacted to the same dry density. The moisture condition of the compacted soil in the calibration box was varied by soaking and subsequent air-drying, while the voltage signal of the sensor and the mass of the soil was continuously measured.

Figure 9 shows example of the calibration curve of the device. Figure 8b shows how the device was installed by directly placing in the compacted fill on-site. The calibration was also carried out in the box while being loaded to simulate the overburden imposed on the device during its use. No significant effect of the overburden load was found on the device reading. In total, 8 moisture sensors were installed along a cross-section of the wall.

Fig. 8 Soil moisture sensor and its installation

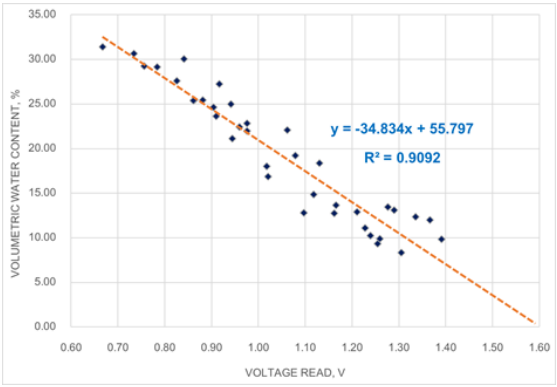

Fig. 9 Calibration curve of the soil moisture sensor

3.3 *Data-logger and rain gauge*

The data-logger used in this study was developed in-house using Arduino microcontroller. The device could take up to 16 signal output from sensors. It was powered on-site using solar panel and a 9volt batter as shown in Figure 10.

Fig. 10 Datalogger system

4 MONITORING RESULTS

4.1 *Soil moisture*

Typical distribution of the soil moisture in the GRS wall is shown in Figure 11, comparing the end of construction period (15 Dec 2017, Figure 11a) with the end of rainy season where water accumulated the most (15 Oct 2018, Figure 11b). The volumetric water content was highest near the base of the wall by the drainage board (TDR1).

Another wetter part of the compacted fill was found at the top right corner (TDR8) below road shoulder. This could be due to infiltration through the joint between concrete shoulder and asphaltic road surface. However, the presence of the geotextile sheets appeared to help imped any further infiltration downward, as evidenced in a much lower water content down at TDR 2 near the wall toe.

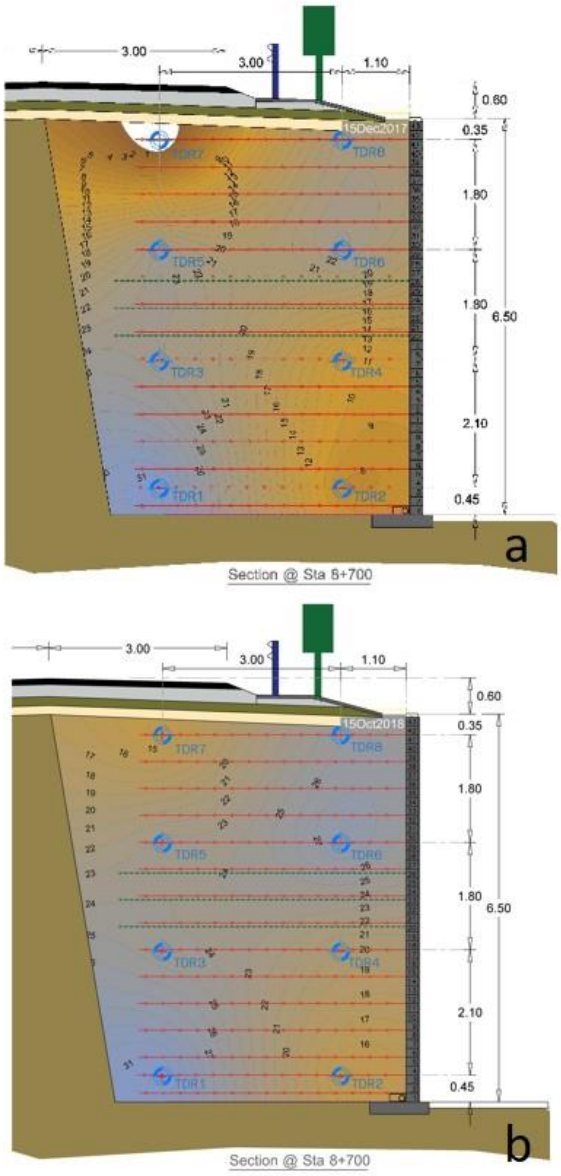

Fig. 11 Typical distribution of volumetric water content in the GRS wall: a) after construction; b) after rainy season

4.2 *Pore-water pressure*

Typical pore-water pressure profile in the reinforced fill behind the modular block facing is shown in Figure 12. The fluctuation of the pore water pressure in response to rainfall was largest at about 1 meter below the ground surface, while the pore water pressue was stable elsewhere. This agrees with the volumetric water content observed earlier. Interesting, while suction or negative pore water pressure were observed in other parts of the fill, a minimal positive pore water pressure was observed at around 3 meter depth near the drainage geotextile sheet. Nevertheless, below the geotextile sheet, the pore water pressure reduced rapidly to negative pressure, which may be an indication of the capillary barrier effect of the geotextile sheet (Iryo and Rowe, 2005).

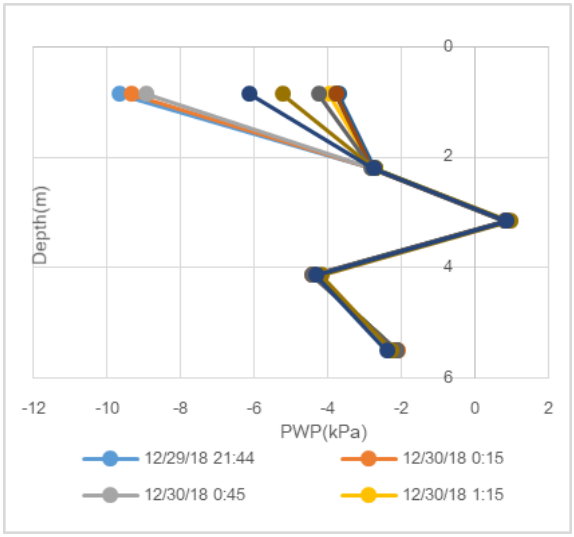

Fig. 12 Typical distribution of pore-water pressure in the reinforced fill behind the modular block facing

5 CONCLUSIONS

This study investigated moisture-suction regime in a geosynthetics reinforced soil fill using an array of soil moisture sensors and tensiometers developed at Kasetsart University. Interestingly, a more fluctuating response of pore-water pressure due to rainfall was found at a shallow depth below the shoulder, while at the other depth the pore water pressure was more stable. This could be indication of infiltration through crack between shoulder and road surface. Below the geotextile sheet intentionally placed at mid-height of the fill, the pore water pressure reduced rapidly to negative value, which may be an indication of the capillary barrier effect of the geotextile sheet The knowledge of water and pore pressure regime in the GRS wall can be used for proper maintenance and more effective design in the future.

ACKNOWLEDGMENTS

This study is supported by the Department of Rural Road, Thailand, and Department of Civil Engineering, Faculty of Engineering, Kasetsart University. The authors also thank Green ground solutions, Co Ltd, students and staffs of Geotechnical Innovation Laboratory at KU for their technical supports.

REFERENCES

Fowze, J.S.M., Bergado, D.T., Soralump, S., Voottipreux, P., Dechasakulsom, M., (2012). Rain-triggered landslide haz practice. Geotextiles and Geomembranes, 30, 50-64. DOI: 10.1016/j.geotexmem.2011.01.007

Iryo, T., and Rowe, R.K., (2005). Infiltration into an embankment reinforced by nonwoven geotextiles, Canadian Geotechnical Journal, 42(4), 1145-1159, DOI:10.1139/T05-035

Jotisankasa, A., Porlila, W., Soralump, S., and Mairiang W. (2007). Development of a low cost miniature tensiometer and its applications. Proc. 3rd Asian Conference on Unsaturated Soils (Unsat-Asia 2007), Nanjing, China, 475-480.

Jotisankasa, A. & Hunsachainan, N., Kwankeo, N., Chunrod, P., and Mancharoen, J. (2010). Development of a wireless landslide monitoring system. Proc. International conference on Slope. Thailand 2010. Geotechnique and Geosynthetics for Slope. Chiangmai, Thailand.

Jotisankasa, A., Mahannopkul, K., Teerachaikulpanich, N., Miyashita, T. and Tada, Y., (2015). Investigation of high-seepage zones in slopes using the Groundwater Aeration Sound (GAS) survey technique in Thailand, Proceedings of the 15th Asian Regional Conference on Soil Mechanics and Geotechnical Engineering, Fukuoka, THA03

Mairaing, W., Jotisankasa, A., and Soralump, S., (2012). Some applications of unsaturated soil mechanics in Thailand: an appropriate technology approach. Geotechnical Engineering Journal of the SEAGS & AGSSEA Vol. 43 No.1, pp. 1-11.

U.S. Department of Transportation (2009) Publication No. FHWA-NHI-10-024: Design and Construction of Mechanically Stabilized Earth Walls and Reinforced Soil Slopes – Volume I

Yoo, C., (2012). Performance of geosynthetic reinforced soil walls under extreme weather conditions. Geosynthetics Asia 2012, 5th Asian Regional Conference on Geosynthetics, Bangkok Thailand.

Laboratory Testing to Calibrate Discrete Element Models Simulating the Effect of Particle Size on Soil Behavior.

S. Dilrukshi
WSP Canada Inc., Vancouver, Canada

J. Mei
Thurber Engineering Ltd., Vancouver, Canada

D. Wijewickreme
Department of Civil Engineering, University of British Columbia, Vancouver, Canada

ABSTRACT: Discrete element modeling (DEM) can be utilized as a tool to study particle-scale interactions and their subsequent effect on overall material behavior. Despite the attractiveness of the technique, the selection of suitable material model microparameters for DEM still is a significant challenge. High-quality data acquired from controlled laboratory element tests are particularly useful in the calibration of DEM models. With this knowledge, a research program was undertaken to study the effect of particle size on the mechanical response of granular materials. Laboratory one-dimensional compression tests of different-sized glass beads and crushed granite were utilized in this regard. Physical tests on glass beads were simulated in a numerically equivalent discrete element model (DEM); the objective herein was to determine suitable DEM particle stiffness micro-parameters that would reproduce the corresponding laboratory results. Through this evaluation of numerical results, it was proposed that a preliminary relationship between "average" constrained modulus for the particle matrix and individual particle stiffness could be established. The results also indicate that DEM simulations of one-dimensional compression tests can be successfully used to calibrate DEM particle stiffness microparameters.

1 INTRODUCTION

The discrete element modelling (DEM) technique allows the users to model granular materials as a collection of separate particles, and in turn, provide an insight into the interactions at particulate level while allowing assessment of the overall material behavior from a continuum point of view. In DEM, the soil particles are considered as rigid bodies, which displace independently from one another and interact via compliant contacts. The behavior at the contacts between the particles is generally characterized by the "soft contact" approach, which accounts for the interaction using normal and shear stiffness values of the particles. The mechanical behavior of the system is described in terms of the movements of the particles due to net inter-particle forces acting at each other, whereas the Newton's law of motion provides the fundamental relationship between the unbalanced inter-particle force and the particle velocity. Frictional slip between the particles is allowed, and it is governed by the friction coefficient between the particles.

It is necessary to use particle contact models to specify the contact characteristics between particles during DEM simulations. Linear contact model and nonlinear Hertz-Mindlin contact model (Itasca, 2016a) have been intensively used by many researchers in this regard.

As reported in the literature, DEM was first applied to rock mechanics and soil by Cundall and Stack (1979). Later, many researchers have demonstrated the capacity of DEM to reasonably represent global soil behavior while taking into account the inter-particle interactions at micro-level (Ting et al. 1989; Cui and O'Sullivan 2006; Chung and Ooi 2007; Belheine et al. 2009; Yu et al. 2011; Yan and Zhang 2013; Dabeet et al. 2015; Tang et al. 2016). Moreover, the technique has been used and considered as a suitable numerical method to analyze the loads applied to rigid bodies by granular materials

(Mak et al. 2012). The technique has also been successfully used to study the soil-pipeline interaction considering the particulate nature of soil (Calvetti et al. 2004; Prisco and Galli 2006; Dilrukshi and Wijewickreme 2017 & 2020).

DEM methodology is well established and its use for considerable number of studies have been reported; however, due to the lack of detailed validation of DEM models to experimental data and methods to calibrate and scale-up DEM models to attain accurate predictions, high computational costs, etc., its use in the industry has become less popular compared to the continuum approaches. One of the critical limitations in using DEM for large-scale engineering simulation is the difficulty of determining the model parameters for a given granular media.

In DEM, it is necessary to use micro-parameters between the particles to characterize inter-particle interaction. It will allow the consideration of particle characteristics preferably with regard to particle size, distribution, shape, and packing arrangement to describe the bulk material properties. Physical measurement of these parameters is extremely challenging; there is no valid theoretical approach to estimate these parameters. Therefore, the use of appropriate calibration techniques to identify model parameters is an important consideration in the modeling process. Many researchers have used trial-and-error methods to determine the suitable micro-property values for the DEM model parameters, and comparing them with related laboratory and in-situ experiments (Ng 2006; Belheine et al. 2009; Plassiard and Belheine 2009; Malone and Xu 2008; Asaf et al 2007; Dabeet et al. 2015, O'Sullivan et al. 2002).

There are many reported research works studying the effect of important microparameters such as particle stiffness, particle friction, and particle shape to the bulk material behavior, with a wide range of different element tests, selected materials and sensitivity studies. However, no published DEM numerical studies can be found with respect to the effect of particle size on the calibrated DEM microparameters of shear or normal stiffness.

The objective of this study is to determine the effect of particle size on calibrated DEM stiffness microparameters, through numerical simulation of specific laboratory experiments. Following the methods utilized by previous DEM calibration studies (Chung and Ooi 2006, Coetzee and Els 2009, Dabeet 2014, Coetzee 2016), DEM re-simulations of one-dimensional compression tests of glass beads were used to identify suitable stiffness microparameters for calibration against laboratory results. The experimental stress-strain responses obtained through one-dimensional compression testing of 1-mm diameter and 9-mm diameter glass beads, were used to calibrate/validate the discrete element models. The calibrated DEM model parameters were then utilized to determine the effect of particle size on bulk material response, as well as its effect on the particle stiffness parameters used in the DEM simulation.

2 EXPERIMENTAL PROGRAM

Tests were conducted on specimens of solid soda-lime glass beads (specific gravity of 2.49) of 1-mm and 9-mm diameter particle sizes. Test specimens were prepared in a polished, rigid, stainless-steel compression chamber setup of 76-mm internal diameter. A compression loading machine was used to apply normal loads to the test specimens at a constant strain rate of 0.013 mm/s. The applied axial loads were measured at top and bottom of the specimen using load cells. A linear potentiometer was used to measure displacement during loading. Five identical compression tests (identified as A,B,C,D and E) were performed on specimens of each of the materials tested. The testing program undertaken is summarized in Table 1. Detail description of the experimental program is given in Mei (2018) and only the summary is given here for brevity.

Table 1. Summary of the testing program

Number of Tests	Size of Glass Beads	Bulk Density of the Sample	Specimen Height
5	1-mm	15.2 (kN/m^3)	53-mm
5	9-mm	15.0 (kN/m^3)	100-mm

3 DISCRETE ELEMENT MODELLING

Three-dimensional (3D) numerical models were developed using commercially available Particle Flow Code software, PFC^{3D} version 5.0 (Itasca, 2016b). Particles were generated using the "particle expansion" method. Herein, a closed cylinder with rigid walls was simulated, and scaled-down particles were generated randomly within the chamber. The

number of particles were determined by creating an assembly with a bulk density similar to the experimental specimen.

After corresponding properties and attributes were assigned to the model, the particle diameters were then multiplied by a scaling factor to obtain the desired particle diameter, and allowed to (numerically) stabilize under gravity. In order to promote particle movement and packing during the initial stabilization process, a considerably smaller particle friction coefficient was assigned to the particles. Following the desired packing arrangement was obtained, the correct coefficient of friction was assigned to the particles, and the system allowed to re-stabilize, before beginning one-dimensional compression.

The normal and shear stiffness between the particles was mostly represented by the linear contact model. A nonlinear Hertz-Mindlin contact model was also used to simulate a test performed with 9-mm size particles, in order to verify the model's ability of accurately capturing the experimental results. For the simulation of one-dimensional compression test specimens with 9-mm diameter particles, the number of particles and the dimensions in the numerical model were made exactly equal to that of the experimental specimens.

Experimental results from one-dimensional compression tests of 1-mm glass beads, indicated that the observed side wall friction was relatively small. Therefore, with the assumption of negligible side wall friction, a numerical specimen with a decreased height (of quarter height) was deemed to be sufficient to represent the experimental one-dimensional compression tests. This approach allowed reducing the high computational effort necessary in running a simulation with considerably large number of particles.

Parameters used in numerical simulations are summarized in Table 2.

In order to match with the laboratory experimental procedure, one-dimensional compression was numerically applied in a displacement-controlled manner and the top plate moved downward at a rate of 0.013 mm/s. Forces generated on the top plate (top axial stress) and bottom plate (bottom axial stress) of the numerical setup, as well as the downward displacement of the top cap were recorded during all simulations.

Table 2. Parameters used in DEM simulations

Parameter	1-mm	9-mm
Normal Stiffness, K_n (N/m)	Varied 2×10^5 to 2×10^6	Varied 7×10^5 to 7×10^6
Shear Stiffness, K_s (N/m)	$= K_n$	$= K_n$
Shear Modulus (GPa)	-	Varied 1.5 to 16.8
Poisson Ratio	-	0.22
Friction Coefficient	0.176	0.176
Particle Density (kg/m^3)	2500	2500

4 RESULTS AND DISCUSSION

4.1 *Experimental and DEM results*

In order to identify the suitable stiffness parameters, the axial stress-strain responses obtained with the selected stiffness parameters during the DEM simulations were compared with the experimental results. For brevity, only the axial stress-strain responses obtained with the selected stiffness parameters during the DEM simulation of 9-mm diameter glass beads are presented (see Fig. 1).

As can be observed from the figures, particle stiffness parameters have a significant effect on the overall bulk material behavior under one-dimensional compression. It can be clearly noted that increasing particle stiffness results in an increase in the bulk stiffness response of the glass-bead specimen under one-dimensional compression.

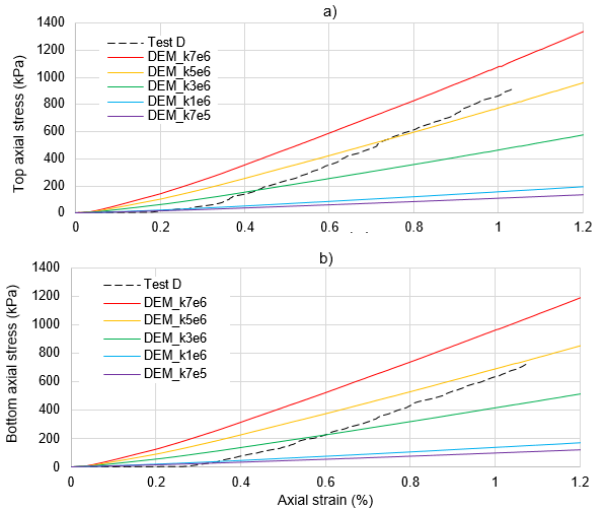

Fig. 1. Comparison experimental results from Test D on 9-mm diameter glass beads, with a series of DEM results obtained for different normal stiffness conducted using the linear contact model - showing axial stress response at: a) top boundary; and b) bottom boundary.

The one-dimensional compression stress-strain response comparisons made (shown as an example in Fig.1) were used to identify suitable stiffness micro-parameters for the simulation of bulk materials in engineering applications. Based on this approach, final calibrated values of K_n , K_s , and G values obtained for the 9-mm and 1-mm particle sizes are presented in Table 3. At this point, the axial stress-strain responses obtained with these specifically selected stiffness parameters during the DEM simulation of 9-mm and 1-mm diameter glass beads are compared with the counterpart experimental results in Figs. 2 and 3, respectively.

As may be noted, experiments displayed somewhat linear stress-strain response after load mobilization. The distinct points of load mobilization are in agreement with Lambe and Whitman (1969), as the stress strain response may be categorized into two distinct sections. Initially, before load mobilization, little stress occurs as strain is governed mainly by particle rearrangement. Further straining past the load mobilization point seem to display a locking phenomenon, where greater stress is needed to deform as contacts become more stable, and elastic deformation of the glass beads begins. Further comparison can be made at the second portion of stress-strain response as described by Lambe and Whitman (1969), where particle contacts become stable after particle rearrangement, and deformation of the glass bead matrix begins to define the stress-strain response. However, The numerical predictions from the linear contact model (shown in dashed lines in Figs. 2 and 3) are unable to capture the non-linear load mobilization responses seen in the experimental results, which occurs initially when strain is governed mainly by particle rearrangement as described by Lambe and Whitman (1969).

With this shortcoming for the linear model in mind, the following sections will compare the experimental results with those from the Hertz-Mindlin contact model. In essence, comparisons were made between the linear and Hertz-Mindlin contact models for the 9-mm glass bead results, to determine the suitability of the two different contact models in capturing bulk material response. Figure 4 compares the numerical results obtained with the Hertz-Mindlin contact model with the experimental results.

Table 3. Parameters used in DEM simulations

Parameter	1-mm	9-mm
Normal Stiffness, K_n (N/m)	5 x 10^5	7 x10^6
Shear Stiffness, K_s (N/m)	= K_n	= K_n
Shear Modulus (GPa)	-	6.5

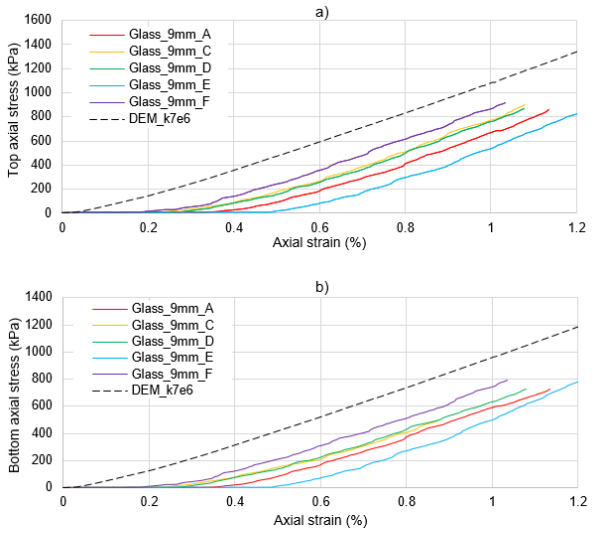

Fig. 2. Comparison of DEM results using linear contact model obtained with $K_n = K_s = 7 \times 10^6$ (N/m) for 9-mm diameter glass beads compared with counterpart experimental results (from Tests A, C, D, E, and F) – showing axial stress response at: a) top boundary; and b) bottom boundary.

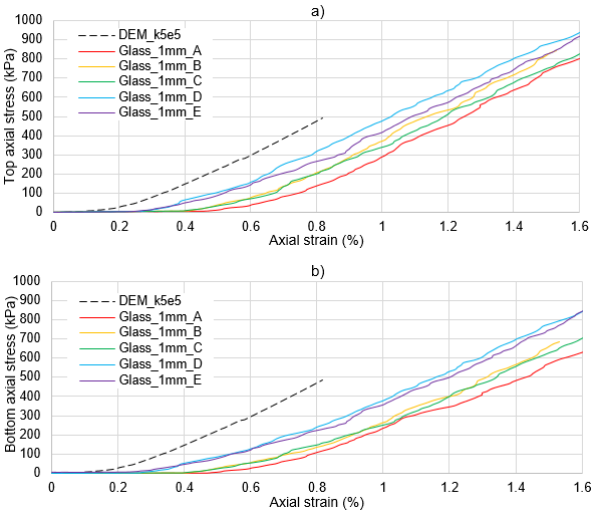

Fig. 3. Comparison of DEM results using linear contact model obtained with $K_n = K_s = 5 \times 10^5$ (N/m) for 1-mm diameter glass beads compared with counterpart experimental results (from Tests A, B, C, D, and E) – showing axial stress response at: a) top boundary; and b) bottom boundary.

4.2 *Evaluation of data*

The stress-strain behaviour of soil is complex, being nonlinear, inelastic, and stress level dependent. The hyperbolic stress-strain model can be considered a simple model that is commonly used to effectively address some key deformation characteristics of soils (Duncan and Chang, 1970). Using this basis,

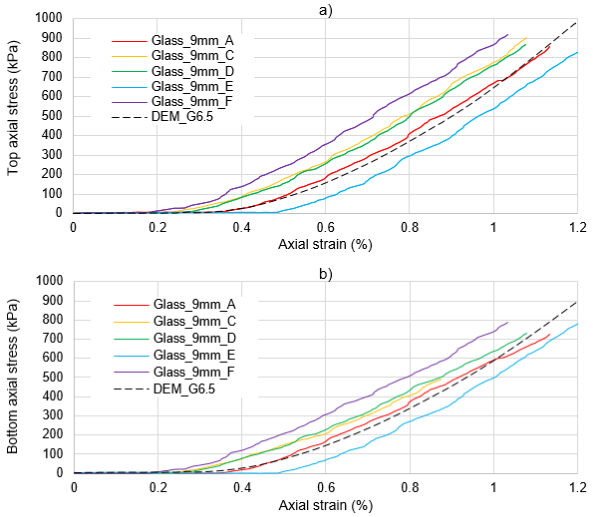

Fig.4. Comparison of DEM calibration results for 1-mm diameter glass beads with experimental results, (Hertz-Mindlin contact model): a) top boundary response, b) bottom boundary response.

Byrne and Eldridge (1982) proposed a three-parameter dilatant elastic stress-strain model for sand. The model accounts for the dependency of material properties on confining stress. The volumetric stress-strain relations are assumed to follow a power law, resulting in bulk moduli that vary with both mean normal effective stress level and relative density as expressed by the following relation:

$$E_t = k_E P_a \left(\frac{\sigma'_m}{P_a}\right)^n \qquad [1]$$

where, E_t = tangent Young's modulus; k_E = soil modulus coefficient, P_a = atmospheric pressure (for normalizing); σ'_m = mean normal effective stress; and n = exponent constant.

Using the above stress level dependency of soil stiffness as the basis, the tangential constrained modulus values were determined from the tangent slope of the experimentally obtained axial stress-strain results at regular strain intervals; this allowed assessing the stress dependency of the constrained modulus across the entire range of axial stresses observed during testing (Note: the stress-strain results from one-dimensional compression testing directly allows computing constrained modulus since the radial strains in the specimen are virtually zero due to the presence of the stainless steel chamber).

It was judged prudent to assess the variation of constrained modulus with respect to the mean normal stress using the formula given in Equation 2:

$$M_t = k_m P_a \left(\frac{\sigma'_m}{P_a}\right)^{0.5} \qquad [2]$$

where, M_t = tangent constrained modulus, and k_m = tangential constrained modulus coefficient. Since the horizontal stress was not measured, it was decided to compute the value of σ'_m assuming a lateral pressure coefficient value at rest (k_0) of 0.5 prevalent with the one-dimensional compression stress conditions. This allowed $\sigma'_m = \frac{2}{3}\sigma'_v$, where σ'_v is the effective vertical stress. With this approach, the M_t values computed for the stress range of σ'_v <500 kPa are plotted with respect to $\sqrt{\sigma'_m}$ (Fig. 5) knowing that the constrained modulus coefficient k_m may be determined from the gradient of the trend line. Linear trend lines and their equations drawn with the intent of determining k_m as well as the coefficient of correlation (R^2) values are also shown in the figures. In this analysis, the tangential constrained modulus coefficient values of 530 and 790 were obtained for 1-mm and 9-mm size glass beads, respectively.

The M_t values could be back-calculated by substituting the above values of k_m back into Equation 2 along with the corresponding axial stress. It is of interest to compare the back-calculated constrained modulus values with the experimental data. Constrained modulus curves developed using Equation 2 are superimposed on experimental results in Fig. 6, labelled as the "M Function", to allow for comparison with experimental results.

4.3 *Effect of particle size on particle stiffness microparameters.*

It was deemed prudent to assess the relationship between calibrated particle stiffness microparameters and the corresponding "average" constrained moduli estimated from simulated stress-strain responses. In addition to the two sets of results from the 1-mm and 9-mm diameter glass beads, it could be argued that particles with zero stiffness would have an "average" constrained modulus of zero – in turn, providing a third point for assessing the relationship.

When these three data points for one-dimensional compression simulations of glass beads were plotted, as shown in Fig. 7, it became apparent that the use of a hyperbolic function in the form shown in Equation 3 would be suitable to describe the relationship between the "average" constrained modulus and particle stiffness.

$$y = \frac{x}{\left|\frac{x}{a}\right| + \frac{1}{b}} \qquad [3]$$

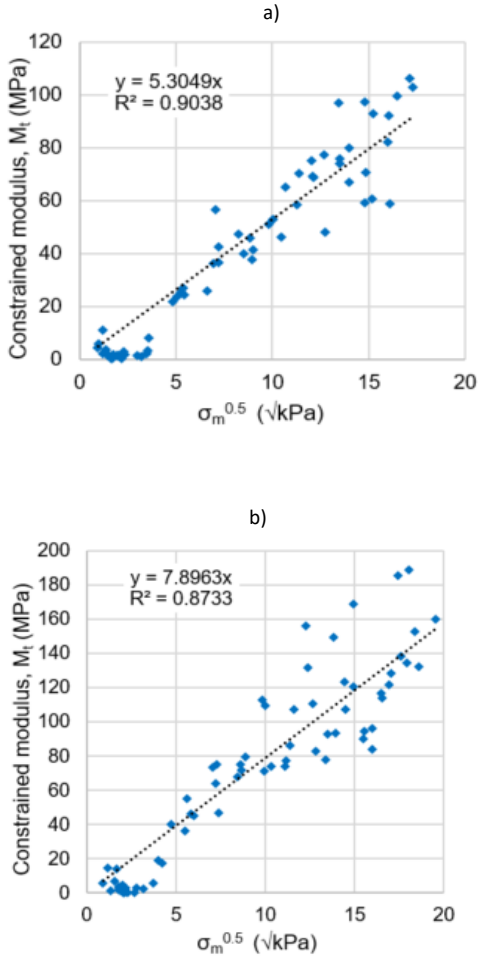

Fig. 5. Determination of constrained modulus number, k_m, for: a) 1-mm diameter, b) 9-mm diameter glass beads.

Curve-fitting of available particle stiffness and "average" constrained modulus data to Equation 3 results in the coefficients as follows:

$$\frac{1}{a} = 0.008 \; and \; \frac{1}{b} = 2197.6$$

Substituting these coefficients back into Equation 3, would lead to Equation 4 to represent the relationship between "average" constrained modulus, Mt and calibrated particle stiffness, k. This curve developed using Equation 4 is superimposed on DEM results in Fig. 7. As expected from the curve-fitting, the curve matches well with the data points.

$$M_t = \frac{k}{\left|\frac{k}{0.008}\right| + 2197.6} \qquad [4]$$

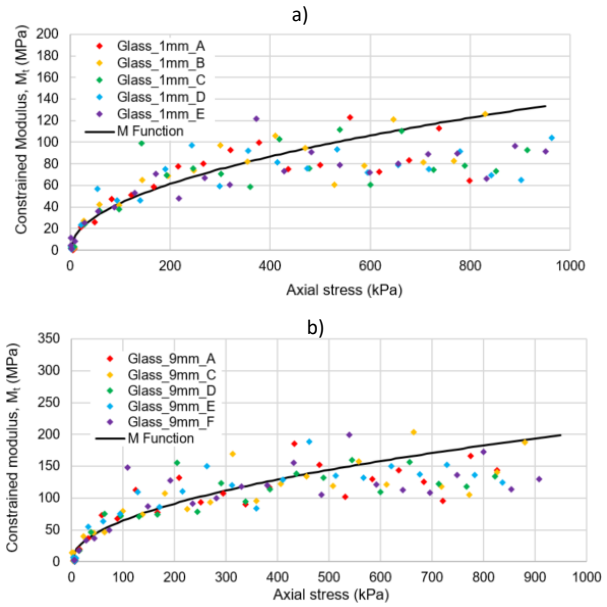

Fig. 6. Stress dependency of the constrained modulus for: (a) 1-mm diameter, (b) 9-mm diameter glass beads.

Based on the presentation in Fig.7, it appears that the particle stiffness (k) for a given material is less sensitive to particle diameter (d) when particle size is smaller (say d < 1 mm) compared to the when d > 1 mm. Although this is based on limited data, it is important to note that the results are arising from careful experimentation combined with DEM analysis. Data from further laboratory testing combined with DEM simulations undertaken on glass beads of different diameters (particularly of diameters less than 9 mm) would add significant value to further confirming this inference.

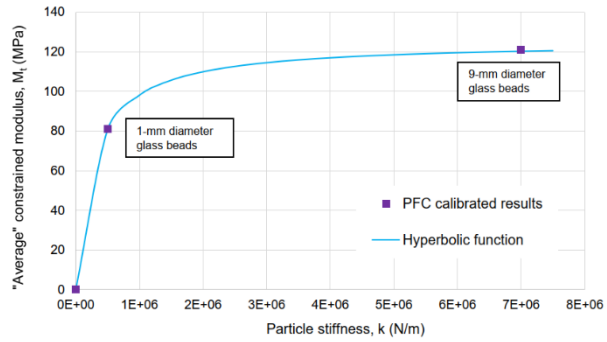

Fig.7. Relationship between average constrained modulus and particle stiffness for one-dimensional compression simulations of glass beads, with superimposed hyperbolic curve.

5 CONCLUSIONS

The results suggest that particle stiffness micro-parameters increase with particle size, for homogeneous, monodisperse mixtures of spherical particles under one-dimensional compression. For 1-mm and 9-mm diameter glass beads, particle stiffness increased by approximately a factor of 14.

A preliminary relationship between "average" constrained modulus and particle stiffness depicted by a hyperbolic curve was suggested based on one-dimensional compression simulations of glass beads of different sizes. Preliminary curve-fitting proved to be successful, however only three data points were available. Additional research needs to be undertaken to investigate this relationship further.

In an overall sense, the findings suggest that particle stiffness microparameters should be carefully selected to represent particle size effects in DEM simulations and, in turn, be utilized in quantitative analysis of geotechnical engineering problems.

ACKNOWLEDGMENTS

The funding provided by the UBC Pipeline Integrity Institute (PII) and Natural Sciences and Engineering Research Council of Canada (NSERC) for supporting this research work is gratefully acknowledged.

REFERENCES

Belheine, N., Plassiard, J.P., Donzé, F.V., Darve, F., and Seridi, A. (2009). Numerical simulation of drained triaxle test using 3D discrete element modeling, Computers and Geotechnics, 36: 320-333.

Byrne, P. M. and Eldridge, T. L. (1982). A three-parameter dilatant elastic stress-strain model for sand. International Symposium on Numerical Models in Geomechanics, Switzerland, 73-79.

Cundall, P.A., and Strack, O.D.L. (1979), A discrete numerical model for granular assemblies, Géotechnique, 29(1): 47-65.

Chung, Y.C., and Ooi J. (2007). Influence of discrete element model parameters on bulk behavior of a granular solid under confined compression, Particulate Sci. Technol., 26(1): 83–96.

Cui, L, and O'Sullivan, C. (2006). Exploring the macro – and micro-scale response of an idealized granular material in the discrete shear apparatus, Géotechniques, 56(7): 455-468.

Calvetti, F., Prisco, C., and Nova, R. (2004). Experimental and numerical analysis of soil-pipe interaction, J. Geotech. Geoenviron. Eng., 130(12), 1292-1299.

Chung, Y., and Ooi, J. (2006). Confined compression and rod penetration of a dense granular medium: discrete element modelling and validation, Modern Trends in Geomechanics, Springer, 223-239.

Dabeet, A., Wijewickreme, D., and Byrne, P. M. 2015. Evaluation of Stress Strain Non-Uniformities in the Laboratory Direct Simple Shear Test Specimens Using 3D Discrete Element Analysis, Geomechanics and Geoengineering, 1-12.

Dilrukshi, S., and Wijewickreme, D. (2017). Evaluation of the trench backfill particle size effects on the development of soil restraints on buried pipelines subjected to relative ground movement, In proc., 3rd Int. Con. on Performance-based Design in Earthquake Geotechnical Engineering (PBD-III), Vancouver, BC, Canada.

Dilrukshi, S., and Wijewickreme, D. (2020). Study of trench backfill particle size effects on lateral soil restraints on buried pipelines using discrete element modelling, ASCE J of Pipeline Systems in Engineering Practice, 11(1): 04019047.

Duncan, J. M., and Chang, C.Y., (1970). Nonlinear analysis of stress and strain in soils-closure, Journal of the Soil Mechanics and Foundations Division, 98(5): 495–498.

Itasca Consulting Group Inc. (2016). PFC- 3D version 5.0 user manual, Monneapolis, USA.

Itasca Inc., (2016). PFC3D (Particle Flow Code in Three Dimensions) version 5.0.

Lambe, T. W., and Whitman, R. V. (1969). Soil Mechanics, Wiley, 116-136.

Mei, J. (2018). Use of laboratory testing to calibrate discrete element models simulating the effect of particle size on soil-pipe interaction, M.A.Sc. Thesis, Department of Civil Engineering, University of British Columbia, Vancouver, Canada.

Mak, J. Chen, Y, and Sadek, M.A. (2012). Determining parameters of a discrete element model for soil-tool interaction, Soil and Tillage Research, 118: 117-122.

Malone FK, Xu BH. (2008) Determination of compact parameters for discrete element method simulations of granular systems. Particuology, 6(6):521-528.

Ng, T. (2006). Input parameters of Discrete Element Methods. ASCE Journal of Engineering Mechanics, 132(7):723-729.

O'Sullivan C, Bray J.D, Riemer M.F. (2002). Influence of particle shape and surface friction variability on response of rod –shaped particulate media. ASCE Journal of Engineering Mechanics, 128(11):1182-1192.

Prisco, C, Galli, A. (2006) Soil-pipe interaction under monotonic and cyclic loads: experimental and numerical modelling. In proceedings of the 1st Euro mediterranean symposium in advances on geomaterials and structures, Hammamet, Tunisia, 755–761.

Plassiard, J-P, Belheine, N., Donze, F.V. A. (2009). spherical discrete element model: calibration procedure and incremental response. Granular Matter, 11(5):293-306.

Tang, H., Zhang, X., and Ji, S. (2016). Discrete element analysis for shear band modes of granular materials in triaxial tests, Particulate Sci. Technol., 35(3): 277–290.

Ting, M.J., Corkum, T.B., Kauffman, C. R., and Greco, C. (1989). Discrete element model for soil mechanics. ASCE Journal of Geotechnical Engineering, 115(3): 379-398.

Yu, Y., and Saxen, H. (2011). Discrete element method simulation of properties of a 3D conical hopper with mono-sized spheres, Advance Powder Technology, 22(3): 324-331.

Yan, W.M. and Zhang, L. (2013). Fabric and critical state of idealized granular assemblage subjected to biaxial shear. Computers and Geotechnics, 49: 43-52.

3-D direct numerical simulation of seepage flow in a soil matrix: Comparison with a model experiment using the method of RIMS

Y. Fukumoto & S. Ohtsuka
Department of Civil and Environmental Engineering, Nagaoka University of Technology, Japan

ABSTRACT: This report presents a validation study for a 3-D direct numerical simulation model of the seepage flow by comparing with a model experiment. The model experiment is based on the method of RIMS (Refractive Index Matching Scanning). In this experiment, the velocities of seepage flow inside the soil matrix can be directly obtained from the image analysis. In addition to such an experimental technique, the direct numerical simulation of the seepage flow, which is based on the coupled LB (Lattice Boltzmann) - DE (Discrete Element) model, was performed in a condition close to the model experiment. In terms of the distribution of the velocities of the seepage flow, the numerical results and the experimental results were compared with each other. It was concluded that the RIMS experiment can contribute to improve the validity and the accuracy of the direct numerical simulation model of the seepage flow.

1 INTRODUCTION

The development of numerical simulation techniques can help our understanding of complex particle-fluid systems, such as a soil particle-pore fluid system in civil engineering. In this study, the validity and the accuracy of a direct numerical simulation model for the seepage flow in the soil matrix are investigated in comparison with a model experiment. The model experiment is conducted by using the method of RIMS (Refractive Index Matching Scanning) (Joshua et al. 2012), which is also called as a method of transparent soils in the field of geotechnical engineering (Ezzein and Bathurst 2011). In the experiment, the flow velocities of silicone oils, which flow through the gaps between acrylic spheres, was directly measured two-dimensionally on a cross section of a green laser sheet. Then, on the basis of the experimental condition, micromechanical numerical analyses of the seepage flow were performed by using the coupled LB (Lattice Boltzmann) - DE (Discrete Element) model (Fukumoto and Ohtsuka 2018). In terms of the distribution of the velocities of the seepage flow, the numerical results and the experimental results were compared with each other and they were found to be in qualitative agreement.

The present paper is organized as follows. At the beginning of the paper, the experimental methods of the RIMS are firstly described. Then, the numerical simulation method based on LB-DE model is briefly explained. Details of the experimental results and the numerical results are given in the following sections. A summary and future prospects are presented in the final section.

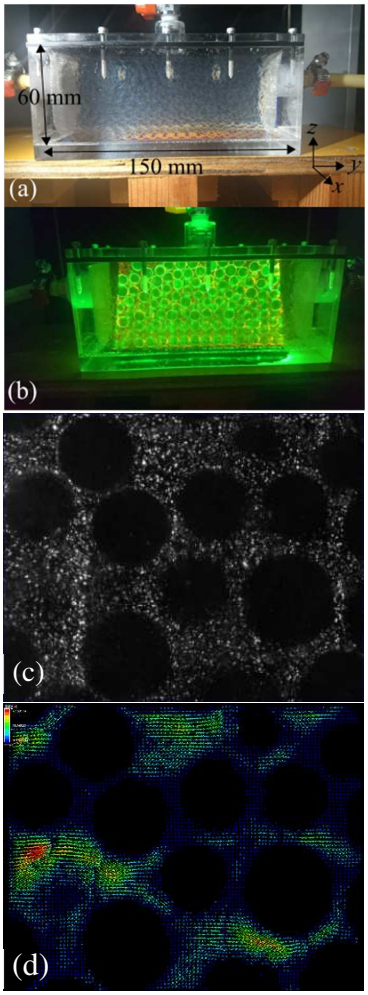

Fig. 1 (a) RIMS with acrylic spheres and silicone oils. (b) A cross-sectional view on a green laser sheet. (c) A black and white image through the optical filter. (d) A velocity distribution obtained by the image analysis.

2 MODEL EXPERIMENT USING THE METHOD OF RIMS

In order to directly observe the seepage flow inside the soils, a model experiment using the RIMS was conducted. The main experimental materials are acrylic spheres, which are substitutes for the soil particles, and silicone oils, which are substitute for the pore water. The average particle size of the acrylic spheres is about 8 mm in diameter and their refractive index is 1.49. Fig. 1 (a) shows that the refractive index of the acrylic spheres is nearly consistent with the silicone oils. To obtain the information of the seepage flow, as shown in Figs. 1 (b) and (c), the behavior of the fluorescent tracer particles suspended in the silicon oils is photographed with a high-speed camera on a cross section of the green laser sheet through an optical filter. After that, the distribution of the two-dimensional flow velocities, as shown in Fig. 1 (d), is obtained by applying an image analysis based on the PIV method to the series of black and white images.

The internal dimensions of the experimental device which is made from acrylic are 60×150×60 mm and the flow of the silicon oils into the device is performed by a pump which can work at a constant flow rate. The magnitude of the flow rate is set so that the Reynolds number can be less than 1. This value for the Reynolds number means the laminar range in the porous flow. In this report, one of the result where the magnitude of the flow rate is 1126.7 ml / min is presented. The area captured by the high-speed camera is approximately 25×25 mm, which is about 3 times longer than the acrylic sphere with a particle size of 8 mm.

3 DIRECT NUMERICAL SIMULATION MODEL FOR SEEPAGE FLOW

A coupled LB (Lattice Boltzmann) - DE (Discrete Element) model is used as a method to directly calculate the seepage flow in the soil matrix (Fukumoto and Ohtsuka 2018). The LB model is a numerical technique for obtaining a flow field by tracking the evolution of the density distribution of the virtual fluid particles that are placed on an orthogonal grid. This numerical scheme is suitable for flows containing complex solid-liquid boundaries. In this study, D3Q19 model for three dimensions is adopted.

Regarding as the resolution of a calculation of fluid flow by the LB model, as shown in Fig. 2, the lattice width is set to be a sufficiently smaller value than the diameter of the soil particles. The solid-liquid interface is handled by employing the PS model (Fukumoto and Ohtsuka 2018), which allows for the

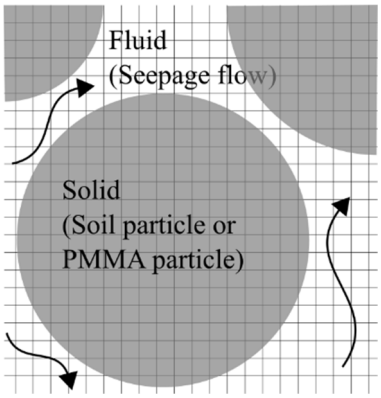

Fig. 2 Resolution of a calculation of seepage flow against the size of soil particle

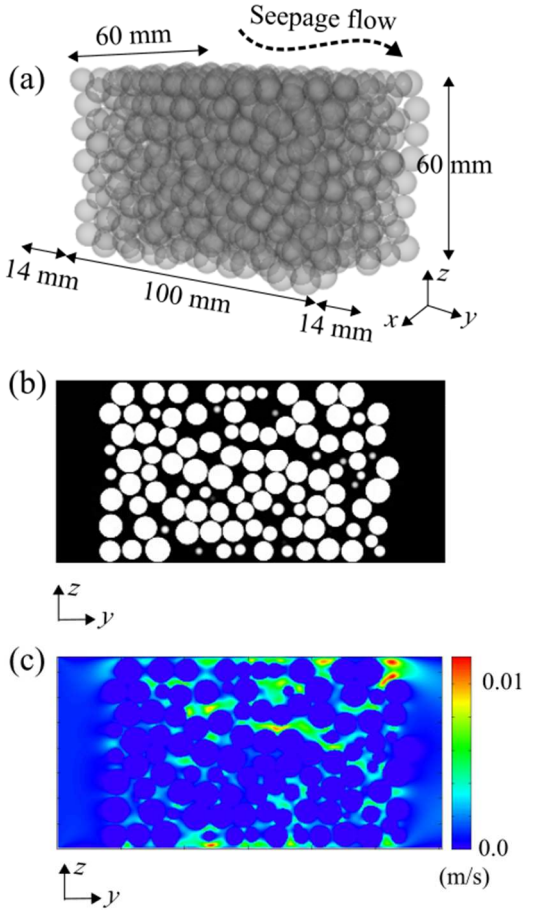

Fig. 3 (a) Full view of numerical porous model, whose sizes is 60×100×60 mm. Seepage flow is generated in positive direction of y axis. (b) Cross sectional view of numerical porous model at x = 30 mm. (c) Colored map for magnitude of flow velocities at x = 30 mm

momentum transfer inside the solid phase. The velocity distribution function at the lattice nodes inside the solid phase is redistributed according to the volume fraction of the solid region. In such a way, non-slip conditions are imposed on the solid-liquid boundary by complementing the spherical shape of interface in the orthogonal lattice space.

A porous model of the numerical simulation is prepared in a close condition to the experiment, as shown in Fig. 3. Fig. 3 (a) is a full view of the numerical porous model and Fig. 3 (b) is a cross-sectional view of the *yz* section at x = 30mm. The arrangement of the soil particles is made by the calculation of the DE model. The average particle size of the soil particles is about 8.0 mm. The analysis area was 60×128×60 mm, whose sizes are corresponding to the sizes of the experimental device. To generate the seepage flow in *y*-direction, the Zou and He pressure boundary condition (Zou and He 1997) is used in the lower and the upper boundaries in the perpendicular direction to the seepage flow. The area occupied by soil particles is 60×100×60 mm. The kinematic viscosity of the fluid was 1.0×10^{-5} m^2/s, which is the same as the physical properties of the silicon oils. The value of the inflow velocity was determined to obtain a laminar flow according to the conditions of the model experiment.

Under the above conditions, simulations of the seepage flow are performed. Fig. 3 (c) shows an example of the result, that is the distribution of the flow velocities in the *yz* section at x = 30mm. It can be seen from the figure that the developed flow inside the porous area can be obtained. All of these calculations are performed on the graphic processing unit. The parallelized algorithm for the LB method are incorporated into our in-house code (Fukumoto and Ohtsuka 2018).

4 COMPARISON BETWEEN EXPERIMENTAL AND NUMERICAL RESULTS

Figs. 4 and 5 show the PDF (Probability Density Function) of the distribution of flow velocity in the porous media. The magnitude of horizontal component of flow velocity, v_y, and vertical component of flow velocity, v_z, are normalized by $\langle v_y \rangle$, which is average value for v_y, respectively. The vertical axis in these figures indicate the frequency of v_y or v_z.

From the PDF of v_y in Fig. 4 (a), it can be seen that the distribution has a peak of frequency at $0 < v_y/\langle v_y \rangle < 1$, which is smaller than the average flow velocity. In addition, the flow velocity which is 9 times larger than the average flow velocity is measured, while the flow velocity having a negative value in the *y* direction is also measured. On the

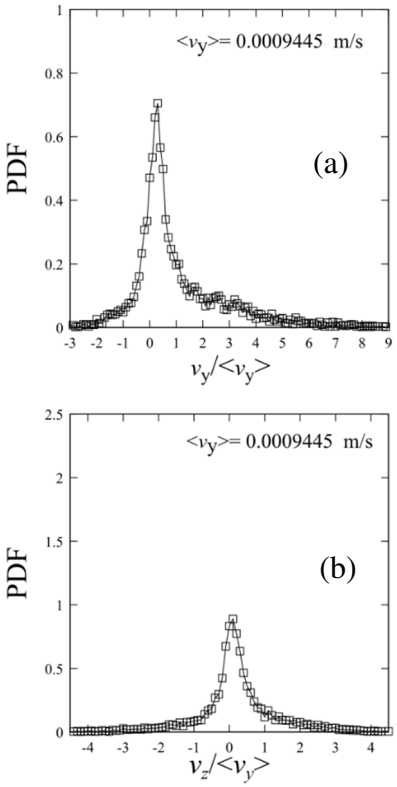

Fig. 4 PDFs of the distribution of horizontal component of flow velocity, v_y, and vertical component of flow velocity, v_z, in the experiment

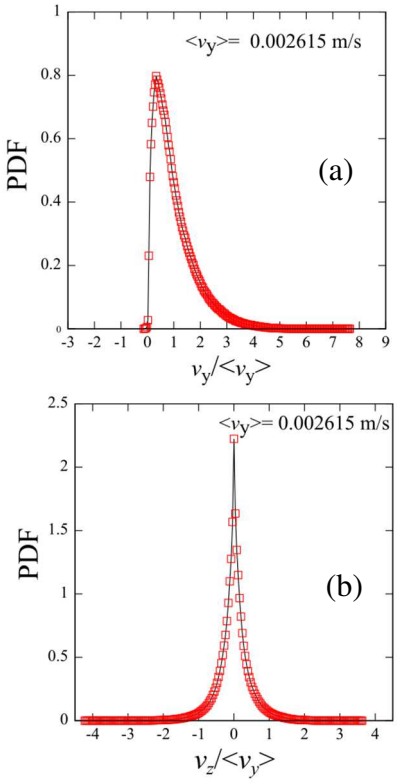

Fig. 5 PDFs of the distribution of horizontal component of flow velocity, v_y, and vertical component of flow velocity, v_z, in the numerical analysis

other hand, the PDF of v_z is a symmetrical shape of distribution with a peak of frequency at near $v_z / \langle v_y \rangle = 0$.

The PDF of v_y obtained from the numerical analysis, as shown in Figure 5, also has a peak of frequency at $0 < v_y / \langle v_y \rangle < 1$ and has the maximum flow velocity which is about 8 times larger than the average flow velocity. In these respects, the numerical result is qualitatively corresponding to the experimental result. However, the fraction of the velocity having a negative value in the numerical simulation is smaller than that in the model experiment. In terms of the PDF of v_z in Fig. 5 (b), the shape of the distribution is symmetric in the same as Fig. 4 (b), but the magnitude of the peak frequency at $v_z / \langle v_y \rangle = 0$ is larger than that in Figure 4 (b).

From the above discussions, it is believed that the qualitative correspondence between the model experiment and the numerical simulation can be obtained. However, there are still a lot of points which are not consistent with each other. In future work, we will identify whether the area of the image analysis in this study can represents the characteristic of the seepage flow in the whole region of the porous media or not. In addition, we plan to further compare with the previous researches (Cenedese and Viotti 1996, Magnic 2003, Dorai et al. 2015, Tachibana et al. 2017).

5 SUMMARY

In the present report, the numerical analysis based on the coupled LB-DE model was performed in a condition close to the model experiment using the technique of the RIMS. The numerical results were found to be in qualitative agreement with the experimental results in terms of the distribution of the flow velocities. From the obtained results, it is thought that the RIMS experiment can contribute to improve the validity and the accuracy of the direct numerical simulation model of the seepage flow.

ACKNOWLEDGMENTS

This work was supported by the fund of Nagaoka University of Technology for young scientists.

References

Cenedese, A. and Viotti, P. (1996). Lagrangian analysis of nonreactive pollutant dispersion in porous media by means of the particle image velocimetry technique, Water resources research, 32(8): 2329-2343.

Dorai, F., Teixeira, C. M., Rolland, M., Climent, E., Marcoux, M. and Wachs, A. (2015). Fully resolved simulations of the flow through a packed bed of cylinders: Effect of size distribution, Chemical Engineering Science, 129: 180-192.

Ezzein, F. M. and Bathurst, R. J. (2011). A transparent sand for geotechnical laboratory modeling, Geotechnical Testing Journal, 34(6):590-601.

Fukumoto, Y. and Ohtsuka, S. (2018). 3-D direct numerical model for failure of non-cohesive granular soils with upward seepage flow, Computational Particle Mechanics, 5(4): 443-454.

Joshua A. Dijksman, Frank Rietz, Kinga A. Lorincz, Martin van Hecke and Wolfgang Losert. Invited Article (2012). Refractive index matched scanning of dense granular materials, Review of scientific instruments, 83(011301): 1-12.

Magnic, P. (2003). Hydrodynamic and transport properties of packed beds in small tube-to-sphere diameter ratio: pore scale simulation using an Eulerian and a Lagrangian approach, Chemical engineering science, 58(22): 5005-5024.

Tachibana, I., Moriguchi, S., Takase, S., Terada, K., Aoki, T., Kamiya, K. and Kodaka, T. (2017). Characterization of transition from Darcy to non-Darcy flow with 3D pore-level simulations, Soils and Foundations, 57(5): 707-719.

Zou, Q. and He, X. (1997). On pressure and velocity boundary conditions for the lattice Boltzmann BGK model, Phys Fluids, 9(6):1591–1598.

Influence of JRC on the bearing capacity of shallow foundations placed on jointed rocks using interface elements

A. D. De Alwis
Department of Civil Engineering, University of Peradeniya, Sri Lanka

L. C. Kurukulasuriya
Department of Civil Engineering, University of Peradeniya, Sri Lanka

ABSTRACT: The study was set to understand the effect of JRC on the bearing capacity of jointed rock masses for joint orientation angles of 0,15,30,45 and 90 for parallel joint sets and orthogonal joint sets. Plane strain analysis was carried out with interface elements to represent the joint, the Barton- Bandis failure criterion was converted to an instantaneous Mohr-Coulomb failure criterion based on 5 selected JRC numbers. The intact rock properties were selected based on published literature and properties corresponding to gneiss rock were selected, considering the lithology of Colombo. The model was calibrated based on results obtained from previously published literature. The bearing capacity was estimated to the nearest 1MPa by selecting the applied footing load, which cause initiation of complete shear failure. The results were plotted as a ratio of the ultimate bearing capacity to intact rock cohesion vs. the JRC number. The results concluded that the JRC number contributes to the bearing capacity adversely or favorably based on the failure mechanism which is governed by the joint orientation.

1 INTRODUCTION

The Mohr-Coulomb failure criterion is most commonly used to numerically simulate the elastic perfectly plastic behaviour of geotechnical materials. Barton (2012) states that the shear strength is more complex and nonlinear in joints of rocks. The shear strength of rock joints is dependent on the undulations of the joint, the weathering condition of the rock and the compressive strength of the rock joints. Barton and Choubey (1976) demonstrated the nonlinear beahviour of the rock joint as,

$$\tau = \sigma_n \tan[\mathrm{JRC}\log_{10}(\mathrm{JCS}/\sigma_n) + \phi_r] \qquad (1)$$

Where τ is the peak shear strength, *JRC* is the joint roughness coefficient, *JCS* is the joint wall compressive strength, σ_n is the effective normal stress and ϕ_r is the residual friction angle. Equation 1 above has been part of the Barton-Bandis joint shear strength and deformability criterion (Barton and Bandis, 1990).

Equation 1 clearly demonstrates the nonlinearity of the joint shear strength and illustrates that the joint conditions must be properly examined in evaluating the strength of a jointed rock mass. However, this study is limited to understanding the effects of JRC and therefore the variable parameter is limited to JRC, whilst the selection of the remaining parameters remain as constants. The basis of selecting these parameters is explained in section 2.2. The JRC value is dependent on the undulation profile of the joint and as illustrated in Fig. 1.

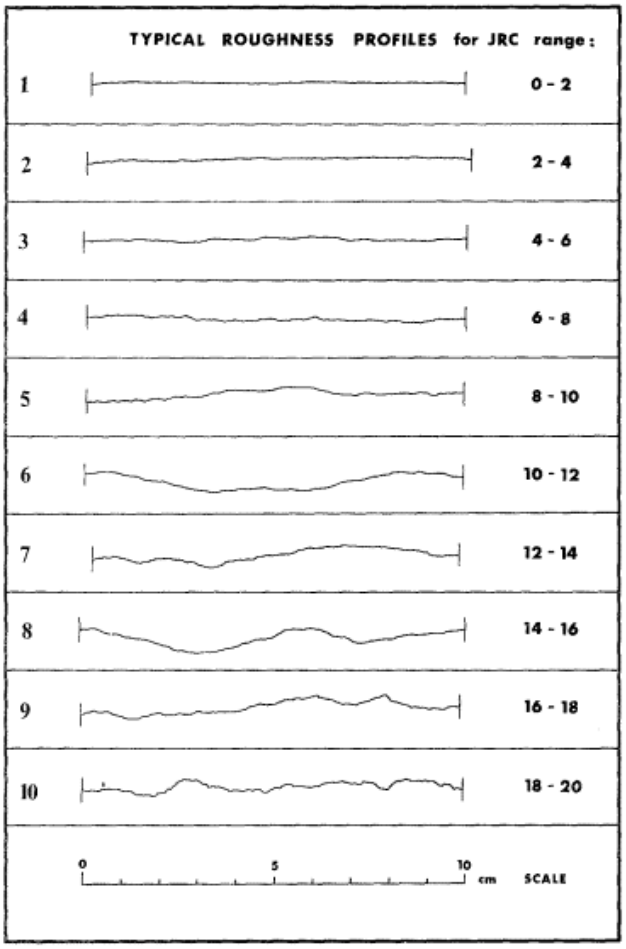

Fig. 1 Roughness profile for JRC numbers, after Barton and Choubey (1976)

Though it is demonstrated that the nonlinear behaviour of rock joints can be accurately described by equation 1, the most common and widely available geotechnical software based on finite element analysis are yet to incorporate the nonlinear behaviour as a material model to numerically simulate rock joints. Hoek (2007) introduced a method by which the nonlinear behavior can be converted to obtain instantaneous Mohr-Coulomb (M-C) shear strength parameters. The instantaneous shear strength parameters obtained from the conversion of equation 1 is illustrated in Fig, 2 and mathematical equations of the conversion are presented in equations 2 to 4.

$$\phi_{in} = \arctan[\partial\tau/\partial\sigma_n] \quad (2)$$

$$\partial\tau/\partial\sigma_n = \tan[\mathrm{JRC}\log_{10}(\mathrm{JCS}/\sigma_n)+\phi_r] - [(\pi\mathrm{JRC})/(180\ln 10)][\tan^2 \mathrm{JRC}\log_{10}(\mathrm{JCS}/\sigma_n+\phi_r)+1] \quad (3)$$

$$C_{in} = \tau - \sigma_n \tan\phi_{in} \quad (4)$$

Where C_{in} is the instantaneous cohesion and ϕ_{in} is the instantaneous friction angle.

Estimating the bearing capacity on a complex geological setting, such as in a jointed rock mass has been studied using numerical methods. Alehossein et al. (1992) presented a solution for obtaining the ultimate bearing capacity of rock using equivalent continuum method based on finite element analysis. Sutcliffe et al. (2004) carried out a study based on lower bound solution (LBS) and finite element analysis to obtain the collapse load for jointed rocks with varying joint orientations that are orthogonal and non-orthogonal. Imani et al. (2012) carried out a study using discrete element modeling to establish an upper bound solution for the ultimate bearing capacity and established the effects of spacing ratio on the bearing capacity. Imani et al. (2012) compared the upper bound solutions established by the studies of Alehossein et al. (1992) and Sutcliffe et al. (2004). This comparison made by Imani et al. (2012) was used for this study to ensure that the parameters used to numerically simulate the joint conditions yielded meaningful results. The calibration process of the model is explained in detail, in section 2.2 of this paper.

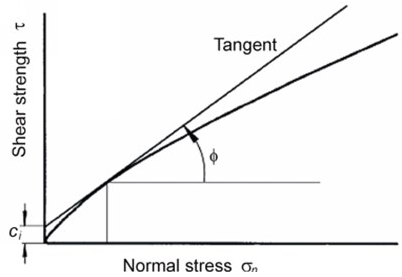

Fig. 2 Graphical representation of the conversion of instantaneous M-C shear strength parameter for nonlinear failure criterion, after Hoek (2007)

2 FINITE ELEMENT MODELING FOR ESTIMATING BEARING CAPACITY ON JOINTED ROCK MASS

2.1 *Model calibration*

This study emphasizes on the use of interface elements to simulate the behavior of joints. MIDAS soilworks ground module, which is a finite element based software is used in this study to simulate the jointed rock mass. In accordance with the constitutive models manual of MIDAS soilworks (MIDAS Information Technology Co., Ltd., 2016) the interface element is based on the Mohr-Coulomb failure criterion. Imani et al. (2012) compared the ultimate bearing strength (UBS) solution with the solutions of Alehossein et al. (1992) and Sutcliffe et al. (2004), to illustrate that the UBS is higher than those obtained from other solutions, and especially that of the solution provided by Sutcliffe et al. (2004), which is based on lower bound solution. Similar to the study of Imani et al. (2012), this study considers orthogonally jointed rock masses with the angle of inclination (α) to the horizontal as 15°, 30° and 45°, the ratio of rock joint cohesion to intact rock cohesion (C_j/C_i) as 0.1 and $\phi_i = \phi_j = 35^\circ$. The compressibility parameters of the intact rock were considered as Modulus of elasticity = 25GPa and the Poisson ratio = 0.25. When considering the modulus of elasticity of rock joint (i.e. the interface element), the recommendations provided in Midas soilworks ground module materials manual (MIDAS Information Technology Co., Ltd., 2016) and the study of Alehossein et al. (1992) were taken into account. The interface element is a zero thickness element that simulates the discontinuity between two materials and thus uses a penalty stiffness. The virtual thickness is not a reflection of an actual joint thickness but is a scale factor since the unit of penalty stiffness is kN/m^3 whereas the unit of modulus of elasticity is kN/m^2.

Alehossein et al. (1992), simulated the joints using an equivalent continuum method describing the Young's modulus of joint in the transverse and normal direction as shown in equations 5 and 6 respectively.

$$k_{si} = E/S_i R_{si} \quad (5)$$

$$k_{ni} = E/S_i R_{ni} \quad (6)$$

Where, S is the spacing of the joint and E is the modulus of elasticity of the intact rock. R is to represent the relative elastic shear and normal compliance.

Considering these two equations the study initially considered $R_{ni} = R_{si} = 1$, 10 and 100 to evaluate its effect on the bearing capacity. The sensitivity analysis was performed with the other 3 studies to check the effect of the modulus of elasticity of the

joint in relation to the intact rock. The objective of the calibration was to ensure that suitable parametric conditions are used for the study, by verifying that the bearing capacity is in between the upper bound and lower bound solutions. Fig. 3 shows that the variation of $R_{ni} = R_{si}$= 1, 10 and 100 has no significant effect and the solution is less than the LBS for both α = 45° and α = 15°. However, the ratio of bearing capacity to intact rock cohesion is higher when $R_{ni} = R_{si}$= 10 for α = 15° and 45° (Fig. 4), which was used for the secondary calibration and for the subsequent analyses.

The study by Alehossein et al. (1992) considers the dilation angle of the joint as equal to that of the friction angle of the rock joint i.e. $\psi_j = \phi_j$. However, the constitutive models manual of MIDAS soilworks (MIDAS Information Technology Co., Ltd., 2016) states that non-associated plastic flow has to be considered when using interface elements to account for excessive fracture opening in the normal direction to the interface. The recommendation from the constitutive manual is to consider $\phi_j - \psi_j \leq 20°$. Considering the particular recommendation, sensitivity analysis was carried out for $\phi_j - \psi_j$ = 0°, 5°, 10°, 15°, 20°, 25° and 30°. The results were compared with the LBS proposed by Sutcliffe et al. (2004) and is shown in Fig. 5. For all angles of α, the closest solution to LBS is observed when $\phi_j - \psi_j$ =15°. Therefore, the study considered the conditions of $R_{ni} = R_{si}$= 10 and for $\phi_j \geq 15°$, $\phi_j - \psi_j$ =15° and for $\phi_j < 15°$, $\phi_j - \psi_j$ =0°, as the calibration factors for the preceding analyses using interface elements, which is envisaged to not consider a low bearing capacity than that of LBS proposed by Sutcliffe et al. (2004)

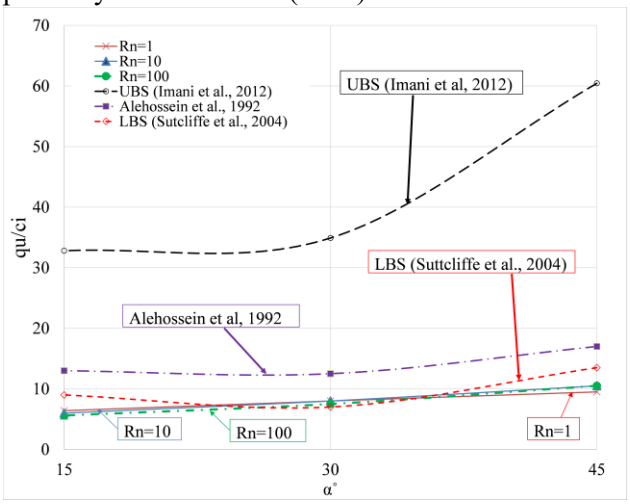

Fig. 3 Comparison of Bearing capacity to intact rock cohesion ratio with varying $R_{ni} = R_{si}$=1, 10 and 100

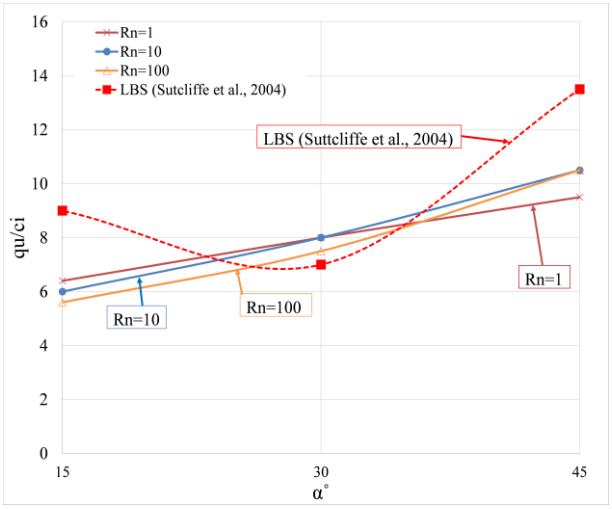

Fig. 4 Comparison of Bearing capacity to intact rock cohesion ratio with varying $R_{ni} = R_{si}$ = 1, 10, 100, considering LBS proposed by Sutcliffe et al. (2004)

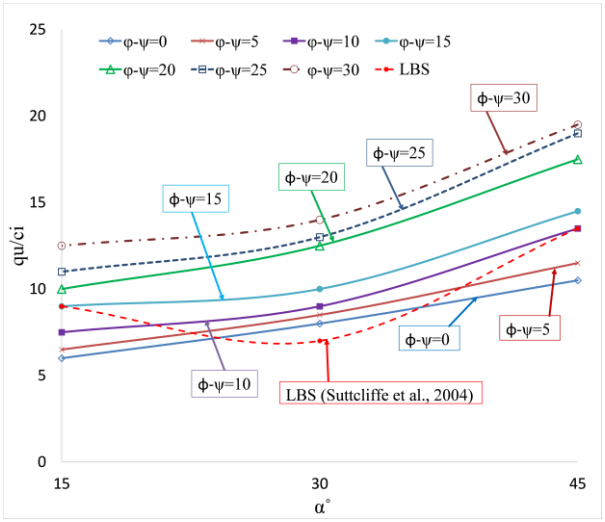

Fig. 5 Comparison of bearing capacity to intact rock cohesion ratio by varying $\phi_j - \psi_j$ with LBS proposed by Sutcliffe et al. (2004)

2.2 *Model setup and parameters selected for analysis*

The study was carried out by introducing single and two joint sets (placed perpendicular to one another). The angle at which the joints are oriented to the horizontal (referred to as α) are 0,15,30, 45 and 90 for the single (parallel) joint set and for the orthogonal (two) joint sets the joint sets are 0;90, 15;105, 30;120 and 45;135. The load was considered to be applied on a horizontal plane and the joints were placed such that the horizontal space between two joint sets is 1m. The uniform ultimate load was applied on the rock mass for a width of 4m. The boundary conditions of the rock mass was placed based on the guidelines stipulated by Alehossein et al. (1992) and was to ensure that the reactions from the boundaries did not reflect to the model. A sketch of the general model setup is shown in Fig. 6.

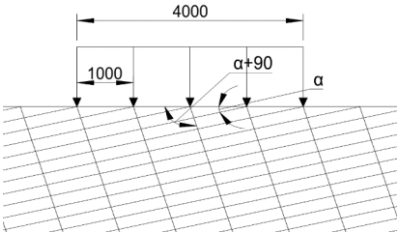

Fig. 6 Sketch of model setup used for the analysis (Orthogonal two joint set model)

To represent the intact rock mass, mechanical and compressibility parameters of gneiss rock was selected; since Colombo region almost exclusively consist of gneiss rock types. The intact rock properties were selected based on the compiled data provided by Pariseau (2007). The properties of the intact rock mass used in the study is provided in Table 1.

The joints were modeled using interface elements and the compressibility parameters used for the interface were based as explained in section 2.1. JRC values of 2, 6, 10, 14 and 18 were considered for this study to represent five undulation profiles. It should be noted that the software inherently has a limitation where in the failure criterion of the interface element is based on the Mohr-Coulomb failure criterion. Thus, the nonlinear failure criterion has to be converted to Mohr-Coulomb failure criterion. The conversion is carried out based on the conversion outline provided by Hoek(2007) as explained in section 1. The conversion, however, is considered as an instantaneous value. Since the study is focused on the effect of the JRC on the bearing capacity, a single point for the conversion was considered for all the selected JRC values i.e. all other parameters were set the same and changing JRC values the corresponding converted (apparent) joint cohesion and joint friction values were considered. The residual friction angle for the rock joint was selected as 24^0 considering the rock type as gneiss (Barton and Choubey, 1976). The joint normal stress σ_n was set at 50MPa and the JCS to σ_n ratio was set as 0.25. Barton and Choubey(1976) recommend to consider the JCS values to be 0.25 of the uniaxial compressive strength σ_c , as a conservative approach if the JCS values are not known. This in turn reflects the slightly - moderate weathering condition of the joint walls. The converted shear strength Mohr-Coulomb parameters for the selected JRC numbers are given in Table 2.

Table 1. Properties of Intact rock used for the Analysis

Property	Description/Value
Rock Type	Gneiss (Foliated)
Unit weight(kN/m^3)	27
Modulus of Elasticity (GPa)	47
Cohesion (MPa)	14.8
Friction angle (^{0})	27.3

Table 2. Joint cohesion and friction angles used for the interface element based on the JRC value

JRC No.	C_j (kN/m^2)	ϕ_j (^{0})	C_j /C_i	ϕ_j / ϕ_i
2	891.87	21.92	0.06	0.80
6	2588.05	17.74	0.17	0.65
10	4189.07	13.54	0.28	0.50
14	5717.93	9.33	0.39	0.34
18	7194.99	5.14	0.49	0.19

Considering all the parametric variables a total of 45 models were analysed to obtain the Ultimate bearing capacities. The rock mass was subjected to an in situ vertical stress due to self-weight as well as an additional pressure of 180kPa (corresponding to a 10m thick overburden). The load was provided in increments of 1MPa from the analysis software. The ultimate load was estimated based to the nearest 1MPa by selecting the load at which shear failure was initiated.

3 RESULTS

The ultimate bearing capacity of the rock mass is obtained when complete shear failure is observed. The load at which deflections begin to show a complete shear failure is recorded. The recorded ultimate load to the intact rock cohesion ratio is demarcated and the best fit polynomial curve is drawn across the recorded points. When considering the failure mechanism a similar failure mechanism was illustrated by Imani et al, (2012). Orthogonal (two) joint sets showed a one sided failure mechanism for joint angle sets of 15; 105 and 30; 120. Fig. 7 shows the displacement diagram when complete shear has occurred for joint orientation 30; 120 to illustrate the failure mechanism (note that this is not the ultimate load which is the load at which complete shear displacement is initiated, but with considerable shear failure to clearly illustrate the failure mechanism). A two sided failure mechanism was observed in joint sets of 45; 135 (Fig. 8) and as well as 0; 90. It should be noted that due to the conditions set by Imani et al.(2012), no analysis was carried out for joint angles of 0;90 in that study. When considering the parallel (single) joint sets for α =15 one sided failure mechanism similar to that of the orthogonal joint set was observed, however, for $\alpha = 30^0$ and 45^0 (Fig.9), a one sided failure mechanism occurred perpendicular to the joint orientation. For $\alpha = 0^0$ and 90^0 two sided failure mechanism could be observed. Fig.10 shows the failure mechanism when $\alpha = 90^0$.

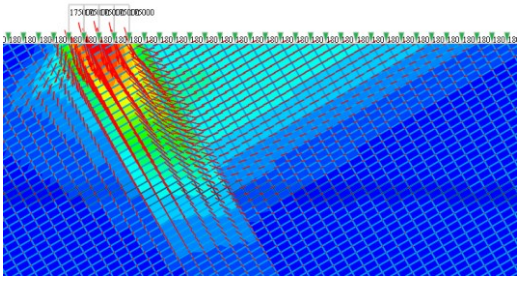

Fig. 7 One sided failure mechanism observed for orthogonal joint sets 30^0;120^0.

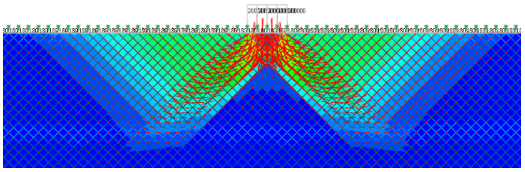

Fig. 8 Two sided failure mechanism observed for orthogonal joint sets 45^0;135^0.

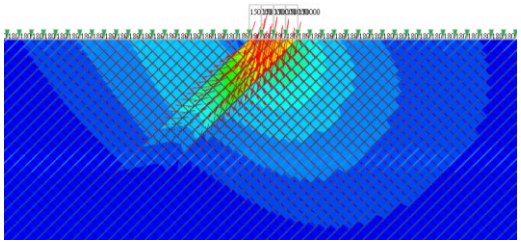

Fig. 9 One sided failure mechanism in the perpendicular direction to the joint orientation observed in $\alpha=45^0$ parallel joint sets.

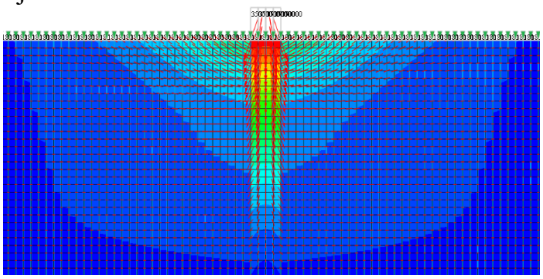

Fig. 10 Two sided failure mechanism observed for parallel joint set with joint orientation $\alpha = 90^0$.

The ultimate load to intact rock cohesion ratio vs. the JRC number for orthogonal and parallel joint sets is presented graphically in Fig. 11 and 12 respectively. It is evident that the highest bearing capacity is obtained for the joint orientation angle $\alpha = 0^0$ for parallel joint sets and 0; 90 for orthogonal joint sets. For the orthogonal joint sets as the JRC number the ultimate bearing capacity increases for $\alpha = 15^0$ and 30^0, where a single failure mechanism was observed. The orthogonal joint set with $\alpha = 45^0$ the ultimate bearing capacity seems to increase to a point until JRC number is approximately 12 and then a decrease can be observed. Considering the parallel joint sets, for the joint orientation angle $\alpha = 15^0$, where a one sided failure mechanism along the joint orientation was observed showed a similar trend with higher values to that of the orthogonal joint set. Similarly, for joint orientation angle $\alpha = 0^0$ (and 90) a higher value was observed for the parallel joint sets. This can be attributed to the fact that additional joints cause failure to occur at a lower applied stress. It should be noted that for $\alpha = 45^0$ the parallel joint set showed a lower bearing capacity than that of the orthogonal joint sets. For $\alpha = 30^0$, parallel joints showed a higher bearing capacity but with the increase in JRC value the capacity decreased than that of the orthogonal joint set. This shows that in considering the ultimate bearing capacity, the joint orientation along with the joint condition has an effect on the bearing capacity of a jointed rock mass.

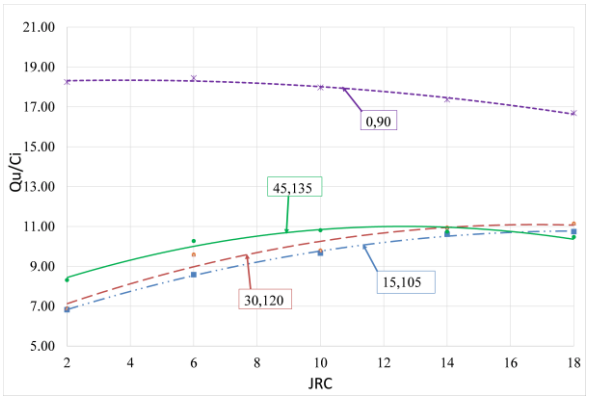

Fig. 11 Plot of bearing capacity to intact rock cohesion ratio vs. JRC for different orientation angles of orthogonal joint sets.

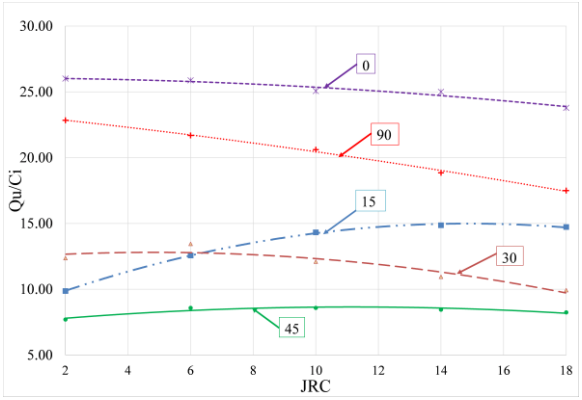

Fig. 12 Plot of bearing capacity to intact rock cohesion ratio vs. JRC for different orientation angles of Parallel joint sets.

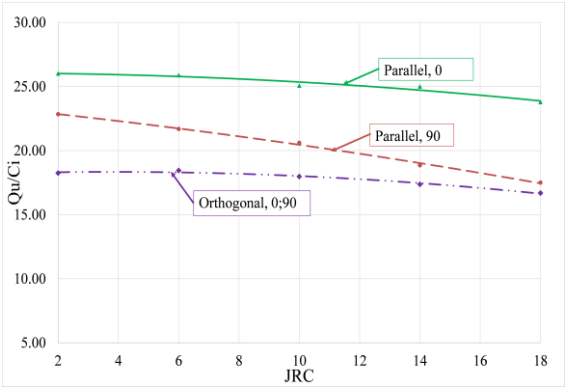

Fig. 13 Plot of bearing capacity to intact rock cohesion ratio vs. JRC for orientation angle 0^0 (90^0)

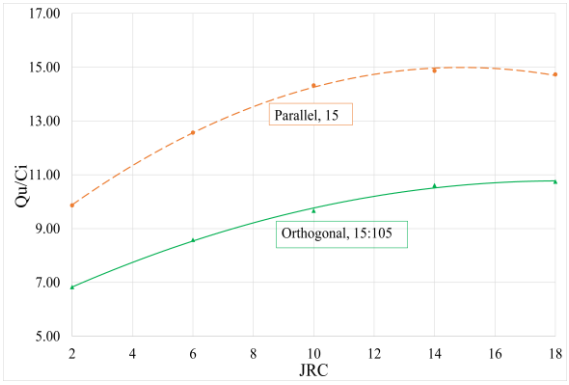

Fig. 14 Plot of bearing capacity to intact rock cohesion ratio vs. JRC for orientation angle 15^0

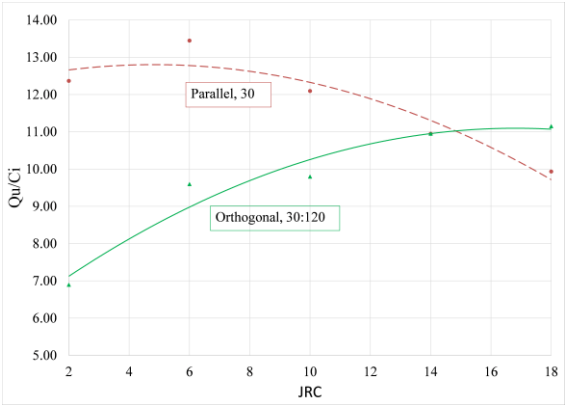

Fig. 15 Plot of bearing capacity to intact rock cohesion ratio vs. JRC for orientation angle 30^0

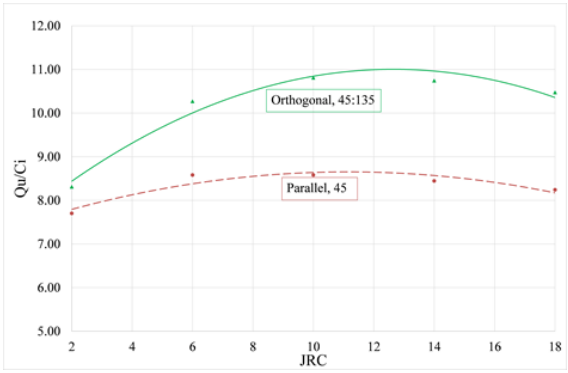

Fig. 16 Plot of bearing capacity to intact rock cohesion ratio vs. JRC for orientation angle 45^0

4 CONCLUSION AND RECOMMENDATION

This study, which was carried out to obtain the effects of JRC on the bearing capacity of jointed rock masses considered the use of interface elements to represent joints. The joint orientations for parallel joint and orthogonal joint sets were 0^0,15^0,30^0,45^0 and 90^0. Based on the results obtained from the study the following conclusions and recommendations can be derived

1. The joint orientation angle has a significant role in the failure mechanism of the jointed rock mass and thus the ultimate bearing capacity.
2. For orthogonal joint sets an increase in the angle of orientation and the JRC number increases the ultimate bearing capacity showing a single sided failure mechanism.
3. For orthogonal joints with $\alpha = 45^0$ the bearing capacity increases to a peak and then decreases, while for $\alpha = 0^0$ the bearing capacity decreases with the increase of JRC.
4. The lowest bearing capacity is shown for parallel joint sets with the failure mechanism shown in the perpendicular direction to the joint orientation, while the most stable joint orientation is the parallel joint set with $\alpha = 0^0$.
5. It should be noted that the study was carried out considering a conversion of the nonlinear failure criterion to a linear failure criterion due to the inherent limitation of the software. Therefore as a further study it is recommended that a similar study is carried out considering the nonlinear failure criterion and the results are compared for verification.
6. A further study will be carried out investigating the effects of rock anchors on the bearing capacity.

ACKNOWLEGEMENTS

Permission granted to use computational facilities by Civil and Structural Engineering Consultants Pvt. Ltd. is greatly appreciated.

REFERENCES

Alehossein, H., Carter, J.P. and Booker, J.R. (1992), Finite element analysis of rigid footing on jointed rock, third International conference on Computational Plasticit,2, 935-945.

Barton, N.R. (2012), Shear strength criteria for rock, rock joints, rockfill and rock masses: Problems and some solutions, Journal of rock mechanics and rock engineering 5, 249-261.

Barton, N. R., and Bandis, S. (1990). Review of predictive capabilities of JRC-JCS model in engineering practice. In Rock joints, proc. int. symp. on rock joints, Loen, Norway, 603-610. Rotterdam: Balkema.

Barton, N.R., and Choubey, V. (1977). The shear strength of rock joints in theory and practice. Rock Mechanics 10, 1-54.

Hoek, E., (2007). Practical Rock Engineering, Evert Consulting Engineering Inc., Canada

Imani, M., Fahimifar, A., Sharifzadeh, M. (2012). Bearing failure modes of rock foundations with consideration of joint spacing, ScientiaIranica 19(6), 1411-1421.

MIDAS Information Technology Co., Ltd., 2016, Soilworks Ground module material manual.

MIDAS Information Technology Co., Ltd., 2016, Soilworks constitutive models manual.

Pariseau, W. G., (2007). Design analysis in rock mechanics, Taylor and Francis, The Netherlands.

Sutcliffe, D.J., Yu, H.S. and Sloan, S.W. (2004), Lower bound solutions for bearing capacity of jointed rock, Computers and Geotechnics 31, 23-36.

Plane-Strain Modelling of Embankment Resting on Soft Soils Stabilized with Gravel Compaction Piles (GCPs)

T. M.D. Thilakarathne & H .S. Thilakasiri
Department of Civil Engineering, Sri Lanka Institute of Information Technology, Malabe

J.Lou & Q.Zhang
China MCC20 Group Corp. Ltd.

ABSTRACT: In this research, the settlement monitoring data which was obtained during the construction of the highway segment is compared with the 1-D FEM simulations. To confirm the modeling process the subsurface condition of the compressible soil deposits from the borehole investigation and installation of the GCP through the same soft compressible soil deposit from a highway construction project in Sri Lanka is used. This numerical simulation was carried out using axisymmetric to plane-strain approach, where the GCPs were converted into equivalent-walls. Satisfactory agreement with the field measurement and the FEM results were observed.

1 INTRODUCTION

Most of the highway development projects in Sri Lanka are located in the low-lying marshy lands and waterlogged areas along the coastal belt of the country which consist of highly compressible soft deposits like peat and organic soils. The excessive settlement and long construction duration of the engineering infrastructure like highways is one of the major concerns in the engineering community. It is important to improve the ground before the construction or it should be properly designed so that the final settlement is within the allowable limits. Preloading without GCPs (Gravel Compaction Piles) is one of the soft soil treatment methods widely used due to its economy and constructability. Whereas, preloading with GCPs (Fig. 1) is commonly used when the soil is highly compressible, weak and the thickness of the soft strata is high. GCPs provide two actions, one is expediting the consolidation process through radial consolidation which speeds up the settlement of the soft deposit and thereby increasing the strength of soft soil deposits faster. Second is the reinforcement action of the stronger GCP enhancing the strength of the soft soil deposit to carry the externally applied load.

The behaviour of GCP-improved soft ground is complex to analyze. Various factors like shear strength of GCPs, strength profile of soft soil, area replacement ratio, geometric conditions and external loading affects its mechanical performance (Terashi et al, 1991). Several researchers have proposed various design approaches based on unit cell concept to understand the bearing capacity, settlement and stability of the soft soil stabilized with

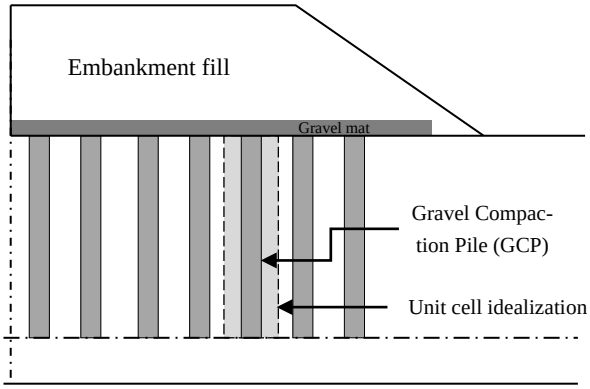

Fig. 1:Embankment stabilized with GCP

GCPs. Among the most significant contributions, the studies by Barron (1948); Priebe (1976); Aboshi et al. (1979); Balaam and Booker (1981) are noteworthy. Most of these solutions are based on unit cell analysis assuming the loaded area of infinite extent. The true nature of the effects of installation of GCPs, the remolding of the surrounding soil and the flexible nature of the embankment loading are not accounted in these design approaches. In order to solve these complex behaviour, numerical modelling is very useful which may help to derive some reliable predictions like settlement, stresses and pore water pressure.

The analysis of embankments with reinforcement, GCPs and multistage construction is not straight forward, and sufficiently accurate Finite Element analysis has to be used. Different researchers have developed different numerical approaches to model the GCPs: (a) axisymmetric model where one GCP is studied (b) plane-strain model where the GCPs are transformed into longi-

tudinal walls (c) axial symmetry technique where GCPs are transformed into cylindrical rings (d) homogenization technique where GCPs and soil are transformed into a homogeneous soil with equivalent properties and (e) full three-dimensional (3D) model (Jorge, 2017).

This paper provides a better understanding of the applicability of modelling an embankment section stabilized with GCPs as a plane strain model including its smear effects. An embankment section in the Outer Circular Highway construction project in Sri Lanka was studied to compare the treated embankment performance with the predicted behaviour.

2 PLANE-STRAIN MODELLING

2.1 *Axisymmetric to plane-strain modelling*

It is impractical to analyze a three-dimensional (3-D) problem of GCP stabilized soft ground due to the large number of GCPs and the 3-D variation of the soil profile. Hence it is often converted into a two-dimensional (2-D) model with equivalent properties and dimensions. The GCP permeability and stiffness are the key factors that need to be converted to obtain an equivalent plane strain model. The high permeability of GCP causes radial dissipation faster. The high stiffness of GCP reduces the stress taken by the soft soil and hence reduces the development of excess pore water pressure.

In several studies of vertical drains, the rate of consolidation has been derived assuming negligible drain stiffness (Barron 1948; Hansbo 1981). However, this may not be applicable to GCPs because the rate of consolidation can be underestimated. Hird et al. (1992) and Indraratna and Redana (1997) proposed methods to convert the axisymmetric unit cell into a plane strain model involving the permeability or geometry-based matching. For GCPs application, the methodology needs to derive the equivalent stiffness to match the plane strain numerical analysis to simulate the consolidation effects. Tan et al. (2008) proposed two methods to obtain the equivalent soil permeability and stiffness of GCPs for 2-D plane strain modelling. In the first method, the geometry of the GCP is kept unchanged while the permeability of soil and the stiffness of GCP are converted (Tan and Oo, 2005). Whereas, in the second method, the thickness of the GCP is converted to match the equivalent area replacement ratio (Tan et al., 2008). Since Method 2 of Tan et al. (2008) is preferable for elastoplastic material modelling, it has been considered in this study.

Generally, GCPs are arranged in triangular or square grids and thus the simplified tributary area

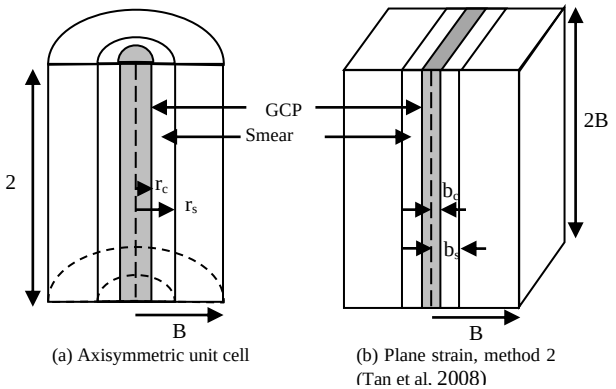

(a) Axisymmetric unit cell (b) Plane strain, method 2 (Tan et al. 2008)

Fig. 2: Cross section unit cell GCP to plane strain conversion

for each GCP is considered as a hexagon or a square, respectively. Barron (1948) showed that the diameter of the influence zone of vertical drain for triangular and square grids are given by R=1.05B and R=1.13B respectively, where R and B are the equivalent radius and equivalent plane strain width of the drainage zone . According to Tan et al. (2008), for a system of GCPs arranged in square grids, the equivalent plane strain parameters can be expressed by (see Fig. 2),

$$b_c = B\frac{r_c^2}{R^2} \quad (01\ a)$$

$$b_s = B\frac{r_s^2}{R^2} \quad (01\ b)$$

$$E_{c,pl} = E_{c,ax} \quad (02\ a)$$

$$E_{s,pl} = E_{s,ax} \quad (02\ b)$$

$$k_{h,pl} = k_{h,ax} \quad (03\ a)$$

$$k_{v,pl} = k_{v,ax} \quad (03\ b)$$

where b_c and b_s denotes the plane strain width of GCP and the plane strain width of smear zone, r_c and r_s denotes the radius of the GCP and the radius of the smear zone, E_c and E_s denotes the elastic moduli of GCP and the elastic moduli of soil, and k_h and k_v denotes horizontal and vertical permeability of soil respectively. Also, the subscripts '*ax*' and '*pl*' are used to denote axisymmetric and plane-strain conditions respectively.

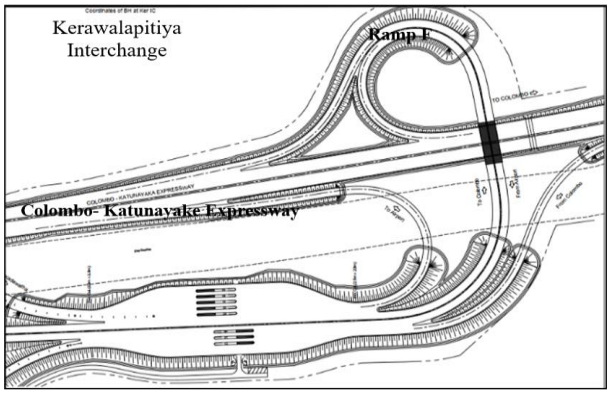

Fig. 3: Ramp F, Kerawalapitiya Interchange, Outer Circular Highway

2.2 *Reference Case*

The basic input geometry and model parameters of the selected study are all taken from an embankment section at Kerawalapitiya Interchange-Ramp F of Outer Circular Highway (Fig. 3), which is 7m high, 17m wide and with a slope gradient of 1:2. This embankment is founded on a 15m thick soft peat layer with the water table at ground level. The layers below the peat consist of medium dense sand materials. GCPs of 0.7m diameter with 1.5m and 1.3m square spacing were installed in square grids to reinforce the ground (Fig.4).

The reference problem was considered as a

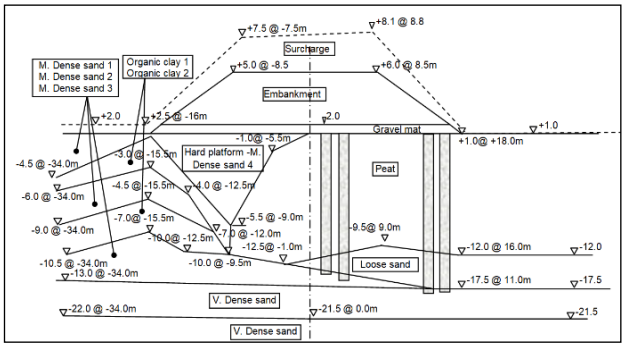

Fig. 4: Cross section of the GCPs supported embankment- section FK0+560m

plane strain two-dimensional (2-D) consolidation at the section FK0+560m chainage using an available Finite Element package PLAXIS 2D. For the numerical modelling of the referenced section, the actual geometry and material parameters were considered while the thickness of the GCP was deduced using Eq. (1a) and Eq. (1b).

2.3 *Boundary condition*

There were few sand layers and soft soil layers found as per the borehole data. The layer underneath 25m is the bedrock and it is considered as the bottom boundary which is assumed completely impermeable and rigid. The vertical boundaries were allowed movement in the vertical direction and horizontal displacement was fixed as shown in Fig. 5. The drainage boundary was taken at the ground level while the lateral boundaries were set impervious and closed.

2.4 *Material model and parameters*

In the present study, borehole logs adjacent to the cracked embankment, variation of applied current during the insertion of GCP mandrel and the laboratory test results on the undisturbed soil sample were used to model the actual soil profile. The parameters deduced from the standard penetration test and laboratory tests result other than values in approved design reports are presented in Table 1 and Table 2.

Table 1: Mohr-Coulomb parameters used in Numerical analysis (other than subsoil)

Parameters	Unit	Embankment Fill	Gravel Mat	GCP in Peat	GCP in Organic Clay
γ_{sat}	kN/m^3	20	22	22	22
γ_{unsat}	kN/m^3	20	21	21	21
k_v	m/s	1.89 x 10^{-5}	10	10	10
k_h	m/s	1.16 x 10^{-5}	10	10	10
ϕ	deg	30	40	40	40
c (D)*	kPa	10	0	0	0
E	kPa	30000	40000	8000	50000
μ	kPa	0.3	0.25	0.3	0.3

*D-Drained

Relationship with Stress Concentration Factor (SCF) and Elastic modulus ratio (E_c/E_s) was proposed by Barksdale and Bachus (1983). Accordingly, modulus ratio of 10 was taken for SCF of 3 and hence the elastic modulus of GCP was yielded as 8000kPa for GCPs in peat and 50000kPa for GCPs in organic clays (Table. 1). Other than the elastic modulus, the properties like permeability and other parameters are all taken from the study

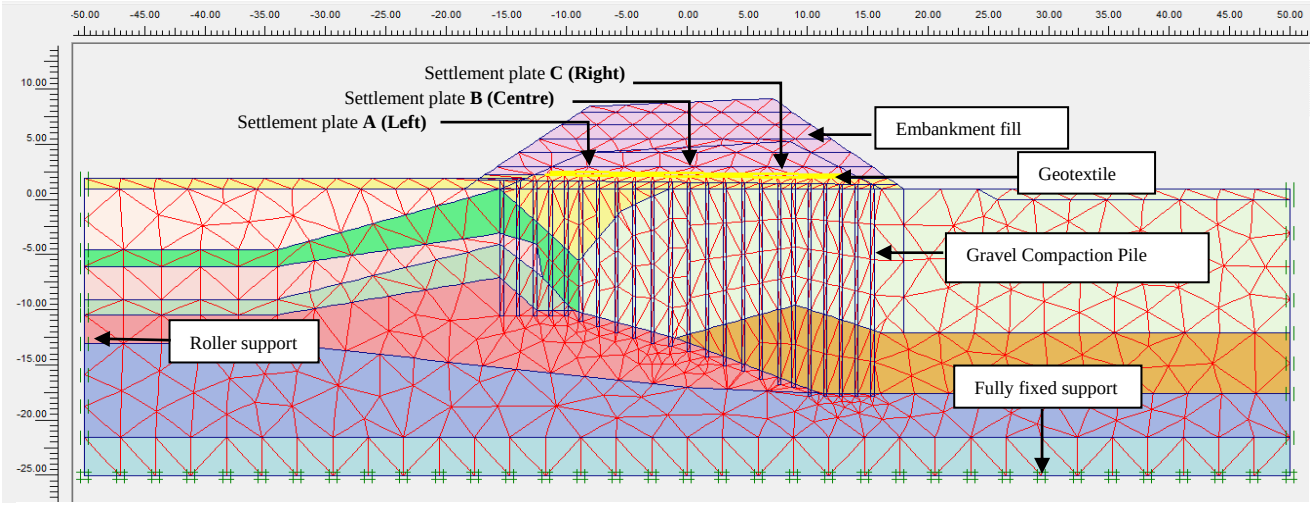

Fig. 5: Model geometry and finite element mesh (Soil profile is same as Fig. 4)

by Tan et al. (2008).

Table 2: Subsoil parameters of used in the analysis

		Soft soil Creep model			Mohr-Coulomb Model					
Parameters	Unit	Peat	O/C 1*	O/C 2	M.D.S 1*	M.D.S 2	M.D.S3	M.D.S4	V.D.S 1	L.S 1
γ_{sat}	kN/m^3	14	15	15	17	18	18	18	19	16
γ_{unsat}	kN/m^3	5	8	8	15	16	16	16	17	14
k_h	m/s	1.73×10^{-10}	1.0×10^{-10}	1.0×10^{-10}	1.16×10^{-5}	1.16×10^{-5}	1.16×10^{-5}	1.16×10^{-5}	5.79×10^{-6}	2.31×10^{-5}
k_v*	m/s	2.82×10^{-10}	1.63×10^{-10}	1.63×10^{-10}	1.89×10^{-5}	1.89×10^{-5}	1.89×10^{-5}	1.89×10^{-5}	9.44×10^{-6}	3.77×10^{-5}
ϕ	deg	0	23	25	32	36	36	32	38	31
c (D)*	kPa	0	3	5	0	0	5	0	10	0
c (UD)*	kPa	20	30	60	-	-	-	-	-	-
E	kPa	800	5000	5000	12000	25000	32000	12000	40000	10000
μ	-	0.4	0.35	0.35	0.3	0.25	0.25	0.3	0.2	0.35
e_0	-	3.913	1.5	1.2	-	-	-	-	-	-
C_c	-	0.97	0.5	0.3	-	-	-	-	-	-
C_s	-	0.1	0.05	0.03	-	-	-	-	-	-
C_α	-	0.074	0.03	0.02	-	-	-	-	-	-

*O/C -Organic Clay, *M.D.S-Medium Dense Sand, *V.D-Very Dense Sand, *L.S-Loose Sand

The hydraulic conductivity (k_v) of the soft soils was calculated using equation $C_v = k/m_v\gamma_w$

The GCPs, gravel mat, embankment fill and sandy soils were modelled as linear elastic-plastic materials with Mohr-Coulomb failure criterion. Whereas soft organic clay and peaty soils were modelled with Soft Soil Creep behaviour to account the secondary consolidation effects.

Since the smear effects likely to develop around the GCPs reduces the initial performance of GCPs and causing a delay in the dissipation of excess pore water pressure, it is important to consider its influence in plane-strain modelling. Investigating a range of field, laboratory tests and numerical back calculations, Bergado et al. (1991) and Indraratna et al. (2001) have obtained the ratio $s=r_s/r_c$ equals 2 where r_s and r_c are the radius of smear zone and radius of GCP respectively. The geometrical transformation of the smear zone can also be done using the same type of equation proposed by Tan et al. (2008). Sharma and Xiao (2000) have obtained the ratio $(\eta = k_{h,ax}/k'_{h,ax})$ of horizontal permeability of the soil layer in the smear zone is approximately 1.3 times smaller than that of the undisturbed zone. Also, it is taken the average value of k_h/k_v of 1.63 for the undisturbed soil and k_h/k_v of 1 for the smear zone (Shogaki et al., 1995). Ignoring the well-resistance, Indraratna and Redana (1997) have proposed equivalent permeability of the smear zone as follows:

$$\frac{k'_{h,pl}}{k_{h,pl}} = \frac{\beta}{\left[ln\left(\frac{n}{s}\right)+\left(\frac{k_h}{k'_h}\right)ln\,S-0.75-\alpha\right]} \qquad (04)$$

where

$$\alpha = \frac{2}{3} - \frac{4b_s^3}{3B^3} + \frac{2b_s^2}{B^2} - \frac{2b_s}{B} \;;$$

$$n = \frac{R}{r_w} \;;\; S = \frac{r_s}{r_c} \text{ and}$$

$$\beta = \frac{b_s^2}{B} - \frac{b_s^3}{3B^3} - \frac{2b_c^3}{3B^3} - \frac{2b_c b_s}{B^2} + \frac{b_c^2}{B^2} + \frac{b_c^2 b_s}{B^3}$$

$$\frac{k_{h,Pl}}{k_h,ax} = \frac{0.67}{ln(n)-0.75} \text{ (Hird et al., 1992)} \qquad (05)$$

Table 3: Coefficient of permeability used for the soft soils in numerical analysis

Material	Axisymmetric parameters	Plane-strain parameters	
		No smear (Hird et al.,1992) $k_{h,pl}$ * (m/s)	With smear $k'_{h,pl}$ * (m/s)
Peat	1.73×10^{-10}	8.62×10^{-10}	8.94×10^{-11}
O/C 1	1.00×10^{-10}	4.98×10^{-10}	5.17×10^{-11}
O/C 2	1.00×10^{-10}	4.98×10^{-10}	5.17×10^{-11}
Improved peat (C)	2.50×10^{-11}	1.24×10^{-10}	1.29×10^{-11}

* $k_{h,pl}$ and $k'_{h,pl}$ are determined from (05) and (04), respectively

2.5 *Mesh Generation and initial conditions*

Fig. 5 shows the finite element discretization of the plane strain model using 15 node triangular elements. Fine meshing was adopted to provide accurate results of the settlement, stresses and pore water pressure.

Table 4: Construction sequence of the embankment

Fill height (m)	Description	Time (Days)
0	Construction of GCP	30
0	Dissipation of pore water pressure	90
0-0.5	Construction of Gravel mat	10
0.5-1.25	Construction of Geotextile and fill that covers up to Geotextile layers	20
0	Dissipation of pore water pressure	10
1.25-2.55	Embankment fill up to the settlement plate installation	10
2.55-3.75	Embankment fill 1	85
3.75-5.05	Embankment fill 2	14
0	Dissipation of pore water pressure	22
5.05-6.25	Embankment fill 3	7
0	Dissipation of pore water pressure	10
6.5-7.1	Embankment fill 4	6
0	Surcharge Duration	227

The initial stresses were calculated based on the K_o procedure while deactivating the embankment. The construction of Ramp F was done in layers as mentioned in Table 4 and the real construction procedure was simulated in the analysis. The Finite Element model was run after assigning material parameters presented in Table 1 and Table 2, and the model was calibrated using the observed data. The parameters at the surcharge period have updated using the back-calculated strength parameters.

3 RESULTS AND DISCUSSION

In the long-term drained stability analysis of the embankment construction, the results from the numerical analysis with and without smear effects are compared with the field settlement data as illustrated in Fig. 7. The monitoring has started 150 days after the construction, and therefore settlement data has compared in the available period. The maximum settlement recorded in the left and right side of the embankment were 0.426m and 1.256m respectively. The values show that a differential settlement has occurred in that section. The main reason for this happening is, the left side of the embankment was already filled with a 10m high soil stockpile before the construction started. This has improved the soil on the left side and caused a differential settlement. The critical slip surface obtained using the shear strain rate and displacement vector from the model also confirms that the possible reason for the excess settlement on the right side was resulted due to the improvement that happened on the left side.

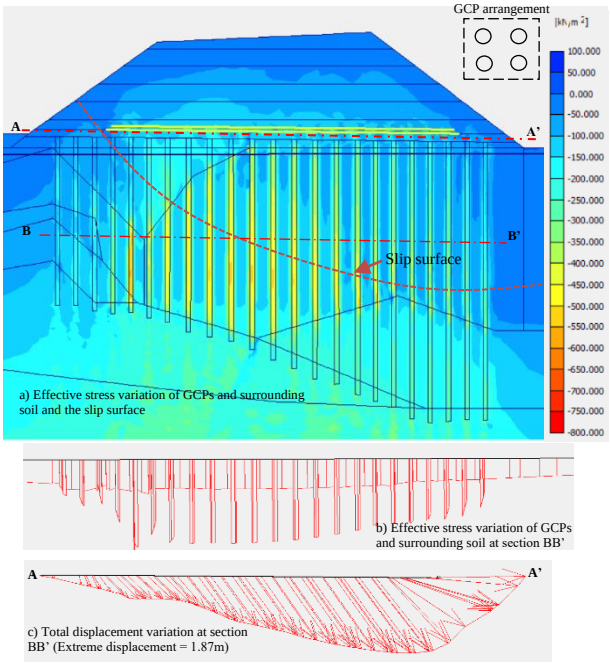

Fig. 6: Effective stress distribution due to embankment loading

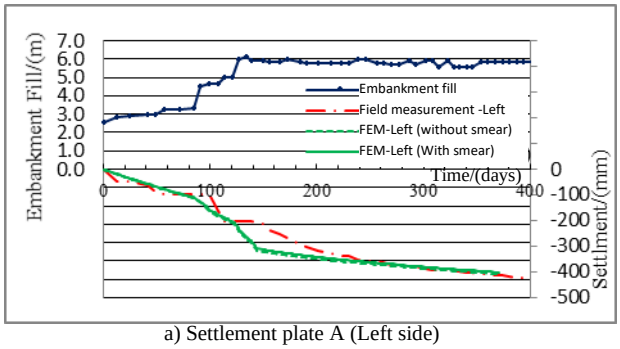

a) Settlement plate A (Left side)

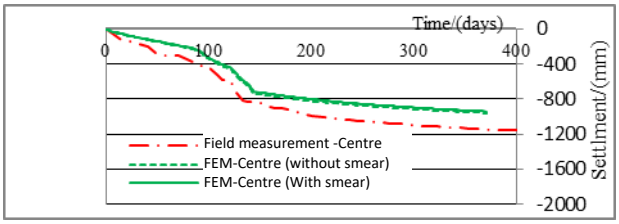

b) Settlement plate B (Centre)

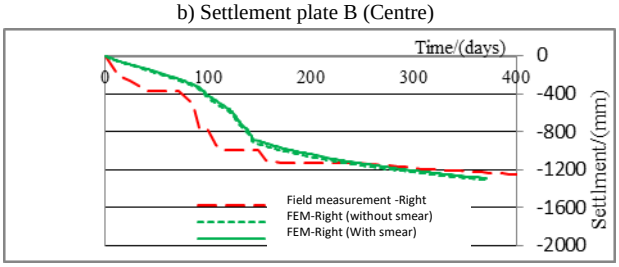

c) Settlement plate C (Right side)

Fig. 7: Variation of predicted settlement and observed settlement

Table 5: Variation of SCF at different MSL

Depth of GCP (MSL)	Average Stress Concentration Factor		
	Left (A)	Centre (B)	Right (C)
-2.0	3.2	3.0	2.8
-4.0	3.2	3.0	2.8
-6.0	3.0	2.8	2.5
-8.0	2.5	2.8	2.8
-10.0	2.0	2.2	2.5
-12.0	-	2.0	-

Fig. 6. shows how the embankment loading are carried by GCPs and the surrounding soil. The vertical stress is distributed between GCPs and surrounding soft soils in the ratio relative to the stiffness of the material and the area replacement ratio. The SCF generally changes with factors like stiffness between GCP and soil, GCP length, area replacement ratio and the characteristic of gravel mat. Although the design and numerical modelling were carried out for the SCF of 3, it is observed that it ranges between 2.0 and 3.5. According to Barksdale & Bachus (1983), a general range of SCF of GCPs lies in the range of 2.5-5.0. Also, it can be observed from Table. 5 that the SCF decreases with depth, but stayed larger than 2.0. A similar variation was found on Sand Compaction Piles by Barksdale and Bachus (1983) and Aboshi

et al. (1979) by conducting field measurement on Sand Compaction Piles at four sites in Japan.

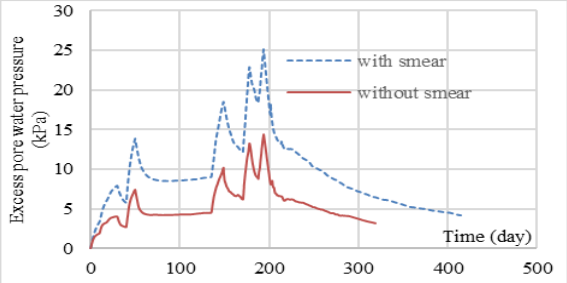

Fig. 8: Excess pore water pressure variation

The predicted excess pore water pressure with and without smear effects, at a depth of 6.0m is shown in Fig. 8. The predicted maximum excess pore water pressure was less than 25kPa; which shows the dissipation of excess pore water pressure is very fast due to the GCPs installation. Fig. 8 also shows, at every stage of embankment loading the excess pore pressure is increased and dissipated gradually. Although there is no much variation in settlement due to the smear effects, the variation of the excess pore water pressure can be seen clearly (Fig. 8).

4 CONCLUSION

In this study, a numerical procedure has been analyzed to transform an axisymmetric GCP stabilized embankment and the settlement variation is compared with the field observation. Through the analysis made, the following conclusions are drawn:

1. The model for the GCP stabilized embankment foundation yielded acceptable results in terms of settlement variation. The differential settlement resulted due to the variation of the ground profile was acceptably predicted by the model.

2. It is seen that the GCPs stabilized foundation stress was shared by GCPs and the surrounding soil in ratio to the relative stiffness of the two material which is based on SCF and area replacement ratio. Hence stiffness of the material and area replacement ratio are significantly important in predicting the behaviour of GCPs stabilized ground.

5 REFERENCES

Aboshi, H., Ichimoto, E., Enoki, M., & Harada, K. (1979). The Composer- a method to improve characteristics of soft clay by inclusion of large diameter sand columns. Proceedings of International Conference on Soil Reinforcements, pp 211-216.

Balaam, N., & Booker, J. (1981). Analysis of rigid rafts supported by granular piles, International Journal for Numerical and Analytical methods in Geomechanics, 5(4): 379-403.

Barksdale, R., & Bachus, R. (1983). Design and construction of stone columns. Springfield, Virginia: National Technical Information Service.

Barron, R. A. (1948). Consolidation of fine-grained soils by drain wells. ASCE, 718-742.

Bergado, D., Asakami, H., Alfaro, M., & Balasubramaniam, A. (1991). Smear effects of drains on soft Bangkok clay. J. Geotech. Engng (ASCE) 117, No. 10, 1509-1530.

Christoulas, S., Giannaros, C., & Tsiambaos, G. (1997). Stabilization of embankment foundation by using stone columns, Geotechnical and Geological Engineering, 247-258.

Cooper, M. R., & Rose , A. N. (1999). Stone column support for an embankment on deepalluvial soils. Proc. Instit. Civil eng. Geotech. Geol. Eng., 31: 1-22, pp 15-25.

Hansbo, S. (1981). Consolidation of fine grained soils by prefabricated drains, Proceeding 10th international conference on Soil mechanics and Foundation Engineering, The Netherlands: Publication committee of ICSMFE, pp 677-682.

Hird, C. C., Russell, D., & Pyrah, I. C. (1992). Finite Element modelling of vertical drainsbeneath embankment on soft ground. Geotechnique, 499-511.

Indraratna, B., & Redana, I. (1997). Plane-strain modelling of smear effects associated with vertical drains, Journal of Geotechnical and Geoenvironmental Engineering, Vol. 123 ,pp 474-478.

Indraratna, B., Bamunawita, C., Redana, I., & Balasubramaniam, A. (2001). Modeling of vertical drains in soft clay, 3rd Int Conf. Soft Soil Engng, Hong Kong, pp 329-137.

Jorge, C. (2017). Modeling Stone Columns. Materials, 782.

Redana, I. W., & Indraratna, B. (1997). Plane-strain modeling of smear effects associated with vertical drains. Geotechnical and Geoenvironmental Engineering, 474-478.

Sharma, J., & Xiao, D. (2000). Characterization of a smear zone around vertical drains by large-scale laboratory tests. Can. Geotech J., 37(6), 1265-1271.

Shogaki, T., Moro, H., Masaharu, M., Kaneko, M., Kogure, K., & Sudho, T. (1995). Effect of sample disturbance on consolidation parameters of anisotropic clay, Proceeding of the international symposium on Compression and Consolidation of Clayey soils, Hiroshima, Vol.1, pp 561-566.

Tan, S., & Oo, K. (2005). Stone Column FEM modeling-2D and 3D considerations illustrated by case history. Proc., Int. Symp. on Tsunami Reconstruction with Geosynthetics, (pp. 157-169). Bangkok, Thailand.

Tan, S., Tjahyono, S., & Oo, K. (2008). Simplified Plane-Strain modeling of Stone-Column Reinforced Ground. Journal of Geotechnical and Geoenvironmental Engineering, 185-194.

Terashi, M., Kitazume, M., & Minagawa, S. (1991). Bearing capacity of improved ground by sand compaction piles, American Society for Testing and Materials, pp 47-61.

Zhen, Z., Jie, H., & Guanboa, G. (2014). Numerical investigation on factors for deep-seated slope stability of stone column-supported embankment over soft clay, Engineering Geology-168, pp 104-113.

One dimensional consolidation analysis considering trapezoidal initial excess PWP

Amit Singh

Dept. of Civil Engineering, Indian Institute of Technology (BHU), India.

Manash Chakraborty

Dept. of Civil Engineering, Indian Institute of Technology (BHU), India.

ABSTRACT: Traditionally, in case of plane strain geotechnical structures consolidation analysis is carried out with the aid of Terzaghi's one-dimensional consolidation theory. In this theory, it is assumed that upon the application of additional external load, the excess pore water pressure (PWP) developed instantaneously within the consolidating layer is distributed uniformly. In most of the geotechnical text books, the analyses are carried out with this uniform PWP distribution. In the present article, an effort has been made to perform consolidation analysis by assuming a trapezoidal distribution of initial excess PWP. The analysis is carried out numerically by employing the explicit and implicit schemes of finite difference method. Different drainage conditions are considered. The isochrones are drawn at few time intervals. The average degree of consolidation with respect to time is plotted and used as a reference to compare the rate of consolidation between the conventional and the present assumptions.

1 INTRODUCTION

The phenomenon of consolidation is a very exciting topic in the field of geotechnical engineering. In this process, *initial excess pore water pressure* (u_0) that is developed instantaneously within the completely saturated clays upon the application of external load, dissipates with the passage of time. To describe this dissipation, Terzaghi (1925) pioneered the one-dimensional linear consolidation theory. The proposed theory as discussed in most of the geotechnical books (Terzaghi 1943; Berry and Reid 1988; Ranjan and Rao 2007; Punamia and Jain 2005) and used by the practicing engineers is primarily based on the assumption that the initial excess pore water pressure is developed uniformly throughout the consolidating layer. However, there is no reason to justify the uniformity of the u_0 loadings for all clays subjected to various type of external loadings. Uniform PWP can be generated beneath of earthen dam or emackment rested on impermeable layer. Few researchers (Terzaghi and Frohlich 1936; Janbu et al. 1956; Singh 2005; Singh and Swamee 2008; Lovisa et al. 2010, 2012; Lovisa and Shivakugan 2014) had considered various other forms of u_o distribution and subsequently proposed the analytical solution for different shape of u_o distribution. Junbu et al (1956) analyzed the average degree of consolidation for linearly increasing and linearly decreasing u_o for single drainage condition where impermeable layer present at the base of the soil. For one-way drainage, Singh and Swamee (2008) analyzed the isochrones for linearly increasing and decreasing case. Lovisa et al. (2010) established an alternate explanation where consolidation of soil represented in terms of normalized isochrones. Lovisa et al. (2012) observed the effect different distribution of u_o for one-way drainage by series solution method. Lovisa and Shivakugan (2014) presented the relationship between percentage of consolidation (U_{avg}) and time factor T_v for different distribution of u_o.

In the present study, an effort has been made to perform consolidation analysis by assuming various trapezoidal distribution of initial excess PWP for one-way as well as two-way drainage conditions. Linear increasing and decreasing trapezoidal form by the sudden drawn down of water table. The analysis is carried out numerically by implicit and explicit schemes of finite difference method. The impact of the trapezoidal u_o loading on the progress of the consolidation phenomenon is presented by a series of normalized isochrones and consolidating curves.

2 PROBLEM STATEMENT

A constant load of magnitude q, as shown in Fig. 1, is applied to homogeneous, isotropic clayey layer having coefficient of consolidation c_v. The thickness of the layer is considered to be H. Due to the application of the external load, trapezoidal u_o is assumed to be generated in the consolidating layer. It is intended to analyze the consolidation behavior of the layer subjected to trapezoidal u_o distribution for both single and double drainage conditions.

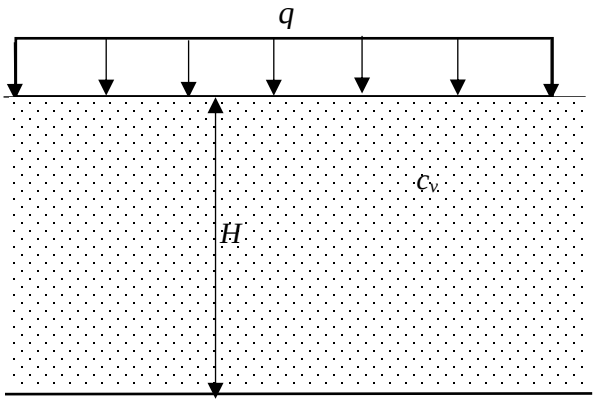

Fig. 1 Consolidating stratum subjected to strip loading

3 ANALYSIS

The numerical analysis is carried out by using Terzaghi's 1-D linear diffusion equation for Darcian flow.

$$\textit{Differential Equation: } c_v \frac{\partial^2 u}{\partial z^2} = \frac{\partial u}{\partial t} \quad (1)$$

Subjected to the following constraints:

$$\textit{Boundary Conditions} \begin{cases} \text{(i)} \quad u(z,0) = u_0 \\ \text{(ii)} \quad u(H,t) = 0 \ \text{(Single Dr.)} \\ \qquad \dfrac{du}{dz}(H,t) = 0 \ \text{(Double Dr.)} \end{cases} \quad (2)$$

$$\textit{Initial Condition: } u(0,t) = 0$$

where, u is the excess PWP at any depth from the top surface (z) corresponding to any arbitrary time, t. The drainage path (D_p) for single and double drainage are, H and $H/2$, respectively.

The initial excess PWP (u_o) is defined as the following:

Shorter base on the vertical axis (Figs. 2)

$$\begin{aligned} u_0 / u_{\max} &= \frac{Z}{b_3} && 0 \le Z < b_3 \\ &= 1 && b_3 \le Z \le b_1 \\ &= \frac{a - Z}{a - b_1 - b_3} && (b_1 + b_3) \le Z \le a \end{aligned} \quad (3)$$

Shorter base on the horizontal axis (Figs. 3 shorter on upward side)

$$u_0 / u_{max} = \frac{Z}{a} + b_2 \left(1 - \frac{Z}{a}\right) \quad (4)$$

Shorter base on the horizontal axis (Figs. 3 shorter on downward side)

$$u_0 / u_{\max} = \frac{a - Z}{a} - b_4 \left(1 - \frac{Z}{a}\right) \quad (5)$$

Here, the shape parameters b_1, b_2, b_3, and b_4, as shown in Figs. 2 and 3 varies between 0 and 1. a is the height of assumed shape

b_1 ($/b_3/b_4$) = 1 implies rectangular distribution

= 0 implies triangular distribution

The analysis is performed by writing a code in *MATLAB* (version *R2018a*).

4 RESULTS AND DISCUSSION

Due to the variation of u_o with depth, the isochrones are presented in the normalized form; where, the normalization along u and z axes are done with respect to maximum u_o (denoted as u_{max}) and thickness of the layer. Figs. 2-5 represent the isochrones for various trapezoidal u_o loadings; Figs. 2-3 display the graphs for doubly-drained clays and Figs. 4-5 show the graphs for one-way drainage condition. In these graphs: (a) the solid line represents the shape of assumed u_o, (b) the dotted curves indicate the isochrones at various time factor $(T_v = c_v t / D_p^2)$ and (c) the dashed line represent the locus of position of maximum excess PWP during the progress of consolidation process (referred here as 'u_{max} path'). The isochrones are computed for four additional T_v, namely, 0.02, 0.06, 0.1 and 0.2.

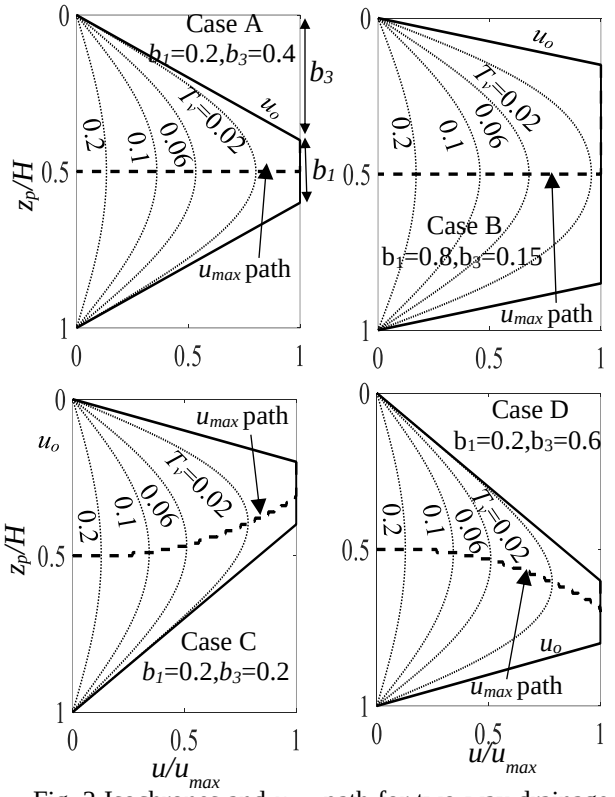

Fig. 2 Isochrones and u_{max} path for two-way drainage and corresponding to trapezoidal u_o loadings having shorter base on the vertical axis

For the symmetric distribution of u_o, as shown in Figs. 2a and 2b, the isochrones always remain to be symmetric during the consolidation phase Fig. 2 shows that the u_{max} path starts almost from the mid-point of b_1 and subsequently proceed to the central portion of the consolidating layer. Similarly, Fig. 3 depicts that the u_{max} path originates from the zone of maximum u_o and after some phase of consolidation it reaches to the central section.

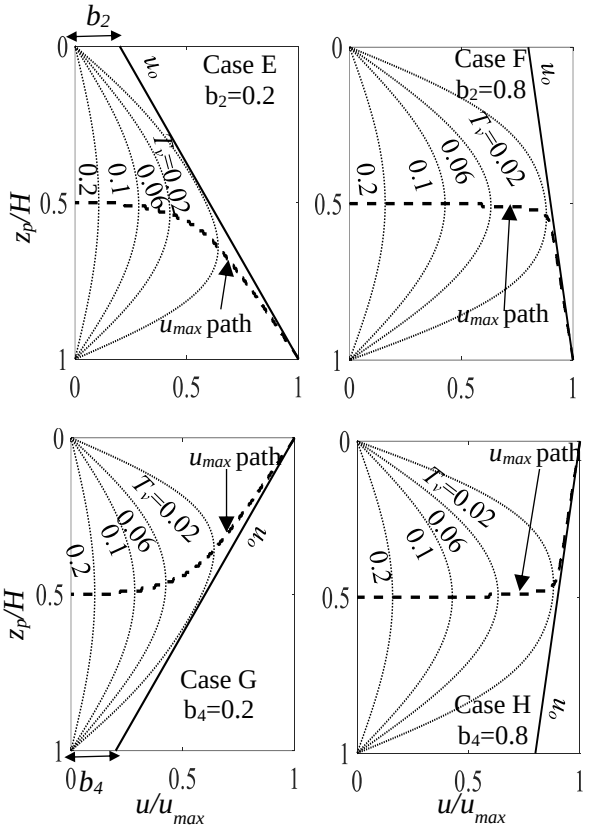

Fig. 3 Isochrones and u_{max} path for two-way drainage clays and corresponding to trapezoidal u_o loadings having shorter base on the horizontal axis

The magnitude of the shape parameters (b_1, b_2, b_3, and b_4) highly influences the speed at which u_{max} path attains a constant direction. The u_{max} path seems to be more effective way for comparing the consolidation process, because, in some sense, it eliminates the need of plotting a number of isochrones in one diagram.

For impervious bottom, pore water can drain out only from the top surface; this restriction results in generation and accumulation of excess pore

water pressure at the bottom surface. The isochrone touches the bottom impervious surface orthogonally. As the process of consolidation continues, the isochrones turn to half parabola and the curvature decreases slowly. The pore water flows in both the direction and eventually creates additional pressure at and near the bottom surface because of its imperviousness which can be the potential reason behind the redistribution of *u* near the impervious surface.

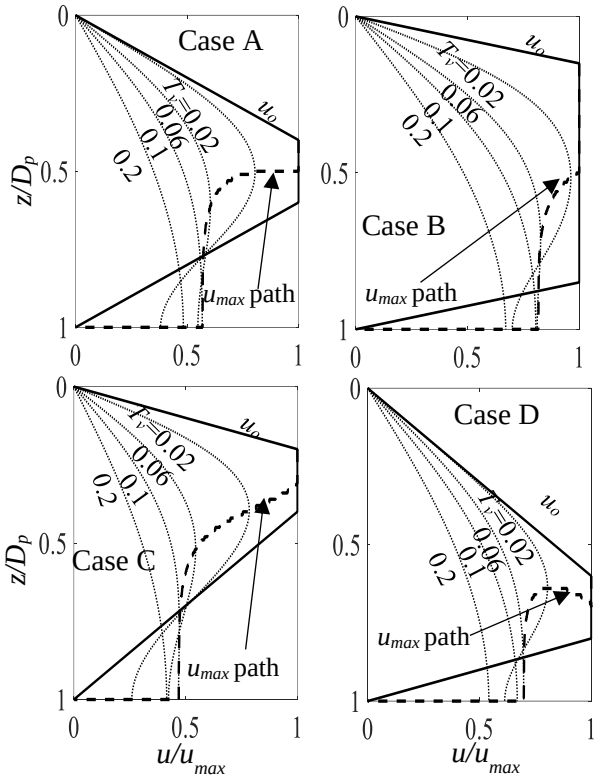

Fig. 4 Isochrones and u_{max} path for one-way drainage clays corresponding to trapezoidal u_o loadings having shorter base on the vertical axis

The u_{max} path originating from the top point of shorter base moves in the downward direction and suddenly drops down to meet the impervious surface.

Fig. 5 represent the shorter base on the X axis. From Fig. 5 it can be observed that if shorter base is at upward side, the u_{max} path passes from the impervious surface only. But in case when shorter base is at bottom side then u_{max} path originates from the right corner and then touches the bottom surface.

It is noteworthy that, u_{max} path always directed towards the central portion of the two-way drained system, whereas, for impervious bottom it is directed towards the impervious surface.

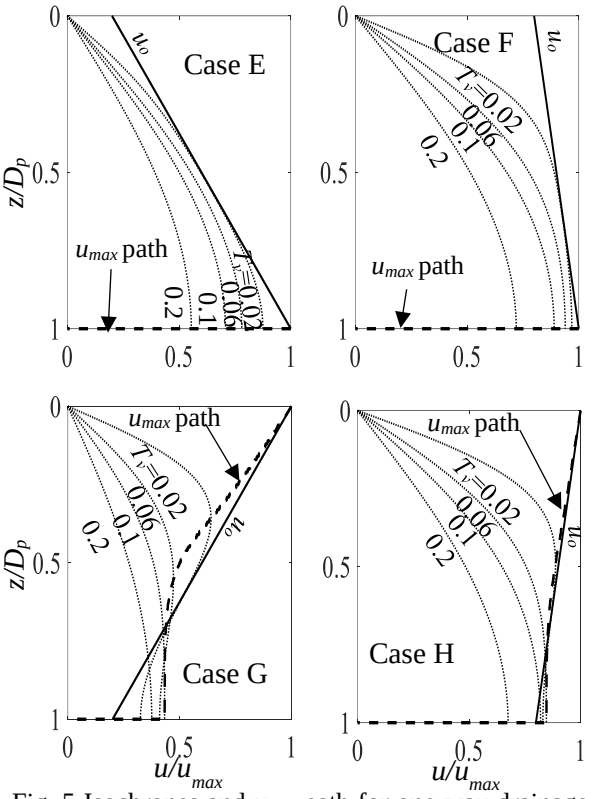

Fig. 5 Isochrones and u_{max} path for one-way drainage clays corresponding to trapezoidal u_o loadings having shorter base on the horizontal axis

Fig. 6 shows that the rate of consolidation is highly dependent on the distribution of u_o. The curves are plotted for PTPB condition. As the value of b_1 increases, the rate of consolidation increases for the symmetrically distributed u_o. For asymmetric distribution, the rate of consolidation is always constant irrespective of the value of b_3.

An interesting observation can be made in case when shorter base is on the horizontal axis. No matter what the value of b_2 and b_4 is, the consolidation curves remain to be the same for all trapezoidal u_o loading as shown for Cases E-H. Therefore, it can be concluded that the isochrones and settlement curves both are required to be presented for showing the entire process of consolidation.

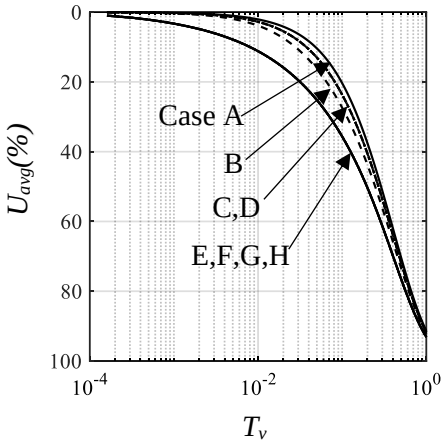

Fig. 6 Relationship between U_{avg} and T_v for two-way drained clays subjected to various trapezoidal u_o loadings

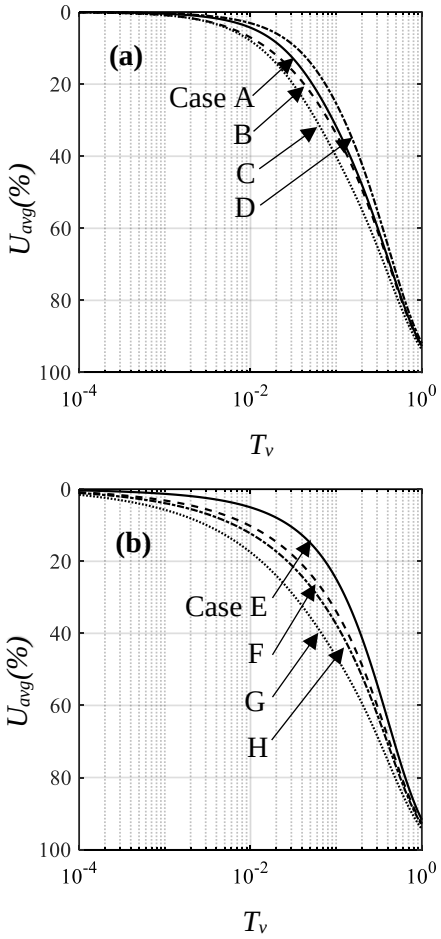

Fig. 7 Relationship between U_{avg} and T_v for two-way drained clays subjected to various trapezoidal u_o loadings: (a) Cases A-D (b) Cases E-H.

Fig. 7 represents the U_{avg} vs T_v curves for Cases A-H and subjected to single drainage condition. It is observed that the deviation between the curves obtained from the single drained clays are far more significant in comparison to its double drained counterpart. Unlike the two-way drained clays, the consolidation curves originating from Cases E-H are unique and distinct. This shows that the value of b_3 and b_4 control the settlement curves for the clayey layers having impervious bottom surface. There is very minute diffrecence between the results obtained by explicit and implicit method.

5 COMPARISON

Fig. 8 depict the comparison of the isochrones generated from the trapezoidal and conventional rectangular u_o distributions; Fig. 8a presents the curves for double drained soils, whereas, Fig. 8b displays the curves for single drained condition. It is observed that irrespective of the drainage conditions, the isochrones for the trapezoidal u_o loadings encompass smaller area than that generated from the uniform u_o distribution.

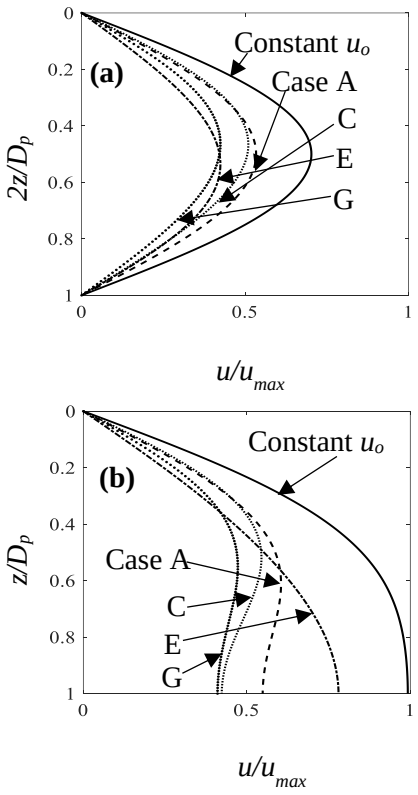

Fig. 8 Comparison of isochrones obtained from different u_o distributions and subjected to (a) two-way (b) one-way drainage.

The present numerical solutions are further compared with the analytical solution of Lovisa et al. (2010, 2012) for both the drainage conditions and corresponding to uniform u_o distribution. The deviations appear to be insignificant as shown in Fig. 9.

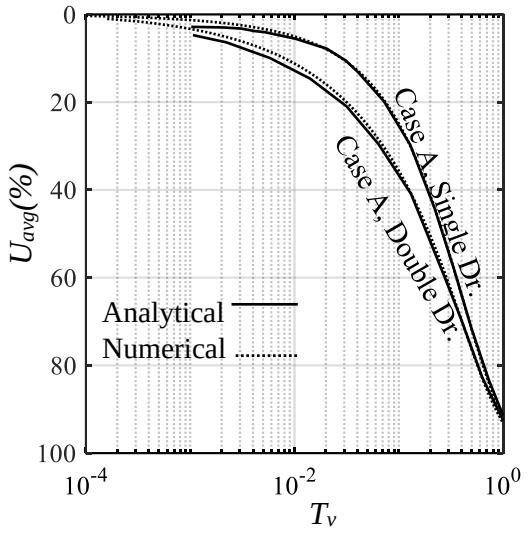

Fig. 9 Comparison analytical and numerical case

6 CONCLUSIONS

In this article the consolidation study is numerically carried out for homogenous and isotropic clays by assuming trapezoidal distribution of initial excess pore water pressure and by considering one- and two- way drainage conditions. The numerical analysis is performed by using the Crank-Nicholson scheme. The solutions are presented in terms of normalized isochrones, settlement curves and newly conceived u_{max} path. These u_{max} path provides the flexibility of representing the impact of the various shapes of u_o distribution in a much concise and compact fashion. The analyses suggest that the assumption of trapezoidal u_o distributions fasten the process of consolidation than the conventional uniform u_o loading.

7 REFRENCE

Berry, P. L., and Reid, D. (1988). An introduction to soil mechanics, McGraw-Hill, England.

Holtz, R. D., Kovacs, W. D., & Sheahan, T. C. (1981). An introduction to geotechnical engineering (Vol. 733). Englewood Cliffs, NJ: Prentice-Hall.

Janbu, N., Bjerrum, L., & Kjaernsli, B. (1956). Veiledning ved løsning av fundamenteringsoppgaver.

Lovisa, J., Read, W., & Sivakugan, N. (2010). Consolidation behavior of soils subjected to asymmetric initial excess pore pressure distributions. International Journal of Geomechanics, 10(5), 181-189.

Lovisa, J., Read, W., & Sivakugan, N. (2012). Consolidation behavior of soils subjected to asymmetric initial excess pore pressure distributions with one-way drainage. International Journal of Geomechanics, 12(3), 318-322.

Lovisa, J., & Sivakugan, N. (2015). A simple method to account for non-uniform initial excess pore water pressures in settlement computations. International Journal of Geotechnical Engineering, 9(1), 89-100.

Punmia, B. and Jain, A.K., 2005. Soil mechanics and foundations. Firewall Media.

Ranjan, Gopal, and A. S. R. Rao. Basic and applied soil mechanics. New Age International, 2007.

Singh, S. K. (2005). "Estimating consolidation coefficient and final settlement: Triangular excess pore-water pressure." J. Geotech. Geoenviron. Eng., 131(8), 1050–1055.

Singh, S. K., and Swamee, P. K. (2008). Approximate simple invertible equations for consolidation curves under triangular excess pore-water pressures. Geotech. Geol. Eng., 26(3), 251–257

Terzaghi, K.(1925). Erdbaumechanik auf bodenphysikalischer Grundlage.

Terzaghi, K. (1943). Theoretical Soil Mechanics. JohnWiley & Sons. New York, 11-15.

Terzaghi, K., and Frohlich, O. K. (1936). Theorie der Setzung von Tonschichten, Leipzig and Wein, Franz Deuticka, Vienna, Austria (in German.)

Experimental validation of element-free Galerkin (EFG) model for SENB sedimentary rocks under varied salinity conditions

P. Dinesh
IITB-Monash Research Academy, IIT Bombay, India
P. G. Ranjith
Department of Civil Engineering, Monash University, Melbourne, Australia
M. R. Behera
Department of Civil Engineering, IIT Bombay, India
W. A. M Wanniarachchi
Department of Civil Engineering, Nanyang Technological University, Singapore
M. Nelson
Department of Mechanical Engineering, IIT Guwahati, India

ABSTRACT: This study aims to investigate the mechanical properties, such as fracture toughness (K_{IC}) and Young's modulus (E) of sandstone saturated under the influence of different salinity level (0 % NaCl to 30 % NaCl). For this purpose, the experiments are performed in Three-Point Bending (TPB) fracture tests using Single-Edge Notched Beam (SENB) configuration. These experimental results are numerically validated using Element Free Galarkin (EFG) model. This model simulates the obtained TPB experimental results, that is load versus displacement plot, and its rock macro parameters, that is E and K_{IC}. Based on the experimental and numerical results, it is concluded that water and brine saturation have a significant effect on the mechanical strength parameters of the rock. The developed EFG model could easily be extended for developing crack path modelling and multiscale modelling for studying the integrity of caprock and reservoir rock in CO_2 storage application in the deep saline aquifers.

1 INTRODUCTION

Storing a large amount of carbon dioxide (CO_2) in deep saline aquifers drastically reduces the rising level of global temperature. Thus, the injected or stored CO_2 reacts with formation fluid, that is, brine, reservoir rock, that is, sandstone and caprock material, that is, siltstone material. This long-term interaction of brine-CO_2-rock minerals results in altering the rocks mechanical properties (Young's modulus (E), Poisson's ratio (ν), fracture toughness, (K_{IC}) and so on) and it is confirmed from the previous studies (Rathnaweera et al., 2015; Zhang et al., 2017). However, an important mechanical property of natural aquifer formation prior to CO_2 injection, i.e. fracture toughness (K_{IC}) is not studied in the past using Single-Edge Notched Beam (SENB) specimen. Therefore, this study aims to investigate the K_{IC} effect of sandstone under the influence of different salinity and its experimental results are validated using Element Free Galarkin (EFG) model. For this purpose, this study performs a group of sedimentary rock bending tests on sandstone which considers effect of brine saturation (% NaCl) on rock compressive strength and fracture toughness (KIC), using three-point bending (TPB) fracture tests respectively. Rock samples are shaped into blocks of specified sizes with a predefined notch for TPB tests as per ISRM and ASTM standards. In order to investigate the brine saturation effect on sandstone, it is divided into dry, water, 10%, 20% and 30% NaCl saturation. The element-free Galerkin (EFG) meshfree method simulates the obtained TPB experimental results that is, load versus displacement plot, and its rock macro parameters that is, elastic modulus, E and Poisson ratio, ν used in the simulation are obtained from dry and respective saturation conditions of TPB tests. In this simulation, the relation between load and deformation and its fracture toughness value and the crack initiation and propagation that is, mode - I crack path are predicted and also compared with experimental results. Based on the experimental and numerical modelling results, it is concluded that water and brine saturation have an extremely significant effect on the mechanical strength parameters (K_{IC}, E and ν) of the rock. The developed EFG model could easily be extended for developing crack path modelling and multiscale modelling for application of CO2 storage in the deep saline aquifers.

2 MODIFIED ELEMENT FREE GALERKIN METHOD

For the type of problem considered in the presence of cracks, the displacement approximation in the proposed EFG method takes the form of,

$$\mathbf{u}(\mathbf{x}) = \sum_{I \in w(\mathbf{x})} \Phi_I(\mathbf{x})\mathbf{u}_I + \sum_{I \in w_j(\mathbf{x})} \Phi_I(\mathbf{x})\{\mathrm{H}(f(\mathbf{x}))\}\mathbf{a}_I \quad (1)$$

where Φ_I is the shape function that is obtained through the moving least square (MLS) technique. The region that is away from the crack tip is modelled with a Heaviside function to introduce displacement discontinuity across the crack faces. The Heaviside enrichment for displacement discontinuity, H(f(x)), is given by

$$H(f(x)) = \begin{cases} 1 & if \quad f(x) \geq 0 \\ -1 & if \quad f(x) < 0 \end{cases} \quad (2)$$

where f(x) is the signed distance function. The set, w_j(x) consists of the Heaviside-enriched nodes with a displacement continuity function.

The crack tip is modelled using the diffraction method (Falzon & Muthu, 2018). The modified distance in the diffracted region is given by

$$d_r = \left(\frac{\mathrm{s}_1 + \mathrm{s}_2(\mathbf{x})}{\mathrm{s}_0(\mathbf{x})} \right)^{\rho} \mathrm{s}_0(\mathbf{x}) \quad (3)$$

The cubic B-spline weight function is given by

$$W(r) = \begin{cases} \frac{2}{3} - 4r^2 + 4r^3 & \text{for} \quad r \leq \frac{1}{2} \\ \frac{4}{3} - 4r + 4r^2 - \frac{4}{3}r^3 & \text{for} \quad \frac{1}{2} < r \leq 1 \\ 0 & \text{for} \quad r > 1 \end{cases} \quad (4)$$

$$W(x - x_I) = W(r) = W\left(\frac{\|x - x_I\|}{R_{dmi}} \right) \quad (5)$$

where R_{dmi} is the radius of the domain of influence (DMI) of node *I*. In this work, the circular DMI of a fixed size (1.75×δ) is used in a rectangular rock domain, where δ is the nodal distance. To improve the accuracy of the numerical integration, Gauss integration of a higher-order is used in the background triangular cells (Muthu et al., 2016).

2.1 *Discrete system of equations*

The governing equation for the 2D problem that is presented in this paper, which was to be solved by the EFG method and which is similar to Dolbow and Belytschko (1999), works as follows:

$$\nabla.\sigma + b = 0 \ in \ \Omega \subset R^2 \quad (6)$$

$$\sigma = C : \varepsilon = C : (\nabla_s u) \quad (7)$$

In the above, the first equation is the equilibrium equation, where σ is the Cauchy stress tensor, and *b* is the body force per unit volume. The constitutive relation is given by the second equation, in which *C* is the elasticity tensor, *u* is the displacement field, and ∇_s denotes the symmetric gradient operator by assuming small deformation kinematics.

The boundary conditions are as follows

$$\begin{aligned} &\sigma.n = \bar{t} \ on \ \Gamma_t \\ &u = \bar{u} \ on \ \Gamma_u \end{aligned} \quad (8)$$

where *n* is the unit outward normal on the boundary, $\Gamma = \Gamma_t \cup \Gamma_u$, with $\Gamma_t \cap \Gamma_u = \emptyset$.

The final discrete system of equations is as follows:

$$\begin{bmatrix} K & G \\ G^T & 0 \end{bmatrix} \begin{Bmatrix} u \\ \lambda \end{Bmatrix} = \begin{Bmatrix} f \\ q \end{Bmatrix} \quad (9)$$

$$K_{IJ} = \int_{\Omega} B_I^T D B_J d\Omega \quad (10)$$

where *D* is plane-strain isotropic elasticity matrix in this work. $B_I = \left[B_I^{std} \mid B_I^{enr} \right]$ is the strain-displacement matrix. B_I^{std} is the standard term, and B_I^{enr} arises due to the enrichment. Ψ_I can be $\mathrm{H}(f(\mathbf{x}))$, depending on the node. B_I^{std} and B_I^{enr} are given by

$$B_I^{std} = \begin{bmatrix} (\Phi_I)_{,x} & 0 \\ 0 & (\Phi_I)_{,y} \\ (\Phi_I)_{,y} & (\Phi_I)_{,x} \end{bmatrix} \quad (11)$$

$$B_I^{enr} = \begin{bmatrix} (\Phi_I)_{,x}\Psi_I + \Phi_I(\Psi_I)_{,x} & 0 \\ 0 & (\Phi_I)_{,y}\Psi_I + \Phi_I(\Psi_I)_{,y} \\ (\Phi_I)_{,y}\Psi_I + \Phi_I(\Psi_I)_{,y} & (\Phi_I)_{,x}\Psi_I + \Phi_I(\Psi_I)_{,x} \end{bmatrix} \quad (12)$$

$$f = \int_{\Gamma} \Phi_I \bar{t} d\Gamma + \int_{\Omega} \Phi_I b d\Omega \quad (13)$$

G is due to the Lagrange multipliers that impose the essential boundary conditions, and N_K are the Lagrange shape functions at the node, *K*.

$$G_{IK} = -\int_{\Gamma_u} \Phi_I N_K d\Gamma \quad (14)$$

$$q_K = -\int_{\Gamma_u} \Phi_I \bar{u} d\Gamma \quad (15)$$

The advantage of EFG over enriched methods such as XFEM and XEFG is that the enriched methods require prior knowledge of the analytical solutions for the crack-tip stress field in order to locally enrich the nodal solution in the vicinity of a crack tip. However, the analytical solution may not be available in all the cases. This is circumvented in the present problem by adding extra nodes around the crack tip without compromising the accuracy. This is possible due to the higher-order nature of the shape functions of the EFG method (Iranmanesh et al., 2018; Lancaster & Salkauskas, 1981; Levin, 1998; Liu, 2009; Samimi & Pak, 2012). Due to these advantages, the EFG method can capture the stress field with an accuracy that is sufficiently close to the strong discontinuity that has a relatively moderate nodal density.

3 SIF EXTRCATION USING EFG METHOD

In order to demonstrate the efficiency of the proposed EFG method, one case study that examines a crack in a rock sample have been considered. The first case study examines the SENB sample to estimate the SIF using interaction or M-Integral under TPB loading.

Case study 1: The Single-edge notched beam (SENB) subjected to TPB loading

Fig. 1 shows the EFG-based SENB model that is subjected to three-point bending (TPB) loading in a block specimen. The dimensions of the 2D model under consideration are similar to the 3D FEM model of Pakdaman et al. (2019). They have used approximately 7800 elements and 35,000 nodes to calculate a dimensionless SIF, which is independent of the applied load. However, in the case of the EFG method, the same SIF values are obtained by using a nodal density of 91 × 21, nodal refinement of 9 × 9, and 3 × 3 diffraction nodes around the crack tip with less than 3.65 % of relative error in comparison to analytical SIF, which is according to ASTM standards (ASTM, 1990), as shown in Eq. (19).

In the present work, mixed-mode SIFs are computed through the popular interaction integral/M-integral (Yau et al., 1980; Yu et al., 2009) and are given by,

$$I = \int_A (\sigma_{ij} u_{i,1}^{aux} + \sigma_{ij}^{aux} u_{i,1} - \sigma_{ik}\varepsilon_{ik}^{aux}\delta_{1j}) q_{,j} dA \quad (16)$$

where A is the area of integration, which is enclosed by the crack tip, as shown in **Fig. 1**. q is a scalar function; it has a value of unity on S_1 and zero on S_2. The area, A_o, shrinks to zero. E and υ are, respectively, Young's modulus and Poisson's ratio. σ_{ij}^{aux}, ε_{ik}^{aux} and u_i^{aux} are auxiliary state values that correspond to the theoretical crack tip solution in a homogenous material. The auxiliary solution for the integral in Eq. (16) is the same as that of the crack tip solution for a homogenous material.

For a crack in an isotropic and homogenous material, the interaction integral/M-integral is equal to Eq. (17).

$$I = \frac{(2K_I K_I^{aux} + 2K_{II} K_{II}^{aux})}{E^*} \quad (17)$$

where E^* is E for the plane stress and $E/(1\text{-}\upsilon^2)$ for the plane strain. K_I is evaluated by setting K_I^{aux} to unity and K_{II}^{aux} to zero. Similarly K_{II} is evaluated by setting K_{II}^{aux} to unity and K_I^{aux} to zero.

The numerical integration is performed by using 13 Gauss points closer to the crack tip and 8 Gauss points for the region that is away from the crack and which has a triangular background mesh. The numerically evaluated dimensionless SIF, *Y*, in Eq. (18), is determined by substituting geometrical parameters such as *W* and *B* with 0.10 m, Mode-I SIF, K_I for a constant load, and *F* as 1000 N for different crack lengths, *a* are shown in **Table 1**.

The SIF values from the analytical solution in Eq. (19), the numerical SIF from the FEM model and the results from the EFG model are plotted in **Fig. 2**. By knowing the dimensionless SIF of a pre-cracked specimen, one can easily identify the maximum load **(**F_{max}**),** which is the load carrying capacity of the same specimen**.** This capacity is obtained by identifying the fracture toughness, K_{IC}, of that material. Therefore, it is important to obtain the property of fracture toughness though laboratory experiments. Such experiments have been performed in this paper in the later sections to verify the developed EFG model by using the load-displacement responses from the SENB specimen. The crack path determined from the EFG method in this SENB model is a straight line, which is also true and matches with a theoretical sample that is under homogeneous and isotropic conditions. Although this crack path is independent of material properties (E, ν and K_{IC}) and the magnitude of the load, it depends on the direction of load application. However, in natural rock samples, the crack path may not be a straight-line propagation due to the inherent heterogeneity in the composition of the mineral.

$$Y = \frac{K_I B W^{3/2}}{Fl} \tag{18}$$

where W is the width of the specimen, B is the thickness of the specimen and l is the length of the specimen.

$$Y = \left[\frac{3\sqrt{r}\left(1.99 - r(1-r)\left[2.15 - 3.93r + 2.7r^2\right]\right)}{2(1+2r)(1-r)^{3/2}} \right] \tag{19}$$

where r is the ratio of crack length, a to the width of the specimen, W.

$$K_{IC} = \frac{F_{max} l}{BW^{3/2}} Y \tag{20}$$

where K_{IC} critical stress intensity factor or fracture toughness of the material. F_{max} is the maximum load obtained from the load displacement plot.

Fig. 2 shows the comparison of all the models namely, the analytical solution of non-dimensional SIF, Y versus $r = a/W$, 3D FEM model results obtained from Pakdaman et al. (2019), and, the modified EFG model results obtained from the present study. Almost all of the simulation results follow the similar trend.

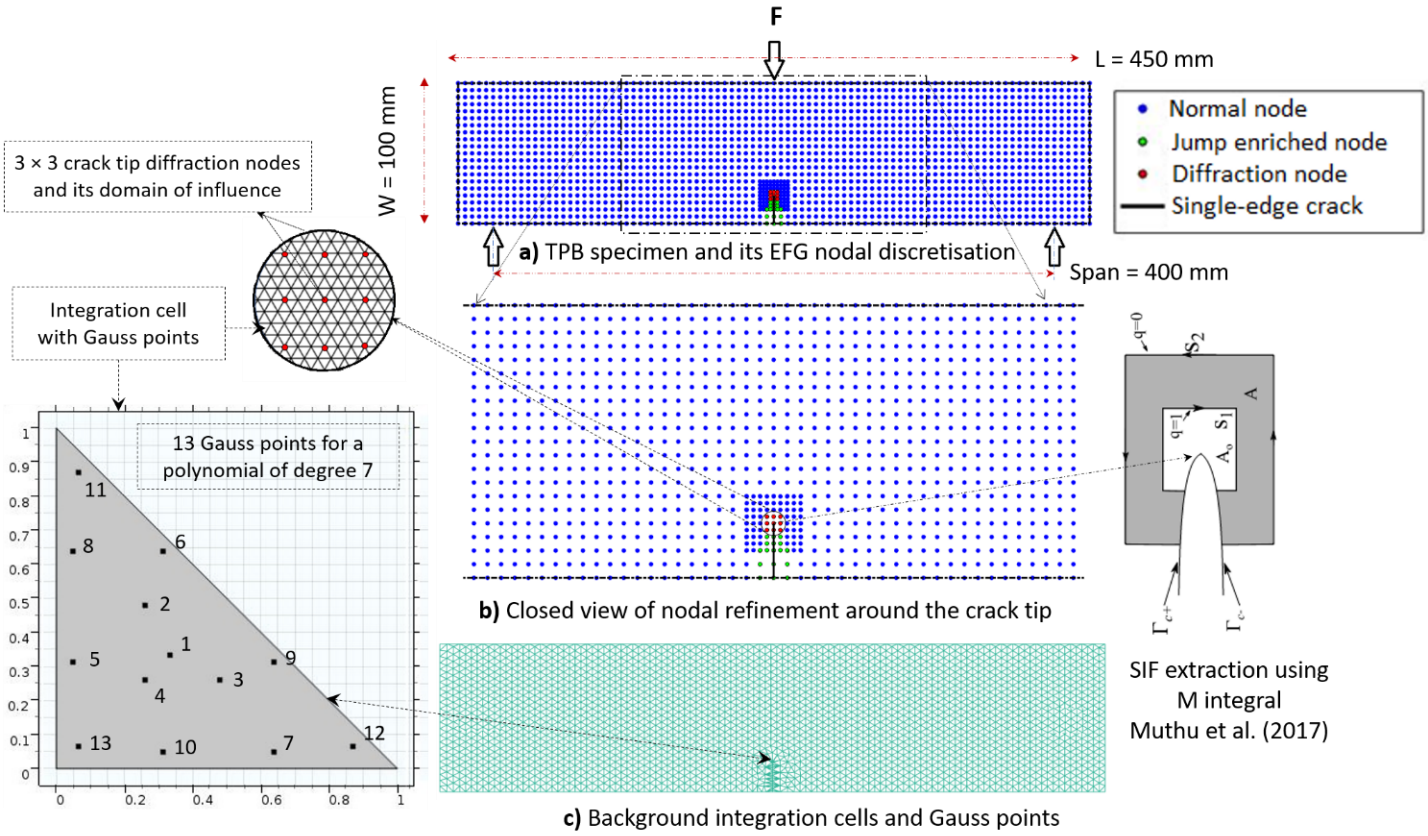

Fig. 1 The SENB sample under TPB loading: a) TPB beam nodal discretisation; b) closer view of nodal discretisation around the crack tip and c) background integration triangular cells for numerical integration.

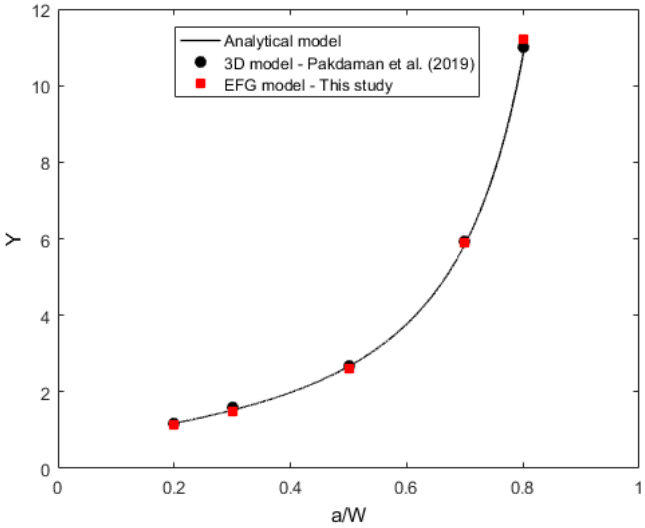

Fig. 2. Comparing the analytical, numerical and EFG values of the dimensionless stress intensity factor in the SENB test.

4 EXPERIMENTAL RESULTS AND DISCUSSION

The following sections describe the experimental methodology of Three-point beam bending (TPB) fracture tests performed on Gosford sandstone under the influence of water and brine saturations as shown in **Fig. 3**. The TPB test was carried out using servo-controlled G95-Instron 4204 50kN Testing Machine, and the strain rate was maintained at 0.02 mm/min for all the tests. The load versus displacement plot for all the representative brine saturated samples are shown in **Fig. 4** and **Table 1**.

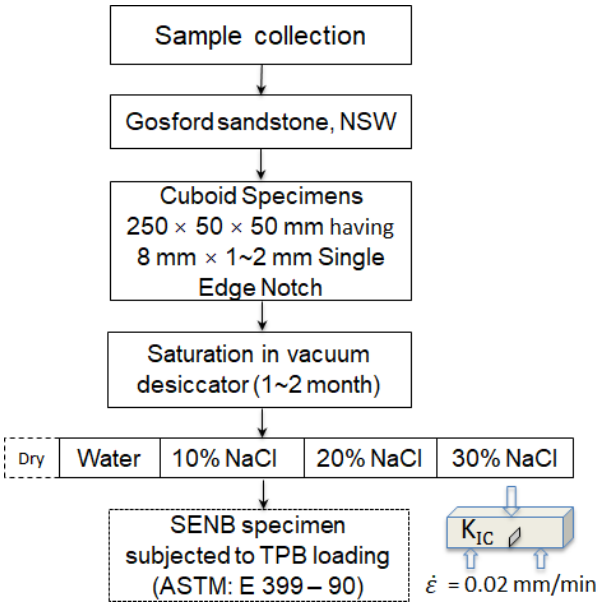

Fig. 3. Experimental methodology used in this work.

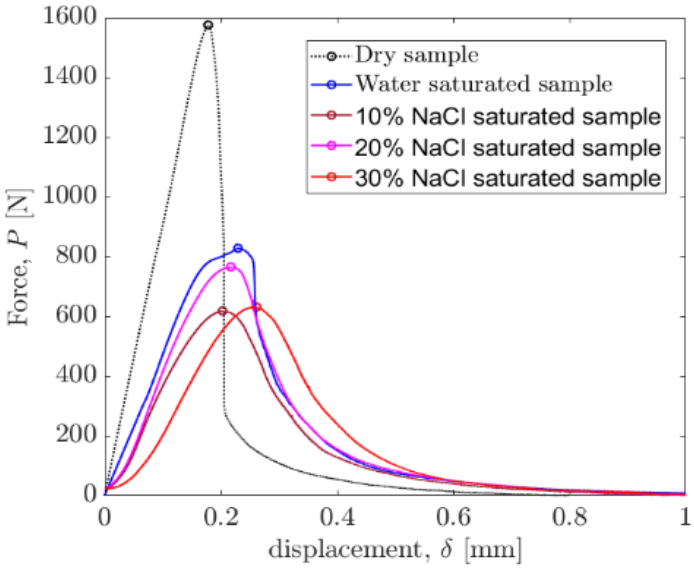

Fig. 4. Force versus displacement, *P-δ* curves obtained from SENB samples of TPB experiments.

Table 1. Comparison of critical load (P_{max}) and displacement (δ) experimental results of sandstone.

Saturation cases	TPB sample name	Peak load, P_{max} (N)	Experimental Displacement at P_{max} δ (mm)	Saturation time
Dry	S1-1	1941.80	0.217	Oven dried
	S1-2	2021.87	0.226	Oven dried
	S1-3	1574.65	0.178	Nominally dry
	S1-4	1527.04	0.217	Nominally dry
water	S2-3	828.00	0.229	1 Month
	S2-4	731.16	0.215	1 Month
	S2-5	724.02	0.253	1 Month
10 % NaCl	S3-1	615.59	0.231	2 Month
	S3-3	748.47	0.225	1 Month
	S3-4	617.38	0.203	1 Month
20 % NaCl	S4-1	583.38	0.209	2 Month
	S4-3	764.75	0.217	1 Month
	S4-4	666.99	0.234	1 Month
30 % NaCl	S5-1	506.38	0.144	2 Month
	S5-2	529.86	0.227	2 Month
	S5-3	651.88	0.328	1 Month
	S5-4	630.52	0.260	1 Month

Fig. 5 shows the variation of peak load results of different saturation condition obtained from the above **Table 1**. The error bar shows the deviation of experimental results with respect to average value of samples saturated with one and two-month brine saturation and the percentage fall in peak load values with respect to dry sample results. **Fig. 6** shows the comparison of experimental and numerical fracture toughness values with its relative error. Zuo et al. (2014) proposed a new method to find the

Young's modulus in TPB tests using the expression, $E = Kl^3/48$ I, in which K is the stiffness value obtained from the linear portion of load versus displacement curve, l is the length of the TPB specimen, and I is the moment of inertia of the cracked cross section, $I = B\ (W-a)^3/12$. In future, one need to study the comparison of Young's modulus under bending and compressional behavior.

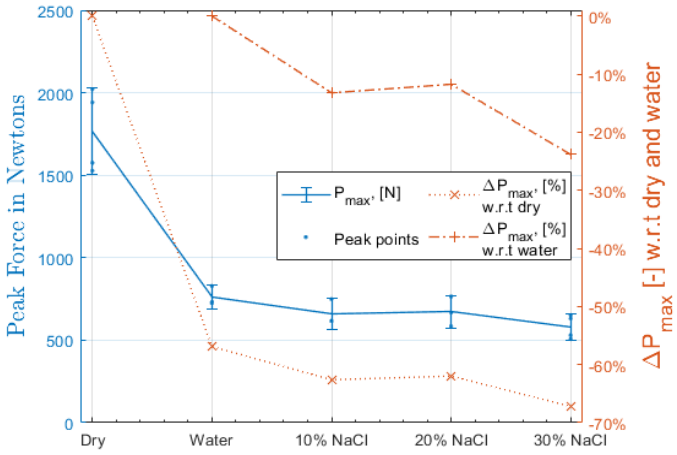

Fig. 5. Peak force variation of varied brine saturated SENB samples and its percentage change in force values with respect to dry and water saturated cases.

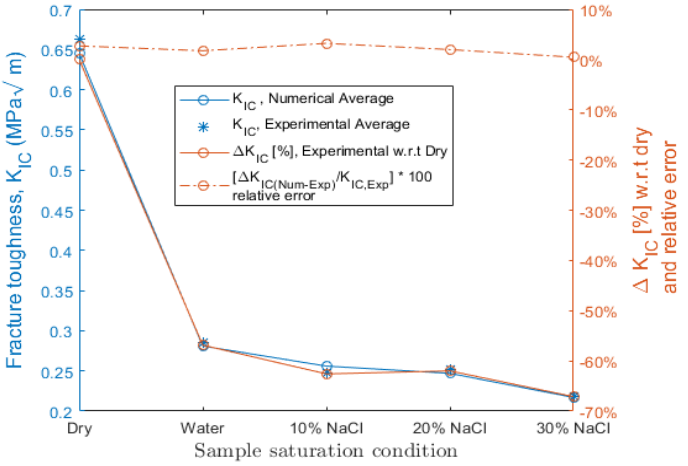

Fig. 6. Fracture toughness variation of varied brine saturated SENB samples and its percentage change in K_{IC} values with respect to dry and water saturated cases

5 CONCLUSIONS

In this paper, the mechanical properties (Elastic modulus, E and fracture toughness, K_{IC} from TPB tests) of Gosford sandstone are studied. The effect of water and brine saturation of sedimentary rocks on the mechanical properties (elastic modulus and fracture toughness) has been studied and the observations were reported. The dry SENB specimens undergo brittle failure when subjected to TPB loading. The water- and NaCl-saturated samples show non-linear softening before failure. The obtained mechanical properties from the TPB tests for water- and brine-saturated specimens, which indicate a degradation in the property of the material. However, for the specimen that is brine-saturated in 30% of NaCl, the KIC decreases when compared to the samples that are brine-saturated in 10% and 2 % of NaCl; this indicates the presence of dissolution mechanism: the formation of rock salt precipitates in the pore space. This has been observed in XRD and SEM studies as well. It has been observed that the elastic modulus and the fracture toughness decrease along with the time taken for saturation, as expected.

ACKNOWLEDGMENTS

The authors are thankful to 3GDEEP laboratory staff members of Monash University for their constant support to carry out this experimental work.

REFERENCES

Dolbow, J., & Belytschko, T. (1999). Numerical integration of the Galerkin weak form in meshfree methods. *Computational mechanics*, *23*(3), 219-230.

Falzon, B. G., & Muthu, N. (2018). 1.13 Micromechanical Modelling of Composite Materials Using the Element-Free Galerkin Approach. In P. W. R. Beaumont & C. H. Zweben (Eds.), *Comprehensive Composite Materials II* (pp. 327-352). Elsevier. https://doi.org/https://doi.org/10.1016/B978-0-12-803581-8.09888-X

Iranmanesh, M. A., Pak, A., & Samimi, S. (2018). Non-isothermal simulation of the behavior of unsaturated soils using a novel EFG-based three dimensional model. *Computers and Geotechnics*, *99*, 93-103.

Lancaster, P., & Salkauskas, K. (1981). Surfaces Generated by Moving Least-Squares Methods. *Mathematics of computation*, *37*(155), 141-158. https://doi.org/Doi 10.2307/2007507

Levin, D. (1998, Oct). The approximation power of moving least-squares. *Mathematics of computation*, *67*(224), 1517-1531.

https://doi.org/Doi 10.1090/S0025-5718-98-00974-0

Liu, G.-R. (2009). *Meshfree methods: moving beyond the finite element method*. CRC press.

Muthu, N., Maiti, S. K., Falzon, B. G., & Yan, W. Y. (2016, Nov). Crack propagation in non-homogenous materials: Evaluation of mixed-mode SIFs, T-stress and kinking angle using a variant of EFG Method. *Engineering Analysis with Boundary Elements, 72*, 11-26. https://doi.org/10.1016/j.enganabound.2016.07.017

Rathnaweera, T., Ranjith, P., Perera, M., Haque, A., Lashin, A., Al Arifi, N., Chandrasekharam, D., Yang, S., Xu, T., & Wang, S. (2015). CO2-induced mechanical behaviour of Hawkesbury sandstone in the Gosford basin: An experimental study. *Materials Science and Engineering: A, 641*, 123-137.

Samimi, S., & Pak, A. (2012). Three-dimensional simulation of fully coupled hydro-mechanical behavior of saturated porous media using Element Free Galerkin (EFG) method. *Computers and Geotechnics, 46*, 75-83.

Yau, J. F., Wang, S. S., & Corten, H. T. (1980). A Mixed-Mode Crack Analysis of Isotropic Solids Using Conservation Laws of Elasticity. *Journal of Applied Mechanics, 47*(2), 335-341. https://doi.org/10.1115/1.3153665

Yu, H., Wu, L., Guo, L., Du, S., & He, Q. (2009). Investigation of mixed-mode stress intensity factors for nonhomogeneous materials using an interaction integral method. *International Journal of Solids and Structures, 46*(20), 3710-3724. https://doi.org/http://dx.doi.org/10.1016/j.ijsolstr.2009.06.019

Zhang, D., Pathegama Gamage, R., Perera, M. S. A., Zhang, C., & Wanniarachchi, W. A. M. (2017). Influence of water saturation on the mechanical behaviour of low-permeability reservoir rocks. *Energies, 10*(2), 236.

Zuo, J.-p., Xie, H.-p., Dai, F., & Ju, Y. (2014, 2014/09/01/). Three-point bending test investigation of the fracture behavior of siltstone after thermal treatment. *International Journal of Rock Mechanics and Mining Sciences, 70*, 133-143. https://doi.org/https://doi.org/10.1016/j.ijrmms.2014.04.005

Large deformation analysis to simulate penetration of offshore pipelines

D.S. Liyanapathirana
School of Engineering, Western Sydney University, Australia

ABSTRACT: This paper presents an investigation into the penetration resistance of offshore pipelines during initial vertical penetration and subsequent lateral penetration, which often occur due to thermal expansion or submarine landslides. Since the soft seabed deformations are large during the penetration process, this problem cannot be simulated using a small strain finite element analysis. Therefore, a Large Deformation Finite Element (LDFE) analysis procedure has been developed using the PYTHON language to simulate this problem utilising the features within the ABAQUS/Standard finite element modelling program. The constitutive behaviour of the soft seabed soil is simulated using the Mohr-Coulomb model. A coupled analysis considering excess pore pressure generation and subsequent dissipation has been performed for the first time for pipeline penetration problem. Results from the LDFE analysis was compared with existing solutions and data collected from centrifuge tests carried out at the Australian National Centrifuge facility at the University of Western Australia to validate the proposed modelling procedure.

1 INTRODUCTION

In deep water, offshore pipelines are laid over seabed directly without any additional restraining mechanisms or trenching. During the laying process, they embed shallowly over the seabed predominantly due to the self-weight. In addition, forces due to wave action and pipe laying equipment may also contribute to the initial positioning. Geotechnical design of pipelines is underdeveloped compared to other common foundation types. At the same time, pipeline design is distinctly different to other foundation types because lateral deformations expected of pipelines during service are relatively large compared to other foundation types such as piles or footings. In general, lateral deformations of pipelines are equivalent to few diameters of the pipeline and often they can exceed more than ten pipe diameters across the seabed. However, for other foundation types, lateral deformations are only a fraction of the foundation diameter. Therefore, pipeline design should consider resistance to both vertical penetration and lateral deformations.

Classical plasticity theory has been widely used to investigate the failure mechanisms and ultimate loads during pipe penetration into the seabed (e.g., Martin and Randolph, 2006; Randolph and White, 2008). Also finite element analysis has been widely used to study this problem considering small-strain (e.g., Aubeny et al., 2005; Merifield et al., 2008, 2009) and large deformation (e.g., Chatterjee et al., 2012; Wang et al., 2010) analysis approaches. Centrifuge test data published by Dingle et al. (2008) are extremely useful as a validation tool for researchers who work in this area using either numerical modelling or developing analytical solutions.

When using small-strain based finite element modelling, it is not possible to simulate penetration of the pipeline from the surface of the seabed. Always analysis was carried out considering a wished-in-place pipeline. Recently published research considering Large Deformation Finite Element (LDFE) analysis by Wang et al. (2010) and Chatterjee et al. (2012), strain softening of the soil and rate effects are incorporated but their analysis procedures are not capable of capturing the pore pressure effects.

When a pipeline is laid over the seabed, excess pore pressures will generate. Hence, it is important to understand how excess pore pressures will influence the resistance to lateral pipeline deformations. Therefore, in this paper, a coupled LDFE analysis has been proposed incorporating the pore pressure effects to simulate the pipeline penetration and subsequent lateral deformations in the soft seabed. First part of the paper presents the development of the LDFE analysis procedure using the PYTHON development environment within the ABAQUS/Standard finite element program. In the second part, the results for penetration resistance during vertical penetration are compared with the centrifuge test data by Dingle et al. (2008), LDFE analysis results by Wang et al. (2010) and Upper Bound (UB) solution by Randolph and White (2008). Finally, the capability of the proposed approach in analysing combined large vertical and lateral penetrations, which cannot be simulated using traditional small-strain based finite element

programs (e.g., ABAQUS/Standard, PLAXIS, PHASE 2&3) is demonstrated.

2 LDFE ANALYSIS PROCEDURE

The LDFE analysis procedure presented in this paper is written by the author using the PYTHON Development Environment (PDE) within the ABAQUS/Standard finite element modelling program. The analysis is carried out in a series of small-strain finite element analysis stages. ABAQUS/Standard input file for each analysis was created using the PYTHON code developed by the author. After each analysis, the deformed boundary of the mesh is captured and a new mesh is generated. The new mesh can have either the same number of elements or it can be changed.

All variables corresponding to integration points and nodes of the old mesh were transferred to the new mesh using the solution mapping algorithm in ABAQUS/Standard. During solution mapping, all variables corresponding to integration points of the old mesh are transferred to nodes of the old mesh and averaged when a node is shared by several elements. Then the interpolation is carried out to the integration points of the new mesh. Similarly, all nodal variables such as pore pressures in a coupled analysis are transferred from nodes of the old mesh to the nodes of the new mesh. The variables transferred from the old mesh to the new mesh will act as initial conditions for the new mesh.

The duration of each analysis should be determined by taking into account the mesh deformations, because the accuracy of analysis depends on the mesh deformations at the end of each remeshing step. Therefore, the criteria for the generation of the new mesh using the boundary of the deformed old mesh should be set before excessive mesh deformations. If there is a discontinuity in the solutions, it can be due to the use of a too coarse mesh or carrying out remeshing, when the elements are excessively distorted. Specific details regarding the LDFE approach presented in this paper will be discussed in the following sections.

3 NUMERICAL MODEL

The problem presented in this paper is about pipeline penetration. Since the length of the pipeline is significantly larger than the diameter, problem is simulated using a two-dimensional plane-strain model as shown in Figure 1. Since the simulation involves vertical penetration and subsequent lateral movement of the pipeline, symmetry in geometry has not been considered when creating the finite element mesh. The soil domain, which represents the seabed in this case, extends sufficiently away from the pipeline, avoiding any boundary effects on measured penetration resistance. The model shown in Figure 1 extends 17.5D in the horizontal direction and 6.25D in the vertical direction, where D is the diameter of the pipeline. The two side edges of the model were restricted to move in the horizontal direction but freed to move in the vertical direction. The bottom boundary was restrained in both vertical and horizontal directions.

The pipe was modelled as an elastic material with a very high Young's modulus compared to the soil as shown in Table 1 to avoid any deformations. The seabed is modelled assuming the Mohr-Coulomb failure criteria. Material properties for both seabed and pipeline are given in Table 1. The Pipeline was modelled using the element CPE4, which is a four-node quadrilateral element. The soil was modelled with the same element but with pore pressure degrees of freedom at the corner nodes, CPE4P. Although CPE4 is a linear element, for the remeshing analysis, linear element could avoid convergence issues faced with the quadratic CPE8R and CPE8RP elements, and CPE8 and CPE8P elements.

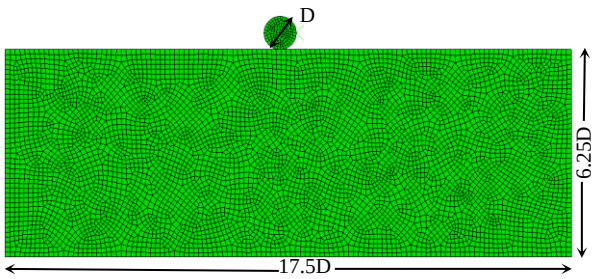

Figure 1. Finite element model

The pipe-soil interaction was modelled using the contact algorithm in ABAQUS/Standard with soil surface as the slave surface and the pipe surface as the master surface. Interaction was modelled using the penalty approach. Different options available within the penalty approach when defining interface friction will be discussed in Section 4.

All the analyses presented in this paper are performed based on the principle of effective stresses considering the pore pressure generation and dissipation. Water table is assumed to be at the surface and simulated using a zero pore pressure boundary in the finite element model.

Pipeline penetration in both vertical and lateral directions were simulated at a rate of 1 mm/s to maintain undrained penetration similar to the centrifuge tests by Dingle et al. (2008). The vertical penetration was carried out for a depth equivalent to one diameter and the lateral movement was also simulated up to a distance of one diameter. For each case presented in this paper, 20 remeshing analyses were performed, with 10 in each direction. That means each

analysis simulated a penetration of 10% of D in respective direction.

Initial and each remeshing analysis consists of two stages. In the first stage of the initial analysis, the initial geostatic stress field is generated by defining the initial vertical stress distribution and coefficient of earth pressure at rest to auto generate the horizontal stress distribution. A body load is defined to bring the initial stress field to an equilibrium state without causing any mesh deformations. Then in the second stage, penetration of 10% of D is applied to the pipeline. In all subsequent remeshing analyses, this initial stage is used to bring mapped stresses (from the old mesh to the new mesh) to an equilibrium state, before applying the 10% of D as a displacement controlled boundary to the pipeline in the second stage of the analysis.

Table 1. Material properties

	Seabed	Pipeline
Unit weight, γ (kN/m^3)	20	
Elastic Modulus, E (MPa)	2.0	1x10^9
Poisson's ratio, v	0.3	0.3
Cohesion, c' (kPa)	5	
Friction angle, ϕ' (°)	20	
Permeability coefficient, k (m/s)	2x10^{-8}	

4 RESULTS

In this section, results from the LDFE analysis are validated against centrifuge test data (Dingle et al., 2008) and previous LDFE analysis results published by Wang et al. (2010). Although Wang et al. (2010) presented LDFE analysis results considering undrained behavior for seabed soil without considering pore pressure effects, a coupled analysis produces undrained penetration, if the adopted penetration rate is sufficiently fast. According to Finnie and Randolph (1994), $vD/c_v > 30$ is required to maintain undrained conditions around a penetrating surface footing, where v is the rate of penetration, D is the footing diameter and c_v is the coefficient of consolidation. If the same analogy is adopted for pipelines, the penetration rate of 1 mm/s selected in this study and the centrifuge test by Dingle et al. (2008) also simulates undrained conditions. This justification makes it valid to compare results from this study with results from undrained analysis of Wang et al. (2010).

4.1 *Mesh sensitivity*

Before comparing results from this study with published data, a mesh sensitivity analysis was carried out to select the suitable element size for the pipeline and the surrounding soil. In the coarse mesh, both pipe and soil were modelled using CPE4 and CPE4P elements, respectively, with 0.2 m node spacing for the soil and 0.1 m node spacing for pipe. In the fine mesh, node spacing for both soil and pipe was selected as 0.1 m. The vertical penetration resistance, R_v, against vertical penetration depth, V, is shown in Figure 2. In Figure 2, dimensionless parameters are used similar to the centrifuge modelling results and LDFE analysis results presented by Dingle et al. (2008), and Wang et al. (2010), respectively. Dimensionless penetration depth is defined as V/D. Dingle et al. (2008), and Wang et al. (2010) computed dimensionless penetration resistance as R_v/Ds_{uo} in their undrained LDFE analysis, where undrained shear strength, s_{uo} at the depth of pipe invert is given by,

$$s_{uo} = s_{um} + kz \quad (1)$$

where, s_{um} = 2.3 kPa is the undrained shear strength at the mudline and k = 3.6 kPa/m is the rate of change of undrained shear strength over depth z measured from the ground surface. In this study, coupled analysis was carried out using the Mohr-Coulomb model. Hence, R_v was converted into a dimensionless term using yield stress, f_y at the invert of the pipe.

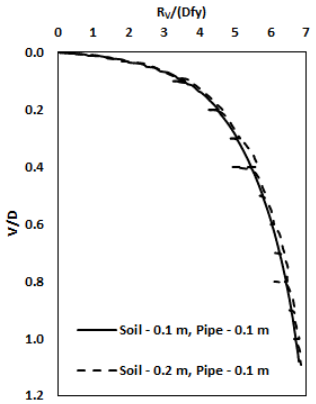

Figure 2. Vertical penetration resistance from fine and coarse meshes.

According to Figure 2, penetration resistance given by both fine and coarse meshes agree well. However, discontinuities observed after each remeshing step is more pronounced in the coarse mesh. Therefore, in what follows, fine mesh with node spacing of 0.1 m has been used.

4.2 *Comparison of vertical penetration resistance*

Figure 3 shows the vertical penetration resistance obtained from the proposed LDFE analysis for three cases: (i) pipe-soil interface is smooth, (ii) friction coefficient at the pipe-soil interface is 0.5 and the limiting shear stress is 2.5 kPa, which is half of c', and (iii) friction coefficient at the pipe-soil interface is 0.5 but there is no limiting shear stress. When the limiting shear stress is not defined, the limiting shear stress at the interface was computed by the contact algorithm for penalty method in ABAQUS/Standard as $\alpha\sigma'_n$, where α is the friction coefficient at the

interface and σ'_n is the effective normal stress at the interface. Also in Figure 3, dimensionless penetration resistance obtained from the centrifuge test (Dingle et al., 2008) is presented.

According to the results shown in Figure 3, it is clear that when the shear stress at the interface is limited, penetration resistance obtained from the remeshing analysis is smooth. When the interface is assumed perfectly smooth, predicted dimensionless penetration resistance is at the lowest due to less resistance to soil flow at the pipe surface compared to the frictional interface. Other two cases with interface friction are not an exact match to the centrifuge test data, but close enough to say that both cases are in good agreement with centrifuge data.

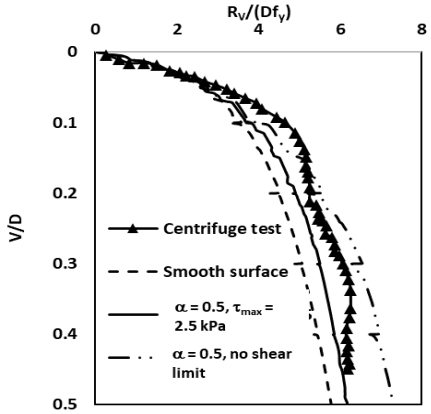

Figure 3. $R_v/(Df_y)$ from centrifuge and LDFE with different conditions at the pipe-soil interface.

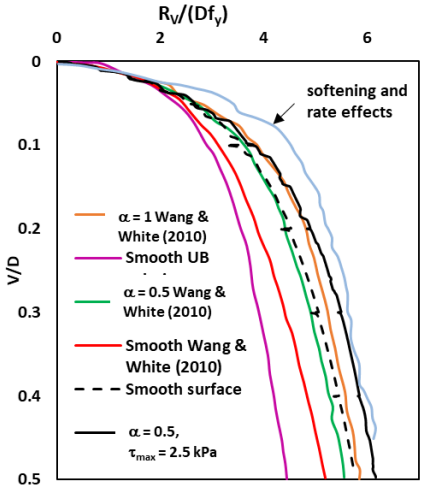

Figure 4. Comparison of LDFE with Wang et al. (2010), and UB (Randolph and White, 2008).

A comparison of results from the proposed LDFE analysis and the LDFE analysis proposed by Wang et al. (2010) is shown in Figure 4. The major difference between the proposed LDFE approach and LDFE by Wang et al. (2010) for cases with no softening and no rate effects, is the pore pressure effects (considered in proposed approach) and the solution mapping from old mesh to new mesh (Wang et al., 2010 performed this outside ABAQUS using their own FOTRAN program based on Zienkiewicz and Zhu, 1992 patch recovery method). Despite these differences, two cases by Wang et al. (2010) with friction coefficients of 1 and 0.5 shows close agreement with results from the proposed approach when interface friction coefficient is 0.5 (with shear limit) or smooth. For smooth interface, Wang et al. (2010) produces lower penetration resistance compared to proposed approach. The difference between two approaches increased with increasing V, indicating that this difference may be due to the increased shear strength with dissipation of pore pressures in the proposed LDFE approach. Another contributing factor is the higher dimensionless submerged unit weight of soil ($\gamma'D/s_{um}$) used in this study, which is 4, compared to 2.26 used by Wang et al. (2010). With the increase in weight of the soil to be pushed upwards during penetration, the force required to push the pipe in the downward direction increases. Due to the same reason, the Upper Bound solution by Randolph and White (2008) for the smooth interface and weightless soil shows the lowest penetration resistance.

4.3 *Soil flow around the pipe - Vertical penetration*

Figure 5 shows the soil flow around the pipeline obtained from the LDFE analysis for three penetration depths, V/D = 0.07, 0.25 and 0.35, same penetration depths as for the centrifuge test by Dingle et al. (2008). These flow patterns match closely with those captured during the centrifuge test using the image analysis. Numerical results show fan shaped soil flow on either side of pipe invert at shallow embedment, forming the failure mechanism. With increasing embedment, fan shaped soil flow enlarges. At deeper embedment, soil underneath the pipe invert also contribute to the failure mechanism.

Although centrifuge tests by Dingle et al. (2008) show nonsymmetry in flow at deeper penetration depths, numerical results show symmetrical soil flow. The nonsymmetry in centrifuge may have caused due to a number of reasons: (i) nonhomogeneous nature of the soil and (ii) rotation or translation of the pipeline during vertical penetration. Although the free meshing technique used for mesh generation has not restricted the mesh to symmetry (Figure 6), due to the uniform soil properties and symmetrical loading used in the analysis, a symmetrical flow was generated around the pipeline.

4.4 *Pore pressure distribution and failure mechanism around the pipe*

Figure 6 shows the excess pore pressure distribution around the pipeline. The maximum excess pore pressure, 60 kPa, was observed at the vicinity of the pipe invert, which shows that significantly high excess pore pressures may generate during the vertical pipe

penetration. Increasing excess pore pressures tend to reduce the shear strength closer to the pipe invert. Hence, soil below the invert has lower shear strength compared to the sides of the pipeline. According to Wang et al. (2010), softening due to accumulated plastic strains and rate effects must be included when simulating the pipeline penetration. In this study, softening due to accumulated plastic strains were not included. Nevertheless, good agreement between results by this study and centrifuge test was observed. The reason may be the reduced shear strength near the pipe invert incorporated in the coupled analysis. Hence one can argue that if a coupled analysis is considered, linking the yield strength of the soil to effective stresses, even an elastic perfectly plastic soil model such as Mohr-Coulomb has the ability to simulate the problem. The shear bands developed around the pipe shown in Figure 7 using LDFE analysis by Wang et al. (2010), considering softening and rate effects, and the proposed LDFE analysis further justifies the above statement.

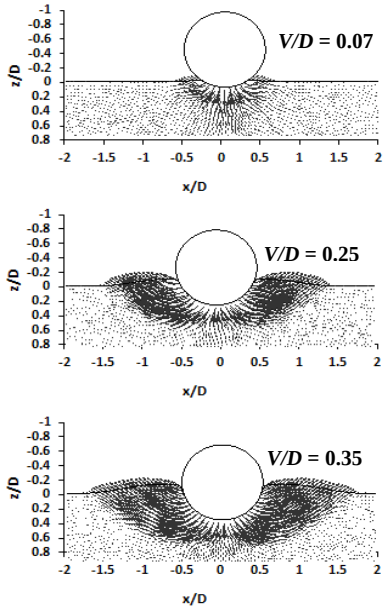

Figure 5. Soil flow around the pipeline.

4.5*Lateral penetration*

During lateral penetration or breakaway of pipeline, it was restrained against vertical movement in this study. Also lateral penetration was carried out after pipe penetrated to a depth of *D* in the vertical direction. Both centrifuge test data and LDFE results from Wang et al. (2010) are not available for this case. Therefore, in this section, the observed soil flow around the pipe, the failure mechanism and penetration resistance from this study will be discussed.

Figure 8 shows the soil flow around the pipeline during the lateral movement. Soil is predominantly displaced in the lateral direction but shows some movement in the upward direction towards the surface increasing the soil heave. Soil moving towards the surface rotates around the pipeline creating new contacts with pipe surface. Although soil movement around the pipeline is large, due to the remeshing approach adopted during the analysis has avoided mesh distortions as can be seen in Figure 9.

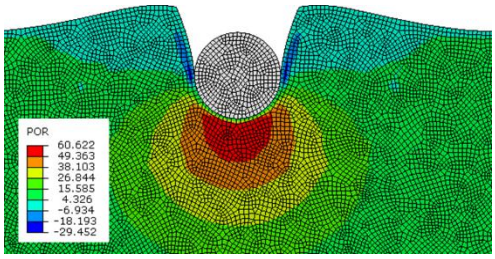

Figure 6. Pore pressure around the pipeline at the beginning of last remeshing analysis for vertical penetration.

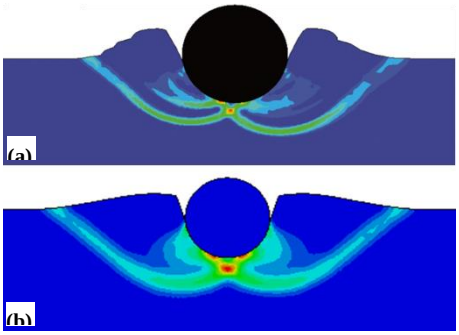

Figure 7. Shear band developed at vertical penetration of *D*/2 (a) Wang et al. (2010) and (b) proposed LDFE (Red to blue – Max to min plastic strain).

During vertical penetration, large excess pore pressures were generated below the pipe invert. However, during lateral penetration, excess pore pressures were not very high due the dissipation of excess pore pressures at the surface, which is close to the region of maximum excess pore pressure.

Figure 10 shows the penetration resistance during lateral penetration of the pipeline. Vertical penetration resistance, R_V, decreases rapidly during the first 0.1D of the lateral penetration and beyond that it shows a steady decline at a very slow rate. This is due to the loss of contact between rear of the pipeline and soil.

The lateral penetration resistance, R_H, also shows a rapid increase up to 0.1D but beyond that shows a steady increase at a very slow rate. The increase in R_H with increasing lateral pipe movement may be due to the formation of new contacts when soil pushed away in front of the pipe tends to rotate around the pipe towards the surface.

Figure 11 shows the development of failure mechanism during pure lateral translation of the pipeline considered in this study. This mechanism is similar to the one given by Randolph and White (2008) for pure translation. The size of the failure surface, which comprises of a fan shaped section and a linear surface, enlarges with increasing U. The boundary of the fan shaped section is part of a circular arc. However, when the pipeline is free to move vertically during lateral translation, which resembles the practical situation in the field, the simple failure mechanism observed in this study may not be valid.

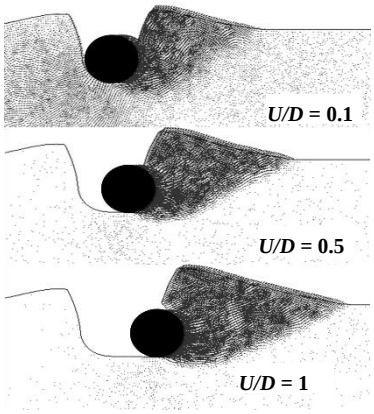

Figure 8. Soil flow around the pipeline.

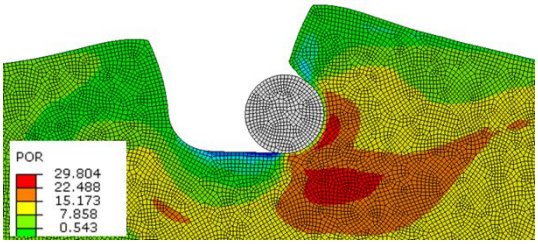

Figure 9. Deformed mesh and excess pore pressure distribution after lateral penetration of D.

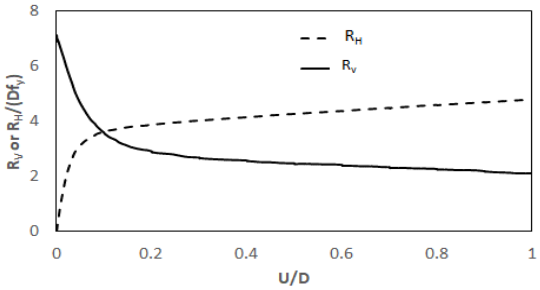

Figure 10. Horizontal, R_H, and vertical, R_V, penetration resistance during lateral penetration.

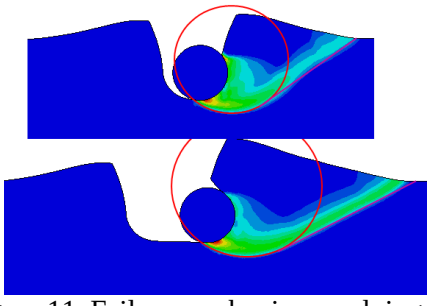

Figure 11. Failure mechanism evolving around pipeline during lateral movement.

5 CONCLUSIONS

In this paper, a remeshing and interpolation based coupled analysis technique developed within PYTHON Development Environment (PDE) in ABAQUS/Standard finite element program is presented. It has the ability to simulate deep penetration problems such as pipeline penetration and subsequent breakaway, which involves large soil deformations, otherwise impossible to simulate using finite element programs based on the small-strain approach. Vertical penetration resistance from the proposed LDFE analysis matches well with centrifuge test data and previous LDFE analysis results for undrained conditions by Wang et al. (2010) confirming that the proposed coupled LDFE approach is a useful tool in simulating deep penetration problems in geotechnical engineering.

REFERENCES

Aubeny, C.P., Shi, H. and Murff, J.D. (2005). Collapse loads for a cylinder embedded in trench in cohesive soil, *International Journal of Geomechanics*, Vol. 5, No. 4, pp. 320-325.

Chatterjee, S., Randolph, M.F. and White, D.J. (2012). The effects of penetration rate and softening on the vertical penetration resistance of seabed pipelines, *Geotechnique*, Vol. 62, No. 7, pp. 573-582.

Dingle, H.R.C., White, D.J. and Gaudin, C. (2008). Mechanics of pipe embedment and lateral breakout on soft clay, *Canadian Geotechnical Journal*, Vol. 45, pp. 636-652.

Finnie, I.M.S. and Randolph, M.F. (1994). Punch-through and liquefaction induced failure of shallow foundations on calcareous sediments. *In Proceedings of the 7th international Conference on the Behaviour Offshore Structures*, Mass., Pergamon, Vol. 1, pp. 217-230.

Martin, C.M. and Randolph, M.F. (2006). Upper bound analysis of lateral pile capacity in cohesive soil. *Geotechnique*, Vol. 56, No. 2, pp. 141-145.

Merifield, R. S., White, D. J. and Randolph, M. F. (2008). The ultimate undrained resistance of partially embedded pipelines. *Geotechnique*, Vol. 58, No. 6, pp. 461–470.

Merifield, R. S., White, D. J. & Randolph, M. F. (2009). Effect of surface heave on response of partially embedded pipelines on clay. J. Geotech. Geoenviron. Engng, ASCE, Vol. 135, No. 6, pp. 819-829.

Randolph, M.F. and White, D.J. (2008). Upper-bound yield envelopes for pipelines at shallow embedment in clay, *Geotechnique*, Vo. 58, No. 4, pp. 297-301.

Wang, D., White, D.J. and Randolph, M.F. (2010). Large-deformation finite element analysis of pipe penetration and large-amplitude lateral displacement, *Canadian Geotechnical Journal*, Vol. 47, pp. 842-856.

Zienkiewicz, O.C., and Zhu, J.Z. (1992). The superconvergent patch recovery and a posteriori error estimates. Part 1: The recovery technique. *International Journal for Numerical Methods in Engineering*, Vol. 33, No. 7, pp. 1331–1364.

Finite Element Stress Based Back Analysis on Retrogressive Failure of Kahagalla Landslide

K.R.K. Lakmal
Department of Civil Engineering, University of Peradeniya, Sri Lanka

L.C. Kurukulasuriya
Department of Civil Engineering, University of Peradeniya, Sri Lanka

ABSTRACT: Landslides are a common geological phenomenon widespread in Central Highlands in Sri Lanka. This research investigates the mode of retrogressive behavior of the saturated sliding mass at Kahagalla, Sri Lanka identified as Kahagalla Landslide. The investigation and instrumentation observations suggest that the mode of movement is retrogressive, as evident by the high length/height ratio of the affected area. Therefore, an in-depth investigation of the slope instability was performed incorporating retrogressive failure using finite element stress-based method for different friction angle values while keeping cohesion value to zero. The deterministic two-dimensional analyses were initially performed using limit equilibrium and finite element methods using SLOPE/W and SIGMA/W software for the phreatic surface established by the inclinometer observations. The study showed that the retrogressive type of failure occurred at the site can be explained by the numerical analyses performed.

Keywords— Landslide, Residual Soil, Back analysis, Progressive behavior, Residual friction angle

1 INTRODUCTION

1.1 *Landslides*

Landslides constitute a major threat to both life and property including infrastructure, in Central highlands of Sri Lanka. These regions are characterized by periods of prolonged rainy weather with periods of intense rainfall. This research is based on the Kahagalla landslide which belongs to an area surrounded by hills covered with cloud forests and tea plantations in Haputale, Sri Lanka and this research mainly focused on interpretation of the landslide failure mechanism.

1.2 *Literature*

There are a limited number of studies available in the literature that explains the mechanisms involved in progressive failure of slopes.

Morgenstern and Price (1965) found that the degree and form of disturbance on the surface of a sliding mass can be used as means for differentiating slope movements that are perfectly circular from those with multiple composite failure zones (Haug et al, 1977). The surface deformation at Kahagalla is of the type found in composite failure surfaces with translational movement along a common failure plane.

1.3 *Study Area*

Kahagalla landslide is located at an elevation of 1,430 m above MSL and has an aerial extent of 3.5 ha on the western slope of the mountain range running northeast from Haputale. The Kahagalla earth slip first occurred in 1987 and A16 road damaged due to its activation during the rainfall.

Sliding events often occur following a rainy period, triggered by intense and prolonged precipitation. In a report published by NBRO in 1989 it was reported that a major slide occurred in May 1987 causing considerable damage to Beragala-Haliela Road (A16 road) blocking the carriageways for a period of over 5 weeks and leaving occasional road subsidence following rains. This led the authorities concerned to take remedial measures.

Fig.1. Road cracks appeared during rainy period (Photo taken on 26-12-2014)

2 GEOLOGY

The subsurface conditions of the landslide site and the adjacent area were determined using information from desk and field studies. The desk study comprised a review of existing data, including the results of the ground investigation carried out by NBRO in 1989 under the ADB funded Second Road Improvement Project. The field studies included post-failure geological mapping and ground investigation done by NBRO during the years 2014 and 2015 under JICA funded Landslide Disaster Protection Project (LDPP) and tests carried out block samples taken at slide boundaries.

The morphology of the earth slip is characterized by hummocky surface terrain (Fig. 2). The general geology of the study site is characterized by Calc gneiss, Charnokitic gneiss, Garnet-biotite gneiss and Khondolite. The material within the slip area consists of colluvial deposits and in-situ weathered residual materials. The site is dominated by sandy silt and silty sand while gravel and rock boulders are distributed in an irregular way. The scar area of the slip has subsided due to sinking into solution cavities of the calc gneiss underneath and the presence of solution cavities were detected during the drilling by experiencing water loss and difficulties in drilling activities.

Fig.2. Site Morphology (Source:Google Earth)

3 METHODOLOGY

Landslides often exhibit features of progressive failure, where downslope removal of material causes unloading of the temporary stable slope, with upper side blocks of soil eventually experiencing active failure, detaching and moving downslope. The methodology comprised of the following two studies.

1. Activation and failure mechanism of the landslide under zero cohesion with varied friction angle.
2. Retrogressive failure causing unloading at toe.

Above two studies were carried out based on a 2D FEM stress based analysis using Geostudio SIGMA/W commercial software. The generated stresses were then imported to SLOPE/W module for stability analysis using Limit Equilibrium Method (LEM). LEM analysis is performed to explore the mode of failure and to explain the mechanisms involved in retrogressive behavior.

3.1 *Borehole investigation data and instrumentation*

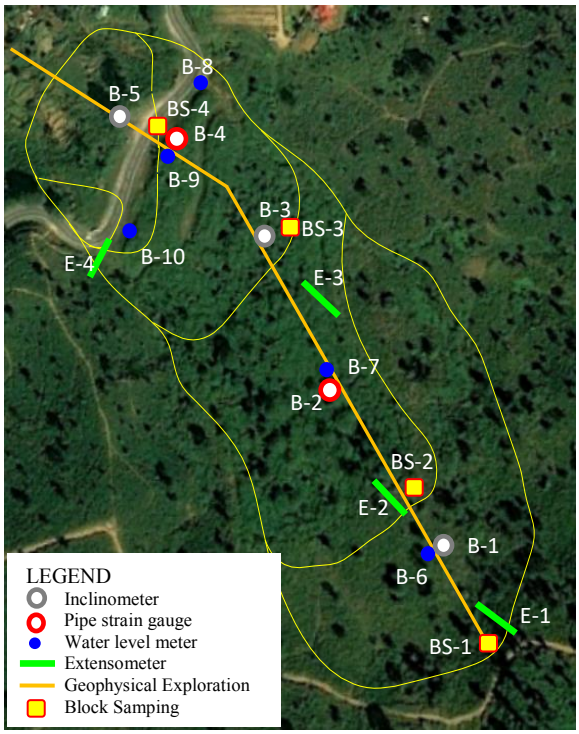

Fig.3. Investigation & Instrumentation in LDPP & Block Sampling

The boreholes were drilled to the bedrock to establish the stratigraphy and for the purpose of landslide instrumentation.

Table 1. Summary of Borehole investigation & instrumentation under LDPP

ID	Type of drilling	Type of the Instrument	Length or Depth/m
B1	Coring	Inclinometer	50.0
B2	Coring	Pipe strain gauge	50.0
B3	Coring	Inclinometer	50.0
B4	Coring	Pipe strain gauge	50.0
B5	Coring	Inclinometer	50.0
B6	Non coring	Water level	20.0
B7	Non coring	Water level	20.0
B8	Coring	Coring only	50.0
B9	Non coring	Water level	20.0
B10	Coring	Coring only	50.0
E1	N/A	Extensometer	10.0
E2	N/A	Extensometer	10.0
E3	N/A	Extensometer	10.0
E4	N/A	Extensometer	10.0

3.2 *Block Sampling*

Four block samples (BS-1 to BS-4) were taken at the Slide Boundaries (location indicated in Fig.3) and Direct Shear tests were carried out for the undisturbed samples to determine the most appropriate value of cohesion for back analysis of FOS. Test results (Table 2) reveal that cohesion can be set to zero for the back calculation of FOS.

Table 2. Direct Shear Test results

ID	Cohesion, c′	Friction Angle, ϕ'
BS1	0.00	8.30
BS2	0.93	9.54
BS3	1.68	9.54
BS4	0.00	9.65

Landslide monitoring is usually done through real time monitoring of parameters related to cause or effect triggering of a landslide.

Currently, local sensor networks are widely used for landslide instrumentation. The techniques based on local sensor networks are based on measurements taken from geotechnical sensors (inclinometers, extensometers, piezometers, geophones, tiltmeters and crackmeters).

3.2.1 *Extensometers*

Wire Extensometers is a simple and low cost device that allows the measurement of relative displacement between two points, where one point is placed in the sliding mass that is in motion and the other in stable ground or a series of extensometers can also be arranged where measurement of relative displacement between two points within a potential sliding mass is possible in which the top most point should be fixed on stable ground.

3.2.2 *Pipe strain gauges*

The pipe strain gauges are used to estimate the slip surface depth. PVC pipes with strain gauges were inserted into boreholes, and the movement is estimated by the change in the strain as the PVC pipe bends.

3.2.3 *Inclinometers*

Inclinometers are instruments placed in the sliding mass. They measure the tilt of the whole ground mass along two orthogonal vertical directions.

3.3 *Geophysical Exploration*

Geophysical exploration consisted of seismic exploration and high density electric exploration. The measuring lines were set parallel to the moving direction of the landslide and the dip direction of the strata as shown in Fig. 3.

3.4 *Rainfall data*

Fairly heavy rainfall of about 75-100 mm is likely at Bandarawela and Haputale area in Uva province during the months of December, January and February which is expected to trigger mass movements. Therefore, instrumentation has been commenced during the month of December 2014 and daily rainfall recorded by the rainfall gauge located at Bandarawela Central College. This study was based on the instrumentation data recorded during rainfall events between 12th of December 2014 and 28th of February 2015.

4 DATA INTERPRETATION

4.1 *Location of the Slip Surfaces*

Primarily, the failure surfaces of the Kahagalla slide were located by examination of borehole samples and the features recognisable in the field. The locations of failure surfaces were identified by NBRO where the wet zones with material of very low consistency were encountered. Identification of the slip surfaces were strengthened using Extensometer, Inclinometer, Pipe strain gauge observations and Geophysical exploration data. Monitoring work has been carried out for nearly one year time period from November 2014 to November 2015 by NBRO. Also the findings of their previous investigations in 1989 were taken into consideration for the determination of slip surfaces.

Kahagalla landslide recognizes four landslide blocks A, B, C, D and their respective slip surfaces identified here as S_4, S_3, S_2, and S_1 (Fig. 4).

S_1 is the largest slip surface which is identified as the major failure and other slip surfaces are located above the toe of S_1. Also, S_4 is the frequently activated failure surface which is located near to the toe of the landslide and it damages the A16 road during heavy rainfall (Fig. 1).

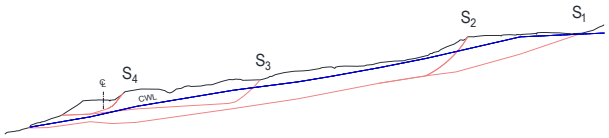

Fig.4. Geometry of the landslide area

4.2 *Location of the Phreatic Surface*

Phreatic surface has continuously been recorded using the ground water level monitoring boreholes. When carrying out stability analyses on the slip surfaces, 'Critical Water Level (CWL)' that refers to the ground water level that is highly susceptible to initiate the landslide during rainfall is consid-

ered (Fig. 4). This activation has been detected at the time the surface cracks appeared supplemented by instrument indications.

4.3 *Rainfall and Landslide activation*

Significant movements are recorded by Extensometers, Pipe strain gauges & Inclinometers during rainfall. Fig. 5 illustrates the surface displacements of Extensometers and rainfall data at the landslide.

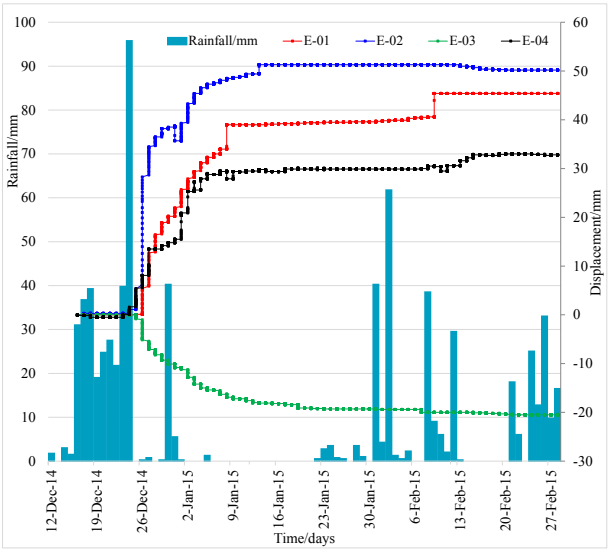

Fig.5. Landslide movement observation through Extensometer data and rainfall

It is seen that the Extensometer E_4 (location indicated in Fig.3) responds early to the surface variations with higher rate of displacement during the rainfall than the others. E_4 is located at the left flank of the landslide closer to the slip surface S_4. Based on Fig. 5, it is apparent that S_4 activates early before the initiation of movement at other slip surfaces showing retrogressive behavior.

It was significantly noted that the ground water level reading at B-09 (location indicated in Fig.3) has gradually increased upto a steady level.

5 STABILITY ANALYSES

The deterministic 2-D analysis is performed based on LEM using SLOPE/W and FEM using SIGMA/W software of Geostudio. Morgenstern-Price method was used for conducting back analysis of the landslide under the CWL.

5.1 *FEM Stress based back calculation*

Stability analyses comprised with FEM stress based back calculation. Since the instrumentation data revealed the order of activation of slip surfaces, sliding mechanism needed to be identified. For that purpose, FOS of each individual slip surface was calculated by varying the friction angle from 14° to 8° while keeping the soil cohesion to zero so that the friction angle which gives a FOS value of unity can be assessed. Material parameters used in these analyses are shown in Table 2 and 3.

Table 3. Material Properties

Name	Elastic Modulus, MPa	Unit weight, kN/m^3	Poisson's Ratio
S_1	13	20.0	0.30
S_2	13	20.0	0.30
S_3	13	20.0	0.30
S_4	13	20.0	0.30
WR	40	22.0	0.25
BR	73	26.5	0.20

WR-Weathered Rock, BR-Bed Rock

Friction angle for Weathered Rock was taken as 38°.

5.2 *Modeling & Boundary conditions*

Boundary conditions used are Fixed X, along the vertical right hand side boundary and Fixed X/Y along the bottom boundary as in calculating stresses for a slope stability problem the boundary for the base is selected as Fixed X/Y, as the displacement in both X and Y directions is not allowed at the base.

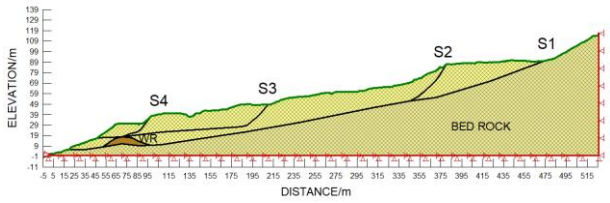

Fig.6. FEM Modeling with SIGMA/W

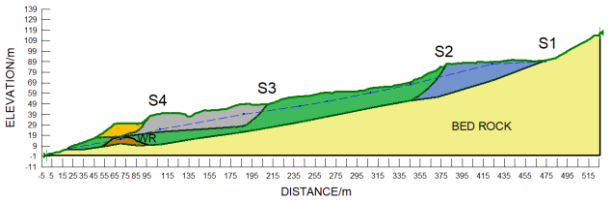

Fig.7. LEM Modeling with SLOPE/W

8. RESULTS

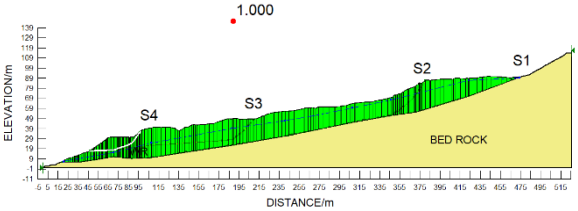

Fig.8. Stability result for S_1 (FOS=1.0 at c′=0, ϕ'=10°)

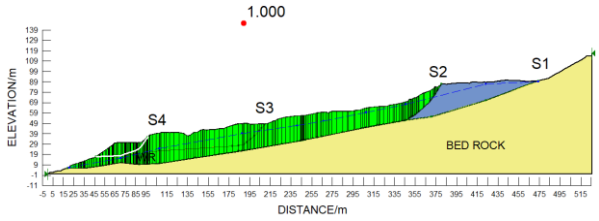

Fig.9. Stability result for S_2 (FOS=1.0 at c′=0, ϕ' = 8.17^0)

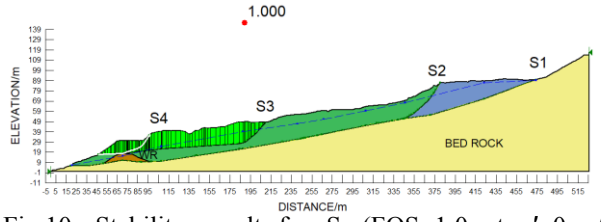

Fig.10. Stability result for S_3 (FOS=1.0 at c′=0, ϕ' =10.11^0)

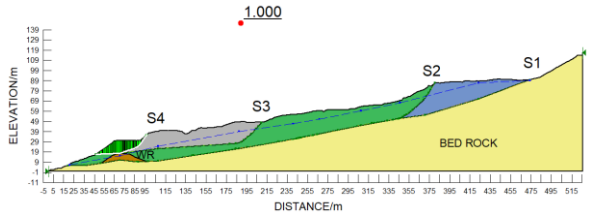

Fig.11. Stability result for S_4 (FOS=1.0 at c′=0, ϕ' =13.24^0)

Table 4. Results of Slope Stability Analyses

Friction angle	FOS			
	S-01	S-02	S-03	S-04
14.00	1.244	1.354	1.398	1.060
13.75	1.228	1.339	1.372	1.040
13.50	1.213	1.323	1.346	1.021
13.25	1.198	1.308	1.321	1.001
13.24	1.197	1.307	1.320	1.000
13.00	1.182	1.292	1.295	0.982
12.75	1.167	1.277	1.269	0.962
12.50	1.152	1.262	1.243	0.943
12.25	1.136	1.246	1.218	0.923
12.00	1.121	1.231	1.192	0.904
11.75	1.106	1.216	1.167	0.884
11.50	1.091	1.200	1.141	0.865
11.25	1.075	1.185	1.116	0.846
11.00	1.060	1.170	1.090	0.826
10.75	1.045	1.155	1.065	0.807
10.50	1.030	1.140	1.039	0.788
10.25	1.015	1.125	1.014	0.769
10.11	1.006	1.116	1.000	0.758
10.00	1.000	1.110	0.989	0.750
9.75	0.985	1.095	0.964	0.731
9.50	0.970	1.080	0.939	0.712
9.25	0.955	1.065	0.913	0.692
9.00	0.940	1.050	0.888	0.673
8.75	0.925	1.035	0.863	0.654
8.50	0.910	1.020	0.838	0.635
8.25	0.895	1.005	0.813	0.616
8.17	0.890	1.000	0.805	0.610
8.00	0.880	0.990	0.788	0.598

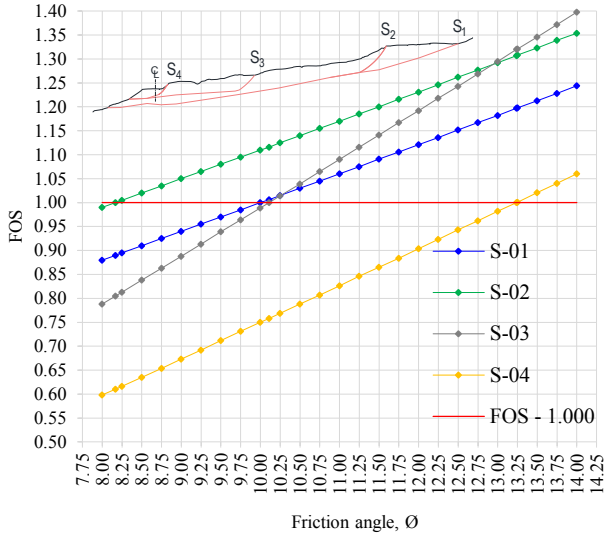

Fig.12. Variation of FOS with Friction angle (ϕ') for identified slip surfaces

Friction angle reduction caused a decrease in FOS of each critical slip surface and its critical ϕ' recorded where the FOS gives a value of unity. Results are shown in Table 4.

Fig.12 shows that the slip surface S_4 appears to be initiating earlier than the other slip surfaces as the FOS approaches unity at a higher value of friction angle (13.24°) while S_1, S_2 & S_3 giving FOS 1.197, 1.307 and 1.320 under ϕ' =13.24°. Similarly, other slip surfaces can be found to be initiating in the order of S_1, S_2 and S_3. It is also noted that both S_3 and S_1 activates at the same time when the friction angle becomes approximately 10°.

The above analyses can be further extended by incorporating the unloading of the toe due to the activation of the slip surface S_4. The following two scenarios are considered in these analyses.

Case 1: The slip surface S_4 has activated thereby considering the removal of the toe support in assessing the stability of surfaces S_1, S_2 & S_3.

Under this scenario, the geometry of the slope and the critical slip surface is shown in Fig.13. Table 5 gives the FOS values of all the slip surfaces from S_1 to S_3.

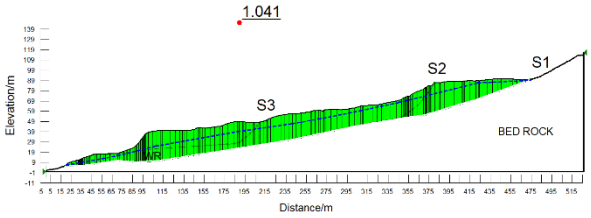

Fig.13. Result of stability analysis under Case 1 (Critical FOS = 1.041, c′=0, ϕ' =13.24°)

Table 5. Results of Stability Analyses of Case 1

Slip Surface	FOS
S_1	1.041
S_2	1.110
S_3	1.183

Case 2: The slip surface S_4 and S_3 are activated thereby considering the removal of the toe support in assessing the stability of surfaces S_1 and S_2.

Under this scenario, the geometry of the slope and the critical slip surface is shown in Fig.14. Table 6 gives the FOS values of the slip surfaces of S_1 and S_2.

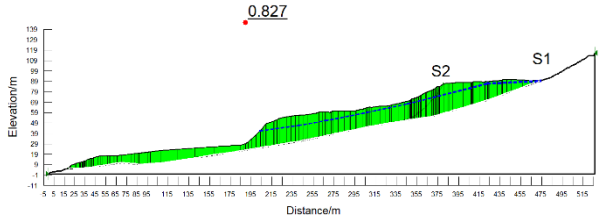

Fig.14. Result of stability analysis under Case 2 (Critical FOS = 0.827, c′=0, ϕ' =13.24°)

Table 6. Results of Stability Analyses of Case 2

Slip Surface	FOS
S_1	0.827
S_2	0.943

The results indicated that the lower block bounded by the slip surface S_4 is activated initially which has the critical FOS as compared with the other slip surfaces. Also, it is significant that there is no much of a difference between FOS values of the other failure surfaces at the time of S_4 becoming unstable.

When the failure occurred in surface S_4, the modified slope becomes unstable again due to loss of toe support and S_1 appears to be the next slip surface where the failure would initiate (critical FOS – 1.041) thus exhibiting the characteristics of a retrogressive type of slope failure. The soil masses bounded by the surfaces S_2 and S_3 which are part of the soil mass bounded by the slip surface S_1 would inevitably become unstable.

6 DISCUSSION

6.1 *Landslide failure mechanism*

The nature of a retrogressive failure mechanism is such that the uphill slides could be triggered by the movement or failure at the toe of the slope. Similarly, the progressive failure downslope reduces the toe support on uphill soil mass, which leads to retrogressive failure and causing subsequent slope instability.

It is seen that the FOS of each slip surface has significantly reduced due to toe unloading causing the slope to become unstable. However, the stability analysis of S_4 shows FOS unity at a higher value of friction angle compared to the others. It is revealed that the S_4 played a dominant role for the global slope instability of Kahagalla site.

The block of mass bounded by the slip surface S_4 provides lateral support to the blocks above it. By examining the values of FOS of slip surfaces, it can be deduced that the activation of slip surfaces can take place in a retrogressive manner as the FOS of slip surfaces uphill of the slip surface S_4 reduces to values that indicates the possibility of failure. According to the instrumentation data too, failure has initiated in the slip surface S_4 followed by the failure along slip surfaces S_1, S_2 and S_3.

7 CONCLUSIONS

The observations suggest that the failure at this site propagates backwards and takes place at different times.

Based on the monitoring results, it is evident that the entire landslide area of this site moves intermittently during rainy seasons. Leading block S_4 at the toe was the first slip surface to activate.

Examination of instrumentation data and the slope stability results provided strong evidence that the mechanism of the landslide at Kahagalla is of retrogressive type.

8 REFERENCES

Geotechnical Investigation Report, January 1989, National Building Research Organisation (NBRO), ADB funded second road improvement Project, Beragala – Hali Ela Road, A016.

Haug, M. D., E. Karl Sauer, and D. G. Fredlund. 1977. "Retrogressive Slope Failures At Beaver Creek, South of Saskatoon, Saskatchewan, Canada." *Canadian Geotechnical Journal* 14(3): 288–301.

Morgenstern.N, Price. 1965. *"The Analysis of the Stability of General Slip Surfaces."* Volume 15 Issue 1, March 1965, pp. 79-93.

Technical Report, August 2015, Report no. A016-010 – Rank C, National Building Research Organisation (NBRO), LDPP.

Some Observations on the Shear Strength of Organic Soils

T. Jayasinghe & D. Wijewickreme
Department of Civil Engineering, University of British Columbia, Vancouver, B.C., Canada

ABSTRACT: Peat or muskeg deposits (i.e., organic soils) can be found in many regions of the world, and they are undesirable from a geotechnical engineering perspective due to the inherent very low strength/stiffness and low compressibility characteristics, combined with high spatial variability. In this study, the behavior of organic soil from a site in Surrey, British Columbia, Canada is investigated through a comprehensive field and laboratory testing program. In particular, the shear strength of the soil was investigated using data from in situ vane shear, cone penetration, and full-flow (ball) penetrometer testing and those from laboratory direct simple shear (DSS) testing of reconstituted specimens, and initial findings are summarized herein.

1 INTRODUCTION

Highly organic soils, generally identified as peat or muskeg, can be found throughout the world in different ecosystems. Peat deposits cover 5-8% of land surface on earth; in Canada, ~15% of the land surface (~1.5 million km^2) is underlain by peatlands (MacFarlane, 1969). It has also been noted that approximately 8-11% of global peat deposits are tropical or subtropical (Mesri and Ajlouni, 2007).

Organic soils pose significant challenges from an engineering viewpoint due to their high water content, low bulk density, and low stiffness/weak strength properties (Mesri and Ajlouni, 2007). These soil deposits are mainly composed of partially decomposed plant matter, and as a result, they are variably fibrous and heterogeneous. It is observed that, strength and stiffness of peat can be expressed as a function of presence of organic fiber layers, fiber orientation, fiber properties (based on source plant species), and degree of humification. With distinct and variable properties compared to inorganic soils such as clays and sands, quantification of different peat structures in terms of their physical, chemical and strength properties has always been a difficult task (Yamaguchi et al., 1985; MacFarlane, 1969). However, understanding the mechanical behavior of organic soils (called as peat hereinafter in this paper) has attracted increasing attention over the past many decades due to the scarceness in land availability to found infrastructure in competent soils.

Due to the high variability and low strength and stiffness, geotechnical engineering in peats is commonly performed considering soil properties with a wide range along with high safety margins. As such, there is an increasing desire to improve the current understanding of the mechanical behavior of peaty soils; in particular, there is a strong need to develop effective in situ and laboratory testing approaches combined with empirical correlations to obtain reliable geotechnical parameters for engineering design in these soils.

The concerns associated with the performance of buried pipelines in organic soils provide one of the good engineering examples in this regard – i.e., strain development in pipelines as a result of subsidence occurring due to drainage and associated potential for upheaval buckling. Thermal changes arising due to operational and environmental reasons have also been recognized as a threat to the structural integrity and safety of buried pipeline systems in organic soils. In an overall sense, the lack of understanding of the mechanical behavior of organic soils has caused an absence of well-adapted soil-pipe interaction assessment methodologies for the design of pipelines buried in these soils.

With this background, a research program involving in situ and laboratory testing has been undertaken at the University of British Columbia, Canada to characterize muskeg soil behavior. This paper presents the initial findings from a component of this study addressing the topic of shear strength. The strength parameters of peats are determined either as undrained shear strength (s_u) or effective friction angle (ϕ'), depending on the drainage considerations. Generally, laboratory shear testing is used to obtain the value of ϕ', whereas s_u is commonly determined from in-situ testing. The present paper focuses on the undrained shear strength aspects. Initially, the results from the field investigation program are presented followed by some limited findings from laboratory element-level testing. s_u values obtained from different approaches are then compared and assessed.

2 FIELD TEST PROGRAM

A field geotechnical investigation program conducted at a site located in Surrey, British Columbia, Canada is considered herein. The specific location of the test site (in Bolivar Park) is shown in Fig. 1; the figure uses a surficial geology map of the Metro Vancouver area as the base; as may be noted, the map identifies the considered test area to be underlain by peat.

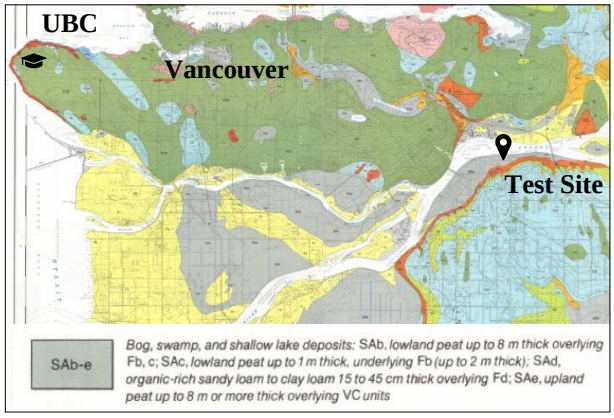

Fig. 1 Location of test site [After Armstrong and Hicock (1979/1980)]

In situ Seismic Cone Penetration Tests (SCPTs), Ball Penetration Tests (BPTs), and electronic Vane Shear Tests (eVSTs) were undertaken in the detailed field test program to characterize organic soils. These field tests are commonly used in interpretation of engineering parameters of inorganic soils. A site layout illustrating the test locations and test groupings is shown in Fig. 2. A summary of test equipment dimensions is presented in Table 1.

Table 1. Summary of test equipment dimensions

Field Test	Equipment Dimensions
SCPT	15 cm^2 cone (4.37 cm dia.), net area ratio: 0.8
BPT	150 cm^2 ball (13.8 cm dia.)
eVST	Double tapered 75 x 150 mm vane

Results from the test program are summarized in Liu et al. (2018), and further details of the in-situ tests will be published in upcoming publications by the research group; only the data interpreted with respect to the determination of s_u are presented herein.

SCPT is a field test that has been used for over 40 years to obtain soil strength and stiffness parameters (Robertson et al., 1986). SCPT consists of a penetrometer with a cone tip, and simultaneous measurements of cone tip and sleeve resistances are recorded as the cone is pushed into the ground, at a typical rate of 2.5 cm/s. Interaction of fibers with the cone has resulted in higher scatter of resistance causing problematic results from traditional cone penetration tests in organic soils. Further, soft nature of organic soils leads to cone resistance measurements lower than the accuracy of the measurement resulting in zero resistance being measured (Boylan et al., 2011).

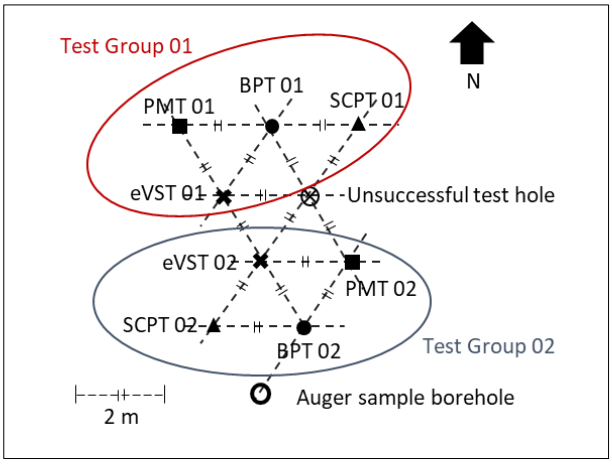

Fig. 2 Schematic test hole layout at the site

BPT is a full flow penetrometer test which is widely used in offshore testing. Compared to the SCPT, BPT uses a ball with a relatively large diameter (~14 cm) instead of a cone. Because of the variable nature and low strength/stiffness, it is considered preferable to characterize organic soils using probing methods such as BPT that would "test" (or mobilize) a relatively large soil volume during penetration.

Field vane shear test is a traditional in-situ test used to obtain the undrained shear strength of fine-grained soils. It consists of a four-blade, stainless steel vane attached to a steel rod which is pushed into the ground and rotated at pre-specified rates to measure the torque at peak and remolded states. In this research, a modified version of field vane test (eVST) was employed to obtain undrained shear strengths of peat at different specific depths.

In addition to in-situ testing, solid-stem auger and Shelby tube sampling were performed at the test site, and the retrieved samples were used to conduct laboratory tests of the main research program.

3 LABORATORY TESTS

Index properties of the tested organic soils were determined by the research team working from the UBC Okanagan Campus (Siddiqua and Elmouchi, 2020). These properties for organic soils material obtained at three different test hole depths are presented in Table 2.

Table 2. Index properties of the tested soil

Test Depth	2 - 4 m	4 - 5.3 m	5.3 - 7 m
Water content (%)	370 ± 20	570 ± 50	620 ± 30
Ash Content (%)	35 ± 4	13 ± 2.5	13 ± 2
Organic Content (%)	65 ± 4	87 ± 2.5	87 ± 2
Liquid Limit (%)	520 ± 20	740 ± 25	880 ± 20
Fiber Content (%)	47 ± 4	51 ± 4	51.5 ± 2.5
Wet Density (g/cm^3)	1.01 ± 0.01	0.95 ± 0.06	0.9 ± 0.04
Dry Density (g/cm^3)	0.75 ± 0.07	0.5 ± 0.1	0.57 ± 0.06
Specific Gravity	1.96 ± 0.1	1.88 ± 0.04	1.8 ± 0.1

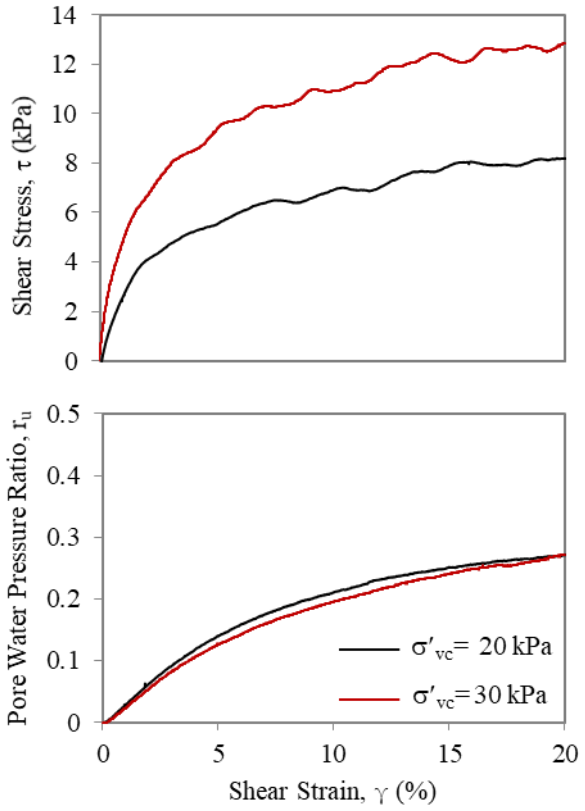

Fig. 3 Results of laboratory monotonic DSS tests

Physical properties of organic soils are important in describing and classification purposes. According to Hobbs (1986), physical properties such as organic content, water content, degree of saturation, void ratio, pH, liquid limit (LL), plastic limit (PL), bulk density and specific gravity indicate the state or condition of peat. These properties are interrelated, and they affect engineering behavior of organic soils to a great extent. Some empirical correlations between index properties and engineering properties of peat (except strength) have been established similar to that done for normally consolidated clays; however, the relationship between undrained shear strength and water content has been found to be not straightforward (Hobbs, 1986).

In addition to index testing, laboratory monotonic direct simple shear (DSS) tests were also performed on reconstituted specimens prepared from bulk samples extracted from the site. Results of two DSS tests conducted on specimens initially consolidated to vertical effective consolidation stresses (σ'_{vc}) of 20 and 30 kPa - corresponding to 2.1 and 3.2 m depths, respectively, calculated based on average bulk density of soil - are presented in Fig. 3. s_u values derived from these tests are included in Figs 4 and 5, for consideration as a part of the discussions on this topic in the next section.

4 INTERPRETATION OF UNDRAINED SHEAR STRENGTH (S_U)

s_u values interpreted from the field tests (SCPTs, BPTs, and eVSTs), along with the laboratory tests, of this study are presented and discussed herein. Methods used to interpret the s_u values are initially presented to serve as background information.

s_u, from eVST was determined adopting the method outlined in ASTM D257 (2015). This test allows measuring both the peak and remolded s_u; only the peak s_u has been considered in this paper. Total of six eVSTs were conducted at different depths at the two test hole locations as shown in Fig. 2.

s_u profile from the SCPTs were determined using the empirical approach given in Equation 1 (Robertson et al., 1986) by considering the resistance factor (N_{kt}) and net penetration resistance (q_{net}). It has been suggested that N_{kt} can typically range from 10 to 20 (Powell and Quaterman, 1988), and a value of 12.5 was assumed for N_{kt} with consideration given to plasticity index, sensitivity, and degree of consolidation of the site.

The s_u profile from BPT was determined using an essentially identical empirical approach as described by Equation 2; herein, an N_{ball} of 11 is used based on literature and information available from extensive experience gathered by a local in situ testing contractor (Weemees et al., 2006). The selected N_{kt} and N_{ball} values fall in the reported range by Boylan et al. (2011) for organic soils. It is of value to note that, unlike for the eVST, SCPT and BPT produce a continuous profile of peak undrained shear strength with depth.

$$s_u = q_{net}/N_{kt} \quad (1)$$

$$s_u = q_{net}/N_{ball} \quad (2)$$

5 COMPARISON OF TEST RESULTS

The variation of s_u values with depth, corresponding to the field Test Groups 01 and 02 (see Fig. 2) are presented in Figs 4 and 5, respectively. Because of the continuous penetration, the SCPT (solid line) and BPT (dashed line) provide an opportunity to obtain a continuous trace for the interpreted plot of s_u versus depth. As may be noted, the results from eVST and DSS tests are also plotted in the same figures as discrete points (with symbols).

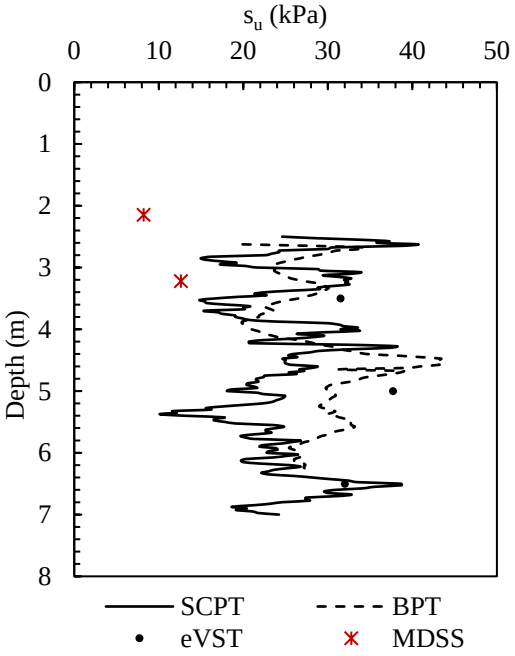

Fig. 4 Variation of s_u with depth - Test Group 01 (see Fig. 2)

The SCPT exhibits a wider variation of interpreted s_u - from 10 kPa to 40 kPa for the test Group 01 and 10 kPa to 75 kPa for the Test Group 02. It appears that the local variations, such as variation of the presence of fibers in organic soil are reflected in the measured cone penetration resistance, and in turn, in the interpreted value of s_u. While the SCPT provides a very effective way of identifying and delineating layering in mineral soil deposits, the results from SCPT may not necessarily represent such layering.

The range of s_u values (20 kPa – 50 kPa for both test groups) interpreted from BPT displays fewer local variations compared to the SCPT results; this is in accord with observations by Boylan et al. (2011). It is also of interest to note that the s_u values from BPT seem to be in good agreement with those from eVST, although eVST is considered not suitable for strength measurements of organic soils due to uncertain failure conditions around the vane circumference (Landva, 1980).

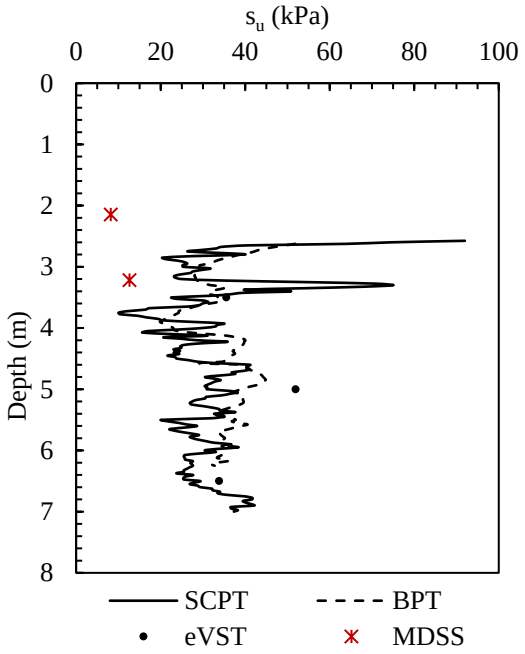

Fig. 5 Variation of S_u with depth - Test Group 02 (see Fig. 2)

According to Table 2, organic content and fiber content of the soil are increasing with depth at the site. However, there is no corresponding increase of the interpreted s_u values in harmony with these trends. This implies that the strength measurements of organic soils and their variations are complex.

The s_u values extracted from the laboratory monotonic DSS test results are also superimposed in Figs 4 and 5, as appropriate. The obtained s_u values are smaller compared to the s_u values determined from different field tests. Lower s_u from laboratory DSS tests are likely to be due to sample disturbance and change in soil fabric during sample reconstitution.

6 SUMMARY

A detailed field and laboratory test program has been undertaken at the University of British Columbia, Canada, to characterize muskeg soils and in turn, contribute to the current pipeline design guidelines. As a part of this program, a series of in-situ and laboratory element tests are conducted to study the strength and deformation parameters for organic soils.

Initial findings suggest that the ball (full-flow) penetration test (BPT) provides a suitable way of estimating undrained shear strength (s_u) of organic soils. The ability of BPT to mobilize a relatively large volume of soil mass during penetration compared to CPT testing is considered preferable to

characterize organic soils, particularly considering their variable nature and low strength/stiffness.

It is to be noted that penetration tests in soft organic soils are likely to be influenced by partial drainage effects related with rate of penetration of the tests (Boylan et al., 2011). These effects have to be critically considered in interpreting strength parameters from penetration tests.

ACKNOWLEDGEMENTS

The authors are grateful for the funding and in-kind support provided by the Industry Partners of the UBC Pipeline Integrity Institute (PII). In particular, the specific support provided by TC Energy, Ledcor, and ConeTec Investigations Ltd is deeply appreciated. The work would not have been possible without the matching funds provided by Natural Sciences and Engineering Research Council of Canada (NSERC) – Ref: NSERC CRD Project CRDPJ 500977-16. The authors would also like to thankfully acknowledge the contributions made to the research program by Jennifer Liu.

REFERENCES

Armstrong, J. E., and Hicock, S. R. (1979/1980). Surficial Geology, Vancouver and New Westminster, West of Sixth Meridian, British Columbia. Geological Survey of Canada, "A" Series Map 1486A and 1484A.

ASTM. D2573/D257. (2015). Standard Test Method for Field Vane Shear Test in Saturated Fine-Grained Soils. ASTM Standard Test Method, D2573/D257, 1–8.

Boylan, N., Long, M., and Mathijssen, F. (2011). In situ strength characterization of peat and organic soil using full-flow penetrometers. Canadian Geotechnical Journal, 1085-1099.

Hobbs, N. B. (1986). Mire morphology and the properties and behavior of some British and foreign peats. Quarterly Journal of Engineering Geology, 19(1), 7–80.

Landva, A. O. (1980). Vane testing in peat. Canadian Geotechnical Journal, 17(1), 1–19.

Liu, J., Wijewickreme, D., Liu, B., and Weemees, I. (2018). Characterization of mus-keg soils for soil-pipe interaction analysis – Some preliminary findings. 71st Canadian Geotechnical Conference, Edmonton, Alberta.

MacFarlane, I. (1969). Muskeg Engineering Handbook. University of Toronto Press, Canada.

Mesri, G., and Ajlouni, M. (2007). Engineering properties of fibrous peats. Journal of Geotechnical and Geoenvironmental Engineering, 133(7), 850–866.

Powell, J., and Quaterman, R. (1988). The interpretation of CPT in clays with particular reference to rate effects. Penetration Testing, ISOPT-1; Proc. int. symp, Orlando 1988. (pp. 903-910). Rotterdam: Balkema.

Robertson, P.K., Campanella, R.G., Gillespie, D., and Greig, J. (1986). USE OF PIEZOMETER CONE DATA. (ASCE (Geotechnical Special Publ n 6)), pp. 1263–1280.

Siddiqua, S. and Elmouchi, A. (2020). Internal UBC Communications.

Weemees, I., Howie, J., Woeller, D., Sharp, J., Cargill, E., and Greig, J. (2006). Improved techniques for the in-situ determination of undrained shear strength in soft clays. 59th Canadian Geotechnical Conference (pp. 89-95). Vancouver: BiTech Publishers Ltd.

Yamaguchi, H., Ohira, Y., Kogure, K., and Shigeru, M. (1985). Undrained shear characteristics of normally consolidated peat under triaxial compression and extension conditions. Soil and Foundations, 25(3): 1-18.

Stabilizer Design for Deep Soil Mixing Using Fly Ash to Stabilize Expansive Soil

J. Sangeetha, J. Dalshica & M.C.M. Nasvi

Department of Civil Engineering, University of Peradeniya, Sri Lanka

ABSTRACT: Stabilization of expansive soils with deep soil mixing (DSM) columns is an effective method to improve expansive soils at deeper depths. A research was carried out to develop a stabilizer design for DSM using ASTM Class F fly ash as the binder. The soil was stabilized with fly ash at various binder contents (10-25%) and the stabilized samples were cured for a period of 28 days at ambient temperature conditions (28 ± 2℃). Index properties, free swell test, swell pressure test and unconfined compressive strength (UCS) test were conducted for all the samples. According to UCS results 15% binder content gives optimum strength to the tested soil. Further, swell pressure reduced with the increase of the binder content up to 25%. Considering both strength and swell criterions, 15% binder content was selected as the optimum binder content. Heave versus area ratio design chart was developed for different DSM column lengths (2-6 m). The developed heave versus area ratio design chart can be used to determine the required area ratio to limit the heave to the project specified value.

Nomenclature

a_r	Area ratio	UCS	Unconfined compressive strength
a_w	Binder content	USCS	Unified Soil Classification System
CL	Low plasticity clay	V	Total volume per one sample mix
DSM	Deep soil mixing	W_b	Weight of binder per sample
FSR	Free swell ratio	$w:b$	Water binder ratio
H_i	Thickness of layer	w_n	Initial water content
ΔH	Surface heave	W_s	Dry weight of soil per sample
LL	Liquid limit	w_T	Total water content of the mix
OPC	Ordinary Portland Cement	$W_{w,slurry}$	Weight of water for slurry
PI	Plasticity index	XRF	X-ray fluorescence
PL	Plastic limit	α	Binder factor
S_w%	Swell percentage of expansive soil-DSM column composite region	γ_b	Bulk unit weight
$S_{w,col}$ %	Swell percentage of treated DSM column	γ_d	Dry unit weight
$S_{w,soil}$%	Swell percentage of untreated expansive soil		

1 INTRODUCTION

Expansive soils are one of the most problematic soils that cause damages to lightly loaded infrastructure built on them due to their undesirable swelling and shrinkage behavior under changing moisture content (Madhyannapu and Puppala, 2014). Expansive clay minerals, such as montmorillonite (smectite group) or some particular types of illite, are responsible for the expansiveness of these soils (Sabtan, 2005; Seco et al., 2010). Deep soil mixing (DSM) is a well-established deep soil stabilization method used to improve physical and mechanical properties of the existing soil and this method is generally used at depths greater than 1.5 m (Bhadriraju et al., 2007; Madhyannapu and Puppala, 2014; Zaika and Rachmansyah, 2017). Two methods of DSM are available based on the method of mixing: (1) Dry method: soil is mixed with a dry binder and this method is used for soils having high moisture content values (2) Wet method: soil is mixed with a slurry of the binder, and this method is used for soils having low moisture content values (Zaika and Rachmansyah, 2017). Since the soil sample used in this study had low moisture content values, the wet method was used in the present study.

The design of DSM column is carried out in two steps: stabilizer design and geometric design. Under

stabilizer design selection of binder type, determination of optimum water-binder ratio and optimum binder content, and development of heave versus area ratio design charts are carried out. In geometric design the geometric parameters e.g. length and diameter of the DSM column and spacing between columns are decided. Since stabilizer design is the main component of DSM design, the present research focuses only on stabilizer design.

Ordinary Portland cement (OPC) and lime are the most commonly used binders in DSM work (Bhadriraju et al., 2007; Madhyannapu and Puppala, 2014). However, production of one ton of OPC emits approximately one ton of CO_2 to the environment and OPC production contributes to 7% of the total global CO_2 emissions (Wardhono et al., 2014; Tee and Mostofizadeh, 2021). Thus, OPC is not a suitable binder with regard to sustainability. On the other hand, the use of fly ash for soil stabilization is better than cement or lime with respect to both sustainability and economic aspects. Fly ash is a by-product of coal-based power plants and its disposal is a major problem of this industry. Fly ash particles have the potential to develop pozzolonic reaction causing reduction in swell of expansive soils due to reduction in surface area and water affinity (Cokca, 2001; Nalbantogulu, 2004). To date, there is no published literature on DSM design using fly ash as a stabilizer; the aim of this research was to develop stabilizer design guidelines for DSM technique to stabilize expansive soil using fly ash as the binder.

2 MATERIALS

2.1 *Expansive soils*

Expansive soil samples were collected from Digana area, Sri Lanka (latitude 7°17'56.8" N, longitude 80°42'37.9"E). Index properties tests: bulk density, moisture content, Atterberg limit test, sieve analysis and hydrometer analysis, were conducted according to the BS1377: Part 2: 1990 to determine the index properties of the soil (Table 1). The initial swell classification of the soil was done based on the free swell test as proposed by Prakash and Sridharan (2004). The free swell ratio (FSR) obtained was 1.6 indicating that the soil used is moderately expansive. In addition, constant volume swell pressure test was conducted in accordance with BS 1377-Part 5-1990 and the swell pressure value obtained for raw expansive soil was 104 kPa.

According to the grain size distribution curve shown in Fig. 1, 45 % of soil particles are sand (4.75 -0.075 mm), 22% of soil particles are slit silt (0.075 – 0.002 mm) and 33% are clay particles (0.002 mm). According to Unified Soil Classification System (USCS), the soil used is low plasticity clay (CL).

Table 1. Index properties of expansive soil

Property	Value
Bulk density (kg/m^3)	1597
Natural moisture content (%)	26
Liquid limit (LL) (%)	45
Plastic limit (PL) (%)	36
Plastic Index (PI) (%)	9

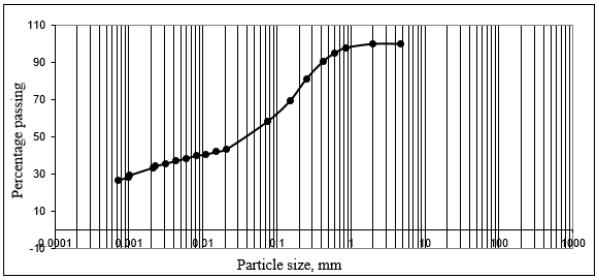

Fig. 1 Gradation curve of expansive soil sample

2.2 *Fly ash*

Coal fly ash was collected from Lakwijaya Coal Power Plant, Norochcholai, Sri Lanka. As per ASTM C618, fly ash can be classified either as ASTM Class F or Class C; the composition requirements of each category are given in Table 2. The chemical composition of the fly ash based on X-ray fluorescence (XRF) is summarized in Table 3. According to the results, the fly ash used in this study is classified as ASTM Class F fly ash.

Table 2. Classification of fly ash as per ASTM C618

Chemical composition requirement	Class F	Class C
$SiO_2 + Al_2O_3 + Fe_2O_3$, minimum (%)	70.0	50.0
SO_3, maximum (%)	5.0	5.0
Moisture content, maximum (%)	3.0	3.0
LOI, maximum (%)	6.0	6.0
Available alkalis (as Na_2O), maximum (%)	1.5	1.5

Table 3. Chemical composition of the fly ash used in the present study

Constituent	Percentage (%)
$SiO_2 + Al_2O_3 + Fe_2O_3$	82.10
SO_3	0.81
CaO	8.40
P_2O_5	2.83
TiO_2	1.93
MgO	1.59
K_2O	0.71
MnO	0.06
Na_2O	0.62

3 METHODOLOGY

3.1 *Selection of binder type*

In this research, fly ash was used as the binder, since it offers sustainable and economical solutions to the issues related to OPC production. Fly ash is rich in divalent ions, such as Ca^{2+}, Mg^{2+}, that produces flocculation of clay particles and limits the expansivity of soil. Furthermore, fly ash will involve in pozzolonic reaction in the presence of water improving mechanical properties of the soil samples (Seco et al., 2011).

3.2 *Selection of optimum water-binder ratio*

In the mixing of the binder and soil, water is an essential component. It supports the hydration process of the binder and enables to achieve an efficient mixing (Bergado and Lorenzo, 2005; Lorenzo et al., 2005). Traditionally, it was assumed that the binder content is the only controlling parameter governing the strength of the DSM columns (Kamon and Bergado, 1991; Bergado et al., 1999). However, recent studies have proven that water-binder (w: b) ratio also can affect the strength of DSM columns (Porbaha et al., 2000; Miura et al., 2001; Lorenzo and Bergado, 2004).

If the water content in the mix is too high, the strength of the treated sample can be low due to the high void ratio. High void ratios will lead to electrostatic attraction loss between clay particles reducing the number of clay-to-clay contact surface to be bonded by pozzolonic reaction. Similarly, low amount of water in the mix affects the strength of the treated soil samples by the presence of air voids, which can reduce the ability of dispersing of binder ions. Low water content can result in unbonded clay-to-clay surfaces due to inefficient mixing. Therefore, an optimum water content needs to be maintained in the mixing of clay with the binder to achieve the best improvement in strength (Bergado and Lorenzo, 2005; Lorenzo et al., 2005). Water to binder ratio (w: b) of 0.6 was selected as this ratio yields high strength values for stabilized samples (Lorenzo et al., 2005).

3.3 *Selection of optimum binder content*

The expansive soil was treated with four different fly ash contents; 10%, 15%, 20% and 25%, to select the optimum binder content by using the method proposed by Bhadiraju et al. (2007). This range of fly ash content (10-25%) was selected based on the binder content values recommended in the literature (Cokca., 2001; Nalbantogulu, 2004; Yadu et al., 2011; Jafer et al., 2018). The following steps were undertaken to select the optimum binder content;

1. The bulk weight of raw soil passing through US Sieve No 10 (2 mm) was oven dried at 105 ^{0}C for 24 hours (Liu et al., 2019).
2. Appropriate amount of binder was decided based on binder factor (α), required amount of dry soil (W_s) and total water content (w_T), which includes the initial water content (w_n)) and amount of water from the water/binder ratio ($W_{w,slurry}$), to prepare the soil binder mixture, as shown in Table 4.

Table 4. Mix design used for stabilizer design

Description and Notation	Equation
Bulk unit weight, γ_b (kg/m^3)	W/V
Initial water content, w_n (%)	Calculated as per BS 1377-2-1990
Dry unit weight, γ_d (kg/m^3)	$\gamma_b/(1+w_n)$
Total volume per one sample mix, V (m^3)	User specific
Dry weight of soil per sample, W_s (kg)	$\gamma_d \times V$
Binder content, a_w in %	W_b/W_s
Binder factor, α (kg/m^3)	$(a_w \times \gamma_b)/100(1+w_n)$
Weight of binder per sample, W_b (kg)	$\alpha \times V$
Water binder ratio, w: b	$W_{w.slurry}/W_b$
Weight of water for slurry, $W_{w.slurry}$ (kg)	$W_b \times (w:b)$
Total water content of the mix, w_T in kg	$w_n + W_{w,slurry}$

3. The desired amount of binder (fly ash) and raw soil, calculated in steps 1 and 2, were mixed in dry state. The total amount of water (w_T) was then added with the dry mixture and it was mixed manually 5-7 minutes until a uniform mixture was obtained.
4. The final mixture was transferred to the compaction mold (100 mm inner diameter and 127 mm height) in three layers. Each layer was compacted by 27 blows using a 2.5 kg light weight hammer free falling from 300 mm. The blows were evenly distributed around the surface of the specimens to prevent any extrusion of soil through the edges and the bottom of the mold. The strength values obtained in the laboratory are usually higher than those obtained in the field and this is attributed to the differences between the mixing efficiencies obtained in a small-scale laboratory sample and the actual field conditions on a large-scale field column (Bhadiraju et al., 2007; Lemos et al., 2020). The ratio between field and laboratory UCS values vary from 0.25 to 0.50 (Lemos et al., 2020).
5. From the compacted soil, samples of 38 mm diameter and 76 mm height were extruded for UCS

test and they were wrapped with airtight plastic bags to prevent any moisture loss. The samples were allowed to cure for a period of 28 days at ambient temperature conditions (28 ± 2 ^{0}C).

6. Constant volume swell pressure test (BS 1377-Part 5: 1990) and UCS test (BS 1377-Part 7:1990) were conducted for all samples.

3.4 *Development of heave versus area ratio charts*

Heave versus area ratio charts were developed for optimum binder content with different column lengths: 2 m, 4 m and 6 m. Schematic view of the DSM improved section considered for heave calculations is given in Fig. 2. Surface heave of composite section (ΔH) was calculated based on the results of constant volume swell pressure test using Equations 1 and 2.

$$S_w\% = S_{w,col}\,\% \times a_r + S_{w,soil}\,\% \times (1 - a_r) \quad (1)$$

where $S_w\%$ is swell percentage of expansive soil-DSM column composite region, $S_{w,col}\,\%$ is swell percentage of treated DSM column, $S_{w,soil}\%$ is swell percentage of untreated expansive soil and a_r is the area ratio which is defined as the ratio between DSM column area and total area of the site. In this study, area ratio values of 0 – 60% were used as per the literature (Madhyannapu and Puppala, 2014; Zaika and Rachmansyah, 2017).

$$\Delta H = \sum_{i=1}^{n}\left[s_{w,i}(\%)\right](H_i)(0.01) \quad (2)$$

where ΔH is surface heave, $s_{w,i}(\%)$ is swell percentage of composite soil and H_i is thickness of layer i as shown in Fig. 2.

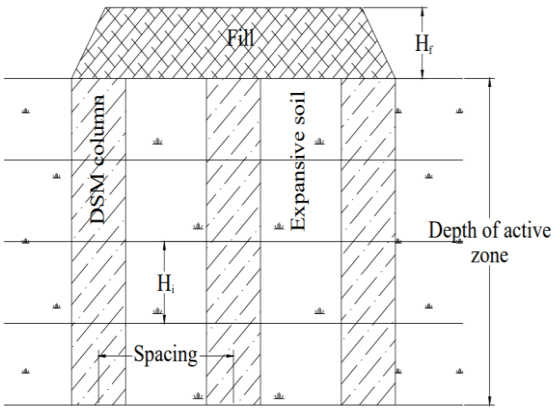

Fig. 2 Schematic view of the DSM improved section considered for heave calculations

4 RESULTS AND DISCUSSION

4.1 *Effect of fly ash on UCS of stabilized soil*

Variation of UCS with binder content is shown in Fig. 3. UCS value of treated soil samples increases with the binder content up to 15% and then reduces with any further addition of binder. The optimum binder content for high strength is 15% and this binder content was chosen to develop the heave versus area ratio design chart.

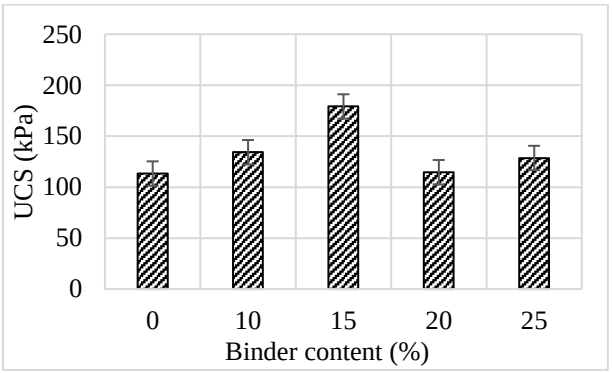

Fig. 3 Variation of UCS with binder content

The percentage increase in UCS up to 15% binder addition is 58% while the reduction in UCS beyond the optimum binder content is 42 %. Initial increase in UCS is due to the increase in dry unit weight with increased binder content as the total weight of solids is increased in the sample (Phani Kumar and Sharma, 2004). Furthermore, there is a cementation process due to the pozzolonic reaction between binder particles and the soil, and this pozzolonic products bind the clay particles together forming a strong bonded matrix. This increases the UCS of the treated soil (Bergado and Lorenzo, 2005; Lorenzo et al., 2005).

The reason for the reduction in the UCS value beyond 15% binder content can be explained as follows. The total water content in soil samples increases with the increase in binder content. If the mixing water content is high, it makes the clay particles to repel each other losing the electrostatic attraction. In addition, the high water content increases the void ratio of treated soil (Bergado and Lorenzo, 2005; Lorenzo et al., 2005). Furthermore, the excess amount of binder introduced to the soil can cause the formation of weak bonds (Yadu et al., 2011; Fattah et al., 2013; Adhikary and Jana, 2016). Due to all these reasons, the UCS value of the treated soil reduces with the increase in the binder content beyond 15%.

4.2 *Effect of fly ash addition on swell pressure*

Fig. 4 shows the variation of swell pressure with the binder content. Swell pressure decreases with an increase in binder content and the percentage decrease is about 53%. The reason for the reduction in the swell pressure with the addition of binder can be explained as follows. The binder (fly ash) particles have potential to provide multivalent cations (Ca^{2+}, Al^{3+}, Fe^{3+}, etc), which promote flocculation of clay particles by cation exchange. As a result, the surface area and water affinity of the samples decrease thereby reducing the swell potential values. With increasing binder content, the amount of exchangeable cations increases, hence the swell pressure reduces (Cokca, 2001; Nalbantogulu, 2004; Zaika and Rachmansyah, 2017). Although the maximum decrease in swell pressure was obtained for binder content of 25%, binder content of 15% was considered for the development of heave versus area design chart considering both strength and the swell reduction criterions.

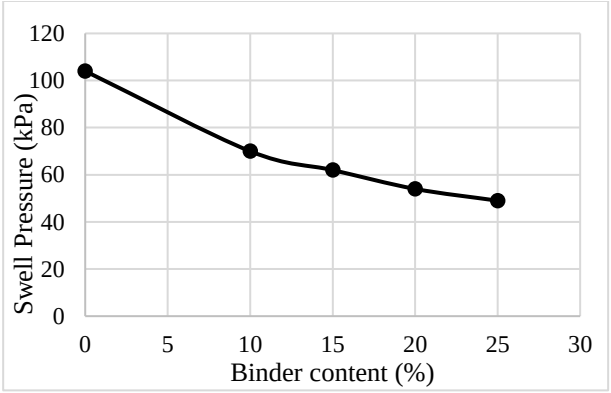

Fig. 4 Variation of swell pressure with the binder content

4.3 *Heave versus area ratio charts*

Heave versus area ratio chart was developed for optimum binder content (15%) obtained based on the UCS results; three different DSM column lengths (2 m, 4 m, and 6 m) were used. The developed heave versus area ratio charts are shown in Fig. 5. The results show that heave is further reduced with the area ratio, because the area covered by the binder increases with the increase in the area ratio. This enables provision of more multivalent cations and reduces the surface area and water affinity of the samples.

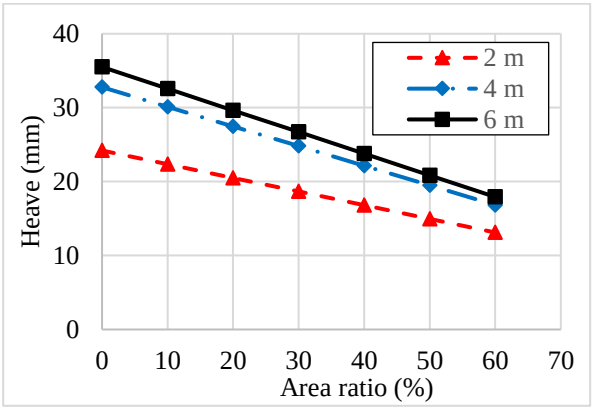

Fig. 5 Heave versus area ratio charts for different column lengths at a binder content of 15%

For a given expansive soil (with certain swell pressure values), figures similar to Fig. 5 can be developed and the required area ratio to limit the total heave to the project specified value can be obtained. For example, allowable heave for flexible pavements, rigid pavements, tunnels and building projects are 12 mm, 18 mm, 10 mm and 40 mm respectively (Madhyannapu and Puppala, 2014). After obtaining the required area ratio from the stabilizer design, geometric design can be conducted to obtain the arrangement of the DSM columns.

5 CONCLUSIONS

A stabilizer design was developed for deep soil mixing (DSM) to stabilize a moderately expansive clay soil using fly ash as the stabilizer. Based on the findings of this research, the following conclusions were drawn;

1. The optimum binder content (fly ash content) for higher UCS value of fly ash stabilized expansive soil is 15% by weight. Initially, the UCS of the stabilized soil increases with the addition of binder content up to 15% and then it reduces with any further increase in the binder content.
2. The swell pressure of the stabilized sample reduces with the increase in the binder content up to 25%. However, when considering both strength and swell criterions, 15% binder content is the optimum binder content for DSM design.
3. The developed heave versus area ratio design chart can be used to determine the required area ratio to limit the total heave to the project specified limit.
4. The DSM technique can be successfully applied to treat expansive soil using fly ash as the stabilizer.

REFERENCES

Adhikary, S. and Jana, K. (2016). Potentials of Rice-husk Ash as a Soil Stabilizer, International Journal of Latest Research in Engineering and Technology (IJLRET), 2(2):40-48.

Bergado, D.T. and Lorenzo, G.A. (2005). Economical Mixing Method for Cement Deep Mixing, Proc. ASCE GeoFrontiers 2005, ASCE, Reaton, Va.

Bergado, D. T., Ruenkrairergsa, T., Taesiri, Y. and Balasubramaniam, A. S. (1999). Deep Soil Mixing to Reduce Embankment Settlement, Ground Improvement Journal, 3(3):1-18.

Bhadriraju, V., Puppala, A.J., Madhyannapu, S. and Williammee, R. (2007). Laboratory Procedure to Obtain Well-mixed Soil Binder Samples of Medium Stiff to Stiff Expansive Clayey Soil for Deep Soil Mixing Simulation, Geotechnical Testing Journal, 31(3):225-238.

Cokca, E. (2001). Use of Class C Fly Ashes for the Stabilization of an Expansive Soil, Journal of Geotechnical and Geoenvironmental Engineering, 127:568-573.

Fattah, M.Y., Rahil, F.H. and Al-Soudany, K.Y.H. (2013). Improvement of Clayey Soil Characteristics Using Rice Husk Ash, Journal of Civil Engineering and Urbanism, 3(1):12-18.

Jafer, H., Atherton, W., Sadique, M., Ruddock, F. and Loffill, E. (2018). Stabilisation of soft soil using binary blending of high calsium fly ash and plam oil fuel ash, Applied Clay Science, 152:323-332.

Kamon, M. and Bergado, D.T. (1991). Ground Improvement techniques, Proc. 9th Asian Regional Conf. on Soil Mechanics and Foundation Engineering, International Society of Soil Mechanics and Foundation Engineering, 2:526-534.

Khemissa, M. and Mahamedi, A. (2014). Cement and lime mixture stabilization of an expansive over consolidated clay, Applied clay science, 95:104-110.

Liu, Y., Chang, C.W., Namdar, A., She,Y., Lin, C.H., Yuan, X. and Yang, Q. (2019). Stabilization of expansive soil using cementing materials from rice husk ash and calcium carbide residue, Construction and Building Materials, 221:1-11.

Lemos, S. G. P., Almeida, M. D. S. S., Consoli, N. C., Nascimento, T. Z., and Polido, U. F. (2020). Field and Laboratory Investigation of Highly Organic Clay Stabilized with Portland Cement, Journal of Materials in Civil Engineering, 32(4): 04020063.

Lorenzo, G.A., and Bergado, D.T. (2004). Fundamental parameters of cement-admixed clay – a new approach, ASCE Journal of Geotechnical and Geoenvironmental Engineering, 130(10):1-9.

Lorenzo, G.A., Bergado, D.T. and Soralump, S. (2005). New and Economical Mixing Method of Cement Admixed Clay for DMM Application, Geotechnical Testing Journal, 29(1): 54-63.

Lu, S.S., Sun, F.F. and Zong, Y.T. (2014). Effect of rice husk biochar and coal fly ash on some physical properties of expansive clayey soil (Vertisol), Catena, 114:37-44.

Madhyannapu, R.S. and Puppala, A.J. (2014). Design and Construction Guidelines for Deep Soil Mixing to Stabilize Expansive Soils, J. Geotech. Geoenviron.Eng, 140(9): 01-15.

Madhyannapu, R.S., Puppala, A.J., Nazarian, S. and Yuan, D. (2010). Quality Assessment and Quality Control of Deep Soil Mixing construction for Stabilizing Expansive Subsoils, Geotechnical and Geoenvironmental engineering, 136(1):119-128.

Miura, N., Horpibulsuk, S. and Nagaraj, T.S. (2001). Engineering behaviour of cement stabilized clay at high water content, Soils Found, 41(5):33-46.

Nalbantogulu, Z. (2004). Effectiveness of Class C Fly Ash as an Expansive Soil Stabilizer, Construction and Building Materials, 18:377-381.

Phani Kumar, B.R. and Sharma, R.S. (2004). Effect of Fly Ash on Engineering Properties of Expansive Soil, Journal of Geotechnical and Geoenvironmental engineering, 130(7):764-767.

Porbaha, A., Shibuya, S. and Kishida, T. (2000). State of the art in deep mixing technology. Part III: geomaterial characterization, Ground Improvement, 4(3):91-110.

Prakash, K. and Sridharan, A. (2004). Free swell Ratio and Clay Mineralogy of Fine-Grained Soils, Geotechnical Testing Journal, 27(2):220-225.

Puppala, A.J., Manosuthikij, T. and Chittoori, B.C.S. (2013). Swell and shrinkage characterizations of unsaturated expansive clays from Texas, Engineering Geology, 164:187-194.

Sabtan, A.A. (2005). Geotechnical properties of expansive clay shale in Tabuk, Saudi Arabia, Journal of Asian Earth Sciences, 25:747-757.

Seco, A., Ramirez, F., Miqueleiz, L. and Garcia, B. (2011). Stabilization of expansive soils for use in construction, Applied clay Science, 151:348-352.

Tee, K. F. and Mostofizadeh, S. (2021). A Mini Review on Properties of Portland Cement Concrete with Geopolymer Materials as Partial or Entire Replacement, Infrastructures, 6(2).

Yadu, L., Singh, D. and Tripathi, R. K. (2011). Comparison of Fly Ash and Rice Husk Ash Stabilized Black Cotton Soil, International Journal of Earth Sciences and Engineering, 4(6):42- 45.

Zaika, Y. and Rachmansyah, A. (2017). The Estimation of Bearing Capacity and Swell Potential of Deep Soil Mixing on Expansive Soil by Small Model Test, International Journal of Geomate, 13:09-15.

Wardhono, A., Law, D.W. and Molyneaux. T. (2014). The mechanicalproperties of fly ash geopolymer in long term performance, The 1st concrete innovation conference (CIC).

Effect of Cementation on Stress-strain and Energy Behavior of Sandy Soil during Undrained Cyclic Loading

M. Shiga
Institute of Industrial Science, the University of Tokyo

T. Kiyota
Institute of Industrial Science, the University of Tokyo

ABSTRACT: Liquefaction characteristics have been investigated in terms of many aspects such as density, soil fabric, and in-situ stress conditions since the 1970s. However, it is still challenging to verify liquefaction characteristics of sand with aging effect. This difficulty is because few previous studies stated how small-strain characteristics represent the combined substantial effects such as cementation and inter-locking, part of the aging effect. In this paper, artificially cemented specimens with different preparation methods were subjected to un-drained cyclic loading to investigate inter-locking and cementation effect on liquefaction characteristics in terms of shear wave velocity and energy concept. The result shows that the specimen prepared by wet tamping required fewer cycles leading up to liquefaction, even under the same cement addition rate. Furthermore, dissipated en-ergy to reach liquefaction is irrespective of the cement addition rate and specimen preparation method.

1 INTRODUCTION

It is necessary to consider the aging effect on liquefaction characteristics of Pleistocene deposits, which has been re-examined due to the large acceleration recently recorded in Japan. The aging effect can be consistent with two effects, fabric stabilization due to over-consolidation and stress history, and chemical stabilization due to cementation effects.

Previous studies discussed the effect of these two stabilizations on the liquefaction characteristics of sandy soils in comparison with dynamic shear modulus, G_d or shear wave velocity, V_s. For instance, Tokimatsu et al. (1986) investigated the effect of pre-shearing or over-consolidation on cyclic resistance ratio, *CRR,* and concluded that dynamic shear moduli could reflect the effect. Kiyota et al. (2009a; b) discussed the difference in aging effect of several in-situ and reconstituted samples in terms of G_d. Kiyota et al. (2019) concluded that without bonding effect, the $V_s - CRR$ trends of the examined soils are consistent regardless of soil type, density, fines content and confining pressure. However, the laboratory tests mentioned in those articles was not intended to examine both stabilization effects contributing to aging effect.

Towhata and Ishihara (1985) studied the stress path dependence of shear work under undrained cyclic loading. They found that the work done externally to reach a specific stress state is independent of stress path. Kokusho (2013) showed that the relationship between normalized cumulative dissipated energy and $\Delta u/\sigma_c'$ is constant regardless of relative density or cyclic shear stress ratio, CSR.

The purpose of this study is to investigate the combined effects on the liquefaction properties of sandy soil by changing specimen preparation methods and cement addition rate.

2 METHODOLOGY

The specimens are composed of silica sand No. 7 (D_{50}=0.153mm, ρ_s=2.617g/cm^3, e_{min}=0.671 and e_{max} =1.145) and early strength Portland cement, which is used as the cementing agent. Cement addition rate, C to silica sand is 0, 1, 2, 3, and 5% by mass. The relative density, D_r, of the specimens are around 65%.

The specimen was prepared by wet tamping (WT), dry temping (DT), and dry vibration (DV) method. First, a plastic bag with pre-measured silica sand, cement, and water in case of wet tamping were shaken for 1 minute. Then, the mixture was thrown into a plastic mold using a funnel and pounded with a hammer to the desired height. The tamping was repeated four times to create a specimen 200 mm in height and 100 mm in diameter, which had been cured in water for seven days. After curing, the plastic mold was removed, the specimen was covered with a membrane and placed in a strain-controlled triaxial apparatus. For the non-cemented specimens,

sand and water mixed in the plastic bag were put into a rigid mold to be tamped by a hammer in case of wet tamping. In contrast, dry sand was poured directly into the mold to be tamped or hit by the hammer for the case of dry tamping and dry vibrating, respectively. The specimen was placed in the test apparatus immediately after it was prepared.

The specimen was initially consolidated at effective confining pressure, σ_c' of 30 kPa. While maintaining σ_c', back pressure was reduced to -100 kPa to remove the air from the specimen. The specimen was saturated with double vacuuming method. The back pressure was gradually increased to 200 kPa after saturation. The B-value of Skempton was confirmed to be above 0.90. Then, isotropic consolidation was performed until σ_c' reached 100 kPa.

A trigger and accelerometer system, initially developed by AnhDan et al. (2002), was used to measure shear wave velocity, V_s of the specimens. A shear wave, in the form of a single sinusoidal wave with a frequency of 1 kHz, was generated by a pair of wave sources (actuators) attached on the top cap that were simultaneously excited in the torsional direction. A pair of accelerometers was employed to measure the arrival time of the shear wave at two different heights.

After the measurement of V_s during consolidation, undrained cyclic loading was applied with a constant amplitude of cyclic deviator stress until double amplitude of axial strain, $\varepsilon_{a(DA)}$ reached 5% at the constant rate of 0.1%/min. The specification of all the tests is shown in Table 1.

3 RESULTS AND DISCUSSION

3.1 *Stress and strain behavior*

Fig. 1 shows the stress-strain relationship and effective stress path of specimens with different cement addition rates. Fig. 2 shows ones with several specimen preparation methods. The number of cycle, N_c shown in Fig. 1 and Fig. 2 is defined by the excess pore pressure ratio, $\Delta u/\sigma_c'$ of 95%. It is observed from the stress-strain relationship that the strain increases in the extension direction regardless of the cement addition rate and specimen preparation method. In addition, V_s and N_c increase significantly as cementation effect becomes dominant. Since all tests except *C*=0% were conducted under the same *CSR* and σ_c', N_c can be corresponded to liquefaction resistance. The fact that liquefaction resistance can be dramatically increased by adding a small amount of cement has been confirmed in many previous studies (Clough et al. 1989; Rasouli et al. 2020; Saxena et al. 1988). Focusing on the effective stress path per cycle, the effective stress with C=1% specimen decreases rapidly, while that of the specimens with C=3% specimen decreases slowly.

As shown in Fig. 2, the difference in preparation methods affects stress-strain behavior and effective stress path. N_c to reach $\varepsilon_{a(DA)}$=5% was 6.5 for wet tamping and 17.5 for dry vibration. In addition, shown in the effective stress path, in wet tamping, Δu increases by about 65 kPa in the first cycle, while in the case of dry vibration, Δu increases by about 30 kPa.

Tatsuoka et al. (1986). conducted various series of tests to investigate the effect of sample preparation on the shear modulus, G_d and concluded that G_d is insensitive to specimen preparation method. Sawangsuriya et al. (2007) compared the effect of the preparation method of rodding and tamping on change in V_s during isotropic consolidation and conduct non-linear fitting to exponential function. They found that there was not significant difference in the fitted parameters of two preparation method. In contrast, the present experiment shows that cement addition and specimen preparation method can mutually affect the shear wave velocity and liquefaction resistance.

Fig. 3 and Fig. 4 show the relationship between the normalized N_c, $\Delta u/\sigma_c'$ and $\varepsilon_{a(DA)}$. The denominator is N_c when $\Delta u/\sigma_c'$ reaches 95% and N_c when *DA* reaches 1%, respectively. Fig. 3 shows that, in the range where the $\Delta u/\sigma_c'$ is less than 95%, and in comparison with non-cemented and cemented specimens, the faster Δu develops in series of cemented specimens. A similar trend was observed in previous articles (Clough et al. 1989; Porcino et al. 2015).

Table 1. Specification of the conducted test

Name	Preparation Method	Cement addition rate, *C*(%)	CSR	N_c ($\varepsilon_{a(DA)}$5%)	N_c ($\varepsilon_{a(DA)}$3%)	N_c ($\varepsilon_{a(DA)}$1%)	N_c ($\Delta u/\sigma_c'$95%)	V_s (m/s)
WT_C00_7	WT	0	0.15	45.5	42.5	37.5	37.5	209.0
WT_C01_3		1	0.30	6.5	2.5	0.5	2.0	227.8
WT_C02_1		2	0.30	6.5	3.5	1.5	2.5	299.1
WT_C03_2		3	0.30	16.5	10.5	4.5	4.5	364.5
WT_C05_1		5	0.30	N/A*	29.5	16.5	12.5	466.8
DT_C02_4	DT	2	0.30	17.5	12.0	6.5	8.5	356.5
DV_C02_2	DV	2	0.30	N/A*	33.5	20.5	17.5	425.4

*$\varepsilon_{a(DA)}$ could not reach to 5% due to the separation of membrane from top cap

3.2 *Number of Cycle and Shear Wave Velocity*

Fig. 5 shows the correlation between V_s and N_c when $\Delta u/\sigma_c'$ reaches 95% or $\varepsilon_{a(DA)}$ reaches 3%. It can be seen that V_s and N_c are positively correlated. It is also noteworthy that V_s is sensitive to the increase in cement addition rate, while N_c to be liquefied is insensitive up to *C*=2%.

For the effect of specimen preparation method on V_s and N_c, although there is a unique positive correlation between V_s and N_c among three methods, the data plot of both DT and DV specimens is not along with the trend of WT specimens.

This trend can be attributed to the difference in the inter-spatial arrangement between cement particles and silica sand particles, as shown in Fig. 6. DT and DV specimens are densified by applying vibration to a dry mixture of cement and silica sand. Meanwhile, cement particles can move freely in the void and may eventually concentrate in the narrow void due to the electrical attraction on the surface of silica sand particles. On the other hand, in the WT specimen, the silica sand particles may have clustered by suction, and cement particles may have been distributed unevenly on the surface of the clustered silica sand. Therefore, it is thought that the cement reaction occurred almost evenly in voids, and the cross-linked structure formed by cement hydrate between silica particles became weaker than that of the DT specimen.

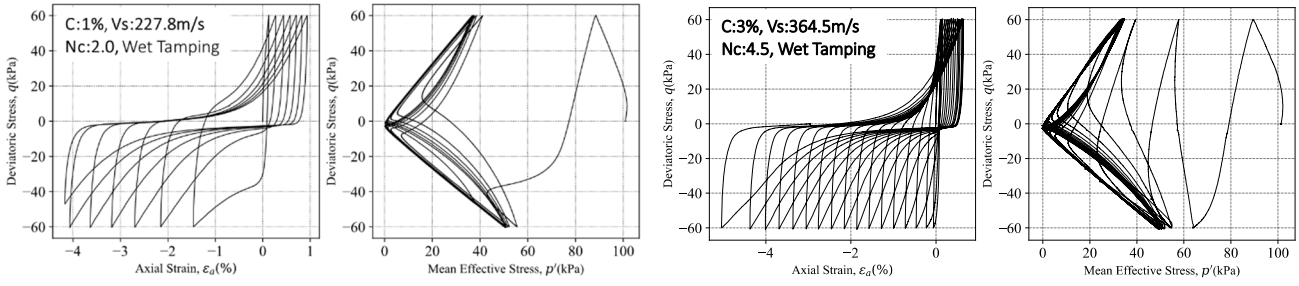

(a) (b)

Fig. 1 Change in stress-strain behavior and stress path with different cement addition rate (a) C=1%, (b) C=3%

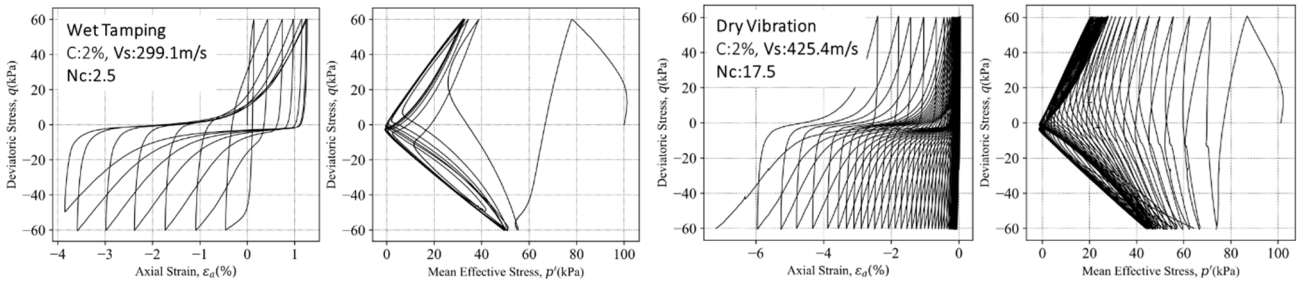

(a) (b)

Fig. 2 Change in stress-strain behavior and stress path with different method (a) Wet tamping, (b) Dry vibration

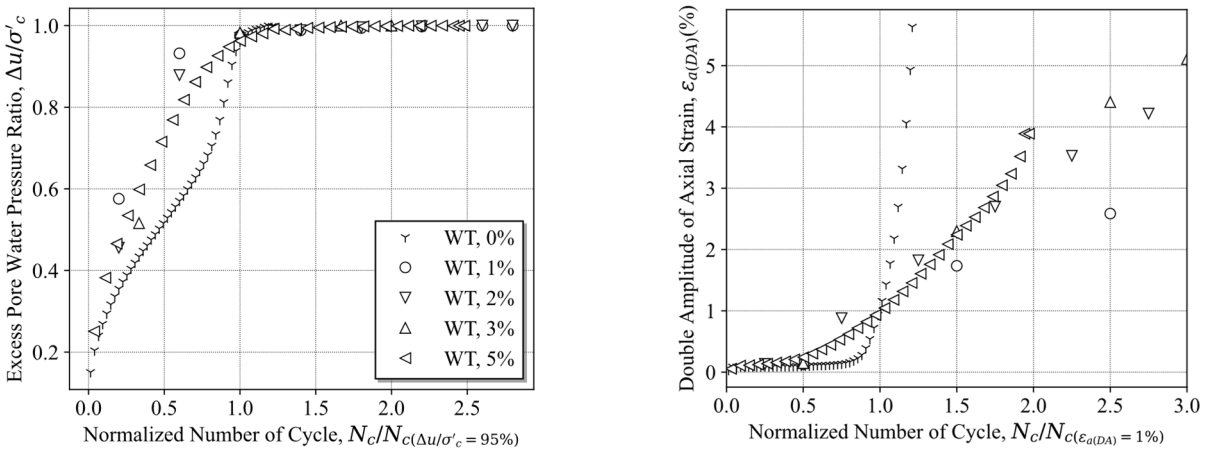

(a) (b)

Fig. 3 The relationship affected by *C* between (a) Normalized N_c and $\Delta u/\sigma_c'$, and (b) Normalized N_c and DA

3.3 *Energy Characteristic*

Fig. 7 shows the relationship between normalized cumulative dissipated energy, E^N and $\Delta u/\sigma_c'$. Based on Kokusho (2013), E^N is defined by the following equation.

$$E^N = \int \tau d\gamma / \sigma_{c0}' \quad (1)$$

where τ, γ and σ_{c0}' are shear stress, shear strain, and initial confining pressure, respectively.

As shown in Fig. 7(a), although the cement addition rate increased, there is no significant differences in the relationship between E^N and $\Delta u/\sigma_c'$, which indicates that the external work required to increase a given Δu is independent of the cement addition rate.

Cuccovillo and Coop (1999) suggested that the stress-induced total work (ΔW) have two components of frictional loss (ΔW_{fric}) and breaking the cementing bond (ΔW_{bond}), i.e.

$$\Delta W = \Delta W_{\mathrm{fric}} + \Delta W_{\mathrm{bond}} \quad (2)$$

where ΔW is equivalent to E^N. As compared in Fig. 7(a), ΔW is likely irrespective of cement addition rate. Also, ΔW_{bond} and cement addition rate should be positively correlated because positive work is required to break bonding, and cement addition increases the total number of bonds. This implies a reduction in ΔW_{fric} in Equation 2. Since ΔW_{fric} are associated with the loss of interlocking of soil particles, i.e., the increase in Δu, ΔW_{fric} and the increment of Δu increase should have a negative correlation. However, such a correlation has not been observed in the experiments. It is necessary to focus on the generation of negative work due to bonding breakage, and further investigations are needed to explain this behavior.

As shown in Fig. 7(b), the $E^N - \Delta u/\sigma_c'$ relationship is not varied significantly by preparation methods under the same cement addition rate, which implies that different bonding patterns shown in Fig. 6 may not influence energy dissipation characteristics during undrained cyclic loading.

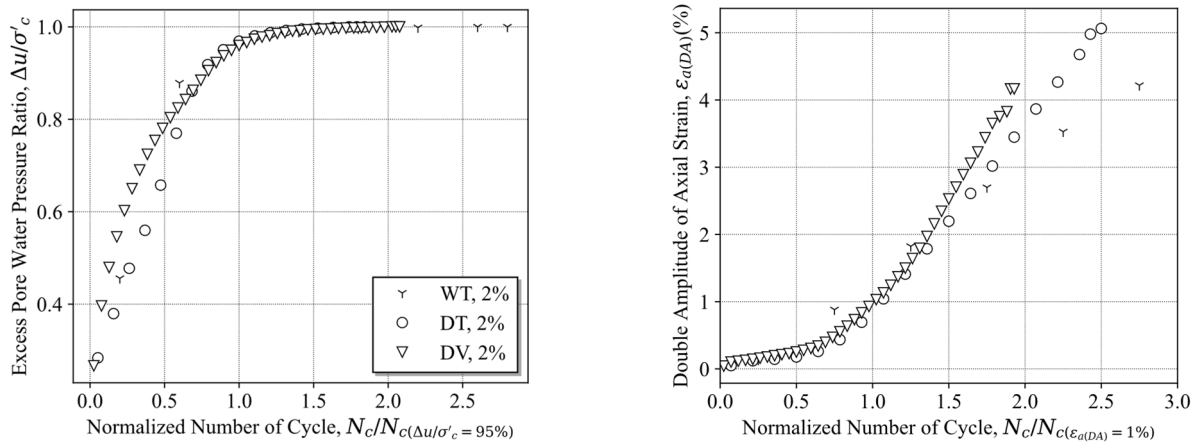

(a) (b)

Fig. 4 The relationship affected by soil fabric between (a) Normalized N_c and $\Delta u/\sigma_c'$, and (b) Normalized N_c and DA

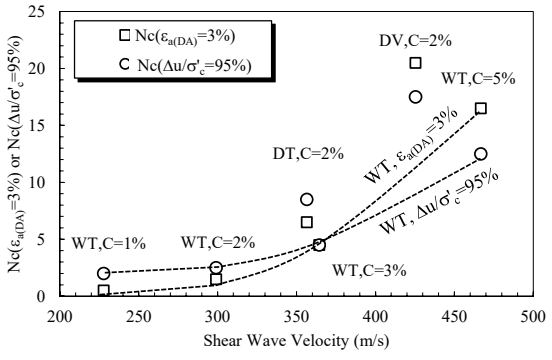

Fig. 5 The correlation between V_s and N_c

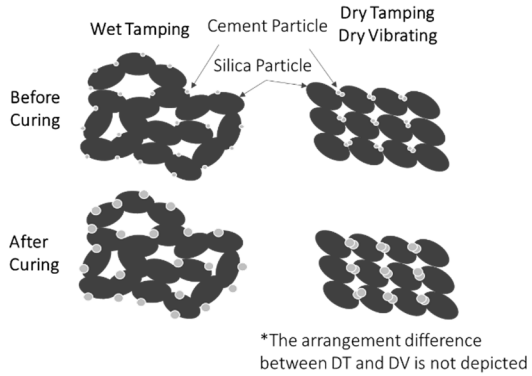

Fig.6 Schematic diagram of the difference in bonding between cement particles and silica sand particles due to their mutual position

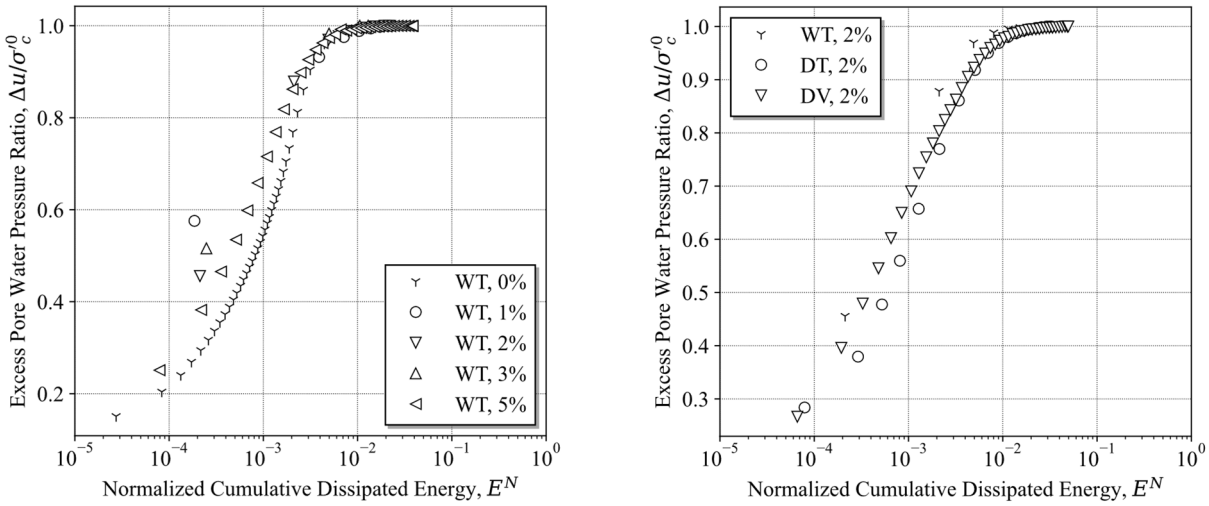

(a) (b)

Fig. 7 The relationship between normalized cumulative dissipated energy and excess pore water pressure ratio (a) different cement addition rate, (b) different preparation method

4 CONCLUSION

Several series of undrained cyclic loading tests were performed to investigate the effect of inter-locking and cementation on liquefaction characteristics. Described is the conclusion of this paper.

1. In the range where excess pore water pressure ratio is less than 0.95, the larger the cement addition rate, the faster the excess pore water pressure develops in terms of normalized number of cycle.

2. There is a positive correlation between shear wave velocity and number of cycle, although the increment in number of cycle is less significant among the specimens with under 2% cement addition rate.

3. Neither the addition of cement nor the specimen preparation methods made a noticeable difference in the relationship between normalized cumulative dissipated energy and excess pore water pressure ratio.

ACKNOWLEDGMENTS

This study was supported by JSPS KAKENHI Grant Number 20H02240 and 19J12349.

REFERENCES

AnhDan, L. Q., Koseki, J., and Sato, T. (2002). "Comparison of Young's moduli of dense sand and gravel measured by dynamic and static methods." *Geotechnical Testing Journal*, 25(4), 349–368.

Clough, G. W., Iwabuchi, J., Rad, N. S., and Kuppusamy, T. (1989). "Influence of cementation on liquefaction of sands." *Journal of Geotechnical Engineering*, American Society of Civil Engineers, 115(8), 1102–1117.

Cuccovillo, T., and Coop, M. R. (1999). "On the mechanics of structured sands." *Géotechnique*, Thomas Telford Services Ltd, 49(6), 741–760.

Kiyota, T., Koseki, J., Sato, T., and Kuwano, R. (2009a). "Aging Effects on Small Strain Shear Moduli and Liquefaction Properties of in-situ Frozen and Reconstituted Sandy Soils." *Soils and Foundations*, 49(2), 259–274.

Kiyota, T., Koseki, J., Sato, T., and Tsutsumi, Y. (2009b). "Effects of sample disturbance on small strain characteristics and liquefaction properties of Holocene and Pleistocene sandy soils." *Soils and Foundations*, Japanese Geotechnical Society, 49(4), 509–523.

Kiyota, T., Maekawa, Y., and Wu, C. (2019). "Using in-situ and laboratory-measured shear wave velocities to evaluate the influence of soil fabric on in-situ liquefaction resistance." *Soil Dynamics and Earthquake Engineering*, Elsevier Ltd, 117, 164–173.

Kokusho, T. (2013). "Applicability of energy-based liquefaction potential evaluation method compared with FL-method." *Japanese Geotechnical Journal*, The Japanese Geotechnical Society, 8(3), 463–475.

Porcino, D., Marcianò, V., and Granata, R. (2015). "Cyclic liquefaction behaviour of a moderately cemented grouted sand under repeated loading." *Soil Dynamics and Earthquake Engineering*, Elsevier, 79, 36–46.

Rasouli, H., Fatahi, B., and Nimbalkar, S. (2020). "Liquefaction and post-liquefaction assessment of

lightly cemented sands." *Canadian Geotechnical Journal*, Canadian Science Publishing, 57(2), 173–188.

Sawangsuriya, A., Fratta, D., Bosscher, P. J., and Edil, T. B. (2007). "S-Wave Velocity-Stress Power Relationship: Packing and Contact Behavior of Sand Specimens." American Society of Civil Engineers (ASCE), 1–10.

Saxena, S. K., Reddy, K. R., and Avramidis, A. S. (1988). "Liquefaction resistance of artificially cemented sand." *Journal of Geotechnical Engineering*, American Society of Civil Engineers, 114(12), 1395–1413.

Tatsuoka, F., Toki, S., Miura, S., Kato, H., Okamoto, M., Yamada, S. I., Yasuda, S., and Tanizawa, F. (1986). "SOME FACTORS AFECTING CYCLIC UNDRAINED TRIAXIAL STRENGTH OF SAND." *Soils and Foundations*, The Japanese Geotechnical Society, 26(3), 99–116.

Tokimatsu, K., Yamazaki, T., and Yoshimi, Y. (1986). "SOIL LIQUEFACTION EVALUATIONS BY ELASTIC SHEAR MODULI." *Soils and Foundations*, The Japanese Geotechnical Society, 26(1), 25–35.

Towhata, I., and Ishihara, K. (1985). "Shear Work and Pore Water Pressure in Undrained Shear." *Soils and Foundations*, Elsevier, 25(3), 73–84.

Study on effect of mixing eggshells with cement for improving characteristics of peaty clay

M.D.S.W.Goonathilake
IESL College of Engineering, Sri Lanka

M.D.J.P.Wickramasooriya
Irrigation Department, Sri Lanka

ABSTRACT: Peat soil may not be suitable for civil engineering constructions as it has critical properties such as high compressibility, low bearing capacity, low specific gravity and high water holding capacity. This research focused on studying the effect caused by the combined action of Egg Shell Powder (ESP) and Ordinary Portland Cement (OPC) stabilization on the geotechnical properties of peat soil. Peat mixed with varying percentages of ESP content by dry weight combined with OPC content. Specific gravity, Proctor compaction, Atterberg limits, direct shear and CBR tests were carried out on treated and untreated samples. The experimental results showed that peaty clay can be enriched by adding of OPC and ESP. Specific gravity of all the treated samples was greater than that of untreated sample. There was a considerable increase in maximum dry density of peat up to 20% of ESP, 15% of OPC with balanced 65% of natural peat sample. Both Shear strength parameters and CBR values increased with 20% ESP and 15% OPC. Further, it was determined that the optimum mix of ESP is 20% by weight mixed with 15% of OPC by weight.

1 INTRODUCTION

Geotechnical engineers face problems when constructing structures on soft peaty clays due to its long-term settlements and shear failure. Peaty clay is one of the most common problematic soils in Sri Lanka. In Sri Lanka, the most commonly used method to construct structures on peaty clay is open cut and replacement method due to its simplicity for shallow depths. However, chemical and mechanical ground improvement methods are also used for deeper depths of peat layers. Therefore, it appears that there is a need to study the improvement methods for peat in an economical and eco-friendly manner.

In addition, waste disposal is an environmental problem that increases year by year in Sri Lanka. Therefore, usage of waste materials for construction purposes is a relief to the environmental pollution also. This study focuses on the effects of mixing of eggshells in wet and dry cement mixing for improving the characteristics of soft peaty clay.

The main objective of this experimental research is to determine the optimum engineering properties of peaty clay by mixing with different percentages of eggshell powder with 15% cement.

The properties of the peat soil were determined, by mixing 15% of cement by weight with increasing percentages of Egg Shell Powder (ESP) by weight such that 10%, 15%, 20% and 25%. Atterberg limit, proctor compaction, specific gravity, direct shear and CBR test were carried out for untreated peat specimens as well as for cement and ESP treated specimens. Munasinghe (2001) determined that the optimum cement content to obtain a considerable improvement in peat is more than 15%. Furthermore, a study by Kulathilaka & Saputhanthri (2002), determined that properties of peat can be enhanced by mixing with 15% of cement. Hence, in this study, cement was added at a constant percentage of 15% by dry soil weight.

2. METHODOLOGY

Firstly, the soil sample was passed through No. 4 (4.75 mm) ASTM sieve. Then Atterberg limit test, organic content test, moisture content test, specific gravity test, standard proctor compaction test, modified proctor compaction test, direct shear test and CBR test were carried out to test the initial properties of natural soil sample. According to the test results, the soil sample was identified.

Egg shells were collected and thoroughly washed from distilled water. Then they were grinded to make egg shell powder (ESP). The ESP was passed through No. 120 (125µm) ASTM sieve. After that, peat was mixed with 15% of constant cement percentage and 10%, 15%, 20% and 25% of egg shell powder by dry soil weight. Spe-

cific gravity test, Atterberg limit test, standard proctor compaction test, direct shear test, modified proctor compaction test and CBR test were carried out to the prepared four test samples to discover the properties after mixing with constant percentage of cement and various percentages of egg shell powder.

2.1 *Materials used*

The peaty clay samples used in this study were collected from Orugodawatta, Sri Lanka. They were was in slurry form and consisted mostly of roots, wood pieces and stones. The collected samples were black, clayey and had the typical smell present in peat soils (Fig 1).

Fig. 1 Sun dried peaty samples

Fig. 2 Collected samples

Approximately 400 numbers of eggshells were collected from two restaurants in Wadduwa town in Sri Lanka. They were washed well and sun dried for 3 days (Fig.2). Dried eggshell waste was grinded using kitchen grinder and then passed through 125µm ASTM sieve. About 4kg of Egg Shell Powder (ESP) was prepared. The peaty samples with smaller particle size were collected for tests because of the availability of larger surface area for fast and more effective chemical reactions. The type of cement used for this study was Ordinary Portland Cement (OPC) (SLS 107)

2.2 *Sample Preparation*

ESP was added to natural peat in varying percentages of 10%, 15%, 20% and 25% by dry weight of soil. Cement added at a constant percentage of 15% by dry soil weight. 5 types of samples were prepared with different amount of ESP and 15% cement by dry weight of soil.

Sample 01 - Natural Peat
Sample 02 - Soil + 15% Cement + 10% ESP
Sample 03 - Soil + 15% Cement + 15% ESP
Sample 04 - Soil + 15% Cement + 20% ESP
Sample 05 - Soil + 15% Cement + 25% ESP

2.3 *Experimental Procedure*

Moisture content (ASTM D 2216-10), organic content (ASTM D 2974) and Atterberg limit (BS 1377: Part 2) tests were carried out on natural peat without adding anything to find out the initial properties of peat. Specific gravity (ASTM D 854-00) test was conducted for all the 5 types of samples using pycnometer (density bottle) method.

Standard proctor compaction test (ASTM D 698) was carried out to obtain the Optimum Moisture Content (OMC) and Maximum Dry Density (MDD) of each type of sample. Dry density verses moisture content graphs were plotted for each sample. From the maximum point of the compaction curve, the MDD and the OMC were obtained for each type of sample.

Direct Shear test (BS 1377: 1990 part 7) was carried out to obtain the shear strength parameters (c and ϕ) of natural peat and treated peat samples. For this test, a direct shear box 60 mm x 60 mm in size was used. The samples were prepared using the standard proctor compaction mould at OMC obtained from the standard compaction test and compacted in 3 layers by giving 25 blows per each layer. The normal stresses applied were 27.25kPa, 54.5kPa and 81.75kPa respectively.

Modified proctor compaction test (ASTM 1557) was carried out only for natural peat and for 15% cement + 20% ESP mixed sample because it was the sample with optimum values for standard proctor compaction test and for direct shear test. A mould with a volume of 943.35cm^3 was used and each sample was compacted in 5 layers by applying 25 blows per layer using a 4.6kg rammer at a dropping height of 460mm. MDD and OMC content of both samples were obtained from the com-

paction curves plotted for modified proctor compaction.

California bearing ratio (CBR) test (ASTM D 1883-87) was conducted to check the suitability of peat sample as an embankment material. Natural peat sample and peat+15% cement+20% ESP mixed sample were used to determine the CBR values. The test was 4 days soaked CBR. The remoulded specimens were prepared at OMC and MDD obtained from modified proctor compaction test. The soil was compacted in 5 layers by applying 56 blows per each layer using 4.6kg rammer. It was then tested under compression with a penetration metal plunger. The graph of stress verses penetration was plotted for both samples. Then, CBR value for 2.5mm and 5.0mm penetration were determined for both untreated and 15% cement with 20% ESP mixed samples.

3 RESULTS AND DISCUSSION

3.1 *Initial Properties*

The general properties of the peat soil were determined as follows (Table 1). According to these results, the soil sample used was identified as a peat sample.

Table 1. General properties

Properties	Values
Soil classification (USCS)	Peat
Specific gravity	1.96
Moisture content	135%
Organic content	25.19%
Atterberg limit	Non-plastic

3.2 Specific Gravity Test Results

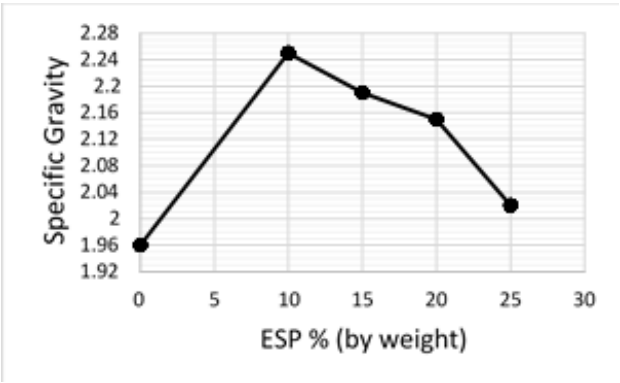

Fig 3 – Specific gravity vs ESP % from all samples

Figure 3 illustrates the variation of specific gravity all the samples with increasing ESP percentage by weight. Specific gravity decreases for treated soil samples when the ESP percentage increases. However, all the treated samples obtained increased specific gravity value more than that of the untreated sample.

The reason for the low specific gravity could be due to the presence of a larger number of hollow spherical particles from which the entrapped air cannot be removed (Pandian, 2004). These hollow spherical particles can be flocs created due to the chemical reaction between cement and ESP. Hence, when the ESP percentage of peat samples increases with 15% cement by weight, consequently floc particles increase and then specific gravity found to be decreased.

3.3 *Compaction Test Results*

The variation of MDD and OMC of all the samples are presented in following fig 04.

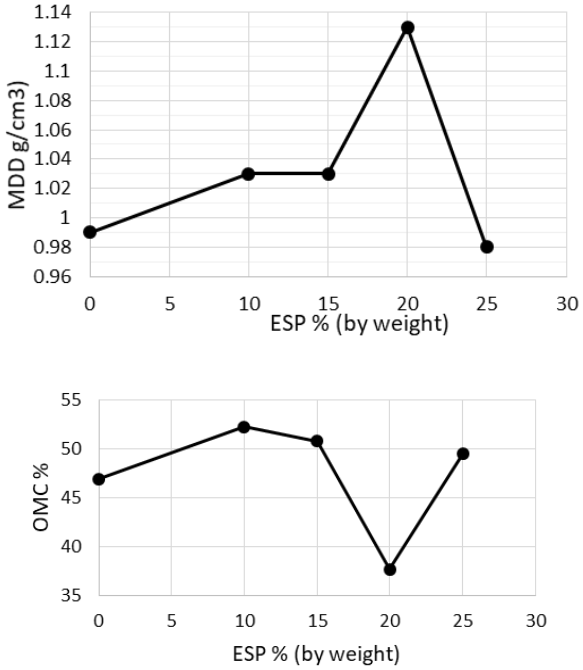

Fig 4 - MDD vs ESP% and OMC vs ESP% graphs for all the samples

The MDD increased and OMC decreased with increasing ESP content up to 20% ESP percentage by weight but at 25% ESP content MDD decreased and OMC increased to the nearest values obtained for untreated peat. 65% peat+20% ESP+15% cement gives the peak value for MDD and dip value for OMC. The MDD could have been increased due to the flocculation of particles as the flocs roll over easily on their own during the compaction process, the particles come closer and voids were reduced (Venuja et al., 2017). At the MDD point, water starts to fill the voids between the particles to prevent the closer packing of the particles. Amount of water needed for this activity was decreased result in reducing OMC of the samples up to 20% of ESP by weight. At that ESP and cement percentage, the MDD of untreated soil increased by about 14% and OMC decreased by about 20 %.

However, MDD decreases when ESP content was increased beyond 20% as a result of large water absorption by un-reacted ESP in the peat-cement-ESP mix. Egg shells were used in powder form so that it had large surface area to contact with water. Therefore, higher moisture content was needed to achieve MDD of the sample result in increased OMC. This result indicates that the addition of cement and ESP had significant effect on compaction properties.

3.4 *Direct Shear Test Results*

The figure 5 indicates that peat + 15% cement+10% ESP and peat+15% cement+15% ESP had obtained lowest shear strengths corresponding to all the normal stresses comparing with untreated peat specimen. But addition of 25% ESP with 15% cement by weight had reached the maximum shear strength 105.5 kPa with the cohesion 28kPa.

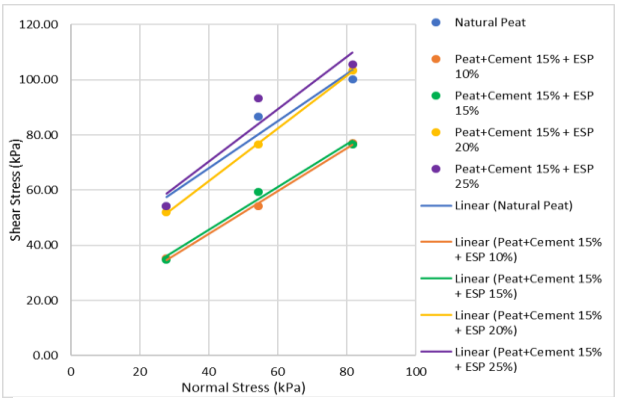

Fig 5 - Direct shear box test result for treated and untreated peat with different normal stresses

The shear strength properties of peat had increased in the range of 20% - 25% of ESP percentage with 15% of cement result in maximum angle of internal friction 43^0.

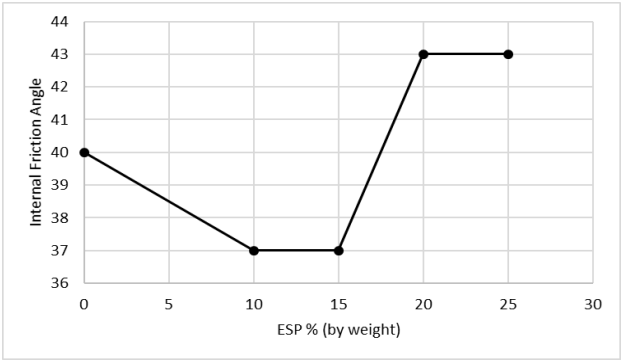

Both cement and egg shells consist of Ca^{2+}. Therefore, their chemical reaction with soil depends on the presence of water and percent of the amount of stabilizer agent (Zembri et al. 2017). The addition of ESP makes strong bond between the soil particles as it consists of Ca^{2+} and thus the soil texture attain change.

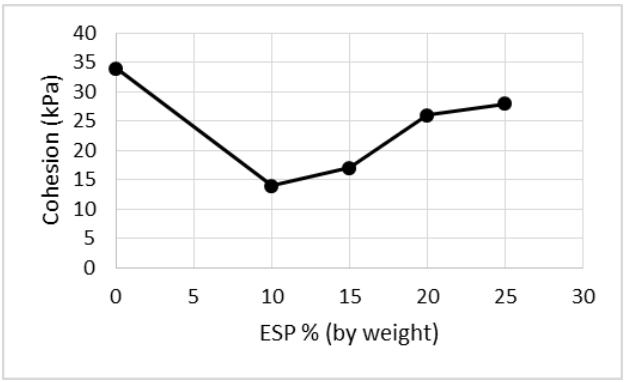

Fig 6 - Angle of internal friction vs ESP% for untreated and treated peat

The main compounds of cement which contribute for strength gaining are Tricalcium silicate ($3CaO.SiO_2$) and Dicalcium silicate ($2CaO.SiO_2$) react with water and produce Calcium Hydroxide (eq 1 & eq2).

$$2(3CaO.SiO_2) + 11H_2O \rightarrow 3CaO.2SiO_2.8H_2O + 3Ca(OH)_2 \quad (1)$$

$$2(2CaO.SiO_2) + 9H_2O \rightarrow 3CaO.2SiO_2.8H_2O + 3Ca(OH)_2 \quad (2)$$

$$Ca(OH)_2 + CO_2 \rightarrow CaCO_3 + H_2O \quad (3)$$

Fig 7 - Cohesion vs ESP% for untreated and treated peat

Peat soil is enriched with Carbon Dioxide (CO_2) and thus when peat is mixed with cement and water CO_2 react with $Ca(OH)_2$ produced. Therefore, $CaCO_3$ is supposed to produce from that reaction (eq3). (Moayedi 2013). The dominating compound of egg shell is $CaCO_3$. Adding egg shell powder for this peat cement mixture would result

in higher calcium carbonate percentage. Hence, this is one of the reasons that the shear strength of the peat samples mixed with cement and ESP was improved.

3.5 *CBR test results*

Table 2 - CBR values of the soil samples

	2.5 mm Penetration	**5.0 mm Penetration**
Untreated peat	3.3%	4.0%
Peat + 15% Cement + 20% ESP	12.0%	14.8%

According to the above table, the CBR value of 65% peat+15% cement+20% ESP sample shows 3.7 times and 3.6 times improved CBR values for 5.0 mm and 2.5mm penetrations respectively than that of the untreated peat sample.

The considerable increase in CBR may be due to the binding action of high percentage of cement and ESP on peat. Therefore, with the increase of MDD, the voids between the soil particles had been reduced result in increased CBR value. Also, with the increase of $CaCO_3$ the strength of the peat sample might have been increased. The inter particle bond had been increased at 15% cement and 20% ESP treated soil.

4 CONCLUSION

This research was carried out as an experimental study to investigate about the properties of peat soil by mixing 15% of cement (by dry soil weight) with 10%, 15%, 20% and 25% of ESP (by dry soil weight). From the study, the proposed sample is 20% ESP (by weight), 15% cement (by weight) with balanced 65% peat because it gained the optimum enriched properties of peat soil. The following conclusions could be drawn from the outcome of this study.

- With addition of constant 15% cement and increasing ESP percentage for balanced percentage of peat, the MDD obtained a considerable increase up to 20% ESP (by weight) and then it was decreased at 25% ESP (by weight). Also, the 65% peat + 15% cement + 20% ESP mixed sample obtained the lowest OMC than natural peat and other additives mixed peat samples.
- The specific gravity of treated peat samples decreasing with the increase of ESP percentage with 15% of cement by weight. Nevertheless, the specific gravity of all the treated samples had been improved more than that of the natural peat sample.
- When ESP percentage ranging from 20% to 25% with 15% cement and balanced 60% to 65% peat, the highest angle of internal friction could be reached and the maximum value was 43^0.
- ESP with cement treated peat samples behaved as non-plastic material according to the Atterberg limit test results.
- CBR values increased for 65% peat + 15% cement + 20% ESP mixed sample compared with untreated natural peat soil.

5 ABBREVIATIONS

ASTM – American Society for Testing and Materials
BS – British standards
Cα –Coefficient of secondary consolidation
CIDA - Construction Industry Development Authority
ESP – Egg Shell Powder
MDD – Maximum Dry Density
OMC – Optimum Moisture Content
RDA – Road Development Authority
SLS – Sri Lankan Standards
UCS – Unconfined Compression Strength
W/C – Water/ Cement ratio

REFERENCES

Afolayan & Olaniyi D. 2017, 'Evaluation of the Effect of Lime and Cement on the Engineering Properties of Selected Soil in a University in Southwestern Nigeria', *Journal of Advancement in Engineering and Technology* Vol. 5, viewed 12 June 2018

Afrin H., 2017, 'A Review on Different Types Soil Stabilization Techniques', *International Journal of Transportation Engineering and Technology* Vol. 3, No. 2, 2017, pp. 19-24., viewed 26 June 2018

Amu O.O., Fajobi A.B., & Oke B.O., 2005, 'Effect of egg shell powder on the Stabilizing potential of lime on an expansive clay soil', *Journal of Applied Sciences,* viewed 30 September 2018

Barazesh A., Saba H., Gharib M. & Rad M.Y., 2012, 'Laboratory Investigation of the Effect of Eggshell powder on Plasticity Index in Clay and Expansive Soils', *European Journal of Experimental Biology* 2012, 2 (6):2378-2384, viewed 15 June 2018

Boobathiraja S., Balamurugan P., Dhansheer M. & Adhikari A., 2014, 'Study on Strength of Peat Soil Stabilised with Cement and Other Pozzolanic Materials', *International Journal of Civil Engineering Research* Vol. 5 Number 4 (2014), pp. 431-438, viewed 27 September 2018

Bujang B.K.H. & Kalantari B., 2008, 'Peat Soil Stabilization, using Ordinary Portland Cement, Polypropylene Fibers, and Air Curing Technique', *EJGE* Vol. 13, viewed 27 September 2018

Kulathilaka S.A.S. & Saputhanthri D.R., 2012, 'Enhancement of engineering characteristics of peaty clay due to mixing with cement', *University of Moratuwa publications*, viewed 27 September 2018

Moayedi H., Kazemian S. & Huat B.B.K., 2013, 'Shear strength parameters of improved peat by chemical stabilizer', *Geotech Geol Eng*, viewed 10th February 2019

Pandian, N. S., 2004. Fly Ash Characterization with Reference to Geotechnical Applications.

Journal of Indian Institute of Science, 84(6), pp.189-216.

Saji G. & Mathew N., 2016, 'Improvement of Clayey Soil by Using Egg Shell Powder and Quarry Dust', *IOSR Journal of Mechanical and Civil Engineering*, viewed 28 September 2018

Standard Specification for Construction and Maintenance of road and bridges, CIDA 2nd edi. 2009.

Sherwood, P., 1993, 'Soil stabilization with cement and lime', *State of the Art Review*. London:

Transport Research Laboratory, HMSO.

Suriya P.A., Subathra P., Gopiprasath P. & Lakshminarayana V., 2017, 'Stabilization of soft soil using stone column – the review', *Journal of Industrial Pollution Control* 33(s2)(2017) pp 1214-1217, viewed 10 June 2018

Susanti R.D., Maulana & Waruwu A., 2017, 'Bearing capacity improvement of peat soil by preloading', *ARPN Journal of Engineering and Applied Sciences* Vol. 12, viewed 10 June 2018_

Tocan A.G.J., 1999, 'Utilization of chick hatchery waste; the nutritional characteristics of day-old chick and egg shells' *Agric wastes,* 4:335-343

Venuja S, Mathiluxsan S. & Nasvi M.C.M., 2017, 'Geotechnical Engineering Properties of Peat, Stabilized with a Combination of Fly Ash and Well Graded Sand', *ENGINEER* Vol. L, No. 02, pp. [21-27], viewed on 10 June 2018

Zambri N.M. & Ghazaly Z.M., 2017, 'Peat Soil Stabilization using Lime and Cement',

CENVIRON Vol. 34, viewed on 28 September 2018

A review of the empirical correlations of peaty and organic soil in Sri Lanka

K. V. D. Vidurapriya
Sri Lanka Institute of Information Technology, Malabe.
Y. Wang
China MCC20 Group Corp. Ltd.
H. S. Thilakasiri
Sri Lanka Institute of Information Technology, Malabe.
S. Zhu
China MCC20 Group Corp. Ltd.

ABSTRACT: Increase in population and high land use rate has resulted in depletion of favourable construction grounds. Hence, treated soft grounds that consist of organic soil has been used for recent infrastructure development projects. To ensure the constructability and long-term performance of structures built on these grounds, it is vital to determine the engineering properties of organic soil. However, to determine these properties, undisturbed soil samples need to be extracted. Due to several reasons extracting an undisturbed organic soil sample is highly costly and difficult. Therefore, empirical correlations can be developed to determine these engineering properties using index soil parameters. Generally, most of these correlations behave differently based on their morphology. In the current paper, recently proposed correlations for Sri Lankan organic soils were reviewed by considering them under two deposits. Significant differences between some correlations were observed and the reasons were discussed successfully.

1 INTRODUCTION

1.1 *Importance of the study*

Expanse of bare land available for construction is depleting rapidly, due to the high land use rates, increase in population and implementation of new development projects. As a result, most of the new infrastructure development projects are proposed to be built on soft grounds consisting of deep layers of organic soils. Organic soils pose a serious challenge for construction than mineral soils. Therefore, it is important to determine the engineering properties of peat to ensure constructability and long-term performance of proposed structures. Strength, Compressibility and Permeability parameters can be considered as the most important properties of organic soils.

It is crucial to extract undisturbed soil samples to determine these properties. However, recovering an undisturbed sample is considerably costly and difficult due to several reasons such as low shear strength of peat, cutting resistance of fibrous materials and difficulty of moving heavy machinery over weak grounds. Upon extraction samples get exposed to comparatively high levels of oxygen and heat, this may increase the biochemical degradation of peat. Hence, tedious and expensive measures need to be taken to preserve the extracted peat samples. Correlations between engineering properties and index soil parameters of organic soils can be successfully applied to curtail these problems.

However, these correlations highly depend on the morphology of organic soil. Comprising plant type and proportion of mineral materials influence the amount of organic content in the soil. Furthermore, humification which is governed by the climate of the accumulating region affects the water content of the soil. Therefore, it is understood that the morphology of organic soil is sensitive to ecology and climate. Hence, unique correlations between properties of peat must be derived for different regions. Correlations for Sri Lankan organic soils were proposed by several research studies. In section 2, these studies are reviewed and compared with well-established correlations.

1.2 *Peat formation*

Peat is greyish black to black and formed by partial decomposition of organic matter under wet and acidic conditions. Coarse fibrous peat, fine fibrous peat and amorphous peat can be identified as the three main types of peat. The secondary compression of peat is generally more prominent than primary consolidation when compared to mineral soils.

In Sri Lanka, peat deposits can be identified in the western and southern provinces especially along coastal areas where the annual rainfall ranges from 1500mm to 3000mm. These lands are situ-

ated in the flood valleys of Maha Oya, Kelani River, Kalu River, Bentota River, Gin River and Nilvala River etc. Therefore, water collected in these regions are well-nourished by inorganic sediments from rivers and slightly acidic due to poor drainage. These conditions provide favourable surroundings for peat accumulation in western and southern provinces in Sri Lanka.

1.3 *Introduction to investigation locations*

The expressway network, which connects Western, Southern and Central provinces is one of the major development projects in Sri Lanka. As shown in Fig. 1, the Southern Expressway, Outer Circular Highway and Colombo – Katunayake Expressway runs through low-lying grounds of Western and Southern provinces. Ground investigation results along these expressways were used for the studies considered in this paper. Table 1 contains the considered studies and their respective areas of concern.

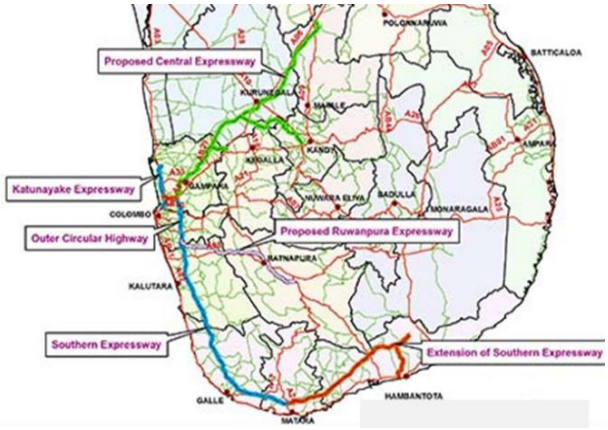

Fig. 1 Expressway network in Sri Lanka

Table 1. Research papers and respective areas concerned

Research Paper	Area
Karunawardena (2007)	Colombo
Ariyarathne (2010)	Along STDP[1]
Thavasuthan (2011)	Along STDP
Hsi et al (2015)	Along CKE[2]

[1]Southern Transport Development Project,[2]Colombo – Katunayake Expressway

As explained in section 1.2, the peat deposits in Sri Lanka are mostly located in the low-lying flood valleys of major rivers in Western and Southern provinces. Therefore, Colombo soft soil deposits were considered to be located in the flood valley of Kelani river and peat deposit in Kalu, Bentota and Nilvala rivers were consider as southern organic soil deposits. Results from Thavasuthan (2011) and Ariyarathne et al (2010) were combined to derive correlations for southern deposits whereas correlations from Karunawardena (2007) were used for Colombo deposits. Hsi et al (2015) presented average soil parameters from soil investigations along CKE project that were conducted before 2003 and during 2003. Out of which the average soil parameters presented for peat and organic soils were considered in the current paper.

2 CORRELATIONS FOR SRI LANKAN ORGANIC SOIL

2.1 *Correlation between index properties of organic soil*

The properties used to classify and identify different soils are known as the index properties of soil. Natural water content (w_0), initial void ratio (e_0), Atterberg limits and organic content (OC) can be considered as the most important index properties of organic soils. Figs. 2 and 4 illustrate the relationships derived between e_0 vs OC and w_0 vs OC for Sri Lankan peaty soils.

These relationships were not presented in the studies mentioned in Table 1 but were derived for the convenience of explaining the behaviour of the correlations proposed later in the current study. Since the data available from Karunawardena (2007) was not enough to derive the correlations in Figs. 2 and 4, data from Outer Circular Highway (OCH) project were used to derive correlations corresponding to Colombo deposits in section 2.1.

When the regression for e_0 vs OC for the two deposits was plotted in the same graph, it was noticed that they yield different relationships. Correlation for Colombo deposit $e_0 = 0.1137OC + 1.34$ falls above the Southern deposit $e_0 = 0.0954OC + 0.17$. The average values of OC and e_0 given by Hsi et al (2015) were introduced to the established correlations as demonstrated in Fig.3. However, it was noticed that these values do not agree with the established correlations. Furthermore, the correlation for Florida organic soil derived by Gunaratne et al (1998) plots closer to the Sri Lankan correlations as shown in Fig. 3.

According to these relationships, e_0 of organic soils increases with the increase in OC. However, for a considered OC, Colombo peat has a higher e_0 than Southern peat. It is further observed that the difference between the two regression lines increases with OC. The e_0 for Colombo peat deposits are higher than Southern peat deposits at OC 0% and 100%. Therefore, it can be suggested that Colombo organic soils are comparatively porous than Southern organic soil. Southern peat deposits might have a higher degree of decomposition than Colombo peat resulting in a less porous structure. However, this can only be validated by conducting a successful investigation on the microstructure of peat in both deposits. Moreover, void spaces pre-

sent inside the mineral portion of an organic soil also contributes towards the overall initial void ratio. This can be suggested as a reason for the excessive scatter observed in Fig. 2.

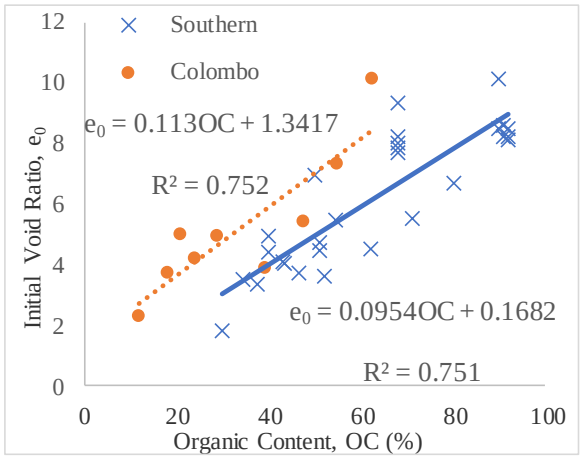

Fig. 2 Correlation between initial void ratio and organic content

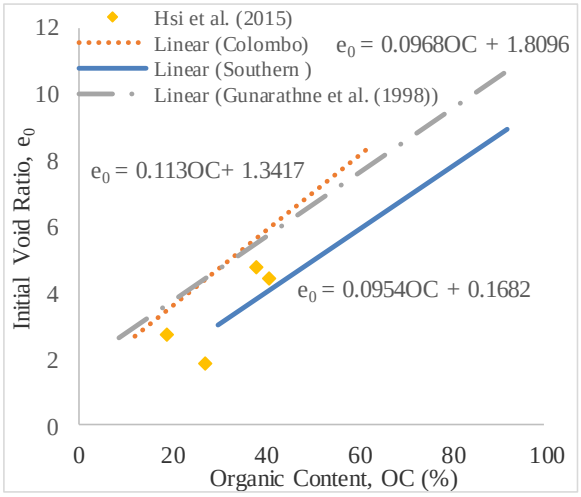

Fig. 3 Comparison of established correlations for initial void ratio vs organic content

The correlations in Fig. 4 suggest that w_0 of organic soil is directly proportional to its OC. However, the data points are considerably dispersed around the plot area. Hobbs (1986) mentioned that the relationship between OC and w_0 is relatively complex as the w_0 of an organic soil mostly depends on the water-retaining ability of the comprised organic matter. Furthermore, the water-retaining ability of organic soil is affected by the degree of decomposition of organic matter. Hence, plots of w_0 against OC display excessive scatter unless the considered samples are in a small range of decomposition. It was noticed that the w_0 of Colombo peat is higher than Southern deposits for a given OC. Which can be partially explained by the fact that the Colombo peat has more voids than Southern peat for the same amount of OC. However, the degree of decomposition of peat might also influence this variation. According to Fig. 5, correlation suggested by Gunaratne et al (1998) plots between the two regressions for Sri Lankan peaty soils. The average soil parameters proposed by Hsi et al (2015) displayed some scatter (Fig. 5) from the regression line derived for the Colombo peat.

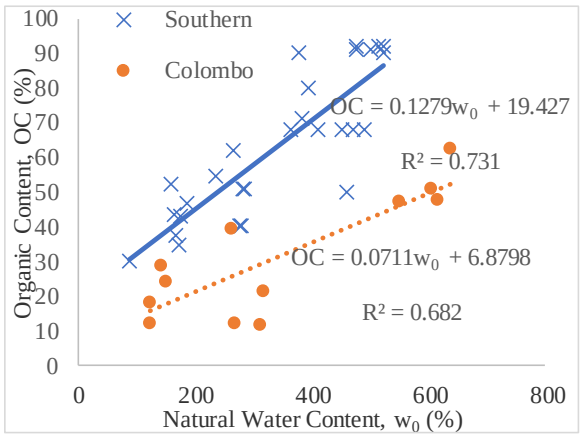

Fig. 4 Correlation between organic content and natural water content

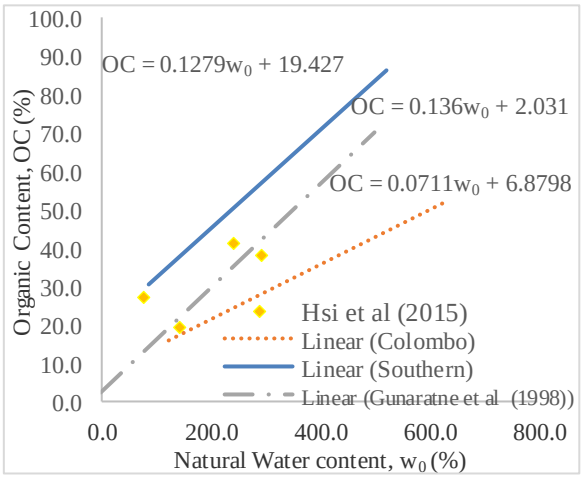

Fig. 5 Comparison between established correlations for organic content vs natural water content

2.2 *Correlation between compression index (C_c) and initial void ratio (e_0)*

Fig. 6 illustrates the linear regression between C_c and e_0 for Southern deposits and Colombo deposits. Hobbs (1986) presented the correlation between C_c and e_0 for UK peat as $C_c = 0.45e_0$, which is closer to both relationships obtained for Sri Lankan conditions. It is also observed that for a given e_0, the C_c of Southern deposits is higher than Colombo deposits. According to the relationship between e_0 and OC given in Fig.2, for a given e_o, higher OC was reported for the Southern deposits.

Rashid and Brown (1975) stated that the compressibility of organic soil increases with the increase in OC. Therefore, for a certain e_0, C_c is higher for Southern peat deposits. Hence, the regression line of C_c vs e_o plots above the regression line for Colombo soil. Evidenced by high values of coefficient of determination (R^2) and the lesser scatter of points, the correlation between e_0 and C_c is comparatively strong. Since the correlation for Colombo peat deposit was based on a limited number of data, it is suggested to verify the above-discussed variation by including more data. The average values of the soil parameters reported in Hsi et al (2015) displayed considerable scatter from the respective correlation for Colombo peat deposits. Relatively low C_c can be considered as the reason for this excessive scatter.

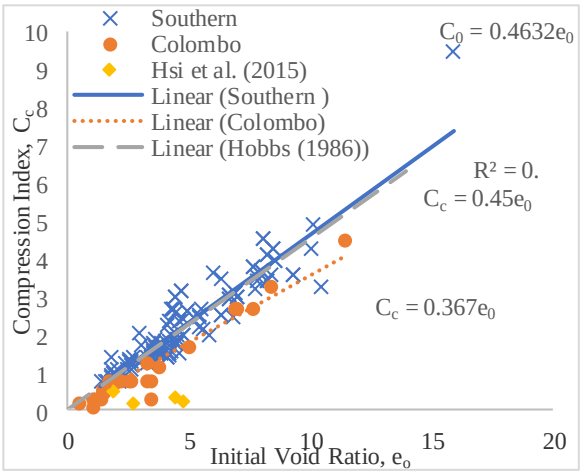

Fig. 6 Correlation between compression index and initial void ratio

2.3 *Correlation between compression index (C_c) and natural water content (w_0)*

When C_c was plotted against w_0 for organic soils, two different linear regressions were produced for Colombo and Southern peat. The correlation for Southern deposit is $C_c = 0.0081w_0$ while for Colombo it is $C_c = 0.007w_0$. According to Hobbs (1986), the correlations for UK bog and fen peat are $C_c = 0.008w_0$ and $C_c = 0.0065w_0$ respectively. Furthermore, Mesri and Ajlouni (2007) proposed $C_c = 0.01w_0$ for fibrous peats. It was observed in Fig. 7, that the regression line for the Southern peat was overlying the regression line for Colombo peat. According to Fig.4, Southern peat contains more OC for a considered w_0 than Colombo peat, evidencing that the Southern peat is more compressive for the same w_0 than Colombo peat. Following the same observation, the data obtained from Hsi et al (2015) shows a considerable amount of dispersion from the established correlations.

Mesri et al (1997) presented the difference between the distribution of peaty soil and clay soils in a C_c vs w_0 graph as represented in Fig. 8. When the data obtained from literature is introduced to this graph, it falls in between peats and clay and silt deposits. Generally, the OC of peat deposits in Sri Lanka is at the lower ranges compared to peat deposits in other countries. Hence, the above behaviour can be expected.

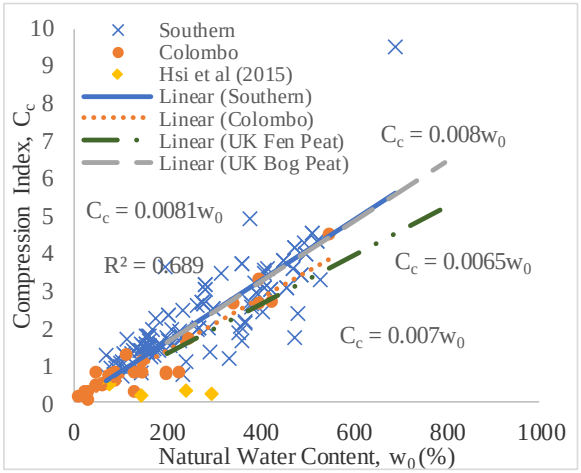

Fig. 7 Correlation between compression index and natural moisture content

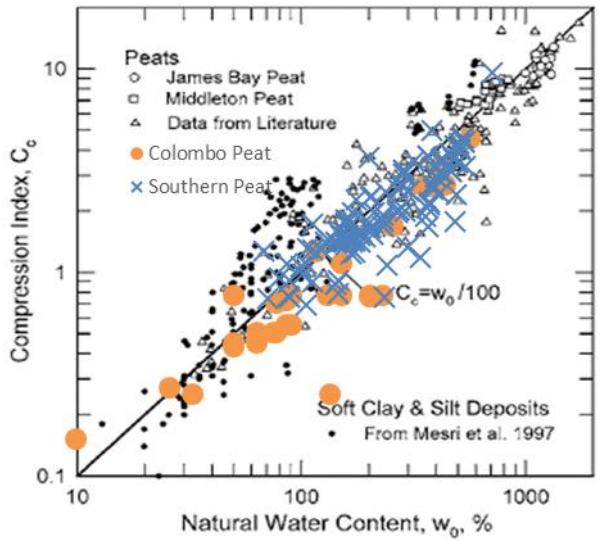

Fig. 8 Plot between compression index and natural water content

2.4 *Correlation between compression index (C_c) and organic content (OC)*

The correlations between Cc and OC proposed for Sri Lankan peat are given in Fig. 9. It is observed that Cc for organic soils increases with the increase in OC, evidencing the statement by Rashid and Brown (1975). However, the relationship developed for Colombo peat plots above Southern peat, showing that Colombo Peat is relatively compressive for a given OC. Since e_0 depicts the variation in compression for a given OC, the relation be-

tween e_0 and OC of Sri Lankan organic soil discussed in section 2.1 is considered here. It is observed that for a certain OC the e_0 is greater for Colombo organic soil and hence, more compressive. However, it is observed that the data points in Fig.9 are dispersed around the regression line, resulting in lower coefficients of determinations. These relationships are derived based on only a limited number of data. Hence, attempts should be taken to improve the correlation by including more data points. The average soil parameters obtained from Hsi et al (2015) falls below the regression line developed for Colombo peat.

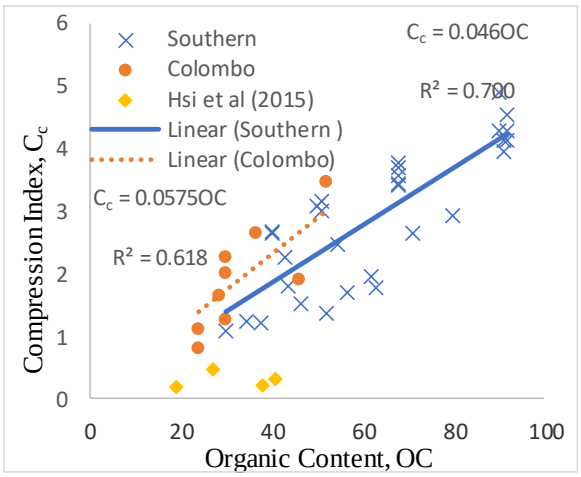

Fig. 9 Correlation between compression index and organic content

2.5 *Correlation between compression index (C_c) and secondary compression index (C_α)*

Secondary compression is more substantial for organic soil than mineral soil. Mesri et al (1997) identified high water contents and void ratios, high C_α/C_c value and lesser duration of primary consolidation as the three major reasons for the observed significance in secondary consolidation. Fig. 10 illustrates the correlations derived for Sri Lankan organic soil deposits. Even though the correlations considered in above sections displayed considerable variation between Colombo and Southern deposits, the observed difference between this correlation is comparatively low. The correlation for Colombo peat and Southern peat are C_α/C_c = 0.0341 and C_α/C_c = 0.0331 respectively. Mesri and Ajlouni (2007) reported that for Middleton peat C_α/C_c = 0.053 and for James Bay peat C_α/C_c = 0.06. Additionally, the $C_c/(1+e_0)$ value range for Colombo peat deposits and Southern peat deposits are 0.1 – 0.36 and 0.56 -0.23 respectively.

According to Mesri et al. (1997), C_α/C_c is in the range of 0.06 ± 0.01 for peat and depends on deformability (including compressibility) of organic particles. Therefore, it is logical to assume that the Sri Lankan organic soil deposits consist of less deformable particles.

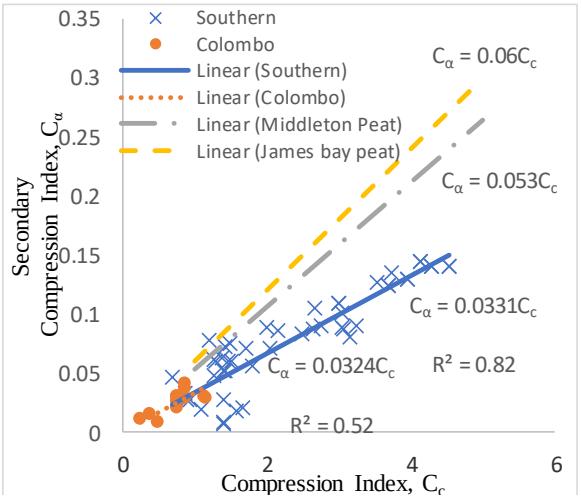

Fig. 10 Correlation between secondary compression index and compression index

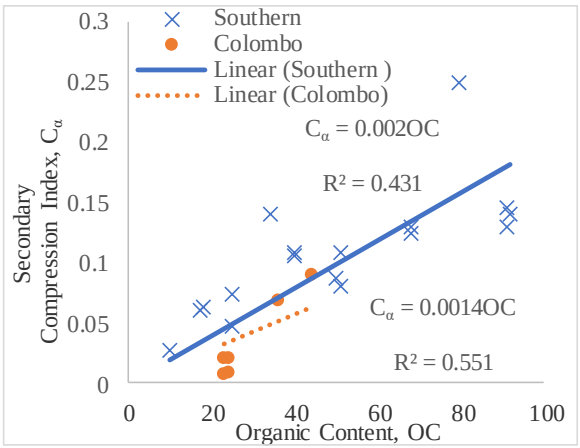

Fig. 11 Correlation between secondary compression index and organic content

Though the variation between the two correlations are lower than other relationships, the Colombo peat has a slightly higher secondary compression. When considering Fig. 11, it is evident that C_α for peat increases with increasing OC. For a given C_α, OC is higher for Colombo peat. Hence, the slight increase in C_α/C_c values for Colombo can be justified. However, the correlations in Fig. 11 are not strong relationships as most data points are dispersed away from the regression line. Difference in deformability of organic particles can be considered as the main reason. Therefore, it is suggested to consider the microstructure of the respective peat deposits before concluding. Furthermore, both the relationships in section 2.5 were derived base on a limited number of data points. Hence, it is suggested to improve these relationships by verifying with more data.

2.6 *Correlation between recompression index (C_r) and compression index (C_c)*

According to Fig. 12 which contains the correlations developed between C_c and C_r, for Colombo deposits $C_r = 0.1015C_c$ and $C_r = 0.1009C_c$ for Southern deposits.

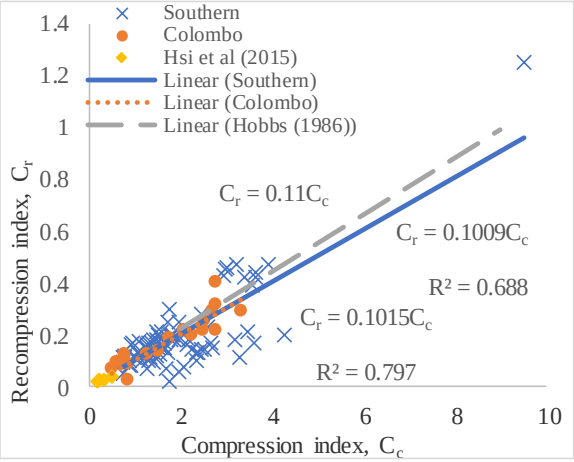

Fig. 12 Correlation between compression index and recompression index

When considering the two regression lines it was noticed that they produce approximately equivalent correlations. Hobbs (1986) mentioned that C_c and C_r are fairly dependent on the method of testing. And rather independent of morphology. The relationships derived for Southern and Colombo deposits agrees well with this statement. Hobbs (1986) further stated that C_r is about 10% of C_c within a range of 5% to 20%, very similar to clay soils and proposed that $C_r = 0.11C_c$ for several UK peat deposits. However, the observed relationship for Sri Lankan peat deposits is $C_r = 0.10C_c$. Generally low organic contents of Sri Lankan peat and excessive scatter in the graph can be considered as the reasons towards the difference between equations suggested by Hobbs (1986) and Sri Lankan correlation. Therefore, these correlations should be validated by the inclusion of more data. Further, it was noticed that the data points plotted by including the Hsi et al (2015) data, falls in very low-value ranges

3 CONCLUSION

Correlations between properties of Sri Lankan organic soils proposed by recent research were successfully reviewed. Data obtained from these studies were separated into two deposits based on their morphology. Noteworthy variations were observed between some correlations proposed for Southern and Colombo deposits and the reasons were briefly discussed. Correlations e_0 vs OC, w_0 vs OC, C_c vs e_0, C_c vs w_0, C_c vs OC and C_α vs OC are the relationships which demonstrated variation depending on the morphology. However, correlations C_r vs C_c and C_α vs C_c did not reveal any contrast based on morphology. An attempt was taken to include the average soil parameters proposed by Hsi et al (2015) into the developed relationships. Nevertheless, these average properties do not agree with the established correlations. Most of these correlations were derived based on a limited number of data and should be further verified by the addition of more data. Attempts must be taken to study the micro-structure of Sri Lankan peats since it helps in understanding the properties and behaviour of peat

REFERENCES

Ariyarathna, P. R. C., Thilakasiri, H. S., Karunawardane, W. A. 2010 Vacuum consolidation of Sri Lankan peaty soils, Proceedings of Annual sessions of Institution of Engineers- 2010, Institution of Engineers, Colombo, pp 27 – 38.

Gunaratne, M., Stinnette, P., Mullins, A. G., Kuo, C., Echelberger, W. F., Jr., (1998)., Compressibility Relations for Peat and Organic Soil, Journal of Testing and Evaluation, 26:01-09

Hsi, J., Gunasekara, C., Nguyen, V. (2015). "Characteristics of soft peat, organic soils and clay, Colombo-Katunayake Expressway, Sri Lanka", *Ground improvement Case Histories*, Indrarathne B. and Chu J., Elsevier Geo-Engineering Book series, Vol. 03., 681-722.

Hobbs, N. B., (1986), Mire Morphology and the Properties and Behaviour of Some British and Foreign Peats, Quarterly Journal of Engineering Geology and Hydrogeology, 19:07-80

Karunawardane, A. W. (2007). "Consolidation Analysis of Sri Lankan Peaty Clay using Elasto-viscoplastic Theory", *Doctoral dissertation*, Kyoto University.

Mesri, G., Ajlouni, M., (2007)., Engineering Properties of Fibrous Peat, Journal of Geotechnical and Geoenvironmental Engineering, 133:850-866

Mesri, G., Stark, T. D., Ajlouni, M. A., Chen, C. S., (1997)., Secondary Compression of Peat with or Without Surcharging, Journal of Geotechnical and Geoenvironmental Engineering, 123: 411-421

Rashid, M. A., Brown, J. D., (1975), Influence of Marine Organic Compounds on the Engineering Properties a Remolded Sediment, Engineering Geology, 9:141-154

Thavasuthan, T. and Thilakasiri, H. S., (2011)., Empirical Correlations for Sri Lankan Peaty Soils, Geotechnical Journal, Sri Lankan Geotechnical Society, 5:27-33

Behavior of ball bouncing and pace on laboratory cricket pitch models made of local soils in Sri Lanka

S. Perera
Department of Civil and Construction Engineering, Swinburne University of Technology, Australia

U. P. Nawagamuwa
Department of Civil Engineering, University of Moratuwa, Sri Lanka

ABSTRACT: Cricket is a complex sport where indirect factors, such as weather and pitch settings, influence significantly on the playing conditions of a particular game. Three locally available clayey soils in Sri Lanka, from Murunkan (MU), Kotawehera (KO) and Tyronne Fernando Stadium in Moratuwa (TY) were selected from previous studies to continue the laboratory model tests of a cricket pitch. Coefficient of restitution (e) of the impact between the ball and the laboratory models with different surface grass conditions were determined by bounce tests. Variation of e values of six laboratory models were analyzed by changing the moisture contents and grass conditions and the pace ratings were evaluated for each model. TY was identified as a slow and low cricket pitch material while MU and KO were selected as the most suitable clays for the further proceedings of the development of fast and bouncy cricket pitches in Sri Lanka.

1 INTRODUCTION

Cricket is an exciting sport for both players as well as the spectators and its importance is no less than any sporting event. Cricket has conquered most parts of the world due to its inherited unpredictability. It seems like a fair battle between a wooden bat and a leather ball, nevertheless, the "Cricket Pitch" plays a major hidden role to ensure the day's winner (Perera et al., 2016).

Unlike many other out-door sports, the turf cricket pitch is not made from artificial, homogeneous material. Consequently, ball behavior is unique from one game to another. Pitches are usually categorized into two types according to their ball behavior, fast and bouncy pitches and slow and low spinning pitches (Nawagamuwa et al., 2009). Cricket playing countries usually construct tailor-made pitches, either fast and bouncy or slow and spinning, according to the strength of their home team.

In most cricket matches, visiting players find it difficult to play on conditions that they do not experience in their home soil. In the Sri Lankan (SL) context, most pitches are tailor-made to assist slow spin bowlers. Hence, SL batsmen lack exposure to quality fast bowling which offers extra pace and bounce in countries like Australia (AUS). This is even common for other cricket playing nations in the Indian sub-continent (Usman et al., 2016). Therefore, development of fast and bouncy pitches is a timely need for cricket playing nations in Asia.

1.1 *Governing factors of the ball behavior of cricket pitches*

McAuliffe and Gibbs (1997) collected objective measurements on the pace and bounce of first-class cricket pitches in New Zealand. A series of mini-trials had been conducted to study the effect of critical factors on speed reduction and bounce height. The results showed that ball age and presence or absence of grass had a significant effect on pace reduction, but less of an effect on bounce height.

Carré et al. (1999) studied the ball bounce and pace while varying the soil and grass types. They discovered that soil type and grass type directly affect the ball behavior. When comparing ball behavior and the soil properties in AUS and SL pitches, Nawagamuwa et al. (2009) identified the fundamental parameters that govern the pitch behavior are the clay content, clay mineralogy, silt content and the plasticity of clays, and Usman et al. (2016) too confirmed the same fact.

1.2 *Fast and Bouncy cricket pitches in Australia*

Western Australian Cricket Assosiation (WACA) cricket pitch in Perth, AUS is considered as the world's fastest cricket pitch. Other than WACA, Gabba in Brisbane is also known as moderately fast and bouncy pitches when compared to other pitches around the world (Usman et al., 2016). As shown in New Zealand Stadium Turf Institute Guide, fast pitches consist of a high clay content in their top clay dressing (McAuliffe and Gibbs, 1997).

1.3 *Laboratory soil tests for cricket pitch materials*

A locally available clayey soil, "Grumusol", in Murunkan, Sri Lanka (SL) was tested and reported by Sobana et al. (2014) as a soil with a clay content between 53% and 60%. Six locally available soil samples were tested for their geotechnical properties by Perera et al. (2016). Grumusol clay from Murunkan (MU), Mannar, SL and a soil from Kotawehera (KO), Nikaweratiya, SL were identified as clay rich soils with a high potential to be used in developing fast and bouncy cricket pitches in SL (Perera et al., 2016).

Moreover, Perera et al. (2017a) further tested MU and KO soils for the clay content and clay mineralogy. Higher clay contents were reported for MU (62%) and KO (64.5%) than TY (45.5%). Also, higher plasticity indexes were reported for MU (47%) and KO (34.7%) than TY (19.3%). X-Ray diffraction tests were carried out to find out the clay mineralogy and MU and KO were found to be smectite clays while TY was a kaolinite clay. According to the results, MU and KO were considered as the best qualified clay types to carry out further testing of friction and bounce.

1.4 *Bounce test*

The vertical rebound height of a ball dropped freely from a fixed height is the most common direct surface assessment, identified as the bounce test. High coefficient of restitution is an important characteristic of a bouncy cricket pitch.

Newtonian impact model developed by Carré (2000) allowed for no deformation of either the surface or the ball and calculated the ball rebound dynamics using a combination of both coefficient of friction (μ) and coefficient of restitution (e). This test well provides a measure of the kinetic energy loss during impact.

Baker et al. (1998) had completed bounce tests of this kind from a height of 3 m. This height relates to a vertical impact speed of 7.67 ms^{-1} which is equal to the mean vertical impact speed of a bowler delivery as measured by James et al. (2004). The e can be determined from Equation (1); the square root of the ratios, vertical rebound velocity (V_{out}) to vertical impact velocity (V_{in}) or the square root of the ratio of rebound height (h) to drop height (H) (James et al., 2005).

$$e = \sqrt{\frac{V_{out}}{V_{in}}} = \sqrt{\frac{h}{H}} \quad (1)$$

1.5 *Friction test*

In order to measure the μ between the cricket ball and pitch surface, friction tests were carried out by James et al. (2005) using a friction sledge system and reported an average μ value for England pitches as 0.35.

Senanayake et al. (2009) adopted the method of inclined surface to evaluate μ by sliding a steel plate on the surface of a compacted soil box at different angles of inclination. The μ value was measured for two soils (currently used soil for pitch preparation in SL, and the same soil mixed with bentonite to have ultimate clay content as 50%) at different moisture contents. Authors reported the least μ as 0.51 at a moisture content (MC) of 7.5%. However, this method is suitable to compare different μ values of different soils but the steel plate surface is different from the real surface of test cricket ball (TCB) in cricket.

Method of using the sledge system in James et al. (2005) was adopted by Perera et al. (2017b). In the study, μ was calculated between the new ball (without touching the seam) and compacted clay material of the laboratory model prepared by three local soils KO, MU and TY, varying the grass conditions continuously for 5 days without adding water to simulate the 5-day test match.

1.6 *Pace rating*

Challenger (1986) reported that during the 1984/85 and 1985/86 seasons, pitches in New Zealand had been assessed by the objective playability method. In this method, quality of a cricket pitch had been related to the ball behavior after the moment of impact.

Murphy (1985) found a significant relationship between pace rating and the subjective assessment of pitch pace as shown in Equation (2).

Pace rating = Ball bounce / Friction (2)

h is measured in cm from H = 4 m as the "Ball bounce" and "Friction" is μ. After testing all first class pitches in New Zealand in 1985, Challenger (1986) defined the pace rating (cm) scale as very slow, slow, easy and fast for the value ranges 0 - 50, 50 - 100, 100 - 300, > 300 respectively.

2 MATERIALS AND METHODS

MU, KO and conventional clay used in SL cricket pitch preparation (TY) were used to continue model tests along with two grass conditions, with surface grass (+GR) and without surface grass.

Nawagamuwa et al. (2009) suggested that top 100 mm-150 mm can be considered to be the most

crucial during a bounce test. 150 mm of clay layer thickness was used for the model tests assuming rigid boundary conditions at the bottom. Soil samples used in this study were compacted in rigid steel molds having internal dimensions of 150 mm ×150 mm ×150 mm.

In the process of constructing cricket pitches, rolling is essential after levelling the surface material. Usman et al. (2016) reported that a typical hand operated heavy roller weighs approximately 1014kg (1 ton, 10kN) and roller compaction was carried out by using different rollers in different stages of the pitch preparation for several days until the pitch was properly consolidated. Usually the rolling was done for 30-40 minutes per session and the process would be repeated until the pitch is able to generate the expected bounce level according to the rules of thumb by the curators. However, a standard duration of time for the rolling process could not be defined (Nawagamuwa et al., 2009).

Considering the total energy applied by a heavy roller for a period of 30 min along the whole length of a cricket pitch (22.56 m) for 10 times per day, the required energy is approximately equivalent to 2 min of 10 kN load application on the surface length of the laboratory model (Shipton, 2008).

2.1 *Procedure of preparing laboratory models*

The maximum dry density and the optimum MC content of MU, KO and TY were pre evaluated by standard Proctor compaction test according to ASTM D698. The required soil mass to achieve the maximum dry density was calculated for each soil and the molds were filled accordingly up to 40 mm layers.

Anthill clay layer of 50 mm was added as the base layer for all laboratory models and compacted to 30 mm by applying a 10 kN (445 kPa) load for 120 s. In local test venues, "*Poa pratensis*" (*Blue Grass*) is planted inside the anthill clay layer, which grows vertically through the above clay layer. The grass stems inside mid clay layer have the ability to hold the clay particles together without cracking during a 5-day test match (Shannon, 2010). The same grass was used in all samples to simulate the grass effect in international test pitches. Four grass plants were planted at each nodal point of a 25 mm ×25 mm grid drawn on the anthill clay layer and grass was fertilized with urea (Carbamide - $CO(NH_2)_2$) and special lawn fertilizer -no. 11 grass fertilizer (N - 12%, P_2O_5 - 9%, K_2O - 4%) according to the pitch preparation method explained by Shannon (2010).

All laboratory models were kept in natural environment after adding each layer of 40 mm of clay on top of the grass. The samples were fertilized for a week until a significant grass growth could be observed. When the height of the grass leaves reached about 50 mm, the 40 mm of uncompacted clay layers were compressed to 30 mm by applying 445 kPa for 120 s. Same procedure was repeated during the second and third layers of compaction.

However, the top grass leaves of the samples without surface grass were trimmed and removed after compacting the final layer. Appearance of the prepared samples before testing is shown in Fig. 1. The three samples of the top row of the Fig. 1 represents the samples without surface grass while the bottom row represents the samples with surface grass.

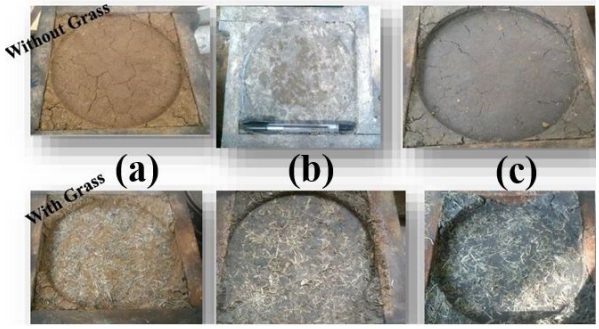

Fig. 1 Final appearance of the prepared six laboratory models; (a) KO, (b) TY and (c) MU

The surface crack density of MU and KO clay surfaces were higher than TY due to the high clay content in KO and MU as explained by Perera et al. (2017).

2.2 *Bounce test for laboratory models*

A compacted soil mold was kept horizontal on a rigid concrete surface in front of a clear white background with a vertical scale. A standard hockey ball (HB) was dropped from a 2 m height above the top clay surface of the model. High definition camera was set to record the motion of the ball and it was mounted on a tripod and placed at a 3.5 m distance away from the line of a vertical ball drop and care was taken to ensure that the camera filmed horizontally to minimize parallax effects. The ball at its peak h was clearly identified and measured by analyzing the high definition video output by the camera. This procedure was followed on each model for five consecutive days to mimic a 5-day test match. The corrections were made for the recorded h values to remove the effect from air drag and respective e values were calculated from Equation (1).

Same laboratory models were used for both friction tests (Perera et al., 2017b) and bounce tests. The μ and e values, calculated respectively, from friction and bounce tests were used to calculate the pace ratings of each laboratory model using Equation (2).

3 RESULTS AND DISCUSSION

3.1 *Comparison of e values*

Average h was calculated for 20 rebounds for a laboratory model, each day and average e values were calculated using Equation (1) for each average h value at H = 2 m and the variation of e values for five days is shown in Fig. 2.

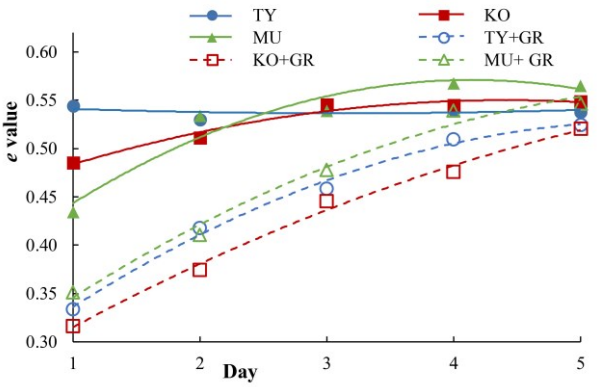

Fig. 2 Variation of e values with days

According to Fig. 2, TY sample starts with a high e value and approximately a flat trend line can be observed during the rest of the days, confirming that there is no increase in e value with time. In contrast, e values of two other samples without surface grass are significantly increased from day 1 to day 4, and nearly becomes a constant from day 4 onwards. Although both e value trend lines for MU and KO show positive gradients, MU shows a higher gradient than KO until day 4, which implies that, e value of MU increases more rapidly than KO with drying time.

Correlations between the pitch measurements, dynamic data and soil characteristics had been analyzed by Carré et al. (1999) and reported that a damp, soft pitch with a high organic matter content leads to a low rebound velocity with high top spin while dry, firm pitches with a low organic matter content leads to a high rebound velocity with low top spin. MU, KO and TY were tested for the soil properties by Perera et al. (2016) and found that MU and KO had less than 5% of organic matter while TY had more than 18% of organic matter. Low organic matter contents of MU and KO had resulted in high e values of their pitch models.

According to Fig. 2, +GR samples show a constant positive gradient in their e value trend lines over the five tested days. As explained by Shannon (2010), grass helps to reduce the moisture trapped inside the mid layers of the impermeable clay layer by its transpiration process. As shown by Carré et al. (1999), the correlation between hardness and MC is strongly negative. MC reduction of +GR samples due to the transpiration of the grass has resulted on increasing gradient of e value trend line throughout the tested five days. Higher rebound could have been achieved if the test was carried out for several days for the samples with grass since there is a significant gradient in their trend lines in the last tested day.

In order to compare and contrast the effect of top grass surface on the e values of the samples, percentage increase of e values in samples without grass with respect to e values of the samples with grass is presented in Fig. 3.

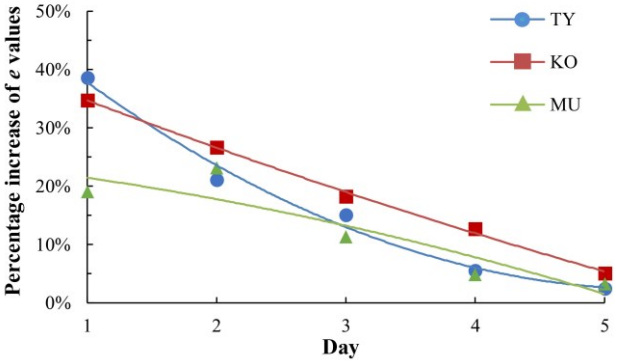

Fig. 3 Percentage increase of e values of the samples without grass with respect to e values of the samples with grass

The Percentage increase of e values of the samples without grass with respect to e values of the samples with grass shown in Fig. 3 are decreased with days for all clays. Rogers and Waddington (1990) reported that shock produced by ball impact on a cricket pitch is reduced due to the presence of a thatch on the turf surface. Since the fresh surface grass is acting like a damping layer, e values are low in samples with surface grass. The top grass including the sheath and leaf buds were dried with time without water and the grass leaves indented inside the top clay due to the ball impact. Therefore, damping due to the surface grass reduced with time and this scenario has resulted on increasing e values of the samples with surface grass with days.

3.2 *Normalized e value by moisture content*

The moisture contents of the samples cannot be controlled due to the addition of water during the grass plantation and due to the natural transpiration of grass. In order to remove the effect of the influence of MC, a normalized e value (e/MC) was obtained by dividing the e value by the MC. Variation of the e/MC with days of samples are presented in Fig. 4.

According to Fig. 4, MU shows a higher e/MC value than KO and TY during all tested days. The e/MC values of MU increase with days while KO and TY show approximately constant values with few fluctuations throughout the tested days. Evidently, MU soil gives higher e values than KO and TY in a given moisture content. High e values of the

ball bounce in MU and TY samples were observed at 10% and 15% of moisture content, respectively.

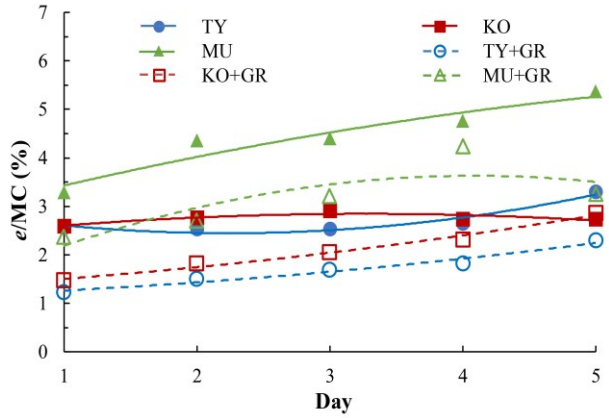

Fig. 4 Variation of *e*/MC

According to Fig. 4, MU+GR sample shows a higher normalized e value during the period than KO+GR and TY+GR and the value reached a peak on day 4. Although, e/MC value of KO+GR and TY+GR increased with days it could go beyond the value for MU+GR during the five days tested. According to Fig. 4, it can be concluded that the MU soil can generate higher bounce than the rest of the tested clays at a given MC for both with or without surface grass conditions.

3.3 *Pace rating*

Bounce test was carried out from H = 2 m in order to minimise the damage caused to the pitch surface. In order to match the input parameters of Murphy (1985) the H values were modified. Bounce test was conducted for five consecutive days by both TCB and HB on a prepared cricket pitch in University of Moratuwa grounds. Balls were dropped from a 2 m height and the h values were recorded. Average h values were calculated from approximately 20 vertical ball bounces from each ball on each day where only non-seam bounces were taken into account from TCB. h values of TCB were plotted against h values of HB as shown in Fig. 5. Trend line for the average h values of the TCB and HB on each day was shown in Fig. 5.

The relationship between h values of TCB (Y) - h values of HB (X) on the prepared cricket pitch is shown by Equation (3).

$$Y = 1.1164\ X + 0.036 \quad (3)$$

h values of HB were converted to h values of TCB by Equation (3) and respective e values were calculated using Equation (1). Accounting for the effects of air drag for H = 3 m, e values were increased by approximately 2% by James et al. (2005). Accordingly, e values were corrected using an increase by 1.67% for H = 2 m.

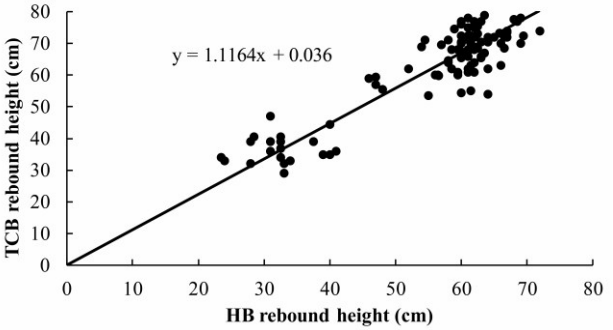

Fig. 5 Rebound heights of TCB - HB on a cricket pitch

Haron and Ismail (2012) studied the variation of e with different H values for the impacts of TCB on wood and steel surfaces. The e values were linearly decreased with H for all impacts. Furthermore, the gradients of the e - H graphs for the impact between one particular ball (HB or TCB) with wood or steel target surfaces is nearly a constant and the gradient values for TCB-wood and TCB-steel were (-)0.020 and (-)0.022, respectively. Average gradient of two trendlines was used to forecast the e value of a TCB - clay impact from H = 4 m. Developed equation of the e - H for a particular TCB – clay surface impact is shown at Equation (4), where $Y = e$, $X = H$ and C is the intercept value.

$$Y = -0.021X + C \quad (4)$$

C for each TCB - clay impact was calculated by substituting Y with experimental e value at X = 2 m of Equation (4). Calculated C values were used to recalculate Y values at X = 4 m from Equation (4). The μ values of the same laboratory models, on same days, for a new TCB (without seam contact) was calculated by Perera at al (2017b). Pace rating was calculated for each case by Equation (2) and the variation of pace rating of all samples during five days is shown in Fig. 6.

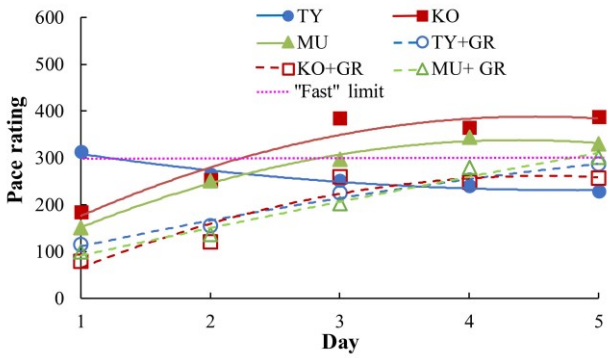

Fig. 6 Variation in pace rating for a new ball

According to Fig. 6, starting from "Easy paced" category, MU and KO have been shifted to "Fast" category from day 3, onwards concluding that MU and KO can be maintained in Fast pace category by maintaining the required MC at the start. However, TY has been shifted from "Fast" to "Easy paced" after day 1. TY exhibits "Fast" nature only in the first day due to the excess surface moisture available at the start. After the evaporation of surface moisture, the TY surface dried and deteriorated with time, hence decreasing the pace rating value. This is an evidence of SL pitches become slow with time due to the absence of fresh grass. Also, the crumbling and deteriorating nature of typical SL kaolinite clays in a dry environment during a five-day test match is demonstrated by TY model. However, pace rating values of the samples with grass increased with time and the peak values could not be obtained within the span of five tested days. Further studies should be carried out to obtain the peak pace rating values of the samples with surface grass.

4 CONCLUSIONS

Laboratory models made from MU soil demonstrated the highest *e* values, in both, without surface grass and with surface grass conditions towards the end of 5-day bounce test. Samples without surface grass showed higher *e* values than samples with surface grass during the five tested days. However, the samples with surface grass displayed higher increase in *e* values than the sample without surface grass throughout the five tested days.

e/MC results showed that MU can generate higher *e* values than any other sample at a given MC. Furthermore, the most suitable range of moisture contents to operate MU, KO and TY in "Fast" category was identified as 10%-12%, 18%-19% and 20%-21%, respectively.

MU and KO can be used to prepare local cricket pitches, under the actual environmental conditions of a cricket match. Pace and bounce tests should be conducted on such field cricket pitches and their values should be compared with the AUS fast and bouncy cricket pitches in further studies.

ACKNOWLEDGMENTS

This study was supported by a Senate Research Grant (SRC/LT/2015/08) of University of Moratuwa, SL and authors would like to thank the ground staff of both University of Moratuwa and Tyronne Fernando Stadium and the staff of Soil Mechanics Laboratory, Department of Civil Engineering, University of Moratuwa, SL.

REFERENCES

Carré, M. J. (2000). The dynamics of cricket and the effects of pitch construction, University of Sheffield, UK, Sheffield. U.K.

Carré, M. J., Baker, S. W., Newell, A. J., & Haake, S. J. (1999). The dynamic behaviour of cricket balls during impact, Sports Engineering, 2:145-160.

Challenger, I. (1986). Cricket and cricket wickets-A discussion of the two, Lincoln College, Christchurch, New Zealand.

Haron, A. & Ismail, K. A. (2012). Coefficient of restitution of sports balls: A normal drop test, IOP Conference Series: Materials Science and Engineering, 36:012038.

James, D. M., Carre, M. J., & Haake, S. J. (2005). Predicting the playing character of cricket pitches, Sports Engineering, 8(4), 193-207. doi:10.1007/bf02844162

McAuliffe, K. W., & Gibbs, R. J. (1997). An investigation into the pace and bounce of cricket pitches in New Zealand, International Turf-grass Society Research Journal, 8:109-119.

Nawagamuwa, U. P., Senanayake, A., Silva, S. A., & Sanjeewa, D. M. I. (2009). Improvement of Local Soils in Order to Make "Fast & Bouncy" Cricket Pitches, Engineer-Journal of the Institution of Engineers Sri Lanka, 42(4), 46-55.

Perera, W. S. U., Nawagamuwa, U. P., & Thilakarathna, G. N. U. (2017a). Identification of clayey properties for cricket pitch surfacing and analysing the variation of surface crack densities in different pitches, Institute of Engineers' Sri Lanka Annual Sessions 2017, Colombo, Sri Lanka.

Perera , W. S. U., Nawagamuwa , U. P., & Wijerathna, H. W. N. (2016). Study on properties of locally available clays to be used in fast and bouncy cricket pitches, Institute of Engineers' Sri Lanka Annual Sessions 2016, Sri Lanka. http://iesl.nsf.ac.lk/handle/1/824

Perera, W. S. U., Nawagamuwa , U. P., & Wijerathna, H. W. N. (2017b). Friction tests on clayey soils for fast and bouncy cricket pitches in Sri Lanka, Proceedings of the 6th International Young Geotechnical Engineers' Conference (iYGEC6), Seoul, Korea.

Rogers, J. N., & Waddington, D. V. (1990). Effects of management practices on impact absorption and shear resistance in natural turf, Natural and artificial playing fields: characteristics and safety features, ASTM International.

Senanayake , A. I. M. J., Silva , S. A., & Sanjeewa, D. M. I. (2009). Imporovement of local soils in order to create "Fast and Bouncy" cricket pitches., University of Moratuwa University of Moratuwa, Sri Lanka.

Shannon, J. (2010). Basic Guide to Turf Cricket Pitch Preparation: VCA.

Shipton, P. M. R. (2008). Optimization of cricket pitch rolling, Cranfield University, Cranfield, UK.

Sobana, A., Mapa, R. B., & Gowthamy, P. (2014). Charactarization of Grumusols in Mannar District in Sri Lanka and their applicability to Agriculture, Proceedings Peradeniya University International Research Sessions (iPURSE 2014).

Usman, H., Hamza, M. M., Hamid, P. M., & Ahmad, T. (2016). Improvement of Geotechnical Properties of Cricket Pitches, Journal of Civil & Environmental Engineering, 6(6): 1-12.

Experimental study of cyclic swell-shrink behaviour of an expansive soil

S. Wijesooriya
Statewide Geotechnical (Aust) Pty Ltd, Australia

S. Costa
School of Engineering, Deakin University, Australia

J. Kodikara
Department of Civil Engineering, Monash University, Australia

ABSTRACT: Expansive clay soils experience large seasonal movements at the ground surface during wet and dry periods. While many have investigated the swelling and shrinking behaviour of expansive soils, very few studies have been conducted to observe their cyclic swell-shrink behaviour during repetitive wet-dry cycles. This paper presents the findings of a series of experiments conducted on an expansive soil to investigate its swell-shrink behaviour using the hydric coefficient as applicable to analysis of desiccation cracking. Hydric coefficient is described as the proportionality constant between potential strain and moisture content change. One dimensional consolidation test was carried out as part of the experimental program. Results indicate that the expansive soil behaviour depends on initial moisture content, initial dry density, net vertical stress, composition of the soil and degree of wetting and drying process.

1 INTRODUCTION

Expansive soils are found in many parts of the world. It is well established that expansive clay soils experience seasonal movements in the ground surface during wet and dry periods. Many studies have been conducted on the swelling and the shrinking behaviour of expansive soils under a single wetting or drying event (Richards et al., 1983; Sharma, 1998). However, only a handful of studies have focused on the cyclic nature of swell-shrink behaviour in expansive soils (Zhao et al. 2019; Tripathy et al. 2002).

The degree of swelling and shrinking of clay depends on the amount and type of minerals in it. However, the volume changing behaviour can be assumed similar for any expansive soil and it varies only in degree (Kodikara 2012; Sharma 1998). When a soil layer is subjected to a sufficient number of wet-dry cycles, it reaches a state where it can act predominantly in an elastic or reversible manner, which is generally referred to as environmental stabilization or ripening in soil science literature (Kodikara et al. 2002). In the environmentally stabilized state, soil achieve a more stable structure. Gould at el. (2011) proposed to use void ratio, gravimetric water content and net stress to model the volumetric behaviour in environmentally stabilized soil. A more generalized approach to describe the volume change characteristics was presented by Kodikara et al. (2020). The concept of environmentally-stabilized line (ESL) in the void ratio (e) – moisture ratio (e_w) space was also established in their work.

In order to analyse the behaviour of unsaturated soils accurately, it is important to determine the stress-strain behaviour of the soils subject to boundary and initial conditions. Unfortunately, there is not a universally accepted model yet to capture the complex behaviour observed by compacted soils. D'onza et al. (2011) presented findings of an interesting collaborative work on constitutive modelling for unsaturated soils. Six published constitutive models were used by six independent teams to model the same set of experimental data for a silty soil including one blind test whose results were not disclosed to the researchers prior to generating the predictions. None of the models agreed reasonably with the experimental data of the blind test showing the need for improvements of constitutive models that are currently available to predict the unsaturated soil behaviour.

In general, many researchers use suction variation to analyse the stresses induced due to moisture content change. As a result, the swell-shrink behaviour is also described as a function of suction. However, the measurements of suction in expansive soils are not straightforward especially under field conditions. Number of techniques such as axis translation (increasing air pressure to generate a curved meniscus while keeping water pressure atmospheric), tensiometer, thermal conductivity sensor and osmotic methods are employed to get the full suction range

covered in laboratory experiments. Some of these techniques are either not able to be employed in the field or may not work well under in-situ conditions. Therefore, although suction is a well-defined parameter of the soil for water flow, its measurement still poses problems to advancement of unsaturated soil mechanics. To overcome this challenge, in this study, moisture content variation is used over suction as advocated by several other researchers (Costa et al., 2008; Gould et al., 2011; Kodikara, 2012).

The cyclic swell-shrink behaviour is related to desiccation crack formation in soil. While the volume reduction during drying gives rise to desiccation cracks, increased volume during wetting initiate self-healing of cracks. This process is reversible through wet-dry cycle where cracks can get reactivated on pre-existing failure zones during subsequent drying (Diel et al. 2019). Therefore, it is important to understand the swell-shrink characteristics of soil from a desiccation cracking analysis point of view. Stress induced by desiccation can be represented either by suction increment or moisture increment. Hydric constant (α) has been used by several researchers to describe the stress generated by moisture content change (Kodikara and Choi 2006; Peron et al. 2009) during desiccation.

However, the behaviour of this α value due to the cyclic swell-shrink behaviour has not been adequately investigated. This paper presents findings of laboratory experiments conducted to study the behaviour of hydric coefficient (α^*), a variable parameter related to hydric constant (α). The relationship between the two parameters and the theoretical formulation is described in the following section.

2 HYDRAIC CONSTANT (α) IN STRESS ANALYSIS

When the stresses are analysed in terms of moisture content variation, the potential strain can be obtained using a constant of proportionality known as the hydric constant (α) and the difference of moisture content similar to heat flow analysis (i.e. $\Delta\varepsilon_{sh} = k\Delta T$, where k is the thermal conductivity, ΔT is the thermal gradient and $\Delta\varepsilon_{sh}$ is the shrinkage strain change)

$$\Delta\varepsilon_{v_{sh}} = \alpha\Delta w \quad (1)$$

However, unlike for thermal expansion coefficient, α is not a constant and its behaviour has not been studied in detail with the cyclic wetting and drying for compacted soils. A theoretical explanation of the hydric coefficient is presented as follows.

According to the MPK framework presented by Kodikara (2012), the net stress in unsaturated soil can be presented as a function of void ratio, e and the moisture ratio, e_w, where:

$$e_w = wG_s \quad (2)$$

Therefore, this functional relationship can be presented as:

$$\sigma = f(e, e_w) \quad (3)$$

By partially differentiating equation (3) gives:

$$d\sigma = \left(\frac{\partial\sigma}{\partial e}\right)_{e_w} de + \left(\frac{\partial\sigma}{\partial e_w}\right)_{e} de_w \quad (4)$$

From the cyclic formula,

$$\left(\frac{\partial\sigma}{\partial e_w}\right)_{e} = -\frac{\left(\frac{\partial e}{\partial e_w}\right)_{\sigma}}{\left(\frac{\partial e}{\partial\sigma}\right)_{e_w}} \quad (5)$$

Substituting equation (5) in equation (4) gives:

$$d\sigma = \left(\frac{\partial\sigma}{\partial e}\right)_{e_w} \left(de - \left(\frac{\partial e}{\partial e_w}\right)_{\sigma} de_w\right) \quad (6)$$

when,

$$\left(\frac{\partial e}{\partial e_w}\right)_{\sigma} = \alpha^* \quad (7)$$

and,

$$\left(\frac{\partial\sigma}{\partial e}\right)_{e_w} = K$$

where K is the bulk modulus at the particle moisture ratio and α^* is the hydric coefficient given by the partial differential of void and moisture ratios at a particular net stress. Then equation (6) becomes,

$$d\sigma = K(de - \alpha^* de_w) \quad (8)$$

K should be replaced by $3K$ if this relation is for only one directional stress. $(\alpha^* de_w)$ represents the free shrinkage. The relation to obtain the potential free shrinkage can be written as,

$$\alpha^* \frac{de_w}{(1+e_0)} = \Delta\varepsilon_{v_{sh}} \quad (9)$$

Hence, from equations (1) and (9),

$$\alpha^* \frac{de_w}{(1+e_0)} = \alpha\Delta w \quad (10)$$

Using equation (2) and substituting it in equation (10) leads to the relationship,

$$\alpha = \alpha^* \frac{G_s}{(1+e_0)} \quad (11)$$

The relationship given by equation (11) can be used to calculate the hydric constant. It is clear that the hydric coefficient depends on the stress level. This coefficient (α^*) can be determined experimentally by following a relatively easy test. The following sections explain the swelling and shrinking experiments conducted to develop the relationships of void and moisture ratios and thereby the variation of the hydric coefficient.

3 EXPERIMENTS

Swell-shrink tests were conducted to determine the hydric coefficient. The material used, experimental procedure and specimen preparation are described in this section.

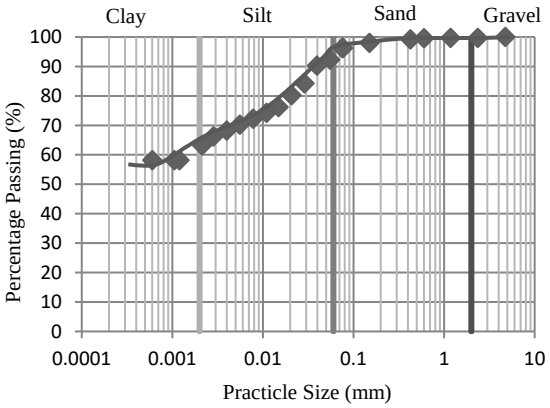

Fig. 1 Particle size distribution of Altona clay

3.1 *Materials*

The expansive soil used was collected from the clay deposits in North Altona in Melbourne, Australia at depths of 0.4 m to 2.0 m. It is light brown in colour when dry, becoming dark when wet. This clay is referred to as Altona clay in this paper. The particle size distribution and the basic properties of Altona clay is given in Fig. 1 and Table 1 respectively.

Table 1. Characteristics of Altona clay

Parameter	Value
Colour	Light brown / biege
Liquid Limit	70.2%
Plastic Limit	21.8%
Plasticity Index	48.4%
Linear shrinkage	16%
Soil class	Inorganic clays of high plasticity (CH)
Standard MDD	14.6 kN/m^3
Standard OMC	23.5%

The main minerals in Altona clay are quartz (59%) and Smectite (31%). The complete mineralogical composition can be found in Gallage et al. (2008).

3.2 *Specimen preparation*

Specimens were prepared in stainless steel oedometer rings of diameter 76.5 ± 0.1 mm and height 19.1 ± 0.1 mm. The height of the sample needed to be small enough to avoid a significant energy loss and heterogeneity (Romero 1999). However, the height should be sufficient to produce considerable volume change with the moisture change. Considering these, the specimen height was selected as 12 mm.

Specimens were prepared carefully and identically in order to maintain homogeneity and repeatability. The initial conditions selected were: moisture content 17 ± 1% and dry unit weight 14.6 ± 0.2 kN/m^3(standard MDD). This point lies on the dry side of the optimum. The behaviour of soils compacted at wet of optimum is reasonably well known and details are available in literature (Romero 1999; Tripathy et al. 2002; Monroy 2006). Behaviour on dry side of the optimum has been neglected although in actual field conditions there is a possibility of soil ending up on dry side. Hence, the dry side of optimum was considered in this study.

The soil was first oven dried at 100^{0}C and sieved to remove the sand-size particles. Powdered clay was then mixed with the required amount of water manually for around 15 min by spraying until moisture was distributed evenly. The wet soil was placed in airtight containers and left for at least 24 hours prior to use.

Static compaction was selected for compacting samples due to its higher potential in repeatability and uniformity over dynamic compaction (Wheeler and Sivakumar 1995). The required quantity of soil was calculated on the basis of the dry density to be achieved and compacted directly into the oedometer ring.

3.3 *Test set-up*

The test programme was designed to observe the change of void ratio over the time when the sample was subjected to controlled wetting and drying conditions. Several types of apparatus can be used for this purpose, and the conventional oedometer is one of them. Monash University Civil Engineering laboratory has oedometers designed and manufactured at Monash as shown in Fig. 2. This oedometer is relatively simple, easy to use and takes less space than the conventional oedometer. Furthermore, wetting and drying tests take longer and the use of Monash oedometers could allow the conventional oedometers to be used for other purposes. The main limitation of the test set-up is the pressure that can

be applied by the loads that can be placed above. Typically about 100kPa pressure is easily achievable.

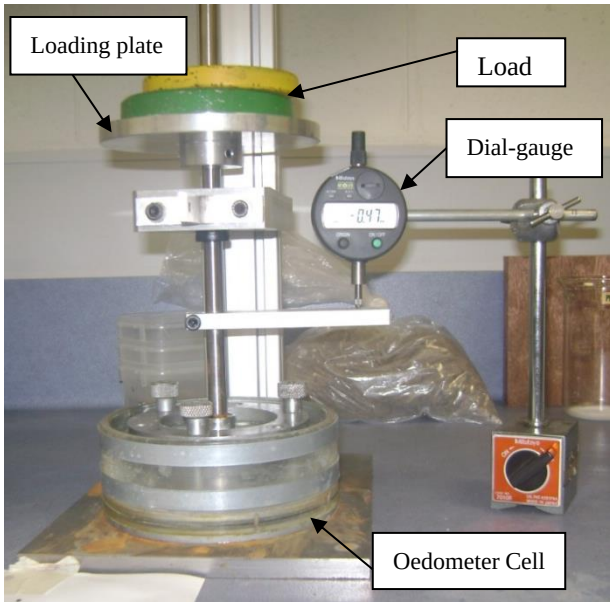

Fig. 2 Monash designed oedometer

The tests conducted had two phases: wetting and drying. A total of 50 specimens were tested. Wetting and drying cycles were continued until the volume change followed the same path for both wetting and drying. This condition was considered as the environmentally stabilized condition for the environment imposed. A static pressure of 5 kPa was applied on the specimens in a temperature controlled room. The temperature was maintained at 25 °C during wetting and increased up to 40 ± 5 °C while drying using halogen working lamps. The pressure used was typically a nominal pressure and is representative of an unloaded clay layer.

When obtaining the swelling path, the moisture content was increased by adding the required amount of water through the holes on the top cap and by inundating the sample in water when the full potential of swell was assumed to have been obtained. About 6 to 10 specimens were tested to obtain one complete wetting or drying path. Each specimen provided a single point in the $e - e_w$ space. The quantity of water to be added was decided allowing 3 to 5 mm water evaporation from the sample during the swelling period. During other periods, the cell was covered with a plastic wrapping to prevent evaporation.

Vertical displacement of the sample was recorded every 24 hrs. At the end of the test, moisture content and unit weight were measured immediately after dismantling the test set-up.

4 RESUTLS AND DISCUSSION

4.1 *Swell – shrink cycles*

The maximum and minimum vertical displacements observed during wetting and drying cycles are plotted in Fig. 3. Samples were compacted at the same initial conditions under the same vertical pressure as described previously. The tests were conducted continually for several wet dry cycles.

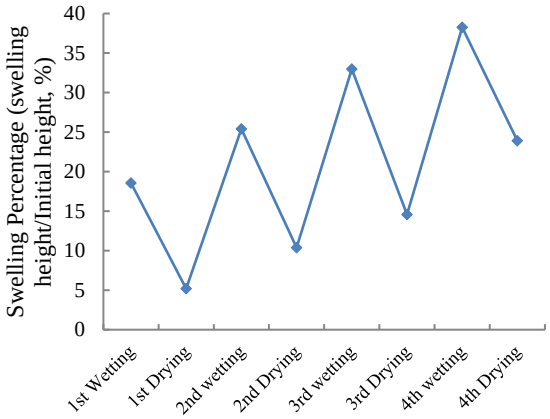

Fig. 3 Average vertical displacement during wet-dry cycles

The results indicate that the initial wetting and initial drying (first cycle) have different vertical displacements variations. The next cycles show a repetitive variation. From Fig. 3, it can be seen that Altona clay shows more than 30% net expansion from the initial height. The change in vertical displacement during wet dry cycles is expected to be around 20% after ageing. This result shows a good agreement with the results of Tripathy et al. (2002).

The variation of void ratio in each cycle is examined and plotted against the moisture ratio. Fig. 4 and Fig. 5 show the first and fourth cycles respectively (intermediate cycles are not included here due to limited space). In each figure wetting is followed by drying to obtain the full cycle.

In Fig. 4, the initial point indicates the point where the sample was compacted. The lower part of the swelling curve from the initial point was obtained by drying the sample. It can be observed that the curves behave wildly at the initial wetting and drying cycle before converging to a stabilized curve achieved in the fourth cycle (Fig. 5).

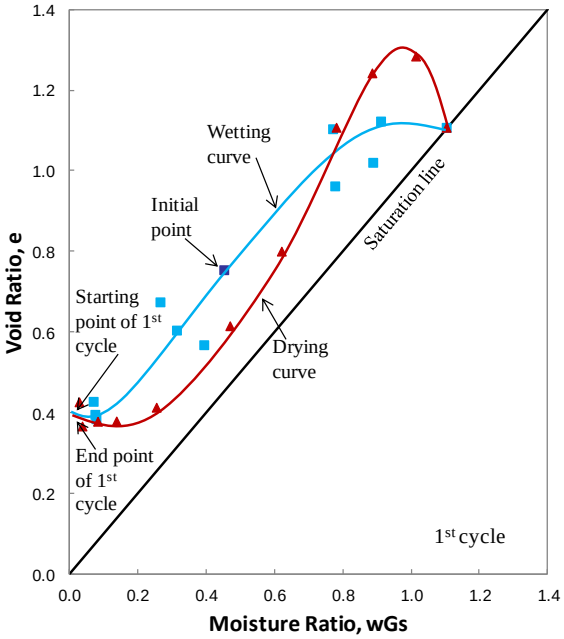

Fig. 4 Swelling and shrinking paths for first cycle

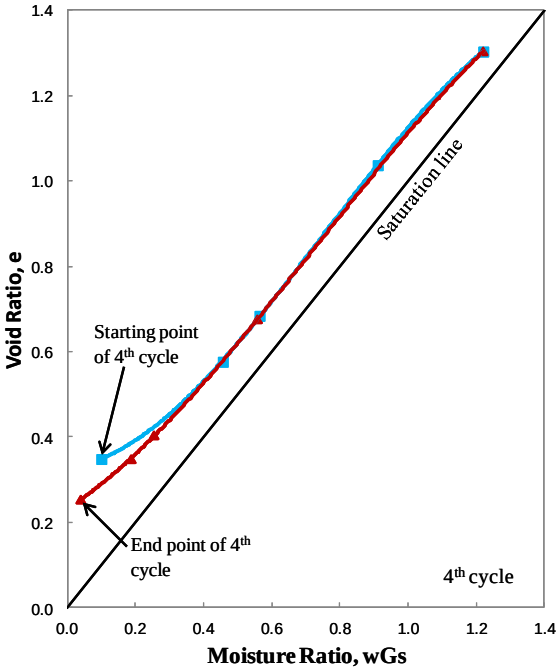

Fig. 5 Swelling and shrinking paths for fourth cycle

In the stabilized curve, both drying and wetting are lying on top of each other. Initially, there is no considerable change in void ratio with moisture content change. Nevertheless, once the moisture ratio is beyond 0.2, void ratio shows substantial increase until close to the saturation However, after approximately 0.2 moisture ratio the void ratio shows a significant change until close to the saturation. This behaviour agrees with results of Tripathy et al. (2002) and the explanation given by Gould et al. (2011).

Variation of hydric coefficient (α^*)The variation of hydric coefficient was examined in relation to number of cycles and moisture content. Fig. 6 and Fig. 7 show the change in hydric coefficient with number of cycles and moisture ratio respectively.

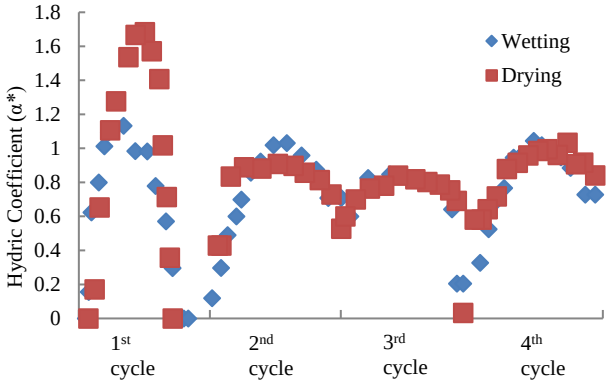

Fig. 6 Variation of α^* with number of cycles

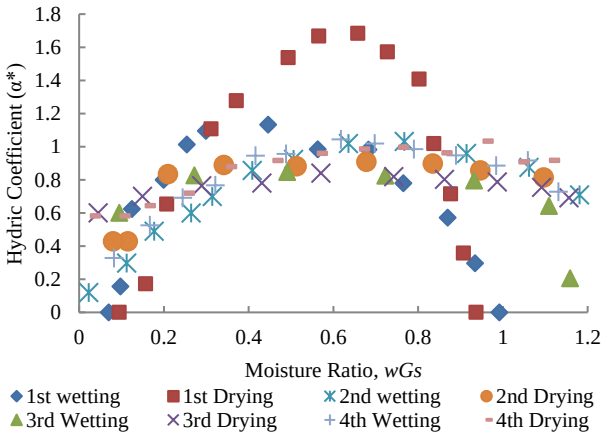

Fig. 7 Variation of α^* with moisture ratio

It can be seen that α^* shows similar behaviour in all swell-shrink cycles, although the first cycle shows little variation in comparison to the other cycles (Fig. 6). However, for both shrinking and swelling curves, similar variation of α^* values can be observed. A careful examination of the figure shows slightly higher values for α^* for shrinking soil than during swelling.

At low moisture contents, α^* is low and increases with the moisture content approximately up to 1 reaching a peak. Then the value remains relatively constant near the peak for a reasonably long range of moisture content. The value of α^* drops swiftly towards the end of the cycle as shown in Fig. 7.

In desiccation crack analysis, hydric constant (α) has been used with the assumption that it remains a constant over a range of moisture content change (Costa et al., 2016). The results presented in Fig. 7 clearly shows the variability of α^* thereby

asserting the variable nature of α. However, a careful observation of α^* in Fig. 7 suggests that assuming a constant value for α is not entirely inaccurate for small ranges of moisture content changes. For large moisture content changes, constant α can be used incrementally.

The higher α^* values during shrinking (drying) than swelling explains why desiccation induced cracks do not get fully repaired during wetting. The higher shrinkage strains generated during drying do not recover in full even under cyclic wetting. Nevertheless, the soil reaches a more reversible condition once the environmentally stabilised condition is achieved.

5 CONCLUSIONS

Experimental results from a one dimensional oedometer test which was carried out to study the swell-shrink behaviour of an expansive clay during wetting-drying cycles were presented in this paper. A theoretical formulation of the coefficient (α^*) is presented and its values were experimentally determined. Hydric coefficient show considerable discrepancies during initial wetting-drying cycles until it reaches a more steady behaviour under environmentally stabilized condition. A slightly higher α^* values are observed during drying cycles than in wetting cycles. It was also found that hydric coefficient does not remain constant during drying. This has implications in desiccation crack analysis where hydric coefficient is normally assumed to be a constant. For small changes in water content, however, it is reasonable to assume a constant value for the hydric coefficient.

REFERENCES

Costa, S., Htike, W. Y., Kodikara, J. and Xue, J. (2016). Determination of *J*-integral for clay during desiccation. Environmental Geotechnics. 3(EG6):372-378.

Costa, S., Kodikara, J. K. and Thusyanthan, N. I. (2008). Modelling of Desiccation Crack Development in Clay Soils. The 12th International Conference of International Association for Computer Methods and Advances in Geomechanics (IACMAG), Goa, India.

Diel, J., Vogel, HJ., Schluter, S. (2019). Impact of wetting and drying cycles on soil structure dynamics. Geoderma 345:63-71.

D'Onza, F., Gallipoli, D., Wheeler, S., Casini, F., Vaunat, J., Khalili, N., Laloui, L., Mancuso, C., Main, D., Nuth, M., Pereira, J. M. and Vassallo, R.. (2011). Benchmark of constitutive models for unsaturated soils, Geotechnique 61: 283-302

Gallage, C., Chan, D., Gould, S. and Kodikara, J. K. (2008). Field Measurement of the Behaviour of an In-Service Water Reticulation Pipe Buried in Reactive Soil (Altona North, Vic). ARC Pipe Linkage Project : Prediction and controlling of pipe failures in buried water and gas pipe systems, Monash University.

Gould, S. J. F., Kodikara, J., Rajeev, P. Zhao, X.-L. and Burn, S. (2011). A void ratio – water content – net stress model for environmentally stabilized expansive soils. Canadian Geotechnical Journal, 48(6):867-877.

Kodikara, J. K. and Choi, X. (2006). A simplified analytical model for desiccation cracking of clay layers in laboratory tests, Fourth International Conference on Unsaturated Soils, Geotechnical Special Publication: 2558-2569.

Kodikara, J., Barbour, S. and Fredlund, D. (2002). Structure development in surficial heavy clay soils: a sysnthesis of mechanisms. Australian Geomechanics, 37(3): 25-40.

Kodikara, J., Jayasundara, C. and Zhou, A.N. (2020). A generalized constitutive model for unsaturated compacted soils considering wetting/drying cycles and environmentally-stabilised line, Computers and Geotechnics, 118.

Kodikara, J.K. (2012). New framework for volumetric constitutive behaviour of compacted unsaturated soils, Canadian Geotechnical Journal, 49:1227-1243.

Monroy, R. (2006). The influence of load and suction changes on the volumetric behaviour of compacted London Clay. PhD Thesis, University of London.

Peron, H., Hueckel, T., Laloui, L. and Hu, L.B. (2009). Fundamentals of desiccation cracking of fine-grained soils: experimental characterization and mechanisms identification, Canadian Geotechnical Journal 46:117-1201.

Richards, B. G., Peter, P. and Emerson, W. W. (1983). The effects of vegetation on the swelling and shrinking of soils in Australia (Adelaide). Geotechnique, 33(2): 127-139.

Richards, B.G.; Peter, P. and Emerson, W.W. (1983). The effects of vegetation on the swelling and shrinking of soils in Australia (Adelaide). Geotechnique 33(2):127-139.

Romero, E. (1999). Characterization and thermo-hydro-mechanical behavoiur of unsaturated Boom clay: an experimental study, PhD Thesis, Technical University of Catalonia.

Sharma, R. S. (1998). Mechanical behaviour of unsaturated highly expansive clays. PhD Thesis, University of Oxford.

Sharma, R.S. (1998). Mechanical behaviour of unsaturated highly expansive clays. PhD Thesis, University of Oxford.

Tripathy, S., Subba Rao, K. S. and Fredlund, D. G. (2002). Water content - Void ratio swell-shrink paths of compacted expansive soils. Canadian Geotechnical Journal 39(4):938-959.

Wheeler, S.J. and Sivakumar, V. (1995). An elasto-plastic critical state framework for unsaturated soil, Geotechnique, 45(1): 35-53.

Zhao, N.F., Ye, W.M., Chen, B., Chen, Y.G. and Cui, Y.J. (2019). Modelling of the swelling-shrinkage behavior of expansive clays during wetting-drying cycles. Acta Geotechnica, 14:1325-1335.

Coupled geotechnical-hydrological modeling of earth slopes subjected to multi-hazards rainfall, earthquake, and excavation

Tharshikka Vickneswaran
Graduate Student, Glenn Department of Civil Engineering, Clemson University, Clemson, SC 29634; Email: tvickne@g.clemson.edu

Nadarajah Ravichandran
Associate Professor, Glenn Department of Civil Engineering, Clemson University, Clemson, SC 29634; Email: nravic@clemson.edu

ABSTRACT: Natural and manmade slopes fail due to many reasons including rainfall, earthquake, and loss of support due to excavation. The focus of this study is to analyze the effect of the individual occurrence of rainfall, earthquake, and excavation and simultaneous occurrence of rainfall-excavation and rainfall-earthquake on the stability and deformation behaviors of earth slopes using coupled Geotechnical-Hydrological finite element software PLAXIS. First, the analysis was carried out by applying the rainfall, earthquake, and excavation individually and then by applying two of these hazards simultaneously i.e., rainfall-excavation and rainfall-earthquake. An abrupt increase of 55 mm was observed in the horizontal movement of the slope subjected to rainfall of duration 17 days. The factor of safety of 1.4 reduced below 1 on the 7th day due to rainfall and on the 6th day due to rainfall-excavation. The utmost horizontal movement of magnitude 725 mm was observed when the earthquake was applied after a heavy rainfall.

1 INTRODUCTION

According to the United States Geological Survey (USGS), slope failures are a catastrophic hazard common in almost every state in the U.S.A which causes $1 billion of damages and about 25 to 55 deaths each year. Common causes for these types of slope failures are heavy rainfall, earthquake, and loss of support due to excavation for transportation and other construction activities. Numerous studies have been carried out on the stability of slopes subjected to heavy rainfall (Cai and Ugai, 2004; Campbell, 1975; Rahardjo et al., 2007). The two-day heavy rainfall in January 2020 caused landslide and flooding in southeastern Brazil which killed at least 30 people (BBC News, 2020). The National Institute of Meteorology reported that the rainfall in this region has been the heaviest recorded in the last 110 years. While the slope failures induced by rainfall can happen within minutes, the infiltration of rainfall which precedes them can take several days to develop (Campbell, 1975). Campbell (1975), concluded that the cause for the slope failures in the Santa Monica Mountains of southern California is due to the infiltration and deep percolation of heavy rainfall. The preconditioning factor for the slope failure occurred in Leyte island, Philippines was found to be the heavy rainfall that occurred four days prior to the slope failure (Evans et al., 2007). The heavy rainfall that lasted for almost four days was the major factor for inducing slope failure that occurred in May 2017 in the village of Bellana, Kalutara district of Sri Lanka (Athas, 2017). The effects of hydraulic characteristics and initial degree of saturation of soils, and rainfall intensity and duration were investigated in a study by Cai and Ugai (2004). It was found that the slopes with low permeability could fail only if the rainfall lasted for sufficient duration even if the rainfall intensity is high. The intensity and duration of rainfall have a significant impact on the slope failures (Cai and Ugai, 2004; Campbell, 1975; Rahardjo et al., 2007).

The other important factor causing slope failures is the inertial forces induced during an earthquake. An Earthquake can engender rock falls, long-distance movement of the slope, and flow of the artificial slopes. Studies were made on the slope failures induced by earthquakes (Lin et al., 2006; Tang et al., 2011). Earthquakes in Central America accompanied by a large number of slope failures caused serious damages and disturbances (Bommer and Rodriguez, 2002). The earthquake that occurred in El-Salvador in 2000 caused debris flow at Las Colinas that killed at least 500 people and slope failure at Las Barrioleras that killed another 100 (Bommer and Rodriguez, 2002). It is necessary to have an awareness about the earthquake-induced slopes failures as there are shreds of evidence in the past.

Apart from the natural hazards causing slope failures, there are records of human-induced slope failures. Improper cutting of hills and mining cause human-induced slope failures (European Geosciences Union, 2018). From the data that was recorded on over 4,800 slope failures during the 13 years revealed that the slope failures resulting from human activities have risen over time (European Geosciences Union, 2018). Among the construction activities, excavations cause an increase in the slope gradient leading to the instability of the slopes. The excavation of the sloping surface makes the slope steep and increases the gravitational forces that may lead to slope failure. Studies have found that the failure on the excavated slopes is due to the release of stress-induced by excavation (Erginal et al., 2008; Rupke et al., 2007).

Heavy rainfall intensity can trigger earthquakes in slopes which are called "disaster triggering disaster" (Brahic, 2008). Shimon Wdowinski of the University of Miami in Florida first noticed a relation between storms and earthquakes. 18 months of time interval was observed between an earthquake with magnitude 7.0 that hit Haiti and several hurricanes and tropical storms (Brahic, 2008). Also, in the same article, it was mentioned that an earthquake of magnitude 6.4 temblors that shook Taiwan in 2009 occurred several months after the Typhoon Morakot which dropped 2.9 m of rain in 5 days.

There is a possibility for the simultaneous occurrence of hazards. Real-world scenarios like heavy rainfall following an earthquake and heavy rainfall in an excavated slope can worsen the stability of the earth slopes. There are few studies that consider the effect of multi-hazards on the stability and deformation behavior of the slopes. For the investigation with rainfall and excavation, first, the slope was analyzed by applying only the rainfall, then the slope was analyzed for various excavations and finally, rainfall was applied to an excavated slope. For the investigation of rainfall and earthquake events, first, the slope was analyzed by applying only the rainfall, then it was analyzed by applying only the earthquake, and finally, it was analyzed by applying heavy rainfall following an earthquake.

2 COUPLED HYDRO-MECHANICAL ANALYSIS OF EARTH SLOPES

Numerical methods are commonly used in slope stability analyses to deal with complex geometries, material anisotropy, non-linear behavior, and coupling flow and deformation, which cannot be performed using limit equilibrium methods. In this study, the fully coupled flow-deformation analysis in the finite element software PLAXIS 2D was used to analyze the slopes subjected to heavy rainfall, excavation, and earthquake. The fully coupled flow-deformation analysis takes in to account the nonlinear behavior of unsaturated soils by considering both deformation and changes in pore water pressure due to water infiltration.

To analyze the effect of natural and human-induced hazards on slope stability, the Meeriyabedda slope failure in the Badulla district was selected for the study. The Meeriyabedda landslide occurred on the 29th of October 2014 causing 16 deaths and property losses which was triggered by continuous rainfall. The details of the numerical modeling are discussed below.

2.1 *Material properties*

Lakmali et al. (2016) did a case study on the Meeriyabedda landslide by analyzing the variation of shear strength parameters with the moisture content and the stability of slope due to rainfall. In that study, soil samples were collected from the Meeriyabedda landslide area and the soil properties were determined by conducting laboratory tests. The soil was classified as poorly graded sand (SP) according to the Unified Soil Classification System based on the sieve analysis carried out by Lakmali et al. (2016). The properties of the soil adopted from Lakmali et al. (2016) are shown in Table 1.

Table 1. Material properties

General properties	Value
Saturated unit weight (kN/m^3)	18.9
Unsaturated unit weight (kN/m^3)	15.7
Saturated Young's modulus (MN/m^2)	30
Poisson's ratio	0.3
Friction angle (Degrees)	30
Cohesion (kN/m^2)	5

2.2 *Constitutive model and model parameters*

The stress-strain behavior of the soil was represented by the Hardening Soil (HS) model available in PLAXIS 2D. The HS model is superior to the Mohr-Coulomb or Linear Elastic models as the HS model is capable of modeling modulus reduction with increasing strain and fits the observed laboratory stress-strain behavior reasonably well (Yang et al., 2002; Youwai et al., 2003). The key input parameters of the HS model that were used in PLAXIS 2D are the secant modulus at 50% of the failure stress (E_{50}^{ref}) of 30,000 kN/m^2, the tangent modulus for primary oedometer loading (E_{oed}^{ref}) of 21,030 kN/m^2, the unloading/reloading modulus (E_{ur}^{ref}) of 90,000 kN/m^2.

2.3 *Soil water characteristics curve*

In this study, the van Genuchten (1980), model was used to describe the hydraulic behavior of unsaturated soils in PLAXIS 2D. The van Genuchten function relating the saturation to the matric suction is expressed as,

$$S(\psi) = S_{res} + (S_{sat} - S_{res})[1 + (g_a \mid \psi \mid^{g_n}]^{g_c} \quad (1)$$

where $S(\psi)$ is the degree of saturation, S_{res} is residual degree of saturation, S_{sat} is degree of saturation at fully saturated state, ψ is the matric suction, g_a is a fitting parameter related to the air entry value of the soil, g_n is a fitting parameter which is a function of the rate of water extraction from the soil once air entry value has been exceeded and g_c is a fitting parameter where $g_c = (1 - g_n) / g_n$. The van Genuchten parameters corresponding to the SP soil and the Soil Water Characteristics Curve (SWCC) are shown in Table 2 and Fig. 1, respectively.

Table 2. van Genuchten parameters

Groundwater parameters	Value
Residual water content	0.1
Saturated water content	1.0
Fitting parameter for air entry value, α (m^{-1})	14.5
Fitting parameter , n	2.68
Void ratio	0.84
Hydraulic conductivity (m/day)	7.13

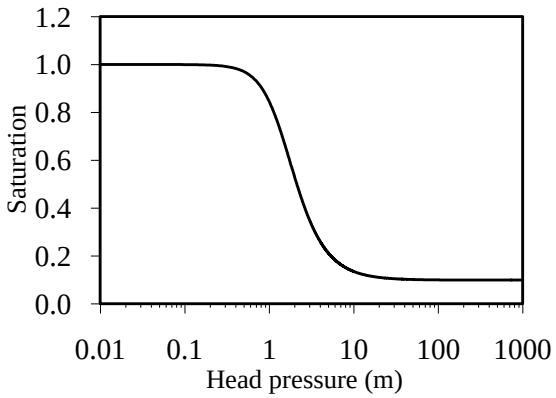

Fig. 1 Soil water characteristics curve

2.4 *Numerical modeling*

Two-dimensional plane strain model in PLAXIS 2D was used to represent the earth slope. The height of the slope was 12 m with a uniform slope angle of 30°. The simulation domain and the mesh used are shown in Fig. 2. The simulation domain was discretized spatially using 15-Node triangular plane strain elements and the mesh near the slope was refined for accurate results. A total of 12,420 elements with 100,865 nodes have been used. Gravity loading function was used to generate the initial stresses by applying the self-weight of the slope. The initial ground water table was assigned at the bottom of the simulation domain.

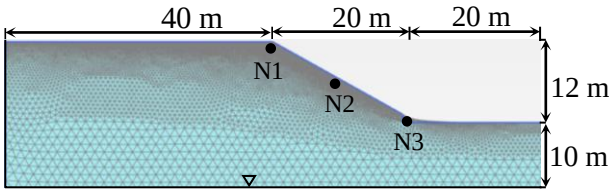

Fig. 2 Simulation domain (where N1 is at 21.8 m, N2 is at 16 m, and N3 is at 10 m from the bottom of the simulation domain)

The deformation boundaries, groundwater flow boundaries, and earthquake boundaries were assigned to the model according to the site conditions. The deformation boundaries used in the analysis restrain deformations of the vertical boundaries against translation in the x-direction and the base of the model against translation in both x and y directions. The flow boundaries were assigned such that flow through the base of the domain and the lateral ends are restricted. The dynamic boundaries were used only for the application of earthquake. The dynamic boundaries used in PLAXIS 2D were viscous boundaries on the vertical sides and a prescribed displacement along the bottom of the model. The prescribed displacement was applied with the acceleration which varies with time according to the acceleration-time history shown in Fig. 3.

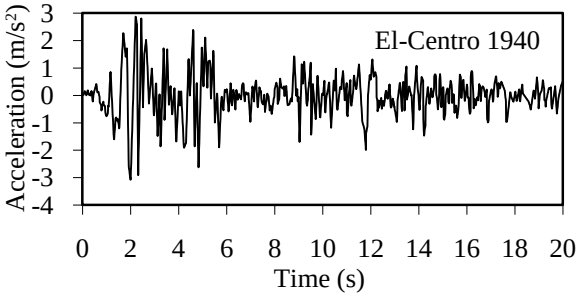

Fig. 3 Acceleration-time history (Vickneswaran and Ravichandran 2020)

3 RESULTS AND DISCUSSION

3.1 *Slope behavior under rainfall*

The rainfall that accumulated over 120 mm during the period of 27th of October to 7th of November 2014 was the main cause for the landslide in Meeriyabedda (Jayamali et al., 2017). Fig. 4 shows the variation of daily rainfall and the accumulated rainfall (AR) with time obtained from Jayamali et al. (2017). Zero on the time axis denotes the 27th of October in Fig. 4. In addition to the deformation and groundwater flow boundaries described in section 2.4, an infiltration boundary with the rainfall hydrograph shown in Fig. 4 was applied to the ground and slope surface. The stability and the deformation behaviors of the slope were analyzed by using coupled hydro-mechanical analysis in PLAXIS 2D. Fig. 5 shows the variation of factor of safety with duration. It can be observed that the factor of safety reached a minimum value after a period of 7-day rainfall. Before any rainfall event, the factor of safety of the slope was 1.4 which decreased to a value of 0.98 (30 %) after 7-day rainfall.

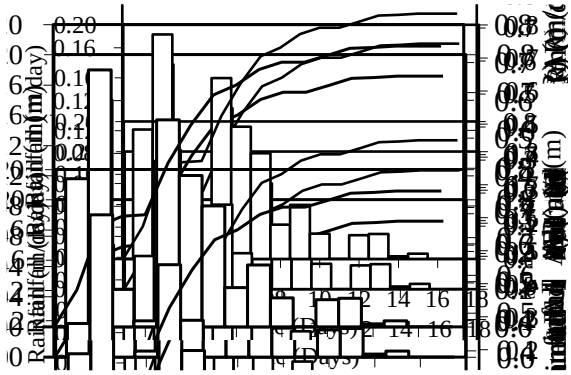

Fig. 4 Rainfall data recorded at Meeriyabedda estate (Jayamali et al., 2017)

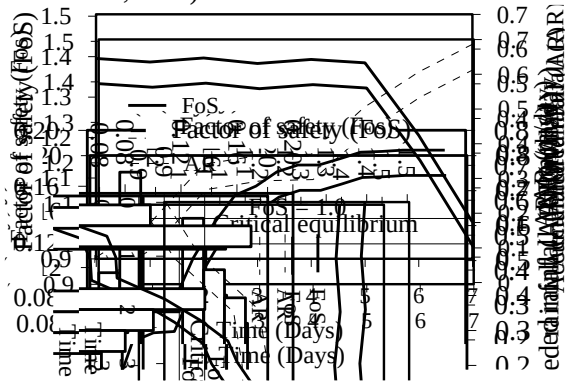

Fig. 5 Variation of factor of safety with time for rainfall

The deformation analysis showed that the variation of horizontal deformation of the slope was higher than the variation of vertical deformation. Therefore, the horizontal deformation-time history was used for further analysis. Fig. 6 shows the horizontal deformation at slope crest (N1), slope midpoint (N2), and slope toe (N3) whose locations are shown in Fig. 2. It is evident that the deformation of the slope exhibited peak value on the 8th day of rainfall. The maximum horizontal deformation of 55 mm was observed near the slope toe.

To capture the sudden increase in the horizontal deformation which is not visibly shown in Fig. 6 after the 8th day was plotted in Fig. 7. It can be seen that an abrupt increase in the horizontal movement occurred within 28 s after the 8th day. The difference between the horizontal deformation at the start of 0 s and end of 28 s after 8th day at N1, N2 and N3 were 15.7 mm, 20.3 mm, and 25.5 mm, respectively. The critical slip surface obtained from PLAXIS 2D is shown in Fig. 8. In addition to this, there could be possibilities when the slope is stable but there can be small movements which could be detrimental. Therefore, it is essential to study the deformation behavior along with the stability.

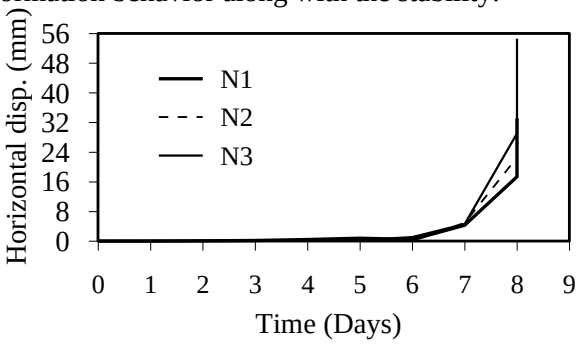

Fig. 6 Horizontal deformation-time history

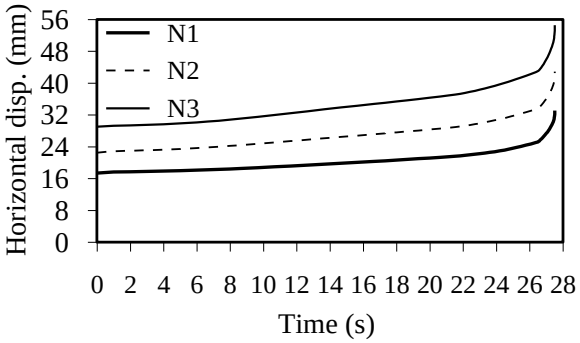

Fig. 7 Horizontal deformation-time history (zero denotes the start of 8th day)

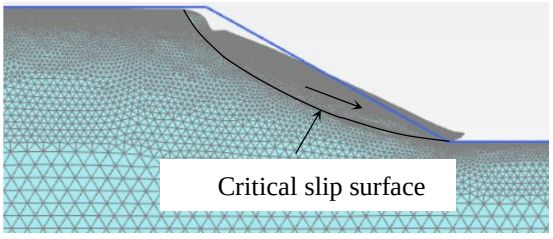

Fig. 8 Failure plane at the end of 7th day (deformation scale factor = 10)

3.2 *Slope behavior under excavation*

The excavation was modeled by removing slices of soil near the toe of the slope with different heights and widths. The limiting excavation height and corresponding width were found by analyzing the stability of the slope for different heights starting from 0.1 m to 2.0 m. The variation of factor of safety against the height of excavation is plotted in Fig. 9. The factor of safety 1.4 prior to any excavations lowered to 0.85 (64.7 %) for an excavation height of 2 m and a corresponding width of 3.5 m. From this analysis, the limiting height of 1.2 m and the corresponding width of 2 m was selected for further analysis.

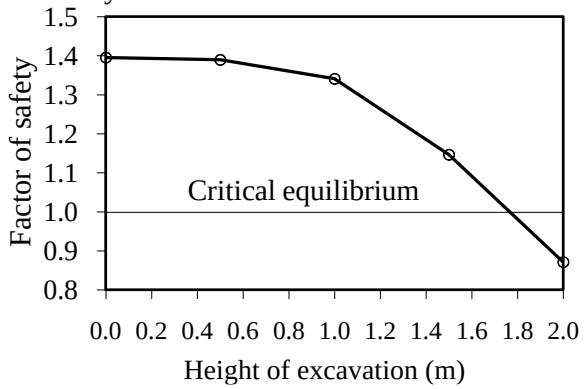

Fig. 9 Variation of factor of safety with height of excavation

3.3 *Slope behavior under rainfall-excavation*

Since the initial factor of safety was 1.4 which is close to 1, any additional excavation to the slope is not desirable. But there may be situations when lack of studies on the initial conditions of the slope result in misleading interpretations. Therefore, it is essential to analyze the stability of the excavated slopes subjected to heavy. The rainfall shown in Fig. 2 was applied to the slope with excavation height 1.2 m and width 2 m. The variation of factor of safety with time for the initial and the excavated slope was plotted against time in Fig. 10.

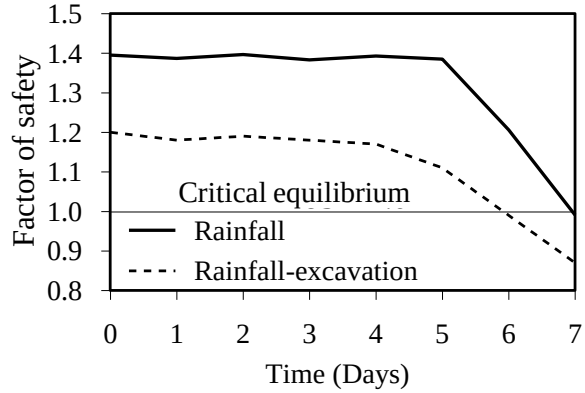

Fig. 10 Variation of factor of safety with time for rainfall and rainfall-excavation

The results indicated that the factor of safety of the slope subjected to rainfall-excavation reduced below 1, one day prior to the slope subjected to rainfall. It is crucial that for any excavations more than the considered excavation height and width can worsen the stability of the slope subjected to heavy rainfall.

3.4 *Slope behavior under earthquake*

The 1940 El-Centro earthquake that struck Imperial Valley, California with a magnitude of 6.9 was used in this study. The slope was analyzed by defining the acceleration-time history of the 1940 El-Centro earthquake shown in Fig. 3. The variation of vertical and horizontal deformation with time for the individual occurrence of earthquake is shown in Figs 11 and 12, respectively. The maximum horizontal and vertical deformations at the toe of the slope were 674.1 mm and 294.7 mm, respectively.

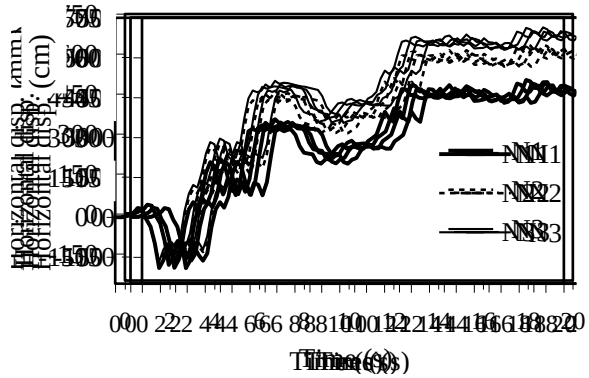

Fig. 11 Horizontal deformation-time history

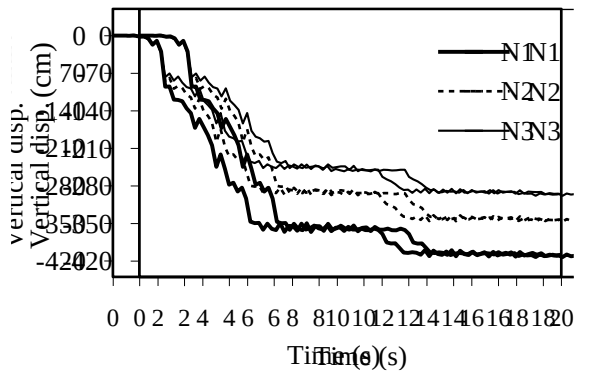

Fig. 12 Vertical deformation-time history

3.5 *Slope behavior under rainfall-earthquake*

In the rainfall-earthquake analysis, the earthquake was applied after the 7th day of heavy rainfall. Due to the limitations in the PLAXIS 2D, the factor of safety was not obtained for the rainfall-earthquake analysis. The variation of horizontal deformation for rainfall, earthquake, and rainfall-earthquake is plotted in Fig. 13. The results show that the slope was vulnerable when the rainfall and earthquake were applied simultaneously. The maximum hori-

zontal deformation of 725 mm (7.6 %) was observed at the toe of the slope when rainfall and earthquake were applied simultaneously. The horizontal movements due to rainfall, earthquake, and rainfall-earthquake were 55 mm, 674.1 mm and 725 mm respectively. Applying rainfall and earthquake simultaneously can worsen the stability of the slope comparing with the individual occurrence of rainfall.

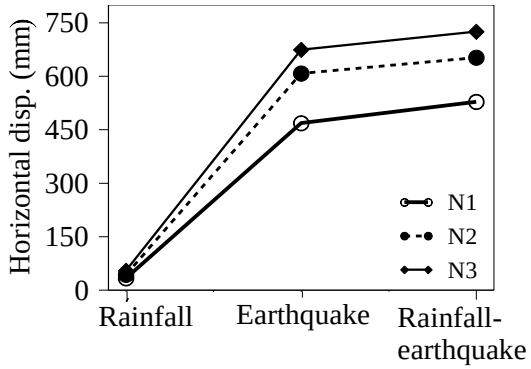

Fig. 13 Horizontal deformation for single hazard rainfall and earthquake, and combined hazard rainfall and earthquake

4 CONCLUSIONS

The effect of the individual occurrence of rainfall, excavation, and earthquake and simultaneous occurrence of rainfall-excavation and rainfall-earthquake on the deformation and stability of slope was analyzed by using Geotechnical-Hydrological finite element software PLAXIS 2D. From the results, it can be concluded that rainfall infiltration due to the considered rainfall hydrograph was responsible for triggering the observed landslide in Meeriyabedda. The factor of safety of 1.4 reduced to 0.98 (30 %) on the 7th day of rainfall and horizontal movement of 55 mm was observed at the toe of the slope during the failure. Further, for the excavation analysis, the factor of safety reduced with the excavation height and reached a minimum value of 0.85 (64.7 %) for an excavation height and width of 2 m and 3.5 m, respectively. The rainfall-excavation analysis was carried out by applying rainfall for the slope with an excavation height of 1.2 m and corresponding width of 2 m. The analysis showed that the factor of safety reduced to 0.9 at the end of the 6th day of rainfall.

The horizontal deformation increased to 725 mm from 674.1 mm (7.6 %) when rainfall and earthquake were applied simultaneously. The results indicate that the combination of multiple hazards can worsen the stability of the slopes and can provoke massive mass movements in the slopes.

REFERENCES

Athas, I. (2017). Heavy rain and floods in Sri Lanka leave 91 dead, government says, *CNN*, <https://www.cnn.com /2017/05/26/asia/sri-lanka-floods/index.html >.

BBC News. (2020). Silent search for Brazil mudslide survivors, <https://www.bbc.com/news/world-latin-america-461 6854 5 >.

Brahic, C. (2008). Five ways to trigger a natural disaster, *New Scientist*,<https://www.newscientist.com/article/dn-14425-five-ways-to-trigger-a-natural-disaster/>.

Bommer, J.J., and Rodrıguez, C.E. (2002). Earthquake-induced landslides in Central America, Engineering Geology, 63:189-220.

Cai, F., and Ugai, K. (2004). Numerical Analysis of Rainfall Effects on Slope Stability, International Journal of Geomechanics, 4(2):69-78.

Campbell, R.H. (1975). Soil slips, debris flow, and rainstorms in the Santa Monica Mountains and vicinity, southern California, U.S, Geological Survey of Professional Paper, 851:51.

Erginal, A.E., Türkeş, M., Ertek, T.A., Baba, A., and Bayrakdar, C. (2008). Geomorphological investigation of the excavation-induced Dündar landslide Bursa-Turkey, Geografiska Annaler (Series A: Physical Geography), 90(A2):109-123.

European Geosciences Union (2018). Landslides triggered by human activity on the rise, *ScienceDaily*, <www.sciencedaily.com/releases/2018/08/180823092049.htm >.

Evans, S. G., Guthrie, R. H., Roberts, N. J., and Bishop, N. F. (2007). The disastrous 17 February 2006 rockslide-debris avalanche on Leyte Island, Philippines: a catastrophic slope failure in tropical mountain terrain, Natural Hazards and Earth System Sciences, 7(1):89-101.

Jayamali , M., Karunasena, M., Wimalasinghe, L., Gunathilake , J., Wu, Y.H., and Bandara, W. (2017). GIS and Numerical Simulation Based Model For Prediction of Vulnerability on Mountain Tsunami at Meeriyabedda, Sri Lanka, Journal of Geological Society of Sri Lanka, 18(2):10.

Lakmali, A., Raveendra, H., and Priyankara, N. (2016). Rain Induced Landslides in Sri Lanka, Civil And Environmental Engineering Society, 2.

Lin, C., Liu, S., Lee, S., and Liu, C. (2006). Impacts of the Chi-Chi earthquake on subsequent rainfall-induced landslides in central Taiwan, Engineering Geology, 86(2-3):87-101.

Rahardjo, H., Ong, T., Rezaur, R., and Leong, E. (2007). Factors Controlling Instability of Homogeneous Soil Slopes under Rainfall, Journal of Geotechnical and Geoenvironmental Engineering, 133(12):1532-1543.

Rupke, J., Huisman, M., and Kruse, H. (2007). Stability of man-made slopes, Engineering Geology, 91(1):16-24.

Tang, C., Zhu, J., Qi, X., and Ding, J. (2011). Landslide induced by the Wenchuan earthquake and the subsequent strong rainfall event: A case study in the Beichuan area of China, Engineering Geology, 122(1-2):22-33.

van Genuchten, M. (1980). A Closed-form Equation for Predicting the Hydraulic Conductivity of Unsaturated Soils, Soil Science Society of America Journal, 44(5):892-898.

Vickneswaran, T., and Ravichandran, N. (2020). Multi Hazard Analysis of Earth Slopes Using Coupled Geotechnical-Hydrological Finite Element Model, Geo-Congress 2020.

Yang, S., Lohnes, R.A., and Kjartanson, B.H. (2002). Mechanical Properties of Shredded Tires, Geotechnical Testing Journal, GTJODJ, 25(1):44-52.

Youwai, S., and Bergado, D.T. (2003). Strength and deformation characteristics of shredded rubber tire-sand mixtures, Canadian Geotechnical Journal, 40(2):254–64.